

AD-A253 647

AGARD-CP-510

①

AGARD-CP-510

AGARD

ADVISORY GROUP FOR AEROSPACE RESEARCH & DEVELOPMENT

7 RUE ANCELLE 92200 NEUILLY SUR SEINE FRANCE

AGARD CONFERENCE PROCEEDINGS 510

DTIC
SELECTE
MAY 07 1992
S B D

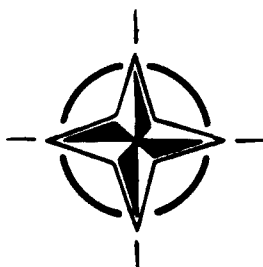
CFD Techniques for Propulsion Applications

(Les Techniques de l'Aérodynamique Numérique pour
les Applications aux Propulseurs)

DISTRIBUTION STATEMENT A

Approved for public release
Distribution Unlimited

*Papers presented at the Propulsion and Energetics Panel 77th Symposium
held in San Antonio, Texas, United States, 27th to 31st May 1991.*



NORTH ATLANTIC TREATY ORGANIZATION

Published February 1992

Distribution and Availability on Back Cover

AGARD

ADVISORY GROUP FOR AEROSPACE RESEARCH & DEVELOPMENT

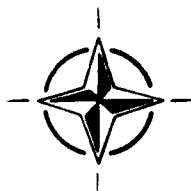
7 RUE ANCELLE 92200 NEUILLY SUR SEINE FRANCE

AGARD CONFERENCE PROCEEDINGS 510

CFD Techniques for Propulsion Applications

(Les Techniques de l'Aérodynamique Numérique pour
les Applications aux Propulseurs)

Papers presented at the Propulsion and Energetics Panel 77th Symposium
held in San Antonio, Texas, United States, 27th to 31st May 1991.



North Atlantic Treaty Organization
Organisation du Traité de l'Atlantique Nord



The Mission of AGARD

According to its Charter, the mission of AGARD is to bring together the leading personalities of the NATO nations in the fields of science and technology relating to aerospace for the following purposes:

- Recommending effective ways for the member nations to use their research and development capabilities for the common benefit of the NATO community;
- Providing scientific and technical advice and assistance to the Military Committee in the field of aerospace research and development (with particular regard to its military application);
- Continuously stimulating advances in the aerospace sciences relevant to strengthening the common defence posture;
- Improving the co-operation among member nations in aerospace research and development;
- Exchange of scientific and technical information;
- Providing assistance to member nations for the purpose of increasing their scientific and technical potential;
- Rendering scientific and technical assistance, as requested, to other NATO bodies and to member nations in connection with research and development problems in the aerospace field.

The highest authority within AGARD is the National Delegates Board consisting of officially appointed senior representatives from each member nation. The mission of AGARD is carried out through the Panels which are composed of experts appointed by the National Delegates, the Consultant and Exchange Programme and the Aerospace Applications Studies Programme. The results of AGARD work are reported to the member nations and the NATO Authorities through the AGARD series of publications of which this is one.

Participation in AGARD activities is by invitation only and is normally limited to citizens of the NATO nations.

The content of this publication has been reproduced directly from material supplied by AGARD or the authors.

Published February 1992

Copyright © AGARD 1992
All Rights Reserved

ISBN 92-835-0659-6



*Printed by Specialised Printing Services Limited
40 Chigwell Lane, Loughton, Essex IG10 3TZ*

Recent Publications of the Propulsion and Energetics Panel

CONFERENCE PROCEEDINGS (CP)

Viscous Effects in Turbomachines
AGARD CP 351, September 1983

Auxiliary Power Systems
AGARD CP 352, September 1983

✓ **Combustion Problems in Turbine Engines**
AGARD CP 353, January 1984

✓ **Hazard Studies for Solid Propellant Rocket Motors**
AGARD CP 367, September 1984

Engine Cyclic Durability by Analysis and Testing
AGARD CP 368, September 1984

✓ **Gears and Power Transmission Systems for Helicopters and Turboprops**
AGARD CP 369, January 1985

✓ **Heat Transfer and Cooling in Gas Turbines**
AGARD CP 390, September 1985

✓ **Smokeless Propellants**
AGARD CP 391, January 1986

✓ **Interior Ballistics of Guns**
AGARD CP 392, January 1986

✓ **Advanced Instrumentation for Aero Engine Components**
AGARD CP 399, November 1986

✓ **Engine Response to Distorted Inflow Conditions**
AGARD CP 400, March 1987

✓ **Transonic and Supersonic Phenomena in Turbomachines**
AGARD CP 401, March 1987

Advanced Technology for Aero Engine Components
AGARD CP 421, September 1987

✓ **Combustion and Fuels in Gas Turbine Engines**
AGARD CP 422, June 1988

Engine Condition Monitoring — Technology and Experience
AGARD CP 448, October 1988

Application of Advanced Material for Turbomachinery and Rocket Propulsion
AGARD CP 449, March 1989

✓ **Combustion Instabilities in Liquid-Fuelled Propulsion Systems**
AGARD CP 450, April 1989

Aircraft Fire Safety
AGARD CP 467, October 1989

✓ **Unsteady Aerodynamic Phenomena in Turbomachines**
AGARD CP 468, February 1990

✓ **Secondary Flows in Turbomachines**
AGARD CP 469, February 1990

Hypersonic Combined Cycle Propulsion
AGARD CP 479, December 1990

✓ **Low Temperature Environment Operations of Turboengines (Design and User's Problems)**
AGARD CP 480, May 1991

ADVISORY REPORTS (AR)

Through Flow Calculations in Axial Turbomachines *(Results of Working Group 12)*

AGARD AR 175, October 1981

Alternative Jet Engine Fuels *(Results of Working Group 13)*

AGARD AR 181, Vol.1 and Vol.2, July 1982

Suitable Averaging Techniques in Non-Uniform Internal Flows *(Results of Working Group 14)*

AGARD AR 182 (in English and French), June/August 1983

✓ **Producibility and Cost Studies of Aviation Kerosines** *(Results of Working Group 16)*

AGARD AR 227, June 1985

Performance of Rocket Motors with Metallized Propellants *(Results of Working Group 17)*

AGARD AR 230, September 1986

✓ **Recommended Practices for Measurement of Gas Path Pressures and Temperatures for Performance Assessment of Aircraft Turbine Engines and Components** *(Results of Working Group 19)*

AGARD AR 245, June 1990

The Uniform Engine Test Programme *(Results of Working Group 15)*

AGARD AR 248, February 1990

✓ **Test Cases for Computation of Internal Flows in Aero Engine Components** *(Results of Working Group 18)*

AGARD AR 275, July 1990

LECTURE SERIES (LS)

✓ **Ramjet and Ramrocket Propulsion Systems for Missiles**

AGARD LS 136, September 1984

✓ **3-D Computation Techniques Applied to Internal Flows in Propulsion Systems**

AGARD LS 140, June 1985

✓ **Engine Airframe Integration for Rotorcraft**

AGARD LS 148, June 1986

Design Methods Used in Solid Rocket Motors

AGARD LS 150, April 1987

AGARD LS 150 (Revised), April 1988

✓ **Blading Design for Axial Turbomachines**

AGARD LS 167, June 1989

Comparative Engine Performance Measurements

AGARD LS 169, May 1990

Combustion of Solid Propellants

AGARD LS 180, July 1991

AGARDOGRAPHS (AG)

Manual for Aeroelasticity in Turbomachines

AGARD AG 298/1, March 1987

AGARD AG 298/2, June 1988

✓ **Measurement Uncertainty within the Uniform Engine Test Programme**

AGARD AG 307, May 1989

✓ **Hazard Studies for Solid Propellant Rocket Motors**

AGARD AG 316, September 1990

REPORTS (R)

✓ **Application of Modified Loss and Deviation Correlations to Transonic Axial Compressors**

AGARD R 745, November 1987

✓ **Rotorcraft Drivetrain Life Safety and Reliability**

AGARD R 775, June 1990

Theme

"CFD Techniques for Propulsion Applications" was the title of this PEP Symposium. The subject of CFD Techniques was very popular in a large number of organisations. The Panel was aware from the beginning of the planning that the Terms of Reference must be directed very specifically to propulsion application.

A first investigation showed that too large a number of papers were available to be considered. The Panel thus restricted the scope to four main subjects for propulsion application: Full 3-D Code Validation, Full 3-D Numerical Technique, Multi-Dimensional Reacting Flow, and Unsteady Viscous Flow.

Special emphasis was given to the validation experiences using the recommendations of AGARD PEP Working Group 18 on Test Cases for the Computation of Internal Flows in Aero Engine Components. The FDP contributed on Computational Methods for Aerodynamic Design (Inverse) and Optimisation, and on Applications of Mesh Generation to Complex 3-D Configurations.

Thème

"Les techniques de l'aérodynamique numérique pour les applications aux propulseurs" était le titre de ce symposium organisé par le Panel PEP. Le sujet de l'aérodynamique numérique avait suscité beaucoup d'intérêt dans de nombreuses organisations. Dès le début du projet de symposium, le Panel a pris conscience que leur mandat devait être orienté très spécifiquement vers les applications aux propulseurs.

Un trop grand nombre de communications a été proposé suite au premier appel de participation. Par conséquent, le Panel a limité le domaine aux quatre grands thèmes suivants: la validation des codes de calcul réellement tridimensionnels, les techniques numériques réellement tridimensionnels, les écoulements à réaction multidimensionnels et les écoulements visqueux instationnaires.

L'accent était mis sur l'expérience acquise lors des travaux de validation effectués conformément aux recommandations du groupe de travail PEP No. 18 sur les cas d'essai pour le calcul des écoulements internes dans les moteurs d'avion. Le Panel FDP avait présenté des communications sur les méthodes de calcul pour la conception aérodynamique (méthodes inverses) et l'optimisation, ainsi que les applications de la génération des maillages aux configurations complexes tridimensionnelles.

Propulsion and Energetics Panel

Chairman: M. l'Ing. Princ. de l'Armement Ph. Ramette
Chef de Programme
Hyperspace
9, rue Salomon de Rothschild
92150 Suresnes
France

Deputy Chairman: Prof. Dr A. Üçer
Middle East Technical University
ODTU
Makina Müh. Bölümü
Ankara
Turkey

PROGRAMME COMMITTEE

Prof. Charles Hirsch (Chairman)
Vrije Universiteit Brussels
Dienst Stromingsmechanica
Pleinlaan 2
1050 Brussel, Belgium

Professor Luigi de Luca
Dipartimento di Energetica
Politecnico di Milano
Piazza Leonardo da Vinci 32
20133 Milano, Italy

Professor Dr-Ing. Leonhard Fottner
Universität der Bundeswehr München
Institut für Strahlantriebe
Werner-Heisenberg-Weg 39
W-8014 Neubiberg, Germany

Mr Keith R. Garwood
Rolls Royce Limited
WH 23, P.O. Box 3
Filton, Bristol B12 7QE,
United Kingdom

Dr Georges Meauze
Chef de Division
ONERA
BP 72
92322 Châtillon Cedex, France

Dr Clifford Moses
Director, Department of Energy
Conversion and Combustion Technology
Southwest Research Institute
P.O. Drawer 28510, 6220 Culebra Road
San Antonio, Texas 78284, United States

Professor Jose J. Salva Monfort
Escuela Técnica Superior de
Ingenieros Aeronauticos
Plaza Cardenal Cisneros 3
28040 Madrid, Spain

Professor George K. Serovy
Anson Marston Distinguished Prof.
Dept. of Mechanical Engineering
3038 ME/ESM
Iowa State University
Ames, Iowa 50011
United States

Prof. Dr A. Üçer
Middle East Technical University
ODTU
Makina Müh. Bölümü
Ankara, Turkey

HOST NATION COORDINATOR

Mr Randolph Grochowski

PANEL EXECUTIVE

Dr Ing. E. Riester

Mail from Europe and Canada:
AGARD—OTAN
Attn: PEP Executive
7, rue Ancelle
F-92200 Neuilly-sur-Seine
France

Mail from US:
AGARD—NATO
Attn: PEP Executive
Unit 21551
APO AE 09777

Tel: 33 (1) 47 38 57 85
Telex: 610176 (France)
Telefax: 33 (1) 47 38 57 99

The Propulsion and Energetics Panel wishes to express its thanks to the National Authorities from the United States of America for the invitation to hold this meeting in San Antonio, Texas, and for the facilities and personnel which made this meeting possible.

Contents

	Page
Recent Publications of PEP	iii
Theme/Thème	v
Propulsion and Energetics Panel	vi
	Reference
Technical Evaluation by L.A. Povinelli	T
 SESSION 1 – TURBOMACHINERY COMPUTATIONS AND VALIDATIONS 	
Computational Techniques for Solving the Navier-Stokes Equations* by D. Hänel	1
Paper 2 withdrawn	
✓ Application of S1BYL2 to the AGARD WG18 Compressor Test Cases by W.J. Calvert	3
✓ A Computational Study of Tip Leakage Flow and Losses in a Linear Turbine Cascade by J. Moore and J.G. Moore	4
Time-Marching Methods for Secondary Flow Analysis in Curved Ducts by M. Marini, A. Massardo and A. Satta	5
Turbine Internal Fluid Flow Analysis and Stokes' Hypothesis by R.E. Gray and W.A. Troha	6
Computation of 3D-Viscous Flow and Heat Transfer for the Application to Film Cooled Gas Turbine Blades by T. Vogel	7
Experimental Verification of a 3D Turbulent Flow Calculation in an Axial Turbine Cascade by J.G.E. Cleak, D.G. Gregory-Smith and N.T. Birch	8
A Mathematical Constraint Placed upon Inter-Blade Row Boundary Conditions Used in the Simulation of Multistage Turbomachinery Flows by J.J. Adamczyk	9
A Critical Evaluation of a Three Dimensional Navier-Stokes Method as a Tool to Calculate Transonic Flows inside a Low-Aspect-Ratio Compressor by C. Hah and S.L. Puterbaugh	10
On the Computation of Unsteady Turbomachinery Flows Part 1 – Euler Equations in Vibrating Cascades by G.A. Gerolymos	11
Paper 12 withdrawn	
Application of CFD in the Design of Gas Turbine Engine Components by A.K. Sehra, M.A. Abolfadl and M.G. Zedan	13

* Contribution by Fluid Dynamics Panel.

	Reference
Validation du Code "Canari" par le Calcul de l'Ecoulement Tridimensionnel Turbulent dans un Distributeur de Turbine par B. Escande et L. Cambier	14
Paper 15 withdrawn	
Computation and Visualization of Specific Flow Phenomena in Turbomachinery Application by J. Haarmeyer and B. Stubert	16
An Integrated CFD System for 3D Turbomachinery Applications by Ch. Hirsch, C. Lacor, C. Dener and D. Vucinic	17
Calcul par Elements Finis de l'Ecoulement 3D Turbulent dans une Pompe Centrifuge par J.F. Combes	18
✓ Predictions and Measurements of 3D Viscous Flow in a Transonic Turbine Nozzle Guide Vane Row by G.C. Horton, S.P. Harasgama and K.S. Chana	19
Paper 20 withdrawn	
Viscous Three-Dimensional Calculations of Transonic Fan Performance by R.V. Chima	21
Navier-Stokes Analysis of Turbine Blade Heat Transfer and Performance by D.J. Dorney and R.L. Davis	22
Calculs 3D Stationnaire et Instationnaire dans un Etage de Turbine Transsonique par A. Le Meur	23
Unsteady Euler Calculations in 3D Internal Aerodynamics by M. Hadzidakis, F. Karagiannis, P. Chaviaropoulos and K.D. Papailiou	24
The Application of a Navier-Stokes CFD Method to Civil Engine Intake Flows by N.T. Birch and E.H. Kitchen	25
SESSION II – FLOW IN DUCTS, INTAKES AND NOZZLES	
CFD Contributions during Hypersonic Airplane Intake Design by N.C. Bissinger and A. Eberle	26
Three Dimensional Solution of Internal Flows using a Cell Vertex Finite Volume Method by E. Oktay, I.S. Akmandor and A.S. Üçer	27
Numerical Representation of Heat Transfer into Turbine Blade Cooling Ducts by C. Taylor, J.Y. Xia, J.O. Medwell and W.D. Morris	28
Presentation d'un Code de Calcul d'Ecoulements Compressibles 3D dans des Canaux et des Cavités de Forme Complexe par D. Dutoya, M. Errera, P.J. Michard et A. Ristori	29
Validation of Non-Orthogonal Three Dimensional Laminar Flow Predictions by P.J. Coelho and J.C.F. Pereira	30
Finite Element Solution of Viscous Compressible Flows in Gas Turbine Ducts and Diffusers by W.G. Habashi, M.F. Peeters, M.P. Robichaud, V-N. Nguyen and M.V. Bhat	31
Aerothermodynamics of Nozzle Flows for Advanced Hypersonic Propulsion Systems by C. Weiland, G. Hartmann and S. Menne	32
Application of Finite Element Methods to Hypersonic Nozzle Flow Computations by W. Koschel, W. Rick and S. Bikker	33

	Reference
Computational Modelling of Turbulent Flow in S-Bends by N.I. Abou Haidar, H. Iacovides and B.E. Launder	34
Three Dimensional Flow in Sharp Bends by K. Fotea, P. Prinos and A. Goulas	35
3-D Navier-Stokes Flow and Temperature Field Computation for a Forced Mixer Nozzle by K. Katheder	36

SESSION III – REACTING FLOWS

Flow Computation in Combustion Chambers using Zonal Nonstaggered Grids by M. Rachner	37
Modelling the Vaporiser and Primary Zone Flows for a Modern Gas Turbine Combustion Chamber by N.R. Bond, J.M. Le Vallois and K.R. Menzies	38
Application of Monte Carlo Simulation for Three-Dimensional Flows by M. Scheurlen, B. Noll and S. Wittig	39
The Coherent Flamelet Model for Propulsion Applications by D. Veynante et al.	40
Paper 41 withdrawn	
Nonequilibrium 3D Flows of Air through Inlets by R. Marsilio and M. Pandolfi	42
Evaluation of the Effects of Finite Rate Chemistry on Nozzle Performance by M. Onofri	43
Numerical Analysis of Converging-Diverging Nozzle Flows in Chemical Non-Equilibrium by R. Walther	44
Calculs Tridimensionnels d'Ecoulements Réactifs dans les Chambres de Combustion Aéronautiques Effectués à l'Aide de Deux Modèles de Combustion par F. Pit, H. Tichtinsky, P. Gilbank et F. Dupoirieux	45



Accession For	
NTIS GRA&I	<input checked="" type="checkbox"/>
DTIC TAB	<input type="checkbox"/>
Unannounced	<input type="checkbox"/>
Justification	
By _____	
Distribution/	
Availability Codes	
Dist	Avail and/or Special
A-1	

TECHNICAL EVALUATION

Louis A. Povinelli
National Aeronautics and Space Administration
Lewis Research Center
21000 Brookpark Road
Cleveland, Ohio 44135 U.S.A.

INTRODUCTION

Thank you, Mr. Chairman. Let me begin these remarks by saying how much I appreciated the opportunity to present the opening remarks and to serve as the technical evaluator for the 77th Symposium of the Propulsion and Energetics Panel on CFD Techniques for Propulsion Applications. I would like to compliment the Program Committee and Panel Members for an outstanding job in the planning and implementation of this meeting. The presenters and the Session Chairmen are also to be complimented for their fine work. This Symposium had a schedule of some 41 technical presentations covering the entire spectrum of propulsion system components. The theme of this meeting was fourfold: to consider (1) Full Three-Dimensional Code Validation, (2) Full Three-Dimensional Numerical Techniques, (3) Multi-Dimensional Reacting Flow, and (4) Unsteady Viscous Flow. All of the topics have direct relevance to the propulsion community which is attempting to develop or to use CFD in the design and analysis of components. In addition, there is now available a compendium of experimental test cases and a corresponding data base published by Working Group 18 of PEP on "Test Cases for the Computation of Internal Flows in Aero Engine Components" (AGARD Advisory Report 275). Those test cases provide an excellent source against which to compare computational results. In addition, it will also provide a focus for code-to-code comparisons. Our goal, therefore, in this Symposium was to evaluate the capability of various three-dimensional Navier-Stokes solvers from the viewpoint of "code validation;" to assess the special features of numerical techniques; to evaluate multi-dimensional reacting flow codes, and to understand new contributions to

unsteady viscous flows. In order to meet the goals, therefore, it is necessary to identify the level of agreement of physical models and numerical solutions with the test data, to identify regions of agreement and disagreement, identify significant missing features, and to assess the sources of error. In addition, of course, is the identification of significant new developments, new capability and new modeling and, finally, the determination of future directions for our research activities. Recommendations for future research will establish the possible impact on future military planning. Before finishing my introductory remarks, it is useful to observe that a single theme Symposium, e.g., Code Validation, would provide a clearer forum for evaluation. That is, with a single theme such as Validation, criteria could be established by which all papers are evaluated. Each paper, then, would be evaluated against the same criteria and judgement made as to how well the codes met the criteria.

As a general comment, the technical level of the meeting was judged as good. It should be said that few, if any of the papers, included all the necessary information for rigorous validation although modeling effects were studied. A large number of papers dealt only with demonstrations of the ability to perform calculations, and a small number provided new solution techniques. Very little information was presented on unsteady viscous solvers and a few papers were primarily examples of propulsion applications.

GENERAL INTRODUCTORY LECTURE

An excellent review was presented by Prof. Hänel on methods for solving the conservation laws using the Navier-Stokes equations. The essential features of the hierarchy of the conservation laws from the Boltzman equation to boundary layer formulations were described. Recognition of the need to resolve relevant length and time scales whose values differ by orders

of magnitude were discussed. It was concluded that nonmodel d small scalings result in undesirable effects on the solution, a point to which I will speak later. Inviscid region scaling was differentiated from viscous region scalings, such as in boundary layers and wakes. The Euler solver is seen as the basic element of the Navier-Stokes solver. And in fact, it is the approximation of the Euler solution in viscous solutions that cause dissipative and dispersive truncation errors in Navier-Stokes solutions. Although the information presented was not new or even specific to turbomachinery/propulsion systems, it did set the stage for the subsequent presentations. That is, the features associated with accuracy, convergence, acceleration, scaling, boundary conditions and gridding were all discussed. In addition, comments regarding the need for Direct Numerical Simulation on massively parallel systems was seen as the trend for the future. This reviewer agrees that DNS holds great promise for the future of propulsion CFD.

EVALUATION

Theme I. Code Validation

It is important to note that CFD codes may be useful at all stages of their development prior to what is considered "complete validation." Research code progress may be thought of passing through various stages beginning with code development and demonstrated capability for simple laminar and/or turbulent flows with consistent numerical stable behavior. The next phase involves application to "realistic" geometries and an assessment of realistic physical behavior. Next comes comparisons with measured profile data and/or total pressure losses. Finally, one arrives at the "validation threshold." Up to this point, the codes may have been used to both assess current designs as well as evaluate new configurations. At this point, a more thorough consideration of many items must now be considered, and include:

- conservation of mass, momentum, energy and species
- numerical accuracy
- numerical stability
- convergence behavior
- grid sensitivity/generation
- numerical dissipation
- turbulence modeling
- transition modeling
- inflow, outflow and wall boundary conditions
- rigorous comparison with detailed data bases

In addition, issues of computational speed and storage are all present. In very few of the papers presented here, were all of these issues addressed. It is recognized that the authors were not asked to address validation; and so simply presenting a three-dimensional numerical scheme satisfied the Symposium's theme. However a high level of user confidence will not be established for any numerical scheme without showing detailed comparisons with data. Three-dimensional variations of flow properties need to be compared with computations. Simple performance comparisons are only the first step.

The critical physics to be modeled for code validation have been discussed previously by this author at the AGARD Fluid Dynamics Panel at Lisbon, 1988. The physics needed to be modeled are shown in the following charts. (Issues related to clearance flow and heat transfer are included as subcategories.) A number of papers in this Symposium dealt with the issues of modeling some of these key physics. For example, the work of Moore, Gregory-Smith and Dorney addressed tip clearance flows, turbulence modeling and transition effects in cascade

flows. This type of activity relates to Chart II directly, and in my opinion, is the proper direction for code validation.

TABLE I. - INLET, DUCT AND NOZZLE CFD VALIDATION

[From Povinelli, L.A., "CFD Validation Experiments for Internal Flows,"
AGARD REPT , 1988.]

Code and critical models requiring validation		Experimental program elements
CFD codes by class	Critical flow physics models	
Three-dimensional subsonic PNS	Turbulence Separation Vortex generation	Transition ducts Offset ducts Vortex generators
Three-dimensional subsonic/ hypersonic PNS	Turbulence Separation Real gas effects Boundary layer bleed Boundary layer transition	Shock-boundary layer interaction Boundary-layer breed High temperature flow
Three-dimensional Navier-Stokes	Turbulence Real gas effects Boundary layer transition	Above experiments Separation flow physics Enhanced jet mixing

TABLE II. - TURBOMACHINERY CFD VALIDATION

[From Povinelli (ibid).]

Code and Critical models requiring validation		Experimental program elements
CFD code by class	Flow physics models	
Steady Euler	End-wall boundary layer Blade surface boundary layer Shock boundary layer interaction	High-speed turbomachinery Low-speed turbomachinery Two-dimensional cascade Shock boundary layer interaction
Steady Navier-Stokes	Turbulence Boundary layer transition	Two-dimensional cascade Low-speed centrifugal Low-speed boundary layer Three-dimensional heat transfer Low-speed axial turbomachinery
Passage-average Navier-Stokes	Closure models	Low-speed multistage High-speed multistage
Unsteady Navier-Stokes (rotor/stator)	Turbulence Boundary layer transition	Low-speed turbomachinery High-speed turbomachinery

TABLE III. - CHEMICALLY REACTING FLOWS CFD VALIDATION

[From Povinelli (ibid).]

Code and critical models requiring validation		Experimental program element
CFD codes by class	Critical flow physics models	
Steady Navier-Stokes	Fuel spray Turbulence Turbulence/combustion Chemical kinetics interaction Radiation/soot formation	Multiphase flow research: phase interaction
Time accurate Navier-Stokes	Turbulence Turbulence/combustion interaction Chemical kinetics	Planar reacting shear layer: Turbulence/combustion interaction Soot/radiation characteristics
Direct numerical simulation	Chemical kinetics	Shock tube chemical kinetics

The work on the validation of the CANARI code by Escande highlighted the necessary numerical considerations required. Detailed information was presented on numerous features of the code and the methodology. Turbulence modeling, differencing method, boundary conditions, accuracy, solution scheme, dissipation, mesh generation and packing, upstream and downstream conditions and cpu time. Transonic computations were shown but as yet no data was compared with the code. Certainly the Working Group test cases should be desirable for comparison with this code.

A good example of the application of Rai's thin-layer Navier-Stokes code (Rotor 3) was given by Dorney and Davis. Careful definition of the inlet and boundary conditions was made for the case of Langston's cascade. A grid sensitivity study was conducted using total pressure and flow angle as criteria. Transition modeling (30 percent chord) allowed fitting of the Stanton number distribution as a function of chord on the suction mid span. Failure of the transition model on the pressure side was interpreted as a failure of turbulence model. Flow angles were generally overpredicted. This activity also focused on improving the modeling required for transition and turbulence.

An intake (inlet) application was presented by Norton using a Navier-Stokes simulation. Various operating regimes were discussed with a focus on high incidence and on spillage conditions. A Jameson formulation was used (finite volume) with a mixing length turbulence model as well as a potential flow method. At low Mach numbers, the potential flow and Navier-Stokes formulations with 20 percent spillage were equivalent. At higher Mach numbers, the potential method does not capture the shock. The Navier-Stokes solution captures incidence physics very well, i.e., shock-boundary layer interaction, spillage and the embedded supersonic region. The ability to capture flow details is related to the transition and turbulence modeling.

Shock-boundary layer interaction plays a major role on pressure recovery. The state of the boundary layer makes prediction difficult. Description of the transition point is critical and testing implies proper boundary layer tripping. The critical issues here are transition and turbulence modeling. Distortions related to shock losses must also be resolved to compute more accurately.

An application of an Euler cell centered finite volume solver by Bissinger with a Riemann solver at the face was applied to the flow field of a hypersonic inlet. Shock capturing was achieved by flux vector blending. Mass flow was conserved to within 0.2 percent for a sidewall compression inlet. The method was also applied to a multi-ramp inlet at M5.25. Fine grids were needed to clarify the shocks and expansions. At M5.65 the external lip shock slip line lies extremely close to the cowl surface. In addition, an expansion from ramp causes throat separation and subsonic flow - hence unstart or unstable operation is possible. This paper illustrated how CFD can be used to examine physics in great detail in order to arrive at an acceptable inlet design. Mass removal was also modeled. Sidewall interactions showed strong three-dimensional effects. It was concluded that Euler computations can be useful for design. Comparison of the computations with data is needed.

Turbulence modeling and boundary conditions were investigated in detail in a finite element model for internal turbine cooling passages by Taylor. This is an important area of research in order to eliminate unneeded coolant in specific regions. The level of detail showed in the internal ribbed passages is remarkable; both for velocity and heat transfer within the cavities. Comparison with data showed good results with a one equation turbulence model. Coriolis effects were shown to be important for smooth pipes and ribs were dominant during rotation.

Analyses for this application may be more advanced than the experimental data. However, a number of questions remain regarding the validity of the computed results.

An algorithm for the conservative form of the Navier-Stokes equations on a non-orthogonal and nonstaggered grid was applied to flow in ducts by Coelho. Convective terms are discretized using a hybrid central differencing/upwind scheme. Reasonable comparisons with incompressible subsonic duct flow in an "S" bend were achieved, however the boundary conditions upstream or downstream need further evaluation.

Iacovides use of a second moment turbulence closure yielded more accurate results for duct flows. Low Reynolds number wall modeling was needed as well as refined near wall turbulence modeling. Extra stabilization was required for Reynolds stress models. A zonal modeling approach was used assuming a fully turbulent outer region and a low Reynolds near wall region (3 to 5 percent R). Algebraic stress models were used in the turbulent region. Near wall modeling used three different formulations based on:

- (1) One equation k transport model
- (2) Two equation low Reynolds number formulation and a
- (3) Low Reynolds number version of ASM (anisotropic model). Based on Gibson-Launder.

Comparison of the computed results with LDV measurements emphasized the flow sensitivity to near wall turbulence, and the criticality of near wall modeling. The best comparison was obtained when a second moment stress model was employed.

Fotea also investigated the turbulence modeling in sharp bends. It was concluded from Navier-Stokes, $k-\epsilon$ computations that modeling improvements are needed, especially for regions of strong recirculation.

Theme II. Full Three-Dimensional Numerical Techniques

We shall now turn to the second theme of the Symposium which is entitled Full Three-Dimensional Numerical Techniques. The theme is somewhat general and as such could include viscous, inviscid, compressible/incompressible, code development/application, steady/unsteady and many other categories. In reality, therefore, this category only requires us to consider three dimensionality. We would look, therefore, at the contributions in this category and the value of the individual presentations relative to new methods, improved difference techniques, applicability and comparison with data.

The paper by Calvert was devoted to a time marching scheme based on Denton's Euler formulation. Integral calculations were used for boundary layers and wakes. An inviscid-viscous matching procedure allows for a valid solution even though shock-boundary layer interaction causes separation. Based on computations of four compressor cascades and three high speed compressors, very good agreement was achieved with data. Problems arise, however, in attempting to compute near the end walls where strong three-dimensional effects occur. The S1-S2 method cannot account for spanwise mixing. More attention is needed for corrections due to radius of curvature and rotational affects. Stream tube thickness distribution appears to be improved but needs to be more carefully described. Loss computations associated with tip clearance flows is modeled to first order by viscous Navier-Stokes. More details of the physics of the clearance flow is being elucidated and modeled. Carefully controlled experiments have led to more refined analyses which has improved the loss prediction. The vortex location is located more correctly than previously obtained; however, the vortex strength is not yet properly computed. Improved grid in the clearance area as well as turbulence model fidelity need further investigation. It appears that turbulence modeling improvements coupled with improved

transition modeling is required; and in fact, the transition effect may be more important than higher order turbulence modeling.

Questions regarding the validity of the Stokes theorem used in the Navier-Stokes equations were raised by Gray when the solution for a cylindrical and for a spherical expansion led to inconsistent results. This result needs to be investigated further to establish the source of the discrepancy or to establish the validity of the stress-strain relationship used in Navier-Stokes solutions. Addition of heat transfer capability to the Dawes Navier-Stokes solver by Vogel was described for turbine computations, including ejection into the freestream. The internal solution was performed with a Laplacian formulation and coupled to the external Navier-Stokes solver. The capability of the method was demonstrated for a turbine stator. No comparisons with data were available, however the demonstrated computations look promising. Comparisons with data are now required for assessment and validation.

Extension of blade row codes to multiple blade row codes was shown by Adamczyk to require certain mathematical constraints related to the conservation of vorticity and the momentum fluxes. The errors associated in the time averaged vorticity field was evaluated relative to requiring continuity of momentum only. Experimental values of the radial gradients of the vorticity terms were used to quantify the effect.

The paper by Hah illustrated the capability available with three-dimensional Reynolds average Navier-Stokes simulations. This code also includes tip clearance flow; and was applied to an Air Force fan configuration. A parametric study identified the most efficient design, which was then analyzed in some detail. Shock structure and shock-boundary interaction was

illustrated with the fan blades. Performance parameters were compared with the computations with good agreement.

The presentation from LEMFI by Gerolymos was a fine example of the unsteady Euler analysis for the study of aeroelasticity. Nonreflecting boundary conditions were used with a moving grid tied to the blade surfaces to provide flutter results. Improvements are required to obtain better agreement with Mach number and bending vibration. Incorporation of viscous effects may provide greater fidelity.

The work of Haarmeyer provides a basis for the visualization work related to streamline and vortex line tracking. Animated particle tracing gives good insight into the stream structure. The integrated CFD system presented by Hirsch provides an attractive package of mesh generator, flow solver, post processing and flow visualization. Such an integrated system is very desirable, provided it does not carry with it excessive complexity for any given problem.

The work by Combes addressed centrifugal pumps using a Reynolds averaged Navier-Stokes solver with $k-\epsilon$ turbulence modeling. The results highlighted some of the difficulties with downstream diffuser conditions and possible tip or hub separation. Improvement over the inviscid computation was significant. Horton's application of Dawes' code to contoured end wall performance and elucidation of flow physics yielded inconclusive results. In addition, reference to a body of work in this field was not recognized.

A good example of current three-dimensional viscous capability is illustrated by the work of Chima. His thin-layer Navier-Stokes solver was applied against one of the AGARD test cases (rotor 67, NASA Lewis Research Center). The tip relative Mach number was 1.38.

Comparison of computations with data showed good agreement as well as exhibiting proper physics relative to vortex formation, flow turning etc. Only tip clearance was unmodeled in the simulation which causes near wall performance to be overly predicted. Post-processing of data and illustration of particle tracings were excellent and sets a standard for CFD researchers. One possible improvement may be the incorporation of an improved turbulence model rather than the Baldwin-Lomax eddy viscosity model. Chima's paper illustrates the continuing validation process as well as the present status of code capability for three-dimensional simulations.

The paper by Marini is an interesting comparison of an explicit finite volume Lax-Wendroff scheme with an implicit Beam-Warming ADI scheme, with a good explanation of secondary flow physics in curved ducts. Further detailed comparisons with data such as in Working Group 18 test cases would be useful.

A comprehensive Lax-Wendroff time advancing scheme with a cell vortex approach has been described comprehensively by Oktay. Many details were provided as to the time advancing and the distribution process to the neighboring nodal points. Additional information is required requiring convergence history and criteria.

A finite element method was described by Weiland and applied to hypersonic nozzles. The method was either an Euler or Navier-Stokes analysis, and employed an explicit Taylor-Galerkin FEM algorithm. Adaptive three-dimensional mesh enrichment was an interesting feature. Comparison of computations was made with nozzle thrust vector angle and nozzle thrust coefficient. Viscous nozzle flow including turbulence modeling, an extension to three-dimensional plug configurations and chemical reactions needed to be added to correctly simulate the flow field.

The aerothermodynamics of nozzle flows for hypersonic systems were investigated by Koschel using two-dimensional boundary layer and Euler methods. Real gas effects were considered. Applications investigated the effect of boundary layer, specific heat ratio, equilibrium gas, injected gas (into nozzle) and propellants in a CD nozzle. A free expansion nozzle was also computed for a gamma value of 1.27 and equilibrium real gas. A free expansion plug was found to exhibit complex flow structure. Navier-Stokes solutions are needed for mixing with special emphasis on turbulence modeling.

The Lycoming paper by Sehra demonstrated current CFD capability in U.S. industry for propulsion components. The MTU paper showed the use of the three-dimensional Reynolds averaged Navier-Stokes SIMPLEST algorithm for mixer lobe application. Only performance values were compared with data; no detailed validation studies were presented.

Theme IV - Unsteady Viscous Solvers

The fourth theme of the Symposium was Unsteady Viscous Solvers. Papers considered to fall into this category were relatively few by comparison with the other themes.

Mathilda is used for the analysis of cooling flows in passages of turbines. It is three-dimensional and unsteady and uses a two equation turbulence model. Cavity flow and internal blade passages were analyzed. Both $k-\epsilon$ and $k-L$ models were used. Numerous issues related to the numerical scheme were presented. Comparison with data is required to assess the turbulence modeling and the validity of the code.

The paper by LeMeur of ONERA presented a approach for computing stage behavior. Maintaining continuity between sub-domains allowed reduction of blade counts. The time change in the flow angle upstream of the rotor, mass flow fluctuations, etc. were calculated. Unsteady blade loadings were also computed. Averaging techniques were used to compare unsteady-averaged values with steady-state results. Some interesting results were obtained which showed that the averaged unsteady results yield solutions quite close to steady-state values.

The paper from NTU (Athens) utilized a Helmholtz decomposition of the velocity field in the development of an unsteady three-dimensional Euler analysis. An ADI technique was used with space varying (linear) and time varying (periodic) boundary conditions. Vorticity conditions were also specified and an exact description of the energy and entropy fields employed. A simple cascade flow was illustrated.

CONCLUDING REMARKS

I would like to finish by making a few points:

(1) The advent of a large number or an "army" of propulsion scientists familiar with computational techniques and numerical simulations is very encouraging and rewarding to those of us who have advocated "Propulsion CFD" for some time. It is believed that the use of CFD for propulsion applications brings its own unique requirements as distinct from the external aerodynamics community. Therefore, it is encouraged that CFD should become an integral part of all presentations and discussions related to propulsion system design and analyses. Propulsion

CFD is simply one more tool available to engineers as is the experimental test cell. Hence we now may have numerical as well as experimental test cells.

(2) Insufficient CFD validation activity has occurred. Now that Work Group 18 test cases are available, a focus validation activity should begin. If three-dimensional numerical simulations for propulsion are to be accepted for design or analysis purposes, then comparisons should be made with the prescribed test cases. These comparisons will provide the initial validation as well as providing code-to-code comparisons. If such a focused validation is undertaken it would also provide a single theme for a future meeting of the PEP Panel, i.e., "CFD Validation for Propulsion Systems."

Validation activity will provide high levels of confidence if all levels of experimental cases are addressed; i.e., ducts, cascades, rotating turbomachinery, combustors and nozzles.

(3) A word of caution is required regarding experimental data. Obviously some data are better than others. Some of the data sets obtained at various labs have high accuracy. It is gratifying for me, since I have been directly involved in that activity for a number of years. However, we must be very careful regarding the validity of experimental data. Most of the data sets are 5 to 10 years old. As we do more comparisons we will be better able to sort out experimental versus computational errors. Also we must move on from "simple" flows to more realistic flows. The simpler cases should only be first steps, not ultimate goals.

(4) It is noteworthy to mention that physics must not be sacrificed for mathematics. For those performing numerical simulations, a good understanding of the flow is necessary.

Collaboration with an experimentalist is a necessity. Education today at the universities is more specialized and the tendency is to neglect aspects of research other than your own.

(5) I mentioned during the Opening Ceremony that CFD methods have undergone significant development, but that a weak part of our effort is related to modeling. Until Direct Numerical Simulation of the Navier-Stokes equations for high Reynolds application becomes available, we shall need to rely on modeling the relevant time and length scales in the engine components. In the long term, DNS and massively parallel systems may be the answer. However for the near term we must face up to the difficulty of turbulence, transition and chemical modeling. Special closure modeling may be required for turbomachinery where unsteady effects may predominate, rather than turbulence per se. Efforts must be expended on compressibility effects, higher order closure, PDF modeling, RNG, DIA and similar activities. Unless we improve these models we shall remain on a plateau in CFD applications. Incorporation of real gas effects, for both chemical and thermodynamic equilibrium and nonequilibrium are needed for the higher Mach numbers.

(6) Three-dimensional Navier-Stokes are essential for propulsion system simulations. Physical flow phenomena inlet, turbomachinery or combustor and nozzle is highly three-dimensional and dominated by turbulent viscous behavior. Euler analysis is helpful in the initial design, but viscous flow details are significantly different. Those differences are crucial in many aspects. In addition, fine scale grids are needed since coarse computations will not normally suffice.

(7) A large amount of activity in propulsion CFD is underway for all components of the propulsion system. These simulations include a fairly good level of detail. Some components are

better modeled than others. Reacting flows pose difficulty. Some progress is underway in modeling injection and burning, but it must be considered the least advanced. PDF modeling promises some advances in this respect.

(8) A large number of algorithms are now available - finite element, finite difference and finite volume. We need now to focus on those features which we recognize to yield good results and not write a new solver with every new researcher. We need to move from the code developer as the only one who understands the code to a body of knowledgeable users, trained in CFD. Their talents will be utilized as they apply and improve the methods.

(9) In regard to whether progress has been made in propulsion CFD, it is clear that the answer is yes for algorithms and codes; for turbulence modeling, progress is limited, for transition modeling very little progress has occurred and for turbulent chemistry some progress has been made with probability density function models. Our physical understanding of the flow in inlets, turbomachinery, ducts and nozzles is very good, and our physical and chemical understanding of combustion is improving. Clearly, the need for better closure modeling is critical for further advances in numerical simulation of propulsion systems.

(10) Finally, in regard to our future direction, I believe the coordination of our activities is important. The PEP panel should consider a focus on selected test cases from Work Group 18 and verify or validate the best cases. Shortcomings as well as success should then be discussed. Following a successful outcome then we should begin to move toward multi-component simulations. The PEP Panel should support and encourage modeling activities for use in three-dimensional viscous simulations and the development of three-dimensional unsteady Navier-Stokes analyses. In addition the Panel should sponsor a Symposium on the topic of "Propulsion CFD Validation."



COMPUTATIONAL TECHNIQUES FOR SOLVING THE NAVIER-STOKES EQUATIONS

D.Hänel

Aerodynamisches Institut, RWTH Aachen

Templergraben 55

D 51 Aachen, Germany

92-16068



Abstract

The paper is concerned with computational techniques for the solution of the Navier-Stokes equations for compressible flows. In the first section the governing equation and their most important approximations are described. A review of computational techniques encloses grid arrangement, conservative discretization, numerical flux formulations, and different methods of solution inclusive multigrid methods. In a last section the influence of the numerical discretization on the accuracy of Navier-Stokes solutions is briefly discussed.

Contents

1	Introduction	1
2	Governing equations	2
2.1	Conservation laws	2
2.1.1	Full Navier-Stokes Equations	2
2.1.2	Thin Layer Approximation	2
2.1.3	Parabolized Navier-Stokes Equations	3
2.1.4	Reduced Navier-Stokes Equations	3
2.1.5	Euler equations	3
2.2	Thermal and caloric relations	4
2.3	Transport Quantities	4
2.4	Boundary conditions	5
3	Computational techniques	5
3.1	Grid generation	6
3.2	Conservative discretization	6
3.2.1	Arrangements of control volumes	7
3.2.2	Conservative approaches	7
3.3	Numerical flux formulation	7
3.3.1	Viscous fluxes	8
3.3.2	Formulation of the inviscid fluxes	8
3.4	Methods of Solution	10
3.4.1	Implicit schemes	11
3.4.2	Explicit Methods	12
3.4.3	Methods on unstructured grids	13
3.4.4	Pressure-correction methods	13
3.4.5	Multigrid methods	14
4	On the accuracy of Navier-Stokes solutions	15
4.1	Numerical dissipation in Euler solutions	16
4.2	Numerical influence in viscous solutions	17

- 1 Introduction

Large progress was made in computational fluid dynamics in the past years, in particular on the field of the Navier-Stokes equations. This progress is based on the one hand on the significantly increased computer capacity, on the other hand on the essentially improved solution methods. The improvement of the methods for the Navier-Stokes equations is the result of experiences with numerical methods for other equations, like the potential equation and Euler equations, over many years. Several years ago potential and streamfunction methods have been the widely used tools for design. Then the Euler solvers became more and more refined, and they are now the next generation of prediction methods. Compared with the potential solvers the Euler solvers are computationally much more expensive, however this drawback is compensated by the greater physical relevance of the results.

The next step will be the use of numerical solutions of the Navier-Stokes equations for prediction. However, at the present state of art a substantial amount of physical, numerical and hardware development is still necessary before the Navier-Stokes solvers become an efficient, accurate, and reliable engineering tool.

Physically an important obstacle for predicting technical flows is the insufficient description of turbulence. This problem requires still much efforts on the experimental and theoretical field in the future.

Numerically essential problems arise from the structure of the Navier-Stokes equations, which involve physical scaling lengths of very different size. The resolution of these scalings requires much finer computational meshes than needed for a corresponding inviscid problem, and with that much more computer storage and time. Therefore computer capacity, the efficiency of numerical methods and the numerical accuracy must be improved.

To increase the efficiency, close cooperation with the applied mathematics is necessary to utilize all the mathematical and potential. A typical example for that is the development of the multigrid methods and their application to hyperbolic and parabolic problems.

The other aim in the development Navier-Stokes solvers has to be the improvement of the accuracy of viscous solutions, in particular for high Reynolds numbers. In this case there is a very sensible balance between inertia and viscous terms. Physically the inertia terms have no dissipative contribution, but their numerical approximation generates a remarkable amount of numerical dissipation superposing to the physical, viscous dissipation. Thus

the accuracy of the viscous solution can be impaired. This effect is amplified in strongly unsteady solutions, and in steady solutions if the spatial resolution is insufficient (which is the usual case in three dimensions). The difficulties, arising in the numerical solution of the Navier-Stokes equations, depend strongly on physical flow problems. Propulsion technique covers a wide field of internal flow problems, ranging from subsonic duct flow to hypersonic inlet flow, in the most cases at high Reynolds numbers. Some specific problems can be solved efficiently by using approximations, like the Parabolized or Reduced Navier-Stokes equations. Such approximations are very well suited for design purposes, but fail if exceeding the limits of the approximations. The most general prediction, but also the most expensive one, is given by the numerical solutions of Navier-Stokes equations. The computational techniques for solving the Navier-Stokes equations for compressible flows is the main subject of this paper. The computational technique consists of different elements, which together define the Navier-Stokes solver. Elements of a solver are the grid arrangement and conservative discretization, the numerical flux formulation, in particular for the Euler terms, and the method of solving the resulting algebraic system. For each of these elements a brief description with references will be given. A section is added in which the numerical influence on viscous, steady and unsteady solution is discussed and demonstrated by several examples.

2 Governing equations

2.1 Conservation laws

In the present paper continuum flow at thermodynamical and chemical equilibrium is considered. The flow is described by the conservation equations for mass, momentum, and energy. These conservation quantities are expressed in a vector Q with the components of specific quantities per volume, which are the specific mass (density ρ), the momentum $\rho\vec{v}$, and the energy ρE . The conservation laws are formulated as the rate of change of the conservative variables Q in a control volume τ , which is balanced by the effect of the generalized fluxes \vec{H} acting normally on the surface A . The conservation laws in the integral form read:

$$\int_{\tau} Q_t d\tau + \oint_A \vec{H} \cdot \vec{n} dA = 0 \quad (1)$$

A differential form (divergence form) can be obtained with the integral theorem of Gauss:

$$Q_t + \nabla \cdot \vec{H} = 0 \quad (2)$$

Herein Q is the vector of the conservative variables

$$Q = (\rho, \rho\vec{v}, \rho E)^T$$

The generalized flux \vec{H} can be split in a vector for inviscid flow \vec{H}_{inv} and in a vector \vec{H}_{visc} describing the contribution viscosity and heat conduction on the flow. The both terms read:

$$\vec{H}_{inv} = (\rho\vec{v}, \rho\vec{v}\vec{v} + p, \rho\vec{v}H_t)^T$$

$$\vec{H}_{visc} = (0, \vec{\sigma}, \vec{\sigma} \cdot \vec{v} + \vec{q})^T$$

where $\vec{\sigma}$ is the stress tensor, and \vec{q} is the heat flux vector. For the sake of simplicity in the following discussion the conservation equations and their approximations will be referred to their formulation in a twodimensional Cartesian system (x, y, t) .

2.1.1 Full Navier-Stokes Equations

The most complete description of continuum flow is given by the Navier-Stokes equations. This system of equations summarizes the conservation of mass, momentum and energy for viscous, heat conducting fluids.

In the Cartesian frame the flux vectors are split up in Cartesian components, i.e. $\vec{H}_{inv} = (F, G)^T$ and $\vec{H}_{visc} = (S, R)^T$. The integral form reads now

$$\int_{\tau} Q_t d\tau + \oint_A (F - S) dy - \oint_A (G - R) dx = 0 \quad (3)$$

and the corresponding divergence form gives

$$Q_t + (F - S)_x + (G - R)_y = 0 \quad (4)$$

Herein is

$$Q = \begin{pmatrix} \rho \\ \rho u \\ \rho v \\ \rho E \end{pmatrix} \quad F = \begin{pmatrix} \rho u \\ \rho u^2 + p \\ \rho uv \\ \rho u H_t \end{pmatrix} \quad G = \begin{pmatrix} \rho v \\ \rho vu \\ \rho v^2 + p \\ \rho v H_t \end{pmatrix}$$

$$S = \begin{pmatrix} 0 \\ \tau_{xx} \\ \tau_{xy} \\ s_4 \end{pmatrix} \quad R = \begin{pmatrix} 0 \\ \tau_{xy} \\ \tau_{yy} \\ r_4 \end{pmatrix}$$

where $s_4 = q_x + u\tau_{xx} + v\tau_{xy}$ and $r_4 = q_y + u\tau_{xy} + v\tau_{yy}$. With the Stokes assumption $\mu_v = -2/3\mu$ the stress terms are expressed by Newtons assumption:

$$\tau_{xx} = 2\mu u_x + \mu_v \nabla \cdot \vec{v}, \quad \tau_{yy} = 2\mu v_y + \mu_v \nabla \cdot \vec{v}, \quad \tau_{xy} = \mu(u_y + v_x)$$

The components of the heat flux vector \vec{q} are given by $q_x = \lambda \frac{\partial T}{\partial x}$ and $q_y = \lambda \frac{\partial T}{\partial y}$.

The Reynolds averaged Navier-Stokes equations for turbulent flows have the same structure and therefore the same approximations and methods of solution.

2.1.2 Thin Layer Approximation

The Thin Layer Approximation of the Navier-Stokes equations is a widely used approximation for the computation of viscous flows at high Reynolds numbers. In this case two very different length scales, the body length L and the boundary layer thickness δ must be resolved. Similar as in the boundary layer theory all the viscous terms with stream-wise derivatives are neglected for the Thin Layer Approximation. However, in contrast to the boundary layer theory, the Thin Layer Approximation retains all the terms of the Euler equations, and the time derivatives, as well. In consequence the Thin Layer Approximation preserves all the properties of the inviscid flow, in particular the information transport along characteristics and discontinuous solutions.

In 2-D Cartesian coordinates, assuming the x-coordinate as the nearly streamwise direction, the Thin Layer Approximation would read:

$$Q_t + F_x + (G - R)_y = 0 \quad (5)$$

where Q , F , and G have the meaning as in the full equations, but the viscous term R contains only that stress terms which have derivatives in normal (y -) direction.

There exists no rigorous theory for the derivation of this approximation, however its range of validity is approximately that of the higher order boundary layer theory. It means that local flow separation and small normal pressure gradients in viscous layers are covered by the approximation.

Computationally a further motivation of using this approximation is given by the fact that due to the disparate scale lengths the step sizes in streamwise direction are much larger than in normal direction. Therefore even when the full equations are used, the streamwise derivatives of the viscous terms are resolved insufficiently. Furthermore most of the turbulence models in use are suited only for boundary layer-like flows.

An important requirement for the application of the Thin Layer approximation is the use of streamline- (surface)-orientated, orthogonal meshes in viscous layers to resolve completely the remaining main stress terms normal to the surface.

The numerical methods of the solution for the full Navier-Stokes equations, and the Thin Layer approximation are nearly identical.

2.1.3 Parabolized Navier-Stokes Equations

The Parabolized Navier-Stokes equations correspond to the Thin Layer approximation, but usually in their steady-state form. For the example of 2-D flow the parabolized equations would read:

$$F_x + (G - R)_y = 0 \quad (6)$$

where the viscous terms R contain only terms with derivatives normal to the main flow, F , and G are the complete Euler fluxes.

Efficient space marching methods are the motivation for using this approximation. Space marching is well suited for stationary, supersonic flow, where all information is transported downstream within the Mach cone. But in the subsonic regions this assumption fails, since the stationary equations become elliptic and upstream influence occurs in main flow direction. Therefore the term "parabolic" is somewhat misleading. To preserve the "parabolic" behaviour, space marching in main flow direction must be enforced numerically by one-sided differences for all derivatives in main flow direction. This numerical manipulation can be justified by the "parabolic" nature of attached boundary layers. However neglecting the upstream influence in subsonic regions, numerical instabilities can arise, which must be suppressed. This can be done with different strategies.

In common marching procedures for external flows either the pressure gradient normal to the wall is assumed to be zero across the subsonic layer, Schiff and Steger [1], or the contribution of the streamwise pressure gradient is decreased in the subsonic layer as a function of the Mach number based on a stability analysis, as proposed by Vigneron [2].

Space marching methods can also be constructed for the time-dependent Thin Layer equations, Eq.(5), using an time marching technique. The solution converges in time in an iteration-like manner for each cross flow plane separately. An usual upwind scheme can be used, where all of

the variables needed downstream of the actual cross section are extrapolated from the upstream sections without further assumption for the pressure, as reported by Menne [3] for computations of external hypersonic flows. An advantage of this strategy is that the same time-marching code can be used in "parabolic" and "elliptic" regimes.

The parabolic assumption is often used for internal, mostly subsonic flows in duct-like geometries of moderate turning. In usual procedures an averaged pressure $\bar{p}(x)$, uniform in one cross section, is introduced in the streamwise momentum equation, which ensures the global mass flux. The other equations retain a separate pressure correction Δp , which can vary over the cross section. A review of different parabolic methods in internal flows has been made e.g. by Rubin [4]. The principle is used by many authors, e.g. by Patankar and Spalding [5], Briley [6], Ghia and Ghia [7], Govindan et al. [8] and others. Since only a single space marching sweep is employed in fully parabolic approximation procedures, the computations become very efficient with respect to the computation time.

Like the boundary layer approximation, the parabolic assumption is not able to deal with flow separation in streamwise direction. In normal direction however, cross flow separation and strong secondary flow can be predicted by this assumption. A sensitivity study in parabolized Navier-Stokes solutions of external supersonic flow was carried out e.g. in [9] with the aim to extend this approximation to more demanding flows at high angle of attack and to improve the accuracy and stability.

The application of parabolic procedures requires initial conditions in two or three cross sections. These conditions have to be taken from other solutions or from experiments.

2.1.4 Reduced Navier-Stokes Equations

The Reduced Navier-Stokes Equations (RNS) correspond to the Parabolized Navier-Stokes equations, but the approximation of the streamwise pressure gradient term is modified to account for the upstream propagation of pressure waves within subsonic zones. In this way the pressure is treated as elliptic and stored in the whole domain. The remaining variables are treated as in the fully parabolic approximation and stored only on some cross section as in space marching procedures. Due to the elliptic treatment of the pressure the approximation enables the calculations of weak streamwise separation and is applied to external and internal flow problems, e.g. by Moore et al. [10], Pratap and Spalding [11], Lai and Khosla [12], Zhu and Fletcher [13] and others.

The RNS solution has shown to be somewhat more expensive than the PNS solution, but much cheaper than the full Navier-Stokes solution as demonstrated e.g. by Power, Barber [14] for external flow over a compression ramp.

2.1.5 Euler equations

The Euler equations, describing the inviscid flow, are an important approximation of the Navier-Stokes equations. They contain the essential mathematical difficulties and therefore determine the properties of Navier-Stokes solutions. Nearly all of the Navier-Stokes solvers for high

Reynolds numbers are based on Euler solvers extended by the viscous terms.

The 2-D Euler equations read in their conservative integral and divergence form:

$$Q_t + F_x + G_y = 0 \quad (7)$$

$$\int_{\tau} Q_t d\tau + \oint_A F dy - \oint_A G dx = 0 \quad (8)$$

The Euler equations form a nonlinear, hyperbolic system of equations with real eigenvalues λ_i . As a consequence of the nonlinearity, the equations show two different types of solutions, discontinuous (weak), and continuous, smooth solutions, as well.

The continuous solution can be expressed by the characteristic solution of the Euler equations. The characteristic form of these equations is obtained by a diagonalization of Jacobian of the Euler fluxes, e.g. $A = \frac{\partial F}{\partial Q}$ with the corresponding eigenvector matrix T . With the diagonal matrix $\Lambda = \text{diag}(\lambda_i) = T^{-1} A T$ the characteristic form reads in 1-D:

$$\frac{\partial W}{\partial t} + \Lambda \frac{\partial W}{\partial x} = 0 \quad (9)$$

The characteristic variables W are defined by $dW = T^{-1} dQ$ and the diagonal matrix is given by the eigenvalues, $\Lambda = \text{diag}(u + a, u, u - a)$. The characteristic form is the basis of the method of characteristics, but also the basis for constructing upwind shock capturing schemes.

The weak solution, describing the jump conditions over a discontinuity (e.g. a shock wave or a slip line), can only be derived from the conservative integral form of the Euler equations. Therefore, if embedded discontinuities are considered, only the conservative form guarantees the correct jump conditions. For a discontinuity C moving with the velocity \tilde{c} , the application of the integral conservation laws results in the jump conditions which read in the general form with the definition $[f] = f_2 - f_1$:

$$\int_C [H - Q\tilde{c}] \cdot \tilde{n} dA = 0 \quad (10)$$

By means of this jump condition the Rankine-Hugoniot relations can be derived, and computationally shock-fitting procedures can be constructed.

2.2 Thermal and caloric relations

The solution of the conservation laws requires additional closure relations to express the thermal and caloric state, and the transport quantities in the flux \tilde{H} as function of the conservative variables Q .

Different situations have to be considered for the formulation of thermal and caloric closure relations. The situations are equilibrium, frozen and nonequilibrium flows. For the present consideration the gas is assumed to be in thermodynamical and chemical equilibrium.

Assuming equilibrium flow, the equations of state can be expressed as algebraic closure relations for the thermodynamical and caloric state as function of conservative flow variables Q . The basic input quantities for these relations usually are the density ρ , and the internal energy ϵ , which can be calculated from the total energy $\rho E = \rho(\epsilon + \tilde{v}^2/2)$.

The caloric equation of state expresses the internal energy ϵ with two thermodynamical variables, e.g. with

ρ and T .

$$\epsilon = \epsilon(\rho, T)$$

For real gases, i.e. a mixture of gases at equilibrium, the caloric equation of gases is the sum of all energy contributions of the species. The single contributions can be calculated with methods of the statistical thermodynamics and with data from measurements (see Vincenti, Kruger [15]).

For a thermally perfect gas (e.g. air $T \leq 2000K$) the caloric equation reduces to $\epsilon = \epsilon(T) = \int c_v dT$, and with the additional assumption of calorically perfect gas (e.g. air $t \leq 600$) it becomes $\epsilon = c_v T$.

The thermal equation of state defines the pressure as function of two variables, e.g. of the internal energy ϵ , and of the density ρ . Assuming that each species of a mixture behaves like perfect gas, the pressure becomes the sum of the partial pressures p_i of each species:

$$p = \sum_i p_i = \sum_i \rho_i \frac{R}{M_i} T = p(\rho, \epsilon) \quad (11)$$

For a thermally perfect gas, e.g. air without dissociation, it yields $p = \rho RT$. In addition for a calorically perfect gas it is $p = (\gamma - 1) \rho \epsilon$.

With the equations of state known, and with the thermodynamical laws all the other quantities can be derived. In general the equations of state for a real, non-perfect gas cannot be formulated in a closed form. The calculation of the state has to be carried out e.g. by an evaluation of the thermodynamical partition functions, from which Mollier diagrams can be constructed.

Computationally it results in a system of nonlinear, algebraic equations, which has to be solved for each state (grid) point. For computational purposes the precalculated variables of state can be subdivided in regions in the ρ, ϵ plane and expressed by curve fits in that regions (e.g. for air by Tannehill [16]). For improving the vectorization the equation of state can also be used in form of interpolation tables with equidistant or stretched step-sizes in the ρ, ϵ plane (e.g. Vinokur [17]).

2.3 Transport Quantities

The computation of viscous, heat conducting flow requires additional relations for the transport coefficients of momentum, (viscosity), of energy (thermal conductivity), and in mixtures of gases for the diffusion of species masses (diffusivity). For the situation of chemical equilibrium, as considered here, the diffusion of species is usually assumed to be negligible.

In laminar flow the transport quantities are functions of the molecular properties, depending on the local thermodynamical state. In general the values and the dependences are well known.

At moderate densities the coefficients of viscosity and heat conduction of a single perfect gas are functions of the temperature only. Then simple models can be used for the calculation of the viscosity of a single component gas, as e.g. the Sutherland formula or potential laws. The corresponding thermal conductivity can be calculated from the viscosity using the Eucken relation (Vincenti, Kruger [15]).

For a mixture of gas at equilibrium, where each component is assumed to be a perfect gas, the composite viscosity can be determined from the semi-empirical mixing law

of Wilke, which takes into account the species viscosity and the corresponding concentration. For the thermal conductivity of a gas mixture a similar law can be defined (for details see e.g. Bird, Stewart, Lightfoot [18]). With such mixing laws the transport coefficients become functions of two variables, e.g. $\mu = \mu(\rho, \epsilon)$. Therefore the calculation of transport coefficients has to be combined with the calculation of the thermal and caloric equations of state. Computationally the transport coefficients can be updated similar to the equations of state in form of interpolation tables or curve fits (e.g. for air by Srinivasan [19]).

In turbulent flow the problem of closures is much more complicated than for laminar flow. Generally all turbulent flow simulations suffer from a lack of correct physical modelling. The complexity of describing turbulent flows is still larger for hypersonic flows due to the effects of compressibility, three-dimensionality, and nonequilibrium mixtures. Therefore the discussion of turbulence modelling is the topic of a separate lecture.

The common attempt to solve the Navier-Stokes equations is based on time-averaging of the variables, which results in the Reynolds-averaged Navier-Stokes equations. Additional closure relations have to be found between the averaged fluctuating quantities (Reynolds stresses), and the mean values of the conservative variables.

An usual formulation of the turbulent stress terms is the eddy viscosity concept, which models these terms similar to the laminar case as an eddy viscosity (turbulent viscosity) multiplied by the velocity gradient. Defining an effective viscosity, $\mu_{eff} = \mu_{lam} + \mu_{turb}$, the Reynolds-averaged Navier-Stokes equations can be written in the same form as for the laminar flow. Thus the mathematical structure of equations is retained, and the numerical methods of solution do not differ essentially for laminar and turbulent flow, beside of the strongly nonlinear transport coefficients and the additional closure relations.

Closure relations can be achieved by additional transport equations, like the $k - \epsilon$ model, or by algebraic relations, like the mixing length assumption. All of these assumptions need parameters to be adapted empirically to the special flow problem. The most of these models are suited for boundary layer-like flows with small separation zones only (which motivates the use of the Thin Layer approximation).

In Navier-Stokes computations an additional difficulty arises from the evaluation of the boundary layer thickness, necessary for the scaling of the models. Therefore special turbulence models were derived for the requirements of Navier-Stokes solutions. At present two widely used models are the two-layer algebraic model by Baldwin and Lomax [20] and the $k - \epsilon$ model. Details can be found in the related literature, a review of turbulence closures in Navier-Stokes solutions is given e.g. in [21].

An additional, and essential problem arises from the prediction of the transition from laminar to turbulent flows. This problem is much more uncovered than the turbulent closures, and requires further investigations in particular for compressible high-speed flow.

2.4 Boundary conditions

The boundary conditions define the specific problem to be considered. Therefore they are an essential part of

computation. In the most of physical situations they can be divided in wall conditions, in- and outflow conditions, and periodic conditions.

Periodic boundary conditions utilize the periodicity of flow field. Their formulation is usually straightforward.

The boundary conditions at the wall for continuum flow at thermodynamical equilibrium are well defined by the conditions of vanishing normal velocity, by the no-slip condition (vanishing tangential velocity v_t), and by the thermal conditions:

$$v_n = 0, \quad v_t = 0, \quad T = T_w \quad \text{or} \quad \frac{\partial T}{\partial n} = 0$$

In rarefied flow and in non-equilibrium flow the formulation of wall conditions is much more complicated and requires additional assumptions and experimental support.

The inflow and outflow boundary conditions

are less unique, since they depend strongly on the flow problem considered. The number of the boundary conditions (conditions from outside) and of the compatibility conditions (conditions from the interior integration domain) can be derived from the differential problem. For the complete Navier-Stokes equation such conditions are discussed e.g. by Dutt [22] and Nordström [23].

For the Thin Layer Approximation additional boundary conditions due to viscous terms are not required since these terms normal to the outflow plane usually are neglected. In this case the number of conditions at a boundary can be deduced from the inviscid, hyperbolic flow by counting the in-going and out-going characteristics normal to the boundary. However which quantities are prescribed or updated from the interior, is the matter of the flow problem to be solved and of the information to be available. In many cases the boundary information on the flow are not complete, since the boundaries cut an unknown, often vortical flow field. Then reasonable conditions have to be deduced from the physical problem. Different assumptions can be made at the boundary, like nearly inviscid flow (characteristic updating of the conditions) and boundary layer-like flow (parabolic behaviour in space, extrapolation from the interior).

3 Computational techniques

The complete Navier-Stokes equations form a system of quasi-linear partial differential equations of parabolic-hyperbolic type in the time-space plane, and of elliptic-hyperbolic type in the space (steady-state). These different types demonstrate the complexity of the solutions.

However the main problems in numerical solutions arise essentially from the many disparate length scales and time scales, which are characteristic for the different physical phenomena. Typical length scales are for example the body length L , the boundary layer thickness $\delta_b \sim L/\sqrt{Re}$, the viscous thickness of a shock wave $\delta_s \sim L/Re$, and the scaling of turbulent eddies $\delta_t \sim L\sqrt{Re}^2$. These scalings differ by orders of magnitude in ordinary flows. Since not all of them can be resolved the unresolved scalings must be modeled, either by physical closures (e.g. turbulence) or by numerical means (e.g. shock capturing schemes), otherwise the accuracy and convergence of a numerical solution is impaired.

For the most of external and internal flows of technical

interest the two most important flow regions are the viscous layers with $\delta_b \sim L/\sqrt{Re}$, and the nearly inviscid flow with scaling of order of L .

The viscous layers (boundary layers, wakes) are characterized by a small extension δ_b normal to the main flow. Within these layers the Euler and viscous terms are nearly balanced. Thus the solution becomes continuous, but shows large gradients and a strong curvature of the variables. This fact can lead to severe problems of accuracy of the numerical method if these layers are not resolved sufficiently well.

In the nearly inviscid regions the Euler terms are dominating and the properties of the solution correspond essentially to that of the hyperbolic Euler equations. Thus continuous and discontinuous solutions can appear, as well.

Although viscous solutions are continuous in principle, discontinuous solutions appear numerically, since in general the viscous structure of a shock wave with the much smaller scale length is not resolved. Therefore the capturing of the discontinuous solutions requires the use of the conservative form of the Navier-Stokes equations and the use an Euler solver with good shock capturing properties.

Thus the Navier-Stokes solution includes all the numerical problems of a Euler solution, and much care has to be taken to avoid undesired interactions between the numerical dissipation of the Euler solver, and the physical dissipation from the viscous terms in the Navier-Stokes equations.

The numerical solution of the conservation equations is based on a discrete approximation of the equations and their initial and boundary conditions, as well. The aim of the numerical solution is to achieve an approximative solution, which converges with decreasing step sizes to the analytical solution of the differential problem. The proof of the convergence for the nonlinear initial-boundary value problems is rather difficult. Therefore in the most cases convergence is assumed, if the equivalence statement by P. Lax [24] is satisfied for a linearized version of the scheme. This proof, valid for initial value problems, requires numerical stability and consistency as necessary and sufficient conditions for convergence. Both requirements are fundamental for the development of converging methods.

The development of methods of solution for conservation equations can be divided in different steps. These steps are the grid generation and arrangement, the conservative formulation in the discrete space, the spatial discretization of the fluxes and boundary conditions, the time discretization, and the solution of the resulting system of algebraic equations.

In the following sections a brief summary of basic numerical approaches will be given and examples for methods of solution will be presented.

3.1 Grid generation

The numerical grid arrangement predefines the quality of the solution with respect to the geometry, the physics and numerical accuracy and stability. The generation of numerical grids can take a large part of total effort for a numerical solution. This effort is growing with increasing geometrical and physical complexity.

The most important requirements to the grid arrangement are accurate representation of geometrical boundaries, clustering of grid points in regions of strong changes, smooth distribution of step sizes and orthogonality and regular grids without mesh singularities.

In general the requirements cannot be sufficiently satisfied at all, therefore compromises must be made. This fact is reflected in the variety of different mesh concepts. Concerning the structure of meshes one can distinguish between structured and unstructured grids. In principle the both concepts show contrary properties, the advantage of one often corresponds to the drawbacks of the other, and vice versa. Both grid concepts are used for CFD, but at present with a majority for structured grids.

In structured meshes the grid points are in a certain order and the mesh can be mapped in a rectangular computational domain. This allows the application of nearly all of the discretization schemes and the efficient use of implicit methods. Vectorization and parallelization becomes easier. Essential drawbacks are mesh singularities, which can arise, and the difficulties for grid adaption, in particular for grid point enrichment and depletion.

Unstructured grids consist of an unordered arrangement of grid cells, thus each cell needs additional information about its connection to neighbouring cells. The essential advantages are the better geometrical flexibility and the capability of enrichment and depletion of grid points, where necessary. But unstructured meshes show drawbacks where structured grids have their advantages. Unstructured grids are mainly used with finite-element methods, but also finite-volume methods can be adapted to complex unstructured grids e.g. [25], [26].

Grid adaption enables optimization of the grid during and by the solution. In principle an optimal mesh would require the solution a priori. The adaption needs a criteria for which the grid points should be concentrated. Such criteria can be estimations of the truncation error of the discrete equations, or can be measures of physical flow gradients. Major techniques for adaption are the grid redistribution and grid enrichment.

Grid redistribution is usually based on a fixed number of grid points, which are rearranged during the solution by applying an adaptivity criteria. Problems can arise from cells becoming too distorted. This technique is mainly applied to structured grids, e.g. [27], but can also be used in unstructured grids.

Grid enrichment techniques are well suited for unstructured meshes. The grid points can locally be added to increase the numerical accuracy, e.g. [28], [29].

The brief discussion of grid generation has shown the variety of different techniques. More informations can be found in review papers, e.g. by Thompson et al. [30] and by Weatherill [31], and e.g. in the proceedings of the Grid Generation Conferences in Landshut (1986), Miami (1988) and the next in Barcelona (June 1991).

3.2 Conservative discretization

The numerical solution requires the preservation of the conservation properties in the discrete space. The conservation equations are applied to a finite control volume (element), which is defined around or between the grid points. The numerical techniques for a conservative spatial discretization differ essentially in the arrangements of the control volume and in the discretization approach.

3.2.1 Arrangements of control volumes

Arrangements of the finite control volumes in a given grid can be defined in different ways.

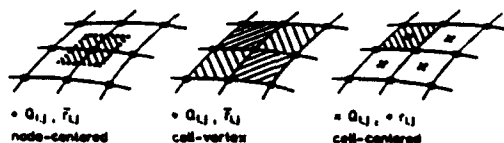


Fig. 1 Arrangements of the control volumes.

Commonly used arrangements are the "node-centered", the "cell-centered", and the "cell-vertex" arrangements, which are sketched in Fig. 1. For node-centered and cell-vertex schemes the variables and the geometry are defined on the same grid point, for cell-centered schemes the variables are defined in the center of the cell. These arrangements of control volumes can be extended straightforward to triangulated, unstructured grids as e.g. in [32].

In a Cartesian grid these arrangements show nearly the same accuracy, but for a curvilinear grid different truncation errors can result. For example using a central scheme it could be shown that for a skewed grid the error from the "cell-centered" arrangement is larger than that for the "cell-vertex" arrangement [33]. Also the node-centered scheme shows a better truncation error for highly skewed meshes, [34].

Near a boundary the different grid arrangements require a different numerical treatment of the boundary conditions, which can be important for the spatial accuracy in particular near geometrical discontinuities, like the trailing edge [34].

Although the truncation error analysis has shown different behaviour for the different arrangements of control volumes, sufficient accurate results were achieved with all of them. The influence of the grid arrangement in combination with the numerical discretization is very complex, therefore no general recommendation can be given for the choice of any arrangement.

3.2.2 Conservative approaches

Conservative discretization of the governing equations can be achieved by using the integral form, and divergence form, as well. In the literature different discretization techniques are applied.

The "Finite-Volume" approach makes use of the integral form, Eq. (1). The surface integral is approximated by the sum over all faces of the control volume. In a simplified form the discrete form reads in 2-D:

$$\frac{\Delta Q}{\Delta t} Vol + \sum_{k=1}^4 (F \Delta y - G \Delta x) = 0 \quad (12)$$

Herein Q is the volume-averaged value, $(F \Delta y - G \Delta x)$ are the normal fluxes summed up over the single cell interfaces. The advantage of the "Finite-Volume" approach is the direct application to the physical (x, y) space, and the easy interpretation in curvilinear meshes. This approach can be used for structured and unstructured meshes, as

well.

The "Finite-Difference" approach, based on the divergence form, Eq. (2), is slightly more expensive in their evolution, since first the differential equations have to be transformed to the curvilinear coordinate system and afterwards the equations are discretized in the transformed plane. The advantage of this approach is given for the more complex terms like the viscous terms in the full Navier-Stokes equations. For the 2-D example the transformed equations in a curvilinear coordinate system (ξ, η) read:

$$\hat{Q}_t + \hat{F}_\xi + \hat{G}_\eta = 0 \quad (13)$$

with $\hat{Q} = QJ$ and $\hat{F} = Fy_\eta - Gx_\eta$. Here J is the metric Jacobian, which can be interpreted as the volume, and x_η , etc. are parts of the surface normal vector. The details can be found elsewhere. After the discretization in the transformed plane with the corresponding (properly discretized) metric formulations, the resulting discretized equations agree with discretization derived by the "Finite Volume" method.

In the "Finite Element" approach, the domain Ω is subdivided into finite elements and the solution vector Q is interpolated using (linear) shape functions. With a weighted residual statement and by use of the Gauss theorem the conservation equation can be cast in an approximate form, e.g. as in [35], [26].

$$M_{j,k} \frac{\Delta Q}{\Delta t} = \int_{\Omega} F_i \frac{\partial N_j}{\partial x_i} d\Omega - \int_{\Gamma} F_i n_i N_j d\Gamma \quad (14)$$

with the finite element matrix $M_{j,k}$. For further details see the related literature. A bibliography on Finite Elements and supercomputing is given by White and Abel [36].

Inspecting the three formulations in more detail, it can be seen, that the Finite Element formulations for conservation laws agree exactly or approximately with those from the Finite Volume or Finite Difference discretizations, see e.g. [26]. It means the different ways of conservative discretization result in equivalent formulations. Remarkable differences for spatial discretization can occur by different arrangements of the control volume, by the different numerical flux formulations, and by the different updating of the cell-interface fluxes.

3.3 Numerical flux formulation

The discretization of the conservation equations for a small control volume results in a system of difference equations for the rate of change of the variables balanced by the normal fluxes over the cell interfaces. The variables used in the time derivatives usually are volume-averaged values, whereas the fluxes in the steady-state operator need cell interface values.

For sake of simplicity the 1-D conservation equations will be used in the following discussion. In a common conservative difference form, they read for a grid point "i":

$$\frac{\Delta Q_i}{\Delta t} + \frac{\hat{F}_{i+1/2} - \hat{F}_{i-1/2}}{\Delta x} = \frac{\hat{S}_{i+1/2} - \hat{S}_{i-1/2}}{\Delta x} \quad (15)$$

Herein $\Delta Q/\Delta t$ is the discretized time derivative, defined later, and $\hat{F}_{i\pm 1/2}$ and $\hat{S}_{i\pm 1/2}$ are the numerical flux

functions for the corresponding inviscid, and the viscous fluxes at the cell interfaces.

3.3.1 Viscous fluxes

The viscous fluxes are usually updated by means of central differences $O(\Delta x^2)$, which corresponds to the elliptic nature of the viscous effects. Then a viscous term of the form $S = \mu u_x$ may be written as

$$S_{i+1/2} = \mu_{i+1/2} \frac{u_{i+1} - u_i}{\Delta x} \quad (16)$$

Cross derivatives can be treated in a similar way.

3.3.2 Formulation of the inviscid fluxes

The numerical formulation of the inviscid fluxes has a great influence on the properties of the solution method, since they contain the essential information of wave spreading. These terms are strongly nonlinear and are mathematically more difficult than the viscous terms. Therefore the most of schemes for the Navier-Stokes equations differ by the formulation of the inviscid flux terms (Euler solver).

The numerical formulation can be divided in two parts, in the evolution of the numerical flux function at cell faces, which should be a consistent approximation of the physical fluxes, and in the projection of the volume-averaged variables to the cell faces for updating the fluxes.

In the "projection-evolution" approach, sometimes called "MUSCL" approach, van Leer [37]), the basic variables, e.g. Q are extrapolated from both sides to the cell interface. With these values a common numerical flux formulation is formulated.

In the "evolution-projection" approach, "non-MUSCL" approach, the flux functions are formed on the grid points, where the variables are stored, thereafter the fluxes are projected to the cell interface. This approach is used e.g. for the "cell-vertex" schemes or in the modified flux approach [38]. Also mixed forms of both may be possible. The numerical flux functions become different for the two approaches, in particular for higher order accurate schemes. However which of the both approaches are to prefer cannot be decided uniquely, discussions about that are made e.g. by Yee [39].

The evolution of numerical fluxes can be considered as the solution of a Riemann problem at the cell interface. Within each cell there exists an averaged value of the conservative variables. The values at the interface to the neighbouring cell result in a jump when they are extrapolated from the left and the right cell-averaged values. According to the theory of the nonlinear hyperbolic Euler equations this jump of the values generates a local Riemann problem, whereby information is transported forward and backward by the different gasdynamical waves and shocks. The solution of the local, exact Riemann problem results in Euler solvers of the Godunow-type [40],[41], which describe very accurately the wave phenomena, but these methods are very expensive. If the jump at the interface is considered to be weak, the Riemann problem can be solved approximately using the characteristic solution of the Euler equations. A large number of numerical flux formulations, called *approximate Riemann solvers* can be derived with this assumption. Widely used approximate Riemann solvers are the schemes of van Leer [42], Roe [43],

Osher, Chakravarthy [44], Steger and Warming [45], and many others.

The derivation of the *approximate Riemann solvers* starts from the 1-D conservative form

$$Q_t + F_x = 0 \quad (17)$$

The characteristic form of the Euler equations is derived by diagonalization of the flux Jacobian $A = \frac{\partial F}{\partial Q}$, which results in an uncoupled system of characteristic Euler equations. These equations describe the information transport along the characteristic directions.

$$W_t + \Lambda W_x = 0 \quad (18)$$

The diagonal matrix $\Lambda = \text{diag}(\lambda_i) = T^{-1}AT$ is formed with the eigenvalues $\lambda_i = (u, u \pm a)$. The relation between the conservative variables Q and the characteristic variables W is given by the eigenvector matrix T , i.e. $T \cdot dW = dQ$.

For subsonic flow, i.e. $-a \leq u \leq a$, the eigenvalue matrix Λ can be split in a positive and a negative part, i.e. $\Lambda = \Lambda^+ + \Lambda^-$. Then the characteristic form results in:

$$W_t + \Lambda^+ W_x + \Lambda^- W_x = 0 \quad (19)$$

An upwind difference formulation of this equation for the cell "i" with the faces $i \pm 1/2$ is:

$$\begin{aligned} \frac{\Delta W}{\Delta t} + \frac{\Lambda^+}{\Delta x} (W_{i+1/2}^+ - W_{i-1/2}^+) \\ + \frac{\Lambda^-}{\Delta x} (W_{i+1/2}^- - W_{i-1/2}^-) = 0 \end{aligned} \quad (20)$$

Herein W^\pm are the backward or forward interpolated variables according to the sign of the eigenvalues. In the simplest (first order accurate) case they are $W_{i+1/2}^+ = W_i$ and $W_{i+1/2}^- = W_{i+1}$.

The desired conservative difference form can be constructed from the characteristic form by assuming a locally constant characteristic field. This is achieved by multiplying the characteristic system, Eq. (20) with the eigenvector matrix T , which results in a conservative form:

$$\frac{\Delta Q}{\Delta t} + \frac{1}{\Delta x} (\hat{F}_{i+1/2} - \hat{F}_{i-1/2}) = 0 \quad (21)$$

where $\hat{F}_{i\pm 1/2}$ is the numerical flux function, which includes the characteristic information.

Using different splitting of the characteristic system, different updating of the cell interface values, and different approximate, conservative back transformation many of the different numerical flux functions can be derived from this formulation.

In the following some typical approaches for approximate Riemann solvers will be discussed briefly.

Flux-vector splitting methods can be derived by a direct application of the conservative back transformation to Eq. (20) and defining $A^\pm = T \Lambda^\pm T^{-1}$, and $F^\pm = A^\pm Q$. Then the split numerical flux results in

$$\hat{F}_{i+1/2} = F^+(Q_{i+1/2}^+) + F^-(Q_{i+1/2}^-) \quad (22)$$

The flux conservation requires that $F = F^+ + F^-$. The values Q^\pm are the cell face values extrapolated from left and right. In the literature there are different formulations for flux-vector splitting.

The flux-vector splitting by Steger, Warming [45]

uses the eigenvalue splitting $\Lambda^\pm = 1/2(\Lambda \pm |\Lambda|)$. Then the numerical fluxes are defined by:

$$\begin{aligned}\tilde{F}_{i+1/2} &= T(\Lambda^+ + \Lambda^-)T^{-1}Q \\ &= (\Lambda^+ + \Lambda^-)Q = F^+ + F^-\end{aligned}\quad (23)$$

This split flux results in a discontinuous numerical eigenvalue whenever the corresponding physical eigenvalue vanishes, van Leer et al. [46]. Therefore it causes a finite dissipation for steady waves, favourable for strong shocks, but too dissipative for viscous computations. This property is utilized for a robust hypersonic code by Eberle et al. [47] using a blended formulation of Steger Warming fluxes and the characteristic flux approach. Furtheron the eigenvalues of Steger Warming fluxes change discontinuously near the sonic point, which reduces the rate of convergence, as found in test calculations.

The flux-vector splitting by van Leer [42]

avoids the latter drawback of the Steger, Warming fluxes by defining the split fluxes as polynomials of the Mach number, such that they are smooth near the sonic point. Since one eigenvalue vanishes over a steady shock, its representation becomes very sharp. Furtheron this splitting if applied in implicit schemes results in very efficient, diagonal-dominant solution methods, e.g. Thomas and Walters [48], Schröder and Hänel [49]. However also this splitting formulation shows a remaining splitting error for steady tangential discontinuities. This drawback influences strongly the accuracy in viscous layers, as shown by Hänel, Schwane [50]. Therefore a number of modifications was developed and reported e.g. by van Leer [51] and by Hänel, Schwane [50]. Using these modifications the accuracy in viscous flows could essentially increased, as shown by Hänel et al. [50], [52].

The flux-difference splitting method, Roe [43],

can be derived from Eq. (20) by using the eigenvalue splitting $\Lambda^\pm = \frac{1}{2}(\Lambda \pm |\Lambda|)$. Rearranging Eq. (20) for Λ and $|\Lambda|$ and applying the conservative back transformation, the numerical flux component $\tilde{F}_{i+1/2}$ of the flux-difference splitting results in:

$$\begin{aligned}\tilde{F}_{i+1/2} &= \frac{1}{2}(F(Q_{i+1/2}^+) + F(Q_{i+1/2}^-)) \\ &+ \frac{1}{2}\tilde{\Lambda}|\tilde{\Lambda}|T^{-1}(Q_{i+1/2}^+ - Q_{i+1/2}^-)\end{aligned}\quad (24)$$

The matrices \tilde{T} and $\tilde{\Lambda}$ are evaluated with Roe averaged values \bar{Q} for the cell interface, which shows an improved shock representation.

The eigenvalues are correct represented by this scheme, even if one eigenvalue vanishes in $\tilde{\Lambda}$. Just this violates the entropy condition in form of expansion shocks and reduces the robustness of schemes. Following Harten [38] the eigenvalues are bounded by a so called entropy correction δ , which is a small number of order of $O(10^{-1})$, scaled by a typical velocity. this correction can be used in different forms, e.g. as in [52]:

$$|\tilde{\Lambda}| = \sqrt{\tilde{\Lambda}^2 + \left(\frac{\delta}{2}\right)^2}\quad (25)$$

Extension to higher order accuracy

The flux-vector and flux-difference splitting schemes are first order accurate, if the direct left and right values Q^\pm

are used as $Q_{i+1/2}^+ = Q_i$ and $Q_{i+1/2}^- = Q_{i+1}$. Higher order accuracy is required for upwind schemes when applied to practical computations. Two widely used ways for extensions to higher order accuracy shall be mentioned here, which are the MUSCL extrapolation by van Leer [37]), and the modified flux approach by Harten [38]. In the MUSCL approach by van Leer [37]), the variables Q^\pm are extrapolated higher order accurate to the cell interface and then substituted in the numerical flux formulation. The MUSCL extrapolation is based on a general polynomial for the forward $Q_{i+1/2}^+$, and backward extrapolated values $Q_{i+1/2}^-$, which can be written as:

$$Q_{i+1/2}^+ = Q_i + 1/4 \varphi_i ((1+\kappa)\Delta^+ Q + (1-\kappa)\Delta^- Q), \quad (26)$$

$$Q_{i+1/2}^- = Q_{i+1} - 1/4 \varphi_{i+1} ((1+\kappa)\Delta^- Q + (1-\kappa)\Delta^+ Q)_{i+1}$$

with $\Delta^+ Q_i = Q_{i+1} - Q_i$ and $\Delta^- Q_i = Q_i - Q_{i-1}$.

Herein φ is a limiter function, and κ is the discretization factor. For $\varphi = 0$ it yields a first order upwind scheme $O(\Delta x)$, with $\varphi = 1$ the scheme becomes higher order accurate, at least second order. In more detail the scheme is then central $O(\Delta x^2)$ with $\kappa = 1$, upwind-biased $O(\Delta x^3)$ with $\kappa = 1/3$, upwind-biased $O(\Delta x^2)$ with $\kappa = 0$, and fully upwind $O(\Delta x^2)$ with $\kappa = -1$.

The limiter functions φ are elements of the numerical flux, which limit the higher order extrapolation to suppress numerical oscillations. In the present definition they vary between 0 and 1, controlled by the solution itself. Such limiter functions can be constructed from the theory of almost monotonic solutions (TVD-theory) and applied approximately to hyperbolic systems in multi-dimensions.

A large number of limiter formulations can be found in the literature, e.g. the Albada limiter [53], the van Leer limiter [37], or the minmod limiter [54]. Comparisons of different limiters are given e.g. by Sweby [55] or by Yee [39].

Common to all of these limiter formulations is their reaction on the changes of the local gradient of the variables, expressed by a function $\varphi_i = \varphi_i(\Delta^+ Q_i, \Delta^- Q_i, \dots)$. The general behaviour of the limiters is given by $1 - \varphi \sim |Q_{xx}/Q_x|$, which can be shown by expanding the differences in the limiter function. Thus in regions of weak changes of Q the limiter remains nearly one, but for strong changes the value decreases, the scheme reduces the accuracy, and stronger numerical dissipation is generated.

The MUSCL extrapolation can be applied to flux-vector splitting as well to flux-difference splitting, if they are expressed by the left/right values Q^\pm .

The modified-flux approach by Harten [38],

modified by Yee [39], is used to increase the accuracy of the flux-difference splitting schemes. The first order flux-difference splitting, Eq. (24) with $Q_{i+1/2}^+ = Q_i$ and $Q_{i+1/2}^- = Q_{i+1}$ consists of a central flux term of $O(\Delta x^2)$ and a first order upwind term. To compensate the first order term an additional term is added to Eq. (24), such that the scheme becomes second order accurate in smooth regions. Near extrema (shocks) the additional flux vanishes, which retains the first order upwind term for capturing the shock. The flux difference splitting for the modified flux approach is usually written in the form:

$$\tilde{F}_{i+1/2} = \frac{1}{2}(F_{i+1} + F_i) + \frac{1}{2}\tilde{T}\tilde{\Phi}_{i+1/2}\quad (27)$$

The second term corresponds to the modified Roes upwind term in Eq. (24), T is the eigenvector matrix and Φ contains cell face differences of the characteristic variables controlled by flux limiters. Examples for this flux splitting are e.g. the "symmetric" and "upwind" TVD schemes of Yee and Harten. A detailed report about the different formulations is given by Yee in [39].

The central schemes can be considered as a special class of approximate Riemann solvers. Then the characteristic range of influence is equally weighted, independently of the Mach number by assuming $\Lambda^+ = \Lambda^- = \Lambda/2$. The numerical flux at the cell interface results in:

$$\bar{F}_{i+1/2} = \frac{1}{2} (F_{i+1} + F_i) \quad (28)$$

The central formulation includes the correct eigenvalues of the flux Jacobian A , and the spatial discretization error is of second order. However since this numerical approach ignores the characteristic range of influence, the numerical solution shows a poor shock capturing capability. Furthermore the central formulation does not include dissipative parts (even derivatives) thus any high-frequency error components of the solution can not be damped. Therefore artificial damping terms for high-frequency damping and shock capturing are added [56]. In general, the damping formulations consist of a linear fourth order term $d^{(4)}$ and of a nonlinear term $d^{(2)}$. Then the numerical flux reads:

$$F_{i+1/2} = \frac{1}{2} (F_{i+1} + F_i) + d_{i+1/2}^{(4)} - d_{i+1/2}^{(2)} \quad (29)$$

The high frequency damping term $d^{(4)}$, necessary to smooth errors of short wave lengths, (e.g. round-off errors) has the form:

$$d^{(4)} = (\epsilon^{(4)} \frac{\Delta x}{\Delta t}) \Delta x^4 \cdot Q_{xxx} \quad (30)$$

where $\epsilon^{(4)}$ is a user specified constant.

The shock capturing term $d^{(2)}$ has to suppress oscillations from the nonlinear terms in particular for shocks.

$$d^{(2)} = (\epsilon^{(2)} \frac{\Delta x}{\Delta t}) \Delta x^2 \cdot Q_x \quad (31)$$

The damping is controlled by the nonlinear coefficient $\epsilon^{(2)}$, which is proportional to a constant, multiplied by the normalized second derivative of the pressure. In smooth regions of pressure the term becomes very small, but it is of $O(\Delta x)$ in regions of strongly varying pressure. Refinements were given by various authors, e.g. by Eliasson, Rizzi [57] for applications to hypersonic flows, formulations and further references for damping terms in viscous flows can be found e.g. in [58], [59].

The preceding consideration of different Euler solvers covers only a small part of existing methods, which are in their details so manifold as the authors are. Therefore critical studies and comparison of the different flux formulations are necessary, in particular for application to viscous flows. Many information can be found in Yee's paper [39]. Analysis of different flux algorithms were carried out e.g. by Grossman and Walters [60], by Montagne, Yee and Vinokur [61] and by Kroll et al. [62]. The behaviour in viscous solutions were studied e.g. by van Leer et al. [46] and Hänel et al. in [63], [50], [64],

[52].

Multi-dimensional Riemann solvers should be mentioned here as an important new tendency for Euler solvers. Whereas the approximate Riemann solvers, as discussed above, are derived from a one-dimensional Riemann problem, the multi-dimensional Riemann solvers take into account multi-dimensional wave propagation and remove the drawback of mesh dependence of the usually one-dimensional Riemann solver. Examples and analysis of multi-dimensional Riemann solvers with further references are given e.g. by Deconinck [65], by Powell, van Leer [66], Rumsey, van Leer, Roe [67].

3.4 Methods of Solution

In general time-dependent Navier-Stokes equations are used for solutions of unsteady, and stationary flow problems, as well. The advantage of using the time-dependent equations for steady-state computations is that the initial-boundary value problem remains parabolic or hyperbolic in the time-space plane, independent from the Mach number range. Therefore one and the same numerical method can cover a broad range of applications. Thus the methods of solution for the time-dependent equations correspond in principle to the methods of integration in time. These methods can be classified by their different properties.

The time integration can either be based on explicit methods or on implicit methods

The explicit methods have the simpler algorithms, only the steady-state operator has to be evaluated from the known initial state, the new state can be computed decoupled for each grid point. The explicit methods are well suited for structured, and unstructured grids, as well. Vectorization and parallelization of the algorithm is much simpler. However the numerical time step of an explicit method is restricted by the numerical stability, depending on the space step divided by the fastest gas-dynamical wave speed, and in viscous flows on the cell Reynolds number. For this reason the explicit schemes become inefficient for stiff equations, when very different scalings have to be resolved.

The implicit schemes have the advantage of being unrestricted stable, or at least allow a much larger time step than an explicit scheme. But the computational work per time step is much higher due to the inversion of large solution matrices. The recursive structure of the inversion algorithms is a handicap for vectorization and parallelization of implicit methods. But nowadays implicit methods can be vectorized in the same high degree as for explicit schemes with appropriate algorithms, improved compilers and sufficient computer storage.

Time integration methods can also be divided in classes of schemes, which are combining space and time integration, and such where space and time integration is independent.

In schemes combining space and time integration an additional term is added to the spatial discretization for increasing the temporal accuracy and stabilizing the scheme. Due to this term these schemes yield steady-state solutions that depend on the time step. To this class of schemes belong the Lax-Wendroff type schemes. Most popular is the predictor-corrector scheme of McCormack [68], which was applied e.g. to complex hyper-

sonic flow by Shang and Scher [69].

Schemes of independent space and time integration are the mostly used types of schemes at present. The major advantage is that the steady-state solutions become independently of the solution method and thus efficient convergence-accelerating means can be used for steady-state calculations. Typical members of this class are the explicit Runge-Kutta type methods and the many implicit schemes based on corrector formulations. Another classification of solution methods can be made for time accurate schemes and such methods for steady-state solutions only.

Time-dependent flow problems require a discretization which is consistent and stable in time and space. Additional care has to be taken for the temporal accuracy, which is influenced by the discretization errors in time and space, as well. For time-accurate computations the explicit scheme results in a tolerable time advance, as long as only one time scale is present in the physical problem, e.g. the gasdynamical scaling in inviscid solutions, just defining the stability restriction. The time step becomes very small and the time accurate computation becomes expensive if additional smaller scale lengths have to be resolved, like in viscous flows at high Reynolds numbers or in stiff chemical rate equations. For this reason time accurate computations with an explicit scheme may be still efficient for inviscid flows and viscous flows at moderate Reynolds numbers, but for high Reynolds numbers some other ways, like implicit schemes or multigrid methods should be taken in consideration.

For steady-state computations the transient solutions have no meaning, as long as the steady-state solution will not be influenced by them. Therefore consistency and accuracy in time is not required, the method of solution (in time) can be chosen e.g. for a optimal rate of convergence. This results in classes of pseudo time-dependent methods which correspond to iteration schemes. Herein different acceleration strategies for improving the convergence can be applied, like e.g. Gauss-Seidel relaxation, Lower-Upper matrix decomposition, local time stepping or the multigrid methods.

The methods of solutions and their variants are numerous, therefore in the following section only some of typical methods of solution for the Navier-Stokes equations will be discussed. For the discussion the two-dimensional Navier-Stokes equations are considered. The treatment of the 3-D equations is analogous. The equations in conservative form, written for a curvilinear coordinate system, let's say (ξ, η, t) , read:

$$\hat{Q}_t + (\hat{F} - \frac{1}{Re} \hat{S})_\xi + (\hat{G} - \frac{1}{Re} \hat{R})_\eta = 0 \quad (32)$$

Details of the transformed equations can be found elsewhere. With a conservative discretization in a way as described above the approximated Navier-Stokes equations (32) read:

$$\frac{\Delta \hat{Q}}{\Delta t} + Res(\hat{Q}) = 0 \quad (33)$$

where $\Delta \hat{Q} / \Delta t$ is the discrete time derivative, and the residual $Res(\hat{Q})$ corresponds to the discretized steady-state operator:

$$Res(\hat{Q}) = \delta_\xi (\hat{F} - \frac{1}{Re} \hat{S}) + \delta_\eta (\hat{G} - \frac{1}{Re} \hat{R}) \quad (34)$$

The fluxes \hat{F} , \hat{S} , etc., are the numerical fluxes, upwind or centrally discretized, and the difference operators δ_ξ , δ_η mean:

$$\delta_\xi f = \frac{f_{i+\frac{1}{2},j} - f_{i-\frac{1}{2},j}}{\Delta \xi}; \quad \delta_\eta f = \frac{f_{i,j+\frac{1}{2}} - f_{i,j-\frac{1}{2}}}{\Delta \eta}$$

Linear multistep methods for the discretized conservation equations were investigated by Beam and Warming [70]. Practical applications are restricted usually to implicit one- and two- step methods. A general method of solution, based on two time levels, may be written as:

$$\frac{\hat{Q}^{n+1} - \hat{Q}^n}{\Delta t} + (1 - \Theta) \cdot Res(\hat{Q})^n + \Theta \cdot Res(\hat{Q})^{n+1} = 0 \quad (35)$$

For $\Theta = 0$ the scheme is explicit of $O(\Delta t)$, with $\Theta = 1/2$ the implicit Crank-Nicholson scheme, $O(\Delta t^2)$, and with $\Theta = 1$ the implicit Euler-backward scheme is achieved.

3.4.1 Implicit schemes

The formulation of an implicit scheme requires time linearization of the unknown fluxes in $Res(\hat{Q})^{n+1}$. This yields:

$$\begin{aligned} Res(\hat{Q})^{n+1} &= Res(\hat{Q})^n + \Delta t \cdot \frac{\partial}{\partial t} Res(\hat{Q})^n + \dots \\ &= Res(\hat{Q})^n + \frac{\partial Res(\hat{Q})}{\partial \hat{Q}} (\hat{Q}^{n+1} - \hat{Q}^n) \end{aligned} \quad (36)$$

The time linearization of the components of $Res(\hat{Q})^{n+1}$ result in the implicit scheme:

$$\begin{aligned} \left[\frac{I}{\Delta t} + \Theta \cdot \{ \delta_\xi \hat{A} + \delta_\eta \hat{B} - \frac{1}{Re} (\delta_\xi \hat{C} + \delta_\eta \hat{D}) \} \right] \Delta \hat{Q}^n \\ = -Res(\hat{Q}^n) \end{aligned} \quad (37)$$

with $\Delta \hat{Q}^n = \hat{Q}^{n+1} - \hat{Q}^n$, and \hat{A} , \hat{B} , \hat{C} , \hat{D} are the Jacobian of the corresponding fluxes \hat{F} , \hat{G} , \hat{S} and \hat{T} .

The discrete steady-state operator on the right hand side (RHS) is usually discretized higher order accurate with a numerical flux formulation, as described before. Thus the RHS determines the spatial accuracy of the solution. For time-accurate solutions, the implicit operator on the left hand side (LHS) has to be developed consistently to the RHS to achieve time accuracy. Then the LHS results in a penta-diagonal block matrix system for each direction.

For steady-state calculations, i.e. $RHS \rightarrow 0$, consistency in time is not required, and therefore the LHS can be manipulated to achieve faster convergence. To reduce the computational work, and to increase the diagonal-dominance of the solution matrix three point stencils are used for the LHS. Thus only systems of tridiagonal block matrices have to be inverted. Such approximations can be achieved in upwind methods by using first order upwinding for the LHS, partially with additional simplifications (e.g. spectral radius instead of complete eigenvalues [71]). This idea is also applicable to central schemes as shown e.g. in [71] or special damping terms are used there.

Even with such approximations for the LHS, the implicit scheme, Eq. (37) requires the inversion of a large system of difference equations. In general the direct inversion of the solution matrix for more than one dimension is too

expensive, therefore in the most of cases the matrix is solved in simpler, approximate steps, using factorization or relaxation methods.

The Approximate Factorization method (AF) by Beam and Warming, [70], was the mostly used implicit scheme in the seventies. The solution matrix is split in one-dimensional operators, which are sequentially inverted by a Gauss elimination method. For the present example, Eq. (37) with $\Theta = 0$, the solution steps of the AF method are:

$$\begin{aligned} \left[I + \Delta t \delta_\epsilon \left(\hat{A} - \frac{1}{Re} \hat{C} \right) \right] \Delta \hat{Q} &= -Res(\hat{Q})^n \\ \left[I + \Delta t \delta_\eta \left(\hat{B} - \frac{1}{Re} \hat{D} \right) \right] \Delta \hat{Q}^n &= \Delta \hat{Q} \end{aligned} \quad (38)$$

This method allows the inversion per time step in a non-iterative way, which is an interesting aspect for time-accurate computations.

The efficiency for steady-state solutions is restricted by the fact that the time step is limited to Courant numbers of $O(10)$ due to the factorization error in 2-D, and in 3-D the method becomes even unstable. However with appropriate formulations of the implicit operator successful algorithms were achieved, e.g. the ARC codes by Pulliam and Steger [72], the diagonalized AF method by Chausee and Pulliam [73], and in the ADI method by Briley and McDonald [74]. The factorization method is used e.g. Lombard et al. [75] for upwind schemes. Examples for the use AF- methods in unsteady viscous flows are given by Anderson et al. [76], by Davoudzadeh et al. [77] for rotating stall, by Kandil and Chuang [78] for oscillating delta wings, by Hosangadi et al. [79] for a forced combustor jet. In the latter paper the dual time approach, known from incompressible solutions, was employed additionally.

The Lower-Upper factorization methods (LU) use a somewhat different idea. In these methods the unfactored implicit operator is approximated by two factors L and U , representing a lower and an upper triangular matrix, and by a diagonal matrix D . For the present example the scheme would read:

$$(L D^{-1} U) \Delta \hat{Q} = -Res(\hat{Q})^n \quad (39)$$

Herein L contains all the unknowns at points $(i-1, j), (i, j), (i, j-1)$, and U the values for $(i+1, j), (i, j), (i, j+1)$, whereas D collects the values in the point (i, j) . The triangular matrices can easily be inverted and the system solved by forward and backward sweeping over the integration domain. The LU method requires strong diagonal-dominance, which can be achieved by first order upwinding on the LHS.

The 3-D Navier-Stokes equations and the $k-\epsilon$ turbulence equations were solved by Yokota [80] with a diagonally inverted LU factored implicit multigrid scheme. A numerical study of chemically reacting flows using a LU symmetric successive overrelaxation scheme was carried out by Shuen and Yoon [81].

An application to hypersonic flow is presented by Rieger and Jameson in [71], where the RHS is centrally discretized and the LHS is made diagonal-dominant by simple upwinding and solved by incomplete LU decomposition (ILU). Numerical experiments of the author and coworkers have shown a similar convergence behaviour of the LU method, used in [71], and of a 5-step Runge-Kutta scheme with implicit residual smoothing, but more

robustness for the ILU method could be stated at high Mach numbers.

Implicit relaxation methods

Relaxation schemes based on classical relaxation methods for elliptic equations (Gauss-Seidel methods) became an alternate, very efficient way for implicit schemes, since strong diagonal-dominant solution matrices could be achieved with the development of upwind schemes. The relaxation schemes make use of an iterative procedure to solve either iteratively the steady-state equations, or for the time-dependent equations an iterative procedure is used for each time step. Time-accurate solutions can be achieved, if the iterative solution converges for each time level. For steady-state solutions the time step is often used to increase the diagonal-dominance in the initial phase, later the time step is increased (to infinity) with decreasing RHS (residual), see e.g. Schröder, Hänel [49].

For the present example, Eq. (37), the iterative procedure from time level n to $n+1$ reads

$$\begin{aligned} \left[\frac{1}{\Delta t} + \delta_\epsilon \hat{A} + \delta_\eta \hat{B} - \frac{1}{Re} (\delta_\epsilon \hat{C} + \delta_\eta \hat{D}) \right]^n \Delta \hat{Q}^\nu \\ = -Res(\hat{Q})^n \end{aligned} \quad (40)$$

where the superscript ν is the iteration index and $\Delta \hat{Q}^\nu = \hat{Q}^{n+1, \nu} - \hat{Q}^n$. The iteration of equation (40) is performed by either a collective point or line Gauss-Seidel relaxation in alternating directions. The iterative procedure is stopped if $\max |\Delta \hat{Q}^{\nu+1} - \Delta \hat{Q}^\nu| \leq \epsilon$ where ϵ is a small number. If the solution matrix is sufficiently well-conditioned and diagonal-dominant the resulting solver becomes very robust and efficient for steady-state solutions since the time step is indeed unrestricted.

The use of relaxation methods has proved valuable in hypersonic flows, where robust behaviour of the methods is required. Results of hypersonic calculations with relaxation-type methods are presented e.g. by Candler and McCormack [82], Lacor and Hirsch [83], Schwane and Hänel [50], Riedelbauch and Brenner [84].

An interesting aspect of the relaxation scheme is that the iterative procedure per time step corresponds to a solution of a quasi-elliptic problem, which is challenging for the application of the multigrid methods, e.g. as used by Schröder, Hänel [49].

3.4.2 Explicit Methods

Among the numerous explicit methods for the solution of conservation equations, the Runge-Kutta time-stepping schemes are most popular member of explicit schemes at present.

Runge-Kutta time-stepping schemes

Considering the equation (33) as a semi-discrete approximation of the time-dependent Navier-Stokes equations, the time discretization can be carried out as a sequence of intermediate steps in the sense of the classical Runge-Kutta method. At present, a version of the Runge-Kutta method, as published by Jameson [85], is widely used for solutions of the Euler and Navier-Stokes equations. This version requires minimum computer storage, but can be extended only to second order accuracy in time. In the original papers central differencing with artificial damping was used, but also upwind schemes are applicable.

For a N-step Runge-Kutta method the scheme for equation (33) reads

$$\begin{aligned} Q^{(0)} &= Q^n \\ &\vdots \\ \Delta Q^{(i)} &= -\alpha_i \Delta t \text{Res}(\hat{Q}^{(i-1)}) \\ Q^{(i)} &= Q^{(0)} + \Delta Q^{(i)} \\ &\vdots \\ Q^{n+1} &= Q^N \end{aligned} \quad (41)$$

In calculations 3, 4, or 5-step Runge-Kutta schemes are employed, with a theoretical maximum Courant number of $N - 1$. The upwind scheme results in a slightly lower Courant number but with a better high frequency damping, which is of advantage for the multigrid treatment. To accelerate the convergence to the steady-state solution local time steps can be used which are dictated by the local stability limit and constant Courant number. The local time stepping allows a faster signal propagation, and thus faster convergence.

A second acceleration technique is the implicit residual smoothing [85], for which with appropriate smoothing coefficients the CFL number can be increased by a factor of two to three.

A further, now widely used acceleration technique, is the multigrid method, as proposed by Jameson [85] for the Runge-Kutta scheme. More details about multigrid are given in a later section.

Applications of the Runge-Kutta method to the 3-D Navier-Stokes equations are reported e.g. by Vatsa and Medan [58], Cima and Yokota [86], Radespiel, Rossow and Swanson [59] on structured grids, and by Mavriplis [26] on unstructured grids. Time-accurate calculations, using the Runge-Kutta method are given e.g. by Meinke and Hänel [87]. Refined formulations of different acceleration strategies can be found in these papers.

3.4.3 Methods on unstructured grids

Finite Element as well Finite Volume methods on unstructured triangulated grids enable geometrical flexibility and adaptive meshing for a high degree. Such methods have proved valuable for solutions of the Euler equations in complex 2-D and 3-D flows, e.g. [28], [25], [88]. The same concept applied to the compressible Navier-Stokes equations for high Reynolds numbers has been not so far developed as for inviscid flows. The major reason is the presence of very different scalings in viscous flows. This has the consequences of higher grid resolution, the directionality of gradients in viscous layers and the corresponding deformation of grid cells. Furtheron the implementation of frequently used algebraic turbulence models is more difficult than in structured grids. About the latter item an approach can be found in [89]. For these reasons attempts are made to combine structured meshes in viscous zones with unstructured meshes outside. Computations on such hybrid meshes are reported e.g. in [90], [91]. Another approach is to use structured meshes in one direction normal to the wall, where viscous terms are important, and in the other directions of a 3-D grid unstructured organization [92] is used.

Despite of the difficulties mentioned above (and because of the advantages against structured meshes) the number of computations for the Navier-Stokes equations on

fully unstructured meshes shows an increasing tendency. Navier-Stokes computations on unstructured grids are shown e.g. in [26], [93], [94], [95], [96] and many other more. A large number of 2-D and 3-D hypersonic applications of finite-element methods for reacting and non-reacting flows were presented by Periaux [97] and Mallet [98], summarizing the works of INRIA and AMD-BA in France.

For the solution of the Navier-Stokes equations on unstructured grids nearly all of the numerical flux approaches were used as known in structured grids. Typical approaches are central Runge-Kutta scheme with multigrid, e.g. Mavriplis [26], central two-step Lax-Wendroff scheme, e.g. [94], [96], Roe's flux-difference splitting, e.g. [99], van Leer's flux-vector splitting, e.g. [100], TVD Osher scheme, e.g. [101], flux-corrected transport approach, e.g. [95]. The methods of solution are explicit as well as implicit schemes, details can be found in the related papers.

Summarizing one can say that methods on unstructured grids for the Navier-Stokes equations have a great potential for geometrical complex flow problems and therefore, the number of applications will increase in the next future.

This is the reason why the author and coworkers have started a research project on grid-adaptive methods [102]. The aim of this project is the development of methods for Euler and Navier-Stokes equations on unstructured grids and comparison of the solutions with that achieved on structured grids. In a first step an adaption method was developed, which enables grid point enrichment, as well as adaptive cell orientation. Adaptive cell orientation means turning of the cells in accordance with the local gradient. The adaptive cell orientation, in addition to grid enrichment, has result in a remarkable improvement of capturing of shocks and slip lines. A demonstrative example is shown in Fig. 2 for a scramjet inlet model. The cells in the adapted shock regions show a distinct orientation normal to the velocity gradient, which was achieved by a gradient-weighted exchange of the cell edges. First results in Navier-Stokes solutions using this adaption techniques are promising.

3.4.4 Pressure-correction methods

Solution methods for the Navier-Stokes equations, based on a pressure correction, traditionally have been developed from methods for incompressible flow. These methods use the pressure as a main variable. They are characterized by the extraction of an equation for the pressure from the continuity equation. The change of density is then considered as a function of pressure, coupled by an equation of state. Many of the pressure-correction methods are developed from the SIMPLE algorithmus by Patankar and Spalding [5], [103]. Extension to compressible flow are presented e.g. by Issa and Lockwood [104], Rhie [105], Karki and Patankar [106] and others. The most of these methods are based on staggered grids, which avoid odd-even decoupling and therefore do not need artificial high-frequency damping. On the other side, formulations of staggered grids become complicated for general non-orthogonal grids.

The main advantage of these methods is the applicability to incompressible or very low subsonic flows, where other methods fail. However the spreading of acoustic waves,

and the Riemann problems, respectively, are strongly approximated due to the special treatment of the pressure, which results in insufficient shock capturing properties at higher Mach numbers. Ideas for improving the shock capturing capability of a pressure-correction method are reported and discussed by McGuirk and Page [107].

3.4.5 Multigrid methods

Multigrid methods are known to be very efficient methods for solving elliptic partial differential equations. The basic concepts of multigrid methods were formulated by Brandt [108],[109]. Encouraged by this success attempts were made to take up the multigrid concept in solution methods for time-dependent, parabolic or hyperbolic problems. Here, of very great interest are the numerical solutions of the conservation equations, which require a large amount of computational work for practical problems. Thus, to reduce the computational work, a number of investigations was made to incorporate the multigrid concept into existing methods of solution for the Euler and Navier-Stokes equations, as well.

A first multigrid approach for explicit Euler solutions was published by Ni [110]. It was generalized and extended to Navier-Stokes equations by Chima, Johnson [111].

A different multigrid concept was developed by Jameson and Baker [85] to accelerate the multi-stage Runge-Kutta scheme. This multigrid scheme has been used very successfully for 2-D and 3-D Euler computations on structured and unstructured grids, e.g. [32], as well for Navier-Stokes solutions [112], [26].

Multigrid can also be combined with implicit Euler solutions, as done e.g. by Hemker [113], Mulder [114] and others.

Navier-Stokes applications can be found e.g. in the paper of Shaw, Wesseling [115], Thomas et al [76], Schröder, Hänel [49], Hemker and Koren [116], [117], Radespiel, Swanson [118], Jameson, Sclari [112], Vatsa and Wedan [58], Abid and Vatsa [119], Radespiel, Rossow and Swanson [59], Mavriplis [26], Yokota [80], Gerolymos [120], Meinke and Hänel [87]. The state of art for multigrid is presented in special multigrid conferences, e.g. the "Copper Mountain Conference on Multigrid Methods", Copper Mountain, Colorado, and the "European Conference on Multigrid Methods", Bonn, Germany.

A common requirement for the application of multigrid formulations is the property of smoothing the high frequency error components by the scheme. This requirement is satisfied in principle by the use of upwind schemes or central schemes with controlled numerical damping. Then the multigrid concept can be applied to implicit and explicit methods and for solutions of the Euler and Navier-Stokes equations, as well.

Brandt [109] has developed a general strategy for the acceleration of nonlinear, iterative schemes, called Full Approximation Storage concept (FAS). The FAS concept is the basis of many multigrid approaches. For example the relations between Ni's, Jameson's and the FAS concept were studied by Chima et al. in [121]. This basic concept shall be briefly explained in the following.

The Full Approximation Storage concept (FAS), as proposed by Brandt [109], is a basic multigrid concept for nearly all of the applications. This concept is developed for the solution of nonlinear equations, and

therefore well suited for the conservation equations.

Consider a grid sequence $G_k, k = 1, \dots, m$ with the step sizes $h_k = 2h_{k+1}$ etc. A finite difference approximation $L_m Q_m = 0$ on the finest grid G_m may be represented after some solution (smoothing) steps by a modified difference approximation on a coarser grid G_{k-1} :

$$L_{k-1} Q_{k-1} = \tau_{k-1}^m \quad (42)$$

where τ is the "fine to coarse defect correction" and referred to as the "discretization error" in the following. It maintains the truncation error of the fine grid G_m on the coarser grids G_{k-1} and is defined by

$$\tau_{k-1}^m = \tau_k^m + L_{k-1}(I_k^{k-1} Q_k) - II_k^{k-1}(L_k Q_k) \quad (43)$$

where I and II are restriction operators from grid G_k to G_{k-1} which are applied to the variable Q_k and the difference approximation $L_k Q_k$, as well. These operators can be used as injection or full weighting operators.

On the coarse grid G_{k-1} equation (42) is solved and the transfer (43) is repeated for the next coarser grid until the coarsest grid is reached. After some solution steps on the coarsest grid the solution is interpolated back to the finer grids with some solution steps in between. According to the FAS scheme only the correction between the "old" fine grid solution Q_{k+1}^{old} and the "new" coarse grid solution Q_k is transferred to the fine grid e.g.:

$$Q_{k+1}^{new} = Q_{k+1}^{old} + I_{k+1}^{k+1}(Q_k - I_{k+1}^{k+1} Q_{k+1}^{old}) \quad (44)$$

Herein I_{k+1}^{k+1} is the interpolation operator, where so far only bilinear interpolation is used. The described multigrid procedure corresponds to a typical cycle (V-cycle). The boundary conditions on the coarser grid have to be corrected in the same way, but also simplifications of the coarse grid boundary conditions, like frozen conditions, were used in the literature.

Different formulations are possible for the restriction operator (fine to coarse grid). The best way is to update the coarse grid values by the values of the fine grid cells that make up one coarse grid cell. This yields the full weighting restriction, e.g. for the residual it is

$$II_k^{k-1} Res_k \hat{Q}_k = \sum_{\text{fine cells}} \beta Res_k \hat{Q}_k \quad (45)$$

where β is a weighting factor. The final formulation of the restriction operators depends on the mesh arrangement and on the degree of approximation of the multigrid scheme used.

Multigrid for implicit schemes can be used to reduce the large computational work of the matrix inversion each time step of an implicit scheme, as given in Eq. (40). Schröder, Hänel [49] have applied the FAS concept to the iterative matrix inversion of an upwind relaxation method, according to Eq. (40). By use of the upwind discretization the scheme becomes sufficiently dissipative. Then the iterative procedure corresponds to a solution of a discrete quasi-elliptic system, which guarantees an efficient use of the multigrid method. On a coarser grid G_{k-1} the relaxation procedure, Eq. (40) is approximated by Eq. (42)

$$LHS_{k-1}^n \Delta \hat{Q}_{k-1}^n + Res_{k-1}(\hat{Q}_{k-1}^n) = \tau_{k-1}^m \quad (46)$$

with the discretization error

$$\tau_{k-1}^m = \tau_k^m + LHS_{k-1}^n(I_k^{k-1} \Delta \hat{Q}_k^n) + Res_{k-1}(I_k^{k-1} \hat{Q}_k^n)$$

$$- \Pi_k^{h-1} [LHS_k^n \Delta \hat{Q}_k^n + Res_k \hat{Q}_k^n] \quad (47)$$

After some relaxation sweeps on every grid level including the coarsest one, the correction $\Delta \hat{Q}_k^n$ (not $\hat{Q}^{n+1,n}$) is interpolated back to the finer grids according to Eq. (44), followed by one relaxation sweep on each grid to smooth the interpolation errors. The V-cycle is completed after the finest grid is reached and in general the next time step is carried out after one or two V-cycles. The method was applied to the 2-D Navier-Stokes equations in curvilinear grids. Different viscous, subsonic and supersonic flow problems were studied in [49]. The estimated gain against single-grid methods was a factor between two and twenty, depending on the flow problem and on the mesh. Multigrid concepts for implicit Euler or Navier-Stokes solvers were used e.g. by Hemker [113], Mulder [114], [113], [114], Shaw, Wesseling [115], Thomas et al [76], Schröder, Hänel [49], Hemker and Koren [116] and others.

Multigrid for explicit schemes is employed directly on the time-dependent solution. The time advances also on the coarser grids. Applied to an explicit scheme the advantage of multigrid is twofold: first, computational time is saved because of the smaller number of grid points on the coarser grids and second, the time steps restricted by the numerical stability can be chosen larger on the coarser grids. This concept can likewise be used for implicit methods.

The principle for explicit method will be discussed briefly by means of the formulation of Meinke and Hänel in [117], [87]. Herein the FAS concept is applied to the explicit Runge-Kutta time-stepping method and used in steady-state and in time-dependent solution of the 2-D Navier-Stokes equations. In a similar manner the multigrid method was successfully used e. g. by Jameson [85] for steady-state Euler calculations. In the studies [117] the Runge-Kutta scheme was used with flux-vector splitting, and with node-centered and cell-vertex central schemes, as well.

Employing the FAS-multigrid procedure, Eq. (42), to the Runge-Kutta scheme, Eq. (41), an intermediate Runge-Kutta step on a coarser grid reads:

$$Q_{k-1}^{(i)} = Q_{k-1}^{(0)} - \alpha_i \Delta t_{k-1} (Res_{k-1} Q_{k-1}^{(i-1)} - \tau_{k-1}^m) \quad (48)$$

The discretization error τ between the fine grid "m" and the coarse grid "k-1" can be split in a time correction and a space correction term:

$$\tau_{k-1}^h = (\tau_{k-1}^h)_{Res} + (\tau_{k-1}^h)_{time} \quad (49)$$

The first part of the discretization error corrects the spatial accuracy on the coarser grid and is defined by:

$$(\tau_{k-1}^{h-1})_{Res} = Res_{k-1} (I_k^{h-1} Q_k) - \Pi_k^{h-1} Res_k (Q_k) \quad (50)$$

The second term preserves the time accuracy on the coarser grids. Approximating the time derivative of Q in the Runge-Kutta algorithm by $\Delta Q / \Delta t$ the term can be written as:

$$(\tau_{k-1}^{h-1})_{time} = \frac{[I_k^{h-1} (Q_k(t^n) - Q_k(t^n - \Delta t_{k-1}))]}{\Delta t_{k-1}} - \Pi_k^{h-1} \left[\frac{Q_k(t^n) - Q_k(t^n - \Delta t_k)}{\Delta t_k} \right] \quad (51)$$

where t^n is the time when the grid level is changed.

For computations of steady-state solutions, simplifications of the multigrid procedure are allowed as long as the steady-state solution is not impaired. Based on this multigrid algorithm the influence of different multigrid parameters were studied in [117], [121] for steady solutions. Typical parameters are e.g. the high frequency damping properties of the basic solver, the grid arrangement, the coarse correction, the coarse grid boundary conditions, the multigrid cycle, the cell aspect ratio and many other more.

The combination of multigrid and Runge-Kutta scheme has become very popular for the solution of two- and three-dimensional conservation equations. Examples for a wide range of applications are given by Radespiel, Swanson [118], Jameson, Siclari [112], Vatsa and Wedan [58], Abid and Vatsa [119], Radespiel, Rossow and Swanson [59], Mavriplis [26], Yokota [80], Gerolymos [120] and others.

Time-accurate multigrid computations require the consequent FAS formulation of the coarse grid correction and the boundary conditions. The present studies have shown that multigrid methods can be used with advantage in highly unsteady flows, like e.g. for vortex shedding on a cylinder by Meinke and Hänel [87].

Summarizing, the multigrid concept can be applied to explicit and implicit solutions of conservation equations with advantage. The gain of computation time by multigrid was found to be high in subsonic and transonic flows. This gain is higher in Euler solutions, but still favourable in Navier-Stokes computations for compressible flow. For the latter a factor of gain between two and ten was reported by different researchers. One reason for that are the high aspect ratios of computational cells, if computing flows at high Reynolds number. Another handicap for multigrid methods can be stated in strongly supersonic (hypersonic) flow, where the solution is hyperbolic in space, and therefore it is in contrast to the "elliptic" multigrid concept. An example for using multigrid in hypersonic flow was presented e.g. by Siclari, Jameson [112].

4 On the accuracy of Navier-Stokes solutions

Methods of solution for the Navier-Stokes equations are usually constructed by adding the viscous terms to a reliable and stable working Euler solver. In general this combination results in efficient Navier-Stokes solvers, stable even for high Reynolds numbers, and well suited for resolving the inviscid flow features. However the Euler solvers generate a certain amount of numerical dissipation, necessary for stabilizing and smoothing the solution. This dissipation is superposed on the physical dissipation in viscous layers, and can impair the solution there. Beside of the numerical dissipation, caused by the truncation errors, other elements of the numerical solution, like grid arrangement and numerical flux formulations, can play a similar role. These effects are summarized as effects of discretization errors.

The aim of this section is to discuss some of such effects in solutions of the Navier-Stokes equations. To do that, a study of the basic discretization schemes for the Euler equations, and inherent sources of numerical dissipation in central and high-resolution schemes is necessary. The

consequences for solutions of the Navier-Stokes equations are considered for steady-state and unsteady solutions, as well.

4.1 Numerical dissipation in Euler solutions

As stated before, the quality of a Navier-Stokes solution is essentially influenced by the numerical dissipation caused by the Euler discretization. The Euler equations are a nonlinear, hyperbolic system of partial differential equations. Two classes of solutions exist, the strong continuous solutions describing the non-dissipative wave transport along characteristics, and the weak, discontinuous solutions, e.g. shocks. An efficient numerical method of solution should resolve both classes of solutions sufficiently well.

Although the exact Euler solutions do not show dissipative behaviour, their numerical approximations always show such effects. Discretizing the Euler equations, the resulting truncation error of the approximation consists of even and odd higher order derivatives, which cause dissipative and dispersive errors in the numerical solution. Particularly the dissipative parts act viscosity-like and cause smearing of the solution and artificial vorticity production. Therefore the aim of the numerical approximation should be to minimize the amount of numerical dissipation.

On the other side a certain amount of numerical damping is necessary to avoid the accumulation of randomly distributed small errors (e.g. round-off errors) during the time or iteration progress. In general, these errors are distributed with smallest resolvable wave length which is in the order of the step sizes. Therefore damping terms have to filter these error components. A widely used approach for such high frequency damping terms is to use fourth order differences, which have a sufficient filter effect and are small of $O(\Delta x^3)$ in smooth solutions. These high frequency damping terms are efficient filters in smooth regions, but fail in regions of captured, stronger discontinuities. Due to the strong changes over a few grid points, stronger oscillations are generated e.g. near a shock by frequency amplification of the nonlinear convection terms. To suppress these oscillations additional shock capturing terms have to be implemented in Euler solvers. Usually, such terms are based on second order differences with a nonlinear viscosity-like coefficient, which activates a strong dissipation within the "shock layer", but vanishes outside in smooth regions.

Both types of damping terms are essential parts of each numerical flux formulation. These terms are either internally generated by the scheme, e.g. in upwind schemes or must be added artificially as in central schemes.

Central schemes are widely used for approximating the Euler equations. However these differences do not result in dissipative truncation errors, therefore artificial damping terms have to be added. In general, the damping formulations consist of a linear fourth order term $d^{(4)}$ and of a nonlinear term $d^{(2)}$, as described in the previous section. The effect of the damping terms becomes evident, when considering the truncation error. Applying the numerical formulation, Eq. (29), to the linear, hyperbolic model equation $Q_t + Q_x = 0$, the truncation

error in space is:

$$\tau_s = (\epsilon^{(2)} \frac{\Delta x}{\Delta t}) \Delta x \cdot Q_{xx} - \frac{1}{6} \Delta x^2 \cdot Q_{xxx} - (\epsilon^{(4)} \frac{\Delta x}{\Delta t}) \Delta x^3 \cdot Q_{xxxx} + \dots \quad (52)$$

Assuming the Courant number $\frac{\Delta x}{\Delta t}$ being $O(1)$, then the artificial damping terms (even derivatives) are of order $O(\Delta x)$, and $O(\Delta x^3)$, resp.. The terms with odd derivatives correspond to dispersive errors caused by the central formulation.

Upwind schemes e.g. flux-vector splitting or flux-difference splitting, take the advantage of the hyperbolic properties in form of an approximated discrete Riemann problem. In general they are used with higher order accurate upwind discretization. Nearly oscillation-free solutions and sharp shock representation is achieved using flux limiters, e.g. in the MUSCL extrapolation (26). The limiter functions φ are elements of the numerical flux, which limit the higher order extrapolation to suppress numerical oscillations. Common to all of these limiter formulations is that they react on the changes of the local gradient of the variables. Thus in regions of weak changes the limiter remains nearly one, but for strong changes the value decreases, the scheme reduces the accuracy, and stronger numerical dissipation is generated. This can be demonstrated by means of the spatial truncation error, analogous to Eq. (52) by applying the extrapolation (26) to the linear model equation $Q_t + Q_x = 0$. The truncation error for Q_x yields:

$$\tau_s = (1 - \varphi) \frac{\Delta x}{2} Q_{xx} - [1 - \frac{3}{2} \varphi (1 - \kappa)] \frac{\Delta x^2}{6} Q_{xxx} - [3(\varphi - \kappa) - (1 - \varphi)] \frac{\Delta x^3}{24} Q_{xxxx} + \dots \quad (53)$$

Similar truncation errors arise from the flux-difference splitting concept and other approximate Riemann solvers.

The truncation errors for a linear model equation, e.g. Eq. (52) and (53) reveal common properties of the different numerical flux formulation. Each truncation error consists essentially of three parts, a shock capturing term $\sim \Delta x Q_{xx}$, a dispersive term $\sim \Delta x^2 Q_{xxx}$, and a high frequency filter term $\sim \Delta x^3 Q_{xxxx}$.

The shock capturing term is controlled by a nonlinear function, a pressure dependent term in central schemes or limiters in high resolution schemes. The nonlinear function reduces the capturing term to at least second order accuracy in smooth regions, but generates first damping near extrema (shocks). The latter effect results in a sharp, non-oscillating resolution of embedded shocks. In viscous layers, however, where strong changes are also present, this term is also activated, since the algorithm cannot distinguish between the large gradients in shocks and in boundary layers. Thus the shock capturing term can significantly impair the viscous solution.

The high frequency filter term of accuracy $O(\Delta x^3)$ is fixed by an user specified constant in central schemes or by the upwind formulation in high resolution schemes. It filters the undesired high frequency error components, but in viscous flows with small viscous scale lengths, it can also suppress small-scale vortical structures. An example for that is given later.

4.2 Numerical influence in viscous solutions

Navier-Stokes solvers are a combination of Euler solver and viscous terms. But in contrast to inviscid flows, the solutions of the Navier-Stokes equations contain very different characteristic scale lengths with corresponding different types of solution. Typical are thin viscous layers with continuously, but strongly changing flow quantities, and large nearly inviscid flow portions with discontinuous solutions. Discontinuities arise from the fact, that the very thin viscous shock structures are not resolved in general. Thus, the solution of the Navier-Stokes equations require good shock capturing properties of the Euler solver and a high accuracy in viscous regions, as well. These requirements are often contradictory, in particular when inviscid and viscous terms are nearly balanced. The most of the Euler solvers work well for inviscid flow problems, mainly due to the implemented damping mechanisms. However these mechanisms usually cannot distinguish between strong gradients in a captured shock and in a boundary layer. Thus in viscous layers, where strong changes of gradients occur, the numerical dissipation can become large and is superposed to the physical viscous effects. This fact can impair essentially the accuracy of the viscous solution. Therefore it is necessary to know the sources of damping in solvers, and to minimize their effects in viscous layers. Important sources of numerical errors can be:

- different upwinding (central to fully upwind)
- limiter functions
- artificial damping terms
- numerical flux formulations
- numerical representation of eigenvalues
- grid stretching and skewing
- numerical boundary conditions, etc.

In general all of these effects are interacting and thus cannot be considered isolated. Therefore numerical experiments and comparisons with other results are useful means to investigate the effects. In the following discussion a number of results demonstrate the influence of different numerical Euler schemes on steady and unsteady viscous flow solutions.

Viscous steady-state solutions

The accuracy of steady-state solutions is mainly governed by the spatial discretization and their corresponding discretization errors. Considering the classical central schemes, Eq. (29), with linear fourth order and nonlinear second order terms the investigations have shown a sufficient spatial accuracy for the boundary layer solution. The reason may be that the linear damping term can be held small per external parameters, and the nonlinear terms controlled by the curvature of the pressure, remain small in shear layers where the normal pressure changes are small. However in boundary layers with strong adverse pressure gradients the deviations become stronger and require a careful analysis.

More attention has to be paid for the high-resolution Euler schemes within a Navier-Stokes solver. Such schemes are very well suited for capturing gasdynamical wave

phenomena by using local approximate Riemann-solvers, higher order upwinding, and TVD flux limiters. The different damping mechanisms are included in the numerical flux formulation, and therefore they cannot be controlled directly by the user.

The numerical damping in Navier-Stokes solutions is mainly caused by the spatial discretization errors of the Euler terms, given by Eq. (52) and (53). The fourth order terms filter essentially the high frequency terms and thus they suppress the smallest physical scalings arising in viscous flows. This effect becomes apparently in highly unsteady flows as shown later. Generally it can be stated, the stronger the upwinding, even higher order, the stronger the dissipative effects.

The second order terms act viscosity-like and reduce the nominal Reynolds number. These terms are mainly controlled by the flux limiters of the upwind schemes, therefore their effects in viscous flows must be studied critically.

The flux limiters react upon the curvature by reducing the higher order terms, which leads in smooth regions to an undesired numerical dissipation. Their influence on a scalar model problem and on Navier-Stokes solutions for laminar boundary layers were studied e.g. in [63]. Concluding from these results, limiter formulations for computations of viscous flows should be less dissipative, which means a weaker reaction on changes. This behaviour is reflected in particular in Navier-Stokes solutions for laminar flows, whereas in turbulent shear layers damping effects from upwinding and from limiters were found to be less critical [52], because of the much stronger turbulent viscosity. Nevertheless the limiter can have significant influence on the results for more complex turbulent flows, e.g. for transonic flows around airfoil. As an example for that, Fig. 3 shows the pressure distribution for transonic flow over a RAE 2822 airfoil [52]. Both results are achieved with a flux-difference scheme in the same grid. The difference in both numerical results were different limiters. In one case a more compressive (less dissipative) minmod-limiter ($\omega = 2$) was used, resulting in a lift and drag coefficient of $c_l = .814$ and $c_d = .0184$. This test case was recomputed with the less compressive Roe limiter ($\omega = 1$) and yields $c_l = .812$ and $c_d = .0203$, an increase of drag of more than 10% by changing the limiter only. The increase of drag stems essentially from the suction peak near the leading edge, where the limiters are activated differently by strong flow gradients. This influences the pressure and thus indirectly the boundary layer. This effect has found to be very crucial for the prediction of drag.

Upwinding and limiters belong to the projection step to update the cell interface values for the evolution of the numerical fluxes.

The formulation of the numerical Euler fluxes

has essential influence on the accuracy in viscous layers. The Euler fluxes represent a composition of information transported along characteristics (eigenvalues of the flux Jacobians) from different directions (signs). Numerically the direction is expressed by left or right extrapolated variables. Depending on the decomposition (flux splitting) the eigenvalues are not always correctly represented by the numerical flux, in particular if they approach zero. The field of linear eigenvalue $\lambda = \bar{v}$ plays a special role

in viscous shear layers, which can be considered as weak tangential discontinuities. The entropy and the tangential momentum is transported along the corresponding characteristics. If they are not correctly represented, then an artificial source flow is induced, which generates dissipation-like effects.

This was found to be an essential reason why van Leer's flux-vector splitting becomes very dissipative in viscous layers, [50]. The dissipation of the flux-vector splitting could be reduced remarkably by introducing one-sided extrapolation of the tangential velocity according to the sign of velocity normal to a cell interface (and later after an idea of van Leer [51] for the total enthalpy, as well [52]). The improved accuracy is demonstrated in Fig. 4 for the skin friction over a flat plate by comparison with the original formulation by van Leer. The same modification of van Leer's splitting is used in 3-D solutions of the Navier-Stokes equations for hypersonic flow over a double-ellipsoidal body [50]. Fig. 5a and 5b show vectors of the local skin friction on the body using the same, relatively coarse mesh, but computed with the original splitting (left), and with the modification (right) from [50]. The remarkable difference between both figures is the reattachment zone on the "canopy", which could be resolved by the computations using the modified fluxes in agreement with experiment.

Another significant influence of the numerical flux formulation in context with van Leer's splitting was noticed in supersonic blunt-body calculations where significant deviations of the computed wall temperature were found in regions of large Mach number gradients [63]. Investigations have shown that this effect is caused mainly by the non-preservation of the total enthalpy H_t using the original split energy flux. This effect is removed substantially by using an alternate split energy flux [63]:

$$F_3^\pm = F_1^\pm \cdot H_t \quad (54)$$

where the enthalpy H_t is transported as a whole by the split mass fluxes F_1^\pm . It has the advantage of being simpler and of being generally valid also in the case of real gases. The improvement of the accuracy by this formulation is clearly demonstrated in Fig. 6 for the wall temperature distribution over an 3-D hemisphere-cylinder body. The idea of this alternate split energy flux, Eq. (54), was extended to generalized flux-vector formulations in [47]. Using this change of split energy flux a better preservation of total temperature could be stated.

The flux-difference splitting of Harten and Yee [39] which is based on the Riemann approach recognizes all different eigenvalues, but it is not free of such effects mentioned above. The entropy correction δ , Eq. (25), which prevents the eigenvalues from diminishing, should be applied to the non-linear eigenvalues to rule out expansion shocks, but is often used for the linear eigenvalues as well to improve the stability of the scheme. However the application to the linear eigenvalues results in similar dissipative effects as found for the flux-vector splitting in viscous layers. The consequences of the entropy correction for viscous transonic flow were investigated by Seider and Hänel in [52] and remarkable effects could be stated, in particular for the drag. To clear up this behaviour numerical experiments were conducted for the flat plate laminar boundary layer. The Fig. 7 shows the skin friction over the plate for different values of the entropy correction δ . With increasing δ the skin friction value deviates from

the Blasius solution with the same tendency as for van Leer's flux-vector splitting in Fig. xxx. Concluding from these results the entropy correction δ for linear eigenvalues should be minimized in viscous flows, in particular across the layers.

These effects of numerical fluxes, in particular the approximate treatment of the eigenvalues, can be remarkable in the formulation of the no-slip conditions at a wall too, as shown e.g. in [64].

In viscous steady-state flow the most of these dissipative effects can be reduced by a better resolution of flow field.

Unsteady viscous flows

Viscous, time-dependent flows are of great importance in fluid mechanics. Typical unsteady problems in turbomachinery are discussed in many papers, e.g. in AGARD proceedings [122] and VKI lectures [123].

The viscous flows can become unsteady either by external excitation or self-induced by interactions between viscous and inviscid forces. Examples for the latter, which are more complicated and thus more critical, are e.g. the formation of a Karman vortex street, the vortex breakdown or the simulation of turbulent flows. Such unsteady flows react very sensitive to small disturbances, physically and numerically, as well. They are characterized by different scale lengths in time and space. Therefore, numerical simulations of these flows require much more care, but also a larger computational effort than an equivalent stationary problem. The temporal accuracy of a numerical solution is strongly related to the spatial accuracy, and therefore in time-dependent computations the spatial resolution plays an important role. But the numerical error can hardly be estimated since both the spatial and the temporal discretization errors influence the time resolution. Furthermore due to the different scale lengths in time and space, an analysis by means of scalar model equations is not sufficient to explain the numerical behaviour of a Navier-Stokes solution. Therefore numerical experiments with solutions of the Navier-Stokes equations can clear up the influence of numerical discretization on the time behaviour.

As long as the scalings in time and space are large compared to the stepsizes, the solutions appear reliable and accurate for the different methods. An typical example for that is the flow around an impulsively started cylinder. Downstream of the cylinder one closed wake is developing. Comparison of its length over the time in Fig. 8 shows close agreement for different methods of solution. However these flow situation alters essentially at a later time or higher Reynolds number, when self-induced separation and formation of a vortex street occur. This flow is a typical test example for highly unsteady and vortical flow. The streaklines of such flow are plotted in Fig. 9. The unsteady separation on the body starts with very small vortices which are growing in time. Due to the fact that numerical dissipation acts filter-like on small scalings, the temporal development of the flow is essential influenced by the scheme and the grid. The numerical influence on the unsteady flow around a cylinder was studied e.g. by Meinke and Hänel [124]. In this paper different grids as well as different solvers, central schemes and flux-vector splitting and multigrid, [87], were used. As an example Fig. 10 shows the lift coefficient over time for several periods for a Reynolds number of 3000 and a

Mach number of 0.3. The flow corresponds to the streaklines shown in Fig. 9.

Grid stretching, in particular in circumferential direction, has been found to be a reason for a unsymmetrical development of the vortex street resulting in a non-vanishing averaged lift coefficient, (Fig. 10a). The vortex street appears then to be shifted above or below the axis of symmetry of the flow. In contrast to Fig. 10a, the lift in Fig. 10b, computed on an equidistant grid (in circumferential direction) results in an vanishing mean value.

The artificial dissipation of the central schemes damps or even suppresses the small scale vortices, and thus influences the further development of the flow. Fig. 10b and 10c shows two time histories of the lift coefficient for two different parameters of the fourth order damping terms. Both the Strouhal number and the amplitude are influenced strongly by the variation of the numerical dissipation. Similar effects were found by Dortmann [34] for laminar separating flow over airfoils.

Similar deformations of the vortex street could be stated if changing the discretization schemes, which were found to be stronger for an upwind scheme than for a central scheme.

The present examples have shown a very large influence of the numerical damping in unsteady solutions. The difficulties of computing viscous unsteady flows grow with increasing geometrical and physical complexity. This refers to three-dimensional problems, as well to strong vortical flow, where the scalings can reach the scalings of turbulent eddies. Such problems cannot be solved sufficiently accurate at present.

Conclusions

An attempt is made to review computational techniques for solutions of the Navier-Stokes equations for compressible flows. The most of methods as discussed here are methods developed and applied for external flows. But also typical approaches for internal flows are mentioned. A concentration on external flow solvers is motivated by the fact that major trends in CFD were first employed to external flows, but are likewise coming up in propulsion technique.

Propulsion technique covers a wide field of different flows, from low subsonic to high supersonic flow. Viscous effects at moderate upto high Reynolds numbers play an important role. There is no universal algorithm for accurate and efficient prediction of the whole flow range. Therefore, approximations of the Navier-Stokes equations as well as adaptations of the methods to specific flow ranges are used with advantage.

Space marching methods for the Parabolized Navier-Stokes equations are fast and fairly accurate in absence of streamwise separation. They are used for internal flows in ducts and turning bends but also for supersonic, external flows. An extension of the Parabolized Navier-Stokes equations to weak separating flow is given by the Reduced Navier-Stokes equations, for which the pressure is treated as elliptic. However these approximations are strongly restricted in their physical validity.

More general are the Full Navier-Stokes equations, and the Thin Layer approximation of the Navier-Stokes equations. Both equations are solved with identical methods.

Pressure correction methods for the Navier-Stokes equations are well suited for subsonic, and even for incompressible flow. But work remains to be done to extend these methods to higher Mach numbers, where improved shock capturing capability is required.

Methods based on the time-dependent Navier-Stokes equations make up the majority of computational methods and are the topic of numerical research. The current status of these methods is quite advanced, which is a result of intensive developments for improved Euler solvers. These methods are able to deal with subsonic flow, but also with high speed flow and distinct gasdynamic phenomena, and even with non-equilibrium situations. A variety of different approaches can be found in the literature.

Differences are given by the use of structured or unstructured meshes. Structured meshes enable very efficient and accurate methods of solution, therefore they form the majority of present-days methods. But the better geometrical flexibility and grid adaptivity are arguments for growing use of Navier-Stokes solvers on unstructured meshes. For both concepts the Finite Difference/ Finite Volume methods as well Finite Element methods are used widely.

The numerical flux formulation of the underlying Euler solver is the most essential part of a Navier-Stokes solver. The central schemes, in particular the artificial damping formulation, are highly developed and applicable to subsonic, transonic and moderately supersonic flows, as well. They are computationally less expensive than high resolution upwind schemes. But upwind schemes can capture strong shocks and complex waves in a more accurate way and therefore they are recommended for flows, where such inviscid phenomena dominate. The better capturing quality has also to be taken into account if strong viscous-inviscid interactions are present.

Implicit as well explicit algorithms are commonly used for the solution of the algebraic system of discretized equations. Implicit schemes, factorization and relaxation methods, are better suited for stiff equations with many disparate length scales, and in solutions with strong changes as in hypersonic flows. For steady-state solutions the explicit schemes with acceleration techniques, in particular with multigrid, become comparable to implicit schemes with respect to the convergence rate.

Despite of the highly sophisticated methods for Navier-Stokes equations the numerical solution remains an approximation of the governing differential problem. To achieve reliable solutions much care has to be taken of the influence of grid resolution and of the numerical scheme on the accuracy. Numerical dissipation is an essential mechanism for stable shock-capturing Euler schemes. In Navier-Stokes solutions the numerical dissipation, caused by the Euler solver, is superposed on the physical dissipation which impairs the viscous solution. Some of typical effects were discussed and demonstrated by number of computational examples. The influence of numerical scheme and grid on viscous solutions become more critical when the smaller scalings are not resolved sufficiently or modeled.

This review has shown the variety of different numerical approaches to predict viscous, compressible flows. The accuracy of the numerical solutions depends on many factors as they are the physical approximation, the numerical modeling, and not to forget, the understand-

ing and experience of the numerical "experimentalist". Therefore, the computational methods need to be validated by analytical and experimental test cases, but also by comparison with other methods. Collections of test cases can be found in the literature for different specific flow problems. An important presentation of test cases for internal flows in aero engines is provided by the AGARD in [125].

References

- [1] Schiff, L.B., Steger, J.L.: Numerical Simulation of Steady Supersonic Viscous Flow. AIAA-paper, No. 79-0130, (1979).
- [2] Vigneron, Y.C., Rakich, J.V., Tannehill, J.C.: Calculation of Supersonic Viscous Flow over Delta Wings with Sharp Supersonic Leading Edges. AIAA-paper, No. 78-1137, (1978).
- [3] Menne, S.: Split-Matrix Marching Methods for Three-Dimensional Viscous and Inviscid Hypersonic Flows. Notes on Numerical Fluid Mechanics, vol 29, Vieweg Verlag, (1990).
- [4] Rubin S.: A Review of Marching Procedures for PNS Equations. 1st Symp. on Num. and Phys. Aspects of Aerodynamic Flows, pp. 171-186, Springer (1980).
- [5] Patankar S. V., Spalding D. B.: A Calculation Procedure for Heat, Mass and Momentum Transfer in Three-Dimensional Parabolic Flow. Int. J. of Heat and Mass Transfer, vol. 15, pp. 1787-1806, (1972).
- [6] Briley W. R.: Numerical Method for Predicting Three-Dimensional Steady Viscous Flow in Ducts. J. Comput. Phys., vol. 5, pp. 205-218, (1977).
- [7] Ghia U., Ghia K. N., Staderus C. J.: Three-Dimensional Laminar Incompressible Flow in Straight Polar Ducts. Comput. Fluids, vol. 5, pp. 205-218, (1977).
- [8] Govindan T. R., Lakshminarayana B.: A Space-Marching Method for the Coputation of Viscous Internal Flows. Computer & Fluids, vol. 16, pp. 21-39, (1988).
- [9] Cline D. D., Carey G.F.: Shock Sensitivity in Parabolized Navier-Stokes Solution of High Angle-of-Attack Supersonic Flow. AIAA Journal, vol. 28, pp. 406-413, (1990).
- [10] Moore J., Moore J. G.: A Calculation Procedure for Three-Dimensional Viscous Compressible Duct Flow. ASME J. of Fluids Eng., vol. 101, pp. 415-422, (1979).
- [11] Pratap V. S., Spalding D. B.: Fluid Flow and Heat Transfer in Three-Dimensional Duct Flows. Int. J. Heat and Mas Transfer, vol. 19, pp 1183-1188, (1976).
- [12] Lai H. T., Khosla P. K.: Global Pressure Relaxation Procedure for Compressible Turbulent Strong Interaction Flows. Comp. & Fluids, vol. 16, pp 217-228, (1988).
- [13] Zhu Z., Fletcher C. A. J.: A Study of Sequential Solutions for the Reduced/ Complete Navier-Stokes Equations with Multigrid Acceleration. Computers & Fluids, vol. 19, pp. 43-60, (1991).
- [14] Power, G.D., Barber, T.J.: Analysis of complex hypersonic flows with strong viscous/inviscid interaction. AIAA-J., vol. 26, No. 7, pp 832-840. (1988).
- [15] Vincenti, W., Kruger, C.: Introduction to Physical Gasdynamics. Wiley and Sons, Inc., New York. (1967).
- [16] Srinivasan, S., Tannehill, J.C., Weilmuenster, K.J.: Simplified curve fits for the thermodynamic properties of equilibrium air. NASA RP 1181. (1987).
- [17] Liu Y., Vinokur M.: Equilibrium Gas Flow Computations. I Accurate and Efficient Calculation of Equilibrium Gas Properties. AIAA paper No. 89-1736, (1989).
- [18] Bird, R.B., Stewart, W.E., Lightfoot, E.N.: Transport Phenomena. Wiley and Sons, Inc., New York. (1960).
- [19] Srinivasan S., Tannehill J.C., Weilmuenster K.J.: Simplified Curve Fits for the Transport Properties of Equilibrium Air. Iowa State Univ., ISU-ERI-Ames 88405, (1987).
- [20] Baldwin, B.; Lomax, H.: Thin Layer Approximation and Algebraic Model for Separated Turbulent Flows. AIAA-paper, No. 78-257, (1978).
- [21] Vandromme D.: Turbulence Modelling and Implementation in Navier-Stokes Solvers. VKI Lecture Series LS 1989-06, von Karman Institut for Fluid Dynamics, Rhode-Saint-Genese, (1989).
- [22] Dutt, P.: Stable Boundary Conditions and Difference Schemes for Navier-Stokes Equations. ICASE report No. 85-37, (1985).
- [23] Nordström, J.: Energy Absorbing Boundary Conditions for the Navier-Stokes Equations. In: Lecture Notes in Physics, vol 264, Springer Verlag. (1986).
- [24] Lax, P.D., Richtmeyer, R.D., Comm. on Pure and Appl. Math., vol 9, (1956).
- [25] Baker, T.J., Jameson, A.: Improvements to the Aircraft Euler Method, AIAA paper No. 87-0452. (1987).
- [26] Mavriplis D. J., Jameson A.: Multigrid Solution of the Navier-Stokes Equation on Triangular Meshes. AIAA Journal, vol. 28, pp. 1415-1425, (1990).
- [27] Nakahashi, K., Deiwert, G.S.: Self-Adaptive Grid Method with Application to Airfoil Flow. AIAA-1 vol 25, pp. 513-520, (1987).
- [28] Löhner, R., Baum, J.D.: Numerical Simulation of Shock Interaction Using a new Adaptive H-Refinement Scheme on Unstructured Grids. AIAA paper No. 90-0700, (1990).
- [29] Ramakrishnan R., Bey K.S., Thornton E. A.: Adaptive Quadrilateral and Triangular Finite Element Scheme for Compressible Flow. AIAA Journal, vol. 28, pp. 5159. (1990).
- [30] Thompson, J.F., Warsi, Z., Mastin, C.W.: Numerical Grid Generation, Foundations and Applications. Pub. North-Holland. (1985).
- [31] Weatherill, N.P.: Mesh Generation in Computational Fluid Dynamics. VKI Lecture Series LS

- 1989-04 on Comp. Fluid Dynamics, von Karman Institut for Fluid Dynamics, Rhode-Saint-Genese, (1989).
- [32] Jameson, A., Baker, T.J.: Euler Calculations for a Complete Aircraft. *Lecture Notes in Physics*, vol. 264, Springer-Verlag Berlin, (1986).
 - [33] Rossow C.: Comparison of Cell Centered and Cell Vertex Finite Volume Schemes. In: Deville, M. (Ed.), *Notes on Numer. Fluid Mech.*, vol 20, pp. 327-334, Vieweg Verlag (1988).
 - [34] Dortmann, K.: Computation of Viscous Unsteady Compressible Flow about Airfoils. In: *Proc. of the IC 11 NMFD, Lecture Notes in Physics*, Springer Verlag, (1989).
 - [35] Löhner, R., Morgan, K., Zienkiewicz: The Solution of Non-Linear Hyperbolic Equation Systems by the Finite Element Method. *Int. J. of Numer. Methods in Fluids*, vol. 4, pp. 1043-1063, (1984).
 - [36] White D. W., Abel J. F.: Bibliography on Finite Elements and Supercomputing. *Com. in Applied Numerical Methods*, vol. 4, pp. 279-294, (1988).
 - [37] van Leer, B.: Towards the Ultimate Conservative Difference Scheme. A second-order sequel to Godunov's method. *J. Comp. Phys.* vol.32, pp.101-136, (1979).
 - [38] Harten, A.: High Resolution Schemes for Hyperbolic Conservation Laws, *J. Comp. Phys.*, vol. 49, pp. 357-393, (1983).
 - [39] Yee H. C.: A Class of High-Resolution Explicit and Implicit Shock-Capturing Methods. In: *VKI Lecture Series 1989-04, Rhode-Saint-Genese*, (1989). also: Yee H. C.: Upwind and Symmetric Shock-Capturing Schemes. NASA TM-89464, (1987).
 - [40] Godunov, S.K.: Finite-Difference Method for Computation of Discontinuous Solutions. (in Russian), *Math. Sbornik* vol.47, pp 271, (1959).
 - [41] Collela, P., Glas, H.M.: Efficient Solution Algorithms for the Riemann Problem for Real Gases. *J. Comp. Phys.*, vol 59, pp 264, (1985).
 - [42] van Leer, B.: Flux-Vector Splitting for the Euler Equations. *Lecture Notes in Physics* vol. 170, pp. 507-512, (1982).
 - [43] Roe, P.L.: Approximate Riemann Solvers, Parameter Vectors and Difference Schemes. *J. Comp. Phys.*, vol. 22, pp. 357, (1981).
 - [44] Osher, S., Chakravarthy, S.: High Resolution Schemes and Entropy Condition. *SIAM J. Num. Anal.*, vol 21 pp. 955-984, (1984).
 - [45] Steger, J.L., Warming, R.F.: Flux-Vector Splitting of the Inviscid Gas Dynamic Equations with Applications to Finite-Difference Methods. *J. Comp. Phys.*, vol 40, pp 263-293, (1981).
 - [46] van Leer, B., Thomas, J. L., Roe, P. L., Newsome, R. W.: A Comparison of Numerical Flux Formulas for the Euler and Navier-Stokes Equations. AIAA paper 87-1104 CP (1987).
 - [47] Eberle A., Schmatz, M., Bissinger, N.: Generalized Fluxvectors for Hypersonic Shock Capturing. AIAA paper No. 90-0390, (1990).
 - [48] Thomas, J.L., Walters, R.W.: Upwind Relaxation Algorithms for the Navier-Stokes Equations. AIAA-paper No. 85-1501, (1985).
 - [49] Schröder, W., Hänel, D.: An Unfactored Implicit Scheme with Multigrid Acceleration for the Solution of the Navier-Stokes Equations. *Comp. & Fluids*, vol 15, pp. 313-336, (1987).
 - [50] Schwane, R., Hänel, D.: An Implicit Flux-Vector Splitting Scheme for the Computation of Viscous Hypersonic Flow. AIAA-paper No. 89-0274, (1989).
 - [51] van Leer B.: Flux Vector Splitting for the 1990's. *CFD Symp. on Aeropropulsion*, NASA Lewis Res. Center, Cleveland, (1990).
 - [52] Seider G., Hänel D.: Numerical Influence of Upwind TVD Schemes on Transonic Airfoil Drag Prediction. AIAA paper 91-0636, 29th Aerospace Sciences Meeting, Reno (USA), Jan. 1991, (1991).
 - [53] van Albada, G. D., van Leer, B., Roberts, W. W.: A Comparative Study of Computational Methods in Cosmic Gas Dynamics. *Astron. Astrophys.* vol. 108, pp.76-84, (1982).
 - [54] Roe, P.L., Baines, M.J.: Algorithms for Advection and Shock Problems. *Proc. of 4th GAMM Conf. on Num. Meth. in Fluid Mech.*, Notes on Num. Fluid Mech., vol 5, Vieweg Verlag (1982).
 - [55] Sweby, P.K.: High Resolution Schemes Using the Flux Limiter for Hyperbolic Conservation Laws, *SIAM J. Numer. Analyt.*, vol. 21, pp.995-1011, (1984).
 - [56] Jameson, A., Schmidt, W., Turkel, E.: Numerical Solution of the Euler Equations by Finite-Volume Methods Using Runge-Kutta Time-Stepping Schemes. AIAA-paper 81-1959, (1981).
 - [57] Eliason, P., Rizzi, A.: Hypersonic Leeside Flow Computations Using Centered Schemes for Euler Equations. In: *Notes on Numerical Fluid Mechanics*, vol. 29, Vieweg Verlag, (1990).
 - [58] Vatsa V. N., Wedan B. W.: Developement of a Multigrid Code for 3-D Navier-Stokes Equations and its Application to a Grid-Refinement Study. *Computers & Fluids*, vol. 18, pp. 391-403, (1990).
 - [59] Radespiel R., Rossow C., Swanson R.C.: Efficient Cell Vertex Multigrid Scheme for the Three-Dimensional Navier-Stokes Equations. *AIAA Journal*, vol. 28, pp. 1464-1472, (1990).
 - [60] Grossman B., Walters R. W.: Analysis of Flux-Split Algorithms for Euler's Equations with Real Gases. *AIAA Journal*, vol. 27, pp. 524-531, (1989).
 - [61] Montagne J.L., Yee H.C., Vinokur M.: Comparative Study of High-Resolution Shock-Capturing Schemes for a Real Gas. *Notes on Numerical Fluid Mechanics*, vol. 20, Vieweg Verlag, Braunschweig/Wiesbaden, (1988).
 - [62] Kroll N., Gaitonde D., Aftosmis: A Systematic Comparative Study of Several High Resolution Schemes for Complex Problems in High Speed Flows. AIAA paper 91-0636, 29th Aerospace Sciences Meeting, Reno, Jan. 7-10, (1991).

- [63] Hänel, D.: On the Accuracy of the Upwind Schemes in Solutions of the Navier-Stokes Equations. AIAA paper No. 87-1105 CP (1987).
- [64] Hänel D.: Effects of Numerical Dissipation in Solutions of the Navier-Stokes Equations. Proc. of Third Intern. Conf. on Hyperbolic Problems. Uppsala, Sweden, June 11-15, (1990).
- [65] Deconinck, H., Struijs, R., Roe, P.L.: Fluctuation Splitting for Multidimensional Convection Problems: an Alternative to Finite Volume and Finite Element Methods. VKI Lecture Series 1990-03, (1990).
- [66] Powell, K., van Leer, B.: A Genuinely Multi-Dimensional Upwind Cell-Vertex Scheme for the Euler Equations. AIAA-paper 89-0095, (1989).
- [67] Rumsey C., van Leer B., Roe P.: A Grid-Independent Approximate Riemann Solver with Applications to the Euler and Navier-Stokes Equations. AIAA paper 91-0239, 29th Aerospace Sciences Meeting, Reno (USA), Jan. 1991, (1991).
- [68] Mac Cormack, W.: The Effect of Viscosity in Hypervelocity Impact Cratering. AIAA paper 69-354, (1969).
- [69] Shang, J.S., Scherr, S.J.: Numerical Simulation of the Flowfield around a Complete Aircraft. AGARD Conf. Proc. 412, (1986).
- [70] Beam, R. M., Warming, R.F.: An implicit factored scheme for the compressible Navier-Stokes equations. AIAA J. vol. 16, pp. 393-402, (1978).
- [71] Rieger, H., Jameson, A.: Solution of steady three-dimensional compressible Euler and Navier-Stokes equations by an implicit LU scheme. AIAA-paper 88-0619 (1988).
- [72] Pulliam T. H., Steger J. L.: Implicit Finite-Difference Simulations of Three-Dimensional Flow. AIAA Journal, vol. 18, pp. 159-167, (1980).
- [73] Chaussee D. S., Pulliam T. H.: Two-Dimensional Inlet Simulation using a Diagonal Implicit Algorithm. AIAA Journal, vol. 19, pp. 153-159, (1981).
- [74] Briley W. R., McDonald H.: On the Structure and Use of Linearized Block Implicit Schemes. J. of Comput. Physics, vol. 34, pp. 34-72, (1980).
- [75] Bardina, J., Lombard, C.K.: Three Dimensional Hypersonic Flow Simulations with the CSCM Upwind Navier-Stokes Method. AIAA paper 87-1114 CP, (1987).
- [76] Anderson, W. K., Thomas, J.L., Rumsey, C. L.: Extension and Application of Flux-Vector Splitting to Calculation on Dynamic Meshes. AIAA paper 87-1152 CP (1987).
- [77] Davoudzadeh F., Liu N. S., Shamroth S. J., Thoren S. J.: Navier-Stokes Study of Rotating Stall in Compressor Cascades. AIAA J., vol. 28, pp. 492-498, (1990).
- [78] Kandil O. A., Chuang H. A.: Unsteady Navier-Stokes Computations past Oscillating Delta Wing at High Incidence. AIAA Journal, vol. 28, pp. 1565-1572, (1990).
- [79] Hosangadi A., Merkle C. L., Turns S. R.: Analysis of Forced Combusting Jets. AIAA J., vol. 28, pp. 1473-1480, (1990).
- [80] Yokota J. W.: Diagonally Inverted Lower-Upper Factored Implicit Multigrid Scheme for the Three-Dimensional Navier-Stokes Equations. AIAA Journal, vol. 28, pp. 1642-1649, (1990).
- [81] Shuen J. S.: Numerical Study of Chemically Reacting Flows Using a Lower-Upper Symmetric Successive Overrelaxation Scheme. AIAA Journal, vol. 27, pp. 1752-1760, (1989).
- [82] Candler G. V., McCormack R. W.: Hypersonic Flow past 3-D Configurations. AIAA paper AIAA-87-0480, (1988).
- [83] Lacor C., Hirsch C.: 3-D Computations of Complex Flow Systems. Proc. of 16th ICAS Congr., (1988).
- [84] Riedelbauch, S., Brenner, G.: Numerical Simulation of Laminar Hypersonic Flow past Blunt Bodies Including High Temperature Effects. AIAA paper No. 90-1492, (1990).
- [85] Jameson, A.: Solution of the Euler Equations for Two-Dimensional Transonic Flow by a Multigrid Method. Appl. Math. and Comput., vol. 13, pp. 327-355, (1983).
- [86] Chima R. V., Yokota J. W.: Numerical Analysis of Three-Dimensional Viscous Internal Flows. AIAA J., vol. 28, pp. 798-806, (1990).
- [87] Meinke M., Hänel D.: Time Accurate Multigrid Solutions of the Navier-Stokes Equations. Proc. of Third European Conf. on Multigrid Methods. Bonn (Germany), (1990). (To be publ. by Birkhauser Verlag).
- [88] Peraire J., Formaggio L., Morgan K., Zienkiewicz: Finite Element Euler Computations in Three Dimensions. AIAA paper No. 88-0032, (1988).
- [89] Mavriplis D.: Turbulent Flow Calculations using Unstructured and Adaptive Meshes. ICASE Rep. No. 90-61, (1990).
- [90] Nakahashi N.: FDM- FEM Zonal Approach for Viscous Flow Computations over Multiple Bodies. AIAA paper No. 87-0604, (1987).
- [91] Weatherill N.P.: A Strategy for the Use of Hybrid Structured- Unstructured Meshes in CFD. In: Numerical Methods for Fluid Dynamics (3), Ed. Morton K. W., Baines M.J., Oxford University Press, (1988).
- [92] Hassan, O., Morgan, K., Peraire, J.: An Adaptive Implicit/Explicit Finite Element Scheme for Compressible Viscous High Speed Flows. AIAA paper No. 89-0363, (1989).
- [93] Prabhu, P.K., Stewart, J.R., Thareja, R.R.: A Navier-Stokes Solver for High Speed Equilibrium Flows and Application to Blunt Bodies. AIAA paper 89-0668, (1989).
- [94] Koschel, W., Vornberger, A.: Turbomachinery Flow Calculation on Unstructured Grids Using Finite Element Methods. Notes on Numerical Fluid Mechanics, vol. 25, Vieweg Verlag, Braunschweig/Wiesbaden, (1989).
- [95] Lohner R., Morgan K., Peraire J., Vahdati M.: Finite Element Flux-Corrected Transport for the Euler and Navier-Stokes Equations. Int. J. for Numer. Meth. in Fluid Mech., vol. 7, pp. 1093-1109, (1987).

- [96] Argyris, J., Doltsinis, I., Friz, H.: Hermes Space Shuttle: Exploration of Reentry Aerodynamics. *Comput. Meth. Appl. Mech. Eng.*, vol 73, (1989).
- [97] Periaux, J.: Finite Element Simulations of Three-Dimensional Hypersonic Reacting Flows around Hermes. *Contrib. on Second Joint Europe-US Short Course on Hypersonics*. Org. by GAMNI-SMAI, Univers. of Texas at Austin, and U.S. Air Force Academy, Colorado Springs, Jan. 1989, 1989).
- [98] Mallet M.: Adapted Finite Element Methods for Hypersonic Reentry Problems. In: *Third Joint Europe-US Short Course in Hypersonics*, RWTH Aachen, Oct. 1990, (1990).
- [99] Venkatakrishnan V., Barth T.J.: Application of Direct Solvers to Unstructured Meshes for the Euler and Navier-Stokes Equations Using Upwind Schemes. AIAA paper No. 89-0364, (1989).
- [100] Desideri J.A., Glinisky N., Hettner E.: Hypersonic Reactive Flow Computations. *Computer & Fluids*, vol. 18, pp. 151-182, (1990).
- [101] Rostand P., Stoufflet B.: TVD Schemes to Compute Compressible Viscous Flows on Unstructured Grids. In: *Notes on Numerical Fluid Mechanics*, vol. 24, pp. 510-520, Vieweg Verlag, Braunschweig/Wiesbaden, (1989).
- [102] Hanel, D., Vilsmeier R.: Solution of the Conservation Equations on Unstructured Grids. Research project supported by the DFG, (1990-1991). Publication submitted for the 9th GAMM-Conf. on Numer. Meth. in Fluid Mech., Lausanne, (1991).
- [103] Patankar S. V.: *Numerical Heat Transfer and Fluid Flow*. McGraw-Hill, Washington, DC, (1980).
- [104] Issa R.I., Lockwood F.C.: On the Prediction of Two-Dimensional Supersonic Viscous Interactions near Walls. *AIAA J.*, vol. 15, pp. 182-188, (1977).
- [105] Rhie C.M.: A Pressure Based Navier-Stokes Solver Using Multigrid Method. AIAA paper No. 86-0207, (1986).
- [106] Karki K.C., Patankar S.V.: Pressure Based Calculation Procedure for Viscous Flows at All Speeds in Arbitrary Configurations. *AIAA J.*, vol. 27, pp. 1167-1174, (1989).
- [107] McGuirk J.J., Page G.J.: Shock Capturing Using a Pressure-Correction Method. *AIAA J.*, vol. 28, pp. 1751-1757, (1990).
- [108] Brandt, A.: Multi-Level Adaptive Solutions to Boundary-Value Problems. *Mathematics of Computation*, vol 31, No. 138, pp. 333-390, (1977).
- [109] Brandt, A.: Guide to Multigrid Development. In: *Lecture Notes in Mathematics* vol 960., pp. 220-312, Springer Verlag Berlin, (1981).
- [110] Ni, R. H.: A Multiple Grid Scheme for Solving the Euler Equations, *AIAA Journal*, vol. 20, No. 11, pp. 1565-1571 (1982).
- [111] Chima, R. V., Johnson, G. M.: Efficient Solution of the Euler and Navier-Stokes Equations with a Vectorized Multiple-Grid Algorithm, *AIAA Journal*, vol. 23, No. 1, pp. 23-32. (1985).
- [112] Siclari, M.J., Del Guidice, P., Jameson, A.: A Multigrid Finite Volume Method for Solving the Euler and Navier-Stokes Equations for High Speed Flow. AIAA paper 89-0283 1989).
- [113] Hemker, P. W., Spekreijse, S. P.: Multiple Grid and Oshers Scheme for the Efficient Solution of the Steady Euler Equations. *Appl. Num. Math.*, vol. 2, pp. 475-493, (1986).
- [114] Mulder, W. A.: Multigrid Relaxation for the Euler Equations. *J. Comp. Phys.*, vol 60, pp. 235-252, (1985).
- [115] Shaw, G., Wesseling, P.: Multigrid Method for the Compressible Navier-Stokes Equations. Rep. of the Dep. of Math. and Inf., Nr. 86-13, Univ. Delft, (1986).
- [116] Hemker, P.W., Koren, B.: Multigrid Defect Correction and Upwind Schemes for the Steady Navier-Stokes Equations. In: *Proc. of Third Conf. on Numerical Methods for Fluid Mech.*, (Morton K. W., Baines M. J., Editors), Oxford, (1988).
- [117] Meinke M., Hänel D.: Application of the Multigrid Method in Solutions of the Compressible Navier-Stokes Equations. *Proc. of the Fourth Copper Mountain Conf. on Multigrid Methods*. (Mandel J. et al, Editors) SIAM, Philadelphia, (1989).
- [118] Radespiel, R., Swanson, R.C.: An Investigation of Cell Centered and Cell Vertex Multigrid Schemes for the Navier-Stokes Equations. AIAA paper 89-0548, (1989).
- [119] Abid R., Vatsa V. N.: Prediction of Separated Transonic Wing Flows with Nonequilibrium Algebraic Turbulence Model. *AIAA Journal*, vol. 28, pp. 1426-1431, (1990).
- [120] Gerolymos G. A.: Implicit Multiple Grid Solution of the Compressible Navier-Stokes Equations Using $k-\epsilon$ Turbulence Closure. *AIAA Journal*, vol. 28, pp. 1707-1714, (1990).
- [121] Chima R.V., Turkel E., Schaffer S.: Comparison of Three Explicit Multigrid Methods for the Euler and Navier-Stokes Equations. NASA TM 88878, (1987).
- [122] *Unsteady Aerodynamic Phenomena in Turbomachines*. AGARD Conf. Proc. No. 468, (1989).
- [123] Giles M.: *Unsteady Methods for Turbomachinery Flow*. VKI Lecture Series LS 1989-06 on Numerical Methods for Flow in Turbomachinery, von Karman Institut for Fluid Dynamics, Rhode-Saint-Genese, May 1989, (1989).
- [124] Meinke M., Hänel D.: Simulation of Unsteady Flows. *Proc of 12th Int. Conf. on Num. Methods in Fluid Mechanics*, Oxford, (1990).
- [125] L. Fottner (Ed.): *Test Cases for Computation of Internal Flows in Aero Engine Components*. AGARD Advisory Report AR 275, (1990).
- [126] Kumar A., Dominion O.: Numerical Analysis of the Scramjet Inlet Flow Field Using Two-Dimensional Navier-Stokes Equations. AIAA paper No. 81-069, (1981).

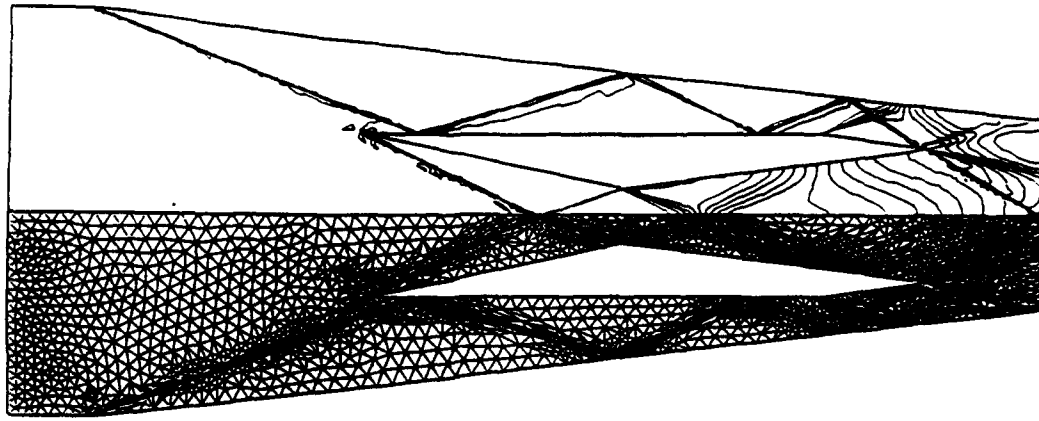


Fig. 2:

Inviscid flow through a scramjet inlet model at $Ma_\infty = 3.6$ (geometry after Kumar [126]). Runge-Kutta solution, central Finite-Volume discretization, and adaptive cell-orientation and grid point adaption. Computations by Vilsmeier [102]. Grid and Mach number distribution after three adaptations with about 5000 points.

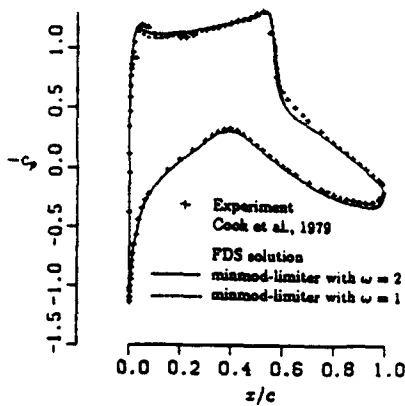


Fig. 3: Influence of different flux limiters on the transonic, turbulent flow around a RAE 2822 airfoil.

Runge-Kutta solution, symmetric TVD flux-difference splitting, Baldwin-Lomax turbulence model. (Results taken from Seider [52]) Min-mod limiter:

$$\varphi_i = \minmod \left\{ \frac{2\omega r}{1+r}, \frac{2\omega}{1+r}; 1 \right\} \quad \text{with} \quad r = \frac{\Delta W_{i+1/2}}{\Delta W_{i-1/2}}$$

$$\omega = 2: \quad c_l = .823, \quad c_d = .0187$$

$$\omega = 1: \quad c_l = .820, \quad c_d = .0216$$

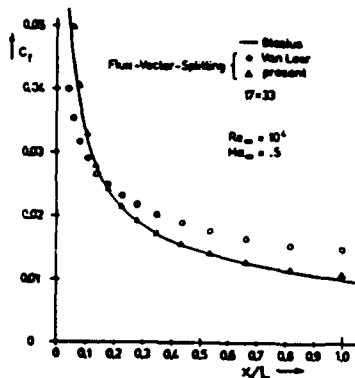


Fig. 4: Solution of the 2-D Navier-Stokes equations for laminar flow over a flat plate. Influence of different formulations for flux-vector splitting on the values of skin friction.

- original flux-vector splitting by van Leer [42]
- △ modified flux-vector splitting, Hänel, Schwane [50]



Fig. 5:

Navier-Stokes solution for hypersonic flow around a double-ellipsoidal body. Vectors of the local skin friction on the body surface ($Ma_\infty = 8.15$, $Re_\infty = 10^6$, $\alpha = 30^\circ$, 60.000 grid points).
a) original van Leer flux-vector splitting [42] b) modification by Hänel, Schwane [50]

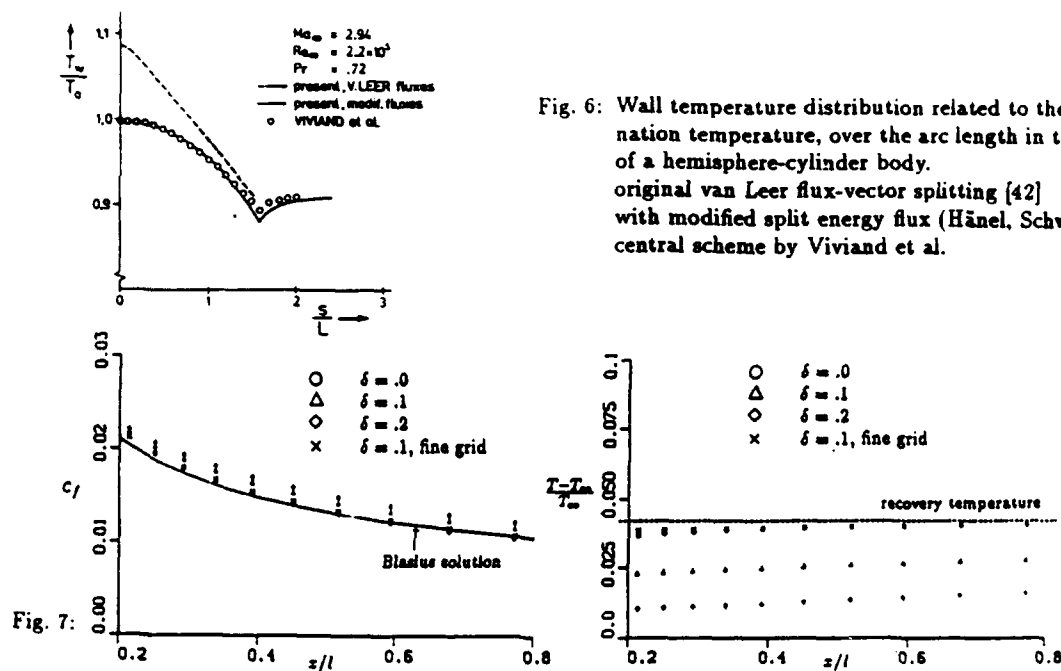


Fig. 7: Solution of the 2-D Navier-Stokes equations for laminar flow over a flat plate. Influence of the entropy correction factor δ on the values of skin friction (left) and on the wall temperature (right) in the symmetric TVD flux-difference splitting (Results taken from Seider [52]).

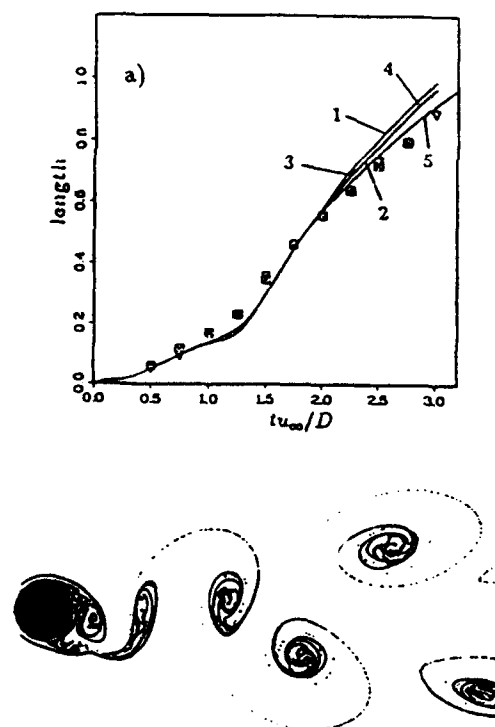


Fig. 9: Computed streaklines of a 2-D Navier-Stokes solution with central differencing for unsteady flow around a circular cylinder, $Re = 3000$, $Ma = 0.3$, 177×113 grid points.

Fig. 6: Wall temperature distribution related to the inflow stagnation temperature, over the arc length in the mid plane of a hemisphere-cylinder body.
original van Leer flux-vector splitting [42]
with modified split energy flux (Hänel, Schwane [63])
central scheme by Viviani et al.

Fig. 8: Unsteady flow around an impulsively started circular cylinder, Navier-Stokes solution, $Re = 3000$, $Ma = 0.3$, 113×81 grid points. Time history of the length of the closed wake for different solution schemes.

- 1 flux-vector splitting, van Leer
- 2 flux-vector splitting, modified by Hänel/Schwane
- 3 node-centered, central
- 4 cell-vertex, central
- 5 node-centered, central, fine grid 225×225

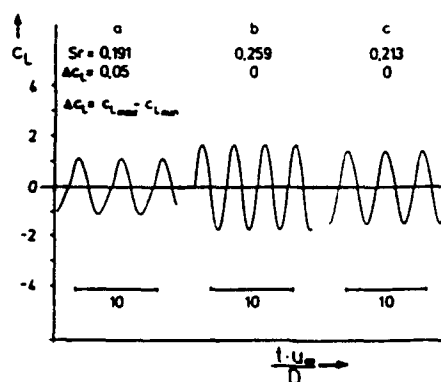


Fig. 10: Time histories of the lift for unsteady flow around a circular cylinder, $Re=3000$, $Ma=0.3$, 177×113 grid points.
a) grid stretched in circumferential direction, coefficient of fourth order damping $\epsilon^{(4)} = 1/256$
b) grid equidistant in circumferential direction, coefficient of fourth order damping $\epsilon^{(4)} = 1/256$
c) grid equidistant in circumferential direction, coefficient of fourth order damping $\epsilon^{(4)} = 1/32$

Discussion

L. FOTTNER, UNIV. OF BUNDESWEHR, GERMANY

Can you briefly comment on the accuracy of the turbulence models used in calculating turbomachinery flow problems, and if there is a need to improve these models?

AUTHOR'S REPLY

Actually, the algebraic turbulence model by Baldwin and Lomax and the $k-\epsilon$ model are widely in use for the Navier-Stokes equations. Their physical validity depends on the degree of approximation and the choice of semi-empirical parameters. Their validity is mainly restricted to boundary-like flows. There is a strong need for improved models for more complex flows.

R. GRAY, WRIGHT LABS, U.S.A.

What are the limitations still preventing the resolution of spatially periodic features such as Tollmien-Schlichting waves?

AUTHOR'S REPLY

So far I know the problems of fluidmechanical instabilities can already be simulated, but for simple conditions (geometries). Essentially, it is necessary to have:

- sufficient computer capacity to resolve the small scaling
- methods which are very accurate in space and time
- appropriate initial and boundary conditions

T. PRINCE, WILLIAMS INTER., U.S.A.

You alluded to the possibility of finding more efficient ways to combine implicit time marching with unstructured grids. In turbomachinery, an implicit time marching scheme must include the rotational periodicity in the implicit formulation. This makes the association between implicit schemes and structured grids even stronger. Is there a way to overcome these obstacles in order to use unstructured grids in implicit schemes?

AUTHOR'S REPLY

This is a difficult question, since I do not have much experience with implicit schemes on unstructured grids. I am remembering examples from the literature:

- use of structured, implicit organization in one direction (e.g., normal to a wall), and unstructured (explicit) in the other plane
- use of semi-implicit schemes (point relaxation methods)
- also explicit multigrid methods may be considered, since they can have similar fast convergence as implicit methods, in particular for steady-state solutions

H. FRÜHAUF, UNIV. OF STUTTGART, GERMANY

Will finer grid computations, which ensure grid independent solutions, reduce the shown influence of numerical damping on the solutions?

AUTHOR'S REPLY

It is the question of convergence!

- For linear problems it is answered by P. Lax (convergence = consistency + stability)
- For nonlinear (CFD) problems it is not cleared, but usually assumed (by comparisons) that the smaller scales are sufficiently modeled or sufficient computer capacity is available for small scale resolution.





APPLICATION OF S1BYL2 TO THE AGARD WG18 COMPRESSOR TEST CASES

by

W.J. Calvert
 Propulsion Department
 Royal Aerospace Establishment
 Pyestock, Farnborough
 Hampshire GU14 0LS
 United Kingdom

92-16069

SUMMARY

S1BYL2 is an inviscid-viscous blade-to-blade method for calculating the detailed aerodynamics and overall performance of compressor blades. It may be applied either on its own to predict the flow for individual blade sections, such as the mid span of a linear cascade, or in conjunction with a throughflow calculation to predict the performance of a complete axial compressor.

A previous AGARD paper by the author described applications of S1BYL2 to most of the compressor cascade test cases which have subsequently been selected by AGARD Working Group 18: generally good agreement was obtained. This current paper presents new predictions for the V2 and ARL S119 cascades and for the high speed compressor cases. It is hoped that this will be one of many sets of calculations for these cases, so that an improved understanding of each case may be obtained, together with an appreciation of the strengths and weaknesses of different computational approaches.

LIST OF SYMBOLS

c	blade chord
H	boundary layer shape factor δ^*/θ
M	Mach number
P	static pressure
α	flow angle, degrees
δ^*	boundary layer displacement thickness
θ	boundary layer momentum thickness
ω	loss coefficient based on upstream conditions
Ω	stream tube contraction (upstream/downstream)

Subscripts

- ¹ conditions at upstream boundary of cascade or inlet to blade row
- ² conditions at downstream boundary of cascade or exit from blade row

1. INTRODUCTION

Validation/calibration of computer codes against suitable test cases is a highly important area of Computational Fluid Dynamics which is rightly receiving increased attention, as shown for example by Ref 1. The current state-of-the-art for turbomachinery test cases is indicated by the selection made by AGARD Working Group 18 (WG18)². These cover a useful range of practical cascades and rotating machines, and provide a reasonable amount of data on the flow fields as well as measurements of overall performance. However, as noted by WG18 in Chapter III, neither the experimental data nor the flow codes are perfect. Also it is not generally possible to obtain

experimental data of many important areas of high speed flows, due primarily to the relatively small scale of turbomachinery blading. Thus some aspects of the codes cannot be adequately validated. Given this situation, there is much to be gained by applying codes to a wide range of test cases and by comparing the results from different codes for the same test cases. An important contribution of WG18 is to have identified a suitable set of test cases to initiate this.

The main code employed in the present work is the RAE S1BYL2 method³. This is an inviscid-viscous interaction technique for predicting the blade-to-blade performance of axial compressors. It can be applied either on its own to individual blade sections, such as the mid span of a linear cascade, or linked to a streamline curvature throughflow method in an S1-S2 system to give a complete quasi-three-dimensional prediction of the flow and overall performance of one or more blade rows.

A brief description of the S1BYL2 and S1-S2 methods is given in section 2 of this paper. Section 3 then reviews the results from previous applications⁴ of S1BYL2 to the compressor cascade test cases chosen by WG18 and presents further predictions for the V2 high subsonic cascade and new predictions for the ARL S119 transonic cascade. Results from the RAE S1-S2 system for the three high speed compressor cases are then given in section 4.

2. GENERAL DESCRIPTION OF METHODS

The RAE S1BYL2 method is an inviscid-viscous interaction technique to predict the blade-to-blade performance of axial compressors. The inviscid part consists of a time marching Euler calculation, based on Ref 5, so it can handle transonic flows: shock waves can be captured and the losses due to them can be predicted. The calculation takes place on a specified axisymmetric stream surface, and it includes the effects of rotation and of varying radius and stream tube thickness in the axial direction. The viscous calculation is an integral technique consisting of three parts to estimate laminar boundary layer development, transition point and turbulent boundary layer development respectively. The inviscid-viscous matching procedure employs mixed modes to allow a valid solution to be obtained even when there are regions of separated flow due to shock wave/boundary layer interactions or to excessive diffusion. The viscous calculations continue in the wake downstream of the bladed region, and a compressible flow mixing calculation is carried out on the downstream boundary to determine the mean exit conditions. Thus the method provides both details of the internal flows, including boundary layer development, and predictions of the blade section overall

performance, such as exit flow angle and losses.

In order to employ the S1BYL2 method to predict the performance of complete blade rows, it must be linked with a throughflow calculation which determines the spanwise variations of the flow and ensures that radial equilibrium is satisfied. A semi-automatic S1-S2 procedure for this is described in Ref 6. This procedure has now been automated, with both the S1BYL2 calculation for the blade-to-blade sections and the streamline curvature calculation for the hub-to-tip flow incorporated into one program, together with the blade geometry and data link routines. The streamline curvature routine is an improved modular version of that previously employed. It allows curved calculating planes to be specified to give an accurate match to the leading and trailing edges of each blade row. Spanwise mixing terms have been added to some versions of the routine, but these were not included in the present S1-S2 calculations.

The basic principles of the S1-S2 interaction remain the same. Essentially there are three parts to each loop:-

- i the performance of the blade-to-blade sections is predicted by S1BYL2 - this involves calculations for up to 9 sections on each blade row.
- ii the hub-to-tip flow throughout the whole compressor is calculated by the S2 streamline curvature method, using the pitchwise averaged data from the S1 solutions.
- iii the relative flow angles and stream tube geometry from the S1 and S2 parts of the calculation are compared to see whether the solution has converged - if not new blade geometry for each section is found by calculating the intersections between the stream surfaces from the current S2 solution and the blade aerofoils.

Target convergence criteria for the complete S1-S2 solution are typically a) S1 and S2 relative flow angles agreeing to within 0.1° , and b) S1 and S2 stream tube thickness variations agreeing to 0.1%. The number of S1-S2 loops required to achieve this depends on the difficulty of the blade section operating conditions and the number of blade rows involved. About eight loops are generally sufficient for one or two blade rows, but more will be needed, for example, if blade choking is significantly affecting the flow distribution. The solutions from the previous loop provide the starting conditions for calculations on the current loop, so that the procedure is quite efficient. For example, a solution for the HP9 type RD stage (see section 4.2) requires about 6 hours CPU on a Stardent 1500 mini-supercomputer.

It should be noted that, in order to obtain realistic losses towards the blade ends, empirically derived extra losses must be

specified as an input to the S1-S2 system. These additional losses are modelled by a constant drag force in the S1 calculation and the effects are fed to S2 via the normal S1-S2 linking. Although the need for such input is one of the limitations of the S1-S2 approach, the ease with which such corrections can be incorporated in order to tune the model for a given compressor can be a distinct advantage in practice. It is emphasised, however, that apart from the stated end losses and annulus wall blockage factors no other corrections were employed for the cases presented here.

3. COMPRESSOR CASCADE TEST CASES

AGARD Working Group 18 selected four compressor cascades suitable for inviscid-viscous blade-to-blade methods:-

- i E/CA-2 V2 High Subsonic Cascade
- ii E/CA-3 ONERA 115 High Subsonic Cascade
- iii E/CA-4 DFVLR L030-4 Low Supersonic Cascade
- iv E/CA-5 ARL SL19 Transonic Cascade

S1BYL2 has previously been applied to the first three of these and the results are given in Ref 4. There was generally good agreement between the test results and predictions, in terms of both internal flow details such as blade surface pressure distributions and overall performance parameters such as static pressure ratio and exit flow angle. The only significant problem area was that increases in losses at high incidence were not predicted directly, but relied on the user noticing the high effective incidence indicated by the solution and specifying revised starting conditions for the surface boundary layer calculation. For cases near optimum incidence, deviation angles were predicted to about $\pm 1^\circ$, static pressure ratios to $\pm 4\%$ and overall loss coefficients to $\pm 2\%$ of inlet dynamic head. These levels of accuracy have been confirmed in applications of the code to other cascades, such as the supercritical designs described in Refs 8 and 9.

The test conditions chosen by WG18 for the ONERA 115 and DFVLR L030-4 cascades are the same as, or similar to, those previously studied. Therefore only calculations for the V2 and ARL SL19 cascades will be presented here.

3.1 V2 Subsonic Compressor Cascade

The V2 cascade is a high camber (56.8°), high solidity (2.22) design with 7% thick DCA blade profiles. Twelve test conditions were selected by WG18, covering inlet Mach numbers from 0.3 to 0.85, inlet flow angles from 47.5° to 54.5° and stream tube contraction ratios from 1.08 to 1.39.

As noted in Refs 2 and 4, the axial variation assumed for stream tube thickness between the measured upstream and downstream values is

critical, but also open to uncertainty. Two plausible assumptions could be (a) a linear variation with streamwise distance between the two measuring planes, and (b) constant values upstream and downstream and a linear variation between the leading and trailing edge planes of the cascade. For the V2 cascade, which has a high aspect ratio of 3.75, the former is more likely to be correct and this is confirmed by the calculations for the test condition with values of $M_1/\alpha_1/\Omega$ of 0.80/54.5/1.39 (Fig 1a). Assumption (a) was therefore adopted for all subsequent calculations for this cascade.

The choice of stream tube thickness variation is a good example of a situation where there is uncertainty in the experimental data; and hence where comparisons against other methods run with the same assumptions would be particularly useful.

An 89 x 16 calculating grid was employed for all calculations of the V2 cascade, with 51 x 16 points equally spaced in the axial and tangential directions within the blade row. Outside the row, the axial spacing was increased by a constant factor to give upstream and downstream boundaries for the calculation domain 0.8 axial chords from the blade row.

The twelve WG18 test conditions can be grouped into three categories: (a) choked flow, (b) operation near optimum incidence and (c) stalled flow. The three choked flow conditions are:- 0.85/49.5/1.20, 0.80/47.5/1.17, and 0.80/49.5/1.27. They demonstrate that, relative to a nominal unchoked condition of 0.80/49.5/1.20, choked flow can be produced by small changes in M_1 , α_1 , or Ω . SIBYL2 successfully predicts this. For example, the predicted Mach number contours, blade surface Mach number distributions and development of the boundary layer displacement thickness and shape factor at 0.85/49.5/1.20 are shown in Fig 1b, together with the test data. There is good agreement between prediction and test, except for the levels of shape factor near the trailing edge of the suction surface.

The point at 0.80/49.5/1.12 is typical of the seven operating conditions near optimum incidence with measured loss coefficients below 5%. The predicted Mach number contours, blade surface Mach number distributions, and boundary layer development are shown in Fig 1c, together with the test data. It can be seen that the overall performance parameters match quite well, although the discrepancy of 1.3° on exit flow angle is higher than usual. There is also close agreement between the predicted inviscid Mach numbers on the blade surfaces and the values deduced from the measured surface static pressures. The agreement between prediction and test for the suction surface boundary layer development is reasonable qualitatively, but the predicted values of shape factor are higher than the test values in the separated flow region near the trailing edge, while the predicted values of displacement thickness near mid chord are lower than the test values. These differences could be due

to many reasons. Some of the more obvious ones are:

- i errors in the prediction of transition between laminar and turbulent flow
- ii the effect of high free-stream turbulence on the turbulent boundary layer - this is not included in the present calculations
- iii the general uncertainty in predicting separated turbulent boundary layers
- iv errors in measuring very thin boundary layers - the measured displacement thickness is only 0.4 mm at 42% chord
- v errors in measuring unsteady flows with a pneumatic probe
- vi errors in measuring reverse flows with a forward facing probe

The level of agreement achieved in this case is typical of that for the test conditions near optimum incidence.

The remaining two operating conditions - 0.80/52.5/1.12 and 0.80/54.5/1.23 - are stalled, with measured loss coefficients of over 10%. As previously noted, such conditions can be identified by the fact that maximum blade loading occurs at the leading edge. The user can then specify that the suction surface boundary layer starts as a turbulent layer, with a momentum thickness Reynolds number of about 500. A solution with the boundary layer tripped in this way for the condition 0.80/52.5/1.12 is shown in Fig 1d. The results for surface Mach number and suction surface displacement thickness agree quite well but the predicted shape factors for the suction surface are much higher than deduced from the boundary layer measurements.

In this context it is interesting to consider the loss produced by applying a compressible flow mixing calculation to the measured suction surface boundary layer parameters at 98% chord. At the two stalled flow conditions this loss exceeds the total loss deduced from the wake traverses by about 25%. Assuming that the suction surface loss should be about the same proportion of the total loss as at the other test conditions (ie 80%) implies that the momentum thickness should be about half of the stated value. This would obviously be in much better agreement with the predicted values of momentum thickness and shape factor.

An alternative approach to tripping the boundary layer would be to employ a grid with much closer axial spacing near the leading edge and to assume that all boundary layers are turbulent. This would give solutions broadly comparable with the Navier-Stokes solutions for the V2 cascade shown in Ref 10. However, a grid giving better modelling of the leading edge region would be needed to obtain grid-independent solutions. Also the process of laminar separation, transition and

turbulent reattachment for high incidence flows needs to be understood better so that more realistic models of the viscous flow (either integral boundary layer calculations or turbulence models) can be developed.

3.2 ARL SL19 Transonic Compressor Cascade

The ARL SL19 transonic compressor cascade was derived from a rotor section of a single stage compressor ¹¹ with a design point pressure ratio of 1.9. It is a thin, high stagger (56.9°), low camber (-1.9°) section with a design point inlet Mach number of 1.616. Cascades with similar blades have been tested in facilities at Detroit Diesel Allison (DDA) ¹², DFVLR ¹³ and ONERA ¹⁴, and one test point from each series was selected by WG18.

A guide to the relevance of each operating condition can be obtained by computing the pressure ratio and efficiency of a corresponding rotor section from the measured overall cascade performance - for this purpose the rotor section was assumed to have zero inlet absolute flow angle and constant stream surface radius. The results for all the DDA test points taken at the design inlet Mach number ¹² were as follows:-

Cascade static pressure ratio	Rotor total pressure ratio	Rotor adiabatic efficiency %
1.220	1.086	67.8
1.468	1.180	77.0
1.672	1.318	81.8
1.870	1.489	84.0
2.036	1.674	84.8
2.097	1.727	83.8
2.220	1.801	81.1
2.300	1.868	82.2

This clearly shows that the points with higher static pressure ratios are of greater practical interest to the compressor engineer, and it is these which the S1BYL2 method was developed to predict. Of the WG18 test conditions only the DFVLR point falls into this category.

For the S1BYL2 calculation of the DFVLR test point the stream tube thickness was assumed to be constant upstream of the cascade leading edge and to reduce linearly with axial distance to the measured value at the traverse plane 47% of gap axially downstream of the blade trailing edge. A 119 x 21 calculating grid was employed for the time marching part of the calculation, with 81 x 21 points within the blade row equally spaced in both axial and tangential directions. The test value of inlet tangential velocity was specified and the operating condition for the solution was chosen such that the main pressure rise on the suction surface occurred close to the measured position.

The predicted Mach number contours, blade surface Mach number distributions and boundary layer development for the design blade shape are shown in Fig 2, together with the Mach numbers deduced from the measured

surface static pressures and the predicted inviscid total pressures. The agreement between prediction and test is generally good. Note that the calculation indicates the presence of strong shock wave/boundary layer interactions on both the suction and pressure surfaces of the blade. It is possible that the pre-shock boundary layer on the pressure surface could be laminar, although transition has been forced upstream of the shock in the S1BYL2 solution, and this might explain the discrepancies between prediction and test in this region. The agreement between measured and predicted overall performance parameters is reasonable - the predicted unique incidence inlet angle and the exit flow angle are both 1° too high, static pressure rise agrees to about 5%, and total pressure loss is 10% compared with a measured value of 12%.

The predictions are quite sensitive to the assumptions made about stream tube thickness. For example, taking a constant value upstream of the initial shock wave reduces the predicted inlet flow angle by 0.8°, while assuming a linear variation between the plane of the upstream static pressure tapings and the downstream traverse plane increases the value by 0.8°. There is also some uncertainty about the appropriate blade shape to use for the calculations, since the two instrumented blades in the cascade both differed slightly from the design intent and some blade deformation due to the aerodynamic loads was observed during testing ¹⁵. Using the measured shape of the suction surface blade given in Ref 2 reduces the predicted inlet flow angle by 0.7°, whereas the shape for the pressure surface blade is much closer to the design intent.

Once again calculations with a number of different codes would be instructive and might enable a consensus view to be reached of the appropriate boundary conditions to be applied.

4. HIGH SPEED COMPRESSOR TEST CASES

As mentioned above, the S1-S2 system incorporating S1BYL2 has been applied to all three high speed compressor test cases selected by WG18 viz:

- i E/CO-2 NASA Transonic Rotor 67
- ii E/CO-3 RR HP9 Subsonic Stage
- iii E/CO-4 DFVLR Transonic Stage

The system was kept the same throughout and similar calculating grids were applied. Nine S1 sections were used to model each blade row and the grids used for the time marching part of the S1BYL2 calculations were similar to those used for the cascades in section 3 above. The S2 solutions typically employed 21 streamlines and there were 4 interblade calculating planes between the leading and trailing edge planes of each blade row.

The inlet total pressure profiles for each compressor were based closely on the measured data, except that no attempt was made to

achieve zero values of velocity at the walls. Small amounts of annulus wall blockage, about 1% for the two transonic fans and 2% for HP9, were included to allow for this. The losses used to model end effects were assumed to affect the outer regions of each row: the loss coefficients were specified to drop from 15% at the annulus walls, to zero at a distance of 1/3 rotor chord from the walls. This assumption is in line with that made for previous S1-S2 calculations of the rotor row of transonic civil fans¹⁴. If more than one stage were being considered, it would obviously be necessary either to include the effect of spanwise mixing within the S2 part of the calculation, or to use a more even distribution of extra loss.

4.1 NASA Transonic Rotor 67

Rotor 67 is the first stage rotor of a two stage fan. It was tested as an isolated row to provide data for comparison with numerical predictions which were free from circumferential variations due to stationary blade rows. The rotor has an aspect ratio of 1.6 based on average span/mid height chord, and at inlet the tip diameter is 514 mm with a hub/tip ratio of 0.375. The design point conditions are a tip speed of 429 m/s, an inlet tip relative Mach number of 1.38, a rotor pressure ratio of 1.63 and a mass flow rate of 33.25 kg/s. Laser anemometry was extensively used to measure details of the internal flow fields, and radial traverses with a combination probe were carried out to determine the inlet and exit variations of total and static pressure, total temperature and flow angle.

Two operating conditions were selected by WG18 - one near peak efficiency and the other near stall. The flow at both conditions was predicted using the S1-S2 system and some of the results are shown in Figs 3 and 4. Considering firstly the overall performance, the mass flow rate at the pressure ratio for the peak efficiency condition was predicted to be 34.0 kg/s, about 1% below the test value. Predicted adiabatic efficiency was 92.3%, compared with a test value of 93%. At the mass flow for the near stall point, the predicted pressure ratio and efficiency were 1.727 and 91.6%, compared with test values of 1.728 and 90.1%. There is also good agreement between the predicted and measured radial profiles of total pressure and temperature at rotor exit, as shown in Fig 3. (The values plotted are relative to the inlet conditions at mid span.)

The predicted Mach number contours at the two conditions for the blade-to-blade sections at 30%, 70% and 90% span from the hub are shown in Fig 4, together with the predicted blade surface Mach numbers and boundary layer development. The contours may be compared directly with the corresponding plots deduced from the test data given in Fig 17 of Ref 2. The agreement is quite good for the outer sections, with the S1-S2 system correctly predicting the dual shock system noted in Ref 17 at the peak efficiency condition, and the single normal shock wave just detached from the blading at the near stall condition.

However, the calculation predicts a more distinct shock in the uncovered passage at 30% blade height for both conditions than was measured with the laser anemometer.

The predicted boundary layer development for the suction surface indicates a trailing edge separation for the sections over the inner third of the span, with the shock wave/boundary layer interaction near mid chord becoming significant and causing some separation over the outer half of the blade. The interaction is sufficiently strong at the peak efficiency condition to cause complete separation of the boundary layer downstream of the shock for the tip sections.

4.2 RR HP9 Subsonic Compressor Stage

The Rolls-Royce HP9 rig is a single stage model of one of the later stages in a civil HP compressor. It therefore has a much higher inlet hub/tip ratio (0.84) and lower rotor aspect ratio (0.9) than the other two WG18 compressor cases. Inlet spoiler rings are employed to generate a suitable inlet velocity profile. The type "RD" case selected by WG18 has conventional blade profiles, a design stage pressure ratio of 1.24, a mass flow rate of 9.1 kg/s and a tip speed of 251.3 m/s at ISA inlet conditions. Tip diameter is 518.2 mm.

All three operating conditions - maximum flow, mid chic and near surge - were studied using the S1-S2 system. The predictions at maximum flow and mid chic were straightforward, but the initial attempts for the near surge point failed. The high incidences for the S1 sections nearest the hub caused very high levels of profile loss to be predicted for this region: these resulted in even more arduous flow conditions being calculated for the next S1-S2 loop by the S2 part of the system and eventually the S1BYL2 calculations failed to converge. The present S1-S2 technique is probably over-sensitive to local flow problems like this, since there is no allowance for spanwise movement of low energy boundary layer flows - inclusion of spanwise mixing in the S2 calculation should help in this respect. Also, the assumption that stream surfaces remain axisymmetric means that the relief of the endwall flow conditions due to three-dimensional flows¹⁵ is neglected, a fundamental limitation of the axisymmetric S1-S2 approach. To enable a solution to be obtained for HP9 at the near surge mass flow, S1 calculations were carried out only between 10% and 90% blade heights (the other S1-S2 solutions included calculations for sections within 5% height of the walls) with extrapolation used to obtain the conditions for stream surfaces closer to the walls.

Predicted Mach number contours and distributions and boundary layer development for the rotor and stator mid height sections at the three operating conditions are shown in Fig 5. These demonstrate the range of operating incidences which are to be expected at different points along a constant speed characteristic for a single stage compressor - high positive blade loadings at the leading edge

near surge, roughly zero loading at mid chord and high negative loadings at maximum flow. The predicted boundary layer behaviour is typical of blade sections with circular arc camber lines. On the suction surface the shape factors are relatively low over most of the chord, indicating attached boundary layers. However, there is rapid growth near the trailing edge where the boundary layer has become too thick to withstand the constant diffusion associated with the circular arc camber line and separates. On the pressure surface the boundary layer remains attached throughout, apart from a possible laminar bubble near the leading edge at the maximum flow point. No interblade measurements are available for comparison with these data.

There is some uncertainty about the rotor exit conditions for this case², and so the comparisons shown between prediction and test (Fig 6) are for the circumferentially averaged conditions downstream of the stator. The main discrepancies are that:-

- i the temperature rises near the outer casing are overestimated - this could be due to the relatively crude allowance for end wall effects, or to neglecting spanwise mixing effects in the S2 throughflow calculation.
- ii the predicted efficiencies at the near surge condition are much higher than measured - this is probably associated with the problems in predicting high incidence flows noted in section 3.1 above. Improved agreement could be obtained by "tripping" the suction surface boundary layers at the blade leading edge.

Apart from this the agreement obtained is reasonable, particularly when the uncertainty due to the manufacturing tolerance of 0.75° on blade stagger angle is considered. If the prediction at the maximum flow point is repeated with the rotor and stator rows restaggered open by this amount, then at the same exit flow function there are increases of 0.9% on mass flow, 0.012 on pressure ratio and 1.2% on efficiency.

4.3 DFVLR Transonic Compressor Stage

The DFVLR transonic fan has an inlet tip diameter of 398 mm, an inlet hub/tip ratio of 0.5 and a rotor aspect ratio of 1.7. The design point pressure ratio is 1.51 at a mass flow rate of 17.3 kg/s and a blade tip speed of 421 m/s. The rotor has been tested with two different stator rows: the laser anemometry measurements of the rotor flow field were taken with the NACA 65/60 stator row and this is the configuration which has been studied using the S1-S2 system.

Predictions were carried out at the same exit mass flow functions as the two test conditions selected by WG18 and the predicted and measured radial distributions of performance are compared in Fig 7. The agreement is much poorer than for the other two compressors. The main problem seems to be that the S1-S2

system over-estimates the rotor efficiency by about 4% at both conditions, and this results in significantly higher pressure ratios being predicted at a given mass flow. The magnitude of this discrepancy is disappointing, given the level of agreement on overall performance for the other two cases and for other transonic fans. In particular the S1-S2 system has not identified any reason for the peak efficiency of the DFVLR rotor being over 5% lower than for NASA rotor 67, which has a similar pressure ratio, tip speed and aspect ratio. It will be interesting to see whether other CFD methods can explain this difference.

Despite the poor agreement on overall performance, the predicted Mach number contours for the rotor at 18%, 45%, 68% and 89% blade heights are in close agreement with those given in Figs 10 and 11 of Ref 2 (See Fig 8). At peak efficiency the solution correctly predicts an oblique leading edge shock near the rotor tip with a maximum suction surface Mach number of about 1.4. At 68% height the shock is becoming more normal, and by 45% height it is detached from the blade leading edge. The predicted diffusion of the flow within the blade passage also matches the test data well. The predicted suction surface boundary layer development shows a gradual progression with blade height, roughly similar to that for NASA rotor 67. Near the hub, separation occurs only near the trailing edge; by about 45% height the shock wave/boundary layer interaction has become strong enough to cause a small separation bubble at about mid chord, and the extent of the separation at the trailing edge has reduced; at 68% height the mid chord separation has increased and the trailing edge separation has disappeared; and at 89% the shock wave/boundary layer interaction is strong enough to cause complete separation for the rear part of the blade.

At the point nearer surge, the shock wave has moved forward and it is just detached from the leading edge at 89% height in both predicted and measured results. The shock becomes further detached at 68% and 45% heights, and at 18% there is only a small region near the leading edge where the flow is supersonic. The predicted boundary layer behaviour is similar to that at peak efficiency except that the shock/boundary layer interaction near the tip is predicted to be slightly weaker and the boundary layer reattaches before the trailing edge. However, given the high effective incidences indicated over the inner half of the blade, it is likely that the actual suction surface boundary layers are rather thicker.

5. CONCLUDING REMARKS

The S1BYL2 inviscid-viscous interaction method has now been applied to all the high speed compressor cascade test cases selected by AGARD WG18, and, linked with a streamline curvature throughflow method in an S1-S2 system, to all the high speed compressor cases. The predictions obtained are generally in encouraging agreement with the experimental data, both in terms of the

features of the internal flows and the overall performance parameters.

For the compressor cascades the blade choking/unique incidence angles and deviation angles are predicted to about $\pm 1^\circ$, the static pressure rise to $\pm 4\%$ and (less satisfactorily) the total loss coefficient to $\pm 2\%$ of inlet dynamic head, for operation below stalling incidence. The increased losses which occur at high positive incidence are not fully predicted automatically, but such situations can be detected by examining the effective incidence predicted for the blade. It is believed that improvements are needed both in the viscous modelling and in the numerical resolution of the leading edge region before this type of flow can be predicted correctly.

For the compressor test cases, the predicted results for the NASA rotor 67 and for the HP9 stage agree well with the measured results. In particular, peak efficiency levels are estimated to within about 1%. The results for the DFVLR stage are less satisfactory: the rotor efficiency is over-estimated by about 4%, despite close agreement between the measured and predicted blade-to-blade Mach numbers. Thus the present method fails to explain the difference of over 5% in measured rotor efficiency between the NASA 67 and DFVLR rotors. It will be interesting to see whether other methods are more successful.

The present applications of the RAE S1BYL2 code to the WG18 compressor test cases have been valuable, both in evaluating the code and in gaining further understanding of the test cases. The author would like to congratulate the Working Group for taking the lead in identifying this set of cases, and he would encourage others to carry out and publish corresponding predictions.

REFERENCES

1. "Validation of Computational Fluid Dynamics", AGARD CP 437, May 1988.
2. "Test Cases for Computation of Internal Flows in Aero Engine Components", AGARD AR275, July 1990.
3. Calvert, W. J., "An inviscid-viscous interaction treatment to predict the blade-to-blade performance of axial compressors with leading edge normal shock waves", ASME Paper 82-GT-135, 1982.
4. Calvert, W. J., "Application of an inviscid-viscous interaction method to transonic compressor cascades", in "Viscous Effects in Turbomachines", AGARD CP 351, June 1983, paper 2.
5. Denton, J. D., "An improved time marching method for turbomachinery flow calculation", ASME Journal of Eng for Power, Vol 105, pp 514-524, 1983.
6. Calvert, W. J., and Ginder, R. B., "A quasi-three-dimensional calculation system for the flow within transonic compressor blade rows", ASME Paper 85-GT-22, 1985.

7. Dunham, J., et al, "A new turbomachinery throughflow program using the streamline curvature method", Unpublished RAE report, 1990.

8. Fuchs, R., et al, "Experimental investigation of a supercritical compressor rotor blade section", in "Advanced Technology for Aero Gas Turbine Components", AGARD CP 421, May 1987, Paper 39.

9. Steinert, W., et al, "Design and testing of a controlled diffusion airfoil cascade for industrial axial flow compressor application", ASME Paper 90-GT-140, 1990.

10. Dawes, W. N., "A comparison of zero and one equation turbulence modelling for turbomachinery calculations", ASME Paper 90-GT-303, 1990.

11. Wennerstrom, A. J., "Experimental study of a high-through-flow transonic axial compressor stage", Proceedings 6th ISABE, Paris, pp 447-457, 1983.

12. Fleeter, S., et al, "Experimental investigation of a supersonic compressor cascade", ARL TR 75-0208, June 1975.

13. Tweedt, D. L., et al, "Experimental investigation of the performance of a supersonic compressor cascade", ASME Paper 88-GT-306, 1988.

14. Fourmaux, A., et al, "Test results and theoretical investigations on the ARL 19 supersonic blade cascade", ASME Paper 88-GT-202, 1988.

15. Schreiber, H. A., and Tweedt, D. L., "Experimental investigation and analysis of the supersonic compressor cascade ARL-2DPC", DFVLR IB-325-02-87, 1987.

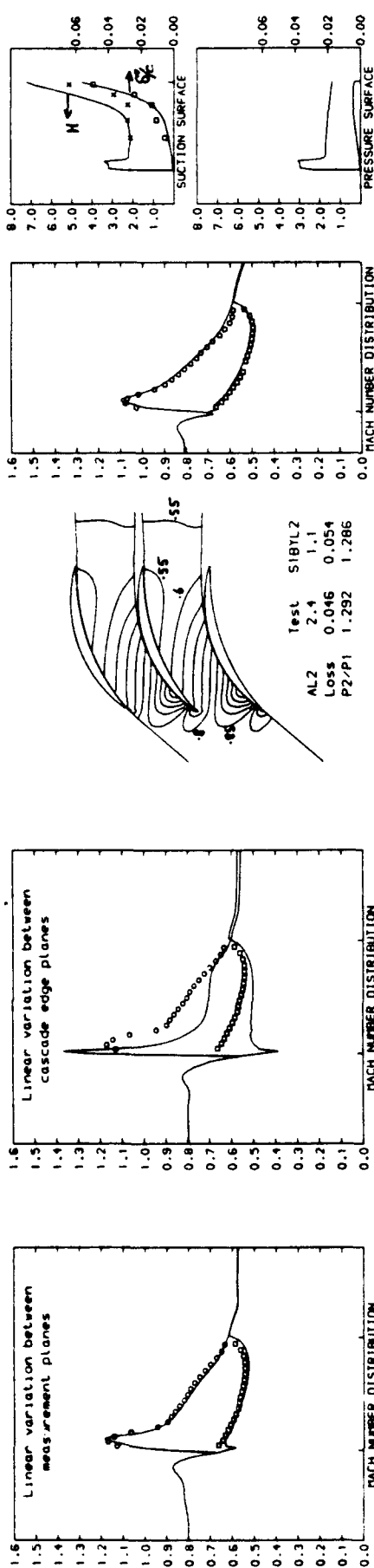
16. Calvert, W. J., et al, "Performance of a civil fan rotor designed using a quasi-three-dimensional calculation system", in "Turbomachinery - Efficiency Prediction and Improvement", Proc I Mech E, 1987-6,

17. Pierzga, M. J., and Wood, J. R., "Investigation of the three-dimensional flow field within a transonic fan rotor: experiment and analysis", ASME Journal of Eng for Gas Turbines and Power, Vol 107, No 2, April 1985, pp 436-449.

18. Wadia, A. R., and Beacher, B. F., "Three-dimensional relief in turbomachinery blading", ASME Journal of Turbomachinery, Vol 112, No 3, pp 587-598, 1990.

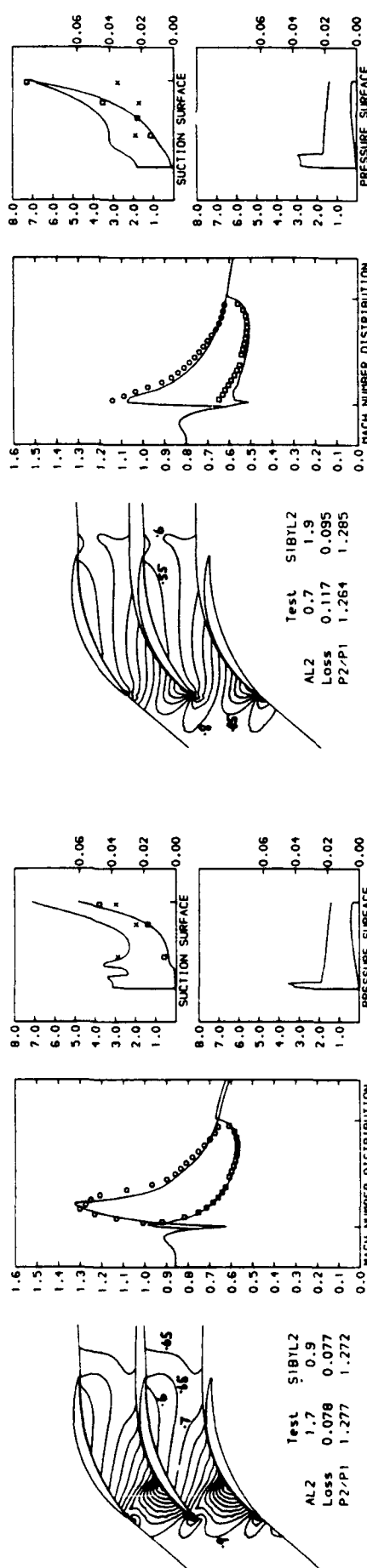
© British Crown Copyright, 1991/MOD

Published with the permission of the Controller of Her Britannic Majesty's Stationery Office.



a. Effect of stream tube thickness at $M_1=0.8$, $AL_1=54.5$, $\Omega=1.39$

c. Optimum incidence case - $M_1=0.8$, $AL_1=49.5$, $\Omega=1.12$



b. Choked flow case - $M_1=0.85$, $AL_1=49.5$, $\Omega=1.20$

d. Stalled flow case - $M_1=0.8$, $AL_1=52.5$, $\Omega=1.12$

Fig 1 SIBYL2 predictions for V2 cascade (symbols indicate test data)

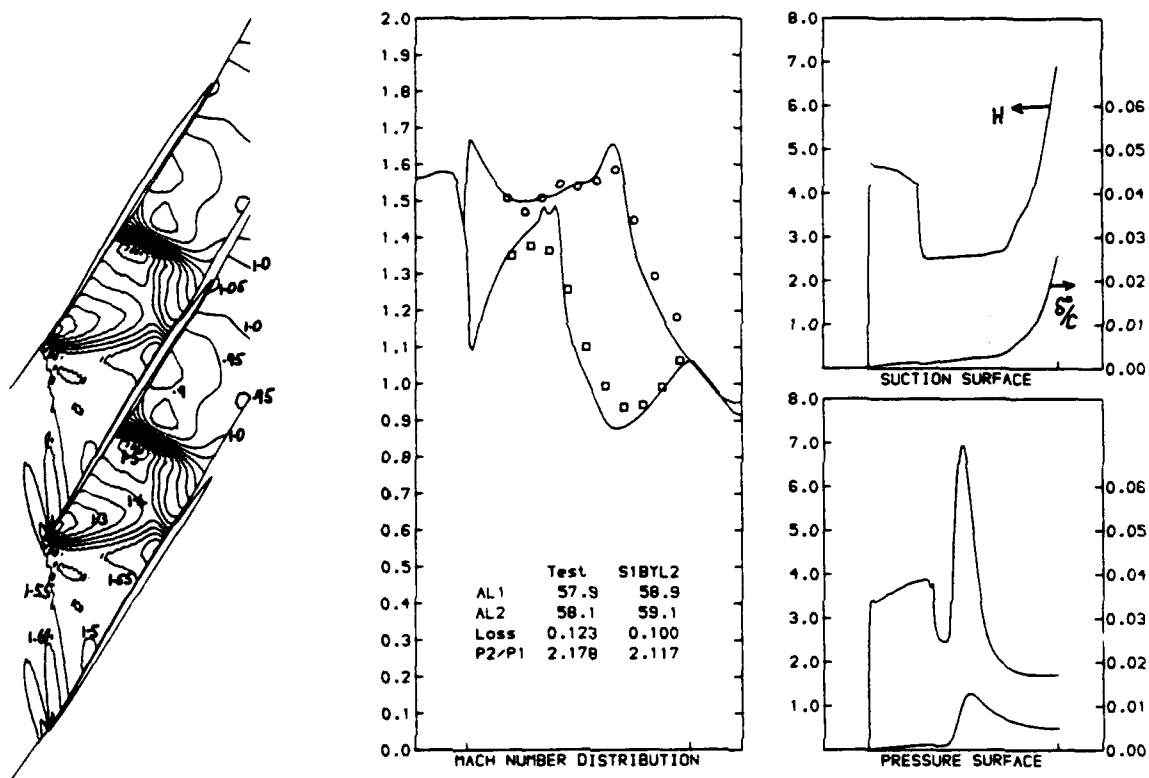


Fig 2 S1BYL2 prediction For ARL SL19 cascade (symbols indicate test data)

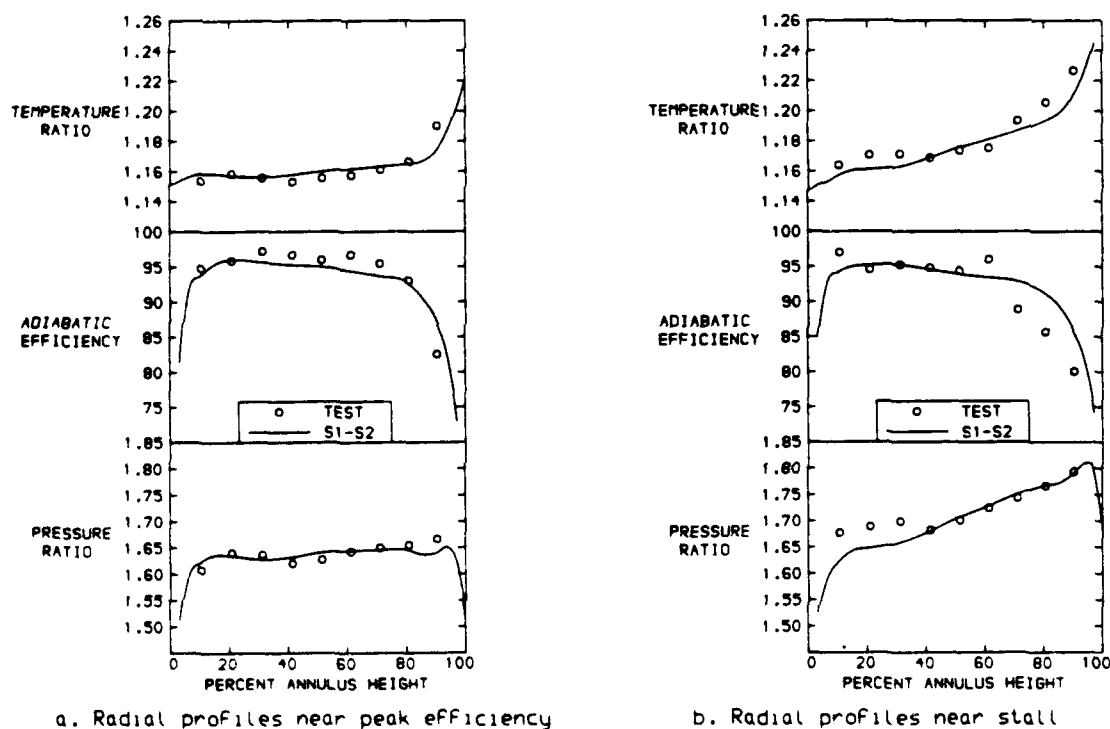


Fig 3 S1-S2 predictions For NASA transonic rotor 67

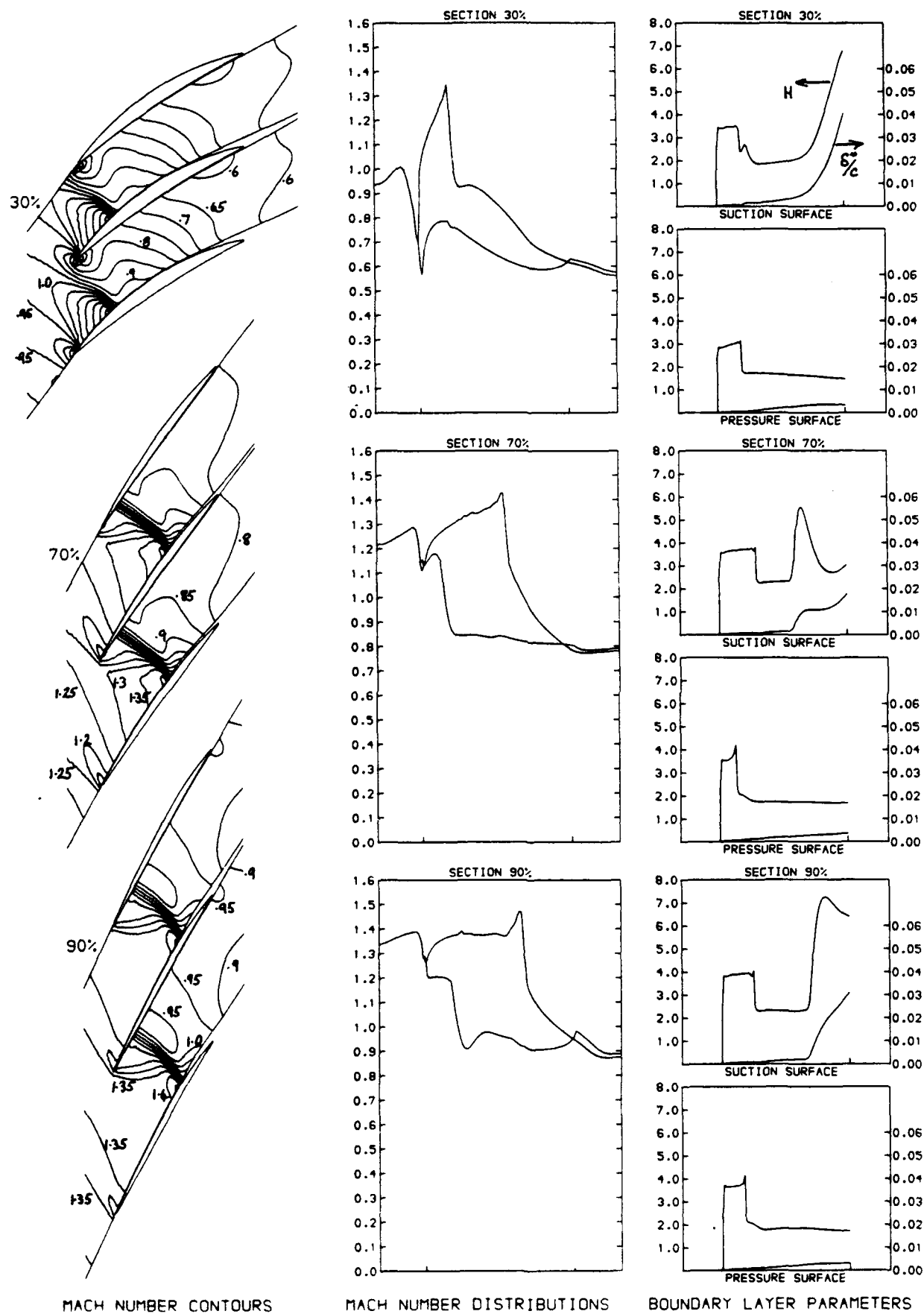


Fig 4a S1BYL2 predictions for NASA rotor 67 at peak efficiency

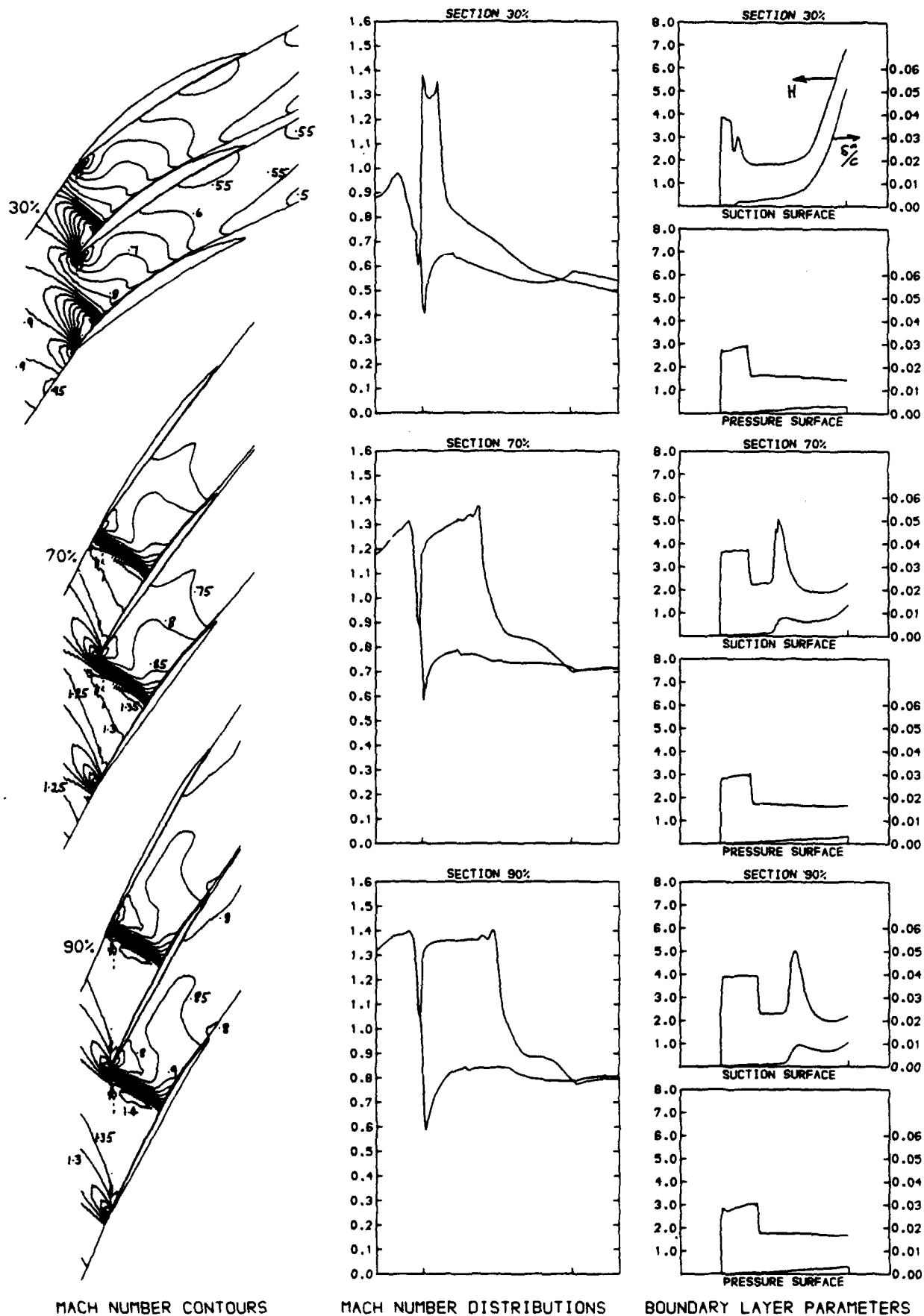


Fig 4b SIBYL2 predictions for NASA rotor 67 near stall

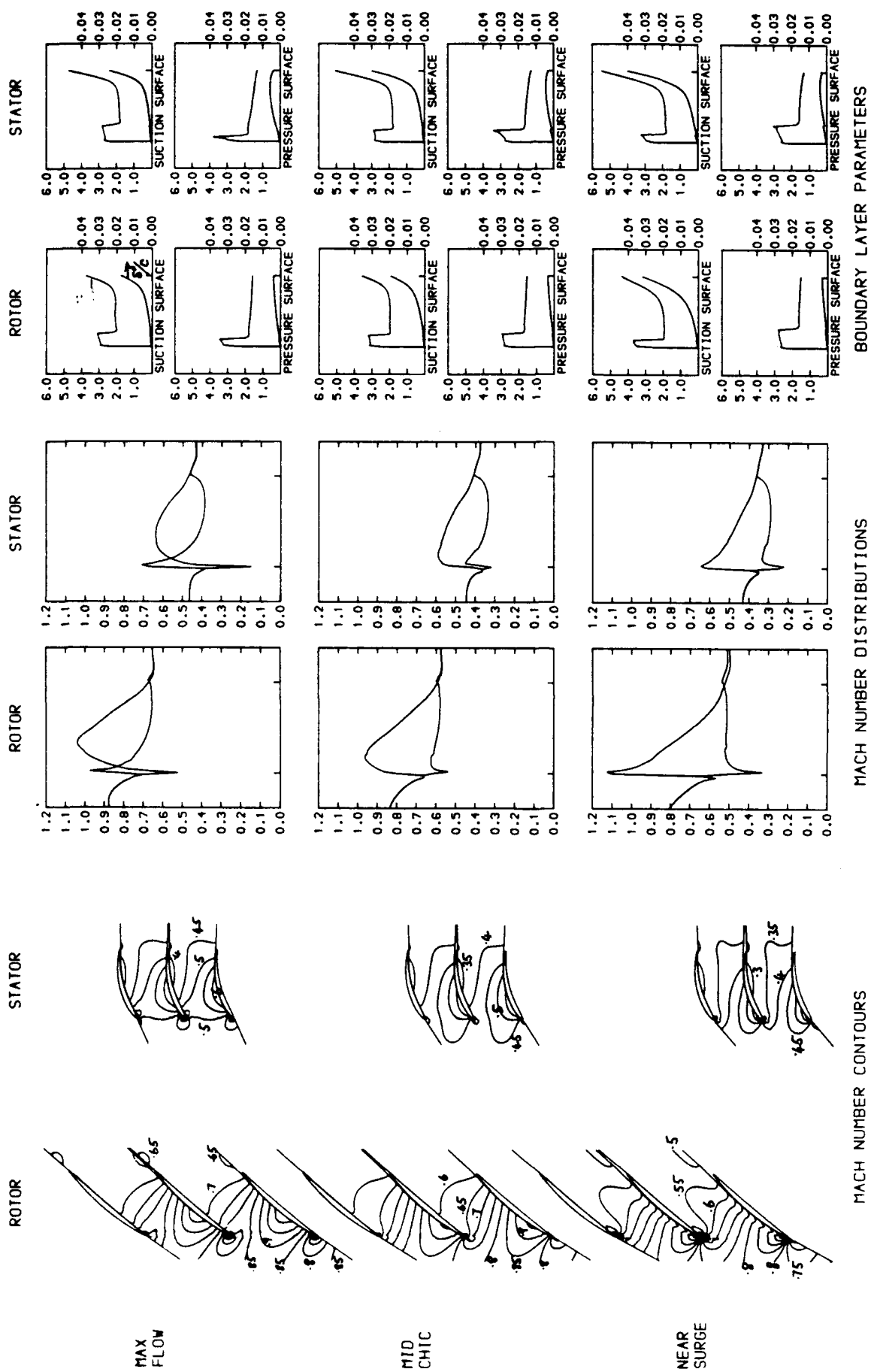


Fig 5 SIBYL2 predictions for Rolls-Royce HP9 mid span sections

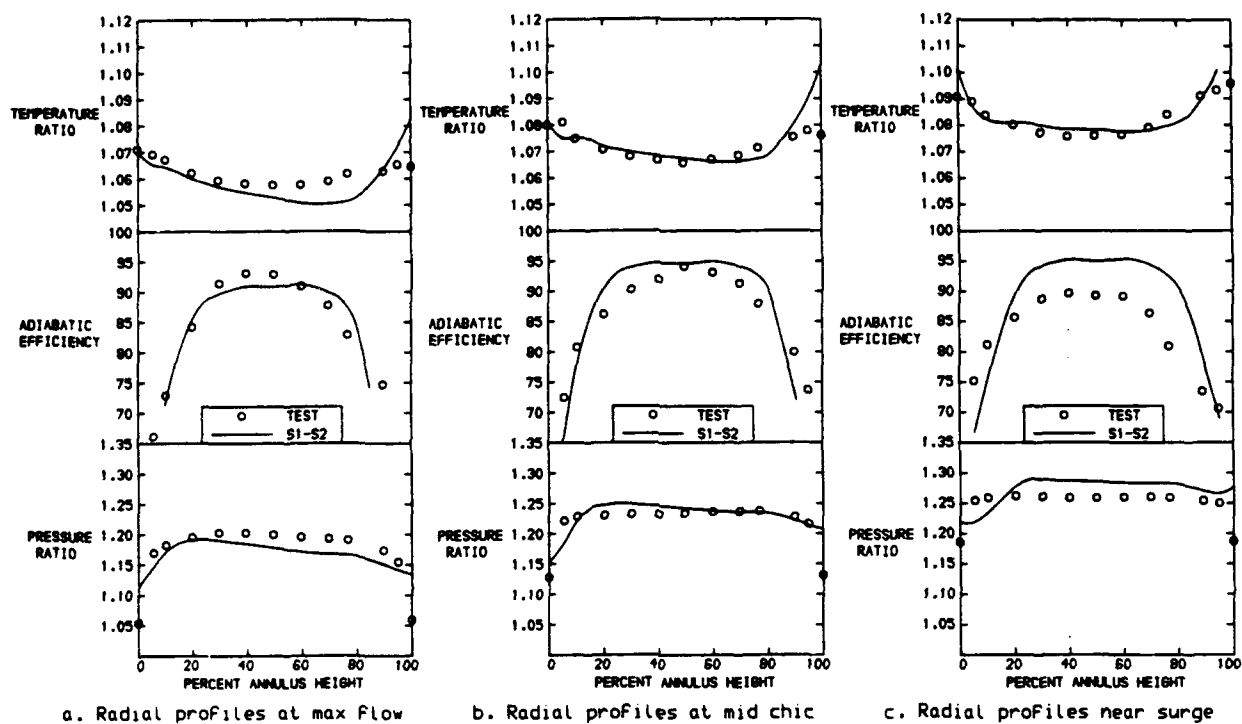


Fig 6 S1-S2 predictions for Rolls-Royce HP9 stage

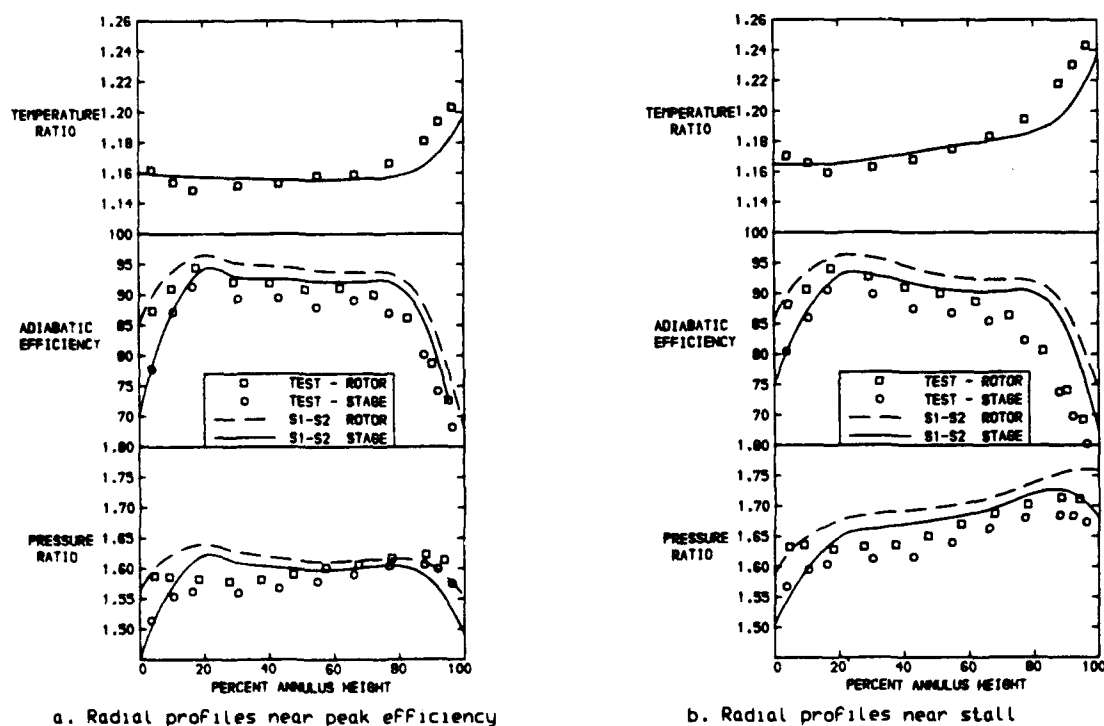
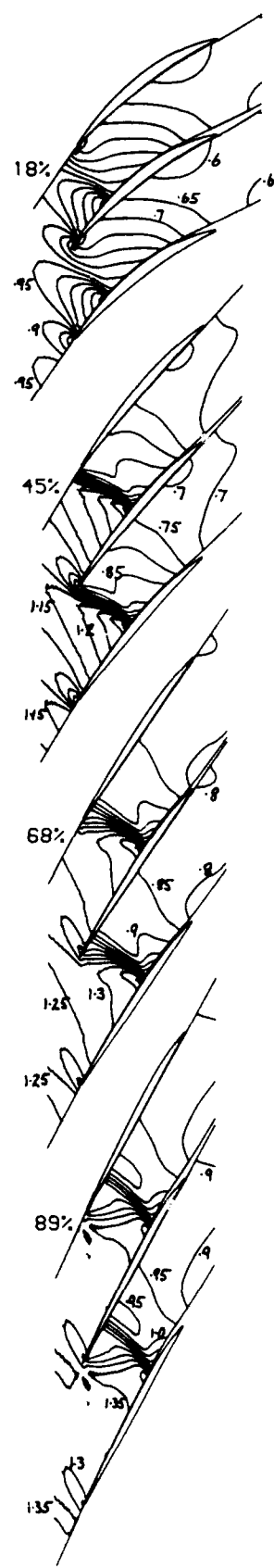
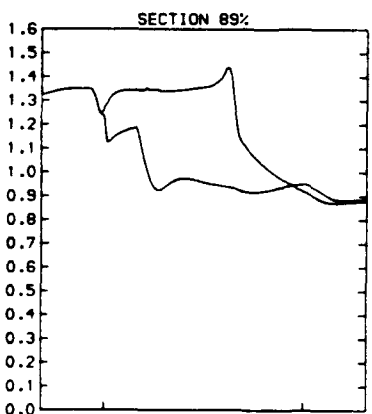
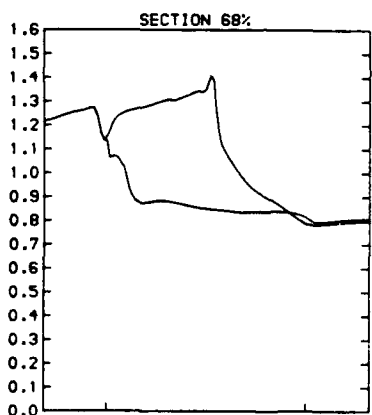
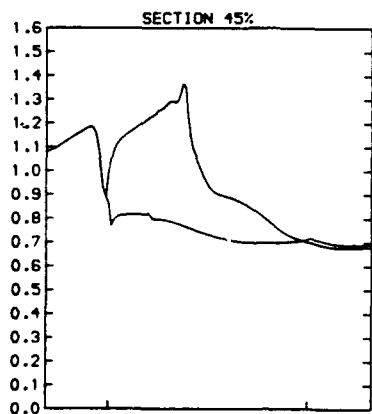
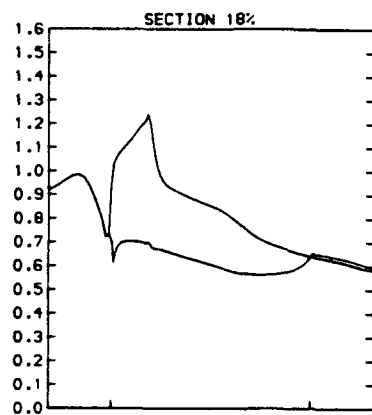


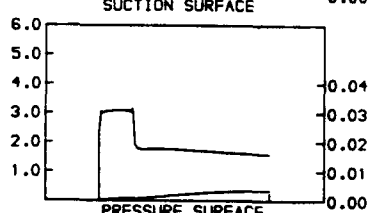
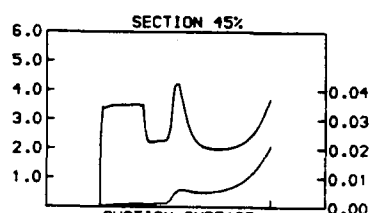
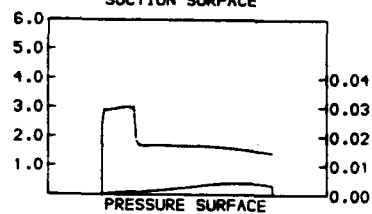
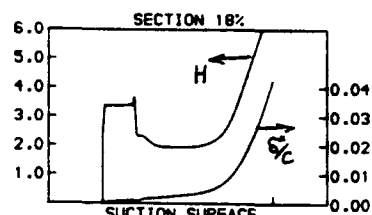
Fig 7 S1-S2 predictions for DFVLR transonic stage



MACH NUMBER CONTOURS



MACH NUMBER DISTRIBUTIONS



BOUNDARY LAYER PARAMETERS

Fig 8a SIBYL2 predictions for DFVLR rotor at peak efficiency

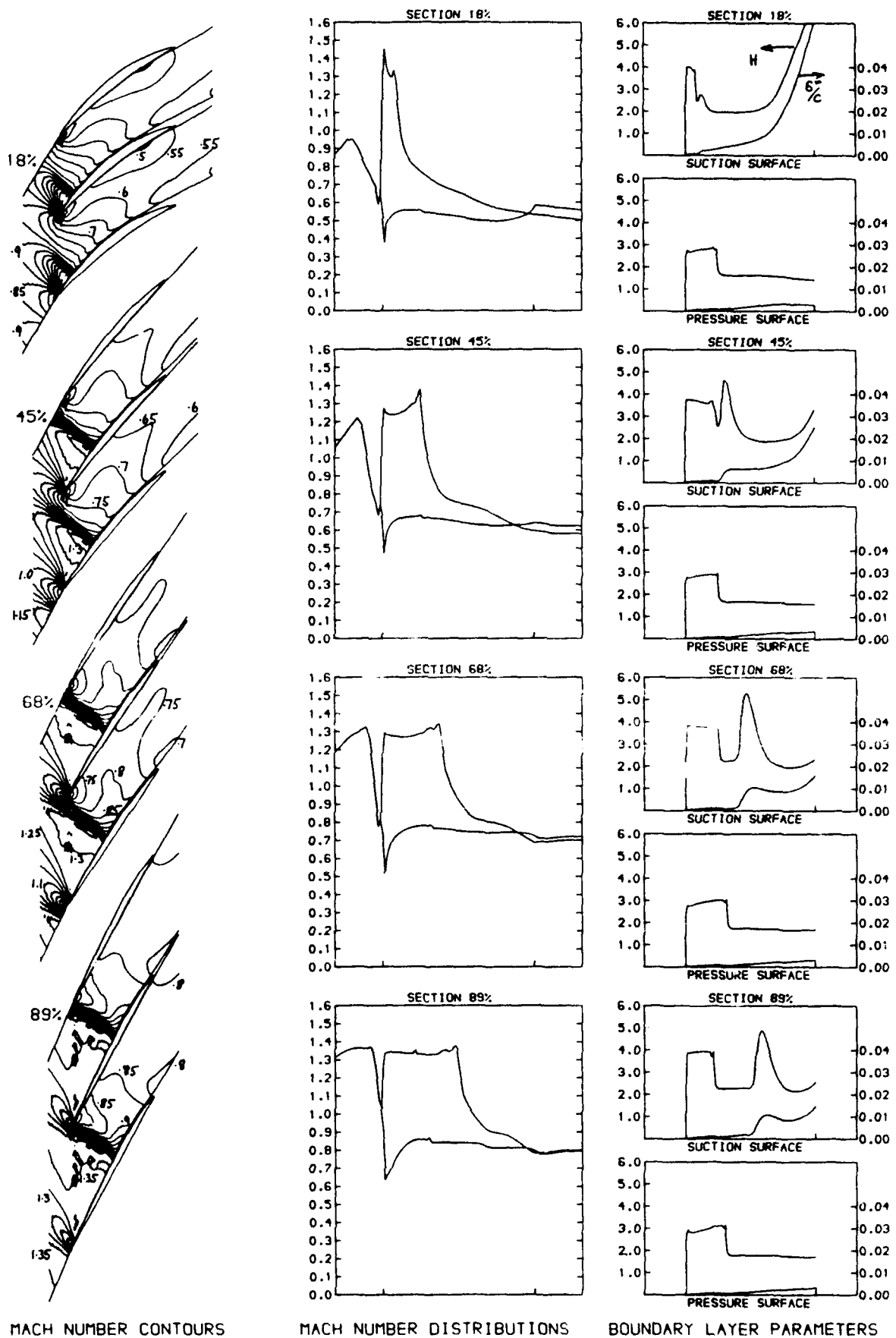


Fig 8b SIBYL2 predictions for DFVLR rotor near surge

Discussion

C. HAH, NASA LEWIS, U.S.A.

- 1) For transonic rotors, the role of tip-clearance flow of spanwise mixing inside the boundary layer is important. How is this effect modeled in your code? If it is not modeled, how can you achieve good results?
- 2) With your method, did you observe shock induced boundary layer separation?

AUTHOR'S REPLY

- 1) All blade end effects are modeled by specifying additional losses for the blade sections near the end walls. Bulk spanwise mixing is not too important for the front blade rows in a compressor, but it becomes more important for later rows: it can be included in the S2 calculation. Spanwise flow in the boundary layer is very noticeable in surface flow visualization, but it does not necessarily seem to have a large effect on the overall flow.
- 2) Shock induced boundary layer separation was predicted for both the NASA and DFVLR rotors at the sections from about mid-span to the tip. It is indicated in Figs. 4 and 8 by the high values of shape factor (H) for the suction surface boundary layer (after the initial region with high values which is associated with the laminar boundary layer).

G. SEROVY, IOWA STATE UNIV., U.S.A.

Could you discuss the method for setting the variation in stream tube thickness (in the blade-to-blade computation) for the cases where both S1 and S2 computations were made, for example in the NASA rotor 67 test case?

AUTHOR'S REPLY

Setting the stream tube thickness distribution is much less of a problem for S1-S2 solutions of a complete compressor than for S1 calculations of a cascade. The S2 throughflow solution provides values of stream tube thickness at the leading and trailing edge planes and at four internal planes for each blade row, and linear variations are assumed in between.

K. BROICHHAUSEN, MTU, MÜNCHEN, GERMANY

In your presentation you mentioned the limitations of S1-S2 calculations regarding endwall effects. Nevertheless your results show remarkable endwall effects, e.g., an accumulation of losses. Could you give an indication, how these phenomena are incorporated into the computation?

AUTHOR'S REPLY

Allowance for endwall effects is made by including additional losses for the outer sections of the blade. These losses were set according to the same rule for all three of the compressor cases, as described in the paper. The losses are specified as input to the S1 part of the solution and fed to the S2 calculation as part of the standard S1-S2 linking.

J. CHAUVIN, LEMFI, FRANCE

- 1) Did you include angle correction to take clearance and secondary flows into account?
- 2) Is the effect of rotation on loss, turning and velocity distribution significant?

AUTHOR'S REPLY

- 1) No corrections were made to the values of flow angle predicted by S1BYL2 in the results shown, and none have been needed for any of the single stage compressors analyzed so far.
- 2) I have not specifically studied the effect of rotation on the solutions, but I would expect it to be significant for blade sections where there is much change in radius.

A COMPUTATIONAL STUDY OF TIP LEAKAGE FLOW AND LOSSES IN A LINEAR TURBINE CASCADE

John Moore and Joan G. Moore

Mechanical Engineering Department
Virginia Polytechnic Institute and State University
Blacksburg, Virginia 24061

92-16070

ABSTRACT

A computational study of 3-D flow in the VPI&SU tip leakage turbine cascade is used to show the level of modelling attainable now. Results for the overall flow development are compared with measurements of flow and losses at the exit of the tip leakage gap and downstream of the blade row. Mechanisms for the additional loss due to tip leakage are discussed. Consideration is given to areas where the modelling of fine scale flow structure may be improved. These include the flow in the tip clearance gap, flow in the tip leakage vortex, and flow separation at the trailing edge.

NOMENCLATURE

C_D	discharge coefficient, Eq. 6
C_{ps}	static pressure coefficient, Eq. 3
C_{pt}	total pressure loss coefficient, Eq. 1
P	static pressure
P_{s0}	cascade inlet static pressure
P_t	total pressure
P_{t0}	cascade inlet total pressure
Q	passage volume flow rate
S_b	tip gap exit length
u	velocity component in primary flow direction
U_0	cascade inlet free stream velocity
u_n	tip gap normal velocity, Fig. 10
u_s	tip gap streamwise velocity
u_t	tip gap total velocity
U_t	tip gap exit velocity based on potential flow
v	velocity component orthogonal to u and w
V	velocity at downstream measurement plane
w	velocity component in spanwise direction
X/c	axial distance from blade leading edge/ axial chord
ΔY	blade pitch
ΔZ	passage height, span
β	flow angle with respect to pitchwise direction, Eq. 2
δ_t	tip gap height
θ	flow angle with respect to axial direction
ρ	fluid density

Subscripts

0	upstream of cascade, reference
ex	tip gap exit plane
x	axial direction
y	pitchwise direction

Overbars

$\bar{}$	area average, average
$\overline{}$	mass average

INTRODUCTION

The calculation of three-dimensional flow in a turbine blade row with leakage through a clearance gap provides an interesting challenge for CFD techniques. It offers an opportunity to simultaneously review numerical and physical modelling

capabilities for a wide range of flow phenomena occurring with quite different length scales and significant variations in flow physics.

At the practical level, one may expect a calculation to give the extra losses due to tip leakage which are known to have an appreciable effect on the efficiency of unshrouded turbine blades [1]. (A decrease of two percentage points for each one percent increase in tip clearance/blade height is typically found.) To model these one needs to compute the flow through the tip gap, the formation of the tip leakage vortex, and the mixing of the leakage vortex with the main passage flow. It is known, for example, that there is fine scale flow structure, such as a vena contracta, within the tip gap which itself is two orders of magnitude smaller than the blade height [2]. It is also known that turbulence and mixing in vortices are influenced by the swirl of the flow [3]. The questions arise as to how well can these effects be modelled. How well can they be modelled not just as isolated flows but in a complete calculation of the flow field in the whole blade row. The answer to this question must depend on computer capability as well as on the numerical technique and the physical modelling. So we find the problem of calculating tip leakage flow and losses in a turbine blade row to be a test of CFD capability, as well as a test of a CFD code.

In the present paper, we review the capability of the Moore Elliptic Flow Program, MEFP, run on an IBM 3084, to model flow in the VPI&SU tip leakage turbine cascade [4,5]. We used a $45 \times 28 \times 26$ grid (32,760 grid points) and 40 hours of CPU time. The basis of the numerical scheme has been described by J.G. Moore [6,7]; it is a pressure correction algorithm for solving the Reynolds-averaged form of the Navier-Stokes equations, see Appendix A. The calculation method uses upwind control volumes chosen for each grid point at each of the forty iterations (twenty pass-pairs). The flow was modelled as having laminar and turbulent flow regions, and the Prandtl mixing length model used previously by the authors formed the basis of the turbulence model [7], see Appendix A. We took this opportunity, however, to try various modifications to the turbulence in several regions of the flow to try to gain insight into the local flow physics, and these are discussed in the last section of the paper.

The paper is structured to first show the overall flow development and the agreement obtained with overall flow properties. The results presented then focus on loss mechanisms associated with tip leakage flow and the extent to which these are modelled. Some areas where improvement of the fine scale modelling was sought are then discussed, including the trailing edge flow where some success was achieved.

VPI&SU Cascade and Computational Mesh

The geometry of VPI&SU tip leakage turbine cascade is shown in Fig. 1. The blade shape is that of a reaction turbine with a turning angle of 109 degrees, and the cascade has an aspect ratio of 1.0. The tip gap is 2.1% of blade height.

The flow through the cascade is incompressible with an inlet free stream velocity $U_0 = 20.5$ m/s and a density of 1.1 kg/m^3 . The Reynolds number based on

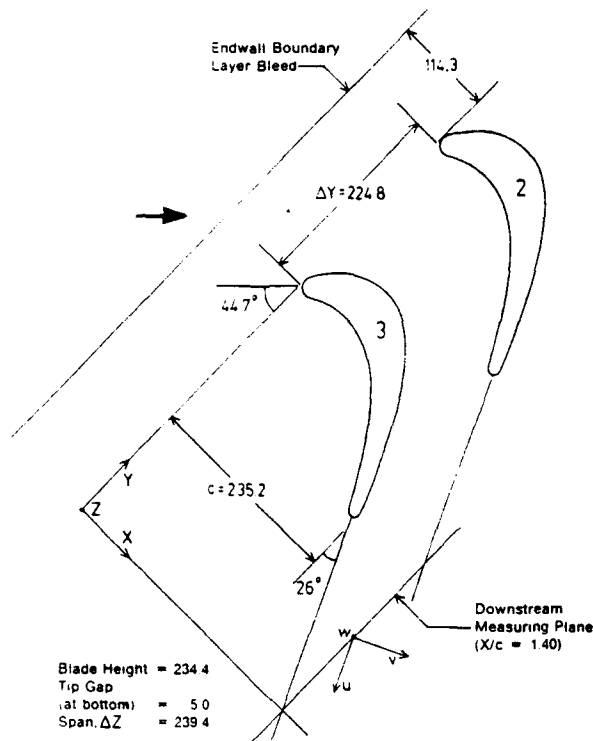


Fig. 1. Cascade geometry with coordinate system for the cascade (X,Y,Z) and showing primary and secondary flow velocities (u,v,w) downstream. Linear dimensions in mm.

blade axial chord and exit velocity was 4.5×10^5 [5].

Thin endwall boundary layers were created about one half an axial chord upstream of the blade leading edges by the use of endwall bleeds. The new boundary layers were tripped and when measured at $X/c = -0.30$ they were turbulent with a thickness of 2.2 mm, less than the 5 mm height of the tip clearance gap [4]. The mass-averaged total pressure loss coefficient at the blade row entrance was low, $\bar{C}_{pt} = 0.0035$, where

$$C_{pt} = (P_{t0} - P_{tc}) / \frac{1}{2} \rho U_0^2. \quad (1)$$

Two views of the computational grid are shown in Fig. 2. The section at mid-passage-height shows an optimised mesh with grid refinement around the leading and trailing edges and upstream and downstream of the blade row. Within the blade passage the basic blade-to-blade spacing chosen to represent the profile boundary layer growth has been preserved. The cross-section midway through the blade row shows simple grid refinement in the bottom half to capture the tip leakage vortex and a relatively coarse grid in the top half where there is no tip leakage flow. There are six points between the blade tip and the stationary endwall describing the velocity profile for flow in the tip gap, and the near-blade-tip point is 5 percent of the tip gap height from the blade tip. In the profile and endwall boundary layers the near-wall points are at a distance of 0.001 axial chords from the wall.

The blade profile boundary layers were tripped just downstream of the blend points with the leading edge circle, in the experiment. They were modelled as fully turbulent in the calculation.

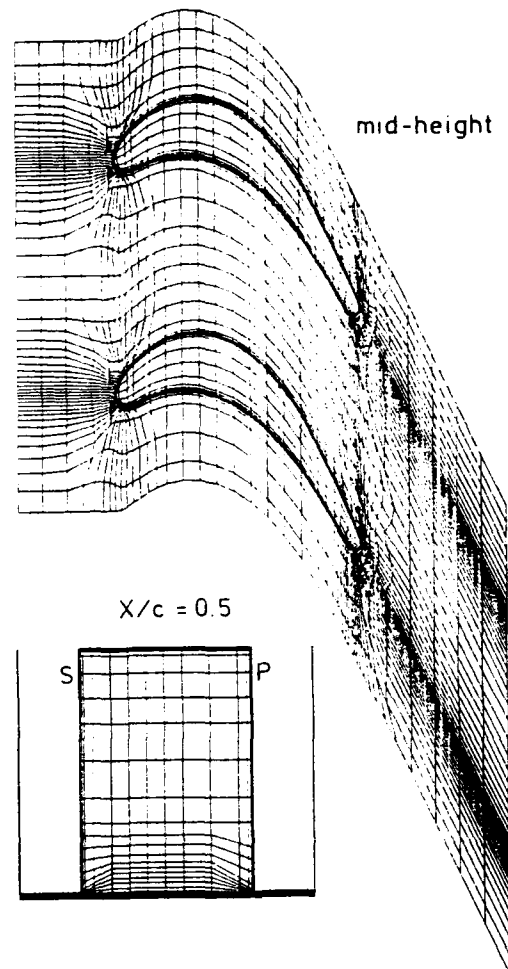


Fig. 2. Calculation grid, 45 x 28 x 26 points. Near wall grid points at 0.001 of axial chord, c.

LEVEL OF MODELLING ATTAINABLE NOW

In this section we consider the overall flow development and the production mechanisms for tip leakage loss, and we show the level of agreement currently attainable.

Overall Flow Development

The calculated flow development may be followed in Fig. 3 which shows contours of total pressure loss coefficient, C_{pt} , on four sections within the blade row and two sections downstream. The two main features seen are the growth of the tip leakage vortex and the development of the suction surface boundary layer and the blade wake. Starting just upstream of the trailing edge the lower passage vortex develops a clear identity above the tip leakage vortex, and convection of low loss fluid appears to be separating the two vortices.

A comparison of the calculated and measured loss distributions at $X/c = 1.4$ is shown in Fig. 4. Here, we view the contours looking upstream along the camber line at the blade trailing edges, i.e. at 26 degrees to the blade-to-blade direction; in this way we are looking essentially along the axes of the trailing vortices. The overall agreement is very good. The size and location of the tip leakage vortex and the lower passage vortex, the shape and thickness of the

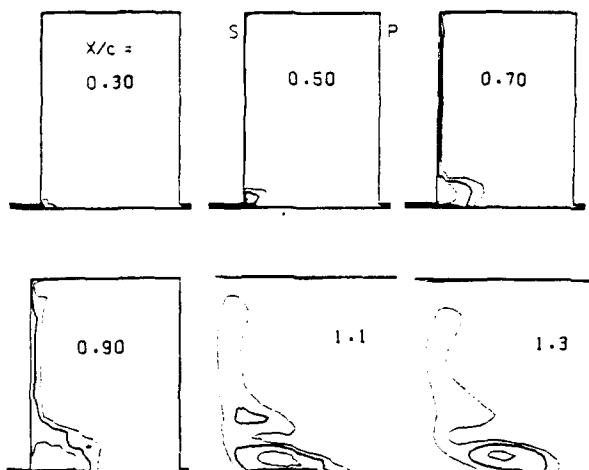


Fig. 3. Calculated flow development. Total pressure loss contours, $C_{pt} = 1, 2, 3$.

blade wake, and the thickness of the upper endwall boundary layer are all well modelled. The peak loss level of $C_{pt} = 3.0$ in the tip leakage vortex also agrees well with the measured value of 2.8. There are three apparent areas for improvement. Near the bottom endwall, there is excessive convection of low loss fluid under the tip leakage vortex; this is probably due to the low turbulence specified in and around the vortex, as discussed below. The peak losses in the blade wake and the lower passage vortex are too high by about $\delta C_{pt} \sim 0.6$, probably due to excessive turbulent viscosity in the blade profile boundary layers. And the passage vortex in the blade wake in the top half of the flowfield is not clearly distinguished, partly because of the coarser grid used in the upper half, see Fig. 2.

The secondary velocity vectors corresponding to Fig. 4 are shown in Fig. 5. Qualitatively the agreement is very good, while quantitatively the calculated secondary velocities appear to be about 30 percent too high.

Mass-Averaged Total Pressure Losses

The build-up of the mass-averaged total pressure losses in the two halves and for the whole flow is shown in Fig. 6. The measured losses at $X/c = 1.4$ are also shown for comparison. In the top half, the losses remain relatively constant until about 80 percent of axial chord; they then rise quite rapidly to the trailing edge; downstream there is again little variation. It appears that the upper endwall boundary layer is contributing little loss and that most of the loss in the upper half is caused by the suction side boundary layer on the uncovered part of the blade row and possibly by mixing of the upper passage vortex. In contrast, in the bottom half, the losses increase steadily through the blade row and downstream. Two important mechanisms are at work here, in addition to those at work in the top half, these are loss production in the tip clearance gap due to mixing and friction, and dissipation of secondary kinetic energy in the tip leakage vortex [5]. The build-up of the loss for the whole passage shown in Fig. 6 is the sum of the development in the two halves.

Quantitatively the losses are well modelled by the calculation. At $X/c = 1.4$, the total loss is $C_{pt} = 0.36$ compared with a measured value of 0.38. In the bottom half, it is 0.25 compared with 0.28, and in the top half it is 0.11 compared with the

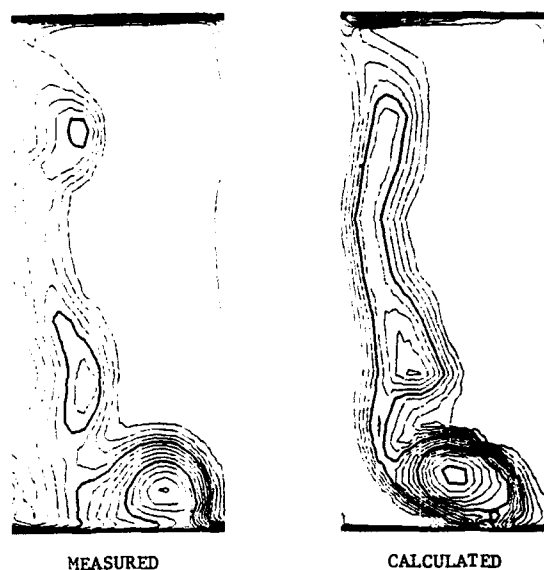


Fig. 4. Comparison of measured and calculated contours of total pressure loss at $X/c = 1.4$. View looking upstream along the blade camber line at the trailing edge. Contours: $C_{pt} = 0.2$ by 0.2 to 3.0.

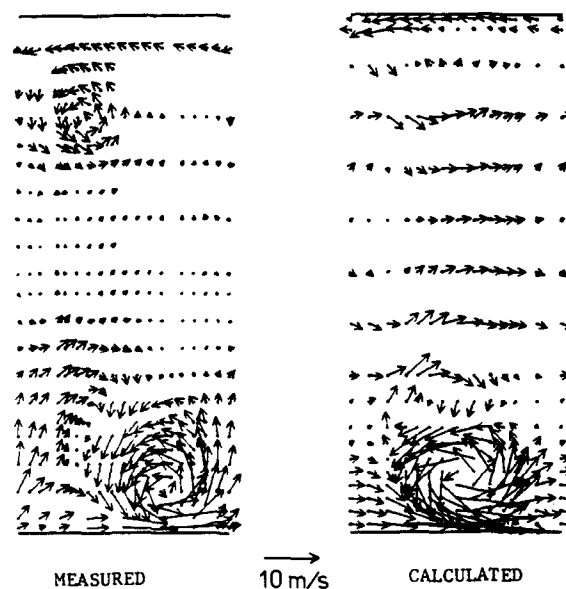


Fig. 5. Measured and calculated secondary velocity vectors at $X/c = 1.4$. View as in Fig. 4. Vectors are resultant of v and w components, see Fig. 1.

measured value of 0.10.

Pitch-Averaged Loss and Flow Angle

Figures 7 and 8 show pitch-averaged total pressure losses and pitch-averaged flow angles at $X/c = 1.4$. For the losses, the agreement is better in the top half than in the bottom half. Even though the fine structure of the upper passage vortex was not modelled, the level and distribution of its losses are quite good. In the bottom half, two effects influence the distribution, the convection of low loss fluid under

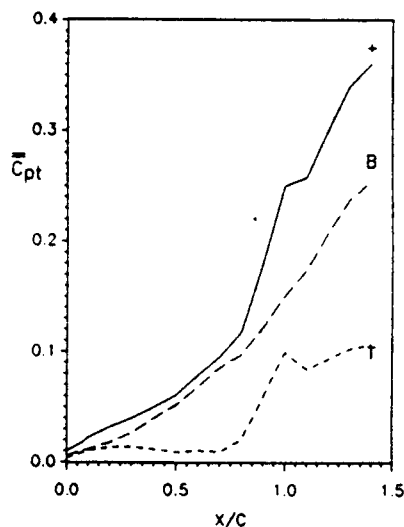


Fig. 6. Development of mass-averaged total pressure losses. Top half: --- calculated; T, measured. Bottom half: --- calculated; B, measured. Total: ——— calculated; +, measured.

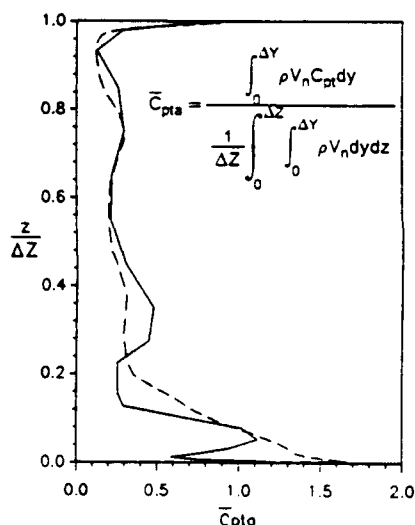


Fig. 7. Pitch averaged total pressure loss coefficient, \bar{C}_{pta} at $X/c = 1.4$. --- measured; ——— calculated.

the tip leakage vortex mentioned previously, and an apparent hijacking of loss by the lower passage vortex from the tip leakage vortex.

The agreement between the measured and calculated exit flow angles is slightly better than for the losses. Here, two curves are shown for the measurements, one giving the data as taken and the second a distribution corrected in an attempt to allow the data to satisfy overall continuity [5]. The difference between the data curves is about 1.8 degrees. The calculation agrees better with the uncorrected data especially in the upper half where it is within 2 degrees. In the lower half, the calculated vortices are too strong giving underturning near the wall and slightly too much overturning

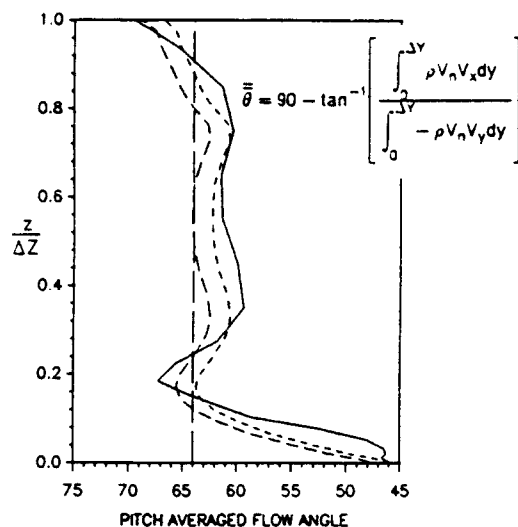


Fig. 8. Pitch averaged flow angles at $X/c = 1.4$. ——— calculated; --- uncorrected measurements; - · - · - corrected measurements; ——— mean camber line at exit.

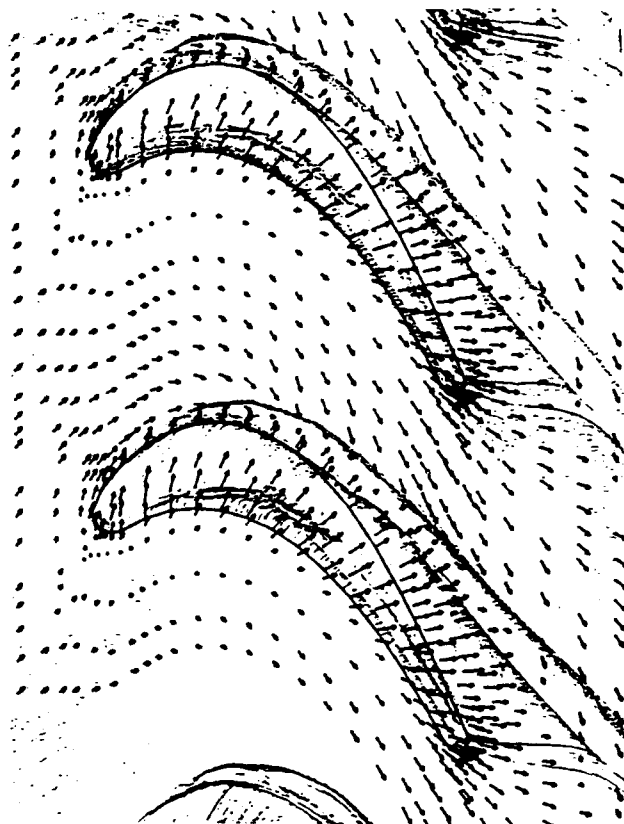


Fig. 9. Superposition of velocity vectors near the bottom endwall on an endwall flow visualization. Note flow under the blade and flow separation in the passage.

between the vortices.

For the whole passage, the exit flow angles,

$$\bar{\theta} = \tan^{-1} \left(\bar{V}_x / \bar{V}_y \right), \quad (2)$$

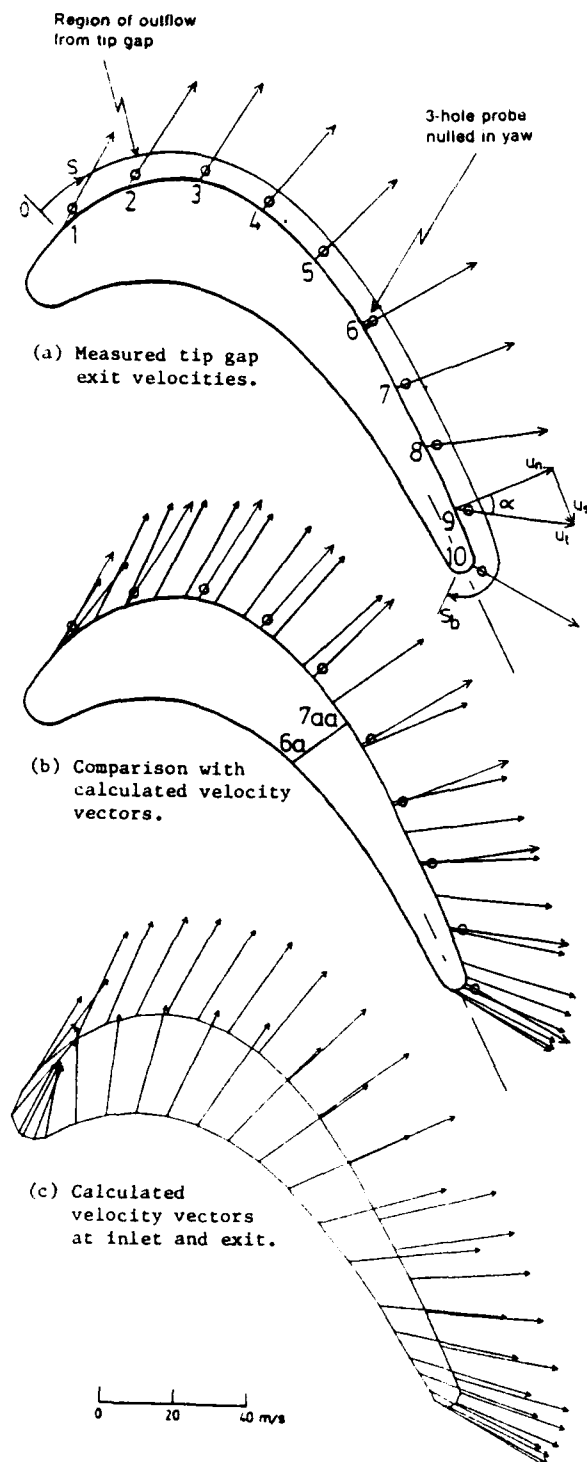


Fig. 10. Measured and calculated velocities at mid-height of tip gap.

were 28.2 degrees from the calculation, 27.9 degrees for the uncorrected data, and 26.1 degrees for the corrected data. A discussion of how the trailing edge flow was modelled to obtain this agreement is given below.

Endwall Flow Visualization

The visualization of the flow near the bottom endwall of the cascade, shown in Fig. 9, has been achieved by overlaying the calculated near-wall velocity vectors and blade outlines on an endwall surface flow visualization. The resulting picture

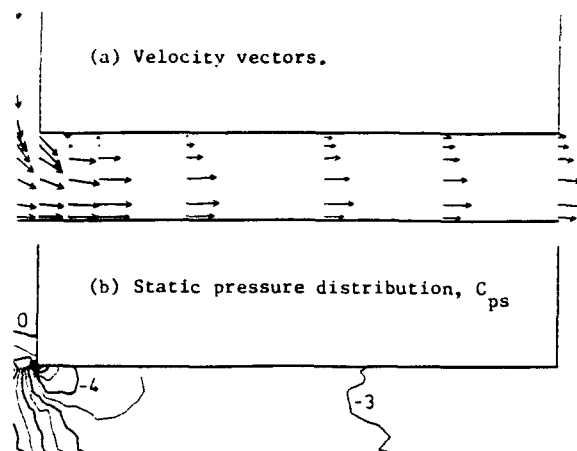


Fig. 11. Flow through the tip gap on plane 6a-7aa, see Fig. 10b.

conveys the impression of flow leaking through the tip clearance gap, moving away from the blade suction surface, and separating from the endwall when it encounters the main passage flow. Within the blade row, the calculated velocity vectors show separation close to the line where the overturned passage boundary layer separates from the endwall. Downstream the calculated separation appears closer to the line of separation of tip leakage fluid. In general, the directions of the leakage vectors follow the directions of the surface streaks quite closely.

Beneath the blades in the oil flow visualization, there was evidence of a laminar flow separation and reattachment [4]. The calculated flow was modelled as turbulent in this region and so the calculation does not show such a separation.

In the pressure-side half of the passage, the vectors show the expected attachment behavior [4]. To the left of this line (following the flow), the flow moves into the tip leakage gap; to the right it is slightly overturned and tends towards the suction side.

Flow at Mid-Height in Tip Gap

Figure 10 shows measured and calculated velocity vectors at the mid-height of the tip gap. At the tip gap exit at this height, the calculated flow directions and velocity magnitudes are in excellent agreement with the measurements. And from pressure side to suction side, there is little change in the calculated flow direction, except near the blade leading edge.

Tip Gap Flow Structure

Within the tip gap, the flow can vary significantly from the blade tip to the endwall, especially near the flow entrance on the pressure side of the blade. Consider the plane 6a-7aa shown in Fig. 10b. The plane runs from $X/c = 0.60$ on the pressure side to $X/c = 0.72$ on the suction side, and it was chosen using the endwall flow visualization to be aligned with the tip leakage flow. Figures 10b and 10c show this to be the case. Figure 11 then shows calculated velocity vectors and the calculated static pressure distribution on this plane.

The flow separates from the corner on the pressure side and forms a vena contracta at about one half to one tip gap height into the gap. It then reattaches on the blade tip at about two tip gap heights. This is typical behavior for a tip gap with a sharp entrance and it is remarkably well modelled considering the near-wall grid spacing near the inlet corner

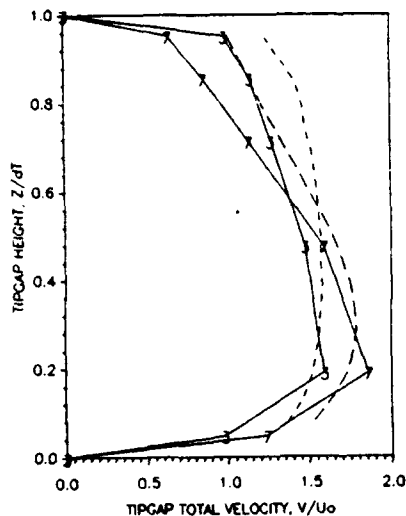


Fig. 12. Tip gap exit total velocity profiles at stations 3 and 7 of Fig. 10a. - - - measured at station 3; - · - measured at station 7; — calculated.

is 5 percent of the tip gap height [8]. Associated with the vena contracta is a region of high velocity and low static pressure. Here, in the calculation, this is evident as contours of $C_{ps} = -4$ and -5 , near the inlet corner, as seen in Fig. 11b. The static pressure coefficient, C_{ps} , is defined as

$$C_{ps} = (P - P_{s0}) / \frac{1}{2} \rho U_0^2 \quad (3)$$

Tip Gap Exit Velocity Distributions

The velocity profile at the exit of the tip gap is non uniform with somewhat lower velocities near the blade tip, as seen in Fig. 11a. This is particularly true near the blade trailing edge where the flow path through the tip gap is shorter. Figure 12 shows a comparison of profiles at two measurement locations, 3 and 7 in Fig. 10a. Location 3 has a profile typical of stations 1-3, and location 7 has a profile like those measured at stations 5-9. The calculation shows the right trend with more non-uniformity at station 7, but the calculated profiles have too little mixing near the blade tip and show about 10 percent too little leakage flow.

Tip Gap Flow Rate

The accumulated flow through the tip gap is shown as a function of axial distance along the blade, for both the measurements and the calculation, in Fig. 13. The agreement is consistent with that seen in Fig. 12, and by the blade trailing edge 5.1 percent of the cascade flow has passed through the tip gap in the calculation, compared with 5.7 percent in the experiment.

Integration of Tip Gap Exit Flow Properties

In reference 5, it was suggested that flow exited the tip gap on the suction side and around the trailing edge over the distance S_b indicated in

Fig. 10a. There was a question about the starting point chosen for the integration at $X/c = 0.075$, but upstream of this point the flow velocities in the tip gap on the suction side are almost tangential to the suction surface, as seen in Fig. 10c. So the net contribution to the flow from the tip gap upstream of this point is only about 1 percent of the tip gap flow.

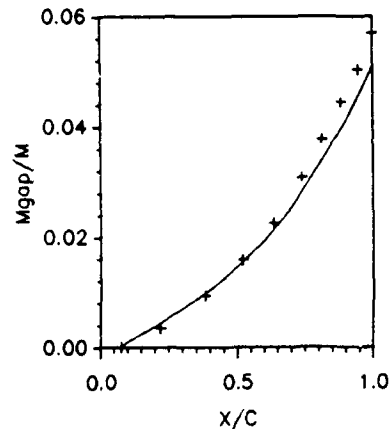


Fig. 13. Accumulated flow rate through the tip gap as a fraction of the flow rate through the cascade. — calculated; +, measured.

For flow exiting the tip gap, the local components of velocity are u_n and u_s , normal and parallel to the suction surface, as shown in Fig. 10a, and the local total pressure is P_t . Overall tip leakage coefficients were defined in reference 5 as

$$\text{Flow Coefficient, FC} = \frac{\int_0^{S_b} \int_0^{\delta_t} \rho u_n dz ds}{\rho Q} \quad (4)$$

and

$$\text{Mass Averaged Flow Property, } \bar{X} = \frac{\int_0^{S_b} \int_0^{\delta_t} \rho u_n X dz ds}{\rho Q U_0^2 / 2} \quad (5)$$

The flow properties, X , considered were

- $(u_n^2 + u_s^2)/2$ - Total Kinetic Energy Coefficient, TKEC,
- $u_n^2/2$ - Normal Kinetic Energy Coefficient, NKEC,
- $u_s^2/2$ - Streamwise Kinetic Energy Coefficient, SKEC,
- $(P_{t0} - P_t)/\rho$ - Total Pressure Loss Coefficient, TPLC.

The calculation gave the following results:

	Measured	Calculated
FC	0.057	0.051
TKEC	0.128	0.101
NKEC	0.109	0.082
SKEC	0.020	0.019
TPLC	0.071	0.071

Further insight into these properties is obtained by plotting their variations as a function of tip gap exit length (0 to S_b). The distributions of tip gap exit flow, and the distributions of the fluxes of kinetic energy and total pressure loss are shown in Fig. 14. The plotted properties are normalized so that the areas under the curves are equal to the coefficients defined in Equations 4 and 5.

Clearly the calculated tip leakage flow has all the variations seen in the measurements; and the relative levels of all the curves are reproduced with remarkable accuracy. The overall difference stems from the flow coefficient being about 11 percent too small, and therefore the normal kinetic energy coefficient is 25 percent too small. The total pressure loss coefficient and the streamwise kinetic energy coefficient are in good agreement.

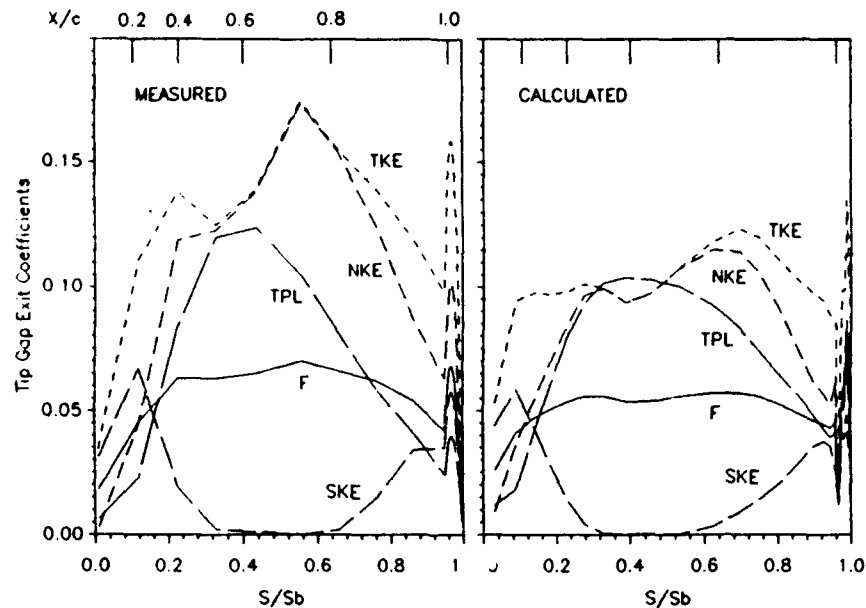


Fig. 14. Variations of flow rate, F , and fluxes of kinetic energy and total pressure loss at the tip gap exit. Fluxes: TKE - total kinetic energy; NKE - normal kinetic energy; SKE - streamwise kinetic energy; TPL - total pressure loss. Areas under the curves correspond to coefficients defined in Eqs. 4 and 5.

Blade Loading

Blade static pressure distributions are presented in Fig. 15. The solid lines show the calculated blade loading at 45 percent of blade height from the top endwall, and the corresponding measurement points are the P's and the S's. The calculated pressures agree well on the pressure side, but on the suction side the measured values are consistently lower. This is in qualitative agreement with the smaller turning and smaller exit flow angle from the calculation, seen in Fig. 8.

At the tip gap exit, some of the static pressures measured on the endwall (E) are lower than in the calculation and some are higher. The difference does not explain the smaller calculated tip gap flow.

Discharge Coefficient

A discharge coefficient for the tip clearance gap has been defined by Moore and Tilton [4] as

$$C_D = \bar{u}_n / U_t \quad (6)$$

\bar{u}_n is the area averaged normal velocity at any section of the tip gap exit; and U_t is the tip gap exit velocity from potential flow analysis based on the cascade inlet free stream total pressure P_{t0} and a local tip gap exit static pressure $P_{s,ex}$.

In references 4 and 5, local static pressures were measured on the endwall in the tip gap exit plane. It was then assumed that there was locally no variation in static pressure between the endwall and the blade tip. The calculation results in Fig. 15 show this to be a good assumption from $X/c = 0.6$ ($S/S_b = 0.4$) to the trailing edge. But upstream, the static pressure on the blade tip is lower. For comparison with the measurements, discharge coefficients for the calculation results are here evaluated using the endwall static pressures at the tip gap exit.

Figure 16 shows a comparison of the measured and

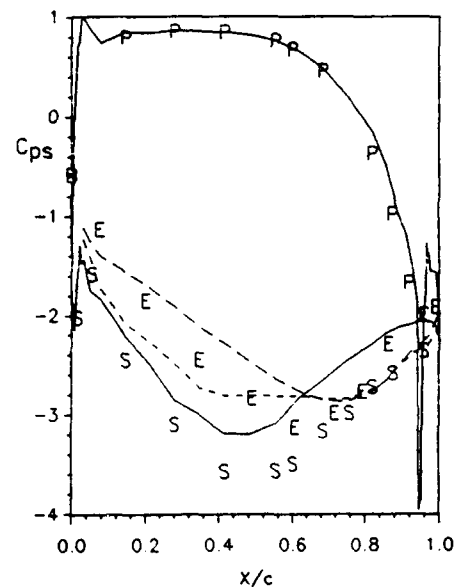


Fig. 15. Blade static pressure distributions. 45 percent span: — calculated; P - measured, pressure surface; S - measured, suction surface. Tip gap exit - endwall: --- calculated; E - measured. Tip gap exit - blade tip: - - - calculated.

calculated discharge coefficients. The calculated values are consistently lower after $X/c \sim 0.2$, averaging about 0.62 compared with an average of about 0.72 for the measurements, in this region. This appears to be the explanation for the lower tip leakage flow and the smaller normal kinetic energy coefficient, in the calculation. The calculated discharge coefficients over most of the blade length differ little from the potential flow value for a simple (two-dimensional) vena contracta.

Loss Coefficient at Tip Gap Exit

The local mass averaged total pressure loss coefficient for flow at the tip gap exit can be evaluated using

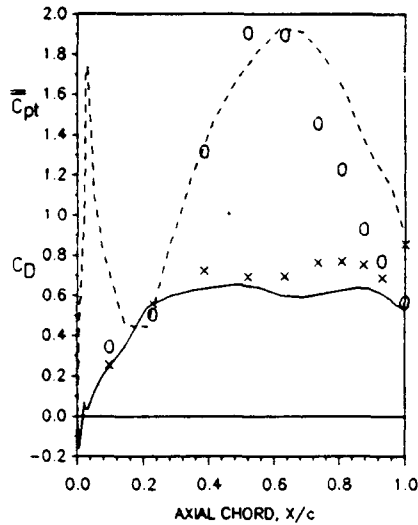


Fig. 16. Discharge coefficients (— calculated; X, measured) and mass-averaged total pressure loss coefficients (- - calculated; O, measured) at the tip gap exit plane.

$$\bar{C}_{pt,ex} = \frac{\int_0^t \rho u_n C_{pt} dz}{\int_0^t \rho u_n dz} \quad (7)$$

The measured and calculated values are also compared in Fig. 16. The calculated results show that the small flow leaving the tip gap upstream of the first measurement location (station 1 in Fig. 10a) has high losses. This is probably mostly due to convection of inlet boundary layer fluid, but the values are locally higher than the maximum loss upstream ($C_{pt} = 1.0$). At mid-axial-chord the losses are in reasonable agreement, but then towards the trailing edge the losses are higher; this is associated with the smaller discharge coefficient and the non-uniform calculated exit velocity profile, seen in Fig. 12. Actually, the total pressure loss coefficient, $TPLC = 0.071$ calculated for the whole tip gap flow agrees with the measured value very closely. This is due to the combination of too little flow having too much loss.

Additional Losses Due to Tip Leakage

Following the analysis by Dishart and Moore [5], we may analyse the additional losses due to tip leakage by considering the top and bottom halves of the flow at $X/c = 1.4$, separately. There it was suggested that the difference between the mass-averaged total pressure loss coefficients for the top and bottom halves is a measure of the extra loss resulting from tip leakage. Thus,

	Measured	Calculated
Bottom half:	0.275	0.254
Top half:	0.101	0.107
Difference:	0.174	0.147

The losses for the top half agree quite closely, and the calculation models the additional loss within 16 percent.

Dishart and Moore also suggested that the additional loss may be estimated by adding the loss incurred within the tip gap, $TPLC$, and the amount of dissipated tip leakage secondary kinetic energy. The latter was found by subtracting the residual tip leakage secondary kinetic energy at $X/c = 1.4$ from the normal kinetic energy coefficient, $NKEC$, at the tip gap exit. Thus

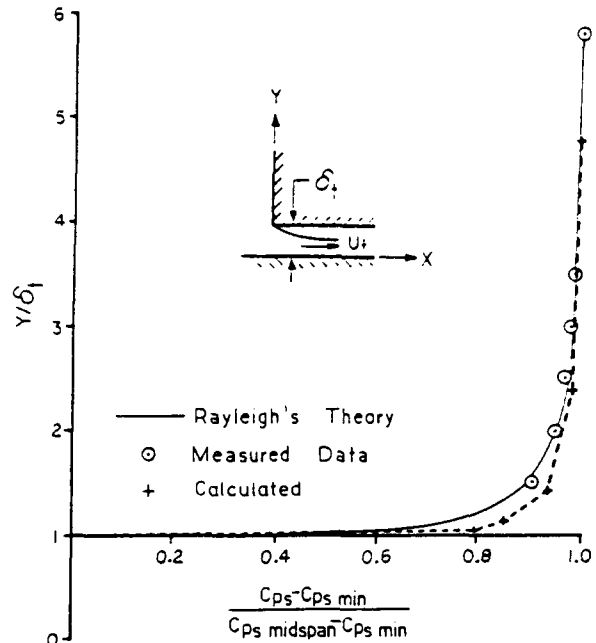


Fig. 17. Calculated pressures on the blade pressure surface compared with measurements and potential flow theory.

	Measured	Calculated
NKEC:	0.109	0.082
Residual tip gap ske:	0.011	0.020
Dissipated tip gap ske:	0.098	0.062
and		
TPLC:	0.071	0.071
Dissipated tip gap ske:	0.098	0.062
Extra tip leakage loss:	0.169	0.133

In the experiment, the additional loss due to tip leakage, 0.174, was almost entirely explained by the sum of the tip gap losses and the dissipated secondary kinetic energy, 0.169. In the calculation, again most of the additional loss, 0.147 is explained by the sum, 0.133. But it appears that the calculated flow has dissipated slightly more primary kinetic energy in the bottom half, probably in the blade wake. Overall though, the calculation supports the use of a simple model of tip leakage loss as due to tip gap loss and dissipated secondary kinetic energy.

AREAS FOR IMPROVEMENT OF FINE SCALE MODELLING

Flow in Tip Clearance Gap

The present calculation did resolve some of the fine scale features of tip leakage flow, as seen in Fig. 11. The flow separation from the blade tip at the inlet, the reattachment at about two tip gap heights into the gap, and the vena contracta with its associated region of low static pressure were all modelled reasonably well, especially considering the near wall grid spacing of 5 percent of the tip gap height. Another feature which was well modelled is the fall in static pressure on the pressure side as the flow approaches the sharp corner at the inlet to the tip gap. Figure 17 shows a comparison of the calculated pressure variation with the measurements of reference 4 and with Rayleigh's two-dimensional potential flow theory for flow from rest entering a slot. The calculation shows the pressure falling over about two tip gap heights, in good agreement with the other results.

A result in Fig. 17, which is important numerically,

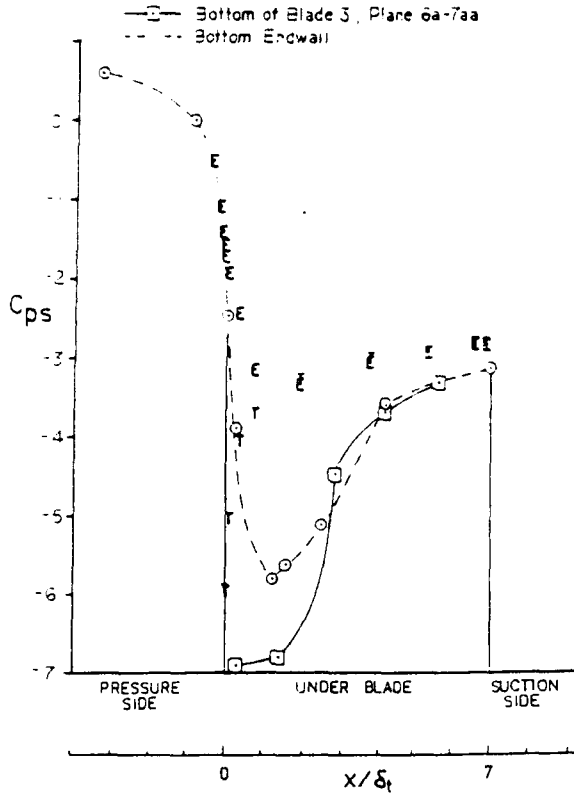


Fig. 18. Tip gap wall static pressure distributions, plane 6a-7aa, see Fig. 10b. Calculated: E - endwall; T - blade tip.

is the difference in static pressure between the corner point and the near corner point up the pressure side. This is seen to be 80 percent of the difference in pressure between midspan and the corner, in this case $\delta C_{ps} = -5.2$. Clearly a finer grid would aid the resolution near the corner.

Under the blade, the static pressure distributions on the blade tip and on the endwall are as shown in Fig. 18. The calculated results are the T's and the E's, respectively. There are two principal differences between the calculations and the measurements; the minimum pressure on the endwall, at $x/\delta_t \sim 2$, is not as low as in the measurements, and the low static pressures on the blade tip do not extend from the corner, at $C_{ps} = -5.9$, under the blade. This basically says the calculated velocities at the vena contracta are not large enough and therefore the discharge coefficient is too small, as seen in Fig. 16. Contributing factors to this may be inadequate mixing after the vena contracta and too much mixing before the vena contracta.

Flow in Tip Leakage Vortex

The tip leakage vortex was modelled quite well as seen in Figs. 4 and 5; the size and location of the vortex and the peak level were in good agreement at $X/c = 1.4$. But it was noticed that the calculated secondary velocity vectors were about 30 percent too high and there was excessive convection of low loss fluid under the vortex. Part of the reason for these differences is that we tried in this calculation to enhance the strength of the leakage vortex.

Figure 19 shows the calculated results for secondary velocity and static pressure just upstream of the trailing edge, at $X/c = 0.96$. The minimum

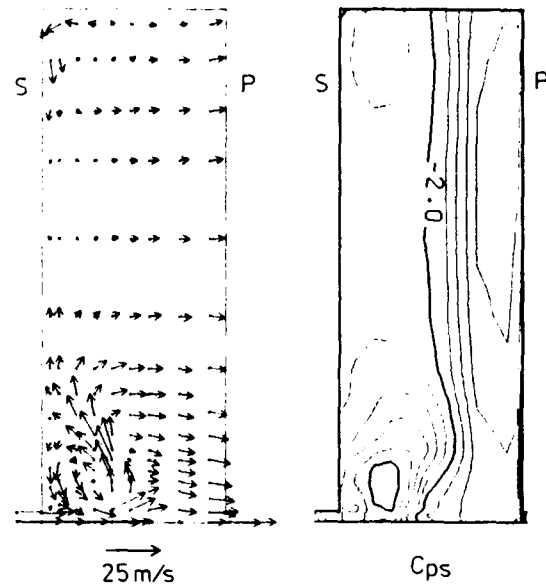


Fig. 19. Calculation results at $X/c = 0.96$. View as in Fig. 4. Contour interval $\delta C_{ps} = 0.1$. Note the vector scale is $1/2.5$ of that C_{ps} in Fig. 5.

static pressure coefficient in the core of the leakage vortex is about $\delta C_{ps} \sim 0.5$ lower than that of surrounding fluid at the same pitchwise location. Some preliminary measurements indicate that this difference is actually about 1.1. So we turned off the turbulent viscosity in the vortex in order to increase the secondary velocities and lower the core static pressure. This viscosity reduction was done for distances larger than the tip gap height away from the endwall and, at $X/c = 0.96$, for distances greater than 10 percent of the pitch away from the suction surface. The net result of this was to change the character of the secondary flow which developed the spanwise outflow seen in Fig. 19a instead of an enhanced circular motion. Correspondingly the reduction in static pressure in the vortex core was not changed significantly.

Trailing Edge Flow

An initial 3-D flow calculation was performed which included a curvature modification for turbulence in the outer part of boundary layers and in shear layers. The modification is described in Appendix A. This calculation gave a mean exit flow angle, β , of 29.5 degrees compared with the corrected value of 26.1 degrees from the measurements. The error was also present at mid-height, suggesting that the cause was two-dimensional in nature. A series of two-dimensional flow calculations was performed to gain understanding of this behavior. This gave the following results:

2-D flow calculations	β_{exit}
Without curvature modification	28.1°
With curvature modification	27.4°
+ Enhanced pressure side turbulence	27.1°
+ Laminar pressure side trailing edge	26.4°

The 3-D flow calculation was then repeated with the curvature modification plus enhanced turbulence in the pressure side boundary layer plus a laminar pressure side trailing edge, and including the laminar vortex flow model discussed above. This gave:

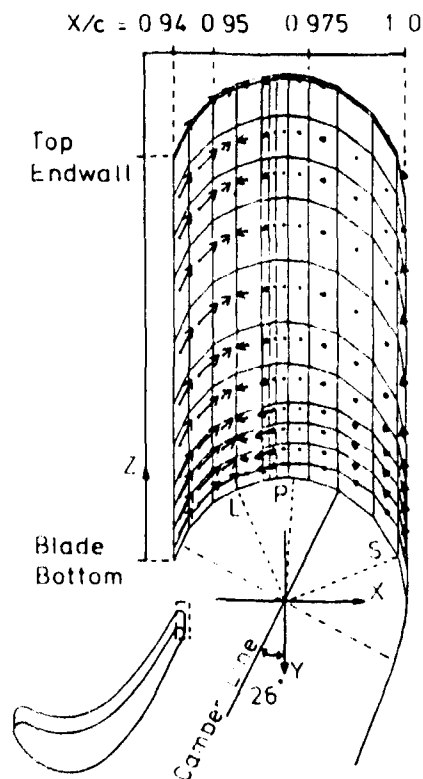


Fig. 20. Near wall velocity vectors around the trailing edge from 3-D flow calculation. Separation points for 2-D calculations: S - suction side; P - pressure side, turbulent flow, no modifications; L - pressure side, laminar trailing edge. Z-dimensions shortened by a factor of 10.

3-D flow calculations	β_{exit}
Basic calculation with curvature modification	29.8°
Calculation with 2-D flow modifications and laminar vortex model	28.2°

The 3-D flow results presented in this paper are all from this second calculation. The near-wall velocity vectors it gave around the trailing edge are shown in Fig. 20. The view is looking upstream from below the blade so that the blade bottom or tip is seen, together with a foreshortened view of the trailing edge. The pressure side is on the left, and the pressure side boundary layer is seen to separate quite uniformly between $X/c = 0.95$ and 0.96 . This separation point is quite close to the separation point in the 2-D laminar pressure side trailing edge calculation, L. It is also significantly upstream of the separation point from the 2-D calculation with no turbulence modifications, P. In that fully turbulent calculation, the flow remained attached almost to the camber line. It was therefore decided to try to promote an earlier separation by thickening the pressure side boundary layer and by causing it to behave as a laminar flow. To accomplish this, the calculated turbulent viscosity in the pressure side boundary layer was increased by a factor of 5 all along the pressure surface. The turbulent viscosity was then turned off from the minimum pressure point on the pressure side of the trailing edge to the camber line and for a distance of approximately two percent of chord away from the blade. These changes had a significant effect on the location of separation and also more importantly on the exit flow angle.

CONCLUSIONS

A calculation of incompressible three-dimensional flow in a turbine cascade with a tip clearance gap has been made. It shows the current capability of modelling overall flow development, including loss production mechanisms, and fine scale flow structure in a single calculation. The computations were performed using a pressure correction method, MEPP, on an IBM 3084, using 32,760 grid points and 40 hours of CPU time. A Prandtl mixing length model formed the basis of the turbulence model. Six grid points were distributed across the tip gap flow.

Overall, the agreement with the measured downstream flow was good. The sizes of the tip leakage vortex and its associated passage vortex, the blade wake, and the thin upper endwall boundary layer were all well modelled. Quantitatively, the losses were in good agreement in both the upper and lower halves of the cascade, as well as overall. Indeed this was true independent of the modelling schemes adopted for the fine scale structure of the flow during this study.

The present calculation gave the additional loss due to tip leakage within 16 percent of the measured value. Thus it appears possible to model the inefficiency of unshrouded turbines due to tip clearance, with a 3-D flow code, now.

The results support the conclusion that the additional loss due to tip leakage may be estimated as the sum of the internal tip gap losses and the tip leakage secondary kinetic energy which has been dissipated. Both of these quantities can be calculated with reasonable accuracy using the currently available level of 3-D flow modelling.

Some of the fine scale flow features were well modelled. The flow velocities at mid-height of the tip gap exit were in excellent agreement with the measurements in both magnitude and direction. However, in the tip gap exit velocity profiles there appeared to be too little mixing near the blade tip, and the wall static pressure distributions within the tip gap were only qualitatively correct. The local discharge coefficients were low and the calculated flow through the clearance gap was 11 percent too small. Overall though the loss produced in the gap was in good agreement. Apparently the smaller flow had larger losses.

Turbulence modelling of the trailing edge flow was found to have a significant influence on the mean exit flow angle. A laminar boundary layer flow on the pressure side from the trailing edge suction peak to the camber line caused earlier flow separation, more lift, and more turning. This together with a curvature correction for turbulent mixing and enhanced turbulence on the pressure side were factors used to obtain reasonable agreement with the measured distribution of exit flow angles.

Reduction of the turbulent viscosity in the core of the tip leakage vortex was not successful in increasing its strength. It changed the character of the flow and influenced the spanwise loss distribution. But the level of static pressure in the vortex core near the blade trailing edge was not appreciably reduced.

ACKNOWLEDGEMENT

The authors wish to thank Peter Clark of Rolls-Royce plc, Aero Division, for his farsighted support of their research over the past sixteen years, and they wish him well in his retirement.

REFERENCES

1. Hourmouziadis, J., and Albrecht, G., "An Integrated Aero/Mechanical Performance Approach to High Technology Turbine Design," AGARD Conference Proceedings No. 421 on Advanced Technology for Aero Gas Turbine Components, Paris, France, 1987.
2. Bindon, J.P., "Measurement of Tip Clearance Flow Structure on the End-Wall and within the Clearance Gap of an Axial Turbine Cascade," I. Mech. E. 1987-6, pp. 43-52, Int. Conf. on "Turbomachinery - Efficiency Prediction and Improvement," Cambridge, England, 1987.
3. Phillips, W.R.C., and Graham, J.A.H., "Reynolds Stress Measurements in a Turbulent Trailing Vortex," Journal of Fluid Mechanics, Vol. 147, 1984, pp. 353-371.
4. Moore, J., and Tilton, J.S., "Tip Leakage Flow in a Linear Turbine Cascade," ASME J. of Turbomachinery, Vol. 110, No. 1, January 1988, pp. 18-26.
5. Dishart, P.T., and Moore, J., "Tip Leakage Losses in a Linear Turbine Cascade," ASME J. of Turbomachinery, Vol. 112, No. 4, October 1990, pp. 599-608.
6. Moore, J.G., "Calculation of 3D Flow Without Numerical Mixing," von Karman Institute for Fluid Dynamics, Lecture Series 1989-06 on Numerical Methods for Flows in Turbomachinery, May 1989.
7. Moore, J.G., "Pressure Correction Calculation Procedures for 3D Viscous Flow," von Karman Institute for Fluid Dynamics, Lecture Series 1989-06 on Numerical Methods for Flows in Turbomachinery, May 1989.
8. Moore, J., Moore, J.G., Henry, G.S., and Chaudhry, U., "Flow and Heat Transfer in Turbine Tip Gaps," ASME J. of Turbomachinery, Vol. 111, No. 3, July 1989, pp. 301-309.

APPENDIX A

Steady Flow Conservation EquationsMass

$$\nabla \cdot \rho \mathbf{u} = 0$$

Momentum

$$\rho \mathbf{u} \cdot \nabla \mathbf{u} - (\nabla \cdot \mu \nabla) \mathbf{u} = \nabla \cdot \mu \nabla \mathbf{u}^T - \nabla p$$

Prandtl Mixing Length Viscosity Model

$$\mu = \mu_{\text{eff}} = \mu_i + \mu_t$$

$$\mu_t = \rho L^2 [\nabla \mathbf{u} : (\nabla \mathbf{u} + \nabla \mathbf{u}^T)]^{1/2}$$

Near-wall grid point correction

$$\mu_{\text{eff}} = [\mu_i (\mu_i + \mu_t)]^{1/2}$$

Mixing length, L

$$L = \text{smaller of } 0.41 \frac{y}{0.08 \delta F}$$

y = distance to the wall
 δ = width of shear or boundary layer
 F = curvature modification factor

Van Driest correction

$$L = 0.41 y (1 - \exp[-y \sqrt{\rho \tau} / 26 \mu_i])$$

Curvature modification

$$\bar{F} = \frac{1}{\delta} \int_0^\delta F dy$$

$$F = 1 - \beta Ri \quad \text{for } Ri < 0$$

$$F = 1 / (1 + \beta Ri) \quad \text{for } Ri > 0$$

$$\beta = 4$$

$$Ri = \frac{[2 \mathbf{u} \cdot (\mathbf{u} \cdot \nabla \mathbf{u})] \cdot [\mathbf{u} \times \mathbf{u} \cdot (\nabla \times \mathbf{u})]}{[\mathbf{u} \times \mathbf{u} \cdot (\nabla \mathbf{u} + \nabla \mathbf{u}^T)]^2}$$

Boundary and shear layer edges

Using Crocco's theorem, for steady inviscid incompressible flow with no body forces,

$$\mathbf{u} \times (\nabla \times \mathbf{u}) = \frac{1}{\rho} \nabla p_t$$

Boundary and shear layers are regions where

$$|(W/u^2) \mathbf{u} \times (\nabla \times \mathbf{u})| > 1$$

W = smaller of $2.5y(\rho y u_i / \mu_i)^{0.2}$, or
characteristic duct width.

APPENDIX B -

CORRECTIONS TO PAPER BY MOORE AND TILTON [4]

The evaluation of the tip gap exit velocities at plane 7aa in reference 4 was in error because of the use of an incorrect tip gap exit static pressure. The velocity distribution in Fig. 8 of that paper is incorrect and should be close to that shown in Fig. 12 for plane 7 in Dishart's measurements [5]. As a result of this, the arguments in reference 4 about the effective contraction coefficient and the discharge coefficient for flow at plane 6a-7aa are incorrect. The corrections are as follows.

Tip Gap Reynolds Number

The corrected mean exit velocity at plane 7aa is 1.46U_o or 29.1 m/s. This gives a tip gap Reynolds number $Re_{\delta t} = \rho u \delta_t / \mu_i = 8500$.

Contraction and Discharge Coefficients for Tip Gap

Rayleigh shows the theoretical contraction coefficient for potential flow is 0.611. A two-dimensional contraction coefficient, σ , calculated from the measurements is

$$\sigma = \frac{\bar{u}}{U_o (C_{pt,1} - C_{ps,min})^{1/2}} = 0.52.$$

An overall discharge coefficient can be evaluated from

$$C_D = \frac{\bar{u}}{U_o (C_{pt,1} - C_{ps,exit})^{1/2}} = 0.72.$$

The effect of mixing in the tip gap, with its corresponding pressure rise, is seen to be an increase in the discharge coefficient from 0.52 to 0.72.

The potential flow with mixing analysis [4] gives

$$C_D = \sigma [1 - 2(\sigma - \sigma^2)]^{-1/2} = 0.844.$$

This agrees well with the data of Wadia and Booth. However, a contraction coefficient, $\sigma = 0.52$, gives $C_D = 0.73$. While this is in good agreement with the discharge coefficient of 0.72, there is a discrepancy here concerning the apparent contraction coefficient which needs to be resolved.

Discussion

M. RACHNER, DLR, GERMANY

A remark and a question:

The remark: This rather complicated recirculating secondary flow might require a higher level turbulence model than the algebraic one you use. In the gap region the velocity gradient will produce a high level of kinetic turbulence energy. So it may be important to take into account the influence of convection/diffusion of turbulence energy and turbulent dissipation. In my opinion a $k-\epsilon$ model (or another two-equation-turbulence model) is minimum here for turbulence closure. As you use a pressure correction scheme it should not be very difficult to implement it.

The question: Do you plan to abandon the present algebraic turbulence model?

AUTHOR'S REPLY

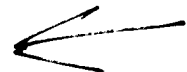
The authors agree that the tip leakage flow produces turbulence kinetic energy as it mixes to fill the tip gap. It would be interesting to use a turbulence model which includes this effect. Two-dimensional flow calculations made by the authors [8] have shown that a higher order turbulence model is not necessary for modeling turbulent flow and heat transfer within the tip gap.

R. CHIMA, NASA LEWIS, U.S.A.

Is there a physical reason why the flow in the tip region should be nearly normal to the blade surfaces?

AUTHOR'S REPLY

Flow entering the tip gap on the pressure side of this blade has little momentum in the throughflow (streamwise) direction. For flow through the tip gap the static pressure is a minimum near the tip gap entrance. Under the action of the resulting pressure gradient, the flow gains a significantly larger momentum normal to the blade upon entering the tip clearance gap.



TIME-MARCHING METHODS FOR SECONDARY FLOW ANALYSIS IN CURVED DUCTS

by

M. Marini, A. Massardo and A. Satta
Dipartimento di Ingegneria Energetica
Università di Genova
Via Montallegro 1, 16145
Genova
Italy

92-16071

SUMMARY

Compressible rotational flows in curved ducts due to inlet total pressure gradients are analyzed. Two different time-marching methods are briefly presented and utilized for the analysis of the development of 3D flows. The former is a finite volume explicit method, the latter is a finite difference implicit method. These methods are successfully compared each other and with other methods. A first analysis of secondary flows concerning constant section curved ducts with a curvature of 90 deg is carried out.

LIST OF SYMBOLS

$c = \sqrt{u^2 + v^2 + w^2}$
e : total energy per unit volume;
EFVM : explicit finite volumes method;
 $\bar{F}, \bar{G}, \bar{H}$: flux vectors;
IFDM : implicit finite differences method;
J : Jacobian of the coord. transformation;
 γ : ratio of specific heats c_p/c_v ;
L : half height of the duct;
n : time level;
p : static pressure;
 p_t : total pressure;
 \bar{Q} : vector of dependent variables;
R : gas constant;
T : absolute temperature;
 T_t : total temperature;
u, v, w : components of velocity in x, y, z directions;
 $U = u \xi_x + v \xi_y + w \xi_z$
 $V = u \eta_x + v \eta_y + w \eta_z$
 $W = u \zeta_x + v \zeta_y + w \zeta_z$
 \bar{V} : elementary transformed volume;
x, y, z : physical reference system;
 ρ : density;
 ϕ : secondary deviation angle;
 δ^+ : forward difference operator;
 δ^- : backward difference operator;
 ϕ : curvature angle;
 σ : explicit method damping coefficient;
 α_i, α_e : implicit and explicit damping coefficients used in the implicit method;
 ξ, η, ζ, r transformed reference system;

Nondimensional variables are referred to inlet total conditions:

$p = p/p_{t1}$, $T = T/T_{t1}$, $c = c/\sqrt{RT_{t1}}$ etc....

Subscripts

l : concerning inlet section;
m : averaged in tangential direction;

$x, y, z, r, \xi, \eta, \zeta$: denotes derivative in x, y, etc. direction.

1. INTRODUCTION

A wide range of flow fields can be solved nowadays with minor simplifying hypotheses thanks to the aid of the current computers more and more powerful.

One of the most fruitful approaches consists of the time-marching methods, especially devoted to the analysis of compressible and transonic flows in complex geometries as turbomachinery cascades. However, the need of easily comparable results makes the study of the flow in simple geometries, as curved ducts with constant transverse section, particularly noteworthy.

The time-marching methods are simple and versatile if compared to other methods capable to face the same problem, so they had a noticeable diffusion. Here the 3D flow within a curved duct is studied through two different time-marching methods, an explicit and an implicit one. The explicit methods have a simple structure but require long CPU times since their stability is strictly conditioned by their time-step. The implicit methods need a heavier analytical and programming work but, at least theoretically, they are strongly stable.

Such characteristics are quite known, in the present work attention is focused on the applications of these methods to the engineering problem of secondary flows. It was analyzed by solving the unsteady compressible Euler equations by means of time-marching techniques, as the phenomenon is essentially inviscid.

For a given simple geometry the methods are compared each other and with results available in literature. Such a test is important in view of the application of time-marching methods to the 3D configurations that are typical of turbomachinery.

2. SOLUTION OF THE FLOW EQUATIONS THROUGH TWO DIFFERENT TIME-MARCHING METHODS

The Euler equations, governing the unsteady 3D compressible flow, written in conservative form and referred to a body-fitted coordinate system are :

$$\frac{\partial \bar{Q}}{\partial \tau} + \frac{\partial \bar{F}}{\partial \xi} + \frac{\partial \bar{G}}{\partial \eta} + \frac{\partial \bar{H}}{\partial \zeta} = 0 \quad (1)$$

where the dependent variable vector \bar{Q} is :

$$\bar{Q} = J^{-1} [\rho, \rho u, \rho v, \rho w, e]^T \quad (2)$$

The flux vector \bar{F} , \bar{G} , \bar{H} have the following form :

$$\begin{aligned} \bar{F} &= J^{-1} [\rho U, \rho u U + \xi_x p, \rho v U + \xi_y p, \rho w U + \xi_z p, (e+p)U]^T \\ \bar{G} &= J^{-1} [\rho V, \rho u V + \eta_x p, \rho v V + \eta_y p, \rho w V + \eta_z p, (e+p)V]^T \\ \bar{H} &= J^{-1} [\rho W, \rho u W + \zeta_x p, \rho v W + \zeta_y p, \rho w W + \zeta_z p, (e+p)W]^T \end{aligned} \quad (3)$$

U, V and W denote the contravariant components of velocity : the velocity components in directions ξ , η and ζ respectively.

The total energy is given by the sum of the internal energy and of a kinetic term; for an ideal gas it is defined :

$$e = \frac{1}{\gamma-1} \rho R T + \frac{1}{2} \rho (u^2 + v^2 + w^2) \quad (4)$$

By recalling the equation of state ($p = \rho R T$) a relation between the static pressure p and the components of \bar{Q} is found :

$$p = (\gamma-1) [e - \frac{1}{2} \rho (u^2 + v^2 + w^2)] \quad (5)$$

The fluid dynamic simulation has been transferred from the physical domain (x,y,z), delimited with the solid walls of the duct and the inflow and outflow plane sections, into a regular computational domain (ξ, η, ζ) as shown in fig.1. The grid generation with the related transferring of the calculation from the reference system (x,y,z) to ξ, η, ζ has been accomplished with an elliptic

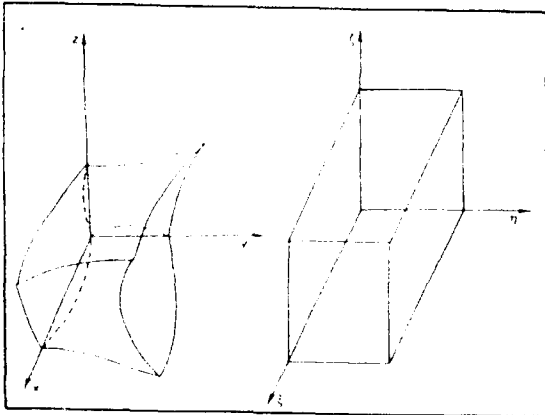


Fig. 1. Physical and computational 3D domain.

technique. It can be applied to the generation of two-dimensional and also to three-dimensional grids [1], [2]. Metrics are calculated with the same approximation used in both time-marching methods. The generation of the three-dimensional grids by solving the full three-variables Poisson system was not strictly necessary for the simple geometries here analyzed, however it enabled to write codes that can be applied to a wide range of geometrical cases.

2.1 The explicit method based on the corrected viscosity scheme

The former method developed for the analysis of inviscid compressible flows takes its origin from the one step explicit method of corrected viscosity [3]. The Euler equations are integrated in time by alternating steps of the Euler and the Lax scheme, in the spatial three dimensions of the transformed space by the technique of finite volumes.

It is useful to introduce the second order dissipation operator D_{AV} :

$$D_{AV} = (\delta_{\xi}^+ \delta_{\xi}^- + \delta_{\eta}^+ \delta_{\eta}^- + \delta_{\zeta}^+ \delta_{\zeta}^-) \quad (6)$$

where δ_{ξ}^+ and δ_{ξ}^- , for example, are the usual forward and backward differences in ξ direction.

The explicit time-marching method of corrected viscosity, to integrate the Euler equations (1) in time, is written :

$$\begin{aligned} \bar{Q}^{n+1} &= \bar{Q}^n + 1/6 D_{AV}(\bar{Q}^n) - \\ &- \sigma/6 D_{AV}(\bar{Q}^*) - \Delta\tau/\bar{V} \sum_{m=1}^6 [\bar{F}_m S_{m\xi} + \\ &+ \bar{G}_m S_{m\eta} + \bar{H}_m S_{m\zeta}] \end{aligned} \quad (7)$$

where :

$$\sigma = c_3 (1 - 1/6 |D_{AV}(p)|)$$

The terms with * are updated every NV iterations in order to achieve a stable scheme that ensures a second order spatial accuracy. The damping term σ must be of order $(1-\Delta\xi)$, as a consequence the coefficient c_3 is chosen.

Since the six lateral faces S_m of the cells are parallel to the coordinate planes $\xi\eta$ or $\xi\zeta$ or $\eta\zeta$, they have a non null projection in a coordinate direction only. In the internal points \bar{V} measures $2\Delta\xi\Delta\eta\Delta\zeta$ and finite volume calculation coincides with finite difference approximation. In the points that lie on a solid wall the cells becomes twice or four times smaller and also the operator D_{AV} has to be modified to keep a second order dissipation. The boundary condition along the channel walls is easily implemented by using finite volumes : only the terms of \bar{F} or \bar{G} including pressure are conveyed through the solid faces of the cell. Details about the calculation in points placed along solid boundaries can be found in [4].

The components of \bar{Q} are updated in the inflow section by applying the continuity equation between the first and the second section in ξ direction, in the outflow section by applying the three equations of linear momentum and the equation of energy between the last and the last but one section.

The time step $\Delta\tau$, for the explicit method here adopted, must satisfy the CFL condition, it is verified every NV iterations.

2.2 The implicit method based on the ADI factorization scheme

The second method presented is an implicit scheme based on Beam and Warming approximate factorization procedure.

The algorithm is fully described in [5] for bidimensional problems; an extension to three dimensional problems has been developed [6].

The solution of equations (1) is temporally advanced as follows:

$$\Delta \bar{Q}^n = \frac{\theta \Delta \tau}{1+\epsilon} \Delta \bar{Q}^{n-1} + \frac{\Delta \tau}{1+\epsilon} \bar{Q}^n + \frac{\epsilon}{1+\epsilon} \Delta \bar{Q}^{n-1} + \rho \left[\left(\theta - \frac{1}{2} - \epsilon \right) \Delta \tau^2 + \Delta \tau^3 \right] \quad (8)$$

$$\Delta \bar{Q}^{n+1} = \bar{Q}^{n+1} - \bar{Q}^n$$

The parameters ϵ and θ may assume different values, resulting in explicit ($\theta < 0$) or implicit ($\theta > 0$), first or second order (if $\theta = \epsilon + 1/2$) temporally accurate schemes.

In the present calculations we chose $\theta = 1$, $\epsilon = 0.5$; we obtained a three-level second-order-accurate scheme.

Spatial derivatives are discretized using central difference; adding an higher order term the equations assume the final factored form:

$$\begin{aligned} & \left(I + \frac{\theta \Delta \tau}{1+\epsilon} \bar{A}_i^n - \bar{n}_i J^{-1} \delta_\xi^- \delta_\xi^+ J \right) \left(I + \frac{\theta \Delta \tau}{1+\epsilon} \bar{B}_\eta^n - \bar{n}_\eta J^{-1} \delta_\eta^- \delta_\eta^+ J \right) \\ & \left(I + \frac{\theta \Delta \tau}{1+\epsilon} \bar{C}_\zeta^n - \bar{n}_\zeta J^{-1} \delta_\zeta^- \delta_\zeta^+ J \right) \Delta \bar{Q}^{n+1} = \\ & = - \frac{\Delta \tau}{1+\epsilon} (\bar{F}_\xi + \bar{G}_\eta + \bar{H}_\zeta) \bar{Q}^n + \frac{\epsilon}{1+\epsilon} \Delta \bar{Q}^{n-1} + \\ & - \bar{n}_e J^{-1} [(\delta_\xi^- \delta_\xi^+)^2 + (\delta_\eta^- \delta_\eta^+)^2 + (\delta_\zeta^- \delta_\zeta^+)^2] J \bar{Q}^n \end{aligned} \quad (9)$$

where $\bar{A}, \bar{B}, \bar{C}$ represent the Jacobian matrix of vectors $\bar{F}, \bar{G}, \bar{H}$. The artificial dissipation terms are weighted by the two coefficient \bar{n}_i and \bar{n}_e .

Equations (9) give three independent sets of block three-diagonal algebraic systems.

Following Steger's approach, $\Delta \bar{Q}^{n+1}$ at the boundary are regarded as zero. Such a procedure leads to a complete decoupling of equations for interior and boundary points, and allows great flexibility in boundary conditions impositions.

At the inlet total pressure, total temperature and flow direction are prescribed; three point extrapolation is used to obtain density.

At the outlet velocity components and density are extrapolated and prescribed static pressure allows energy calculations.

Static pressure on solid walls is given by the normal momentum equation, obtained from a scalar product between eqs. (1) and the vector $N' = (0, \eta_x, \eta_y, \eta_z, 0)$. In simple geometries, such as the curved ducts presented, where solid walls are represented by cylinder with generatrices parallel to cartesian axis x, y or z , the normal momentum equation reduces to a simple tridiagonal algebraic systems, as in the 2-D case. Density and velocity at the wall are given by extrapolation in the phisical space; tangent flow condition is imposed ignoring the normal contravariant component on the solid surface.

A computer code has been developed and implemented on an Apollo DN4000 workstation; this hardware allows three dimensional computations in simple

geometries, such as curved ducts, in 8-10 hours.

The metrics of the transformation are calculated within the code, as is essential, for a conservative formulation, the use of the same difference scheme for the metrics discretization and the solver. The boundary procedures are isolated in a single subroutine; this strongly simplifies the treatment of different kind of physical boundaries, and is made possible by the decoupling of interior and boundary point equations previously described.

The code has been tested in various test case, both 2-D and 3-D, to verify its accuracy and stability [6]

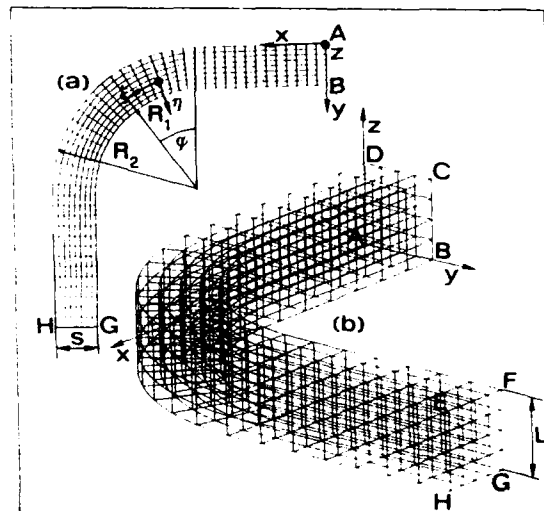


Fig. 2. Geometry of the curved duct here studied : a) projection onto the coordinate plane $z = \text{const}$, b) 3D view of the grid.

3. COMPARISON BETWEEN THE TWO METHODS

The computational codes implementing the just described time-marching methods were applied to a test-case, about which flow field data were known, and compared each other.

An example of 2D solution of the flow within an elbow was chosen in order to obtain a first check as regards the stability and the accuracy of the methods. The incompressible flow analyzed by Johnson [7] cannot be solved directly through a time-marching method that makes use of the Euler equations in conservative form. An adequate value of the outlet pressure p_2 guarantees a low subsonic flow where the influence of compressibility can be neglected. In a constant section curved duct the static pressure in extreme sections is the same, so the fixed outlet pressure corresponds, through isentropic relations to Mach = 0.2 both at inlet and at outlet. The geometrical parameters of the 2D duct are shown in fig.2a, the reference length is the duct width s , the internal and external curvature radii are $R_1 = 2.5$, $R_2 = 3.5$, two rectilinear extensions both upstream and downstream the elbow complete the computational domain.

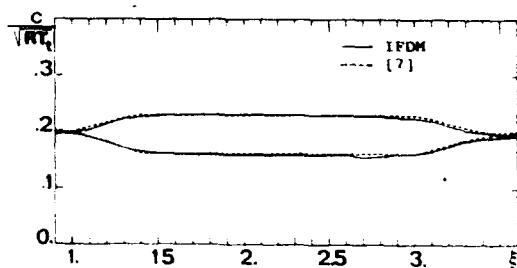


Fig. 3. Variation of velocity along walls of the curved duct.

In fig.2b the 3D duct, extension of the grid of fig.2a, is illustrated. The two reference systems used (see fig.1) are indicated in both figures; the transformed coordinate ξ follows the curvilinear axis of the duct, the η constant lines are orthogonal to it, the coordinate ζ coincides with the cartesian coordinate z . The first calculation concerned a square section ($\xi = \text{const}$) duct, the dimensions of the related grid were $47 \times 9 \times 9$. Only half of the grid points in every direction are represented in fig.2b for simplicity.

The boundary conditions in the extreme sections are the total pressure and temperature (p_{t1} and T_1) and the two flow angles (β_1 and β_2) at inlet, the static pressure p_2 at outlet.

If the fixed quantities are set uniform all over the extreme sections, a two-dimensional flow is born. It was solved by means of two codes with 3D structure. In fig.3 the velocities along the suction side and the pressure side lateral walls carried by Johnson [7] are compared with the velocities obtained with the implicit method. The agreement between the velocity distributions is quite good, it was repeated for different surfaces $\xi = \text{const}$ to verify that the codes simulated a flow actually 2D. The results of the explicit method, not plotted here, are close to those of fig.3.

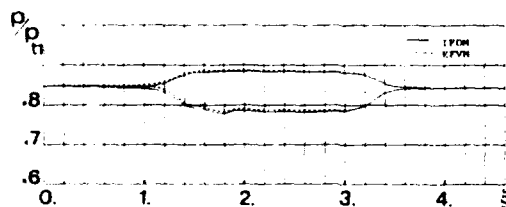


Fig. 4. Variation of static pressure along walls of the curved duct.

In fig.4 the distributions of static pressure along the lateral solid walls according to the implicit and the explicit time-marching method are compared. The outlet static pressure was decreased (corresponding to Mach = 0.5) to consider a case where compressibility played a significant role. The pressure diagrams of fig.4 are almost coincident, showing a good accordance between the methods.

A 3D analysis was then performed by considering the development of secondary flows after a non uniform total pressure distribution at the inlet of the curved duct. The inlet total pressure distribution and the corresponding inlet

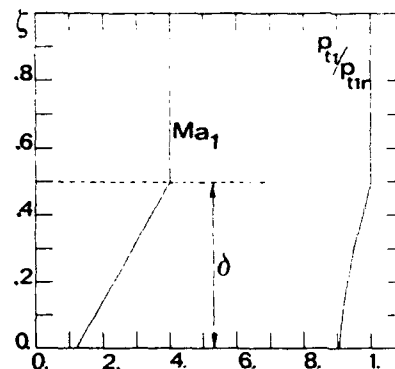


Fig. 5. Inlet total pressure gradient and corresponding inlet Mach number.

Mach number are shown in fig.5. The reference total pressure is its maximum value (p_{t1r}). The variation of p_{t1} within δ is corresponding, through isentropic relations, to a linear variation of Mach number from its maximum value to 30 per cent of it. By imposing the condition of symmetry, rather than the condition of

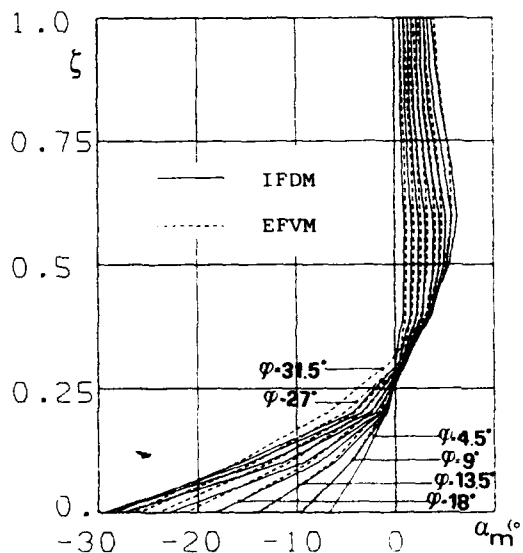


Fig. 6. Averaged secondary deviation angles according to the two time-marching methods.

solid wall, along the upper boundary $\xi = \xi_{\text{max}}$, only the lower half of the duct was analyzed. The hypothesis is that the radial distribution of p_{t1} at the inlet of the duct, whose height is $2L$, is symmetrical respect to DC (fig.2).

In fig.6 the average secondary deviation angles, averaged according to the local mass flow rate, along the different sections of the duct, are

illustrated. The continuous line joins the results from the implicit method, while the dotted line joins the results from the explicit method.

The primary flow is the flow in streamwise direction $\xi = \text{const}$, as a consequence the velocity components in the transverse directions η and ζ are the secondary velocities.

$$U' = \frac{u \xi_x + v \xi_y + w \xi_z}{\sqrt{\xi_x^2 + \xi_y^2 + \xi_z^2}} \quad (10)$$

$$V' = \frac{u \eta_x + v \eta_y + w \eta_z}{\sqrt{\eta_x^2 + \eta_y^2 + \eta_z^2}}$$

The local secondary deviation angle is :

$$\alpha = \text{atan}(V'/U') \quad (11)$$

The average secondary deviation angle is defined :

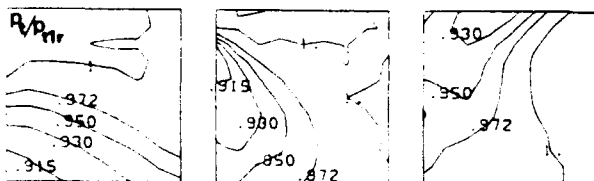
$$\alpha_m = \text{atan}(V'_m/U'_m) \quad (12)$$

$$\text{with : } U'_m = \frac{\int \rho U' U' d\eta}{\int \rho U' d\eta}$$

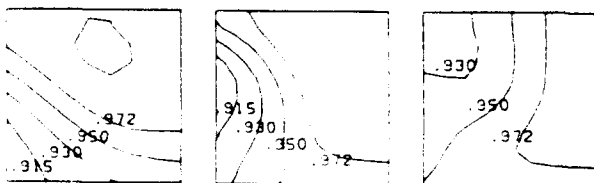
$$V'_m = \frac{\int \rho U' V' d\eta}{\int \rho U' d\eta}$$

The accordance of the averaged deviation angles of fig.6 is mainly qualitative, as an attentive observer can notice, because the curves superimposed are sometimes shifted. A better result would be achieved probably with more grid points in any direction.

In fig.7 the contours of total pressure in different surfaces $\xi = \text{const}$ of the duct for the same inlet total pressure distribution are shown. In this case the two methods outline contours that are somewhat similar but not coincident, however both the methods find that the surfaces $p_t = \text{const}$ rotate in accordance with the secondary vortex growing within the elbow. Such a rotation is well known and has been pointed out and examined by other authors.



Explicit method: planes $\varphi=30^\circ$, $\varphi=60^\circ$, $\varphi=90^\circ$.



Implicit method: planes $\varphi=30^\circ$, $\varphi=60^\circ$, $\varphi=90^\circ$.

Fig. 7. Comparison between the methods.

4. THE SECONDARY FLOWS IN A RECTANGULAR SECTION CURVED DUCT

The analysis of the secondary flows that arise and develop within curved ducts has been carried out with procedures that are classical at this time [8]. Some hypotheses are to be made in order to evaluate the three-dimensional effects induced by the deflection of a non uniform inflow, without solving the full fluid dynamic equations.

In the turbomachinery field an important parameter is the secondary deviation angle. Several authors suggested simple correlations to evaluate it approximately from the knowledge of few basic elements of the cascade. The angle provided has to be attributed to the whole section varying in radial direction. So it is interesting to calculate an average deviation angle from the three-dimensional results (see previous paragraph) to be eventually compared to deviation angles from correlations.

Some features that are peculiar of the three-dimensional flow necessarily escape the simplified calculations, indeed these features are captured by solving the governing equations of the inviscid compressible flow by means of the time-marching methods, for example. In fact the phenomenon of secondary flows, as stated

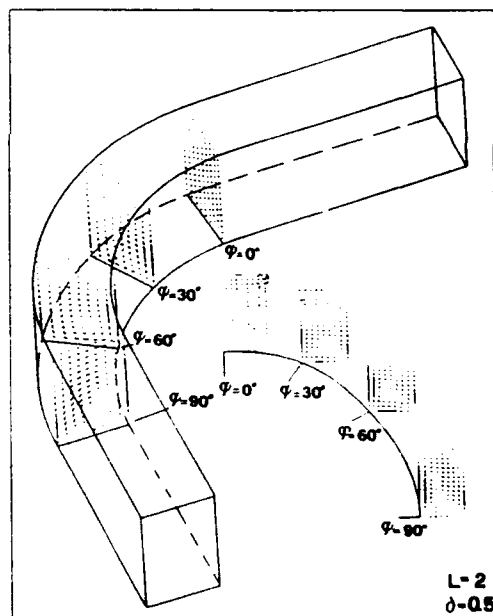


Fig. 8. Secondary components of velocity in $\xi = \text{const}$ surfaces and vortex development within the elbow.

before, is mainly inviscid.

Following the successful tests discussed in the previous paragraph, some calculations of the 3D flow in curved ducts with constant curvature radius and transverse rectangular section were performed.

The displacement of the centre of the secondary vortices along the ξ coordinate has been considered in detail. The secondary velocities in different sections $\xi = \text{const}$ along the axis of the duct, for the inlet total pressure gradient of fig.5 are shown in fig.8. It is clear that the

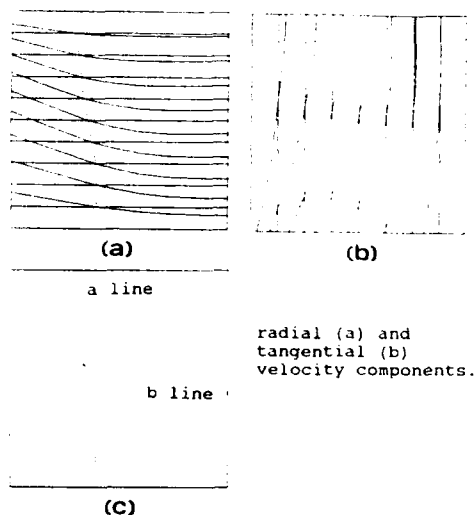


Fig. 9. Determination of the vortex centre.

intensity of the secondary vortex increases while its centre moves both in radial and tangential direction. In fig.9a, 9b and 9c a procedure to determine the position of the vortex centre is presented. The centre is found from the intersection of the lines joining the points where the radial or tangential components of velocity are null.

The fig.10 shows the displacement of the centre of the vortex for two different thicknesses ($\delta=0.5$ and $\delta=0.25$) where the inlet total pressure varies. In both cases the direction of the movement is almost the same, the vortex moves towards the suction side and towards the midspan. Obviously the position is kept lower in radial direction when $\delta=0.25$ respect to $\delta=0.5$, furthermore such a radial displacement in every section in the elbow is nearly constant. Meanwhile a greater displacement in tangential direction stands out; at the outlet of the elbow the vortex centre is nearer to the suction side wall when $\delta=0.25$. The total pressure gradient is stronger for $\delta=0.25$ than for $\delta=0.5$ because the same variation of p_t takes place in a shorter distance. The stronger is the secondary flow the longer is the distance the vortex centre goes through.

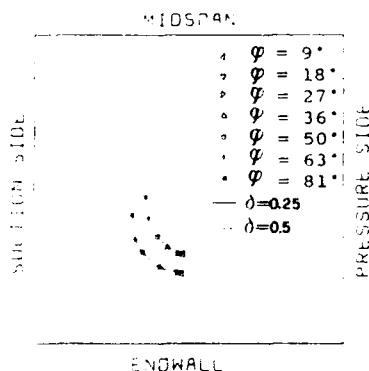


Fig.10. Secondary vortex centre displacement along the duct for two different values of δ .

In fig.11 the displacements of the vortices for two different half-heights of the duct, $L=1$ and $L=2$ respectively, are compared. In both cases vortices move towards the suction side and the midspan but the vortex centre keeps its position closer to the endwall when $L=1$. In this case too the vortex moves in a different way in tangential direction, the secondary flow seems to be stronger when the frontal section area is smaller even though the total pressure gradient is the same.

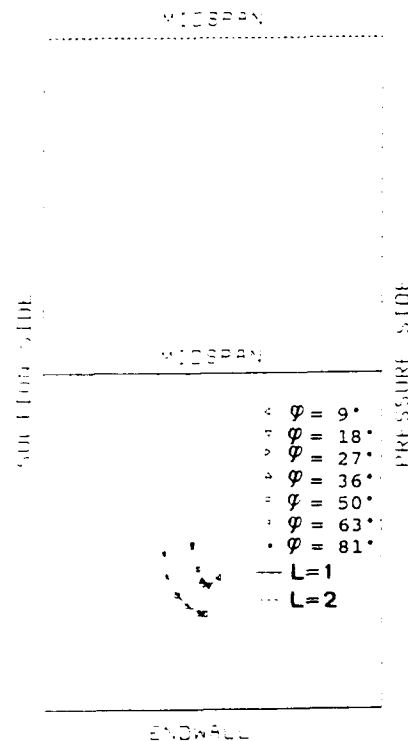


Fig.11 Secondary vortex centre displacement along the duct for two different aspect ratios of it.

5. CLOSURE

Two computational methods have been set up, compared each other and utilized to analyze 3D flows within simple geometries. The comparison between the methods and with results from literature has been fairly satisfactory.

These preliminary calculations allow to show the outstanding characteristics of secondary flows and the possibilities of 3D time-marching methods. However the necessity to develop them on more powerful computers making use of finer grids has come out.

In the paper the development of secondary flows has been shown, pointing out the movement of vortex centres and the influence of the aspect ratio and of the thickness of the total pressure gradient zone on it.

REFERENCES

1. Marini, M., Satta, A., " Meshes by developed elliptic systems in the CAD procedures for turbomachinery analy-

- sis", (in Italian), in "Proceedings of the 44th ATI Conference", September 1989, pp.IIID-207-220.
2. Marini M. " An elliptic technique to generate orthogonal grids along boundaries", Paper accepted to the "1991 Fluid Machinery Forum Asme/Jsme", Seattle, June 1991.
 3. Arts, A., " Study of the 3D flow in a stage of transonic turbine", (in French), Thesis of doctorate, Université Catholique de Louvain, 1982.
 4. Marini, M., "A time-marching method for the 3D analysis of the flow in turbomachinery passages ", (in Italian), in " Proceedings of the 45th ATI Conference", September 1990, pp.IIIB-57-72.
 5. Wang, Y.Y, Fujiwara, T., " Numerical analysis of transonic flow around a two-dimensional airfoil using full Navier-Stokes equations ", in " Memoirs of the Faculty of Engineering, Nagoya University ", Vol.36, No.2 (1985)
 6. Satta, A., Croce, G., " An implicit method to analyze 3D flows " (in preparation)
 7. Johnson, M.W., " An over-relaxation technique for 3D incompressible inviscid duct flow ", in "Three-dimensional flow phenomena in fluid machinery", ASME FED-Vol.32 (1985).
 8. Bardon, M.F., Moffatt, W.C., Randall, J.L., " Secondary flow effects on gas exit in rectilinear cascades ", J. of Eng. for Power, January 1975, pp.93-100.

Discussion

F. KARAGIANNIS, NAT. TECH. UNIV., GREECE

Could you mention the CPU time necessary for the calculation, and how many steps are necessary for the convergence to the steady state solution?

AUTHOR'S REPLY

4000 time steps were necessary to achieve reliable results by using the explicit method, 1000 time steps as regards the implicit method. But the total CPU time is not very different in the two cases since every iteration of the implicit method requires a longer time. A few days on a HP APOLLO 4005 are needed.

M. IACOVIDES, UMIST, U.K.

Curved duct secondary flow is generated by the interaction between the boundary layer fluid and the cross-stream pressure gradients which are induced by curvature. Did the authors neglect the viscous effects in order to be able to develop their code more quickly or do they envisage that inviscid comparisons can make a contribution to the understanding of such flows?

AUTHOR'S REPLY

Both the methods presented in the paper solve the Euler equations that govern compressible inviscid flows. The nonuniform inlet flow, that gives rise to secondary flow development within the duct, can be due to upstream viscous effects or other causes. Since the phenomenon of secondary flows is essentially inviscid the solution of the Euler equations enables one to carry out a significant analysis of this interesting example of rotational flow.



TURBINE INTERNAL FLUID FLOW ANALYSIS AND STOKES' HYPOTHESIS

Robert E. Gray
Turbine Analysis Engineer
&

Dr William A. Troha
Turbine Technical Area Manager
WL/POTC

Wright-Patterson Air Force Base Ohio 45433-6563
United States of America

92-16072

I. SUMMARY

Two-dimensional Navier-Stokes solvers are beginning to appear for the purpose of analyzing fluid flow and heat transfer phenomena in turbomachinery. It is often assumed that the Navier-Stokes' equations represent the ultimate in precision and generality possible when the fluid is modelled as a continuum. Therefore, the advent of the high-speed computer has spawned a number of finite differencing schemes aimed at solving these equations for steady and unsteady flows, both internal and external. In the case of compressible flows with heat transfer, some of these schemes have had questionable success in the approximation of experimental data despite use of accepted solution techniques and reasonable care in maintaining rigor in boundary conditions. Stokes' hypothesis, with its implication of zero bulk viscosity for a viscous fluid, may have a bearing on some of these anomalies. This paper identifies two viscous, compressible flow phenomena, in the form of expansion waves, for which the level of irreversibility implied by Stokes' hypothesis appears to be suspect.

List of Symbols

$\sigma_{xx}, \sigma_{yy}, \sigma_{zz}$	Normal stresses
$\sigma_{xy}, \sigma_{xz}, \sigma_{yz}$	Shear stresses
U	x - velocity component
V	y - velocity component
W	z - velocity component, total work
δ	small but not infinitesimal variation
ζ_{xx}, ζ_{yy}	normal strain rates
ζ_{xy}	shear strain rate
P	absolute or thermodynamic pressure
ρ	mass density
T	absolute or thermodynamic temperature
K	thermal conductivity
e	internal energy per unit mass
μ	dynamic viscosity
λ	second coefficient of viscosity
$\frac{D}{Dt}$	substantial derivative of indicated variable
v	specific volume = $1/\rho$
S	control volume diagonal, matrix of strain rate component representations in (x, y) coordinates, entropy
S_u	diagonal matrix of principal strain rate components
S	matrix of stress components in rotated coordinates
P	diagonal matrix representation of thermodynamic pressure

Marks above symbols

.	rate of change with respect to time
-	variable represented on base vectors aligned with principal axes
-	variable represented on base vectors with arbitrary angular orientation relative to principal axes.
-	indicates vector
*	indicates special case

II. INTRODUCTION

The analysis of viscous flow fields using the Navier-Stokes equations has represented a daunting task since their introduction in modern form by G. G. Stokes in 1845. In fact, most of the problems which could be solved using these equations were either trivial or of interest only in demonstrating the properties of the equations themselves. The problem lay in the complexity of the velocity derivatives associated with the deviatoric stresses.

For many fluid flows, such as a high Reynold's number flow found in the neighborhood of an airfoil, frictional effects are very intense close to the airfoil surface, where a no-slip condition is satisfied. As distance from the airfoil surface is increased, the effects of fluid friction rapidly diminish until they are negligible provided that turbulence is not a prominent feature of the flow. Furthermore, many interesting flows around airfoils are essentially two-dimensional in nature. In 1904 (Ref. 1), L. Prandtl observed that the Navier-Stokes equations could be significantly simplified for such flows without great loss of accuracy except in the immediate neighborhood of a stagnation point or flow separation. The two-dimensional boundary layer equations, used extensively in flow analysis of airfoils, are the simplified form of the two dimensional Navier-Stokes equations derived by Prandtl.

The success of Prandtl's boundary layer equations in the analysis of flows important to aircraft and turbomachinery designers has often been cited as evidence of the validity of the Navier-Stokes equations. As mentioned in the summary, it is frequently assumed that the Navier-Stokes equations represent the ultimate in precision and generality when employed for such flows. Nevertheless, problems continue to arise in the corroboration of calculated heat transfer coefficients from both Navier-Stokes solvers and boundary

layer solvers. In many recent heat transfer experiments performed on gas turbine stages, analytical predictions of heat transfer coefficients have fallen well below measured values. The deviation appears to be endemic to compressible flow regimes. Hence, the writers of this paper became curious about Stokes' hypothesis concerning the relationship of deviatoric stresses to pressure, and its consequences for compressible, viscous flow calculations; particularly with regard to the Navier-Stokes Equations.

III. TWO DIMENSIONAL ANALYSIS

State of Stress and Taylor's Theorem

Let us consider the state of stress acting on a rectangular element of unit height on the plane, and locate the origin of coordinates at the center of the rectangle. Suppose the sides of the rectangle to be of lengths δx and δy , as shown in Figure 1. Consider a stress represented by a point function σ , which is infinitely differentiable to any order in the interior and on the boundaries of Figure 1. Then by Taylor's theorem, one may find an expansion representing σ on the rectangular domain to any desired degree of accuracy. The expansion on the domain

$$-\frac{\delta x}{2} \leq x \leq \frac{\delta x}{2}$$

$$-\frac{\delta y}{2} \leq y \leq \frac{\delta y}{2}$$

may be written as

$$\begin{aligned} \sigma = & \sigma(0) + \frac{\partial \sigma(0)}{\partial x} \cdot x + \frac{\partial \sigma(0)}{\partial y} \cdot y + \frac{\partial^2 \sigma(0)}{\partial x^2} \cdot \frac{x^2}{2} + \\ & \frac{\partial^2 \sigma(0)}{\partial x \partial y} \cdot x \cdot y + \frac{\partial^2 \sigma(0)}{\partial y^2} \cdot \frac{y^2}{2} + \dots \end{aligned} \quad (1)$$

Now let (e_1, e_2) be a vector basis such that

$$e_1 = (1, 0)$$

$$e_2 = (0, 1)$$

The resultant surface force acting on face f_1 is

$$\begin{aligned} \delta \vec{F}_1 = & e_1 \cdot \left\{ \sigma_{xx}(0) \cdot \delta y + \frac{\partial \sigma_{xx}(0)}{\partial x} \cdot \frac{\delta x \cdot \delta y}{2} + \right. \\ & \left. \frac{\partial^2 \sigma_{xx}(0)}{\partial x^2} \cdot \frac{\delta x \cdot \delta y}{8} + \frac{\partial^2 \sigma_{xx}(0)}{\partial y^2} \cdot \frac{(\delta y)^3}{24} + \dots \right\} + \\ & e_2 \cdot \left\{ \sigma_{xy}(0) \cdot \delta y + \frac{\partial \sigma_{xy}(0)}{\partial x} \cdot \frac{\delta x \cdot \delta y}{2} + \dots \right\} \end{aligned} \quad (2)$$

Regardless of the scale of the rectangle, the expansion of equation (2) may be continued to the required degree of accuracy.

The resultant surface force acting on face f_2 is analogous, and designated as $\delta \vec{F}_2$.

Let

$$\delta \vec{F} = \delta \vec{F}_1 + \delta \vec{F}_2 \quad (3)$$

As the rectangle is reduced in a sequence such that the limit is infinitesimal,

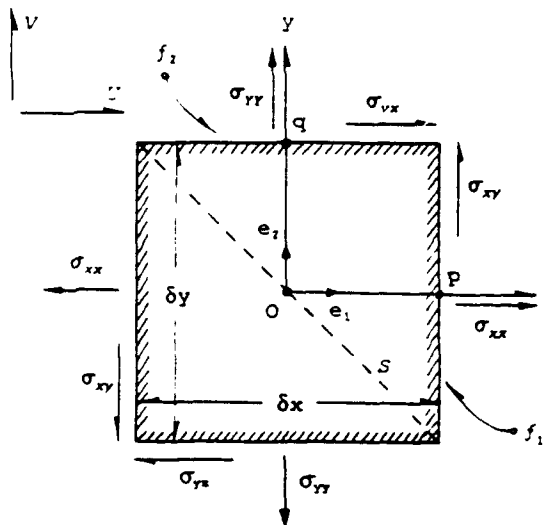


Fig. 1 Rectilinear control volume.

points p in face f_1 and q in face f_3 become coincident with center O. In the limit, $\delta \vec{F}$ is the infinitesimal surface force acting through plane S at point O. The representation of $\delta \vec{F}$ is

$$\begin{aligned} \delta \vec{F} = & e_1 \cdot [\sigma_{xx}(0) \cdot \delta y + \sigma_{yx}(0) \cdot \delta x] + \\ & e_2 \cdot [\sigma_{xy}(0) \cdot \delta y + \sigma_{yy}(0) \cdot \delta x] \end{aligned} \quad (4)$$

Now let α_m be the maximal angular acceleration at any point in or on the rectangle of Figure 1, and let ρ_m be the maximal fluid mass density for unit height interior to, or on the boundaries of the control volume. Utilizing Taylor's theorem, an expression for the moment applied to the rectangle by the surface forces can be developed, which results in the following inequality.

$$\begin{aligned} & \left| -\frac{\partial^2 \sigma_{xx}(0)}{\partial x \partial y} \cdot \frac{(\delta y)^2}{12} + \sigma_{xy}(0) + \frac{\partial^2 \sigma_{xy}(0)}{\partial x^2} \cdot \frac{(\delta x)^2}{8} + \right. \\ & \frac{\partial^2 \sigma_{xy}(0)}{\partial y^2} \cdot \frac{(\delta y)^2}{24} + \frac{\partial^2 \sigma_{yy}(0)}{\partial x \partial y} \cdot \frac{(\delta x)^2}{12} - \sigma_{yx}(0) - \\ & \left. \frac{\partial^2 \sigma_{xy}(0)}{\partial x^2} \cdot \frac{(\delta x)^2}{24} - \frac{\partial^2 \sigma_{yx}(0)}{\partial y^2} \cdot \frac{(\delta y)^2}{8} + \dots \right| \\ & \leq \left| \rho_m \cdot \alpha_m [(\delta x)^2 + (\delta y)^2] \right| \end{aligned} \quad (5)$$

One can construct a sequence by which the rectangular figure may be reduced in scale approaching an infinitesimal limit at point O. It is clear that equation (5) implies $|\sigma_{xy}(0) - \sigma_{yx}(0)| = 0$ in this case, showing that the stress tensor is symmetric at an arbitrary point. This is a crucial fact for any analysis to follow, but it is dependent on the existence of the aforementioned sequence. Although hypotheses leading to symmetry of the stress tensor fit many flow conditions, it is recognized that they may not apply to rarefied flows, or to highly turbulent flows. In fact, in fluids with discrete molecular structure, the required limit cannot be found.

Orthogonal Transformation and Principal Stresses

The vector basis (e_1, e_2) is orthonormal. Consider a new orthonormal vector basis (α_1, α_2) rotated through angle θ at point O, and let variable representations in the new system be barred. Then

$$\delta \vec{F} = e_1 \delta F_x + e_2 \delta F_y \quad (6)$$

$$\delta \vec{F} = \alpha_1 \delta \bar{F}_x + \alpha_2 \delta \bar{F}_y$$

and

$$\delta \bar{F}_x = \delta F_x \cdot \cos \theta + \delta F_y \cdot \sin \theta \quad (7)$$

$$\delta \bar{F}_y = -\delta F_x \cdot \sin \theta + \delta F_y \cdot \cos \theta$$

Let:

$$\delta \eta = \begin{bmatrix} \delta F_x \\ \delta F_y \end{bmatrix} \quad \delta \bar{\eta} = \begin{bmatrix} \delta \bar{F}_x \\ \delta \bar{F}_y \end{bmatrix}$$

$$A = \begin{bmatrix} \sigma_{xx} & \sigma_{xy} \\ \sigma_{yx} & \sigma_{yy} \end{bmatrix}$$

$$\delta \epsilon = \begin{bmatrix} \delta y \\ \delta x \end{bmatrix} \quad \delta \bar{\epsilon} = \begin{bmatrix} \delta \bar{y} \\ \delta \bar{x} \end{bmatrix}$$

$$C = \begin{bmatrix} \cos \theta & \sin \theta \\ -\sin \theta & \cos \theta \end{bmatrix}$$

Equation (4) is a vector description of the surface force acting through a small element of plane S at point O of Figure 1. The following matrix equation may be extracted from it, taking the first of equations (6) into account.

$$\delta \eta = A \cdot (\delta \epsilon) \quad (8)$$

Now note that

$$\delta \epsilon = C' \cdot (\delta \bar{\epsilon})$$

where

C' is the transpose of matrix C .

Hence,

$$\delta \bar{\eta} = (C \cdot A \cdot C') \cdot (\delta \bar{\epsilon}) \quad (9)$$

The purpose of developing the orthogonal relations is to find the value of θ which admits the simplest representation of the stress system. In view of the fact that $\sigma_{x_1} = \sigma_{y_1}$, the coefficient matrix for equation (9) may be written in the following way:

Let $S_s = C \cdot A \cdot C'$

Then

$$S_s = \begin{bmatrix} S_{11} & S_{12} \\ S_{21} & S_{22} \end{bmatrix} \quad (10)$$

where:

$$S_{11} = \frac{(\sigma_{xx} + \sigma_{yy})}{2} + \frac{(\sigma_{xx} - \sigma_{yy})}{2} \cdot \cos 2\theta + \sigma_{xy} \sin 2\theta$$

$$S_{12} = -\frac{(\sigma_{xx} - \sigma_{yy})}{2} \sin 2\theta + \sigma_{xy} \cos 2\theta$$

$$S_{21} = S_{12}$$

$$S_{22} = \frac{(\sigma_{xx} + \sigma_{yy})}{2} - \frac{(\sigma_{xx} - \sigma_{yy})}{2} \cdot \cos 2\theta - \sigma_{xy} \sin 2\theta$$

It is clear that matrix S_s will be diagonalized if the following condition is satisfied:

$$\cos 2\theta = \frac{\sigma_{xx} - \sigma_{yy}}{2\sqrt{\left(\frac{\sigma_{xx} - \sigma_{yy}}{2}\right)^2 + \sigma_{xy}^2}} \quad (11)$$

$$\sin 2\theta = \frac{\sigma_{xy}}{\sqrt{\left(\frac{\sigma_{xx} - \sigma_{yy}}{2}\right)^2 + \sigma_{xy}^2}}$$

When θ satisfies equations (11),

$$C \cdot A \cdot C' = \begin{bmatrix} \bar{\sigma}_{xx} & 0 \\ 0 & \bar{\sigma}_{yy} \end{bmatrix} \quad (12)$$

where:

$$\bar{\sigma}_{xx} = \frac{(\sigma_{xx} + \sigma_{yy})}{2} + \sqrt{\left(\frac{\sigma_{xx} - \sigma_{yy}}{2}\right)^2 + \sigma_{xy}^2}$$

$$\bar{\sigma}_{yy} = \frac{(\sigma_{xx} + \sigma_{yy})}{2} - \sqrt{\left(\frac{\sigma_{xx} - \sigma_{yy}}{2}\right)^2 + \sigma_{xy}^2}$$

It is evident that when the rectangle of Figure 2 is near-infinitesimal and rotated through angle θ about O, the stresses acting on the faces of the control volume are strictly normal. These normal stresses, embodied by $\bar{\sigma}_{xx}$ and $\bar{\sigma}_{yy}$, are the principal stresses. It is also evident that the work done on the rectangular element of unit height may be characterized

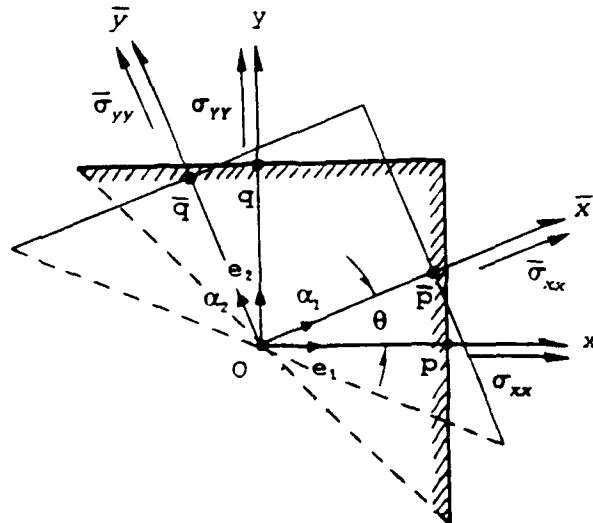


Fig. 2 Orthogonal transformation of base vectors to principal axes.

by these normal stresses. A discussion of the linear relation between the local stress and the local rate of strain is required in order to develop the implications of Stokes' hypothesis under the Second Law of Thermodynamics.

Rotational and Rate-of-Strain Relationships

Let U and V represent velocity components in the x and y directions respectively in Figure 1. Utilizing Liebnitz's formula, the total differentials of these components are expressible as,

$$dU = \left\{ \frac{\partial U}{\partial x} \cdot dx + \frac{1}{2} \left(\frac{\partial U}{\partial y} + \frac{\partial V}{\partial x} \right) \cdot dy \right\} + \left\{ \frac{1}{2} \left(\frac{\partial U}{\partial y} - \frac{\partial V}{\partial x} \right) \cdot dy \right\} + \left\{ \frac{\partial U}{\partial t} \cdot dt \right\} \quad (13)$$

$$dV = \left\{ \frac{1}{2} \left(\frac{\partial U}{\partial y} + \frac{\partial V}{\partial x} \right) \cdot dx + \frac{\partial V}{\partial y} \cdot dy \right\} + \left\{ \frac{1}{2} \left(\frac{\partial V}{\partial x} - \frac{\partial U}{\partial y} \right) \cdot dx \right\} + \left\{ \frac{\partial V}{\partial t} \cdot dt \right\} \quad (14)$$

The local rate of rotation associated with the fluid motion may be expressed as,

$$\omega = \left| \frac{1}{2} \text{curl } \vec{v} \right| \quad (15)$$

Equations (13) and (14) imply that the components of the velocity differential may be written in the form of the matrix equation

$$\begin{bmatrix} dU \\ dV \end{bmatrix} = \begin{bmatrix} 0 & -\omega \\ \omega & 0 \end{bmatrix} \begin{bmatrix} dx \\ dy \end{bmatrix} + \begin{bmatrix} \frac{\partial U}{\partial x} & \frac{1}{2} \left(\frac{\partial U}{\partial y} + \frac{\partial V}{\partial x} \right) \\ \frac{1}{2} \left(\frac{\partial U}{\partial y} + \frac{\partial V}{\partial x} \right) & \frac{\partial V}{\partial y} \end{bmatrix} \begin{bmatrix} dx \\ dy \end{bmatrix} + \begin{bmatrix} \frac{\partial U}{\partial t} \cdot dt \\ \frac{\partial V}{\partial t} \cdot dt \end{bmatrix} \quad (16)$$

Let:

$$dV_t = \begin{bmatrix} dU \\ dV \end{bmatrix} \quad dL = \begin{bmatrix} dx \\ dy \end{bmatrix} \quad \delta H = \begin{bmatrix} \frac{\partial U}{\partial t} \cdot dt \\ \frac{\partial V}{\partial t} \cdot dt \end{bmatrix}$$

$$R = \begin{bmatrix} 0 & -\omega \\ \omega & 0 \end{bmatrix}$$

$$S = \begin{bmatrix} \frac{\partial U}{\partial x} & \frac{1}{2} \left(\frac{\partial U}{\partial y} + \frac{\partial V}{\partial x} \right) \\ \frac{1}{2} \left(\frac{\partial U}{\partial y} + \frac{\partial V}{\partial x} \right) & \frac{\partial V}{\partial y} \end{bmatrix}$$

Then equation (16) should be written as

$$dv_t = R \cdot dL + S \cdot dL + \delta H \quad (17)$$

It is evident that equation (17) is a linear combination of components such that $R \cdot dL$ embodies the effects local rotational motion, $S \cdot dL$ embodies the effects of dilatation and distortion, and δH embodies the effects of local temporal acceleration.

Orthogonal Transformation and Principal Strain Rates

Note that the elements of matrix S represent the local strain rates, which also form a symmetric tensor of second order.

Let:

$$\zeta_{xx} = \frac{\partial U}{\partial x} \quad \zeta_{yy} = \frac{\partial V}{\partial y}$$

$$\zeta_{xy} = \zeta_{yx} = \frac{1}{2} \left(\frac{\partial U}{\partial y} + \frac{\partial V}{\partial x} \right)$$

Then,

$$S = \begin{bmatrix} \zeta_{xx} & \zeta_{xy} \\ \zeta_{xy} & \zeta_{yy} \end{bmatrix}$$

Consulting Figure 2, it is apparent that

$$d\vec{v} = e_1 \cdot dU + e_2 \cdot dV \quad (18)$$

$$d\vec{v} = \alpha_1 \cdot d\bar{U} + \alpha_2 \cdot d\bar{V} \quad (19)$$

In the barred coordinate system rotated through angle θ , equation (17) may be written as

$$dV_t = (C \cdot R \cdot C') \cdot d\bar{L} + (C \cdot S \cdot C') \cdot d\bar{L} + C \cdot \delta H \quad (20)$$

The rate-of-strain tensor in the barred system is embodied in the elements of the matrix $C \cdot S \cdot C'$.

Now suppose θ is such that

$$\cos 2\theta = \frac{\zeta_{xx} - \zeta_{yy}}{2 \sqrt{\left(\frac{\zeta_{xx} - \zeta_{yy}}{2} \right)^2 + \zeta_{xy}^2}} \quad (21)$$

$$\sin 2\theta = \frac{\zeta_{xy}}{\sqrt{\left(\frac{\zeta_{xx} - \zeta_{yy}}{2} \right)^2 + \zeta_{xy}^2}}$$

Then

$$C \cdot S \cdot C' = \begin{bmatrix} \bar{\zeta}_{xx} & 0 \\ 0 & \bar{\zeta}_{yy} \end{bmatrix} \quad (22)$$

where:

$$\bar{\zeta}_{xx} = \frac{(\zeta_{xx} + \zeta_{yy})}{2} + \sqrt{\left(\frac{\zeta_{xx} - \zeta_{yy}}{2} \right)^2 + \zeta_{xy}^2}$$

$$\bar{\zeta}_{yy} = \frac{(\zeta_{xx} + \zeta_{yy})}{2} - \sqrt{\left(\frac{\zeta_{xx} - \zeta_{yy}}{2} \right)^2 + \zeta_{xy}^2}$$

The rate-of-strain tensor has principal axes, just as the stress tensor does. When the base vectors (α_1, α_2) are rotated to angle θ defined by equations (21), they are aligned with the principal axes, upon which the local rate of strain is characterized by pure dilatation components $\bar{\zeta}_{xx}$ and $\bar{\zeta}_{yy}$. Likewise, when θ is defined by equations (11), base vectors (α_1, α_2) are aligned with the principal axes of the stress tensor.

We next observe that for any angle of rotation θ , including that defined by

equations (21), $C \cdot R \cdot C' = R$. Let us restrict θ to values satisfying equations (21), and let \bar{C} designate the special cases of matrix C corresponding to those values of θ . Then let:

$$S_a = \bar{C} \cdot S \cdot \bar{C}'$$

$$\delta \bar{H}_a = \bar{C} \cdot \delta H_a$$

Hence, when base vectors (α_1, α_2) are aligned with the principal axes of the rate-of-strain tensor, equation (20) becomes,

$$dV_c = R \cdot d\bar{L} + S_a \cdot d\bar{L} + \delta \bar{H}_a \quad (23)$$

where

$$S_a = \begin{bmatrix} \bar{\zeta}_{xx} & 0 \\ 0 & \bar{\zeta}_{yy} \end{bmatrix}$$

It may be seen that the exact differential of the velocity vector is invariantly a linear combination of the effects of rotational motion, dilatation and distortion, and temporal acceleration.

The local state of stress is represented by the elements of matrix A . This system of components forms the second order stress tensor. The deviatoric stresses are those due to the local dilation and distortion rates in a field of viscous fluid flow. They are obviously null when the fluid is static. We now come to the task of expressing the linear relationships between the deviatoric stress components and the local strain rate components.

Linear Connection of Stress Components and Strain Rate Components

Schlichting and Lamb (Ref. 1 and 2) both gave extensive discussion of the Navier-Stokes equations, and they both put forth the hypothesis that the normal components of the stress tensor are linear combinations of the deviatoric normal stresses, and the thermodynamic pressure. Neither author offered any support of this, but we shall leave it unchallenged for the moment, referring to it as the deviatoric stress hypothesis.

These authors would treat the two-dimensional flow fields being considered here as special cases of three-dimensional fields. Let z designate a third axis perpendicular to the x and y axes, and let $-P$ be the conventional representation of thermodynamic pressure (Ref. 1). They would give the deviatoric normal stresses as,

$$\sigma_{xx}' = \sigma_{xx} + P \quad (24)$$

$$\sigma_{yy}' = \sigma_{yy} + P \quad (25)$$

$$\sigma_{zz}' = \sigma_{zz} + P \quad (26)$$

Following Stokes, Lamb (Ref. 2) showed that for a point in a field of flow, the arithmetic mean of the normal stresses acting on each of three mutually

perpendicular planes intersecting at a point remains fixed regardless of the orientation of the planes. Also after Stokes, both Lamb and Schlichting concluded that this arithmetic mean is equivalent to the local thermodynamic pressure. We shall also leave this hypothesis unchallenged. It appears, however, that one of these two hypotheses leads to a problem with the Second Law of Thermodynamics in one of two cases: either an expansion wave with cylindrical symmetry, or an expansion wave with spherical symmetry.

Continuing with our formulation,

$$P_m = \begin{bmatrix} -P & 0 \\ 0 & -P \end{bmatrix} \quad (27)$$

The deviatoric stress tensor may be represented by the following matrix;

$$D = \begin{bmatrix} \sigma_{xx}' & \sigma_{xy}' \\ \sigma_{xy}' & \sigma_{yy}' \end{bmatrix} \quad (28)$$

Then

$$A = D + P_m$$

Let A_a be the matrix representation of the stress tensor on base vectors (α_1, α_2) , and let D_a be the matrix representation of the deviatoric stress tensor on (α_1, α_2) . Suppose angle of rotation θ is defined by equations (11) so that (α_1, α_2) are aligned with the principal axes of stress tensor. The deviatoric stress hypothesis implies that $\sigma_{xx} - \sigma_{yy} = \sigma_{xx}' - \sigma_{yy}'$, and hence that base vectors (α_1, α_2) are also aligned with the principal axes of the deviatoric stress tensor in this case. Clearly, the deviatoric stress tensor, and the stress tensor itself, have coincident principal axes. Consequently,

$$A_a = D_a + P_m \quad (29)$$

where

$$D_a = \begin{bmatrix} \bar{\sigma}_{xx}' & 0 \\ 0 & \bar{\sigma}_{yy}' \end{bmatrix}$$

The assumptions that the fluid is Newtonian and isotropic clearly imply that the stress tensor and the rate-of-strain tensor are in alignment. This means that the principal axes are aligned, and that the axis of maximum shear stress corresponds to the axis of maximum shear rate in the two-dimensional system being considered here.

The alignment requirement is weaker than it might at first seem. In fact, it gives rise to the need for a second coefficient to describe the effects of fluid friction. Since dynamic viscosity is the only property of a Newtonian fluid which could produce the effects of fluid friction, an additional connecting relation is required in consequence. Stokes' hypothesis provides such a relationship; the question being, "is it correct?" We shall first examine the appearance of the second property in two-dimensional flow fields.

Suppose that θ satisfying equations (11)

and (21) is fixed. In this case, the principal axes of the deviatoric stress tensor and the rate-of-strain tensor are in alignment. Now consider Figure 3 in which the base vectors (β_1, β_2) are shown rotated through arbitrary angle φ relative to (α_1, α_2). Let (\bar{x}, \bar{y}) designate a point in space referenced to the new system. We shall express the components of the deviatoric stress tensor, and the rate-of-strain tensor on base vectors (β_1, β_2).

Referring to Figure 3, we define orthogonal matrix G as,

$$G = \begin{bmatrix} \cos \varphi & \sin \varphi \\ -\sin \varphi & \cos \varphi \end{bmatrix} \quad (30)$$

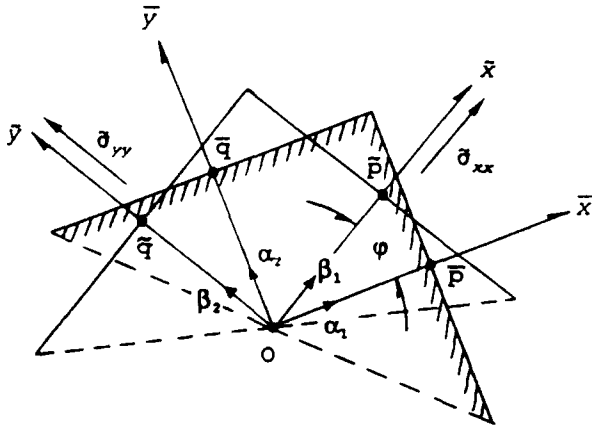


Fig. 3 Orthogonal transformation of base vectors from principal axes to arbitrary orientation.

Let \sim denote representation in the new system. Then

$$\delta \bar{\eta} = \bar{A} \cdot (\delta \bar{\xi}) \quad (31)$$

$$d\bar{V}_e = R \cdot d\bar{L} + \bar{S} \cdot d\bar{L} + \delta \bar{H} \quad (32)$$

where:

$$\delta \bar{H} = G \cdot \delta \bar{H}$$

$$\bar{A} = G \cdot D_e \cdot G' + P_m$$

$$\bar{D} = G \cdot D_e \cdot G'$$

$$\bar{S} = G \cdot S_e \cdot G'$$

G' is the transpose of G .

The elements of \bar{D} and \bar{S} are respectively the components of the deviatoric stress tensor, and the rate-of-strain tensor represented on base vectors (β_1, β_2). The matrices \bar{D} and \bar{S} are written out as,

$$\bar{D} = \begin{bmatrix} \bar{\sigma}_{xx} & \bar{\sigma}_{xy} \\ \bar{\sigma}_{xy} & \bar{\sigma}_{yy} \end{bmatrix} \quad (33)$$

$$\bar{S} = \begin{bmatrix} \bar{\zeta}_{xx} & \bar{\zeta}_{xy} \\ \bar{\zeta}_{xy} & \bar{\zeta}_{yy} \end{bmatrix} \quad (34)$$

where:

$$\bar{\zeta}_{xx} = \frac{\partial \bar{U}}{\partial \bar{x}} \quad \bar{\zeta}_{yy} = \frac{\partial \bar{V}}{\partial \bar{y}}$$

$$\bar{\zeta}_{xy} = \bar{\zeta}_{yx} = \frac{1}{2} \left(\frac{\partial \bar{U}}{\partial \bar{y}} + \frac{\partial \bar{V}}{\partial \bar{x}} \right)$$

Recalling equations (22) and (29), it is at once clear that the elements of \bar{D} may be expressed in terms of $\bar{\sigma}_{xx}'$, $\bar{\sigma}_{yy}'$, and angle φ . The elements of \bar{S} , correspondingly, may be expressed in terms of $\bar{\zeta}_{xx}'$, $\bar{\zeta}_{yy}'$, and angle φ . The expressions for the elements of both matrices may thus be written as:

$$\bar{\sigma}_{xx}' = \frac{(\bar{\sigma}_{xx}' + \bar{\sigma}_{yy}')}{2} + \frac{(\bar{\sigma}_{xx}' - \bar{\sigma}_{yy}')}{2} \cos 2\varphi \quad (35)$$

$$\bar{\sigma}_{yy}' = \frac{(\bar{\sigma}_{xx}' + \bar{\sigma}_{yy}')}{2} - \frac{(\bar{\sigma}_{xx}' - \bar{\sigma}_{yy}')}{2} \cos 2\varphi \quad (36)$$

$$\bar{\sigma}_{xy} = \bar{\sigma}_{yx} = - \frac{(\bar{\sigma}_{xx}' - \bar{\sigma}_{yy}')}{2} \sin 2\varphi \quad (37)$$

$$\bar{\zeta}_{xx} = \frac{(\bar{\zeta}_{xx}' + \bar{\zeta}_{yy}')}{2} + \frac{(\bar{\zeta}_{xx}' - \bar{\zeta}_{yy}')}{2} \cos 2\varphi \quad (38)$$

$$\bar{\zeta}_{yy} = \frac{(\bar{\zeta}_{xx}' + \bar{\zeta}_{yy}')}{2} - \frac{(\bar{\zeta}_{xx}' - \bar{\zeta}_{yy}')}{2} \cos 2\varphi \quad (39)$$

$$\bar{\zeta}_{xy} = \bar{\zeta}_{yx} = - \frac{(\bar{\zeta}_{xx}' - \bar{\zeta}_{yy}')}{2} \sin 2\varphi \quad (40)$$

Examination of Equations (35) - (40) shows that even though the fluid is isotropic and Newtonian, alignment of the stress and rate-of-strain tensors does not preclude the need for two viscosity coefficients. Next consider two possibly distinct viscosity coefficients, a and b , and orient (β_1, β_2) so that they are aligned with the maximum shear axis of both the deviatoric stress and rate-of-strain tensors. In this case, $\varphi = \frac{\pi}{4}$ and we have,

$$\bar{\sigma}_{xx}' = \frac{(\bar{\sigma}_{xx}' + \bar{\sigma}_{yy}')}{2} = a \frac{(\bar{\zeta}_{xx}' + \bar{\zeta}_{yy}')}{2} = a \bar{\zeta}_{xx} \quad (41)$$

$$\bar{\sigma}_{yy}' = \bar{\sigma}_{xx}'$$

$$\bar{\sigma}_{xy} = - \frac{(\bar{\sigma}_{xx}' - \bar{\sigma}_{yy}')}{2} = -b \frac{(\bar{\zeta}_{xx}' - \bar{\zeta}_{yy}')}{2} = b \bar{\zeta}_{xy} \quad (42)$$

Note that

$$\frac{(\bar{\zeta}_{xx}' + \bar{\zeta}_{yy}')}{2} = \frac{1}{2} \left(\frac{\partial \bar{U}}{\partial \bar{x}} + \frac{\partial \bar{V}}{\partial \bar{y}} \right) = \frac{1}{2} \left(\frac{\partial \bar{U}}{\partial \bar{x}} + \frac{\partial \bar{V}}{\partial \bar{y}} \right)$$

Hence, for this special case,

$$\bar{\sigma}_{xx}' = \bar{\sigma}_{yy}' = \frac{a}{2} \left(\frac{\partial \bar{U}}{\partial \bar{x}} + \frac{\partial \bar{V}}{\partial \bar{y}} \right) \quad (43)$$

We thus conclude that the normal stresses are purely the result of dilatation rate on the axis of maximum shear. Of course,

$$\sigma_{xy} = \frac{b}{2} \left(\frac{\partial \bar{u}}{\partial \bar{y}} + \frac{\partial \bar{v}}{\partial \bar{x}} \right) \quad (44)$$

It is clear that frictional resistance to shear could be distinct from frictional resistance to dilatation; so coefficients a and b are possibly distinct, isotropic coefficients which must be connected by a constraining relation. At the risk of creating a non sequitur, we shall attempt to show that Stokes' hypothesis constraining a and b fails on either the cylindrical expansion wave, or the spherical expansion wave.

The components of the deviatoric stress tensor for any arbitrary value of angle φ may be written as

$$\bar{\sigma}_{xx}' = \frac{a}{2} (\bar{\epsilon}_{xx} + \bar{\epsilon}_{yy}) + \frac{b}{2} (\bar{\epsilon}_{xx} - \bar{\epsilon}_{yy}) \cos 2\varphi \quad (45)$$

$$\bar{\sigma}_{yy}' = \frac{a}{2} (\bar{\epsilon}_{xx} + \bar{\epsilon}_{yy}) - \frac{b}{2} (\bar{\epsilon}_{xx} - \bar{\epsilon}_{yy}) \cos 2\varphi \quad (46)$$

$$\bar{\sigma}_{xy} = -\frac{b}{2} (\bar{\epsilon}_{xx} - \bar{\epsilon}_{yy}) \sin 2\varphi \quad (47)$$

Examination of equations (45)-(47) shows that alignment of the deviatoric stress tensor with the rate-of-strain tensor is completely preserved, even though a and b may be distinct.

In case of a rotation of base vectors (β_1, β_2) through angle φ relative to the principal axes, the following relations hold between the principal rate-of-strain components and partial velocity derivatives in the rotated system:

$$\bar{\epsilon}_{xx} - \bar{\epsilon}_{yy} = \left(\frac{\partial \bar{u}}{\partial \bar{x}} - \frac{\partial \bar{v}}{\partial \bar{y}} \right) \cos 2\varphi - \left(\frac{\partial \bar{u}}{\partial \bar{y}} + \frac{\partial \bar{v}}{\partial \bar{x}} \right) \sin 2\varphi \quad (48)$$

$$\frac{\partial \bar{u}}{\partial \bar{y}} + \frac{\partial \bar{v}}{\partial \bar{x}} = - \left(\frac{\partial \bar{u}}{\partial \bar{x}} - \frac{\partial \bar{v}}{\partial \bar{y}} \right) \tan 2\varphi \quad (49)$$

$$\bar{\epsilon}_{xx} + \bar{\epsilon}_{yy} = \frac{\partial \bar{u}}{\partial \bar{x}} + \frac{\partial \bar{v}}{\partial \bar{y}} = \frac{\partial \bar{u}}{\partial \bar{x}} + \frac{\partial \bar{v}}{\partial \bar{y}} \quad (50)$$

It follows that for any value of φ ,

$$\bar{\sigma}_{xx}' = \frac{a}{2} \left(\frac{\partial \bar{u}}{\partial \bar{x}} + \frac{\partial \bar{v}}{\partial \bar{y}} \right) + \frac{b}{2} \left(\frac{\partial \bar{u}}{\partial \bar{x}} - \frac{\partial \bar{v}}{\partial \bar{y}} \right) \quad (51)$$

$$\bar{\sigma}_{yy}' = \frac{a}{2} \left(\frac{\partial \bar{u}}{\partial \bar{x}} + \frac{\partial \bar{v}}{\partial \bar{y}} \right) - \frac{b}{2} \left(\frac{\partial \bar{u}}{\partial \bar{x}} - \frac{\partial \bar{v}}{\partial \bar{y}} \right) \quad (52)$$

Utilizing equations (24) and (25), the relation of the stress tensor to the rate-of-strain tensor may be written as

$$\bar{\sigma}_{xx} = -P + \frac{(a-b)}{2} \left(\frac{\partial \bar{u}}{\partial \bar{x}} + \frac{\partial \bar{v}}{\partial \bar{y}} \right) + b \frac{\partial \bar{u}}{\partial \bar{x}} \quad (53)$$

$$\bar{\sigma}_{yy} = -P + \frac{(a-b)}{2} \left(\frac{\partial \bar{u}}{\partial \bar{x}} + \frac{\partial \bar{v}}{\partial \bar{y}} \right) + b \frac{\partial \bar{v}}{\partial \bar{y}} \quad (54)$$

$$\bar{\sigma}_{xy} = \frac{b}{2} \left(\frac{\partial \bar{u}}{\partial \bar{y}} + \frac{\partial \bar{v}}{\partial \bar{x}} \right) \quad (55)$$

Letting μ be the coefficient of dynamic viscosity, it is apparent from equation (55) that $b = 2\mu$. Since " a " remains unconstrained, we may define a second coefficient λ such that

$$\lambda = \frac{(a-b)}{2}$$

Equations (53)-(55) retain their form regardless of the value of φ . We shall retain the tilde, and use barred variables to signify values taken on principal axes in subsequent discussion. Equations (53)-(55) may be written as

$$\bar{\sigma}_{xx} = -P + \lambda \left(\frac{\partial \bar{u}}{\partial \bar{x}} + \frac{\partial \bar{v}}{\partial \bar{y}} \right) + 2\mu \cdot \frac{\partial \bar{u}}{\partial \bar{x}} \quad (56)$$

$$\bar{\sigma}_{yy} = -P + \lambda \left(\frac{\partial \bar{u}}{\partial \bar{x}} + \frac{\partial \bar{v}}{\partial \bar{y}} \right) + 2\mu \cdot \frac{\partial \bar{v}}{\partial \bar{y}} \quad (57)$$

$$\bar{\sigma}_{xy} = \mu \left(\frac{\partial \bar{u}}{\partial \bar{y}} + \frac{\partial \bar{v}}{\partial \bar{x}} \right) \quad (58)$$

Equations (56)-(58) constitute the stress tensor in two dimensions. The distinction between λ and μ is based on the conditions of symmetry and isotropy. They are fluid property functions which should have consistent consequences under the Second Law of Thermodynamics.

IV Work and Energy Relations

Next, we consider the action of the two-dimensional stress system with regard to the conservation laws. Consider the rectangle of Figure 1 to be a control volume of unit height upon the (x, y) plane, as before. We shall assume that body force terms are negligible, and that there is no mechanical work done on the surroundings of this control volume. Let the rectangle be rotated through angle θ about point O defined by equations (11). If the rotated rectangle be reduced in a sequence toward an infinitesimal limit, then the surface forces acting through the faces of the control volume which are normal to the (x, y) plane are the result of the principal normal stresses, $\bar{\sigma}_{xx}$, and $\bar{\sigma}_{yy}$. One can see that when the rectangle axes are aligned with the principal axes of the stress tensor, then the flow work and momentum balance may be characterized in terms of $\bar{\sigma}_{xx}$ and $\bar{\sigma}_{yy}$. The components of the stress tensor taken on these axes are:

$$\bar{\sigma}_{xx} = -P + \lambda \left(\frac{\partial \bar{u}}{\partial \bar{x}} + \frac{\partial \bar{v}}{\partial \bar{y}} \right) + 2\mu \cdot \frac{\partial \bar{u}}{\partial \bar{x}} \quad (59)$$

$$\bar{\sigma}_{yy} = -P + \lambda \left(\frac{\partial \bar{u}}{\partial \bar{x}} + \frac{\partial \bar{v}}{\partial \bar{y}} \right) + 2\mu \cdot \frac{\partial \bar{v}}{\partial \bar{y}} \quad (59)$$

$$\bar{\sigma}_{xy} = 0$$

As before, the (\bar{x}, \bar{y}) coordinates are upon base vectors (α_1, α_2) which are aligned with the principal axes of the stress tensor. On these base vectors, the conservation equations take the following form:

Continuity

$$\frac{\partial \rho}{\partial t} + \frac{\partial(\rho \bar{u})}{\partial \bar{x}} + \frac{\partial(\rho \bar{v})}{\partial \bar{y}} = 0 \quad (60)$$

Momentum

$$\begin{aligned}\frac{\partial \bar{U}}{\partial t} + \frac{\partial \bar{U}}{\partial x} \cdot \bar{U} + \frac{\partial \bar{U}}{\partial y} \cdot \bar{V} &= \frac{1}{\rho} \cdot \frac{\partial \bar{\sigma}_{xx}}{\partial x} \\ \frac{\partial \bar{V}}{\partial t} + \frac{\partial \bar{V}}{\partial x} \cdot \bar{U} + \frac{\partial \bar{V}}{\partial y} \cdot \bar{V} &= \frac{1}{\rho} \cdot \frac{\partial \bar{\sigma}_{yy}}{\partial y}\end{aligned}\quad (61)$$

First Law of Thermodynamics (Energy)

$$\begin{aligned}\frac{\partial}{\partial x} \left(\kappa \cdot \frac{\partial T}{\partial x} \right) + \frac{\partial}{\partial y} \left(\kappa \cdot \frac{\partial T}{\partial y} \right) &= \rho \cdot \frac{\partial e}{\partial t} + \\ \rho \cdot \frac{\partial e}{\partial x} \cdot \bar{U} + \rho \cdot \frac{\partial e}{\partial y} \cdot \bar{V} - \bar{\sigma}_{xx} \cdot \frac{\partial \bar{U}}{\partial x} - \bar{\sigma}_{yy} \cdot \frac{\partial \bar{V}}{\partial y}\end{aligned}\quad (62)$$

Equation (62) was derived for an open thermodynamic system. However, in examining expansion wave phenomena, we are particularly concerned with the unsteady stagnation region at the center in Figures (4) and (5). The stagnation region, in

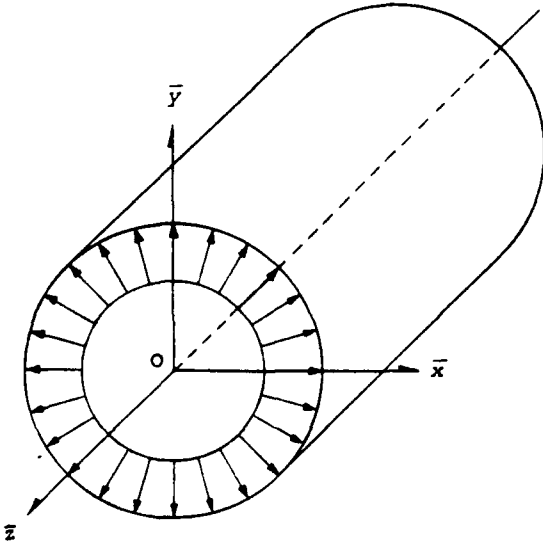


Fig. 4 Cylindrically symmetrical expansion wave.

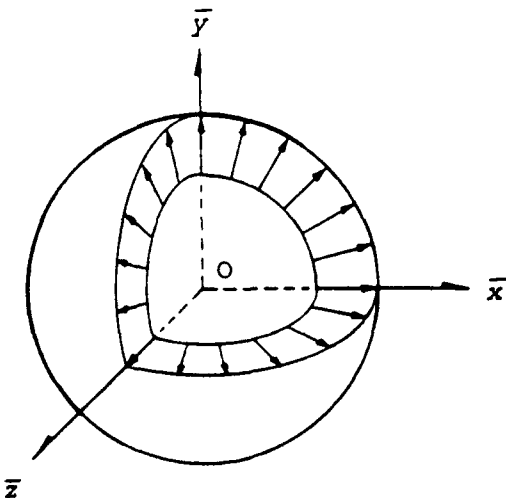


Fig. 5 Spherically symmetrical expansion wave.

fact, forms a closed system. There is an expansion process which takes place, but there is no inflow or outflow. If the near-infinitesimal control volume, Y , is oriented so that its principal axes align with the principal axes of the stress tensor, as in Figure 2, then the rate at which work is done on the control volume is expressible as

$$\dot{W}_f = \left[\frac{\partial (\bar{\sigma}_{xx} \cdot \bar{U})}{\partial x} + \frac{\partial (\bar{\sigma}_{yy} \cdot \bar{V})}{\partial y} \right] \cdot \delta \bar{x} \cdot \delta \bar{y} \quad (63)$$

when $\delta \bar{x}$ and $\delta \bar{y}$ are sufficiently small. Taking the momentum and continuity equations into account, equation (63) becomes,

$$\begin{aligned}\dot{W}_f = \left\{ \frac{P}{\rho} \cdot \frac{D\rho}{Dt} + (\lambda + \mu) \cdot \left[\frac{1}{\rho} \frac{D\rho}{Dt} \right]^2 + \mu \cdot \left[\frac{\partial \bar{U}}{\partial x} - \frac{\partial \bar{V}}{\partial y} \right]^2 + \right. \\ \left. \frac{\rho}{2} \cdot \left[\frac{D\bar{U}^2}{Dt} + \frac{D\bar{V}^2}{Dt} \right] \right\} \cdot \delta \bar{x} \cdot \delta \bar{y}\end{aligned}\quad (64)$$

where the operator $\frac{D}{Dt}$ signifies a substantial derivative.

Let \dot{T}_i be the net inflow rate of total energy, and let \dot{T}_v be the rate of accumulation of total energy within our near-infinitesimal control volume. Taking the continuity equation into account, we note that,

$$\dot{T}_v - \dot{T}_i = \left\{ \rho \frac{De}{Dt} + \frac{\rho}{2} \cdot \left[\frac{D\bar{U}^2}{Dt} + \frac{D\bar{V}^2}{Dt} \right] \right\} \cdot \delta \bar{x} \cdot \delta \bar{y} \quad (65)$$

Let \dot{Q} be the rate of heat addition to the control volume. Noting that the control volume forms an open system, the First Law of Thermodynamics may be written as,

$$\dot{Q} = \dot{T}_v - \dot{T}_i - \dot{W}_f \quad (66)$$

The expansion of a cylindrical column of gas which is infinite in height provides an interesting exposition of the influence of the normal deviatoric stresses. It has a stagnation region in which the velocity is zero for all time, but in which there is an expansion which must be resisted by viscous stress as well as pressure. We may imagine such a flow being created by an expansion wave with polar symmetry, concentric with the center of the column, propagating inward toward the center or stagnation region. The wave is assumed to be perfectly axisymmetric for all time.

The cylindrical expansion wave considered here is infinite in the z -direction, so it may be represented as a planar flow. For the sake of simplicity, we shall confine our analysis to the plane, recognizing that with respect to the use of the constitutive equations, the stress field should be considered as three-dimensional, with rates of strain in two dimensions in the case of planar flow.

Suppose that control volume, Y , encloses point O of Figure 4, which is the unsteady stagnation axis of an expansion wave with polar symmetry. For a control volume of unit height, we write, $Y = \delta \bar{x} \cdot \delta \bar{y}$. We wish to show that as Y contracts about O , it forms a closed thermodynamic system with a direct interpretation of irreversibility.

If m is the totality of mass contained in Y at an instant, we may write,

$$m = \rho(0) \cdot (\delta\bar{y}) \cdot (\delta\bar{x}) + \frac{1}{24} \frac{\partial^2 \rho(0)}{\partial \bar{x}^2} \cdot (\delta\bar{y}) \cdot (\delta\bar{x})^3 + \frac{1}{24} \frac{\partial^2 \rho(0)}{\partial \bar{y}^2} \cdot (\delta\bar{y})^3 \cdot (\delta\bar{x}) + \dots \quad (67)$$

It is clear that for sufficiently small Y containing point O , we are left with,

$$(\delta\bar{x}) \cdot (\delta\bar{y}) = \frac{m}{\rho} \quad (68)$$

It is understood that ρ is taken at the central point of Y .

Equations (63), (64), and (65) are the result of writing the required point functions as Taylor's expansions in terms of their values at the central point of Y ; then contracting the indicated Y to near-infinitesimal size. Hence, the values of the variables within the brackets in these equations are the instantaneous values at the central point of Y . Let this be understood in the discussion following.

Note that when the central point of Y coincides with the expansion wave center,

$\frac{D\bar{U}}{Dt}$ and $\frac{D\bar{V}}{Dt}$ must each be zero. In this special case, then we may write

$$\dot{W}_f = \left\{ \frac{P}{\rho^2} \cdot \frac{D\rho}{Dt} + \frac{(\lambda + \mu)}{\rho} \cdot \left[\frac{1}{\rho} \cdot \frac{D\rho}{Dt} \right]^2 + \frac{\mu}{\rho} \cdot \left[\frac{\partial \bar{U}}{\partial \bar{x}} - \frac{\partial \bar{V}}{\partial \bar{y}} \right] \right\} \cdot m \quad (69)$$

Also as a result of Y being sufficiently small with the wave center at its central point, the convective terms of $\frac{De}{Dt}$ vanish, and we may write

$$\dot{T}_v - \dot{T}_f = \dot{e} \cdot m \quad (70)$$

Note that when Y is greater than infinitesimal, m fails to be a control mass. It only becomes so in the limiting case of contraction of Y about the wave center.

Now let Y' be a volume on the order of Y in size, but let it vary in time such that m is fixed. Then Y' forms a closed system. We may write the First Law of Thermodynamics for Y' as,

$$\frac{\dot{Q}'}{m} = \dot{e} + \frac{\dot{W}}{m} \quad (71)$$

where:

W is the rate at which Y' does work on its surroundings.

e is the total rate of change of e in Y' .
 \dot{Q}' is the total rate of heat transfer into Y' .

On the other hand, equation (66) implies that on Y , at the instant it contains m ,

$$\frac{\dot{Q}}{m} = \dot{e} - \frac{\dot{W}_f}{m} \quad (72)$$

If we suppose that point O is contained in both Y and Y' , and that m is reduced to zero by contracting both Y and Y' to their

limit at O , we conclude that,

$$\frac{\dot{Q}'}{m} = \frac{\dot{Q}}{m} \quad (73)$$

Note that in the limit,

$$\frac{De}{Dt} = \dot{e} \quad (74)$$

$$\frac{\dot{W}}{m} = - \frac{\dot{W}_f}{m} \quad (75)$$

We conclude that the open and closed systems have the same limit at point O . Now let S be the rate of entropy change in Y' . In this case, the Second Law of Thermodynamics may be stated for the closed system Y' , and we write (Ref. 3)

$$\frac{\dot{S}}{m} = \frac{\dot{Q} + \dot{I}}{m \cdot T} \quad (76)$$

where

$\dot{I} = \dot{W}$ (reversible) - \dot{W} (irreversible)
 T = thermodynamic temperature

The variable \dot{I} is known as the internal irreversibility or lost work. In a system which is not in thermal equilibrium, \dot{Q} is generally irreversible. Since the work integral is path-dependent, the variable \dot{I} generally includes the effects of thermal non-equilibrium and viscous dissipation. Equation (69) shows that the viscous dissipation may be isolated as a linear component of the work rate associated with the near-infinitesimal volume Y , located at the center of the expansion wave in the case of a Newtonian fluid. We let \dot{I}_f be the component of irreversible work due strictly to viscous effects.

In a Newtonian fluid the gas mass m , as it expands, meets frictional resistance proportional to the rate of strain as Y' changes. Letting v be the rate at which the specific volume changes, it may be seen that when viscous dissipation is absent, we may write

$$\frac{\dot{W}}{m} = P v \quad (77)$$

as Y' is contracted about point O in Figure 4.

Finally, the normal stress at the unsteady stagnation point O of the cylindrical or polar expansion wave is not dependent on angle ϕ shown in Figure 3. Equations (45) and (46) then require that $\bar{\zeta}_{xx}$ and $\bar{\zeta}_{yy}$ be equal. Setting $\phi = 0$, we find that $\frac{\partial \bar{U}}{\partial \bar{x}} = \frac{\partial \bar{V}}{\partial \bar{y}}$ in this case. It is

notable that the shear stress is zero for any orientation at point O when this condition is satisfied, rendering angle θ of Figure 2 arbitrary. This is to say that any set of mutually orthogonal axes, \bar{x} and \bar{y} , centered at O is a set of principal axes for the polar expansion wave stagnation point.

Referring to equation (69), we should write

$$\dot{W}_f = \left\{ \frac{P}{\rho^2} \cdot \frac{D\rho}{Dt} + \frac{(\lambda + \mu)}{\rho} \cdot \left[\frac{1}{\rho} \cdot \frac{D\rho}{Dt} \right]^2 \right\} m \quad (78)$$

for sufficiently small Υ containing point O. Letting $\dot{\rho}$ represent the rate of change of ρ at point O; and noting that as Υ is contracted to the limit at point O, equation (75) holds, one may write,

$$\frac{\dot{W}}{m} = P\dot{V} - \frac{(\lambda + \mu)}{\rho} \cdot \left(\frac{\dot{\rho}}{\rho} \right)^2 \quad (79)$$

Let $l = \lim_{m \rightarrow 0} \frac{\dot{W}}{m}$ as Υ is contracted about point O. It is clear at once that, the dissipation function for the cylindrical expansion wave may be written as

$$l = \frac{(\lambda + \mu)}{\rho} \cdot \left(\frac{\dot{\rho}}{\rho} \right)^2 \quad (80)$$

At this point, we have completed description of the required stress and work relationships.

V. INTERPRETATION OF VISCOUS DISSIPATION FUNCTION

Consider an expansion wave with spherical symmetry analogous to the cylindrical expansion wave just described. Suppose the wave to be set in (x, y, z) coordinates with stagnation point located at the origin, as shown in Figure 5. Let barred variables denote variables on principal axes.

On principal axes, the components of the stress tensor may be expressed as

$$\bar{\sigma}_{xx} = -P - \lambda \left(\frac{1}{\rho} \frac{D\rho}{Dt} \right) + 2\mu \frac{\partial \bar{U}}{\partial \bar{x}} \quad (81)$$

$$\bar{\sigma}_{yy} = -P - \lambda \left(\frac{1}{\rho} \frac{D\rho}{Dt} \right) + 2\mu \frac{\partial \bar{V}}{\partial \bar{y}} \quad (82)$$

$$\bar{\sigma}_{zz} = -P - \lambda \left(\frac{1}{\rho} \frac{D\rho}{Dt} \right) + 2\mu \frac{\partial \bar{W}}{\partial \bar{z}} \quad (83)$$

$$\bar{\sigma}_{xy} = \bar{\sigma}_{yx} = 0 \quad (84)$$

$$\bar{\sigma}_{xz} = \bar{\sigma}_{zx} = 0 \quad (85)$$

$$\bar{\sigma}_{yz} = \bar{\sigma}_{zy} = 0 \quad (86)$$

It is important to note that expressions (81) - (86) are specialized forms applying only when the base vectors of the coordinate system are aligned with the principal axes of the stress tensor.

If Υ is a rectangular parallelepiped control volume of small extent containing a point in (x, y, z) coordinates, and oriented such that its principal axes are aligned with those of the stress tensor, then the work rate may be expressed as,

$$\dot{W}_f = \left[\frac{\partial(\bar{\sigma}_{xx} \cdot \bar{U})}{\partial \bar{x}} + \frac{\partial(\bar{\sigma}_{yy} \cdot \bar{V})}{\partial \bar{y}} + \frac{\partial(\bar{\sigma}_{zz} \cdot \bar{W})}{\partial \bar{z}} \right] \cdot \delta \bar{x} \cdot \delta \bar{y} \cdot \delta \bar{z} \quad (87)$$

The momentum relations are:

$$\frac{D\bar{U}}{Dt} = \frac{1}{\rho} \frac{\partial \bar{\sigma}_{xx}}{\partial \bar{x}} \quad (88)$$

$$\frac{D\bar{V}}{Dt} = \frac{1}{\rho} \frac{\partial \bar{\sigma}_{yy}}{\partial \bar{y}} \quad (89)$$

$$\frac{D\bar{W}}{Dt} = \frac{1}{\rho} \frac{\partial \bar{\sigma}_{zz}}{\partial \bar{z}} \quad (90)$$

The continuity relation is

$$\frac{\partial \bar{U}}{\partial \bar{x}} + \frac{\partial \bar{V}}{\partial \bar{y}} + \frac{\partial \bar{W}}{\partial \bar{z}} = -\frac{1}{\rho} \cdot \frac{D\rho}{Dt} \quad (91)$$

In the light of these, equation (87) becomes

$$\dot{W}_f = \left\{ \frac{P}{\rho} \cdot \frac{D\rho}{Dt} + \lambda \cdot \left(\frac{1}{\rho} \frac{D\rho}{Dt} \right)^2 + 2\mu \cdot \left[\left(\frac{\partial \bar{U}}{\partial \bar{x}} \right)^2 + \left(\frac{\partial \bar{V}}{\partial \bar{y}} \right)^2 + \left(\frac{\partial \bar{W}}{\partial \bar{z}} \right)^2 \right] \right\} \cdot \delta \bar{x} \cdot \delta \bar{y} \cdot \delta \bar{z} \quad (92)$$

Now suppose Υ to contain the stagnation region of the spherical expansion wave. Let m be the mass contained in Υ , and suppose Υ to be contracted about point O, the origin of coordinates and center point of the spherical wave. In view of the spherical symmetry of the expansion wave, we note that at the origin,

$$2\mu \cdot \left[\left(\frac{\partial \bar{U}}{\partial \bar{x}} \right)^2 + \left(\frac{\partial \bar{V}}{\partial \bar{y}} \right)^2 + \left(\frac{\partial \bar{W}}{\partial \bar{z}} \right)^2 \right] = \frac{2}{3} \mu \cdot \left(\frac{1}{\rho} \frac{D\rho}{Dt} \right)^2 \quad (93)$$

Hence, if Υ is sufficiently small, equation (92) becomes

$$\dot{W}_f = \left\{ \frac{P}{\rho^2} \cdot \frac{D\rho}{Dt} + \left(\lambda + \frac{2}{3} \mu \right) \cdot \frac{1}{\rho} \cdot \left[\frac{1}{\rho} \cdot \frac{D\rho}{Dt} \right]^2 \right\} \cdot m \quad (94)$$

at point O.

As shown for the cylindrical expansion wave, the thermodynamic process at point O may be described as the limiting case of a closed system process. As Υ is reduced to zero,

$$\frac{\dot{W}}{m} = P\dot{V} - \frac{1}{\rho} \left(\lambda + \frac{2}{3} \mu \right) \cdot \left(\frac{\dot{\rho}}{\rho} \right)^2 \quad (95)$$

For the spherical expansion wave, the viscous dissipation function at the unsteady stagnation point is expressible as,

$$l = \frac{1}{\rho} \left(\lambda + \frac{2}{3} \mu \right) \cdot \left(\frac{\dot{\rho}}{\rho} \right)^2 \quad (96)$$

The expression $\lambda + \frac{2}{3} \mu$ is commonly known as the bulk viscosity, and Stokes' hypothesis is that the bulk viscosity is zero. Since the coefficient of dynamic viscosity, μ , is a property of the fluid, Stokes' hypothesis clearly implies that the second coefficient of viscosity, λ , is also a fluid property. Furthermore, λ appearing in equation (80) must be the same as that appearing in equation (96). This may be seen as follows:

Let $(\bar{x}, \bar{y}, \bar{z})$ be aligned such \bar{x} and \bar{y}

coincide with the coordinate basis of Equations (56)-(58). Clearly, we may consider a two-dimensional flow as a flow in $(\bar{x}, \bar{y}, \bar{z})$ coordinates in which $\bar{w} = 0$ at every point, and in which \bar{u} and \bar{v} do not depend on \bar{z} . In this case, the components of the stress tensor in $(\bar{x}, \bar{y}, \bar{z})$ become

$$\bar{\sigma}_{xx} = -P + \lambda \left(\frac{\partial \bar{u}}{\partial \bar{x}} + \frac{\partial \bar{v}}{\partial \bar{y}} \right) + 2\mu \cdot \frac{\partial \bar{u}}{\partial \bar{x}} \quad (97)$$

$$\bar{\sigma}_{yy} = -P + \lambda \left(\frac{\partial \bar{u}}{\partial \bar{x}} + \frac{\partial \bar{v}}{\partial \bar{y}} \right) + 2\mu \cdot \frac{\partial \bar{v}}{\partial \bar{y}} \quad (98)$$

$$\bar{\sigma}_{zz} = -P + \lambda \left(\frac{\partial \bar{u}}{\partial \bar{x}} + \frac{\partial \bar{v}}{\partial \bar{y}} \right) + 0 \quad (99)$$

$$\bar{\sigma}_{xy} = \bar{\sigma}_{yx} = \mu \left(\frac{\partial \bar{u}}{\partial \bar{y}} + \frac{\partial \bar{v}}{\partial \bar{x}} \right) \quad (100)$$

$$\bar{\sigma}_{xz} = \bar{\sigma}_{zx} = 0 \quad (101)$$

$$\bar{\sigma}_{yz} = \bar{\sigma}_{zy} = 0 \quad (102)$$

Clearly, equations (56)-(58) are a subset of equations (97)-(102). Hence, equations (80) and (96) may be compared on the basis of Stokes' hypothesis. We find that the viscous dissipation function for the cylindrical expansion wave must be

$$I = \frac{1}{\rho} \cdot \frac{\mu}{3} \cdot \left(\frac{\rho}{\rho} \right)^2 \quad (103)$$

On the other hand, Stokes' hypothesis implies the enigmatic result that I expressed by equation (96) for the unsteady stagnation point of the spherical expansion wave vanishes. This implies that the expansion occurring here has no internal dissipation, a conclusion seemingly inconsistent with equation (103).

VI. CONCLUSIONS

The appearance of a second coefficient of viscosity in order to complete the connection of the stress tensor to the rate-of-strain tensor for the flow of a Newtonian, isotropic fluid is well-known and often documented. In flows with two-dimensional symmetry, the orthogonal transformations required to rotate the local coordinate system onto the principal axes of either the rate-of-strain tensor, or the stress tensor, are particularly simple and result in transparent formulae for the principal values of these tensor components. The derivation of the formulae given here elucidates the following three points:

1) The symmetry of the stress tensor is dependent on the assumption that each control volume containing a point in space has a properly contained control volume on which the flow is continuous and differentiable, and which also contains the point. This dependence is clear in the two-dimensional arguments presented here, and may also be shown to hold in three dimensions. The assumption clearly fails for all real fluids which have discrete molecular structure. Hence, one must

reckon with the possibility that the Navier-Stokes' equations could lead to paradoxical results for some flows of practical interest.

2) The isotropy assumption requires that the stress tensor, and the rate-of-strain tensor, be in alignment with respect to their principal axes, and axis of maximum shear. This restriction is weak, and the required alignment is, in fact, guaranteed when two distinct coefficients of viscosity, λ and μ , are defined in accordance with equations (56)-(58). One must then constrain λ in order to obtain unique values for the stress components at a point in the flow field. This is the obvious intent of Stokes' hypothesis, the validity of which is difficult to verify.

3) The assumption that the fluid is Newtonian implies that λ and μ are both fluid properties, and are not dependent on the dimensional symmetry of the flow field. The equations for the components of the three-dimensional stress tensor, when specialized to two dimensional symmetry, take on the form of equations (97)-(102). This shows that if the deviatoric stress hypothesis holds, then λ and μ as defined from equations (53)-(55) are identical to those defined in the three-dimensional flow field.

Based on the derivations and reasoning set forth in this paper, the writers feel that Stokes' hypothesis that $\lambda + \frac{2}{3}\mu = 0$ leads to a thermodynamic enigma.

It is evident that Stokes' hypothesis is equivalent to asserting that the thermodynamic pressure is the mean of the normal stresses acting on three orthogonal planes intersecting at a point. It is also evident that in a closed thermodynamic system, the work passing the system boundary is strictly due to the action of the thermodynamic pressure if and only if there is no friction. In this case, the irreversibility of the system is due strictly to non-equilibrium heat transfer—there being no change in entropy due to work transfer.

We have shown that the work rate/unit mass at the center point of a cylindrical expansion wave is equivalent to the work rate/unit mass of an infinitesimal, closed thermodynamic system located at the center. It seems clear enough that the same may be inferred for a spherically symmetric expansion wave.

Now by Stokes' hypothesis, the viscous dissipation function at the center of the spherically symmetric expansion wave as expressed by equation (96) is zero. The dilatation of an infinitesimal element of mass located at the center of the wave is unopposed by fluid friction during the course of the expansion in this case. Since the element would be expanding outward in all directions equally, the notion that there would be no internal dissipation in an isotropic, Newtonian fluid is unsettling.

On the other hand if the viscous dissipation function actually does vanish

at the center of the spherical expansion wave, one would expect the same to occur at the center of an expansion wave with cylindrical or polar symmetry. Under Stokes' hypothesis, this is clearly not the case. Equation (103) expresses the viscous dissipation function at the center of a cylindrical expansion wave, and it is greater than zero. This does not contradict the Second Law of Thermodynamics, but the inconsistency of these results seems apparent.

The writers have concluded that both expansion wave forms must, in fact, be dissipative in their stagnation point expansions. The fact that Stokes' hypothesis results in one wave form being dissipative, while the other is not, would appear on the surface to leave the hypothesis suspect, since both of these expansion waves are non-trivial, compressible flows. Examination of equations (62) and (76), which embody the First and Second Laws of Thermodynamics, suggests that in flows where internally dissipative irreversibility is important, one could introduce profound errors in the local state point and heat transfer rate calculations if the viscous dissipation function is in error. In flows where compressibility effects may dominate, such as rotor relative flows in high temperature, single-stage gas turbines, the second coefficient of viscosity, λ , must be known with good accuracy if one is to avoid this difficulty. The example expansion waves taken in this analysis raise the possibility that Stokes' hypothesis, and therefore the Navier-Stokes Equations themselves, lacks consistency at times with the Second Law of Thermodynamics.

Acknowledgements

The authors would like to acknowledge the assistance of Dr Michael Crawford of the University of Texas at Austin, who generously provided his extensive knowledge of viscous flow phenomena, and considerable time, to us. We hope we have used these wisely. We wish to thank Major Jerold Friddell, USAF, Turbine Group Technical Manager, who provided the illustrations in this paper, as well as the editorial assistance necessary to produce this paper on very short notice. We also wish to thank Ms Wanda Comstock for her unending patience as she prepared this text.

References

1. Schlichting, H., "Boundary Layer Theory", 6th ed., McGraw-Hill, New York, pp 55-60.
2. Lamb, Sir Horace, "Hydrodynamics", 6th ed., Cambridge (Eng.), The University Press, 1932, pp 571-574.
3. Huang, F., "Engineering Thermodynamics: Fundamentals and Applications", Macmillan Publishing Co., Inc., New York, pp 57-60, pp 69-75.

Discussion

C. HAH, NASA LEWIS, U.S.A.

Very interesting paper. Is there any evidence that the issues discussed in the paper have some effects on turbine heat transfer calculation?

AUTHOR'S REPLY

We have no rigorous evidence that the issues addressed in the paper are crucial to accurate analysis of blade heat transfer in turbines. However, we are disturbed by the inconsistency of analytical predictions for convective heat-transfer coefficients with respect to short-duration experiments such as performed by Dr. M. Dunn on isolated turbine stages. We suspect that there is more thermodynamic irreversibility associated with these experiments than closure with turbulence models can account for. This study is an attempt to understand how this could happen, and how thermal design parameters could be affected.

M. RACHNER, DLR, GERMANY

A remark: I compute turbulent flows in combustion chambers using the $k-\epsilon$ turbulence model. In the Eddy-Viscosity assumption (the $k-\epsilon$ model is based on) one can extend the laminar Stokes law to the eddy viscosity and a turbulent bulk viscosity. I found that it had a nonnegligible influence on solutions I obtained, whether this bulk viscosity term was dropped or not. From that I feel, that the validity of Stokes law is more than only an academic question.

AUTHOR'S REPLY

Thank you for your remark. We are unable to predict Stanton numbers for turbine blade rows with sufficient accuracy to satisfy our design requirements. We feel that we need a sharper understanding of the fundamental hypotheses on which the Navier-Stokes equations rest in order to remedy this situation. Our view coincides with yours. The true nature of the Stokes law needs to be addressed. The incineration of a full-scale high-pressure turbine stage due to faulty design analysis is not an academic matter to us.

M. FORDE, UNIV. TRONDHEIM, NORWAY

1) In regard to the transformation of the rectilinear control volume in Fig. 1 into another coordinate system in order to avoid the symmetry assumption of σ_{xy} and σ_{yx} ; isn't the transformation just the same assumption?

2) Is Stokes' hypothesis valid both in steady and unsteady conditions? Can a really unsteady turbulent flow change the hypothesis?

AUTHOR'S REPLY

1) The subject transformation has the purpose of finding the simplest representation of the fluid stress system. In this system, there exists an orientation in which the effect of the surface forces upon the control volume is manifest through purely normal stresses. The symmetry condition ($\sigma_{xy} = \sigma_{yx}$) guarantees that this orientation can be found. The interpretation of the energy relations is much easier in a coordinate system with this orientation. We are not avoiding the symmetry condition; but utilizing it to simplify the stress and strain-rate equations.

2) In principal, if the fluid flow is a continuum, and the fluid is Newtonian, then Stokes' hypothesis should hold for unsteady flow as well. However, it is conceivable that intense turbulence could change the alignment of the stress and strain rate tensors, or cause the continuum assumption to fail. Under these conditions, the Stokes hypothesis could become invalid.

J. ADAMCZYK, NASA LEWIS, U.S.A.

What is the Knudsen number associated with your flows?

AUTHOR'S REPLY

The Knudsen number was not checked for the flows in question. I believe the question here concerns the limits on the existence of the required sequence to guarantee symmetry of the stress tensor. These limits were only pointed out to demonstrate the nature of the conditions on the Navier-Stokes equations. The dissipative enigma described in this paper, in fact, holds partly as a consequence of the symmetry of the stress tensor, and the linearization of the normal fluid stress components. If the enigma is true, then one of the standard hypotheses fails. If one can establish by experiment that the enigma is false, then the authors will have been shown to be in error.

L. POVINELLI, NASA LEWIS, U.S.A.

1) The examples you have shown indicate the Stokes hypothesis used in the solution of the Navier-Stokes equations, leads to inconsistent results for the cylindrical and spherical expansions. Have you looked at other flows to see if this same inconsistency exists?

2) It would be of interest to see some further results because the invalidation of Stokes hypothesis would have severe consequences for the numerical solution techniques that are being pursued.

AUTHOR'S REPLY

1) These are the only two cases studied so far. It has been a progression from boundary layer theory into an examination of the Navier-Stokes theory and into gas kinetic theory.

2) This is not the first time that Stokes' hypothesis has been called into question. It has been controversial since the 1800's. Here are two examples where difficulties are encountered and one must be cautious regarding the physics described.

H. WEYER, DLR, GERMANY

First thing to do is to define and execute a sophisticated basic experiment to demonstrate if there exists the physical effect you try to calculate.

AUTHOR'S REPLY

Thank you for your remark. We have begun consideration of an expansion wave experiment which could quantify the influence of the Stokes relation.



COMPUTATION OF 3D-VISCOUS FLOW AND HEAT TRANSFER FOR THE APPLICATION
TO FILM COOLED GAS TURBINE BLADES

by

Thorsten Vogel
DLR, Institut für Antriebstechnik
Linder Höhe, D-5000 Köln 90
Germany

92-16073

SUMMARY

The mechanism of film cooling and heat transfer on gas turbine blades and endwalls is theoretically investigated by simultaneously solving the 3D Navier-Stokes equations for the flow field and the 3D heat conduction equation for the cooled blade.

The coupling of flow calculation and heat conduction calculation in the turbine blades supplies the wall temperatures and heat fluxes at the blade surfaces. These have to be taken from measurements if a traditional boundary layer approach is used for calculating the corresponding heat transfer coefficients.

Heat transfer coefficients and film cooling efficiencies resulting from the 3D solution are presented.

Additionally a comparison between measured and calculated data is shown.

List of symbols

α	blowing angle
c_p	specific heat
D	dissipation
E	energy
\vec{e}	vector
H	rothalpy
k	Von Karman's constant, $k = 0.4$
κ	ratio of specific heats
λ	thermal conductivity
μ	viscosity
Pr	Prandtl number
p	pressure
ρ	density
S	surface
s	distance along wall
T	temperature
t	time
τ	shear stress
V	velocity
Ω	finite volume
ω	rotational speed
$ \omega $	vorticity
x, y, z	cartesian coordinates
x, φ, r	cylindrical coordinates
y	distance from wall

subscripts

blow	blowing
B, b	blade
c	cooling fluid
e	edge of the boundary layer
eff	effective
g	gas side
l	molecular
n	normal direction
nw	next cell to the wall
Rey	Reynolds-stresses
t	total
turb, t	turbulent
τ	friction
x, y, z	in direction of cartesian coordinates
x, φ, r	in direction of cylindrical coordinates
w	wall
∞	primary fluid at definition point

superscripts

T	transposed
+	wall coordinate

1 Introduction

Euler and Navier-Stokes (NS) methods have found increased use as tools for turbomachinery blade analysis. Especially the problem of film cooling connected with heat transfer at the cascade walls leads to strong three dimensional viscous flow. Compared with ordinary CFD-methods (streamline curvature, potential flow solver connected with boundary layer approaches, method of characteristics) NS-methods give additional information about the following important effects connected with film cooling:

- film cooling ejection affects the boundary layer and primary channel flow. NS-methods account for this effect.

- interaction between film cooling and secondary flow

Furthermore there is no need for additional boundary conditions at the edge of the boundary layer. Today the following disadvantages have generally to be taken into account if NS-methods are applied:

- computer memory capacity is limited, so the fineness of the computational mesh, especially near walls, will be coarser than the computational mesh of any boundary layer method. The boundary layer flow and its phenomena is described more simply. The coarse mesh on the blade surfaces provides only a rough description of the film cooling geometry, (holes etc.).
- CPU-time!

These disadvantages are strongly connected to computer performance and will decrease with increasing computer power. The NS-code used in this paper is based on Dawes' code [1] which was extended to take care of the following aspects:

- heat conduction and heat transfer at the passage walls
- viscous terms in energy equation (diffusion)
- comprehensive representation of the stress tensor in cylindrical coordinates with respect to finer grids
- the turbulence model includes the effect of turbulent heat transfer
- film cooling and effusion cooling (coolant flow)
- additional calculation of the 3D-temperature-field in the blade subject to the channel flow and boundary conditions at hub and tip.

⇒ Coupling of Navier-Stokes and temperature field calculation in the blade.

Furthermore the code is vectorized for application on CRAY - YMP and IBM-3090. On CRAY-computers multitasking [2] is possible under UNICOS.

The code is handled on two different processors, one computes the flow field and the other one works out the temperature distribution in the blade at the same time

2 Analysis

The Navier-Stokes equations in integral form using body fitted cylindrical coordinates (x, φ, r) can be written as follows:

Continuity equation:

$$\frac{\partial}{\partial t} \int_{\Omega} \rho d\Omega + \oint_S \rho \vec{V} d\vec{S} = 0 \quad (1)$$

and Momentum equation in x-direction:

$$\frac{\partial}{\partial t} \int_{\Omega} \rho \tilde{V}_x d\Omega + \oint_S (\rho V_x \tilde{V} + p) d\tilde{S}_x = \oint_S \bar{\tau} d\tilde{S}_x + \int_{\Omega} \rho f_{ex} d\Omega \quad (2)$$

Momentum equation in φ -direction:

$$\frac{\partial}{\partial t} \int_{\Omega} \rho \tilde{V}_{\varphi} r d\Omega + \oint_S r (\rho V_{\varphi} \tilde{V} + p) d\tilde{S}_{\varphi} = \oint_S \bar{\tau} d\tilde{S}_{\varphi} + \int_{\Omega} \rho f_{e\varphi} d\Omega \quad (3)$$

Momentum equation in r -direction:

$$\frac{\partial}{\partial t} \int_{\Omega} \rho \tilde{V}_r d\Omega + \oint_S (\rho V_r \tilde{V} + p) d\tilde{S}_r = \oint_S \bar{\tau} d\tilde{S}_r + \int_{\Omega} \rho f_{er} d\Omega \quad (4)$$

Energy equation:

$$\frac{\partial}{\partial t} \int_{\Omega} \rho E d\Omega + \oint_S \rho H \tilde{V} d\tilde{S} = \oint_S \bar{\tau} \tilde{V} d\tilde{S} + \oint_S \lambda \frac{\partial T}{\partial n} d\tilde{S} \quad (5)$$

and the equation of state:

$$p = \rho(\kappa - 1)(E - \frac{1}{2}(\tilde{V}\tilde{V} - (\omega r)^2)) \quad (6)$$

n is the direction normal to the surface S .

with: $\tilde{V} = (V_x, V_{\varphi}, V_r)^T$

$f_{ex} = 0$, $f_{e\varphi} = -2\omega r V_r$, $f_{er} = V_{\varphi}^2/r + r\omega^2 + 2\omega V_{\varphi}$

Rothalpy: $H = c_p T_{lo} - \frac{1}{2}(\omega r)^2$

The stress tensor in cylindrical coordinates:

$$\bar{\tau} = \begin{pmatrix} \tau_{xx} & \tau_{x\varphi} & \tau_{xr} \\ \tau_{\varphi x} & \tau_{\varphi\varphi} & \tau_{\varphi r} \\ \tau_{rx} & \tau_{r\varphi} & \tau_{rr} \end{pmatrix}$$

$$\tau_{xx} = 2\mu(\frac{\partial V_x}{\partial x} - \frac{1}{3}\nabla\tilde{V}), \quad \tau_{x\varphi} = \mu(\frac{1}{r}\frac{\partial V_x}{\partial\varphi} + \frac{\partial V_{\varphi}}{\partial x})$$

$$\tau_{xr} = \mu(\frac{\partial V_x}{\partial r} + \frac{\partial V_r}{\partial x}), \quad \tau_{\varphi x} = \tau_{x\varphi}$$

$$\tau_{\varphi\varphi} = 2\mu(\frac{1}{r}\frac{\partial V_{\varphi}}{\partial\varphi} + \frac{V_{\varphi}}{r} - \frac{1}{3}\nabla\tilde{V}), \quad \tau_{\varphi r} = \mu(\frac{1}{r}\frac{\partial V_{\varphi}}{\partial r} - \frac{V_r}{r} + \frac{\partial V_r}{\partial\varphi})$$

$$\tau_{rx} = \tau_{xr}, \quad \tau_{r\varphi} = \tau_{\varphi r}, \quad \tau_{rr} = 2\mu(\frac{\partial V_r}{\partial r} - \frac{1}{3}\nabla\tilde{V})$$

O. Reynolds introduced the idea of time-averaging all quantities of \tilde{V}, p, T, ρ to account for the turbulent fluctuations appearing in turbulent flows:

$$\tilde{V} = \overline{\tilde{V}} + \tilde{V}', \quad p = \bar{p} + p', \quad T = \bar{T} + T', \quad \rho = \bar{\rho} + \rho'$$

The overlined quantity represents the averaged value and the "prime"-marked quantity represents the time-averaged turbulent fluctuation. These formulas are inserted into Eqs. 1-6.

All additional new terms are neglected with exception of the so-called *Reynolds stresses*. The resulting Reynolds-stress-tensor τ_{Rey} is expressed by:

$$\tau_{Rey} = (\tau_{ij})_{turb} = -\overline{V_i \rho' V_j'} - \bar{p} \overline{V_i' V_j'} - \overline{\rho' V_i' V_j'} - \overline{V_j \rho' V_i'} \quad (7)$$

The Reynolds-averaged energy equation is completed by the turbulent dissipation term D_{turb} :

$$D_{turb} = \overline{\tau'_{ij} \frac{\partial V_i'}{\partial x_j}} \quad (8)$$

τ_{Rey} and D_{turb} are described with the help of a *Turbulence Model*.

2.1 Turbulence Model

The system of equations is closed by an algebraic, zero equation, turbulence model accounting for the turbulent shear stresses and the turbulent dissipation mentioned above. The molecular viscosity μ_t is replaced by an effective viscos-

ity μ_{eff} , defined by:

$$\mu_{eff} = \mu_t + \mu_i \quad (9)$$

where μ_t is the eddy (or turbulent) viscosity. The eddy viscosity relates the Reynolds stresses to the mean velocity gradient. The turbulent heat transport is modelled by manipulating the molecular thermal conductivity λ_t . This manipulation leads to an additional term in the energy equation representing the turbulent heat conduction. The resulting effective heat conduction is now described by an effective thermal heat conductivity λ_{eff} . λ_{eff} is calculated by assuming a turbulent Prandtl Number. A connection of two different models is applied to describe the turbulent viscosity and the turbulent heat conductivity. Both models are described below.

Model 1 consists of the Baldwin-Lomax [3] mixing length model, coupled with the Cebecchi-Smith [4] near wall damping model. The eddy viscosity is given by:

$$\mu_{eff} = \begin{cases} \mu_{t,inner} & \text{for } y \leq y_{crossover} \quad \text{inner layer} \\ \mu_{t,outer} & \text{for } y > y_{crossover} \quad \text{outer layer} \end{cases}$$

$y_{crossover}$ is the smallest value of y at which values from inner and outer formulas are equal.

The inner layer is modelled by the Prandtl-van Driest formulation

$$\mu_{inner} = \rho l^2 |\omega| \quad (10)$$

with $l = k y (1 - \exp(-y^+/A^+))$ and $|\omega|$ is the magnitude of the vorticity:

$$|\omega| = \sqrt{(\frac{\partial V_x}{r\partial\varphi} - \frac{\partial V_{\varphi}}{\partial x})^2 + (\frac{\partial V_{\varphi}}{\partial r} - \frac{\partial V_r}{r\partial\varphi})^2 + (\frac{\partial V_r}{\partial x} - \frac{\partial V_x}{\partial r})^2} \quad (11)$$

and

$$y^+ = \frac{\rho_w U_{\tau}}{\mu_w} y \quad (12)$$

In the Baldwin-Lomax model A^+ is held constant: $A^+ = 26$, whereas in this paper the Cebecchi-Smith near wall damping model is incorporated to define A^+ as a function of the freestream pressure gradients p_t^+ and p_x^+ :

$$A^+ = \frac{26}{\sqrt{1 - 11.8(p_t^+ + p_x^+)}} \quad (13)$$

For stationary flow solutions p_t^+ is set equal to zero and

$$p_x^+ = \frac{\mu_t}{U_{\tau}^2} \frac{\partial U_{\tau}}{\partial x} \quad \text{with } U_{\tau} = \sqrt{\frac{\tau_w}{\rho_w}}$$

This approach accounts for the influence of freestream pressure or velocity gradient on the viscous sublayer [5]. The outer layer turbulent viscosity is described by the Clauser formulation:

$$\mu_{outer} = K_1 C_{cp} \rho F_{wake} F_{Kleb}(y) \quad (14)$$

where K_1 and C_{cp} are constants and $F_{wake} = y_{max} F_{max}$. The quantities of y_{max} and F_{max} are determined from the function:

$$F(y) = y |\omega| (1 - \exp(-y^+/A^+)) \quad (15)$$

F_{max} is the maximum value of $F(y)$ that occurs in a profile with $F(y_{max}) = F_{max}$. The function $F_{Kleb}(y)$ is the Klebanoff intermittency factor given by:

$$F_{Kleb}(y) = (1 + 5.5(C_{Kleb} y / y_{max})^8)^{-1} \quad (16)$$

Model 2:

The turbulent thermal conductivity λ_t is described with the help of a turbulent Prandtl Number Pr_t and the eddy viscosity:

$$\lambda_t = \frac{c_p \mu_t}{Pr_t} \quad (17)$$

λ_t links the heat conductivity to the turbulent viscous effects. Pr_t is found from an expression given by Kays and Moffat [7]:

$$Pr_t = (\alpha^2/2 + \alpha cPet - (cPet)^2(1 - \exp(-\frac{\alpha}{cPet})))^{-1} \quad (18)$$

with $Pet = \mu_t/\mu_l Pr$ and $\alpha = 1/\sqrt{Pr_t u}$

The programmed value of c is 0.2 and the suggested value of Pr_t for large y^+ is 0.86. The effective thermal conductivity is expressed by:

$$\lambda_{eff} = \frac{c_p \mu_{eff}}{Pr_{eff}} \quad (19)$$

with

$$Pr_{eff} = \frac{1 + \mu_t/\mu_l}{1/Pr + (\mu_t/\mu_l)/Pr_t} \quad (20)$$

the effective Prandtl Number.

2.2 Film Cooling Boundary Condition

Film cooling is simulated by varying the fixed-wall boundary conditions and satisfying all governing equations. The solution of the film cooling flow field should be stable and is naturally strongly influenced by the manner in which boundary conditions are given. In this paper a blowing-rate M_{blow} , blowing angles α_z and α_r and the total temperature T_{tc} of the coolant are used to describe the film cooling flow. The assumption of equal-pressure-mixing closes the system of film cooling boundary conditions. M_{blow} is defined by:

$$M_{blow} = \frac{\rho_c V_c}{\rho_{\infty} V_{\infty}} \quad (21)$$

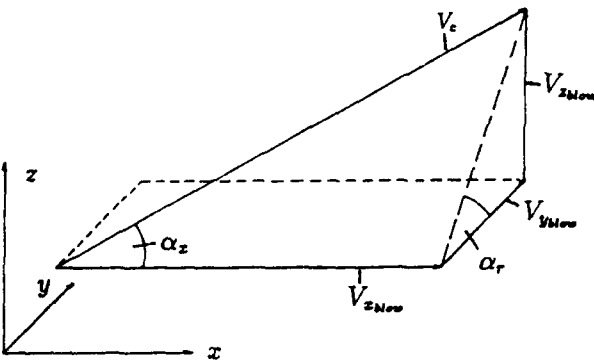


Figure 1: Definition of blowing angles

The coolant flow is calculated from the following equations:

$$V_{xblow} = V_c \cos \alpha_z \quad (22)$$

$$V_{yblow} = V_c \sin \alpha_z \cos \alpha_r \quad (23)$$

$$V_{zblow} = V_c \sin \alpha_z \sin \alpha_r \quad (24)$$

or in cylindrical coordinates:

$$V_{xblow} = V_{zblow} \quad (25)$$

$$V_{yblow} = V_{zblow} \sin \varphi - V_{xblow} \cos \varphi \quad (26)$$

$$V_{zblow} = V_{yblow} \cos \varphi + V_{xblow} \sin \varphi \quad (27)$$

The determination of the density ρ_c of the coolant presents a difficulty. If ρ_c is given as a boundary condition the system of equations (1-6) is redundant in determination. Therefore the total pressure of the coolant flow is determined by means of the following implicit formula (Eq.28) and the assumption $p_c = p_{\infty}$.

$$M_{blow} = \sqrt{\frac{T_{t\infty}}{T_{tc}}} \left(\frac{p_{tc}}{p_{t\infty}} \right)^{\frac{\gamma-1}{\gamma}} \frac{\sqrt{(1 - \frac{p_{tc}}{p_{t\infty}})^{\frac{\gamma-1}{\gamma}}}}{\sqrt{(1 - \frac{p_{\infty}}{p_{t\infty}})^{\frac{\gamma-1}{\gamma}}}} \quad (28)$$

The coolant density is calculated with the help of this formula and the relationship $\rho_c = \rho_{tc} \cdot (p_c/p_{tc})^{1/\gamma}$.

2.3 Fourier/Laplace Equation

The heat conduction in the gas turbine blade is described by Fourier's equation as follows:

$$\frac{\partial}{\partial t} \int_{\Omega} (\rho c)_B T d\Omega = \oint_S \lambda_B \frac{\partial T}{\partial n} \tilde{c}_n dS \quad (29)$$

n is again the direction normal to the surface S .

Because of the stationary character of the flow field solution of the Navier-Stokes calculation the time dependence of the temperature in the blade can be neglected: $\partial T/\partial t = 0$. If heat sources in the blade are neglected and constant properties $\lambda_B, (\rho c)_B$ are assumed, Fourier's equation is reduced to the well known Laplace equation:

$$\oint_S \frac{\partial T}{\partial n} \tilde{c}_n dS = 0 \quad (30)$$

2.4 Coupling of Navier-Stokes and Laplace Calculation

The connection of both independent calculations is worked out with regard to common boundary conditions at the blade surfaces.

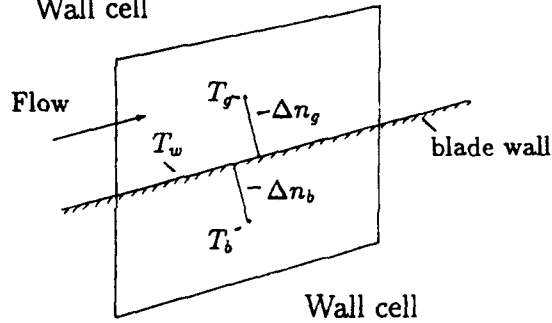
Wall cell

Figure 2: Coupling and energy balance at blade surface

For diabatic walls the heat fluxes through the blade surfaces can be described on the gas side and on the blade material side by means of an energy balance at the blade surface as follows: $q_g = q_b$ (Fig.2).

with:

$$-\lambda_g \frac{\partial T_g}{\partial n_g} = -\lambda_b \frac{\partial T_b}{\partial n_b} \quad (31)$$

or discretized:

$$\lambda_g \frac{T_g - T_w}{\Delta n_g} = \lambda_b \frac{T_w - T_b}{\Delta n_b} \quad (32)$$

The wall temperature T_w , the heat fluxes and the heat transfer coefficient α_g are expressed with this equation.

α_g is defined as:

$$\alpha_g = \frac{-\lambda_g \frac{T_g - T_w}{\Delta n_g}}{T_w - T_{\infty}}$$

3 Numerical Procedure

The Reynold-averaged Navier-Stokes equations are numerically solved using a finite volume technique with centred difference approximation to represent the convection terms. It is possible to use I-Grids in the case of unfavourable curvature at the leading and trailing edge of the blade profile. As far as possible H-Grids should be applied because they are much more recommendable using less computer storage and time. I-Grids require a full matrix of nine projected cell face areas and the cylindrical coordinates (x, φ, r) depend on all node indices (i, j, k) , whereas H-Grids only require seven projected areas and the coordinate-directions (x, r) only show (j, k) dependence. The computational grids are quickly generated and controlled before starting the actual computational procedure. The applied grid-generator is described in detail in [6]. The grid needed for the Laplace-calculation in the blade is automatically generated at the beginning of each calculation procedure. Because of the use of centred difference approximation two main numerical difficulties occur especially in convection dominated flow:

- wiggles and shock-smearing
wiggles: short waves representable on a given mesh may interact and form nonphysical long waves
shock-smearing: shocks are smeared over several mesh cells
- unstable time marching algorithm in some cases

The first difficulty is resolved by adding a certain amount of artificial dissipation to the NS-model [8] to prevent wiggles and to permit shock capture. The second problem requires a stable algorithm in time such as the implicit schemes of Beam-Warming [9] or Briley-McDonald [10]. The disadvantages of these schemes (not only these ones) being that they require the solution of the implicit step to be retained in computer memory. The artificial dissipation values are additionally stored upon the viscous values of each equation (with exception of the dissipation quantity of the continuity equation). With regard to this the numerical discretization of the governing equations becomes:

$$\frac{\Delta \bar{U}_{ijk}}{\Delta t} \Delta VOL_{ijk} = \sum_{Cell, i, j, k} \bar{F}_{iE} \Delta \bar{S} + \sum_{Cell, i, j, k} \bar{F}_{iN} \Delta \bar{S} + \rho \bar{F}_{A, i, j, k} \Delta VOL_{ijk} + \bar{D}(\bar{U})_{ijk} \quad (33)$$

with

$$\bar{U} = (\rho, \rho V_x, \rho V_\varphi, \rho V_r, \rho E)^T$$

$$\bar{F}_{iE} = (\rho \bar{V}, \rho V_x \bar{V}, \rho V_\varphi \bar{V}, \rho V_r \bar{V}, \rho H \bar{V})^T$$

$$\bar{F}_{iN} = (0, \bar{\tau} \bar{e}_x, \bar{\tau} \bar{e}_\varphi, \bar{\tau} \bar{e}_r, \bar{\tau} \bar{V} \bar{e} + \lambda \Delta T / \Delta n)^T$$

$$\bar{F}_A = (0, 0, -2\omega r V_r, V_\varphi^2 / r + r\omega^2 + 2\omega V_\varphi, 0)^T$$

$$\text{and } \bar{D}(\bar{U}) = \bar{D}_I + \bar{D}_J + \bar{D}_K$$

the dissipative operator, where $\bar{D}_I, \bar{D}_J, \bar{D}_K$ represent the contributions from each of the curvilinear coordinate directions. [1] and [8] describe the dissipative operator in detail.

The discretization of Laplace's equation results in:

$$\sum_{Cell, i, j, k} F_{ijk} \bar{e}_n \Delta S = 0 \quad (34)$$

with $F_{ijk} = (\Delta T / \Delta n)_{ijk}$

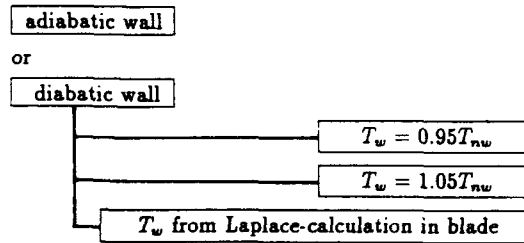
Usually elliptical equations such as Laplace's equation (Eq. 34) are solved using any matrix-solvers to find the more or less correct values of the dependant quantity (here: temperature) at any grid node (i, j, k) . Due to the coupling of the channel flow and blade temperature problem the boundary conditions of Laplace's equation change with any time-step during the Navier-Stokes calculation. For this reason

the heat conduction problem in the blade material is solved using Banach's iteration in space [11]. Eq. 35 shows the principle steps involved:

$$T(i, j, k) = F(T(i+1, j, k), T(i-1, j, k), T(i, j+1, k), T(i, j-1, k), T(i, j, k+1), T(i, j, k-1)) \quad (35)$$

The function F depends on the geometry of the blade. Eq. 35 is solved for every mesh cell and the iteration is homogeneously fitted to the alternating boundary conditions. To solve film cooling problems it is very important to build up a very general input procedure which enables the user to simulate blowing situations of different kinds. Therefore a special input routine was drawn up enabling the user to address every wall mesh cell of the computational grid and to put in every amount of coolant flow. The main restriction is: The coolant flow properties have to be the same as the primary flow properties.

The user can choose between the following calculation options:



Film cooling may be connected with all options.

4 Results and Discussions

The first part of this section treats the comparison between calculated and measured data and the second one deals with evaluations concerning a real gas turbine stator available at the DLR (MTU-VT1B). Because of the difficulty to get experimental data from measurements on heat transfer and film cooling in real gas turbine passages the code validation is carried out for a simple test case. All calculations took place on CRAY-YMP. The flow was considered to be turbulent without any transition in all cases. The obtained results are presented in the following sections.

4.1 Comparison between measured and calculated film cooling data

Experimental data obtained by C. Liess [12] (1975) are used for code validation. Liess measured adiabatic wall effectiveness and heat transfer coefficients on a flat plate downstream of a row of inclined circular film cooling ejection holes. The adiabatic film cooling efficiency (or adiabatic wall effectiveness) is defined as:

$$\eta_{ad} = \frac{T_w - T_{t\infty}}{T_{tc} - T_{t\infty}}$$

The flow field downstream of the ejection holes is found to be very complex and three-dimensional. Due to the complex flow field experimental data for film cooled turbine blades are very rare.

The range of flow conditions is listed in Table 1.:

Main flow Mach number	$M_\infty \approx 0.3$
Main flow upstream of ejection	turbulent
Blowing rate	0.1-2.0
Ejection angle	$\alpha_e = 35 \text{ deg.}$
Spacing to diameter of ejection holes	$s/d = 3.0$
Stagnation temperature of ejected flow	$\approx 350 \text{ K}$
Stagnation temperature of main flow	$\approx 276 \text{ K}$

Table 1.: Experimental flow conditions.

The experimental test section had a height of 10 cm, a width of 5 cm and rectangular cross sections. The numerical experiment was restricted to only one part of the test flow channel with periodic boundaries and the ejection influence of only three holes. The upper part of Fig.3 shows the test section flow channel and the lower part of this figure illustrates the discretization of the ejection holes on the given mesh. Adiabatic wall effectiveness and heat transfer coefficient were measured over a maximum downstream distance of $x/d = 80$, which corresponds to the interesting range of gas turbine blades. The computational mesh consisted of $53 \cdot 169 \cdot 39 = 331968$ mesh cells. Convergence was reached after 2500 Time-steps or approximately 10.5 hours CPU-Time on CRAY - YMP. Fig.4 shows the heat transfer coefficient as a function of x/d for the experimental and numerical data without any ejection. The agreement is good. Fig.5 presents the distribution of the adiabatic wall effectiveness for blowing rates $M_{low} = 0.16/0.34/0.91$ as a solution to the computation mentioned above compared to the experimental data. Inaccuracies occur in the complex 3D-flow region downstream of the ejection holes. The inaccurate modelling of the ejection holes (Fig. 3) and the inexact description of the incoming boundary layer are some reasons for these effects.

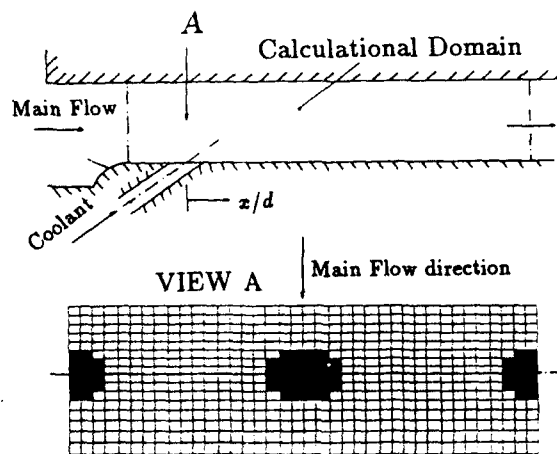


Figure 3: Test section and modelling of the ejection holes.

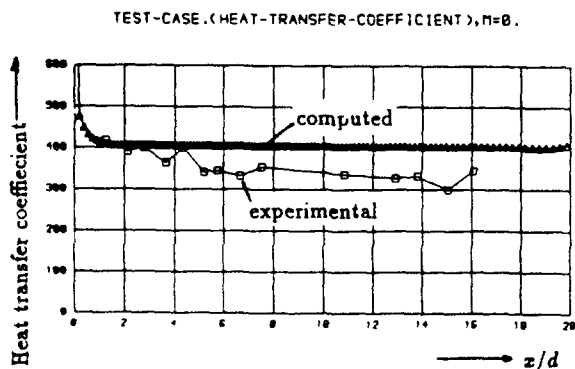


Figure 4: Comparison between experimental and numerical data: Heat transfer coefficient without blowing.

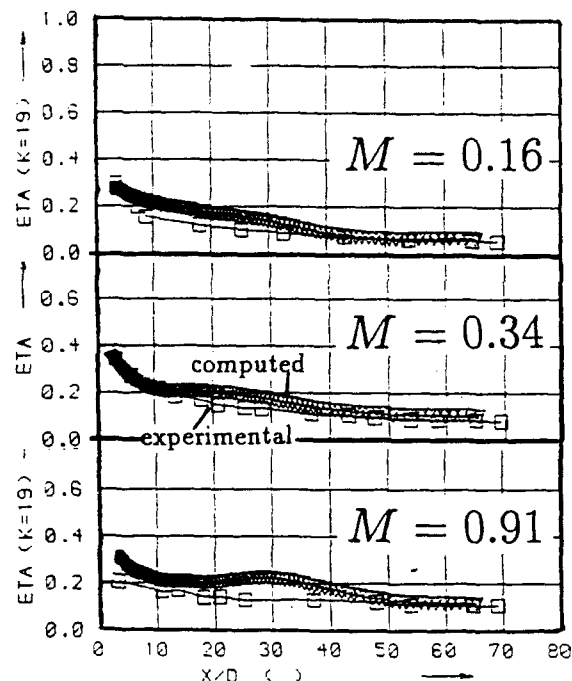


Figure 5: Comparison between experimental and numerical data: Film cooling efficiency.

4.2 Turbine stator calculations

Table 2 presents the most important information concerning the blade geometry parameters and main flow conditions.

Aspect ratio	0.61
Number of blades	25
Inlet flow angle	90.0 deg
Outlet flow angle	21.1 deg
Exit Mach number	0.9
Pressure ratio	0.54
Inlet stagnation temperature	500 K
Inlet stagnation pressure	1.70 bar
Reynolds number	1.00E+6
Mass flow	4.7 kg/s

Table 2.: Main flow conditions and stator baseline data.

In the following two subsections two test calculations and their solutions are presented. Option 1 treats a calculation *without* any film cooling but incorporates heat transfer at the turbine passage walls. The calculation of the blade temperature distribution is coupled to the passage flow calculation. The gas turbine blade is cooled at hub and tip with constant temperature ($T_{hub} = T_{tip} = 380K$). Option 1 treats a calculation *with* film cooling and adiabatic walls. 3000 time steps are required for convergence in Option 1. Convergence is also reached after 3000 time steps in the case of Option 2.

4.2.1 Option 1: Diabatic walls without film cooling, wall temperatures from Laplace calculation

Table 3 provides information on the mesh sizes used for the flow and heat conduction calculation, about the Rate of Data Processing (RDP) and the Computer Memory Requirement (CMR):

Simulation	IM /JM /KM	mesh cells
Navier-Stokes	53/149/45	338624
Laplace	28/ 80/45	93852
RDP	$4.5 \cdot 10^{-5} \frac{\text{sec}}{\text{step-cell}}$	
CMR	$118.4 \cdot 10^6$ Bytes	

Table 3.: Mesh configurations, RDP and CMR.

IM, JM, KM are the maximum mesh size indices in circumferential, axial and radial directions. After every time step of the Navier-Stokes calculation nt iteration steps take place in Laplace calculation. nt is given by the user. In this special case nt is set to 8. The viscid calculation starts after a certain time step number ($nstart$) which is set by the user. All viscid effects are neglected if n (time step counter) is smaller than $nstart$. Coupling and energy balance (Section 2.4) is handled after every time step greater than $nstart$. The stagnation temperature and pressure distributions at the blade surfaces are plotted as a function of radius (r) and distance along the wall (s).

Fig.6 shows the computational mesh at mid span for both calculation options and Fig.7 illustrates the computational mesh for the Laplace calculation in the blade. Fig.8 presents the local Mach number isolines on this mesh. The boundary layer contains three to six mesh cells, therefore the local Mach number strongly decreases at the blade walls. The temperature isolines in the blade are shown in Fig.9 at mid span and at a cross-sectional plane at 40% of the axial chord length. Fig.10 compares the stagnation temperature in the flow channel at the suction side and the temperature in the cooled blade at the same blade surface. Data is given in the centers of the mesh cells which are close to the wall. Very hot areas are identified at mid span at trailing and leading edge of the blade and cooler areas are found at hub and tip as expected. The pressure side temperature distribution looks similar but is found on a higher temperature level. Fig.11 shows the stagnation temperature isolines at a cross sectional plane at the position $J=115$ (trailing edge: $J=123$). The pressure surface is warmer and at the edges of hub/pressure surface and tip/pressure surface very hot bubbles are concentrated. Fig.12 illustrates the distribution of the heat transfer coefficient as a function of the axial chord length on the pressure side (square symbol) and on the suction side (triangle symbol). The heat transfer coefficient obviously increases at the leading and trailing edge as it should be.

4.2.2 Option 2: Adiabatic walls with film cooling

Table 3 presents the film cooling input configuration and the mesh size.

Ejection angles: α_s and α_r	35-40 deg./90 deg.
Blowing rate	0.9
Stagnation temperature T_{ic}	350 K
Mesh size, IM/JM/KM	53/149/45 = 338624 cells
Blowing at pressure side: two rows of holes, at	$J=65/66$ and $J=75/76$ 23% and 37% of c_{ax}
Blowing at suction side: one row of holes, at	$J=65/66/67$ 23% of c_{ax}

Table 3.: Film cooling input and mesh configuration.

$$RDP = 4.2 \cdot 10^{-5} \frac{\text{sec}}{\text{step-cell}}$$

$$CMR = 13.4 \text{ Mw} = 107.2 \cdot 10^6 \text{ Bytes}$$

Fig.13 shows the positions of the ejection holes at the suction and pressure side on the given mesh. Fig.14 presents the local Mach number isolines at mid span comparable to Fig.8. Fig.15 shows the stagnation temperature isolines at the same cross-sectional plane as described in subsection 4.2.1. The cooling film is pressed to the pressure side of the blade and

sucked away from the suction side. The influence of the secondary flows is visible. Near the hub the cooling films from both blade surfaces combine. Fig.16 presents the stagnation temperature isolines at the suction side of the blade. The wall mesh cells where coolant flow is ejected are clearly visible. Due to the influence of the secondary channel flows the cooling film drifts away from hub and tip. At the trailing edge not far away from tip a small separation bubble appears. The effect of heat conduction clearly occurs in the boundary layer where heat transport takes place in opposite direction to the main flow direction. Fig.17 shows the same effects on the pressure side, but no separation bubble occurs and the influence of the secondary flow is weaker. Fig.18+19 present the stagnation pressure isolines at the suction and pressure blade surfaces. Big losses appear at the trailing edge as expected. Fig.20 shows the distribution of the film cooling efficiency as a function of the axial chord length c_{ax} at mid span. The triangle marked curve shows the efficiency at the suction side ($\eta_{ad,suc}$), the square marked curve presents the efficiency at the pressure side ($\eta_{ad,pres}$). The two peaks of $\eta_{ad,pres}$ and the peak of $\eta_{ad,suc}$ show the place of blowing. The adiabatic wall temperature is extrapolated with the help of the static temperatures at the mesh cell centres close to the wall. So the wall temperatures will reach the stagnation temperature only for infinitely fine computational meshes. Due to this phenomena on finite meshes η_{ad} is computed bigger than it should be. This sets the maximum values of η_{ad} above the real maximum of 1.0. At the trailing edge of the blade strongly viscous effects affect η_{ad} .

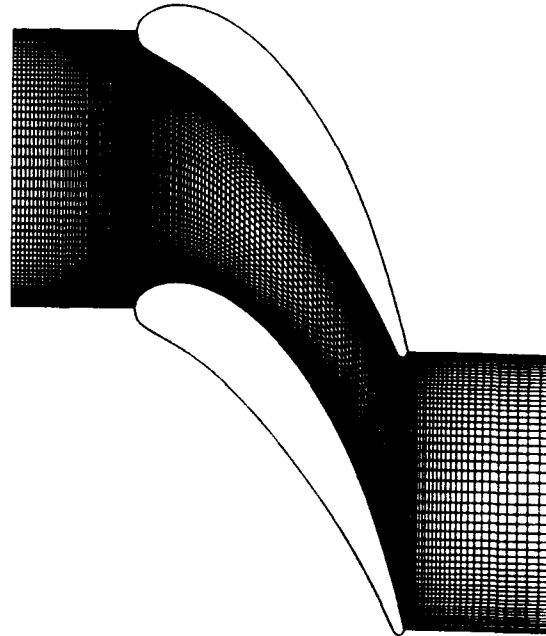


Figure 6: Computational mesh at mid span in the flow channel.

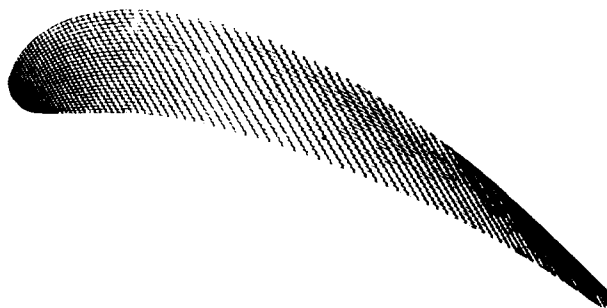


Figure 7: Computational mesh at mid span in the blade.

5 Conclusions

A numerical method for computing the 3D compressible and viscous turbomachinery flow is presented.

The analysis solves the Reynolds-averaged Navier-Stokes equations coupled with the stationary heat conduction equation describing the turbulent channel flow and the temperature distribution in the gas turbine blade.

The effects of blade and endwall heat transfer, film and effusion cooling are additionally taken into account.

The solutions of the 3D simulations presented in Fig. 8-20 are significant and the comparison between computed and experimental data for a simple test case (Fig. 4-5) show good agreement and encourage to further development and investigations. So far the presented computer code is a useful tool describing the complicated relationships between turbomachinery passage flow, ejection of coolant and heat transfer. It is possible to investigate the influence of blade cooling on the temperature field in the blade and on the flow. Nevertheless the code should be improved in future relative to:

- calculations on finer meshes to improve the detection of the wall temperature gradient describing the heat transfer problem,
- improved modelling of the turbulent flow near ejection holes,
- improved description of the laminar/turbulent transition,
- code validation with the help of measurements concerning the application to gas turbine flows,
- numerical and experimental investigation of the effect of film cooling on secondary passage flows,
- consideration of the influence of cooling channels in the blade.

REFERENCES

- [1] Dawes, W.N.: 'A computer program for the analysis of three dimensional viscous compressible flow in turbomachinery blade flows', Whittle Laboratory, Cambridge, U.K., (1988)
- [2] CRAY Research: 'UNICOS User Commands Reference Manual', SR-2011
- [3] Baldwin, B. and Lomax, H.: 'Thin layer approximation and algebraic model for separated turbulent flows', AIAA Paper 78-257 (1978)
- [4] Cebecci, T.: 'Calculation of unsteady two-dimensional laminar boundary layers with fluctuations in external velocity', Mechanical Engineering Department, California State University at Long Beach (1977)
- [5] Boyle, R.J.: 'Navier-Stokes Analysis of Turbine Blade Heat Transfer', ASME 90-GT-42, Brussels (1990)
- [6] Heselhaus, A.: 'Erstellung eines Programms zur Generierung von 3D-Turbinenschaufeln für die numerische Strömungssimulation', Diplomarbeit, DLR Inst. Antriebstechnik (1990)
- [7] Crawford, M.E., Kays, W.M. and Moffat, R.J.: 'Heat transfer to a full-coverage film-cooled surface with 30 deg. slant-hole injection', NASA Contractor Report, NASA CR-2786
- [8] Jameson, A. and Baker, T.J.: 'Multigrid solution of the Euler equations for aircraft configurations', AIAA Paper 84-0093 (1984)
- [9] Warming, R.F. and Beam, R.M.: 'On the construction and application of implicit factored flows', SIAM-AMS Proceedings, VOL. 11, 1978
- [10] Weinberg, B.C. and McDonald, H.: 'Solution of three-dimensional time-dependent viscous flows', Eighth International Conference on Numerical Methods in Fluid Dynamics' Aachen, 1982
- [11] Jeltsch, R.: 'Mathematik für Ingenieure, Teil A, Inst. f. Geometrie u. Praktische Mathematik, RWTH-Aachen, 5. Aufl. (1986)
- [12] Liess, C.: 'Experimental investigation of film cooling with injection from a row of holes for application to gas turbine blades', Journal of Engineering for Power, (Jan. 1975)

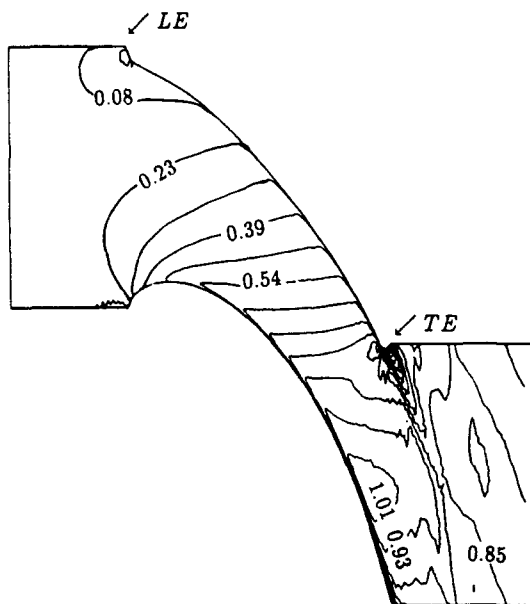


Figure 8: Local Mach number isolines at mid span, cooled blade, without film cooling.

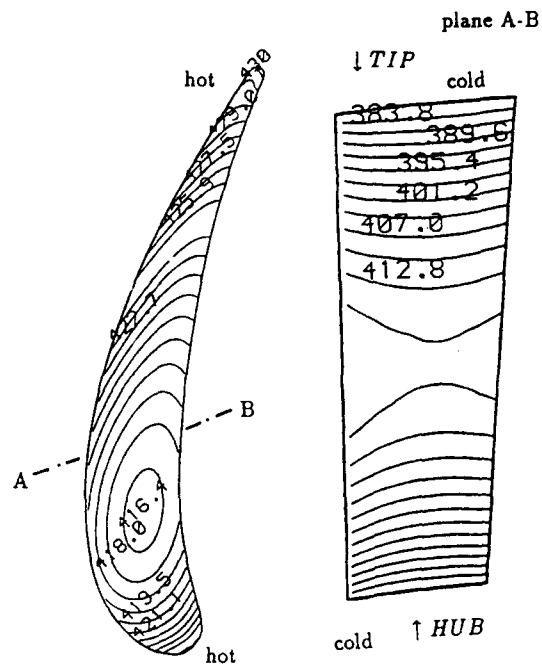


Figure 9: Temperature isolines in the blade at mid span and at a cross section.

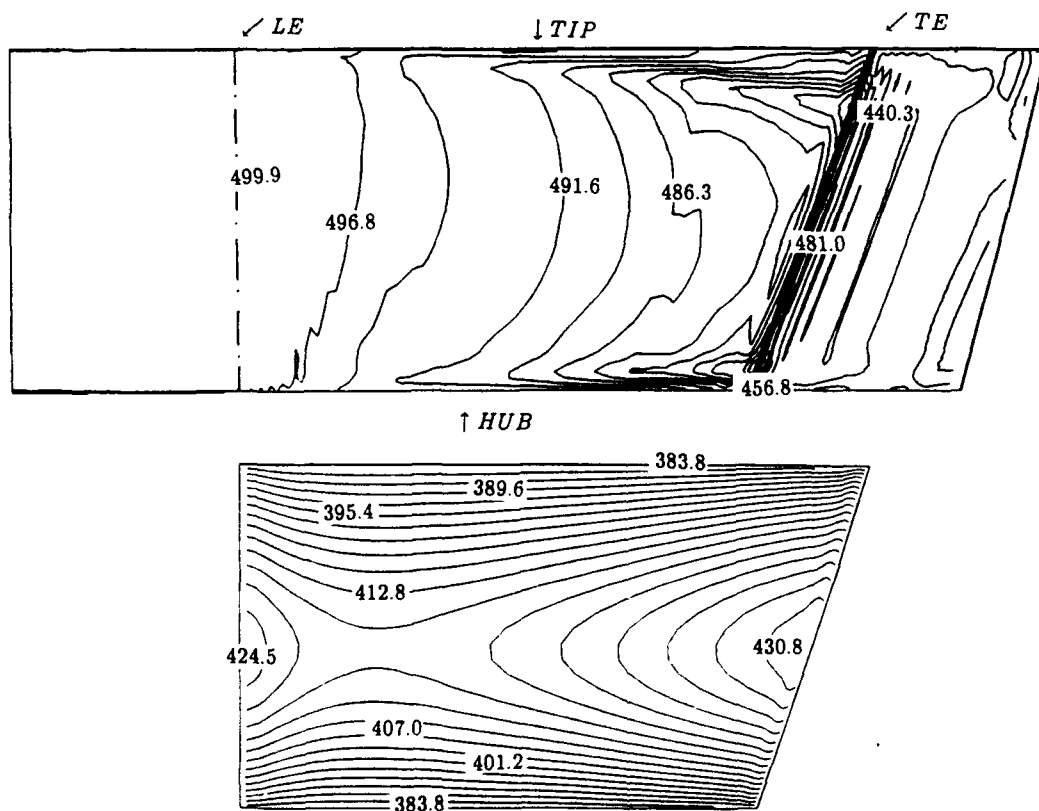


Figure 10: Upper part: Stagnation temperature isolines at the suction side in the flow channel. Lower part: Temperature isolines at the suction side in the blade (without film cooling).

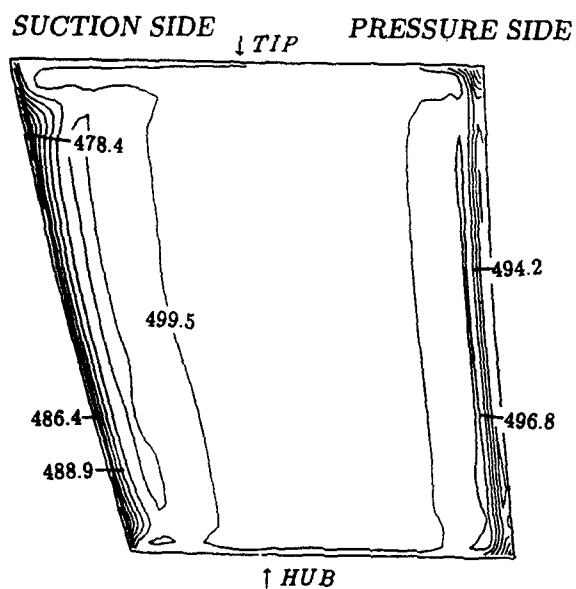


Figure 11: Stagnation temperature isolines at a cross sectional plane (without film cooling).

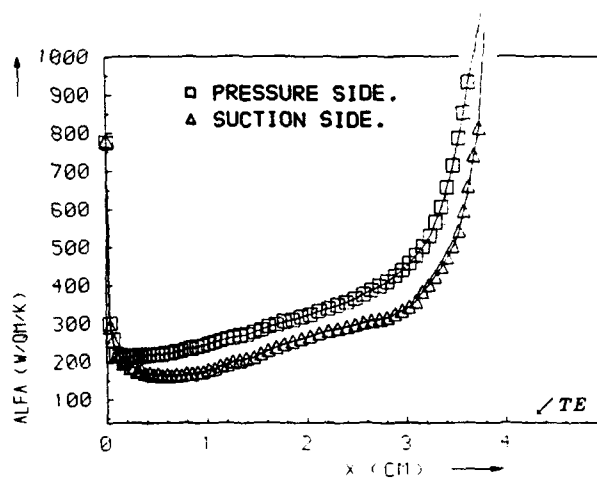


Figure 12: Heat transfer coefficient at mid span.

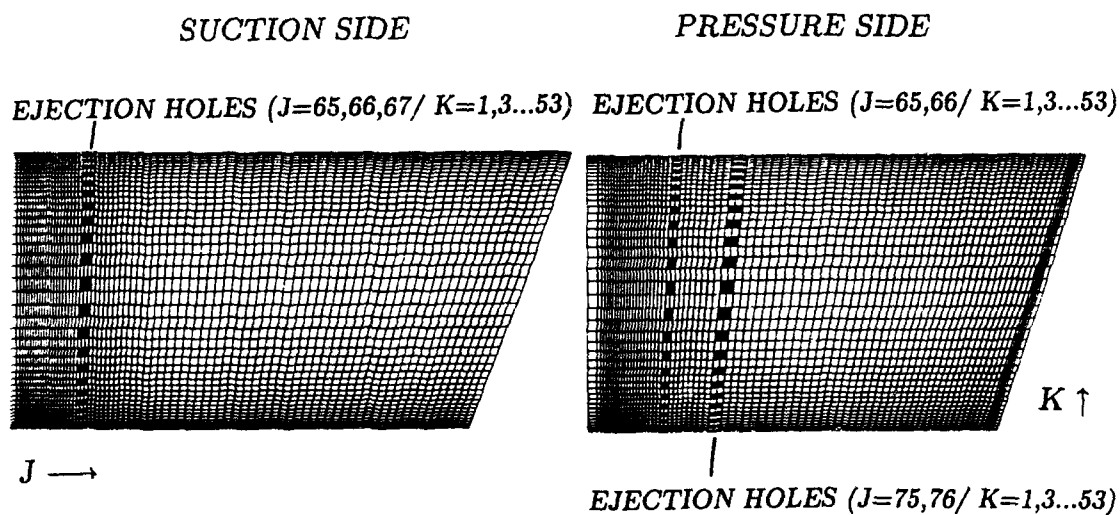


Figure 13: Position of the ejection holes on suction and pressure surface

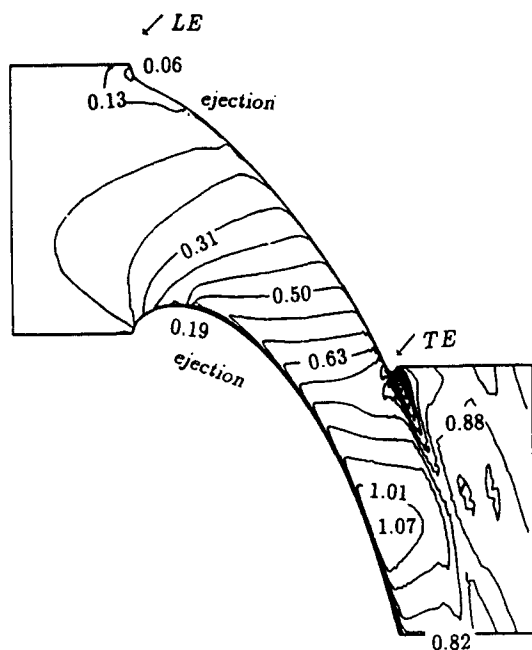


Figure 14: Local Mach number isolines at mid span, film cooled blade.

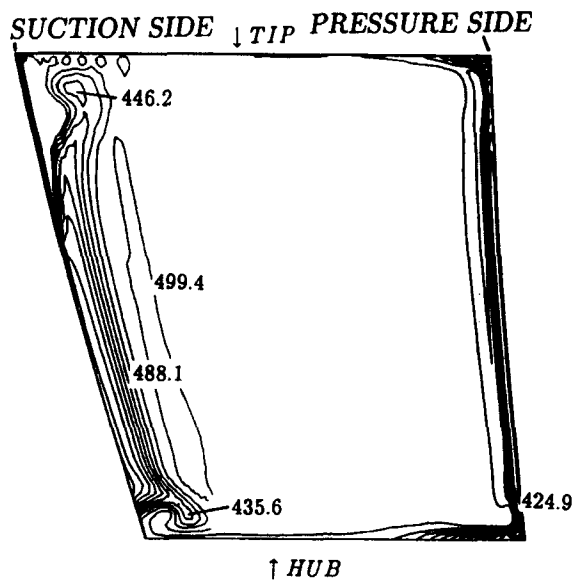


Figure 15: Stagnation temperature isolines at a cross section (with film cooling)

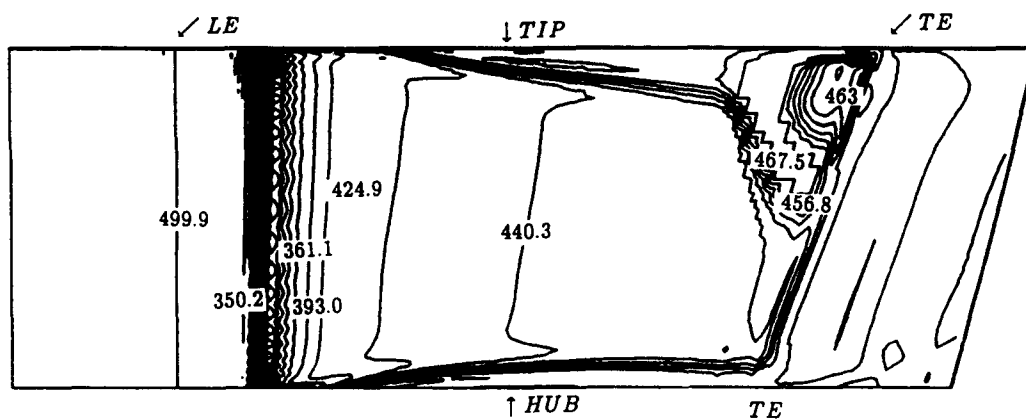


Figure 16: Stagnation temperature isolines and film cooling at the suction side.

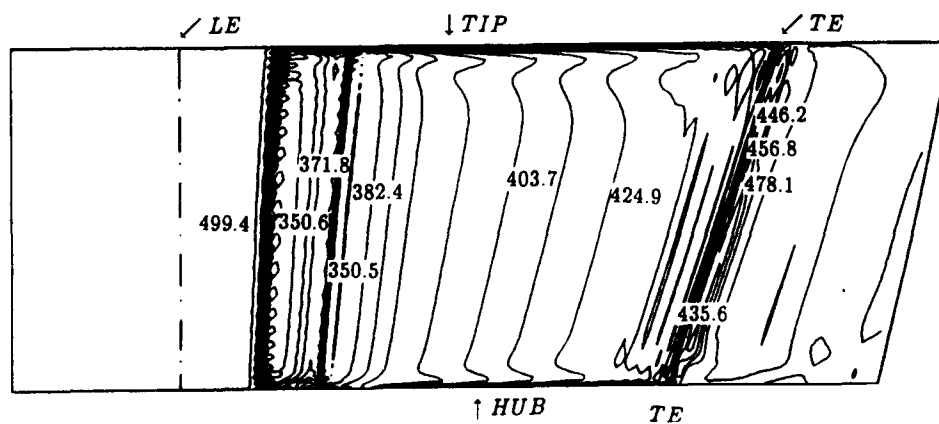


Figure 17: Stagnation temperature isolines and film cooling at the pressure side.

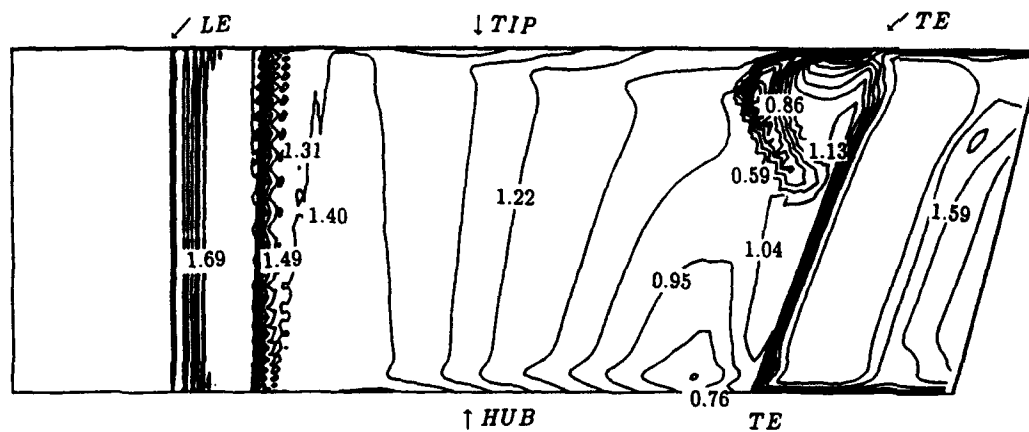


Figure 18: Stagnation pressure isolines and film cooling at the suction side.

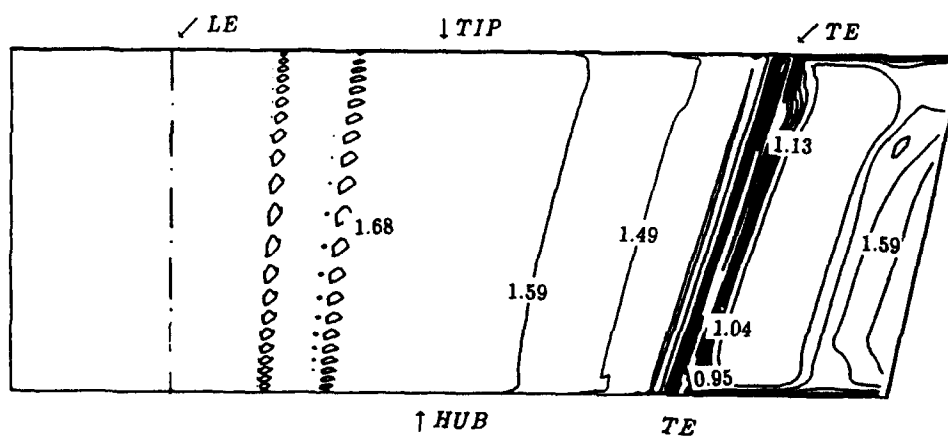


Figure 19: Stagnation pressure isolines and film cooling at the pressure side.

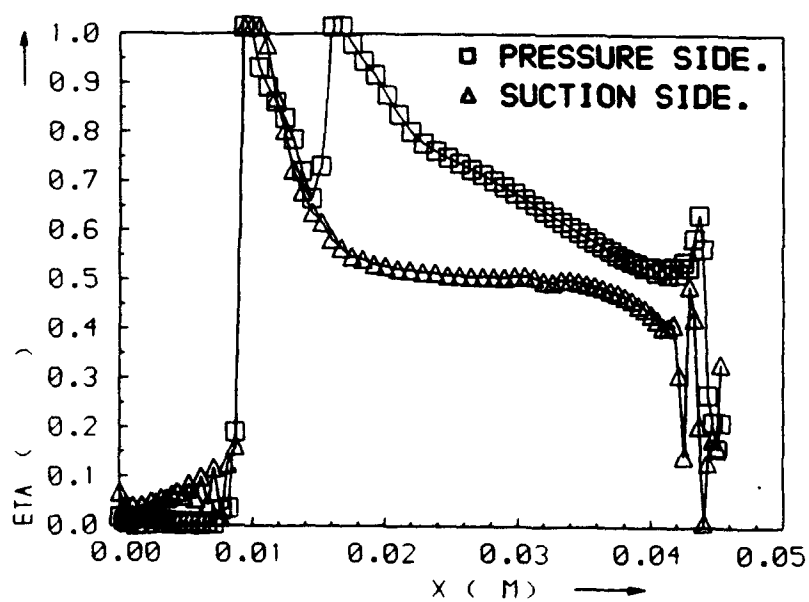


Figure 20: Film cooling efficiency at pressure and suction side.

Discussion

M. FORDE, UNIV. OF TRONDHEIM, NORWAY

- 1) Did you have any convergence problems?
- 2) Did you try any variation of the density of the mesh near the wall and did you see the influence?

AUTHOR'S REPLY

- 1) No, I had no convergence problems. I have to mention that film cooling accelerates the convergence of the calculated problems.
- 2) The density of the mesh near the wall has a big influence on the heat transfer. The heat transfer coefficient increases with an increasing density of the mesh. The influence of the mesh density is low for very dense meshes.

K. BROICHHAUSEN, MTU, MÜNCHEN, GERMANY

What special handling of the turbulence model did you use at the wall?

AUTHOR'S REPLY

A Baldwin-Lomax mixing length model was used, coupled with a Cebeci-Smith near wall damping model. A turbulent Prandtl number from the expression by Keyes and Moffit was used.

M. IACOVIDES, UMIST, U.K.

What was the y^+ value at the near-wall nodes?

AUTHOR'S REPLY

The y^+ value at hub and tip amounts to 2.5. At the blade surfaces y^+ is about 1 to 1.5.

R. GRAY, WRIGHT LABS, U.S.A.

Were there any examples in your computations of situations resulting in increased wall heat flux as a result of film injection?

AUTHOR'S REPLY

No, I did not observe this. But this also depends on the temperature field in the interior of the cooled turbine blade.

F. LEBOEUF, ECOLE CENTRALE LYON, FRANCE

Are you able to capture the main kinematic features of the jet flow, particularly near the orifice (counter-rotating vortices in the jet), for the turbine case?

AUTHOR'S REPLY


I am able to do this for test cases, where the injection holes are described well on the given mesh. Here you can detect the jet vortices. For the turbine case I don't have enough computer storage to describe the small injection holes. Only four to six mesh cells at the wall simulate an ejection hole. This is not enough.

M. IACOVIDES, UMIST, U.K.

What is the value of y^+ at your first node from the wall?

AUTHOR'S REPLY

I don't know offhand.



EXPERIMENTAL VERIFICATION OF A 3D TURBULENT FLOW CALCULATION IN AN AXIAL TURBINE CASCADE

by

J.G.E. Cleak and D.G. Gregory-Smith
School of Engineering and Applied Science
University of Durham, Durham DH1 3LE
United Kingdom

N.T. Birch
Rolls-Royce plc., Derby
United Kingdom

92-16074

SUMMARY

A Navier-Stokes computer code has been used for the calculation of the three-dimensional secondary flow in a cascade of axial turbine blades. A comparison is made with experiment of the results of various applications of a mixing length model within the code. The results are compared on the basis of mean flow data and also turbulent Reynolds shear stresses. Substantial grid independence was obtained with a grid of 20,000 points; further grid refinement had a significant effect only on midspan loss. Large variations in the results were obtained with the different applications of the model, the best results overall being obtained with laminar flow being imposed for up to 80% of the axial chord away from the end wall. The high turbulence activity in the vortex core was not predicted; the flow close to the endwall and blade surfaces appeared to dominate the calculated flow. The need for higher order turbulence modelling is indicated, but probably of greater importance is the accurate prediction of transition.

1. INTRODUCTION

The development of computer codes for the calculation of the viscous three-dimensional flow such as found in turbomachinery blade rows has received much attention in recent years. The rapid advance in the power of computers has allowed the code developers to consider an ever widening range of techniques and problems. There is thus a parallel requirement to ensure that the codes are modelling the physics of the flow with increasing accuracy. The three-dimensional flows that are generated in the secondary flow region near the end wall of a high turning turbine blade passage provide a particularly severe case for the calculation methods.

As codes are developed they are normally checked by comparison with experimental data. However through lack of time or sufficiently detailed data, the comparisons may be fairly limited. For instance, only the inlet and exit flow for a blade row may be compared and not the flow within the blade passage, or only flow velocities and not losses may be compared. Whether such detailed comparisons are necessary depends on the use to which the code is to be put, and for some purposes a limited comparison may be sufficient. However as turbomachinery design advances, the increasing demands for high efficiency and the need to control the flow within the blading mean that the requirements for a useful code are becoming more stringent.

A pressure correction code that has received a lot of attention and that is used extensively by Rolls-Royce, is that of Moore and Moore [1]. A recent paper by Northall, Moore and Moore [2] shows a comparison of the method for the VKI low speed annular cascade of turbine nozzles (Sieverding et al. [3]). Satisfactory comparisons are made at three planes, one near the blade passage exit and two downstream, and include flow

angles, static pressures and losses. This paper describes a much more detailed comparison of the flow through a large scale linear cascade of high turning rotor blades which produce intense secondary flows. Two experimental data sets were used, which differed in that the first had low inlet turbulence, and the second had high inlet turbulence created by a grid placed upstream of the cascade. For the first, mean flow data had been obtained with a five hole probe at several stations through the cascade as reported by Walsh and Gregory-Smith [4] and Cleak [5]. This data set is used to provide comparisons for the development of the secondary velocities and loss through the cascade. The second data set consists of turbulence quantities obtained by hot wire traverses, (Gregory-Smith and Cleak, 6) and these are used to assess the effectiveness of the turbulence modelling within the Moore code.

2. CASCADE DATA

The first set of experimental data used in this comparison is mainly taken from that presented by Walsh and Gregory-Smith [4]. They were studying the effects of inlet boundary layer skew in a cascade, and presented results for negative, zero and positive inlet skew. For this comparison, only the results for zero skew are used. Their data for zero skew were subsequently extended by Cleak [5], who carried out one extra traverse within the row and additional traversing downstream. The cascade consisted of large scale rotor blades of 111° of turning. Full details are given by Walsh [7], but the main design parameters are given in Table 1. A notable feature of the profile design is that while it was based on the root section of a typical high pressure turbine, it was not directly geometrically similar. Rather the profile was modified to give a similar profile pressure distribution at low speed to that of the actual blade operating at transonic design speed.

TABLE 1
Cascade Design Data

Flow Inlet Angle	42.75°
Blade Exit Angle	-68.60°
Blade Chord	224 mm
Axial Chord	181 mm
Blade Span	400 mm
Blade Pitch	191 mm
Reynolds Number (Chord and exit velocity)	4×10^5

The blades were set in the cascade with traversing slots cut in one end wall as shown in Figure 1 which also shows the position of the turbulence generating grid used for the second data set. Traverses were made with five hole pressure probes at eight slot positions, slot 1 upstream of the cascade, slots 3, 5, 7 and 8 within the blade passage, and slots 9 to 11 downstream. The traversing was carried out for the half blade span opposite to the wall with the traverse slots, so that reliable data close to the end wall could be obtained. Upstream of the cascade the end wall consisted of a belt whose motion provided the inlet skew. For the data presented here, the belt was kept stationary.

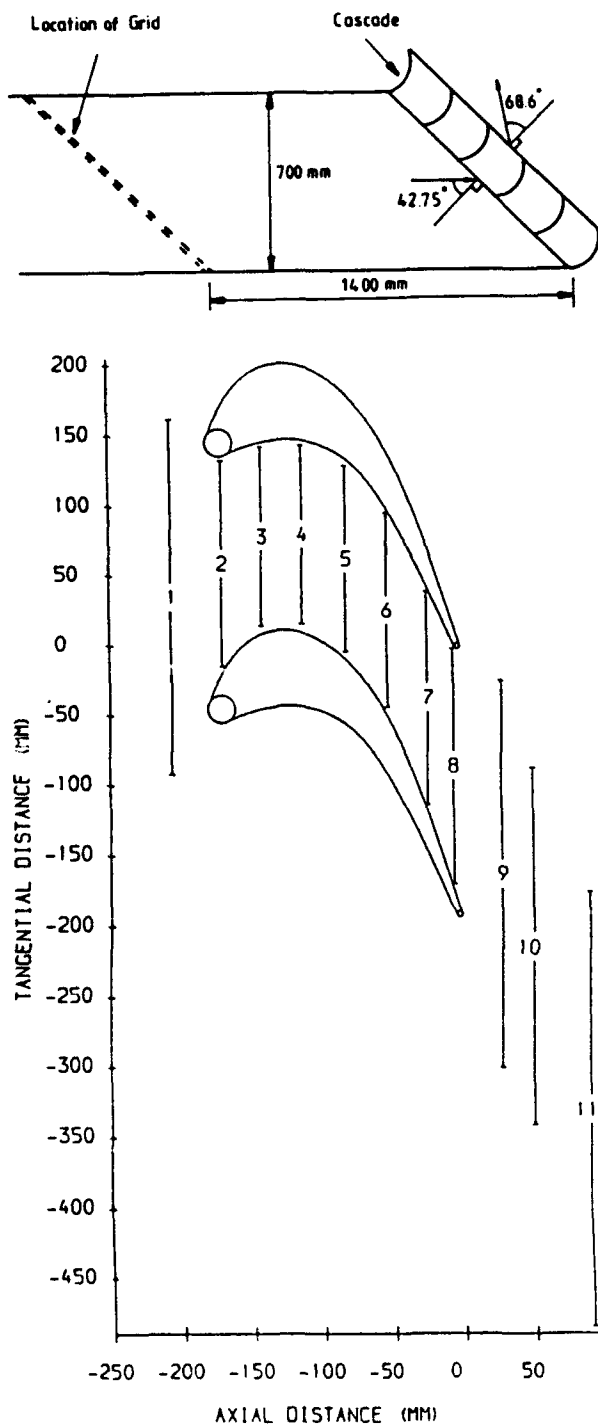


FIGURE 1. Cascade and Traverse Slots

The second data set was obtained with the grid placed upstream of the cascade as shown in Figure 1. The hot-wire traverses were carried out at slot 1 at inlet, slot 5 at 55% axial chord, slot 8 just before the trailing edge and slot 10 downstream. As described by Gregory-Smith and Cleak [6], the technique involved a double traverse with cross-wire probes, which gave the three normal Reynolds stresses and two of the three shear stresses. For this comparison the two shear stresses are of interest, viz. the streamwise/cross passage correlation ($u'v'$) and the streamwise/spanwise correlation ($u'w'$).

The grid raised the inlet turbulence level to about 4.5%, and also reduced the inlet boundary layer thickness. The inlet flow definition for the computer runs was taken by pitch averaging the flow at slot 1. The boundary layer details with and without the grid are given in Table 2.

TABLE 2
Inlet Boundary Layer

	No Grid	Turbulence Grid
99% Nominal Thickness	39.6 mm	37.4 mm
Displacement Thickness	6.0 mm	4.2 mm
Momentum Thickness	3.6 mm	2.2 mm
Shape Factor	1.7	1.9
Inlet Loss Coefficient	0.041	0.025

As reported by Walsh and Gregory-Smith [4], surface flow visualisation studies without the grid showed a laminar separation bubble on the suction surface of the blades at about 80% axial chord position. In the spanwise direction the bubble extended from midspan to about 40mm from the end wall, where it met the separation line due to the suction side leg of the horseshoe vortex running up the suction surface of the blade. With the grid, Cleak [8] observed that the separation bubble was suppressed, and he concluded that transition was taking place a little upstream of the 80% axial chord position.

3. MOORE CODE

The computational method is that described by Moore and Moore [1]. It solves the equations for fluid flow by a control volume discretisation process, which is different for the continuity and Reynolds averaged momentum equations. The continuity equation is integrated over a control volume with the corners being eight grid points. The momentum equation is integrated over upwinded control volumes as described by Moore [8]. This feature of the method allows the use of central differencing to reduce numerical mixing, and yet provides a stable set of finite difference equations. A minimum of numerical mixing or 'numerical viscosity' is important for a viscous flow code which is to be used for estimating losses.

A mixing length model is used to allow for the Reynolds shear stresses in the momentum equation. Because no convection equation is used for turbulence quantities, it is easy to specify regions in the flow domain where the turbulence model is disabled and the flow is only affected by laminar viscosity. Thus boundary layer transition can be simulated provided some prior estimate of the transition point can be made.

A three-dimensional non-orthogonal 'i-j-k' calculation grid is used. In this comparison the constant 'i' planes are approximately axial, the 'j' planes are aligned approximately with the midspan flow direction through the cascade, and the 'k' planes are parallel to the end wall. A typical grid is shown in Figure 2. It can be seen that some grid points lie within the blade, a switch being used to activate the calculations at a given point. This feature, together with a distortion of the basic grid shape, is used to increase the orthogonality of the grid around the leading and trailing edges.

4. COMPUTED CASES

Comparisons of the computed results and experimental data were made with three parameters being varied. These were:

Comparison 1: Effect of varying mixing length specification in the turbulence model.

Comparison 2: Effect of varying the regions in which the turbulence model operated.

Comparison 3: Effect of grid refinement.

A summary of the conditions are given in Table 3, and the details are described below.

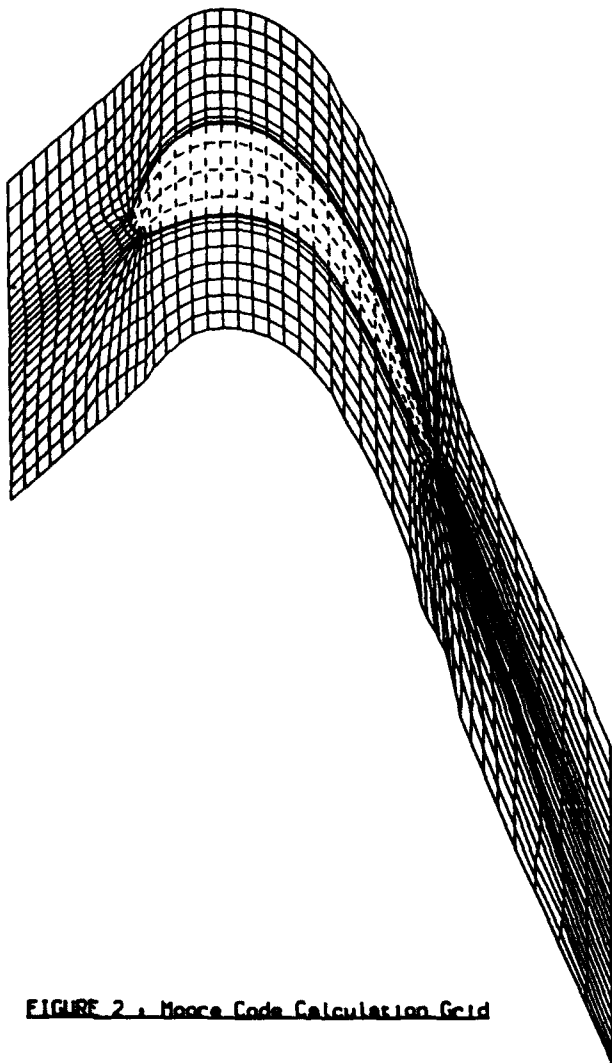


FIGURE 2. Moore Code Calculation Grid

Comparison 1: Mixing Length Definition

The mixing length in the Moore code follows the usual Prandtl formulation, i.e.

$$l_0 = \text{MIN} (K n E_v, \lambda \delta)$$

where n is the distance to the nearest solid boundary and δ is the shear layer thickness. K and λ are constants, 0.41 and 0.08 respectively, and E_v is the Van-Driest damping factor to allow for the near wall effects. In the complex three-dimensional flow within the cascade, a problem arises as to the definition of the shear layer thickness. In this comparison three definitions are investigated, and these are termed MXL1, MXL2 and MXL3.

The shear layer thickness, δ , is determined by looking at gradients of a shear layer parameter. In MXL1, this parameter was related to the non-dimensional loss of total pressure, such that it is unity in the free stream and zero on the walls. A search was made along each of the grid directions, until some arbitrarily low cut-off value of gradient signified the edge of the shear layer. The values obtained by the searches in the three directions were then averaged. However the originators noticed that with the model set up in this way, blade wakes appeared to mix out more rapidly than occurred in experiment. Thus a modified model, MXL2, was produced which searched only along the direction of maximum gradient of shear layer parameter to give the shear layer thickness. This tended to reduce the shear layer thickness in the wakes, and thus also the mixing length there, leading to a slower mixing out of the wakes.

The third model, MXL3, used a different definition for the shear layer parameter, basing it on mean flow vorticity rather than total pressure loss. The reason for this was that with the previous definition, a single spurious value of pressure could lead to the detection of a shear layer when none really existed. It was hoped that a vorticity based shear layer thickness would be less prone to error and yield more smoothly varying values for the mixing length.

Comparison 2: Turbulence Regions

As shown below it was found that if the whole flow was specified as turbulent, the prediction of the loss in the cascade was poor. In particular the blade boundary layers, and hence the profile loss, were excessive. In practice the blade boundary layers are substantially laminar, and the end wall may have a laminar boundary layer downstream of the separation line caused by the suction side leg of the horse-shoe vortex (References 6 and 9). Thus it was decided to investigate the effect of different areas being specified laminar or turbulent as described below and illustrated in Figure 3.

- a) Laminar Flowfield. The flow was specified as laminar throughout the flowfield, except in the blade boundary layer region from 80% axial chord to the trailing edge and also in the blade wake (Figure 3b). As mentioned above for data set 1, a laminar separation bubble was observed at 80% axial chord on the suction surface of the blades.
- b) Turbulent Flowfield. The flow was specified as turbulent everywhere.

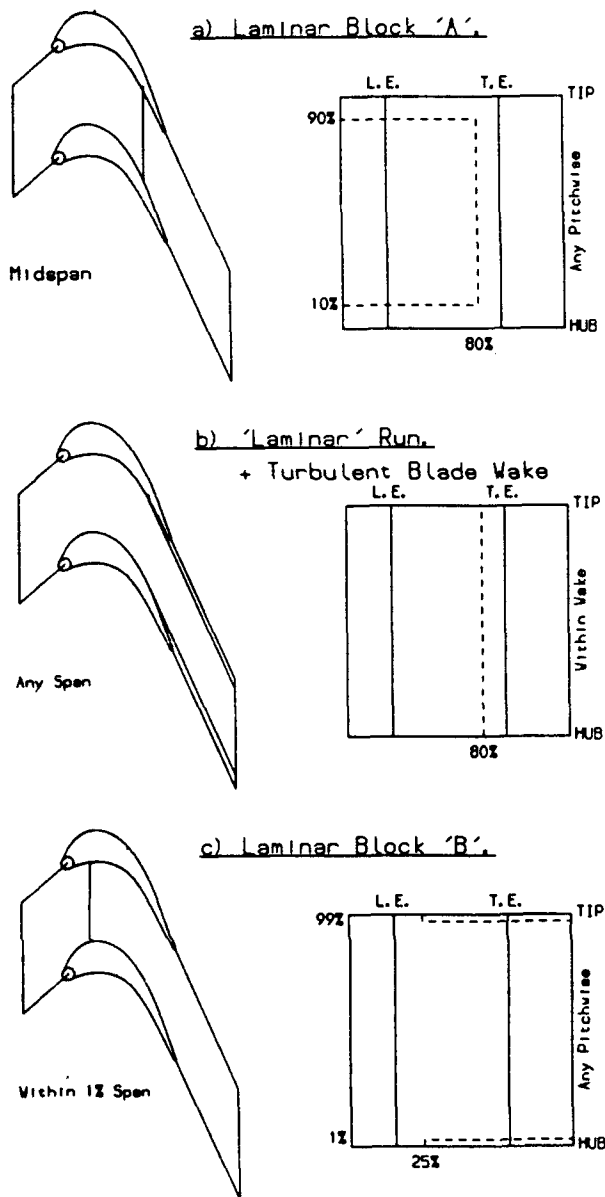


FIGURE 3. Laminar Blocking Arrangements

- c) Laminar Block A. The flow was specified as turbulent everywhere except for a laminar region, which was in axial extent from inlet to 80% axial chord, in spanwise extent from 40mm from the end wall to midspan (Figure 3a), and across the blade pitch.
- d) Laminar Blocks A + B. The flow was specified as turbulent everywhere except for the laminar block A, and a second region, block B shown in Figure 3c. This extended downstream from the 25% axial chord position for flow within 3 mm of the end wall.

This comparison used both data sets, as indicated in Table 3. Comparison 2(a) used data set 1 to compare mean flow results for the four different regions described above. Comparison 2(b) used data set 2 to compare turbulent shear stresses. Although mean flow data are also available from set 2, comparisons are not made here because the results were qualitatively similar to set 1.

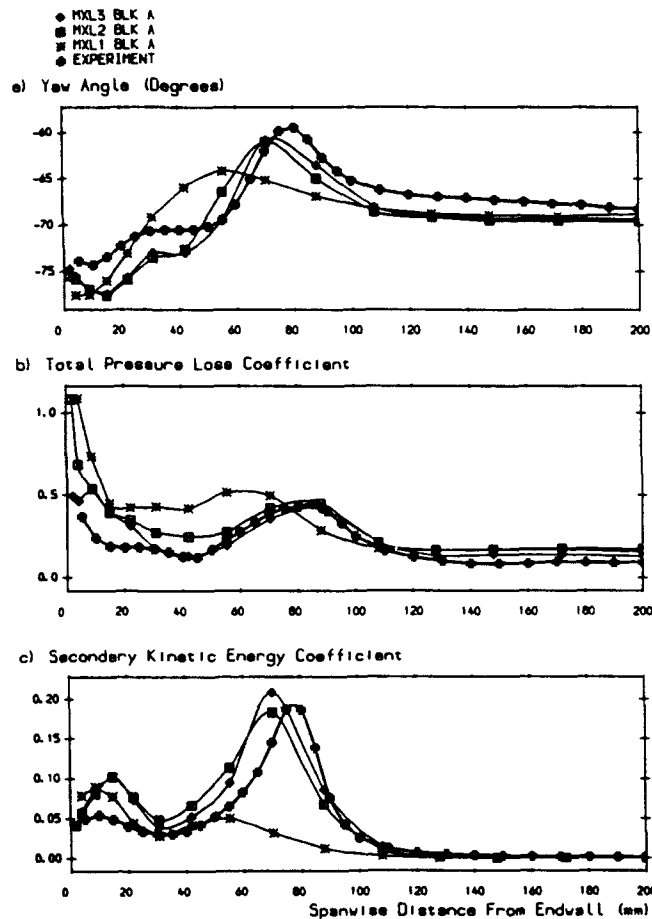


FIGURE 4. Pitch Averaged Results For Slot 10

Comparison 3: Grid Refinement

The majority of runs were done with the 'coarse' grid shown in Figure 2. This contained 47 axial by 25 tangential by 17 radial grid points, a total of 19,975 points. The grid points in the plane parallel to the end wall were arranged with the aim of minimising the skewness of cells and any rapid changes in grid spacing. A 'fine' grid was generated to test the sensitivity of the results to grid size. This grid contained 60 axial by 36 tangential by 30 radial grid points (64,800 points), with the shape of the grid similar to that shown in Figure 2.

It may be seen from Table 3 that the common computed set for all the comparisons is mixing length type MXL2, with Laminar Block A and the Coarse Grid.

The comparisons are made by means of area plots of secondary velocity vectors and total pressure loss, graphs of pitch averaged yaw angle, loss and secondary kinetic energy, and area averaged results for loss and secondary kinetic energy to show their growth through the cascade. Of necessity, a selection of the results is presented here, chosen to illustrate the main features.

5. COMPARISON 1: MIXING LENGTH DEFINITION RESULTS

5.1 Vortex and Loss Core Development

A notable feature of the measured mean flow is the way the passage vortex develops through the cascade, and the consequent effect on the loss. A full description is given by Gregory-Smith and Graves [10] for a slightly different cascade and by Walsh and Gregory-Smith [4] for this cascade.

TABLE 3
Computed Data

	Comparison 1	Comparison 2a	Comparison 2b	Comparison 3
Topic	Mixing length Definition	Turbulence Regions	Turbulence Regions	Grid Refinement
Mixing length Type	MXL1 MXL2 MXL3	MXL2	MXL2	MXL2*
Laminar Blocks	Block A	Turbulent Block A Block A+B Laminar	Turbulent Block A Block A+B	Block A*
Grid	Coarse	Coarse	Coarse	Coarse Fine
Experimental Data Set	Mean Flow Set 1	Mean Flow Set 1	Turbulence Set 2	Mean Flow Set 1

* Some loss results for MXL3 with Block A and MXL2 with Turbulent are presented also.

The development may be seen in the subsequent figures, but it is helpful to give a brief summary here. The centre of the vortex appears at slot 3 close to the endwall and nearer to the pressure than the suction surface. The secondary velocities are low, and so the effect on the total pressure loss contours is small; they are still nearly parallel to the end wall. Proceeding downstream the passage vortex grows in strength and its centre moves towards the suction surface and then away from the end wall, and finally back towards the centre of the passage as defined by the blade wakes downstream of the blades. The loss on the end wall is swept up into a loss core, and a counter vortex in the suction surface and end wall corner generates extra loss in the corner. The three-dimensional separation lines on the suction surface feed loss from near the surface into the main flow, causing a double loss peak for the loss core.

The area plots are not shown for Comparison 1. The development of the vortex and loss core for MXL2 are shown in Comparison 2a. Figures 6 to 8 and MXL3 gives a similar development. The results for MXL1 and the comparison with MXL2 and MXL3 are described as follows.

At slot 5, the experimental vortex centre is close to the suction surface, and the sweeping up of the end wall loss is quite advanced (Figure 6). The vortex is fairly central for MXL1, and slightly closer to the suction surface for MXL2 and MXL3. Proceeding towards the trailing edge MXL1 still has the vortex stuck in the centre of the passage, with too low secondary velocities, and thus the loss core is not realistically produced. The secondary velocities for MXL2 and MXL3 are more accurate, and they show some movement of the vortex centre. MXL3 slightly more than MXL2. Downstream at slot 10, MXL2 and MXL3 show reasonable vortex convection away from the end wall and a reasonable loss core, although the blade wakes appear too deep, a common feature of most calculations as seen in Figure 8. All the computations appear to give too much loss on the end wall.

5.2 Mass Averaged Data

Mass averaging the data across the blade pitch gives a quantitative assessment of some of the features seen qualitatively in the area plots. Only one position is shown here, that at the downstream slot 10, Figure 4, since many of the

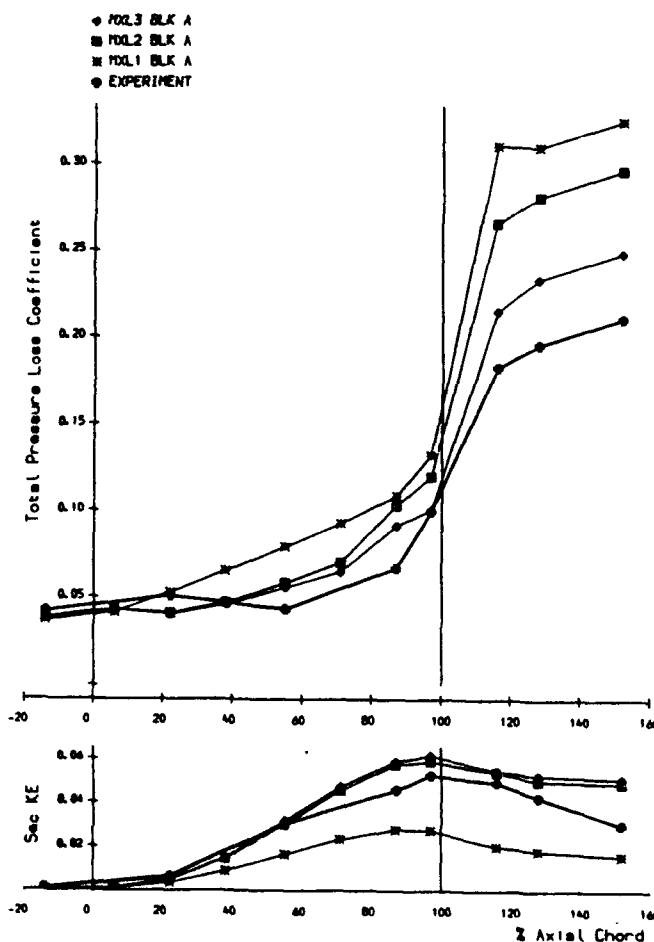


FIGURE 5 . Mass Averaged Loss & Secondary KE.

features seen at slot 8 are repeated. The secondary kinetic energy and underturning peaks follow the same pattern, with outward convection of the peaks as the vortex moves away from the end wall for MXL2 and MXL3. MXL1 gives a shallow peak and little convection. Closer to the end wall, the computations give too much secondary kinetic energy and hence too much overturning. The loss shows that at midspan, MXL3 gives least loss, with MXL1 and MXL2 giving similar values. The loss peak has also been convected outwards and appears to be predicted well by MXL2 and MXL3 but poorly by MXL1. Near the end wall all the computations give too much loss (although MXL3 does drop back very close to the wall), indicating too rapid growth of the end wall boundary layer.

Figure 5 shows the growth of loss and secondary kinetic energy through the cascade. Experimentally the latter grows fairly steadily through the cascade, reaching a maximum at slot 8 just before the trailing edge, and then decaying downstream fairly rapidly after slot 9 at 115% axial chord. The three computations follow the trend up to the trailing edge, with MXL1 giving about half the measured maximum, and the other two giving similar values, a little higher than that measured. This accords with the descriptions of the vortex, where MXL1 generally gives too little secondary kinetic energy, the other two being fairly similar. Downstream, there is a drop to slot 9, but thereafter the measured decay in secondary kinetic energy is not computed with any of the models.

The measured loss is substantially constant up to slot 5, but then starts to rise with an increasing gradient up to the trailing edge. The computed results start to rise earlier, which must be due, at least in part, to the lack of measurements in the blade boundary layers. MXL1 gives the most loss and MXL3, the least. Across the trailing edge there is a jump in loss to slot 9, as trailing edge loss is included. The too deep blade wakes (e.g. Figure 8) are reflected in the too large computed jumps in loss, with MXL1 giving the highest and MXL3 the lowest loss. The rate of loss increase downstream is computed generally well, but since the secondary kinetic energy is not being dissipated correctly, the loss increase is probably coming from the too rapid growth of the end wall boundary layer, which was noted in Figure 4. Additional evidence for this comes from the calculation of mixed out loss. Any increase in this should come from new loss on the end wall. From slot 9 to slot 11, the measured mixed out loss increases from 0.2337 to 0.2432, that is by 0.0095, or 4.1%. For MXL3, for instance, the mixed out loss increases from 0.2816 to 0.3097, that is by 0.0281, or 10.0%.

5.3 Discussion

The difference in definition of the shear layer as used by the mixing length models MXL1 and MXL2 has a significant effect on the results. MXL1 gives a weaker vortex, which is much less mobile and it produces too much loss. As described above, the shear layer in MXL1 is defined so as to be larger than in MXL2, so that away from surfaces the mixing length and hence shear stresses are larger for the same strain rate (or velocity gradients). Thus it is to be expected that more loss is produced and the generation of secondary velocities is inhibited. This comparison has allowed some quantification of the differences which arise.

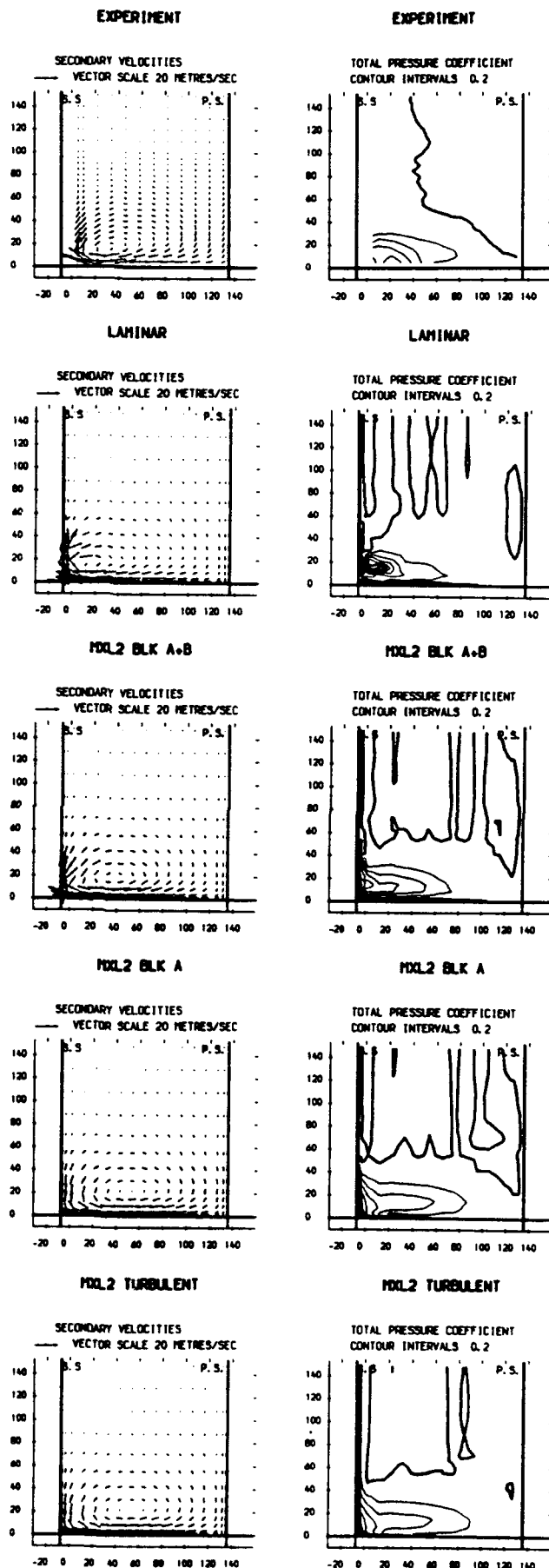


FIGURE 6 : Area Plots For Slot 5

The differences between MXL2 and MXL3, which uses the vorticity gradient to derive the shear layer, appear to be much less. The secondary flowfields are very similar, with MXL3 giving slightly more secondary kinetic energy and more mobility of the vortex. However, although the maximum secondary kinetic energy, given at slot 8, is greater than that measured, the vortex is not convected far enough from the end wall. The net secondary loss for MXL2 and MXL3 are very similar, with the main difference being in the midspan or profile loss, where MXL2 gives a higher value.

All these comparisons were for computed cases with laminar block A, chosen because of the observed laminar flow on blade suction surface at midspan up to 80% axial chord. It has been noted that these computations give too much growth of the end wall boundary layer loss downstream of the blades. Thus the laminar block B described earlier (Figure 2) might be a way of reducing that loss. In order to clarify the effect of turbulent and laminar regions in the flow, the second comparison was made.

6. COMPARISON 2: RESULTS OF VARYING TURBULENCE REGIONS

6.1 Comparison 2(a): Mean Flow Data, Set 1

Figures 6 to 8 show a comparison of the experimental data and the computed results with the mixing length model MXL2 for laminar flowfield, laminar blocks A + B, laminar block A, and turbulent flowfield.

6.1.1 Area Plots

The results at slot 5 are shown in Figure 6. A striking feature is the movement of the centre of the vortex shown by the laminar case, which is in contrast with the vortex centred in the middle of the passage for the turbulent case, and the laminar block A case. In fact the laminar case has the vortex centre moved too far towards the suction surface corner, with very high secondary velocities close to the corner. Laminar block A + B shows some movement, but not as much as the experiment. This movement shown by block A+B is somewhat surprising when compared with the block A results, since laminar block B extends only out from the end wall by 3 mm, and starts at only 25% axial chord (slot 5 is at 55% axial chord). Clearly the inclusion of block B has a significant effect on the secondary velocities. The loss contours show virtually no differences between the turbulent and laminar block A cases, with a little more distortion evident for the block A + B and laminar cases.

The results for slot 7 are not shown, but they show a similar sequence to those for slot 8, Figure 7. The turbulent case shows very slight displacement of the vortex centre toward the suction surface, laminar block A shows a little more, but both block A + B and the laminar cases show significant movement of the vortex centre away from the end wall, and for the laminar case, back towards the passage centre. The laminar results show some transverse velocities close to the suction surface edge, and this is a consequence of some difficulties with convergence for this case, with some oscillation of the solution around the trailing edge. This may also explain the area of negative loss contours (dashed) seen for the laminar case. The other three cases all show the feeding of loss from the suction surface into the core at 70 mm from the end wall, as shown by experiment.

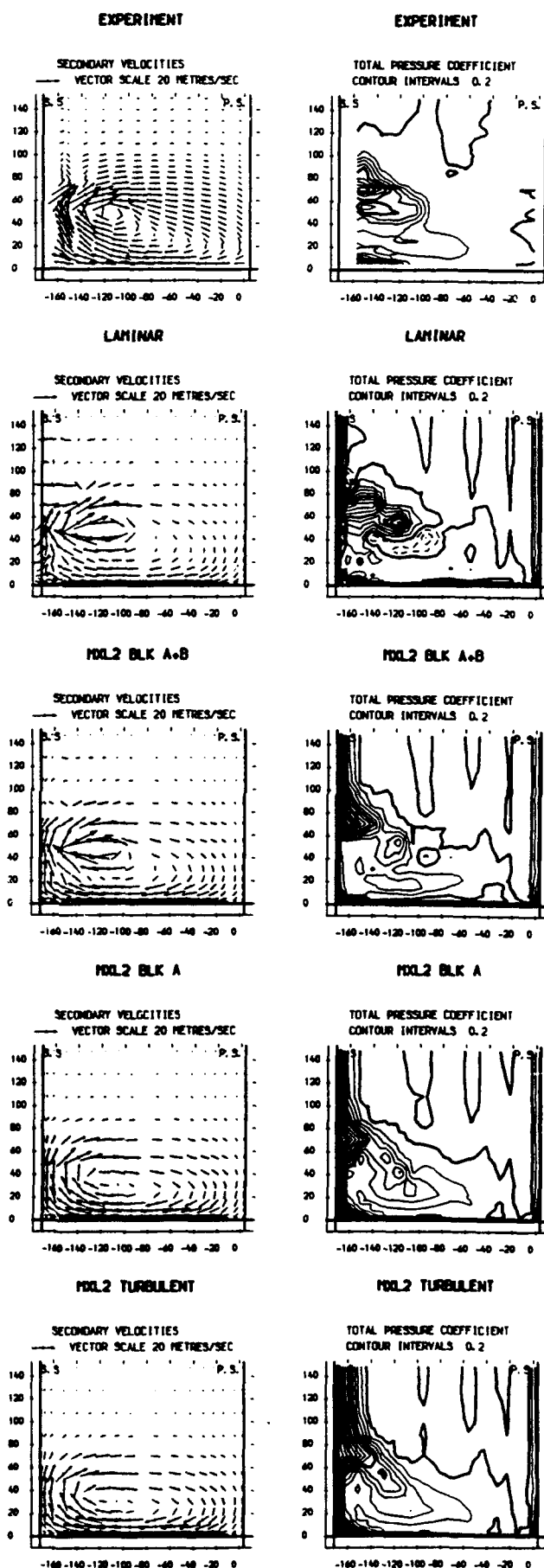


FIGURE 7. Area Plots For Slot 8

Figure 8 shows that at slot 10, the secondary velocities look very similar for the laminar and block A + B cases. The convection of the vortex centre is not quite enough, being at about 60 mm from the end wall, compared with the experimental 65 mm, and tangentially at about -260 mm, compared with the experimental -240 mm. All the computed loss contours show too deep blade wakes compared with the experiment, with the turbulent case the thickest, and the laminar case the thinnest. It should be remembered here that the laminar case has a turbulent wake specified. The laminar and block A + B cases give a clear double peak to the loss core, although the lower of the two peaks (on the right) is too far from the end wall. The block A and turbulent cases do show a double peak, but the lower one is not so clearly defined.

6.1.2 Mass Averaged Data

Only the pitch averaged results for the downstream Slot 10 (Figure 9) are shown here, since they illustrate most of the features seen at the other slots. The laminar and block A + B results show similar values of secondary kinetic energy, with a peak value much greater than experiment, although not far enough from the end wall, reflecting the slight under-convection of the vortex centre. The turbulent case gives too low a peak, but reference to Figure 4 shows that the block A case has the peak at about the right level. Near the end wall, the turbulent and block A cases show a definite lower peak, which is only just seen for the experiment and the laminar and block A + B cases. These secondary kinetic energy results are reflected in the yaw angle, with the laminar and block A + B results giving too high an overturning peak (bearing in mind the midspan error), the block A peak being about right and the turbulent case peak too low. The laminar and block A + B results then show a high overturning peak, which is a consequence of the large secondary velocities just below the vortex centre seen in the vector plots of Figure 8.

In Figure 9b the midspan loss values all show too much wake loss, also noted in Figure 8. The sequence is as expected with laminar giving the lowest and turbulent the highest value. The results for block A + B and block A are very similar, as would be expected, since block B is close to the end wall and should not affect the midspan flow. At around 80 mm from the end wall, the loss peak for laminar and block A + B is too high, whereas block A is about right and the turbulent case too low, compared with the midspan error. The effect of block B, which has laminar flow close to the end wall, is seen to be strong when block A + B and block A (Figure 4b) are compared. Close to the wall, block A gives a value of 1.08, and block A + B, 0.58.

Figure 10 shows the growth of loss and secondary kinetic energy through the passage. The secondary kinetic energy for the laminar and block A + B cases show peak values at Slot 8 about 40% higher than the experiment, whereas block A (Figure 5) gives about 10% too much. Again the addition of block B to block A is seen to have a large effect on the vortex. The turbulent case gives about the right values. However, block A and the turbulent case do not decay the secondary kinetic energy rapidly enough. The laminar and block A + B give roughly the right decay rate, but at a higher level. The loss growth curves show that the laminar and block A + B cases appear to underestimate the loss growth in the blade passage (the experiment must be an underestimate), but give too large a jump across the trailing edge, so that even the laminar case gives too much loss. Overall the turbulent case gives the greatest overestimate, with reducing values for block A,

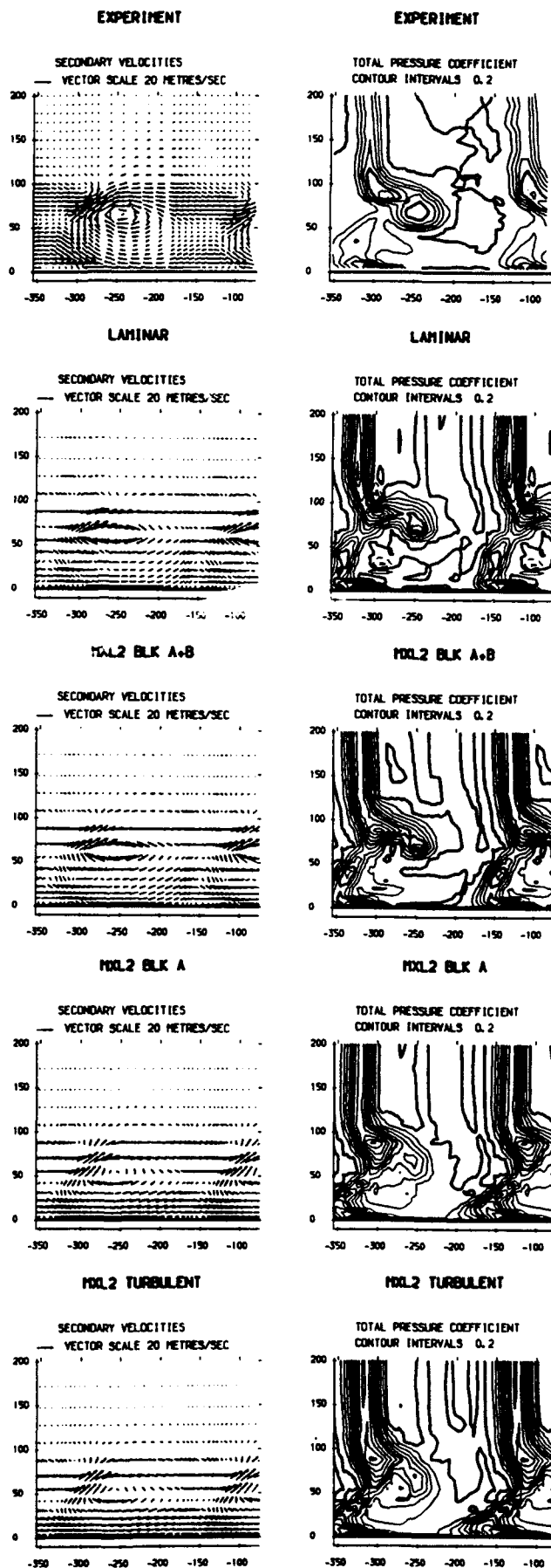


FIGURE 8. Area Plots For Slot 10

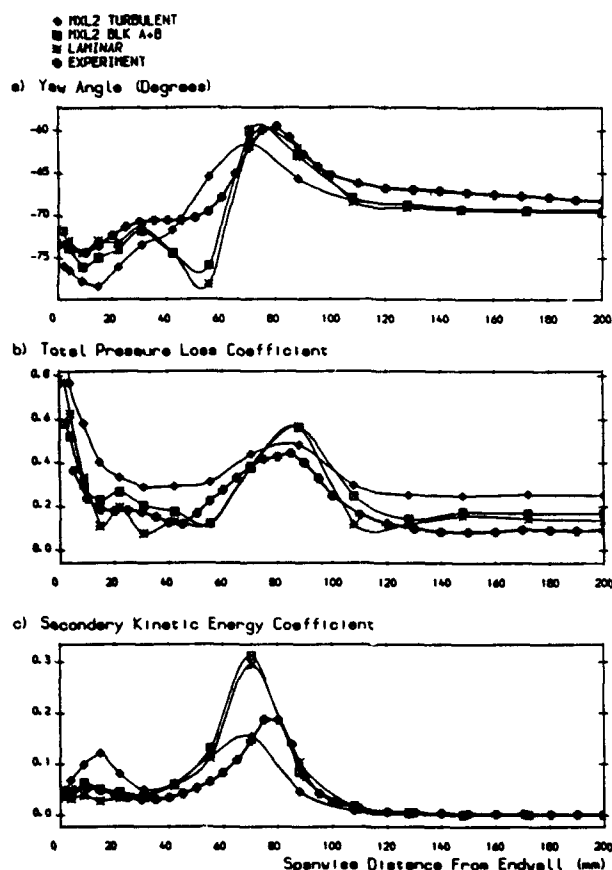


FIGURE 9. Pitch Averaged Results For Slot 10

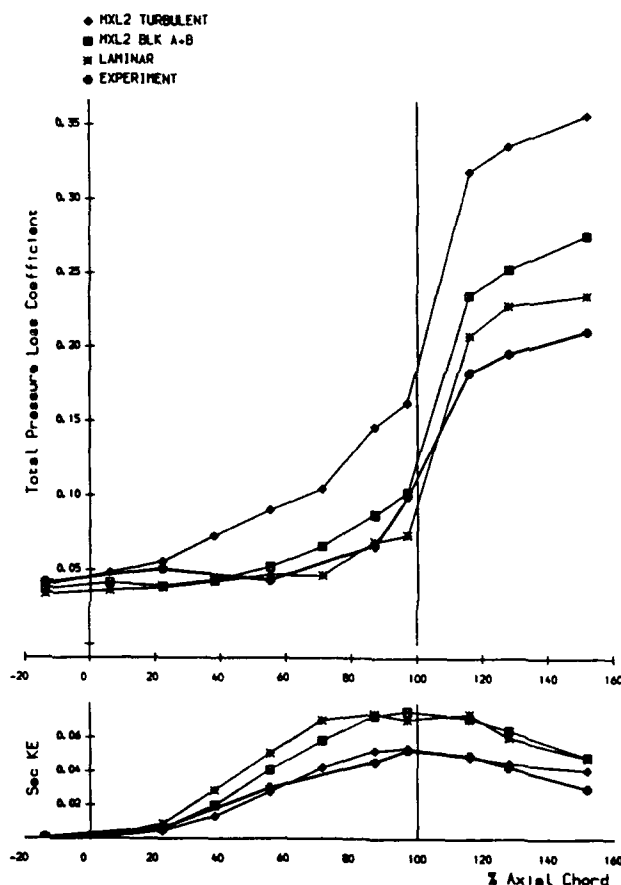


FIGURE 10. Mass Averaged Loss & Secondary KE.

TABLE 4
Mixed Out Losses, Slot 10

	Experiment	Laminar	Block A+B	Block A	Turbulent
Total loss	0.239	0.296	0.321	0.342	0.397
- Midspan loss	0.095	0.139	0.168	0.183	0.269
- Gross Sec. loss	0.144	0.157	0.153	0.159	0.128
- Inlet loss	0.041	0.034	0.037	0.038	0.040
- Net Sec. loss	0.103	0.123	0.116	0.121	0.088

block A + B and laminar cases. The addition of block B does seem to reduce the end wall boundary layer growth since block A + B gives about the same loss growth rate downstream, but is decaying the secondary kinetic energy more rapidly. From slot 9 to slot 11, block A + B gives a rise in mixed out loss of 1.9% whereas block A gives 7.0% compared to the experimental value of 4.1%.

Table 4 shows the mixed out loss values at slot 10. Apart from the turbulent case, which gives a low value, the other three cases give a slightly high value of net secondary loss. The midspan loss is accounting for most of the error, the value increasing progressively from the laminar to the turbulent case. The latter has a very high value, resulting in the low secondary loss value.

6.2 Comparison 2(b): Turbulent Data, Set 2

The second part of this comparison shows the experimental data set 2 and the predictions of turbulent shear stresses given by the computations for laminar blocks A + B, laminar block A and the fully turbulent case. The laminar case is omitted, since it would show no shear stresses except in the blade wakes.

Figure 11 shows the results at slot 5, with the top row showing the streamwise/cross passage ($u'v'$) correlation. The full contours are for positive values, i.e. negative shear stress. The values are non-dimensionalised with respect to upstream velocity. The experiment shows strong positive values in the secondary flow region which is perhaps just hinted at by the computations. Close to the suction surface the negative (dashed) contours represent the expected positive shear

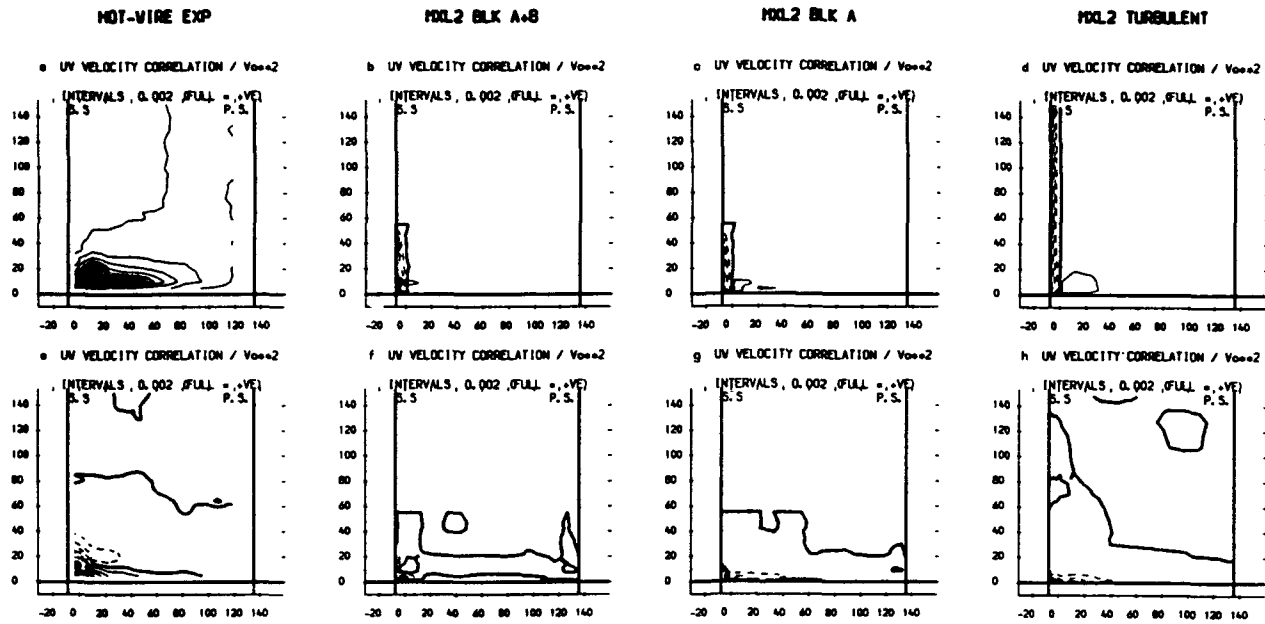


FIGURE 11 : Area Plots For Slot 5

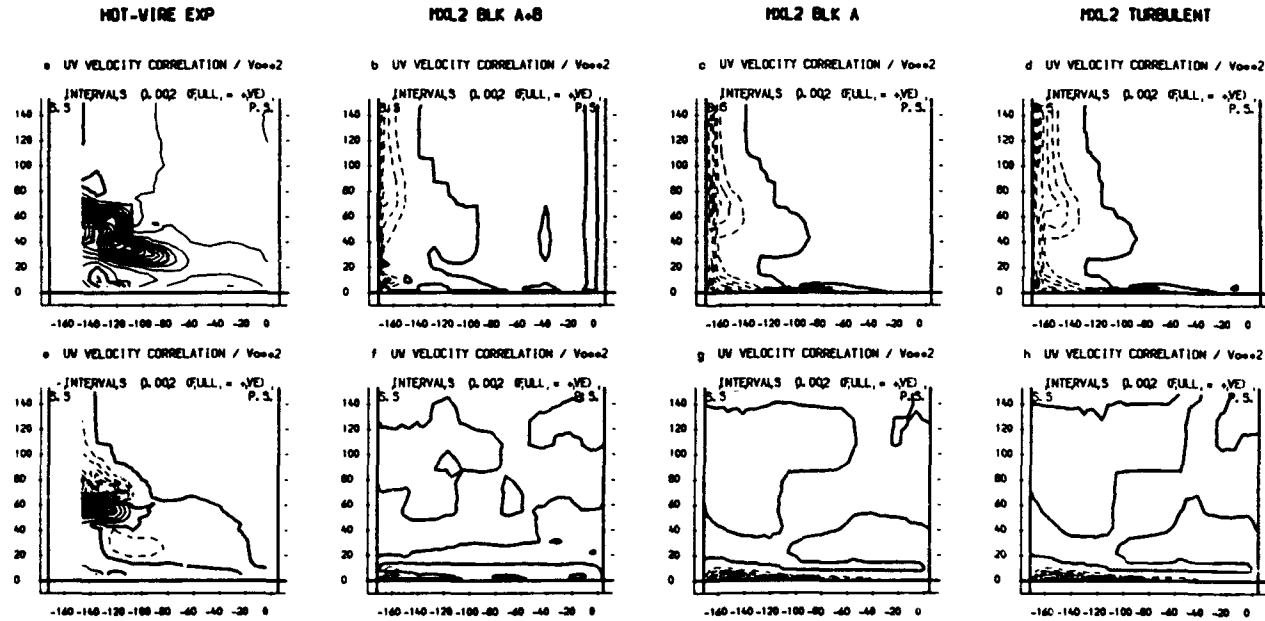


FIGURE 12 : Area Plots For Slot 8

stress in the boundary layer. The operation of block A is clearly seen in restricting turbulent flow to within 40 mm of the end wall (the contours go a little higher due to the contouring routine, the cell spacing there being 15 mm in the spanwise direction). The streamwise/spanwise ($u'w'$) correlation shows the turbulent and block A cases giving negative values, i.e. positive shear stress, close to the end wall. The addition of block B prevents this, but none of them show the sign change across the vortex centre seen for the experiment.

Slot 8 is downstream of where block A ends, and so in Figure 12, all the computations show $u'w'$ turbulent stresses up to midspan on the suction surface. However their appearance is like a boundary layer distorted by the secondary flow, quite unlike the experimental contours which are of opposite sign. The computation of $u'w'$ values show a similar end wall boundary layer for the turbulent and block A cases, with the addition of

block B preventing the turbulence. The strong experimental sign change at about 70 mm from the end wall is associated with the suction surface separation line (see Gregory-Smith and Cleak [6]). The computations miss this feature, although the zero contour with negative values above and positive below does meet the suction surface at about the same position.

In Figure 13, the blade wakes at slot 10 are clearly seen with the $u'w'$ correlation, for both the experiment and computations. The turbulent case gives the strongest values as might be expected. However none of the computations give the large negative values seen experimentally in the secondary vortex region. It may be noted that this region shows a dramatic sign change from slot 8, and this somewhat surprising result is discussed in some detail by Gregory-Smith and Cleak [6]. Again the computations show $u'w'$ shear stresses in the end wall boundary layer, but miss the experimental values in the vortex region.

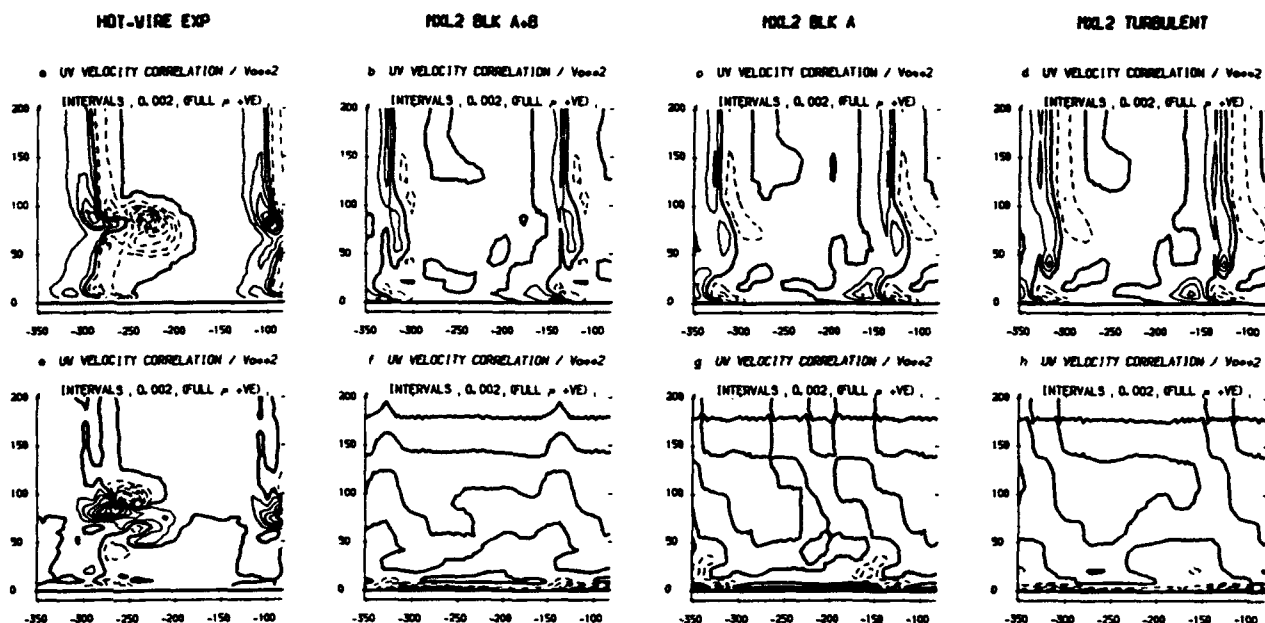


FIGURE 13 , Area Plots For Slot 10

6.3 Discussion

This comparison of the effects of different areas of the flow being specified as laminar or turbulent shows large differences in the computed results for the different cases tried. While this is hardly surprising, what is unexpected is that in terms of loss and mobility of the vortex, the flow specified as nearly all laminar appears to do best, although the best prediction of vortex strength as defined by secondary kinetic energy is given by the fully turbulent case. The comparison with measured Reynolds shear stresses show that even for the fully turbulent case, the computed turbulent activity is confined mainly close to the blade and end wall surfaces and the blade wake. The very high levels measured in the passage vortex region are largely missed. The effects of this are seen in the general failure of the computations to decay the secondary kinetic energy sufficiently rapidly downstream of the cascade.

Overall it might be said that the case with laminar block A provides a good compromise, giving reasonable predictions of vortex strength and mobility, with not the excessive loss prediction of the fully turbulent case. The effect of block B, which was introduced to simulate the laminar flow of the end wall boundary layer, is quite remarkable on the movement and strength of the passage vortex. This suggests that the restraint on vortex exercised by the mixing length model acts mainly through the flow close to the surfaces, and accords with the remarks made above on the shear stress predictions.

The effect of the blocks on the mixed out loss (Table 4) is seen mainly in the midspan mixed out value. This suggests some inadequacy, at least as far as loss is concerned in the modelling of the two-dimensional flow around the blade profile. One obvious source of error may be an insufficiently fine grid. This topic is addressed in the third comparison.

7. COMPARISON 3: RESULTS OF GRID REFINEMENT

For this comparison, only the detailed results at slot 10 are presented here, the other slots showing very similar features as far as comparing the results with the coarse and fine grid. As described above the comparison was made with MXL2 with laminar block A.

7.1 Area Plots

Figure 14 shows the results at slot 10 for the coarse and fine grid, the greater number of vector arrows giving a visual impression of the refinement in an axial plane. The vortex appears very similar, both in strength and position with both grids. The fine grid gives slightly more movement, with the centre at co-ordinates $(-250, 55)$ compared to $(-260, 50)$ with the coarse grid. The loss contours also look very similar overall, although the fine grid shows some extra fine detail. It may be noted that at midspan, the fine grid gives a thinner wake, although still too deep compared with the experiment (see Figure 8).

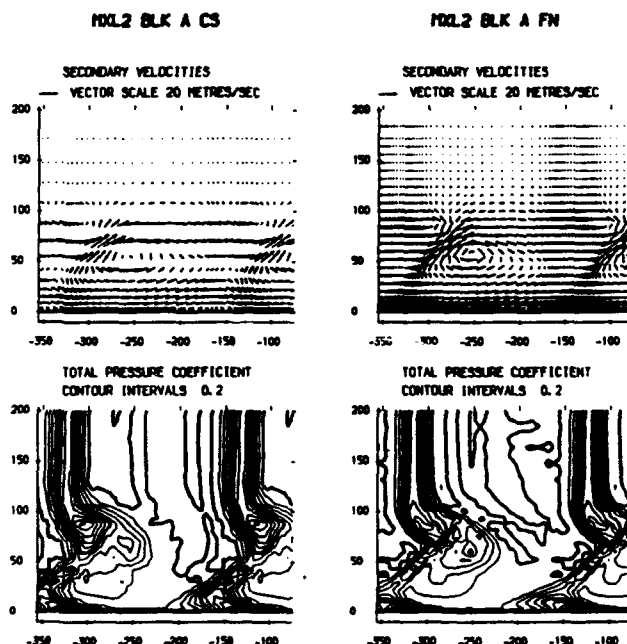


FIGURE 14 , Area Plots For Slot 10

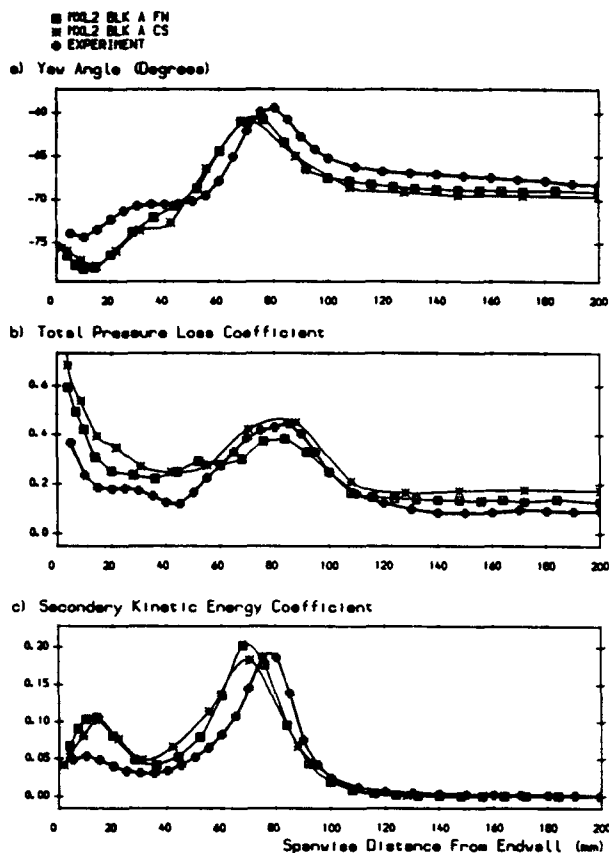


FIGURE 15. Pitch Averaged Results For Slot 10

7.2 Mass Averaged Data

Figure 15 shows results with the coarse and fine grids and the experimental data pitch averaged at slot 10. The fine grid gives a slightly higher secondary kinetic energy peak, but with still not enough outward convection. The yaw angle graphs also show very similar values. At midspan, refinement of the grid gives a value closer to the experiment. The actual values are -69.6° with the coarse grid and -69.1° with the fine grid, compared with -68.1° and -68.4° for the experiment, averaged over the right hand and left hand wakes respectively (Figure 14). In Figure 15, the average value is plotted. Probably refinement of the grid is improving the modelling of the trailing edge flow to meet the Kutta condition, and this has an effect on the exit angle. The loss curve also shows an improvement in midspan or profile loss with the finer grid. In general, the finer grid predicts lower loss, but the curves are very similar, and the experimental loss peak lies between them.

The area averaged secondary kinetic energy curves again show in Figure 16 very similar results for the two grids, with the fine grid being closer to the experiment. The loss growth with the fine grid is above that with the coarse grid, but the former then gives a much lower jump across the trailing edge, illustrating the improved trailing edge modelling. It appears that the greatest quantitative effect of the grid refinement is on the loss, and this is also seen in the mixed out loss values in Table 5. The main reduction in loss is in the midspan value, although there is a slight reduction in secondary loss as well.

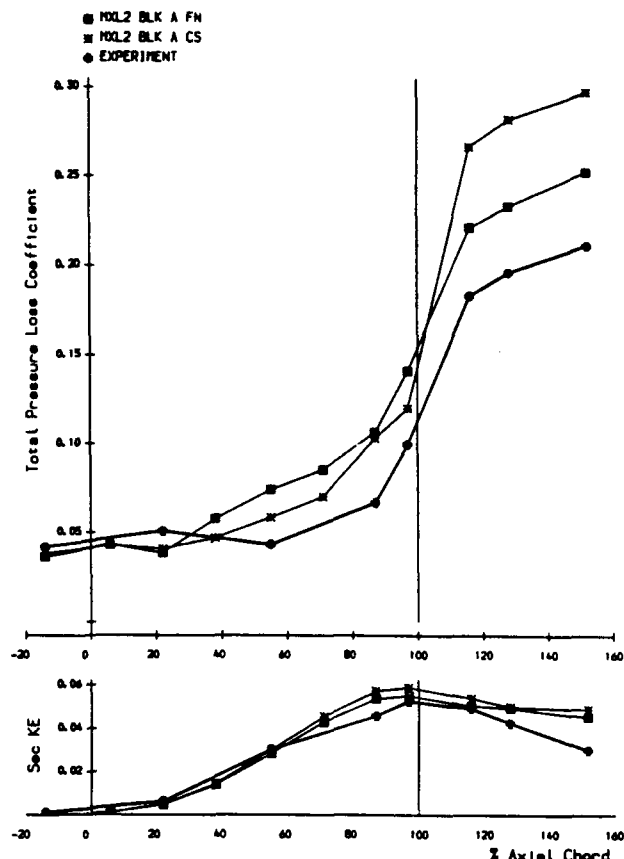


FIGURE 16. Mass Averaged Loss & Secondary KE.

Hah [11] suggested that the reduction in loss predicted by a computer code was roughly linear with the inverse of the number of grid points. Figure 17 shows such a plot, not only for the MXL2 turbulence model with laminar block A, but also MXL2 fully turbulent and MXL3 with block A. It can be seen that all three show a similar reduction, with the projection of the MXL3 with block A to an infinite number of points being very close to the experimental value. Obviously, other grid numbers would be required to confirm the linear relationship, but the trend is clear.

For the coarse grid the resource required was typically 5,000 CPU seconds on a CRAY XMP2, with 18 Mbytes of storage. Convergence was achieved usually with less than 40 iterations. For the fine grid typically 20,000 CPU seconds were required with 44 Mbytes of storage.

7.3 Discussion

The comparison of the coarse and fine grid shows that in terms of the overall flow pattern the results are qualitatively very similar, both for the secondary velocities and loss contours. The secondary kinetic energy results are also quantitatively similar, and so the use of the coarse grid for the first two comparisons is justifiable in view of the large saving in computer resource required. The main quantitative effect of grid refinement is on the loss, particularly on the downstream loss at midspan, where there is also an effect on the exit flow angle. It is to be expected that accurate modelling of the trailing edge flow and the blade boundary layers requires a fine grid, whereas due to its larger scale, the passage vortex is modelled fairly well by the coarse grid.

TABLE 5
Mixed Out Loss, MXL2 Block A, Slot 10

	Experiment	Coarse Grid	Fine Grid
Total Loss Coefficient	0.239	0.342	0.289
- Midspan Loss	0.095	0.183	0.138
- Gross Sec. Loss	0.144	0.159	0.151
- Inlet Loss	0.041	0.038	0.038
- Net Sec. Loss	0.103	0.121	0.113

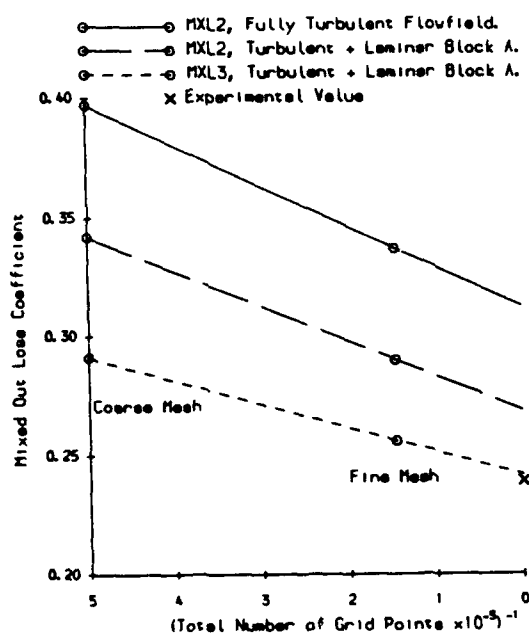


FIGURE 17 - Effect of Mesh on Loss

8. OVERALL DISCUSSION

In order to study the effect of applying turbulence models, a prior requirement is to have a computer code which generates sufficiently small numerical error in terms of artificial losses, so that the differences are not masked by the numerical error. The Moore code has proved to meet this requirement, and thus the results of the comparisons presented here should have a wider significance for the application of turbulence models in other codes.

The results show that the turbulence modelling can have a large effect on the computed results. There is a clear link between the level of turbulence activity and the strength and mobility of the passage vortex, and the generation of losses. While this is intuitively reasonable, these comparisons show that the differences are quantitatively large, with for instance secondary kinetic energy varying from 50% to 150% of the experimental value. Apparently a small change in the specification of regions of laminar flow, viz. the addition of block B close to the end wall, has an unexpectedly large effect on the results. The comparison of turbulent shear stresses in Figure 11 to 13, show that the mixing length models are most active near the surfaces, with low activity in the vortex, and so the control of the vortex may be being exercised through the shear on the

walls. The failure of the models to predict the very high turbulent shear stresses in the passage vortex means that the secondary kinetic energy is not decayed sufficiently rapidly downstream of the cascade. It may also explain why the distribution of secondary velocities through the vortex is not correct. This is seen not only in the secondary velocity vector plots, but also in the fact that the cases which give the loss nearest to experiment and the most migration of the vortex (e.g. MXL2, laminar), have much too much secondary kinetic energy. By contrast MXL2, fully turbulent, gives almost exactly the correct maximum secondary kinetic energy (Figure 10), but little vortex migration (Figure 7). One might have expected that correct prediction of secondary kinetic energy would give good migration of the vortex, but if the velocity distribution is incorrect, this may not be the case.

The prediction of the passage vortex does not change significantly when the finer grid is employed. The main effect of grid refinement is on the prediction of loss. The plot, Figure 17, suggested by Hah [11] shows the reduction in overall loss, and Table 5 shows this is due substantially to the reduction in midspan loss. Whether the plot is linear must depend to some extent to the way in which the grid refinement is made. The fact that midspan loss is most affected suggests that refining the grid only around the blade might achieve the same reduction. The agreement with experiment shown by an extension of the MXL3 values to an infinite number of points, must be a little fortuitous in view of the observation that the velocity field and Reynolds shear stresses are not modelled correctly.

The mixing length model was originally developed from two-dimensional shear layers, where local equilibrium for turbulence holds with local dissipation and generation being much larger than convection. The flow in the blade passage has high curvature, rapid accelerations and three-dimensional separations, and so local equilibrium is unlikely to exist. Moreover the experimental results suggest that such a simple Boussinesq eddy viscosity model is inadequate (e.g. Figure 12). Thus higher order modelling is suggested if more accurate results are required, and a successor to this paper, Cleak and Gregory-Smith [12], studies the application of a one-equation and a k-epsilon model. However, since the results here also show that the regions over which the model operates are very important, the clear need exists for good prediction of transition. This may well be more urgent than higher order modelling, since with a good prediction of transition point, here provided by experiment, quite good results for pitch averaged angle and loss can be obtained.

9. CONCLUSIONS

- a) The low numerical error shown by the Moore code means that of these comparisons should have wide application to other high quality codes.
- b) The way in which the turbulence model is applied can be very important. In some cases a laminar flow prediction may be better than that with an over active turbulence model.
- c) A mixing length shear layer defined in terms of maximum gradient of total pressure loss or vorticity gradient gave the best results.
- d) The computational grid of 20,000 points showed substantial grid independence. The main effect of grid refinement to 65,000 points was a reduction in midspan loss.
- e) The greater the turbulence activity, the greater is the loss, and the less is the passage vortex strength and mobility. However the secondary velocity distribution in the vortex is not predicted accurately, so that with the correct vortex strength the vortex shows too little mobility.
- f) The high turbulence activity in the vortex core is not predicted by the mixing length model, and this indicates the need for higher order modelling.
- g) The appropriate use of laminar regions in which the turbulence model was turned off gives quite good predictions of the main features of the secondary flow, including loss. This indicates the importance of a good method for transition modelling.
- h) The best results overall were obtained with laminar block A, i.e. up to 80% axial chord away from the end wall, although the vortex mobility and end wall loss, the addition of block B was beneficial, i.e. laminar flow within 3 mm of the end wall downstream of 25% axial chord.
- i) In view of the dominant effect in the calculations of flow near the surfaces, transition modelling is probably more important than higher order turbulence modelling.

ACKNOWLEDGEMENT

The authors gratefully acknowledge support from Rolls-Royce plc and their permission to publish this paper. Further support is also acknowledged from the Science and Engineering Research Council.

REFERENCES

1. Moore J. and Moore J.G., Performance evaluation of linear turbine cascades using three-dimensional viscous flow calculations. ASME, J.Eng. GT & Power, Vol. 107, pp 969-975. (1985)
2. Northall J.D., Moore J.G. and Moore J., Three-dimensional viscous flow calculations for loss prediction in turbine blade rows. Proc. I.Mech.E., Turbomachinery-Efficiency Predictions and Improvement, Paper C267/87, pp 63-71. (1987)
3. Sieverding C.H., Van Hove W. and Boletis E., Experimental study of the three-dimensional flow field in an annular turbine nozzle guide vane. ASME, J.Eng. G.T. and Power, Vol. 107, pp 969-975. (1984)
4. Walsh J.A. and Gregory-Smith D.G., The effect of inlet skew on the secondary flows and losses in a turbine cascade. Proc. I.Mech.E., Turbomachinery-Efficiency Predictions and Improvement, Paper C275/87, pp 15-28. (1987)
5. Cleak J.G.E., Validation of viscous, three-dimensional flow calculations in an axial turbine cascade. Ph.D. Thesis, Durham University. (1989)
6. Gregory-Smith D.G. and Cleak J.G.E., Secondary flow measurements in a turbine cascade with high inlet turbulence. ASME Paper 90-GT-20 (to be published in J. Turbomachinery). (1990)
7. Walsh J.A., Secondary flows and inlet skew in axial turbine cascades. Ph.D. Thesis, Durham University. (1987)
8. Moore J.G., Calculation of 3D flow without numerical mixing, AGARD-LS-140, Paper No. 8. (1985)
9. Harrison S., Secondary loss generation in a linear cascade of high turning turbine blades. ASME Paper 89-GT-47. (1989)
10. Gregory-Smith D.G. and Graves C.P., Secondary flow and losses in a turbine cascade. AGARD CP-531, Paper No. 17.
11. Hah C., A Navier-Stokes analysis of three-dimensional turbulent flows inside turbine blade rows at design and off design conditions. ASME, J. Eng. Gas Turbines and Power, Vol. 106, pp 421. (1984)
12. Cleak J.G.E. and Gregory-Smith D.G., Turbulence modelling for secondary flow predictions in a turbine cascade. To be presented at ASME Gas Turbine Congress, Orlando. (1991)

Discussion

D. HOBBS, PRATT & WHITNEY, U.S.A.

Your computations show a rapid rise of the total pressure loss across the cascade trailing edge plane. What is the cause of this rise?

AUTHOR'S REPLY

This is primarily the profile and trailing edge loss. As Table 4 shows, subtracting the mid-span loss from the total loss gives a much more reasonable estimate of secondary loss.

M. IACOVIDES, UMIST, U.K.

Do the authors intend to try to account for near-wall transition effects without moving to a higher order model?

AUTHOR'S REPLY

It is probably necessary to go to a higher order of turbulence modeling to produce a transition model. However, our point is that it is the aspect of transition modeling that is most important, rather than the turbulence modeling per se.

L. LANGSTON, UNIV. OF CONNECTICUT, U.S.A.

Well-documented experimental results show that the very-important passage vortex is located in the endwall-suction side corner (slot 8, Fig. 7) in the region of uncovered turning. A key feature of CFD calculations that make use of two-dimensional boundary layer turbulence models (e.g., your MXL2 (Fig. 7), Hah (Ref. 11) and Moore and Moore (Ref. 1)) is an incorrect centered passage vortex (MXL2, Fig. 7). Your laminar (no turbulence) case (Fig. 7) shows a (correct) noncentered passage vortex position that is very close to the experiment result. Should one conclude from your results that the extensive use of relatively simple turbulence models for such a complex three-dimensional flow is worse (and misleading!) than no turbulence model at all?

AUTHOR'S REPLY

There is some truth in your comment, as is implied in the Conclusion 9.b). The movement of the secondary vortex is best predicted by the laminar flow, but it should be noted that the strength of the secondary flow is too great, as Fig. 10 shows. Turbulent action is required to reduce the strength to the experimental level, although as the turbulence comparisons show in Figs. 11 and 12, none of the applications of the mixing model predict anything like the correct turbulence shear stresses in the vortex. In the ASME paper 91-GT-57 (Ref. 12) we have tried a one equation and a two equation model, with some limited success in predicting the vortex turbulence.





**A MATHEMATICAL CONSTRAINT PLACED UPON
INTER-BLADE ROW BOUNDARY CONDITIONS USED IN THE
SIMULATION OF MULTISTAGE TURBOMACHINERY FLOWS**

J. J. Adamczyk
NASA Lewis Research Center
Cleveland, OH 44135

92-16075



ABSTRACT

A number of researchers have suggested using an inter-blade row boundary condition to extend isolated blade row flow solvers to multiple blade row configurations. This suggestion is worth consideration for it appears to result in codes that are computationally more efficient than those based on other schemes that have been suggested to accomplish the same task. The present work is concerned with the development of a mathematical constraint which this boundary condition must satisfy to insure the proper transfer of momentum and vorticity across the plane. Using experimental data, the present work quantifies the error in the time-averaged vorticity field which results from simply requiring continuity across the boundary plane of the momentum based on the time-averaged velocity fields associated with a multiple blade row configuration.

INTRODUCTION

Today numerous studies in computational flow modeling has been directed towards extending well established three-dimensional isolated blade row codes to multiple blade row configurations. The motivation behind this activity is quite clear. These isolated blade row simulation codes have made a significant impact in our ability to analyze the complex flow field surrounding a high speed fan rotor. Now is the time to see if computational fluid dynamics codes can have a similar impact on our ability to analyze multistage turbomachinery. There are a number of approaches by which these isolated blade row codes could be extended to multistage configurations. One such approach is the use of inter-blade row boundary conditions, through which information is exchanged between what are essentially steady state intra-blade row flow solvers. This approach is attractive because it may lead to codes which are computationally more efficient than codes based on other suggested approaches. It should be understood that the simulation codes we are referring to in this paper are those that simulate the time-averaged intra-blade row flow field associated with a typical blade row passage, not those which attempt to simulate the unsteady flow field.

The function of the inter-blade row boundary condition is to transfer information between two time-averaged flow representations, one fixed to the rotor frame of reference, the other to the stator frame of reference. An illustration showing the location of the boundary plane, where these conditions are applied,

relative to a rotor and stator is shown in Figure 1. The views are in both the meridional and the cascade plane. The flow is from left to right, with the rotor rotating in the direction indicated. The boundary which separates the two time-averaged flow representations for this configuration is the dashed line. For blade row spacings typical of multistage machinery, the inter-blade row boundary condition must implicitly or explicitly account for the effects introduced by a reference frame transformation on the time-averaged flow states. The objective of the present work is not the development of the inter-blade row boundary condition, but to call attention to a mathematical constraint this condition must satisfy in order for the intra-blade row flow fields to be physically correct. An attempt will be made to quantify these constraints using experimental results.

The flow field description we are after is of the time-averaged flow state in the rotor and stator frames of reference. The field equations associated with these flow states can be derived from the Navier Stokes equations. These equations, given in Reference 1, are referred to as the average passage equation system. We will use the results of the analysis in Reference 1 to derive a mathematical constraint which the inter-blade row boundary condition connecting the two average passage flow descriptions must satisfy in order for them to be physically correct. In the development of these conditions, we will restrict the discussion to a single stage (i.e., a rotor followed by a stator). We will assume that the inter-blade row flow field is continuous in both time and space, and that the time and space derivatives of the primitive flow variables are also continuous. We shall also neglect any density variation in the flow field.

**INTER-BLADE ROW BOUNDARY
CONDITION ANALYSIS**

The configuration to be studied is depicted in Figure 1. It is composed of two blade rows, the first being a rotor; the second, a stator. The dashed line between these blade rows is the location of an inter-blade row boundary condition which transfers information between the two time-averaged flow states on either side of the boundary plane. The analysis which follows will be executed in a cylindrical coordinate system in which r , θ , and z are the radial, tangential, and axial coordinates, respectively, and t denotes time. The two time-averaged flow descriptions are governed by the average passage equation system expressed with respect to a coordinate system

fixed to the rotor and the stator. Both of these flow descriptions are defined over the entire flow domain of the machine, that is, from the inlet to the exit. It can be shown that the axisymmetric average of these two flow states are identical and that this average satisfies the axisymmetric equations of motion for turbomachinery as derived by Marble in Reference 2. We will exploit this fact to derive a mathematical constraint which an inter-blade row boundary condition must satisfy in order for the time-averaged intra-blade row flow fields to be physically correct. Specifically, the axisymmetric components of both the momentum flux and the vorticity field must be continuous across the inter-blade row boundary plane.

The absolute velocity field as viewed in the stator frame of reference can be expressed as:

$$\vec{u}(r, \theta^{(S)}, z, t) = \vec{u}^E(r, \theta^{(S)}, z, t) + \vec{u}'(r, \theta^{(S)}, z, t) \quad (1)$$

where $\theta^{(S)}$ is the tangential position in the stator frame of reference. The vector \vec{u}^E is the time resolved or deterministic component of the velocity field. This component correlates directly in time with an integer multiple of the shaft rotation speed. The vector \vec{u}' is the time unresolved component, which includes turbulence. The superscript E represents an ensemble or phase-locked average. The time resolved velocity field may be further decomposed as

$$\vec{u}^E(r, \theta^{(S)}, z, t) = \vec{u}^{(S)} + \vec{u}^{(R)} \quad (2)$$

with respect to the stator frame of reference. Similarly with respect to the rotor frame,

$$\vec{u}^E(r, \theta^{(R)}, z, t) = \vec{u}^{(R)} + \vec{u}^{(S)} \quad (3)$$

where $\vec{u}^{(S)}$ represents the time-averaged velocity field in the stator frame of reference and $\vec{u}^{(R)}$ is the corresponding velocity field in the rotor frame of reference. The unsteady, deterministic (i.e., time resolved) components $\vec{u}^{(R)}$ and $\vec{u}^{(S)}$ may be written as

$$\vec{u}^{(R)} = [\vec{u}^{(R)}(r, \theta^{(S)} - \Omega t, z) - \vec{u}^{AX}(r, z)] + \vec{u}^{(R)''}(r, \theta^{(S)}, z, \theta^{(S)} - \Omega t) \quad (4)$$

$$\vec{u}^{(S)} = [\vec{u}^{(R)}(r, \theta^{(R)} - \Omega t, z) - \vec{u}^{AX}(r, z)] + \vec{u}^{(S)''}(r, \theta^{(R)} + \Omega t, z, \theta^{(R)}) \quad (5)$$

where Ω is the shaft rotational speed and \vec{u}^{AX} is the axisymmetric component of the deterministic velocity field. In what follows, the expression $\vec{u}^{(R)} - \vec{u}^{AX}$ will be denoted as

$$\vec{u}^{(R)} = \vec{u}^{(R)}(r, \theta^{(S)} - \Omega t, z) - \vec{u}^{AX}(r, z)$$

and $\vec{u}^{(S)} - \vec{u}^{AX}$ as

$$\vec{u}^{(S)} = \vec{u}^{(S)}(r, \theta^{(R)} - \Omega t, z) - \vec{u}^{AX}(r, z)$$

The vectors $\vec{u}^{(R)}$ and $\vec{u}^{(S)}$ are determined from the average passage equation system for the respective blade row. The axisymmetric average of these vectors is equal to the velocity vector \vec{u}^{AX} . The vector $\vec{u}^{(R)}$ ($\vec{u}^{(S)}$) is periodic in the tangential direction with a spatial periodicity inversely proportional to the number of blades in the rotor (stator). Thus the time average as well as the axisymmetric average of $\vec{u}^{(R)}$ and $\vec{u}^{(S)}$ are identically zero. Furthermore, the vector $\vec{u}^{(R)}$ ($\vec{u}^{(S)}$) will be periodic in time; the period being an integer multiple of the product of the shaft speed and the number of rotor (stator) blades. The vector $\vec{u}^{(R)''}$ ($\vec{u}^{(S)''}$) is that part of the velocity field which results from a rotor-stator unsteady aerodynamic interaction. It is periodic in time in either the rotor or stator frame of reference, the period being an integer multiple of the shaft speed. Its time average (i.e., average over the time it takes the shaft to turn one revolution) as well as its axisymmetric average is zero.

The outlined decomposition of the velocity field should not be taken to imply that the components which comprise the decomposition are linearly independent. On the contrary, it will be shown that a set of correlations exists which mathematically link the components to one another.

In addition to the outlined velocity decomposition, an equivalent decomposition exists for the vorticity field. This decomposition in the stator frame of reference can be written as

$$\begin{aligned} \vec{\zeta}(r, \theta^{(S)}, z, t) = & \vec{\zeta}^{(S)}(r, \theta^{(S)}, z) \\ & + \vec{\zeta}^{(R)}(r, \theta^{(S)} - \Omega t, z) \\ & + \vec{\zeta}^{(R)''}(r, \theta^{(S)}, z, \theta^{(S)} - \Omega t) \\ & + \vec{\zeta}^{(S)''}(r, \theta^{(S)}, z, t). \end{aligned} \quad (6)$$

The development of the constraining relationship associated with placing an inter-blade row boundary plane between the two time-averaged flow states is begun by examining the flux of momentum (defined in terms of the absolute velocity field) across the inter-blade row boundary plane shown in Figure 1. This flux in either frame of reference is equal to

$$\vec{F} = \rho u_z \vec{u} \delta A_z \quad (7)$$

where ρ is the density of the fluid stream, δA_z is a differential area element of the inter-blade row boundary plane, and u_z is the axial velocity component. Recall that we are restricting the present analysis to subsonic flows and hence will neglect variations in density. Since the flux as defined by Eqn. (7) is a vector, it is independent of the reference frame. Using Eqn. (7), we establish the time resolved representation of the momentum flux on either side of the boundary plane. The flux to the left of the plane (see Figure 1) is evaluated with respect to the rotor

frame of reference, while that to the right is evaluated with respect to the stator reference frame. With respect to either frame of reference, the time resolved representation is constructed from an ensemble average of Eqn. (7) in which a data sample consists of a continuous length of data recorded over one shaft revolution. The resulting averaged flux can be shown to be independent of the coordinate system in which it is constructed and is expressed as

$$\overline{\rho u_z \tilde{u}}^E \delta A_z = \rho \tilde{u}_z^E \tilde{u}^E \delta A_z + \rho \tilde{u}_z^E \tilde{u}'^E \delta A_z. \quad (8)$$

The first quantity on the right of the equal sign is the momentum flux associated with the deterministic velocity field, while the second expression represents the contribution originating from the time unresolved velocity component. Since both of these expressions are identical in both the rotor and stator reference frame, there can be no change in the momentum flux associated with either the time resolved or time unresolved velocity field across the inter-blade row boundary plane. Similarly, it may be shown that the time resolved vorticity field is continuous across the boundary plane.

To construct the time-averaged momentum flux on either side of the boundary plane, one averages over time the time resolved momentum flux. The time scale associated with this averaging operation is equal to one shaft revolution cycle. In the stator frame of reference, the expression for the time-averaged momentum flux is

$$\begin{aligned} \overline{\rho u_z \tilde{u}}^{t(s)} \delta A_z &= \rho u_z^{(s)} \tilde{u}^{(s)} \delta A_z \\ &+ \overline{\rho \tilde{u}_z^{(R)} \tilde{u}^{(R)}}^{t(s)} \delta A_z \\ &+ \overline{\rho u_z' \tilde{u}'}^{t(s)} \delta A_z \end{aligned} \quad (9)$$

where the superscript $t(s)$ denotes a time-average operation with respect to the stator reference frame. The corresponding expression for the time averaged momentum flux with respect to the rotor frame of reference is

$$\begin{aligned} \overline{\rho u_z \tilde{u}}^{t(R)} \delta A_z &= \rho u_z^{(R)} \tilde{u}^{(R)} \delta A_z \\ &+ \overline{\rho \tilde{u}_z^{(s)} \tilde{u}^{(s)}}^{t(R)} \delta A_z \\ &+ \overline{\rho u_z' \tilde{u}'}^{t(R)} \delta A_z. \end{aligned} \quad (10)$$

Based on the definition of the time-averaging operation given in Reference 1, this averaging operation does not yield a result which is independent of the frame of reference. Thus Eqn. (9) is not equal to Eqn. (10). This can be seen by examining the time resolved flow field downstream of an isolated rotor. The time-averaged momentum flux in the rotor frame of reference is a function of tangential position, while in the laboratory or fixed frame of reference it is independent of the tangential position. Thus unless the

flow field is axisymmetric, the time-averaged momentum flux will not be continuous across the inter-blade row boundary plane.

Next we consider the axisymmetric component of the time-averaged momentum flux on either side of the inter-blade row boundary plane. By virtue of their construction, it was shown in Reference 1 that these two momentum fluxes must be equal, hence from Eqns. (9) and (10) we obtain the result

$$\begin{aligned} \overline{\rho u_z^{(s)} \tilde{u}^{(s)}}^{AX} \delta A_z + \overline{\rho \tilde{u}_z^{(R)} \tilde{u}^{(R)}}^{t(s)} \delta A_z &= \\ \overline{\rho u_z^{(R)} \tilde{u}^{(R)}}^{AX} \delta A_z + \overline{\rho \tilde{u}_z^{(s)} \tilde{u}^{(s)}}^{t(R)} \delta A_z \end{aligned} \quad (11)$$

where the superscript AX denotes an axisymmetric average operation. Based on the definitions of $\tilde{u}^{(R)}$ and $\tilde{u}^{(s)}$ and Eqn. (4) and (5), Eqn. (11) may be rewritten as

$$\begin{aligned} \overline{\rho u_z^{(s)} \tilde{u}^{(s)}}^{AX} \delta A_z + \overline{\rho \tilde{u}_z^{(R)} \tilde{u}^{(R)}}^{t(s)} \delta A_z &= \\ \overline{\rho u_z^{(R)} \tilde{u}^{(R)}}^{AX} \delta A_z + \overline{\rho \tilde{u}_z^{(s)} \tilde{u}^{(s)}}^{AX} \delta A_z \end{aligned} \quad (12)$$

where we have used the fact that the temporal correlation $\overline{\tilde{u}_z^{(R)} \tilde{u}^{(R)}}^{t(s)}$ is independent of the tangential position. Finally, if we interchange the axisymmetric average of the product $u_z^{(R)} \tilde{u}^{(R)} \delta A_z$ with its equivalent temporal average, and define the axisymmetric average of the product $\rho u_z^{(s)} \tilde{u}^{(s)} \delta A_z$ as

$$\overline{\rho u_z^{(s)} \tilde{u}^{(s)}}^{AX} \delta A_z = \rho u_z^{(s)} \tilde{u}^{(s)} \delta A_z^{AX}$$

and similarly

$$\overline{\rho \tilde{u}_z^{(s)} \tilde{u}^{(s)}}^{AX} \delta A_z = \rho \tilde{u}_z^{(s)} \tilde{u}^{(s)} \delta A_z^{AX}$$

we obtain the result

$$\begin{aligned} \rho u_z^{(s)} \tilde{u}^{(s)} &= \overline{\rho u_z^{(R)} \tilde{u}^{(R)}}^{t(s)} \\ &- [\overline{\rho \tilde{u}_z^{(R)} \tilde{u}^{(R)}}^{t(s)} - \rho \tilde{u}_z^{(s)} \tilde{u}^{(s)}] \end{aligned} \quad (13)$$

Eqn. (13) is the expression we sought to derive at the start of this analysis. It links the momentum flux across the inter-blade row boundary plane to the time-averaged velocity field on either side of the plane. Requiring these two velocity fields to satisfy this equation insures that their axisymmetric components as well as the axisymmetric components of the two time-averaged vorticity fields are continuous across the boundary plane. This condition must be satisfied in order for the time-averaged velocity field on either side of the boundary plane to be physically correct. In the next section an example will be presented which will help in interpreting and quantifying several of the correlations that appear in Eqn. (13).

Before we leave this section, consider an inter-blade row boundary condition suggested by a number of researchers wherein the time-averaged flux of momentum per unit area associated with the rotor flow field is set equal to the axisymmetric average of the momentum flux per unit area based on the stator's time-averaged velocity field. This boundary condition implies that the two terms which appear within the brackets in Eqn. (13) are zero or negligible. We shall see that this is a reasonable approximation if the magnitude of the nonaxisymmetric component of the axial or tangential time-averaged vorticity field at a particular radial location on the boundary plane is small. As we shall show this negates the use of this boundary condition in the endwall region or at any location where the secondary vorticities generated by the rotor intersect the boundary plane.

VORTICITY TRANSFER ACROSS AN INTER-BLADE ROW BOUNDARY PLANE

Figure 2 from Reference 3 shows the output signal from a hot wire anemometer probe placed downstream of a rotor whose tip speed is 800 ft/sec. The spanwise location of the wire and the throttle position are noted. At the near minimum loss operating point and at .35 inches immersion from the outer case, the shape of the output signal comes from the velocity deficit in the wake. As the wire is raised towards the case, the form of the signal begins to change. The change in the shape is brought about by the tip leakage vortex produced by the clearance flow. The figure shows that the wake and the leakage vortex are two distinct features which remain distinct from one another over the entire stable operating range of the rotor. Of these two structures, the leakage vortex appears to be the dominant structure.

A number of researchers have shown that the leakage vortex has a velocity deficit in its core with rotational motion about its center line. When formed by an upstream rotor, this vortex will appear as a three-dimensional unsteady structure to an observer in the stator frame of reference. With respect to the stator frame of reference, this structure will possess both an axial and tangential component of vorticity which contribute to the time-averaged vorticity field entering the stator. Since this time-averaged vorticity field is one of the main contributors to the development of secondary flow within the stator, the transfer of the rotor's tip leakage vortex across the boundary plane must be addressed.

The analysis which follows will use the results derived in the previous section in addressing this issue. It will focus on the transfer of the axial component of the vorticity field of the leakage vortex across the inter-blade row boundary plane. The transfer of the other components associated with this structure would follow a similar procedure and therefore will not be presented.

The time-averaged axial vorticity with respect to

the stator's frame of reference is defined as

$$\zeta_z^{(S)} = \frac{1}{r} \frac{\partial}{\partial r} r u_\theta^{(S)} - \frac{1}{r} \frac{\partial}{\partial \theta} u_r^{(S)} \quad (14)$$

which can be rewritten as

$$\begin{aligned} \zeta_z^{(S)} = & \frac{1}{r} \frac{\partial}{\partial r} r u_\theta^{AX} \\ & + \left\{ \frac{1}{r} \frac{\partial}{\partial r} r (u_\theta^{(S)} - u_\theta^{AX}) \right. \\ & \left. - \frac{1}{r} \frac{\partial}{\partial \theta} (u_r^{(S)} - u_r^{AX}) \right\} \end{aligned} \quad (15)$$

At the inter-blade row boundary plane, we shall consider the nonaxisymmetric component of the stator's time-averaged velocity field as a small perturbation to an axisymmetric rotational velocity field (i.e., a velocity field whose vorticity field is finite). This assumption appears to be quite reasonable since the nonaxisymmetric component is the result of a potential disturbance generated by the flow field near the leading edge of the stator. Thus to lowest order, the contribution of the terms within the brackets in Eqn. (15) may be neglected, thus yielding

$$\zeta_z^{(S)} \approx \frac{1}{r} \frac{\partial}{\partial r} r u_\theta^{(S)} \quad (16)$$

Since it is the transfer of the leakage vortex across the inter-blade row boundary plane that we are considering, we need to express u_θ^{AX} as a function of the tangential momentum associated with the rotor's time-averaged velocity field. As has been shown this insures the correct transfer of momentum and vorticity across the boundary plane. This relationship is derived from the tangential component of Eqn. (13)

$$\begin{aligned} \widehat{u_z^{(S)} u_\theta^{(S)}} = & \overline{u_z^{(R)} u_\theta^{(R)}} t^{(S)} \\ & - [\overline{u_z^{(R)} u_\theta^{(R)}}] t^{(S)} - \widehat{u_z^{(S)} u_\theta^{(S)}} \end{aligned} \quad (17)$$

and the two definitions

$$\begin{aligned} u_z^{(S)} &= u_z^{AX} + (u_z^{(S)} - u_z^{AX}) \equiv u_z^{AX} + \hat{u}_z^{(S)} \\ u_\theta^{(S)} &= u_\theta^{AX} + (u_\theta^{(S)} - u_\theta^{AX}) \equiv u_\theta^{AX} + \hat{u}_\theta^{(S)} \end{aligned}$$

Forming the correlation $\widehat{u_z^{(S)} u_\theta^{(S)}}$ from these definitions and introducing the result into Eqn. (17) yields

$$u_z^{AX} u_\theta^{AX} = \overline{u_z^{(R)} u_\theta^{(R)}} t^{(S)} - \overline{\hat{u}_z^{(R)} \hat{u}_\theta^{(R)}} t^{(S)}$$

or

$$u_\theta^{AX} = \frac{\overline{u_z^{(R)} u_\theta^{(R)}} t^{(S)}}{u_z^{AX}} - \frac{\overline{\hat{u}_z^{(R)} \hat{u}_\theta^{(R)}} t^{(S)}}{u_z^{AX}} \quad (18)$$

The first term in Eqn. (18) on the right of the equal sign is the mass-averaged tangential velocity component associated with the rotor's time-averaged flow

field. The second term represents the tangential momentum transported across the stream surfaces of the stator's time-averaged flow field. Introducing Eqn. (18) into Eqn. (16) yields

$$\zeta_z^{(S)} = \frac{1}{r} \frac{\partial}{\partial r} \frac{\overline{ru_z^{(R)} u_\theta^{(R)}}^{t(S)}}{u_z^{AX}} - \frac{1}{r} \frac{\partial}{\partial r} \frac{\overline{ru_z^{(R)} \dot{u}_\theta^{(R)}}^{t(S)}}{u_z^{AX}} \quad (19)$$

Similarly, one can construct the following approximation for the tangential vorticity component on the stator's side of the boundary plane,

$$\zeta_\theta^{(S)} = \frac{\partial}{\partial r} \frac{\overline{u_z^{(R)} u_z^{(R)}}^{t(S)}}{u_z^{AX}} - \frac{\partial}{\partial r} \frac{\overline{\dot{u}_z^{(R)} \dot{u}_z^{(R)}}^{t(S)}}{u_z^{AX}} \quad (20)$$

Eqns. (19) and (20) show that the unsteady flow field generated by the rotor's clearance vortex influences the time-averaged vorticity field entering the stator through a radial gradient of the correlations $\overline{\dot{u}_z^{(R)} \dot{u}_\theta^{(R)}}^{t(S)}$ and $\overline{\dot{u}_z^{(R)} \dot{u}_z^{(R)}}^{t(S)}$. To assess the magnitude of these correlations, we shall examine the measurements reported in Reference 4. Figure 3 taken from Reference 4 shows the values of the six velocity correlations based on \bar{u} as a function of span measured 10% of chord downstream of an isolated rotor. The flow coefficient is 0.85. The correlations have been normalized with respect to the wheel speed at midspan squared. Of the six correlations, the largest two outboard of mid-span are $\overline{\dot{u}_z^{(R)} \dot{u}_z^{(R)}}^{t(S)}$ and $\overline{\dot{u}_z^{(R)} \dot{u}_\theta^{(R)}}^{t(S)}$. The reported relative total pressure field in the rotor's frame of reference associated with these correlations is reproduced in Figure 4. The contours of total pressure clearly show the existence of the clearance vortex as well as the rotor wake. The rapid raise in the value of the correlations outboard of mid-span is caused by the clearance vortex. The velocity deficit associated with the wake appears to contribute little to these correlations at this operating condition.

Figure 5 shows a plot of the measured axisymmetric component of the velocity field as a function of span. The location of these measurements is identical to the location for the measurements shown in the two previous figures. These velocity components have been normalized with respect to the wheel speed at mid-span. The reduction in the axial and tangential velocity components u_z^{AX} and u_θ^{AX} beginning at 80% of span will result in the generation of axial vorticity, and a decrease in tangential vorticity. Eqns. (19) and (20) indicate that the error in defining the time-averaged axial and tangential vorticity in terms of the mass-averaged axial and tangential velocity exiting the rotor is equal to the ratio of the radial gradient of the correlations $\overline{\dot{u}_z \dot{u}_\theta}^{t(S)} / u_z^{AX}$ and

$\overline{\dot{u}_z \dot{u}_z}^{t(S)} / u_z^{AX}$ to the radial gradient of u_z^{AX} . Using the data presented in Figures 3 and 5 to estimate this error, one finds that the error in the magnitude of the axial vorticity can be as large as 34%, while the error in the magnitude of the tangential vorticity approaches 14%. Furthermore, the radial gradient of the axial-tangential velocity correlation outboard of 95% of span implies that the axial vorticity estimated from the mass-averaged tangential velocity profile is finite, while the correct value based on the time-averaged tangential velocity plotted in Figure 5 is near zero. These estimates of the impact of the temporal velocity correlations associated with the leakage vortex on the vorticity transferred across the boundary plane are obviously not insignificant. However, at any region on the boundary plane (i.e., both sides) where the nonaxisymmetric components of the axial and tangential vorticity are small, the use of the mass-averaged velocity field to define the vorticity field appears to be a reasonable engineering approximation.

SUMMARY AND CONCLUSIONS

A relationship was developed which linked the momentum flux based on the time-averaged velocity field generated by a rotor to the axisymmetric averaged mass flux entering a stator. This relationship is a mathematical constraint which the velocity fields on either side of an inter-blade row boundary plane must satisfy in order that the momentum and vorticity field associated with these velocity fields be correctly transferred across this plane. The derivation of this relationship identified a set of velocity correlations whose acknowledgement insures that this constraint is met. From an examination of experimental data taken downstream of a rotor, it was concluded that the leakage vortex associated with rotor clearance flow contributed significantly to the magnitude of these correlations, while at operating points near peak efficiency of a well designed rotor, the contribution of the rotor wake was minimal. Hence if the endwall flow field is to be correctly predicted one must attempt to account for these correlations in simulations which employ an inter-blade row boundary condition to transfer information between intra-blade row solvers.

ACKNOWLEDGMENT

The author wishes to express his gratitude to Dr. R. Dring of the United Technologies Research Center for providing him with plots of his experimental results.

REFERENCES

- 1 Adamczyk, J. J., "Model Equations for Simulating Flows in Multistage Turbomachinery," NASA TM-86869 and ASME 85-GT-226, 1984.
- 2 Hawthorne, W. R., "Aerodynamics of Turbines and Compressors," High Speed Aerodynamics and Jet Propulsion, Vol. X, Princeton University Press,

1964.

- 3 Fessler, T. E. and Hartmann, M. J., "Preliminary Survey of Compressor Rotor-Blade Wakes and Other Flow Phenomena With A Hot-Wire Anemometer," NACA RM-E56A13, June, 1956.
- 4 Dring, R. P., Joslyn, H. D. and Hardin, L. W., "Experimental Investigation of Compressor Rotor Wakes," Technical Report AFAPL-TR-2107, January, 1980.

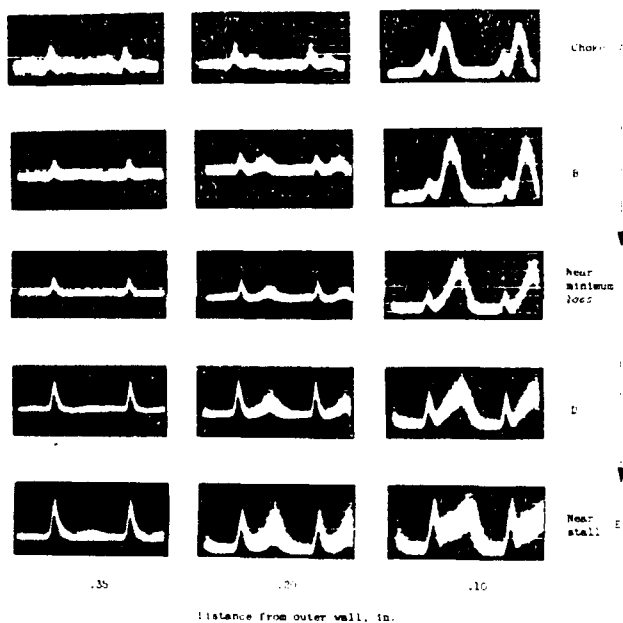


Figure 2. Hot wire traces of compressor rotor-outlet flow conditions. Five operating conditions, corrected tip speed, 800 ft/sec.

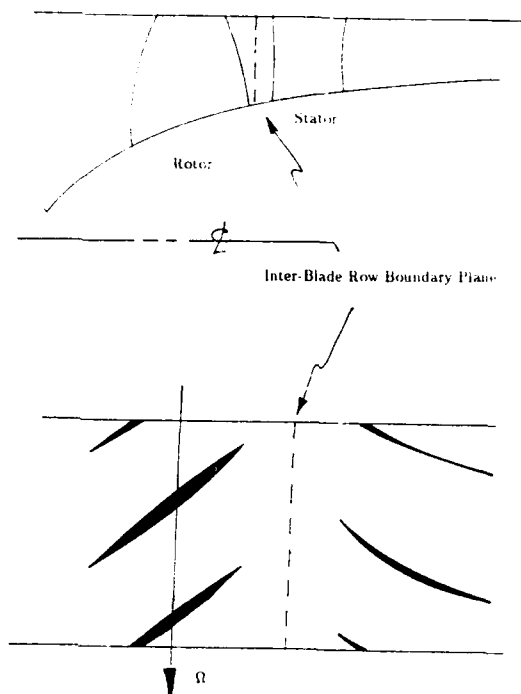


Figure 1. Location of Rotor Relative to Stator.

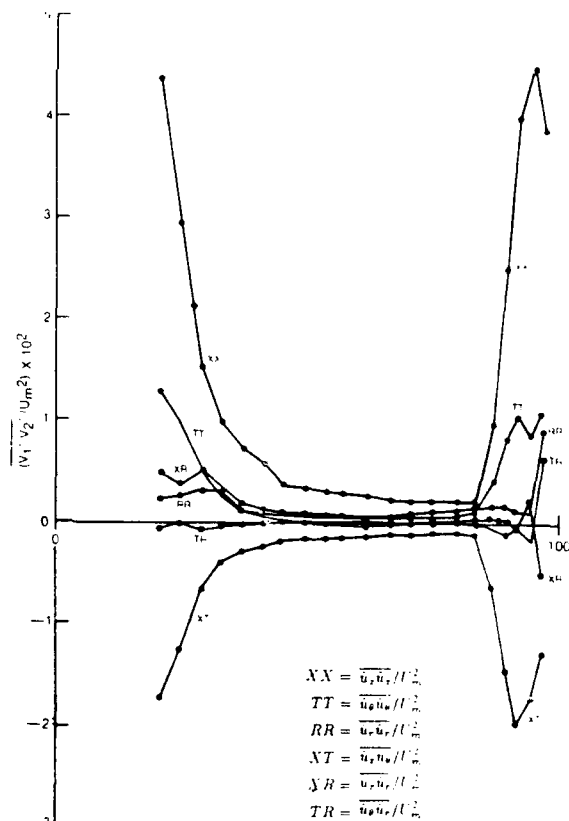


Figure 3. Spanwise Distributions of Fluctuation Terms 10% Aft. $(\frac{C}{U_m}) = 0.85$

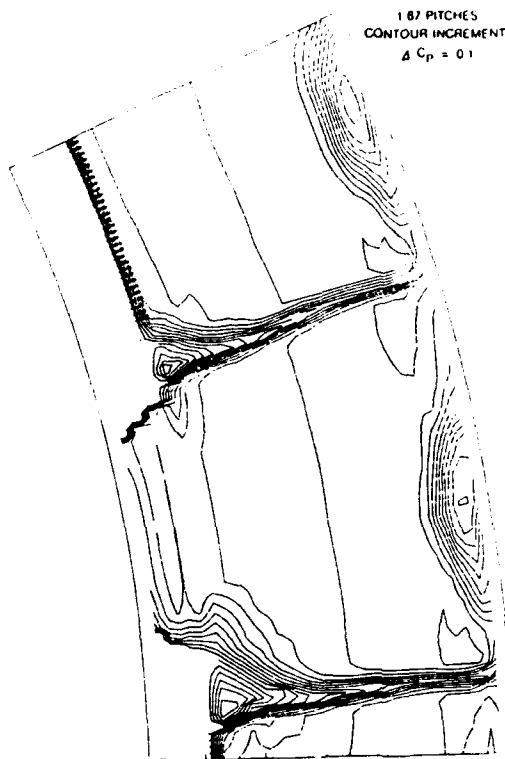


Figure 4. Total Pressure Contours. 10% Aft. $(\frac{C_x}{U_m}) = 0.85$.

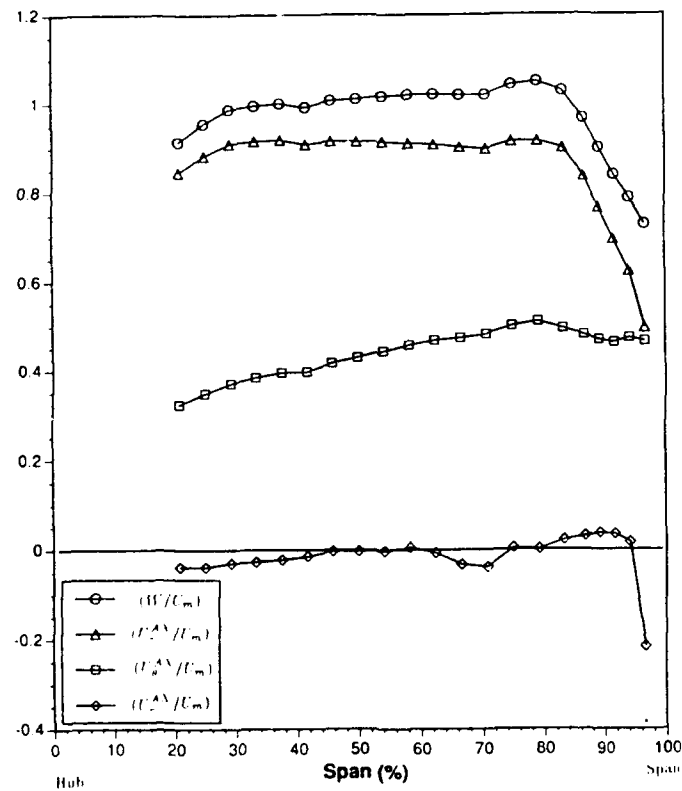


Figure 5. Time Averaged Velocity Components. $(\frac{C_x}{U_m}) = 0.85$, $(\frac{\Delta C_p}{U_m}) = 0.10$

Discussion

T. PRINCE, WILLIAMS INTER., U.S.A.

Are the additional terms in your model of time-averaged blade row interaction more important with small numbers of blades? How much error are we committing by performing three-dimensional calculations one row at a time, with matching to a throughflow computation?

AUTHOR'S REPLY

I do not know what effect blade count has on the terms I spoke about in my talk. I do know that spanwise loading distribution is important. One cannot match the incoming velocity profile of a three-dimensional simulation to a throughflow calculation without accounting for the correlations associated with the unsteady flow generated by the rotor. The error in the vorticity field entering a stator as shown in the paper can be as large as 30 percent.

J. MOORE, VPI, U.S.A.

How much of the fluctuation term $\overline{u_z u_z}^{t(s)}$ in Fig. 3 is caused by the Reynolds normal stress $\overline{u_z' u_z'}^{E^{t(s)}}$? One might expect this Reynolds stress to grow in an adverse pressure gradient.

AUTHOR'S REPLY

The only unsteady process that contributes to $\overline{u_z u_z}^{t(s)}$ comes from the unsteady velocity field associated with the nonaxisymmetric component of the time averaged velocity field of the rotor. What little data there is suggests that the time averaged kinetic energy associated with the turbulent field generated by the rotor, measured in the stator frame of reference (i.e.,

$\overline{u_i' u_i'}^{E^{t(s)}}$), is comparable to the kinetic energy associated with the rotor's unsteady

deterministic velocity field (i.e., $\overline{u_i u_i}^{t(s)}$). However, it appears that the radial gradient of the deterministic kinetic energy is larger than that of the turbulent field generated by the rotor.

D. HOBBS, PRATT & WHITNEY, U.S.A.

Can you quantify the effect of the additional terms in the matching plane conditions on the downstream airfoil row?

AUTHOR'S REPLY


These terms are associated with spanwise mixing within a stator attribute to an upstream rotor as given by the Adkins and Smith mixing model. One may estimate the magnitude of this effect by estimating the mixing within a stator produced by the secondary flows generated by an upstream rotor.

H. WEYER, DLR, GERMANY

With the time averaged flow field ahead of stator the unsteady (periodic) flow phenomena (blade wakes, secondary vorticity, etc.) are suppressed. How do you account for their effects on transition or separation of the stator blade boundary layers?

AUTHOR'S REPLY

Although the details of the time history of transition and unsteady separation has been filtered out by the averaging procedure, nevertheless the time averaged effect of such processes on a stators time averaged flow field is taken into account through a generalized Reynolds stress.





A CRITICAL EVALUATION OF A THREE-DIMENSIONAL NAVIER-STOKES METHOD AS A TOOL TO CALCULATE TRANSONIC FLOWS INSIDE A LOW-ASPECT-RATIO COMPRESSOR

CHUNILL HAH

NASA LEWIS research center
Cleveland, Ohio 44135

STEVEN L. PUTERBAUGH

Aeropropulsion Laboratory
Wright Patterson AFB, Ohio 45433

92-16076



SUMMARY

A numerical study to evaluate a three-dimensional Navier-Stokes method as a tool to predict the detailed flow field inside a low-aspect-ratio compressor at various operating conditions has been conducted.

The details of the flow structure inside a low aspect-ratio-compressor (three-dimensional shock structure, shock-boundary layer interaction, tip leakage vortex, etc.) and the overall aerodynamic performance at design and off-design conditions are numerically analyzed and the results are compared with the available experimental data.

The flow field inside a state-of-the-art transonic compressor is used for the purpose of the evaluation.

μ	Viscosity
ν	Kinematic viscosity
ω	ρ/κ
ρ	Density
<u>Subscripts</u>	
0	Inlet total condition
2	Exit condition
eff	Effective value
w	Surface conditions (wall)

*Original contains color
plates: All DTIC reproductions
will be in black and
white.

NOMENCLATURE

C_1	Constant in turbulence closure models
C_2	Constant in turbulence closure models
C_3	Constant in turbulence closure models
C_4	Constant in turbulence closure models
c_μ	Constant in turbulence closure models
J	Jacobian of transformation
k	Turbulent kinetic energy
M	Mach number
p	Pressure
P	Production of turbulence
Pr	Prandtl number
Re	Reynolds number
St	Stanton number
T	Temperature
Tu	Turbulence intensity
U, V, W	Mean velocity components
u, v, w	Fluctuating velocity components

Greek Symbols

ϵ	Turbulence dissipation rate
δ_{ij}	Kronecker delta
κ	Thermal conductivity of the fluid

INTRODUCTION

In the mid 1970's a very successful transonic High-Through-Flow single stage fan was designed and demonstrated by the Compressor Research Group, Technology Branch, Turbine Engine Division, Air Force Aero Propulsion Laboratory. The results were reported by Wennerstrom [1984]. The success of this stage, particularly the rotor, and its state-of-the-art geometry (e.g. low aspect ratio, arbitrary airfoils, etc.) made it an ideal baseline for a parametric design investigation. The intent of the investigation was to quantify the effect of several design parameters by designing, fabricating, and testing a series of rotors, each differing as much as practical from the baseline by a single design parameter. The parameters varied were those which were thought to be important to performance but have not been included in the loss models of contemporary design systems. These specific parameters include chordwise location of maximum thickness, several cascade area ratios, and leading edge sweep. This series of rotors were tested in the late 1980's.

One of the design parameters varied in this series was the throat-to-inlet area ratio including a specified suction surface shape near the passage shock. It is possible to achieve a net precompression of the flow in high speed cascades by steepening the suction surface angle ahead of the passage shock. The effect is a decrease in average Mach number ahead of the shock and therefore a decrease in shock strength. However, this results in a decreased throat-to-inlet area ratio, i.e. throat margin. In order

to maintain sufficient throat margin while exploiting this precompression, a rapid change in blade mean line angle may be required near the passage shock which would tend to worsen shock-boundary layer interaction. A rotor in the series was therefore designed with less throat margin than the baseline and a suction surface shape was tailored to lessen the shock boundary layer interaction. The design was performed by the General Electric Co. under the Air Force contract.

The rotor described above was selected as the subject of the current computational analysis. This geometry is somewhat more representative of transonic rotors in use today than the swept rotor (also a member of the test series) which was analyzed and reported by Hah and Wennerstrom [1990].

Over the last decade, computational methods for turbomachinery aerodynamics have significantly advanced from two-dimensional inviscid analysis to fully three-dimensional Navier-Stokes method. In recent years, significant progress has been reported in applying various numerical methods based on Reynolds-averaged Navier-Stokes equation to the investigation of detailed flow physics inside turbomachinery (Davis *et al.* [1987], Dawes [1986], Denton [1986], Giles [1988], Hah [1986], Moore and Moore [1985], Rao and Delaney [1990], etc.).

The primary objective of applying a Navier-Stokes method is to analyze detailed flow phenomena inside the flow passage and to predict aerodynamic performance as accurately as possible with the least empiricism. Because of the very complex geometry and the various viscous flow phenomena inside the flow passage (three-dimensional boundary layer development, secondary flow, shock-boundary layer interaction, tip-leakage flow, radial mixing, etc.), accurate prediction of the aerodynamic performance of low-aspect-ratio transonic rotors has been considered to be very difficult.

In this study, a numerical method based on the Reynolds-averaged Navier-Stokes equation is applied to predict the above mentioned transonic rotor at design and off-design operating conditions. Three-dimensional shock structure, shock-boundary layer interaction, tip-leakage flow, and the overall efficiency are numerically studied and the results are compared with the available measured data.

EXPERIMENT

The subject rotor was tested as a complete stage. The configuration and instrumentation was identical to that used for the swept rotor discussed by Hah and Wennerstrom [1990].

Data from twelve high-frequency Kulite pressure transducers, which were mounted on the casing, were obtained at 100 percent and 90 percent of rotor design speed. The measured data were then spatially resolved and contour plotted to give an indication of the tip flow characteristics. Several of these plots are compared with the numerical solutions. Rotor exit total temperature and total pressure profiles are used to calculate the aerodynamic efficiency of the rotor. It must be kept in mind, however, that rotor exit profiles are inferred from the stage exit data using standard techniques assuming axisymmetric through flow. Therefore mixing, which inevitably occurs in the stator, will tend to skew the rotor outlet profiles somewhat. Therefore, comparison of the computational results with the experimentally determined profiles must be done carefully.

GOVERNING EQUATIONS

The following Reynolds-averaged Navier-Stokes equations are solved for the current problem.

$$\frac{\partial}{\partial x_i} (\rho U_i) = 0 \quad (1)$$

$$\begin{aligned} \frac{\partial}{\partial x_j} (\rho U_i U_j) + 2\rho \epsilon_{ijk} \Omega_j U_k = & - \frac{\partial p}{\partial x_i} \\ & + \frac{\partial}{\partial x_j} \left[\mu \left(\frac{\partial U_i}{\partial x_j} + \frac{\partial U_j}{\partial x_i} - \frac{2}{3} \frac{\partial U_k}{\partial x_k} \delta_{ij} \right) - \overline{\rho u_i u_j} \right] + F_i \end{aligned} \quad (2)$$

$$\begin{aligned} \frac{\partial}{\partial x_j} (\rho U_j e) = & \frac{\partial}{\partial x_j} \left[\left(\frac{\mu}{Pr} \right)_{eff} \frac{\partial T}{\partial x_j} \right] - \frac{\partial}{\partial x_j} (\rho U_j) + U_i F_i \\ & + \frac{\partial}{\partial x_j} \left[U_i \mu \left(\frac{\partial U_i}{\partial x_j} + \frac{\partial U_j}{\partial x_i} - \frac{2}{3} \frac{\partial U_k}{\partial x_k} \delta_{ij} \right) \right] \end{aligned} \quad (3)$$

$$p = \rho RT \quad (4)$$

where U_i = mean velocity, u_i = fluctuating velocity, e = total energy, Ω_i = angular velocity,

$$\left(\frac{\mu}{Pr} \right)_{eff} = \left(\frac{\mu}{Pr} \right)_{laminar} + \left(\frac{\mu}{Pr} \right)_{turbulent}$$

and

$$e = C_v T + \frac{1}{2} U_i U_i$$

It is well known that neither the conventional mixing length type turbulence model nor any standard two-equation type turbulence model describes turbulence stresses properly in the region behind a shock wave or in the separated flow regions. Several recent studies indicate that significant improvement can be achieved when the standard two-equation model is modified to include the low Reynolds number effects. For the current study, a standard two-equation model is modified to include the low Reynolds number effects following the studies of Chien [1982]. The following additional transport equations are solved for the turbulent shear stresses.

$$\frac{\partial (\rho U_i k)}{\partial x_i} = \frac{\partial}{\partial x_i} \left[\frac{\mu_{eff}}{\sigma_k} \frac{\partial k}{\partial x_i} \right] - \rho \overline{u_i u_j} U_{i,j} - \rho \epsilon - \frac{2\mu k}{l^2} \quad (5)$$

$$\begin{aligned} \frac{\partial (\rho U_i \epsilon)}{\partial x_i} = & \frac{\partial}{\partial x_i} \left[\frac{\mu_{eff}}{\sigma_\epsilon} \frac{\partial \epsilon}{\partial x_i} \right] + C_1 \frac{\rho \epsilon}{k} (\overline{u_i u_j} U_{i,j}) \\ & - \frac{\rho \epsilon}{k} \left[C_2 f \epsilon + \frac{2\nu k \epsilon^{-C_3 \mu^{1/4}/\nu}}{l^2} \right] \end{aligned} \quad (6)$$

where

$$\mu_{eff} = \mu + C_\mu (k^2/\epsilon) (1 - e^{-C_\mu^{1/4}/\nu})$$

and

$$f = 1 - \frac{0.4}{1.8} e^{-(k^2/\epsilon \nu)^2}$$

No attempt was made to optimize the constants of the turbulence transport equations for the current study. Therefore, standard values for the constants are used; these values are

$$C_\mu = 0.09, C_1 = 1.35, C_2 = 1.8, \sigma_k = 1.0, \sigma_\epsilon = 1.3, \\ C_3 = 0.0115, C_4 = 0.5$$

NUMERICAL METHOD

Although significant progress has been made in numerical techniques during the last decade, obtaining an accurate numerical solution of the flow field inside the transonic compressor remains to be one of the more difficult problems. The development of three-dimensional boundary layers on the blade surface and end walls as well as shock-boundary layer interaction, and the tip-clearance flow should all be accurately calculated to capture the overall flow field correctly.

For the current study, the governing equations are solved with an implicit relaxation method using a fully conservative control volume approach. A third-order accurate interpolation scheme is used for the discretization of the convection terms and central differencing is used for the diffusion terms. The method is of second-order accuracy with smoothly varying grids. Details of the current method and, applications to transonic flows are given by Hah [1987] and by Hah and Wennerstrom [1990].

The computational grid used for the current study is shown in fig. 1. The current computational grid was generated to give an orthogonal grid near the leading edge and near the blade surface where the most important flow phenomena (passage shock, shock-boundary layer interaction, etc.) occur. With this grid, spatial periodicity at the periodic surfaces is not enforced for the grid, so the physical periodicity condition is handled inside the code using an interpolation function. The grid consists of 50 nodes in the blade-to-blade direction, 46 nodes in the spanwise direction, and 152 nodes in the streamwise direction. Six grid nodes in the spanwise direction are used to describe the tip-clearance region of the compressor. Inside the tip gap, the grid is closed in the blade-to-blade direction and the periodicity condition is applied. The standard boundary conditions for the transonic flow in a compressor are used (Hah and Wennerstrom [1990]). About two of Cray YMP single processor CPU hours are required to get a fully converged solution for each operating conditions.

RESULTS AND DISCUSSION

In the current design procedure, three-dimensional Navier-Stokes CFD is frequently used to verify the final design, which has been derived with various simpler methods (streamline curvature, three-dimensional potential, Euler method, etc.). The primary objective of the current study is to examine how well a three-dimensional Navier-Stokes method can calculate the aerodynamic performance of a state-of-the-art low-aspect ratio transonic fan at various operating conditions. To assess the performance of the code and to anchor the code for design application, the detailed flow field and the overall aerodynamic performance are analyzed and compared with the available experimental data.

SHOCK STRUCTURE NEAR THE SHROUD

Numerical analysis was performed for three operating conditions (near stall, peak efficiency, and near choke) at the 100 percent and the 90 percent rotor speed. For each rotational speed of the rotor, different blade stress analysis was performed to obtain the true deflected geometry of the rotor. This running geometry of the rotor was used for the numerical analysis of the corresponding flow field. In figure 2, time averaged static pressure contours on the casing are compared between the numerical solution and the Kulite measurement. At the near stall condition, both the measured data and the calculation show that the passage shock near the endwall is located ahead of the blade passage. Also, the leading edge shock is not normal to the incoming relative flow angle. The numerical results indicates that there exists a strong interaction between the passage shock and the tip-leakage vortex.

At the design condition, the leading edge shock moves into the blade passage and the shock becomes nearly normal to the incoming relative flow. The interaction between the tip-leakage vortex and the passage shock is evident. However, the effect of this interaction is somewhat diminished compared to the near stall condition. At the choke condition, the passage shock becomes again oblique to the relative flow direction. The passage shock is reflected on the suction surface and a second shock appears on the pressure side, which results in further aerodynamic loss due to the shock-boundary layer interaction. Comparisons in figure 2 show that the numerical solutions do calculate the shock structure correctly at different flow conditions. Various existing shock loss models (Miller et al [1962], Wennerstrom and Puterbaugh [1984]) assume that the passage shock is normal to the relative flow direction. The current study indicates that this assumption is valid only near the peak efficiency condition. Therefore, an improved shock loss model, which include an oblique shock, similar to the approach by Koch and Smith [1976], might represent the flow more realistically. The interaction between the passage shock and the tip-leakage vortex is significant at all operating conditions. This interaction becomes stronger when the flow rate is reduced.

FLOW STRUCTURE NEAR THE BLADE

Calculated static pressure contours on the blade surfaces at the 100 percent rotor speed are shown in figures 3 and 4. In figure 3, the static pressure distribution on the blade surface is shown for the entire rotor blade. The calculated static pressure contours on a projected plane are shown in figure 4. The change of the shock structure due to the flow rate is clearly displayed with the numerical solutions. At all three flow conditions, the shock shape is three-dimensional with the shock quite oblique away from the endwall. However, the shock becomes normal to the endwall near the casing due to the physical constraint. As shown in figures 3 and 4, most changes in flow structure with the various mass flow rates happen between the casing and 50 percent span height.

Relative velocity vectors inside the suction surface boundary layer are shown in figure 5 for the three operating conditions. Velocity vectors follow the conventional stream surfaces before the passage shock. However, strong radial flow develops immediately after the shock. This strong radially outward flow inside transonic compressors was previously observed and discussed (Kerrebrock [1980], Kotidis and Epstein [1990], Hah and Wennerstrom [1990]). For the

current rotor, no axially reversed flow region is calculated except near the tip-clearance area for all the flow rates. The radially outward flow is due to the shock-boundary layer interaction near the casing (above 40 percent of the span) while traditional secondary flow phenomena cause the radial flow near the hub. Particle traces inside the blade passage are shown in figure 6. Particle traces in figure 6 illustrate spanwise mixing and detailed structure of the tip-clearance vortex. Swirling motion of fluid particles due to this vortex is clearly shown in figure 6. This tip-clearance vortex and its interaction with the passage shock seem to dominate the endwall flow phenomena. Therefore, proper control of this vortex might improve the compressor efficiency significantly.

OVERALL PERFORMANCE

Spanwise distribution of the blade section efficiency is compared in figure 7. The agreement between the measurement and the calculation is quite good considering the complexity of the flow field. Although the absolute value of the aerodynamic loss is not calculated exactly, the differences in the efficiency at different flow conditions are very well calculated. The results in figure 7 show that the differences in efficiency are mainly from the near tip section. Below 20 to 30 percent span from the shroud, the blade section performance remains almost constant. Contours of entropy at the trailing edge surface are shown in figure 8 for different flow conditions. For the rotating system, entropy is a better quantity for loss analysis than total pressure. The aerodynamic losses are much larger on the suction surface than the pressure surface due to the shock. There is a large loss region immediately below the shroud which is associated with the tip-clearance vortex. This high loss region moves from the suction side of the blade to the pressure side of the blade when the mass flow rate is reduced (from choke condition to the stall condition). The entropy contours in figure 8 show the accumulated loss at the trailing edge surface. Again, most of the loss is generated and accumulated on the suction side of the blade and near the shroud of the rotor at all three operating conditions.

An experimentally measured efficiency map of the rotor is compared with the calculated map in figure 9. The variation of the aerodynamic performance of the rotor at various flow rates is quite well calculated. However, the calculated peak efficiency is somewhat lower than the measured value. Several attempts were made to reduce mass flow rate beyond the currently reported value for the numerical solution by raising the exit static pressure. However, the numerical solution becomes unstable and no steady state solution can be obtained. Probably this numerical instability might be interpreted as an indication of the real compressor stall. But, further investigation might be necessary to apply the current numerical method to study flow phenomena near stall condition.

CONCLUDING REMARKS

This paper describes a numerical study to evaluate a three-dimensional Navier-Stokes method as a tool to predict the detailed flow field inside a low-aspect-ratio compressor at various operating conditions. The details of the flow structure and the overall aerodynamic performance of a state-of-the-art compressor rotor have been studied at the design rotor speed and at the 90 percent speed.

The currently applied numerical method along with the turbulence model calculate details of the flow field with the accuracy acceptable for engineering application. The aerodynamic behavior of the rotor at different rotor speeds and mass flow rates is also calculated well. Some disagreement in aerodynamic loss calculation, especially near the tip region, might be improved if a more realistic turbulence model along with a further refined grid are used. The current numerical capability could be used to conduct a parametric study of transonic fan design. Also a preliminary evaluation of revolutionary designs can be done using such a tool.

ACKNOWLEDGMENTS

The authors would like to thank Dr. A. R. Wadia of the G. E. Aircraft Engine Company for his many useful discussions during the course of the current work.

REFERENCES

- Chien, K.Y., 1982, "Prediction of Channel and Boundary-Layer Flows With a Low Reynolds Number Turbulence Model," *AIAA Journal* Vol. 20, No. 1, pp. 33-38.
- Davis, R.L., Hobbs, D.E., and Weingold, H.D., 1988, "Prediction of Compressor Cascade Performance Using a Navier-Stokes Technique," *ASME Journal of Turbomachinery*, Vol.110, No. 4, pp. 520-531.
- Dawes, W.N., 1986, "Development of a 3D Navier-Stokes Solver for Application to All Types of Turbomachinery," *ASME paper 86-GT-70*.
- Denton, J.D., 1986, "The Use of a Distributed Body Force to Simulate Viscous Flow in 3D flow Calculations," *ASME Paper 86-GT-144*.
- Giles, M.B., 1988, "Stator/Rotor Interaction in a Transonic Turbine," *AIAA Paper 88-3093*.
- Hah, C., 1987, "Calculation of Three-Dimensional Viscous Flows in Turbomachinery With an Implicit Relaxation Method," *AIAA Journal of Propulsion and Power*, Vol. 3, No. 5, pp. 415-422.
- Hah, C., and Wennerstrom, A.J., 1990, "Three-Dimensional Flowfields Inside a Transonic Compressor with Swept Blades," *ASME Paper 90-GT-359*.
- Kerrebrock, J.L., 1980, "Flow in Transonic Compressors," *AIAA Journal*, Vol.19, No. 4.
- Koch, C.C. and Smith, L.H., 1976, "The Loss Sources and Magnitude in Axial Flow Compressors," *Journal of Engineering for Power*, Vol. 98, pp 411-424.
- Kotidis, P.A., and Epstein, A.H., 1990, "Unsteady Radial Transport in a Transonic Compressor Stage," *ASME Paper 90-GT-133*. *ASME Paper No. 86-GT-21*.
- Miller, G.G. Lewis, G.W., and Hartmann, M.J., "Shock Losses in Transonic Rotor Rows," *ASME Journal of Engineering for Power*, Vol. 83, pp. 235-242.
- Moore, J., and Moore, J.E., 1985, "Performance Evaluation of Linear Turbine Cascade Using Three-Dimensional Viscous Flow Calculations," *ASME Journal of Engineering for Gas Turbines and Power*, Vol. 17, No. 1, pp. 969-975.
- Rao, K. and Delaney, R., 1990, "Investigation of Unsteady Flow Through Transonic Turbine Stage," *AIAA Paper 90-2408*.

Wennerstrom, A.J., 1984, "Experimental Study of a High-Through-Flow Transonic Axial Compressor Stage," *Journal of Engineering for Gas Turbine and Power*, Vol. 106, No. 3, pp. 552-560, July, 1984.

Wennerstrom, A.J. and Puterbaugh, S.L., 1984, "A Three-Dimensional Model for the Prediction of Shock Losses in Compressor Blade Rows," *Journal of Engineering for Gas Turbines and Power*, Vol. 106, No. 2, pp 295-299, April 1984.

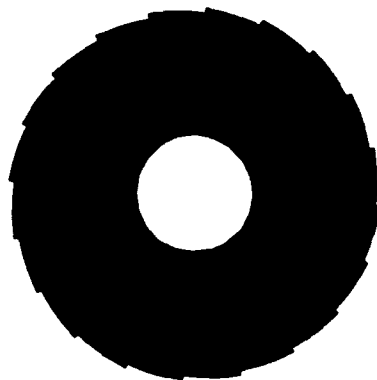


Fig. 1a. Front view of rotor 4.

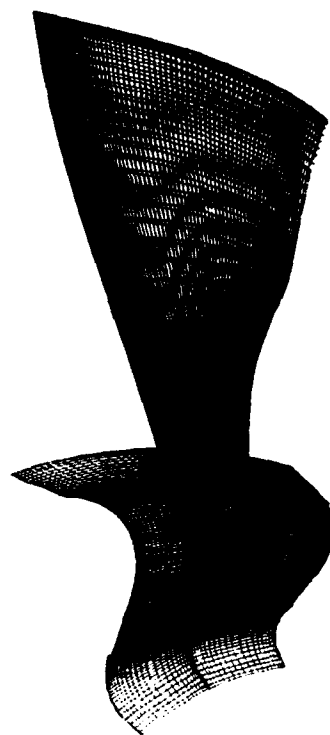
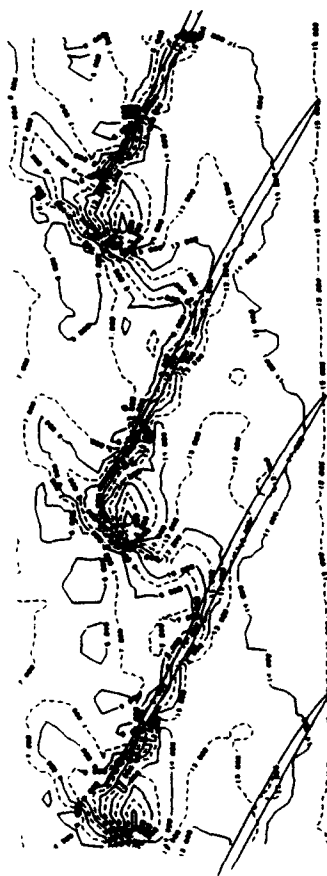


Fig. 1b. Rotor 4 computational grid (6 nodes inside tip clearance).



measurement



calculation

Fig. 2a. Comparison of shroud static pressure at stall condition (100 % rotor speed).

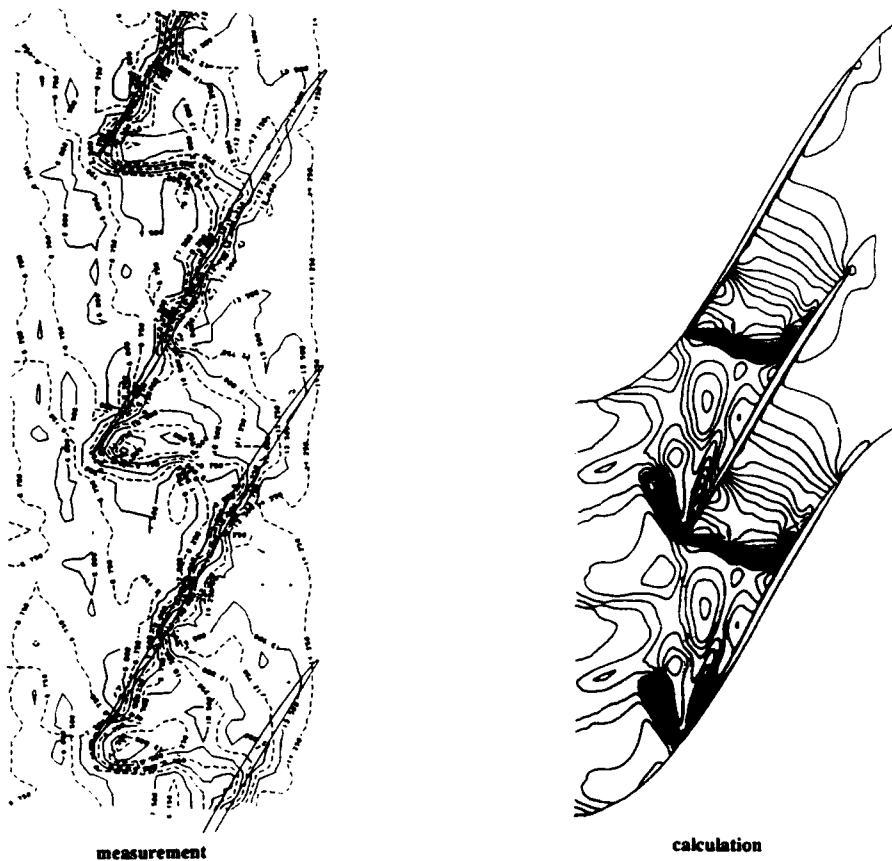


Fig. 2b. Comparison of shroud static pressure at design condition (100 % rotor speed).

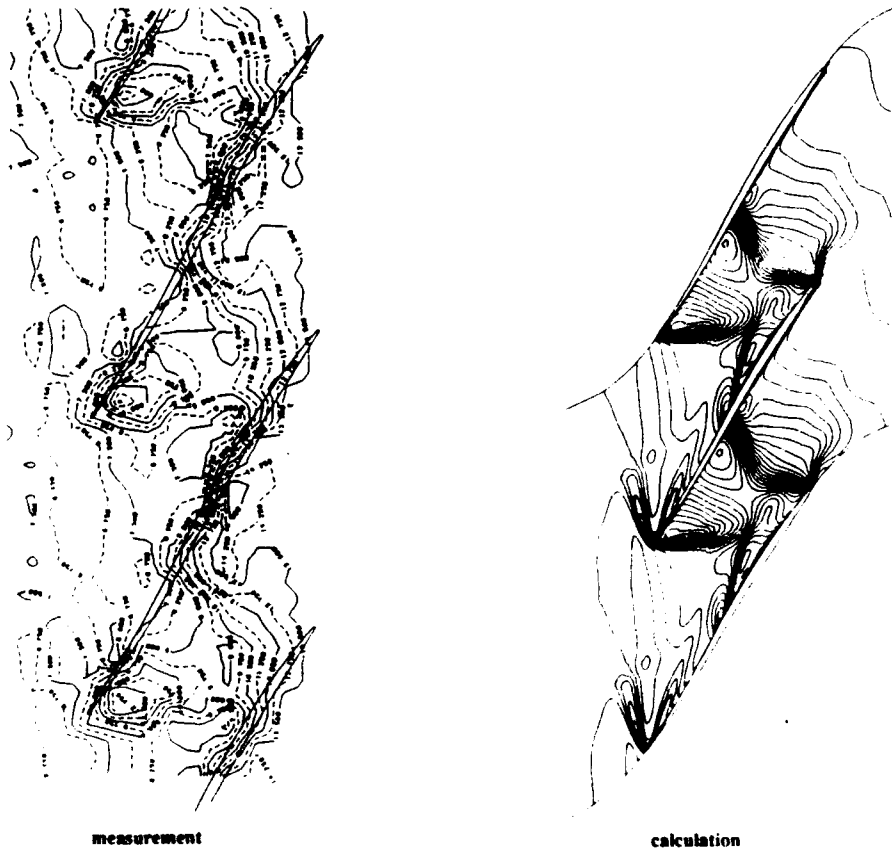
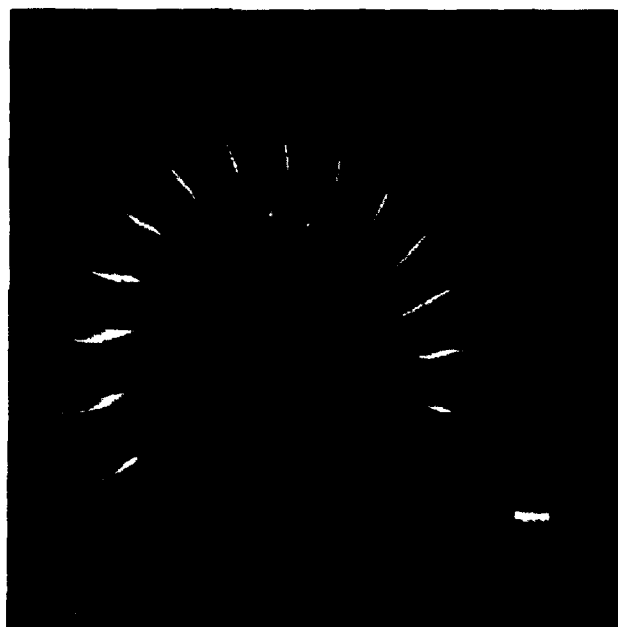
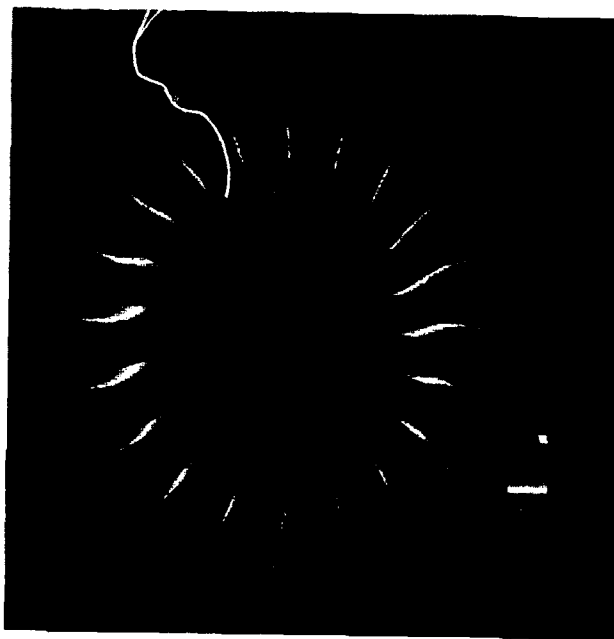
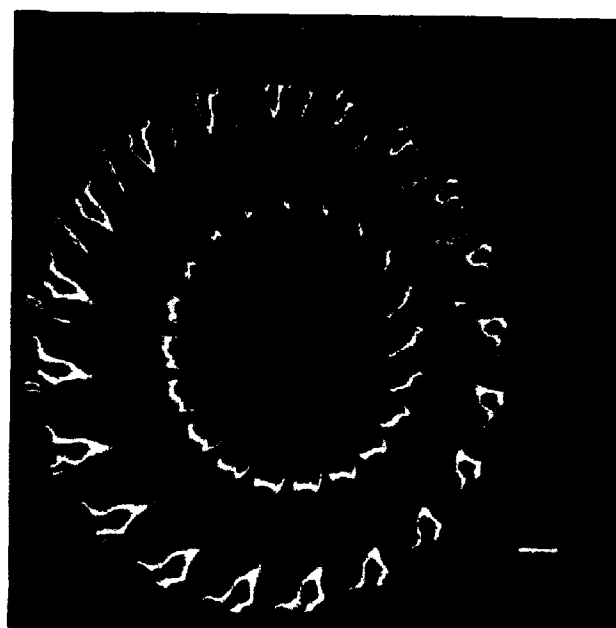


Fig. 2c. Comparison of shroud static pressure at choke condition (100 % rotor speed).

**Fig. 3a. Static pressure distribution
at stall condition (100 % rotor speed).**



**Fig. 3b. Static pressure distribution
at design condition (100 % rotor speed).**



**Fig. 3c. Static pressure distribution
at choke condition (100 % rotor speed).**

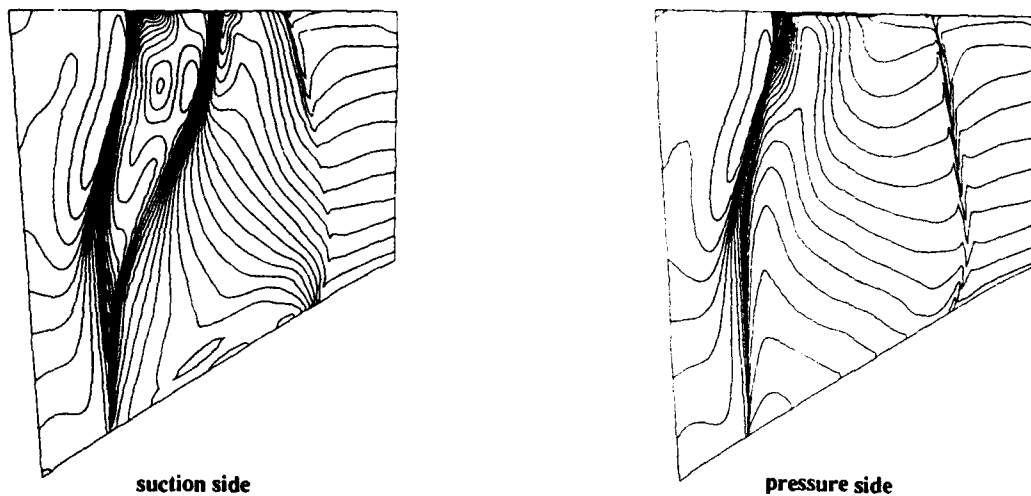


**Fig. 4a. Calculated static pressure contours
at stall condition (100 % rotor speed).**

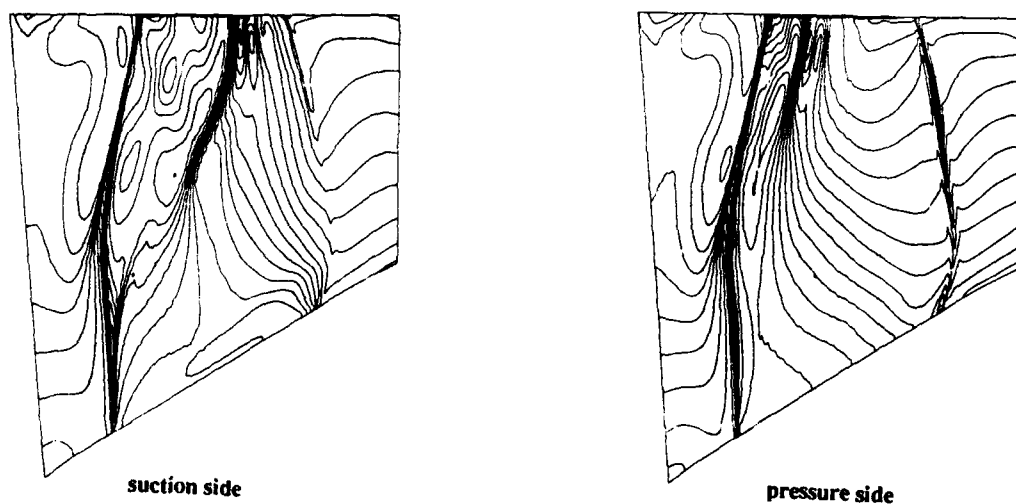


**Fig. 4b. Calculated static pressure contours
at design condition (100 % rotor speed).**

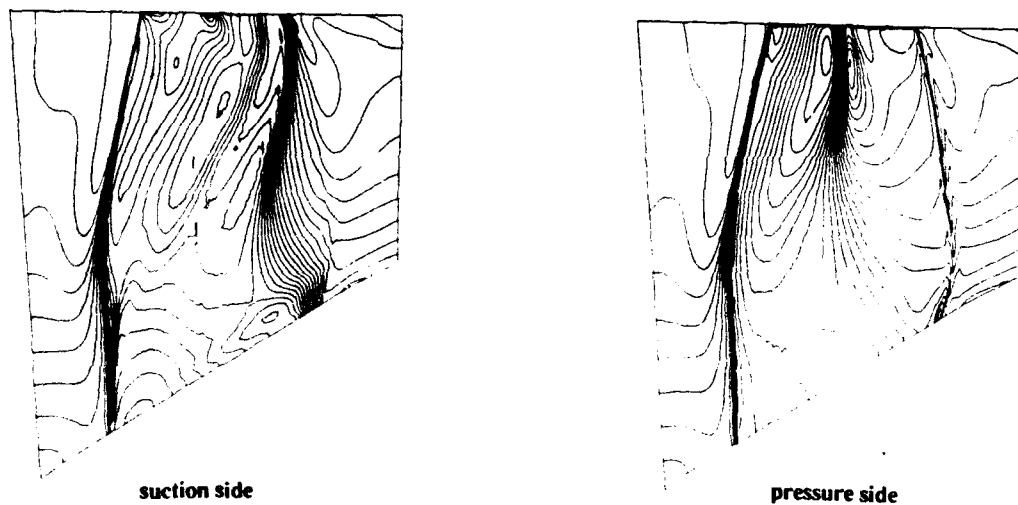


**Fig. 4c. Calculated static pressure contours
at choke condition (100 % rotor speed).**

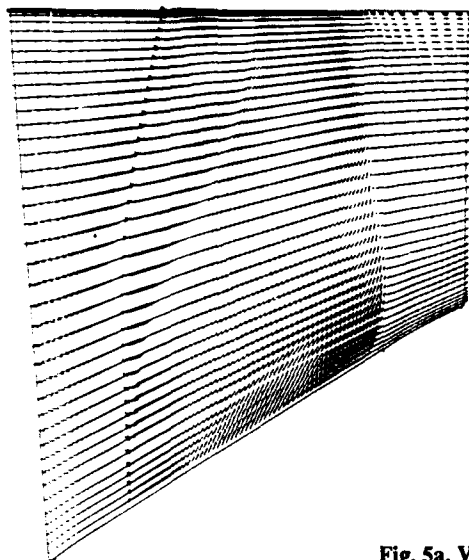


Fig. 5a. Velocity vectors near the suction surface at stall condition (100 % rotor speed).

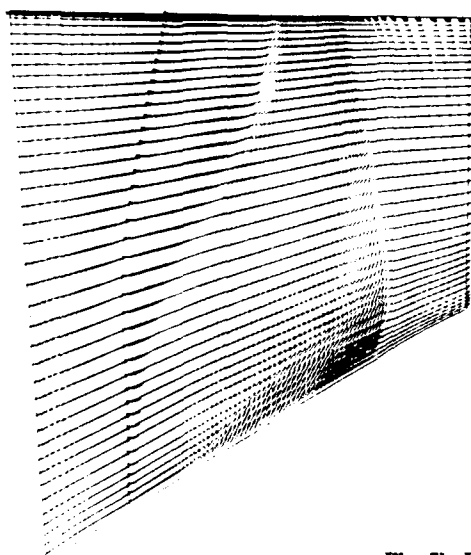


Fig. 5b. Velocity vectors near the suction surface at design condition (100 % rotor speed).

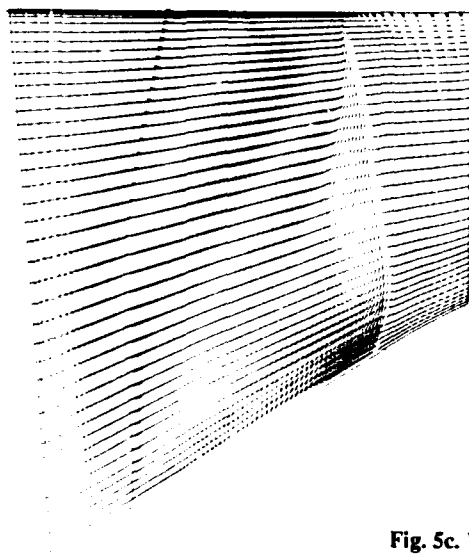


Fig. 5c. Velocity vectors near the suction surface at choke condition (100 % rotor speed).



Fig. 6a. Particle traces near the blade surface.



Fig. 6b. Structure of the tip-clearance vortex.

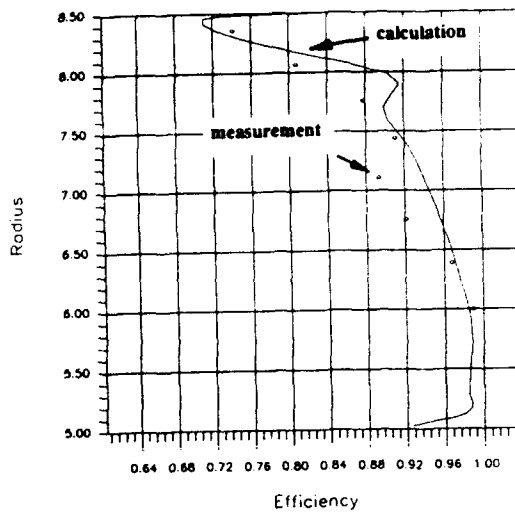


Fig. 7a. Comparison of blade section efficiency at stall condition (100 % rotor speed).

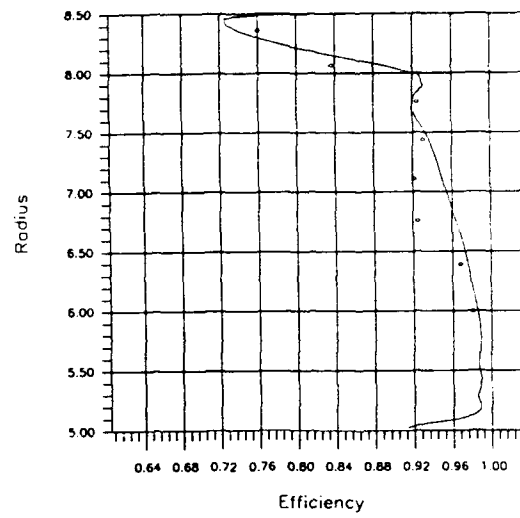


Fig. 7b. Comparison of blade section efficiency at design condition (100 % rotor speed).

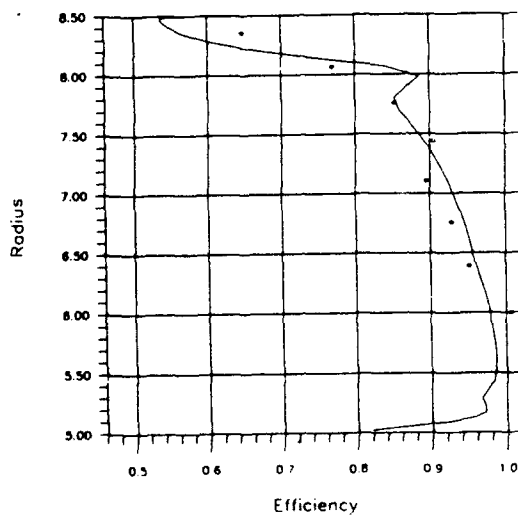


Fig. 7c. Comparison of blade section efficiency at choke condition (100 % rotor speed).

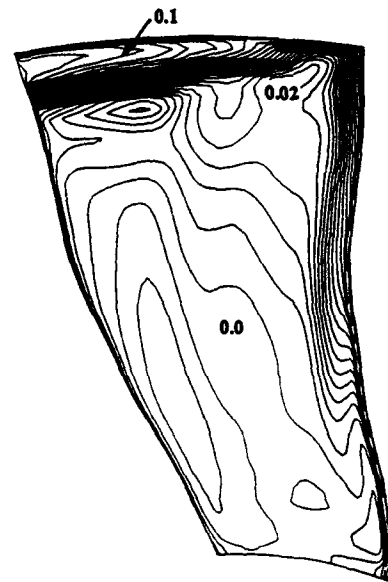


Fig. 8a. Entropy contours at the trailing edge at stall condition (100 % rotor speed).

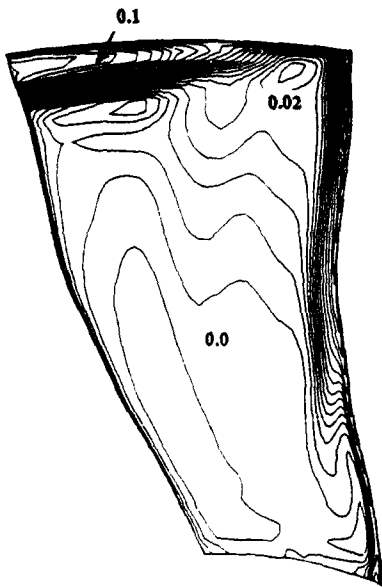


Fig. 8b. Entropy contours at the trailing edge at design condition (100 % rotor speed).

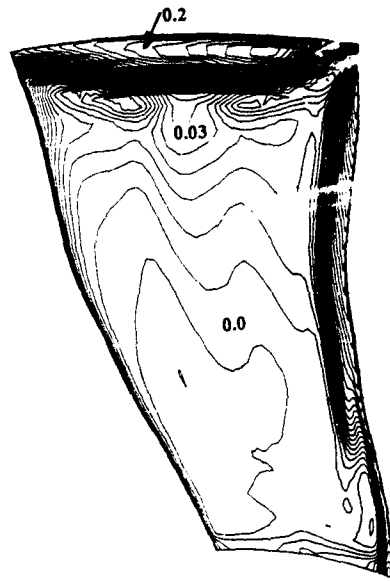


Fig. 8c. Entropy contours at the trailing edge at choke condition (100 % rotor speed).

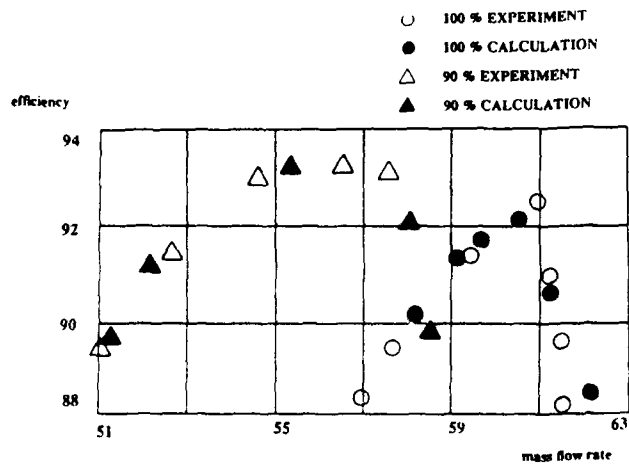


Fig. 9. Comparison of rotor efficiency map.

Discussion

J. ADAMCZYK, NASA LEWIS, U.S.A.

The data shown in Fig. 9 shows the rotor at 100 percent speed chokes at a mass flow of 61 lb/sec, your simulation shows no evidence that the rotor is choked at this flow rate or at the low back pressure case for which the computed flow rate is 62 lb/sec. What is the computed choke flow rate for this machine?

AUTHOR'S REPLY

First of all, the test rig was not operated for fully choked condition because of the restriction of the test facility. Therefore, flow behavior near the choke condition was not studied very well experimentally. The computed mass flow rate at choke seems slightly higher than the experimentally derived value.

P. RAMETTE, DASSAULT AVIATION, FRANCE

In your model, turbulence is computed with a standard two equation model with a low Reynolds number extension. Could you comment on the modifications made in order to include low Reynolds number effects? What could be the next improvement to take into account turbulence effects?

AUTHOR'S REPLY

Our code is programmed so that the low-Reynolds-number correction is automatically activated when the grid y^+ is less than 11. To account for the effects in the numerical solution, we need typically 10 to 25 points inside the boundary layer. Near the shock/boundary-layer interaction area, the grid is fine and most of the correction is included. We are also studying alternate ways to improve the turbulence modeling aspect of the code.

R. GRAY, WRIGHT LABS, U.S.A.

The ability to characterize three-dimensional shock surfaces is very good. Can you comment on remaining work to correctly calculate the shock-boundary layer interaction, which must be quite complex?

AUTHOR'S REPLY

We have demonstrated our capability to capture shock/boundary-layer interaction, we are further looking into the improvements of both numerics of physical modeling. Probably, we need further refined grid near the interaction area and some improvements in turbulence modeling.

K. BROICHHAUSEN, MTU, MÜNCHEN, GERMANY

The Mach number in the tip region of the fan is about 1.5. Could you comment on the regular flow pattern near the end wall without a pronounced separation?

AUTHOR'S REPLY

The compressor is a state-of-the-art design. The relative motion of endwall and tip clearance flow energizes the flow near the tip-region and no large flow separation is observed.

D. HOBBS, PRATT & WHITNEY, U.S.A.

Did your analysis of the various rotors in the parametric series show significant differences in these designs and their respective performance levels and flow fields?

AUTHOR'S REPLY

All the numerical results for different rotors show considerable variation of performance. We are studying various reasons for these differences. Hopefully, some of the results will be released to the community.





ON THE COMPUTATION OF UNSTEADY TURBOMACHINERY FLOWS PART 1 - EULER EQUATIONS IN VIBRATING CASCADES

by

Georg A. Gerolymos*
Université Pierre & Marie Curie
Building 511, 91405 Orsay
France

92-16077



ABSTRACT

The purpose of this paper is to present a methodology for unsteady flow analysis in vibrating transonic compressor cascades, using Euler equations. After a brief discussion of the problem, the numerical algorithm is presented, for the 3-D case, with particular emphasis on grid displacement procedures, slip surface-fitting, boundary-conditions and their effect on computational results. Chorochronic flow periodicity and modal superposition are briefly discussed. Several results from realistic aircraft engine turbomachinery configurations are presented. The lack of, and urgent need for 3-D experimental data combining unsteady pressure measurements and vibrating modeshapes are stressed. The methods are then validated through comparison with time-linearized flat-plate cascade theory (analytical) and experimental data from annular and linear cascades. A method for computing the aeromechanical coupling is presented. Finally a discussion concerning the taking into account of viscous effects is undertaken.

Euler methods is not an end to itself, but a first step towards the development of Navier-Stokes solvers.

1. positive incidence subsonic
2. unstarted flutter
3. high back-pressure started
4. low back-pressure started
5. choke
6. negative incidence subsonic

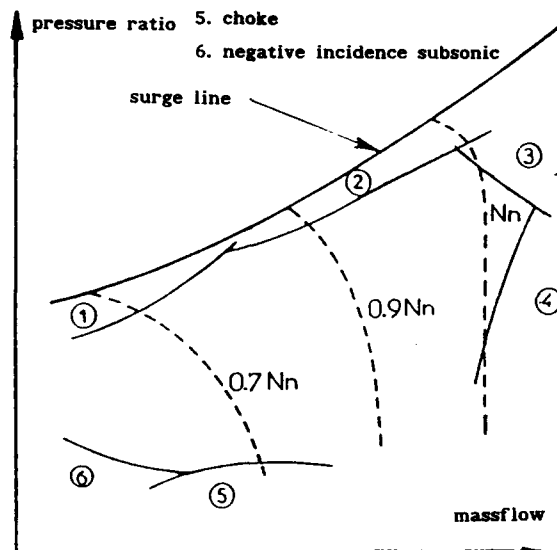


Fig. 1 Compressor map showing typical flutter boundaries.

1 INTRODUCTION

Transonic compressors are susceptible to flutter in various regions of their pressure-ratio vs. mass-flow-rate operating map. Various, but not radically different definitions of flutter types exist in the literature, e.g. Sisto.¹⁹⁸⁷ Focussing our interest on modern high-tip-speed transonic compressors the diagramme of Fig. 1, largely inspired from the work of Lubomski^{1979,1981} is introduced. At high mass-flow, viz. in zones 3-4-5 of Fig. 1, flutter is most probably due to unsteady shock motion, and may be analyzed with quantitatively satisfactory results, using Euler equations. It should nevertheless be made clear that the development of

A simple system-approach to explaining flutter is presented in Fig. 2, in the form of a potentially unstable feedback-loop, where random or quasi-random blade oscillations are amplified and then sustained by extracting energy from the flowfield (cf. Bisplinghoff & Ashley¹⁹⁶²). Quite often, in the case of wing-flutter the coupled structure/flow system is numerically time-marched in order to determine the response to an initial perturbation, providing a straightforward stability or instability criterion, e.g. Guruswamy.¹⁹⁸⁹ This fully integrated approach is not applicable to single-interblade-channel

* mail to: Dr. G.A. Gerolymos, LEMFI, Bldg 511, UPMC, F-91405 Orsay, FRANCE

simulations for turbomachinery applications, due to the variable-amplitude pitchwise traveling-waves (cf. Lane¹⁹⁵⁶) which are not compatible with usual nonlinear numerical implementations of chorochronic periodicity (cf. Gerolymos,^{1990b} Giles,¹⁹⁸⁸ He¹⁹⁸⁹). The only known alternative is coupling the aerodynamic and structural operators in the frequency domain (e.g. Bendiksen¹⁹⁸⁸), even in the case of a time-nonlinear aerodynamic operator.

The present work is mostly concerned with the aerodynamic operator, in the form of a 3-D time-marching Euler solver, and its $2\frac{1}{2}$ -D counterpart. The development of time-marching Euler solvers for use as aerodynamic operator in an aeroelastic stability prediction methodology is relatively new in turbomachinery. There are very few references on this subject in the *AGARD Manual on Aeroelasticity in Axial-Flow Turbomachinery* (cf. Acton & Newton¹⁹⁸⁷). In a more recent review by Bendiksen¹⁹⁹⁰ several references on Euler solvers are given, and the interested reader may consult this reference for further details. Reviews on time-linearized unsteady turbomachinery aerodynamics have been published by Verdon.^{1987,1992} For subsonic inviscid flows, the vibrating cascade problem can be treated quite successfully using time-linearized methods. When, however, shock-waves are embedded in the flowfield, several theoretical and practical problems are encountered. Williams^{1979,1980} has shown that the motion of shock-waves is nonlinear even from the point-of-view of a linearized solver. The work of Williams can certainly be

used, in conjunction with time-linearized solvers, when one uses shock-fitting techniques (Hall & Crawley¹⁹⁸⁹ have developed a time-linearized Euler solver using shock-fitting techniques). The general trend in CFD (Computational Fluid Dynamics) has been (cf. Hussaini¹⁹⁸⁹), for almost 2 decades now, to abandon shock-fitting in favour of shock-capturing, on the basis of the weak solutions concept of Lax.^{1957,1957} The underlying reason is that shock-fitting, although in theory feasible (e.g. Salas¹⁹⁷⁶), can become an intractable problem in the case of complex 3-D flowfields, with many interacting shock-waves. The state-of-the-art of shock-capturing in unsteady time-linearized solvers is not well enough developed yet (but has development potential!). That is the reason why many authors (e.g. Fransson & Pandolfi,¹⁹⁸⁶ Gerolymos,^{1988,1990a,1992a} He,¹⁹⁸⁹ Bendiksen¹⁹⁹⁰) have developed time-nonlinear Euler solvers, based on time-marching schemes, both for the 3-D and the $2\frac{1}{2}$ -D problems, despite the substantially higher computing-time requirements in comparison with time-linearized methods.

The time-marching Euler solver could be used to produce a modal data base and then coupled, in the frequency domain, with the structural operator. Such a procedure was in fact used by Henry & Vincent.¹⁹⁹⁰ It is however both expensive and tedious to manually construct such a modal aerodynamic data-base, making this procedure cumbersome for use in the design process. An alternative, is mode-modification during the time-marching iterations (cf. Gerolymos^{1992b}), which will be discussed at the end of the present report.

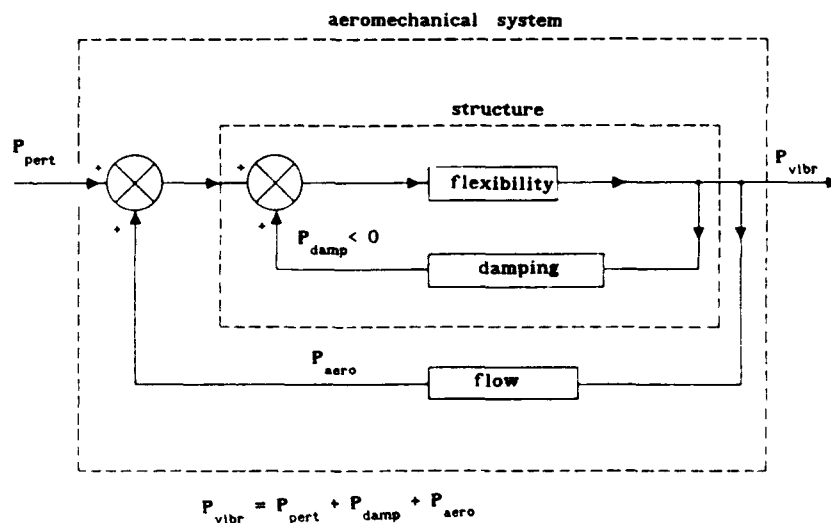


Fig. 2 Schematic block-diagram for the coupled flow/structure system.

In the following the numerics of a time-marching Euler solver are discussed, with particular emphasis on boundary-conditions. After presenting summary results for a typical aircraft engine fan, a coupled aeromechanical solver, using the mode-modification technique is described, and assessed by presenting some typical results. The validation of time-nonlinear Euler methods is discussed in detail, and comparisons of computational results with both theory and experiment are presented. Finally some remarks are made on future research for computing the viscous flowfield, and extending this methodology to subsonic flutter analysis.

2 BASIC STRUCTURAL OPERATOR

The unsteady 3-D solver needs a vibratory mode input. This is computed using an existing finite-element solver, in the present case SAMCEF.* The structural method is based on the work on rotationally periodic structures by Thomas,¹⁹⁷⁹ Henry,¹⁹⁸⁰ and Henry & Ferraris.¹⁹⁸⁴ Steady aerodynamic loading and centrifugal stiffening are taken into account in the computations.

3 3-D EULER SOLVER

3.1 Flow Description & Problem Position

Using Euler methods, one can expect satisfactory results only in the operating-map regions where viscous effects are not overwhelmingly important. It should be reminded that the problem at hand is the determination of the aeroelastic stability of a given configuration, and not the estimation of efficiency, i.e. the problem is to obtain an accurate prediction of pressure distributions around the airfoil, both for the steady flow, and the vibration-driven oscillatory flow.

For started flow on the nominal-speed-line, Euler solvers are expected to give a good qualitative description of the shock-waves system inside the rotor (cf. Epstein & al.,¹⁹⁷⁹ Kerrebrock,¹⁹⁸¹ Karadimas¹⁹⁸⁸). Experience with aeroelastic studies (cf. Gerolymos,^{1988,1990a} Gerolymos & al.¹⁹⁹⁰) suggests that the same is true for unstarted flow as well, at least at high rotational speeds (nominal or near-nominal). A plausible explanation is that stalling (in the

sense of the impossibility of higher pressure-ratios) and upstream incidence increase from the unique-incidence-angle (inducing lower mass-flow-rates at constant speed) are associated with the detached leading-edge shock-system, which turns the flow to near-unique-incidence before the interblade-channel entrance, and that viscous effects are not very important. The previous argument concerns shock-system structure and pressure distributions, but not efficiency and losses.

Consequently, the Euler solvers that will be described in the sequel, aim at determining the flowfield response to a prescribed bladed-disk vibration, for operation in zones 3-4-5, i.e. for predicting started and unstarted supersonic flutter.

3.2 Euler Equations & Numerical Scheme

The flowfield is modelled by the unsteady 3-D Euler equations (e.g. Vavra¹⁹⁶⁰),

$$\frac{\partial \rho}{\partial t} + \nabla \cdot (\rho \vec{W}) = 0 \quad (1a)$$

$$\frac{\partial \rho \vec{W}}{\partial t} + \nabla \cdot (\rho \vec{W} \otimes \vec{W} + p \mathbf{I}) + 2 \vec{\Omega} \times \vec{W} + \nabla \cdot (-\Omega^2 \vec{R}^2 / 2) = 0 \quad (1b)$$

$$\frac{\partial \rho E}{\partial t} + \nabla \cdot (\rho \vec{W} h_{tr}) = 0 \quad (1c)$$

completed by the perfect-gas equation-of-state,

$$p = \rho R_g T \quad (2)$$

where ρ is the density, t the time, ∇ the gradient operator, \vec{W} the relative flow velocity, h_{tr} the rothalpy ($h_{tr} = h + W^2/2 - (\Omega R)^2/2$), h the static enthalpy, E the total energy in the rotating frame ($E = h_{tr} - p/\rho$), $\vec{\Omega}$ the rotational velocity vector, R the radius with respect to the rotation axis, p the static pressure, T the static temperature, R_g the gas-constant, and \mathbf{I} the identity 3x3 tensor.

The numerical method used for integrating the Euler equations is presented in detail in Gerolymos,^{1990a,1992a} and will be only briefly described here. The unsteady Euler equations are discretized in a moving grid, using a finite-volume technique based on 3-linear isoparametric brick elements. The resulting semi-discrete equations are then integrated in time using the 5-stage Runge-Kutta scheme devised

* SAMCEF (Système d'Analyse des Milieux Continus par Éléments Finis) is a computer program by SAMTech [B].

by Jameson & al.,¹⁹⁸¹ and used by Venkatakrishnan & Jameson¹⁹⁸⁸ for the computation of unsteady flows over isolated airfoils. Shock-capturing is achieved through use of a combined 2-order nonlinear and 4-order smoothing dissipation operator, following Jameson & al.,¹⁹⁸¹ Pulliam,^{1986a,1986b} and Olsson & Johnson.¹⁹⁸⁹ A typical H-grid, for a wide-chord fan is shown in Fig. 3. The computational grid is displaced at every iteration to conform with the vibrating blades. Grid generation and displacement are done algebraically and are described in Gerolymos.^{1988,1990a}

The flow-diagram for the 3-D computer-program MANIAC-2 (Methodology for Aeroelastic Numerical Instability Analysis in Compressors) is depicted in Fig. 4.

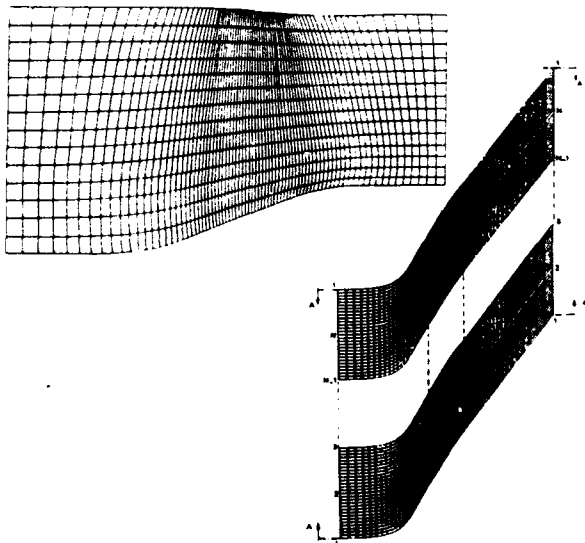


Fig. 3 Typical computational H-grid for a wide-chord fan.

3.3 Boundary Conditions

3.3.1 General Remarks: Boundary conditions are applied using the theory of characteristics. The particular numerical implementation follows closely the work of Brochet¹⁹⁸⁰ and Cambier & al.,^{1985,1989} (for details cf. Gerolymos^{1992a}). In the following, boundary conditions will be discussed mostly from the physical point-of-view.

3.3.2 Blade Boundary Conditions: On the blades' surface ∂B the unsteady nonpenetration condition is applied,

$$\vec{W}(t, \vec{x}) \cdot \vec{n}(t, \vec{x}) = \vec{q}_t(t, \vec{x}) \cdot \vec{n}(t, \vec{x}) \quad \forall \vec{x} \in \partial B \quad (3)$$

where \vec{n} is the unit normal vector on the blades surface, \vec{x} is the position vector, \vec{q} is the blade surface position vector (mean position + instantaneous vibratory displacement), and \vec{q}_t is the time-derivative of \vec{q} . It should be noted that when using the 5-stage Jameson scheme boundary conditions (and particularly nonpenetration) should be applied at the end of every stage of the Runge-Kutta cycle, and not only at the end of the cycle (in this connexion the work of Gottlieb & Turkel¹⁹⁷⁸ can be consulted).

3.3.3 Inflow Boundary Conditions: At the inflow boundary, in the present version of the 3-D code a 1-D nonreflecting boundary condition, following the theory by Hedstrom,¹⁹⁷⁹ which for the present case may be summarized as:

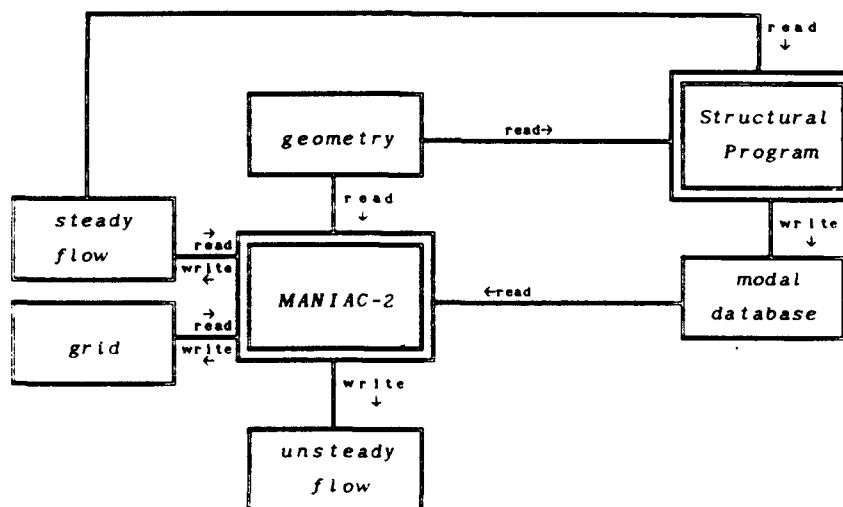


Fig. 4 Flow-diagram of the 3-D computer-program MANIAC-2.

$$p_{,t} + \rho a (\vec{W} \cdot \vec{n})_{,t} = 0 \quad (4a)$$

$$S_{,t} = 0 \quad (4b)$$

$$[\angle(\vec{V}, \vec{e}_u)]_{,t} = 0 \quad (4c)$$

$$[\angle(\vec{V}, \vec{e}_r)]_{,t} = 0 \quad (4d)$$

where $(\cdot)_{,t}$ denotes partial derivation with respect to time, $\angle(\vec{a}_1, \vec{a}_2)$ is the angle between the 2 vectors \vec{a}_1 and \vec{a}_2 , \vec{n} is the ingoing unit normal vector at the upstream boundary (invariably the positive axial direction), p the static pressure, ρ the static density, a the sound velocity, \vec{W} the relative flow velocity, S the entropy, \vec{V} the absolute flow velocity, \vec{e}_u the unit vector in the tangential direction, and \vec{e}_r the unit vector in the radial direction. Conditions 4c and 4d imply that the absolute flow angles (tangential and radial) are fixed, since they remain equal to those of the initialization.

It should be remarked that the present boundary condition is not nonreflecting in the 3-D case. Results using this boundary condition or a classical reservoir boundary condition are identical insofar as blade pressures are concerned, as shown in Gerolymos & al.¹⁹⁹⁰ In another study, concerning wake/rotor interaction (cf. Chapin¹⁹⁹²) the multi-dimensional nonreflecting boundary condition that was developed by Thompson^{1987,1990}, has been implemented in the $2\frac{1}{2}$ -D code. In a test case, consisting of a 2-D channel, with uniform nonviscous flow for $t < 0$, where at $t = 0$ a wake appears at the inflow boundary and is then convected to the outflow, Thompson's condition gave spectacularly better results near the boundary (in fact no perturbation whatsoever of the wake profile was introduced). However the error introduced when using Hedstrom's condition is only local, and as numerical tests have shown does not propagate upstream (it creates, in the sense of Moretti,¹⁹⁶⁹ a numerical boundary-layer). Work on implementing Thompson's nonreflecting boundary condition in the 3-D code, and on testing its effects for vibrating cascade configurations at resonance conditions is currently under way.

3.3.4 Outflow Boundary Conditions: At the outflow boundary again a 1-D nonreflecting boundary condition, following Hedstrom,¹⁹⁷⁹ is applied,

$$p_{,t} + \rho a (\vec{W} \cdot \vec{n})_{,t} = 0 \quad (5)$$

where $(\cdot)_{,t}$ denotes partial derivation with respect to time, \vec{n} is the ingoing unit normal vector at the outflow boundary (invariably the negative axial direction), p the static pressure, ρ the static density, a the sound velocity, \vec{W} the relative flow velocity.

3.3.5 Supersonic Throughflow Machinery: The above boundary conditions are valid in the case of conventional subsonic throughflow machinery where the normal to the boundary Mach number is subsonic ($|M_n| < 1$). In the supersonic throughflow case, lately drawing much attention (cf. Wood & al.¹⁹⁸⁸ for steady flow analysis and design and Kielb & Ramsey¹⁹⁸⁹ for aeroelastic studies) all variables are fixed at the inflow boundary, and none is fixed at the outflow. The unsteady problem is indeed much simpler, since no upstream-propagating waves appear, as can be seen e.g. in the work of Lane.¹⁹⁵⁷

3.3.6 Cut Condition: At the permeable pitchwise boundaries, a matching condition between adjacent channels is applied, following Cambier & al.^{1985,1989} The problem of reconstructing the flow on the 2 neighbouring channels, making use of chorochronic periodicity conditions, is discussed in 3.3.8. The matching condition, is applied by discretizing the characteristic equations on the surface that separates the 2 channels and taking only upwind information, in the sense of information propagation along characteristics. Thus if the normal to the interface Mach number is supersonic, only the characteristic equations from the 'upstream' channel are used. If it is subsonic, the characteristic equation of the 'upstream'-traveling pressure-wave is taken from the 'downstream' channel, and all 4 others from the 'upstream' channel (for details cf. Gerolymos^{1992a}).

3.3.7 Slipsurface Fitting: Downstream the trailing-plane of the blades, a simple matching condition between adjacent channels might be looked upon with some suspicion. The problem touches upon the old, but still actual unsteady Kutta condition issue (cf. Sears,¹⁹⁷⁶ McCroskey,¹⁹⁷⁷ Satyanarayana & Davis,¹⁹⁷⁸ Fleeter,¹⁹⁸⁰ Crighton,¹⁹⁸⁵ Amiet¹⁹⁹⁰). One solution, which has been used by this author, both in $2\frac{1}{2}$ -D and 3-D, is to attach a slipsurface to the trailing-plane of the blades. This is not so difficult, as it would be in external 3-D aerodynamics, because of the existence of the hub

and tip surfaces, which provide material limits to the slipsurface, thus avoiding any roll-up problems, that make such a procedure impossible in external aerodynamics. As explained in Cambier & al.¹⁹⁸⁵ for the computation of this contact discontinuity, all compatibility relations (in both domains) are used; the matching conditions apply the equality of pressures and normal velocities, and allow for differences in tangential velocities and entropy (computed separately in each domain, using the corresponding characteristic equations). The flow velocity normal to the contact discontinuity and relative to it (normal flow velocity, W_n , minus normal slipsurface displacement velocity, U_n) must be 0 (cf. Lax^{1954,1957}). Therefore, at every iteration, the slipsurface is displaced using the computed flow velocity. In order that the slipsurface remain a smooth surface, and that no instabilities occur during the displacement procedure, the grid points on the slipsurface are displaced in a purely circumferential direction (with a velocity whose projection on the normal to the slipstream gives the normal displacement velocity U_n), and slopes on the slipsurface are always upstream-biased. For further details cf. Gerolymos.^{1992a}

A typical slipsurface plot, for Fan A which is described in section 4 'Sample Results' (cf. Tab. 2) is presented in Fig. 5. It represents the slipsurface, for the steady-flow computation, at nominal operation. It should be observed that the variation of flow-angles with radial position introduce a tendency to stretch the slipsurface, and, at the same time to roll it round the hub. For this reason (quite representative of reality)

numerical computations may become unstable, due to grid degeneracy, if the outflow-boundary is positioned very far downstream. This problem does not appear in $2\frac{1}{2}$ -D computations, where the whole blade-to-blade surface is unrolled and mapped onto a plane. Positioning the outflow-boundary near the trailing-plane might be unattractive, especially when the cascade and vibration parameters correspond to propagating waves (cf. Whitehead¹⁹⁸⁷). Furthermore, Thompson's nonreflecting boundary condition has presented problems when used at the outflow-boundary, in combination with slipsurface-fitting. Therefore studies are under way in order to use a simple matching condition in lieu of a fitted-slipsurface, and especially in order to determine the price one must pay in terms of higher circumferential resolution for the same accuracy (the problem of capturing a contact discontinuity, which as noted by Lax^{1954,1957} will have the tendency to spread with time). One can also note the enhanced robustness induced by slipstream fitting, especially in supersonic-throughflow machinery computations, as remarked by Dumas.¹⁹⁹²

3.3.8 Chorochronic Periodicity: When one is concerned with the response of the flowfield to a traveling-wave vibration of the bladed-disk, spectacular gains in computing-time are obtained by computing only one interblade-channel making use of the chorochronic periodicity of the flow (cf. Fig. 6). Chorochronic periodicity is introduced because, as shown by Lane,¹⁹⁵⁶ the aeroelastic eigenmodes of a perfectly tuned (with perfect cyclic symmetry) bladed-disk are traveling-waves, decaying, propagating or

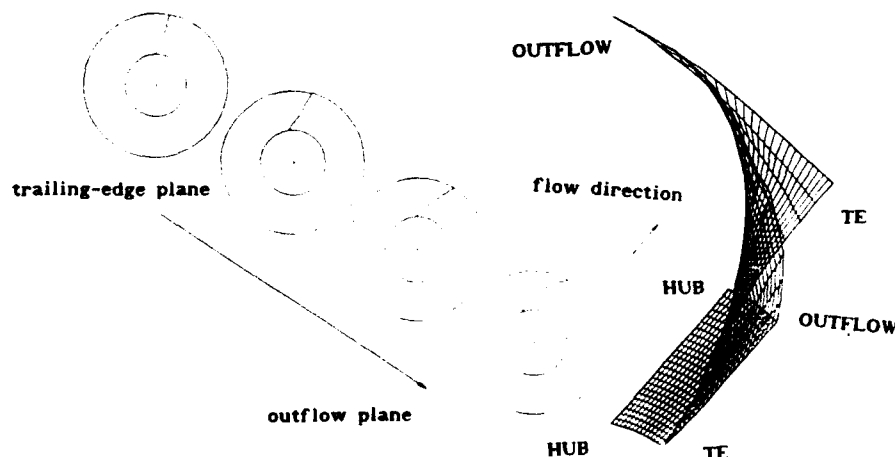


Fig. 5 Typical slipsurface plot for a wide-chord fan.

amplifying, depending on the aeroelastic stability of the system (under the sole assumption that the coupled aeromechanical system is linear), viz. that the vibration of the bladed-disk is of the form,

$$q(t, x, R, \theta + 2k\pi/N) = e^{-\zeta\omega t} \operatorname{Re} \left\{ q_0(t, x, R, \theta) e^{i(\omega t + k\beta_r)} \right\} \quad (6)$$

where q is the vibratory displacement vector, t the time, x the coordinate along the engine axis, R the radius, θ the azimuthal angle of a reference sector ($0 \leq \theta < 2\pi/N$), q_0 the vibratory displacement vector of the reference sector, ω the angular vibration frequency, ζ the damping factor, β_r the interblade-phase-angle, N the number of blades and $k \in \mathbb{Z}$. Eq. 6 is the symbolic representation of the traveling-wave mode, where all the blades vibrate in the same way as their neighbour, but with a phase-difference one-from-another of β_r , and an amplitude varying as $e^{-\zeta\omega t}$ with time.

for every aeromechanical quantity F , where t is the time, x the coordinate along the engine axis, R the radius, θ the azimuthal angle, ω the vibration frequency, β_r the interblade-phase-angle, N the number of blades and $k \in \mathbb{Z}$.

There are 2 different ways for the numerical treatment of chorochronic periodicity, either the Time-Inclining (TI) method, introduced by Giles,^{1988,1990} or the Signal-Storage-and-Reconstruction (SSR) technique, introduced by Erdos & al.,¹⁹⁷⁷ and used by various authors either in vibrating cascades (e.g. Gerolymos,^{1988,1990a,1992a} He¹⁹⁸⁹) or in wake/rotor interaction (e.g. Hodson,¹⁹⁸⁵ Koya & Kotake,¹⁹⁸⁵ Lewis & al.¹⁹⁸⁹). This author has used the SSR technique, with storage of a discretized temporal signal and reconstruction using piecewise quintic interpolation.

3.4 $2\frac{1}{2}$ -D Euler Solver

A similar code has been developed for the $2\frac{1}{2}$ -D case, solving the blade-to-blade Euler equations,

$$\frac{\partial(\rho b R)}{\partial t} + \frac{\partial(\rho b R W_m)}{\partial m} + \frac{\partial(\rho b R W_u)}{\partial \theta} = 0 \quad (8a)$$

$$\frac{\partial(\rho b R W_m)}{\partial t} + \frac{\partial(\rho b R W_m^2 + b R p)}{\partial m} + \frac{\partial(\rho b R W_u W_m)}{R \partial \theta} = -p \frac{d(b R)}{dm} - \rho b (W_u + \Omega R)^2 \frac{dR}{dm} \quad (8b)$$

$$\frac{\partial(\rho b R W_u)}{\partial t} + \frac{\partial(\rho b R W_u W_m)}{\partial m} + \frac{\partial(\rho b R W_u^2 + b R p)}{R \partial \theta} = \rho b W_m (W_u + \Omega R) \frac{dR}{dm} \quad (8c)$$

$$\frac{\partial(\rho b R E)}{\partial t} + \frac{\partial(\rho b R E W_m + b R p W_m)}{\partial m} + \frac{\partial(\rho b R E W_u + b R p W_u)}{R \partial \theta} = 0 \quad (8d)$$

In practice, for reasons that will be discussed in detail in section 3.1 'Traveling-Waves', aerodynamic computations are done for a constant-amplitude traveling-wave vibration input. For such an input it is assumed (and has been verified through comparison with full annular cascade computations in Gerolymos^{1990b}) that the same chorochronic periodicity is found in the flowfield. Hence, computations are performed on a single channel, applying the following chorochronic periodicity conditions at the permeable pitchwise boundaries,

$$F(t, x, R, \theta) = F(t - k\omega^{-1}\beta_r, x, R, \theta + 2k\pi/N) \quad (7)$$

where t is the time, m is the meridional coordinate, θ is the azimuthal angle, $R(m)$ the radius of the streamsurface which is assumed axisymmetric, ρ the static density, p the static pressure, E the total energy ($E = e + (W_m^2 + W_u^2)/2 - (\Omega R)^2/2$), $W_m = \vec{W} \cdot \vec{e}_m$, $W_u = \vec{W} \cdot \vec{e}_u$, and $b(m)$ the streamsheet blockage. In the above Eq. 8, the assumption is made that b and R are not functions of time (viz. $b_t = 0$ and $R_t = 0$).

An earlier version of the code (cf. Gerolymos¹⁹⁸⁸) used MacCormack's explicit scheme (MacCormack¹⁹⁷¹) to solve the Euler equations. In the current version of the $2\frac{1}{2}$ -D code Ni's explicit scheme (Ni¹⁹⁸²) is used (the particular numerical implementation follows closely Gerolymos^{1990c}).

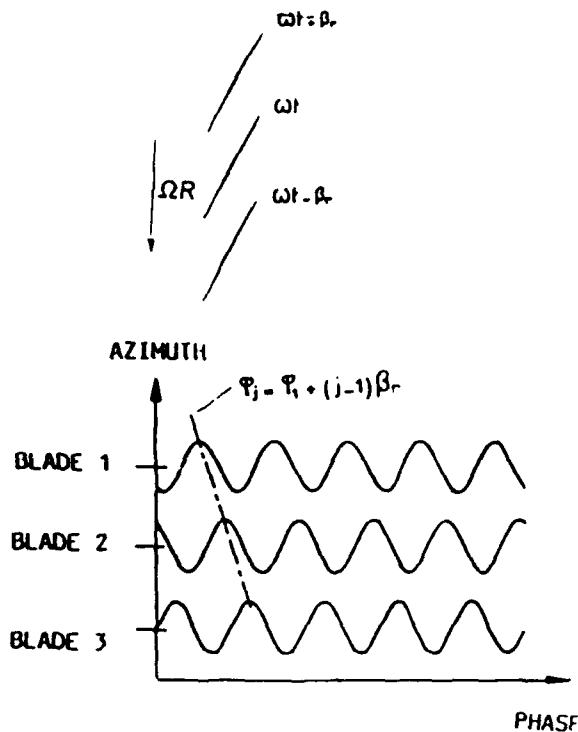


Fig. 6 Constant-Amplitude Traveling-Waves (CATW) chorochronic periodicity.

4 CHOROCHRONIC PERIODICITY & EULER METHODOLOGY

4.1 Traveling-Waves

It was noted in 3.3.8 that the aeromechanical eigenmodes of perfectly tuned bladed-disks are Variable-Amplitude Traveling-Waves (VATW) of the Eq. 6 type. If one was interested in simulating the entire N-blade rotor, a VATW vibratory motion (with positive or negative damping) could be applied to the blades, and its development followed in time. This would be the more interesting in view of coupling the aerodynamic computation with a structural one, as is at present becoming usual practice for aeroelastic computations over wings (e.g. Guruswamy,¹⁹⁸⁹ Bendiksen & Kousen¹⁹⁸⁷). In that case, as illustrated in (Fig. 7.), the amplitude of oscillation of any aeromechanical quantity will increase or decrease in time.

In practice, however, computations are done in a single channel, with chorochronic periodicity conditions on the permeable pitchwise boundaries. In view of Fig. 7, it becomes clear that damping, in the sense of amplitude modification from one period to the other, should be taken into account

when computing chorochronic periodicity conditions. If a linearized computation is made, this is trivial. It is not so, in the case of a general nonlinear (containing many harmonics) oscillation, unless one assumes that all harmonics are damped (with positive or negative damping) in the same way (or following some prescribed law). It is believed that chorochronic periodicity, in the case of VATW modes is an important field for further developments.

Current state-of-the-art is to compute separately the unsteady aerodynamic pressures, on the blade surface, by imposing a constant-amplitude traveling-wave vibration of the blades, in which case chorochronic periodicity in the sense of Eq. 7 and Fig. 6 applies. This kind of computation of Constant-Amplitude Traveling-Wave (CATW) has been presented by a number of authors for 2-D or $2\frac{1}{2}$ -D (e.g. Fransson & Pandolfi,¹⁹⁸⁶ Gerolymos,¹⁹⁸⁸ Kau & Gallus,¹⁹⁸⁹ He,¹⁹⁸⁹ Bendiksen¹⁹⁹⁰) and for 3-D (Gerolymos^{1990a,1990b}) methods. The basic justification of using CATW codes is that the characteristic time of the traveling-wave amplitude variation is much larger than the period of vibration (in other words that the damping ratio ζ is very small).

A note on bifurcation phenomena is in order here. Bendiksen¹⁹⁹⁰ discusses the case of a subsonic cascade, oscillating at large amplitudes, where the trailing-edge region becomes transonic for a part of the period, thus invalidating the classical Kutta condition used in linearized cascade theory (because of the change of wave-propagation structure in the supersonic region). This would be a serious problem for a linearized method because, as stated by

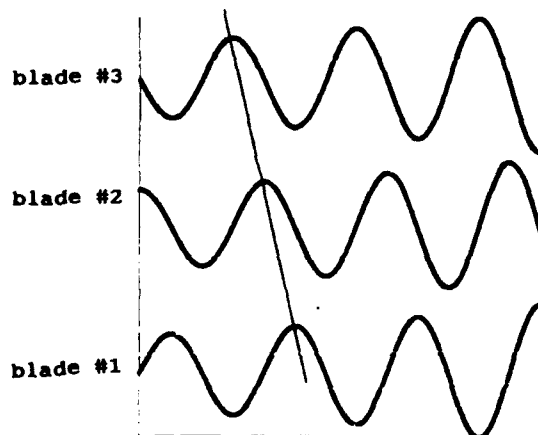


Fig. 7 Variable-Amplitude Traveling-Waves (VATW) quasi-periodicity.

within measuring accuracy the same as those obtained for a traveling-wave vibration. A numerical investigation by Gerolymos^{1990b} came to the same conclusions (cf. Fig. 11).

The computational interest of the influence-wave computation (IW) is the possibility to compare with experimental data obtained in the same type of configuration, i.e., as remarked by Fleeter & Jay,¹⁹⁸⁷ experiment and computation simulate exactly the same configuration.

4.3 Euler Solvers System

The Euler solvers that are used in this paper are summarized in Tab. 1. The MultiChannel method (MC) was developed for the study of modal superposition and unsteady periodicity. The Influence-Wave (IW) method was developed for comparing directly with experimental data obtained in an influence-wave setup. It should be noted that there is no particular gain in using an influence-wave computation for aeroelastic stability analyses, since the same results can be obtained by computing a limited number of traveling-waves, with the TW method, and analyzing the results to compute the influence coefficients.

5 SAMPLE RESULTS

This section is concerned with presenting typical results that can be obtained using the 3-D Euler equations in vibrating cascades (CATW computations). The rotor that will be considered is Fan A (cf. Tab. 2).

The measured compressor operating map is shown in Fig. 12. On the nominal speed line are shown 4 points computed with the 3-D Euler code (Gerolymos^{1990a}). If the computed points are plotted as π/π_{nominal} vs. $\dot{m}/\dot{m}_{\text{nominal}}$ and reported on the measured operating map the agreement of Fig. 12 is obtained, provided that the computed and measured nominal values are used for nondimensionalizing the computed and measured values, respectively. This conclusion is rather general on the nominal speed line, where the evolution π vs. \dot{m} is governed mostly by the evolution of the shock-waves system, meaning that the evolution of the flowfield near nominal speed is well predicted by Euler methods (although dimensional values are ~5% in error). In particular the success of the computation for the unstarted flow point 4, near the surge-line should be noted.

The steady-state isoMachs for the design point (point #3 in Fig. 12) are shown in Fig. 13. The flow is started with a strong in-passage shock-wave. The computed point is near stall, and the shock-wave has moved forward in the interblade-channel. Unsteady computations will be presented for the 3. mode, which, as shown in Fig. 14, is essentially torsional. At standard ISA conditions, at sea-level, and with 0 aircraft velocity, the corresponding vibration frequency is 707 Hz. Computations are performed for a number of periods, until the unsteady results (in the sense of pressure-harmonics) converge. Unsteady convergence was quantified by the error L2-norm

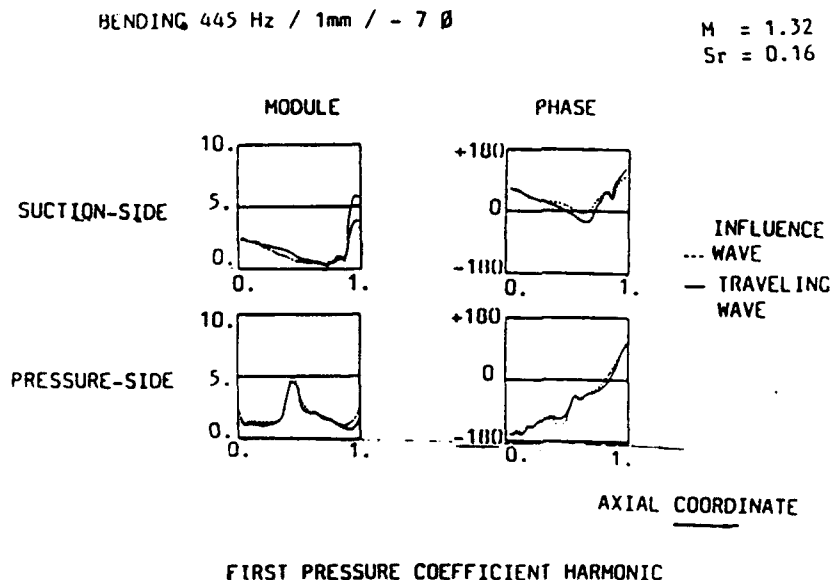


Fig. 11 Comparison of IW and CATW computations.

error =

$$\frac{1}{T S_B} \sqrt{\iint_{\partial B} dS \int_{t_0}^{t_0+T} dt \left\{ \frac{p(t) - p(t-T)}{p(t-T)} \right\}^2} \quad (6)$$

where t_0 is the time at the start of the period, T the vibration period, ∂B the blade surface of area S_B , and p the static pressure. The error is defined as the rms relative variation of pressure during the last vibration period. A typical result

of unsteady convergence is shown in Fig. 15. As a general rule engineering accuracy is obtained within 4 periods, and even sooner if only global results (aerodynamic damping) are required.

At the end of the simulation pressure-histories are post-treated to obtain pressure-harmonics on the blade surface, and, more importantly the mean-accumulated-power i.e. the mean value of the power accumulated by the blade, at every point of its surface, during one vibration period, defined by

Tab. 1 Euler Codes for Vibrating Cascades.

Methods	# of channels ¹	# of computations ²
2 $\frac{1}{2}$ D methods		
MultiChannel method (MC)	N	N
Traveling-Wave method (TW)	1	1
Influence-Wave method (IW)	7+9	N
3-D methods		
Traveling-Wave method (TW)	1	N

¹ for an N-blade rotor

² for 1 operating point and 1 blade-mode

Tab. 2 Rotors studied.

Case	Fan A	Fan C
# of blades	22	38
RPM at design point	9551.	4836.
part-span shroud	no	yes

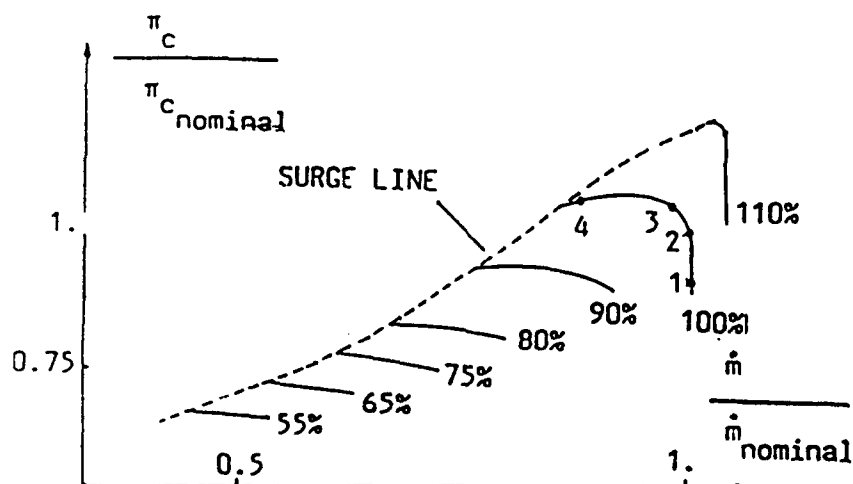


Fig. 12 Fan A operating map.

$$map(\vec{x}) = \frac{1}{T} \int_{t_0}^{t_0+T} p(t) \vec{V}(\vec{x}, t) \cdot \vec{n}(\vec{x}, t) dt \quad \forall \vec{x} \in \partial B \quad (10)$$

where map is the mean-accumulated-power, T the period, t_0 the time at the start of the simulated period, \vec{V} the velocity on the surface of the blade, and \vec{n} the normal to the blade's surface. The isomaps for torsional vibration at a 0-order ($\beta_r=0$) traveling-wave are presented in Fig. 16. It is evident that the mode studied is a very stable one.

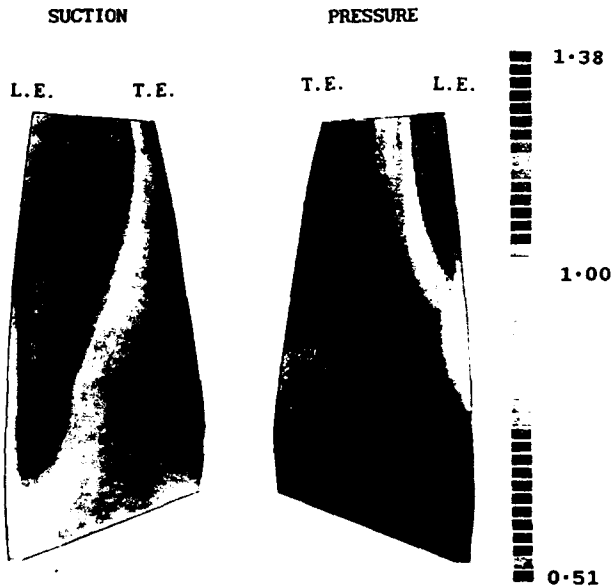


Fig. 13 Steady-state isoMachs on the blade-surface of Fan A.

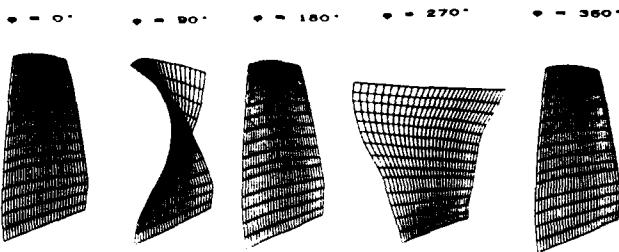


Fig. 14 Schematic representation of the 3. blade-mode of Fan A.

The stability assessment of a given configuration is obtained considering the aerodynamic damping, as defined by Carta,¹⁹⁶⁷

$$\delta_{aero} = - \frac{1}{4 f \overline{KE}} \iint_{\partial B} map dS \quad (11)$$

where δ_{aero} is the aerodynamic damping, f the

vibration frequency, and \overline{KE} the mean vibration kinetic energy of the blade. The evolution of δ_{aero} vs. β_r for the 4 operating points of Fig. 12, for vibration in the 3. mode (Fig. 14), is presented in Fig. 17.

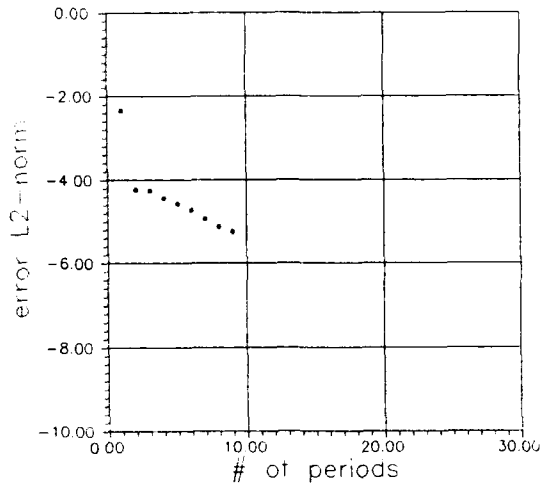


Fig. 15 Typical unsteady convergence plot.

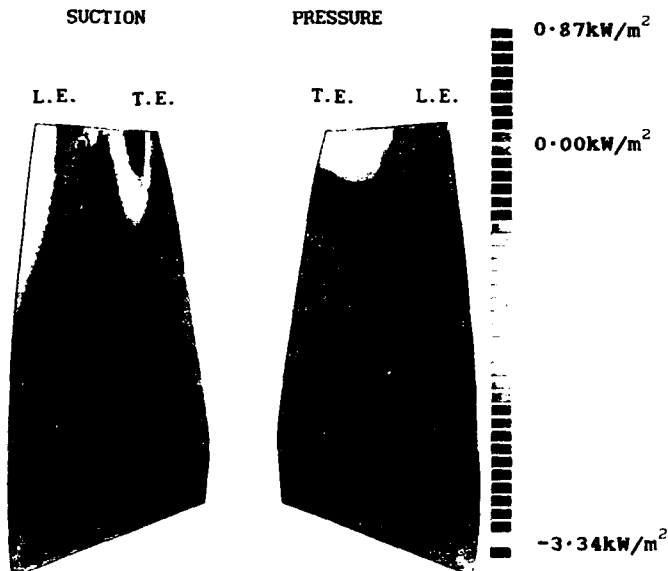


Fig. 16 Isomaps for the 0-order traveling-wave of the 3. mode of Fan A.

6 COUPLED 3-D AEROELASTIC ANALYSIS

6.1 Theory

The computations presented in section 4 'Sample Results' were purely aerodynamic. The vibratory mode was obtained by a finite-element code and was not modified by the unsteady aerodynamic forces. Consequently the use of these results for assessing the aeroelastic stability of a given configuration, is tantamount to assuming that the

eigenmodes computed taking into account centrifugal stiffening and steady aerodynamic loads, are not substantially modified by the fluctuating aerodynamic loads which are generated by blade vibration.

A typical time-marching Euler computation of the 3-D unsteady flow in a vibrating cascade requires $\sim \frac{1}{2}h$ on a CRAY-XMP computer. This computation is done for a given vibratory mode and a given interblade-phase-angle. If one were to use the 3-D Euler solver for computing a modal database, then for every interblade-phase-angle, N_{modes}^2 Euler computations are required, if N_{modes} modes are used for the modal projection. Hence for a typical $N_{\text{modes}} = 6$, 36 Euler computations would be required, resulting to unrealistic computing-times.

In order to circumvent this problem, a method of mode-modification during the time-marching iterations was developed (cf. Gerolymos^{1992b}). The basic idea is to compute the coupled eigenmode for a given β_r , by running only one unsteady 3-D Euler computation. The procedure is schematically described in Fig. 18. After computing the steady-state flowfield, the steady pressures are used for computing the steady aerodynamic loads, for use in the structural computation. The results of the structural computation generate a mechanical modal basis (mechanical* aeromechanical), identified by the couple,

$$\left\{ \begin{array}{l} \mathbf{M}(\ell, r) \quad | \quad 1 \leq \ell \leq N_{\text{modes}} \\ \quad \quad \quad | \quad 1 \leq r \leq N-1 \end{array} \right\} \quad (12)$$

where ℓ is the blade-mode number, N_{modes} the number of modes used for the subsequent modal synthesis, r the traveling-wave order defining the interblade-phase-angle β_r , N the number of blades. Based on the orthogonality of mechanical eigenmodes of different β_r (cf. Thomas,¹⁹⁷⁹ Lane¹⁹⁵⁶) the computation of the aeromechanical eigenmode $\mathbf{A}(\ell=m, r=n)$ uses the following modal basis,

$$\left\{ \begin{array}{l} \mathbf{M}(\ell, n) \quad | \quad 1 \leq \ell \leq N_{\text{modes}} \end{array} \right\} \quad (13)$$

At the end of the aerodynamic simulation of each period, of the aeromechanical mode $\mathbf{A}(m, n)$, the aeromechanical mode is reactualized by the contributions of the modes of Eq. 13, computed on the basis of the unsteady pressures generated by $\mathbf{A}(m, n)$. The details on the coupling relations are given in Gerolymos^{1992b}.

3rd MODE - / 707 Hz

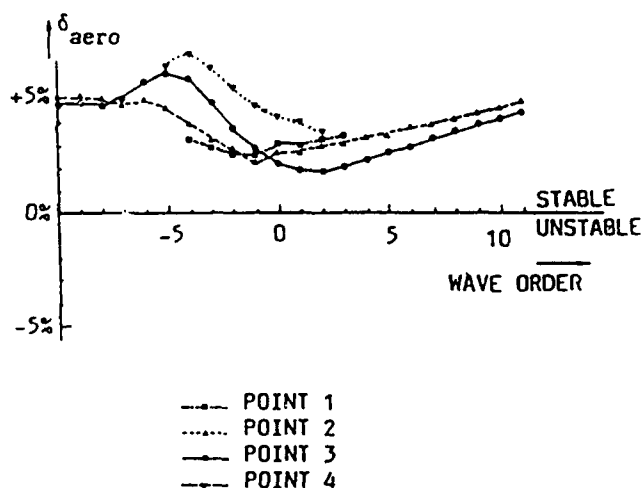


Fig. 17 Evolution of aerodynamic damping for Fan A.

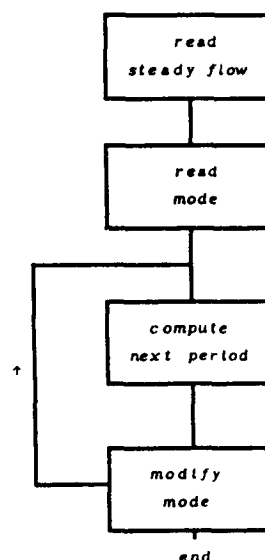


Fig. 18 Procedure for coupled aeromechanical computation.

6.2 Results

Results of the coupled aeromechanical method are given for Fan C (cf. Tab. 2), on the operating line at 107% speed. This fan has a part-span shroud, which was not taken into account into the aerodynamic simulations (it was however included in the mechanical model, where it has a great influence on vibration modes, as explained in the work of Carta¹⁹⁶⁷). Although the shock-waves system of the rotor is influenced by the part-span shroud, with important effects on efficiency (cf. Derrien¹⁹⁸⁶), it is not expected to substantially influence the unsteady aerodynamics of the vibrating cascade. The inclusion of the shroud

into the aerodynamic model will be the subject of a future study. The corresponding steady isoMachs are shown in Fig. 19, where one remarks, on the pressure-side, the penetration of the supersonic region down to the hub. In Fig. 20 are shown the isomaps for the 4. mode -4-order traveling-wave. This mode is marginally unstable, despite the existence of stabilizing peaks at the tip-sections ($\delta_{aero} \approx -0.44\%$). The participation of the other mechanical modes in the resulting aeromechanical mode is negligible, as may be seen in Tab. 3. The most important contribution (from mode #3, whose frequency is closest to mode #4) is $\sim 5\%$. This was found to be so for all the cases that were studied (for further results and discussion cf. Gerolymos^{1992b}).

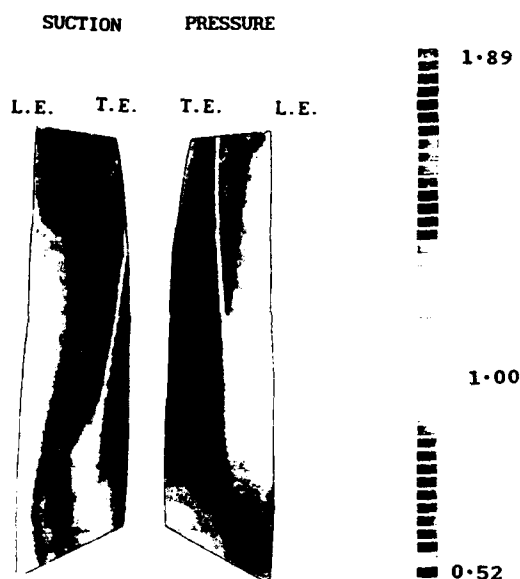


Fig. 19 Steady-state isoMachs on the blade-surface of Fan C.

7 ON THE VALIDATION OF TIME-NONLINEAR EULER METHODS

7.1 The Validation Problem

The problem of validating the methods presented herein for application to the prediction of aircraft engine flutter is twofold. Euler methods must be validated as to whether they are a representative model of the flowfield, and particular codes must be validated for eventual programming errors.

Unfortunately 3-D data are scarce, if not unavailable. A 3-D experimental database for turbomachinery flutter should contain accurate

Tab. 3 Coupled 4. aeromechanical mode for Fan C -4-order traveling-wave.

mode #	frequency	η
1	235. Hz	0.1%
2	408. Hz	0.7%
3	626. Hz	5.0%
4	688. Hz	100.0%
5	805. Hz	1.4%
6	901. Hz	0.7%

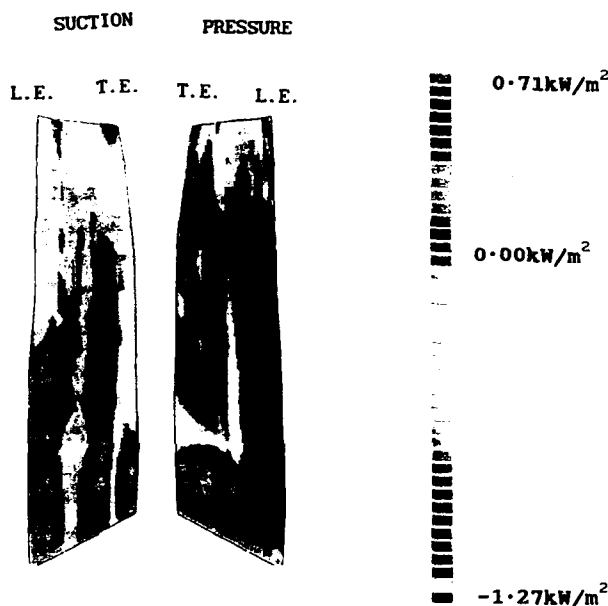


Fig. 20 Isomaps for the -4-order traveling-wave of the 4. mode of Fan C.

measurements of both vibratory modeshape of, and unsteady pressures on the blade. The only existing such data were those used by Halliwell & al.,¹⁹⁸⁴ for validating a stacked $2\frac{1}{2}$ -D time-linearized method derived from the steady method of Whitehead & Newton,¹⁹⁸⁵ but unfortunately these data (of insufficient resolution on the blades) are not available in the open literature (geometry + modeshapes + unsteady pressures). There exist however theoretical results by Namba & Ishikawa,¹⁹⁸² Namba,¹⁹⁸⁷ and Salaün.¹⁹⁸⁷ The comparison of Euler results with these theories has not yet been undertaken, and should be the subject of future research.

In order to assess the potential of Euler solvers, comparisons were undertaken with available theoretical and experimental results in 2 dimensions.

Tab. 4 Cascades studied

Case	Cascade A	Cascade B
# of blades in cascade	9	9
chord, mm	100.	100.
solidity	1.44	1.23
setting angle, deg	56.2	62.4
stagger angle, deg	33.8	27.6

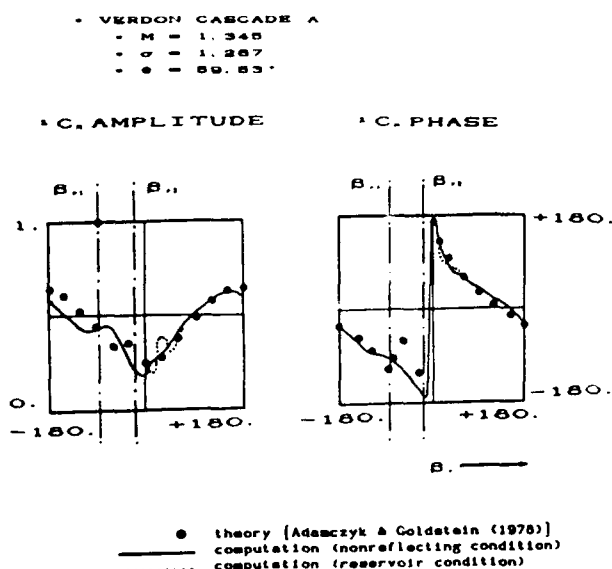


Fig. 21 Comparison of theory and numerical computations.

7.2 Comparison with Theory

By theoretical results are understood results obtained through analytical or semi-analytical methods, and consequently free of numerical errors (or at least with negligible numerical errors). A number of theories exist for flat-plate cascades (cf. Whitehead,¹⁹⁸⁷ Bendiksen,¹⁹⁹⁰ Gerolymos & al.¹⁹⁹⁰), producing virtually identical results. The comparison of these theories with Euler computations is described in Gerolymos & al.¹⁹⁹⁰ Results are presented in Fig. 21, for the so-called Verdon Cascade A, which is a typical test case for time-linearized theories and computations. It is a flat-plate cascade at 0 incidence, whose solidity is 1.267, and has a 59.53° setting-angle with respect to the axial direction. The inflow Mach number is 1.345. In Fig. 21 are plotted the amplitude and phase-angle of the first moment-coefficient harmonic $1C_M$ vs. interblade-phase-angle β_r , for torsional vibration around midchord at $Sr_x = 0.096$. The agreement between the Euler computations and the theory by

Adamczyk & Goldstein,¹⁹⁷⁸ is globally satisfactory, and computational results do not seem dependent on the upstream boundary condition used, insofar unsteady pressures on the blades are concerned. Nonetheless discrepancies occur at resonance, where despite the very good agreement in phase-angle the computation does not predict any amplitude-peak at resonance. Since theory is known to break down at resonance, it cannot be stated with certainty whether the computations are correct at resonance (neither that they are incorrect). It is believed that the issue of resonance in vibrating flat-plate cascade should be further investigated, and is the subject of current research.

7.3 Comparison with Experiment

Comparison of Euler computations with theory, for flat-plate cascades is important for validating the methods against simple, well documented configurations. It is as important to compare Euler results with experimental data from realistic configurations in order to determine with what confidence Euler results may be used in aeroelastic stability computations. Comparisons with experimental data from realistic transonic compressor cascades have been presented in Gerolymos,¹⁹⁸⁸ and Gerolymos & al.¹⁹⁹⁰

Sample results are presented for 2 cascades tested by ONERA (cf. Tab. 4). In Fig. 22 are presented the steady-state wall-Mach-number distributions for 3 operating points of ONERA Cascade A, Flow I being at low back-pressure, Flow II at nominal back-pressure and Flow III at high back-pressure (unstarted configuration). The agreement is in general satisfactory except at the shock-wave/boundary-layer interaction regions, as might be expected from any nonviscous method.

Comparisons for unsteady computations are presented in Fig. 23. These results are for the unsteady pressures on the vibrating blade, for an influence-wave setup. There is globally reasonably good agreement, with the exception of the phase-angle downstream the shock-waves, where the phase-shift introduced by the shock-wave/boundary-layer interaction is not predicted by the inviscid model. It should be noted that the best agreement is for the unstarted Flow III.

A global comparison is presented in Fig. 24, for an influence-wave setup of ONERA Cascade B. The computed and experimental imaginary part of the first harmonic of the moment coefficient are plotted against interblade-phase-angle. In both cases the moment coefficient for different interblade-phase-angles is reconstructed by superposition of the computed or measured influence coefficients. It is seen that the agreement is very satisfactory, and indeed much better than the agreement in detailed unsteady pressure distributions. In general, and from experience from other comparisons (cf. Gerolymos, 1988 Gerolymos & al. 1990) a $\pm 15\%$ (and often better) accuracy in stability predictions can be expected from Euler computations, in the supersonic flutter region.

7.4 Unanswered Questions & Validation Perspectives

For flows in vibrating cascades, the effort for the validation of Euler methods, and indeed of computational methods in general, is relatively new. The basic issues are:

7.4.1 Resonance: All linearized methods, both semi-analytical and numerical, present an erratic behaviour at resonance, or at least some local and sharp amplitude peaks. Preliminary numerical computations have shown no particular behaviour at

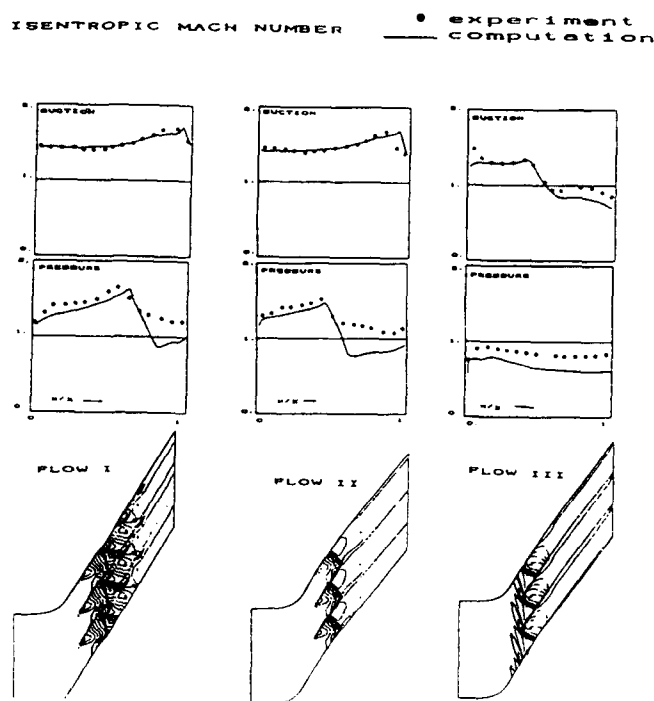


Fig. 22 Comparison of steady computed and experimental results.

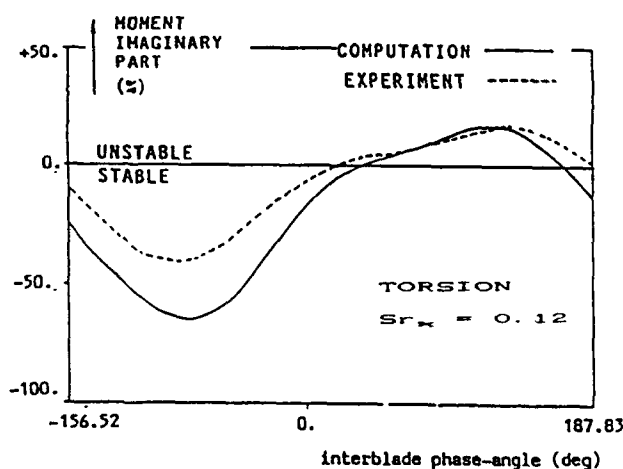


Fig. 24 Comparison of computed and experimental $\text{Im}(C_M)$.

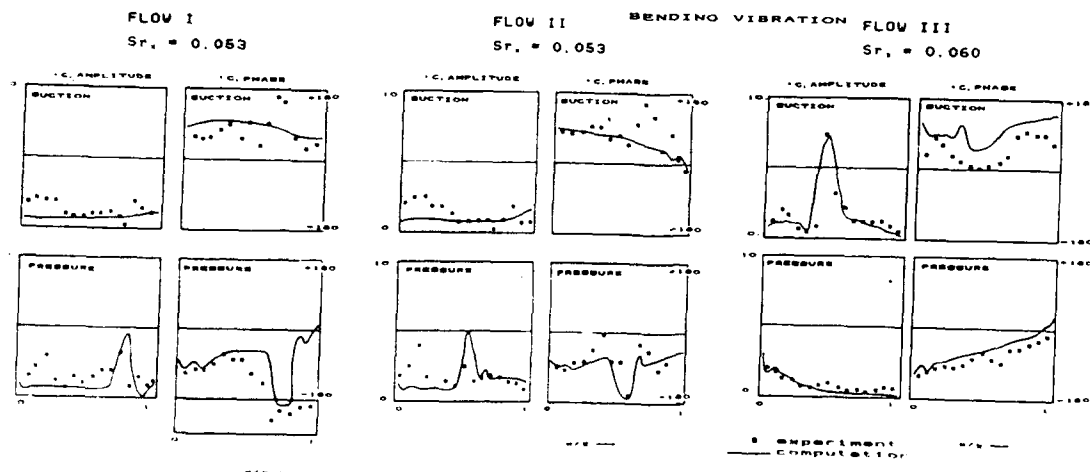


Fig. 23 Comparison of unsteady computed and experimental results.

resonance (Gerolymos & al.¹⁹⁹⁰). Further computations and theoretical studies are needed to clarify this matter.

7.4.2 3-D Effects: The evaluation of 3-D effects by comparing results from stacked $2\frac{1}{2}$ -D computations with those of a fully 3-D should be the subject of a future research.

7.4.3 3-D Code Validation: Although the comparison proposed in 7.4.2 could serve to this purpose, comparison with linearized 3-D theory (e.g. Namba & Ishikawa,¹⁹⁸³ Namba,¹⁹⁸⁷ Salaün¹⁹⁸⁷) should be undertaken in a future study.

7.4.4 Comparison with Experimental Data:

Comparisons with experimental data presented by various authors (e.g. Gerolymos,¹⁹⁸⁸ Kau & Gallus,¹⁹⁸⁹ Gerolymos & al.¹⁹⁹⁰) are encouraging. However a systematic comparison with the existing $2\frac{1}{2}$ -D database should be undertaken.

7.4.5 3-D Experimental Data Base: Well documented reliable 3-D measurements, combining blade vibration and unsteady pressures are not available in the literature. Although engine measurements are an ultimate goal, they are far too difficult to provide reliable data in the near future. Therefore, a simple wind-tunnel experiment, as the one described in Fig. 25 should be undertaken. In the absence of rotation precise 3-D blade vibration measurements are within present state-of-the-art capabilities, and such measurements are indispensable for code validation.

8 ON VISCOUS EFFECTS

As stated in the introduction, Euler methods are not an end to themselves, but a first step towards the development of viscous flow solvers. Several interesting works on Navier-Stokes solvers have appeared in the literature, mostly for blade-row-interaction problems (e.g. Jorgenson & Chima,¹⁹⁸⁹ Rai & Dring,¹⁹⁹⁰ Rai & Madavan,¹⁹⁹⁰ Krouthén & Giles¹⁹⁹⁰), and their extension to computations in vibrating cascades does not seem complicated. However, computing times are prohibitively large, especially taking into account the number of computations (operating-points \times blade-modes \times interblade-phase-angles) needed for aeroelastic stability prediction (which is just an emerging possibility for 3-D Euler solvers).

In view of this, although Navier-Stokes solvers

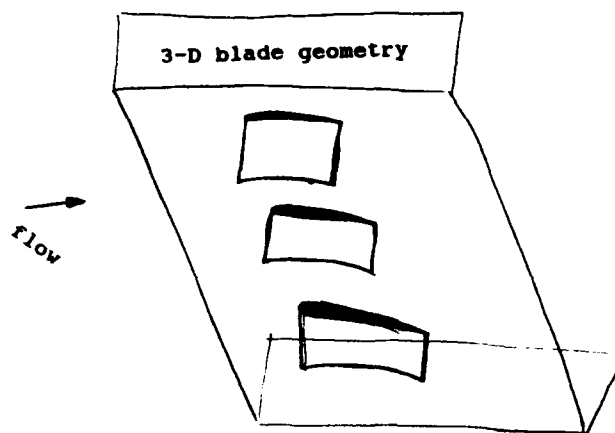


Fig. 25 Proposal of a 3-D aeroelastic test configuration.

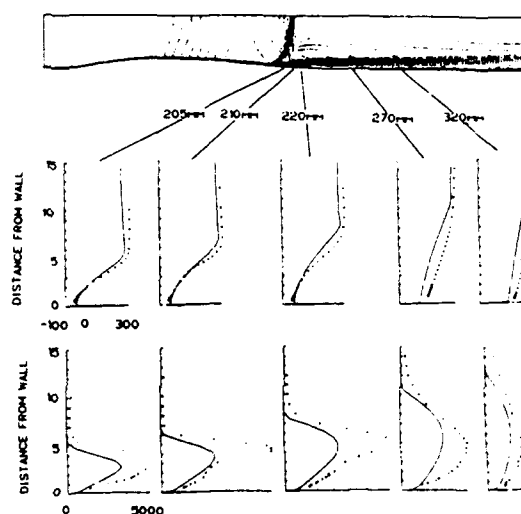


Fig. 26 Comparison of $k-\epsilon$ computations with experiment in channel flow.

development must be undertaken, faster methods, based on integral boundary-layer corrections of the Euler solvers are bound to play an important role in the development of predictive capabilities of aeroelastic stability. It is hoped that such methods will make possible the prediction of subsonic positive incidence flutter, where with the exception of the recently presented incompressible method of Sisto & al.,¹⁹⁸⁹ no computational method exists.

It is believed, however, that the parallel development of unsteady Navier-Stokes solvers, with advanced turbulence-transport closures is of equal importance. An example of preliminary (steady) work in this field is illustrated in Fig. 26, where are compared $k-\epsilon$ computations with measured data, for flow in a transonic channel (cf. Gerolymos^{1990c}). The agreement is certainly not perfect (but much better than inviscid model predictions). In view of such turbulence-modeling

problems Denton¹⁹⁹⁰ has stated that 'in the complex turbomachinery environment the accuracy of such viscous calculations is severely limited by the limitations of turbulence modelling so that at present only qualitatively accurate results can be obtained from even the most sophisticated turbulence models'. However this author feels that the development of solvers using such sophisticated, computationally expensive, and yet inaccurate turbulence models is necessary for their evaluation, and subsequent modification.

9 CONCLUSIONS & DISCUSSION

A coupled 3-D aeroelastic computation, based on a 3-D Euler solver and a mode-modification technique, was described. Despite a number of unanswered questions, it is argued that 3-D Euler

solvers in vibrating cascades is a well developed analysis tool. Interest should be focussed on the development of viscous flow solvers, both for improving accuracy of stability analysis in the supersonic flutter region, and, more importantly, for predicting subsonic stall flutter.

ACKNOWLEDGMENTS

The studies on turbomachinery aeroelasticity for the development of *MANIAC-1* (Gerolymos^{1990a}) and *MANIAC-2* (Gerolymos^{1992a,1992b}) were financed by *SNECMA*. The present paper is published with the permission of *SNECMA*. Special thanks are due to Alex Ribère of *SNECMA-Villaroche* who made available the graphics software for postprocessing the results in Gerolymos^{1992a,1992b} and to J.P. Mascarel of *SNECMA-Villaroche* who provided the *SAMCEF* results.

REFERENCES

- ACTON E. & NEWTON S.G. *AGARDograph* 298 (1987) 6-1-6-21
 ADAMCZYK J.J. & GOLDSTEIN M.E. *AIAA J.* 16 (1978) 1248-1254
 AMIET R.K. *AIAA J.* 28 (1990) 1718-1727
 BENDIKSEN O.O. & KOUSEN K.A. *AIAA Paper* 87-0911 (1987)
 BENDIKSEN O.O. *J. Propulsion Power* 4 (1988) 164-171
 BENDIKSEN O.O. *AIAA Paper* 90-1157 (1990)
 BISPLINGHOFF R.L. & ASHLEY H. *Principles of Aeroelasticity* (1962)
 BÖLCS A. & al. *AGARD Conf. Proc.* 468 (1989) 5-1-5-19
 BROCHET J. *Rech. Aérop.* 1980-5 (1980) 301-315
 BUFFUM D.H. & FLEETER S. *J. Phys.* III (1992) to appear
 CAMBIER L. & al. *Rech. Aérop.* 1985-3 (1985) 181-186
 CAMBIER L. & al. *Rev. Franç. Méc.* 1988-4 (1988) 11-26
 CARTA F.O. *ASME J. Eng. Power* 89 (1967) 419-426
 CHAPIN V. *Doct. Diss. Université Pierre & Marie Curie* (1992) in progress
 CRAWLEY E.F. *AGARDograph* 298 (1988) 19-1-19-24
 CRIGHTON D.G. *Ann. Rev. Fluid Mech.* 17 (1985) 411-445
 DENTON J.D. *ASME Paper* 90-GT-19 (1990)
 DERRIEN T. *AGARD Conf. Proc.* 401 (1986) 14-1-14-15
 DOWELL E.H. & al. *AIAA J.* 21 (1983) 38-46
 DUMAS M. *Doct. Diss. Université Pierre & Marie Curie* (1992) in progress
 EPSTEIN A.H. & al. *AIAA J.* 17 (1979) 375-379
 ERDOS J.I. & al. *AIAA J.* 15 (1977) 1559-1568
 FLEETER S. *AIAA J.* 18 (1980) 497-503
 FLEETER S. & JAY R.L. *AGARDograph* 298 (1987) 8-1-8-18
 FRANSSON T.H. & PANDOLFI M. *ASME Paper* 86-GT-304
 FRANSSON T.H. *ASME Paper* 90-GT-225
 GEROLYMOS G.A. *AIAA J.* 26 (1988) 1483-1492
 GEROLYMOS G.A.^a *Int. J. Turbo Jet Eng.* 7 (1990) (a.e. *ASME Paper* 88-GT-255)
 GEROLYMOS G.A.^b *Int. J. Turbo Jet Eng.* 7 (1990) (a.e. *ASME Paper* 88-GT-136)
 GEROLYMOS G.A.^c *AIAA J.* 28 (1990) 1707-1717
 GEROLYMOS G.A. & al. *ASME Paper* 90-GT-373 (1990)
 GEROLYMOS G.A.^a *ASME 1992 Gas Turbine Conference* (1992) in writing
 GEROLYMOS G.A.^b *ASME 1992 Gas Turbine Conference* (1992) in writing
 GILES M.B. *J. Propulsion Power* 4 (1988) 356-362
 GILES M.B. *J. Propulsion Power* 6 (1990) 621-627
 GIRAULT J.P. *Rech. Aérop.* 1984-1 (1984) 57-66
 GOTTLIEB D. & TURKEL E. *J. Comp. Phys.* 26 (1978) 181-196
 GURUSWAMY G.P. *AIAA J.* 27 (1989) 788-793
 HALL K.C. & CRAWLEY E.F. *AIAA J.* 27 (1989) 777-787
 HALLIWELL D.G. & al. *ASME J. Vibr. Acoust. Rel. Des.* 106 (1984) 198-203
 HANAMURA & al. *Bull. Jap. Soc. Mech. Eng.* 23 (1980) 880-887
 HE L. *ASME Paper* 89-GT-279 (1989)
 HEDSTROM G.W. *J. Comp. Phys.* 30 (1979) 222-237
 HENRY R. *J. Méc. Appl.* 4 (1980) 61-82
 HENRY R. & FERRARIS G. *ASME J. Eng. Gas Turb. Power* 106 (1984) 2-10
 HENRY R. & VINCENT B. *Bull. Soc. Franç. Méc.* 1990-1 (1990) 23-32
 HODSON H.P. *ASME J. Eng. Gas Turb. Power* 107 (1985) 337-344

- HUSSAINI M.Y. *Lect. Notes Phys.* 323 (1989) 3-17
 JAMESON A. & al. *AIAA Paper* 81-1259 (1981)
 JORGENSEN P.C.E. & CHIMA R.V. *AIAA J.* 27 (1989) 743-749
 KARADIMAS G. *ASME J. Turbom.* 110 (1988) 419-425
 KAU H.P. & GALLUS H.E. *AGARD Conf. Proc.* 468 (1989) 2-1-2-10
 KERREBROCK J.L. *AIAA J.* 19 (1981) 4-19
 KIELB R.E. & RAMSEY J.K. *ASME J. Turbom.* 110 (1989) 462-467
 KOYA M. & KOTAKE S. *ASME J. Eng. Gas Turb. Power* 107 (1985) 945-952
 KROUTHÉN B. & GILES M.B. *J. Prop. Power* 6 (1990) 769-776
 LANE F. *J. Aero. Sci.* 23 (1956) 54-66
 LANE F. *J. Aero. Sci.* 24 (1957) 65-66
 LAX P.D. *Comm. Pure Appl. Math.* 8 (1954) 159-193
 LAX P.D. *Comm. Pure Appl. Math.* 10 (1957) 537-566
 LEWIS J.P. & al. *ASME J. Turbom.* 111 (1989) 387-393
 LUBOMSKI J.F. *NASA Tech. Mem.* 79805 (1979)
 LUBOMSKI J.F. *NASA Tech. Mem.* 81500 (1981)
 MacCORMACK R.W. *Lect. Notes Phys.* 8 (1971) 151-163
 McCROSKEY W.J. *ASME J. Fluids Eng.* 99 (1977) 8-30
 MORETTI G. *Phys. Fluids* 12 (1969) 11-13-11-20
 NAMBA M. & ISHIKAWA A. *ASME J. Eng. Power* 105 (1983) 138-146
 NAMBA M. *AGARDograph* 298 (1987) 4-1-4-30
 NI R.H. *AIAA J.* 20 (1982) 1565-1571
 OLLSON P. & JOHNSON S.L. *J. Sci. Comp.* 4 (1989) 159-195
 PULLIAM T.H. *AIAA J.* 24 (1986) 1931-1940
 PULLIAM T.H. *Appl. Num. Math.* 2 (1986) 441-474
 RAI M.M. & DRING R.P. *J. Prop. Power* 6 (1990) 276-282
 RAI M.M. & MADAVAN N.K. *ASME J. Turbom.* 112 (1990) 377-384
 SALAS M.D. *AIAA J.* 14 (1976) 583-588
 SALAÜN J.P. *AGARDograph* 298 (1987) 5-1-5-17
 SATYANARAYANA B. & DAVIS S. *AIAA J.* 16 (1978) 125-129
 SEARS W.R. *AIAA J.* 14 (1976) 216-220
 SITO F. *AGARDograph* 298 (1987) 1-1-1-13
 SITO F. & al. *AIAA J.* 27 (1989) 455-461
 S ECHENYI E. *AGARDograph* 298 (1987) 10-1-10-16
 THOMAS D.L. *Int. J. Num. Meth. Eng.* 14 (1979) 81-102
 THOMPSON K.W. *J. Comp. Phys.* 68 (1987) 1-24
 THOMPSON K.W. *J. Comp. Phys.* 89 (1990) 439-461
 VAVRA M.H. *Aerothermodynamics and Flow in Turbomachines* (1960) 107-132
 VERDON J.M. *AGARDograph* 298 (1987) 2-1-2-31
 VERDON J.M. *J. Phys. III* (1992) to appear
 VENKATKRISHNAN V. & JAMESON A. *AIAA J.* 26 (1988) 974-981
 WHITEHEAD D.S. & NEWTON S.G. *Int. J. Num. Meth. Fluids* 5 (1985) 115-132
 WHITEHEAD D.S. *AGARDograph* 298 (1987) 3-1-3-30
 WILLIAMS M.H. *AIAA J.* 17 (1979) 394-397
 WILLIAMS M.H. *AIAA J.* 18 (1980) 615-624
 WOOD J.R. & al. *ASME J. Turbom.* 110 (1988) 270-279



APPLICATION OF CFD IN THE DESIGN OF GAS TURBINE ENGINE COMPONENTS

by

Arun K. Sehra, Mohamed A. Abolfadl and Mohamed G. Zedan

Textron Lycoming
550 S. Main Street
Stratford, CT 06497
United States

ABSTRACT

The primary focus of this paper is to illustrate the application of three-dimensional viscous procedures for optimizing the turbomachinery component geometry. Specific cases presented in the paper include the application of three-dimensional viscous analyses to a transonic axial compressor rotor, a splintered axial compressor rotor, a turbine rotor, and an exhaust mixer-nozzle. Application of an axisymmetric Navier Stokes solver to the inlet particle separator, and a two-dimensional inverse design procedures for customizing compressor airfoil geometry are also briefly included.

NOMENCLATURE

C_p	Pressure coefficient
H	Inlet Particle Separator width
L	Inlet Particle Separator length
M	Mach number
p_a	ambient pressure
P_t	total pressure
R	outer radius
T_t	total temperature
T_{t1}	total temperature at inlet
V	velocity
X	axial distance
y, Y	radial distance
μ	particle size
Subscript	
avg	average value
a	ambient
abs	absolute value
c	core flow (engine flow)
f	fan flow (bypass flow)
t	total

92-16078



1. INTRODUCTION

The trend in the aircraft power plants is towards energy efficient, compact, lightweight systems. In terms of the propulsion parameters, the goal is to increase the thermal efficiency (lower specific fuel consumption), the specific power (power per unit airflow), and the specific weight (power per unit weight of the engine). Whereas the thermal efficiency of a gas turbine engine is a direct function of the overall cycle pressure ratio and thermodynamic efficiencies of individual components, the specific power primarily depends on the overall cycle temperature. High strength, lightweight materials, and reduced number of turbomachinery stages are the primary elements for achieving higher specific weight. A key technology area for achieving higher aerodynamic efficiency of individual components and increased average stage pressure ratio (fewer stages) is the use of advanced Computational Fluid Dynamics (CFD) methods in the aerodynamic design process. This is the basic focus of this paper.

During the past decade, the use of Computational Fluid Dynamics for understanding the complex flowfield prevailing in the gas turbine engine has dramatically increased. The result is that a number

of fully three-dimensional Navier Stokes solvers have reached a degree of sophistication that can make them potential design tools for future engines. With the advent of high speed super computers, the possibility of routinely applying fully three-dimensional Navier Stokes solvers to complex gas turbine engine component geometries is within reach. Unfortunately, most of the schemes that are currently used in the industry suffer from several inherent problems. These include lack of code robustness, user unfriendly system, and slow convergence rate. Consequently, the application of these codes has been limited to the role of research tools for CFD experts. The primary thrust at Textron Lycoming in the CFD area is to address these limitations, thereby changing the role of these advanced analytical procedures from research tools to design tools.

Currently, the use of two and three-dimensional Navier Stokes solvers is restricted to the flow analysis mode wherein a designer specifies the component geometry along with inlet/exit flow conditions, and the code computes the internal flowfield. For application of these procedures in the design process, a designer has to iteratively optimize the component geometry to achieve the desired level of performance. This is a cumbersome process and its effectiveness strongly depends on the background and experience level of the designer.

More recently, Textron Lycoming has started concentrating on another approach which has come to be known as "inverse design technique". In this type of scheme one prespecifies an optimum flow distribution and the code generates a geometry that will produce the prespecified flow. Currently, the application of inverse design procedures is restricted to two-dimensional inviscid and inviscid-viscous modes. In the latter technique, an inverse boundary layer calculation is coupled with an inverse Euler calculation. A two-dimensional inverse blade-to-blade design method when coupled with an inverse meridional flow calculation [1] provides an inverse quasi three-dimensional system which can be used to generate an airfoil shape reasonably close to the final optimum geometry. Another advantage of using an inverse design scheme is that it can generate geometries that cannot be evolved with conventional evolutionary logic.

This paper is intended to illustrate the application of a number of Navier Stokes solvers to various gas turbine engine components. Selection of these solvers was based on their meeting the criteria for use as design tools. Also, to emphasize the inherent benefit of inverse design procedures, an illustration of the application of a two-dimensional inverse design scheme to a stator airfoil is included in this paper. Table 1 summarizes the test cases presented in this paper.

TEST CASE	COMPONENT	TYPE OF CODE	REFERENCE
1	Transonic Compressor Rotor	3-D Viscous-Implicit	9
2	Splittered Rotor	3-D Viscous-Implicit	9
3	Turbine Rotor	3-D Viscous-Implicit 3-D Viscous-Explicit	9 3
4	Exhaust Mixer-Nozzle	3-D Viscous-Implicit	16
5	Inlet Particle Separator	Axisymmetric Viscous-Implicit	26
6	Compressor Stator	Inverse Design-Inviscid	31

2. TURBOMACHINERY ROTORS

Integration of the three-dimensional viscous analysis codes into the turbomachinery engineering design/analysis process has been a major concern of many research institutions and industry in the recent past. Extensive code validation against experimental data is required before relying on these codes in the turbomachinery design process. Two three-dimensional Navier Stokes codes, which have reached the desired degree of sophistication for qualifying as design tools, are reviewed here. These codes have been successfully applied to a series of advanced turbomachinery stages, and the predicted flowfield compared against detailed experimental data. The test cases reviewed here include (a) a high tip speed, highly loaded transonic compressor rotor, (b) a high work turbine rotor, and (c) a 3:1 pressure ratio splitter axial compressor rotor. The first two were designed and tested at Textron Lycoming; the splitter rotor [2] was designed and tested at the Air Force Aeronautics Research Laboratory.

Codes Description

LYCVIS3D: This code was developed at Textron Lycoming by Subramanian and Bozzola [3]. It is based on an explicit, four-stage Runge-Kutta integration scheme originally proposed by Jameson et al [4]. It solves the Reynolds averaged time dependent three-dimensional Navier Stokes equations in stationary/rotational cylindrical coordinates and uses the Baldwin-Lomax algebraic eddy viscosity turbulence model [5]. LYCVIS3D has been successfully run for a variety of compressor and turbine cascades and the predictions are in very good agreement with available test data [6-8].

BTOB3D: Textron Lycoming has acquired a three-dimensional viscous code, BTOB3D, developed by Dawes [9] at Cambridge University, England. This code is extensively used in the industry. The numerical scheme, a new efficient implicit time marching algorithm similar to the Beam-warming algorithm [10], is used to solve the Navier Stokes equations for compressible flows with an in-built multigrid algorithm to enhance the convergence rate. It also uses the Baldwin-Lomax turbulence model. The current version of

this code is highly versatile and can be applied to turbofan bypass geometry, splittured rotors, and full turbomachinery stages.

Boundary Conditions

A variety of boundary conditions are employed in these codes. At the inflow, the absolute total pressure, total temperature, and the absolute flow angle are fixed. For the other numerical condition required at the inflow, the left running Riemann invariant, or the static pressure is extrapolated from the interior. At the outflow, the hub static pressure is specified. The radial distribution of the static pressure is calculated using the radial equilibrium condition. The rest of the variables are extrapolated from the interior points.

For the cell adjacent to solid boundaries, zero flux condition is imposed. Wall static pressure is calculated by using the normal momentum equation. The no slip condition is specified on the wall for evaluating wall velocities. Periodic boundaries are treated as interior points in the calculation.

Application of these codes to a transonic compressor rotor, a high work turbine rotor, and a splittured axial compressor rotor will be presented below.

Transonic Compressor Rotor

To meet the challenge of the next generation compact compressors, Textron Lycoming has designed and developed a series of axial compressor rotors with design pressure ratios ranging from 2.0:1 to 2.6:1. Design features that characterize these highly loaded transonic rotors include very low aspect ratio (0.5-1.0) and very high tip speed (1500-1700 ft/sec). Both swept and unswept airfoils have been analytically and experimentally evaluated. The flow field through these rotors comprises several complex flow phenomena including three-dimensional shock, shock boundary layer interaction, and secondary flows due to tip clearance and endwall boundary layer.

The test case presented here is the first stage rotor (Figure 1) of a multistage axial compressor. This is an unswept rotor having an aspect ratio below 0.8 and a design tip speed in excess of 1650 ft/sec; the design pressure ratio is higher than 2.4:1 (for proprietary reasons, actual design numbers are not given here). Dawe's three-dimensional viscous code, BTOB3D, was applied to this stage using a 31x85x31 nodes computational grid, shown in Figure 2. The results presented here correspond to the peak efficiency operating point, which happens to be very close to the design point of this rotor.

Figure 3 shows a tangentially mass averaged spanwise distribution of total pressure ratio at design point. Predicted results are in excellent agreement with experimental data in the region of 15 to 85 percent span. The code, however, slightly over predicts the pressure ratio near the tip and under predicts in the hub region. A comparison between the computed total temperature ratio and experimental data is presented in Figure 4. It is interesting to note that the code underpredicts the total temperature ratio over the entire span. This discrepancy in temperature is expected because the rotor exit temperature was measured at the stator leading edge, where the presence of the stator exerts a local throttling effect causing the work to increase. The phenomenon of the circumferential variation of the rotor exit temperature caused by the downstream stators is discussed in detail in Reference [11].

Mach number contours at midspan section for near design and near stall conditions are illustrated in Figure 5. Near the design condition, the flow is characterized by an oblique shock followed by slow diffusion, but close to the stall, the flow is dominated by a strong normal shock upstream of the blade leading edge.

High Work Turbine Rotor

This high work turbine was designed and tested at Textron Lycoming. The flow field in this turbine is highly three-dimensional with high exit Mach number and large flow turning.

Both LYCVIS3D and BTOB3D were applied to this turbine rotor and the flowfield was computed for 120 percent, 100 percent and 80 percent of design rotational speeds. The results for the 80 percent speed case, for which test data is available, are presented here in detail. The experimental evaluation was conducted at cold similarity test conditions with rotor inlet temperature of 710°R and a mass flow rate of 3.2 lb/sec. The exit relative Mach number at this operating condition is about 1.07.

A computational grid of 31x85x31 nodes (Figure 6) in pitchwise, streamwise, and spanwise directions respectively, was used for both LYCVIS3D and BTOB3D codes. The inlet boundary conditions were based the measured total pressure and flow angles downstream of the isolated stator. The next two figures (Figures 7 and 8) present radial distributions of tangentially mass averaged values at an axial station located at approximately 50 percent of the axial chord downstream of the rotor. Figure 7 shows the exit total pressure normalized with respect to the average exit total pressure. The LYCVIS3D code demonstrates better agreement with data near the hub. However, near the tip, BTOB3D code is in better agreement with data. The predicted absolute Mach numbers, shown in Figure 8, are in good agreement with experimental data, except near the hub.

Figure 9 illustrates the meridional projection of the velocity vector in proximity of the blade suction surface. A clockwise vortex is seen upstream of the intersection of the hub and blade leading edge. A larger counter clockwise vortex is seen upstream of the intersection of the shroud and blade leading edge. These are typical turbine endwall phenomena: the initial boundary layer rolls up and forms the horseshoe vortices. The detailed physical explanation of this endwall phenomenon was described by Langton's measurement [12]. Inside the blade passage, the inward motion of the boundary layer flow from the walls toward mid-span is quite evident. The mechanism for the accumulation of the losses at mid-span downstream of the rotor is the strong secondary flow system that develops in the high

turning (about 110°) rotor blading. The general agreement with the test data gives confidence in the trend of the secondary flow pattern established by the calculation. The secondary velocity vectors for the cross flow plane, at approximately 10 percent chord downstream of the rotor trailing edge, is presented in Figure 10. The primary flow direction is assumed to follow the streamwise grid lines, and the secondary velocity is the velocity component perpendicular to the primary flow direction. The two strong passage vortices which dominate the secondary flow can be clearly seen in these figures. The secondary flow features were described in detail by Sieverding [13]. The total pressure loss contours corresponding to this location are given in Figure 11. As result of the secondary flows, the maximum loss accumulates in the mid span region.

Splittered Axial Compressor Rotor

Incorporation of partial vanes (splitters) between the principal rotor airfoils is a technique for achieving very high pressure ratios with minimum efficiency penalty. It helps to control the trailing edge separation without having to pay a very heavy penalty associated with increased solidity when a full length airfoil is used. It also ensures that the flow capacity of the blade (which is controlled by the entrance region) will not be compromised since the solidity in the entrance region is not increased. A three-dimensional viscous analysis is an essential step in the design of a highly loaded blade row such as a splattered rotor. Some of the flow phenomena that need to be closely examined from viscous solutions include the boundary layer growth, shock/boundary layer interaction, shock structure, flow capacity, and potential areas of flow separation.

Wennerstrom's 3:1 pressure ratio splattered rotor [2], shown in Figure 12, was analyzed using BTOB3D code. A $21 \times 85 \times 19$ grid was used for this analysis. Results from this analysis were compared with those obtained from Denton's 3-D inviscid analysis [14] to demonstrate the importance of 3-D viscous effects. These results were also compared with global test performance provided by Wennerstrom [15].

Figures 13 and 14 show the Mach number contours and velocity vectors on a blade-to-blade plane near hub, near mid, and near tip sections, respectively. The corresponding Mach number contours computed by Denton's inviscid code are shown in Figure 15. At all sections, a weak oblique shock from the leading edge of the principal blade is predicted. In the splitter vane region, an oblique shock is seen followed by a passage normal shock on the splitter vane suction surface. On its pressure surface, a normal shock from the leading edge is observed. This shock structure is qualitatively similar to that predicted by the three-dimensional inviscid code. However, near the tip section (Figure 13), a huge separation occurs on the principal blade suction surface immediately downstream of the splitter leading edge shock, which has moved upstream of the splitter leading edge. This separation could be induced by the shock or could be due to the excessive diffusion rate in that channel. In either case, this important aspect cannot be predicted by an inviscid analysis. The experimental data taken at the Air Force Aeronautical Research Lab [15] confirmed significantly lower work and efficiency (as compared with design intent) from mid-span to the tip region of the rotor.

3. EXHAUST MIXER-NOZZLE

Significant performance gains (thrust and SFC) can be achieved in turbofan engines at various flight conditions, including cruise, by mixing the hot core stream with the cooler fan stream prior to expansion through the exhaust nozzle. Theoretical thrust gain (complete mixing with minimum losses) is primarily dependent on the temperature ratio between the core and fan streams. The actual performance gain, however, is lower because of the incomplete mixing, and total pressure losses associated with the mixing process and wall friction. The challenge, therefore, is to design a mixing system that can achieve adequate mixing, with low total pressure loss. A lobed type of forced mixer (Figure 16) has been found to be most successful in achieving these goals. An efficient design of such a mixer strongly depends on our ability to compute the detailed flow field in the mixer and exhaust system. The test case presented here represents a mixer-nozzle system for Textron Lycoming LF500 series engines. Relationship of this mixer to the engine flow path is shown in Figure 17.

Two robust and versatile computational procedures were employed for solving the complex three-dimensional viscous flows in the entire mixer-nozzle of a turbofan engine. A basic solver [16] developed by Severdrup Technology (known as PARC-3D) was combined with a NASA LeRC developed code for grid generation [17] (known as INGRID).

Solver

A modified version of the PARC-3D code was used for computing the complex flow field of the high bypass ratio turbofan mixer. It is a general purpose Navier Stokes solver which was developed by Severdrup Technology, Inc., and is capable of solving combined internal and external flows. The basic algorithm is based on the NASA Ames ARC-3D code [18]. The major advantage of PARC-3D is its flexibility, through the use of grid patches and boundary segments, to compute flows through complex geometries with specified boundary conditions. The code uses the Beam-Warming appropriate factorization algorithm [10] and Pulliam's Scalar pentadiagonal transformation to produce a steady-state solver [19]. For turbulent flows, the code uses the Thomas formulation [20] of the Baldwin and Lomax model [5], which has demonstrated good simulation for free shear layers [21].

Computational Grid

The computational domain considered in this analysis is shown in Figure 17 and labeled as forced mixer. Flow symmetry and geometric periodicity require a solution only for a sector comprising half a lobe of the mixer. This computational sector is shown in Figure 18. A $70 \times 35 \times 30$ (X,R, θ) grid which represent 73,500 mesh points was used. Figure 19, shows a picture of this grid. This body fitted

grid was generated, packed and passed through an elliptic smoother by using INGRID-3D [17] computer code.

Boundary Conditions

The boundary conditions at flow inlet are the prescribed total pressure and total temperature for both core and fan flows. At the exit station, static pressure was specified. Symmetry boundary conditions were assumed along the edges of the half-lobe sector. Walls were treated as adiabatic surfaces with no slip. At the nozzle exit plane, an extra constant-area downstream duct was added to accommodate the zero-gradient condition across the outlet.

Comparison with Experimental Data

The above computational procedure was applied to a 12 lobed mixer design, which was subsequently fabricated and tested at Fluidyne Engineering Corporation.

The predicted total temperature distribution was in close agreement with the measured values. This is illustrated for three different angular locations at the nozzle exit plane in Figure 20. The predicted total temperature contours at the same plane are presented in Figure 21. As seen, these contours are able to reproduce the mushroom-shaped hot spike depicted experimentally in References [22] and [23] and analytically in References [24] and [25].

Figure 22 shows the predicted secondary flow field downstream of the lobe exit plane. This figure shows an inwardly directed, radial velocity on the fan-side of the mixer, and an outwardly directed, radial velocity of an almost similar magnitude, on the core-side of the mixer. This velocity field represents a streamwise vortex which is responsible for pushing the hot core flow into the cold fan one, creating the mushroom-shaped hot spike, resulting in better mixing between the two streams. The radial position of the vortex center moves outwards toward the shroud surface, as it propagates downstream along the axial direction. This eventually breaks the hot gas region into two parts. Similar results were predicted by Povinelli and Anderson [25] and Malecki and Lord [24]. It should be pointed out here that, the depiction of this secondary flow, which is the key physical phenomenon contributing to the mixing process, has been made possible by a fully three-dimensional viscous computation. A simplified computational scheme, for example, a parabolized Navier Stokes solver would fail to capture this physics.

It is interesting to note that despite the previously mentioned code simplifications and the relatively coarser grid resolution, the predicted total temperature distributions (Figure 20) are in excellent agreement with data. This indicates that the large scale vortex (Figure 22) is the dominant mechanism controlling the mixing process.

4. INLET PARTICLE SEPARATOR

Modern aircraft gas turbine engines operate at higher rotational speeds than gas turbines of a decade ago. Ingestion of sand and dust into these engines can lead to a rapid erosion of the compressor and turbine airfoils and blockage of the cooling passages with attendant performance degradation. This engine performance degradation can be reduced significantly by using an Inlet Particle Separator (IPS).

Typically, an inertial type of IPS comprises an inlet duct followed by a splitter that divides the flow into an outer bypass stream and a core engine stream (Figure 23). Such a configuration allows the entering airflow to turn inward at the splitter lip toward the engine centerline. The larger inertia of the particles, however, propels them along the outer periphery where they are collected in the bypass duct and dumped overboard. Larger particles hit the inner hub wall, which is angled to deflect the particles toward the outer periphery and, hence, out the bypass.

Solver

The flow analysis scheme used for computing the IPS flow field [26] is based on the solution of the full Navier Stokes and continuity equations in two-dimensional axisymmetric plane using a recently proposed scheme by Karki [27]. In this scheme, a steady state pressure correction formulation is used to solve the Navier Stokes equations.

Grid System

The computational grid shown in Figure 24 comprises of elliptic H-grids for the core and the scavenge regions. The two grids are patched from the splitter leading edge to the inlet along the mid-span line. This grid system provides good resolution around the splitter and also avoids the numerical errors introduced from patching of H-grid with C-grid [28,29]. The grid structure also minimizes the numerical diffusion of the highly turning turbulent flow around the splitter.

Boundary Conditions

The total pressure P_t , the total temperature T_t , and the inlet flow angle are prescribed at the inlet section. Along the hub, shroud, and flow splitter walls a non-slip condition is imposed. At the exit section, a uniform static pressure is prescribed. The required mass flow rate through the core and scavenge ducts are achieved by adjusting the specified exit static pressure in both ducts.

The grid cells on the patching line, located between the splitter leading edge and the inlet plane, are treated as interior cells. This provides an implicit coupling between the solution of the core and scavenge ducts and improves convergence rate.

Comparison with Experimental Data

The test vehicle selected for code validation was a small vaneless IPS which was earlier designed and developed using an axisymmetric inviscid calculation. Experimental results were obtained at the core flow rate of 5 lb/sec with a bypass ratio of 20 percent. The experimental test rig is shown in Figure 25.

The flow and particle trajectory models were applied to the above 5 lb/s flow size vaneless inlet particle separator. Three of the measurement locations (locations 1 to 3) upstream of the splitter and the scavenge are indicated in Figure 24. Figure 26 illustrates the detailed velocity field and Mach number contours. As seen, the flow is characterized by local separation regions at the hub and splitter leading edge, and large separation region in the scavenge duct which starts upstream of the splitter leading edge. These flow characteristics are attributed to the large hub ramp, the splitter proximity, and a significantly lower bypass flow as compared with the core flow. This resulted in high diffusion in the bypass duct, and a positive splitter incidence angle, which in turn moved the stagnation point on top of the splitter lip. As the flow reverses and follows the sharp turn of the splitter lip, it undergoes rapid acceleration followed by abrupt deceleration which produces a thick boundary layer in that region.

Figure 27 compares the measured and predicted static pressure distributions along the hub and shroud. As seen, excellent agreement exists between the analytical and experimental results. The predicted total pressure upstream of the splitter and in the scavenge region is compared with the test data for locations 1, 2 and 3 in Figure 28. Again, good agreement between the predicted and test results is demonstrated. Figure 29 presents the predicted total pressure distribution in the core region for locations 4, 5, and 6 (no experimental data is available). This figure indicates that the inner wall profile of the splitter needs more refinement to minimize the total pressure loss in this region.

Particle Trajectory Analysis

The above flow field was used to predict its influence on the sand separation efficiency for a given particle size distribution. This requires trajectory prediction for various particle sizes as they are acted upon by the aerodynamic forces. In this particle trajectory analysis, five particles of the same size are introduced at the IPS inlet at equal spacing across the span with initial velocity equal to the gas velocity. Display routines incorporated in the code give trajectory plots showing rebound, acceleration, and deceleration of the particles. Figure 30 illustrates the particle trajectories of three different-sized particles in the separator. Of particular interest are the trajectories of 5- μ particles, which show that some of the particles are actually being carried back around the splitter into the core. This is a result of stagnation point located on top of the splitter. As indicated by Breitman et al [30], this important region is difficult to predict. The capability of the aerodynamic solver to accurately predict the flow field in this region is vital in the design of the splitter lip.

The 10 μ particles have similar trajectories as that of 5 μ . The primary difference is that, whereas, some of the 5 μ particles reverse the direction and follow the core flow, the 10 μ particles are not able to do so. The larger inertia of the 10 μ particles propels them to the outer periphery where they are collected and dumped overboard. As a result, the sand separation efficiency of 10 μ particles is 42 percent higher than that of 5- μ particles. The representative trajectories of the 50 μ particles show that most of them hit the inner hub wall, which is angled to deflect the particles toward the outer periphery and, hence, out the bypass.

It can be concluded from Figure 30 that the smaller particles are primarily separated through the influence of the flow field on their trajectories, while the larger particles are separated by their impact with the contoured hub. These two effects, when properly combined, can result in high separation efficiency over a wide range of particle sizes.

5. INVERSE DESIGN

An inverse design scheme developed for cascades by Giles and Drela [34 and 35] was modified for application in a quasi-three-dimensional design system for multistage axial compressor. The modified code accounts for the streamtube thickness and radius variations, and can be used in the analysis, fully inverse, and mixed inverse modes. The mixed inverse mode refers to a procedure where the pressure or velocity distribution is specified only over a portion of the airfoil.

In this code, the Euler equations are written in terms of density and displacement normal to streamlines and the solution for the flow field and grid displacement are strongly coupled. An efficient Newton procedure is used to solve the system of equations.

Application to Stator Hub

The fully inverse and mixed inverse schemes have been checked out for many rotor and stator airfoils that are representative of highly loaded, high pressure ratio, transonic stages [31]. Low aspect ratio, high solidity, high inlet Mach number, and significant stream tube contraction are some of the design features of these stages.

The test case chosen for presentation in this paper is intended to demonstrate the application of the mixed inverse scheme to the stator hub section of a transonic stage.

The aim was to ensure that the airfoil suction surface is free of any shock, and also achieve a gradual diffusion from the peak Mach number point to the exit. First of all, an approximate airfoil geometry (Figure 31), generated in the quasi-three-dimensional design system with the aid of the cascade data, was evaluated in the analysis mode; the resulting Mach number contours are shown in Figure 32. As seen, the flow accelerates at the suction surface L.E. from Mach number (M) of 0.98 to peak value of 1.34, followed by a strong normal shock to $M = 0.76$ in the front part of the airfoil. It is then diffused very slowly over the rest of the airfoil.

To improve the above flow characteristic and to eliminate the shock, a new pressure distribution over most of the airfoil suction surface was prescribed. The base airfoil (plus signs) and prescribed (solid curve) pressure distributions are shown in Figure 33. The two vertical lines in this figure define the portion of the suction surface that the code was allowed to modify, rest of blade geometry is fixed. The resulting surface pressure distribution of the inverse output is shown in this figure by dashed line. The difference between the specified pressure distribution and the pressure distribution corresponding to inverse mode output is due to two degrees of freedom introduced in the specification of pressure to satisfy geometric continuity (see References [32] and [33]).

The new blade geometry, Figure 34, has eliminated the shock and spread the flow diffusion over the entire suction surface. What is more interesting is that the code has eliminated the shock by increasing the blade thickness; current design procedures based on conventional thinking would invariably lead to a thinner airfoil.

6. CONCLUDING REMARKS

Application of advanced CFD codes to gas turbine engine components has been illustrated. It is shown that several fully three-dimensional viscous solvers have reached a level of maturity to qualify for use in the routine design process. Code robustness, user friendly system, fast convergence rates have played a key role in achieving the current level of sophistication. Current three-dimensional Navier Stokes solvers are able to accurately predict the flowfield in such complex geometries as splintered rotors and exhaust mixers. Considering the rate at which the computing speed is increasing, it would be entirely possible to routinely run multiblade row unsteady analysis schemes before the turn of the century. Recent advances in the use of inverse design procedures indicates that this area of CFD is likely to have a major impact in speeding up the design process. It is firmly believed that CFD systems will help to drastically reduce the development cost and time of the gas turbine engine components.

ACKNOWLEDGEMENT

The authors would like to thank Drs., A. Mostafa, K. Tzuoo and J. Liu who helped running particle trajectory, Denton and LYCVIS3D codes, respectively.

The authors would also like to thank Textron Lycoming for permission to publish this paper. This work was performed as a part of Textron Lycoming's Independent Research and Development Program. The computer time for part of this effort was made available by NASA Lewis Research Center.

REFERENCES

1. Law, C.H. and Puterbaugh, S.L., "A Computer Program for Axial Compressor Design (UD0300M)," AFWAL-TR-82-2074, 1982.
2. Wennerstrom, A.J. and Frost, G.R., "Design of a Rotor Incorporating Splitter Vanes for a High Pressure Ratio Supersonic Axial Compressor Stage," ARL-TR-74-0110, 1974.
3. Subramanian, S.V. and Bozzola, R., "Numerical Simulation of Three-Dimensional Flowfields in Turbomachinery Blade Rows Using the Compressible Navier Stokes Equations," AIAA Paper 87-1314, June 1987.
4. Jameson, A., and Baker, T.J., "Multigrid Solution of the Euler Equations for Aircraft Configurations," AIAA Paper 84-0093, January 1984.
5. Baldwin, B., and Lomax, H., "Thin Layer Approximation and Algebraic Model for Separated Turbulent Flows," AIAA Paper 78-25 January 1978.
6. Subramanian, S.V., Bozzola, R., and Povinelli, L.A., "Computation of Three-Dimensional, Rotational Flow Through Turbomachinery Blade Rows for Improved Aerodynamic Design Studies," ASME Paper 86-GT-26, June 1986.
7. Liu, J.S., and Subramanian, S.V., "Multigrid Solution of the Euler Equation for Three-Dimensional Cascade Flows," AIAA Paper 89-1818, June 1989.
8. Subramanian, S.V., "Three-Dimensional Multigrid Navier Stokes Computations for Turbomachinery Applications," AIAA Paper 89-2453, July 1989.
9. Dawes, W.N., "BTOB3D - A Computer Program for the Analysis of Three-Dimensional Viscous Compressible Flow in Turbomachinery Blade Rows," University of Cambridge, U.K., 1986.
10. Warming, R.F., and Beam, R.M., "On the Construction and Application of Implicit Factored Schemes for Conservation Laws," SIAM-AMS Proceedings, Vol. 11, 1978.

11. Epstein, A.H., Giles, M.B., Shang, T. and Sehra, A.K., "Blade Row Interaction Effects on Compressor Measurements", AGARD, Conference, Proceedings No. 468, August 1989.
12. Langston, L.S., "Crossflows in a Turbine Cascade Passage," Journal of Engineering for Power, Vol. 102, Oct., 1980, pp. 866-874.
13. Sieverding, C.H., "Recent Progress in the Understanding of Basic Aspects of Secondary Flows in Turbine Blade Passages," Trans. of the ASME, Journal of Eng. for Gas Turbine and Power, Vol. 107, April 1985, pp. 248-251.
14. Denton, J.D., "An Improved Time Marching Method for Turbomachinery Calculation," ASME Paper 82-GT-239, June 1982.
15. Wennerstrom, A.J., "Some Experiments with a Supersonic Axial Compressor Stage," Journal of Turbomachinery, Vol. 109, No. 3, July, 1987.
16. Cooper, G.K., and Sibaugh, J.R., "PARC Code: Theory and Usage", AEDC TR-89-15, Arnold Engineering Development Center, Tullahoma, TN, December 1989.
17. Dorrell, Jr., E.W., and McClure, M.D. "3D IGRID: Interactive Three-Dimensional Grid Generation," AEDC-TR-87-40, April 1988.
18. Pulliam, T.H., "Euler and Thin Layer Navier Stokes Codes: ARC2D, ARC3D", notes for Computational Fluid Dynamics User's Workshop, The University of Tennessee Space Institute, Tullahoma, TN, (UTSI Pub. E02-4005-023-84), March 12-16, 1984, pp. 15.1-15.85.
19. Pulliam, T.H. and Steger, J.L., "Implicit Finite - Difference Simulations of Three-Dimensional Compressible Flow," AIAA, J. Vol. 18, 1980, pp. 159-167.
20. Thomas, P.D., "Numerical Method for Predicting Flow Characteristics and Performance of Nonaxisymmetric Nozzles Theory", Langley Research Center, NASA CR3147, September 1979.
21. Cooper, G.K. and Sirbaugh, J.R., "The PARC Distinction: A Practical Flow Simulator," AIAA Paper, NO. 90-2002, 26th Joint Propulsion Conference, Orlando, FL, July 16-18, 1990.
22. Kozlowski, H., and Larkin, M., "Energy Efficient Engine Exhaust Mixer Model Technology Report," NASA CR-165459, June 1981.
23. Larkin, M.J., and Blatt, J.R., "Energy Efficient Engine Exhaust Mixer Model Technology Report Addendum Phase III Test Program," NASA CR-174799, April 1984.
24. Povinelli, L.A., and Anderson, B.H., "Investigation of Mixing in a Turbofan Exhaust Duct, Part II: Computer Code Application and Verification, AIAA J. Vol. 22, No. 4, 1984, pp. 518-525.
25. Malecki, R. and Lord, W., "Navier Stokes Analysis of a Lobed Mixer and Nozzle," AIAA paper, No. 90-0453, 28th Aerospace Sciences Meeting, Reno, NV, January 8-11, 1990.
26. Zedan, M., Hartman, P., Mostafa, A. and Sehra, A., "Viscous Flow Analysis for Advanced Inlet Particle Separators," AIAA-90-2136 AIAA/SAE/ASME/ASEE 26th Joint Propulsion Conference, July 16-18, Orlando, FL, 1990.
27. Karki, K.C., "A Calculation Procedure for Viscous Flows at All Speeds in Complex Geometries," Ph.D. Thesis, University of Minnesota, 1986.
28. Vital, B.V.R., Tipton, D.L. and Bennett, W.A., "Development of an Advanced Vaneless Inlet Particle Separator for Helicopter Engines," J. Propulsion, 2, 1986, pp. 438-444.
29. Sheih, C.F., Delaney, R.A., and Tipton, D.L., "Analysis of the Flow Field in an Engine Inlet Particle Separator," Computation of Internal Flows: Methods and Applications, ASME Fed-Vol 14, Feb. 1984, pp. 23-28.
30. Breitman, D.S., Dueck, E.G., and Mahashi, W.G., "Analysis of a Split-Flow Inertial Particle Separator by Finite Elements," J. Aircraft, 1985, pp. 135-140.
31. Zedan, M., Sehra, A., "Application of an Inverse Design Procedure to Axial Compressor Blading," ASME 90-GT-67 June 11-14, Brussels, Belgium, 1990.
32. Giles, M., Dreia, M., and Thompkins, Jr., W.T., "Newton Solution of Direct and Inverse Transonic Euler Equations," AIAA Paper No. 85-1530-CP, Cincinnati, Ohio, 1985.
33. Dreia, M., and Giles, M., "Viscous Inviscid Analysis of Transonic and Low Reynolds Number Airfoils," AIAA paper No. 86-1786-CP, 1986.



Figure 1: Transonic Compressor Rotor

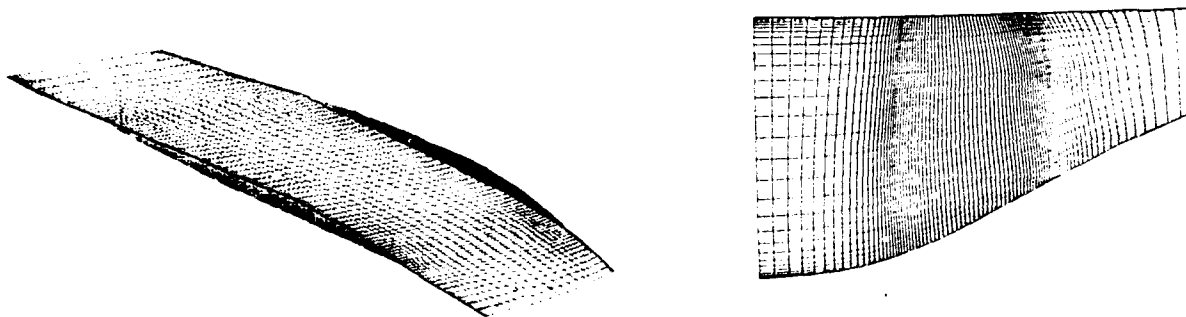


Figure 2 Transonic Rotor Grid, Blade to Blade (Mid Span Section) and Meridional

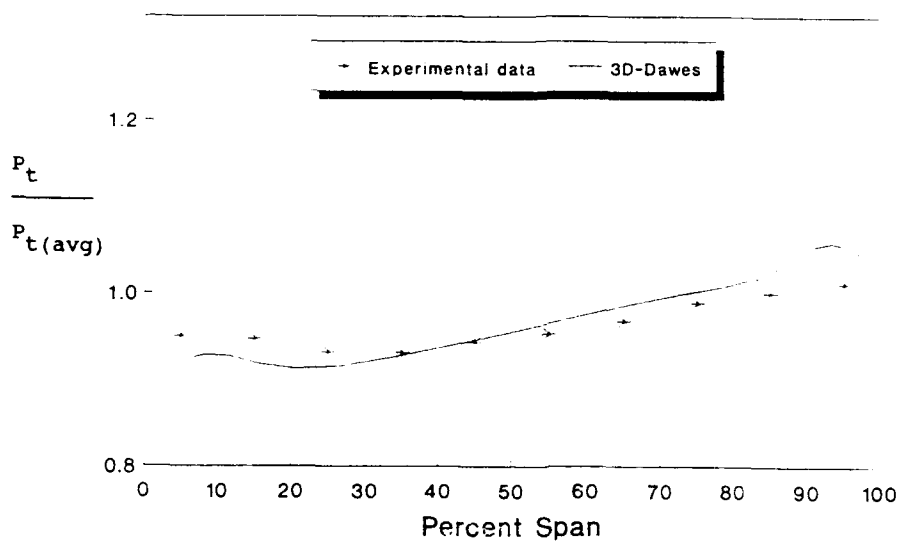


Figure 3 Exit Normalized Total Pressure Distribution

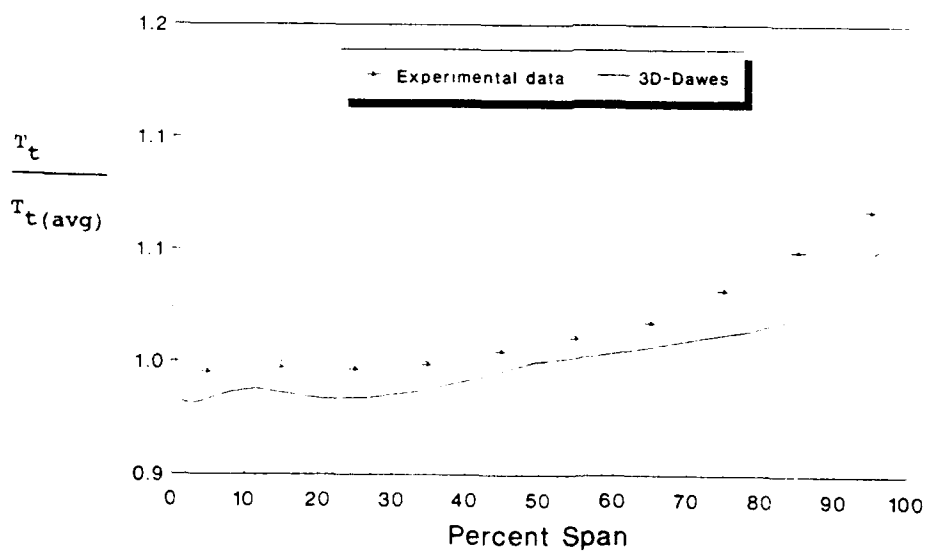


Figure 4 Exit Normalized Total Temperature Distribution

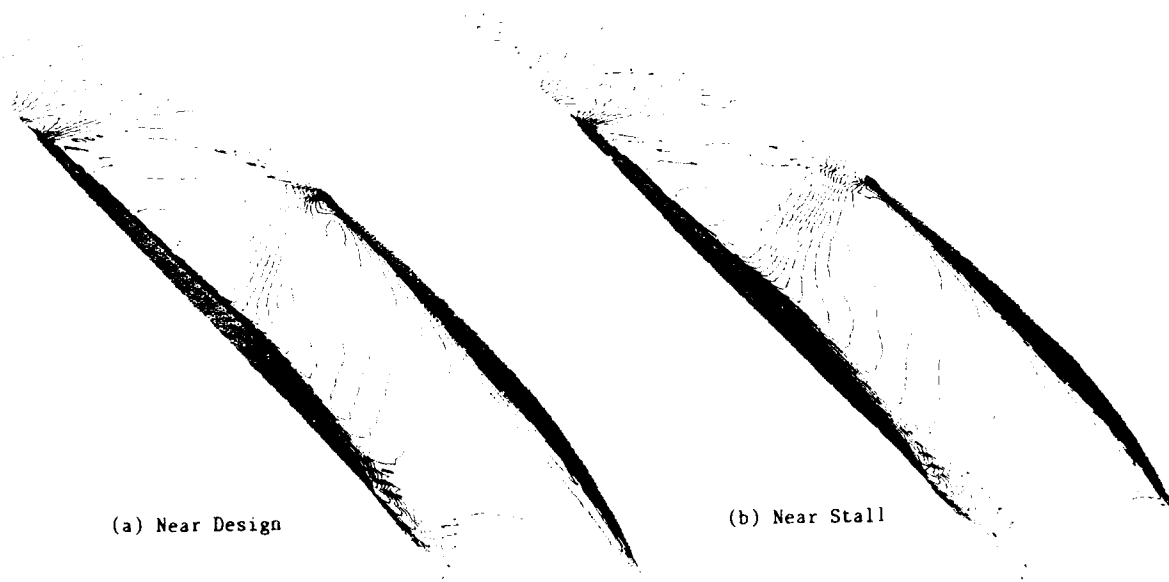


Figure 5 Predicted Mach Number Contours

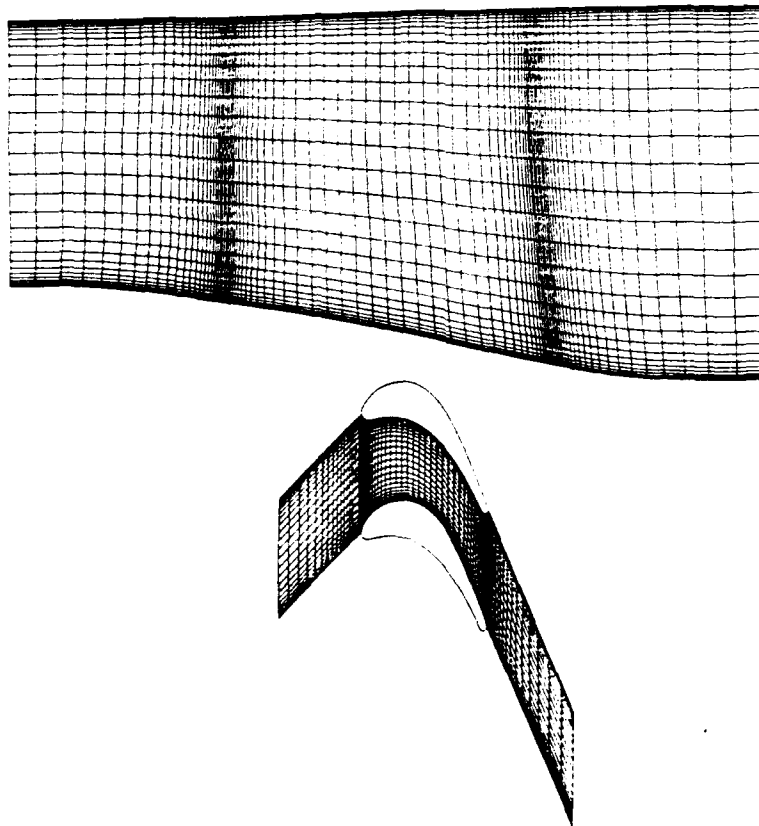


Figure 6 Computation Grid for High Work Turbine Rotor

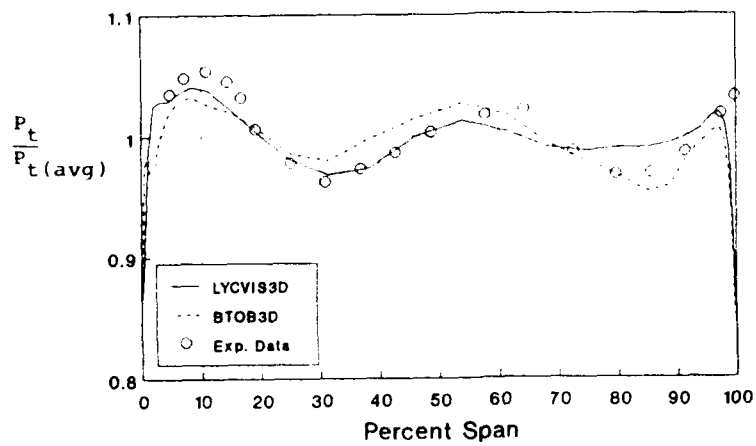


Figure 7 Exit Normalized Total Pressure Distribution

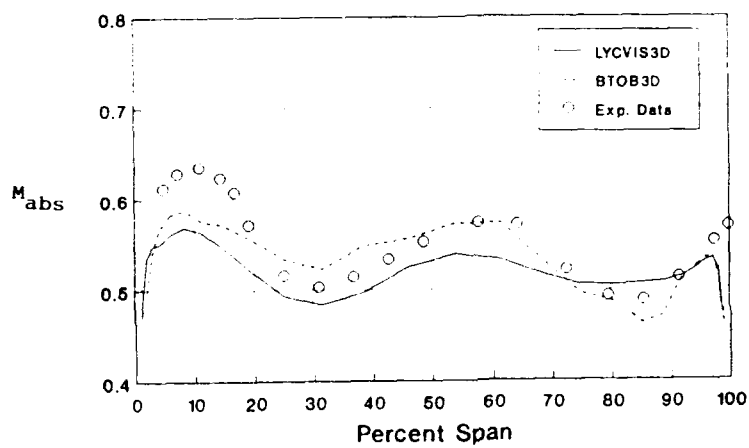


Figure 8 Exit Absolute Mach Number Distribution

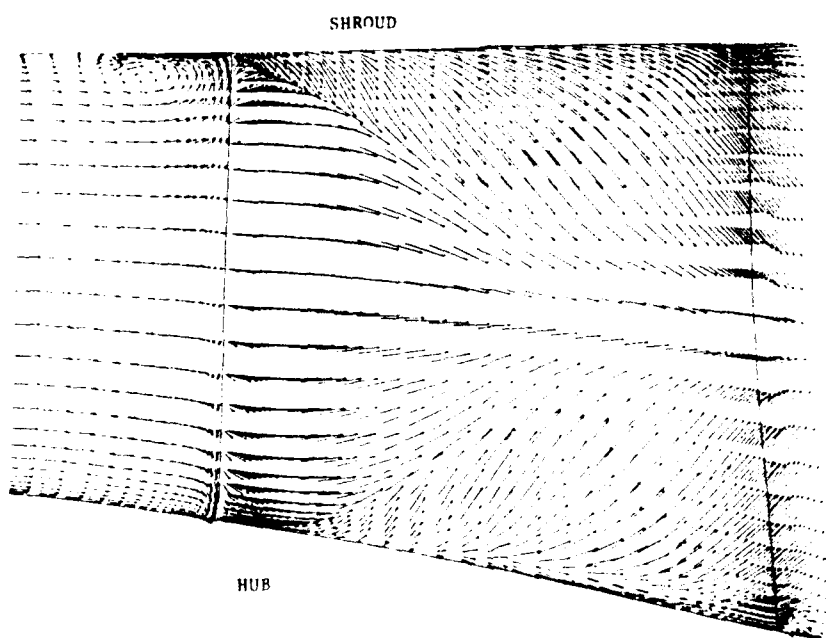


Figure 9 Meridional Projection of the Relative Velocity Vectors Near Suction Surface

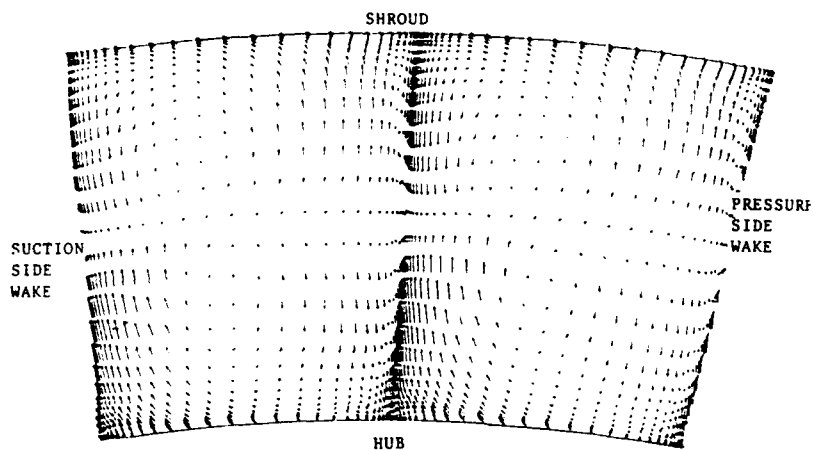


Figure 10 Relative Secondary Velocity for the Cross Flow Plane at 10 Percent Chord Downstream of the Rotor Trailing Edge (two passages)

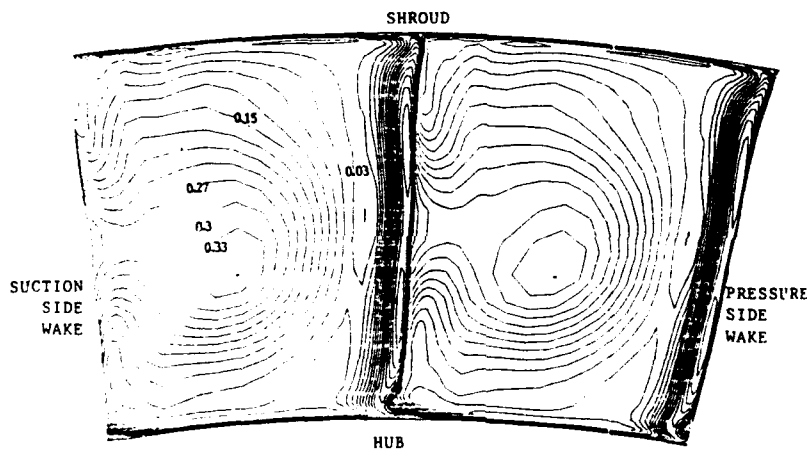


Figure 11 Total Pressure Loss Contours for the Cross Flow Plane at 10 Percent Chord Downstream of the Rotor Trailing Edge (two passages)

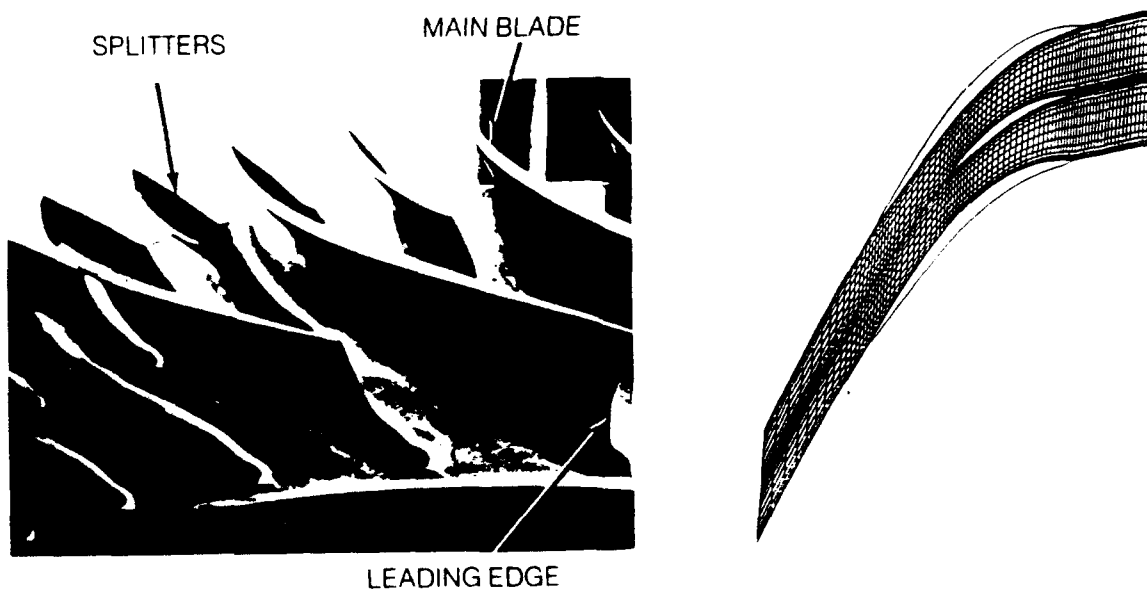


Figure 12 Wennerstrom's Splitted Rotor



Figure 13 Mach Number Contours of Wennerstrom's Splintered Rotor Predicted by Daves' Viscous Code

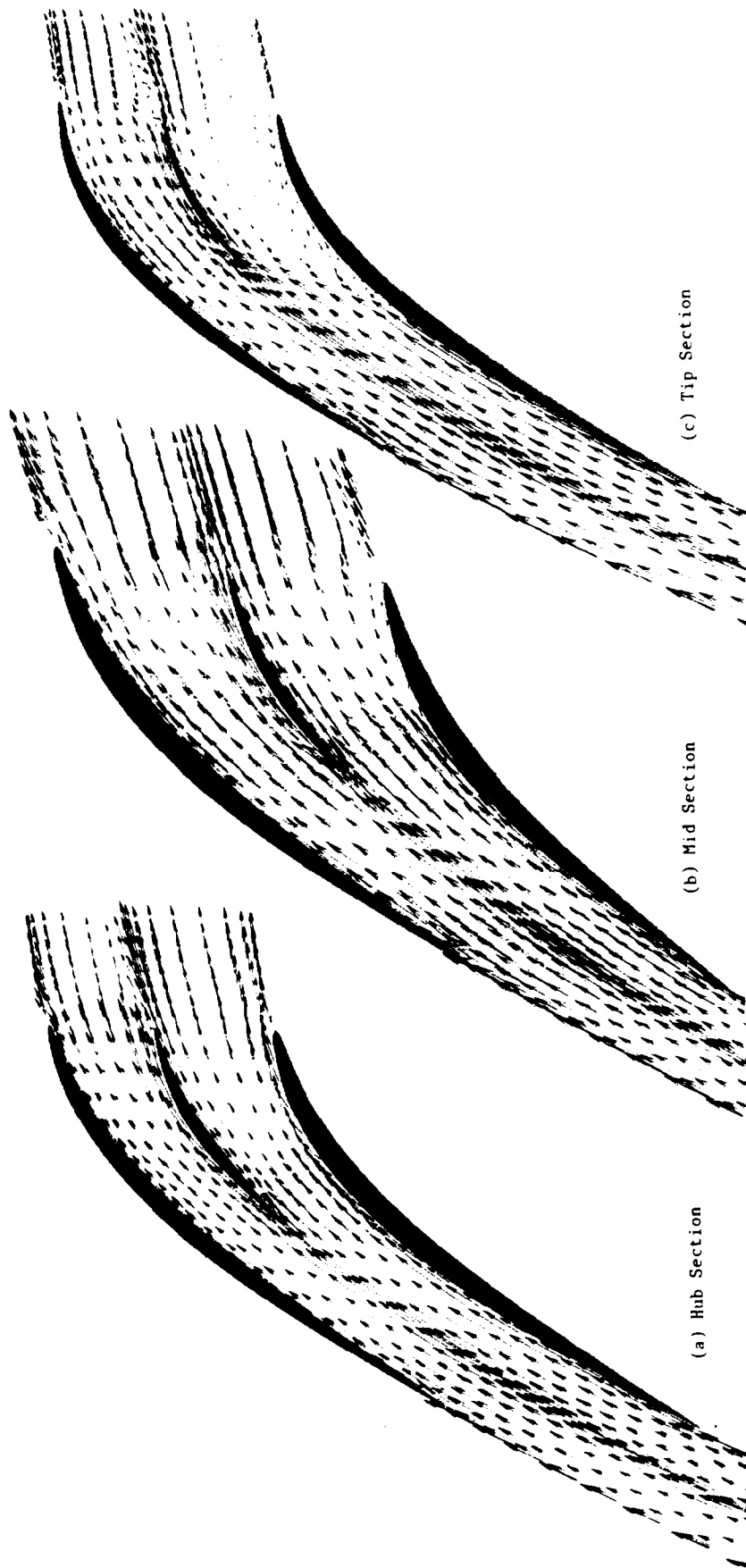


Figure 14 Velocity Vectors of Wennerstrom's Splittered Rotor Predicted by Dawes' Viscous Code

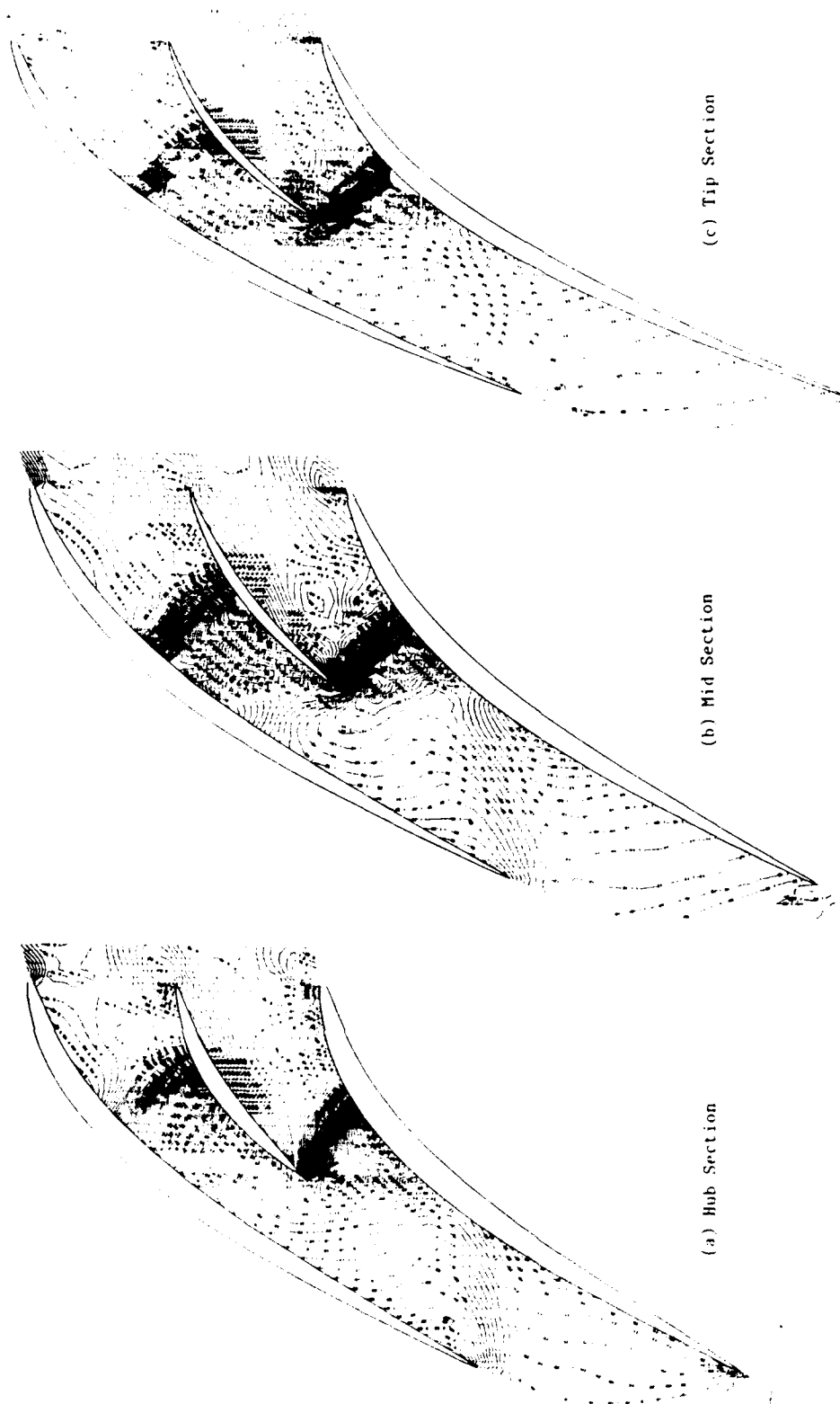


Figure 15 Mach Number Contours of Wennerstrom's Splintered Rotor Predicted by Denton's Inviscid Code

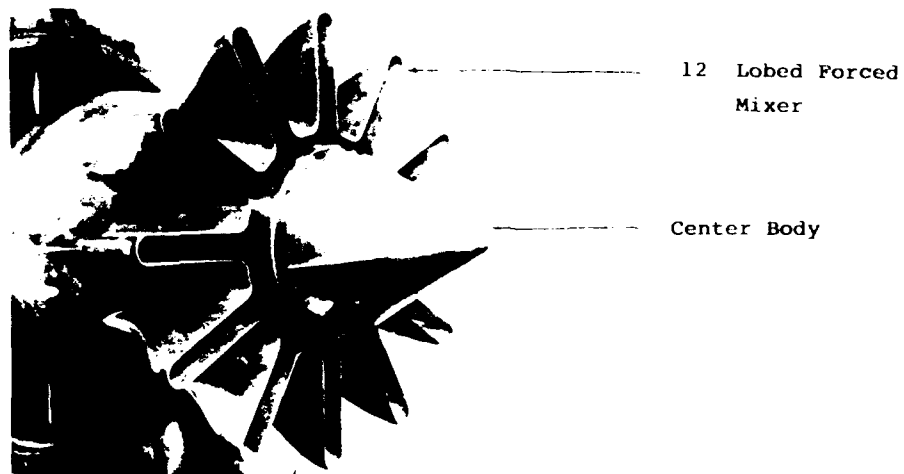


Figure 16 A Typical 12 Lobed Forced Mixer

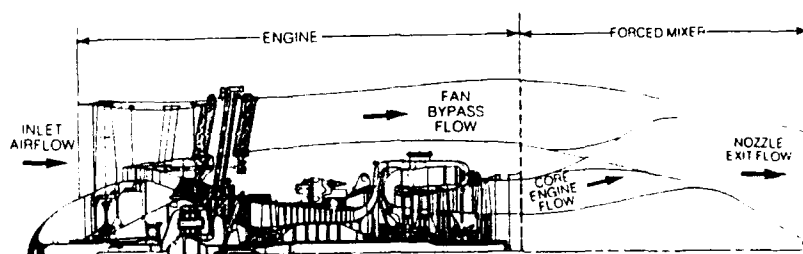


Figure 17 Textron Lycoming LF500 Engine with Forced Mixer

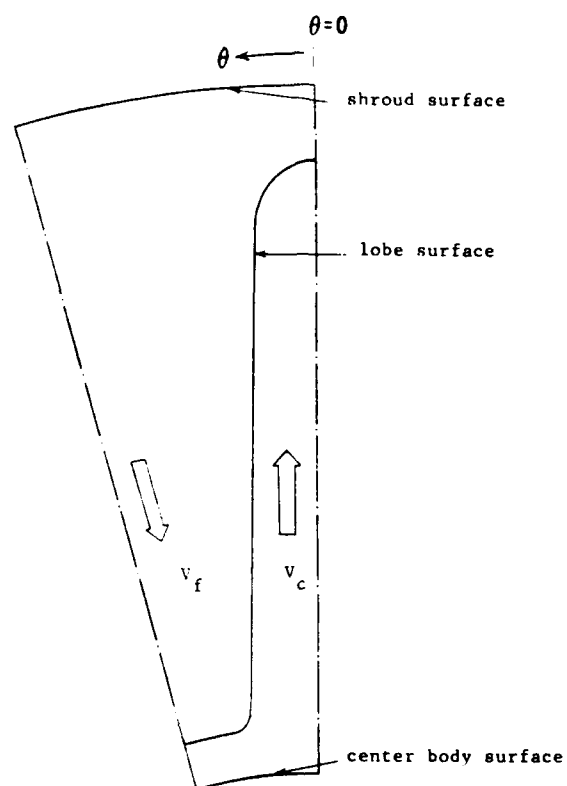


Figure 18 Transverse Computational Segment

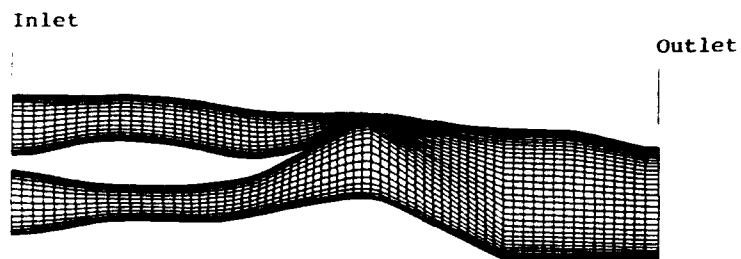


Figure 19 Grid Mesh for Mixer and Exit Nozzle

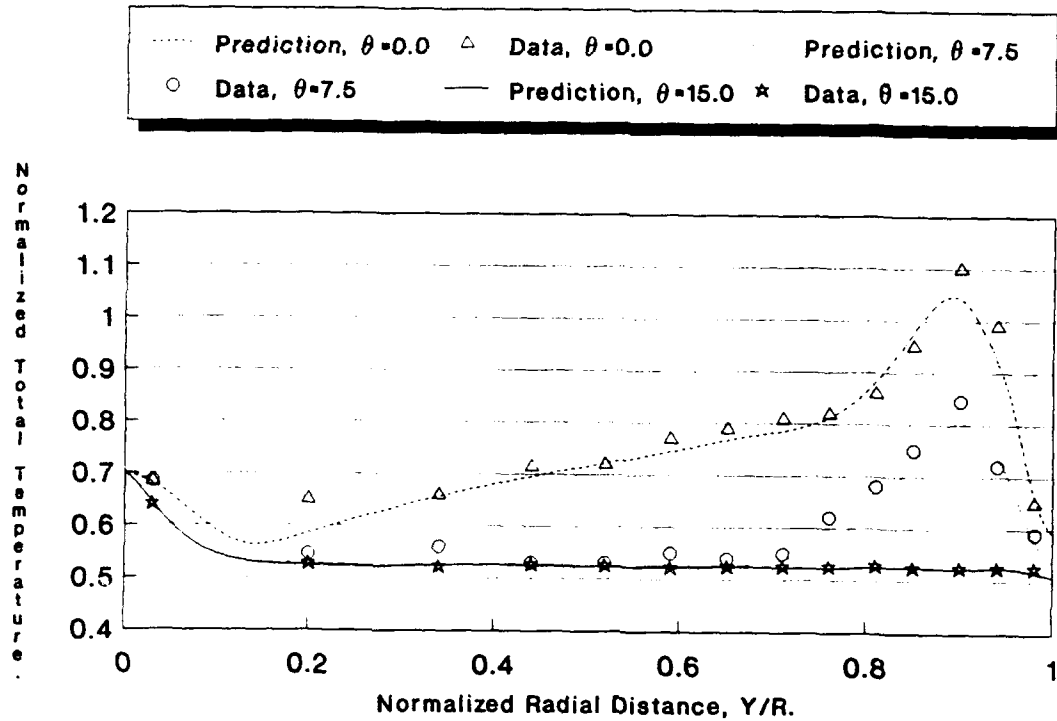


Figure 20 Comparison of Computed and Measured Total Temperature Profiles at Different Circumferential Location of the Nozzle Exit-Plane

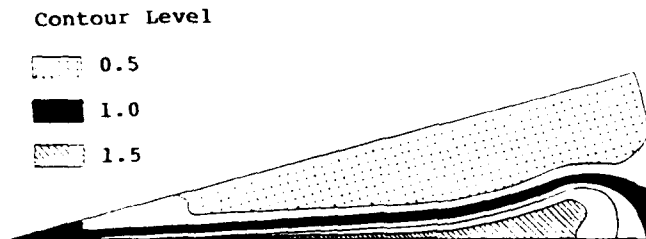


Figure 21 Predicted Total Temperature Contours at Nozzle Exit-Plane

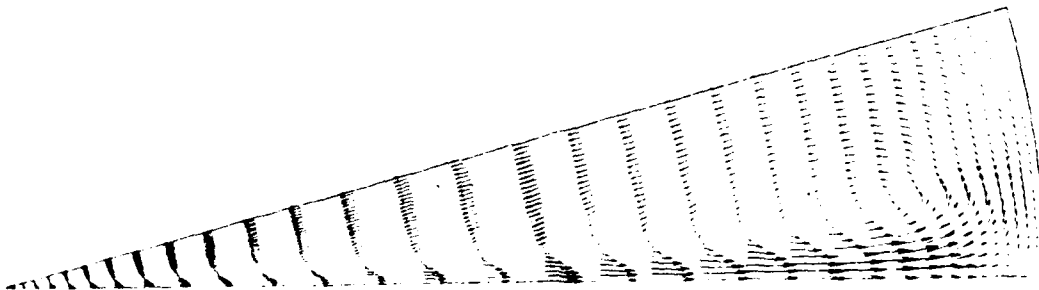


Figure 22 Predicted Secondary-Flow Velocity Field at the Nozzle Exit-Plane

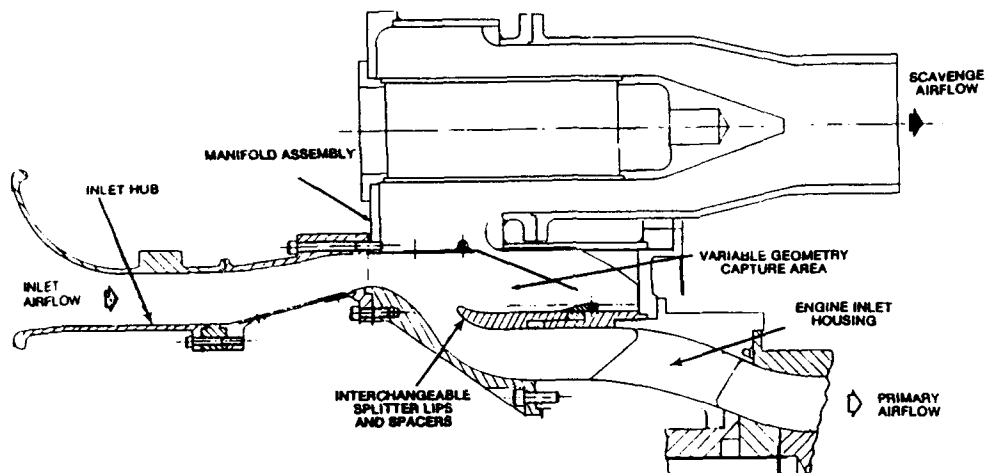


Figure 23 5 lb/s IPS Technology Demonstrator Test Rig

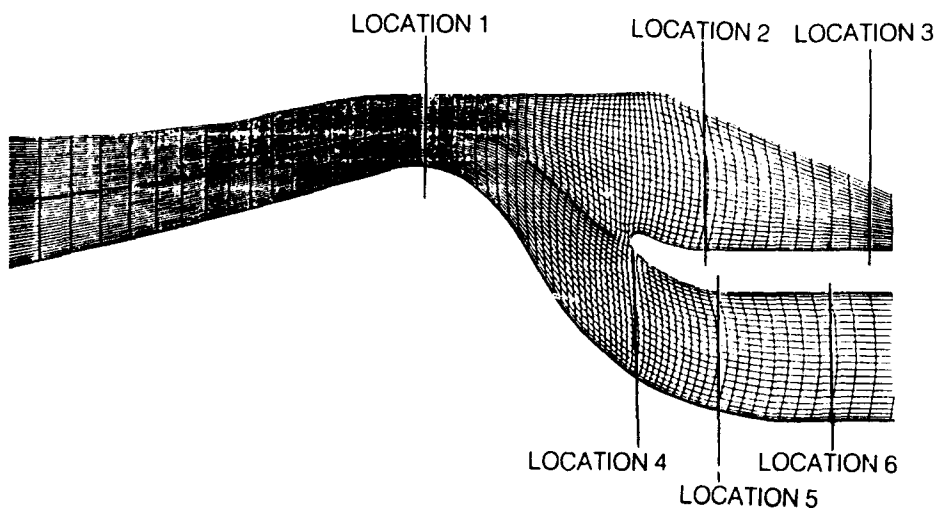


Figure 24 Computational Grid & Measurement Locations

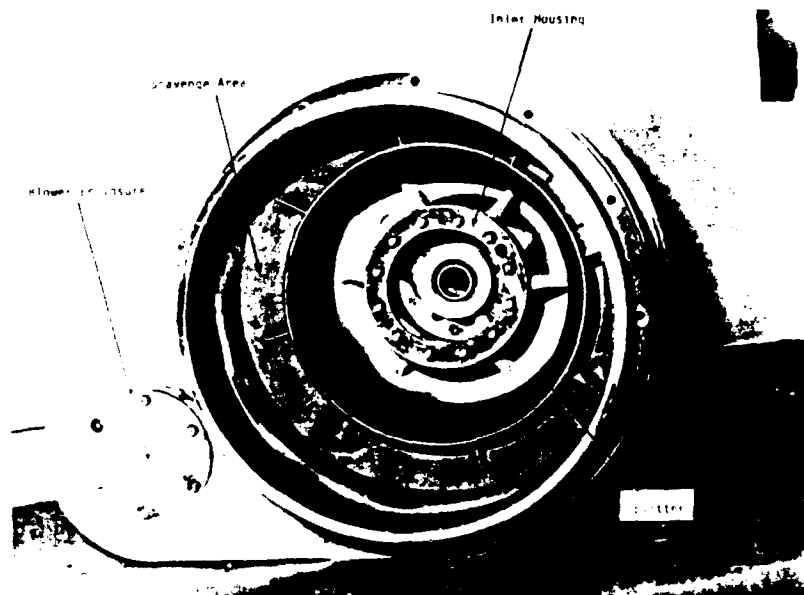


Figure 25 5 lb/s IPS with Splitter Exposed

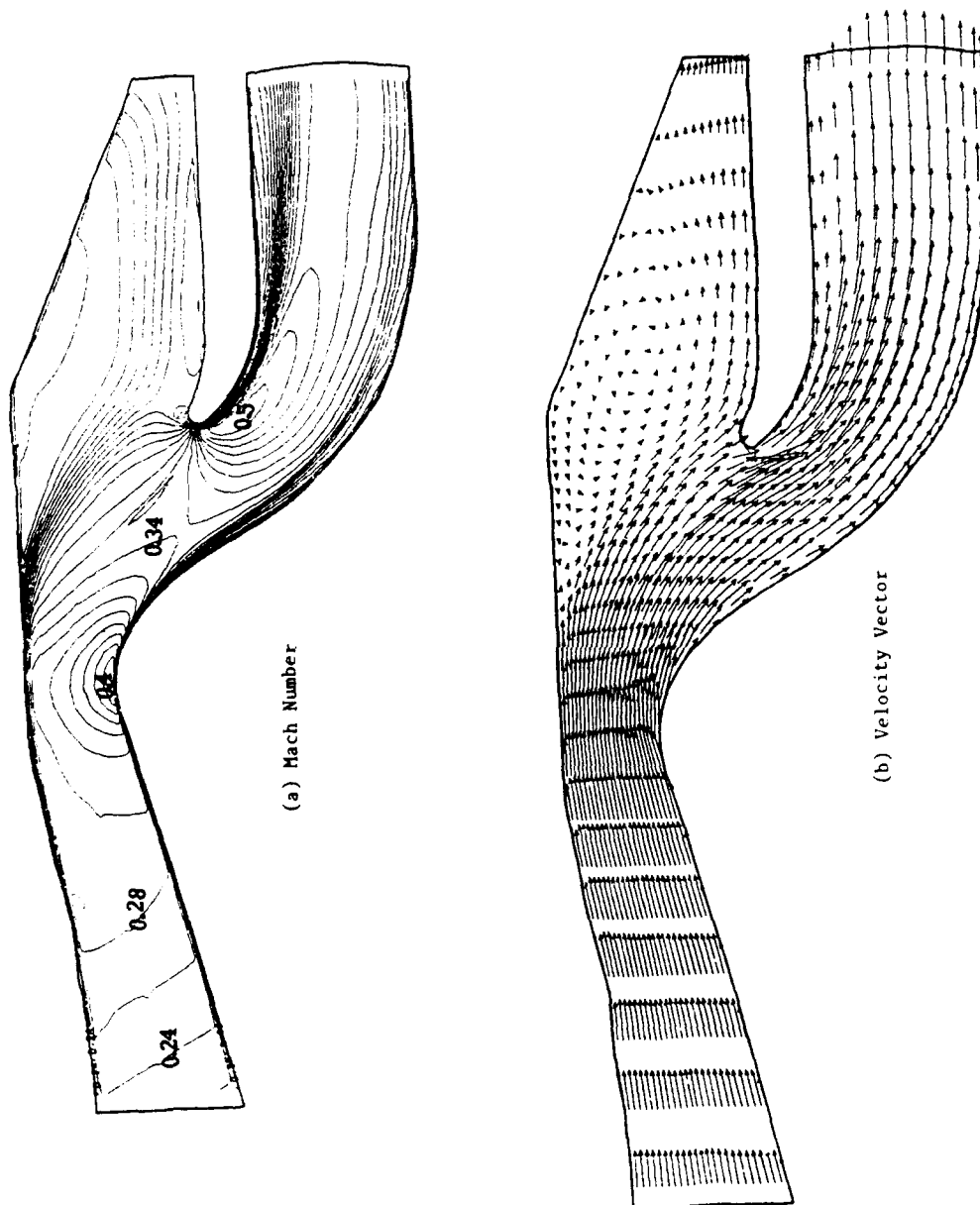


Figure 26 Predicted Flow Field

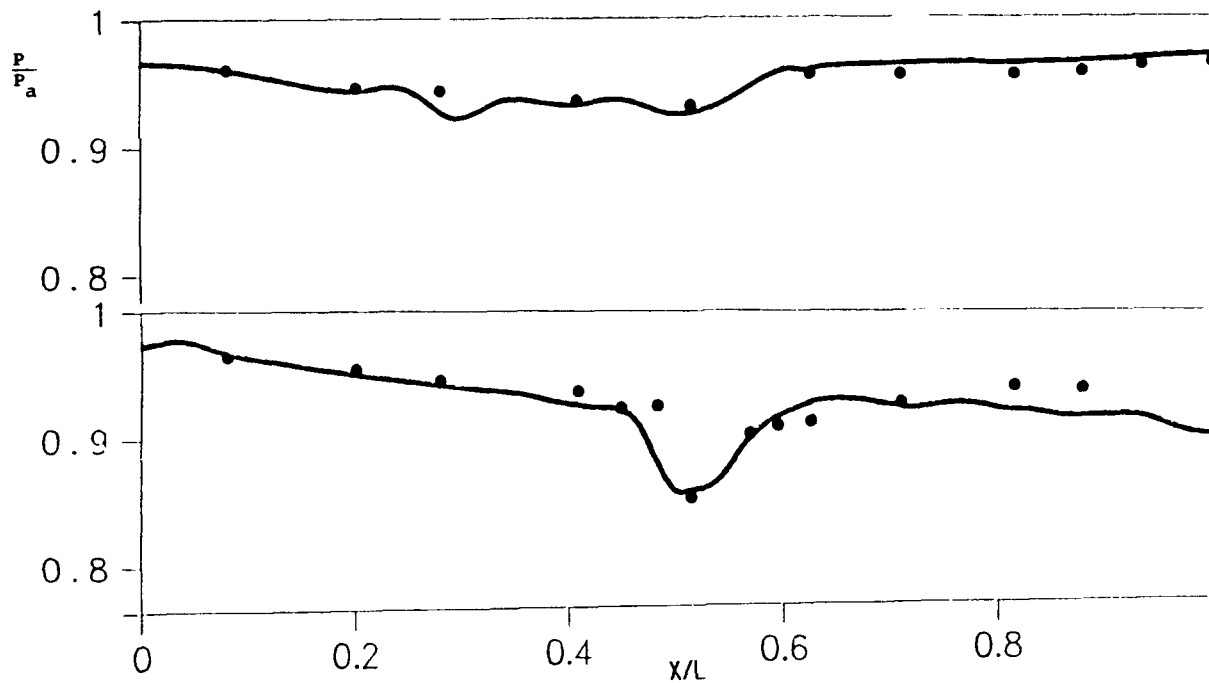


Figure 27 Comparison Between Experimental Results and Predictions for Static Pressure Distribution

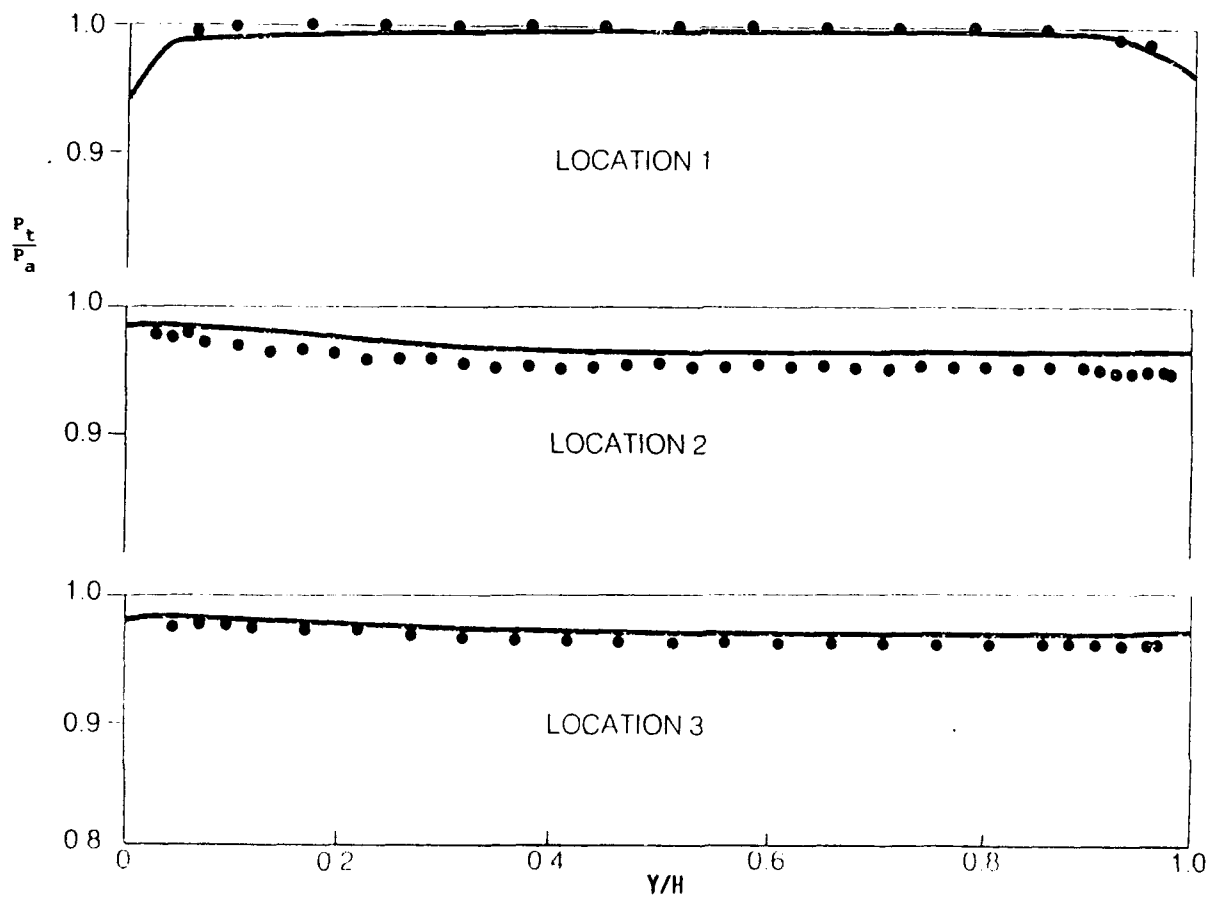


Figure 28 Comparison Between Experimental Measurements and Predictions for Total Pressure Distribution

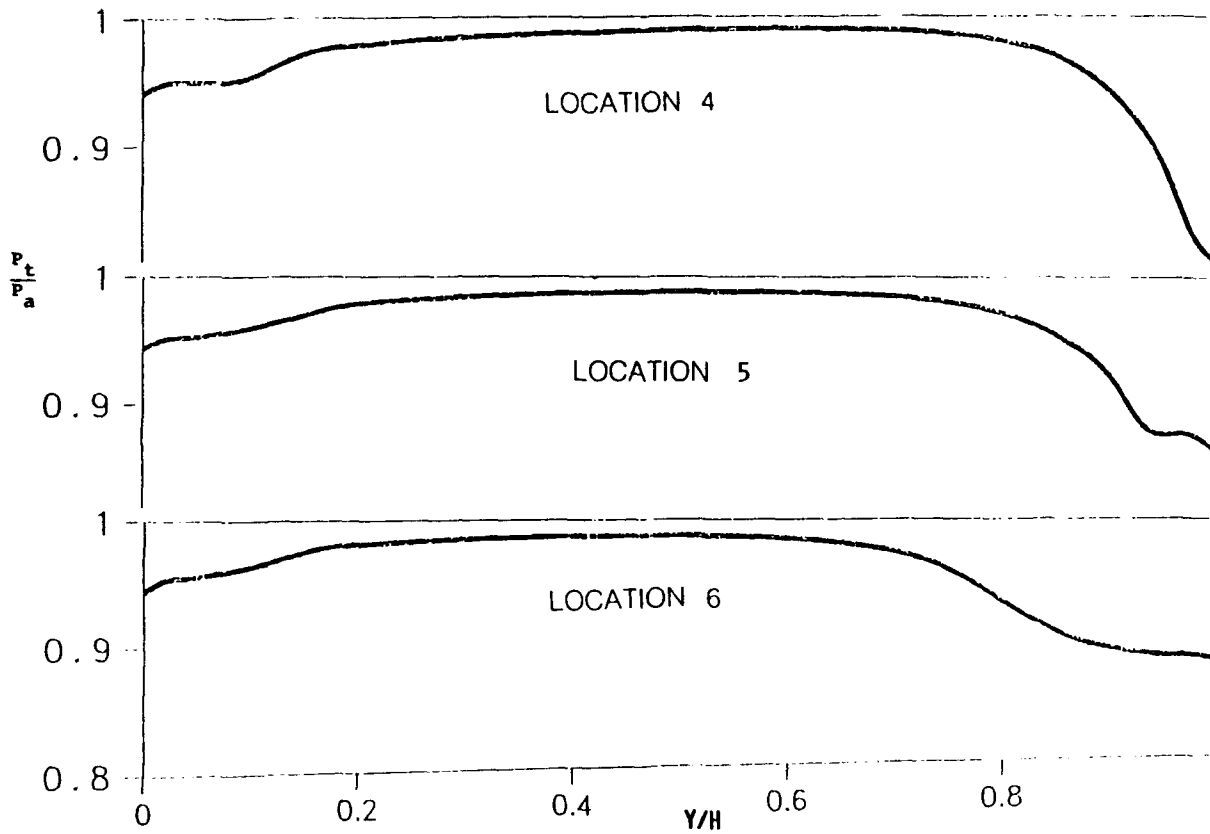


Figure 29 Predicted Core Total Pressure Distribution. Survey Locations Shown in Figure 24

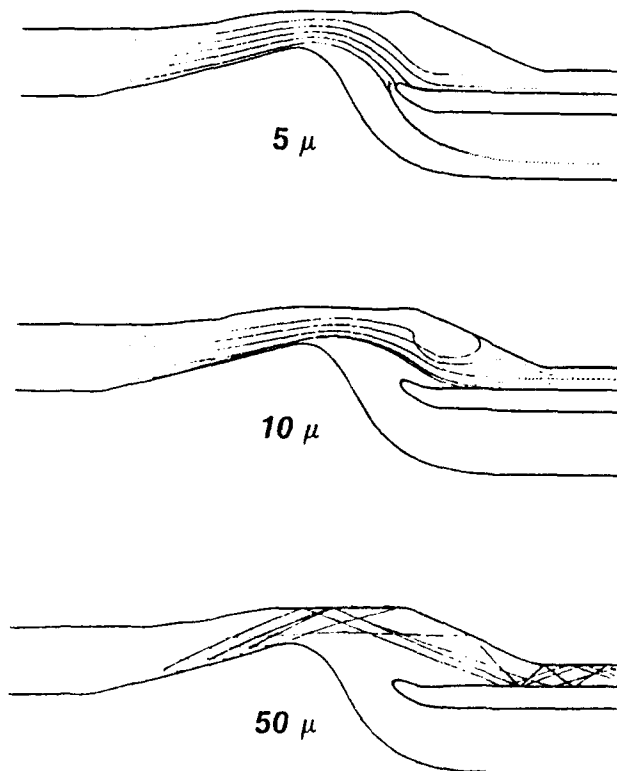


Figure 30 Predicted Particle Trajectories for Three Particle Sizes.
Smaller Particles are Influenced by Recirculation Zone

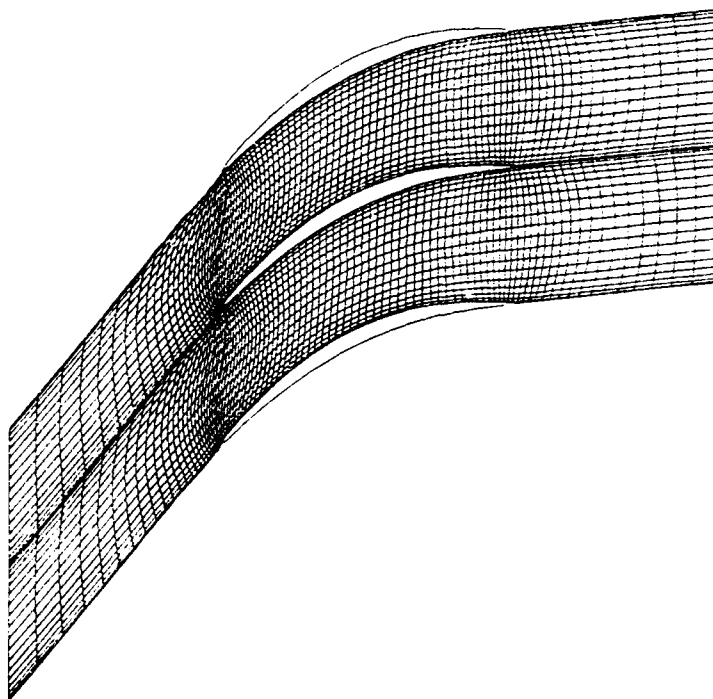


Figure 31 Stator Airfoil at Hub and Grid System

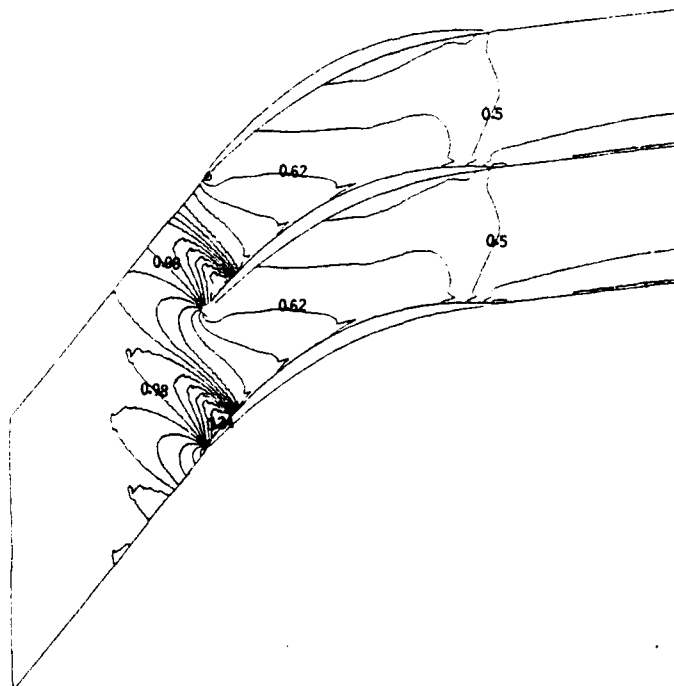


Figure 32 Stator Airfoil at Hub and Mach Number Contours

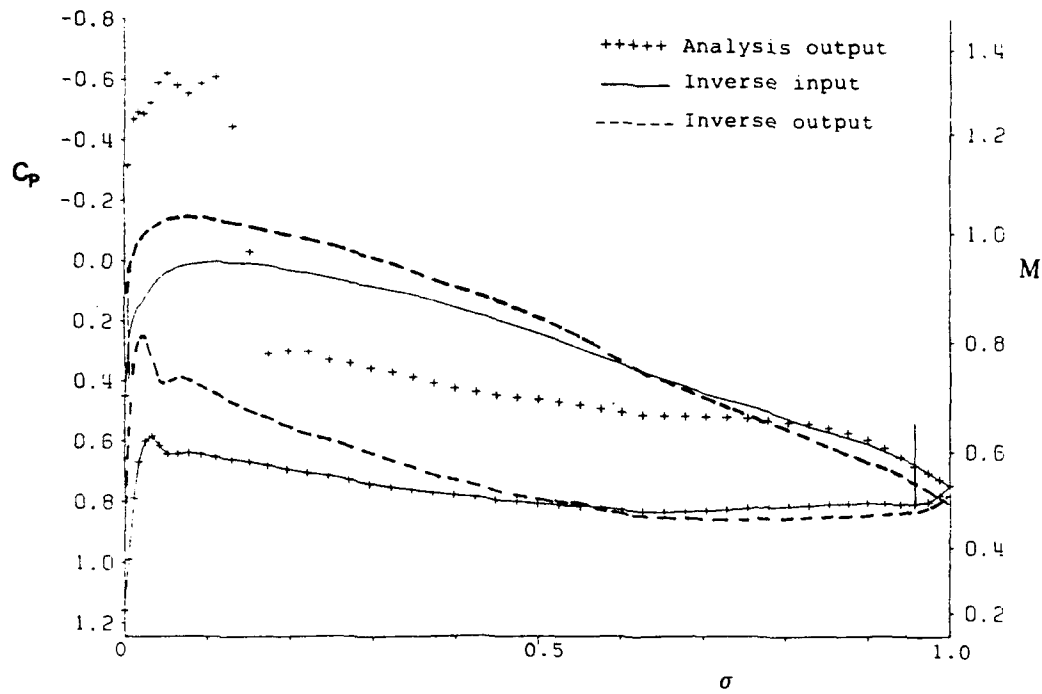


Figure 33 Stator Airfoil Surface Pressure Distributions at Hub

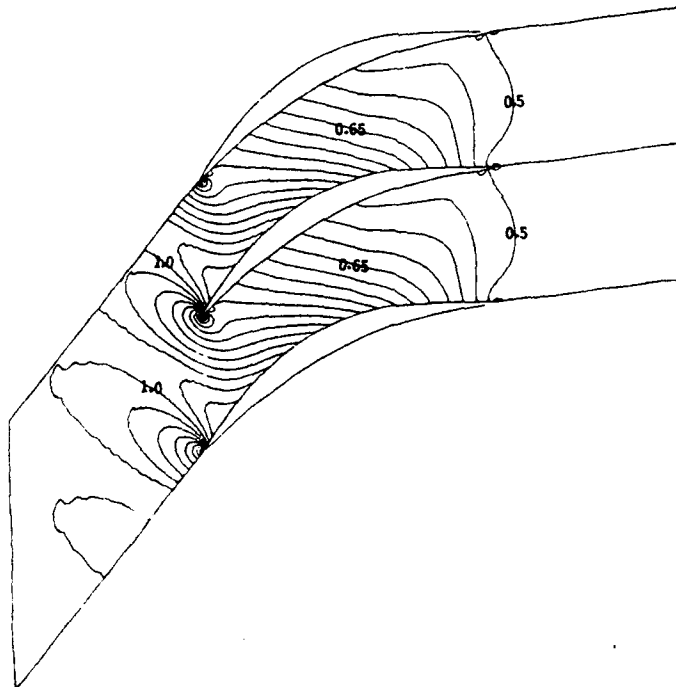


Figure 34 Modified Stator Airfoil at Hub and Mach Number Contours

Discussion

P. RAMETTE, DASSAULT AVIATION, FRANCE

In addition to improving thrust and specific fuel consumption with the modified mixer you presented, did you also measure some improvement in noise reduction?

AUTHOR'S REPLY

This design was not carried out for noise reduction. However the mixer does reduce the noise level of this engine still further than the original design.

R. GRAY, WRIGHT LABS, U.S.A.

In the bypass mixer for which a total-pressure discrepancy was found, how close were the results to those for an inviscid mixer?

AUTHOR'S REPLY

The total pressure at the inlet in the core flow and the bypass flow are known experimentally and used as input. From that we predicted the loss due to mixing.

VALIDATION DU CODE "CANARI" PAR LE CALCUL DE L'ÉCOULEMENT TRIDIMENSIONNEL TURBULENT DANS UN DISTRIBUTEUR DE TURBINE

Béatrice ESCANDE
Laurent CAMBIER

Office National d'Études et de Recherches Aérospatiales (ONERA)
B.P. N° 72 - 92322 CHATILLON Cedex (France)

RESUME

L'objet de cette communication est de présenter les résultats préliminaires obtenus en vue d'une validation du code CANARI en turbomachine. Ce code, développé à l'ONERA, prend en compte les équations de Navier-Stokes moyennées tridimensionnelles compressibles; il est ici appliqué au calcul de l'écoulement dans une grille distributrice de turbine haute pression. Ce calcul a pour caractéristique l'utilisation d'un maillage en O fortement resserré autour des aubes et de maillages en H en amont et en aval, afin de permettre une description précise des phénomènes de bord d'attaque et de bord de fuite. Le cas considéré est celui d'un montage expérimental récemment réalisé à l'ONERA pour la validation détaillée des programmes de calcul (montage VEGA).

ABSTRACT

The object of the paper is to present the preliminary results obtained in order to validate the CANARI code in a turbomachinery case. This code, developed at ONERA, solves the Reynolds averaged compressible three-dimensional Navier-Stokes equations. It is here applied to the flow computation through a high-pressure turbine annular cascade. This computation is characterized by the use of a highly stretched O-mesh around the blades and of H meshes for the upstream and downstream regions, in order to allow an accurate description of the leading- and trailing-edge phenomena. The configuration studied is an experimental set-up which has been recently realized at ONERA for the validation of computational codes (VEGA set-up).

1. INTRODUCTION

Pour répondre aux objectifs de plus en plus ambitieux des constructeurs de moteurs aéronautiques, il est maintenant nécessaire de mettre au point des méthodes de calcul de plus en plus complexes, capables de décrire les phénomènes physiques suivants: tridimensionnalité des écoulements, effets visqueux, effets de la turbulence, effets transsoniques.

L'outil "idéal" demandé aujourd'hui par les industriels est alors un code de résolution des équations de Navier-Stokes tridimensionnelles, compressibles, moyennées, comprenant une modélisation de la turbulence.

Un tel code fournit de manière exhaustive les caractéristiques locales de l'écoulement en tout point d'une grille d'aubes, mais une vue plus globale est indispensable: les grandeurs fondamentales du point de vue du constructeur sont en effet des grandeurs moyennées azimutalement sur un pas. Ce sont elles qui permettront par exemple d'ajuster les caractéristiques d'un rotor à l'écoulement qui sort d'un distributeur. À ce niveau, l'apport d'un code Navier-Stokes 3D est en représentation beaucoup plus précise des effets secondaires, qui ne pouvaient être que modélisés par les calculs méridiens.

Dans cette optique, l'ONERA développe depuis 1980 un code nommé CANARI (Code d'Analyse par Navier-Stokes en Aérodynamique) d'une fourchette isolée, destiné au calcul d'écoulements stationnaires dans les grilles de turbine et de compresseur.

La présente communication est consacrée au calcul de l'écoulement dans une grille de type distributeur de turbine haute pression. Ce cas de grille annulaire est caractérisé par de forts effets tridimensionnels et transsoniques.

2. RAPPEL DES CARACTERISTIQUES DE LA METHODE

Les équations de Navier-Stokes compressibles moyennées, associées à un modèle de turbulence de type longueur de mélange, sont la base mathématique du solveur. Ces équations ont été présentées de manière complète dans [1].

L'implantation du modèle de longueur de mélange nécessite un soin particulier dans le cas présent, où l'écoulement se développe entre des parois solides au nombre de quatre: moyeu, carter, intrados et extrados de l'aube.

En effet, le calcul de la longueur de mélange en un point courant du domaine de calcul suppose la détermination de deux quantités: la distance à la paroi d et l'épaisseur de couche limite δ . Comme décrit dans [1], la prise en compte de l'influence des différentes parois solides a été effectuée au moyen d'un calcul de "distance modifiée" proposé par Buleev [2]. Lorsque le point considéré se trouve dans le sous-domaine situé en amont de la grille, cette "distance" est calculée au moyen des distances séparant ce point du moyeu et du carter. Pour un point situé dans le sous-domaine entourant l'aube ou dans le sous-domaine aval, cette "distance" fait intervenir de plus les distances à l'extrados et à l'intrados de l'aube.

Le modèle de turbulence est appliqué dans tout l'écoulement. Actuellement, le code ne comporte pas la possibilité de décrire la transition laminaire-turbulent, mais une étude est en cours sur ce sujet.

La méthode numérique est décrite dans la référence [3], et est dérivée des méthodes présentées dans les références [4] et [5]. La discrétisation des équations utilise un schéma explicite centré de type Lax-Wendroff à deux pas. La stabilité du calcul est améliorée par deux termes de viscosité artificielle, permettant de capturer les discontinuités dans les régions de fluide parfait. La progression en temps de la solution se fait en utilisant un pas de temps local. L'évolution temporelle de la solution n'ayant ici pas de sens physique, il est impossible d'effectuer une simulation instationnaire.

Le programme CANARI utilise une approche multi-domaines. Un de ses atouts est sa modularité, qui permet, avec des modifications très limitées, de prendre en compte des géométries et des topologies variées. Dans le cas des turbines, il est ainsi possible d'utiliser un maillage en O autour des aubes afin de représenter avec un grand degré de détail les phénomènes dans les régions de bord d'attaque et de bord de fuite.

3. LA GRILLE ANNULAIRE "VEGA"

3.1. Données générales

On va ici considérer le cas pour lequel on a calculé l'écoulement dans le code CANARI: une grille distributrice annulaire de type turbine haute pression. Cette grille définit une géométrie

industrielles, a été conçue pour valider le code CANARI dans un cas d'écoulement complexe. La grille comprend 25 aubes cylindriques, avec un rayon de tête de 245 mm, et un rapport de moyeu de 0.775. La veine présente une divergence de 1° au carter, sur la portion située en aval de la grille. Les conditions aérodynamiques du calcul sont les suivantes:

- nombre de Mach amont : 0.15
- angle de l'écoulement amont : 0°
- nombre de Mach aval moyen : 1.1
- angle de l'écoulement aval moyen : -74.5°

Les conditions expérimentales sont proches des valeurs ci-dessus, mais les résultats sont encore indisponibles actuellement. Par conséquent, il n'est hélas pas possible ici de présenter de comparaison entre le calcul et l'expérience. Nous nous sommes cependant efforcés de donner dans la présente communication des résultats aussi complets que possible, en espérant ainsi fournir une illustration suffisante des possibilités du code CANARI.

Le maillage de calcul (Fig. 1) est composé de trois sous-domaines: un sous-domaine amont où l'on définit un maillage en H, un sous-domaine central constitué d'un maillage en O et un sous-domaine aval, lui aussi, maillé en H. Le maillage tridimensionnel est constitué d'un empilement de maillages surfaciques, définis sur des nappes de révolution entre le moyeu et le carter. Le maillage est fortement resserré au voisinage des parois (moyeu, carter, aube), de manière à obtenir une bonne représentation des couches limites. A titre indicatif, la taille de maille aux parois est d'environ un dix-millième de l'encombrement axial de l'aube.

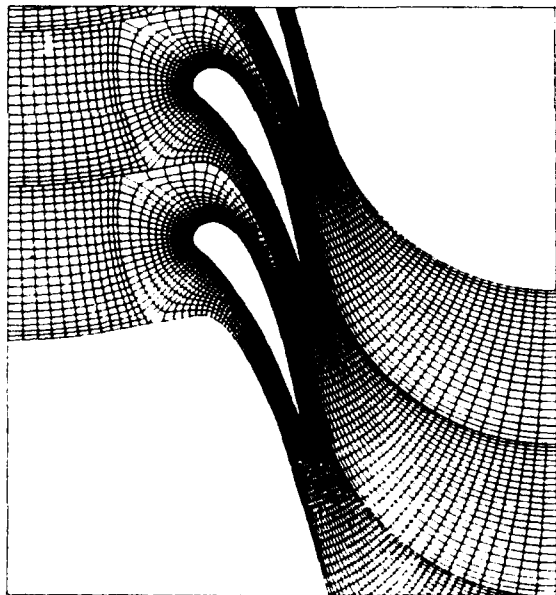


Fig. 1 - Vue bidimensionnelle du maillage

La même taille de maille est utilisée sur les différentes parois: nous avons en effet constaté que les couches limites au moyeu et au carter sont complètement "balayées" par les écoulements secondaires à l'entrée dans la grille: il est donc nécessaire de prévoir un maillage beaucoup plus serré que ne l'exigeraient les échelles des couches limites en amont. Le nombre de points de maillage se répartit comme suit:

maillage "H" amont	15 × 21 × 69
maillage "O" central	185 × 41 × 69
maillage "H" aval	49 × 25 × 69

soit au total 626 310 points. Le domaine de calcul ainsi maillé s'étend en amont du bord d'attaque et en aval du bord de fuite sur des distances valant

respectivement 1.7 et 2.4 fois l'encombrement axial de la grille. Ces dimensions, ainsi que le nombre de points de maillage choisi sont le fruit d'un compromis entre le temps de calcul raisonnablement envisageable, le degré de détail que l'on attend de ce type de calcul, et des exigences numériques ou physiques.

Le calcul utilise, dans le cas que nous présentons, les conditions aux limites suivantes:

- frontière amont: la direction de la vitesse et les profils de température totale et de pression totale sont imposés; ce dernier est déduit d'un profil initial analytique de vitesse obtenu à partir de la formule de Whitfield [6].

- frontière aval: le calcul est initié sur un certain nombre d'itérations en imposant un profil axisymétrique de pression statique obéissant à un équilibre radial simplifié; le calcul est ensuite poursuivi avec une condition de non-réflexion, afin de pouvoir représenter les hétérogénéités azimutales telles que les ondes de choc.

- parois solides: sur l'aube, le moyeu et le carter on impose une condition de non-glissement et la valeur de la température. La valeur de la pression est obtenue en supposant nul son gradient suivant la normale à la paroi, approchée par la ligne de maillage passant par le point considéré.

La convergence du calcul est suivie au moyen du niveau des résidus et de l'aspect visuel du champ. Les résultats présentés ici correspondent à une décroissance des résidus d'environ trois ordres de grandeur et à un état jugé stabilisé. Le temps de calcul est ici de 13.5 micro secondes par itération et par point, et représente au total un peu plus de 18 heures sur un ordinateur de type CRAY-2.

3.2. Résultats

Tout en ayant conscience de la difficulté d'extraire une information synthétique à partir d'une grande masse de résultats, nous présentons ici un nombre important de figures, de façon à donner une idée assez complète des résultats. Une première série de figures concerne des résultats extraits sur des surfaces, et représentés sous forme de cartes de lignes iso valeurs ou de vecteurs vitesses. Nous présentons ensuite des résultats globaux, obtenus par des moyennes azimutales sur un pas, ainsi qu'il est d'usage en turbomachines.

La figure 2 représente les lignes iso-nombre de Mach sur une surface de maillage située à 2% de hauteur de veine, donc très proche du pied. On y aperçoit le système d'ondes de choc et de détente issues du bord de fuite des aubes, ainsi que les interactions avec la couche limite extradados et les sillages. A 50% de hauteur de veine (Fig.3), le nombre de Mach moyen en sortie de l'aubage est nettement moins élevé, d'où des interactions transsoniques beaucoup moins marquées. Au voisinage du carter, à 98% de hauteur de veine (Fig.4), l'écoulement est essentiellement subsonique. Il est frappant de constater à quel point la structure de l'écoulement varie suivant la hauteur: cet effet tridimensionnel résulte avant tout des différences d'accélération subie par le fluide entre le pied et la tête (équilibre radial).

La tridimensionalité de l'écoulement est également due pour une large part aux écoulements secondaires. Ils sont constitués de structures tourbillonnaires prenant naissance devant le bord d'attaque de la grille. La figure 5 illustre la trace du tourbillon "en fer à cheval" au moyen d'une coupe du champ de vecteurs vitesses par un plan méridien passant approximativement par le bord d'attaque de l'aube. La paroi solide représentée en bas de la figure correspond au moyeu, et la paroi située à droite est celle de l'aube. Les vecteurs vitesse permettent de distinguer le décollement de la couche limite de moyeu, qui est à l'origine du tourbillon "en fer à cheval". Il faut mentionner que les vecteurs vitesse n'ont pas été tracés en tous les points du maillage au voisinage des parois, afin de préserver

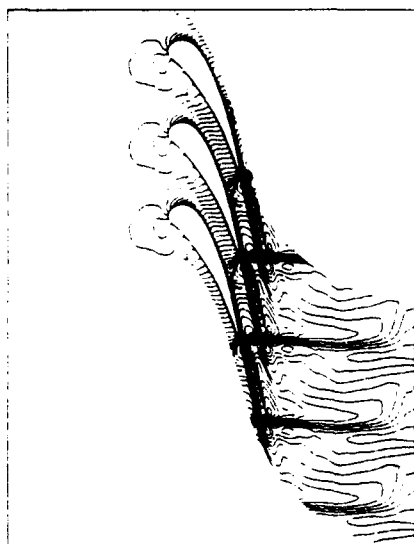


Fig. 2 - Lignes iso-nombre de Mach à 2% de hauteur de veine

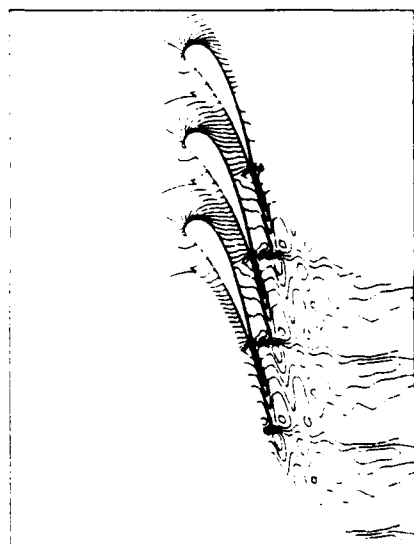


Fig. 3 - Lignes iso-nombre de Mach à 50% de hauteur de veine



Fig. 4 - Lignes iso-nombre de Mach à 98% de hauteur de veine

la lisibilité de la figure. Il est toutefois possible de visualiser une structure tourbillonnaire supplémentaire en agrandissant fortement la zone du coin formé par le moyeu et l'aube (Fig. 6). Ce tourbillon, tournant en sens inverse du précédent, est parfois appelé tourbillon "secondaire", par opposition au tourbillon en fer à cheval, appelé tourbillon "primaire" [7]. Ces deux dernières figures confirment que ce résultat de calcul représente convenablement la naissance des écoulements secondaires.

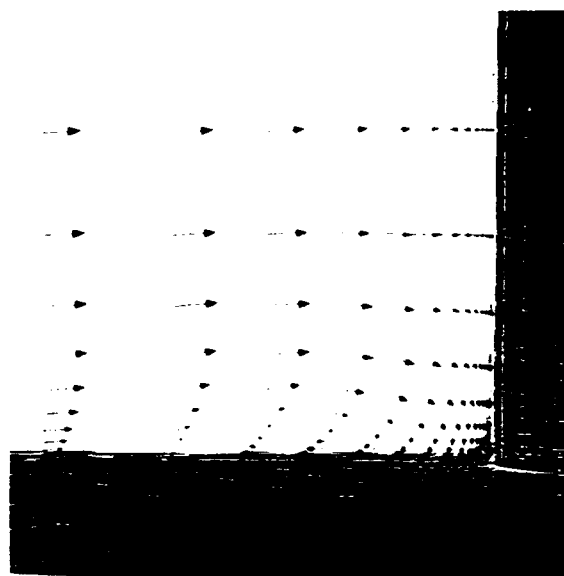


Fig. 5 - Champ de vecteurs vitesse en amont du bord d'attaque - Coupe du tourbillon en fer à cheval

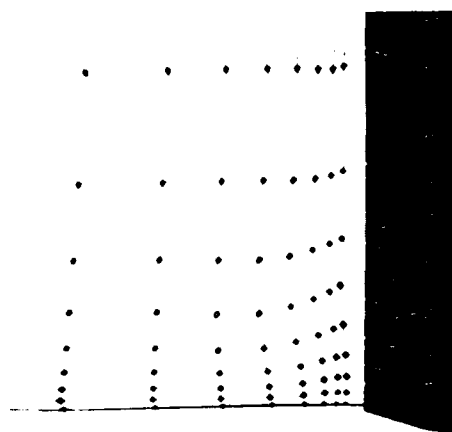


Fig. 6 - Champ de vecteurs vitesse en amont du bord d'attaque (agrandissement) - Coupe du tourbillon secondaire

Les figures suivantes représentent des résultats dans trois plans perpendiculaires à l'axe de la grille et correspondant à trois positions en aval du bord de fuite.

- plan 1 : 10% de C_x derrière le bord de fuite.
 - plan 2 : 25% de C_x derrière le bord de fuite.
 - plan 3 : 70% de C_x derrière le bord de fuite.
- où C_x représente l'encombrement axial de l'aube. Les vues sont prises en regardant vers l'amont. Les traces sont reproduites sur trois pas afin de représenter le caractère périodique du champ. Un segment de droite marque la frontière de périodicité du domaine de calcul.

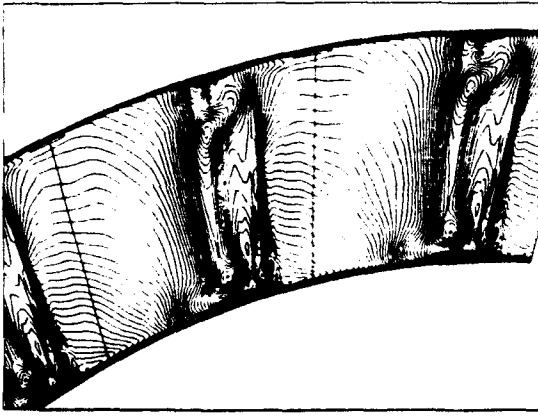


Fig. 7 - Lignes iso-nombre de Mach dans le plan 1 ($x/C_x = 0,1$)

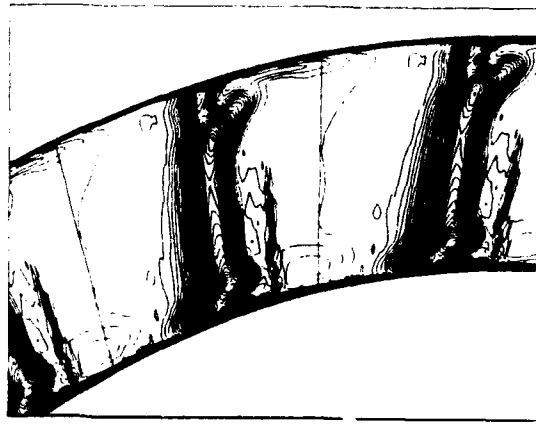


Fig. 10 - Lignes iso-pression totale dans le plan 1 ($x/C_x = 0,1$)

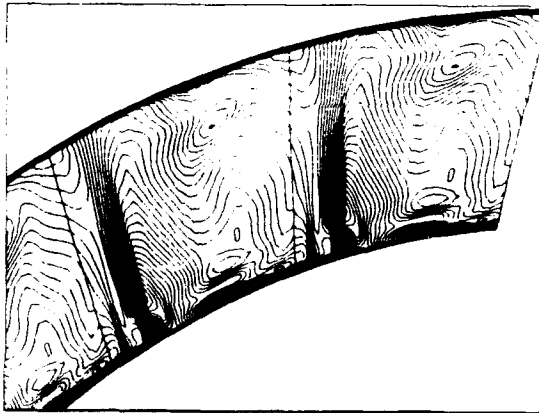


Fig. 8 - Lignes iso-nombre de Mach dans le plan 2 ($x/C_x = 0,25$)

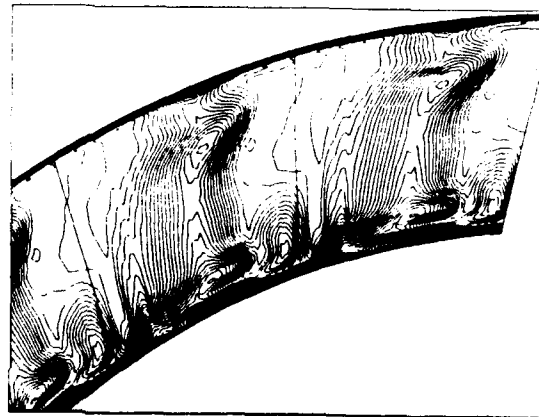


Fig. 11 - Lignes iso-pression totale dans le plan 2 ($x/C_x = 0,25$)

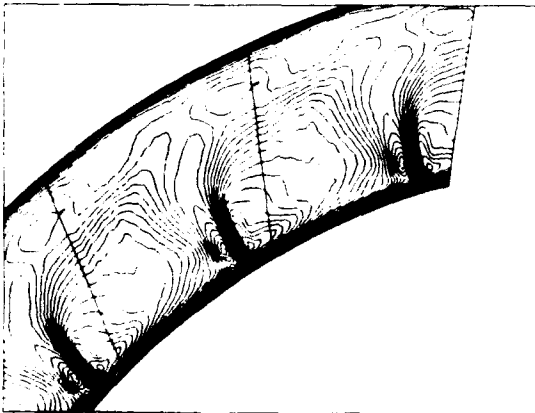


Fig. 9 - Lignes iso-nombre de Mach dans le plan 3 ($x/C_x = 0,7$)

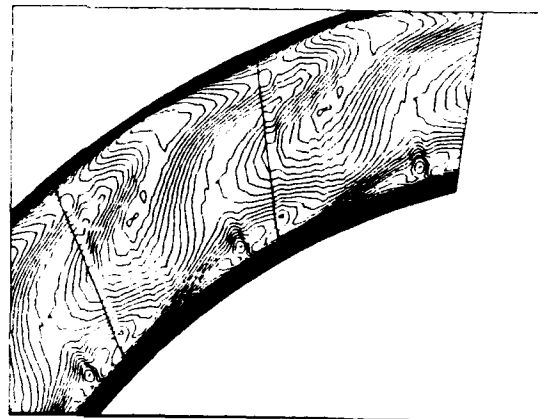


Fig. 12 - Lignes iso-pression totale dans le plan 3 ($x/C_x = 0,7$)

Les lignes iso-nombre de Mach dans les trois plans sont données par les figures 7, 8 et 9. La figure 7, correspondant à la position la plus proche du bord de fuite, montre nettement la trace de l'onde de choc issue du bord de fuite côté extradorsal, qui s'évanouit en s'approchant du carter. Le sillage est visible sous la forme de deux couches cisailées séparées par une zone de basses vitesses. Au voisinage de la tête et du pied, des "poches" se forment sur le sillage, sous

l'effet des écoulements secondaires, ainsi que cela sera montré plus loin. La région de fluide parfait présente l'évolution radiale que l'on attend dans ce type de grille. Lorsque l'on passe au plan suivant (Fig. 8), l'onde de choc s'est décalée vers la droite et a franchi la frontière de périodicité du domaine de calcul; elle se trouve donc légèrement étalée du fait de la différence de densité du maillage de part et d'autre de l'interface. Dans le dernier plan, situé à

70% de corde derrière la grille, l'aspect du champ est très particulier: en effet, à cette abscisse, l'onde de choc rencontre le sillage dans la région de pied, et ce dernier est très incliné sous l'effet des gradients dans la direction radiale.

Les figures 10, 11 et 12 représentent les lignes iso-pression totale dans les trois plans. On constate bien ici l'épaississement considérable des couches limites. En particulier, la couche limite sur le moueu atteint une épaisseur d'au moins 15% de la hauteur de veine.

Pour mettre en évidence les écoulements secondaires en sortie de la grille, nous avons représenté (Fig. 13, 14 et 15) les "vitesses secondaires" sous forme de vecteurs dans les trois plans utilisés ci-dessus. La "vitesse secondaire" est définie ici en soustrayant à la vitesse de l'écoulement sa composante suivant une direction azimutale "moyenne" arbitrairement choisie. Le vecteur résultant est ensuite projeté dans le plan perpendiculaire à l'axe pour une représentation bidimensionnelle. Dans le cas de la grille VEGA, nous avons utilisé pour calculer les vitesses secondaires un angle azimutal moyen de -74.5° . Bien évidemment, pour un écoulement fortement tridimensionnel comme c'est le cas ici, cette définition de la vitesse secondaire n'est pas pleinement satisfaisante. Néanmoins, il est possible d'avoir une idée assez claire de la structure de l'écoulement, comme le montre la figure 13, correspondant au plan le plus proche du bord de fuite. En tête, le tourbillon de passage est visible sans ambiguïté. En pied, plusieurs structures apparaissent: le tourbillon de passage au-dessus de la couche limite, un tourbillon contrarotatif très aplati au voisinage immédiat du moueu, et un enroulement dans le même sens que le tourbillon de passage dont seule la partie gauche (intrados) subsiste, par suite de l'intersection avec l'onde de choc. Ces deux dernières structures pourraient être interprétées [8], pour la première, comme étant liée à la branche "extrados" du tourbillon en fer à cheval et au tourbillon de bord de fuite, et pour la deuxième, comme résultant soit des nappes issues du bord de fuite, soit du décollement de la couche limite extrados sous l'effet de l'onde de choc. Ces hypothèses demandent à être vérifiées.

Les figures 14 et 15, représentant les vecteurs vitesse dans les plans 2 et 3, montrent que la position des tourbillons varie fortement d'un plan à l'autre. Seule une analyse réellement tridimensionnelle (lâcher de particules, lignes de courant) permettrait de comprendre précisément la structure de l'écoulement, qui est ici compliquée par la présence d'ondes de choc. Il est toutefois important de remarquer (Fig. 15) que les vitesses secondaires transportent le fluide depuis la couche limite du moueu jusqu'au voisinage du carter.

Comme cela est mentionné plus haut, l'exploitation des résultats tridimensionnels doit être complétée par le calcul de grandeurs globales. Dans le cas des grilles d'aubes, les grandeurs utilisées sont des moyennes azimutales sur un pas pondérées par le débit. L'évolution radiale de ces moyennes renseigne sur les performances de la grille et sur les caractéristiques moyennes de l'écoulement. Les figures 16 et 17 présentent les évolutions radiales des angles de sortie (angle azimutal et angle méridien) dans les plans 1, 2 et 3 en aval de la grille. La figure 18 et 19 présentent respectivement les distributions du nombre de Mach et de la pression totale également dans les plans 1, 2 et 3. Les évolutions obtenues pour chacune de ces grandeurs sont tout à fait représentatives d'un écoulement comprenant d'importants effets secondaires. Cependant, le niveau de pertes semble un peu élevé, probablement à

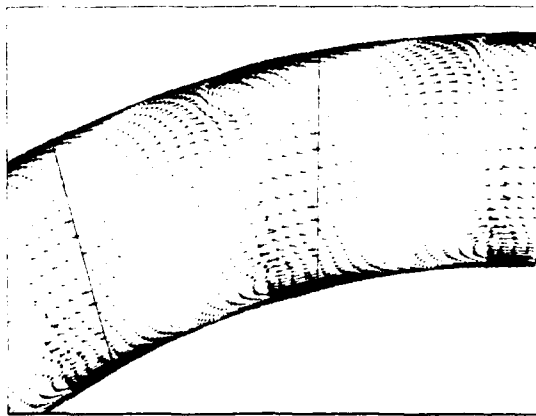


Fig. 13 - Vecteurs vitesse "secondaires" dans le plan 1 ($x/C_x=0,1$)

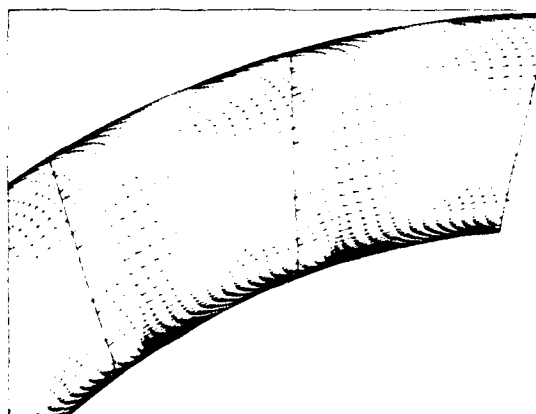


Fig. 14 - Vecteurs vitesse "secondaires" dans le plan 2 ($x/C_x=0,25$)

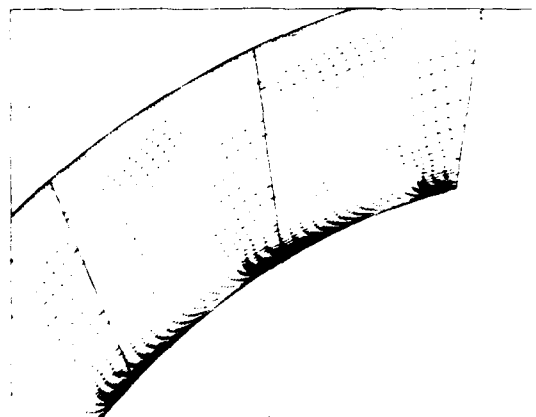


Fig. 15 - Vecteurs vitesse "secondaires" dans le plan 3 ($x/C_x=0,7$)

cause de couches limites turbulentes trop épaisses sur l'aube, et du fait de la non prise en compte des écoulements laminaires et transitionnels.

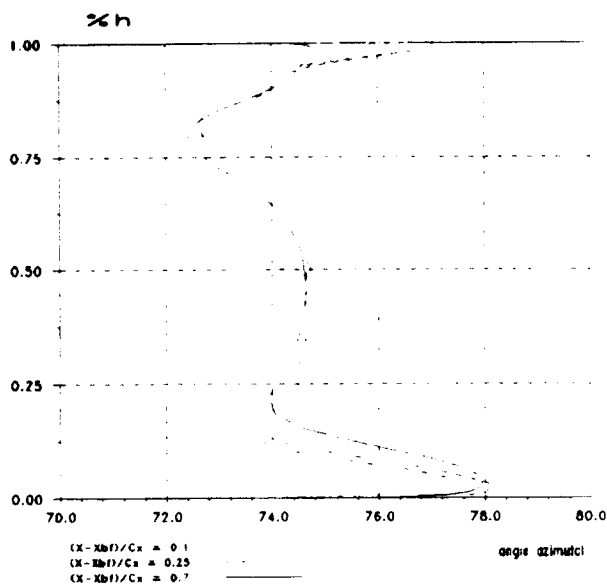


Fig. 16 - Evolutions radiales de l'angle azimutal moyen dans les plans 1, 2 et 3

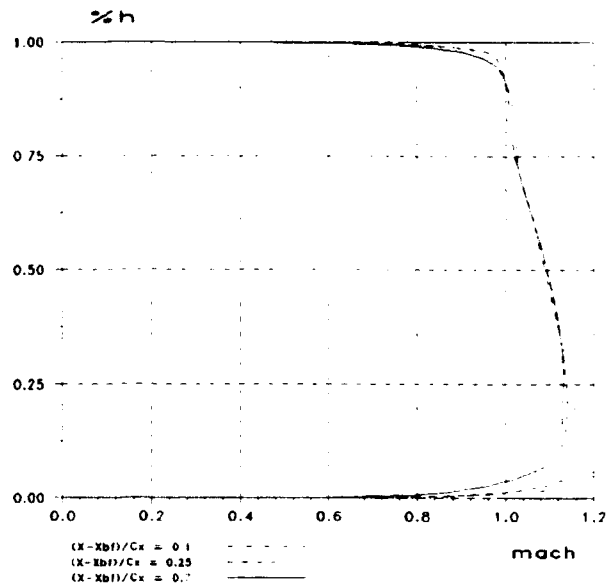


Fig. 18 - Evolutions radiales du nombre de Mach moyen dans les plans 1, 2 et 3

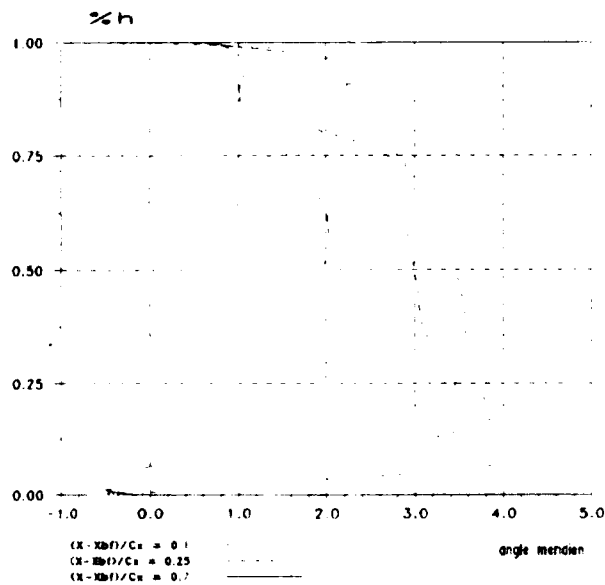


Fig. 17 - Evolutions radiales de l'angle méridien moyen dans les plans 1, 2 et 3

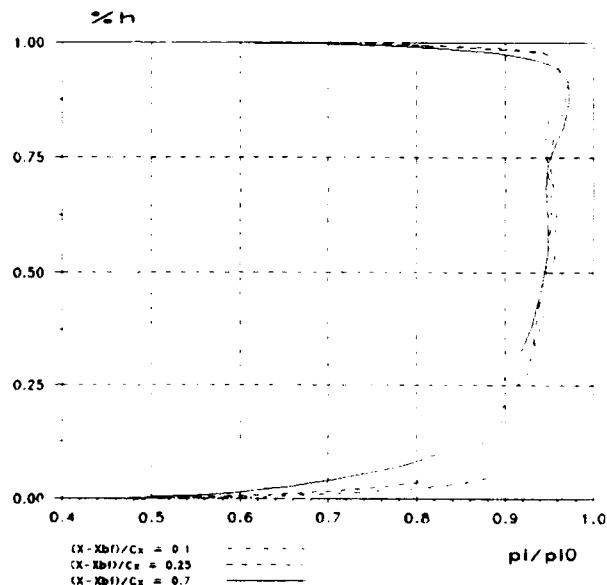


Fig. 19 - Evolutions radiales de la pression totale moyenne dans les plans 1, 2 et 3

4. CONCLUSION

Bien que la comparaison à l'expérience n'ait pu être présentée, les résultats donnés par le code "CANARI" sur une grille annulaire de distributeur haute pression confirment que ce code permet d'analyser un écoulement transsonique de structure complexe. Les renseignements obtenus sont de nature à intéresser directement les constructeurs. Au niveau global, les résultats moyennes représentent un apport par comparaison aux méthodes de prédiction employées jusqu'à présent. Au niveau local, les résultats permettent une compréhension fine de l'écoulement, ce que ne permettent pas les méthodes expérimentales. Des perspectives immédiates consisteront à valider quantitativement le code par comparaison aux résultats expérimentaux, dès que ceux-ci seront disponibles.

REFERENCES

- [1] L. CAMBIER et B. ESCANDE
"Calcul de l'écoulement tridimensionnel turbulent dans un aubage rectiligne de turbine". AGARD/PEP 74th Meeting on Secondary Flow in Turbomachines, Luxembourg, 1989.
- [2] N.I. BULEEV
"Theoretical Model of the Mechanism of Turbulent Exchange in Fluid Flow". Teploperedacha, pp. 64-95, Moscow, USSR, 1967 and AEEF Translation 955, Atomic Research Establishment, Harwell, England, 1967.
- [3] L. CAMBIER et B. ESCANDE
"Calculation of a Three Dimensional Shock

- Wave Turbulent Boundary Layer Interaction", AIAA Journal, Vol. 29, pp. 1762-1763, 1991, November 1991.
- 141 L. CAMBIER, V. QUAILLIERE and V. VUILLIET
"Résolution numérique des équations des Navier-Stokes à l'aide d'une méthode multigrille", in Recherche Aéronautique, 1988 2, pp. 25-42, 1988.
- 151 A.M. VUILLIET
"A Multi-Domain Euler Solver for Flows in Turbomachines", Proceedings of the 9th ISABE Symposium, Athens, Sept. 1989.
- 161 D.L. WHITFIELD
"Analytical Description of the Complete Turbulent Boundary Layer Velocity Profile", AIAA Paper 78-1158, 1978.
- 171 W.A. PETERLE and L.M. LANFSTON
"Torsionless Vortex Formation around a Cylinder", ASME J. of Turbom., 109, pp. 284-285, April 1991.
- 181 J.H. CIEVERDING
"Recent Progress in the Understanding of Basic Aspects of Secondary Flows in Turbine Blade Passages", ASME Paper n°84-GT-16, 1984.

REMERCIEMENTS

Le travail présenté ici a été effectué sous contrat de la Direction des Recherches, Etudes et Techniques de la Délégation Générale pour l'Armement.

Discussion

C. HAH, NASA LEWIS, U.S.A.

These are very impressive results. In Fig. 2, the shock might have to extend all the way to the exit. To have this feature numerically, exit boundary conditions might have to be handled differently. At the exit plane, the static pressure cannot be specified constant in the tangential direction. How is this exit boundary condition handled in the code?

AUTHOR'S REPLY

The static pressure on the downstream boundary is prescribed only in the first hundreds of time steps. The prescribed value is uniform in the tangential direction and corresponds to a radial equilibrium relation. Obviously, this condition is not suitable when a shock wave crosses the downstream boundary. For this reason, in a second phase, the downstream condition is a nonreflecting condition, which allows circumferential pressure variations but still keeps the memory of the radial evolutions previously prescribed. If we had used the nonreflecting condition from the beginning of the calculation, the downstream values would have been influenced by the initial conditions, which do not represent radial equilibrium. In Fig. 2, the shock wave vanishes towards the downstream boundary because of the growth of the subsonic boundary layer on the hub. In Fig. 3, we can see that the shock wave is still remaining and crosses the downstream boundary without reflection.

J. MOORE, VPI, U.S.A.

Are you planning to validate your code by comparison with experimental data? If so, when do you expect to publish the results?

AUTHOR'S REPLY

In the case of this turbine stator, the comparison to experimental results is planned, as soon as the experimental data are processed. I must note that we have already compared our code's results to experimental data in a transonic channel flow case (see Ref. 3).

R. GRAY, WRIGHT LABS, U.S.A.

How are the characteristic relations used to determine the correct inlet total pressure and temperature to the cascade?

AUTHOR'S REPLY

The total pressure and temperature at the inlet must be either prescribed, or computed, for the initial field. In the present case, the total temperature is assumed uniform (and equal to its value in the reservoir conditions). The total pressure profile is deduced from an analytical velocity profile (see Ref. 6) for the hub and tip boundary layers. The assumption is that the static pressure is constant. The boundary layer profile requires the following data: the displacement and momentum thicknesses, the skin friction coefficient, and the outer velocity.

F. LEBOEUF, ECOLE CENTRALE LYON, FRANCE

Dans le Fig. 3 il existe une interaction entre le choc issu du bord de fuite et le sillage issu de l'aubage adjacent. Le sillage accélère-t-il jusqu'à un régime supersonique et comment cette interaction se produit-elle?

AUTHOR'S REPLY

- Le sillage, qui est fortement accéléré en supersonique subit une interaction forte avec le choc, et un fort ralentissement; ce ralentissement peut localement causer un épaissement du sillage et même une bulle de décollement.
- Malheureusement ces calculs sont très récents et nous n'avons pas encore eu ni le temps ni les moyens d'analyser finement le détail de cette interaction.

C. HAH, NASA LEWIS, U.S.A.

About Prof. Leboeuf's remark; we also observe similar behavior of flow for this type of H.P. turbine. The overall physics of the flow looks correctly calculated. The interaction between the shock and the wake is very well calculated.

T. VOGEL, DLR, GERMANY

- 1) How much computer storage do you need for your calculation?
- 2) What are your convergence criteria?

AUTHOR'S REPLY

1) The present calculation required less than 40 million words of computer storage on a CRAY 2. This code is written for computers having large memory, in order to minimize CPU time.

2) The convergence is evaluated by following the level of the residuals and the visual aspect of the solution. The final solution corresponds to a three-order of magnitude decrease of the residuals.





Computation and Visualization of Specific Flow
Phenomena in Turbomachinery Application

J. Haarmeyer
B. Stubert
MTU München GmbH
Dachauer Straße 665
D-8000 Munich 50

92-16079

Summary

Capacity and speed in industrial computer hardware today allows the complete numerical evaluation of the three-dimensional flow field through turbomachinery blading. Detailed consideration of specific flow phenomena like horseshoe vortex or tip clearance effects will be of increasing importance in the design process. It is therefore necessary to study the influence of such phenomena in more depth.

The large amount of data produced by a three-dimensional calculation requires separate development of algorithms for visualization of the computational results. Numerical techniques for the integration of both streamlines and vortex lines through three-dimensional vector fields are needed to identify fluid flow features based on values at discrete grid points. This paper covers such an integration technique which includes a search algorithm for places of local rotations. By way of illustration some evaluations of Euler calculations in a turbomachinery application are shown.

List of Symbols

x, y, z	cartesian coordinates of physical space
ξ, η, ζ	coordinates of numerical space
v, v, w	velocity vector in physical, in numerical space, and in cylindrical coordinates
v_x, v_y, v_z	components of the velocity
w_r, w_u, w_z	components of the velocity cylindrical coordinates
$\frac{\partial x}{\partial \xi}, \frac{\partial x}{\partial \eta}, \dots$	partial derivatives
J	Jacobian
$\frac{dx}{dt}, \frac{dy}{dt}, \frac{dz}{dt}$	derivatives with respect to time
(α, β, γ)	arbitrary point

Abbreviations

ODE	ordinary differential equation
IV	initial value

1. Introduction

A fluid flow computer simulation may give highly detailed information of a complex flow field. The 3D-computation which commonly is carried out on a supercomputer produces a large amount of data. A small computational grid consists of approximately 100,000, e.g. $100 \times 30 \times 30$ grid points, but engineers now are dealing with grids which have up to one million points. It is simply impossible to get any benefit by only listing this data. Rather a post-processing is needed to produce objects which can be visualized and so easier can be interpreted. These objects are velocity vectors, iso-lines, iso-surfaces, streamlines, vortex lines, etc.

The main subject of this paper are the streamlines. We only consider the steady case and here streamlines are identical with trajectories of fluid particles, so they can also be compared with pictures of experimental simulation. A 3D-calculation computes the flow field not everywhere in space but only at discrete points which usually are the knots of a computational grid. To obtain streamlines from such kind of data, first an interpolation routine is needed and second some integration technique is to be carried out.

In a 3D flow-field the streamlines are a two-parametric family of curves. The parameters can be seen as the starting points of a fluid particle. These starting points must be seeded intelligently to produce a picture of the specific phenomena one is looking for. User interaction may be called for this selection. This paper presents an algorithm which detects points in regions with local rotations. These points can be taken as such starting points.

2. Interpolation

In a turbomachinery cascade mostly computational grids of H-type or C-type are used (fig. 1, 2). For our purpose (calculation of streamlines) these adjusted grids are not usable. Instead we better deal with orthogonal grids for which interpolation routines are faster.

We call the coordinates of the physical space (x, y, z) and the coordinates of the computational space (ξ, η, ζ) . The original grid points are:

$$(x_i, j, k, y_i, j, k, z_i, j, k), \\ 1 \leq i \leq i_{\max}, 1 \leq j \leq j_{\max}, 1 \leq k \leq k_{\max}.$$

The computational grid points (ξ_i, η_j, ζ_k) are defined as follows (H-type grid):

$$\xi_i := 0, \xi_{i+1} := \xi_i + \\ \text{mean}((x_{i+1, j, k} - x_{i, j, k}), 1 \leq j \leq j_{\max}, 1 \leq k \leq k_{\max}),$$

$$\eta_j := 0, \eta_{j+1} := \eta_j + \\ \text{mean}((y_{i, j+1, k} - y_{i, j, k}), 1 \leq i \leq i_{\max}, 1 \leq k \leq k_{\max}),$$

$$\zeta_k := 0, \zeta_{k+1} := \zeta_k + \\ \text{mean}((z_{i, j, k+1} - z_{i, j, k}), 1 \leq i \leq i_{\max}, 1 \leq j \leq j_{\max}).$$

Thus the points of the computational grid are not equally spaced but behave like the original points. They are closer in those regions where it is desirable (e.g., at the leading or trailing edge of the blade) (fig. 3). In the case of a C-type grid the definition of the computational grid is slightly different. The periodic conditions in the physical space lead to a symmetric numerical grid with respect to the plane ($\xi = \xi_i$, $i = (i_{\max} + 1)/2$).

When the computational grid is defined an interpolation routine is to be chosen. For two reasons we want to get data that are as smooth as possible. One reason is that the vortices and the rotations can be better represented with smooth curves than with piecewise straight lines. The other reason is that the high-order integration routines which will be described later require smooth data.

There are several interpolation methods which can process given data on orthogonal grids. We prefer the method of parabolic blending [1]. This is a local method, which means that in order to obtain a value at a specific point in space, only the values on gridpoints in the neighbourhood are used. The result is a function which is everywhere twice continuously differentiable with respect to the coordinates (ξ, η, ζ).

The chosen interpolation method then defines the mapping from computational to physical space: (ξ, η, ζ) \rightarrow (x, y, z). At grid-points this mapping is already done by setting:

$$(\xi_i, \eta_j, \zeta_k) \rightarrow (x_i, y_j, z_k).$$

So by interpolation we get:

$$\begin{aligned} x &= x(\xi, \eta, \zeta), \\ y &= y(\xi, \eta, \zeta), \\ z &= z(\xi, \eta, \zeta) \end{aligned}$$

We can also compute the Jacobian:

$$J = \begin{vmatrix} \frac{\partial x}{\partial \xi} & \frac{\partial x}{\partial \eta} & \frac{\partial x}{\partial \zeta} \\ \frac{\partial y}{\partial \xi} & \frac{\partial y}{\partial \eta} & \frac{\partial y}{\partial \zeta} \\ \frac{\partial z}{\partial \xi} & \frac{\partial z}{\partial \eta} & \frac{\partial z}{\partial \zeta} \end{vmatrix}$$

The transformation of the velocities takes place with the inverse of J:

$$v = J^{-1} \bar{v}$$

Observe that we have defined a mapping from the computational to the physical space and not the inverse. If one needs to know a point (ξ, η, ζ) which corresponds to a given (x, y, z) a non-linear 3x3 system of equations has to be solved.

3. Streamlines

We understand streamlines as trajectories of fluid-particles. Consider a particle at a point (x, y, z) in a velocity-field $v(x, y, z)$. The dynamic description is:

$$\begin{aligned} \frac{dx}{dt} &= v_x(x, y, z) \\ \frac{dy}{dt} &= v_y(x, y, z) \\ \frac{dz}{dt} &= v_z(x, y, z) \end{aligned} \quad (\text{ODE})$$

This is a system of ordinary differential equations. If a point (x_0, y_0, z_0) is seeded, (ODE) together with the condition:

$$\begin{aligned} x(0) &= x_0 \\ y(0) &= y_0 \\ z(0) &= z_0 \end{aligned} \quad (\text{IV})$$

form an initial value problem which can be solved numerically.

The simplest numerical method is due to Euler. Choose a time-step h , and set:

$$\begin{aligned} x(t+h) &:= x(t) + h \cdot v_x(x(t), y(t), z(t)) \\ y(t+h) &:= y(t) + h \cdot v_y(x(t), y(t), z(t)) \\ z(t+h) &:= z(t) + h \cdot v_z(x(t), y(t), z(t)) \end{aligned}$$

Starting with $t=0$ and repeating this several times a sequence can be computed:

$$(x(i \cdot h), y(i \cdot h), z(i \cdot h)), i=0, 1, 2, \dots)$$

This sequence can be considered as an approximation of some discrete points on the streamline.

The accuracy of this approximation depends only on the chosen step size h . It is well known that this simple algorithm needs a very small time-step for a satisfactory accuracy. So during the calculations of the streamline a high number of function evaluations are to be carried out. Each function evaluation is a computation of the three components of the velocity by means of the interpolation method.

Mathematicians have developed several algorithms for solving initial value problems like (ODE), (IV) faster than the simple Euler-method does. The most popular are the Runge-Kutta methods. Less known are the multi-step methods by Adams-Moulton or by Gear [2]. All these high-order methods require smooth data (i.e., a velocity field which is sufficiently often differentiable with respect to the coordinates x, y , and z). If the data are not smooth, e.g., at a shock in the flow field, the ODE-solver will automatically reduce the step-size. In this case the benefit of the high-order method will decrease again.

When the computation of the streamline is carried out with a high-order algorithm, the number of function evaluation and so the time and the costs are reduced. Because of the greater time step (which may vary) less discrete points on the streamline are computed. This may result in a problem when the streamline is to be plotted. For a smooth curve one needs many plot points and it seems to be necessary that intermediate points have to be generated by interpolating between the few ones.

On the other hand the multi-step methods use an internal approximation of the solution curve which is a polynomial. Thus one can use this internal representation and evaluate the polynomial at as much points as one needs. This is known as a high-order-method with dense output.

As a result of the arguments we have decided to use the multi-step-method by Adams-Moulton. The implementation in FORTRAN is available on the software-market (for example in the libraries of IMSL or NAG), and the only work which is to be done is to adopt such a routine to one's own code.

4. Vortex Lines

Vortex lines can be treated in the same way as streamlines when the velocity field is replaced by the curl. So the remaining problem is to compute the curl of the velocity. This however can easily be done by means of the interpolation routine.

The physical dimension of the velocity is [m/s] while the dimension of the curl is [1/s]. So in the streamline case the parameter t is actually a time, while in the vortex line case the parameter t is only artificial.

5. Local Rotations

The concept of local rotation is due to Vollmers et al. [3]. We intuitively understand a vortex as a locally rotating part of the fluid where in a cross section the streamline patterns have centres or foci.

Consider a small vector:

$$\mathbf{r}(t) = (x_1, y_1, z_1) - (x_0, y_0, z_0)$$

attached at (x_0, y_0, z_0) . After a small time step h we have:

$$\mathbf{r}(t+h) = \mathbf{r}(t) + h \cdot \mathbf{J}(\alpha, \beta, \gamma) \cdot \mathbf{r}(t)$$

where \mathbf{J} is the Jacobian of the velocity field \mathbf{v} and (α, β, γ) is a point in the neighbourhood of (x_1, y_1, z_1) and (x_0, y_0, z_0) . This leads us to consider the eigenvalues and eigenvectors of \mathbf{J} .

\mathbf{J} is a real 3x3 matrix with either three real eigenvalues and eigenvectors or two complex eigenvalues with corresponding complex eigenvectors and one real eigenvalue and eigenvector. For a symmetric Matrix \mathbf{J} the eigenvectors are orthogonal and we may construct the well-known ellipsoid of principal stresses. If two eigenvalues become complex, the real eigenvector is the axis of a local rotational displacement. Thus by distinguishing the complex eigenvalues of the Jacobian of the velocity vector we can detect a region where axes of local rotation may occur.

An observer who moves with the fluid and looks parallel to the direction of the local velocity vector will not generally see rotations. It is only if the principal axis is almost parallel to the direction of displacement that a local rotation is observed.

So our procedure to find local rotations is: search for grid points where complex eigenvalues of the Jacobian of the velocity occur. If the angle of the real eigenvector and the velocity vector is less than a (user-)given limit, the point will be selected to become a starting point of a streamline which will be computed forward. A second streamline which is evaluated backwards may then be concatenated.

6. Euler Calculation

The numerical scheme of the Euler calculation is based on a finite volume discretization for the Euler equations in cylindrical coordinates on the rotating frame. A nodal point technique with overlapping control volumes in all coordinate directions is used on an H-type or C-type grid according to the blade geometry. The discretization in time is formulated by the so-called "Damping Surface Technique" [4,5].

Several conditions for the boundary grid points must be specified as follows:

- in the inlet plane the relative total pressure, the relative total temperature, the flow angles $\arctan(w_r/w_z)$, and $\arctan(w_u/w_z)$ or instead of the latter the relative velocity component in circumferential direction (w_u).
- at midspan of the outlet plane the static pressure which is set constant in circumferential direction.

Values at the remaining boundary grid points are part of the solution namely in the outlet plane and at the periodic boundaries. On the solid boundaries neither mass flux nor energy flux is permitted and after every timestep the tangential condition for the velocity is computed additionally.

The calculation of two thousand time steps on a grid with 225x27x33 points requires about 20 minutes on a Cray-YMP.

7. Applications

Two applications of the prescribed numerical integration scheme are discussed. Firstly the horse-shoe vortex formation in a turbine stator and secondly the flow in the tip clearance region of an axial compressor fan. In both cases main interest and therefore numerical grid points are concentrated on the secondary flow regions.

To seed the starting points of the streamlines that are to be calculated we first apply our procedure that detects local rotations (as described in paragraph 5). The result will be a whole bundle of streamlines that look rather disordered. Now we select one streamline and set some other points in the neighbourhood of the selected one. Two neighbouring lines may be connected to ribbons which we call stream ribbons.

Figure 4 shows starting points, marked as crosses, where a forward and backward integration of the velocity field begins up to the outlet and inlet positions of those streamlines which go through these points. This technique provides in a relatively simple manner an insight to known secondary flow regions.

Two classes of pictures are made to visualize the flow pattern of the two examples. A number of neighbouring streamlines allows an insight more into local details of the flow whereas a few stream ribbons provide more clearly distinct flow paths and their rotation over the whole physical domain.

a) Turbine Stator

The development of a horse-shoe vortex formation in a frictionless calculation is reached by a total pressure variation in the inlet boundary of the numerical domain to simulate an oncoming boundary layer flow near a side wall. The profile is given by a measurement in a turbine test facility not specially for this test case but for comparable flow conditions.

In order to save computer storage the computational domain is reduced to the hub region only. The inlet boundary layer thickness therefore covers thirty percent of the flow channel in radial direction. Figure 5 shows the coaxial channel contour in meridional projection.

In figures 6a+b, the backward flow in front of the leading edge clearly can be seen until it rolls up to the horse shoe vortex. It is interesting to see that the backward flow from the starting points forms two neighbouring quasi meridian stream surfaces. Particles from these surfaces build up downstream of the suction side leg and the pressure side leg of the horse shoe vortex. The corresponding rotations can be observed in figures 7a+b. In these figures a further stream ribbon is represented to illustrate the passage vortex. It is interesting to follow the interaction of the suction side leg of the horse shoe vortex and the passage vortex. An animation of this picture in a coloured version carries out more clearly than a monochrome plot the change in rotation of the suction side leg due to numerical diffusion. The passage vortex is seen here as the dominant phenomenon.

To be more illustrative, a vortex line of the horse-shoe vortex has been calculated, too (fig. 8). This vortex is dominant in approximately thirty percent of the passage while the main part of the passage is dominated by the passage vortex. The change of direction of rotation happens near the turning point of the vortex line. The pressure side leg of the horse shoe vortex initially rotates in the same direction as the passage vortex.

Observe that although the curl of the velocity field is periodical the computed vortex line is not. This would only happen in the special case that an end point of a vortex line meets its own starting point shifted by a period. But if one repeats the vortex line by rotating the periodical pattern will immediately be seen.

b) Compressor Rotor

Main interest of this example is concentrated on the tip clearance region. In order to maintain the H-type grid topology the original blade geometry and the numerical grid are modified as shown in fig. 9. It should be pointed out that the focus is not on the details of the tip clearance flow but rather on the global interaction between the suction and the pressure side region. Therefore the grid density seemed to be sufficient. The flow field computation again is carried out by an Euler calculation. Again, the streamline (figures 10a+b) and stream ribbon (figures 11a+b) technique are used to visualize the flow pattern. It is possible to divide the flow across the tip clearance in more or less undisturbed regions and sections which are influenced by a vortex directly. Obviously the third ribbon from the left in fig. 11 contains the core of the tip vortex.

8. Conclusions

We have introduced a technique for calculation and visualization of streamlines and vortex lines. The above algorithms can be integrated into a 3D display system which may run on a modern workstation.

The main advantage of such a visualization technique is that it permits one to determine the location in the oncoming flow of fluid patches of interest in the downstream flow field. Comparisons with experimental visualization techniques can easily be carried out.

References

- [1] Rogers, D.F. and Adams, J.A., "Mathematical Elements for Computer Graphics", McGraw-Hill, New York, 1976, pp. 133-138
- [2] Gear, C.W., "Numerical Initial-Value Problems in Ordinary Differential Equations", Prentice-Hall, Englewood Cliffs, New Jersey, 1971
- [3] Vollmers, H., Kreplin, H.-P., and Meier, H.U., "Separation and Vortical Type Flow around a prolate Spheroid", AGARD-CP-No. 342, paper no. 14, 1983
- [4] Happel, H.-W. and Stubert, B., "Computation of Transonic 3D Cascade Flow and Comparison with Experiments", AGARD-CP-No. 437, paper no. 31, 1988
- [5] Couston, M., McDonald, P.W., and Smolderen, J.J., "The Damping Surface Technique for Time Dependent Solutions to Fluid Dynamic Problems", VKI TN 109, 1975

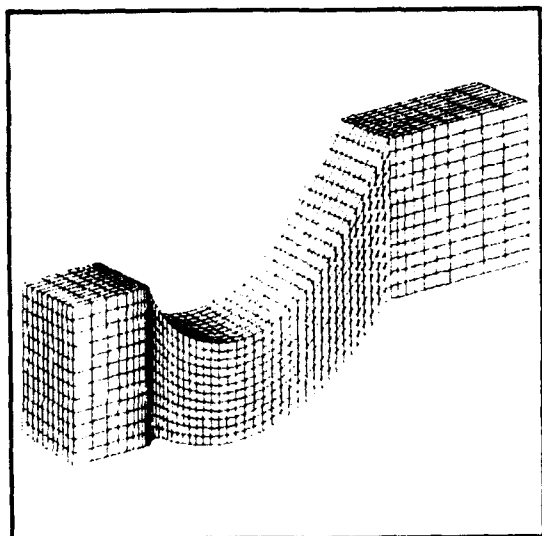


Fig. 1: 3D H-Type Grid

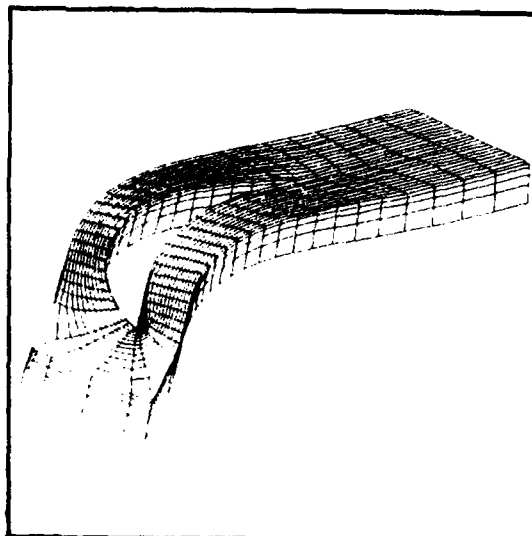


Fig. 2: 3D C-Type Grid

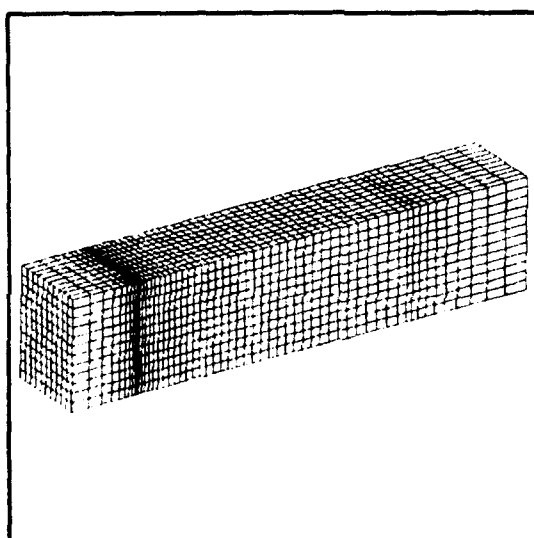


Fig. 3: Numerical Grid

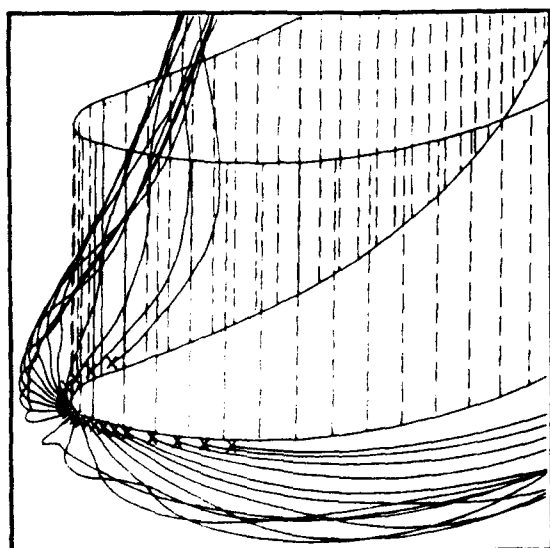


Fig. 4: Starting Points for Horse-Shoe-Vortex Streamlines

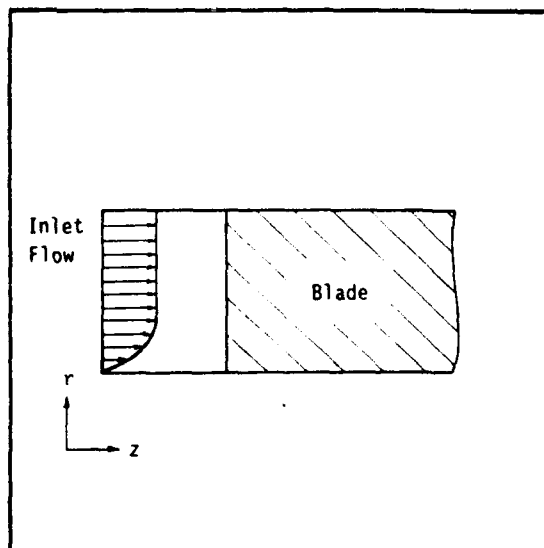


Fig. 5: Inlet Total Pressure Distribution

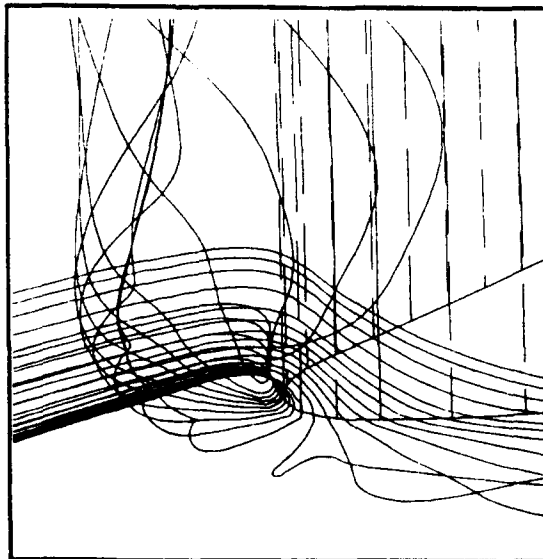
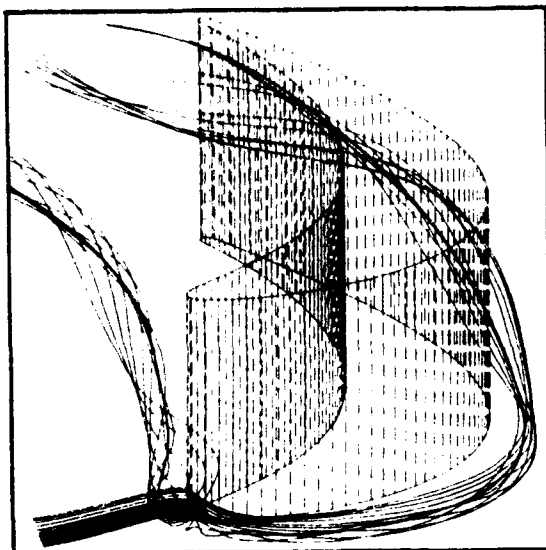


Fig. 6a, b: Horse-Shoe-Vortex Streamlines
computed forward and backward

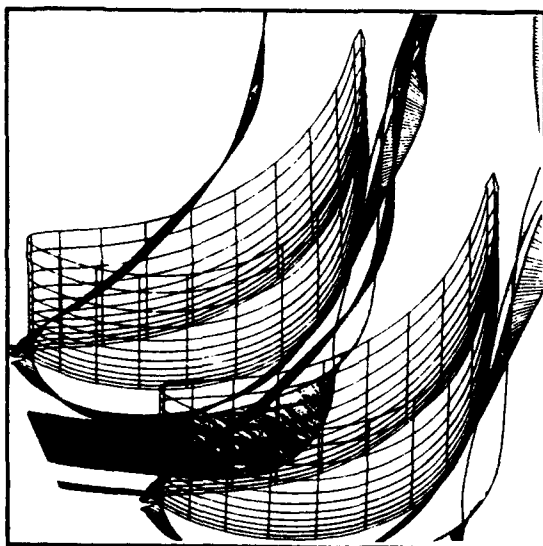
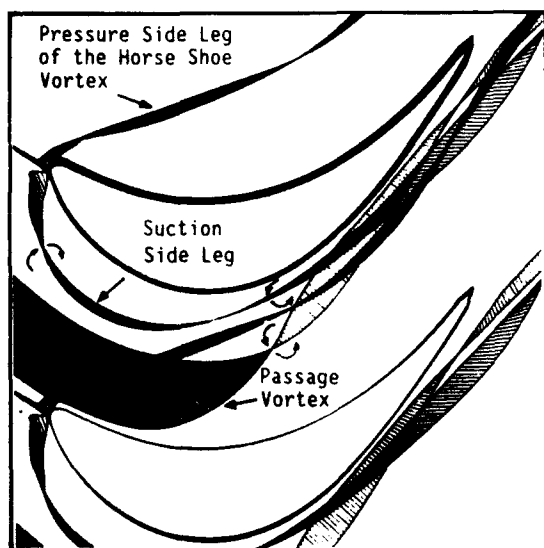


Fig. 7a,b: Horse-Shoe-Vortex Streamribbons

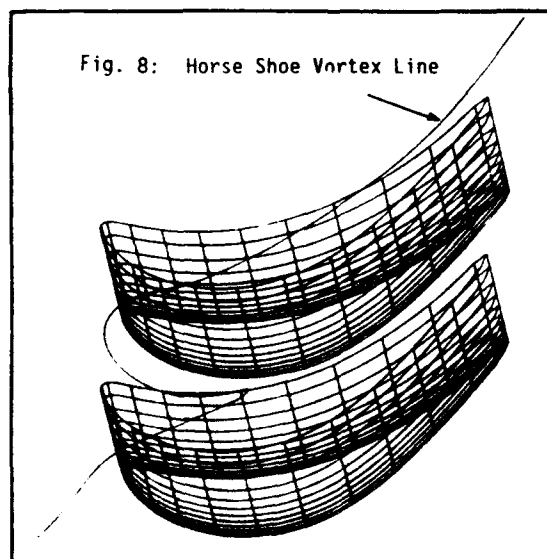


Fig. 8: Horse Shoe Vortex Line

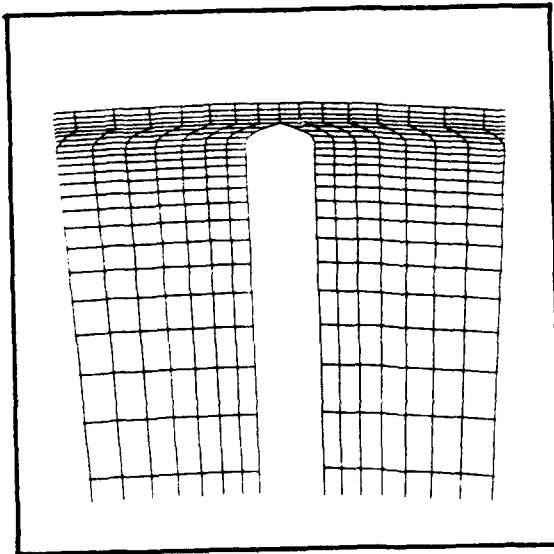


Fig. 9: Tip Clearance Discretization

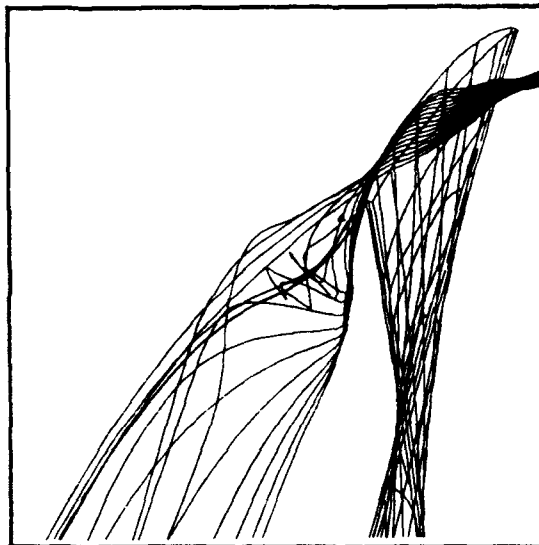
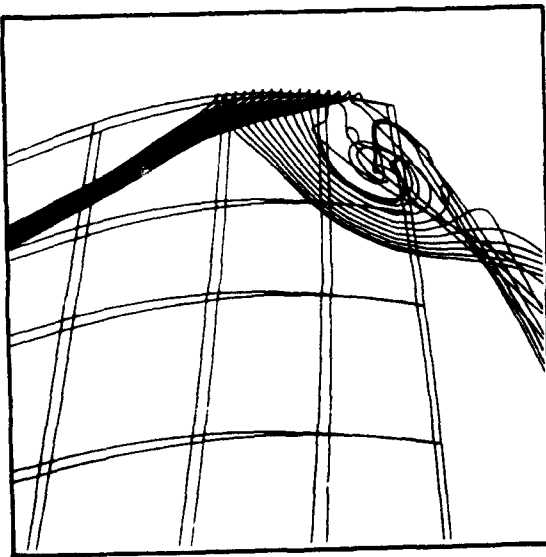


Fig. 10a,b: Streamlines in Tip Clearance

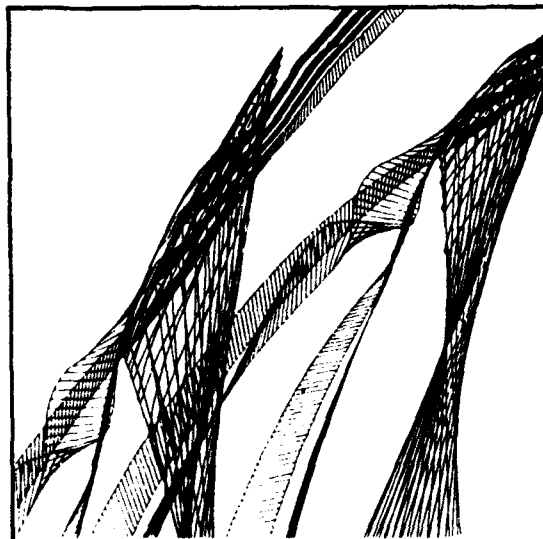


Fig. 11a,b: Streamribbons in Tip Clearance

Discussion

J. MOORE, VPI, U.S.A.

What weighting function do you use to interpolate between the parabolas?

AUTHOR'S REPLY

The weighting function we use is a cubic.

M. FORDE, UNIV. OF TRONDHEIM, NORWAY

Is the search for the next streamline point the most time-consuming part of the algorithm?

AUTHOR'S REPLY

Obviously the computation time needed for the search algorithm depends on the size of the grid whereas the streamline computation does not. The time may be reduced if the calculation of the Jacobian matrix is already carried out in the initializing procedure of the computer program. The Jacobian is helpful to support the ODE-solver anyhow.

R. GRAY, WRIGHT LABS, U.S.A.

Please provide a physical interpretation of the complex eigenvalues of the Jacobian of the velocity field. Does matrix J decompose into symmetric and antisymmetric components?

AUTHOR'S REPLY

Every matrix can be decomposed into a symmetric and an antisymmetric component. Consider a symmetric Jacobian, all eigenvalues are real. The corresponding eigenvectors are orthogonal and we may construct the ellipsoid of principal stresses. Consider an antisymmetric Jacobian, we have one real eigenvector which is the vorticity vector and vanishing corresponding eigenvalue. The two other eigenvalues are $\pm iw$, where w is the absolute value of the vorticity. In the general case we can say that the antisymmetric component is dominant when there exist complex eigenvalues of the Jacobian matrix.

AN INTEGRATED CFD SYSTEM FOR 3D TURBOMACHINERY APPLICATIONS

Ch. HIRSCH **, C. LACOR **, C. DENER * and D. VUCINIC *

Computational Fluid Dynamics Group
Department of Fluid Mechanics
Vrije Universiteit Brussel
Pleinlaan 2, 1050 Brussels
Belgium

1. SUMMARY

A complete CFD system, composed of an interactive mesh generator, an efficient flow solver and an advanced, portable, flow visualization system is presented for turbomachinery applications. The mesh generator (IGG) and the visualization system (CFView) have the same user interface and call on Object Oriented Programming, on top of X-Windows. The flow solver is developed within a multigrid method, where the time integration schemes are considered as 'smoothers'. Both explicit or implicit time integration methods can be chosen. The explicit integration is based on the Runge-Kutta method and the implicit solver uses relaxation methods with Gauss-Seidel point or line strategies. The space discretization allows for central as well as upwind schemes and algebraic or two equation turbulence models are available. The application to an annular turbine blade row is shown.

2. INTRODUCTION

The development of efficient Navier-Stokes solvers and their increasing application in industrial environments, emphasize the need for complete CFD systems, including advanced pre- and post-processing components, such as mesh generation and flow analysis through graphical visualization.

For many 3D applications to complex geometries, such as turbomachinery blades, inlets, combustion chambers, or external flow configurations, the generation of an adequate mesh can be a lengthy, and therefore costly, part of the flow simulation. Similarly the adequate analysis of the generated flow data calls upon efficient qualitative and quantitative visualization tools, in order to gain a valid knowledge of the numerical and physical features of the flow solution.

The present work aims at the development of an integrated CFD system comprising a highly interactive grid generator IGG, an advanced flow solver and an interactive flow visualization system CFView. These tools require highly developed languages, such as the object oriented language C++, coupled to the X-windows system and the PHIGS graphical standard library, to ensure portability over the large variety of available workstations.

The flow solver is developed for structured, multiblock meshes, as a multigrid system with different options for the time integration as well as for the space discretization. Explicit and implicit methods can be selected with central or upwind schemes, allowing the user to select the best adapted options according to the configuration or Mach

number level. Various physical models for the gas laws, including chemical relations, are introduced, together with different turbulence models.

The following sections describe successively the structure of the interactive grid generator, the flow solver and the visualization system, followed by applications for an annular turbine.

3. INTERACTIVE GRID GENERATION SYSTEM

The interactive grid generator (IGG) has been developed as the preprocessor part of the system. The IGG includes advanced geometry modelling and grid generation features, designed to minimize man-machine interaction in creating grids around complex configurations.

IGG version 2.2 is capable of generating structured or unstructured multiblock grids around 2D geometries (Dener (1991)). With version 3.0, these capabilities are extended to 3D geometries with additional features for surface modelling / grid generation and for structured multiblock grid generation in a multiwindow environment.

The IGG system consists of three main modules :

- an advanced interactive graphical user interface;
- a built-in geometry modeller;
- a grid generator.

The user interface is designed for maximum portability. The geometry modeller is developed as a built in CAD system to construct and manipulate the 2D / 3D grid boundary curves and surfaces. The grid generator integrates various generation algorithms to deal with a wider spectrum of applications and introduces new interactive techniques for fast generation of grids, as well as the evaluation and enhancement of grid quality.

The IGG system is implemented by using the principles of object oriented programming (OOP) and C++. A brief discussion on the basic concepts of OOP is given in Section 5.2. All the basic concepts of implementation are defined as separate objects (abstract data types). The main design goal is to specify what to do with an object, rather than how something gets done.

For the first time in the domain of interactive graphics, the Programmer's Hierarchical Interactive Graphics Standard (PHIGS) and InterViews (an object oriented toolkit based on the X window system) were integrated at the C++ level, to create a portable graphical user interface for the IGG and CFView systems. IGG and CFView classes are designed to have a simple data structure and a high degree of generality in order to facilitate derivation of new classes for other CFD applications.

** Professor, * Research Asst.

3.1 Interactive Graphical User Interface

An overall picture of the IGG interactive graphical user interface, with all the menu options and interaction areas on the display, is shown in Figure 3.1. There are three input options (mouse, keyboard and file) for user interaction and six operating modes (grid, block, face, edge, segment and parameter) for editing and grid generation. The mouse controlled quick buttons are available for viewing operations and the dialogue boxes are used for file management, topology definition, active segment selection, surface and cell scrolling, editing and setting the grid generation/adaptation parameters. Each menu item has also a key binding for fast menu activation. Window positions and viewing coordinates can be interactively changed by the user. The interactive colour map editor, visibility filters, reverse video option, grid structure repetition and descriptive text insertion are other tools provided to customize the display area. Active status of the system is displayed and updated on user interaction areas. Warning messages are given for wrong input and selections.

3.2 Geometry Modelling

A curve and surface construction part has been developed within the code in order to define grid boundaries. The 2D or 3D curve generation options include line, multiline, cubic spline, cubic B-spline, circle, circular arc, ellipse, elliptical arc and algebraic function, in which the user interactively enters an algebraic function and its variable limits to define an analytical curve. Surface construction is based on interpolation from four boundary curves (Coon's patch), or from surface cross sections defined by spline coefficients. Other CAD system outputs can also be read and edited by the code.

A boundary segment is the smallest element in building and editing blocks. There are three geometrical elements (data, grid and normal points) considered for the construction of boundary segments and these are displayed in different colors and shapes. A segment can be selected as the active segment, with one of the input modes. Once it is selected, all operations are effective on this segment. By changing the operation mode, one can extend the scope of operation to active boundary, to active block or to the entire grid. Beside standard editing capabilities, such as rotation, translation, scaling, mirroring and copying, it is also possible to save or recover each boundary segment at any stage of curve construction, to add, modify or delete a data point, to divide a segment or to connect opposite boundaries by straight lines or arcs. A shape change option is also included to convert a multiline to a cubic spline or vice versa.

3.3 Grid Generation

A structured multiblock grid can be created in three steps. First, the grid topology and block boundary information are provided by the user through interactive dialogue boxes. Then, grid boundaries are constructed by a number of segments to capture discontinuities. During this process, at least two opposite block boundaries are needed to be specified for grid generation. On each segment, grid point and boundary normal distributions can be interactively specified by cubic B-spline based control functions. Grid point clustering can be defined at either or both ends of a segment or at a location in between. Boundary normal angles can also be fixed at

the end points of each segment separately. Finally, the grid is created within these boundaries, the quality is observed, and the modifications or adaptations are made.

A variety of generation options have been provided for the user to select the best suited one for a specific geometry. As a new feature, it is possible to define surface normal lengths for grid points on each block face, by interpolating from the user specified distributions on four edges. Thus in 3D transfinite interpolation, cubic B-spline based interpolation functions can be used to enhance orthogonality in 3D space. For multigrid solvers, different coarse grid levels can be interactively analyzed and saved.

The 3D grids are analyzed by selecting arbitrary block surfaces through a surface scroller. The cell skewness or aspect ratio can be displayed on all selected surfaces for assessment of grid quality. Individual 3D grid cells can also be scanned to check cell distortions. Solid model representations of block surfaces and removal of hidden lines are other visualization tools implemented in the system.

The following grid generation features have been implemented in the system:

- Six-boundary interpolation (linear or cubic) to create 3D block grids,
- Four-boundary interpolation (linear or cubic), as an extension of the B-spline based surface generation methods, for generation of surface and block grids,
- Two-boundary interpolation (linear or cubic) with user specified or hyperbolic tangent stretching, for surface and block grids,
- Body wrapping technique for C and O type structured surface grids, enforcing orthogonality on the solid body,
- Local smoothing in a user specified region of a surface grid,
- Interactive adaptation of structured surface grids,
- Local grid point refinement in structured blocks by segment subdivision.

For 3D multiblock configurations, the block connectivities and boundary conditions of each face are interactively specified by start and end values of the variable indices on that face and the type of boundary conditions, respectively. The system automatically connects the corresponding segments with proper orientation. In order to minimize the effort to define grid boundaries for specific applications, such as 3D turbomachinery components, a number of predefined data file formats can be used. The colour representations of grid cell skewness and aspect ratio also provide visual aids for the evaluation of grid quality..

The H-type 3D grid created for the test case E/TU-1, low speed annular turbine blade row, Sieverding(1990), has been shown in Figure 3.2, by a number of selected surfaces with hidden line removal. Figure 3.3 is an example of a C-type grid created for a 2D turbine blade. Figure 3.4 presents the 2D unstructured grid created for the above test case profile, using the same boundary information. Currently, the IGG system is being extended to deal with a broader spectrum of 3D applications with new surface modelling and grid generation options in a multiwindow environment.

4. MAIN FEATURES OF THE SOLVER

4.1 Introduction

The solver which has been developed with FFA, the Aeronautical Research institute of Sweden, is based on a solution of the Reynolds Averaged Navier-Stokes equations. It is applicable to a wide range of flow problems varying from internal flows in turbomachinery, channels and inlets to external flows about complete airplane or shuttle configurations. The Mach number range is from low subsonic up to hypersonic. Though the emphasis is on steady state calculations, time-accurate problems can be treated too.

The code is based on the use of structured meshes. A multi-block approach is adopted for reasons of flexibility. In the current version of the code, continuous gridlines are assumed between different blocks. In a new version discontinuous gridlines will be allowed.

The 'heart' of the solver is the multigrid method. This method is used to drive the solution towards its steady state, with a maximum efficiency.

Within this context, the time integration schemes are considered as 'smoothers' for the multigrid. Their aim is to eliminate high frequency errors in the solution.

Either explicit or implicit methods can be chosen. The explicit integration is based on the Runge-Kutta method, where the user can specify the desired number of stages and the Runge-Kutta coefficients for optimal smoothing. The implicit solver uses relaxation methods with Gauss-Seidel point or Gauss-Seidel line strategies.

The accuracy of the obtained solution is determined by the spatial discretization. Different schemes are implemented into the present code, based either on a central or on an upwind discretization of the convective terms, cf. Müller and Rizzi (1989), Eliasson and Rizzi (1990), Lacor and Hirsch (1988a,b). Within the upwind option different alternatives are coded, cf. Section 4.3.2.

The turbulence models are currently being implemented. Both the algebraic model of Baldwin-Lomax and the two-equation k-ε model will be available.

Finally, some real gas effects will be introduced for hypersonic applications.

The treatment of the data within the code, is handled by a set of utility routines. The complete set of data, stored in a integer and real workvector, is available at all levels of the code. The utility routines allow to store and/or retrieve data from the workvectors in a flexible, user-friendly way. This simplifies the addition of new routines.

4.2 Multigrid Method

The multigrid method is based on the use of FAS cycles. Both V-cycles and sawtooth cycles can be chosen.

The loop over the different grids is outside the loop over the different blocks, leading to faster convergence rates than the alternate solution where a complete multigrid cycle is performed on one block at a time, cf. Yadlin and Caughey (1990).

The basic strategy is shortly described below.

Consider a set of meshes denoted with an index $l = 1, \dots, L$ with L the finest level. The Navier-Stokes problem on the finest level can be written as :

$$\frac{\partial U^L}{\partial t} + N_L(U^L) = 0 \quad (4.2.1)$$

where $N_L(U^L)$ is the spatial discretization of the Navier-Stokes operator on the finest mesh L . Note that the temporal discretization has been left unspecified so far.

The problem is then approximated on coarser levels l as :

$$\frac{\partial U^l}{\partial t} + N_l(U^l) = F_l \quad (4.2.2)$$

with F_l the forcing function, defined recursively as :

$$F_l = N_l(I_{l+1}^1 U^{l+1}) + \hat{I}_{l+1}^1 [F_{l+1} - N_{l+1}(U^{l+1})] \quad (4.2.3)$$

where I_{l+1}^1 and \hat{I}_{l+1}^1 represent restriction operators of resp. the unknowns and the residuals. In the present code they are defined as :

$$\hat{I}_{l+1}^1 R^{l+1} = \sum R^{l+1} \quad (4.2.4)$$

$$I_{l+1}^1 U^{l+1} = \frac{\sum \Omega^{l+1} U^{l+1}}{\sum \Omega^{l+1}} \quad (4.2.5)$$

where R^{l+1} is defined as :

$$R^{l+1} = F_{l+1} - N_{l+1}(U^{l+1}) \quad (4.2.6)$$

and Ω represents the cell volume. The summation in eqs. (4.2.4), (4.2.5) is over the 8 fine cells contained within a coarse cell.

After temporal discretization, eq.(4.2.2) can be written as

$$S \Delta U^l + N_l(U^{l(0)}) = F_l \quad (4.2.7)$$

is the current solution on mesh l , around which the equations have been linearized (in an implicit method) and which has to be smoothed. One has:

$$U^{l(0)} = I_{l+1}^1 U^{l+1} \quad (4.2.8)$$

ΔU^l is an update of $U^{l(0)}$ and is to be calculated. S is the smoother. It is an operator that depends on the chosen time discretization. For an Euler explicit method one has :

$$S = \frac{1}{\Delta t} \quad (4.2.9)$$

whereas for an implicit method, S can symbolically be written as :

$$S = \frac{1}{\Delta t} + \frac{\partial N}{\partial U^l} \quad (4.2.10)$$

The linear problem (4.2.7) can be solved for ΔU^l . Note that for implicit schemes combined with iterative solvers, (4.2.7) will only be solved approximately. The updated solution U^l will be smooth (provided S is a good smoother) and can be restricted to the next coarser level, according to eq. (4.2.8) with l replaced by $l-1$. Alternatively one can perform another linearization on the same level l , before proceeding to a coarser level. This is achieved by putting $U^{l(0)} = U^l$ and repeating the steps above.

Once the solution on the coarsest mesh is smoothed, the coarse-to-fine sweep of the multigrid cycle is initiated. The current solutions on finer grids are updated with the solution on the next coarser level :

$$U = U^j + I_{j-1}^j (U^{j-1} - I_{j-1}^{j-1} U^j) \quad (4.2.11)$$

The operator I_{j-1}^j is a the prolongation operator, in the present code piecewise constant prolongation : in each of the 8 fine cells contained within a coarse cell, the prolonged correction is taken to be the coarse cell correction, i.e.

$$I_{j-1}^j \Delta U = \Delta U \quad (4.2.12)$$

In a V-cycle the new solution on the finer mesh is smoothed before proceeding to the next finer level. This is achieved by solving eq. (4.2.7) with $U^{(0)} = U^j$.

In a sawtooth cycle this smoothing step is omitted and the solution is immediately prolonged to the next grid level.

4.3 Spatial Discretization Methods

Consider the Euler / Navier-Stokes system in multi-dimensions :

$$\frac{\partial U}{\partial t} + \frac{\partial F}{\partial x} + \frac{\partial G}{\partial y} + \frac{\partial H}{\partial z} = 0 \quad (4.3.1)$$

This equation is discretized in space by the control volume approach, based on a cell centered method :

$$\int_{\Omega} \frac{\partial U}{\partial t} d\Omega + \oint_S \vec{F} \cdot \vec{n} dS = 0 \quad (4.3.2)$$

The surface integral is approximated as :

$$\oint_S \vec{F} \cdot \vec{n} dS = \sum_{\text{faces}} (\vec{F} \cdot \vec{n})_{\text{face}} \Delta S \quad (4.3.3)$$

where the subscript 'face' indicates the flux through the cell face, which is the so-called numerical flux .

A general framework for different numerical schemes is provided by expressing the numerical flux as, cf. Hirsch (1990):

$$(\vec{F} \cdot \vec{n})_{i+1/2}^* = \vec{F}(U_{i+1/2}) \cdot \vec{n}_{i+1/2} - d_{i+1/2} \quad (4.3.4)$$

Note that the indices j,k which do not vary, are dropped in equation (4.3.4). This will consistently be done in the remaining of this text in order to enhance clarity.

The first term in the right-hand-side of (4.3.4) corresponds to a central discretization. The second term can be seen as a general dissipation term.

Note that in the central part, the cell face flux is obtained from the average primitive variables on the cell face, $U_{i+1/2}$. In this averaging procedure, the possibly different lengths of the cells on both sides of the cell face, have been accounted for.

The dissipation term may be a classical artificial dissipation, used in combination with central schemes, or the dissipation associated with upwind schemes.

4.3.1 Central Schemes

The artificial dissipation term $d_{i+1/2}$ of eq. (4.3.4) is given by :

$$d_{i+1/2} = \varepsilon_{i+1/2}^{(2)} (U_{i+1} - U_i) + \frac{\varepsilon_{i+1/2}^{(4)} + \varepsilon_{i-1/2}^{(4)}}{2} (U_{i+1} - 2U_i + U_{i-1}) - \frac{\varepsilon_{i-3/2}^{(4)} + \varepsilon_{i-1/2}^{(4)}}{2} (U_i - 2U_{i-1} + U_{i-2}) \quad (4.3.5)$$

The coefficients ε are determined as :

$$\varepsilon_{i+1/2}^{(2)} = \lambda_{i+1/2} \kappa^{(2)} \max\{v_{i+2}, v_{i+1}, v_i, v_{i-1}\} \\ \varepsilon_{i+1/2}^{(4)} = -\max\{0, \lambda_{i+1/2} \kappa^{(4)} - \varepsilon_{i+1/2}^{(2)}\} \quad (4.3.6)$$

The variables v in the first formula are shock sensors, aimed to activate the second order dissipation in the regions of shocks and to deactivate it elsewhere. They are based on the pressure and defined as :

$$v_i = \frac{|p_{i+1} - 2p_i + p_{i-1}|}{|p_{i+1} + 2p_i + p_{i-1}|} \quad (4.3.7)$$

λ^* is a measure of the fluxes, and is commonly chosen as the spectral radius of the flux Jacobians multiplied with the cell face area :

$$\lambda_{i+1/2}^* = \lambda_{i+1/2} = [|\vec{U} \cdot \vec{n}| + c]_{i+1/2} S_{i+1/2} \quad (4.3.8)$$

Within the cell centered approach, the flow variables are defined only in cell centers, and hence :

$$\vec{U}_{i+1/2} = \frac{1}{2} [\vec{U}_i + \vec{U}_{i+1}] \\ c_{i+1/2} = \frac{1}{2} [c_i + c_{i+1}] \quad (4.3.9)$$

Equation (4.3.8) corresponds to a purely isotropic definition of λ . According to Martinelli (1987) this is not a good choice on high aspect ratio grids. In 2D, he proposes to include a contribution of the spectral radius in the other direction. His ideas have been extended into 3D by Vatsa and Wedan (1989), leading to :

$$\lambda_{i+1/2}^* = \lambda_{i+1/2} + \sqrt{\lambda_{i+1/2} \lambda_{i-1/2} \lambda_{i-1/2}} \quad (4.3.10)$$

The dissipation coefficients $\kappa^{(2)}$ and $\kappa^{(4)}$ are constants to be supplied by the user.

4.3.2 Upwind TVD Schemes

The numerical flux is again given by (4.3.4), but the dissipation term is more complicated and more in accordance with the physics of the flow :

$$d_{i+1/2} = \frac{1}{2} R_{i+1/2} \text{diag}(\alpha_{i+1/2}^l) R_{i+1/2}^{-1} (U_{i+1} - U_i) \quad (4.3.11)$$

The matrices R and R^{-1} are resp. formed by the right and left eigenvectors of the Jacobian matrix , i.e. they satisfy

$$\vec{A} \vec{n} = A.n_x + B.n_y + C.n_z = R \Lambda R^{-1} \quad (4.3.12)$$

where A,B,C are the Jacobians of the flux vectors in resp. x,y,z direction, noted F,G,H :

$$A = \frac{\partial F}{\partial U}, B = \frac{\partial G}{\partial U}, C = \frac{\partial H}{\partial U} \quad (4.3.13)$$

U represents the vector of conservative variables. The notation $\text{diag}(\alpha_{i+1/2}^l)$ represents a diagonal matrix with $\alpha_{i+1/2}^l$ as element in row and column l.

Depending on the expression for a different upwind schemes are defined. In the code, a TVD version of flux

difference splitting, cf. Roe (1981) and the symmetric TVD scheme of, Yee (1987) have currently been implemented.

They correspond to the following choices :

$$(\alpha_{k+1/2}^l)^{FDS} = |\alpha_{k+1/2}^l| - \psi(R_{k+1/2}^+) \alpha_{k+1/2}^l + \psi(R_{k+1/2}^-) \alpha_{k+1/2}^l \quad (4.3.14)$$

for flux difference splitting and

$$(\alpha_{k+1/2}^l)^{STVO} = |\alpha_{k+1/2}^l| [1 - Q_{k+1/2}^l(r_{k+1/2}^-, r_{k+1/2}^+)] \quad (4.3.15)$$

where $\alpha_{k+1/2}^l$ represents the l-th eigenvalue of the Jacobian of eq. (4.3.12).

The dissipation of eq. (4.3.11) together with eqs. (4.3.14), (4.3.15) corresponds to second-order accurate upwind type schemes. The functions ψ and Q are limiters which introduce a non-linearity in the scheme to make it monotone. If the limiters are taken to be zero, both flux difference splitting and symmetric TVD, lead to the same first-order accurate upwind scheme.

The limiter arguments are based on variations of the characteristic variables, and are defined as :

$$R_{k+1/2}^+ = \frac{\alpha_{k+1/2}^+ (w_k^+ - w_{k-1}^+)}{\alpha_{k+1/2}^+ (w_{k+1}^+ - w_k^+)} \\ R_{k+1/2}^- = \frac{\alpha_{k+1/2}^- (w_{k+2}^- - w_{k+1}^-)}{\alpha_{k+1/2}^- (w_{k+1}^- - w_k^-)} \quad (4.3.16)$$

in equation (4.3.14) and

$$r_{k+1/2}^+ = \frac{w_k^+ - w_{k-1}^+}{w_{k+1}^+ - w_k^+} \\ r_{k+1/2}^- = \frac{w_{k+2}^- - w_{k+1}^-}{w_{k+1}^- - w_k^-} \quad (4.3.17)$$

in equation (4.3.15).

The superscript l refers to the l-th component of the vector of characteristic variable variations. This vector is obtained from the conservative variable variations through the following relation :

$$W_{k+1} - W_k = R_{k+1/2}^l (U_{k+1} - U_k) \quad (4.3.18)$$

Different limiters can be chosen. Currently the minmod limiter and the superbee limiter have been implemented. This corresponds to the following expressions for the functions ψ and Q :

$$\psi(R) = \minmod(1, R) \quad (4.3.19)$$

$$Q(r, r^+) = \minmod(1, r) + \minmod(1, r^+) - 1 \quad (4.3.20)$$

$$\psi(R) = \max\{0, \min(1, 2R), \min(2, R)\} \quad (4.3.21)$$

$$Q(r, r^+) = \max\{0, \min(1, 2r), \min(2, r)\} \\ + \max\{0, \min(1, 2r^+), \min(2, r^+)\} - 1 \quad (4.3.22)$$

Expressions (4.3.19), (4.3.20) represent the minmod limiter, eq. (4.3.21), (4.3.22) superbee.

Note that different limiters may be chosen for different components of the characteristic variables, cf. Yee (1987).

4.4 Time Integration

The chosen time integration fixes the smoothing operator as defined in eq.(4.2.7).

In the code both explicit Runge-Kutta time stepping and an implicit scheme with an iterative solver based on relaxation methods have been implemented.

The time integration is decoupled from the spatial discretization, in the sense that both methods may be combined with any of the spatial discretization operators.

4.4.1 Runge-Kutta Methods

The user can specify the number of stages. A m-stage scheme is coded as :

$$U^1 = U^n + \beta_1 \Delta t R(U^n)$$

$$U^2 = U^1 + \beta_2 \Delta t R(U^1)$$

$$U^m = U^{m-1} + \beta_m \Delta t R(U^{m-1})$$

$$U^{n+1} = U^m \quad (4.4.1)$$

where R is defined as in eq.(...) and β are the Runge-Kutta coefficients to be specified by the user.

The Runge-Kutta solver is combined with local time stepping to enhance the convergence rate. The user has also the option of using residual smoothing.

4.4.2 Implicit Methods

The implicit operator will be derived for the upwind schemes. The same operator however can also be used in combination with central schemes.

The following family of explicit and implicit schemes can be defined :

$$\frac{\Omega M \Delta V}{\Delta t} + \theta \sum_{\text{faces}} [(\vec{F} \cdot \vec{n})_{\text{face}}]^{n+1} \Delta S = \\ -(1 - \theta) \sum_{\text{faces}} [(\vec{F} \cdot \vec{n})_{\text{face}}]^n \Delta S \quad (4.4.2)$$

where

$$\Delta V = V^{n+1} - V^n \quad (4.4.3)$$

and the numerical flux is given by (4.3.4). In view of the linearization, the primitive variables V are used instead of the conservative variables. This leads to much simpler Jacobians. The matrix M in eq.(4.4.2) describes the transformation from primitive to conservative variables :

$$\Delta U = M \Delta V \quad (4.4.4)$$

with

$$M = \frac{\partial U}{\partial V} \quad (4.4.5)$$

The numerical flux at time level $n+1$ is rewritten as :

$$(\vec{F} \cdot \vec{n})_{k+1/2}^{n+1} = \vec{F}(V_{k+1/2}^{n+1}) \cdot \vec{n}_{k+1/2} \\ - \frac{1}{2} R_{k+1/2}^{n+1} \text{diag}[(\alpha_{k+1/2}^l)^{n+1}] (L_{k+1/2}^{-1})^{n+1} (V_{k+1} - V_k)^{n+1} \quad (4.4.6)$$

where L diagonalizes the Jacobians of the primitive variables, denoted \tilde{A} :

$$\tilde{A}n = L \Lambda L^{-1} \quad (4.4.7)$$

The numerical flux is now linearized following a similar procedure as proposed by Yee (1987).

The fluxes of the first term in the rhs are linearized according to:

$$\begin{aligned} \tilde{F}(V_{i+1/2}^{n+1}) &= \tilde{F}(V_{i+1/2}^n) + \tilde{A}_{i+1/2}^n \Delta V_{i+1/2} \\ &= \tilde{F}(V_{i+1/2}^n) + \frac{1}{2} \tilde{A}_{i+1/2}^n (\Delta V_i + \Delta V_{i+1}) \end{aligned} \quad (4.4.8)$$

\tilde{A} is not to be confused with \tilde{A} and is given by

$$\tilde{A}n = \frac{d(\tilde{F}n)}{dV} = R \Lambda L^{-1} \quad (4.4.9)$$

The second term in the rhs of eq.(4.4.6) is linearized by treating the matrix, multiplying the variation of the primitive variables, at time level n .

The resulting linearized system in two dimensions is:

$$\begin{aligned} &E_{i-1,j} \Delta U_{i-1,j} + E_{i,j} \Delta U_{i,j} + E_{i+1,j} \Delta U_{i+1,j} \\ &+ E_{i,j-1} \Delta U_{i,j-1} + E_{i,j+1} \Delta U_{i,j+1} \\ &= -\lambda \sum_{\text{faces}} (\tilde{F}n)_{\text{face}} \end{aligned} \quad (4.4.10)$$

with

$$\begin{aligned} E_{i-1,j} &= -\frac{\lambda \theta}{2} [P_{i-1/2} + K_{i-1/2}] \\ E_{i,j-1} &= -\frac{\lambda \theta}{2} [P_{j-1/2} + K_{j-1/2}] \\ E_{i+1,j} &= +\frac{\lambda \theta}{2} [P_{i+1/2} - K_{i+1/2}] \\ E_{i,j+1} &= +\frac{\lambda \theta}{2} [P_{j+1/2} - K_{j+1/2}] \\ E_{i,j} &= M + \frac{\lambda \theta}{2} [P_{i+1/2} - P_{i-1/2} + P_{j+1/2} - P_{j-1/2}] \\ &+ \frac{\lambda \theta}{2} [K_{i+1/2} + K_{i-1/2} + K_{j+1/2} + K_{j-1/2}] \end{aligned} \quad (4.4.11)$$

and

$$\begin{aligned} P_{i+1/2} &= (\tilde{A}n)_{i+1/2} \\ K_{i+1/2} &= R_{i+1/2} \text{diag}[(\alpha_{i+1/2})] (L_{i+1/2}^{-1}) \end{aligned} \quad (4.4.12)$$

From eqs. (4.4.10-12) the following observations can be made.

Though the spatial accuracy is of second-order the resulting implicit operator corresponds to a 5 point stencil in 2D (and 7 point in 3D). The Jacobians appearing in the operator are Jacobians of the full fluxes and not of split fluxes.

The implicit operator can be simplified if only first-order accurate spatial discretization is used. The variables α reduce then to the absolute value of the eigenvalues, cf. eqs. (4.3.14), (4.3.15). Hence

$$K_{i+1/2} = |P_{i+1/2}| \quad (4.4.13)$$

and the matrices E simplify to positive and negative Jacobians:

$$\begin{aligned} E_{i-1,j} &= -\lambda \theta P_{i-1/2}^+ \\ E_{i+1,j} &= +\lambda \theta P_{i+1/2}^- \\ E_{i,j} &= M + \lambda \theta [P_{i+1/2}^+ - P_{i-1/2}^- + P_{j+1/2}^- - P_{j-1/2}^+] \end{aligned} \quad (4.4.14)$$

with similar expressions for $E_{i,j-1}$ and $E_{i,j+1}$.

Further simplification of the implicit operator is still possible if one replaces K with its spectral radius.

The linearized system (4.4.10) with (4.4.11) or (4.4.14) is solved iteratively with a Gauss-Seidel point or line relaxation. In the latter case block-tridiagonal systems have to be solved.

4.5 Structure and Data Management

The flexibility of the code is guaranteed by a set of utility routines that take care of all the management of data, such as for instance storage and retrieval. These routines are designed to work around the limitations of Fortran static arrays.

The basic storage is done in two large one-dimensional work vectors with fixed sizes, one for real and one for integer data.

On central memory machines the workvectors are either kept in memory at all times or sliced in pieces of which most are kept on external storage, being read in the memory as needed.

On a computer with distributed memory, there will be a local set of workvectors for each processor.

Through the use of the utility routines, these work vectors appear to the programmer as a common tree structure. The data stored in the work vectors is addressed through the use of a system of pointers, each containing the starting address of the corresponding data.

The complete tree structure is set up at run time and is dynamic in the sense that one may allocate space for arbitrary data with a size determined at run time. One can however not delete data from the tree and reclaim the memory locations for new purposes. In order to have truly dynamic memory allocation a stack is used.

Within this data management approach data is treated as local as possible, with no data appearing in other routines than the ones that actually need it. This allows several programmers to work on the code at once and simplifies the addition of new modules.

Finally, the use of commons is avoided, making the code more easily transportable to distributed memory computers.

5. COMPUTATIONAL FLOW VISUALIZATION SYSTEM

The computational flow visualization system (CFView) is a highly interactive and portable postprocessor, with integrated windowing environment, menus and mouse controls. Considerable attention has been focused on the design of the graphical user interface (GUI) and on the development of numerical probes, the new tools for interactive quantitative and qualitative data field analysis.

The data fields can be generated either from the output of numerical simulation codes or from experimental data.

CFView allows the visualization of 2D and 3D fields on structured and unstructured meshes in multidomain (multiblock) configurations. The geometry and field data specifications are supported in the cartesian, cylindrical and meridional stream surface coordinate systems.

The CFView system is designed using an object-oriented programming (OOP) approach and implemented in C++. Based on PHIGS and InterViews, class libraries were developed to ensure full integration of 3D graphics and GUI.

5.1 Objectives

Numerical simulation of flow problems produce vast volumes of data, which require appropriate tools for analysis and interpretation. With the present development of efficient workstations, graphical representation and visualization of flow properties are the best adapted approach.

The objective of CFView (Vucinic(1989), Vucinic(1991)) is to establish an environment, in which the researchers may interactively probe, visualize and extract quantitative field information. The visualization, as a postprocessing tool must be powerful, easy to use, flexible and must allow the user to make an in-depth investigation to identify peculiarities in his model, to check out his own simulation codes running on test cases, or simply to extract guide lines for a better tuning of parameters in a solver.

Because the visualization is a common activity for all numerical simulation systems, it is a logical idea to develop a visualization system which can be used across different flow solvers and computer systems. The objective is to give the user a fully interactive graphics package with as much functionality as possible and with the simplest possible interface.

The state of art in the development of visualization systems, specifically for CFD, is represented by several computer packages : PLOT3D, developed at NASA Ames for steady data and multiple structured grids (Buning(1985)), VISUAL2 and VISUAL3 at MIT implemented on graphics supercomputer workstation for structured and unstructured grids (Giles(1990)), AGPS used at The Boeing Company (Capron(1991)), and FLOVIS at CIRA (FLOVIS(1988)).

Another group represents general visualization systems: DataVisualizer from Wavefront, FieldView from Intelligent Light and AVS from Stardent Computer Inc.

5.2 Object Oriented Approach

Object oriented programming (OOP) (Goldberg(1983), Gorlen(1990)) is a useful software development technique for structuring large programs by assembling interchangeable, reusable software components, called objects. Objects are computer analogs for entities in the real world, meaningful to the CFD user. OOP allows reusing of existing software through data abstraction and inheritance. The data abstraction is a programming technique for the creation of abstract data types (classes in C++). An abstract data type (ADT) is a user defined data type which integrates the data and the operations

that can be performed on them. The inheritance simplifies the creation of a new ADT that is similar to an existing ADT by enabling the user to specify just the difference between the new ADT and the existing one.

The OOP approach is applied to develop the object oriented model of PHIGS functional graphics library. The C++ binding and class library related to PHIGS are created to improve object oriented implementation of CFView. The GUI is developed using InterViews library, Linton (1987), in combination with PHIGS graphics classes. GUI is similar to the emerging PEX standard (the PHIGS Extension to X windows) for high performance graphics, and is completely written in C++ for software reusability and maintainability. The combination of PHIGS and InterViews library classes provides a user friendly environment for GUI and 3D graphics implementations.

5.3 Advanced System Features In an Interactive User Environment

CFView has a powerful context-sensitive, mouse-operated GUI. GUI consists of a set of pulldown-pullright menus and dialogue boxes, that allow the selection and combination of various representations. Viewing operations and interactive interrogation of the computational fields are ensured through the use of the cursor and view manipulation buttons. A general layout of the system is illustrated in Figure 5.1.

In addition, the system supports a generalized multiwindow concept in which 2D or 3D graphics can be independently displayed and manipulated through the use of the menus. In order to avoid system limitations, the number of windows and the task assigned to them is free to the user. Any representation of the flow field may be applied and combined inside one or more views. The multiwindow environment of CFView allows the user to simultaneously load different data sets during the same run and to manipulate them for comparative analysis. In the same way, different field quantities of a same file may be visualized at the same time.

The colormap editor and interactive light positioning can improve the appearance of 3D representations.

CFView offers additional facilities, such as undoing commands, setup files and interactive picking for the selection and removal of graphical objects. Setup files may be generated when the user wants to apply the same configuration to different data sets. The setup file typically consists of parameters used to define the viewing positions, arbitrary cutting planes, particle traces starting positions and some other user preferences.

5.4 Field Representations

The number and type of field quantities are defined by the user. In addition, new field quantities can be generated interactively from the existing quantities by specifying an analytical function. According to the type of quantity, the representations are subdivided into scalars and vectors. The analysis of the complete field can be performed on different types of interactively selected zones. These zones are grouped according to their space dimension as 0D, 1D, 2D or 3D zones inside the computational field. A summary of all zone groups can be given as follows :

Zone Types :

0D general points inside the computational domain.

1D general curves:

- constant mesh line (for structured mesh),
- arbitrary curve section,
- general curve resulting from the intersection of two surfaces (e.g. solid boundary and arbitrary section),
- particle paths.

2D general surfaces:

- mesh boundaries,
- constant I, J, or K surfaces (for structured grids)
- arbitrary cutting planes,
- isosurfaces,
- surface-tangent vector (e.g. streamsurface).

3D general volumes:

- complete mesh,
- single domain of the mesh,
- arbitrary submesh interactively generated.

In the next section, more detailed description of the 2D general surface concept is explained together with the possible modes of operations on extracted or user generated surfaces.

In addition to the volumetric data input, CFView can treat surface and validation data. Surface data include quantities confined to solid boundaries, such as the heat transfer coefficient. Validation data are the results of experiments or other computations, that can be used to facilitate the comparison of displayed results.

5.5 Surface Concept

CFView makes an extensive use of the surface concept, because most representations are primarily related to them. The surfaces represent the most natural way to extract data from the volume data set.

For structured meshes the user can scan the computational volume instantaneously by moving through constant I, J or K surfaces. The scanning enables the user to browse through grid surfaces and to select the ones with which the user is particularly interested. The scanning is available in geometrical and quantity mode. The geometrical mode allows to visualize surface geometry while the quantity mode allows analysis with shaded contours. Interactively the user can switch between these two modes without interrupting the surface creation process. This scanning feature give the user the possibility to rapidly localize interesting field features in an animated way.

Another way of scanning the entire volume is by applying arbitrary cutting planes. The orientation of the cutting plane can be defined numerically or interactively with scrolling or rotating about an arbitrary axis. In this way, the result of the surface creation process is an unstructured surface. The CFView system is unifying the handling of the structured and unstructured surfaces to enable all the representations that are available for structured surfaces to be used for unstructured surfaces too. After the surface creation process, the surfaces are automatically selected for the active view. The user is then able to use them as geometrical reference for different field representations. For more flexibility the displayed surfaces can become active or inactive, which means that the field representations will be applied or not to them. This feature enable the user to superpose two or more

different quantity representations in the same view on different surfaces.

5.6 Numerical probes

Beside classical field representations, like isoline, contour shading and thresholding, CFView provides a set of very powerful diagnostic tools for the interactive QUANTITATIVE analysis of the field. The important tools are local values, quantity distribution along curves (arbitrary or grid lines) and local profiles.

The local profile numerical probe is a very special tool, which allows the user to locally blow up a region of the field and to display the quantity distribution in a cartesian plot. This feature is very useful when boundary layer phenomena are considered. The local value probe displays the numerical value of the active quantity at a point, interactively selected by the user. The user can also interactively select a section line and visualize any quantity distribution along it. In Figure 5.2, beside the grid geometry and isoline representations, the numerical probes, local profile and local value are shown for scalar and vector quantities. In addition, the user can select different types of boundaries (solid, inlet,...) and restrict his investigations to these regions.

The particle path numerical probe is also available as a standard tool for vector field analysis. All previously mentioned probes are available for 3D computations, as shown in Figure 5.3.

In addition to surface representations CFView allows the user to compute isosurfaces of scalar field quantities. On these unstructured surfaces other quantities can be analysed using numerical probes and surface representations (isoline, colour contours...).

6. RESULTS

Since parts of the solver are currently still under development, preliminary results are shown for a laminar Navier-Stokes calculation of an external flow problem at high Mach number.

The geometry consists of two perpendicular flat plates forming a 90 degree corner. Figure 1 shows the mesh in the two plates and in a cross-section. The bold lines on figure 1 indicate the outer boundaries of the plates. The mesh was extended beyond the plates, where a symmetry condition was imposed, and in front of the plates. The flow enters the corner at zero angle of attack and at zero yaw angle with a Mach number of 4. Due to the displacement effect of the boundary layers, two shocks are formed at the sharp leading edges of both plates. The mesh used, consisted of $45 \times 29 \times 29$ points.

Calculations were performed with the central scheme and the second order accurate flux difference splitting TVD scheme. In the latter calculation the Van Albada limiter was used to ensure monotonicity. In both cases a four stage Runge-Kutta scheme was used for the time integration.

Figure 6.2 shows the convergence history for the central scheme calculation. The multigrid which is implemented but not properly tested yet, was switched off in the present runs. Both calculations start from a converged solution on a coarser grid.

Figures 6.3 and 6.4 give a qualitative comparison of the results obtained with both schemes. In figure 6.3 the total pressure distribution is shown in 3 different sections of the mesh. Figure 6.4 shows the distribution of the Stanton number, which is a measure of the wall heat flux, on the horizontal and vertical plate.

Finally, figure 6.5 gives the velocity distribution in the outlet section, obtained with both schemes. Note that not the same scaling was used in both plots. There is an indication of a vorticity in the flow, but this should be confirmed in calculations on still finer meshes.

7. REFERENCES

- Buning P. and Steger J. L., (1985), "Graphics and Flow Visualization in CFD", AIAA paper 85-1507.
- Capron W. K. and Smit K. L., (1991), "Advance Aerodynamic Applications of an Interactive Geometry and Visualization System", AIAA paper 91-0800.
- Dener C. and Hirsch Ch. (1991) "IGG - An Advanced Interactive Grid Generation System", The 3rd International Conference on Numerical Grid Generation, Barcelona, Spain, 3-7 June 1991.
- Eliasson P., Rizzi A., (1990) "Hypersonic Leeside Flow Computations Using Centered Schemes for Euler Equations", Proc. 8th GAMM Conf. Num. Meth. Fluid Mech.(ed) P. Wesseling, NNFM 29, Vieweg, Braunschweig.
- FLOVIS, (1988), a Graphic Postprocessor for Fluid Dynamic Solvers", CIRA, Technical report DLC-INT-TN-001
- Giles M. and Haimes R., (1990), "Advanced Interactive Visualization for CFD", Computing Systems in Engineering, Vol. 1, No. 1, pp. 51-62.
- Goldberg A., Robson D. (1983) "Smalltalk-80 The Language and its Implementation", Addison-Wesley, Reading, Massachusetts.
- Gorlen K. E., Orlow S. W., Plexico P. S. (1990) "Data abstraction and object-oriented programming in C++", John Wiley & Sons.
- Hirsch Ch., (1990), "Numerical Computation of Internal and External Flows. Volume 2", John Wiley & Sons.
- Lacor C., Hirsch Ch., (1988a), "3D Computations of Complex Flow Systems", presented at the 16th ICAS Congress, Jerusalem, 28/8-2/9/1988.
- Lacor C., Hirsch Ch., (1988b), "Numerical Simulation of the Three-Dimensional Flow Around a Butterfly Valve", Proceedings of Symposium on Flows in Non-Rotating Turbomachinery Components, ASME Winter Annual Meeting, Chicago, FED-Vol.69, pp. 1-12.
- Linton, M.A., Calder, P.R. and Vlissides, J.M., (1987), "InterViews : A C++ Graphical Interface Toolkit", Proceedings of the USENIX C++ Workshop, November 1987.
- Martinelli L. , (1987), 'Calculation of Viscous Flows with Multigrid Methods', Ph D Dissertation, MAE Dept., Princeton University.
- Müller B., Rizzi A., (1989), "Navier-Stokes Calculations of Transonic Vortices over a Round Leading Edge Delta Wing", Int. J. Numerical Methods Fluid Mechanics, Vol. 9, pp. 943-962.
- Sieverding, C.H., (1990), "Experimental Test Cases for Turbines-Test Case E/TU-1", AGARD-AR-275, PEP WG18, "Test Cases for Computation of Internal Flows in Aero Engine Components".
- Roe P.L. (1981). 'Approximate Riemann solvers, parameter vectors and difference schemes', J. Comp. Physics, Vol. 43, pp. 357-382.
- Stroustrup, B., (1986), "The C++ Programming Language", Addison-Wesley.
- Vatsa V.N., Wedan B.W., (1989), "Development of an Efficient Multigrid Code for 3-D Navier-Stokes Equations", AIAA paper 89-1791, AIAA 20th Fluid Dynamics, Plasma Dynamics and Lasers Conference.
- Yadlin Y., Caughey D.A. (1990), 'Block Multigrid Implicit Solution of the Euler Equations of Compressible Fluid Flow" AIAA paper 90-0106, 28th AIAA Aerospace Sciences Meeting.
- Yee H.C. (1987), 'Construction of Explicit and Implicit Symmetric TVD Schemes and their Applications', Journal of Computational Physics, Vol. 68, pp. 151-179.
- Vucinic D. and Hirsch Ch., (1989), 'Computational Flow Visualization System at VUB - CFView 1.0', VKI Lecture Series on Computer Graphics and Flow Visualization in CFD, September 1989.
- Vucinic D., Pottiez M., Sotiaux V., Hirsch Ch., (1991) 'CFView an advanced interactive visualization system based on object-oriented approach', Open Forum of the AIAA 10th CFD Conference, Honolulu, June 1991.

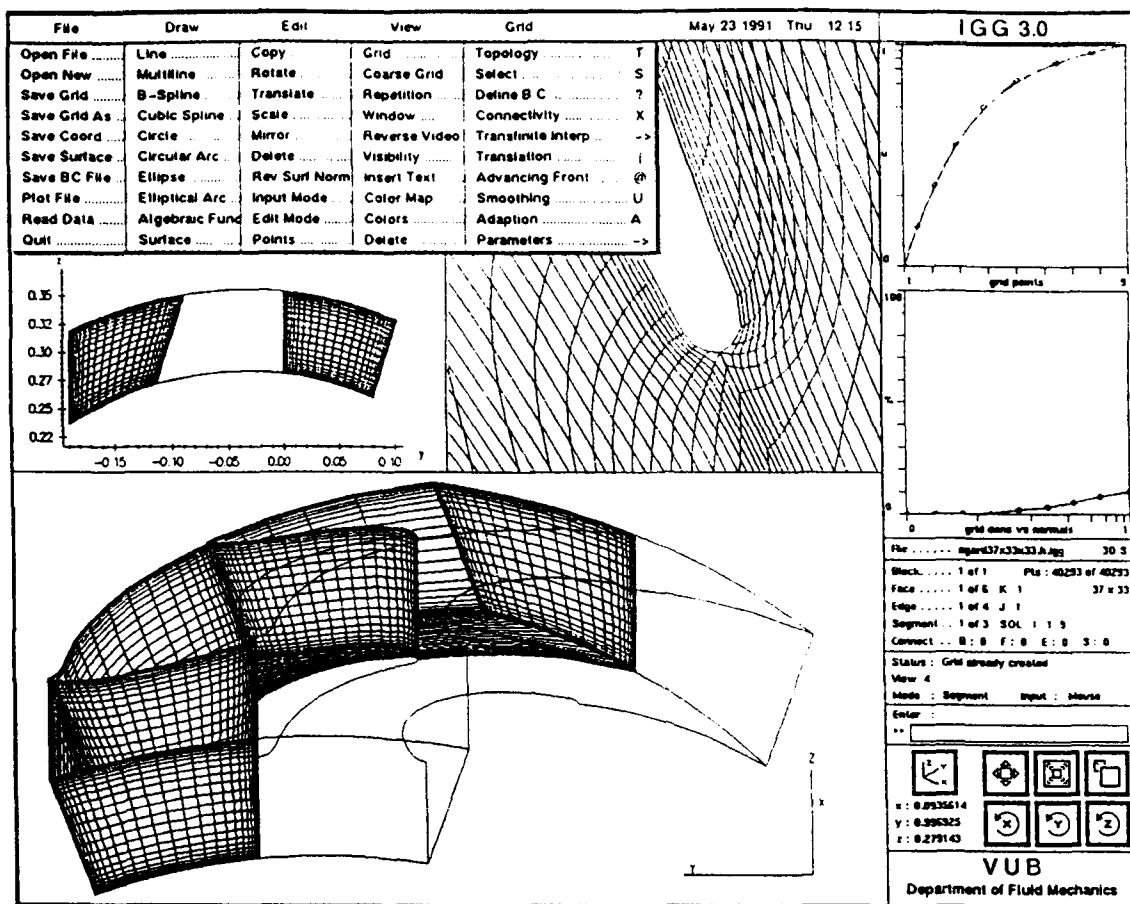


Figure 3.1 General layout of the IGG interactive graphical user interface.

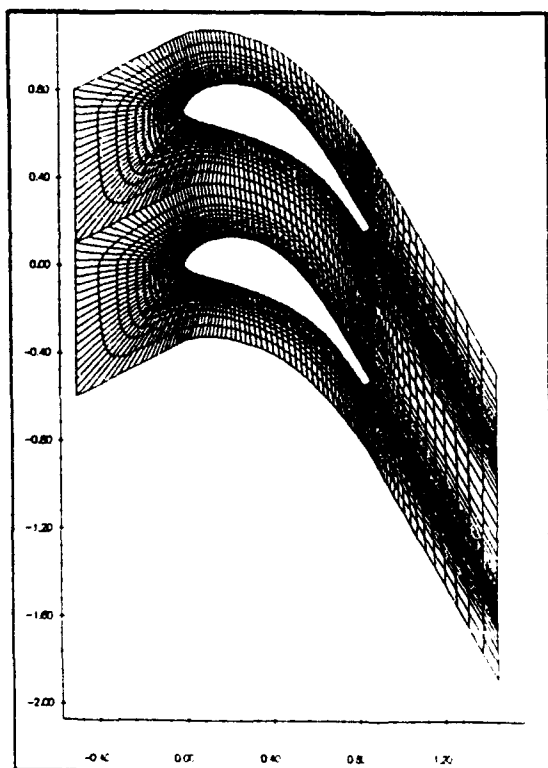


Figure 3.2 C-type grid created for a turbine blade.

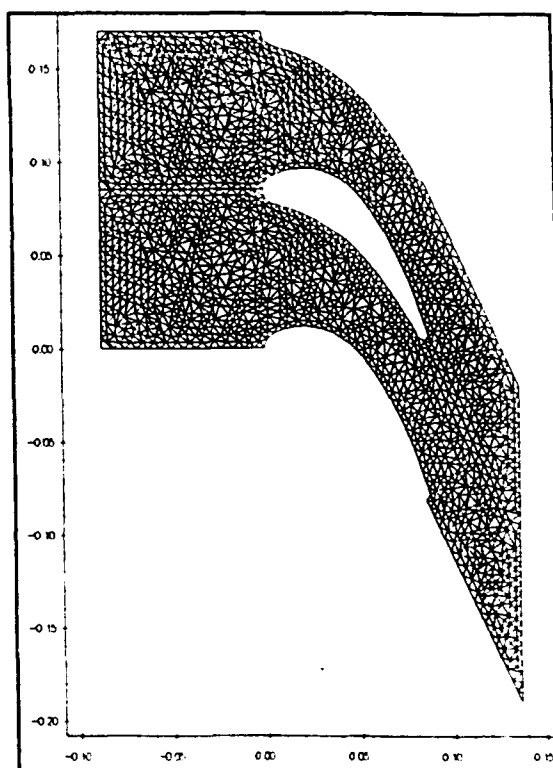


Figure 3.3 An unstructured grid created for the same boundary data given in Figure 3.4.

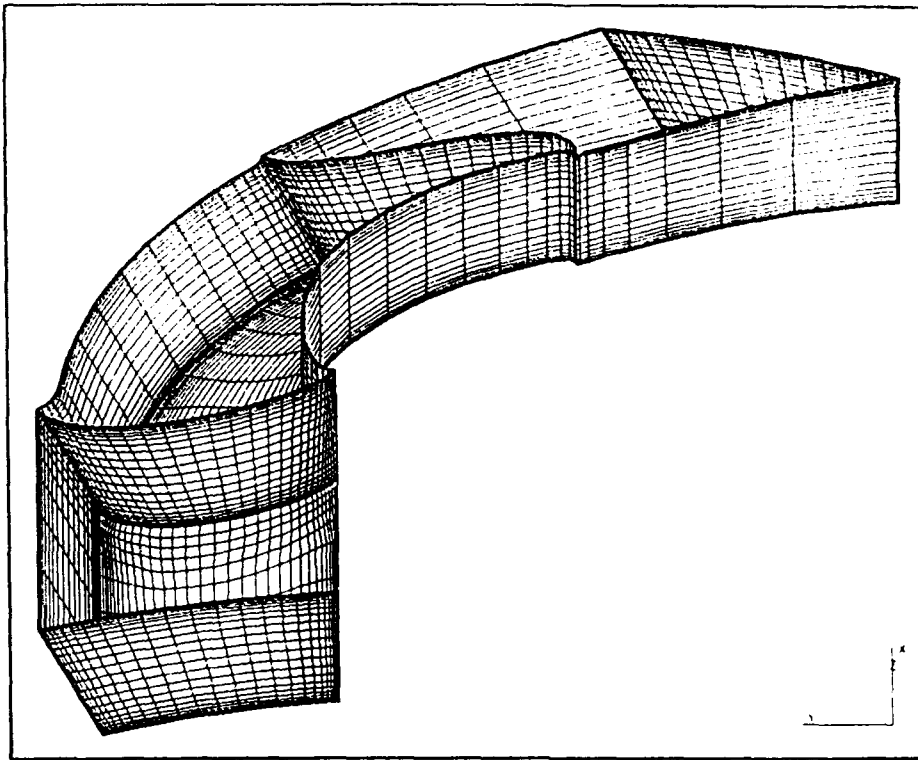


Figure 3.4 Selected surfaces on the H-type grid, created for the test case E/TU-1 low speed annular turbine blade.

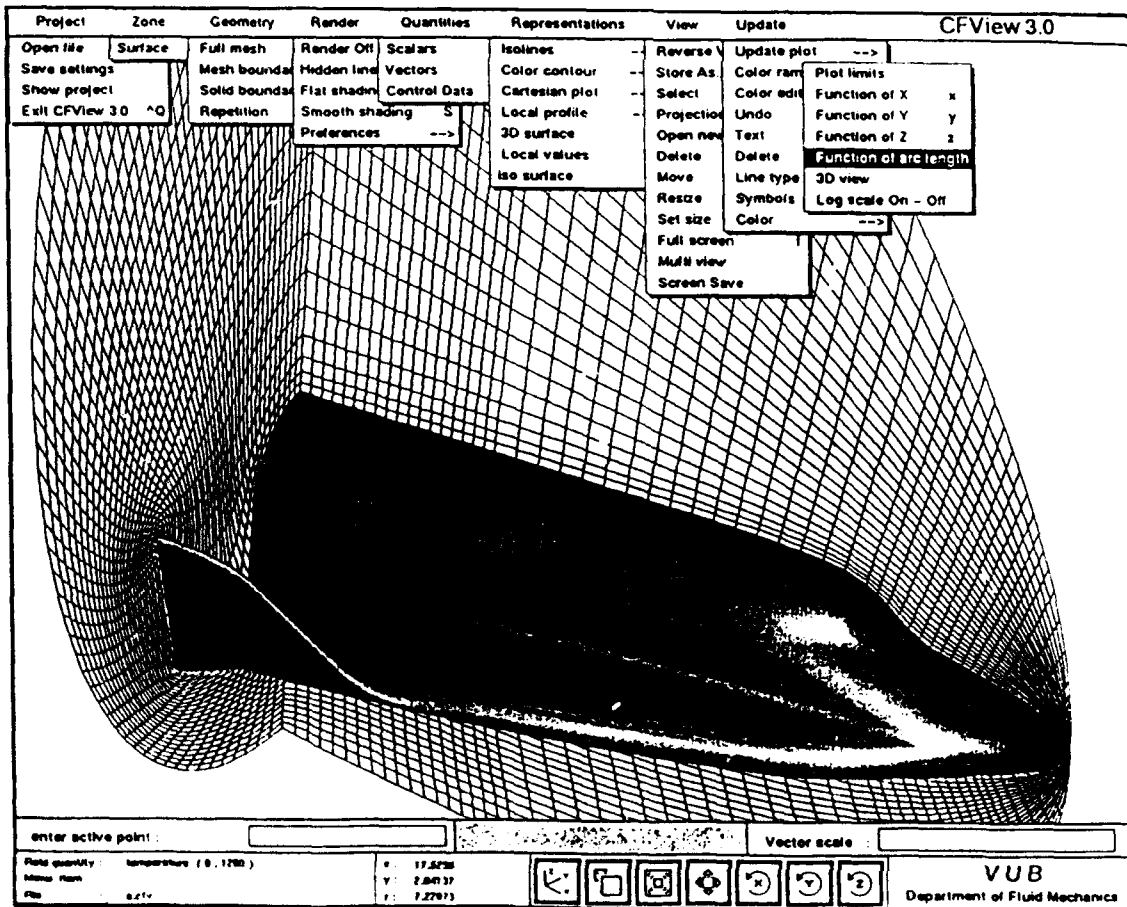


Figure 5.1 General layout of the CFView interactive graphical user interface.

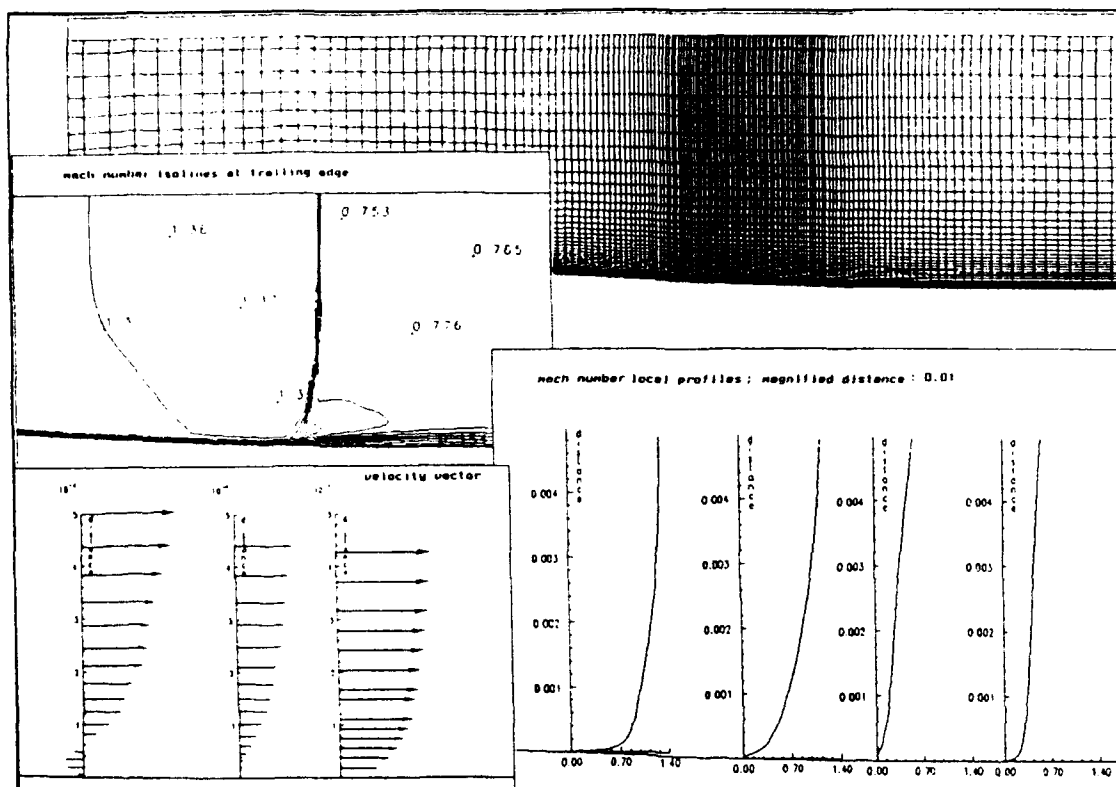


Figure 5.2 Numerical probes : local profiles and values.

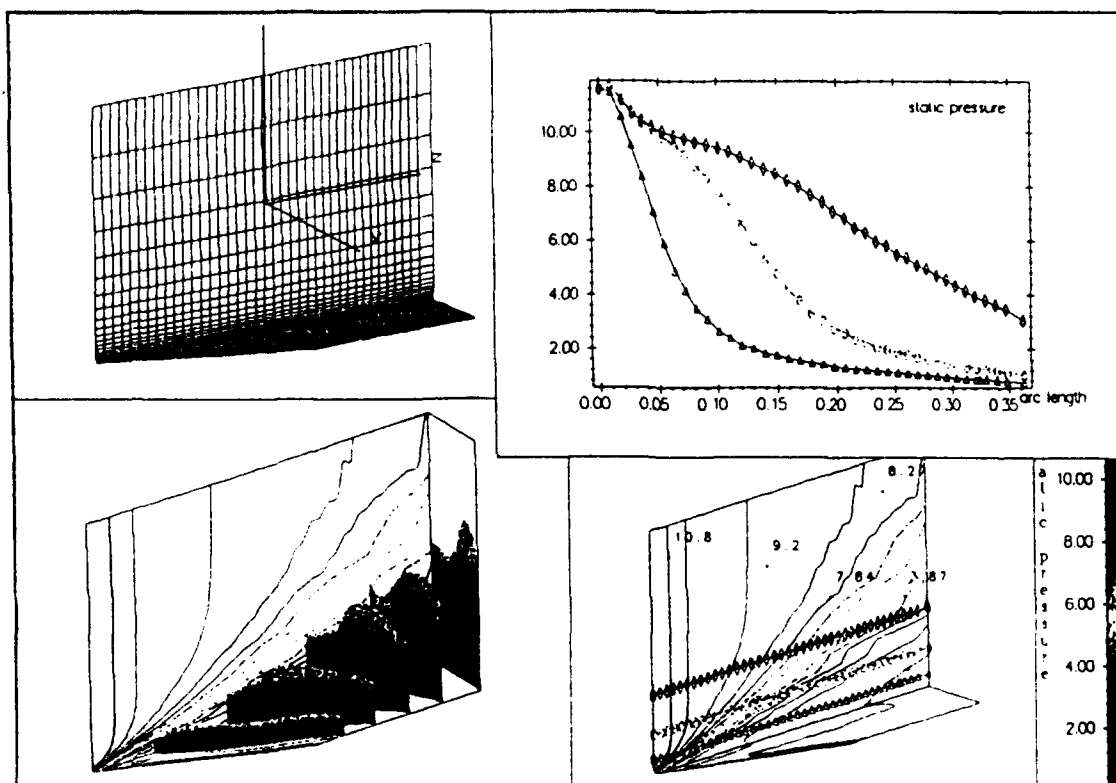


Figure 5.3 Different types of representations for the interactive qualitative and quantitative field analysis.

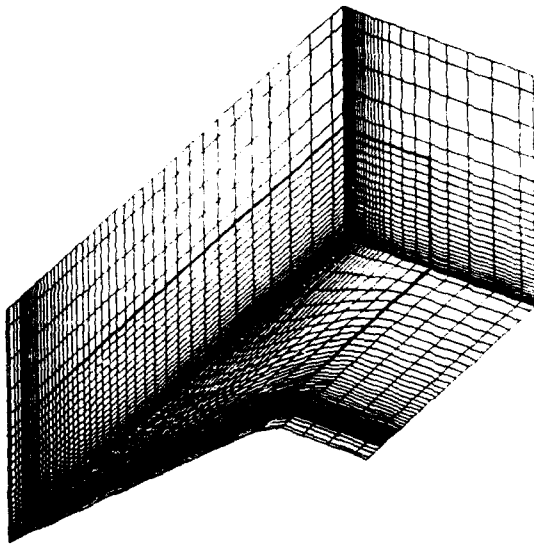


Figure 6.1 Part of the 3D mesh for the corner flow problem.

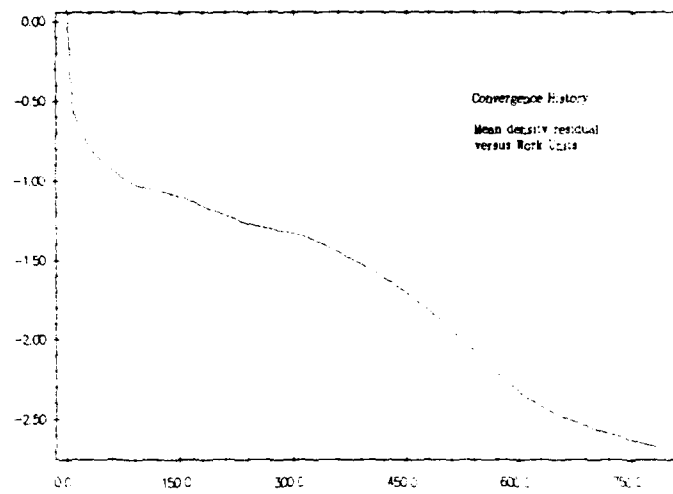


Figure 6.2 Convergence history for the central scheme.

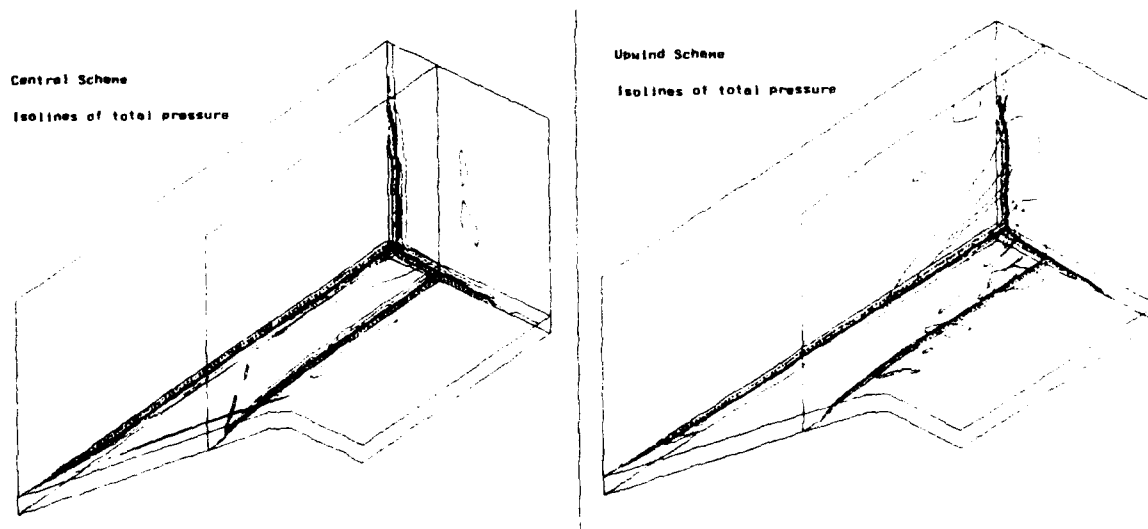


Figure 6.3 Comparison of total pressure distribution in different sections.

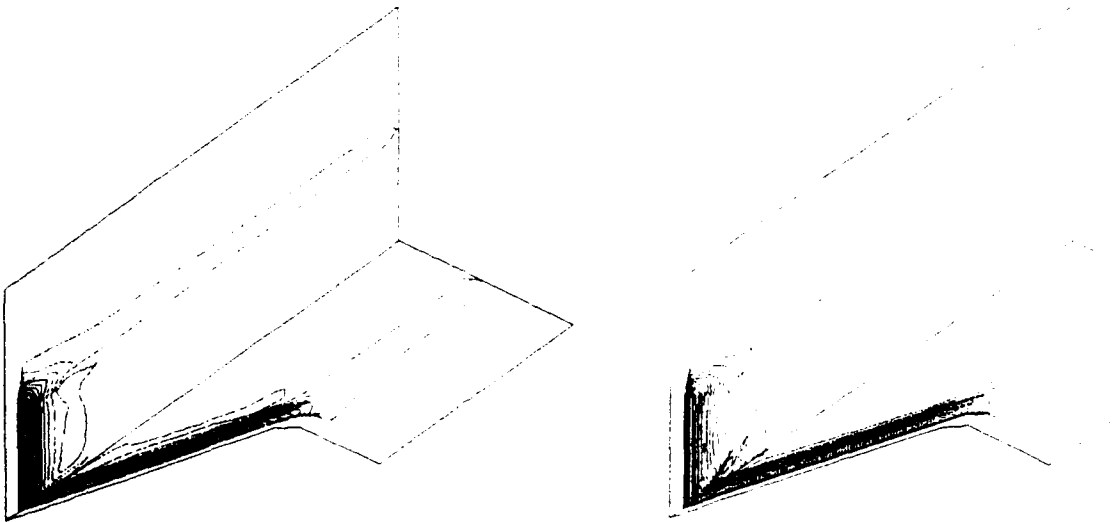


Figure 6.4 Comparison of Stanton number distributions in the vertical and the horizontal plate. (left:central scheme , right : upwind scheme)

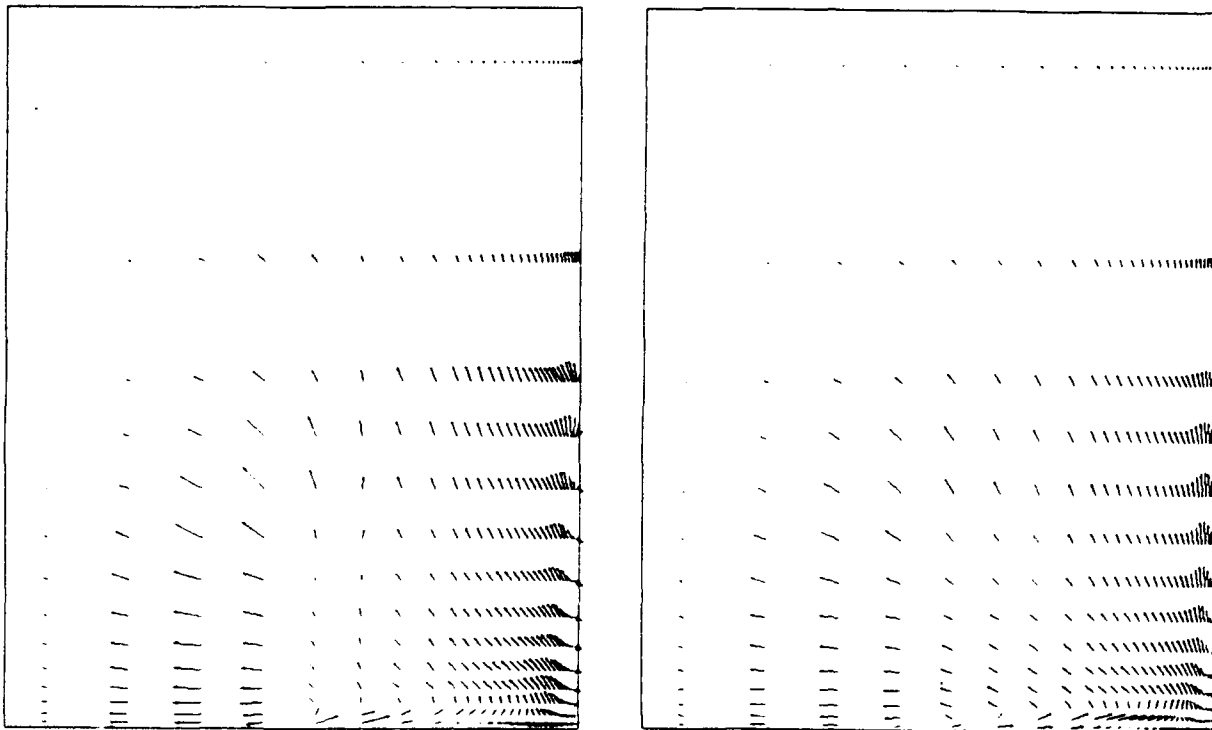


Figure 6.5 Velocity distribution in the outlet cross-section obtained with central (left) and upwind (right) schemes.

Discussion

H. WEYER, DLR, GERMANY

You showed exciting results of numerical simulation of shock-boundary layer interaction. Did you apply different turbulence models with your calculations and what are the effects on the calculated flow field?

AUTHOR'S REPLY

Calculations were done with different turbulence models. The results indicate that the turbulence models essentially affect the behavior at the foot of the shock, namely the shock induced separation. This interaction is very sensitive to turbulence models and there is, at present and as far as we know, no model, that shows unequivocally better performance. Although there might be some indications that the Reynolds stress models give better predictions, more tests have to be done to confirm these indications.

M. FORDE, UNIV. OF TRONDHEIM, NORWAY

Can your mesh generator generate a Navier-Stokes mesh based on an Euler mesh and solutions?

AUTHOR'S REPLY

The mesh generator has an option whereby a certain number of mesh lines can be "wrapped" around the body with a user defined clustering law and defined between the surface and a fixed initial mesh line. The "wrapping" leads to a series of mesh lines which are everywhere parallel to the surface along orthogonal directions. Hence, a local "Navier-Stokes" mesh can be inserted between the surface and a first "Euler" mesh line. In the present state, the clustering law is not connected to the flux solution.

H. FRÜHAUF, UNIV. OF STUTTGART, GERMANY

Do you have experience applying either the upwind or central differencing mode in the near wall regions of high Reynolds number flows? How do the solutions compare in regard to accuracy?

AUTHOR'S REPLY

The upwind schemes have to be treated carefully in the near wall regions. It is known that the flux vector splitting schemes such as Steger-Warming or Van Leer are too diffusive in the boundary layer regions. Improvements on the Van Leer flux splitting scheme are discussed in Dr. Hänel's lecture in order to achieve better accuracy. On the other hand, Roe's flux difference upwind scheme gives excellent results as well as central schemes, if the dissipation terms are kept low enough.

CALCUL PAR ELEMENTS FINIS DE L'ÉCOULEMENT 3D TURBULENT DANS UNE POMPE CENTRIFUGE

J.F. COMBES
Dept. Machines, EDF/DER
6 quai Watier
78400 Chatou
FRANCE

Résumé

Afin de résoudre des problèmes d'écoulements industriels dans des géométries complexes, la Direction des Etudes et Recherches d'Electricité de France a développé un code de calcul par éléments finis appelé N3S. Ce code permet de calculer des écoulements incompressibles et instationnaires 2D ou 3D en résolvant les équations de Navier-Stokes moyennées couplées au modèle de turbulence k- ϵ . Pour permettre de traiter des écoulements dans les turbomachines hydrauliques, on a développé dans ce code le traitement de conditions de périodicité, ainsi que la prise en compte des termes de rotation (force centrifuge et force de Coriolis).

Ce code est basé sur une méthode à pas fractionnaires: chaque pas de temps est décomposé en une étape de convection qui est traitée par une méthode de caractéristiques, une étape de diffusion pour les quantités scalaires et un problème de Stokes résolu grâce à un algorithme d'Uzawa. La discrétisation en espace fait appel à une méthode d'éléments finis avec une formulation mixte pour la vitesse et la pression.

Dans cet article nous présentons une application de ce code au calcul de l'écoulement dans une pompe centrifuge qui a fait l'objet d'essais sur plusieurs boucles en eau, et pour laquelle de nombreux calculs en fluide parfait ont été réalisés. Pour le calcul avec N3S le maillage d'un canal à aube comprend environ 28000 tétraèdres et 43000 noeuds. On a utilisé le modèle k- ϵ avec des lois de paroi. Les résultats de calcul seront comparés aux résultats expérimentaux pour le débit nominal.

Abstract

In order to solve industrial flow problems in complex geometries, a finite element code, N3S, has been developed at Electricité de France. It allows the computation of a wide variety of 2D or 3D unsteady incompressible flows, by solving the Reynolds-averaged Navier-Stokes equations together with a k- ϵ turbulence model. Some recent developments of this code concern turbomachinery flows, where one has to take into account periodic boundary conditions, as well as Coriolis and centrifugal forces.

The numerical treatment of the Navier-Stokes equations together with the k- ϵ ones is based on a fractional step method: at each time step, we solve successively an advection step by means of a characteristics method, a diffusion step for the scalar terms, and finally, a Generalized Stokes Problem by using a preconditioned Uzawa algorithm. The space discretization uses a standard Galerkin finite element method with a mixed formulation for the velocity and the pressure.

In this paper, we present an application of this code to the flow inside a centrifugal pump which has been extensively tested on several air and water test rigs, and for which many quasi-3D or Euler calculations have been reported. The present N3S calculation is made on a finite element mesh comprising about 28000 tetrahedrons and 43000 nodes. The k- ϵ turbulence modelling is used together with wall functions. The numerical results are compared to the experiments.

Nomenclature

A	: matrice de diffusion	V	: vitesse absolue
B	: matrice de divergence	W	: vitesse relative
k	: énergie cinétique de la turbulence	ϵ	: dissipation
n	: normale	ν	: viscosité cinématique
p	: pression statique	ν_t	: viscosité turbulente
P	: production d'énergie turbulente	ρ	: masse volumique
r	: rayon	σ	: contrainte
t	: temps	Ω	: vitesse de rotation
u*	: vitesse de frottement		

1- INTRODUCTION

La mise au point au cours des dernières années de codes de calcul basés sur une modélisation de plus en plus fine des écoulements a permis de faire des progrès importants dans l'analyse du fonctionnement des turbomachines. Pour le calcul de roues isolées, on est ainsi passé de modélisation 2,5D à des calculs Euler 3D, et maintenant la simulation d'écoulements turbulents est possible avec des codes tels que ceux décrits dans les références [1], [2], [3] et [4]. Ces développements ont porté surtout sur la modélisation des écoulements compressibles dans les compresseurs et les turbines. Les turbomachines hydrauliques ont suivi cette évolution avec quelques années de retard: les calculs Euler 3D ne sont couramment utilisés que depuis peu [5], [6], et très peu de calculs Navier-Stokes en pompe ont été publiés [7]; les méthodes numériques utilisées sont souvent dérivées de méthodes utilisées en compressible (compressibilité artificielle).

Par contre, des calculs d'écoulements turbulents sont faits de façon courante depuis plusieurs années en hydraulique industrielle avec des méthodes spécifiques pour les écoulements incompressibles. C'est ainsi que la Direction des Etudes et Recherches d'Electricité de France a développé plusieurs codes [8], résolvant les équations de Reynolds en 2D ou en 3D, en différences finies ou en éléments finis, pour traiter des problèmes de thermohydraulique. Parmi eux, le code N3S [9], utilisant une formulation en éléments finis, permet de calculer des écoulements incompressibles et instationnaires 2D ou 3D en résolvant les

équations de Navier-Stokes moyennées couplées au modèle de turbulence k-ε. Il a déjà été appliqué à des éléments fixes de turbomachines, tels qu'un diffuseur de turbine hydraulique [10]. Pour permettre de traiter des écoulements dans les roues, on a développé dans ce code le traitement de conditions de périodicité, ainsi que la prise en compte des termes de rotation (force centrifuge et force de Coriolis).

Dans cet article nous présentons une application de ce code au calcul de l'écoulement dans une roue de pompe centrifuge qui a fait l'objet d'essais sur plusieurs boucles en air et en eau [11], [12], [13], [14], et pour laquelle de nombreux calculs en fluide parfait ont été réalisés [15], [16].

II- MODELISATION DE L'ECOULEMENT

II-1 Equations

On se place dans le cas d'un écoulement turbulent de fluide incompressible dans un repère animé d'un mouvement de rotation uniforme. En utilisant l'hypothèse de Boussinesq, on peut écrire les équations de Navier-Stokes moyennées sous la forme:

$$\frac{\partial \vec{W}}{\partial t} + \vec{W} \cdot \vec{\nabla} \vec{W} = -\frac{1}{\rho} \vec{\nabla} p + \vec{\nabla} \cdot \left((\nu + \nu_t) \vec{\nabla} \vec{W} \right) - 2\vec{\Omega} \times \vec{W} + \Omega^2 \vec{r}$$

$$\vec{\nabla} \cdot \vec{W} = 0$$

où les deux termes $-2\vec{\Omega} \times \vec{W}$ et $\Omega^2 \vec{r}$ représentent respectivement l'accélération de Coriolis et l'accélération centrifuge.

La viscosité turbulente ν_t est liée à l'énergie cinétique de la turbulence k et au taux de dissipation ϵ par la relation :

$$\nu_t = C_\mu \frac{k^2}{\epsilon}$$

k et ϵ sont solution des deux équations de transport-diffusion suivantes:

$$\begin{aligned} \frac{\partial k}{\partial t} + \vec{W} \cdot \vec{\nabla} k &= \vec{\nabla} \cdot \left(\left(\nu + \frac{\nu_t}{\sigma_k} \right) \vec{\nabla} k \right) + \tilde{P} - \epsilon \\ \frac{\partial \epsilon}{\partial t} + \vec{W} \cdot \vec{\nabla} \epsilon &= \vec{\nabla} \cdot \left(\left(\nu + \frac{\nu_t}{\sigma_\epsilon} \right) \vec{\nabla} \epsilon \right) + \frac{\epsilon}{k} (C_{\epsilon 1} \tilde{P} - C_{\epsilon 2} \epsilon) \end{aligned}$$

où $\tilde{P} = \nu_t \frac{\partial W_i}{\partial x_j} \left(\frac{\partial W_i}{\partial x_j} + \frac{\partial W_j}{\partial x_i} \right)$ représente un terme de production par cisaillement.

Les constantes du modèle k-ε sont les constantes standard:

$$C_\mu = 0.09, \quad \sigma_k = 1, \quad \sigma_\epsilon = 1.3, \quad C_{\epsilon 1} = 1.44 \quad \text{et} \quad C_{\epsilon 2} = 1.92$$

II-2 Conditions aux limites

- en entrée, on utilise des conditions de Dirichlet pour toutes les variables sauf la pression.
- en sortie, la formulation variationnelle conduit naturellement à des conditions de contrainte:

$$\sigma_n = -p + \mu_c \frac{\partial W_n}{\partial n} \quad \text{pour la contrainte normale}$$

pour k et ϵ , on utilise une condition de Neuman homogène: $\frac{\partial k}{\partial n} = \frac{\partial \epsilon}{\partial n} = 0$

- au niveau des parois, la condition naturelle d'adhérence conduirait à utiliser un maillage très raffiné et un modèle à bas Reynolds pour la modélisation de la turbulence. On utilise de préférence des lois de paroi: en supposant la frontière du maillage à une distance y de la paroi, d'après la loi de Reichardt, la vitesse sur cette frontière est donnée par:

$$\frac{u}{u^*} = 2.5 \ln(1 + 0.4y^*) + 7.8 \left[1 - \exp\left(-\frac{y^*}{11}\right) - \frac{y^*}{11} \exp(-0.33y^*) \right]$$

où u^* représente la vitesse de frottement liée à la contrainte tangentielle σ^* par

$$\sigma^* = -p u^{*2}, \quad \text{et} \quad y^* = y \frac{u^*}{\nu}$$

u^* et y^* sont calculés itérativement en chaque noeud de paroi à chaque pas de temps.

Les conditions aux limites correspondantes pour k et ϵ sont les suivantes:

$$k = \frac{u^{*2}}{\sqrt{C_\mu}} \quad \text{et} \quad \epsilon = \frac{|u^*|^3}{K y}$$

- pour le calcul dans la pompe, on a supposé que l'écoulement est périodique, c'est à dire le même dans chacun des canaux interaubes. Aussi, le domaine de calcul correspond à un seul de ces canaux, et on applique des conditions de périodicité pour la vitesse, la pression, k et ϵ sur les frontières latérales.

II-3 Méthode numérique

La méthode numérique utilisée est décrite en détail dans la référence [9].

II-3-1 Discrétisation en espace

Le code N3S utilise une discrétisation en éléments finis. Pour assurer l'existence et l'unicité d'une solution au problème de Stokes discrétisé, et éviter des modes parasites de pression, les éléments retenus satisfont à la solution inf-sup. On peut ainsi utiliser des triangles ou tétraèdres P1-P2 ou P1-isoP2, ou des quadrangles ou briques Q1-Q2. Pour le calcul de l'écoulement dans la pompe SHF, on a utilisé des tétraèdres P1-isoP2 à 10 noeuds, dans lesquels la vitesse, k et ϵ sont discrétisés de façon linéaire par sous-élément, et la pression de façon linéaire. La pression est continue d'un élément à l'autre.

II-3-2 Discrétisation en temps

La résolution des équations de Reynolds et des équations du modèle k - ϵ est basée sur un schéma à pas fractionnaires; à chaque pas de temps on résoud successivement les étapes suivantes:

Convection

Les termes non linéaires de convection sont traités par une méthode de caractéristiques: pour résoudre l'équation type $\frac{\partial \tilde{C}}{\partial t} + w_j^n \frac{\partial \tilde{C}}{\partial x_j} = S_c$, où \tilde{C} représente la vitesse, k ou ϵ , w_j^n la vitesse au pas de temps précédent et S_c un terme source, on calcule entre t^n et t^{n+1} la courbe caractéristique - trajectoire des particules fluides - passant par le noeud i au temps t^{n+1} , et on intègre l'équation précédente le long de cette courbe par une méthode de Runge-Kutta. Cette méthode explicite est inconditionnellement stable dans le cas où il n'y a pas de terme source. Par contre, un traitement semi-implicite des termes sources du modèle k - ϵ a été rendu nécessaire pour assurer la robustesse du schéma.

Diffusion

après l'étape de convection, les équations pour k et ϵ peuvent se mettre sous la forme:

$$\frac{C^{n+1} - \tilde{C}}{\Delta t} = \vec{\nabla} \cdot \left(\left(\nu + \frac{\nu_t}{\sigma_c} \right) \vec{\nabla} C^{n+1} \right)$$

la discrétisation par une méthode de Galerkin (GFEM) de cette équation implicite conduit à un système linéaire qui est résolu par une méthode de gradient conjugué préconditionné par une décomposition incomplète de Cholesky (ICCG).

Problème de Stokes

les équations de Navier-Stokes deviennent après l'étape de convection:

$$\frac{w_i^{n+1} - \tilde{w}_i}{\Delta t} = - \frac{1}{\rho} \frac{\partial p^{n+1}}{\partial x_i} + \frac{\partial}{\partial x_j} \left(\left(\nu + \nu_t \right) \frac{\partial w_i^{n+1}}{\partial x_j} \right)$$

$$\frac{\partial w_i^{n+1}}{\partial x_i} = 0$$

elles ne comportent pas les termes correspondant à la rotation: le terme de Coriolis peut être traité comme terme source de l'équation de convection et la force centrifuge est prise en compte en rajoutant à la pression en post-traitement la quantité $\rho \Omega^2 r$

Après discrétisation par éléments finis (GFEM), on obtient un système matriciel de la forme:

$$\begin{aligned} A W + B^t P &= S \\ B W &= 0 \end{aligned}$$

en éliminant la vitesse entre ces deux équations, on obtient le système en pression suivant:

$$(B A^{-1} B^t) P = B A^{-1} S$$

qui est résolu par un algorithme d'Uzawa, préconditionné de façon à assurer une convergence rapide.

Les conditions aux limites - parois, périodicité - sont prises en compte par l'intermédiaire d'un opérateur de projection.

III- CAS TEST : POMPE SHF

III-1 Présentation

Depuis plusieurs années, la Société Hydrotechnique de France (SHF) consacre un effort important à l'étude du fonctionnement à débit partiel des turbomachines. Dans ce cadre, le sous-groupe de travail 1-ef de la SHF a conduit un double programme de recherche, expérimental et théorique. C'est ainsi qu'une géométrie de pompe centrifuge a été définie, deux maquettes ont été réalisées et essayées, et des calculs ont été effectués à plusieurs débits avec des modélisations différentes (quasi-3D, 3D Euler, couches limites) [15], [16], [17]. Des essais en air [11], [14] ont été réalisés sur une maquette de diamètre 516.8 mm à l'ENSAM de Lille, et des essais en eau sur une maquette de diamètre 354.4 mm à L'INSA de Lyon [13], à l'Ecole Polytechnique Fédérale de Lausanne et dans le laboratoire de la Société HYDROART à Milan. Les caractéristiques de la pompe SHF sont représentées sur la figure 1.

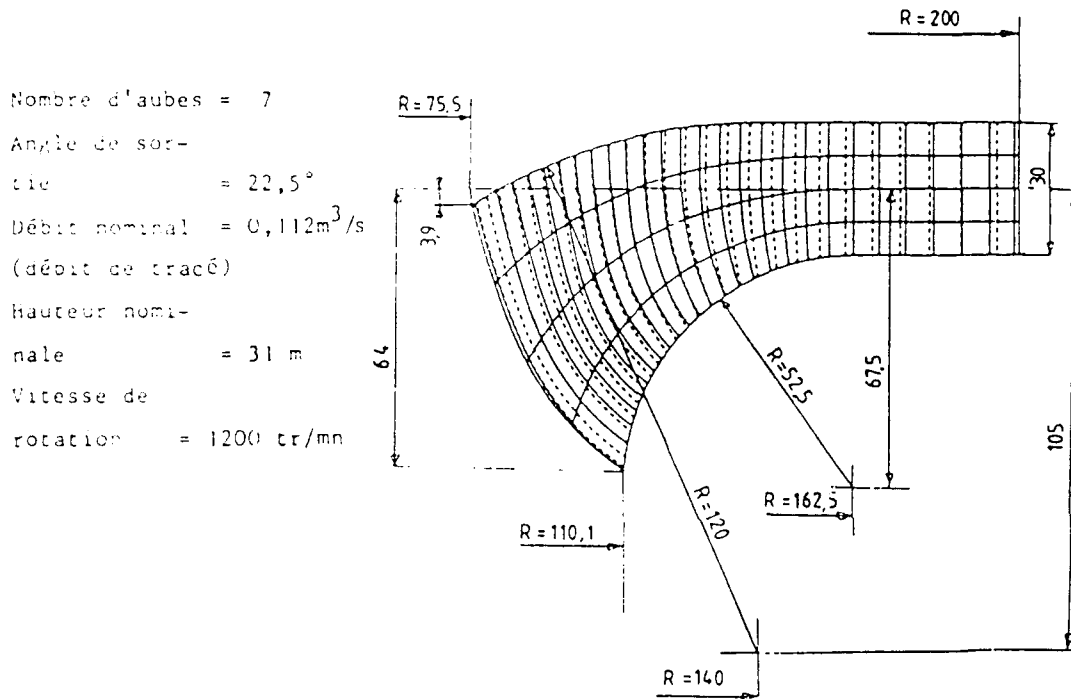


Figure 1: Vue méridienne et caractéristiques de la roue SHF

Mesures

Des mesures détaillées de champ de vitesse dans la roue et le diffuseur ont été réalisées à l'INSA de Lyon sur la maquette en eau, grâce à un système de vélocimétrie laser Doppler à deux composantes [13]. Les mesures ont été effectuées pour 5 débits différents, 3 positions radiales dans la roue, et 5 dans le diffuseur. Pour chaque section, il y a une quinzaine de relevés de vitesse. La pompe essayée à l'INSA comportait un diffuseur de 6 aubes.

Nous comparons également les résultats de calcul à des mesures dans le diffuseur lisse de la maquette en air essayée à l'ENSAM à Lille [11], [14]. Dans ce cas, la vitesse a été mesurée à l'aide d'une sonde à 4 trous pour 4 positions radiales et plusieurs positions circonférentielles.

Les différentes positions radiales retenues pour la comparaison entre mesures et calcul sont les suivantes:

INSA :	$R/R_2 =$	0.818,	0.978,	1.045	
ENSAM :	$R/R_2 =$		1.039,	1.194	

III-2 Calcul de l'écoulement dans la pompe SHF

Maillage

Le domaine de calcul correspond à la roue SHF, avec à l'amont un tronçon de tuyauterie droite et à l'aval un diffuseur lisse de diamètre 500 mm ($R/R_2 = 1.25$). En utilisant des conditions de périodicité, on n'a maillé que 1/7 de ce domaine.

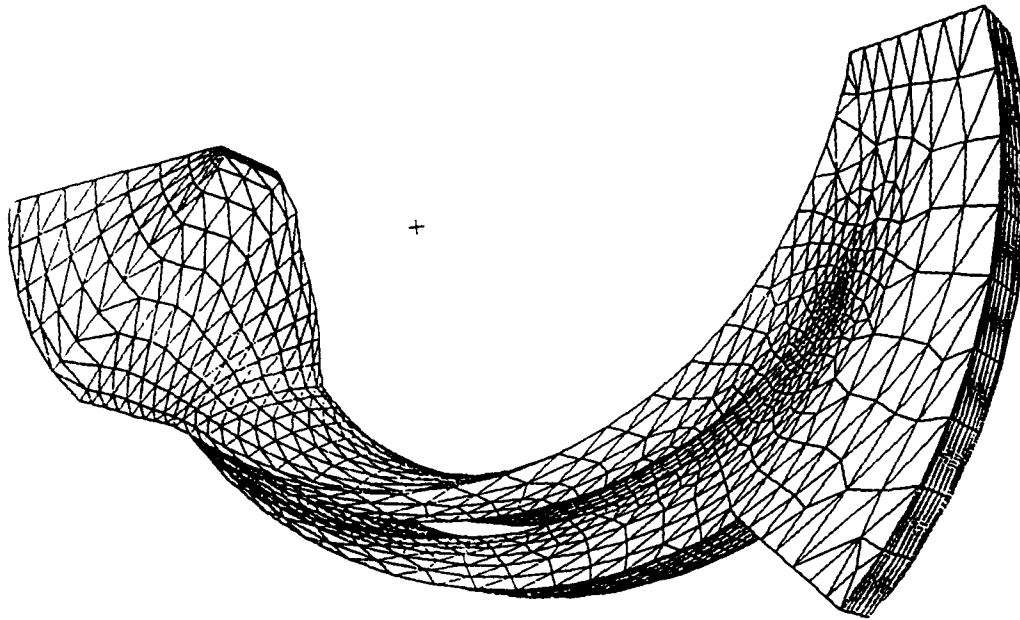


Figure 2 : Vue en perspective du maillage

Le maillage en éléments finis a été réalisé de la façon suivante:

- maillage structuré en H (I-J-K) du domaine de calcul.
- remaillage 2D en triangles d'une surface $I=Cte$ à l'aide du logiciel I-DEAS de SDRG, en concentrant les mailles près du bord d'attaque et du bord de fuite.
- report de la topologie de ce maillage sur toutes les surfaces I du maillage initial.
- constitution d'un maillage 3D en prismes et redécoupage de chaque prisme en trois tétraèdres.

Le maillage final, représenté sur la figure 2, comprend 28080 éléments tétraédriques et 43206 noeuds. Il a été constitué de façon à ce qu'il y ait correspondance deux à deux des faces d'éléments et des noeuds sur les frontières de périodicité.

Conditions aux limites

Le calcul est effectué au débit nominal ($0.1118 \text{ m}^3/\text{s}$) sans prérotation à l'amont. Le nombre de Reynolds basé sur la vitesse débitante et le diamètre d'entrée est alors voisin de 650000. L'écoulement est turbulent.

Les différentes conditions aux limites sont les suivantes:

- en entrée, on impose les trois composantes de la vitesse relative, ainsi que k et ϵ , correspondant à un profil turbulent établi dans la tuyauterie amont.
- sur toutes les surfaces solides, on utilise des lois de paroi. On prend ainsi en compte le frottement sur les parois fixes dans le repère en rotation - aubes, moyeu, carter - et l'entraînement par les parois mobiles dans ce repère - tuyauterie amont et diffuseur lisse.
- en sortie, on a essayé différents types de conditions aux limites - contraintes normale et tangentielle imposées, condition de Neuman sur la vitesse, ... Les résultats présentés correspondent à une pression statique constante sur la frontière aval.
- en chacun des points des frontières latérales, on impose des conditions de périodicité pour la vitesse, la pression, k et ϵ .

Caractéristiques du calcul

Le calcul complet a été réalisé de la façon suivante:

- maillage en prismes sur station de travail HP 9000 suivant la procédure indiquée ci-dessus.
- vérification et enrichissement du maillage initial (découpage en tétraèdres, création des noeuds milieu d'arêtes), introduction des conditions aux limites, constitution des fichiers d'entrée de N3S: passage du programme STBN3S sur CRAY-YMP.
- calcul de l'écoulement avec le programme N3S. Le calcul a duré environ 10 heures sur CRAY-YMP avec une occupation mémoire de 8 Mmots.
- exploitation des résultats à l'aide du logiciel GRAFN3S sur IBM 3090 ou station de travail HP9000.

Autres calculs

Dans le cadre du groupe de travail de la SHF, l'écoulement dans la pompe a été calculé à l'aide de nombreux programmes de calcul (quasi-3D, Euler 3D, couches limites, écoulements secondaires) par une dizaine d'organismes européens [15]. Nous comparons ici les résultats du calcul N3S avec des calculs en fluide parfait réalisés avec un code d'écoulement potentiel 3D en éléments finis [16]. Ces résultats sont représentatifs de l'ensemble des calculs en fluide parfait réalisés sur cette géométrie.

IV- RESULTATS

L'allure générale de l'écoulement dans la pompe calculé avec N3S correspond aux champs de vitesse relative et de pression statique représentés sur les figures 3 et 4 pour deux canaux interaubes consécutifs. Ces champs sont donnés sur un plan perpendiculaire à l'axe coupant la pompe à $z = -0.012$ m (carter : $z = -0.015$ m, moyeu : $z = 0.015$ m). Les points figurant sur la figure 4 indiquent les positions radiales où les calculs ont été comparés aux mesures : les points A et B dans la roue, C et D dans le diffuseur. Ne disposant pas de mesures de pression dans la roue, la comparaison avec les mesures n'a porté que sur les champs de vitesse. La représentation du champ de pression semble cependant correcte et très proche du calcul en fluide parfait.

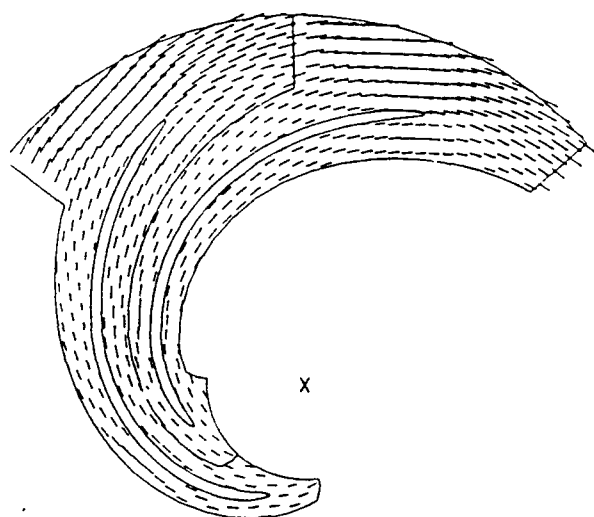


Figure 3 : Vitesse relative sur un plan orthogonal à l'axe

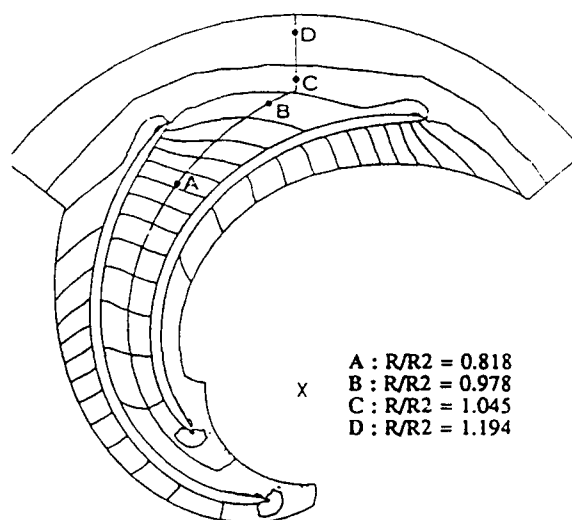


Figure 4 : Pression statique

Sur les figures 5 et 6 on a représenté l'évolution de la vitesse radiale et de la vitesse tangentielle moyennées sur un pas, entre le carter ($z = -0.15$ m) et le moyeu ($z = 0.15$ m) pour les quatre rayons A, B, C et D. On note un bon accord sur les profils de vitesse radiale avec les mesures en eau et en air. La vitesse radiale moyenne dans la roue est presque uniforme avec une légère remontée le long des parois. Dans le diffuseur, le profil de vitesse radiale bascule progressivement avec une survitesse au carter et une sous-vitesse au moyeu, pour atteindre près de la sortie du diffuseur lisse, une zone de recirculation. Ce phénomène est plus accentué dans le cas des mesures en air à l'ENSAM Lille où le diffuseur était légèrement plus large. Maroufi [14] avait observé le même comportement pour cette pompe, en calculant l'écoulement dans le diffuseur à l'aide d'un modèle de Senoo [18].

L'accord est correct également pour les vitesses tangentielles, dans la roue et en entrée de diffuseur où le calcul donne des résultats intermédiaires entre les deux mesures. Par contre, dans la zone de sortie du diffuseur, la valeur calculée est surestimée, sans doute à cause d'un choix de conditions aux limites en sortie inadapté : l'écoulement possède en effet une très forte composante tangentielle et la vitesse radiale est négative dans la zone proche du moyeu. Le calcul en fluide parfait donne en sortie des vitesses radiale et tangentielle uniformes, mais avec un niveau correct de vitesse tangentielle. On peut noter également sur la figure 6 l'inversion entre la roue et le diffuseur des profils de vitesse tangentielle au niveau des parois ; cet effet correspond au changement de référentiel : la vitesse de paroi vaut Ωr dans la roue et 0 dans le diffuseur.

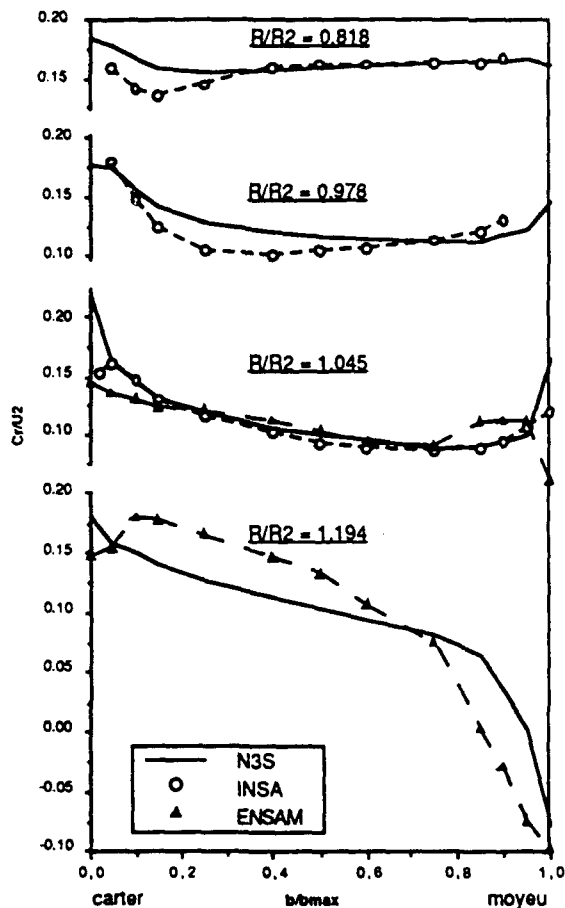


Figure 5 : Vitesse radiale moyennée sur un pas

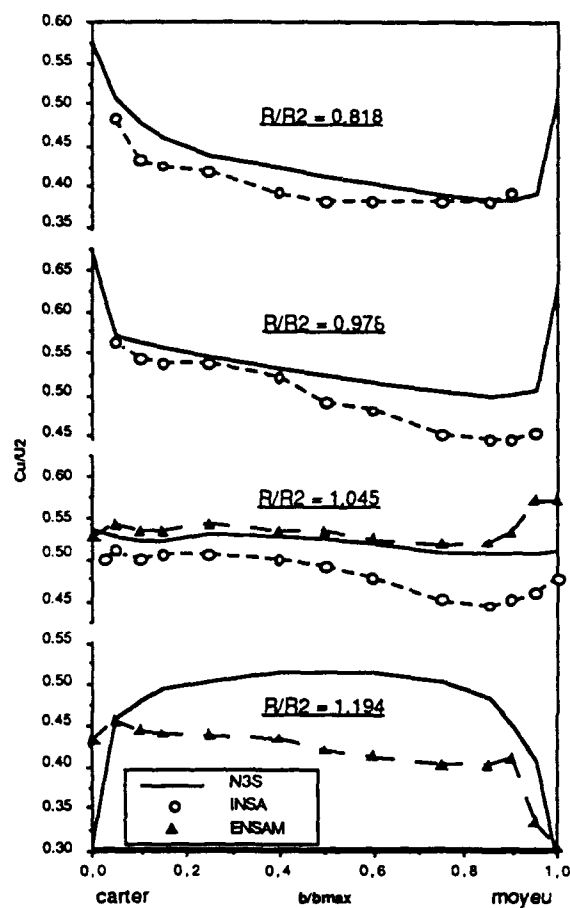


Figure 6 : Vitesse tangentielle moyennée sur un pas

Les figures 7 à 10 donnent l'évolution sur un pas de la vitesse radiale et de la vitesse tangentielle pour les deux rayons A et B, en des points de mesure proches du moyeu et du carter ($z = -0.0135$ m et $z = 0.0135$ m). Près du moyeu, comme pour la plus grande partie de la largeur du canal, on a une bonne correspondance entre les mesures et les calculs en fluide parfait et en fluide visqueux, bien que la vitesse tangentielle au niveau du bord de fuite soit surestimée par les calculs. L'évolution rapide de la vitesse relative sur la face en pression entre le point A et le bord de fuite est bien prédite par les deux codes.

On observe un comportement tout à fait différent dans la zone proche du carter. Alors que le calcul en fluide parfait fournit la même évolution que dans le reste du canal, les mesures et le calcul avec N3S montrent un comportement de type sillage dans le coin situé entre le carter et la face en dépression. A ce niveau, la vitesse relative est très ralentie (vitesse radiale plus faible et vitesse tangentielle plus élevée), et on observe un basculement complet du profil de vitesse radiale au niveau du bord de fuite (point B), le débit se reportant vers la face en pression pour compenser le déficit de vitesse radiale sur la face en dépression. Cette zone de sillage correspond à une zone de pertes importantes comme le montre la figure 11 où sont représentées les courbes iso-pression totale relative au niveau de la section A sur deux canaux interaubes consécutifs.

V- CONCLUSION

L'écoulement turbulent dans une pompe centrifuge a été calculé à l'aide du code aux éléments finis N3S. Le calcul a été réalisé à débit nominal, en utilisant le modèle $k-\epsilon$ standard et des lois de paroi relatives aux parois fixes et mobiles. Les résultats ont été comparés à des calculs en fluide parfait et à des mesures de vitesse par vélocimétrie laser dans la roue et dans le diffuseur sur une maquette en eau à l'INSA de Lyon et par sondage dans le diffuseur sur une maquette en air à l'ENSAM de Lille. Les champs de vitesse calculés avec N3S sont en bon accord avec l'expérience, même dans les zones où l'écoulement est fortement perturbé par les effets visqueux - recirculation en sortie de diffuseur côté moyeu, et zone de sillage dans le coin entre le carter et la face en dépression. La prédiction de l'écoulement est alors bien meilleure qu'en fluide parfait.

Cette première simulation de l'écoulement turbulent dans une roue de pompe est donc très encourageante et permet d'augurer de bons résultats également à débit partiel dans les cas où les calculs en fluide parfait ne sont plus représentatifs. Les prochains développements concernent l'amélioration des modèles de turbulence et des lois de paroi, et une diminution des temps de calcul. La validation se poursuivra à débit partiel et sur d'autres géométries.

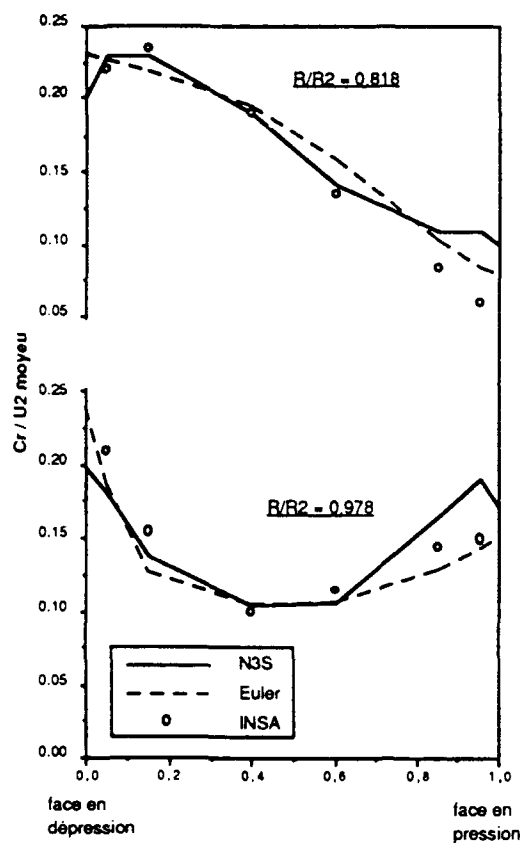


Figure 7: Vitesse radiale près du moyeu

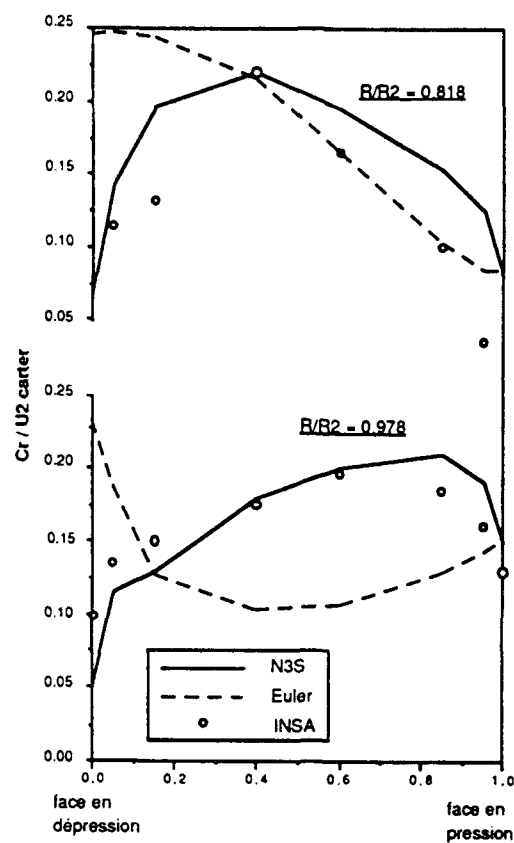


Figure 8: Vitesse radiale près du carter

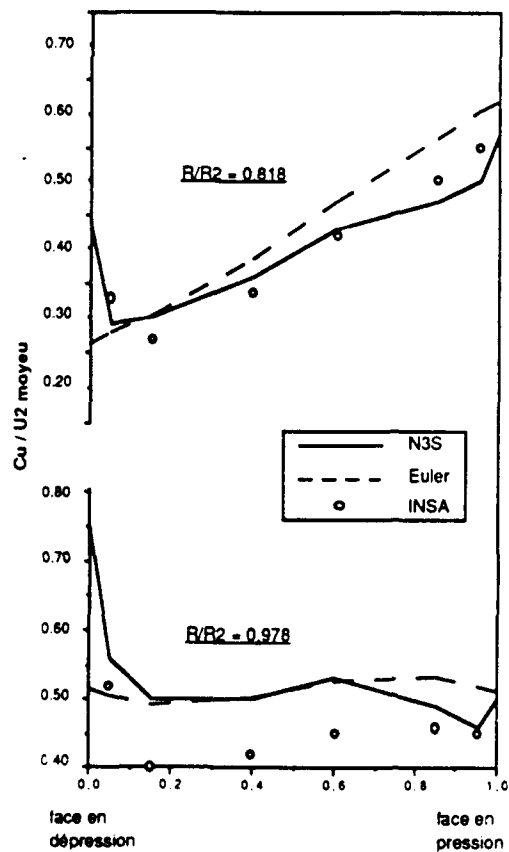


Figure 9: Vitesse tangentielle près du moyeu

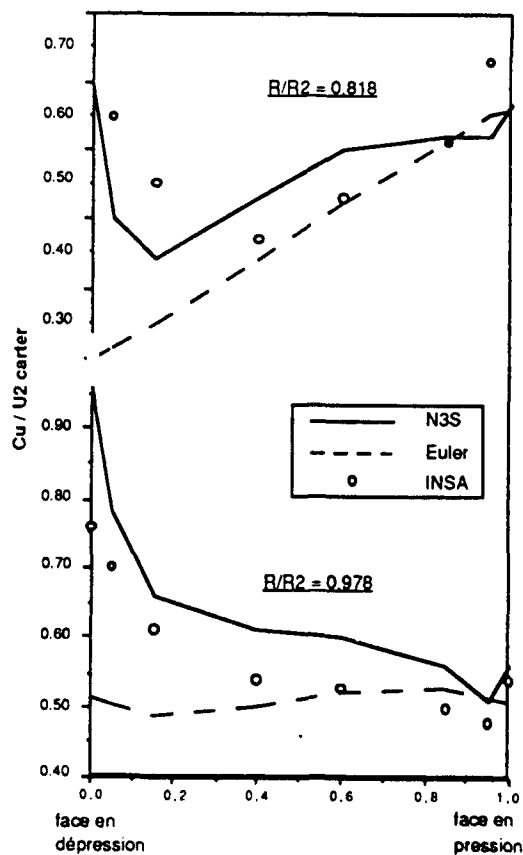


Figure 10: Vitesse tangentielle près du carter

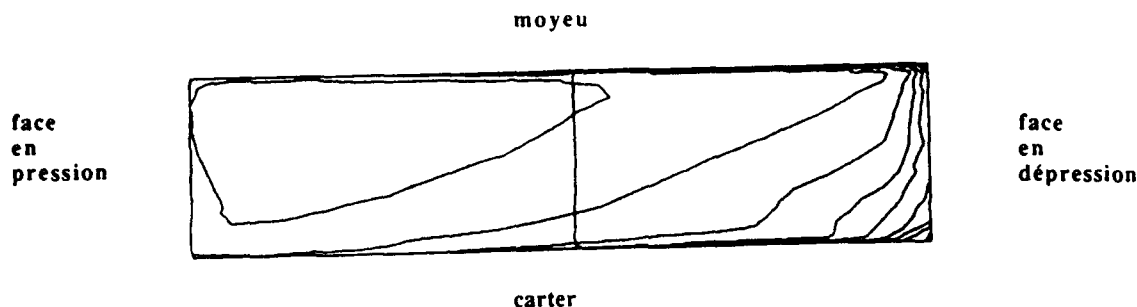


Figure 11 : Champ de pression totale au rayon $R/R_2 = 0.818$

Références

- [1] HAH, C. : "A Navier-Stokes analysis of 3D turbulent flows inside turbine blade rows at design and off-design conditions", ASME paper 83-GT-40, 1983
- [2] DAWES, W.N. : "Development of a 3D Navier Stokes Solver for Application to all Types of Turbomachinery", ASME paper 88-GT-70, 1988
- [3] CHIMA, R.V., YOKOTA, J.W. : "Numerical analysis of 3D viscous internal flows", AIAA paper 88-3522, 1988
- [4] MOORE, J. : "Performance evaluation of flow in turbomachinery blade rows". AGARD LS-140, 1985
- [5] CAUDIU, E., GRIMBERT, I., EL GHAZZANI, E.M., VERRY, A., PHILIBERT, R. : "Calculs d'écoulements tridimensionnels. Application à une pompe hélico-centrifuge et à une turbine Francis", Symposium AIRH 1988, Trondheim, Norvège.
- [6] ERIKSSON, L.E., RIZZI, A., THERRE, J.P. : "Numerical solutions of the steady incompressible Euler equations applied to water turbines", AIAA Appl. Aerodynamics Conf., Seattle, 1984.
- [7] GOTO, A. : "Study of Internal Flows in a Mixed-Flow Pump Impeller at Various Tip Clearances Using 3D Viscous Flow Computations", ASME paper 90-GT-36, 1990
- [8] CHABARD, J.P., COMBES, J.F., GABILLARD, M., LAURENCE, D., POT, G., : "Refined Modelling of Industrial Flows, Applications and prospect", Symposium on Advances in Numerical Simulation of Turbulent Flows, Joint ASME/JSME Conference, Portland, June 23-26, 1991
- [9] CHABARD, J.P., METIVET, B., POT, G., THOMAS, B. : "An efficient finite element method for the computation of 3D turbulent incompressible flows", to appear in Finite Element in Fluids, vol.8.
- [10] COMBES, J.F., VERRY, A., DELORME, M., PHILIBERT, R., VANEL, J.M. : "Numerical and experimental analysis of the flow inside an elbow draft tube", Symposium AIRH 1990, Belgrade, Yougoslavie
- [11] CAIGNAERT, G., DESMET, B., MAROUFI, S., BARRAND, J.P. : "Velocities and Pressure Measurements and Analysis at the Outlet of a Centrifugal Pump impeller", ASME paper 85-WA/FE-6, Miami Beach - november 17-21, 1985
- [12] CAIGNAERT, G., BARRAND, J.P. : "Débits critiques de recirculation: synthèse de l'ensemble des résultats expérimentaux sur les roues SHF essayées en air (ENSAM Lille) et en eau (INSA Lyon, EPF Lausanne, Hydroart Milan)", 20^{èmes} journées de l'Hydraulique SHF, Lyon, avril 1989
- [13] BOIS, G., RIEUTORD, E. : "Etude de l'écoulement en sortie de roue de pompe centrifuge depuis le débit nominal jusqu'au débit critique de recirculation", Compte rendu de fin d'étude de contrat MRT no 88H0636, octobre 1990.
- [14] MAROUFI, S. : "Contribution à l'étude de l'apparition des recirculations en sortie de roue dans une pompe centrifuge fonctionnant à débits partiels", Thèse de 3^{ème} cycle, Univ. de Lille, 7 mai 1986.
- [15] UBALDI, M., PHILIBERT, R., VERRY, A. : "Examen des possibilités et limites d'utilisation des calculs d'écoulement pour la prévision des débits de recirculation d'une roue de pompe centrifuge", Symposium AIRH 1986, Montréal, CANADA
- [16] COMBES, J.F. : "Calcul de l'écoulement tridimensionnel potentiel dans une roue de pompe centrifuge à débit partiel", La Houille Blanche n°5, 1985
- [17] UBALDI, M. : "Calcul de l'écoulement visqueux dans un canal de pompe centrifuge", La Houille Blanche n°5, 1985
- [18] SENOO, Y. : "Vaneless diffusers" Von Karman Institute for Fluid Dynamics, LS 1984-07 : Flow in centrifugal compressors, 1984

Discussion

C. HAH, NASA LEWIS, U.S.A.

For the exit boundary condition, do you fix static pressure at the exit plane? How is the total mass flow rate set for the numerical solution?

AUTHOR'S REPLY

At the exit, uniform values for the normal and tangential stress components are fixed. It corresponds approximately to a uniform static pressure. The mass flow rate was constant all over the calculation. It was determined by the imposed inlet velocity distribution.

J. MOORE, VPI, U.S.A.

With your Navier-Stokes code, how well did you calculate the head rise, the efficiency, and the slip factor of the impeller? May I also make a comment about flow in your vaneless diffuser. If you go to larger radius ratios, you will probably find it easier to satisfy the exit flow boundary condition in a constant area vaneless diffuser. This will reduce the tendency to reversed flow in the radial direction due to separation on the diffuser walls.

AUTHOR'S REPLY


Thank you for your comment. The radius ratio was chosen according to the measurements in ENSAM Lille. The comparison with experimental results was done at present only for velocity fields. It will be pursued for pressure and efficiency at nominal and partial flow rates.

H. WEYER, DLR, GERMANY

The Navier-Stokes-calculation - in good agreement with experiments - differs considerably from Euler results. There is obviously a jet-wake flow within the impeller (due to separation) as the experiments confirm. Does the Navier-Stokes-calculation present the separation? What did you do for modeling?

AUTHOR'S REPLY

There was no special modeling for the separation zones. In the wake region, the radial velocity goes down nearly to zero, but no reverse flow was found.





PREDICTIONS AND MEASUREMENTS OF 3D VISCOUS FLOW IN A TRANSONIC TURBINE NOZZLE GUIDE VANE ROW

by

G.C.Horton, S.P.Haragama and K.S.Chana
Royal Aerospace Establishment
Pyestock, Farnborough
Hampshire GU14 0LS
United Kingdom

92-16080



SUMMARY

In recent years improvements in algorithms and computing power have allowed the regular use of three-dimensional viscous flow programs to analyse the flows in turbines. Before these programs can be used with confidence by the turbine designer, however, they must be validated by comparison with high quality experimental data taken at realistic conditions.

A transonic turbine nozzle guide vane has been tested in an annular cascade with two different endwall geometries. The measurements were taken at engine-representative flow conditions and include surface static pressures and a downstream area traverse of total pressure.

The flow through these geometries has been modelled at the test conditions using a three-dimensional viscous flow program. The effects of different mesh densities and two turbulence models have been studied. Predictions of secondary flow and loss have been obtained and are compared with the experimental measurements.

1. INTRODUCTION

The use of three-dimensional viscous flow programs to analyse the flow in turbomachinery blade passages has become widespread in recent years. In general these methods are currently used to analyse existing designs or to check specific features of a new design in the final stages of the design process. If these methods are to realise their full potential for radically improving turbomachinery design they must be used much earlier in the design process. This requires the designer to have confidence in the capability of the program and also a good understanding of the effect of the available options, such as mesh size and density, or different turbulence models.

To help prove this confidence, a turbine nozzle guide vane (ngv), designed for transonic flows, has been tested in annular cascade form with two different endwall shapes in the Isentropic Light Piston Cascade (ILPC) facility at RAE Pyestock. The same nozzle geometry has been analysed using a three-dimensional viscous flow program with different meshes and turbulence models. This paper reports the results of these computations and makes comparisons with the experimental results.

2. THE NGV DESIGN

The ngv tested was designed at the Royal Aerospace Establishment as part of a high work capacity, high blade speed turbine known as the High Rim Speed Turbine. The design philosophy and test performance have been

described in a previous AGARD paper (Ref 1) and blading aerodynamic and heat transfer measurements in Ref 2. The blade design is illustrated in figure 1. The design features a variation of exit flow angle along the span and a curved tangential stack of the trailing edge to control secondary flows by setting up spanwise pressure gradients. At the design condition the exit Mach number is 1.05 and the Reynolds number (based on exit conditions and axial chord) is 1.73×10^6 . The original ngv was designed for cylindrical endwalls, but as part of an investigation of potential improvements to the turbine efficiency, profiled hub shapes were also considered.

The blading design has been tested with two of these endwall shapes, which are here termed the bellmouth and S-bend profiles (see figure 1). The aim of these endwall shapes was to reduce the secondary effects by re-energising the flow near the endwall. The distribution of curvature, and hence the local acceleration provided to the flow, varied between the two designs.

3. THE ILPC FACILITY

The Isentropic Light Piston Cascade, or ILPC, (Ref 3) is a short duration facility designed to allow high quality heat transfer and aerodynamic measurements to be taken for a full-size annular cascade of turbine vanes. Its design and operation has been described in an AGARD paper presented in 1985 (Ref 3). A major extension of the facility, to enable heat transfer data to be taken from a rotating rotor mounted downstream of the nozzle row, has been designed and will be installed in 1991. The aerodynamic conditions upstream of the cascade, to match the engine parameters of exit Mach number, Reynolds number and gas-to-wall temperature ratio, are obtained by the isentropic compression of air in a large pump tube. This compression is performed by a free piston driven along the tube by high pressure air. When the correct conditions are achieved, a fast-acting plug valve opens allowing the air to flow through the cascade giving steady operating conditions for approximately 0.5 second, during which time aerodynamic and heat transfer data can be acquired.

For this series of tests the instrumentation consisted of static pressure tapings at a total of 188 locations on the vane surfaces and endwalls. An area traverse of total pressure was performed on a plane 0.2 axial chord downstream of the trailing edge. This was built up from a series of 27 circumferential sweeps at different radii, each sweep requiring a separate run of the ILPC facility. The circumferential extent of a sweep was approximately 1.5 vane pitches. As it was desired to traverse through two vane wakes on each sweep and the vane wakes were

significantly curved, regular adjustment of the location of the traverse mechanism was necessary to produce a full area traverse. As a result, producing the area traverse took a considerable time and so was done for only one endwall profile, the bellmouth profile. Results reported previously for the cylindrical endwall geometry (Ref 4) were obtained with a three-hole probe with high-response transducers mounted near the tip. These results suffered from a high degree of noise, much of it aerodynamic. For the current series of traverses a modified probe configuration was used. This configuration had three transducers with lower frequency response mounted 500 mm from the probe head. This distance between the probe head and the transducers appears to damp out the aerodynamic noise effectively while providing enough response to capture adequately the vane wakes. The natural frequency of the system is now approximately 400 Hz.

The manner of operation of the traverse mechanism presented some difficulties when measuring near the hub. To overcome these difficulties two different probe tips were used: a straight tip for the traverses above mid-height and a "swan-necked" tip for those below (figure 2). By using these two probe tips it was possible to traverse to within 7.5% vane height of both endwalls.

4. ANALYSIS METHOD

The method used to analyse the flow is the three-dimensional viscous flow program of Dawes (Ref 5). This solves the unsteady Reynolds averaged Navier Stokes equations for a steady solution using an implicit time marching algorithm. Turbulent stresses are modelled using an eddy viscosity concept. Two formulations of eddy viscosity are available: an algebraic method due to Baldwin and Lomax (Ref 6) and a one-equation method patterned after that of Birch (Ref 7). The latter model includes an additional transport equation for turbulent kinetic energy which is solved using a space-marching algorithm. In the Baldwin-Lomax model laminar-turbulent transition is modelled by specifying locations for the start and end of transition on both suction and pressure surfaces. A value of intermittency is then calculated for each mesh point by linear interpolation between these specified transition locations. For the current series of calculations transition on the suction surface was set to start at 25% axial chord (Cax) and end at 60% Cax. The corresponding figures for the pressure surface were 40% and 90%. The one-equation method models transition through a low Reynolds number damping term.

Spatial discretisation is achieved using a sheared, cell-centred H-mesh. Two different densities of mesh were employed; calculations with meshes 1 and 2 used 25 points circumferentially, 25 radially and 89 axially, a total of 55625 mesh points, while those with meshes 3 and 4 used a 33 x 33 x 119 mesh (129591 mesh points). In each case the mesh was refined considerably near solid surfaces

and also near the leading and trailing edges. For the bellmouth endwall shape a limited investigation of mesh distribution was performed by varying the refinement at the leading and trailing edges for the same overall number of mesh points. Results from all the different mesh densities and distributions are presented.

The convergence of the program is accelerated using a multigrid algorithm. Previous experience indicated that good convergence was obtained after 2000 time steps and so this number was used for the results presented here. At this point the rms value of axial momentum residue was 2.6×10^{-4} on mesh 4. The program was run on a Stardent 1500 mini-supercomputer and 2000 time steps on mesh 4 required approximately 48 hours of cpu time.

5. MESH COMPARISON

The four meshes employed for modelling the bellmouth profile are compared in figures 3 and 4. The different mesh refinements at leading and trailing edges and near solid surfaces resulted in the mesh spacings shown in table 1. The endwall boundary layer at the first plane, one axial chord upstream of the leading edge was set to have a thickness of 6% annulus height. This resulted in 6 points in this inlet boundary layer for meshes 1 and 2, and 8 points for meshes 3 and 4.

The mid-height distributions of isentropic Mach number predicted with the different meshes are compared in figure 5. The main variations occur on the pressure surface between the leading edge and 60% axial chord (Cax) and on the suction surface at about 60% Cax. The latter feature corresponds to the impingement of the trailing edge shock on to the suction surface and the differences are probably due to the different modelling of the trailing edge flow with the various meshes. This shock is modelled best with mesh 4, which has the finest spacing at the trailing edge. Contours of Mach number near the trailing edge are illustrated for meshes 2 and 4 in figure 6. The pressure surface boundary layer upstream of the trailing edge is considerably thinner with the finer mesh leading to delayed separation and higher peak Mach number at the trailing edge. This produces the stronger shock evident where it impinges on the suction surface. On the forward pressure surface the isentropic Mach number is higher with the finer meshes than the coarser. The differences appear to be associated with the finer cross-stream mesh rather than the axial refinement, suggesting that they are due to the improved modelling of the pressure surface boundary layer as a result of the finer spacing of meshes 3 and 4 in this region.

Figure 7 compares the secondary flows near the suction surface for meshes 1 and 4. The manner in which the endwall crossflow was swept onto the suction surface can be clearly seen in both cases. The finer mesh (4) has

resolved two separate points of impingement onto the suction surface for each endwall at approximately 50% Cax and 85% Cax with the flow nearly parallel to the endwall between the two. The coarser mesh has modelled the first impingement very similarly to the finer mesh but has not picked up the second.

The development of mass-averaged loss along the passage is shown for each mesh in figure 8. The results from the finer meshes have a lower overall loss than those from the coarser meshes reflecting the improved modelling of the blade and endwall boundary layers with the finer meshes. Also they exhibit a more realistic growth of loss through the blade passage; the loss with the coarser meshes grows from the leading edge to about 30% Cax, then diminishes before growing again towards the trailing edge. At the trailing edge mesh 4 shows a very rapid growth of loss with little further growth downstream whereas the other results, particularly meshes 1 and 3, show less growth at the trailing edge but significant further growth downstream. This is attributed to the increased mixing of the flow at the trailing edge with mesh 4 due to the finer mesh spacing in this region. The total losses at the exit plane (1.0 axial chord downstream of the trailing edge) for meshes 1 and 4 are 0.081 and 0.052 respectively.

Contours of total pressure on a cross-stream plane at 120% axial chord are compared for all four meshes in figure 9. The distinctive curved wake is due to the curved trailing edge and the radial variation of exit angle. In each case the peak loss (minimum total pressure) occurs in a thick region around mid-height, the level of this peak loss being similar for all the meshes. Meshes 1 and 4 give narrower wakes than (respectively) meshes 2 and 3 suggesting that the finer mesh in the trailing edge region has changed the modelling of the flow in the mixing region downstream of the trailing edge. Also, the wake with mesh 4 is narrower than with mesh 1 indicating that the improved modelling of the suction and pressure surface boundary layers due to the finer near-wall mesh has resulted in thinner boundary layers being predicted at the trailing edge.

6. TURBULENCE MODEL COMPARISON

The above results were all produced using the Baldwin-Lomax turbulence model with the specified transition locations. Calculations have also been performed using the one equation turbulence model on meshes 1 and 4. The development of the mass averaged loss along the vane passage is compared for these meshes with both turbulence models in figure 10. There are only small differences between the results with the two turbulence models, particularly with the coarser mesh. This is consistent with the findings of Dawes (Ref 8) which he attributes to most of the loss being generated very close to solid surfaces, within a laminar sub-layer region which is common to both models.

7. COMPARISON WITH EXPERIMENT

The total pressure traces obtained from the centre hole of the three hole probe for the experimental sweeps at 10% and 50% vane height are shown in figure 11. A small amount of smoothing has been applied to the traces to remove some high frequency noise. The vane wakes can be seen clearly in both plots, the wake at 50% height being considerably wider than that at 10% height. Also evident are some oscillations in the traces between the wakes. These are due to fluctuations with time in the total pressure upstream of the vanes arising from piston velocity variations during the operation of the rig. Because of the manner in which the traverse is performed, a variation with time appears as a variation with position when the trace is plotted. These oscillations can be largely removed by further analysis to allow for the variation in upstream total pressure; the results at 10% and 50% height after this additional processing are shown in figure 12.

The individual experimental sweeps, after processing, have been combined to form a complete area traverse and contours of total pressure are shown in figure 13 together with the predictions using both turbulence models on mesh 4. The predictions both show wakes which are wider at mid-height than near the endwalls. The wake in the prediction with the one-equation model is wider (23% pitch at mid-height) than that with the Baldwin-Lomax model (20%); the experimental results show a wake which is slightly wider than either prediction (25%). The one-equation model predicts a similar deficit of total pressure in the centre of the wake to the experimental value but the Baldwin-Lomax model does not capture the full deficit. In common with the experimental results neither prediction has identifiable regions of secondary loss though the Baldwin-Lomax results do exhibit some thickening of the wake near the hub. The experimental results show greater curvature of the wake near mid-height and a more acute angle between the wake and the endwall, particularly near the tip, than either prediction, with again the one-equation model giving a slightly closer result.

8. COMPARISON OF ENDWALL PROFILES

Measurements of surface static pressure were taken for both the bellmouth and S-bend endwall profiles. These are shown on figure 14 in the form of isentropic Mach number distributions at 10% and 50% span, together with predictions for both endwall profiles, using mesh 1 spacings. At 10% span the S-bend hub profile has increased the Mach number on the early part of the suction surface and slightly increased the strength of the shock at approximately 70% Cax. The effect on the pressure surface is small. At 50% span there is very little difference between the two sets of experimental results, though the S-bend does still have a slightly higher Mach number over the early suction

surface. Each of these differences has been well modelled by the flow program, though neither prediction captures the full shock strength. The effect of the endwall profile on the predicted secondary flows is illustrated in figure 15 by the velocity vectors near to the suction surface. It appears that the passage cross-flow on the hub impinges on to the suction surface slightly further downstream with the S-bend profile but that it does so at a greater angle resulting in a greater spanwise extent of the vane being affected by the secondary flow. The effect on the losses is small as is shown by contours of total pressure on the plane at 120% Cax in figure 16. There is very little difference between the shape of the vane wakes or the total pressure deficits for either endwall profile. The total loss is 0.081 of exit dynamic head for the bellmouth profile and 0.084 for the S-bend.

9. CONCLUSIONS

A transonic turbine nozzle guide vane has been tested in an annular cascade facility with two different endwall profiles. Vane surface static pressures have been measured and a traverse of the total pressure field downstream of the trailing edge has been performed for one of the profiles.

The new area traversing technique has given good results. It has been found necessary to process the results to remove the effect of piston oscillation.

The Dawes three-dimensional viscous flow program has been used to model the flow through the nozzle. A variety of mesh densities and distributions have been investigated as have two different turbulence models. Good agreement has been obtained for the pressure distributions and realistic secondary flows have been predicted. It was found that the finer meshes gave better predictions of the static pressure distributions and reduced levels of loss as a result of the improved modelling of the vane surface boundary layers.

The different turbulence models were found to have little effect on the predicted overall loss though there were differences in the distribution and the shape of the vane wakes. The one-equation turbulence model produced wakes which had similar levels of total pressure deficit to the experiment and had a more similar shape than those with the Baldwin-Lomax algebraic model.

REFERENCES

1. R. C. Kingcombe, J. D. Bryce and N. P. Leversuch, "Design and Test of a High Blade Speed, High Work Capacity Transonic Turbine", AGARD CP-421, 1987.
2. R. C. Kingcombe, S. P. Harasgama, N. P. Leversuch and E. T. Wedlake, "Aerodynamic and Heat Transfer Measurements on Blading for a High Rim-Speed Transonic Turbine", ASME Paper 89-GT-228.
3. A. J. Brooks, D. E. Colbourne, E. T. Wedlake, T. V. Jones, M. L. G. Oldfield, D. L. Schultz and P. J. Loftus, "The Isentropic Light Piston Annular Cascade Facility at RAE Pyestock", AGARD CP-390, 1985.
4. G. C. Horton, "Secondary Flow Predictions for a Transonic Nozzle Guide Vane", AGARD CP-469, 1990.
5. W. N. Dawes, "A Numerical Method for the Analysis of 3D Compressible Flow in Turbine Cascades; Application to Secondary Flow Development in a Cascade With and Without Dihedral", ASME Paper 86-GT-145, 1986.
6. B. S. Baldwin and H. Lomax, "Thin Layer Approximation and Algebraic Model for Separated Turbulent Flows", AIAA Paper 78-257 1978.
7. N. T. Birch, "Navier-Stokes Predictions of Transition, Loss and Heat Transfer in a Turbine Cascade", ASME Paper 87-GT-22, 1987.
8. W. N. Dawes, "A Comparison of Zero and One Equation Turbulence Modelling for Turbo-machinery calculations", ASME Paper 90-GT-303 1990.

Copyright
©

Controller HMSO London
1991

	Mesh 1	Mesh 2	Mesh 3	Mesh 4
Axial spacing at leading edge (% axial chord)	0.36	0.43	0.30	0.10
Axial spacing at trailing edge (% axial chord)	0.36	0.43	0.30	0.10
Spanwise spacing at endwall (% blade height)	0.39	0.49	0.24	0.24
Tangential spacing at blade surfaces (% pitch)	0.39	0.39	0.24	0.24

Table 1. Mesh spacings for different meshes

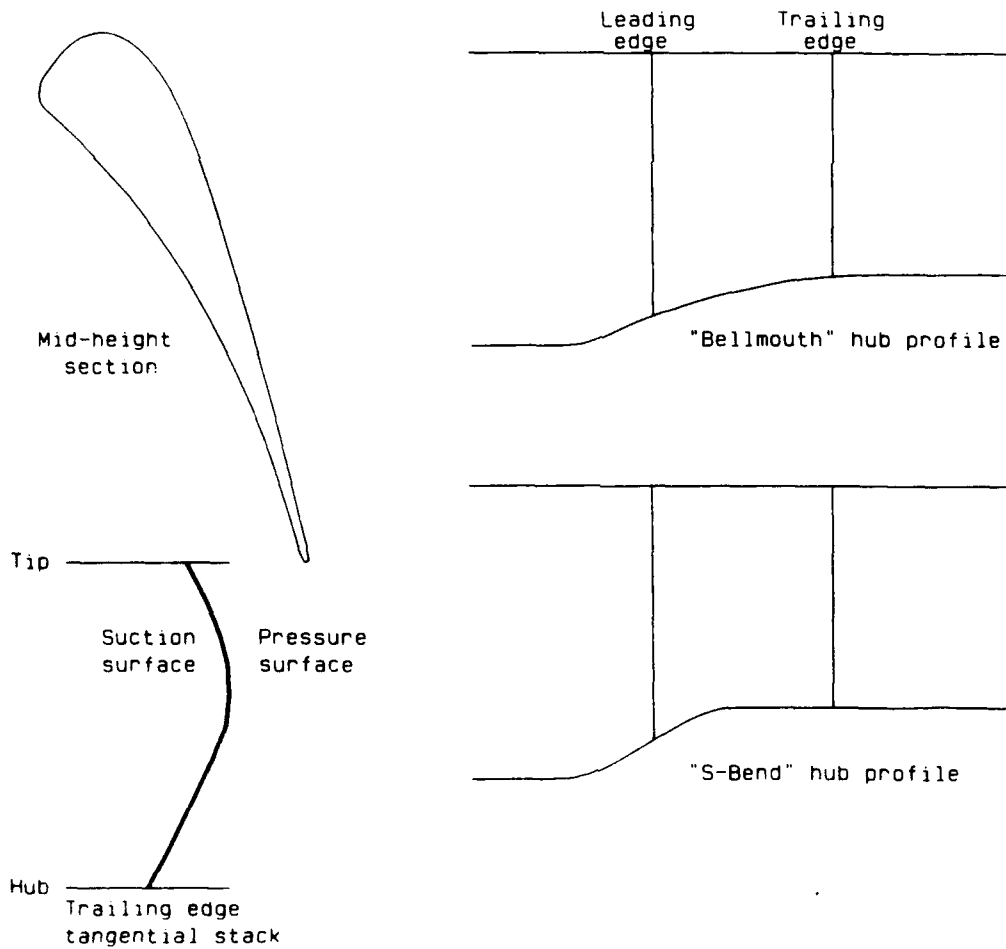


Fig 1. Illustration of ngv design

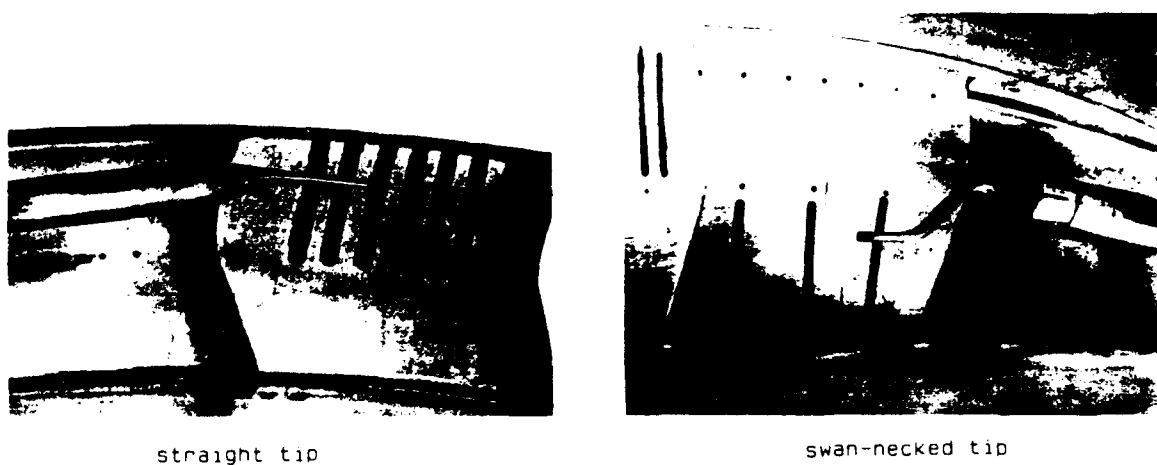


Fig 2. The two traverse probes

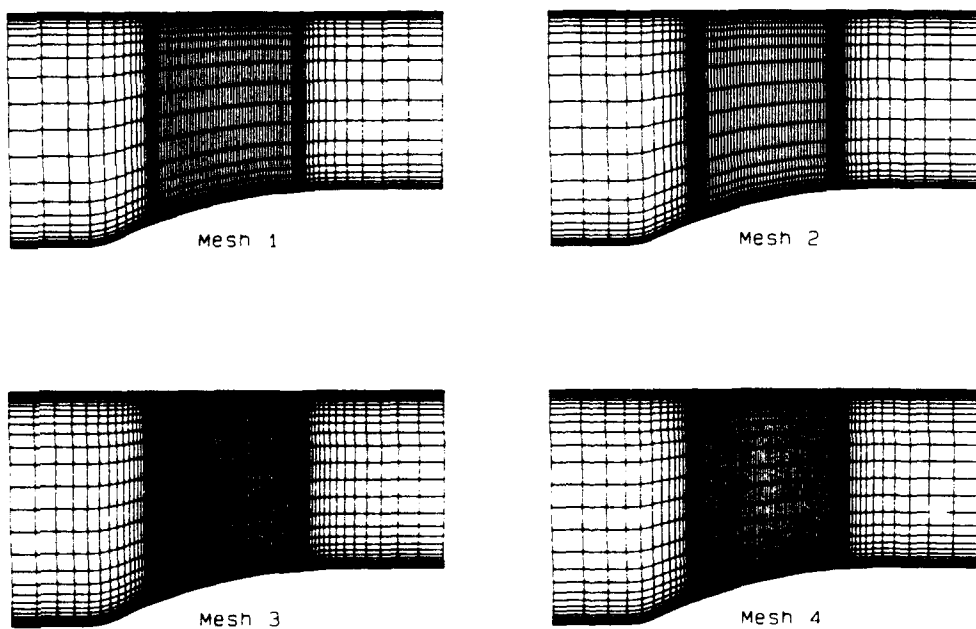
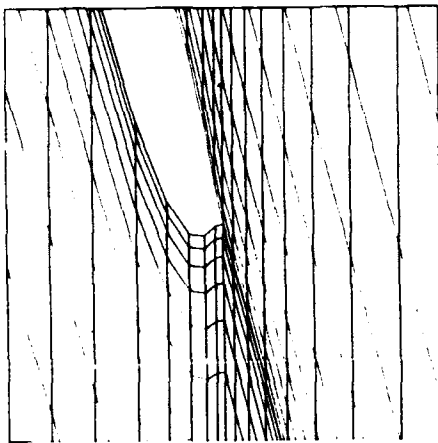
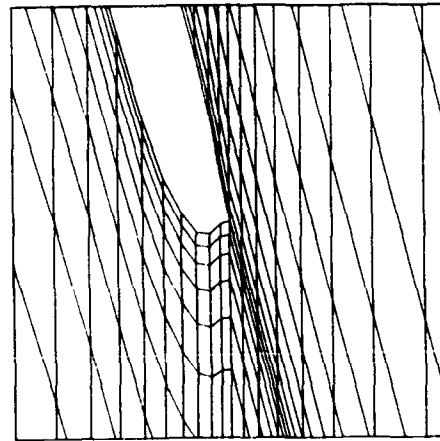


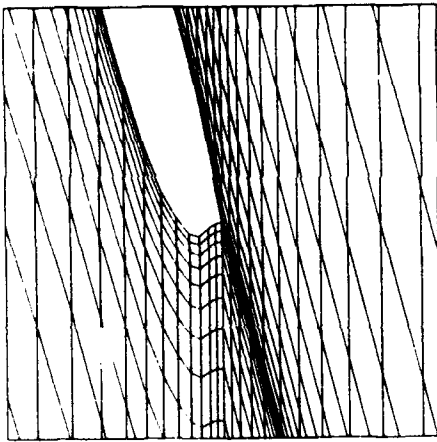
Fig 3. Details of calculation mesh



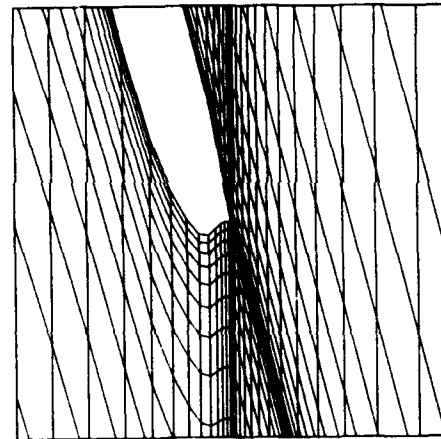
Mesh 1



Mesh 2



Mesh 3



Mesh 4

Fig 4. Details of mesh near trailing edge

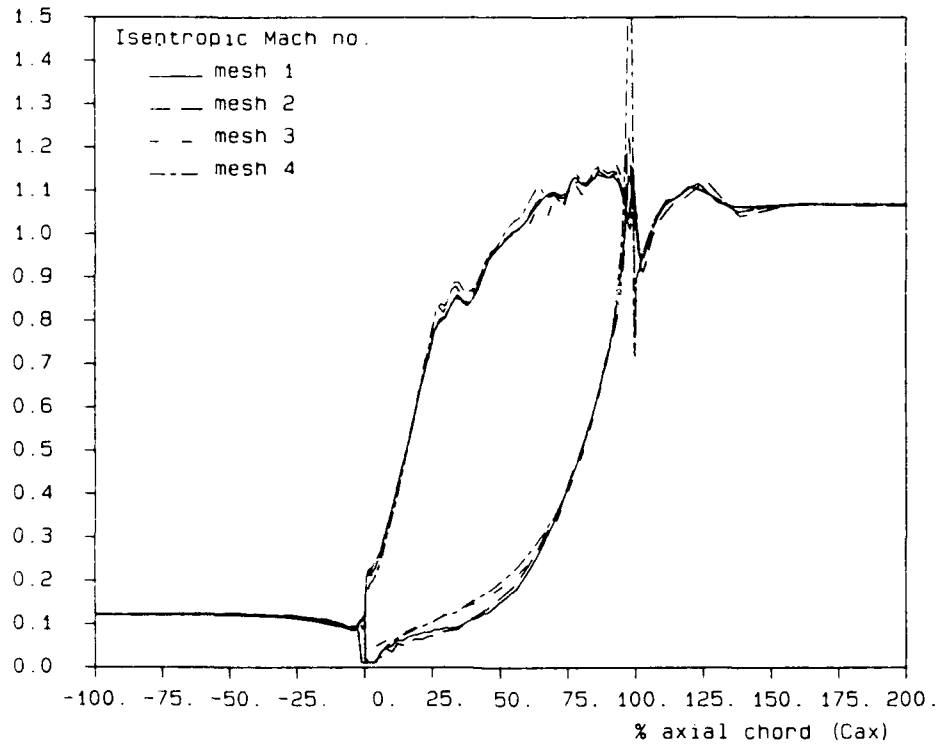


Fig 5. Comparison of mid-height isentropic Mach number distributions with different meshes

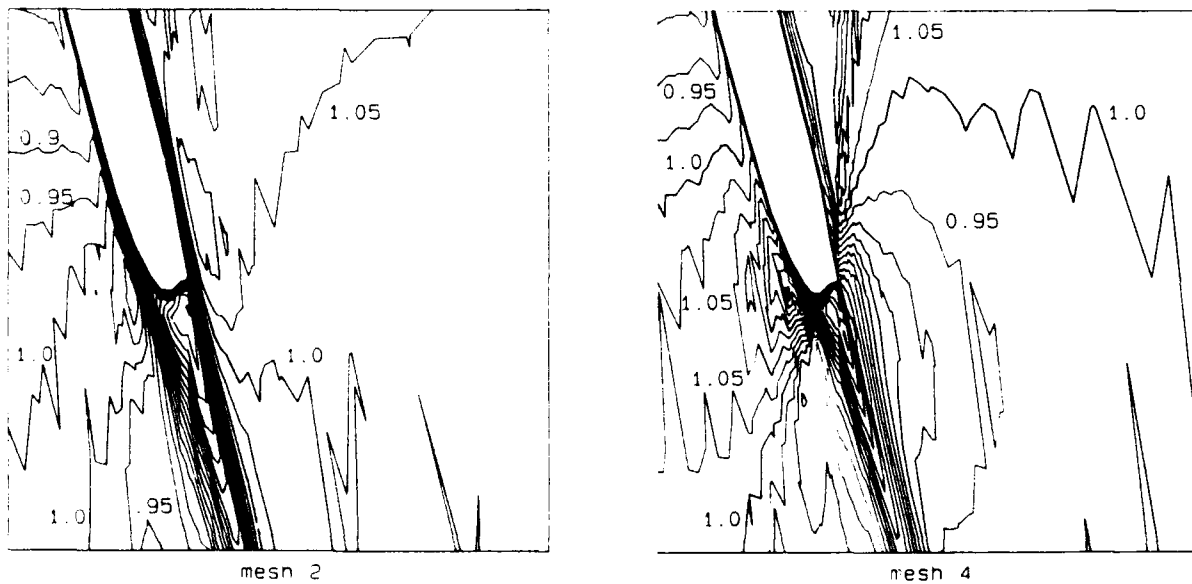


Fig 6. Contours of Mach number near trailing edge

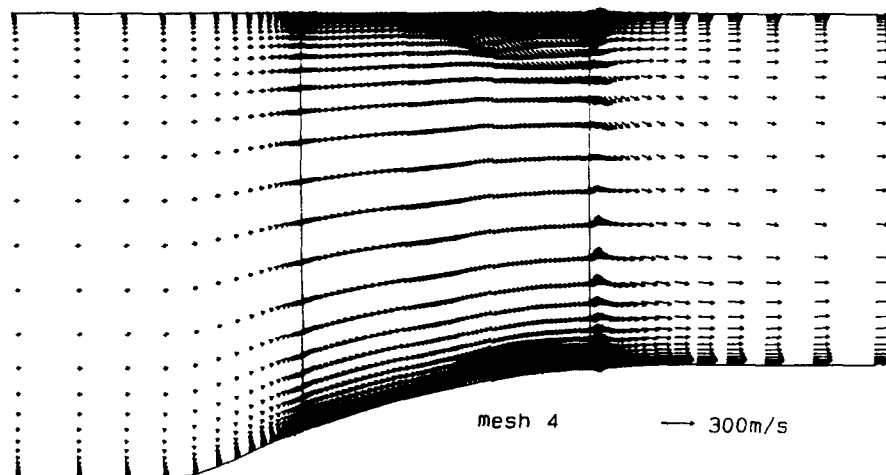
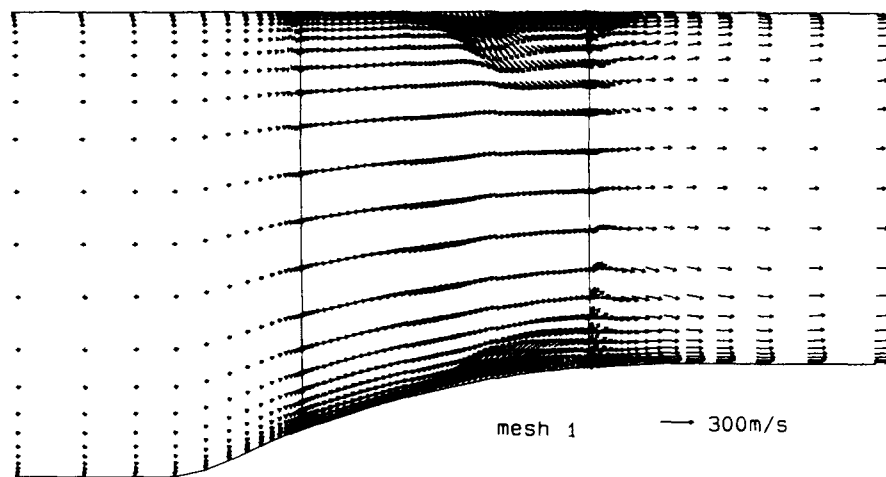


Fig 7. Suction surface flows with meshes 1 and 4

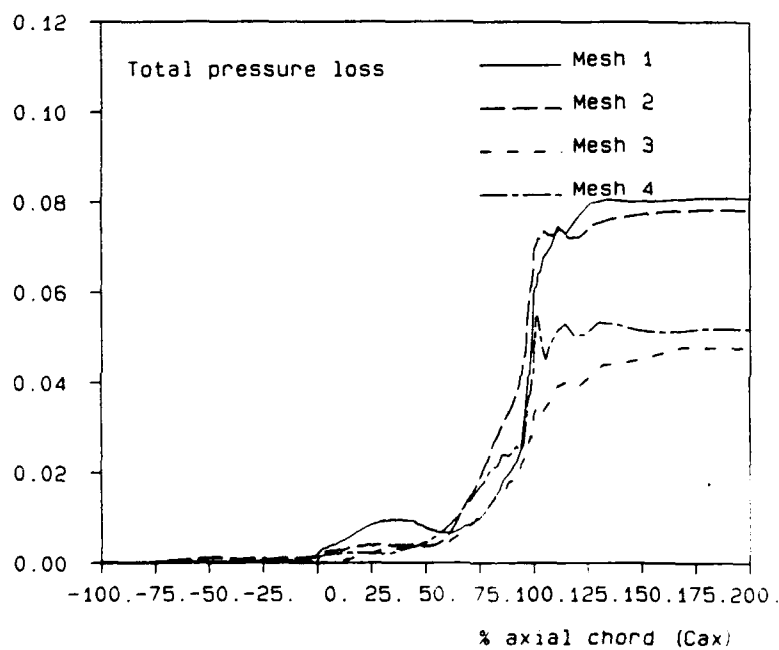


Fig 8. Development of total pressure loss with different meshes

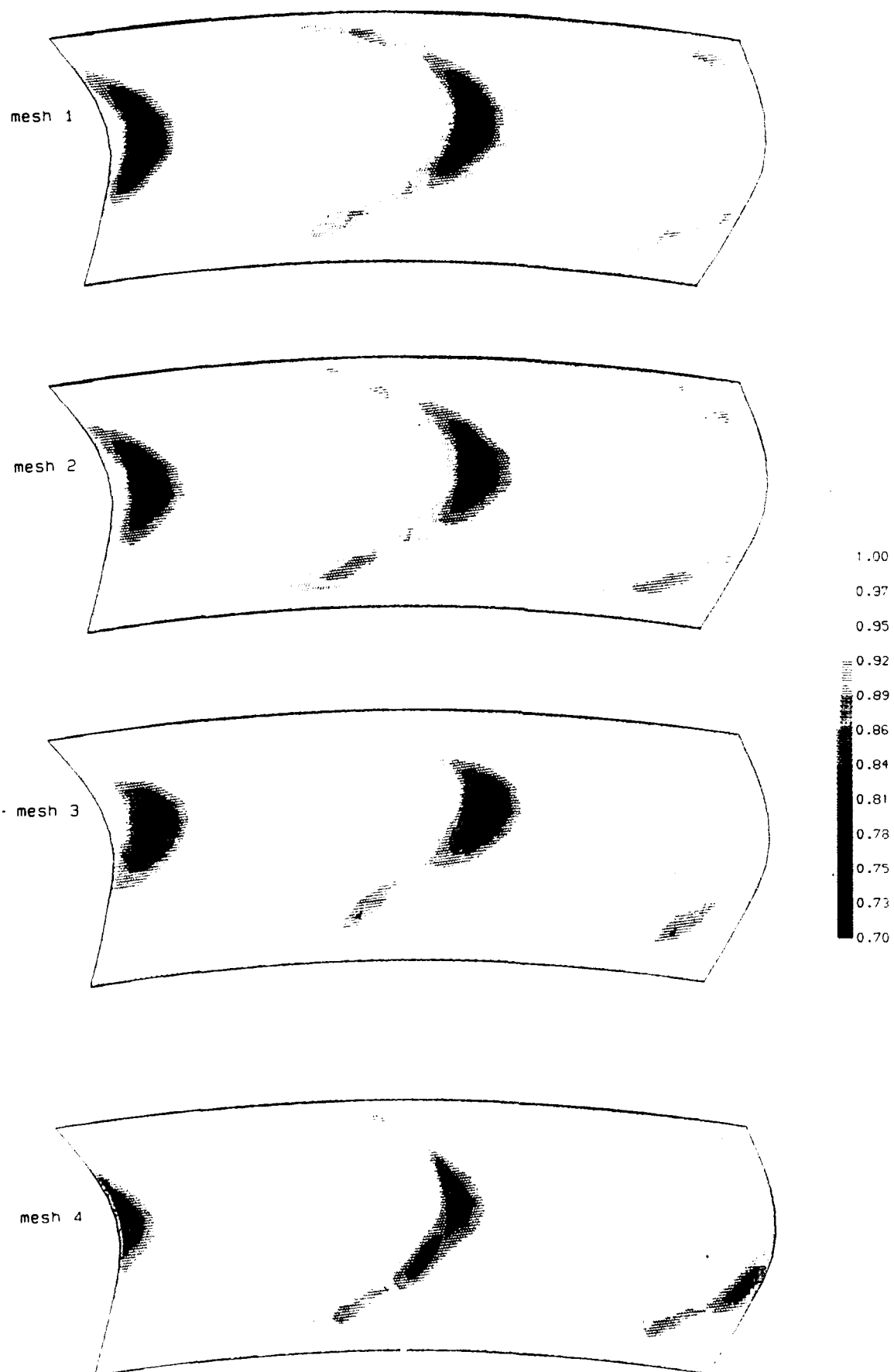


Fig 9. Contours of total pressure on a plane at 120% axial chord
Comparison of results with different meshes

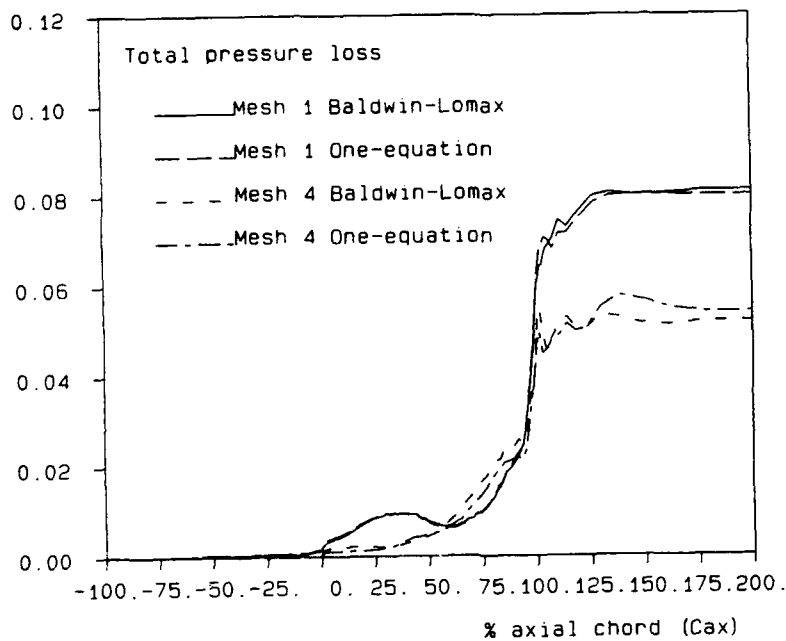


Fig 10. Development of total pressure loss with different turbulence models

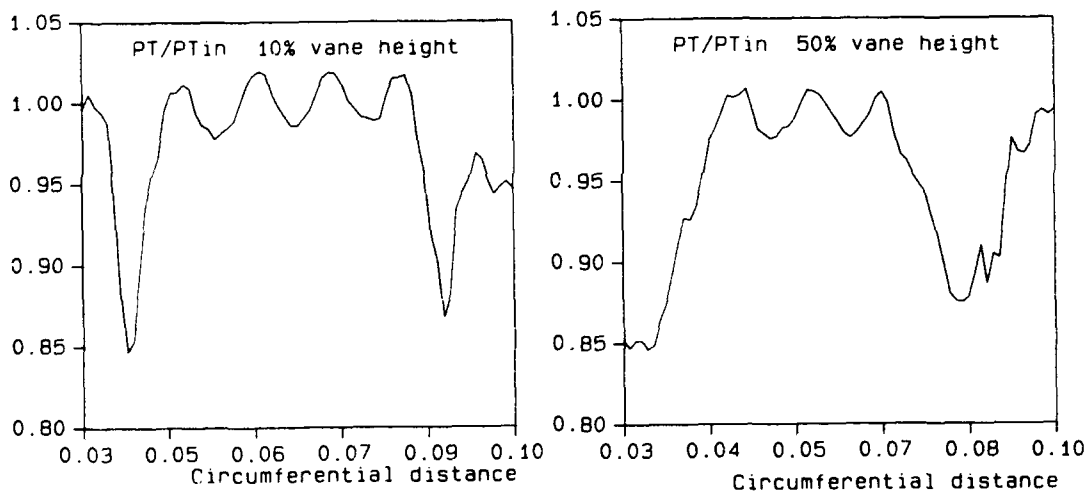


Fig 11. Total pressure traverse sweeps before processing

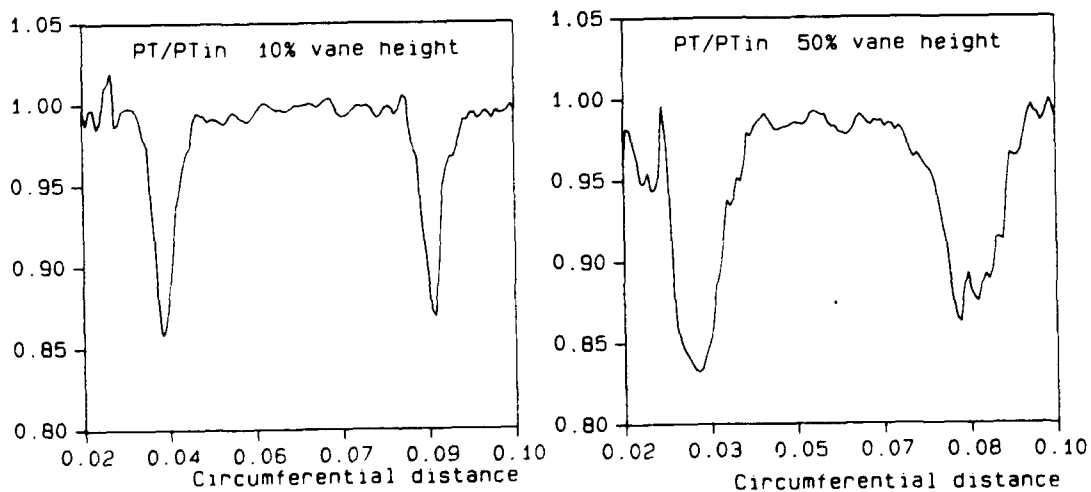


Fig 12. Total pressure traverse sweeps after processing

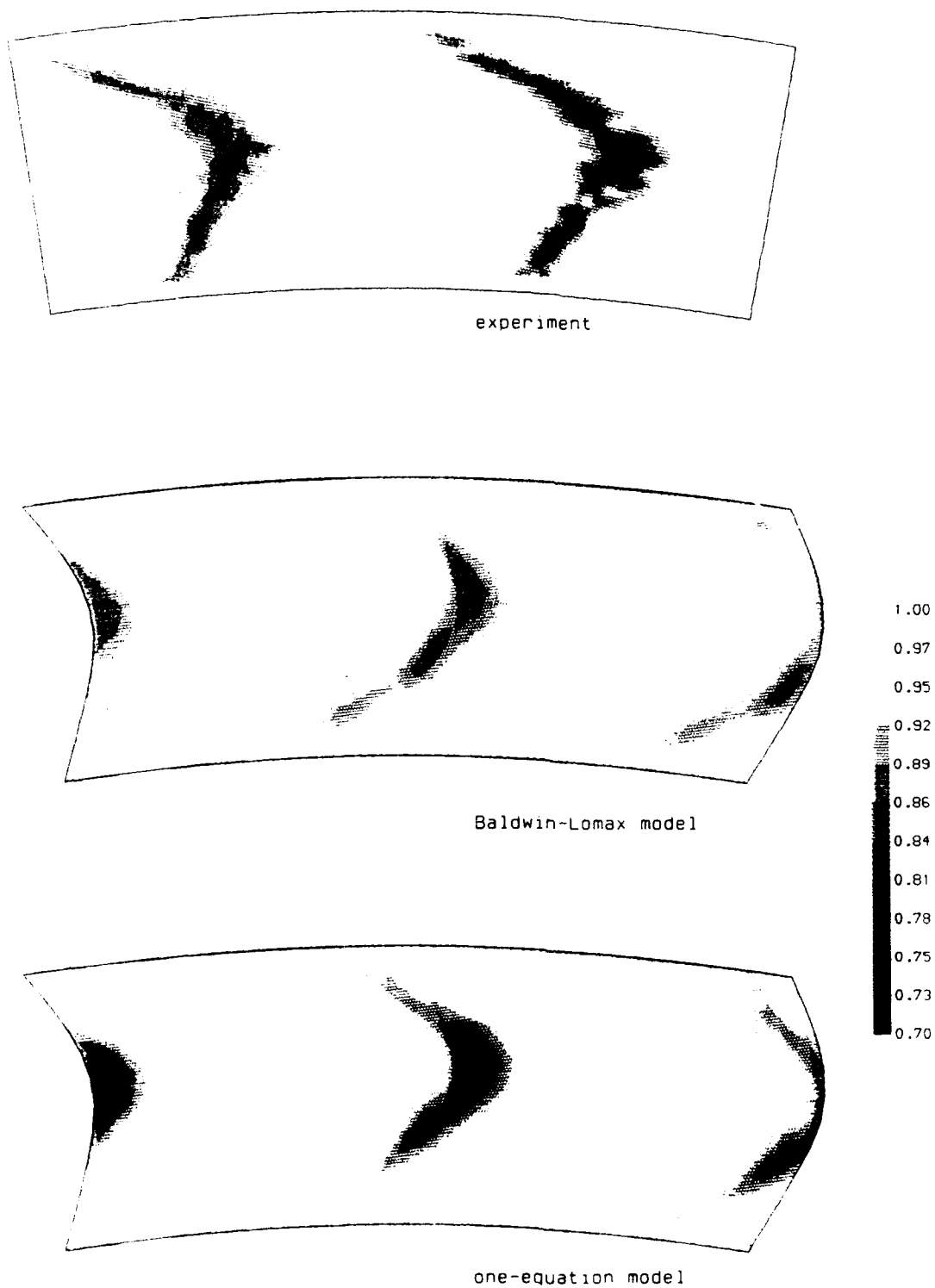


Fig 13 Total pressure contours on a plane at 120% axial chord
Comparison of different turbulence models with experiment

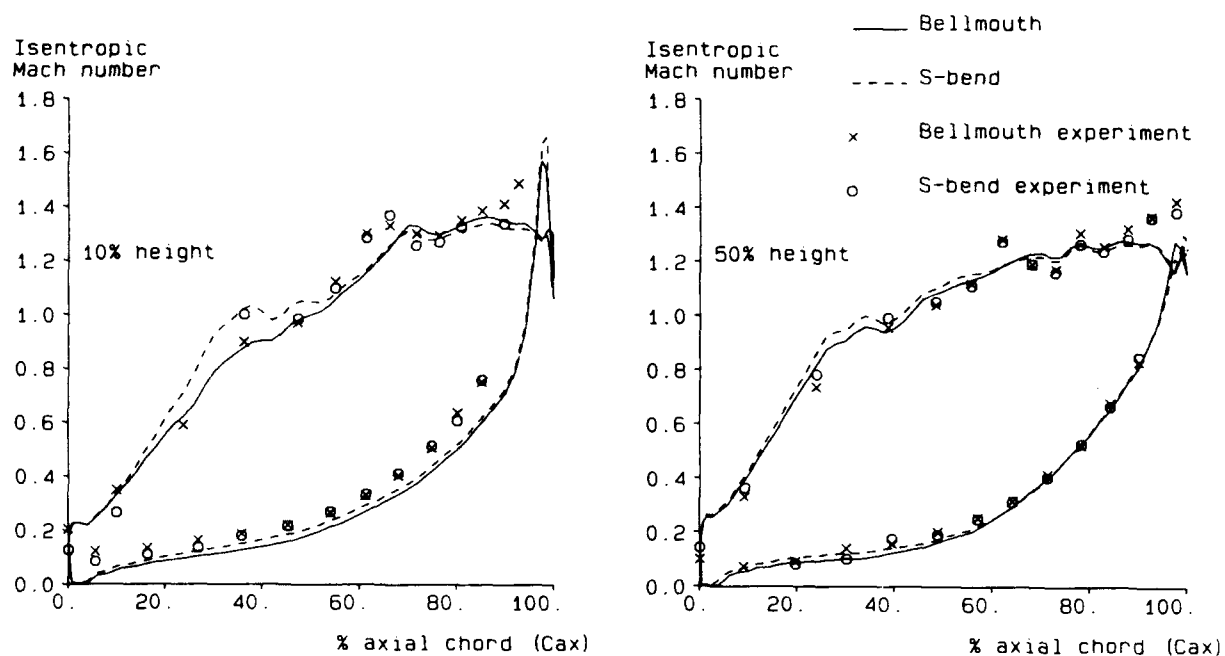


Fig 14. Mach number distributions with different endwall profiles

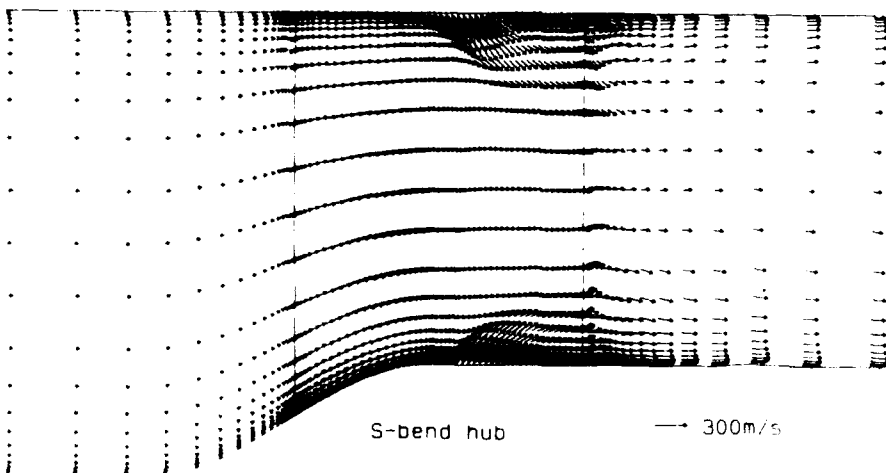
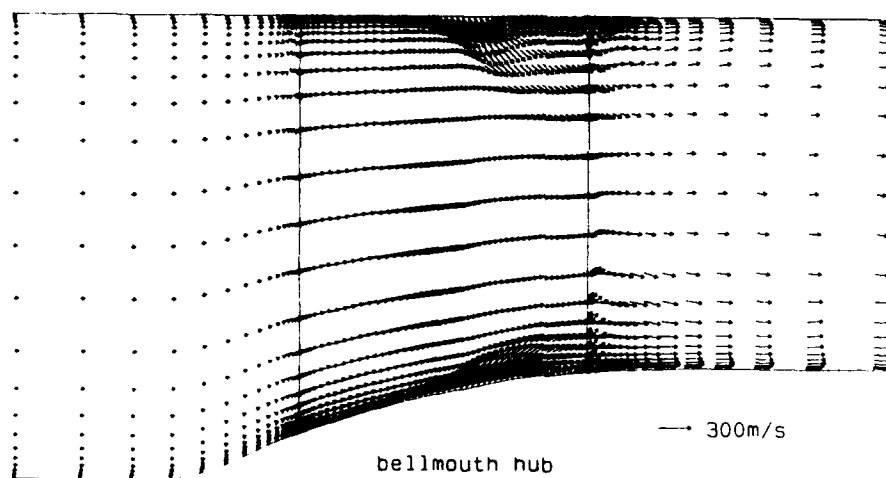


Fig 15. Suction surface flows with bellmouth and S-bend hub profiles

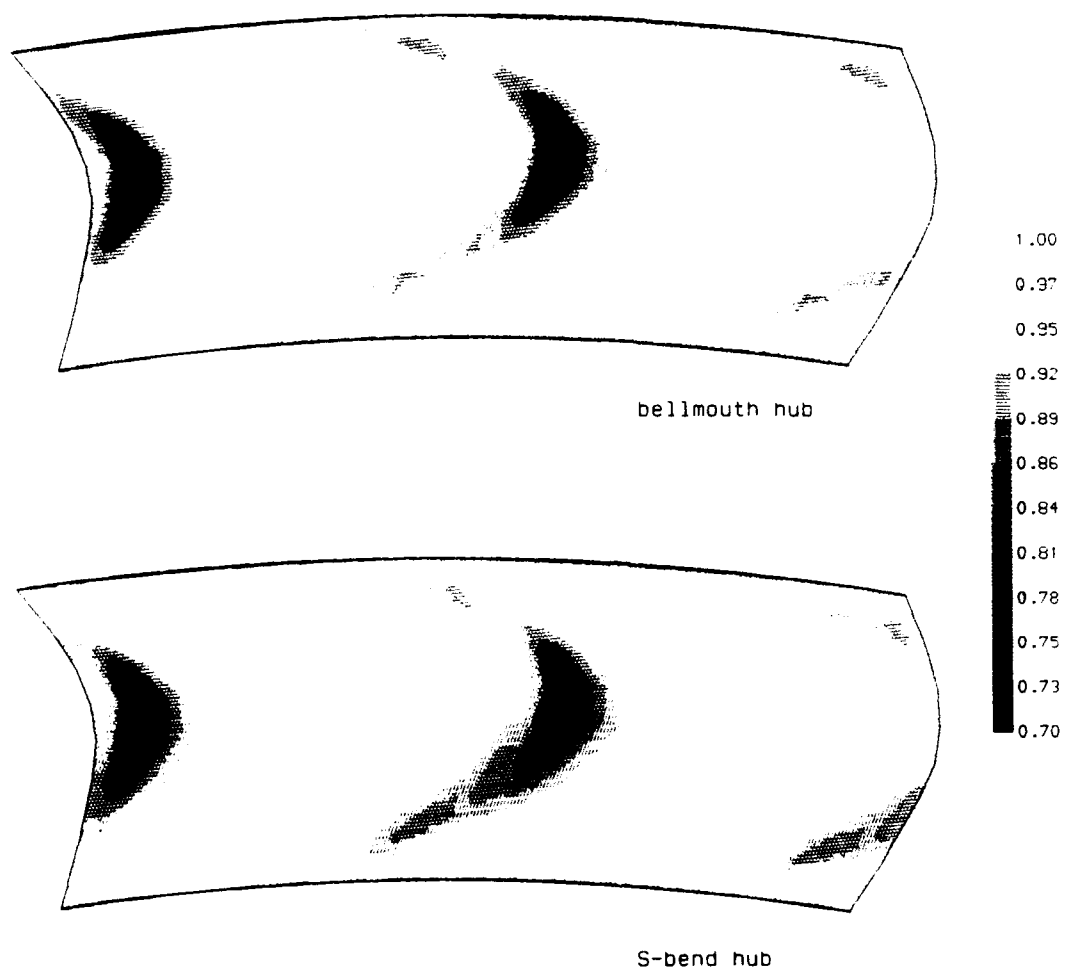


Fig 16. Total pressure contours on a plane at 120% axial chord
for bellmouth and S-bend hub profiles

Discussion

F. BASSI, UNIV. OF CATANIA, ITALY

How did you measure three-dimensional flow field with a three-hole probe? Did you neglect the radial component of velocity?

AUTHOR'S REPLY

The results that I have presented are derived from only the center hole of the three hole probes. The probes have now been fully calibrated and further analysis will be possible. We are not able to measure the radial component of velocity with the three-hole probes.

K. BROICHHAUSEN, MTU, MÜNCHEN, GERMANY

Could you give some information on the rational behind your S-bend endwall design?

AUTHOR'S REPLY

Both endwalls were designed to reduce the secondary flow by using the endwall curvature to re-energize the flow near the wall. The two different shapes were considered to investigate whether the probable advantage of the greater curvature of the S-bend profile was outweighed by the probably disadvantage of the higher peak Mach number.

C. HAH, NASA LEWIS, U.S.A.

- 1) Did you compare the measured loss to the calculated values?
- 2) What is exit Mach number?
- 3) Do you expect any trailing edge shock?
- 4) Further refined grids might have to be used to study grid dependence of the solution. Is the trailing edge shown in Fig. 4 the real geometry?

AUTHOR'S REPLY

- 1) The area traverse did not include the endwall boundary layers so it was not possible to compare the total losses.
- 2) The exit Mach number is approximately 1.05 to 1.10.
- 3) I expect a weak trailing edge shock.
- 4) Further refined meshes have been used but not on this geometry. The correct trailing edge has a round geometry.

D. HOBBS, PRATT & WHITNEY, U.S.A.

- 1) What was the average loss of the straight cascade?
- 2) Did the S-bend results show a reduced secondary flow on the outer endwall consistent with earlier Russian experimental results?

AUTHOR'S REPLY

- 1) I have not run the straight walled cascade with the finer meshes reported and do not have a figure for a coarse mesh on hand.
- 2) There was a slight effect of the S-bend endwall on the secondary flow near the opposite wall, but the main effect was on the secondary flow near the profiled wall.

SAVINI, NATIONAL RES. COUNCIL, ITALY

From your vector plots it is apparent that there is radial motion associated with secondary vortices, but from the total pressure contours there seems to be no loss core associated with secondary flows. Could you comment on this?

AUTHOR'S REPLY

We believe that the strong secondary flows on the suction surface are connecting the secondary loss cores to mid-height. This is the reason why the wakes are so wide at mid-height.

T. PRINCE, WILLIAMS INTER., U.S.A.

1) As this nozzle vane was designed to increase static pressure at hub end tip by curved stacking, was there an effort to determine the optimum degree of curve stacking? Would such an analysis show advantages for a more moderate degree of curved stacking?

2) What precautions were taken to establish uniformly swirling flow with a corresponding radial pressure gradient in the measurement section, and prevent downstream plenum effects from altering these conditions?

AUTHOR'S REPLY

1) A three-dimensional Navier-Stokes analysis method was not available when this vane was designed, so it was not possible to perform such an optimization study. As so much loss has been connected to mid-height, it is possible that a more moderate stack may produce benefits.

2) A second throat was installed downstream of the cascade. This was intended to avoid a change in downstream conditions during the run but this will also have helped avoid the plenum disturbing the radial pressure gradient at the exit of the cascade.



AD-P007 695



92-16081



Viscous Three-Dimensional Calculations of Transonic Fan Performance

Dr. Rodrick V. Chima
NASA Lewis Research Center
Cleveland, Ohio, 44135, USA
(216) 433-5919

ABSTRACT

A three-dimensional flow analysis code has been used to compute the design speed operating line of a transonic fan rotor, and the results have been compared to experimental data. The code is an explicit finite difference code with an algebraic turbulence model. It is described in detail in the paper. The transonic fan, designated Rotor 67, has been tested experimentally at NASA Lewis Research Center with conventional aerodynamic probes and with laser anemometry, and has been included as one of the AGARD test cases for computation of internal flows. The experimental data are described briefly. Maps of total pressure ratio and adiabatic efficiency versus mass flow have been computed and are compared to the experimental maps, with excellent agreement between the two. Detailed comparisons between calculations and experiment are made at two operating points, one near peak efficiency and the other near stall. Blade-to-blade contour plots are used to show the shock structure. Comparisons of circumferentially-integrated flow quantities downstream of the rotor show spanwise distributions of several aerodynamic parameters. Calculated Mach number distributions are compared to laser anemometer data within the blade row and the wake to quantify the accuracy of the calculations. Finally, particle traces are used to illustrate the nature of the secondary flow in this fan.

INTRODUCTION

One goal of computational fluid dynamics (CFD) for turbomachinery is the prediction of component performance, for example pressure ratio and efficiency. Since a small improvement in engine efficiency can amount to huge savings in yearly fuel costs for a fleet of commercial aircraft, turbomachinery designers are extremely interested in tools that give good quantitative predictions of turbomachinery performance.

However most of the CFD results for turbomachinery published more than a few years ago show only qualitative comparisons with experimental Mach contours, or quantitative comparisons with surface pressures. This is not to diminish the importance of these results; in the hands of a good turbomachinery designer

a shock location or surface pressure distribution can be extremely useful. However CFD for turbomachinery has evolved to a point where it can now provide the designer with reasonable predictions of overall performance of isolated blade rows.

In more recent literature several researchers have presented more detailed predictions of turbomachinery performance. Davis et al. [1] predicted loss buckets for 2D transonic compressor cascades. Chevrin and Vuillez [2] have predicted loss and exit flow angle for turbine and fan cascades using the 2D code of Cambier et al. [3]. Boyle [4] investigated effects of turbulence modelling on turbine blade heat transfer predictions using the 2D code of Chima [5]. In 3D, Pierzga and Wood [6] predicted the static pressure ratio versus mass flow curve of a transonic fan using Denton's code [7], and Dawes [8] has predicted exit total pressure and temperature distributions in a multistage turbine. Adamczyk et al. [9] investigated the effects of tip clearance on stall for the fan considered in the present work, and predicted pressure ratios and efficiencies for that fan. In [10] Chima used the present code to predict the overall efficiency of an annular turbine stator.

There are many reasons for the scarcity of turbomachinery performance calculations in the early literature. One reason is that pressure field calculations are relatively independent of viscous effects and can be calculated with simple models. Conversely, efficiency and loss calculations are highly dependent on viscous effects and require careful attention to the viscous terms, turbulence modeling, artificial viscosity, and grid resolution for successful calculation. Secondly, computers capable of performing large viscous flow calculations have become generally available only recently. A final reason is that detailed experimental data is difficult to obtain in turbomachinery due to the small size and high speeds of the components involved. Experimental surface pressures are available from many linear and annular cascade tests, which may account for many of the comparisons appearing in the literature. However wake surveys and loss data are often available for the same tests, but tend to be overlooked.

With the publication of AGARD Advisory Report No. 275, *Test Cases for Computation of Internal Flows*

in *Aero Engine Components* [11], researchers now have access to some excellent data for the validation of CFD codes for turbomachinery.

In the present work the experimental data described by Strazisar, et al. in [12] and by Wood, et al. in [11, pp. 165–213] was used to validate the 3D Navier-Stokes code first referenced by Chima and Yokota in [10]. The code, RVC3D (Rotor Viscous Code 3-D), is described, with emphasis on the boundary conditions and artificial viscosity. A new 3D grid code for turbomachinery is also introduced. The test case, a transonic fan rotor (Rotor 67, shown in Fig. 1) is described briefly.

Several operating points were computed along the 100 percent speed line of the rotor. The computed operating curves of adiabatic efficiency and total pressure ratio versus mass flow are compared to the experimental data. Two operating points are examined in detail: one near peak efficiency and one near stall. At each point qualitative comparisons are made between computed and experimental Mach number contours. Comparisons are then made with laser anemometer measurements within the blade row and across the wake, and with conventional aerodynamic measurements downstream. Finally, particle traces are used to illustrate the nature of the secondary flows in this machine.

GOVERNING EQUATIONS

The Navier-Stokes equations are written in a Cartesian (x, y, z) coordinate system rotating with angular velocity Ω about the x -axis. The rotation introduces source terms in the y - and z -momentum equations. The Cartesian equations are mapped to a general body-fitted (ξ, η, ζ) coordinate system using standard techniques. A C-type grid was used in the present work, with the ξ -coordinate roughly following the flow, the η -coordinate running blade-to-blade, and the ζ -coordinate running spanwise. The thin-layer approximation is used to drop all viscous derivatives in the ξ -direction. All viscous terms in the cross-channel (η, ζ) plane are retained. The resulting equations are as follows:

$$\partial_t q + J[\partial_\xi \hat{E} + \partial_\eta \hat{F} + \partial_\zeta \hat{G} - Rc^{-1}(\partial_\eta \hat{F}_V + \partial_\zeta \hat{G}_V)] = H \quad (1)$$

where:

$$q = J^{-1} \begin{bmatrix} \rho \\ \rho u \\ \rho v \\ \rho w \\ e \end{bmatrix} \quad E = J^{-1} \begin{bmatrix} \rho l'' \\ \rho u l'' + \xi_x p \\ \rho v l'' + \xi_y p \\ \rho w l'' + \xi_z p \\ e l'' + p l' \end{bmatrix}$$

$$H = \Omega \begin{bmatrix} 0 \\ 0 \\ -\rho w \\ \rho v \\ 0 \end{bmatrix} \quad F = J^{-1} \begin{bmatrix} \rho V'' \\ \rho u V'' + \eta_x p \\ \rho v V'' + \eta_y p \\ \rho w V'' + \eta_z p \\ e V'' + p V' \end{bmatrix}$$

$$G = J^{-1} \begin{bmatrix} \rho W'' \\ \rho u W'' + \zeta_x p \\ \rho v W'' + \zeta_y p \\ \rho w W'' + \zeta_z p \\ e W'' + p W' \end{bmatrix} \quad (2)$$

Again, these equations are written in a rotating Cartesian coordinate system attached to the moving blade. The code solves for the *absolute* velocity components u, v , and w , which point in the x, y , and z coordinate directions, respectively. The *relative* velocity components u', v' , and w' are defined with respect to the same rotating coordinate system by subtracting the appropriate components of the blade speed from the absolute velocities, giving:

$$\begin{aligned} u' &= u \\ v' &= v - \Omega z \\ w' &= w + \Omega y \end{aligned} \quad (3)$$

The relative contravariant velocity components are given by:

$$\begin{aligned} l'' &= \xi_x u + \xi_y v' + \xi_z w' \\ V'' &= \eta_x u + \eta_y v' + \eta_z w' \\ W'' &= \zeta_x u + \zeta_y v' + \zeta_z w' \end{aligned} \quad (4)$$

Note that although $u' = u$, $U' \neq U$.

The energy and static pressure are given by:

$$e = \rho \left[C_v T + \frac{1}{2}(u^2 + v^2 + w^2) \right] \quad (5)$$

$$p = (\gamma - 1) \left[e - \frac{1}{2}\rho(u^2 + v^2 + w^2) \right] \quad (6)$$

Using Stokes' hypothesis, $\lambda = -\frac{2}{3}\mu$, the viscous flux \hat{F}_V can be written as follows:

$$\hat{F}_V = J^{-1} \mu [0, F_2, F_3, F_4, F_5]^T \quad (7)$$

where

$$\begin{aligned} F_2 &= C_1 \partial_\eta u + C_2 \eta_x + C_3 \partial_\zeta u - C_4 \eta_x + C_5 \zeta_x \\ F_3 &= C_1 \partial_\eta v + C_2 \eta_y + C_3 \partial_\zeta v - C_4 \eta_y + C_5 \zeta_y \\ F_4 &= C_1 \partial_\eta w + C_2 \eta_z + C_3 \partial_\zeta w - C_4 \eta_z + C_5 \zeta_z \\ F_5 &= \frac{\mu \gamma}{Pr} (C_1 \partial_\eta (C_v T) + C_3 \partial_\zeta (C_v T)) \\ &\quad + u F_2 + v F_3 + w F_4 \end{aligned} \quad (8)$$

and

$$\begin{aligned} C_1 &= \eta_x^2 + \eta_y^2 + \eta_z^2 \\ C_2 &= \frac{1}{3}(\eta_x \partial_\eta u + \eta_y \partial_\eta v + \eta_z \partial_\eta w) \\ C_3 &= \eta_x \zeta_x + \eta_y \zeta_y + \eta_z \zeta_z \\ C_4 &= \frac{2}{3}(\zeta_x \partial_\zeta u + \zeta_y \partial_\zeta v + \zeta_z \partial_\zeta w) \\ C_5 &= \eta_x \partial_\zeta u + \eta_y \partial_\zeta v + \eta_z \partial_\zeta w \end{aligned} \quad (9)$$

Terms multiplied by C_1 and C_2 lead to non-mixed second derivative viscous terms like $u_{\eta\eta}$, while terms multiplied by C_3 – C_5 lead to mixed-derivative terms like $u_{\eta\zeta}$. The viscous flux vector \hat{G} can be written similarly by interchanging directions η and ζ and replacing F with G everywhere.

Metric terms are defined using the following relations:

$$\begin{bmatrix} \xi_x & \eta_x & \zeta_x \\ \xi_y & \eta_y & \zeta_y \\ \xi_z & \eta_z & \zeta_z \end{bmatrix} = J \begin{bmatrix} y_\eta z_\zeta - y_\zeta z_\eta & y_\zeta z_\xi - y_\xi z_\zeta & y_\xi z_\eta - y_\eta z_\xi \\ x_\zeta z_\eta - x_\eta z_\zeta & x_\xi z_\zeta - x_\zeta z_\xi & x_\eta z_\xi - x_\xi z_\eta \\ x_\eta y_\zeta - x_\zeta y_\eta & x_\zeta y_\xi - x_\xi y_\zeta & x_\xi y_\eta - x_\eta y_\xi \end{bmatrix} \quad (10)$$

where:

$$J = (x_\xi y_\eta z_\zeta + x_\zeta y_\xi z_\eta + x_\eta y_\zeta z_\xi - x_\xi y_\zeta z_\eta - x_\eta y_\xi z_\zeta - x_\zeta y_\eta z_\xi)^{-1} \quad (11)$$

Terms like x_ξ , x_η , etc. are found using second order central differences. The Jacobian is computed using (11) and stored for the entire grid. All other metric terms are computed as needed using (10.)

The equations are nondimensionalized by arbitrary reference quantities (here the inlet total density ρ_{0ref} and the total sonic velocity c_{0ref} were used,) and the Reynolds number Re and Prandtl number Pr are defined in terms of these quantities. The equations assume that the specific heats C_p and C_v and Prandtl number are constant, that Stoke's hypothesis is valid, and that the effective viscosity for turbulent flows may be written as

$$\mu_{eff} = \mu_{lam} + \mu_{turb} \quad (12)$$

where the laminar viscosity is calculated using a power law function of temperature:

$$\frac{\mu_{lam}}{\mu_{ref}} = \left(\frac{T}{T_{ref}} \right)^n \quad (13)$$

with $n = 2/3$ for air.

The turbulent viscosity μ_{turb} is computed using an adaptation of the Baldwin-Lomax turbulence model [13] on cross-channel planes. Briefly, the model is applied independently in the blade-to-blade and spanwise directions, and the resulting turbulent viscosities are added vectorially. The 2D Buleev length scale based on the distance from the hub and blade is used. The vorticity is calculated in the absolute frame, but the wall shear and wake velocities are calculated in the relative frame. See [10] for details on the 3-D implementation.

BOUNDARY CONDITIONS

Many boundary conditions for turbomachinery are best expressed in cylindrical coordinates, but the code

is formulated in Cartesian coordinates. For the boundary conditions, coordinate systems are transformed as needed using:

$$\begin{aligned} v &= (v_r y + v_\theta z)/r \\ w &= (v_r z - v_\theta y)/r \\ v_r &= (vy + wz)/r \\ v_\theta &= (vz - wy)/r \\ r &= \sqrt{y^2 + z^2} \end{aligned} \quad (14)$$

At the inflow boundary the total temperature, total pressure, whirl, and meridional flow angle were specified, and the upstream-running Riemann invariant was extrapolated from the interior. The inlet total temperature T_0 was specified as a constant (standard conditions). The inlet total pressure was specified as a constant in the core flow (also standard conditions) and reduced in the endwall regions according to a 1/7 power law velocity profile, with the inlet boundary layer heights estimated from the experimental data to be 12 mm on both the hub and the casing. At the inlet v_θ was set to zero, and v_r was chosen to make the flow tangent to the meridional projection of the inlet grid lines. The upstream-running Riemann invariant R^- based on the total absolute velocity $Q = \sqrt{u^2 + v^2 + w^2}$ was calculated at the first interior point and extrapolated to the inlet. The Riemann invariant is given by:

$$R^- = Q - \frac{2c}{\gamma - 1} \quad (15)$$

The total velocity is found from T_0 and R^- using:

$$Q = \frac{(\gamma - 1)R^- + \sqrt{2(1 - \gamma)(R^-)^2 + 4(\gamma + 1)C_p T_0}}{\gamma + 1} \quad (16)$$

The velocity components are then decoupled algebraically, and the density is found from P_0 , T_0 , and Q using an isentropic relation.

At the exit the hub static pressure is specified and ρ , ρu , ρv , and ρw are extrapolated from the interior. The local static pressure is found by integrating the axisymmetric radial equilibrium equation:

$$\frac{dp}{dr} = \frac{\rho v_\theta^2}{r} = \frac{\rho}{r^3}(vz - wy)^2 \quad (17)$$

A periodic C-grid was used in the present work. The periodic boundary was solved by setting periodic flow conditions (in terms of cylindrical velocity components) on a dummy grid line outside the boundary. Fourth-difference artificial dissipation terms are neglected on the outer boundary so that only one dummy grid line is needed.

On the blade surface and the rotating part of the hub, $U' = V' = W' = 0$. The hub was specified to be stationary 13.4 mm upstream of the leading edge and 3.35 mm downstream of the trailing edge by setting

$u = v = w = 0$. The tip casing was assumed to be stationary, that is, the blade was assumed to scrape along the casing with zero tip clearance.

Surface pressures were found from the normal momentum equation. On the hub ($\zeta = 1$) and tip ($\zeta = \zeta_{max}$):

$$(\zeta_x \xi_x + \zeta_y \xi_y + \zeta_z \xi_z) \partial_\xi p + (\zeta_x \eta_x + \zeta_y \eta_y + \zeta_z \eta_z) \partial_\eta p + (\zeta_x^2 + \zeta_y^2 + \zeta_z^2) \partial_\zeta p = -\rho[\Omega(\zeta_y w - \zeta_z v)] \quad (18)$$

On the blades ($\eta = 1$) the normal momentum equation can be found by replacing ζ with η everywhere in (18.) Surface temperatures were found from an adiabatic wall condition implemented as in (18) with p replaced by T and a right-hand side of zero.

MULTISTAGE RUNGE-KUTTA SCHEME

The governing equations are discretized using a node-centered finite difference scheme. Second-order central differences are used throughout.

The multistage Runge-Kutta scheme developed by Jameson, Schmidt, and Turkel [14] is used to advance the flow equations in time from an initial guess to a steady state. If (1) is rewritten as:

$$\partial_t q = -J[R_I - (R_V + D)] \quad (19)$$

where R_I is the inviscid residual including the source term, R_V is the viscous residual, and D is an artificial dissipation term described in the next section, then the multistage Runge-Kutta algorithm can be written as follows:

$$\begin{aligned} q_0 &= q_n \\ q_1 &= q_0 - \alpha_1 J \Delta t [R_I q_0 - (R_V + D) q_0] \\ &\vdots \\ q_k &= q_0 - R_k \\ &= q_0 - \alpha_k J \Delta t [R_I q_{k-1} - (R_V + D) q_0] \\ q_{n+1} &= q_k \end{aligned} \quad (20)$$

Here a standard four-stage scheme was used, with $\alpha_i = 1/4, 1/3, 1/2, 1$. For efficiency both the physical and artificial dissipation terms are calculated only at the first stage, then are held constant for subsequent stages.

ARTIFICIAL DISSIPATION

The dissipative term D in (19) is similar to that used by Jameson et. al. [14]. It is given by:

$$Dq = (D_\xi + D_\eta + D_\zeta) q \quad (21)$$

where the ξ -direction operator is given by

$$D_\xi q = C_\xi (V_2 q_{\xi\xi} - V_4 q_{\xi\xi\xi\xi}) \quad (22)$$

The terms V_2 and V_4 are given by:

$$\begin{aligned} V_2 &= \mu_1 + \mu_2 \max(\nu_{i+1}, \nu_i, \nu_{i-1}) \\ V_4 &= \max(0, \mu_4 - V_2) \end{aligned} \quad (23)$$

where:

$$\nu_i = \frac{|P_{i+1} - 2P_i + P_{i-1}|}{\min(P_{in}, |P_{i+1} + 2P_i + P_{i-1}|)} \quad (24)$$

and subscript i corresponds to the ξ direction, etc.

The constant μ_1 scales a first-order artificial viscosity that is useful for maintaining stability at startup. The constant μ_2 scales a first-order artificial artificial viscosity that is switched on at shocks detected by (24). The denominator in (24) is normally constant at the inlet pressure P_{in} , making the operator roughly symmetric across shocks. The more common term $|P_{i+1} + 2P_i + P_{i-1}|$ is included to switch on the second-difference dissipation when the pressure becomes very small, usually due to numerical problems. The constant μ_4 scales a uniform third-order artificial viscosity that is switched off at shocks by (23). In this work μ_1 was set to $1/4$ for the first 200 iterations and zero thereafter, $\mu_2 = 1/2$, and $\mu_4 = 1/32$.

C is an arbitrary coefficient that can have a large impact on the stability and accuracy of the solution. The subscript indicates that C may be different in each direction.

In [10] a directionally homogeneous coefficient was used for 3D problems. To minimize dissipation in viscous regions C was reduced to zero linearly over several grid points near walls. In [5] a directionally biased coefficient was used for 2D problems. The dissipation was proportional to the grid spacing in each direction, thus reducing it across finely-gridded viscous regions. This worked well in 2D but did not generalize to 3D. Martinelli and Jameson [15] proposed a directionally biased coefficient that works well but can still have large directional variations on highly stretched 3D grids. Kunz and Lakshminarayana [16] proposed a modified form of the Martinelli and Jameson coefficient:

$$\begin{aligned} C_\xi &= \frac{1}{J \Delta t_\xi} \left(1 + \frac{\Delta t_\xi}{\Delta t_\eta} + \frac{\Delta t_\xi}{\Delta t_\zeta} \right)^\sigma \\ C_\eta &= \frac{1}{J \Delta t_\eta} \left(1 + \frac{\Delta t_\eta}{\Delta t_\xi} + \frac{\Delta t_\eta}{\Delta t_\zeta} \right)^\sigma \end{aligned} \quad (25)$$

etc., where $\sigma = 2/3$.

In the present work the 1D time step is approximated as a length scale over a velocity scale. In general the length scale must vary with grid spacing, but the normalized velocity scale can be approximated as one, giving:

$$\Delta t_\xi = \frac{\Delta s_\xi}{V_\xi} \approx \Delta s_\xi \quad (26)$$

Dissipation coefficients given by (25,26) seem to give a very good distribution of the dissipative terms in each direction, and have been used throughout this work.

THREE-DIMENSIONAL STABILITY LIMIT

The following expression is used for the time step:

$$\Delta t \leq \frac{\lambda^*}{l_x |u| + l_y |v'| + l_z |w'| + \sqrt{c^2(l_x^2 + l_y^2 + l_z^2) + \Omega^2}}$$

where:

$$\begin{aligned} l_x &= |\xi_x| + |\eta_x| + |\zeta_x| \\ l_y &= |\xi_y| + |\eta_y| + |\zeta_y| \\ l_z &= |\xi_z| + |\eta_z| + |\zeta_z| \end{aligned} \quad (27)$$

and λ^* is the maximum Courant number for the particular multistage scheme. For the standard four-stage scheme $\lambda^* \approx 2.8$.

To accelerate convergence to a steady state the maximum permissible time step at each grid point was used giving a constant Courant number everywhere. The time step was updated every 50 iterations.

IMPLICIT RESIDUAL SMOOTHING

To further accelerate convergence it is desirable to use a time step even larger than the stability limit given by (27). To maintain stability, the residual calculated in (19) is smoothed after each Runge-Kutta stage by an implicit smoothing operator, i.e.,

$$(1 - \epsilon_\xi \delta_{\xi\xi})(1 - \epsilon_\eta \delta_{\eta\eta})(1 - \epsilon_\zeta \delta_{\zeta\zeta})\bar{R}_k = R_k \quad (28)$$

where $\delta_{\xi\xi}$, $\delta_{\eta\eta}$, and $\delta_{\zeta\zeta}$ are standard second difference operators and ϵ_ξ , ϵ_η , and ϵ_ζ are smoothing parameters. Linear stability analysis shows that the Runge-Kutta scheme may be made unconditionally stable using implicit residual smoothing if the smoothing parameters ϵ are made sufficiently large [17]. In one dimension:

$$\epsilon \geq \frac{1}{4} \left[\left(\frac{\lambda}{\lambda^*} \right)^2 - 1 \right] \quad (29)$$

gives unconditional stability if λ^* is the Courant limit of the unsmoothed scheme, and λ is a larger operating Courant number. In three dimensions different ϵ 's may be used in each direction, and their magnitudes may often be reduced below the value given by (29). Courant numbers $\lambda^* \approx 2.8$, $\lambda = 5.0$, and smoothing parameters $\epsilon_\xi = 0.4$, $\epsilon_\eta = 0.55$, and $\epsilon_\zeta = 0.45$ were used in the present work.

COMPUTATIONAL GRID

A three-dimensional grid code for turbomachinery has been developed by the author (currently unpublished.) The code, called TCGRID for Turbomachinery C-GRID, generates three-dimensional C-type grids using the following technique:

1. A coarse, equally-spaced meridional grid is generated between the specified hub and tip.
2. Blade coordinates are found at the meridional grid points by interpolation of the input blade geometry.
3. Two-dimensional blade-to-blade grids are generated along the meridional grid lines in $(m, \bar{r}\theta)$ coordinates using a version of the GRAPE code developed by Steger and Sorenson [18]. Here m is

the arc length along the meridional surface, and \bar{r} is some mean radius. The GRAPE code allows arbitrary specification of inner and outer boundary points, then generates interior points as the solution of a Poisson equation. Forcing terms in the Poisson equation are chosen to maintain the desired grid spacing and angles at the boundaries.

4. The $(m, \bar{r}\theta)$ coordinates are transformed back to (z, r, θ) .
5. The two-dimensional grids are reclustered spanwise using a hyperbolic tangent stretching function to make a full three-dimensional grid.
6. Finally the (z, r, θ) coordinates are transformed to (x, y, z) and stored in a standard format.

Figure 2 shows the 185x40x49 grid used for Rotor 67. The C-shaped grids used here give good resolution of the round leading edge of the blade, as shown in Fig. 3. The initial grid spacing is about 0.015 mm at the blade, 0.03 mm at the hub, and 0.045 mm at the tip.

COMPUTATIONAL DETAILS

All computations were run on the Cray Y-MP computer at NASA Ames Research Center, under support from the Numerical Aerodynamic Simulation (NAS) Project Office.

The grid code required about 3 million words (Mw) of in-core storage and ran in about 15 seconds for the grid shown in Figs. 2 and 3 (362 600 points.) The flow solver required about 6.5 Mw of storage and 3.6 Mw of solid state device storage (SSD.) The SSD storage is used to hold the old solution q_0 and the dissipative terms $R_V + D$ during the four stages of the multistage scheme (20.)

The spanwise inlet profile was used as an initial guess, and 250 iterations were run with an exit pressure corresponding to the peak efficiency point. About 20 minutes of CPU time were required for this startup solution. All subsequent calculations were restarted from this solution and run an additional 1550 iterations, requiring about 2.5 CPU hours per case.

EXPERIMENTAL DETAILS

Experimental details are described briefly below. Full details may be found in [11,12].

Test Rotor - The test rotor, NASA designation Rotor 67, is shown in Fig. 1. It is the first-stage rotor of a two-stage fan, with a design pressure ratio of 1.63 at a mass flow of 33.25 kg/sec. The rotor has 22 blades. The tip radius varies from 25.7 cm at the leading edge to 24.25 cm at the trailing edge, and the hub/tip radius ratio varies from 0.375 to 0.478. At the design rotational speed of 16 043 rpm the tip speed is 429 m/sec and the tip relative Mach number is 1.38.

Aerodynamic Performance Measurements - The rotor mass flow was determined using a calibrated orifice. Radial surveys of total pressure and temperature,

static pressure, and flow angle were made 2.54 cm upstream of the leading edge and 2.02 cm downstream of the trailing edge using conventional probes.

Laser Anemometry Measurements – A single-channel fringe anemometer was used for the measurements described below. Optical access to the fan was through a glass window in the casing. Fluorescent oil droplets with a diameter of about 1.0–1.4 μm were used to seed the flow.

Measurements were made by holding the probe volume fixed in space as the blades rotated by. Measurement were taken in 50 intervals going from the suction surface of one blade to the suction surface of the next blade. In [11,12], and in the present work the term *windows* is used interchangeably with the term *intervals* in referring to laser measurement locations. Within the blade row the blade itself obscures the last few windows. Measurements were taken in 17 consecutive blade passages, then averaged. Only axial and tangential velocities were measured; however Pierzga and Wood [6] have shown numerically that neglecting the radial component has a minimal effect on calculated Mach numbers.

RESULTS

The computed total pressure ratio and adiabatic efficiency at 100 percent speed are plotted against normalized mass flow and compared to experimental data in Fig. 4. The computed and experimental mass flows are normalized by their respective choking mass flows, as suggested by Pierzga and Wood [6]. This normalization removes any uncertainties in the experimental mass flows. The choking mass flow was measured as 34.96 kg/sec using a calibrated orifice, and the computed value was 34.54 kg/sec, a difference of 1.2 percent. The computed pressure ratios and efficiencies agree very well with the experimental data, except that they are slightly high near stall.

Figures 5–8 show detailed results at an operating point near peak efficiency. Figure 5 shows a comparison of relative Mach number contours at 10, 30, and 70 percent span from the tip. The experimental contours were drawn from laser anemometry data using smoothing and interpolation procedures outlined in [6]. At 10 percent span the inlet Mach number is about 1.35, and a bow wave stands ahead of the blade. A weak oblique shock crosses the passage inside the blade row, and a strong normal shock sits near the trailing edge. The flow exits at a Mach number of about 0.95. The flow is qualitatively similar at 30 percent span, except that the shock sits more forward. At 70 percent span the inlet Mach number is about 0.95. A small supersonic bubble forms on the forward portion of the suction surface. It is not clear if this bubble is terminated by a shock.

Figure 6 shows a comparison of computed and measured blade-to-blade profiles of relative Mach number versus laser window number at two axial locations for

each of three spanwise locations. The first axial location is within the blade row and the second is within the wake. Again, 50 laser windows are defined from the suction surface of one blade (window 0) to the suction surface of the next blade (window 50.)

Within the blade row the computed profiles agree reasonably well with the laser data and predict the shock locations accurately. At 70 percent span near the pressure surface (laser windows greater than 40), few seed particles were observed and the data is statistically uncertain.

Within the wake the computed Mach numbers are somewhat low near the tip, and get progressively better towards the hub. The computed wake profiles are deeper than the measured profiles. It is thought that this is because the seed particles used for the laser anemometer measurements could not follow the high shear rates found at the center and edges of the wake.

The computational results were averaged blade-to-blade using a so-called "energy average" procedure developed by D. L. Tweedt at NASA Lewis Research Center (unpublished.) On each blade-to-blade grid line the procedure integrates the mass flow, radial and tangential momentum, total enthalpy, and ideal total enthalpy $P_0^{\frac{\gamma-1}{\gamma}}$. The radial distributions were mass-averaged spanwise to produce the overall averages shown previously in Fig. 4. Since the integrations give total conditions directly, they can be expected to give good predictions of efficiency. Other quantities like average static pressure or flow angle are found as nonlinear algebraic combinations of the primitive integrated quantities, and thus may not agree as well with experimental data.

Experimentally the exit total conditions and flow angle were measured with a self-nulling combination probe, and static pressure was measured using a separate self-nulling wedge probe. Total conditions are thought to be fairly accurate, but flow angle and static pressure accuracy depend on the frequency response and blockage of the instrumentation.

With these thoughts in mind, radial surveys of several aerodynamic parameters measured 2.02 cm downstream of the rotor (at the grid exit) are shown in Fig. 7. The computed exit total temperatures and total pressures agree very well with the measurements along the span, but the computed static pressures are somewhat high, and computed exit flow angles are two to three degrees high over much of the span.

Figure 8 shows several particle traces to illustrate some of the secondary flows in this fan. The overall view shows particles introduced upstream so as to pass over the suction surface of the blade. Most of the particles pass straight through the blade row, but those in the endwall boundary layer roll up into a vortex that climbs the leading edge. The enlargement of the leading edge shows that the flow in the hub boundary layer sees a high blade incidence and separates near the lead-

ing edge. The low-momentum fluid in this separated region is centrifuged radially outwards. Eventually the incidence decreases and the flow turns abruptly in the streamwise direction. The trailing edge enlargement shows a large separation bubble fed by fluid from the endwall that migrates radially outward and ends up in the wake. The complicated flow pattern in this region may explain the scarcity of laser seed particles observed in this region.

Figures 9-12 show detailed results at an operating point near stall. Figure 9 shows a comparison of relative Mach number contours, again at 10, 30, and 70 percent span from the tip. At 10 percent span the inlet Mach number is about 1.4. A normal shock stands ahead of the blade and crosses the passage. The computed shock is somewhat stronger than, and ahead of, the measured shock. The exit Mach number is about 0.85. At 30 percent span the results are similar. The flow at 70 percent span is similar to the peak efficiency case, except that the supersonic bubble is smaller and has a better-defined (though smeared) terminating shock.

Figure 10 shows a comparison of relative Mach number profiles, again at two axial locations and three spanwise locations. At the tip the computed shocks are ahead of and stronger than the measured shocks, which accounts for the high predicted pressure ratios near stall. Adamczyk, et al. [9] have shown numerically that interaction of the tip leakage vortex and the tip shock has a large effect on the near-stall performance of this rotor, and that lack of a tip clearance model can account for the discrepancies in shock position and strength seen here. At 70 percent the computed Mach numbers are slightly low, but agree qualitatively with the data.

In the wake, the computed Mach numbers are somewhat low near the tip, and get progressively better towards the hub. Again the computed wakes are deeper than the measured wakes. There is considerable uncertainty in the laser data in the center of the wake at 70 percent span, where computed particle traces shown later indicate a large separation.

Figure 11 compares radial surveys downstream of the rotor. The computed total temperatures and pressures are slightly high along the span, consistent with the high adiabatic efficiency shown in Fig. 4. Again the computed static pressures are high. Computed exit flow angles agree well near the tip but are a few degrees high at lower radii.

Figure 12 shows particle traces at the near-stall operating point. The overall view shows more radial migration of the endwall flow than at peak efficiency. At this lower mass flow the blade sees a higher relative incidence than at peak efficiency, causing the flow near the hub to migrate tangentially away from the suction surface, as shown in the leading edge enlargement. The trailing edge enlargement shows a separation bubble similar to that seen near peak efficiency. The trailing

edge separation appears to be slightly larger at the near-stall point.

SUMMARY

A flow analysis code has been developed for 3D viscous flows in turbomachinery. The analysis solves the Navier-Stokes equations written in a general body-fitted coordinate system, including rotation about the x -axis. The thin-layer approximation is made in the streamwise direction but all viscous terms are included in the cross-planes. The Baldwin-Lomax eddy-viscosity model is used for turbulent flows.

An explicit multistage Runge-Kutta scheme is used to solve the finite-difference form of the flow equations. A variable time step and implicit residual smoothing are used to accelerate the convergence of the scheme. The code is highly vectorized for the Cray Y-MP, and solutions can be computed on fairly fine grids in two to three hours.

The code was used to compute the operating map of a transonic fan at design speed, and showed good agreement with measured values of total pressure ratio and adiabatic efficiency. The computed results are slightly optimistic near stall, probably due to the lack of a tip clearance model.

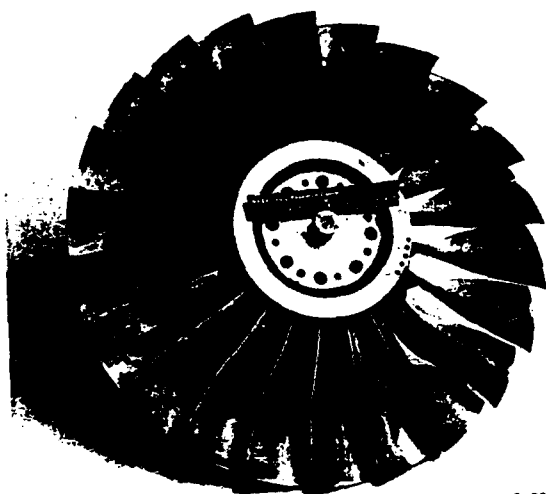
Detailed comparisons were made with experimental data at two operating points, one near peak efficiency and one near stall. Comparisons were made with aerodynamic surveys downstream of the fan. In general, exit total temperature and total pressure were predicted quite accurately, but static pressure and flow angle showed some disagreement with the data. Comparisons were also made with laser anemometry data in the blade row and in the wake. Shock location and strength were predicted closely near peak efficiency, but were over-predicted near stall. Predicted wake profiles had about the right spread, but were off in location in some cases. Predicted wakes were much deeper than measured wakes, probably due to lack of resolution in the laser data.

Particle traces showed separated flow at both the leading and trailing edges at both operating points. The leading edge separation is too small to be seen in the laser data. The trailing edge separation may have been suggested indirectly by the scarcity of seed particles in this region. The ability of the code to predict these separated flow features suggests that the code could be used to guide experimental work aimed at resolving these features, or to eliminate such features during design.

Overall the code showed very good agreement with a variety of experimental data, thereby increasing confidence that the code can reliably be used to predict the performance of other machines as well.

References

- [1] Davis, R. L., Hobbs, D. E., Weingold, H. D., "Prediction of Compressor Cascade Performance Using a Navier-Stokes Technique," ASME Paper 88-GT-96, June, 1986.
- [2] Chevrin, P.-A., Vuillez, C., "Viscous Flow Computations in Turbomachine Cascades," ASME Paper 90-GT-76, June, 1990.
- [3] Cambier, L., Escande, B., Veuillot, J. P., "Computation of Internal Flows at High Reynolds Number by Numerical Solution of the Navier-Stokes Equations," *Rech. Aérop.*, No. 1986-6, pp 27-44.
- [4] Boyle, R. J., "Navier-Stokes Analysis of Turbine Blade Heat Transfer," ASME Paper 90-GT-42, June, 1990.
- [5] Chima, R. V., "Explicit Multigrid Algorithm for Quasi-Three-Dimensional Viscous Flows in Turbomachinery," *J. Propulsion and Power*, Vol. 3, No. 5, Sept.-Oct. 1987, pp. 397-405.
- [6] Pierzga, M. J., Wood, J. R., "Investigation of the 3-D Flow Field Within a Transonic Fan Rotor: Experiment and Analysis," *J. Eng. Gas Turbines and Power*, Vol. 107, No. 2, Apr. 1985, pp. 436-449.
- [7] Denton, J. D., "An Improved Time Marching Method For Turbomachinery," ASME Paper 82-GT-239, Apr. 1982.
- [8] Dawes, W. N., "Towards Improved Throughflow Capability: The Use of Viscous Flow Solvers in a Multistage Environment," ASME Paper 90-GT-18, June, 1990.
- [9] Adamczyk, J. J., Celestina, M. L., Greitzer, E. M., "The Role of Tip Clearance in High-Speed Fan Stall," to be presented at the 1991 ASME Gas Turbine Conf., June 3-6, 1991, Orlando, FL.
- [10] Chima, R. V., Yokota, J. W., "Numerical Analysis of Three-Dimensional Viscous Internal Flows," AIAA J., Vol. 28, No. 5, May 1990, pp. 798-806.
- [11] Fottner, L., ed., *Test Cases for Computation of Internal Flows in Aero Engine Components*, Propulsion and Energetics Panel Working Group 18, AGARD Advisory Report No. 275, July, 1990, Specialised Printing Services Ltd. Essex, U.K.
- [12] Strazisar, A. J., Wood, J. R., Hathaway, M. D., Suder, K. L., "Laser Anemometer Measurements in a Transonic Axial Flow Fan Rotor," NASA TP-2879, Nov. 1989.
- [13] Baldwin, B. S., Lomax, H., "Thin-Layer Approximation and Algebraic Model for Separated Turbulent Flows," AIAA Paper 78-257, Jan. 1978.
- [14] Jameson, A., Schmidt, W., Turkel, E., "Numerical Solutions of the Euler Equations by Finite Volume Methods Using Runge-Kutta Time-Stepping Schemes," AIAA Paper 81-1259, June 1981.
- [15] Martinelli, A., Jameson, A., "Validation of a Multigrid Method for the Reynolds Averaged Equations," AIAA Paper 88-0414, Jan. 1988.
- [16] Kunz, R., F., Lakshminarayana, B., "Computation of Supersonic and Low Subsonic Cascade Flows Using an Explicit Navier-Stokes Technique and the $k - \epsilon$ Turbulence Model," in *Computational Fluid Dynamics Symposium on Aeropropulsion*, NASA Conference Publication 10045, Apr. 24-26, 1990.
- [17] Jameson, A., Baker, T. J., "Solution of the Euler Equations for Complex Configurations," AIAA Paper 83-1929, July 1983.
- [18] Steger, J. L., Sorenson, R. L., "Automatic Mesh-Point Clustering Near a Boundary in Grid Generation with Elliptic Partial Differential Equations," *Journal of Computational Physics*, Vol. 33, No. 3, Dec. 1979, pp. 405-410.



C-88-05331

Figure 1. Rotor 67 test hardware.

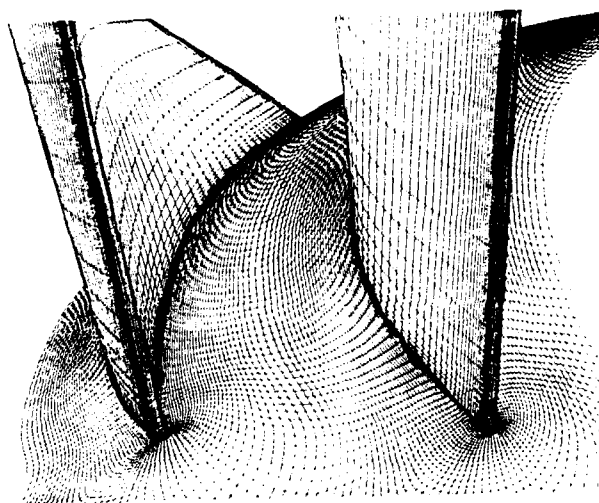


Figure 3. Grid leading edge enlargement.

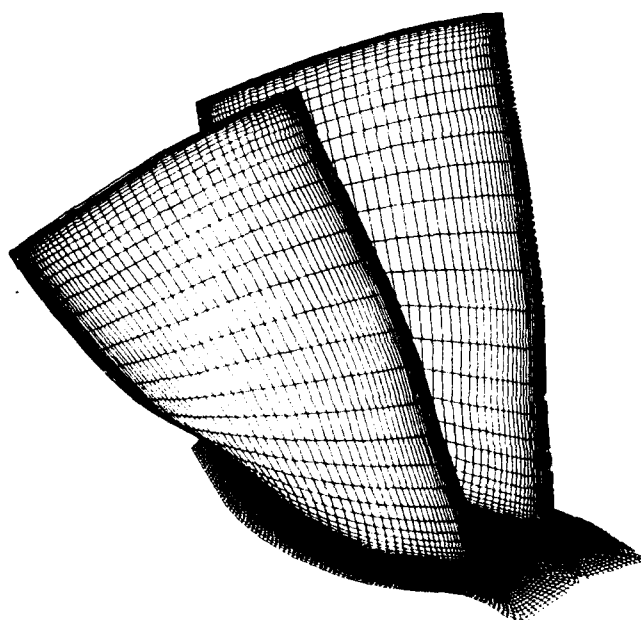
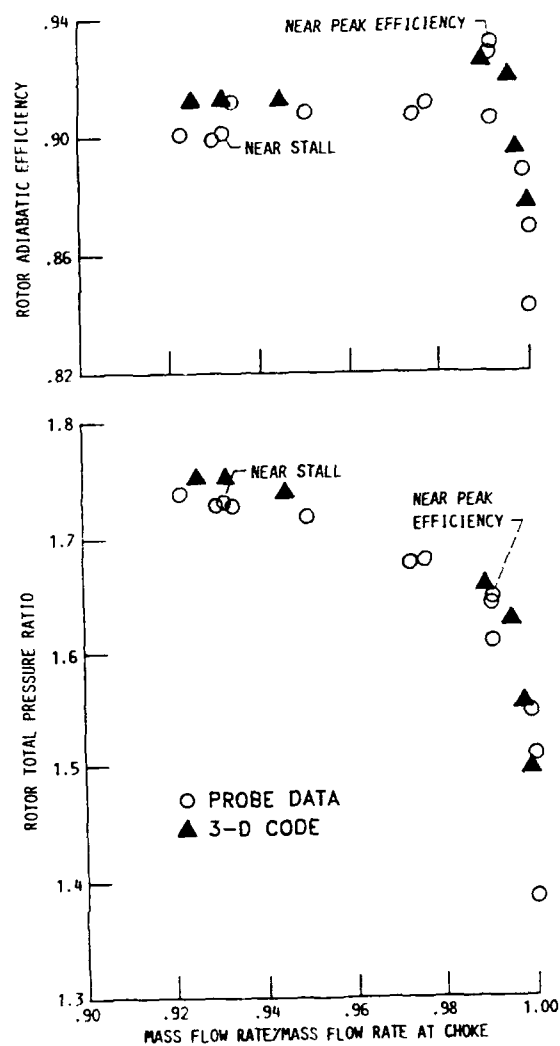
Figure 2. Computational grid.
185 C x 40 tangential x 49 spanwise points.

Figure 4. Comparison of computed and measured adiabatic efficiency and total pressure ratio characteristic at 100 percent speed. Points labelled "NEAR STALL" and "NEAR PEAK EFFICIENCY" are discussed in detail in the text.

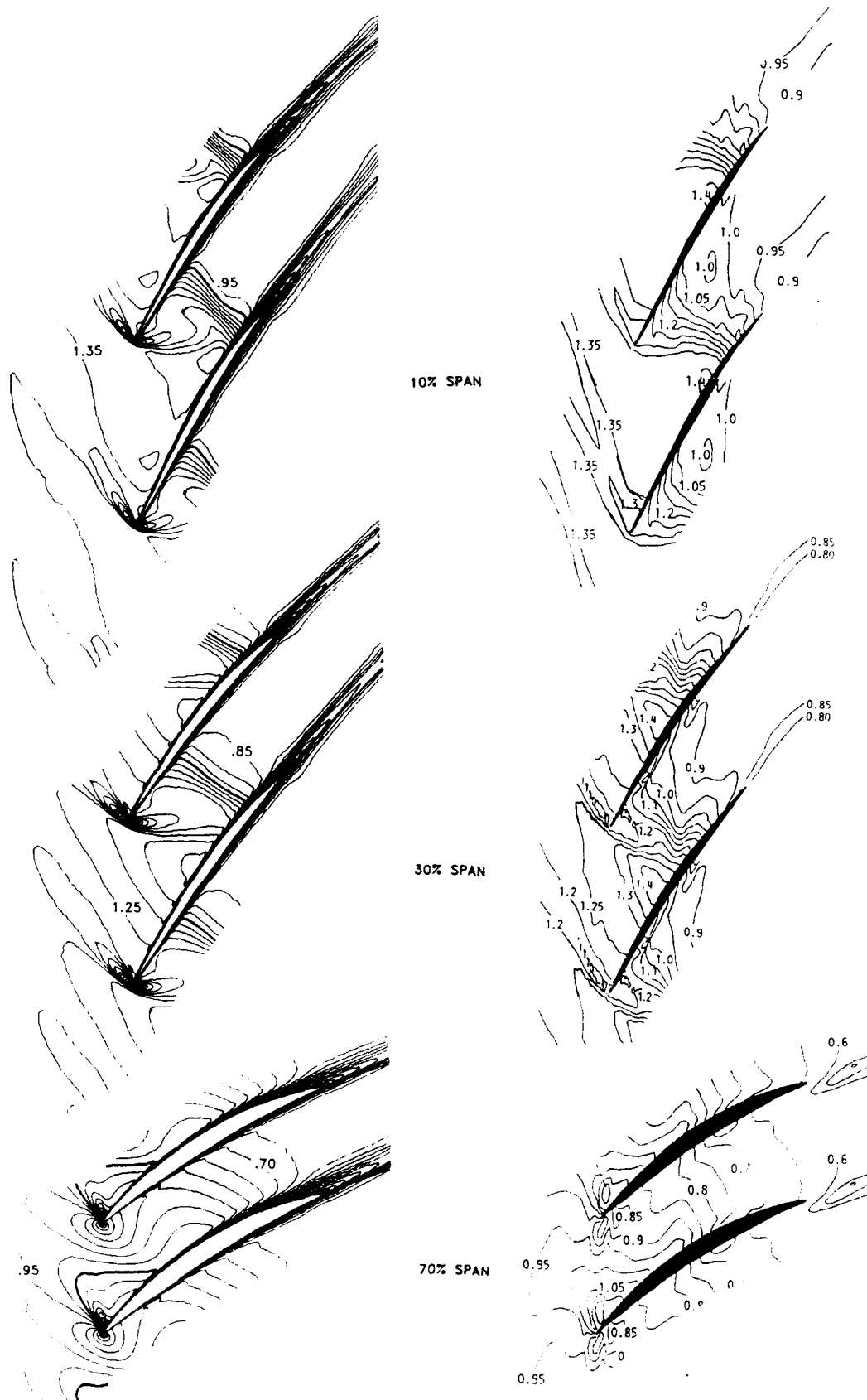


Figure 5. Computed contours of relative Mach number, near peak efficiency. Heavy line is $M = 1.0$, contour increment = 0.05.

Measured contours of relative Mach number, near peak efficiency.

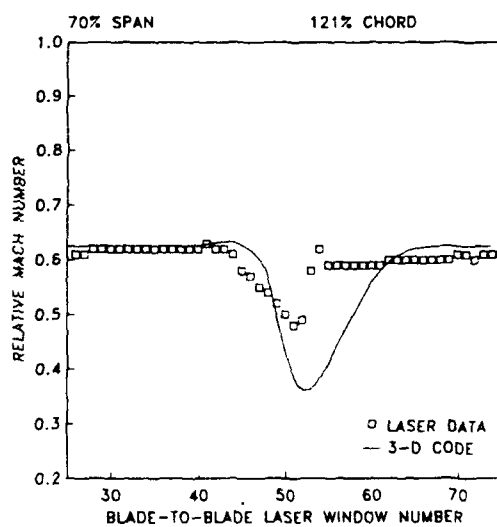
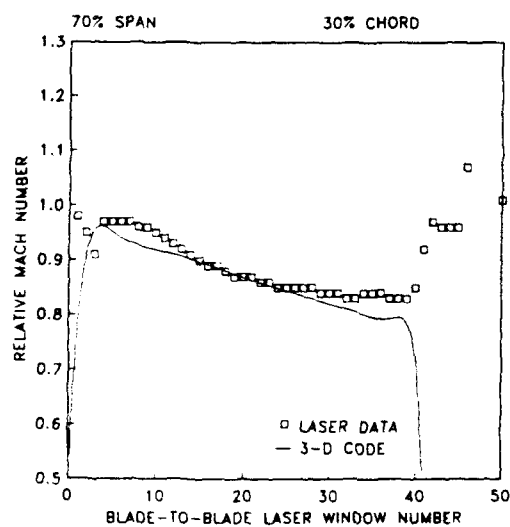
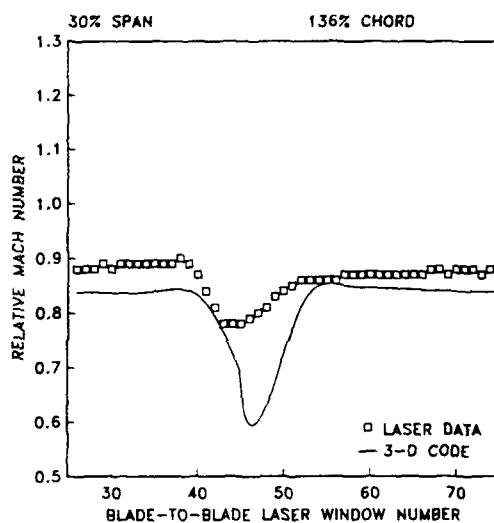
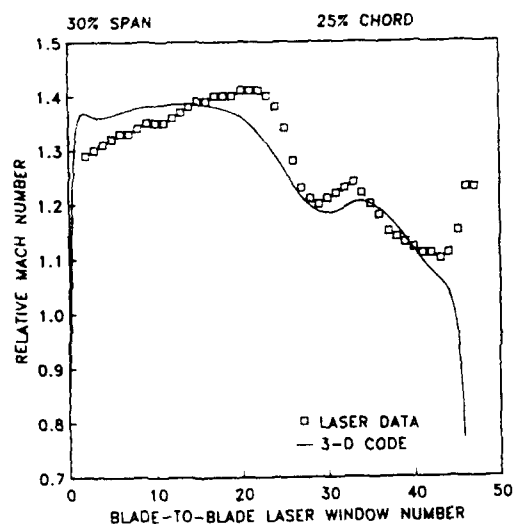
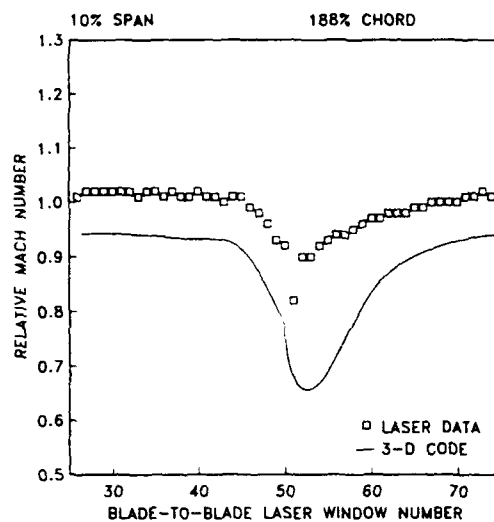
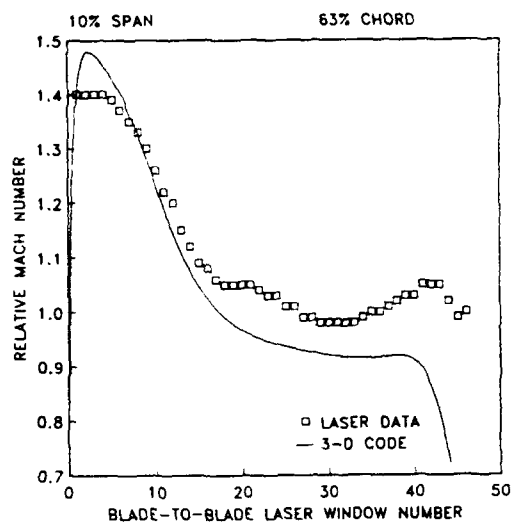


Figure 6. Comparison of computed and measured blade-to-blade distributions of relative Mach number, near peak efficiency.

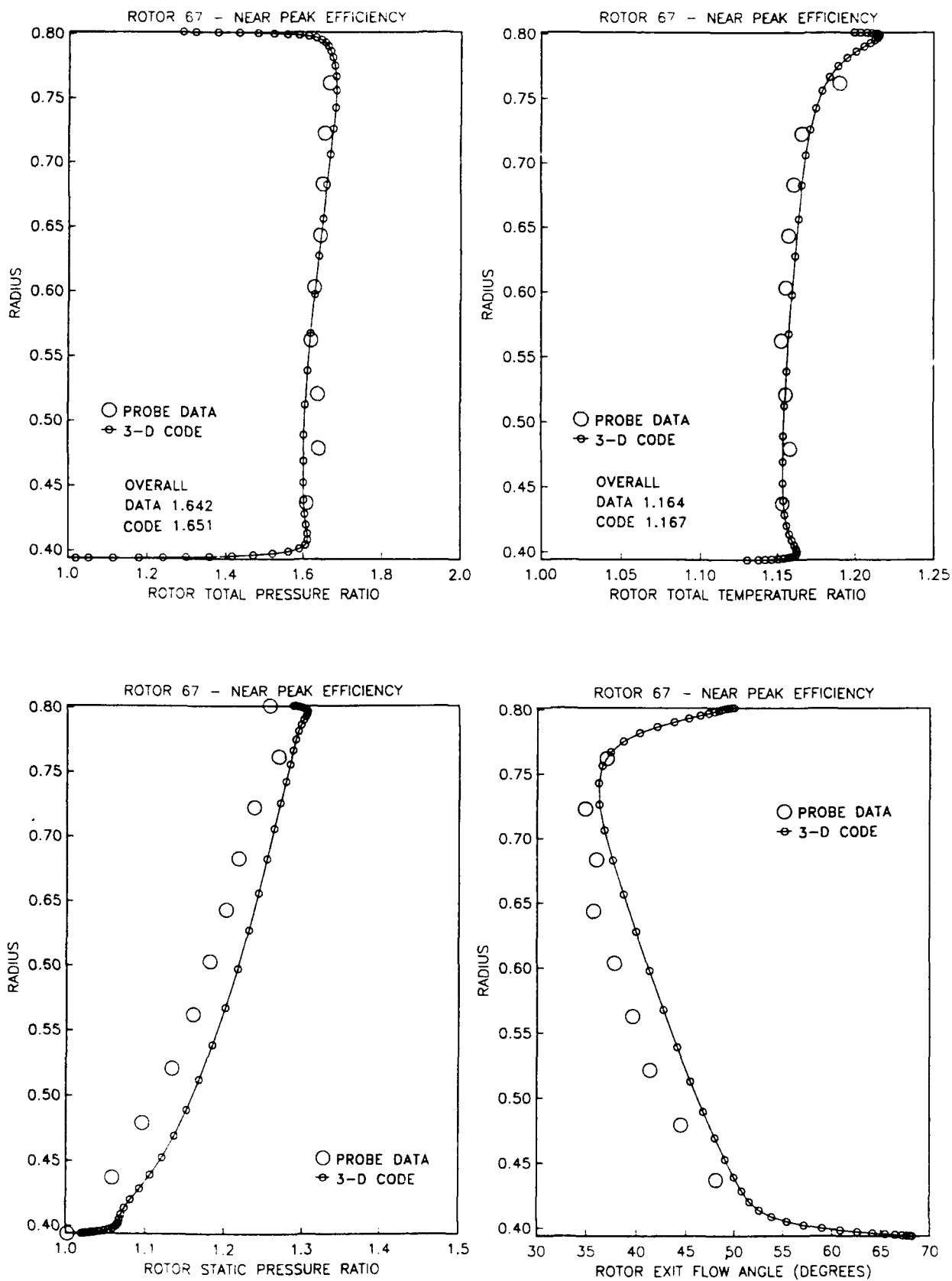


Figure 7. Comparison of computed and measured spanwise distributions of total pressure, total temperature, static pressure, and flow angle downstream of the rotor, near peak efficiency.

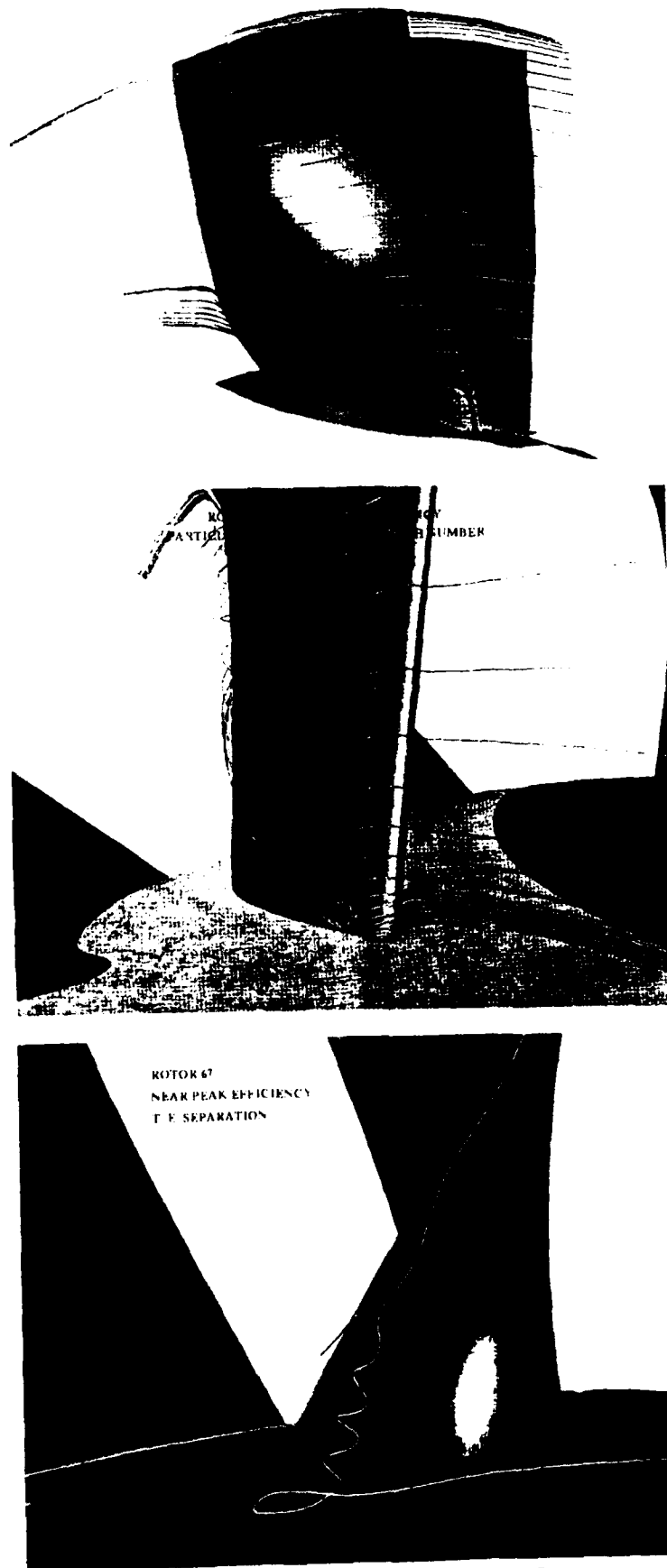


Figure 8. Computed particle traces, near peak efficiency.
 Top: Suction surface overview.
 Center: Leading edge enlargement looking downstream.
 Bottom: Trailing edge enlargement looking upstream.

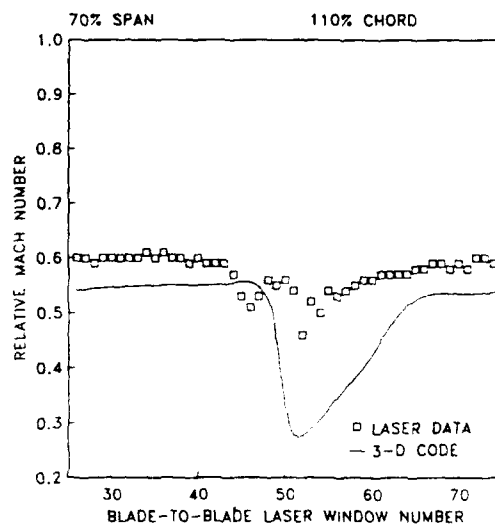
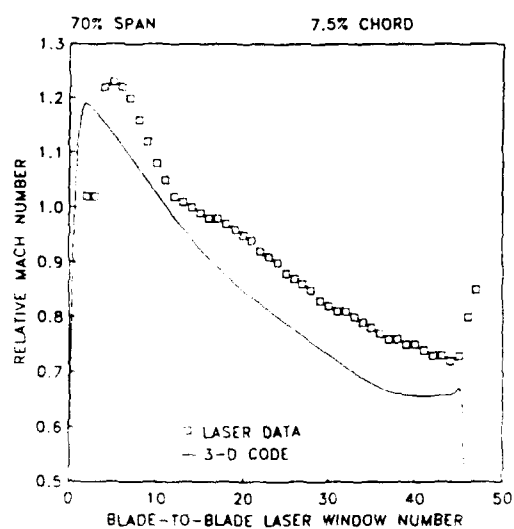
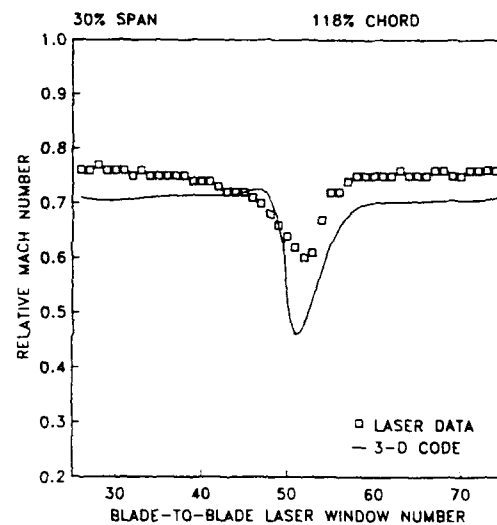
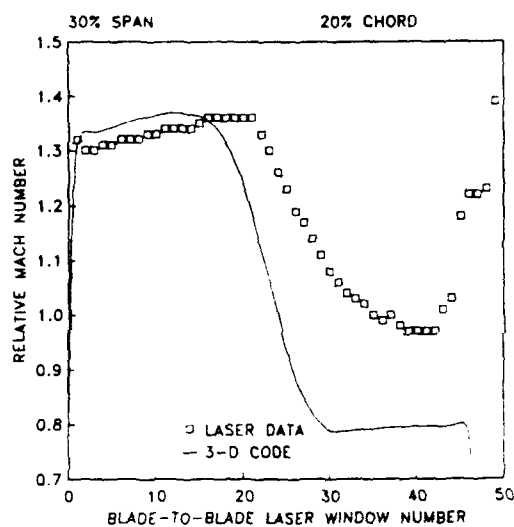
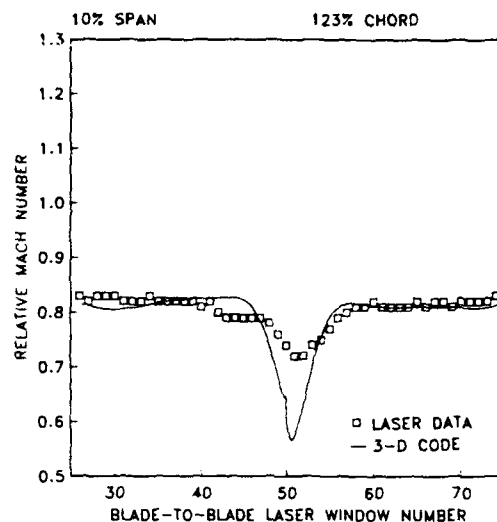
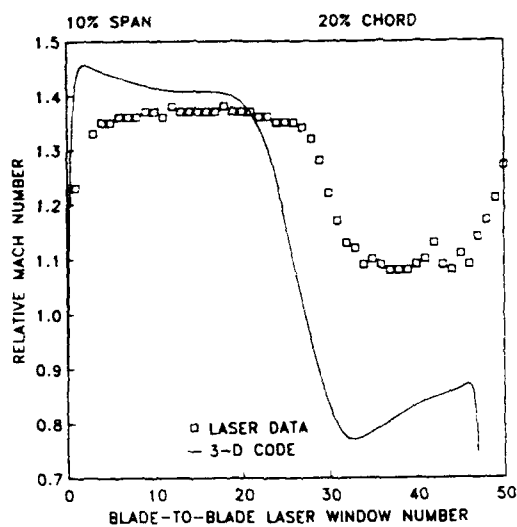


Figure 10. Comparison of computed and measured blade-to-blade distributions of relative Mach number, near stall.

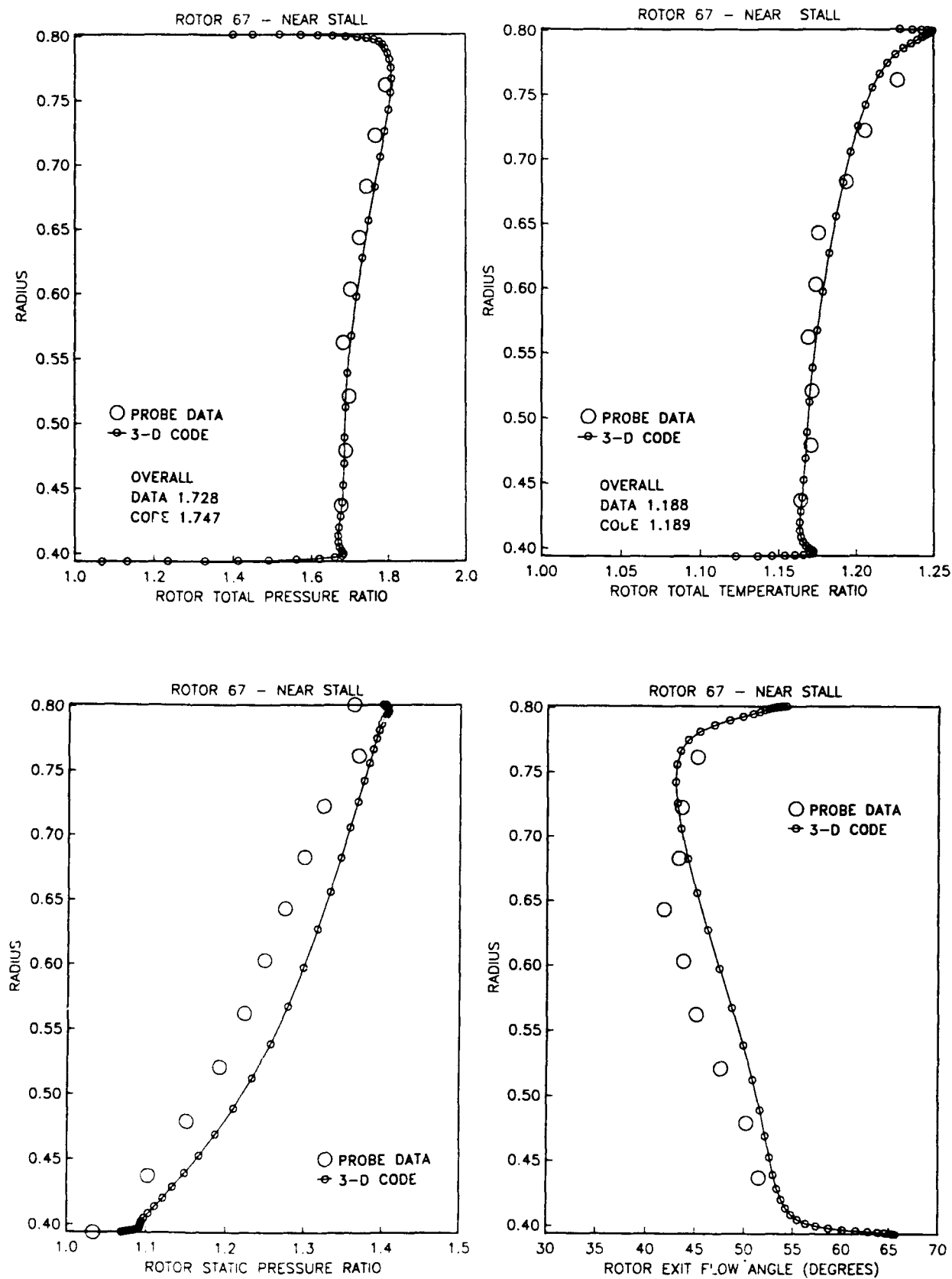


Figure 11. Comparison of computed and measured spanwise distributions of total pressure, total temperature, static pressure, and flow angle downstream of the rotor, near stall.

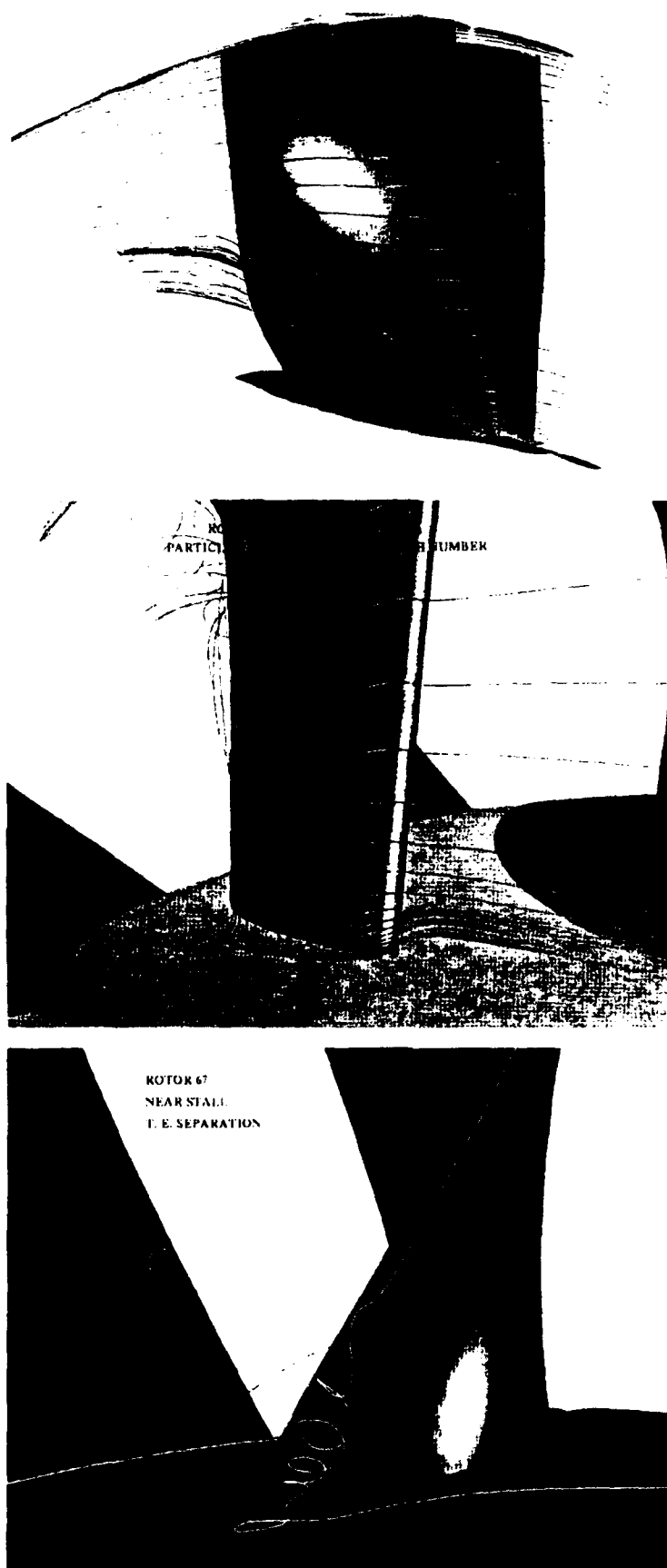


Figure 12. Computed particle traces, near stall.
 Top: Suction surface overview.
 Center: Leading edge enlargement looking downstream.
 Bottom: Trailing edge enlargement looking upstream

Discussion

T. PRINCE, WILLIAMS INTER., U.S.A.

Have you investigated the hysteresis effect, where Rotor 67 exhibits two distinct levels of performance at the peak efficiency point?

AUTHOR'S REPLY

The efficiencies computed when approaching peak efficiency from either side seemed to follow the speculation of the experimentalists. The difference in the computed efficiencies was about half the measured differences. The differences in the flows were hard to detect - slight differences in shock location and strength. I suspect that the hysteresis effect is computable, but will require a very precise and systematic computational study. I also suspect that the final results will not show dramatic differences between the two solutions.

P. RAMETTE, DASSAULT AVIATION, FRANCE

- 1) What is the extent of the separation zone at the trailing edge near the hub?
- 2) Did you compute the flow near the tip, taking into account tip clearance effects?

AUTHOR'S REPLY

- 1) The trailing edge separation covers roughly the last 25 percent chord and the bottom 20 percent span of the blade.
- 2) There is no tip clearance model in the present code. The blade is assumed to scrape without leakage against a stationary endwall.

W. CALVERT, RAE PYESTOCK, U.K.

- 1) I notice from your paper that your calculations underestimated the mass flow of this fan by 1.2 percent, which is consistent with the results from my calculations using a S1-S2 system. Can you comment on whether this is a common feature for all CFD predictions carried out on this fan?
- 2) What transition model is used in your code?

AUTHOR'S REPLY

- 1) The mass flow for the fan was found experimentally both by use of a calibrated orifice and by integrating measured inlet profiles. The two methods give somewhat different results, but the orifice value is generally taken as correct. My computed choking mass flow differs from the orifice value by 1 to 2 percent (lower than measured). I don't know how close other researchers have come to predicting the choking mass flow. Pierzga and Wood (Ref. 6) have recommended normalizing the computed mass flows at other operating points by the computed choking mass flow in order to minimize uncertainties in the experimental mass flows. That procedure was used for the operating curves shown in Fig. 4.
- 2) The Baldwin-Lomax turbulence model uses the following transition model: The turbulent viscosity is computed for a given velocity profile. If the maximum value is less than 14 times the laminar viscosity, the flow is assumed to be laminar, and the turbulent viscosity is reset to zero. When the maximum value exceeds 14 times the laminar viscosity, the flow is taken to be turbulent.

C. HIRSCH, UNIV. OF BRUSSELS, BELGIUM

- 1) What is the CFL number and convergence levels of your computation?
- 2) Can you comment on the validity of the thin shear layer approximation compared to full Navier-Stokes, taking into account the fact that your results show regions of large three-dimensional separations.

AUTHOR'S REPLY

1) The calculations were all run at a Courant number of 5.0. Each case was run for a total of 1800 iterations, at which point the residuals were reduced about three orders of magnitude. Several other parameters were monitored for convergence. Global mass conservation was generally better than 0.2 percent, and adiabatic efficiency was converged to three decimal places.

2) The thin shear layer approximation neglects all viscous derivatives along streamwise grid lines, based on the fact that the streamwise grid spacing may be several orders of magnitude larger than the spacing across the viscous layer. Even if streamwise viscous terms are included, their effects cannot be resolved on the relatively coarse streamwise grid. Several papers, notably one by Steger, have demonstrated this in the past. Although the thin shear layer approximation superficially resembles the boundary layer approximation, the normal momentum equation is retained, allowing calculation of separated flows.

F. BASSI, UNIV. OF CATANIA, ITALY

Have you tried or do you plan to use a multigrid technique in your code?

AUTHOR'S REPLY

Although I have worked with multigrid in the past, my three-dimensional code does not use multigrid. I may add it in the future.





NAVIER-STOKES ANALYSIS OF TURBINE BLADE HEAT TRANSFER AND PERFORMANCE

by

Daniel J. Dorney* and Roger L. Davis†
 United Technologies Research Center
 411 Silver Lane, MS-20
 East Hartford, CT 06108-1049
 United States

92-16082



Summary

A three-dimensional Navier-Stokes analysis of heat transfer and aerodynamic performance is presented for a low speed linear turbine cascade. The numerical approach used in this analysis consists of an alternate-direction, implicit, approximate-factorization, time-marching technique. An objective of this investigation has been to establish the computational grid density requirements necessary to accurately predict blade surface and endwall heat transfer, as well as the exit plane aerodynamic total pressure loss and flow angle distributions. In addition, a study has been performed to determine a viable implementation strategy for the three-dimensional modelling of transition and turbulence in the turbine blade passage. Results are presented which demonstrate that the present procedure can accurately predict 3-D turbine blade heat transfer as well as the absolute level and spanwise distribution of aerodynamic performance quantities.

List of Symbols

a	- Speed of sound
c_p	- Specific heat ratio at constant pressure
e	- Specific energy
e_t	- Total energy
k	- Thermal conductivity
L	- Reference length (2.54 cm)
M	- Mach number
P	- Static pressure
Pr	- Prandtl number
P_T	- Stagnation pressure
q	- Heat flux
Re	- Free stream inlet reference Reynolds number
T	- Static temperature
u	- x component of velocity
v	- y component of velocity
w	- z component of velocity
λ	- Second coefficient of viscosity
μ	- First coefficient of viscosity
ρ	- Density
τ	- Shear stress

Subscripts

i	- Inviscid
L	- Laminar quantity
t	- Stagnation quantity
T	- Turbulent quantity
v	- Viscous
x, y, z	- First derivative with respect to x, y or z
xx, yy, zz	- Second derivative with respect to x, y or z
1	- Inlet quantity
2	- Exit quantity

Introduction

The accurate prediction of three-dimensional turbomachinery blade row heat transfer and aerodynamic performance, including total pressure loss and flow turning, remains a challenging task for most Navier-Stokes numerical procedures. The very large computational grid densities necessary to accurately resolve the viscous flow physics and properly convect the vorticity require computational resources which far exceed those available to most engineering facilities. Thus, in most instances, it has not been possible to produce grid-independent three-dimensional flow solutions for turbomachinery blade rows which ensure the accuracy required for reliable predictions.

The proper modelling of transition and turbulence within turbomachinery blade passages is also often compromised in order to reduce computational times to acceptable levels. The effects of turbulence in the flow are quite often modelled with an algebraic eddy viscosity correlation which has its basis in two-dimensional boundary layer data, even though the flow in a blade row passage has strong secondary and occasional reversed flows. The modelling of transition in most Navier-Stokes approaches is practically non-existent due to the lack of reliable correlations for three-dimensional internal blade row flows and due to the numerical instabilities caused by the unsteady movement of the transition region as the flow field develops. Unfortunately, it is unlikely that improvements in turbulence and transition modelling will improve beyond the current state-of-the-art for three-dimensional turbomachinery flows until Navier-Stokes procedures can affordably and reliably produce grid-independent solutions. Only then will researchers be able to separate out the turbulence modelling effects on the flow from those caused by truncation error and numerical viscosity.

Several investigations have been made recently in which three-dimensional Navier-Stokes procedures have been used to predict the heat transfer and/or aerodynamic performance of the Langston linear turbine cascade [1, 2]. Among these numerical investigations, Chan and Sheedy [3] have used a pressure correction method with a two equation ($k - \epsilon$) turbulence model to predict the losses in the Langston cascade for a thick (3.3 cm) inlet boundary layer. Their predicted results indicate the numerical procedure is very sensitive to spanwise computational grid density. Even the use of comparatively fine computational grids, however, was not adequate to achieve the flow field resolution needed to accurately predict aerodynamic performance quantities. Hah [4, 5] has also used a pressure correction technique with a two equation ($k - \epsilon$) turbulence model to predict endwall Stanton numbers [4] and losses as a function of axial distance [5] for the Langston cascade with a thick inlet boundary layer. The predicted endwall Stanton numbers show fair agreement with the experimental data, but it is unclear if a sufficiently fine computational grid was used to attain grid independent solutions. Moore [6, 7] has used a pressure correction method with an algebraic turbulence model to predict losses and secondary flows for the Langston cascade with a thick inlet boundary layer. Lee and Knight [8] solved the thin layer Navier-Stokes equations using an approximate factorization technique and the two equation ($q - \omega$) turbulence model to study heat transfer for the Langston cascade with a thick inlet boundary layer. A portion of their

*Associate Research Engineer, Theoretical & Computational Fluid Dynamics Group

†Senior Research Engineer, Theoretical & Computational Fluid Dynamics Group

investigation focused on the effects of different grid topologies (H- and O-H grids) on the predicted heat transfer quantities. In their study, it was determined that grid topology, as well as computational grid density, can impact the predicted solutions.

The objective of the current investigation has been to provide guidance as to the computational grid density requirements which are necessary to produce reliable and accurate Navier-Stokes predictions of turbomachinery blade row flows. Simulations of transitional flow through the Langston cascade [1, 2] with a thin inlet boundary layer (0.41 cm) have been performed where the focus has been to conduct a computational grid refinement study to determine the computational grid density necessary to properly resolve surface heat transfer and aerodynamic performance quantities. As part of this investigation, a study was performed to determine a viable strategy for implementing an algebraic turbulence model for three-dimensional internal blade row flows and to determine the limitations of using an algebraic turbulence model on the accuracy of the exit plane distributions of total pressure loss and flow angle. Also, a brief study was conducted to demonstrate the importance of modelling laminar/turbulent transition for these flows.

Numerical Integration Procedure

The governing equations considered in this study are the time dependent, three-dimensional Navier-Stokes equations:

$$U_t + (F_i + F_v)_x + (G_i + G_v)_y + (H_i + H_v)_z = 0 \quad (1)$$

where

$$U = \begin{bmatrix} \rho \\ \rho u \\ \rho v \\ \rho w \\ e_t \end{bmatrix} \quad (2)$$

$$F_i = \begin{bmatrix} \rho u \\ \rho u^2 + P \\ \rho uv \\ \rho uw \\ (e_t + P)u \end{bmatrix} \quad F_v = - \begin{bmatrix} 0 \\ \tau_{xx} \\ \tau_{xy} \\ \tau_{xz} \\ \tau_{hx} \end{bmatrix} \quad (3)$$

$$G_i = \begin{bmatrix} \rho v \\ \rho uv \\ \rho v^2 + P \\ \rho vw \\ (e_t + P)v \end{bmatrix} \quad G_v = - \begin{bmatrix} 0 \\ \tau_{yx} \\ \tau_{yy} \\ \tau_{yz} \\ \tau_{hy} \end{bmatrix} \quad (4)$$

$$H_i = \begin{bmatrix} \rho w \\ \rho uw \\ \rho vw \\ \rho w^2 + P \\ (e_t + P)w \end{bmatrix} \quad H_v = - \begin{bmatrix} 0 \\ \tau_{zx} \\ \tau_{zy} \\ \tau_{zz} \\ \tau_{hz} \end{bmatrix} \quad (5)$$

where

$$\begin{aligned} \tau_{xx} &= 2\mu u_x + \lambda(u_x + v_y + w_z) \\ \tau_{xy} &= \mu(u_y + v_x) \\ \tau_{xz} &= \mu(u_z + w_x) \\ \tau_{yz} &= \tau_{zy} \\ \tau_{yx} &= 2\mu v_y + \lambda(u_x + v_y + w_z) \end{aligned}$$

$$\begin{aligned} \tau_{yz} &= \mu(v_z + w_y) \\ \tau_{zx} &= \tau_{xz} \\ \tau_{zy} &= \tau_{yz} \\ \tau_{zz} &= 2\mu w_z + \lambda(u_x + v_y + w_z) \\ \tau_{hx} &= u\tau_{xx} + v\tau_{xy} + w\tau_{xz} + \gamma\mu P_r^{-1}e_x \\ \tau_{hy} &= u\tau_{yx} + v\tau_{yy} + w\tau_{yz} + \gamma\mu P_r^{-1}e_y \\ \tau_{hz} &= u\tau_{zx} + v\tau_{zy} + w\tau_{zz} + \gamma\mu P_r^{-1}e_z \\ e &= \frac{P}{(\rho(\gamma - 1))} \\ e_t &= \rho e + \frac{\rho(u^2 + v^2 + w^2)}{2} \end{aligned} \quad (6)$$

For the present application, the second coefficient of viscosity is calculated using Stokes' hypothesis, $\lambda = -2/3\mu$. The equations of motion are completed by the perfect gas law.

The viscous fluxes are simplified by incorporating the thin layer assumption [9]. In the current study, viscous terms are retained in the direction normal to the hub surface (z-direction) and in the direction normal to the blade surface (y-direction). To extend the equations of motion to turbulent flows, an eddy viscosity formulation is used. Thus, the effective viscosity and effective thermal conductivity can be defined as:

$$\begin{aligned} \mu &= \mu_L + \mu_T \\ \frac{k}{c_p} &= \frac{\mu_L}{P_r L} + \frac{\mu_T}{P_r T} \end{aligned} \quad (7)$$

The turbulent viscosity, μ_T , is calculated using the Baldwin-Lomax [9] algebraic turbulence model. The specific techniques used to implement this model for three-dimensional flows in turbomachinery blade rows will be described below.

The numerical procedure for the three-dimensional analysis consists of a time marching, implicit, third-order spatially accurate, upwind, finite difference scheme. The inviscid fluxes are discretized using a combination of central, forward, and backward differences depending on the local eigenvalues of the flux Jacobians according to the scheme developed by Roe [10]. The viscous fluxes are calculated using standard central differences. The alternate direction, approximate-factorization technique of Beam and Warming [11] is used to compute the time rate changes in the primary variables. An inner Newton iteration can be used to increase stability and reduce linearization errors. For all cases investigated in this study, one Newton iteration was performed at each time step. Further details of the three-dimensional numerical technique can be found in Refs. [12, 13].

Grid Generation and Geometry

The three-dimensional Navier-Stokes analysis uses zonal grids to discretize the turbine flow field. A combination of O- and H-grid sections are generated at constant radial spanwise locations in the blade-to-blade direction extending upstream of the airfoil leading edge to downstream of the airfoil trailing edge. Algebraically generated H-grids are used in the regions upstream of the leading edge, downstream of the trailing edge and in the inter-blade region. The O-grid, which is body-fitted to the surface of the airfoil and generated using an elliptic equation solution procedure, is used to properly resolve the viscous flow in the blade passages and to easily apply the algebraic turbulence model. Computational grid lines within the O-grid are stretched in the blade-normal direction with a fine grid spacing at the wall. The combined H- and O- overlaid grid sections are stretched in the spanwise direction away from the hub and shroud regions with a fine grid spacing located adjacent to the hub and shroud.

Boundary Conditions

The theory of characteristics is used to determine the boundary conditions at the passage inlet and exit. For subsonic inlet flow, the total pressure, v and w velocity components and the downstream running Riemann invariant, $R_1 = u + \frac{2a}{\gamma-1}$, are specified while the upstream running Riemann invariant, $R_2 = u - \frac{2a}{\gamma-1}$, is extrapolated from the interior of the computational domain. For subsonic outflow the pressure ratio, P_2/P_{t1} , is specified while the v and w velocity components, entropy, and the downstream running Riemann invariant are extrapolated from the interior of the computational domain. Periodicity is enforced along the outer boundaries of the H-grids in the circumferential (θ) direction.

Dirichlet conditions, in which the time rate change in the vector U of Eq. (2) is set to zero, are imposed at the overlaid boundaries of the O- and H-grids. The flow variables of U at zonal boundaries are explicitly updated after each time step by interpolating values from the adjacent grid. Because of the explicit application of the zonal boundary conditions, large time steps may necessitate the use of more than one Newton iteration. The zonal boundary conditions are non-conservative, but for subsonic flow this should not affect the accuracy of the final flow solution.

No-slip boundary conditions are enforced at the hub and shroud endwalls of the turbine passage and along the surface of the airfoil. In addition, a specified heat flux or wall temperature distribution is held constant in time along the solid surfaces. In the present investigation, a specified heat flux given by

$$q_{wall} = -k \frac{\partial T}{\partial n} \quad (8)$$

is prescribed over all solid surfaces at a level consistent with the experimental conditions. Upon discretizing Eq. 8 using a first order backward difference, a Neumann boundary condition arises which is held during the implicit sweep of lines normal to the surface. The implicit update of the solid boundary flow variables is followed by a second order accurate explicit update. Further information describing the implementation of the boundary conditions can be found in Refs. [12, 13, 14].

Turbulence/Transition Model

The Baldwin-Lomax [9] two-layer algebraic turbulence model is used to represent the turbulent eddy viscosity in the flow field. This turbulence model is based upon two-dimensional boundary layer data, and as such, is not well suited for corner flows such as those at the blade/endwall juncture. Previously, the treatment used to implement this turbulence model in the corner regions was the technique proposed by Hung and Buning [15, 16]. In this technique, the Baldwin-Lomax turbulence model is computed separately for each endwall and the blade surface. The mixing length in the corner region depends on the computational indices of a given node. For instance, consider the case when the J =constant computational lines run normal to the blade surface and the K =constant lines run normal to the endwall. For any computational node whose J -wise index is less than its K -wise index, the 'normal' distance is defined as the distance from the blade surface to the grid point and the 'parallel' distance is defined as the distance from the endwall to the grid point. The mixing length for the inner region of the boundary layer is then calculated as

$$l = 2sn/(s + n + \sqrt{s^2 + n^2}) \quad (9)$$

where s is the parallel distance and n is the normal distance. The eddy viscosity is then based on the flow variables along a computational grid line from the airfoil surface (normal direction) to the grid point under consideration. Likewise, for any computational node whose J -wise index is greater than its K -wise index,

the parallel distance is measured from the blade surface to the grid point and the normal distance is measured from the endwall to the grid point. The eddy viscosity is then based on the flow variables along a computational grid line from the endwall to the grid point. Two significant problems arise from this particular three-dimensional implementation of the Baldwin-Lomax turbulence model. First, the eddy viscosity distribution in the corner regions is discontinuous across the $J=K$ computational lines which can cause large gradients to occur in the velocity field. Secondly, this particular blending is highly dependent upon the computational grid density and stretching in both computational directions. It was determined, based upon numerical simulations, that the steady-state solution in the blade/endwall region was extremely sensitive to changes in the computational grid structure.

In the present investigation, a blending function has been used to smoothly vary the eddy viscosity distribution between the blade and endwall. Separate eddy viscosity distributions are computed for the blade and endwall surfaces along the computational lines which run normal to each surface respectively. The eddy viscosity in the corner flow regions is then computed based upon the following blending function according to the work of Vatsa and Wedan [17]:

$$\mu_T = \frac{d_{ew}^2 \mu_{T_b} + d_b^2 \mu_{T_{ew}}}{d_b^2 + d_{ew}^2} \quad (10)$$

where d_b is the distance from the blade surface to a given node, d_{ew} is the distance from the endwall surface to the node, and μ_{T_b} , $\mu_{T_{ew}}$ are the eddy viscosities computed from the blade and endwall flows, respectively. This type of blending greatly reduces the dependence of the eddy viscosity distribution on the computational grid and creates a smooth eddy viscosity distribution in the corner regions.

As will be shown below, results from a number of computations demonstrate the importance of correctly modelling transition of the flow from laminar to turbulent on the blade surface. In the present investigation in which turbine blade heat transfer is being predicted, the modelling of transition is essential for the accurate prediction of Stanton number distributions. In this study, transition was modelled using a prescribed location for the onset of transition. The onset of transition was varied as a function of span, with the endwalls assumed to be fully turbulent, and mid-span transition beginning at the 20% axial chord location on the suction surface according to the experimental data. Transition was assumed to occur as an instantaneous process. As will be discussed below, a means of accurately predicting transition especially in turbine blade rows clearly must be developed in order to reliably and accurately predict heat transfer.

Results

A set of viscous three-dimensional numerical simulations of flow through the Langston low speed turbine cascade with a thin inlet boundary layer (0.41 cm), including heat transfer and transition, have been performed and the predicted results compared to experimental data [1, 2]. The heat flux values at the endwall and airfoil surfaces were specified to be the same as in Ref. [2]. The inlet Mach number was set to $M_1 = 0.0917$ and the inlet flow angle was specified to be $\beta_1 = 44.7$ degrees. The inlet Reynolds number was set to $Re_1 = 25590$ per cm and the ratio of the exit static pressure to the inlet total pressure was fixed at $P_2/P_{t1} = 0.9847$ based on the experimental data.

A computational grid refinement study has been performed to establish the grid density required to produce essentially grid-independent solutions in both the blade-to-blade and spanwise directions. A combination of two- and three-dimensional simulations were performed to establish the required grid density and wall spacing in the blade-to-blade direction to accurately predict turbine blade heat transfer. As a result of the two-dimensional

Case	Grid Density stream × tang × span	Δy_{blade} (y^+)	$\Delta y_{endwall}$ (y^+)	Profile $\Delta P_T/P_{T1}$	Total $\Delta P_T/P_{T1}$	Profile β_2	Total β_2	Trns
1	H-70 × 31 × 25 O-101 × 31 × 25	0.00100 (4.260)	0.00300 (7.430)	0.20846	0.19065	27.96	27.34	yes
2	H-70 × 31 × 25 O-101 × 31 × 25	0.00010 (0.384)	0.00100 (2.920)	0.16102	0.18373	27.49	27.36	no
3	H-70 × 31 × 25 O-101 × 31 × 25	0.00010 (0.379)	0.00100 (2.781)	0.16100	0.18372	27.49	27.58	yes
4	H-70 × 31 × 51 O-101 × 31 × 51	0.00010 (0.360)	0.00010 (0.266)	0.14575	0.17271	27.67	27.38	yes
5	H-70 × 31 × 71 O-101 × 31 × 71	0.00010 (0.351)	0.00010 (0.266)	0.13898	0.17075	27.73	27.26	yes
6	H-70 × 31 × 91 O-101 × 31 × 91	0.00010	0.00010	0.13051	0.17064	27.75	27.25	yes
2-D	O-131 × 61 H-71 × 21	0.00002 (0.059)	—	0.12030	—	26.58	—	yes
EXPT	—	—	—	0.13000	0.17437	26.80	26.32	—

Table 1: Grid refinement study

simulation, it was determined that a computational grid consisting of 70 × 21 grid points in the H-grid and 131 × 61 grid points in the O-grid with an average wall spacing of .00002 ($y^+ = .059$) produced grid-independent solutions. Once this was established, a similar grid topology and density were used in the blade-to-blade direction for the three-dimensional simulations. The wall spacing adjacent to the airfoil surface was then refined during a series of three-dimensional simulations to insure the accuracy of the three-dimensional blade-to-blade solution. Finally, the spanwise computational grid was refined both in terms of endwall spacing and density until the exit total pressure loss and exit flow angle distributions remained unchanged and exhibited close agreement with the experimental data.

A summary of the cases executed during this investigation are given in Table 1. The columns labelled 'Total' in Table 1 indicate area-averaged values in the spanwise direction, while the columns labelled 'Profile' refer to mid-span values. The area-averaged values were calculated using trapezoidal integration and only the computational grid points at the experimental data locations were included in the integration (a total of 13 locations for the half-span) in order to be consistent with the experimental area-averaged exit loss and flow angle values. The column labelled 'Trns' indicates whether or not transition was modelled. Since the geometry was symmetric about the mid-span, the numerical simulations were performed for only the half-span and a symmetry boundary condition was used along the symmetry plane. The spanwise grid densities given in Table 1 are for the half-span geometry. Figure 1, which illustrates the 'Total' exit flow angle and total pressure loss, \sim Eq. 13) values as a function of grid point density, demonstrates that a half-span grid-independent solution was obtained with approximately 450,000 grid points. Except where noted, the predicted results shown below are for this fine grid (Case 6) solution.

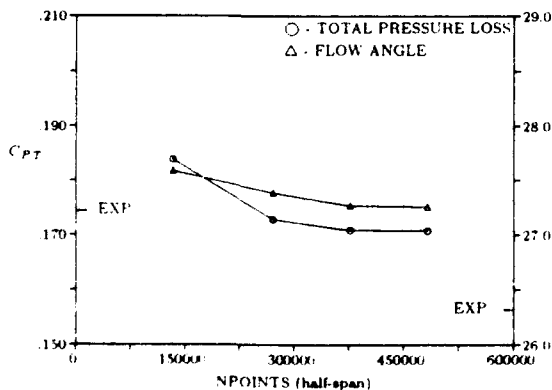


Figure 1: Exit flow angle and total pressure loss as a function of grid point density

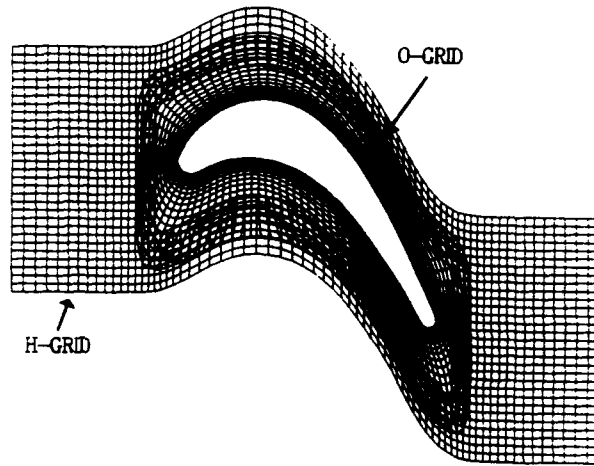


Figure 2: Blade-to-blade computational grid for Langston cascade

Figure 2 illustrates an example of the blade-to-blade computational grid used in the numerical simulations. Planes of blade-to-blade computational grids such as shown in Figure 2 are stacked in the spanwise direction to create the discretized geometry. Computational grid lines are clustered adjacent to the airfoil surface and endwall to properly resolve the viscous flow.

Figure 3 illustrates the predicted fine grid (Case 6) and experimentally measured pressure coefficient distributions along the surface of the airfoil at the 2.9, 12.5, 25.0, and 50.0% span locations, where the pressure coefficient is defined as:

$$C_p = \frac{2(P - P_1)}{\rho U_1^2} \quad (11)$$

and U_1 is the total inlet velocity. Experimental data was taken on two separate blades in the cascade and both sets of data are presented for each spanwise location. There is close agreement between the predicted results and the experimental data for the entire span of the cascade. In both the predicted results (Cases 4-6 in Table 1) and the experimental data the effects of the endwall secondary flow on the pressure distribution are visible on the suction surface of the airfoil near the trailing edge at 12.5% span. This phenomenon was not present in the coarser grid calculations (Cases 1-3).

The predicted and experimental [2] endwall static pressure coefficient contours are illustrated in Figures 4 and 5, respectively. Comparison of the two figures show that the predicted results and experimental data agree very well. Both figures show a pressure "island", corresponding the minimum pressure point, located on the suction surface at approximately 60% axial chord.

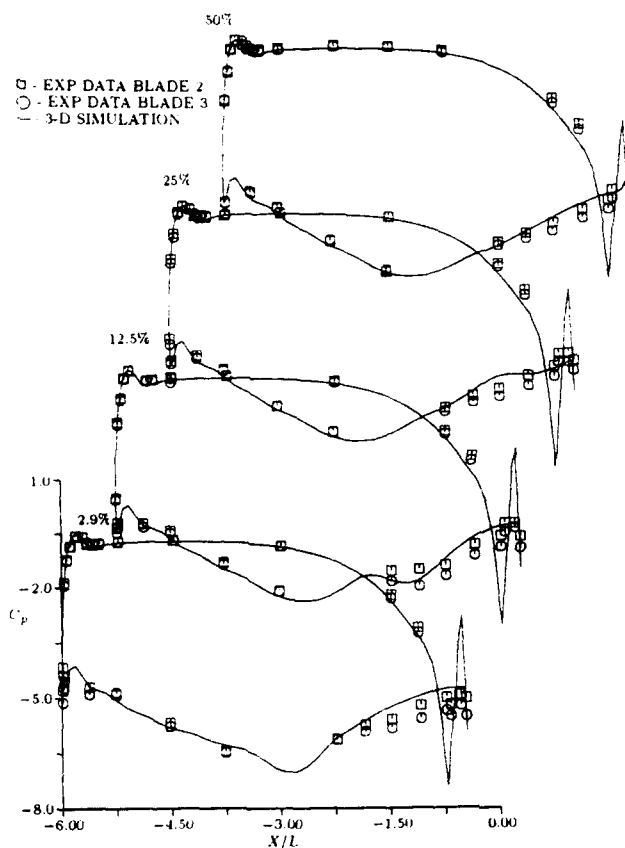


Figure 3: Airfoil surface static pressure coefficient distributions 22

The predicted static pressure coefficient contours for the suction and pressure surfaces of the airfoil are shown in Figures 6 and 7, while the experimental contours for both surfaces are shown in Figures 8 and 9, respectively. It is important to note that Figures 6 and 7 are three-dimensional renderings of the airfoil surface, while Figures 8 and 9 are two-dimensional projections of the airfoil surface. There is good agreement between the predicted results and experimental data on both surfaces of the airfoil. The static pressure island associated with the minimum pressure point, located at 38% axial chord on the suction surface, is shown in both the predicted and experimental results. The effects of the endwall boundary layer are visible in Figures 6 and 8 just downstream of the mid-axial chord location. In both the predicted results and the experimental data, the static pressure changes very little for the first 50% axial chord of the pressure surface (see Figures 7 and 9), then decreases very rapidly as the flow accelerates near the trailing edge.

The predicted limiting streamlines for the suction surface of the airfoil are shown in Figure 10. Limiting streamlines obtained experimentally using surface flow visualization techniques are included for comparison in Figure 11. The predicted limiting streamlines (Figure 10) show close agreement with the experimental data. The flow in the mid-span region of the suction surface is two-dimensional, while the flow in the endwall region is highly three-dimensional. A separation streamline forms at the airfoil leading edge in the endwall region and extends spanwise to approximately the 25% span position at the trailing edge. As the flow moves towards the exit of the blade passage, it is forced towards mid-span by the endwall secondary flow. The predicted pressure surface limiting streamlines are shown in Figure 12. The corresponding experimental pressure surface limiting streamlines are presented in Figure 13. The leading edge stagnation line is well illustrated in Figure 12 and it is evident from both the predicted and experimental limiting streamlines that the flow on the pressure surface is predominantly two-dimensional in nature.

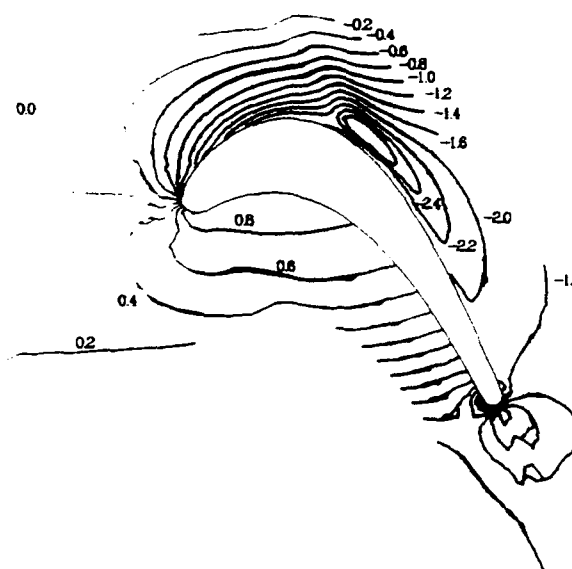


Figure 4: Predicted 3-D endwall static pressure coefficient contours

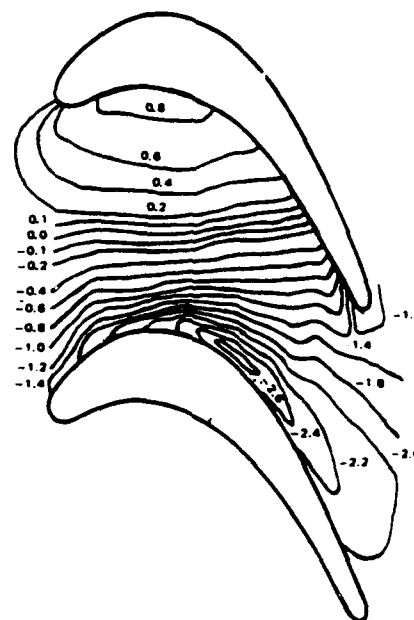


Figure 5: Experimental 3-D endwall static pressure coefficient contours

The predicted endwall limiting streamlines from the fine grid simulation are shown in Figure 14, while the experimental endwall limiting streamlines are shown in Figure 15. In both Figures 14 and 15, a saddle point is evident near the pressure surface leading edge of the airfoil. In the numerical simulation, the saddle point location is predicted somewhat further upstream than that observed in the experiment. This may indicate that the predicted endwall boundary layer is slightly too thick. In Reference [2] it was demonstrated that the location of the saddle point moves upstream as the endwall boundary layer is thickened. In both Figures 14 and 15, the flow in the leading edge region moves onto the suction side of the passage and intersects the suction surface near the minimum pressure point. The flow on the pressure side of the passage migrates towards the suction surface, intersecting it in the region downstream of the minimum pressure point.

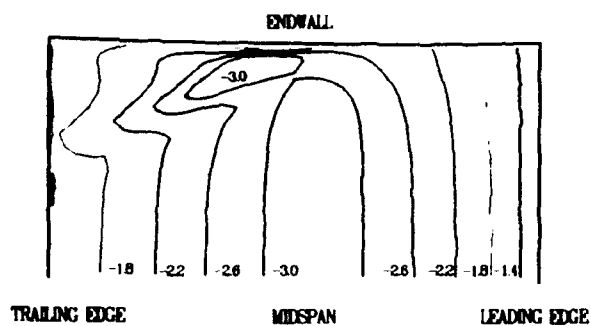


Figure 6: Predicted suction surface static pressure coefficient contours

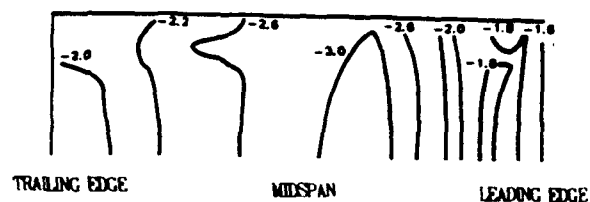


Figure 8: Experimental suction surface static pressure coefficient contours

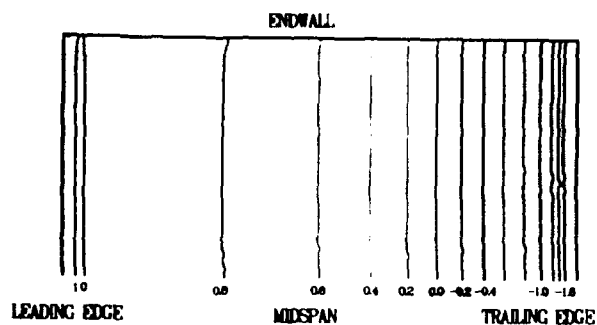


Figure 7: Predicted pressure surface static pressure coefficient contours

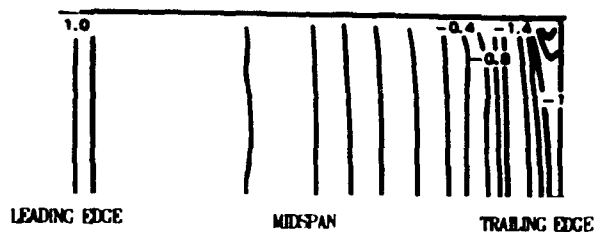


Figure 9: Experimental pressure surface static pressure coefficient contours

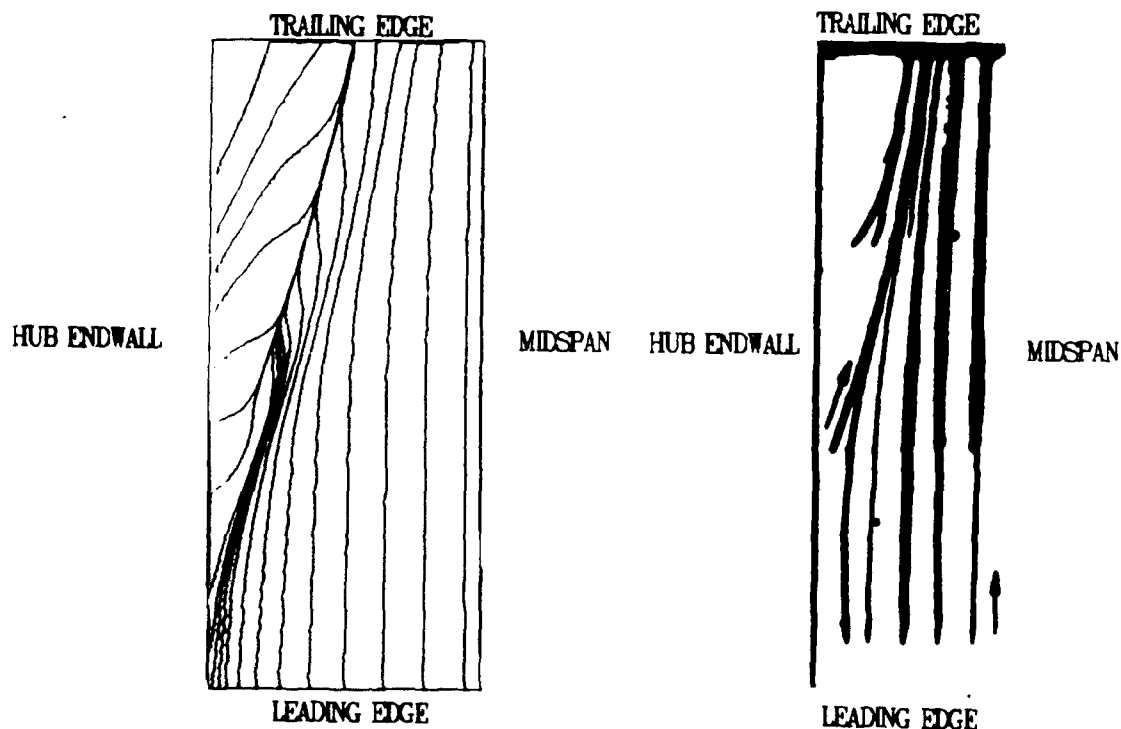


Figure 10: Predicted suction surface limiting streamlines



Figure 11: Experimental suction surface limiting streamlines

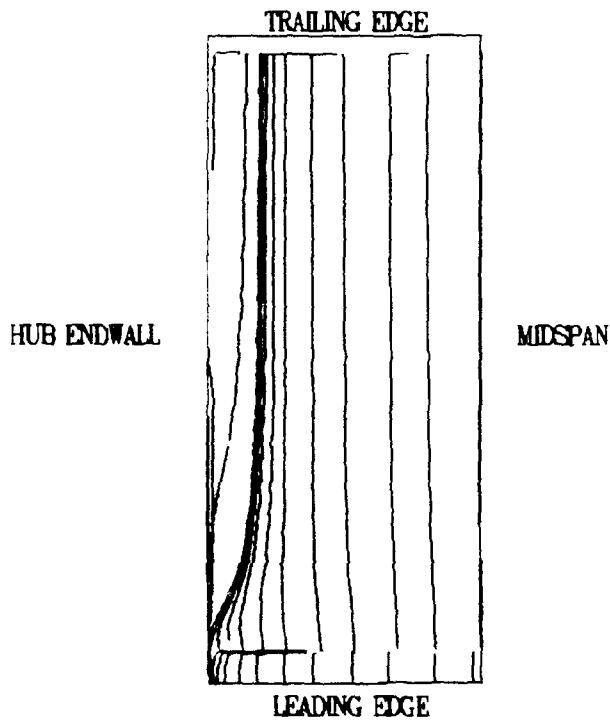


Figure 12: Predicted pressure surface limiting streamlines

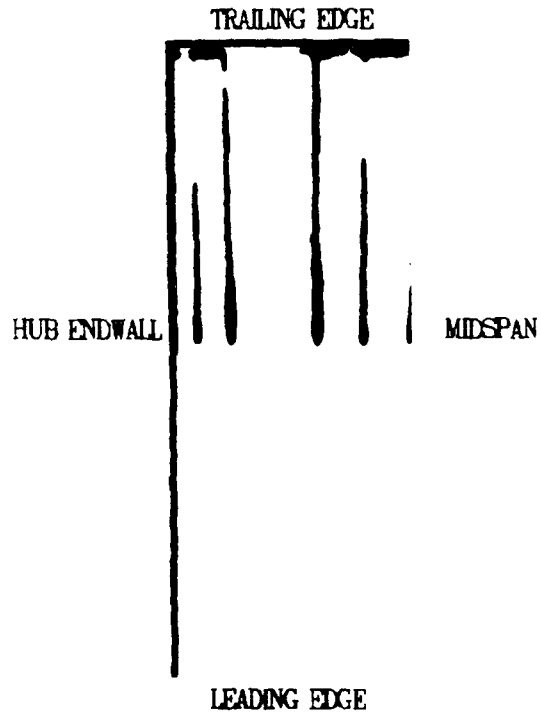


Figure 13: Experimental pressure surface experimental limiting streamlines

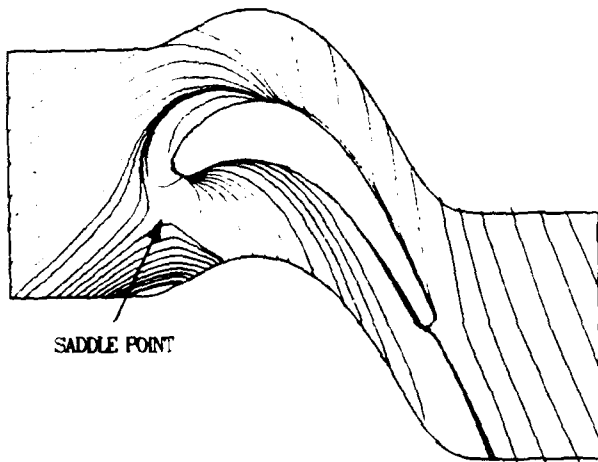


Figure 14: Predicted endwall limiting streamlines

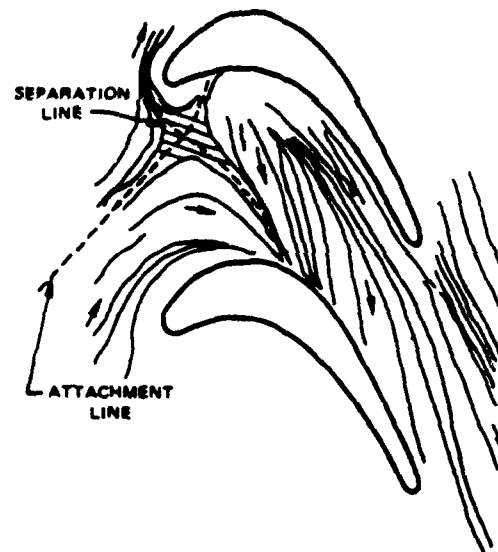


Figure 15: Experimental endwall limiting streamlines

To assess the ability of the present Navier-Stokes analysis to predict heat transfer, the Stanton number was calculated along the surface of the airfoil and compared with the experimental data [2]. The Stanton number is defined as:

$$St = \left(\frac{\partial h}{\partial n} \right) / (RePr(h_{aw} - h_w)) \quad (12)$$

and n is the normal distance from the wall, h_{aw} is the adiabatic enthalpy at the wall, and h_w is the enthalpy at the wall. Figure 16 compares the predicted suction surface mid-span Stanton number distributions obtained with and without transition, the predicted results from the two-dimensional simulation, and the experimental data. The fully turbulent calculation overpredicts the Stanton number in the first 25% of the axial chord, demonstrating the importance of modelling transition. As discussed earlier, mid-span

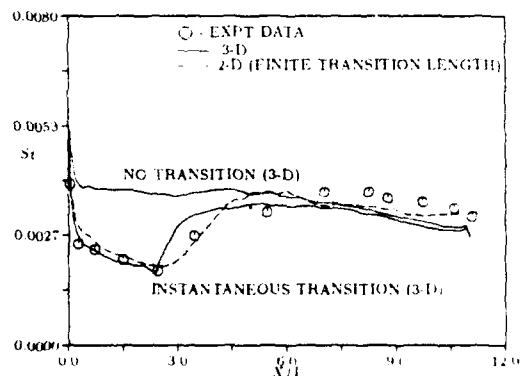


Figure 16: Mid-span suction surface Stanton number distributions

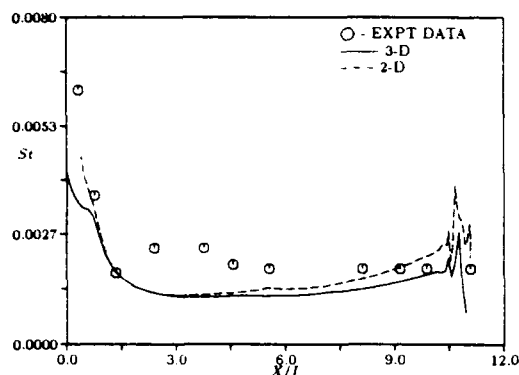


Figure 17: Mid-span pressure surface Stanton number distributions

transition was prescribed, according to the experimental data, to be instantaneous at the 25% axial chord position. The effects of transition are evident from the rapid increase in the Stanton number at the 25% axial chord location. The Stanton number is predicted very well ahead of transition but is slightly underpredicted aft of the transition point. It has been found, based upon a number of two-dimensional simulations, that this small discrepancy is due to the instantaneous transition model currently used in the three-dimensional procedure. Very good agreement was found to exist between the predicted Stanton number distribution and the experimental data in the two-dimensional simulations when transition was modelled over a region extending between 25 - 60% axial chord (see Figure 16).

A comparison of the predicted three-dimensional mid-span pressure surface Stanton number distribution with the experimental data is presented in Figure 17. The three-dimensional predicted results demonstrate only fair agreement with the experimental data. A series of two-dimensional simulations were performed to determine if the differences between the predicted Stanton number and the experimental data near the 25% axial chord location was due to transition, similar to the suction surface. The results from these two-dimensional simulations showed that transition had little effect on the pressure side Stanton number distribution in this region of the flow. Further investigation is required to determine the contributing factor of this difference.

The predicted three-dimensional fine grid suction surface Stanton number contours are shown in Figure 18. The experimental suction surface Stanton number contours are illustrated in Figure 19. The predicted results demonstrate good quantitative agreement with the experimental data, except along the hub endwall downstream of the separation streamline, where the experimental data indicates increased amounts of heat transfer. In Figure 20, the variation of the transition location with span is apparent in the leading edge endwall regions. Both the predicted results and the experimental data indicate enhanced heat transfer at the airfoil leading edge in the endwall regions and downstream of the endwall separation line.

Figures 20 and 21 illustrate the predicted fine grid and experimental Stanton number contours for the pressure surface. The predicted Stanton number distribution shows close agreement with the experimental data. Both the predicted results and the experimental data reveal much less heat transfer taking place on the pressure surface, as indicated by smaller values of the Stanton number.

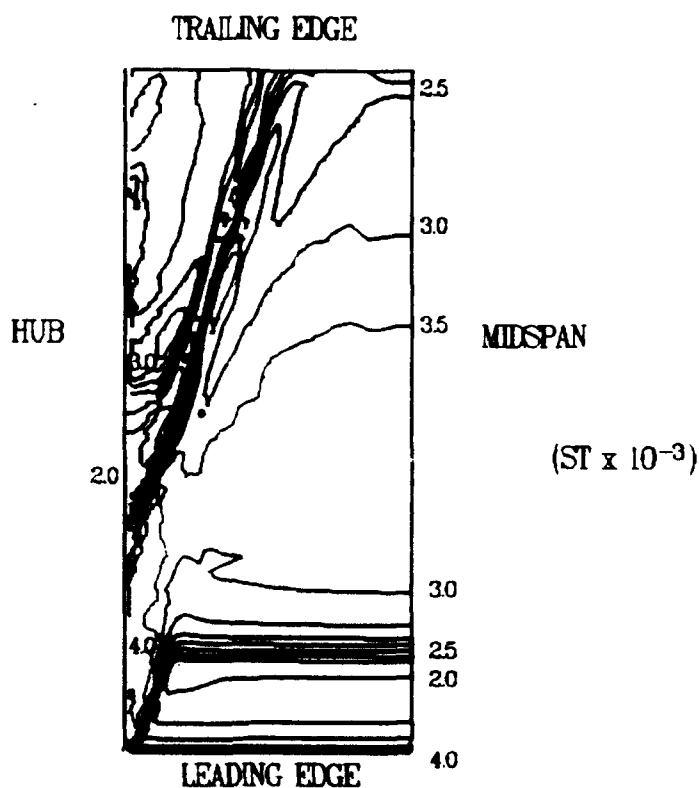


Figure 18: Predicted suction surface Stanton number contours

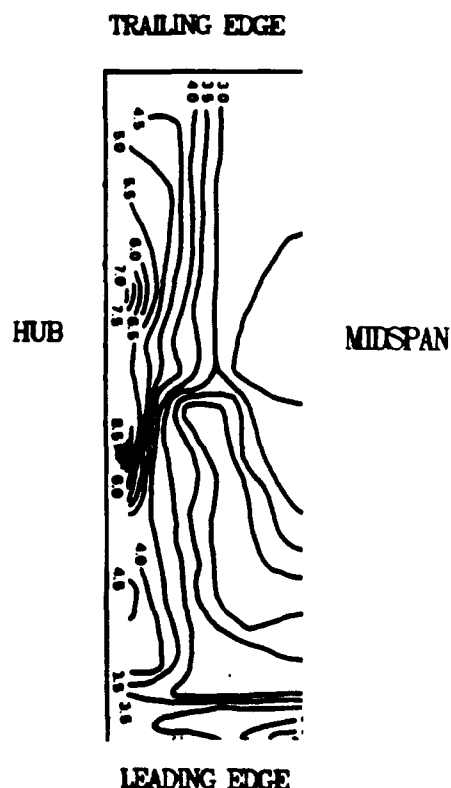


Figure 19: Experimental suction surface Stanton number contours

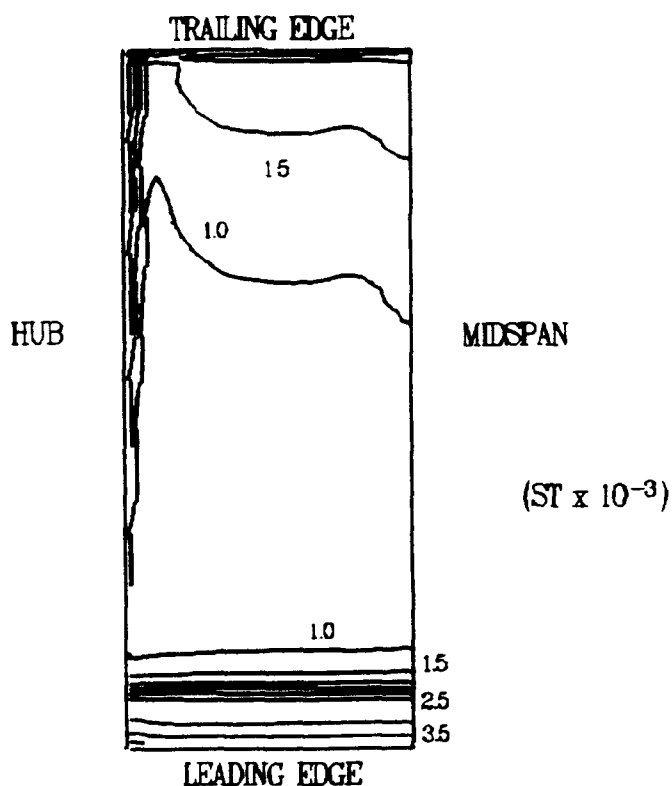


Figure 20: Predicted pressure surface Stanton number contours

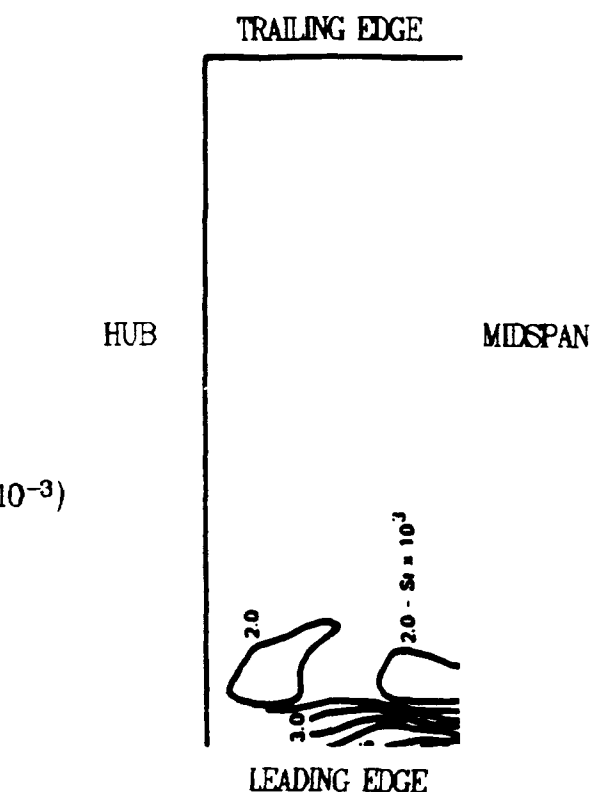


Figure 21: Experimental pressure surface Stanton number contours

Figures 22 and 23 present the predicted fine grid and experimental Stanton number contours for the endwall. In both the predicted results and the experimental data, the lowest values of the endwall Stanton number are located on the pressure surface, beginning just downstream of the saddle point and extending to the trailing edge. In both figures, a region of increased heat transfer is located near the suction surface leading edge and in the vicinity of the minimum pressure point on the suction surface.

In the wake region, discrepancies exist between the predicted results and the experimental data. The predicted results indicate a small amount of heat transfer in the wake region, while the experimental data indicates larger amounts of heat transfer. These discrepancies are probably due to the use of an O-grid around the airfoil, which precludes the use of wake modelling in the algebraic turbulence model. Other than in the wake region, the predicted results show good agreement with the experimental data.

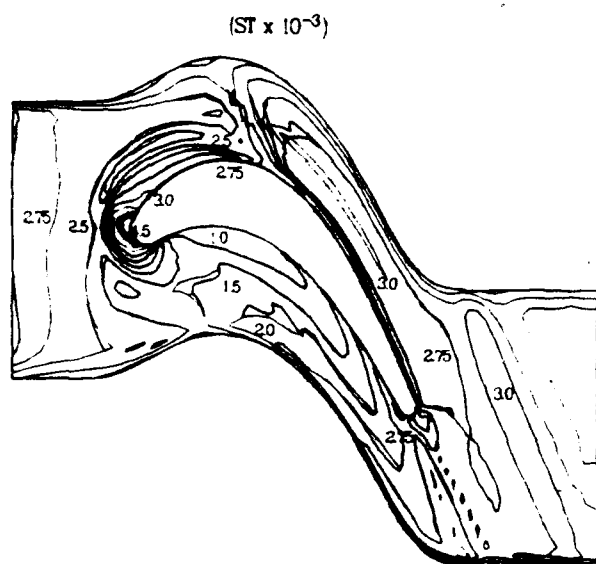


Figure 22: Predicted endwall Stanton number contours

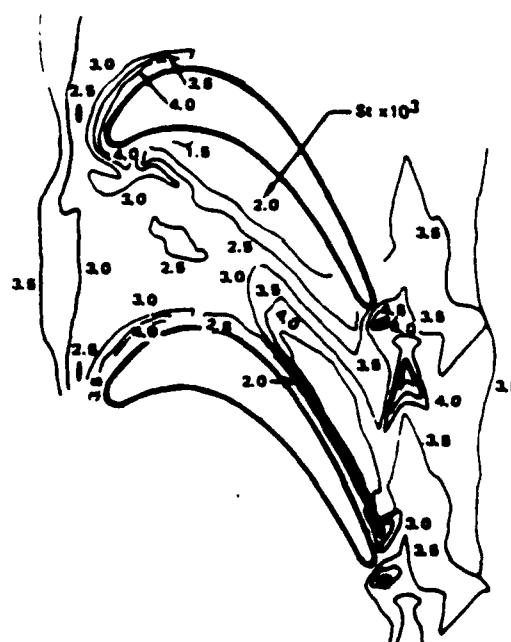


Figure 23: Experimental endwall Stanton number contours.

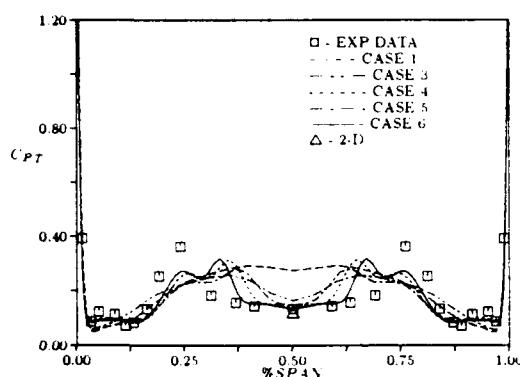


Figure 24: Gap-averaged total pressure coefficient distributions

The predicted spanwise distributions of the total pressure loss coefficient downstream of the trailing edge for all of the cases given in Table 1 are compared with the experimental data in Figure 24. The total pressure loss coefficient is defined as:

$$C_{PT} = \frac{2(P_T - P_{T1})}{\rho U_1^2} \quad (13)$$

The mid-span profile loss is accurately predicted using the fine grid, but overpredicted using the coarser grids. The predicted fine grid spanwise loss distribution shows similar features as the

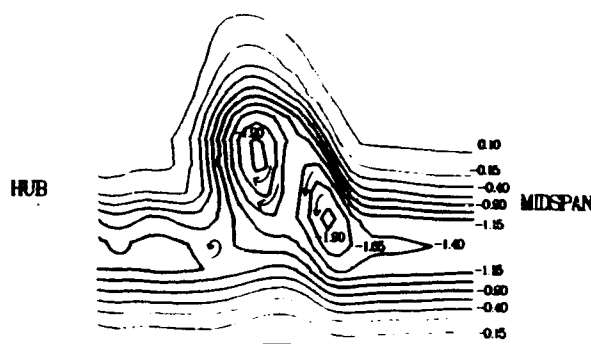


Figure 25: Predicted total pressure loss coefficient contours at exit of turbine passage

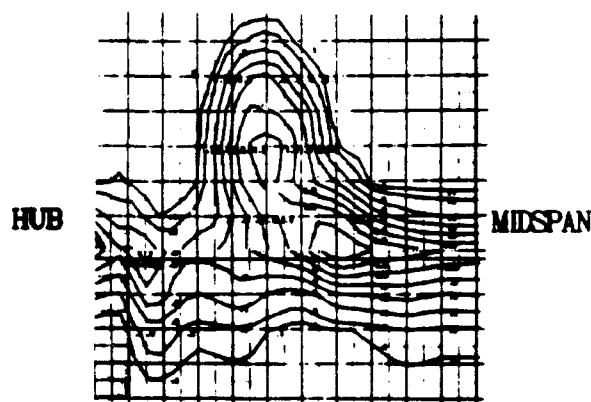


Figure 26: Experimental total pressure loss coefficient contours at exit of turbine passage

experimental data. The profile loss at mid-span is predicted very well by the current procedure, but the peak loss region near the 25% span location is not being accurately predicted. The predicted loss in this region associated with the secondary flow is predicted to be lower and more towards mid-span. The small rise in the predicted loss distribution in the endwall region (Cases 5-6) agrees well with the experimental data.

Table 1 provides the area-averaged total pressure loss for each of the curves shown in Figure 24. These values of area-averaged loss were computed using C_{PT} values at the experimental data locations in order to be consistent. Table 1 shows that for the finest grid solution, a 2% error exists between the predicted and experimental area-averaged losses. The primary source of this error is the underprediction of the secondary flow loss near the 25% span location as shown in Figure 24. Since an essentially grid-independent solution was achieved using the finest grid (see Figure 1), this error can be mainly attributed to the algebraic turbulence model and the transition model.

Figures 25 and 26 illustrate the predicted and experimental total pressure loss contours at the exit plane of the turbine passage. The effects of the passage vortex and endwall secondary flow on the total pressure loss distribution are accurately predicted by the numerical analysis. Both the predicted and the experimental total pressure loss contours indicate the existence of three peak loss regions. These peak loss regions may be associated with three separate vortices which form a triangle bounded by the airfoil suction surface and the hub endwall. The largest vortex, associated with the secondary flow, is located at the apex of the triangle [2]. By examining the vorticity field, it was determined that the secondary flow vortex rotates in the clockwise direction (see Figure 25). A slightly smaller vortex, which may possibly be associated with the suction side leg of the horseshoe vortex, rotates in the counter-clockwise direction and is located more towards the mid-span region than the secondary flow vortex [2]. The smallest vortex, which may be associated with the suction side corner vortex, also rotates in the counter-clockwise direction and is located closer to the hub endwall than the other two vortices.

The predicted spanwise distribution of the gap-averaged flow angle (in the pitch-wise direction) downstream of the trailing edge for the cases given in Table 1 are compared with the experimental data in Figure 27. The shape of the predicted three-dimensional flow angle distribution demonstrates good qualitative agreement with the experimental data, but the numerical values are uniformly larger than the experimentally measured flow angles by approximately 1 degree. As shown in Table 1, the exit flow angle changed very little with increasing grid density, indicating that grid dependence is not the cause of the discrepancy between the predicted and experimental flow angles. The 3.5% difference between the predicted area-averaged exit flow angle and the experimental data could possibly be due to inadequacies in the modelling of transition and turbulence.

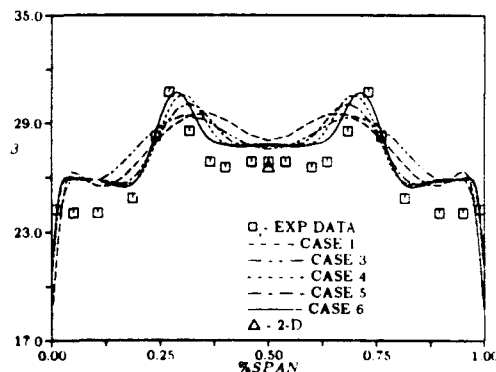


Figure 27: Gap-averaged flow angle distributions

Conclusions

A three-dimensional, implicit, upwind Navier-Stokes procedure has been used to predict heat transfer and aerodynamic performance quantities in the Langston cascade for a thin inlet boundary layer. A grid resolution study has been performed which indicates that approximately 900,000 (full span) computational grid points are required for a single turbomachinery blade row to produce grid-independent solutions for flows at Reynolds numbers typical of those in gas turbine engines. In addition, this study has shown that overall aerodynamic turbomachinery blade row performance can be predicted within 2% using these fine computational grids with the Baldwin-Lomax algebraic turbulence model. Also, the importance of modelling transition from laminar to turbulent flow within the blade passage for the accurate prediction of heat transfer is demonstrated. Clearly, further progress in reducing the computational time required for three-dimensional Navier-Stokes procedures is required to enable reliable and affordable grid-independent solutions for turbomachinery blade row flows. This capability is required before major improvements in turbulence modelling can be made and three-dimensional heat transfer and aerodynamic performance quantities can be routinely and accurately predicted.

Acknowledgements

This work was supported by the Naval Air Systems Command under NAVAIR contract N00140-88-0677 from the office of George Derderian with Raymond Shreeve of the Naval Post Graduate School acting as technical monitor and the United Technologies Research Center under the Corporate Research Program. The three-dimensional simulations performed during this investigation were performed on the NAS Numerical Aerodynamic Simulation CRAY-2 supercomputer. The authors would like to thank Man Mohan Rai and Linda Haines of the NASA Ames Research Center for assistance in computational aspects of this investigation. The authors appreciate the helpful discussions with Om Sharma of Pratt & Whitney and Mike Blair and Bob Dring of the United Technologies Research Center concerning interpretation of the experimental results.

References

- [1] Langston, L. S., Nice, M. L., and Hooper, R. M., "Three-Dimensional Flow Within a Turbine Cascade Passage," ASME Paper No. 76-GT-50, March, 1976.
- [2] Graziani, R. A., Blair, M. F., Taylor, J. R., and Mayle, R. E., "An Experimental Study of Endwall and Airfoil Surface Heat Transfer in a Large Scale Turbine Blade Cascade," *Journal of Engineering for Power*, Vol. 102, No. 2, April, 1980, pp.257-267.
- [3] Chan, D. C. and Sheedy, K. P., "Turbulent Flow Modeling of a Three-Dimensional Turbine," AIAA Paper 90-2124, July, 1990.
- [4] Hah, C., "Numerical Study of Three-Dimensional Flow and Heat Transfer Near the Endwall of a Turbine Blade Row," AIAA Paper 89-1689, June, 1989.
- [5] Hah, C., "A Navier-Stokes Analysis of Three-Dimensional Turbulent Flows Inside Turbine Blade Rows at Design and Off-Design Conditions," *Journal of Engineering for Gas Turbines and Power*, Vol. 106, April, 1984, pp. 421-429.
- [6] Moore, J. and Moore, J. G., "Performance Evaluation of Linear Turbine Cascades Using Three-Dimensional Viscous Flow Calculations," *ASME Journal of Engineering for Gas Turbines and Power*, October, 1985.
- [7] Moore, J. and Ransmayr, A., "Flow in a Turbine Cascade: Part I - Losses and Leading Edge Effects," *ASME Journal of Engineering for Gas Turbines and Power*, Vol. 106, April, 1984, pp. 400-408.
- [8] Lee, D. and Knight, C. J., "Evaluation of an O-H Grid Formulation for Viscous Cascade Flows," AIAA Paper 89-0207, January, 1989.
- [9] Baldwin, B. S. and Lomax, H., "Thin-Layer Approximation and Algebraic Model for Separated Turbulent Flows," AIAA Paper 78-257, January, 1978.
- [10] Roe, P. L., "Approximate Riemann Solvers, Parameter Vectors, and Difference Schemes," *Journal of Computational Physics*, Vol. 43, pp.357-372, 1981.
- [11] Beam, R. M. and Warming, R. F., "An Implicit Factored Scheme for the Compressible Navier-Stokes Equations," AIAA Paper 77-645, 1977.
- [12] Rai, M. M., "Three-Dimensional Navier-Stokes Simulations of Turbine Rotor-Stator Interaction," *Journal of Propulsion and Power*, Vol. 5, May-June, 1989.
- [13] Rai, M. M. and Madavan, N. K., "Multi-Airfoil Navier-Stokes Simulations of Turbine Rotor-Stator Interaction," AIAA Paper 88-0361, 1988.
- [14] Rai, M. M., "An Implicit, Conservative, Zonal-Boundary Scheme for Euler Equation Calculations," AIAA Paper 85-0488, 1985.
- [15] Hung, C. M. and Buning, P. G., "Simulation of Blunt-Fin Induced Shock Wave and Turbulent Boundary Layer Interaction," AIAA Paper 84-0457, January, 1984.
- [16] Hung, C. M. and McCormack, R. W., "Numerical Solution of Three-Dimensional Wave and Turbulent Boundary Layer Interaction," AIAA Paper 78-161, January, 1978.
- [17] Vatsa, V. N. and Wedan, B. W., "Navier-Stokes Solutions for Transonic Flow Over a Wing Mounted in a Wind Tunnel," AIAA Paper 88-0102, January, 1988.
- [18] Dhawan, S. and Narasimha, R., "Some Properties of Boundary Flow During Transition from Laminar to Turbulent Motion," *Journal of Fluid Mechanics*, Vol. 3, 1958, pp.418-436.
- [19] Johnson, D. A. and King, L. S., "A Mathematically Simple Turbulence Closure Model for Attached and Separated Turbulent Boundary Layers," *AIAA Journal*, Vol. 23, No. 11, November 1985, p. 1684.

Discussion

C. HAH, NASA LEWIS, U.S.A.

- 1) When you use a compressible flow code for the current flow, how did you specify exit static flow condition?
- 2) For Figs. 4 and 5, the experimental data with thick inlet boundary layer shows results (unlike your prediction (footprint of vortex)). Any comments about this?

AUTHOR'S REPLY

- 1) The exit static pressure was obtained from the experimental results.
- 2) The endwall boundary layer in our simulation developed slightly faster than that observed experimentally. Therefore, our boundary layer at the inlet to the blade passage was approximately 3 percent greater than that in the experiment. This may explain the presence of the "footprint" in the numerical predictions and not in the experiment. The use of an algebraic turbulence model in the endwall region may also contribute to the "footprint" phenomenon in the numerical simulation.

L. LANGSTON, UNIV. OF CONNECTICUT, U.S.A.

The endwall static pressure data shown in Fig. 5 is for the thin ($\delta = 0.41$ cm) boundary layer case, where the effects of the secondary flow are less dramatic and less pronounced than for the thick ($\delta = 3.3$ cm) boundary layer case (the case calculated by Hah in Ref. 4) of Ref. 1. The calculated results shown in Fig. 4 would be somewhat indicative of a slightly thicker boundary layer than that of the experiment (Fig. 5). This can be seen by a study of Fig. 6 of Ref. 1. I am somewhat surprised that you are off in the prediction of the exit angle! Your airfoil pressure distributions are very close to the experiment. Since these are a direct measure of lift (and hence, turning) I do not see why the exit angle is off.

AUTHOR'S REPLY

We believe our exit flow angles were accurately calculated, however we agree that the pressure distributions would suggest better agreement between the predicted exit flow angle distribution and the experimental data. The matter is currently being investigated.

D. GREGORY-SMITH, DURHAM UNIV., U.K.

In view of the Durham experience of the sensitivity of the flowfield to assumed laminar flow areas I would ask two questions -

- 1) Did you observe any change in the mobility or strength of the secondary vortex when you added the specified transition point on the suction surface?
- 2) There is evidence of laminar flow on the end walls for this type of cascade. Did you investigate the effect of having a laminar flow specification on the endwall?

One last point, Fig. 1 looks better when plotted as $1/NPOINTS$ rather than $NPOINTS$ (i.e., as total pressure and angle versus mesh spacing).

AUTHOR'S REPLY

1) Yes, when the suction surface was assumed to be fully turbulent, the main passage vortex was observed to migrate more towards mid-span than the experimental data indicated. When transition was specified, the numerical results exhibited closer agreement with the experimental data. This comparison, however, was performed on one of the coarser grids used in the series of simulations. I should also note that in both instances, with and without transition specified, the endwall flow was assumed to be fully turbulent.

2) No, in all the cases investigated the endwall flow was assumed to be fully turbulent. The basis of this decision was careful investigation of the experimental data and discussions with M. Blair, one of the experimental investigators. Based on your experiences at Durham University, I do intend to perform an additional test case with laminar (or transitional) flow specified on the endwall.

CALCULS 3D STATIONNAIRE ET INSTATIONNAIRE DANS UN ETAGE DE TURBINE TRANSSONIQUE

par Alain LEMEUR

Office National d'Etudes et de Recherches Aéronautiques
29, Avenue de la Division Leclerc
92320 - CHATILLON (France)

RESUME

Ce papier est destiné à donner des éléments de réponse aux problèmes très importants suivants :

Quelle est la meilleure approche pour obtenir les caractéristiques moyennes (en espace et en temps) de l'écoulement en utilisant directement un calcul 3D sur un étage complet de turbomachine ?

En effet l'écoulement vrai est complètement 3D et instationnaire. Ceci entraîne qu'une simulation rigoureuse de l'écoulement ne peut être qu'instationnaire. Alors, est-il nécessaire de faire un calcul instationnaire plus ou moins exact ? ou bien peut-on directement faire un calcul stationnaire moyen dans la mesure où l'on ne s'intéresse qu'aux grandeurs moyennes comme c'est souvent le cas au stade de la conception ?

Fondamentalement deux approches différentes sur la façon de mener les calculs sur un étage de turbine HP fortement chargé seront montrées et analysées :

- l'approche stationnaire où l'on redistribue à chaque itération un écoulement moyen entre les deux roues. On obtient ainsi une solution stationnaire moyenne.
- l'approche instationnaire avec prise en compte de plusieurs canaux dans les roues. Le calcul est purement instationnaire avec une périodicité en temps c'est-à-dire qu'à convergence, si l'on obtient un résultat pour un instant donné, on doit retrouver la même chose à l'instant qui correspond à une période supplémentaire. Il suffit alors d'effectuer une moyenne en temps sur une seule période pour obtenir la solution 3D moyenne.

STEADY AND UNSTEADY 3D FLOW COMPUTATION THROUGH A TRANSONIC TURBINE STAGE

by Alain LEMEUR

ABSTRACT

The aim of this paper is to give some information on the following important problems :

What is the best approach in order to obtain the average characteristics of the flow field by directly using a 3D computation on a complete turbomachinery stage ?

As a matter of fact the real flow is absolutely 3D and unsteady. This implies that numerical simulation of the flow must be unsteady.

Therefore is it necessary to make more or less rigorous unsteady computation or can we directly perform averaged steady computation, in so far as we are interested in the averaged data, often required at the design stage ?

Two different ways to carry out computation on a highly loaded turbine stage will be shown and analysed here :

- steady approach where we redistributed at each iteration the average flow between the both rows. In this way we obtained the average steady solution.
- unsteady approach by taking into account several channels on both rows. The computation is purely unsteady with a time periodicity ; i.e., if a result is obtained at time t , we must find exactly the same result at time $t + T$, T being the time period. In these case we have to make a time average over a period in order to obtain the 3D flow field averaged.

1. INTRODUCTION

L'amélioration des performances des moteurs en général et plus particulièrement des turbomachines aéronautiques nécessite à l'heure actuelle la mise en oeuvre de méthodes numériques sophistiquées permettant de donner une bonne restitution de l'écoulement.

Pour obtenir une description correcte de l'écoulement qui est complètement tridimensionnel et instationnaire il faudrait par exemple si on s'intéresse à un étage de turbine, calculer tous les canaux successifs du distributeur et de la roue mobile.

Bien entendu aujourd'hui que ce soit avec la résolution des équations d'Euler et a fortiori celles des équations de Navier-Stokes il n'est pas envisageable de calculer tous les canaux d'un étage de turbine ou de compresseur. Les temps et les coûts de calcul deviendraient prohibitifs surtout dans le cas d'applications systématiques.

Il est donc nécessaire de faire des hypothèses simplificatrices permettant une réduction du nombre de canaux à calculer pour obtenir une solution instationnaire satisfaisante. Par ailleurs il faut savoir si l'on peut effectuer un calcul stationnaire moyen quand seule la solution moyenne est recherchée.

Autrement dit, est-il nécessaire dans le cas où on ne s'intéresse uniquement qu'aux grandeurs moyennes, d'effectuer un calcul 3D instationnaire, puis de faire une moyenne en temps donnant ainsi la solution moyenne ?

Des comparaisons entre les deux approches seront montrées et analysées ainsi que des confrontations calculs-expériences.

2. RAPPELS

De façon à mieux cerner les problèmes qui se posent dans ce genre d'étude il n'est peut être pas inutile de faire quelques rappels sur les phénomènes qui régissent l'écoulement ainsi que sur la méthode de calcul et les hypothèses simplificatrices qui permettent de déterminer les principales grandeurs physiques indispensables à la compréhension de l'écoulement.

2.1. Phénomènes instationnaires

Considérons par exemple un premier étage de turbine (distributeur fixe suivi d'une roue mobile). L'écoulement réel sortant du foyer est fortement non-uniforme aussi bien dans le sens radial qu'azimutal [1] et il faudrait en toute rigueur calculer l'ensemble de la couronne distributrice. On fera ici l'hypothèse que cet écoulement est stationnaire et azimutalement uniforme. Toutefois, même dans ce cas simplifié, l'écoulement dans l'étage est non seulement tridimensionnel par suite du gauchissement des nappes de courant, mais aussi complètement instationnaire à cause de l'interaction des deux roues.

Le nombre d'aubes de chaque roue permet alors de distinguer deux cas :

- soit ces nombres sont identiques et on retrouve donc à chaque instant la périodicité en espace sur un pas.
- dans le 2ème cas qui reflète mieux la réalité, les nombres d'aubes sur les deux roues successives sont en général premier entre eux. Dans cette configuration il est en toute rigueur indispensable de calculer tous les canaux non seulement de la roue fixe mais également de la roue mobile.

Bien entendu dans ce cas on se trouve confronté au problème du coût et des temps de calcul, dû aux nombres de point de maillage très élevés.

Par exemple entre le premier cas et le cas réel il peut y avoir un rapport de 50. Ces nombres prohibitifs imposent d'utiliser des hypothèses simplificatrices.

2.2. Hypothèses simplificatrices

D'après le point développé ci-dessus, on est donc amené à réduire le domaine de calcul à une taille raisonnable. C'est-à-dire de trouver un compromis ayant un bon rapport qualité-prix et donnant des résultats satisfaisants pour la compréhension des phénomènes que l'on désire étudier.

Certaines de ces hypothèses ont déjà été étudiées en détail dans les références [2] et [3]. Mais il n'est peut être pas inutile de rappeler en quelques lignes les principaux éléments qui permettent de faire un calcul approché.

Considérons un étage comportant N_1 aubes dans la roue amont et N_2 dans la roue aval. On choisit tout d'abord deux entiers K_1 et K_2 aussi petits que possible, mais tels que les rapports K_1/K_2 et N_1/N_2 soient voisins. K_1 et K_2 représentent les nombres de canaux effectivement calculés respectivement dans la roue amont et la roue aval.

Les extensions azimutales de chaque groupe de canaux sont :

- pour la roue 1 $e_1 = K_1 p_1 = K_1 \times 2\pi/N_1$
- pour la roue 2 $e_2 = K_2 p_2 = K_2 \times 2\pi/N_2$.

On définit alors une extension moyenne par :

$$e_c = 1/2 (e_1 + e_2)$$

ainsi que :

$$\lambda_1 = e_c/e_1 \quad \lambda_2 = e_c/e_2 \quad \frac{\lambda_1}{\lambda_2} = \frac{e_2}{e_1} = \frac{N_1}{N_2} \times \frac{K_2}{K_1}$$

Les quantités λ_1 et λ_2 servent, au cours du calcul, à dilater ou contracter les gradients azimutaux à l'interface des deux roues de façon à les rapporter à l'extension circonférentielle commune e_c à travers laquelle on assure la continuité axiolo-radiale. Par ce biais il est alors possible d'appliquer la condition de périodicité spatiale sur les frontières hautes et basses de chaque groupe de canaux.

Quelques remarques :

- comme on le voit, il s'agit seulement d'un traitement aux frontières de continuité (frontières fluides internes) du domaine de calcul. En particulier, il est important de noter que les géométries réelles des canaux ne sont pas affectées, et que n'importe quel type de machine peut être pris en compte ;
- les approximations induites sont d'autant plus faibles que K_1/K_2 est proche de N_1/N_2 : la solution est d'ailleurs exacte si $K_1/K_2 = N_1/N_2$;
- il est aisé de démontrer que les valeurs moyennes (dans le temps) de grandeurs globales comme le débit ou la charge sur les roues sont indépendantes du choix des nombres K_1 et K_2 ;
- cette technique peut être étendue à un nombre de roues supérieur à 2 par :

$$e_c = \frac{1}{n} \sum_{i=1}^n K_i \times p_i \quad \lambda_i = e_c/e_i$$

Par exemple si on considère un cas où le rapport N_1/N_2 est voisin de 0,58 la réduction du domaine de calcul peut être $k_1 = 3$ pour la 1ère roue et $k_2 = 5$ pour la 2ème, soit $k_1/k_2 = .60$ ou $k_1 = 1$ et $k_2 = 2$ ce qui donne $k_1/k_2 = .5$.

Des vérifications ont été effectuées en bidimensionnel entre les approximations 1-1, 1-2 et 3-5 évoquées ci dessus et le cas "réel" obtenu par la solution rigoureuse prenant en compte le nombre exact de canaux sur les deux roues, réf. [4].

Les résultats ont montré que les écarts restent faibles entre les trois dernières solutions, alors que le cas 1-1 présente des différences non négligeables.

2.3. Méthode de calcul

Voici brièvement les principales caractéristiques de la méthode utilisée :

Les équations d'Euler (équations de continuité, de quantité de mouvement et d'énergie) sont directement discrétisées dans l'espace physique qui peut comporter plusieurs domaines de calcul. Le repère choisi est un repère cylindrique (R, θ , Z).

Les équations discrétisées sont résolues à l'aide d'un schéma de Mac Cormack, capable de calculer les écoulements compressibles avec ondes de choc.

La viscosité artificielle utilisée est celle de "Tukel et Jameson", réf. [5].

Le traitement des conditions aux limites du domaine (ou des sous-domaines) de calcul utilise la théorie des relations caractéristiques, ou relations de compatibilité. Les détails sur ces techniques numériques pourront être trouvés dans les références [6], [7] et [8].

2.4. Traitement numérique sur l'interface dans le cas stationnaire.

Sur l'interface (frontière commune aux deux roues), la technique de réduction du nombre de canaux exposée au paragraphe 2.2. permet d'appliquer localement la condition de continuité axiolo-radiale. Cette approche est donc fondamentalement instationnaire.

Mais on peut aussi envisager des approches stationnaires en effectuant à chaque itération une moyenne azimutale sur des grandeurs caractérisant l'écoulement. Ces approches ont l'intérêt évident de ne nécessiter qu'un seul canal de calcul par roue ($k_1 = k_2 = 1$).

La première de ces approches consiste à calculer, à chaque rayon, un écoulement azimutalement uniforme, par exemple en calculant une moyenne des grandeurs de calcul ($\rho, \rho v_r, \rho v_\theta, \rho v_z, p, E$). Les conséquences sont les suivantes :

- à l'aval du premier domaine, on impose une pression statique moyenne venant du deuxième domaine.
- à l'amont du second domaine, on impose la pression et la température d'arrêt ainsi que deux angles (valeurs moyennes issues du premier domaine).

Cette approche est cependant rarement utilisable. En effet dans le cas d'un étage de turbine transsonique, il n'est pas réaliste d'imposer une pression constante sur une frontière circonferentielle très proche du distributeur, qui est précisément traversée par des ondes de choc et de détente.

La seconde approche consiste à utiliser de façon originale les possibilités offertes par les relations caractéristiques.

Rappelons ces relations :

$$(1) p^{(n+1)} - (\rho a) V_n^{(n+1)} = p^* - (\rho a) V_n^*$$

$$(2) p^{(n+1)} - (a^2) \rho^{(n+1)} = p^* - (a^2) \rho^*$$

$$(3, 4) \vec{V}_t^{(n+1)} = \vec{V}_t^*$$

$$(5) p^{(n+1)} + (\rho a) V_n^{(n+1)} = p^* + (\rho a) V_n^*$$

où p = pression statique

ρ = masse volumique

a = célérité du son

V_n = vitesse normale à la frontière

\vec{V}_t = vitesse tangentielle

avec les indices supérieurs $(n+1)$: relatif à la $(n+1)^{\text{ème}}$ itération

* : valeurs issues du schéma.

Ces relations sont ordonnées de (1) à (5) selon les valeurs croissantes des valeurs propres. Le choix du vecteur normal détermine la première relation disponible : si la normale entre dans le domaine de calcul, on prend d'abord la relation (1) puis éventuellement (2, 3, 4) enfin (5) (sauf indication contraire, c'est cette convention qui est adoptée).

Sur l'interface, à l'aval de la première roue, la vitesse normale est subsonique et sort du domaine de calcul ($V_{n1} < 0$) : on utilise les quatre premières relations de compatibilité, et une cinquième équation est nécessaire. Celle-ci ressemble à la condition de non réflexion et s'écrit :

$$p^{(n+1)} + (\rho a) V_n^{(n+1)} = \bar{p}_1 + (\rho a) \bar{V}_{n1}$$

Dans les cinq équations, a^2 et a sont calculés au point considéré du domaine 1, à partir des grandeurs "calcul" $\rho, \rho^{v_r}, \rho^{v_\theta}, \rho^{v_z}, \rho E$, au pas de temps précédent, indicé (n) , c'est-à-dire :

$$a^2 = (a^2)_1^{(n)} \quad (\rho a) = (\rho a)_1^{(n)}$$

\bar{p}_1 et \bar{V}_{n1} proviennent du second domaine. Ce sont les moyennes arithmétiques de la pression statique et de la vitesse normale sur le pas de la deuxième roue, (valeurs "schéma"), soit :

$$\bar{p}_1 = \bar{p}_2$$

$$\bar{V}_{n1} = -\bar{V}_{n2} \quad (\text{compte tenu du changement de repère})$$

Un traitement symétrique est effectué à l'amont du second domaine. Là, la vitesse normale, toujours subsonique, entre dans le domaine de calcul ($V_{n2} > 0$). Seule la première relation de compatibilité est disponible :

$$p^{(n+1)} - (\rho a) V_n^{(n+1)} = p^* - (\rho a) V_n^*$$

(évidemment $a^2 = (a^2)_2^{(n)}, \rho a = (\rho a)_2^{(n)}$: domaine aval, itération précédente).

Les autres équations sont :

$$p^{(n+1)} - (a^2) \rho^{(n+1)} = \bar{p}_2 - (a^2) \bar{\rho}_2$$

$$V_t^{(n+1)} = \bar{V}_{t2}$$

$$V_\theta^{(n+1)} = \bar{V}_{\theta 2}$$

$$p^{(n+1)} + (\rho a) V_n^{(n+1)} = \bar{p}_2 + (\rho a) \bar{V}_{n2}$$

dans lesquelles $\bar{p}_2, \bar{\rho}_2, \bar{V}_{t2}, \bar{V}_{\theta 2}, \bar{V}_{n2}$ sont issues de moyennes faites sur un pas du premier domaine, c'est-à-dire :

$$\bar{p}_2 = \bar{p}_1^*$$

$$\begin{aligned}\bar{\rho}_2 &= \bar{\rho}_1^* \\ \bar{V}_{n2} &= -\bar{V}_{n1}^* \quad (\text{changement de repère}) \\ \bar{V}_{t2} &= \bar{V}_{t1}^* \\ \bar{V}_{\theta 2} &= \bar{V}_{\theta 1}^*\end{aligned}$$

Contrairement à la première approche (écoulement azimuthalement uniforme) des gradients en θ existent à l'interface, et le cas d'une turbine transsonique peut être traité sans ennui numérique. Toutefois, ces gradients ne sont pas les mêmes de part et d'autre de l'interface (autrement dit, l'écoulement n'est pas continu axialement). Comme, de plus, cette approche est stationnaire à cause de l'utilisation de moyennes, la signification physique de la solution ainsi obtenue reste discutable dans les cas où l'on soupçonne des effets instationnaires importants. L'un des buts de cet article est précisément d'apporter une réponse à cette interrogation.

2.5. Prise en compte des effets visqueux

La simulation des effets visqueux [9] et [10] consiste à imposer une force pariétale qui a pour effet de ralentir la vitesse de l'écoulement à la paroi. Cette force est directement liée à un coefficient de frottement donné tant que l'écoulement n'est pas ralenti, sinon elle dépend du gradient de vitesse locale.

Par suite de la viscosité numérique nécessaire au calcul, il est créé au voisinage de la paroi, une couche ralentie dont une caractéristique globale peut être identique à celle d'une couche visqueuse comme par exemple la même quantité de mouvement. Le profil des vitesses est certainement différent de celui de la couche visqueuse réelle et en particulier, il n'y a généralement pas de vitesse nulle à la paroi, mais si l'on utilise un maillage adéquat pas trop serré, on peut espérer obtenir une épaisseur globale ayant un ordre de grandeur correct. On notera qu'avec une modélisation aussi simplifiée, il n'est pas possible de simuler à la fin l'épaisseur de déplacement et l'épaisseur de quantité de mouvement, puisque l'on n'agit que sur un paramètre qui est la force à la paroi.

Néanmoins, cette simulation simplifiée des effets visqueux donne, lorsque l'on effectue des comparaisons "calcul-expérience", des résultats satisfaisants dans l'ensemble, par exemple sur les évolutions radiales de certaines grandeurs physiques en aval d'une roue mobile d'un étage de turbine.

3. CARACTERISTIQUES PRINCIPALES DE LA TURBINE ETUDIEE

Les calculs ont été faits avec les caractéristiques suivantes communes aux essais effectués sur la turbine expérimentale :

. Taux de détente	: $\zeta = 3,49$
. Pression d'arrêt amont	: $P_{10} = 3,56 \text{ } 10^5 \text{ Pa}$
. Température d'arrêt	: $T_{10} = 399,7 \text{ K}$
. Rapport des chaleurs spécifiques	: $\gamma = 1,397$
. Chaleur spécifique à pression constante	: $C_p = 1 \text{ } 015 \text{ Jkg}^{-1}\text{K}^{-1}$
. Vitesse de rotation	: $N = 19 \text{ } 600 \text{ t/mn}$
. Nombre d'aubes distributeur	: $Z_1 = 31.$
. Nombre d'aubes roue mobile	: $Z_2 = 53.$

4. DESCRIPTION DU BANC D'ESSAI

Le schéma descriptif du banc d'essai de turbine froide est représenté sur la figure n° 1.

La veine expérimentale est composée, de l'amont vers l'aval, d'un divergent suivi d'une partie cylindrique jusqu'au distributeur. Ensuite, vient la roue mobile qui peut être décalée axialement de façon à effectuer des sondages sur l'interface. Enfin, à l'aval de la roue, il y a une longue partie divergente qui arrive dans un caisson de tranquillisation.

L'installation comporte différents plans de mesure :

Plan 0

Ce plan est à environ 40 mm de l'axe d'empilage du distributeur où il est possible de relever non seulement les pressions statiques aux parois, mais aussi de faire des sondages en pression d'arrêt afin de connaître son évolution radiale en amont du distributeur.

Notons que ce plan de sondage est légèrement en avant de la frontière amont du maillage utilisé pour le calcul.

Plan 1

Ce plan se trouve juste en aval du distributeur. Il est possible de faire des sondages radiaux en pression d'arrêt en retirant la roue mobile de façon à connaître l'évolution que donne le distributeur seul.

Notons que l'exploration de l'écoulement se fait sur un secteur angulaire au moins égal à un canal inter-aubes du distributeur avec une sonde NACA permettant de déterminer les valeurs moyennes en pression statique et en pression d'arrêt.

Plan 2

Ce plan se trouve à l'aval de la roue mobile.

La pression totale moyenne dans le plan de sortie est calculée à l'aide des paramètres suivants :

- . Débit Q.
- . Température totale moyenne prise égale à la température dans la chambre de tranquillisation.
- . Pression statique P.
- . Angle moyen de l'écoulement par rapport à l'axe de la machine.

De plus, sur les distributeurs il existe, pour trois hauteurs différentes, un certain nombre de prises de pression, aussi bien sur l'extrados que sur l'intrados, permettant de connaître la distribution de pression. Il existe également dans le canal inter-aubes un certain nombre de prises de pression aussi bien sur le moyeu que sur le carter extérieur.

5. RAPPELS SUR LES RESULTATS INSTATIONNAIRES DEJA OBTENUS

Avant d'analyser les résultats de calcul obtenus par les différentes approches dont nous avons parlé plus haut, il n'est pas inutile de rappeler les ordres de grandeurs des fluctuations instationnaires de l'écoulement, déjà largement analysées dans la référence [11].

Par exemple les variations de l'angle relatif en amont d'une roue mobile de turbine ainsi que les variations des débits donnent une bonne idée de l'importance de ces effets instationnaires.

5.1. Cas sans perte

L'évolution en fonction du temps des valeurs locales de l'angle relatif pour la coupe de pied et pour la coupe de tête sont représentées, sur les figures 2 et 3 pour différentes positions azimutales repérées par le schéma de la figure 2.

Une analyse des évolutions montre que les amplitudes ont des valeurs élevées de l'ordre de 23 à 24° au centre non seulement pour la coupe de pied mais également pour la coupe de tête.

Les planches 4 et 5 montrent les variations de débit instantanées en fonction du temps, au bord d'attaque et au bord de fuite, dans les deux canaux de la roue mobile. Il est visible en examinant ces évolutions que, à chaque instant, les variations de débit dans chaque canaux sont relativement grandes. L'on remarque également que les amplitudes sont plus faibles à la sortie qu'à l'entrée de la roue, celle-ci jouant probablement un rôle d'amortisseur pour le fluide qui la traverse.

5.2. Cas avec pertes

De même que dans le cas sans perte l'évolution en fonction du temps des valeurs locales de l'angle relatif pour la coupe de pied et la coupe de tête sont représentées sur les planches 6 et 7 pour différentes positions azimutales de la roue mobile défilant devant son distributeur.

L'analyse des évolutions montre que dans le cas avec pertes, les amplitudes ont des valeurs beaucoup plus élevées que dans le cas sans coefficient de frottement constant aux parois. Par exemple, au centre du canal c'est-à-dire devant l'aube centrale, on relève une amplitude de l'ordre de 32°, soit approximativement 10 à 12° de plus que dans le cas sans perte, suivant que l'on considère la coupe de pied ou la coupe de tête.

Comme dans le cas sans perte, il est indiqué sur les figures 8 et 9 les variations du débit instantanées en fonction du temps, juste après le bord d'attaque et juste avant le bord de fuite, des deux canaux relatifs à la roue mobile.

Si on effectue une comparaison de ces évolutions avec les planches 4 et 5, il est visible que les amplitudes sont beaucoup plus fortes dans le cas avec pertes que dans celui où il n'y a pas de frottement à la paroi pour l'évolution concernant l'entrée de la roue, et du même ordre de grandeur pour celles qui concernent la sortie des canaux.

Pour terminer ces rappels indiquons que le fait d'avoir une simulation des effets visqueux diminue les effets instationnaires sur les aubes de la roue mobile. D'après ce qui précède on voit donc que les effets instationnaires sont très importants. D'ailleurs cela a été mis en évidence par des animations numériques du champ des pressions sur les aubes d'un étage complet.

6. RESULTATS DE CALCUL

Dans ce paragraphe nous allons considérer deux cas bien distincts à savoir les calculs sans et avec pertes, ces deux cas étant eux-mêmes découplés en deux parties différentes c'est-à-dire les calculs avec l'approche stationnaire et ceux avec l'approche instationnaire suivis d'une moyenne en temps de façon à obtenir la solution de l'écoulement moyenné.

Les maillages utilisés sont présentés sur la figure 10. La figure 10a représente le cas où l'on prend en compte un canal dans le distributeur et deux canaux dans la roue mobile et la figure 10b représente le maillage méridien utilisé dans tous les cas.

Différentes grandeurs telles que le Mach relatif, l'angle relatif et l'angle absolu qui sont des grandeurs bien représentatives de l'écoulement seront montrées et analysées dans différents plans successifs. Pour fixer les idées les plans seront repérés par rapport au bord d'attaque et au bord de fuite de la roue mobile. En ce qui concerne les deux plans en amont de la roue mobile les abscisses sont respectivement $x = -3,05$ mm et $x = 0,37$ mm. De même pour les quatre plans en aval du bord de fuite les distances sont : $x = 1,323$ mm, $x = 6,764$ mm, $x = 8,654$ et $x = 16,591$ mm.

6.1. Calcul sans perte

Les calculs sont effectués avec des coefficients de viscosités artificielles et des paramètres aérodynamiques identiques dans les différents cas de façon à faire des comparaisons valables.

6.1.1. Résultats avec l'approche stationnaire

Dans ce cas on redistribue à chaque itération certaines grandeurs moyennes (voir paragraphe 2.4) sur l'interface entre les deux domaines de calcul jusqu'à obtention d'une bonne convergence. On obtient alors la solution moyenne des grandeurs physiques régissant le fonctionnement de l'étagé.

Les figures 11 et 12 montrent les évolutions des 3 paramètres choisis pour les deux plans amont et les quatre plans aval. On remarque qu'il y a une certaine évolution radiale en fonction du cheminement amont-aval en particulier en tête, en ce qui concerne les angles amont et pour toutes les grandeurs dans la zone en aval de la roue mobile.

6.1.2. Résultats avec l'approche instationnaire

Cette fois le calcul est purement instationnaire et il suffit lorsque les critères de convergence sont atteints d'effectuer sur une seule période une moyenne en temps pour obtenir la solution de l'écoulement moyenné. Deux cas sont alors à distinguer soit il a été effectué un calcul en prenant en compte un seul canal sur chaque roue, soit de façon à améliorer la prise en compte des effets instationnaires comme il a été expliqué au paragraphe 1 le calcul est effectué avec prise en compte d'un canal côté distributeur et de 2 canaux sur la roue mobile.

a) Cas 1-1

Comme il a déjà été dit dans les références [3], [4] le cas où l'on prend en compte 1 canal dans chaque roue donne des résultats du point de vue uniquement instationnaire différents du cas 1-2. Malgré ces différences qui sont loin d'être négligeables on pouvait se poser la question de savoir si oui ou non les moyennes en temps étaient susceptibles de donner les mêmes résultats ou du moins des résultats identiques.

Les figures 13 et 14 présentent les résultats pour les différents plans considérés et les remarques effectuées dans le cas ci-dessus sont applicables dans cette configuration.

b) Cas 1-2

Du point de vue instationnaire cette configuration se rapproche plus de la réalité. Comme dans les cas précédents les évolutions radiales des différentes grandeurs caractéristiques sont données sur les planches 15 et 16 avec les mêmes remarques déjà dites ci-dessus. On peut quand même ajouter que les évolutions en grandeurs sont relativement fortes entre des plans éloignés, mais que les écarts sont faibles entre deux plans très proches. Ceci permet d'éviter des interpolations lorsque l'on veut des résultats moyens pour une même abscisse alors que les lignes de maillage sont très faiblement inclinées dans le sens radial.

6.1.3. Comparaison entre les deux approches sans perte

Les moyennes entre les cas où l'on prend en compte 1 canal sur chaque roue et le cas où il y a deux canaux sur la roue mobile, donnant rigoureusement les mêmes résultats les comparaisons ne sont faites qu'entre les cas 1-1 stationnaire et 1-2 instationnaire plus moyenne en temps. De plus pour les comparaisons en aval de la roue mobile les confrontations entre les deux approches ne sont faites que dans trois plans, le plan intermédiaire étant celui correspondant au plan où sont relevés les grandeurs expérimentales c'est-à-dire celui dont la distance au bord de fuite est $x = 8,654$ mm.

La figure 17 présente les comparaisons pour les évolutions radiales du nombre de Mach relatif moyen pour les deux plans situés en amont du bord d'attaque de la roue mobile. Dans le plan situé le plus en amont on constate qu'il y a une légère différence constante sur toute la hauteur de la pale. Pour le plan situé juste devant le bord d'attaque l'écart est pratiquement nul pour les 50 % côté coupe de tête alors que du côté de la coupe de pied les différences sont plus significatives tout en restant faibles. La figure 18 montre les comparaisons pour les angles moyens. On constate des écarts

très faibles dans le plan amont et pratiquement pas d'écart sauf du côté coupe de pied pour les résultats dans le plan juste en amont du bord d'attaque. Notons pour fixer les idées que ces petites variations sont inférieures au degré.

Les planches 19, 20 et 21 donnent les comparaisons des évolutions radiales pour les trois grandeurs physiques considérées et cela dans les différents plans en aval de la roue mobile. En ce qui concerne le nombre de Mach il n'y a pas de différence pour les deux premiers plans dans le 3ème plan un très léger écart apparaît du côté coupe de tête.

Pour l'évolution radiale des angles relatifs moyens on notera que les écarts sont là aussi très faibles, de l'ordre de $0,5^\circ$ et que pour les angles absolus moyens, les écarts peuvent atteindre $1,5^\circ$ localement du côté de la coupe de tête.

Remarque : Il est déjà possible de dire que dans le cas des calculs effectués en fluide parfait il n'y a pas ou presque pas de différence sur les évolutions radiales des paramètres caractéristiques de l'écoulement entre les différentes façons de mener les calculs.

6.2. Calculs avec pertes

Les différents calculs ont été effectués avec les mêmes coefficients de frottement sur les aubes, moyeu et carter. Cependant dans cette étude la prise en compte du jeu sur la roue mobile n'a pas été faite.

6.2.1. Résultats avec l'approche stationnaire

Les figures 22 et 23 représentent l'évolution radiale des différents paramètres, dans les deux plans amonts et les 4 plans en aval de la roue mobile. Par rapport au cas sans perte les évolutions sont très différentes en niveau, mais les allures des courbes sont les mêmes sauf en ce qui concerne les angles absolus en aval de la roue mobile.

6.2.2. Résultats avec l'approche instationnaire

a) Cas 1-1

Les figures 24 et 25 donnent les évolutions radiales comme dans le cas sans perte et l'on peut faire les mêmes constatations que ci-dessus.

b) Cas 1-2

Les figures 26 et 27 montrent les évolutions des différents paramètres choisis. Comme dans le cas sans perte on constate avec des niveaux différents, que les évolutions successives entre deux plans très proches donnent des écarts faibles et même nuls en ce qui concerne les angles absolus puisque les courbes sont confondues, entre les plans 2 et 3 distants, rappelons-le de 1.89 mm.

6.2.3. Comparaison entre les deux approches avec pertes

La figure 28 montre les comparaisons pour les évolutions radiales du nombre de Mach relatif moyen, pour les deux plans situés en amont du bord d'attaque de la roue mobile. Contrairement au cas sans perte il n'y a pratiquement aucune différence entre les deux approches.

La figure 29 donne les comparaisons pour les angles moyens. Comme dans le cas sans perte on constate des écarts inférieurs au degré dans le plan le plus en amont et des évolutions semblables sans écart significatif dans le plan juste en amont du bord d'attaque de la roue mobile.

Enfin les planches 30, 31 et 32 donnent dans les différents plans en aval de la roue les comparaisons des évolutions radiales pour les 3 paramètres choisis comme étant le plus caractéristique de l'écoulement. Pour ce qui est des évolutions radiales du nombre de Mach moyen il apparaît des écarts relativement faibles sur presque toute la hauteur de pale et contrairement au cas sans perte ceci a lieu dans les 3 plans considérés.

En ce qui concerne l'évolution radiale des angles relatifs moyens il n'y a pas ou presque pas de variations entre les différentes façons d'effectuer les calculs. Cette remarque s'applique également pour les évolutions des angles absolus moyens.

6.3. Comparaison "calcul-expérience"

Nous allons maintenant donner quelques comparaisons "calcul-expérience" pour les paramètres tels que l'angle relatif, le débit et la pression d'arrêt.

La figure 33 présente d'une part les comparaisons entre les évolutions radiales de pression statique et d'autre part les évolutions radiales du rapport $P_t/P_{t\infty}$ de la pression d'arrêt locale sur la pression d'arrêt à l'infini amont.

L'analyse de l'évolution de la distribution radiale de la pression d'arrêt montre qu'il y a une assez bonne concordance entre l'expérience et le calcul dans toute la partie centrale de l'écoulement. Par contre en ce qui concerne les valeurs expérimentales aussi bien du côté bas et haut de la veine, on note qu'il y a des écarts non négligeables.

La figure 34 montre l'évolution radiale de l'angle que forme la vitesse résiduelle avec l'axe de la machine. Comme dans le cas précédent, on note que la comparaison entre les résultats expérimentaux et ceux donnés par le calcul sont satisfaisants pour les 3/4 de la hauteur de veine. Par contre, en ce qui concerne l'évolution sur la partie basse on note encore quelques petites différences.

Enfin, la figure 35 représente l'évolution radiale des débits spécifiques ; là aussi, on constate que les évolutions données par le calcul recoupent bien l'expérience en ce qui concerne la partie centrale de l'écoulement.

7. CONCLUSIONS

Cette étude qui a été entreprise de façon à donner des éléments de réponse, aux questions qui se posaient au vu des résultats de calculs instationnaires montrant des variations de fortes amplitudes amènent les remarques suivantes.

Si on s'intéresse aux grandeurs instationnaires, pour avoir une meilleure connaissance des maxi et mini des fluctuations des différentes grandeurs physiques, régissant l'écoulement de façon par exemple à analyser un phénomène local plus finement, il faut nécessairement faire un calcul instationnaire. Le découpage d'une période, en fonction du temps permettra d'avoir une évolution des paramètres avec une très grande précision. Cela nécessite de prendre en compte au minimum un canal sur la roue fixe et deux canaux sur la roue mobile.

Maintenant si pour différentes raisons, par exemple l'avant-projet d'une machine, on ne s'intéresse qu'aux grandeurs moyennes globales de l'écoulement, l'étude ci-dessus sous peine d'investigations plus poussées montre qu'il est pratiquement indifférent d'effectuer un calcul 3D avec les trois approches explicitées.

Bien entendu toutes ces simplifications et approximations ne sont admissibles que si l'on considère l'écoulement en amont du distributeur comme homogène. Or ce n'est pas le cas dans la réalité car l'écoulement est fortement, non homogène, instationnaire radialement et azimutalement. De toutes façons dans ce cas il n'est pas possible à l'heure actuelle de faire un tel calcul prohibitif en temps et en coût.

REFERENCES

- [1] - SHYY W., BRAATEN M.E.
A numerical study of flow in coas-turbine combustor. AIAA Paper 87-2132, june 29-july 2, 1987, San Diego, California.
- [2] - MEAUZE G., FOURMAUX A.
Numerical simulation of flows in axial and radial turbomachines using Euler solvers. Cours au VKI, 15-18 juin 1987.
- [3] - FOURMAUX A., LE MEUR A.
4th Symposium on Unsteady Aerodynamics and Aeroelasticity of Turbomachines and Propellers. Aachen, 6-10 septembre 1987.
- [4] - FOURMAUX A., BILLONNET G., LE MEUR A., LESAIN A.
Numerical simulation of three-dimensional unsteady flows in turbomachines. 74-A PEP/AGARD, Luxembourg, 4-6 septembre 1989.
- [5] - COUAILLIER V.
Multigrid method for solving Euler and Navier-Stokes equations in two and three dimensions. 8th GAMM conference on Numerical Methods in Fluid Dynamics, Delft (Pays-Bas), September 27-29, 1989.
- [6] - SOVRANO R.
Calcul de l'écoulement transsonique dans un compresseur centrifuge par une méthode pseudo-instationnaire. AGARD/PEP "Centrifugal Compressors, Flow Phenomena and Performance", Bruxelles, 1980, TP ONERA n° 1980-42.
- [7] - VIVIAND H., VEUILLOT J.P.
Méthodes pseudo-instationnaires pour le calcul d'écoulements transsoniques. Publication ONERA n° 1978-4.
- [8] - VEUILLOT J.P., MEAUZE G.
A 3D Euler method for internal transonic flows computation with a multi-domain approach. AGARD/PEP, LS 140, ONERA TP n° 1985-41.
- [9] - MEAUZE G., PAULON J., DEHONDT D.
Numerical simulation of turbomachinery flow with a simple model of viscous effects-comparison with experimental data. 9th International Symposium on Air Breathing Engines, Athens (Greece), september 4-9, 1989.
- [10] - MEAUZE G., PAULON J.
Numerical simulation of nonreactive flows in turbomachines. La Recherche Aérospatiale n° 1990-2 (english edition).

[11] - LE MEUR A.

Three-dimensional unsteady flow computation in transonic axial turbine stage. AIAA 88-0362, 26th Aerospace Science Meeting, Reno (Nevada), 11-14 january 1988.

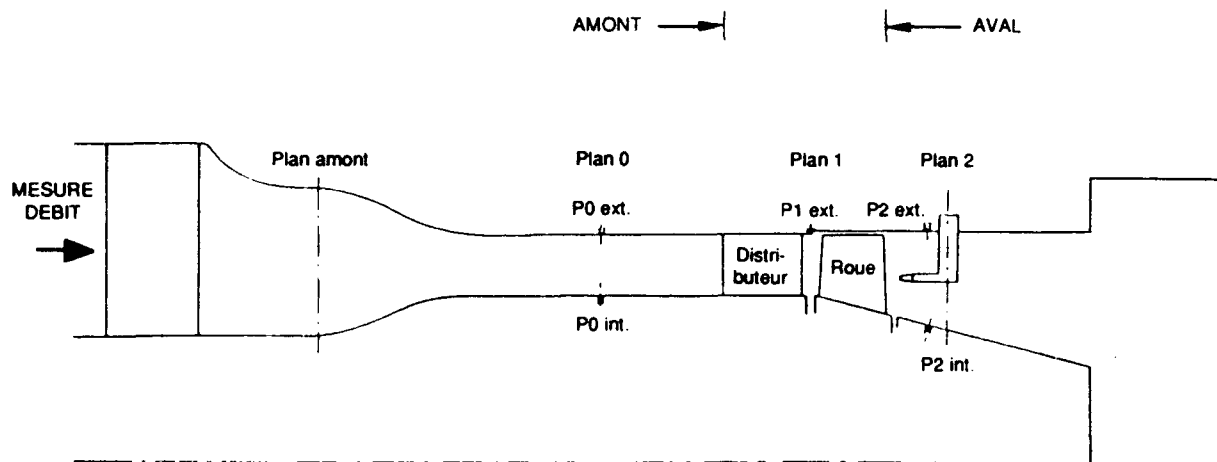


Figure 1 - Schéma du banc d'essai de turbine

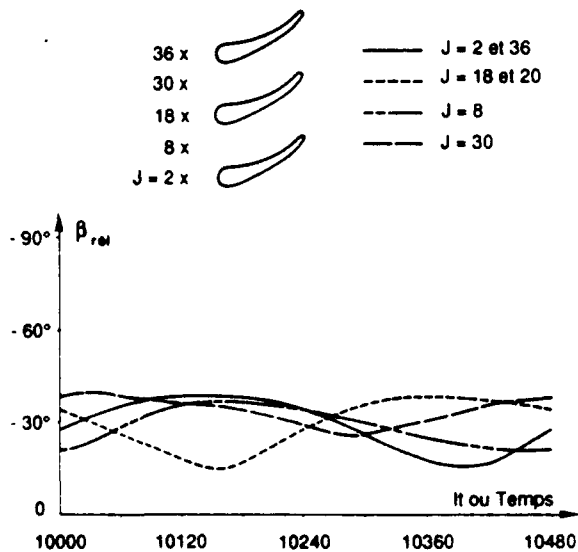


Figure 2 - Evolution en fonction du temps des valeurs locales de l'angle relatif en amont de la roue mobile pour 4 positions azimutales coupe de tête sans perte

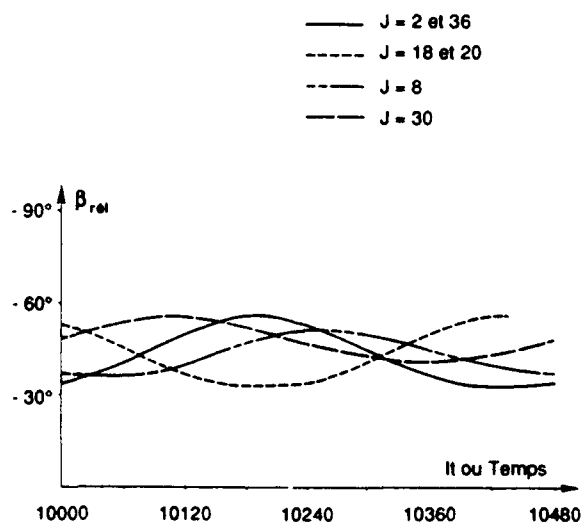


Figure 3 - Evolution en fonction du temps des valeurs locales de l'angle relatif en amont de la roue mobile pour 4 positions azimutales coupe de pied sans perte

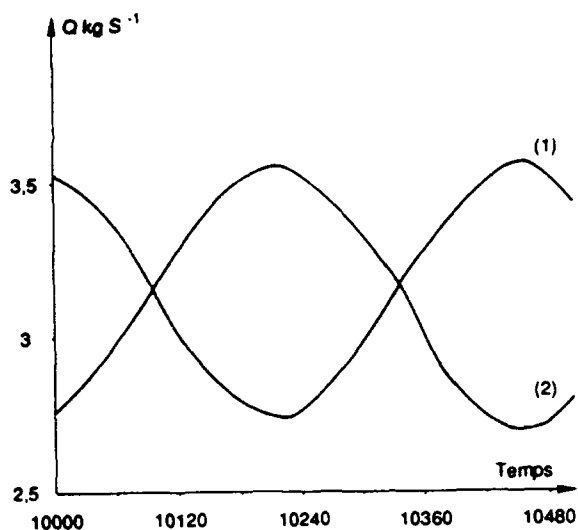


Figure 4 - Variation du débit instantané dans une tranche (bord d'attaque) pour les deux canaux de la roue mobile sans perte

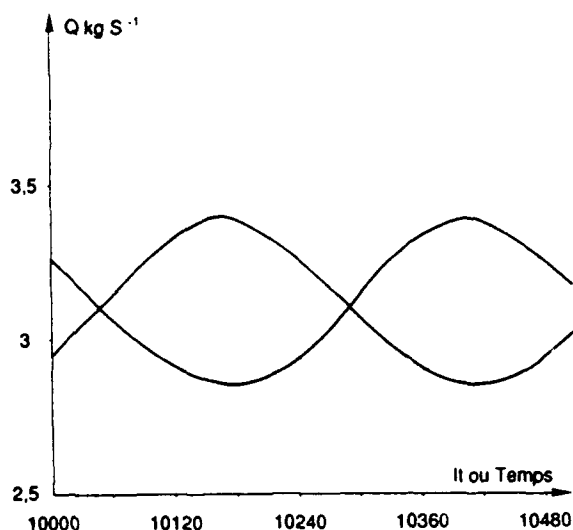


Figure 5 - Variation du débit instantané dans une tranche (avant bord de fuite) pour les deux canaux de la roue mobile de l'étage sans perte

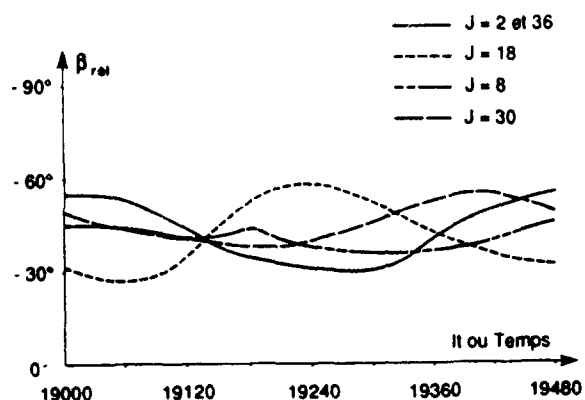


Figure 6 - Evolution en fonction du temps des valeurs locales de l'angle relatif en amont de la roue mobile pour 4 positions azimuthales coupe de pied avec pertes

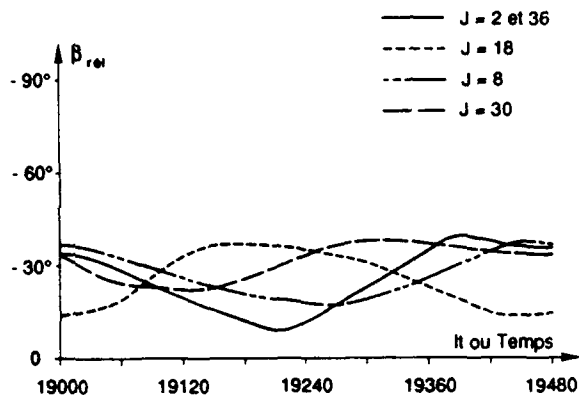


Figure 7 - Evolution en fonction du temps des valeurs locales de l'angle relatif en amont de la roue mobile pour 4 positions azimuthales coupe de tête avec pertes.

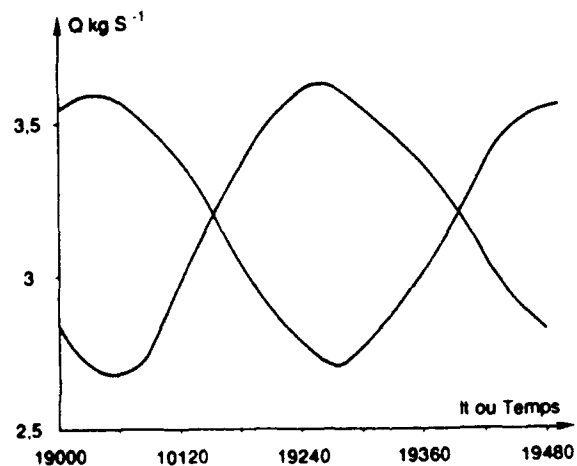


Figure 8 - Variation du débit instantané dans une tranche (bord d'attaque) pour les deux canaux de la roue mobile avec pertes

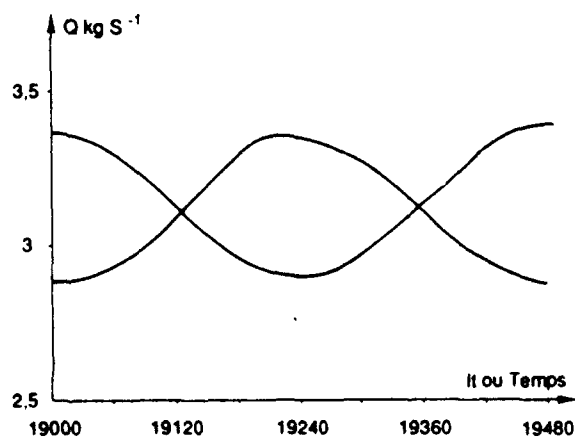
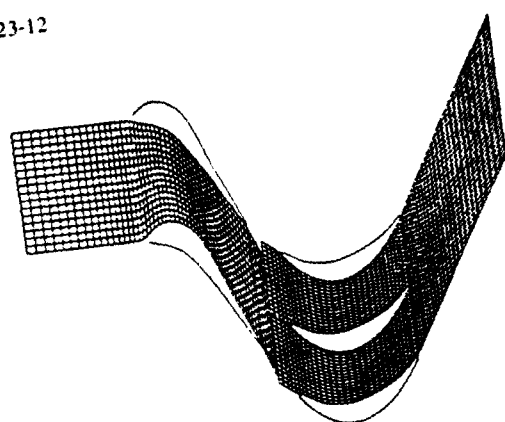
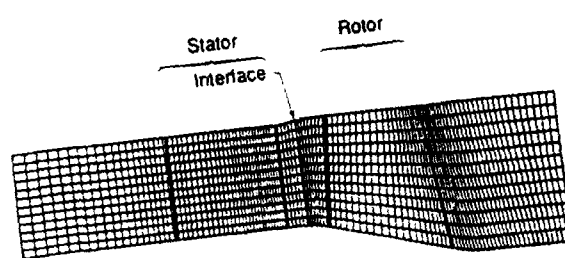


Figure 9 - Variation du débit instantané dans une tranche (bord de fuite) pour les deux canaux de la roue mobile avec pertes

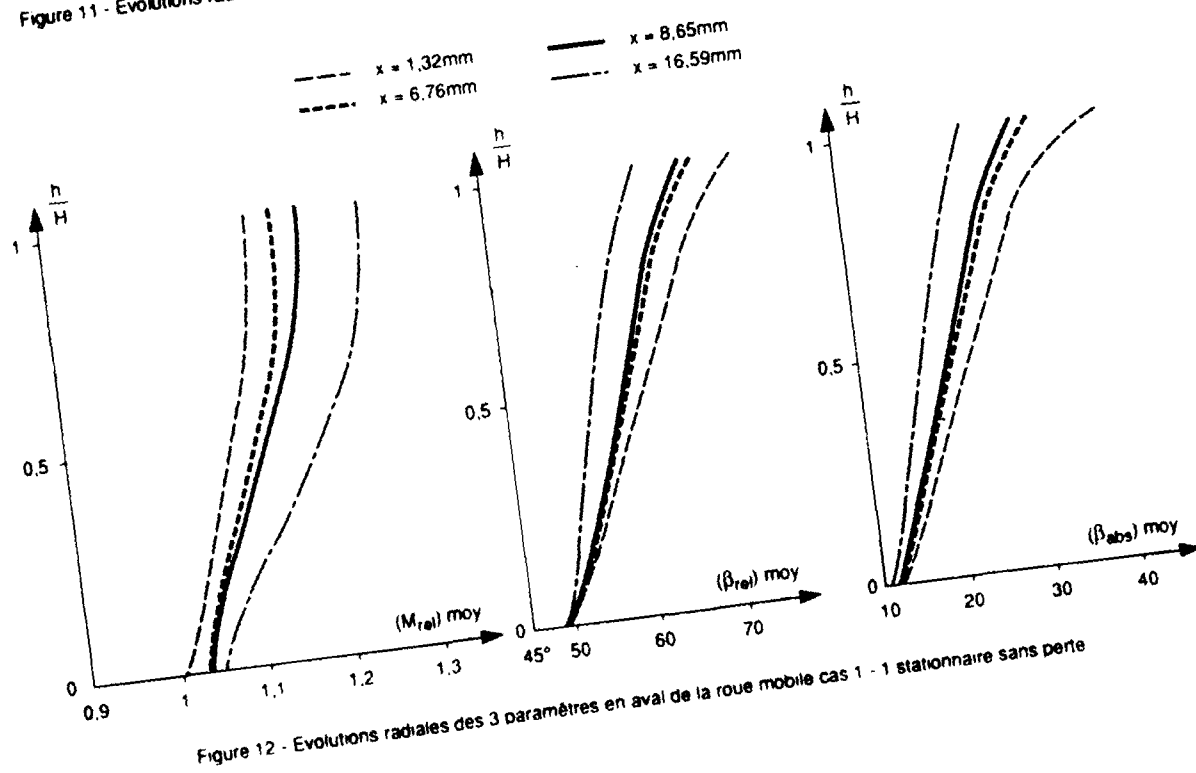
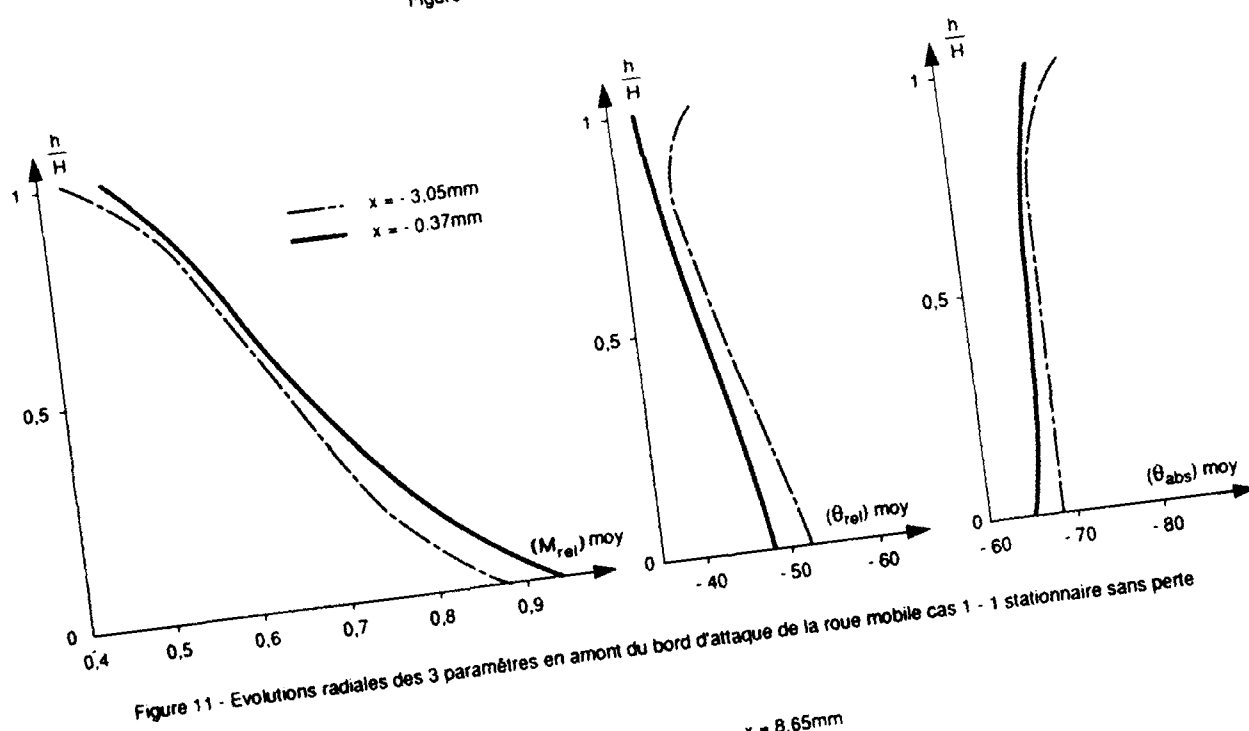


a) - Maillages aube à aube



b) - Maillage inter-dien

Figure 10 - Maillages pour le calcul 3-D



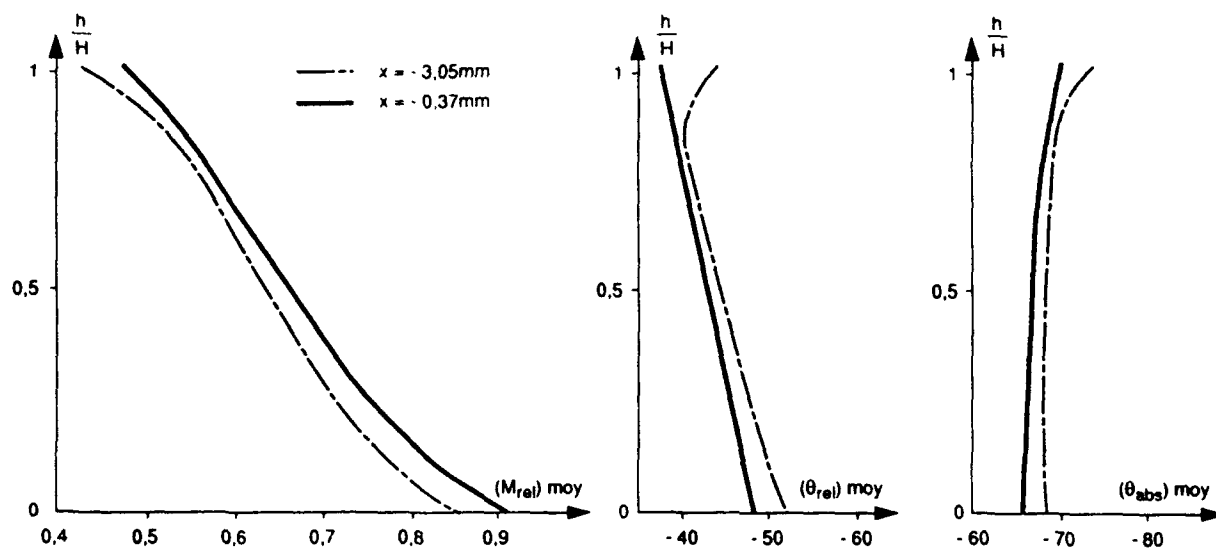


Figure 13 - Evolutions radiales des 3 paramètres en amont de la roue mobile - cas 1 - 1 instationnaire plus moyenne - sans perte

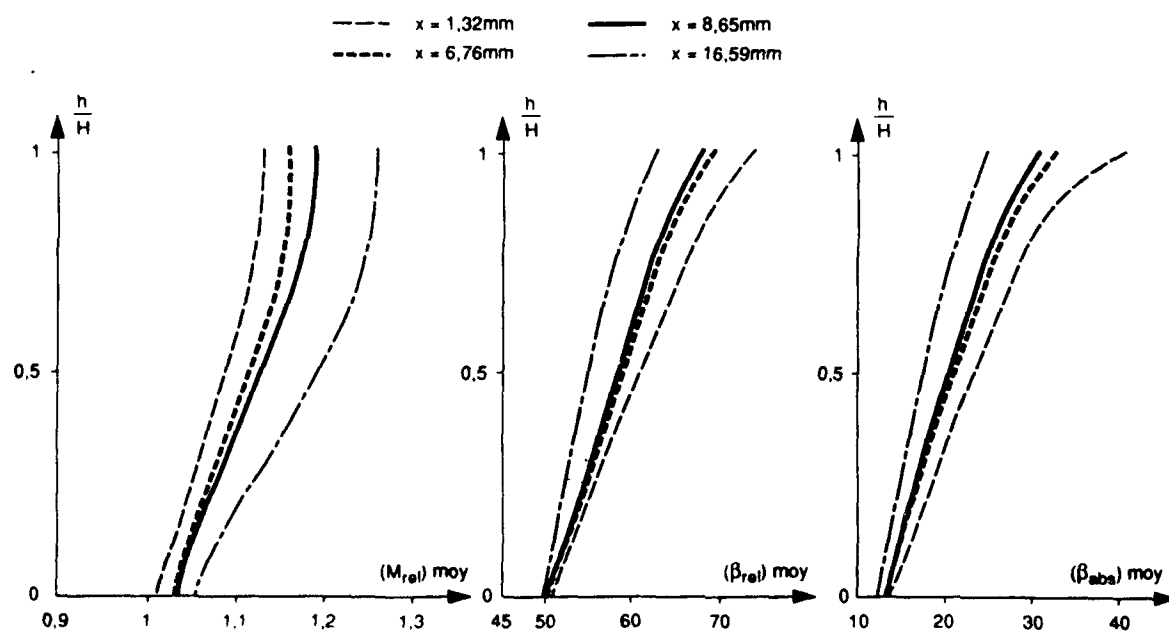


Figure 14 - Evolutions radiales des 3 paramètres en aval de la roue mobile - cas 1 - 1 instationnaire plus moyenne - sans perte -

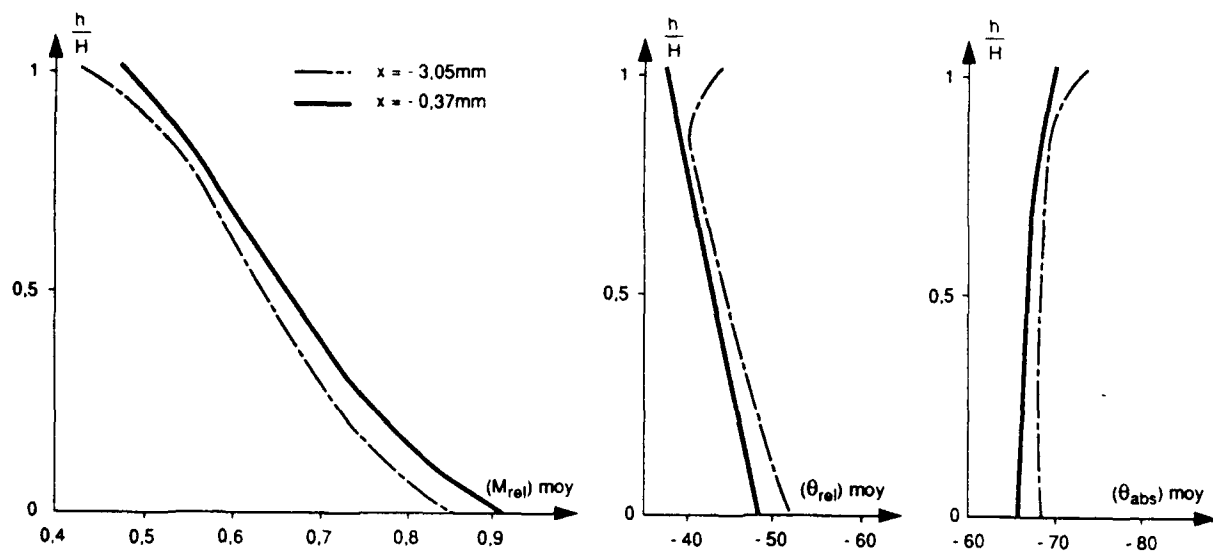


Figure 15 - Evolutions radiales des 3 paramètres en amont de la roue mobile - cas 1 - 2 instationnaire plus moyenne - sans perte -

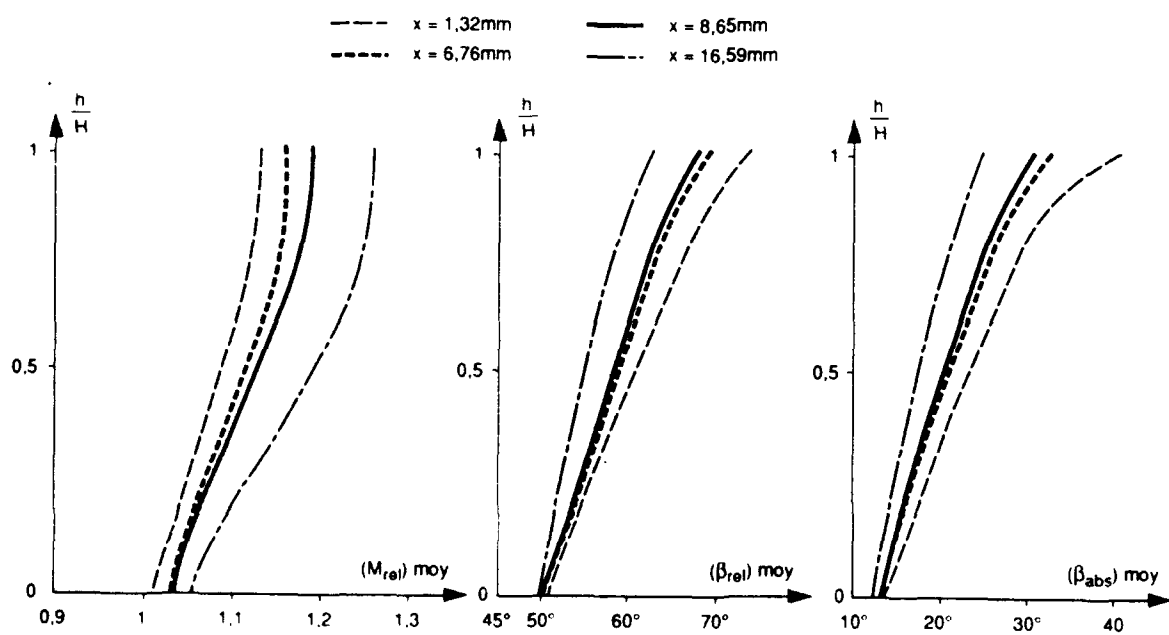


Figure 16 - Evolutions radiales des 3 paramètres en aval de la roue mobile - cas 1 - 2 instationnaire plus moyenne - sans perte -

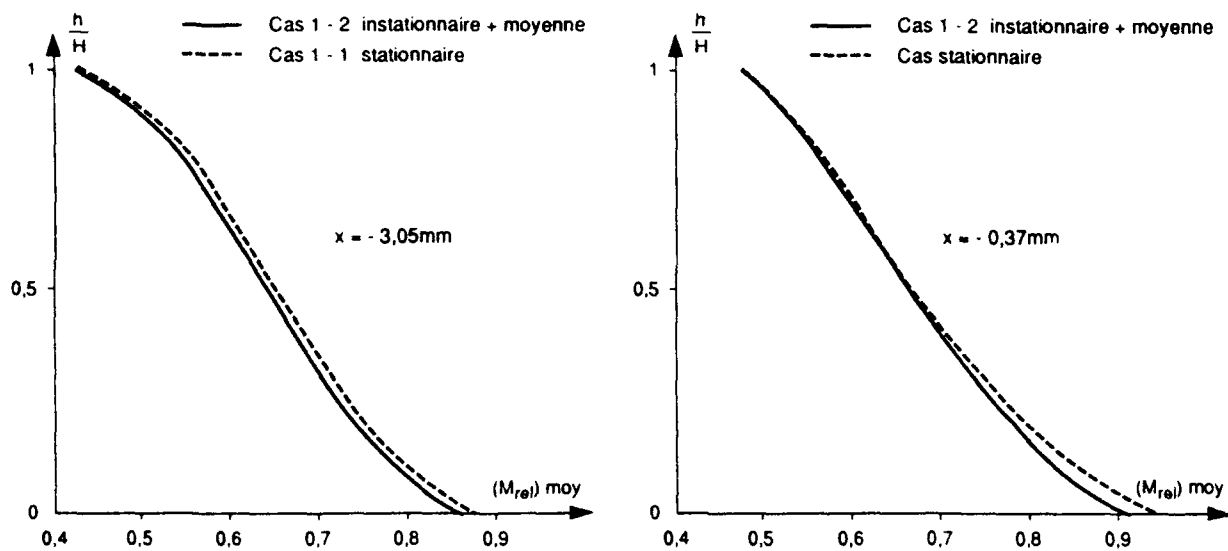


Figure 17 - Comparaisons des évolutions radiales du nombre de mach en amont de la roue mobile - sans perte -

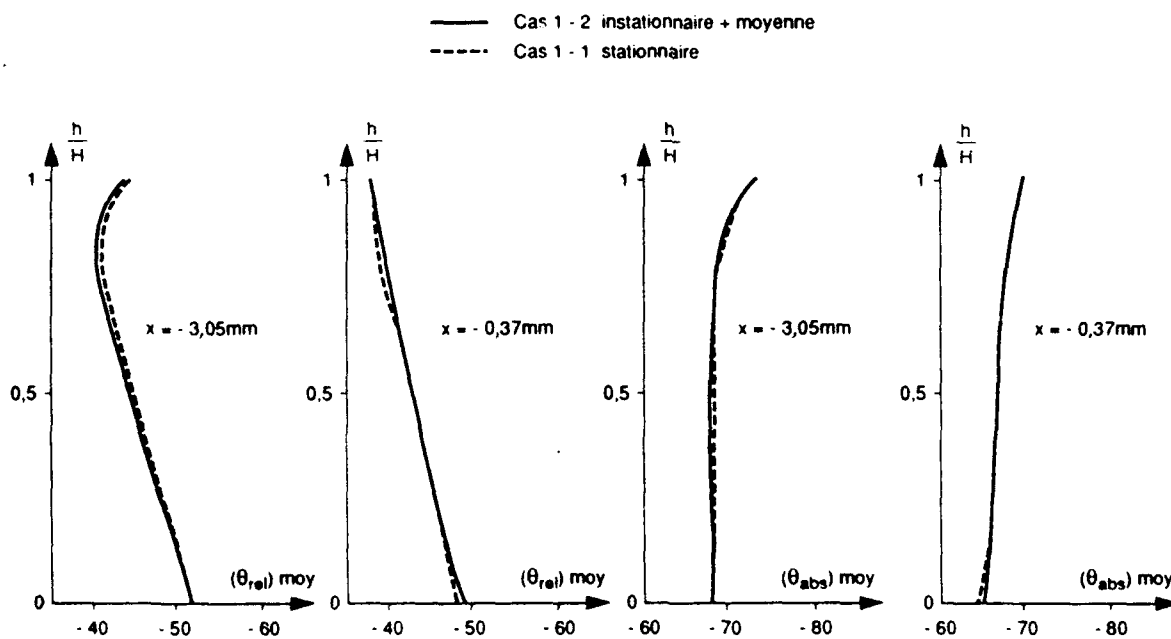


Figure 18 - Comparaisons des évolutions radiales des angles relatifs et absolus en amont de la roue mobile - sans perte -

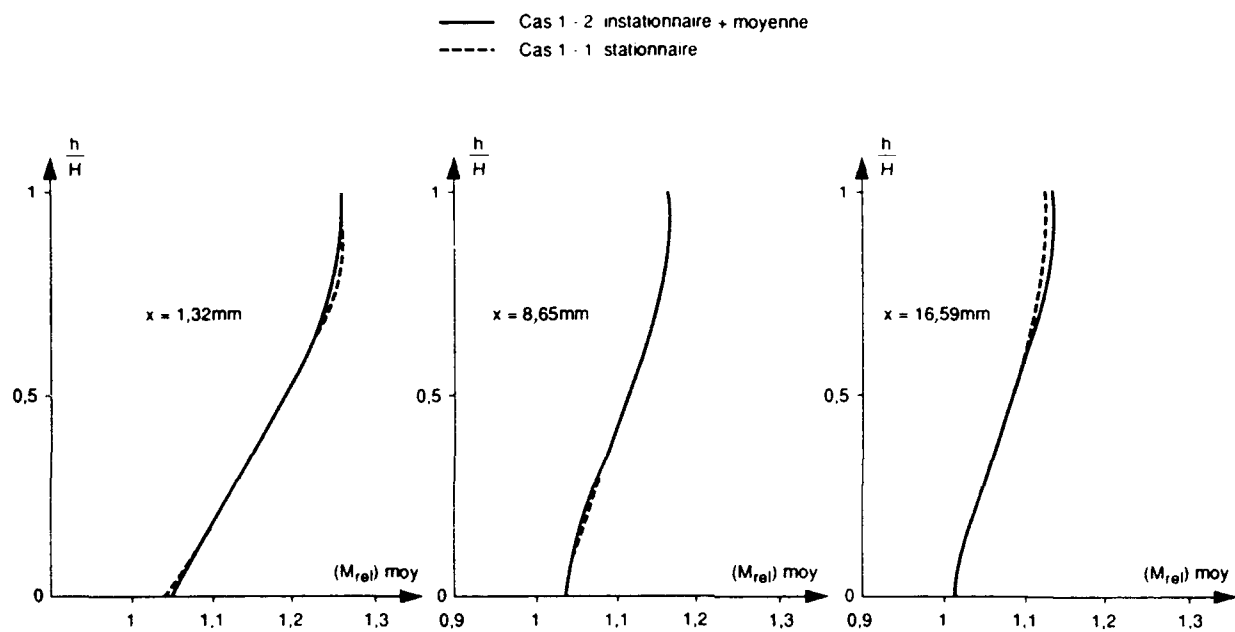


Figure 19 - Comparaisons des évolutions radiales du nombre de mach en aval de la roue mobile - sans perte -

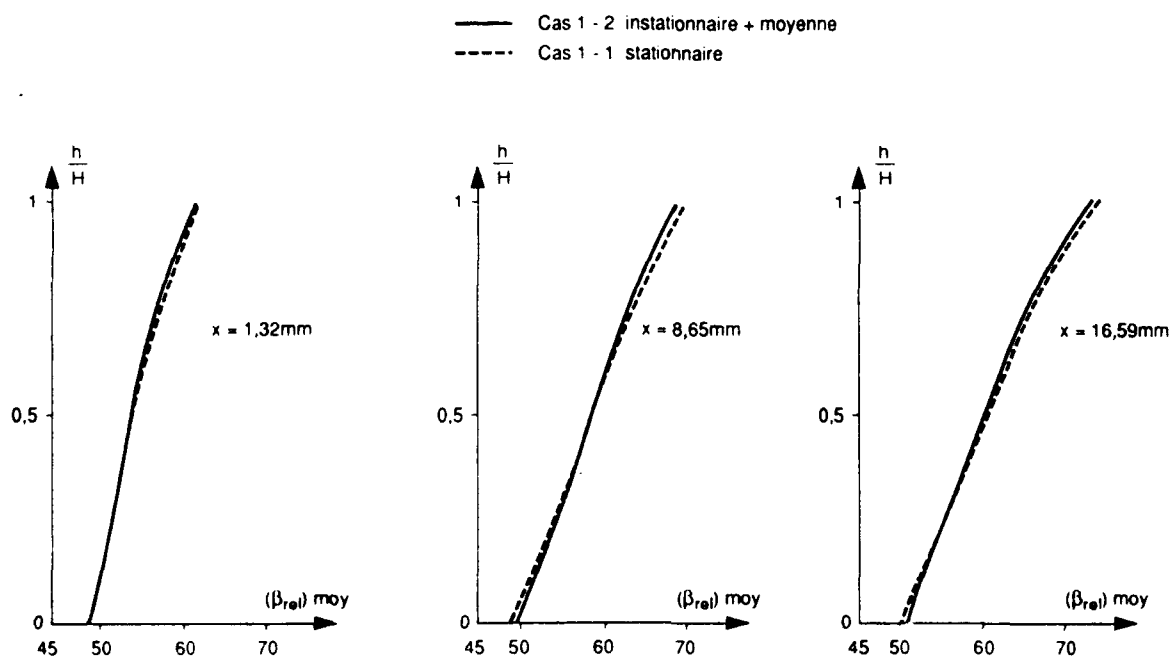


Figure 20 - Comparaisons des évolutions radiales des angles relatifs en aval de la roue mobile - sans perte -

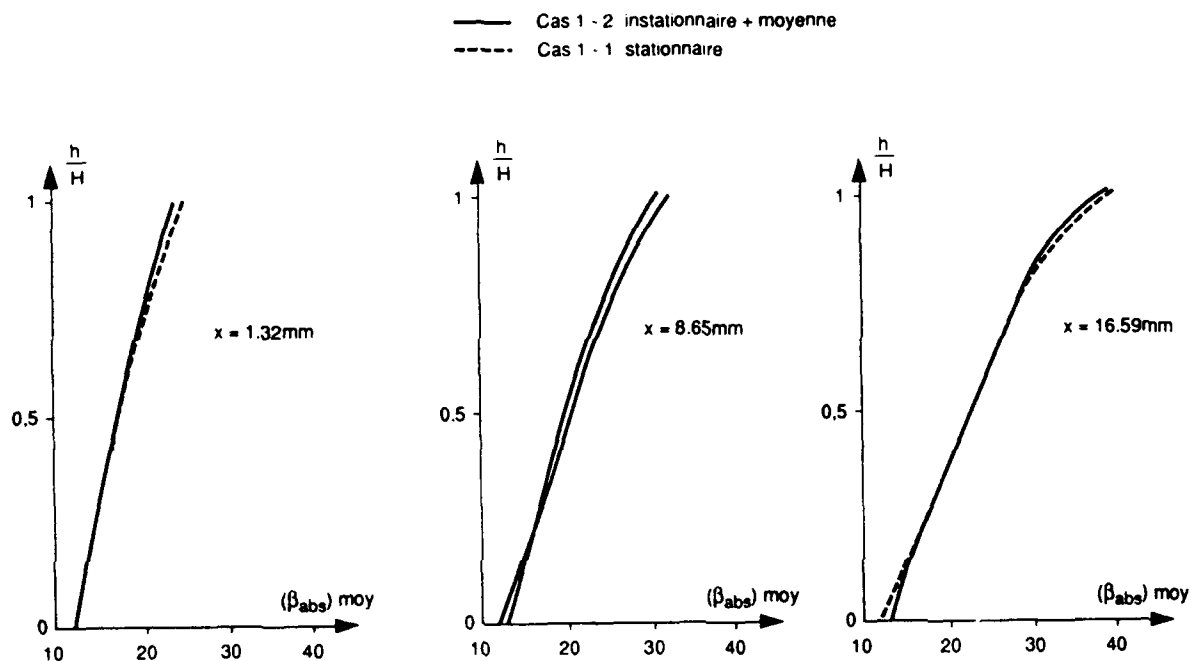


Figure 21 - Comparaisons des évolutions radiales des angles absolus en aval de la roue mobile - sans perte -

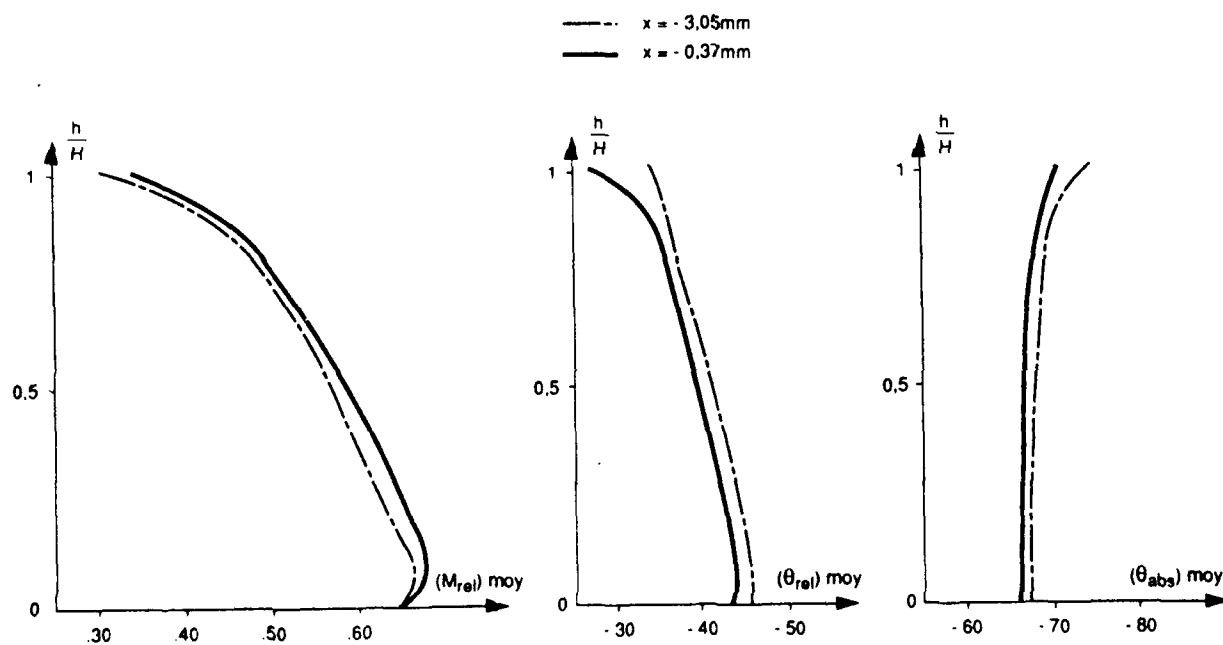


Figure 22 - Evolutions radiales des 3 paramètres en amont du bord d'attaque de la roue mobile - cas 1 - 1 stationnaire avec perte

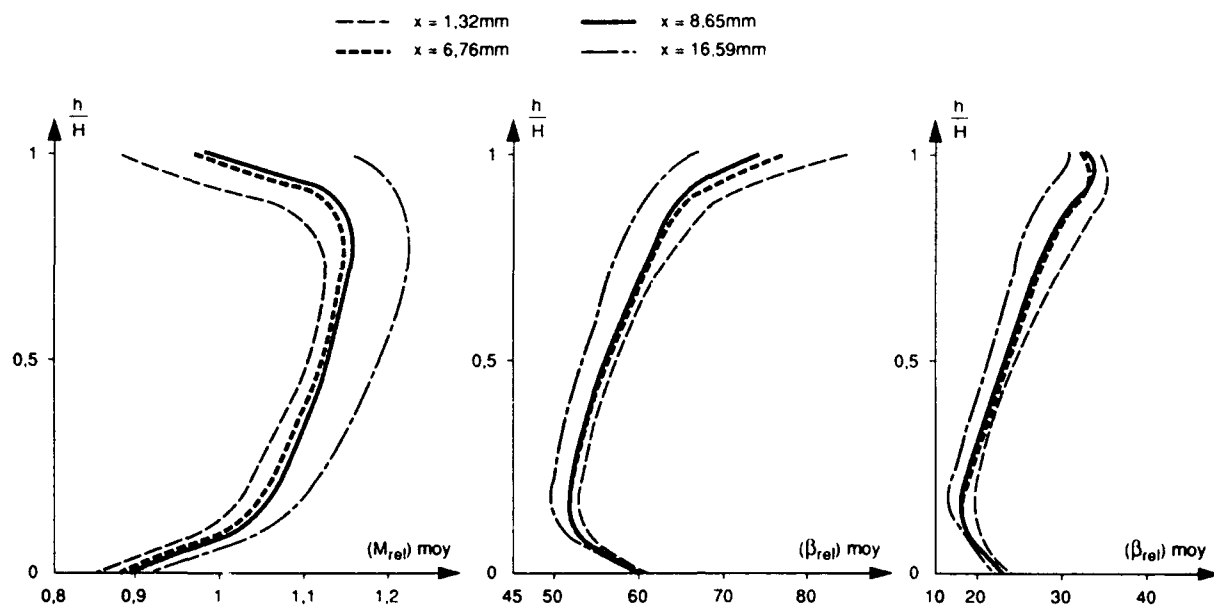


Figure 23 - Evolutions radiales des 3 paramètres en aval de la roue mobile - cas 1 - 1 stationnaire plus moyenne avec pertes

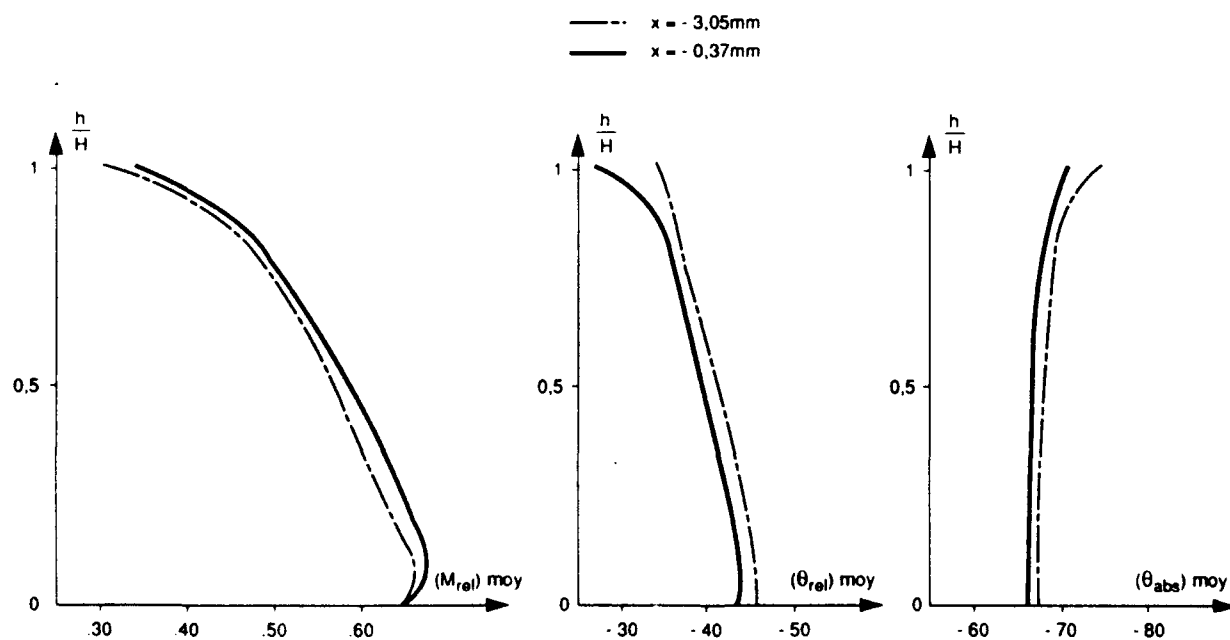


Figure 24 - Evolutions radiales des 3 paramètres en amont de la roue mobile - cas 1 - 1 instationnaire plus moyenne - avec pertes -

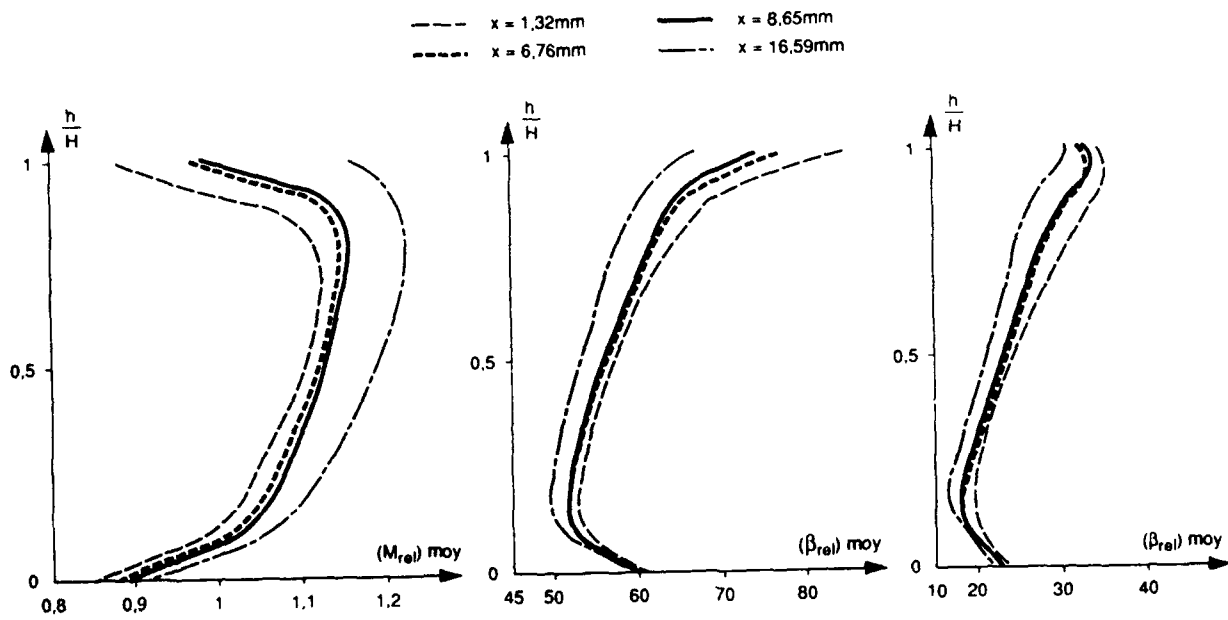


Figure 25 - Evolutions radiales des 3 paramètres en aval de la roue mobile - cas 1 - 1 instationnaire plus moyenne avec pertes

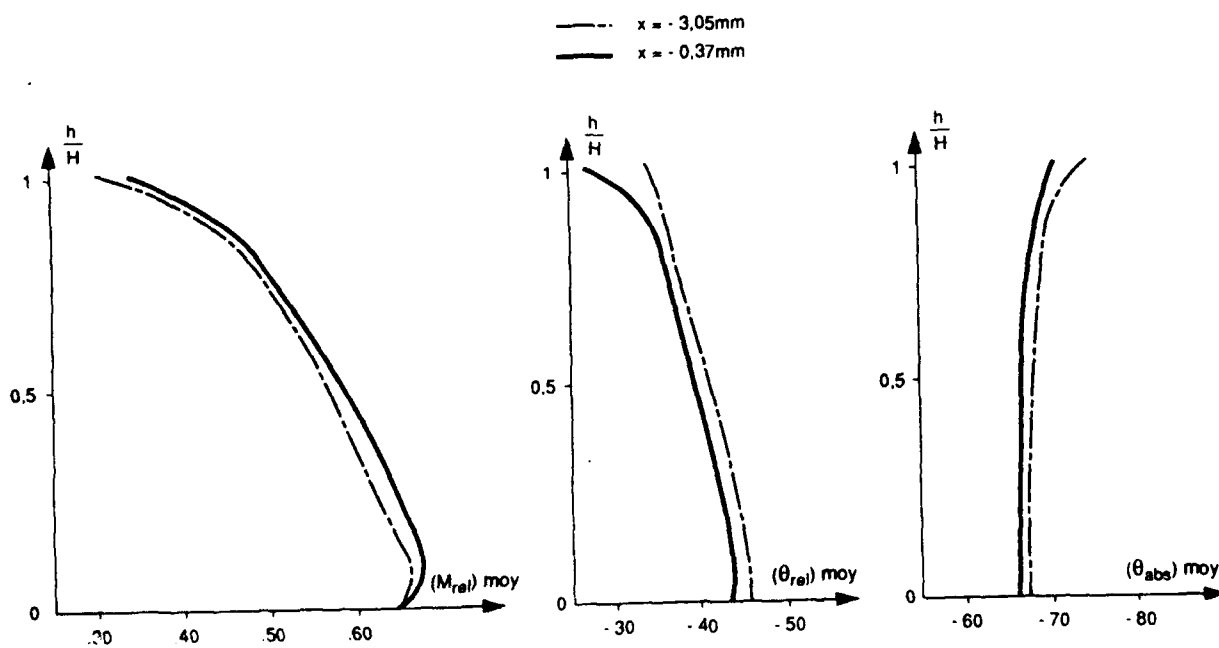


Figure 26 - Evolutions radiales des 3 paramètres en amont de la roue mobile - cas 1 - 2 instationnaire plus moyenne - avec pertes -

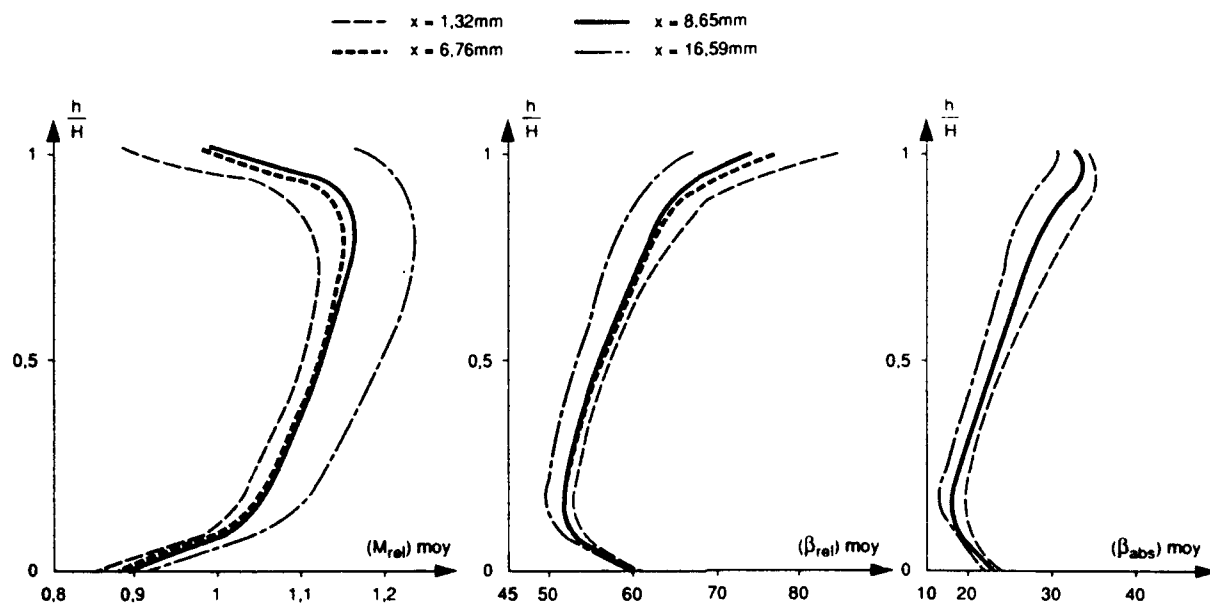


Figure 27 - Evolutions radiales des 3 paramètres en aval de la roue mobile - cas 1 - 2 instationnaire plus moyenne avec pertes

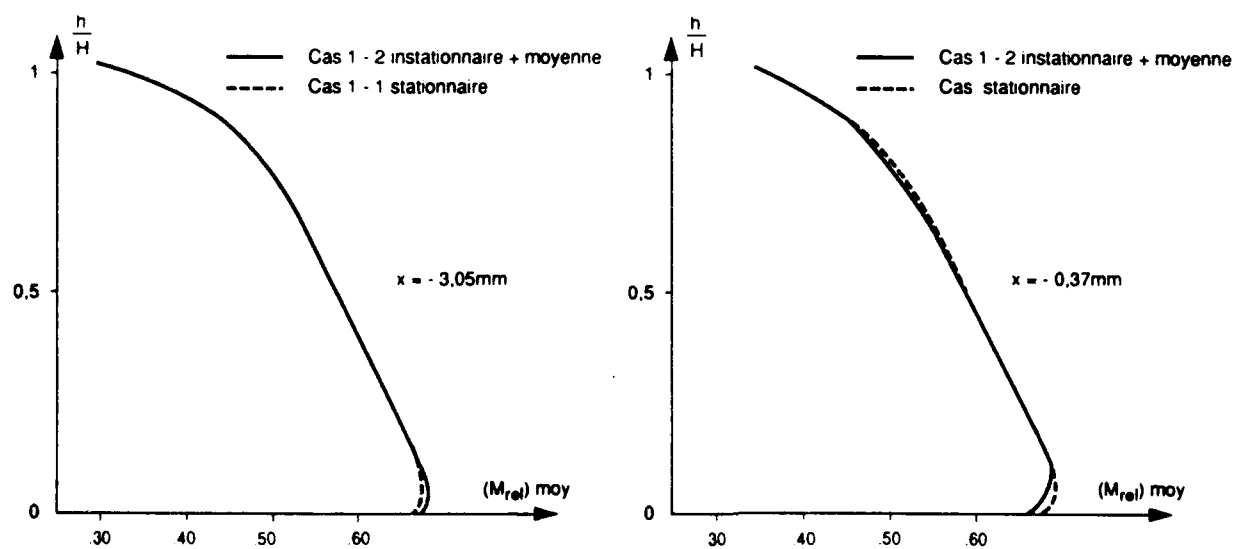


Figure 28 - Comparaisons des évolutions radiales du nombres de Mach en amont de la roue mobile - avec pertes -

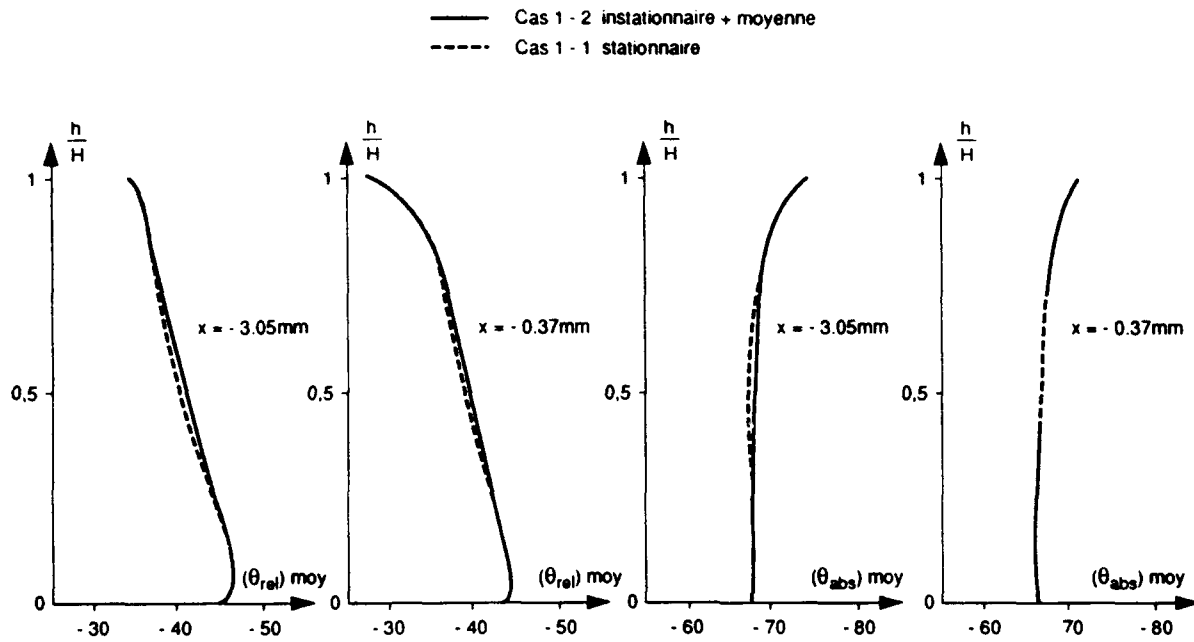


Figure 29 - Comparaisons des évolutions radiales des angles relatifs et absolus en amont de la roue mobile - avec pertes -

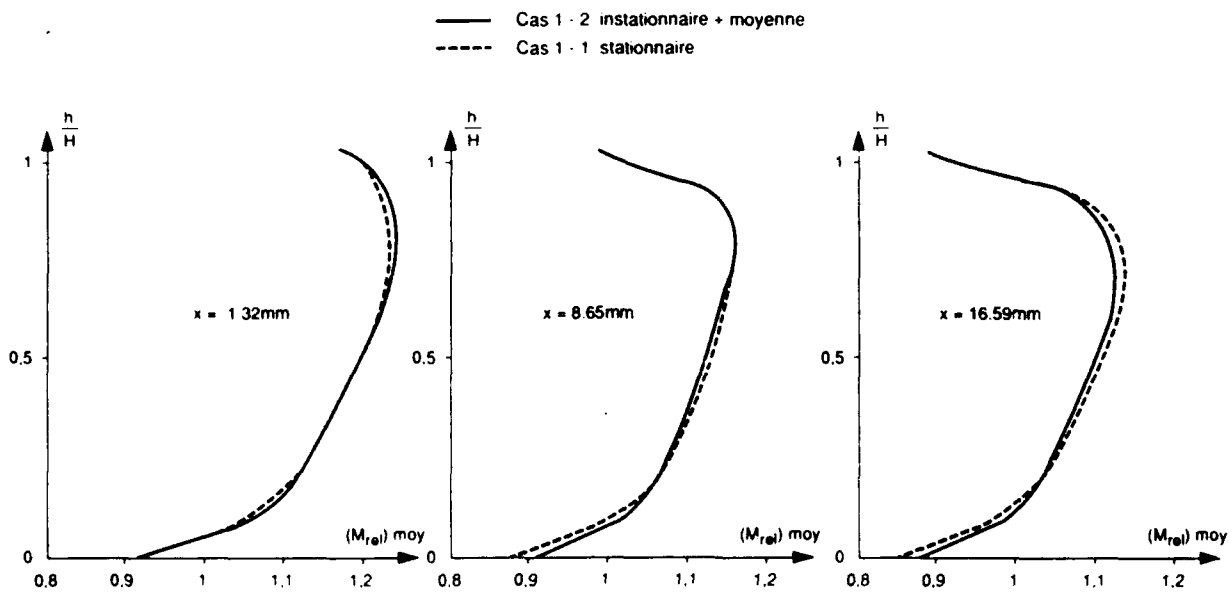


Figure 30 - Comparaisons des évolutions radiales du nombre de Mach en aval de la roue mobile - avec pertes -

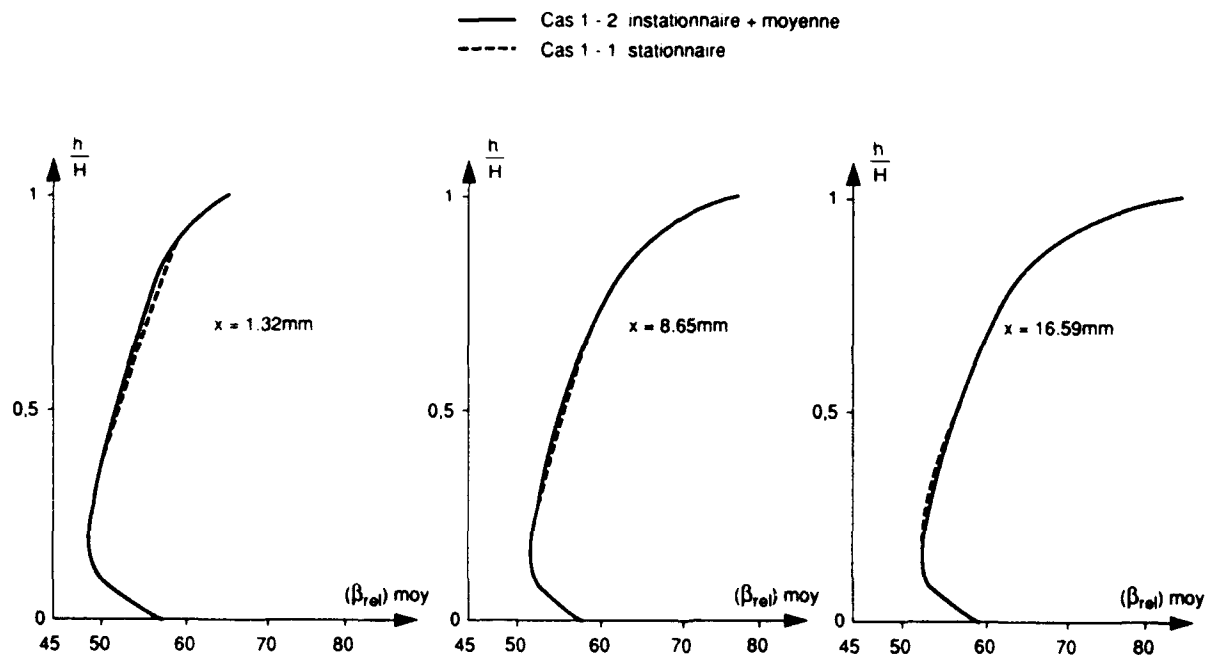


Figure 31 - Comparaisons des évolutions radiales des angles relatifs en aval de la roue mobile - avec pertes -

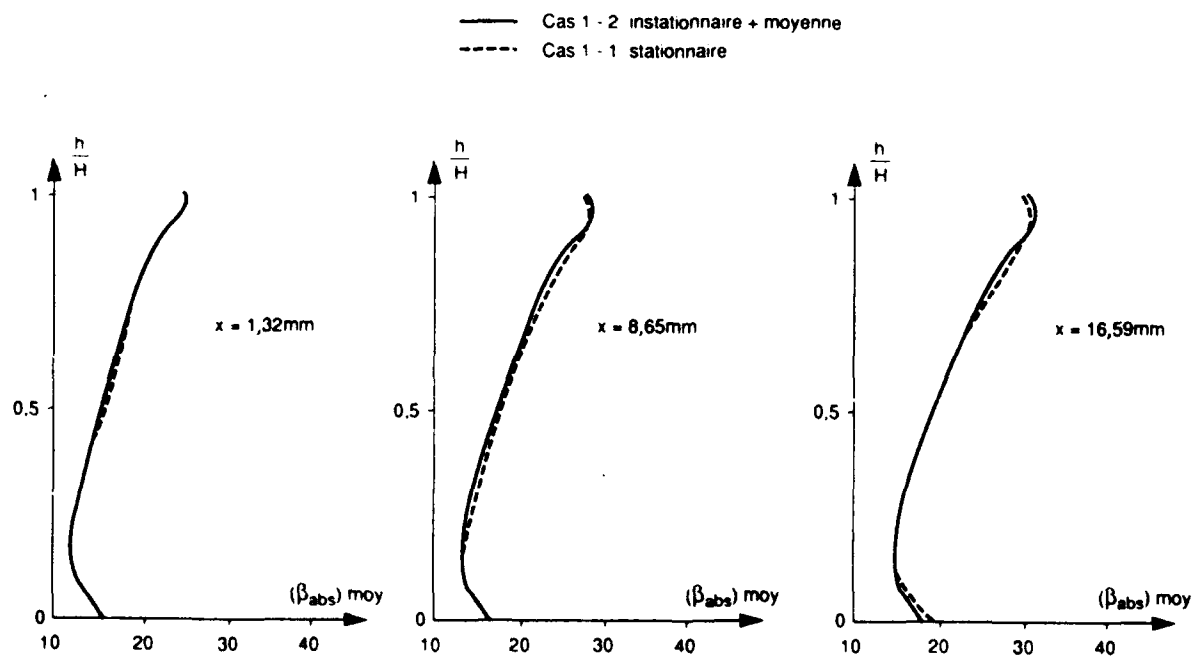


Figure 32 - Comparaisons des évolutions radiales des angles absolus en aval de la roue mobile - avec pertes -

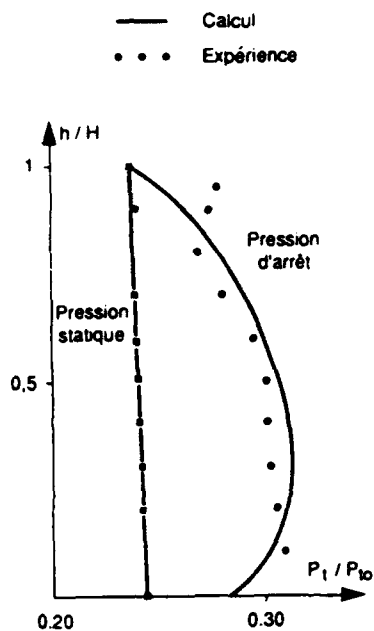


Figure 33 - Evolution radiale de la pression d'arrêt locale sur la pression d'arrêt amont dans le plan de mesure n°2

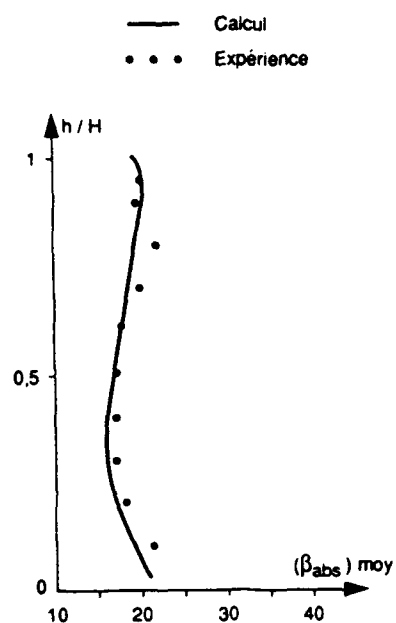


Figure 34 - Evolution radiale de l'angle absolu dans le plan de mesure n°2

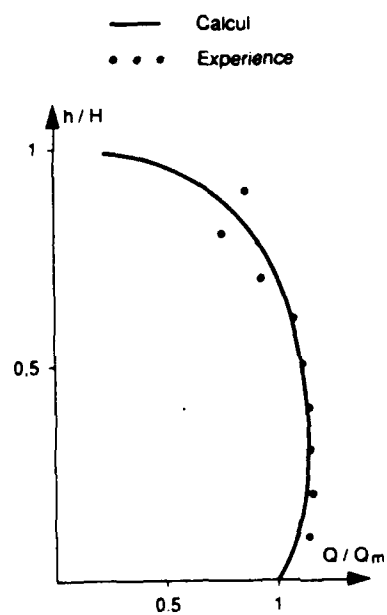


Figure 35 - Evolution radiale des débits dans le plan de mesure n° 2

Discussion

C. HIRSCH, UNIV. OF BRUSSELS, BELGIUM

de l'excellente concordance entre les distributions moyennes et les distributions rationnel que vous avez montrée, mais compte tenir des fortes difference' dans les , pensez-vous que cette bonne concordance est un hazard heureux, ou bien fait-on en tirer des conclusions plus généraux.

AUTHOR'S REPLY

Il faut se méfier de tirer des conclusions générales à partir de l'étude d'une seule configuration et nous avons l'intention d'étudier d'autres configurations (en particulier compresseur). Cependant il nous semble que dans le cas d'un calcul Euler ce type de résultats doit être assez général, d'autant plus que la configuration étudiée est l'une de celle qui donne le plus d'effets instationnaires. Nous ne sommes pas du tout certains de retrouver un résultat équivalent dans le cas d'un calcul Navier-Stokes surtout si les effets instationnaires créent des phénomènes d'hystérésis importants au niveau des décollements sur les aubes.





UNSTEADY EULER CALCULATIONS IN 3D INTERNAL AERODYNAMICS

M. Hadzidakis
F. Karagiannis
P. Chaviaropoulos
K.D. Papailiou

92-16083



National Technical University of Athens
Lab. of Thermal Turbomachines
P.O. Box 64069, 157 10 Athens, Greece.

SUMMARY

This paper presents an implicit finite difference algorithm which solves the unsteady Euler equations in three dimensional ducts. The present work is based on the Helmholtz decomposition of the unsteady velocity field into a potential and a rotational part. The geometry does not change with time, thus the unsteady nature of the flow is due to the time dependent inflow and outflow boundary conditions. The flow at the inlet is supposed to be rotational. Vorticity is introduced by means of velocity, total enthalpy or even entropy profile slope. The presented results cover a wide range of reduced frequencies in the subsonic flow regime.

LIST OF SYMBOLS

h	static enthalpy
K	Reduced frequency
R_g	gas constant
S	entropy
t, τ	time
T	static temperature
V	velocity vector
x, y, z	Cartesian coordinates
ξ, η, ζ	Curvilinear coordinates
α	speed of sound
γ	isentropic exponent
λ	function defining the secondary vorticity
ρ	static density
ϕ	scalar potential
ψ	vector potential
ω	vorticity
w	angular velocity
sl	number of time steps per cycle

Subscripts

t	stagnation values
∞	free stream values
o	normalization values
in	normal to the inlet boundary component
ex	exit values

Superscripts

$n, *$	time level values
--------	-------------------

1 INTRODUCTION

The calculation of three dimensional unsteady flows in internal aerodynamics is necessary for the understanding of the behaviour and performance of turbomachinery. A very commonly encountered case is that of unsteady flows with introduced vorticity at the inlet by means of velocity, total enthalpy or even entropy profile slope. The unsteady full potential

model cannot simulate these flows and the solution of the unsteady Euler equations is imperative, even in the subsonic flow region.

In the past researchers have dealt with the solution of unsteady Euler Equations in two dimensions {1}, {2} and in three dimensions {3}, {4}. These efforts treated external aerodynamics flow problems where the inlet boundary conditions were irrotational and thus no vorticity was introduced in the domain. Internal aerodynamics flow problems (unsteady flows in ducts) with irrotational inlet boundary conditions have also been tackled {5}. Recently two dimensional unsteady flows in cascades with rotational inlet boundary conditions were published {6}. The solution of three dimensional unsteady Euler equations in cascades is a topic that has been dealt with by very few researchers {7}. However all the above mentioned research efforts solve the Euler equations using the primitive variables formulation.

The proposed method applies the Helmholtz decomposition on the velocity vector. This leads to a scalar and vector potential as working variables. The rest working variables are the total enthalpy, entropy and secondary vorticity (or elicity). It can be stated that the total enthalpy and entropy fields, being primitive variables in this formulation, are computed more accurately {8} than with primitive variables solvers, where the need of artificial viscosity impairs the convective character of the flow. Implicit finite difference schemes are used for the solution of the governing equations. The proposed decomposition leads to a second order unsteady equation for the scalar potential, a vector Poisson equation for the vector potential and transport equations for entropy, total enthalpy and secondary vorticity. The proposed formulation is an extension to a solver already developed by the authors for the two-dimensional case {9}.

As in the two dimensional case, the solution procedure is divided in two steps. The first step is a linearization around the known "n" time level values which provides an estimation of the "n+1" values. The second one is a linearization around these estimated values and provides the correct "n+1" values. Thus the unsteady equations are satisfied at each time level, since they are converged using the second step. This fact reduces disturbing truncation errors which occur if a simple time integration scheme (explicit or implicit) is followed. Greater time steps than those permitted by time integration

schemes are used.

2 GOVERNING EQUATIONS

In order to permit the accurate description of the boundary conditions the governing equations are written in a body-fitted coordinate system (ξ, η, ζ) of the form

$$\xi = \xi(x, y, z)$$

$$\eta = \eta(x, y, z)$$

$$\zeta = \zeta(x, y, z)$$

$$\tau = t$$

The form of the governing equations in this system can be found in Appendix I. The equations in vector form are:

2.1 Velocity Definition

$$\vec{V} = \nabla \phi + \nabla \times \vec{\psi}$$

2.2 Continuity Equations

$$\frac{\partial \rho}{\partial \tau} + \nabla \cdot (\rho \vec{V}) = 0$$

2.3 Vector Potential and Vorticity

$$\vec{\Omega} = \frac{\vec{V}}{|\vec{V}|} \left(\frac{\vec{\Omega} \cdot \vec{V}}{|\vec{V}|} \right) + \frac{\vec{V}}{|\vec{V}|^2} \times \left[\nabla S - \nabla h_t - \frac{\partial \vec{V}}{\partial \tau} \right] =$$

$$= \lambda \rho \vec{V} + \frac{\vec{V}}{|\vec{V}|^2} \times \left[\nabla S - \nabla h_t - \frac{\partial \vec{V}}{\partial \tau} \right]$$

$$\nabla \times \vec{\psi} = -\vec{\Omega}$$

$$\nabla \cdot \vec{\Omega} = 0 \quad \text{or}$$

$$-\frac{1}{\rho} \frac{\partial \rho}{\partial \tau} \lambda + \vec{V} \cdot \nabla \lambda = -\frac{1}{\rho} \nabla \cdot \left[\frac{\vec{V}}{|\vec{V}|^2} \times (\nabla S - \nabla h_t - \frac{\partial \vec{V}}{\partial \tau}) \right] \quad (6)$$

2.4 Entropy Equation

$$\frac{\partial S}{\partial \tau} + \vec{V} \cdot \nabla S = 0$$

2.5 Energy Equation

$$\vec{V} \cdot \nabla h_t = -\vec{V} \cdot \frac{\partial \vec{V}}{\partial \tau} - T \frac{\partial S}{\partial \tau}$$

2.6 Equation of State

$$S - S_{ref} = R_g \ln \left[\frac{(h_t / h_{tref})^{1/\gamma-1}}{\rho_t / \rho_{tref}} \right]$$

2.7 Density Equation

$$\rho = \rho_t \left(1 - \frac{|\vec{V}|^2}{2h_t} \right)^{1/\gamma-1}$$

3 THE SOLUTION ALGORITHM

As in the two dimensional case (9), the solution procedure is divided in two steps. The first one is the "initial guess" which provides an estimation of the "n+1" time level values by linearizing around the known "n" time level values. The second step is a non-linear one which linearizes around the estimated "n+1" values and provides the correct "n+1" values.

3.1 Initial Guess

An estimation of the "n+1" time level values (denoted as "*" values) is made. Let

$$\begin{aligned} \phi^* &= \phi_n + \Delta \phi, \quad \vec{\psi}^* = \vec{\psi}_n + \Delta \vec{\psi}, \quad S^* = S_n + \Delta S, \\ h_t^* &= h_{tn} + \Delta h_t, \quad \lambda^* = \lambda_n + \Delta \lambda \end{aligned} \quad (11)$$

3.1.1 Continuity Equation

Considering that $\rho = \rho(\phi, \vec{\psi}, h_t, S, \lambda)$ the density at "n+1" time level can be expressed as

$$\begin{aligned} \rho^{n+1} &= \rho^n + \left(\frac{\partial \rho}{\partial \phi} \right)^n \Delta \phi + \left(\frac{\partial \rho}{\partial \vec{\psi}} \right)^n \Delta \vec{\psi} + \\ &+ \left(\frac{\partial \rho}{\partial h_t} \right)^n \Delta h_t + \left(\frac{\partial \rho}{\partial S} \right)^n \Delta S + \left(\frac{\partial \rho}{\partial \lambda} \right)^n \Delta \lambda \end{aligned} \quad (12)$$

and the density derivative as

$$\frac{\partial \rho}{\partial \tau} = \frac{k_1 (\rho^{n+1} - \rho^n)}{\Delta \tau} + \frac{k_2 (\rho^n - \rho^{n-1})}{\Delta \tau} \quad (13)$$

$$k_1 = \frac{4-\theta}{4-2\theta}, \quad k_2 = \frac{-\theta}{4-2\theta} \quad (14)$$

where $\theta=0$ for first order in time accuracy or $\theta=1$ for second order in time accuracy.

The density derivative terms can be computed from the density equation (10). Since though $\Delta \vec{\psi}, \Delta h_t, \Delta S, \Delta \lambda$ are not known a priori the density is linearized as in the irrotational case (11), (13)

$$\rho^{n+1} = \rho^n + \left(\frac{\partial \rho}{\partial \phi} \right)^n_{POT} \Delta \phi, \quad \text{where}$$

$$\left(\frac{\partial \rho}{\partial \phi} \right)^n_{POT} = \beta^n \left(\frac{\partial}{\partial \tau} + \vec{V}^n \cdot \nabla \right) \quad (15)$$

If eqs. (13)-(15) are taken into account, the continuity equation takes the form

$$\begin{aligned} \frac{k_1}{\Delta \tau} \beta^n \left(\frac{\partial}{\partial \tau} + \vec{V}^n \cdot \nabla \right) \Delta \phi + \nabla \cdot (\rho^n \nabla \Delta \phi) &= \\ = -\nabla \cdot (\rho \vec{V})^n - \frac{k_2}{\Delta \tau} (\rho^n - \rho^{n-1}) \end{aligned} \quad (16)$$

where

$$\beta^n = \frac{-\rho^n}{(\gamma-1)h_n} \quad (17)$$

Thus $\Delta \phi$ can be computed from eq. (16) which is solved using an ADI approximate factorization scheme. Thus a \vec{V}^* and ρ^* can

be computed as

$$\vec{V}^* = \vec{V}\phi^* + \vec{V}\psi^* \quad (18)$$

$$\rho^* = \rho_t^n \left[1 - \frac{|\vec{V}^*|^2}{2h_t^n} \right]^{1/\gamma-1}$$

3.1.2 Entropy equation

The entropy equation is cast in the following form

$$(1 + \Delta\tau \vec{V} \cdot \nabla) \Delta S = -\Delta\tau \vec{V} \cdot \nabla S^n \quad (19)$$

and is solved by the A.F. scheme of Rao et al. (10).

3.1.3 Energy equation

The energy equation is cast in the form

$$\vec{V} \cdot \nabla h_t^* = - \frac{1}{\Delta\tau} [\vec{V} \cdot \nabla (\Delta\phi) + T^n \Delta S] \quad (20)$$

It is seen that a $\partial h_t / \partial \tau$ term does not exist. The rotational part of the term $\partial \vec{V} / \partial \tau$ does not exist as well, since $\Delta\psi$ is not yet evaluated. The A.F. scheme of Rao et al is used but eq. (20) is not fully converged. Only a few iterations are performed using a local time step which corresponds to a certain CFL number.

3.1.4 Vorticity transport

The transport equation (6) is solved as

$$-\frac{1}{\rho^*} \left(\frac{\partial \rho^*}{\partial \tau} \right) \lambda^* + \vec{V} \cdot \nabla \lambda^* =$$

$$= - \frac{1}{\rho^*} \nabla \cdot \left[\frac{\vec{V} \cdot \nabla}{|\vec{V} \cdot \nabla|^2} \times [T^n \nabla S^* - \vec{V} h_t^* - \frac{1}{\Delta\tau} \nabla (\Delta\phi)] \right] \quad (21)$$

The solution procedure is the same as that of the energy equation. Thus λ^* leads to the computation of $\vec{\Omega}^*$ as

$$\vec{\Omega}^* = \lambda^* \rho^* \vec{V} + \frac{\vec{V} \cdot \nabla}{|\vec{V} \cdot \nabla|^2} \times [T^n \nabla S^* - \vec{V} h_t^* - \frac{1}{\Delta\tau} \nabla (\Delta\phi)] \quad (22)$$

3.1.5 Poisson equation for $\vec{\psi}$

The Poisson equation is written in a quasi-unsteady form

$$(1 - \Delta\tau \vec{V} \cdot \nabla) \Delta\psi = \Delta\tau (\vec{\Omega}^* + \vec{V} \cdot \nabla \vec{\psi}^n) \quad (23)$$

This equation (in fact three scalar equations for ξ, η, ζ) is solved by a block-ADI scheme where $\Delta\tau$ represents a local time step which corresponds to a certain CFL number. Thus $\vec{\psi}^*$ is evaluated and the estimation of the velocity field is

$$\vec{V}^* = \vec{V}\phi^* + \nabla \times \vec{\psi}^* \quad (24)$$

The vector potential $\vec{\psi}$ is represented using covariant coordinates. This formulation leads to coupled differential equations with simple boundary conditions. This formulation was introduced in the corresponding steady three dimensional

solver (14) and is presented in Appendix I.

3.1.6 Density equation

The density ρ^* is computed explicitly from eq. (10) as

$$\rho^* = \rho_t^n \left(1 - \frac{|\vec{V}^*|^2}{2h_t^*} \right)^{1/(\gamma-1)} \quad (25)$$

where ρ_t^* is explicitly computed from eq. (9) after S^* and h_t^* are found. Thus all quantities are updated at "n+1" time level and the non-linear step will be activated in order to find the correct "n+1" values.

3.2 Non-Linear Step

3.2.1 Continuity equation

Let

$$\vec{\psi}^{n+1} = \vec{\psi}^* + \Delta\vec{\psi}, \quad \phi^{n+1} = \phi^* + \Delta\phi, \quad h_t^{n+1} = h_t^* + \Delta h_t, \quad (26)$$

$$S^{n+1} = S^n + \Delta S, \quad \lambda^{n+1} = \lambda^* + \Delta\lambda$$

thus the density linearization around the "n+1" time level values yields

$$\rho^{n+1} = \rho^* + \left(\frac{\partial \rho^*}{\partial \phi} \right) \Delta\phi + \left(\frac{\partial \rho^*}{\partial \psi} \right) \Delta\psi + \left(\frac{\partial \rho^*}{\partial h_t} \right) \Delta h_t +$$

$$+ \left(\frac{\partial \rho^*}{\partial S} \right) (S^{n+1} - S^*) + \left(\frac{\partial \rho^*}{\partial \lambda} \right) \Delta\lambda \quad (27)$$

The density linearization procedure is the same as the one used in the initial guess. Thus

$$\rho^{n+1} = \rho^* + \left(\frac{\partial \rho^*}{\partial \phi} \right)_{\text{POT}} \Delta\phi = \rho^* + \beta^* \left(\frac{1}{\Delta\tau} + \vec{V}^* \cdot \nabla \right) \Delta\phi \quad (28)$$

Using eq. (28), the continuity equation takes the form

$$\left(k_1 \beta^* \left(\frac{1}{\Delta\tau^2} + \vec{V}^* \cdot \nabla \right) + \nabla \cdot (\rho^* \vec{V}) \right) \Delta\phi =$$

$$= - \left[\frac{k_1}{\Delta\tau} (\rho^* - \rho^n) + \frac{k_2}{\Delta\tau} (\rho^n - \rho^{n-1}) + \nabla \cdot (\rho \vec{V})^* \right] \quad (29)$$

$$\beta^* = - \frac{\rho^*}{(\gamma-1)h^*} \quad (30)$$

which is solved by an AF scheme. Note the subtle difference between the time terms of eqs. (15) and (28). More details are provided in (11).

After $\Delta\phi$ is found, the velocity is updated as

$$\vec{V}^{n+1} = \vec{V}\phi^{n+1} + \nabla \times \vec{\psi}^n \quad (31)$$

3.2.2 Entropy equation

The equation is cast in the form

$$(1 + \Delta\tau \vec{V} \cdot \nabla) \Delta S = -\Delta\tau \vec{V} \cdot \nabla S^n \quad (32)$$

and is solved as in the initial guess step.

3.2.3 Energy equation

Since $\bar{\Psi}^*$ is evaluated, the equation takes the form

$$\bar{V}_{n+1} \cdot \nabla h_{t,n+1} = - \frac{1}{\Delta \tau} \{ \bar{V}_{n+1} \cdot [\nabla(\phi_{n+1} - \phi_n) + \nabla x(\bar{\Psi}_{n+1} - \bar{\Psi}_n)] + T_{n+1} \Delta S \} \quad (33)$$

The solution procedure is the same as that of the initial guess step.

3.2.4 Vorticity transport equation

This equation becomes

$$- \frac{1}{\rho^*} \left(\frac{\partial \rho^*}{\partial \tau} \right) \lambda_{n+1} + \bar{V}_{n+1} \cdot \nabla \lambda_{n+1} = - \frac{1}{\rho^*} \nabla \cdot \left[\frac{\bar{V}_{n+1}}{|\bar{V}_{n+1}|^2} \times \left\{ T_{n+1} \nabla S_{n+1} - \nabla h_{t,n+1} - \frac{\partial \bar{V}_{n+1}}{\partial \tau} \right\} \right] \quad (34)$$

and is solved as in the initial guess

3.2.5 Poisson equation for $\bar{\Psi}$

The Poisson is written in the form

$$(1 - \Delta t f \nabla^2) \Delta \bar{\Psi} = \Delta t f (\bar{\Omega}_{n+1} + V^2 \bar{\Psi}^*) \quad (35)$$

and the same solution procedure as in the initial guess is followed. Thus the updated velocity is

$$\bar{V}_{n+1} = \nabla \phi_{n+1} + \nabla \times \bar{\Psi}_{n+1} \quad (36)$$

3.2.6 Density equation

The density ρ_{n+1} is

$$\rho_{n+1} = \rho_{t,n+1} \left(1 - \frac{|\bar{V}_{n+1}|^2}{2 h_{t,n+1}} \right)^{1/\gamma-1} \quad (37)$$

where $\rho_{t,n+1}$ is explicitly computed from eq.(9) after the evaluation of $h_{t,n+1}$ and S_{n+1} .

It is noted that the unsteady equations of energy, continuity, vorticity transport and Poisson appear at the right hand side of the non-linear formulation. If these residuals are minimized to a desired level, the non-linear step ends with the explicit density computation. If not, the current "n+1" values are set as "n" values and a new non-linear step is activated. In practice several non-linear steps are required for convergence.

4 BOUNDARY CONDITIONS

The definition of the boundary conditions is the most difficult topic in internal aerodynamics, especially when the flow is rotational at the inlet plane. The present test cases consider ducts with orthogonal inlet planes and the tangential velocity components at the inlet will be assumed zero. The inlet normal velocity profile will be assumed linear and its defining law for the steady state is

$$u_{in}(y, z, 0) = u_\infty (1 + 0.1 y / y_{max}) \quad (38)$$

where u_∞ corresponds to a given free stream Mach number (here $M_\infty = 0.4$).

The imposed inlet normal velocity profile for the unsteady case is defined as

$$u_{in}(y, z, \tau) = u_{in}(y, z, 0) (1 + 0.2 \sin(k\tau)) \quad (39)$$

The governing equations are normalized by some characteristic values. Their form remains the same after the normalization. x, y, z are normalized by c_0 , V by V_0 , h_t by V_0^2 , τ by $\tau_0 = c_0 / V_0$, ρ by ρ_0 . For convenience $V_0 = u_\infty$, $\rho_0 = \rho(M_\infty)$, $c_0 = c$ (the length of the duct). Thus the reduced frequency K is

$$K = \frac{\omega c_0}{V_0} = \frac{\omega c}{u_\infty} \quad (40)$$

The entropy at the inlet must also be specified at each time step. Here the flow is assumed to be fully isentropic which is the most realistic for subsonic flow problems, but generally the code can handle entropy variations.

The total enthalpy must be derived from the compatibility condition that the introduced inlet vorticity from the velocity profile must be the same as that of the entropy and total enthalpy fields. Since the tangential velocity components at the inlet are assumed zero, no secondary vorticity is introduced in the domain ($\lambda=0$). The inlet plane is assumed to be orthogonal, so a local Cartesian coordinate system can be attached. Thus the compatibility condition is

$$\Omega = \nabla x \bar{V} = \frac{\bar{V}}{|\bar{V}|^2} \times \left[T \nabla S - \nabla h_t - \frac{\partial \bar{V}}{\partial \tau} \right] \quad \text{where } \bar{V} = u(y) \cdot \bar{i} \quad (41)$$

which gives

$$\frac{\partial h}{\partial y} = \frac{1}{c_p} \frac{\partial S}{\partial y} \quad (42)$$

If $\partial S / \partial y$ is independent of y (linear entropy profile) the enthalpy is

$$h_t(y, z, \tau) = (h_t(0, z, \tau) -$$

$$- \frac{u_{in}^2(0, z, \tau)}{2}) \exp(\partial s / \partial y \cdot y / c_p) + \frac{u_{in}^2(y, z, \tau)}{2} \quad (43)$$

where $h_t(0, z, \tau)$ is specified as

$$h_t(0, z, \tau) = h_{t0} - \frac{\partial \phi(y=0)}{\partial \tau} \quad (44)$$

The final quantity needed is the exit normal velocity. It is well known that in an one dimensional unsteady potential flow the disturbances propagate with $(u+\alpha)(\tau=0)$ speed if they are small and with $(u+\alpha)(\tau)$ speed if they are large. A coherent set of boundary conditions can be set if it's assumed that the disturbances propagate with $(u+\alpha)(0)(y=y_{max})$ speed. Thus the time delay is approximated as

$$\Delta \tau_{del} = \frac{c}{(u+\alpha)(\tau=0, y=y_{max})} \cdot \frac{1}{\tau_0} \quad (45)$$

and the exit normal velocity follows the law

$$u_{ex}(y,z,\tau) = \begin{cases} u_{in}(y,z,0) & \text{if } 0 \leq \tau \leq \Delta t_{del} \\ u_{in}(y,z,0)(1 + 2\sin(k \cdot (\tau - \Delta t_{del}))) & \text{otherwise} \end{cases} \quad (46)$$

It must be noted that the imposed boundary conditions are quasi three dimensional. More complex boundary conditions (p.ex. secondary vorticity at the inlet) could be imposed which would lead to must more complex compatibility relations for all quantities involved.

5 RESULTS AND DISCUSSION

The presented results cover the subsonic compressible flow region in a three dimensional duct. It is the classical "bump" test case (12) in three dimensions. Generally the code can handle a secondary vorticity distribution at the inlet plane but in this test case this distribution will be assumed zero. This leads to a quasi three dimensional flow in the duct which demonstrates the ability of the code to degenerate in simpler solutions while operated at its general form. The reduced frequency K will be equal to 1 and the boundary conditions will be those described in the previous chapter. Both first and second order in time runs will be presented. Unfortunately no similar effort for either two or three dimensional unsteady rotational flows in ducts has been found in order to validate the presented results.

Fig.1 presents a first order in time run with $sl=100$. The Mach number distribution on the lower boundary is plotted for the steady case and for each 90° , up to 540° . Note the considerable difference at the exit Mach number between the steady state, 180° and 360° . It is also seen that a slight transition exists between 90° and 450° . The difference at the exit Mach number between 0° , 180° and 360° is due to the phase difference of the exit normal velocity, where at the inlet the Mach number is the same.

A second order in time run for the same test case is presented in fig.2. There are not many differences between these figures except that the observed transition between 90° and 450° is somewhat bigger than in the first order in time run. 15 non-linear steps per time step were used for both runs and the calculations were performed on a $50 \times 10 \times 6$ grid.

The same number of non-linear steps per time step were used for the second order in time run in the bump with $K=0.5$, $sl=160$. Since $\Delta \tau = 2\pi/K \cdot sl$, the time step for this test case is greater than the one used in the previous case. Fig.3 presents the Mach number distribution on the lower boundary for the steady case and the first two cycles, at each 90° . It is seen that the Mach number distribution for 180° and 360° is very close to the steady state, in contrast with the case of $K=1$. This is expected because the flow tends to the steady state as the reduced frequency diminishes.

6 CONCLUSIONS

The three dimensional unsteady rotational flow in ducts was discussed and some results were presented. The boundary conditions were the same as those of a two dimensional flow and fully three dimensional ones could be imposed in the future. The introduced vorticity was treated without severe problems and the proposed code seems to be promising. For the moment the flow is limited to the subsonic region. The next step will be the testing of the code in more complicated geometries.

7 REFERENCES

1. Kandil, O.A., Chuang, A.H., "Unsteady Transonic Airfoil Computation Using Implicit Euler Scheme on Body-Fixed Grid", AIAA Journal, Vol.27, No 8, 1989, pp.1031-1037.
2. Venkatakrishnan, V., Jameson, A., "Computation of Unsteady Transonic Flows by the Solution of Euler Equations", AIAA Journal, Vol.26, No 8, 1988 pp.974-981.
3. Guruswamy, G.P., "Unsteady Aerodynamic and Aeroelastic Calculations for Wings Using Euler Equations", AIAA Journal, Vol.28, No 3, 1990, pp.461-469.
4. Anderson, W.K., Batina, J.T., "Accurate Solutions, Parameter Studies, and Comparisons for the Euler and Potential Flow Equations", AGARD-CP-437, Vol. 1, "Validation of Computational Fluid Dynamics", 1988.
5. Allmaras, S.R., "A Coupled Euler/Navier-Stokes Algorithm for 2-D Unsteady Transonic Shock/Boundary-Layer Interaction", GTL Report # 196, Ph.D. Thesis, MIT, 1989.
6. Servaty, S., Gallus, H.E., "Unsteady Blade Loads Due to Wake Influence", AGARD-CP-468, "Unsteady Aerodynamic Phenomena in Turbomachines", 1989.
7. Fourmaux, A., Billonnet, Gilles, Le Meur, A., Lessain, A., "Simulation Numerique des Ecoulements Tridimensionnels et Instationnaires dans les Turbomachines", AGARD-CP-468/469-Unsteady Aerodynamic Phenomena in Turbomachines, 1989.
8. Chaviaropoulos, P., Giannakoglou, K., Papailiou, K.D., "Numerical Computation of Three-Dimensional Rotational Inviscid Subsonic Flows, Using the Decomposition of the Flow Field Into a Potential and a Rotational Part", ASME Paper 86-GT-169, International Gas Turbine Conference and Exhibit, Dusseldorf, June 8-12, 1986.
9. Hadzidakis, M., Karagiannis, F., Chaviaropoulos, P., Papailiou, K.D., "Unsteady Euler Calculations in 2-D Internal Aerodynamics with Introduced Vorticity", ASME Paper, to appear at the 1991 Intl. Gas Turbine Conference and Exhibition, Orlando, Florida, USA.

10. Rao, K.V., Steger, J.L., Pletcher, R.H., "A Three-Dimensional Dual Potential Procedure for Inlets and Indraft Wind Tunnels", AIAA Paper 87-0598.
11. Shankar, V., Ide, H., Gorski, J., Osher, S., "A Fast, Time-Accurate, Unsteady Full Potential Scheme", AIAA Journal, Vol. 25, No. 2, 1987, pp. 193-198.
12. Rizzi, A., Viviani, H. (ed.), "GAMM Workshop on Numerical Methods for the Computation of Inviscid Transonic Flows with Shock Waves", Vieweg editions, 1981.
13. Hadzidakis, M., Chaviaropoulos, P., Papailiou, K.D., "A Two-Dimensional Unsteady Potential Solver in Internal Aerodynamics Flow Problems", Proceedings of the Vth International Symposium on Numerical Methods in Engineering, Lausanne, Switzerland, 1989.
14. Chaviaropoulos, P., Giannakoglou, K., Papailiou, K.D., "Novel Scalar-Vector Potential Formulation for Three-Dimensional, Inviscid, Rotational Flow Problems", AIAA Journal, Vol. 28, No. 10, October 1990, pp. 1734-1739.
- $$\Omega_i = \lambda \rho U_i + F_i \quad (A1.10)$$
- $$F_i = J(A_2 B^3 - A_3 B^2) \quad (A1.11)$$
- $$F_2 = J(A_3 B^1 - A_1 B^3) \quad (A1.12)$$
- $$F_3 = J(A_1 B^2 - A_2 B^1) \quad (A1.13)$$
- $$A^i = \frac{U^i}{|\vec{V}|^2} \quad (A1.14)$$
- $$B^i = T\alpha^i - \beta^i - \frac{\partial U^i}{\partial \tau} \quad (A1.15)$$
- $$\alpha^i = g^{ij} \frac{\partial S}{\partial u_j} \quad (A1.16)$$
- $$\beta^i = g^{ij} \frac{\partial h_t}{\partial u_j} \quad (A1.17)$$
- $$U_i = U_j g_{ij} \quad (A1.18)$$
- Vorticity Transport
- $$-\frac{1}{\rho} \frac{\partial \rho}{\partial \tau} \lambda + U^i \frac{\partial \lambda}{\partial u_i} = -\frac{1}{\rho} \nabla \cdot (F_i \vec{g}^i) \quad (A1.19)$$

8 APPENDIX I

If we set $u_1 = \xi$, $u_2 = \eta$, $u_3 = \zeta$, the equations at the computational domain are

Continuity Equation

$$\frac{\partial(\rho J)}{\partial \tau} + \frac{\partial}{\partial u_i} (\rho J U^i) = 0 \quad (A1.1)$$

Entropy Equation

$$\frac{\partial S}{\partial \tau} + U^i \frac{\partial S}{\partial u_i} = 0 \quad (A1.2)$$

Poisson

$$\vec{\Psi} = \Psi_i \vec{g}^i \quad (A1.3)$$

where on $u_\kappa = ct$

$$\Psi_i = 0, \quad \forall i \neq \kappa \quad (A1.4)$$

$$\begin{aligned} & \frac{\partial}{\partial u_i} (J g^{i\kappa}) \Psi_\kappa + J g^{i\kappa} \frac{\partial}{\partial u_i} (\Psi_\kappa) = \\ & = -J g^{\kappa\lambda} \frac{\partial}{\partial u_\kappa} (\Psi_\lambda) \end{aligned} \quad (A1.5)$$

$\lambda \neq \kappa$, no summation on κ

$$\vec{\Omega} = \Omega_i \vec{g}^i \quad (A1.6)$$

$$\nabla^2 \Psi_i - \frac{\partial \Psi_j}{\partial u_\mu} \alpha_{j\mu} - \Psi_k \beta_k^i = -\Omega_i \quad (A1.7)$$

$$\alpha_{j\mu}^i = 2\Gamma_{\nu i}^j g^{\mu\nu} \quad (A1.8)$$

$$\beta_k^i = \left(\frac{\partial \Gamma_{\nu i}^k}{\partial u_\mu} - \Gamma_{j i}^k \Gamma_{\mu\nu}^j - \Gamma_{\nu j}^k \Gamma_{\mu i}^j \right) g^{\mu\nu} \quad (A1.9)$$

where U^i are the contravariant velocity components

$$U^i = g^{ij} \frac{\partial \Phi}{\partial u_j} + U_{r^i} \quad (A1.25)$$

\vec{g}^i the contravariant vectors, J the jacobian of the transformation, g_{ij} the contravariant metrics, g_{ij} the covariant metrics and $\Gamma_{j\kappa}^i$ the Christoffel symbols of the second kind.

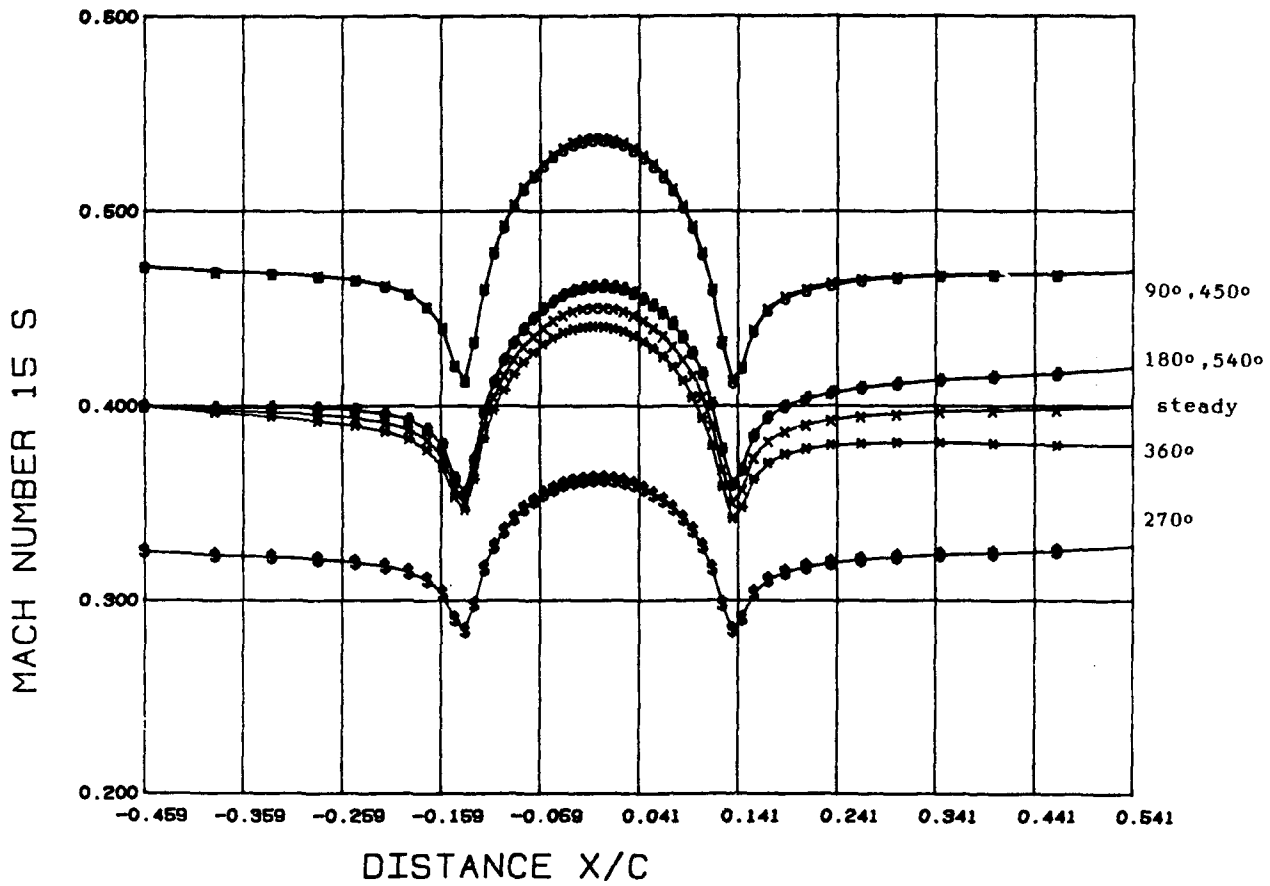


Fig. (1): Mach number distribution on the "bump" lower boundary for $K=1$, $sl=100$. First order in time run.

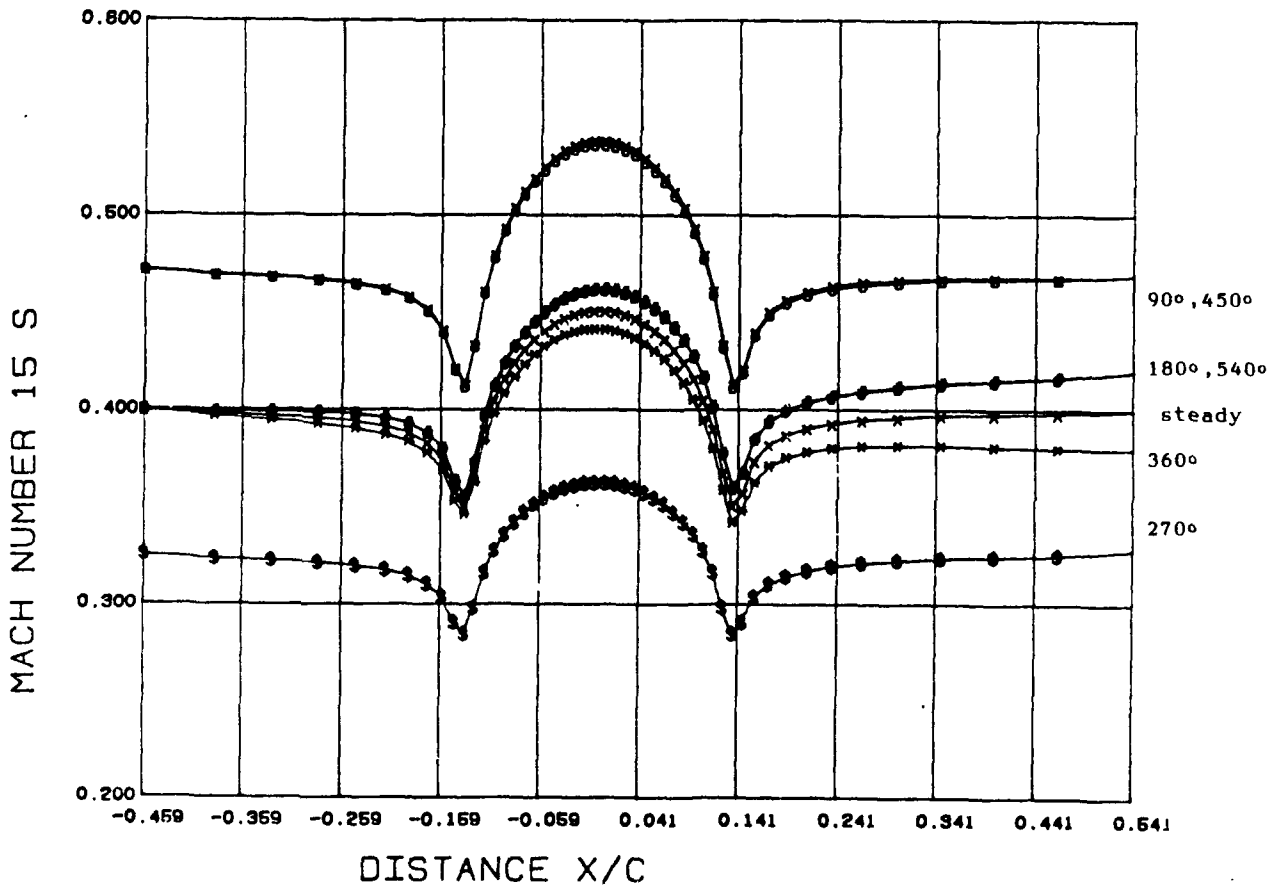


Fig. (2): Mach number distribution on the "bump" lower boundary for $K=1$, $sl=100$. Second order in time run.

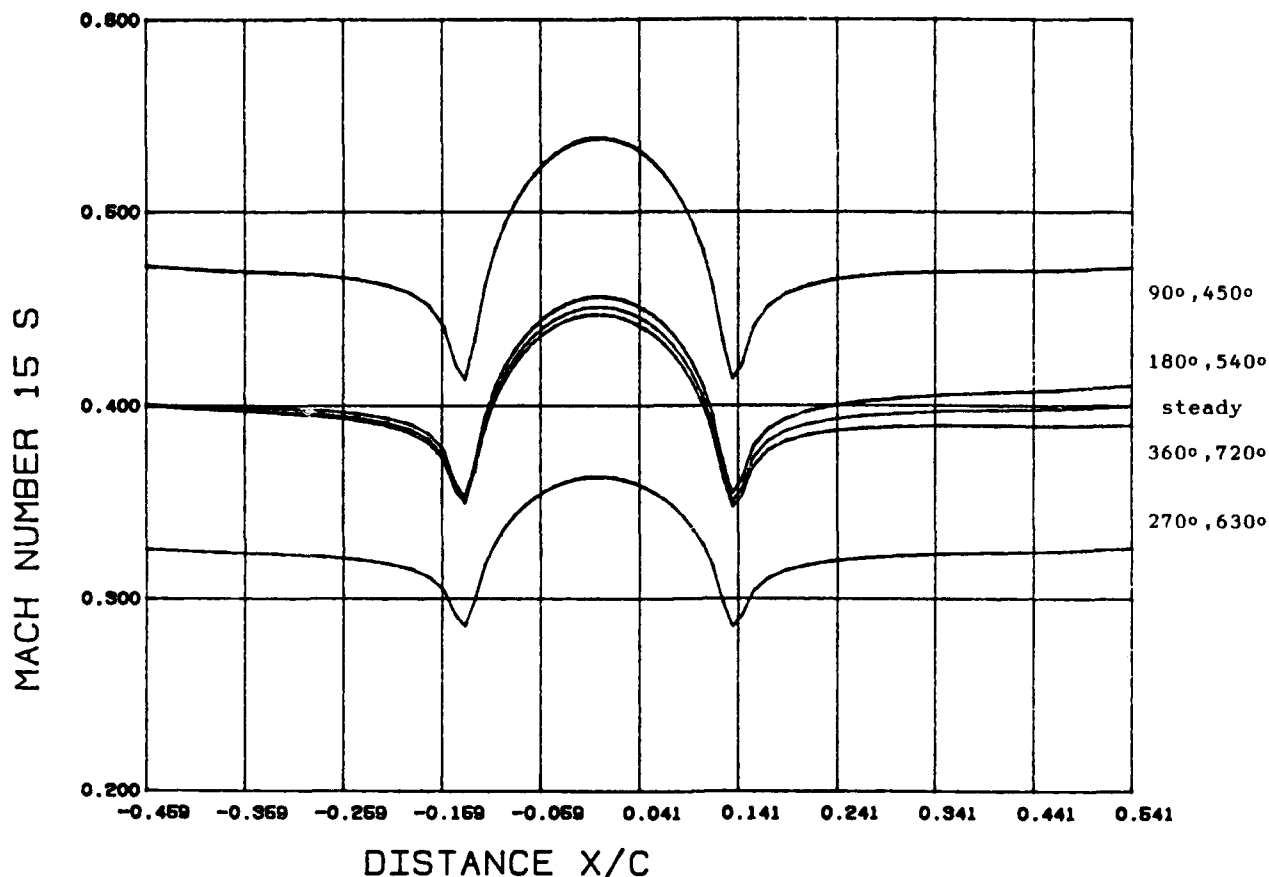


Fig. (3): Mach number distribution on the "bump" lower boundary for $K=0.5$, $sl=160$. Second order in time run.

Discussion

F. LEBOEUF, ECOLE CENTRALE LYONS, FRANCE

1) Pouvez-vous comparer les avantages et les inconvénients des formulations de Helmholtz et de Glebsk?

2) La condition à la limite amont (Eq. (43)) signifie-t-elle que vous ne pouvez pas choisir h_t et S indépendamment?

3) L'équation (42) est-elle correcte? Elle implique que $\partial p / \partial y = 0$?

AUTHOR'S REPLY

1) Nous avons choisi la décomposition Helmholtz pour les raisons suivantes:

- Il existe déjà une expérience très solide sur ce sujet en écoulements stationnaires
- Nous avons une description précise des champs d'entropie S et d'enthalpie totale h_t , puisque ces deux grandeurs sont utilisées comme variables indépendantes du problème.
- Nous n'introduisons pas de viscosité artificielle dans nos calculs.

2) L'enthalpie totale h_t est compliquée à définir, à cause de la formulation choisie. En tous cas dans le cas simple que nous présentons ici, l'enthalpie est indépendante de l'entropie dans le sens où $h_t(o,r)$ est définie à un point (à l'entrée) indépendamment de S . La définition arbitraire du profil de h_t nous conduirait à des solutions sans sens physique, et une éventuelle divergence du code.

3) L'équation (42) doit être correctement écrite de la façon suivante:

$$\frac{\partial h}{\partial y} = \frac{1}{c_p} \cdot \frac{\partial S}{\partial y} \cdot h$$

AD-P007 698



92-16084



THE APPLICATION OF A NAVIER-STOKES CFD METHOD TO CIVIL ENGINE INTAKE FLOWS

by

Dr. N. T. Birch and Dr. E. H. Kitchen
Rolls-Royce plc, P. O. Box 31, Derby, DE2 8BJ, U.K.
Dr. R. J. G. Norton,
Rolls-Royce, Inc., 1895 Phoenix Boulevard, Atlanta, USA.

SUMMARY

Three-dimensional flows around civil engine intakes have been calculated by a Navier-Stokes method. The full Reynolds-averaged Navier-Stokes equations for viscous flow are solved by an explicit time-marching cell-centred finite-volume algorithm. To ensure numerical stability, Jameson's formulation of fourth-order and second-order smoothing is used. Second-order smoothing is switched on only in regions of strong pressure gradient such as shocks. The flow may be laminar or turbulent; turbulence is treated by a mixing-length eddy viscosity model. The algorithm is applied on a body-fitted C-type computational grid.

The method is applicable to studies of intake flow capacity, Reynolds number scaling, separation limits, pressure recovery and distortion, and nacelle drag. A series of flow conditions may be analysed to produce, for example, a curve of intake pressure recovery and distortion coefficient against mass flow. Initially the method was applied to an axisymmetric intake, for which experimental surface pressures are available as well as results from a potential flow method with inviscid/viscous interaction. Calculations were then performed for a 3D intake at high incidence conditions and compared to both experimental data and inviscid/viscous interaction results, over a range of engine mass flows. The results show that the Navier-Stokes method successfully predicts the trend of increasing loss and distortion over the full range of mass flow. The results are also shown to be sensitive to Reynolds number and the assumed position of laminar/turbulent transition.

NOMENCLATURE

(Symbols not defined explicitly in the text.)

ρ	density
x, y, z	Cartesian co-ordinates
u, v, w	Cartesian velocity components
e	internal energy
τ_{xx}, τ_{xy}	viscous shear stress components
p	static pressure

μ	viscosity
t	time
T	temperature
R_g	gas constant
Pr, Pr_t	laminar, turbulent Prandtl number
c_p	specific heat
γ	ratio of specific heats

1. INTRODUCTION

The aerodynamic design of the engine nacelles of modern civil subsonic transport aircraft is becoming increasingly important in determining the overall aircraft performance. As the bypass ratio (and hence fan diameter) of the modern turbofan engine has increased, together with the recent popularity of the wide-bodied twin-engined aircraft, so the nacelle drag has tended to become a more important component of total aircraft drag. In addition, ground proximity limitations for underwing powerplant installations have tended to lead to nacelle locations closer to the wing resulting in the increased risk of nacelle/wing aerodynamic interference.

These trends have increased the desirability of producing nacelles with the smallest possible maximum diameter. This, in turn, has led to increased attention being paid to the intake design, for example through the reduction and circumferential variation of intake lip contraction ratio and the increased circumferential asymmetry of the external nacelle profile.

The choice of geometric design parameters defining the intake represents a compromise between achieving the best possible performance at design point (cruise) conditions, and ensuring acceptable engine face and external flow at a wide variety of off-design conditions. To prevent degradation of the engine performance and stability, the intake must deliver flow to the fan face with minimal pressure losses and low distortion at various extreme conditions including high incidence, static and crosswind situations, for varying engine mass flows. Likewise, the external intake profile must be carefully chosen to ensure that nacelle drag does not increase at high flight speeds, at reduced engine mass

flows, and at high incidence. Figure 1 illustrates the various critical off-design conditions that must be considered in the intake design.

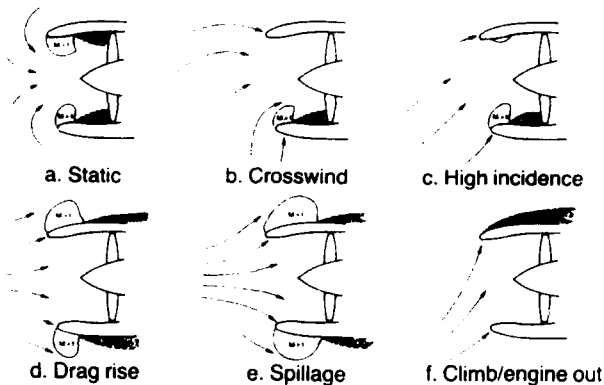


Figure 1. Intake off-design conditions

The desirability of reduced intake contraction ratio means that extreme care must be taken to ensure that the intake aerodynamics is acceptable at all these off-design conditions with a minimal margin for error. For example, the aircraft manufacturer will normally define the maximum aircraft incidence at which safe engine operation must be guaranteed, over a range of flight Mach numbers (normally the aircraft buffet boundary). The intake will then usually be designed to ensure separation-free flow up to these limitations of the flight envelope. To demonstrate this, a model of the intake may be tested in the windtunnel over a range of incidence and Mach number to obtain internal separation boundaries and limiting flow distortion parameter values. Since windtunnel models will normally be tested at sub-scale Reynolds numbers such results will usually be pessimistic, leading either to conservative intake designs, or increased risk of engine problems at these extreme conditions. This highlights the need for both improved design rules in generating the intake internal and external aerodynamic profiles and an accurate 3D viscous CFD analysis method, which can predict both cruise and off-design performance at an early stage of the design process, and which can allow for scale effects.

In recent years, the 3D analysis of subsonic intake aerodynamics has mostly been performed using methods based on the Full Potential Flow or Euler Equations. Chen & Caughey (Ref. 1), Vadyak & Atta (Ref. 2), Nakamura (Ref. 3) and Peace (Ref. 4) solved the potential flow equation on body-fitted meshes for intake configurations. Reyhner (Ref. 5) used a Cartesian mesh to analyse intake flows, the advantage being that the problem of generating a smooth, body-fitted grid is avoided. Viscous effects were modelled by Vadyak & Atta (Ref. 2) by linking an axisymmetric integral boundary layer method to the potential flow scheme. The published reports on these methods show good agreement between predicted and

measured intake/nacelle surface pressure distributions at cruise-type conditions (high Mach number, low angle of attack). Schmilovich (Ref. 6) used a finite volume potential flow method coupled to an inverse, axisymmetric differential boundary layer method, due to Cebeci and Smith (Ref. 7). This was used to overcome the well-known numerical stability problems associated with direct inviscid-viscous coupling at off-design conditions, where the boundary layer tends to separate. Schmilovich used this economical scheme to show regions of separation in the intake at off-design conditions, although no experimental data were shown to validate the boundary layer behaviour.

A number of methods based on the Euler equations have also been used to analyse the flow in subsonic intakes. Chen et al (Ref. 8), Hirose and Akai (Ref. 9) and Vadyak (Ref. 10) have analysed nacelle flows with embedded shocks. The main advantage of the Euler type of method is in its ability to more accurately predict rotational effects (e.g., shock waves), which are not allowed for by the potential flow equations. Viscous effects again may be included by coupling the Euler solutions to a boundary layer method. Whilst the direct-coupled inviscid/viscous interaction type of method would normally be expected to give good performance predictions at cruise or moderately off-design conditions, this approach has shortcomings at extreme conditions. This is because the direct coupling of the inviscid and viscous regions becomes increasingly numerically unstable as separation is approached, and, at least for high incidence conditions, the flow field becomes increasingly three-dimensional. This makes the application of a two-dimensional or axisymmetric boundary layer technique invalid and demands the use of either a coupled 3D boundary layer method or the use of a Navier-Stokes method. The latter approach has been used by Shrewsbury et al (Ref. 11). The advantage of the Navier-Stokes approach is that it may be possible to analyse extreme off-design conditions, e.g., high incidence separation boundaries, where limiting engine face distortion parameter values are required. This type of information would normally be obtained from a windtunnel model test at a sub-scale Reynolds number. A Navier-Stokes method could also be used to extrapolate model test results to full-scale. The difficulties with the Navier-Stokes approach are well-known. They include the difficulty of grid generation, turbulence modelling and the balancing of long computer run-times with high resolution grids for accuracy.

The objective of this paper is to present a 3D Navier-Stokes method for the prediction of subsonic engine intake flows. The first part of the paper describes the governing equations and numerical algorithm employed, the choice of computational grid, and some details of the turbulence modelling. The remainder of the paper is concerned with the application of the method to both an axisymmetric intake, and a more representative three-dimensional intake geometry. Results are obtained for both full and sub-scale Reynolds numbers and are compared

to those from a potential flow method and experimental data. These examples illustrate the usefulness of a Navier-Stokes approach for the analysis of intake flows at off-design conditions.

2. DESCRIPTION OF METHOD

2.1 Governing Equations

The three-dimensional Reynolds-averaged Navier-Stokes equations for compressible viscous flow may be written in a Cartesian co-ordinate system as

$$\frac{\partial U}{\partial t} + \frac{\partial F}{\partial x} + \frac{\partial G}{\partial y} + \frac{\partial H}{\partial z} = 0 \quad (1)$$

where U is the state vector and F, G, H are the flux vectors:

$$U = \begin{pmatrix} \rho \\ \rho u \\ \rho v \\ \rho w \\ \rho e \end{pmatrix}$$

$$F = \begin{pmatrix} \rho u \\ \rho u^2 + p - \tau_{xx} \\ \rho uv - \tau_{xy} \\ \rho uw - \tau_{xz} \\ \rho uI - u\tau_{xx} - v\tau_{xy} - w\tau_{xz} + q_x \end{pmatrix}$$

$$G = \begin{pmatrix} \rho v \\ \rho uv - \tau_{xy} \\ \rho v^2 + p - \tau_{yy} \\ \rho vw - \tau_{yz} \\ \rho vI - v\tau_{xy} - w\tau_{yz} + q_y \end{pmatrix}$$

$$H = \begin{pmatrix} \rho w \\ \rho uw - \tau_{xz} \\ \rho vw - \tau_{yz} \\ \rho w^2 + p - \tau_{zz} \\ \rho wI - w\tau_{xz} - v\tau_{yz} - u\tau_{zz} + q_z \end{pmatrix} \quad (2)$$

Assuming that turbulent stresses can be modelled by a viscosity coefficient in the same way as viscous stresses (Boussinesq hypothesis), the components of the stress tensor are

$$\begin{aligned} \tau_{xx} &= \mu \frac{2}{3} \left(2 \frac{\partial u}{\partial x} - \frac{\partial v}{\partial y} - \frac{\partial w}{\partial z} \right) \\ \tau_{yy} &= \mu \frac{2}{3} \left(2 \frac{\partial v}{\partial y} - \frac{\partial u}{\partial x} - \frac{\partial w}{\partial z} \right) \\ \tau_{zz} &= \mu \frac{2}{3} \left(2 \frac{\partial w}{\partial z} - \frac{\partial u}{\partial x} - \frac{\partial v}{\partial y} \right) \\ \tau_{xy} &= \tau_{yx} = \mu \left(\frac{\partial u}{\partial y} + \frac{\partial v}{\partial x} \right) \\ \tau_{yz} &= \tau_{zy} = \mu \left(\frac{\partial v}{\partial z} + \frac{\partial w}{\partial y} \right) \\ \tau_{zx} &= \tau_{xz} = \mu \left(\frac{\partial u}{\partial z} + \frac{\partial w}{\partial x} \right) \end{aligned} \quad (3)$$

Pressure, temperature and density are related by the gas law

$$p = \rho R_g T \quad (4)$$

and the internal energy e and enthalpy h are given by

$$e = \frac{1}{\gamma - 1} \frac{p}{\rho} + \frac{1}{2} (u^2 + v^2 + w^2) \quad h = e + \frac{p}{\rho} \quad (5)$$

The heat flux components are

$$(q_x, q_y, q_z) = -k \left(\frac{\partial T}{\partial x}, \frac{\partial T}{\partial y}, \frac{\partial T}{\partial z} \right) \quad (6)$$

Effective viscosity μ and thermal diffusivity k are given by

$$\mu = \mu_l + \mu_t \quad k = c_p \left(\frac{\mu_l}{Pr} + \frac{\mu_t}{Pr_t} \right) \quad (7)$$

μ_l is the laminar viscosity. Turbulent viscosity μ_t is zero for laminar flow, and otherwise is given by a suitable turbulence model. The laminar and turbulent Prandtl numbers are taken as 0.72 and 0.92 respectively.

2.2 Numerical Scheme

The numerical technique used to solve the equations is based on that developed by Jameson et al (Ref. 12) for the Euler equations, and is similar to the Navier-Stokes method of Swanson and Turkel (Ref. 13). This is a finite-volume method in which the equations are written as a balance of fluxes over hexahedral cells, with the flow variables evaluated and stored at the cell centres. The resulting discrete form of the equations can be written as

$$\frac{\partial U_{ijk}}{\partial t} + Q_{ijk} + V_{ijk} - D_{ijk} = 0 \quad (8)$$

where i, j, k are cell labels in a structured grid. Q arises from the inviscid terms in the equations, V from the viscous and heat flux terms, and D represents smoothing or artificial dissipation which is added to the equations. Following Jameson, D is a blend of fourth order smoothing to suppress odd-even point oscillations, and second order smoothing which is activated only in regions of strong pressure gradient such as shocks, to suppress pre- and post-shock oscillations.

Equation (8) is marched forward in time by a two-step predictor-corrector method. The physical residual for the solution at time level n is

$$R(U^{(n)}) = -Q^{(n)} - V^{(n)} \quad (9)$$

The predictor step is

$$U^{**} = U^{(n)} + \Delta t (R(U^{(n)}) + D(U^{(n)})) \quad (10)$$

and the corrector step is

$$U^{(n+1)} = U^{(n)} + \Delta t (R(U^{**}) + D(U^{**})) \quad (11)$$

Since the scheme is explicit, there is a time-step restriction of the form

$$\Delta t < C \tau \quad (12)$$

where τ is an expression depending on the local velocities and grid metric coefficients for each cell, and C is a constant. Hence, the maximum allowable time-step

varies from cell to cell. Normally the code is run by taking

$$\Delta t = C_1 \tau \quad (13)$$

where C_1 is an input parameter typically chosen as 0.8.

The boundary conditions are as follows:

Freestream: specified values of farfield static pressure and temperature, Mach number, and flow angles (pitch and yaw). Small perturbations to these farfield conditions are imposed at the boundary using characteristic based extrapolation.

Walls: zero velocity, zero normal pressure gradient, and either a specified wall temperature or zero normal temperature gradient.

External downstream boundary: specified static pressure (= freestream value).

Intake downstream boundary: specified static pressure.

Other variables at the two downstream boundaries are obtained by extrapolation of 1D flow characteristics.

Boundary conditions are implemented using dummy computational cells along each boundary. The grid axis, where one face of each cell contracts to a line, is not a physical boundary but merely a topological boundary, where the dummy cell data is obtained from the cell physically across the axis.

For grids with around 40,000 points, changes in state vector variables typically have reduced by 3 to 4 orders of magnitude after around 5,000 iterations. This level of convergence ensures that calculated total pressure losses can be quoted to precision better than that of experimental data.

2.3 Grid Structure

The natural type of computational grid structure for civil intake flowfields is a C-type grid (Fig. 2) in which the grid lines wrap around the body. This grid system has been used previously in Refs. 2, 3, 4 and 6 and is also used for the potential flow calculations described in this paper. For Navier-Stokes calculations, the grid need only be modified by adding extra C-lines close to the intake surface, to resolve the internal and external boundary layers. A 3D grid is produced by circumferential stacking of grid sections around a common centreline. The only disadvantage with this grid system is a tendency for skewed grid cells to be generated, particularly in the vicinity of the centreline upstream of the intake. This leads to the possibility of the generation of numerical errors in this region if the algorithm is sensitive to skewness in the grid. The relationship between grid quality and algorithm behaviour is further discussed in Section 3.

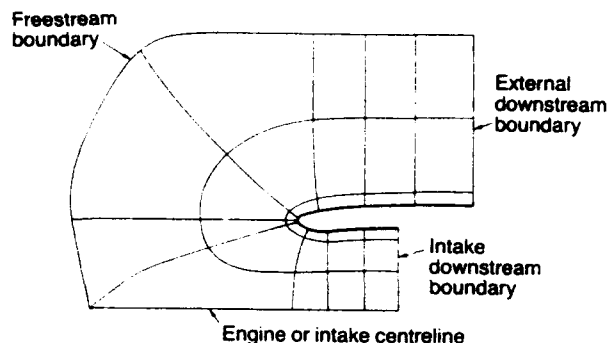


Figure 2. C-type grid (schematic)

A master grid is created which describes the body surface with sufficient accuracy. If required, linear interpolation in the master grid is used to produce a calculation grid. For example, the number of calculation points in the boundary layer region may be increased without regenerating the master grid.

2.4 Turbulence Modelling

In the Prandtl mixing length model, as implemented by Moore and Moore (Ref. 14), the turbulent (eddy) viscosity is given by

$$\mu_t = \rho l^2 D \quad (14)$$

where l is the mixing length and D is a generalised velocity gradient. The mixing length in shear layers or boundary layers is given by

$$l = \min(\kappa n E_v, \lambda \delta) \quad (15)$$

where n is the distance to the nearest wall, δ is the shear layer thickness, and κ and λ are constants taken as 0.41 and 0.08, respectively. E_v takes the value 1 except in the near-wall region where it is the van Driest damping factor,

$$E_v = 1 - \exp \left[\frac{-n \sqrt{\rho(\mu + \mu_t) D}}{A \mu_t} \right] \quad (16)$$

A is a constant taken as 26. Because μ_t appears on the right-hand side of (16), it must be calculated iteratively (by successive substitution) in the near-wall region. The shear layer thickness δ is determined within the code by the behaviour of the gradient of a shear layer parameter δ^+ . Two choices of δ^+ are available, one based on total pressure and the other on flow vorticity.

In regions away from any shear or boundary layers, the mixing length l is either input directly, or is given in terms of free-stream turbulence intensity T_∞ and a characteristic length L , by

$$l = 0.387 T_\infty L \quad (17)$$

Clearly this is a rather ad hoc and approximate treatment of freestream turbulence.

The generalised velocity gradient D is given by

$$D = \sqrt{\left| \frac{\partial u_i}{\partial x_j} \right| \left(\frac{\partial u_i}{\partial x_j} + \frac{\partial u_j}{\partial x_i} \right)} \quad (18)$$

(summation over indices i and j).

Laminar/turbulent transition may be modelled within the code by de-activating the turbulence model in specified regions of the computational grid.

2.5 Potential Flow Method

Intake flowfields are routinely calculated by a potential flow method with coupled boundary layer. The three-dimensional compressible flow equation in non-conservative form is discretised by finite differences in the manner of Jameson (Ref. 15), using rotated differences to maintain computational stability in supersonic regions. The resulting discrete system of equations is solved by an implicit approximate factorisation technique, namely the AF3 scheme described by Baker and Forsey (Ref. 16). Viscous effects are treated by an integral boundary layer method which can deal with laminar, transitional and turbulent flow. This method is applied quasi-axisymmetrically to profile sections along the intake, and the boundary layer is coupled to the inviscid flow by surface transpiration.

3. APPLICATIONS

3.1 Axisymmetric Flow

The first application of the Navier-Stokes method is to an axisymmetric model intake (ARA6) which was tested at the Aircraft Research Association Ltd. (Ref. 17). This geometry and test data has been used to evaluate various CFD codes in recent years. Calculated results for this case are presented here to establish that the Navier-Stokes method can give similar quality solutions to a more conventional (potential flow) method, at well-behaved flow conditions. In the present study two sets of flow conditions are considered: a subsonic case with freestream Mach number of 0.4 and intake mass flow ratio 0.697, and a transonic case with Mach number 0.85 and mass flow ratio 0.587. (Intake mass flow ratio is defined as A_0/A_1 where A_0 is the cross-sectional area, at a large distance upstream, of the streamtube comprising all of the flow entering the intake, and A_1 is the intake highlight area.) Flow incidence angle for both cases is zero, hence the flow is axisymmetric as well as the geometry.

Figure 3 shows results for the subsonic case ($M = 0.4$). The grid used has 99 wraparound \times 35 radial points. The predicted pressure distribution agree well with the measured data. Also shown in Fig. 3 is the prediction from the potential flow method described in 2.5 which in this case is of similar quality to the Navier-Stokes predictions.

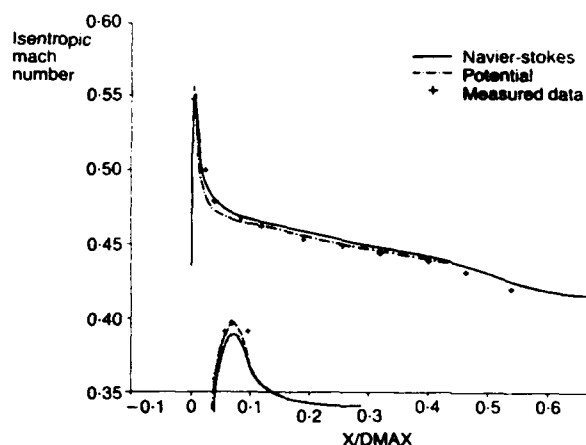


Figure 3. Axisymmetric subsonic case

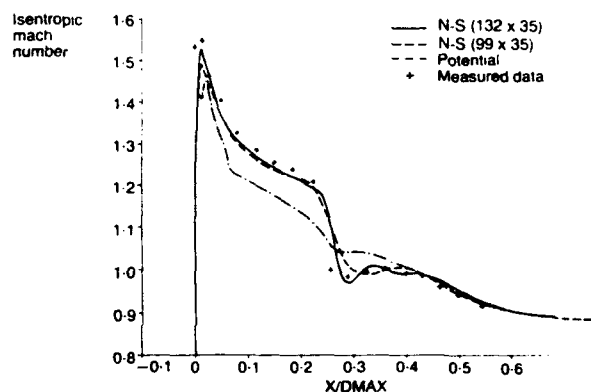


Figure 4. Axisymmetric transonic case

Figure 4 shows results for the transonic case ($M = 0.85$). The peak is somewhat underpredicted and the shock is smeared in the potential flow solution. Better results are obtained, though still with some underprediction for a Navier-Stokes solution on a grid with 99 wraparound points. By increasing this to 132 wraparound points the predicted peak and shock are improved as shown in Fig. 4. Earlier attempts for this case displayed some localised, spurious total pressure losses (up to 2% of P_0) emanating from a region near the axis upstream of the intake, where some of the grid cells were very skewed (angles between faces less than 10°). The grid was modified to reduce the skewness (avoiding angles less than 30°), and the resulting total pressure field was substantially improved (to about $\frac{1}{3}$ % of P_0).

The shock location in the transonic case has been found to be sensitive to the value of freestream Mach number. Though nominally $M = 0.85$, there is some uncertainty over the wind tunnel blockage correction to Mach number (Ref. 17).

3.2 Three-Dimensional Flow

The Navier-Stokes method has been applied to a Rolls-Royce plc research intake, typical of modern civil intake designs in that the geometry is substantially three-dimensional with local contraction ratio varying circumferentially around the intake. This type of intake has been designed for a modern high bypass ratio engine in an underwing, twin-jet installation. The intake is drooped (i.e. intake and engine centrelines are not co-incident) to align the intake with the incident flow at cruise conditions, which is subjected to wing-induced upwash. The contraction ratio on the bottom lip is increased relative to that at the top, to give improved tolerance to high incidence conditions. In addition the highlight is markedly non-circular, with a flattened bottom sector, to meet representative stringent ground clearance criteria.

A 1/10 scale model of the intake was tested in the transonic wind tunnel at the Aircraft Research Association Ltd., Bedford, UK. This test covered a range of high speed-low incidence, and low speed-high incidence conditions to establish the intake performance. Internal performance was measured using a 5-arm, rotating rake array containing 50 static and total pressure probes. This was located at a position equivalent to the turbofan compressor face. In addition, the model was instrumented with a series of streamwise rows of static pressure tappings to assess surface distributions. Intake mass flow was measured by a venturi system.

The particular cases studied here have a freestream Mach number of 0.35 and a flow incidence of 21° , for a range of intake mass flows. This is close to the intake high incidence separation boundary illustrated in Fig. 1c. Fully turbulent calculations have been performed using both the Navier-Stokes and potential flow methods, at full and model scale. The Navier-Stokes solutions used a grid with 99 wraparound x 35 radial x 9 circumferential points. To appreciate the nature of the flow, Figs. 5a, b show the predicted bottom lip Mach number and total pressure fields, respectively, at $A_0/A_1 = 1.32$, for the full-scale Navier-Stokes calculation. Clearly evident is the shock located near the intake throat, the subsequent thickening of the boundary layer downstream of the shock (Fig. 5a), and the losses arising from the shock (Fig. 5b). Thus, prediction accuracy is dependent on adequate modelling of shock losses and shock/boundary layer interaction.

As the engine mass flow increases the supersonic region on the bottom lip increases in size, terminating in a shock of increasing strength. At the highest mass flows there may be a shock-induced separation. Losses and distortion in total pressure at the fan face are due to the boundary layer and the shock, with the latter contribution becoming increasingly important as mass flow increases. Hence curves of total pressure recovery and distortion coefficient against mass flow function are reasonably flat at first, then

have a 'knee' leading to a rapid fall-off as shock losses become dominant.

Pressure recovery is defined as

$$\frac{\bar{P}_1}{P_0} = 1 - \frac{\Delta P}{P_0} \quad (19)$$

where \bar{P}_1 is the mean total pressure at the fan face location and P_0 is the freestream total pressure. For Navier-Stokes solutions the pressure recovery may be calculated directly from the flowfield, whereas for potential flow solutions with coupled boundary layer it may be expressed in terms of boundary layer parameters as

$$\frac{\bar{P}_1}{P_0} = 1 - \frac{(H+1)\theta_\gamma M_1^2}{R_f} \quad (20)$$

where H is shape factor and θ is momentum thickness, both averaged circumferentially around the intake. M_1 is one-dimensional Mach number and R_f intake radius, both at the fan face location.

$$(M = 0.35, \alpha = 21^\circ, A_0/A_1 = 1.32)$$

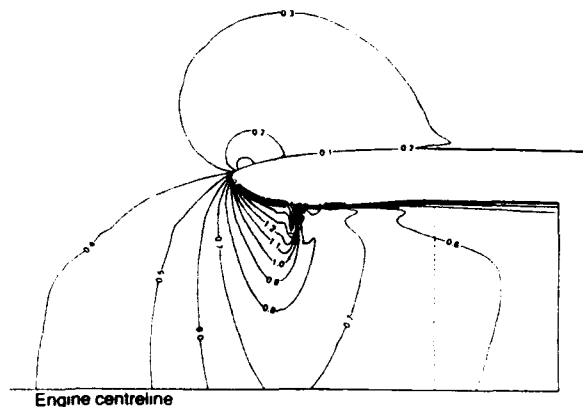


Figure 5a. 3D intake bottom lip Mach number

$$(M = 0.35, \alpha = 21^\circ, A_0/A_1 = 1.32)$$

$$P_0 = 101.35 \text{ kPa}$$

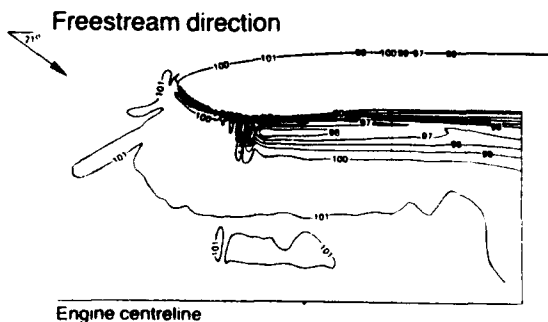


Figure 5b. 3D intake bottom lip total pressure (kPa)

Distortion coefficient is defined in terms of the 60° sector containing the greatest total pressure loss around the fan face plane. In the high incidence cases here the worst sector occupies 30° on either side of the intake bottom line. The coefficient is defined as

$$DC_{60} = \frac{\overline{P_{t60}} - P_1}{\frac{1}{2}\rho U^2} \quad (21)$$

where $\overline{P_{t60}}$ is the minimum mean total pressure over a 60° sector, and $\frac{1}{2}\rho U^2$ is mean dynamic head at the fan face plane. For Navier-Stokes solutions DC_{60} may be calculated directly from the flowfield, while for potential flow with boundary layer it is expressed as

$$DC_{60} = -\frac{(H_{60} + 1)\theta_{60}\gamma M_1^2}{R_f} \left(\frac{\overline{P_1}}{\frac{1}{2}\rho U^2} \right) \quad (22)$$

where H_{60} and θ_{60} are shape factor and momentum thickness averaged over the worst 60° sector.

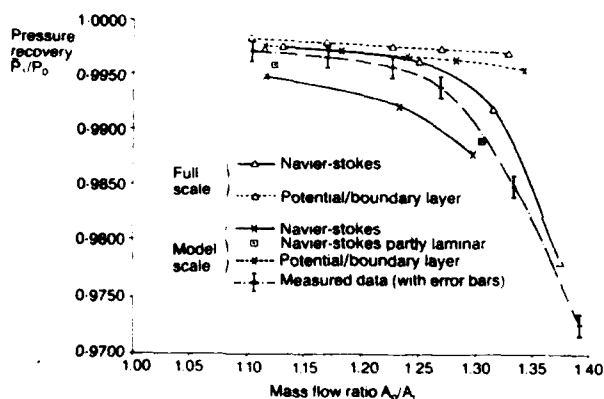


Figure 6. Pressure recovery of 3D intake at $M = 0.35$, $\alpha = 21^\circ$

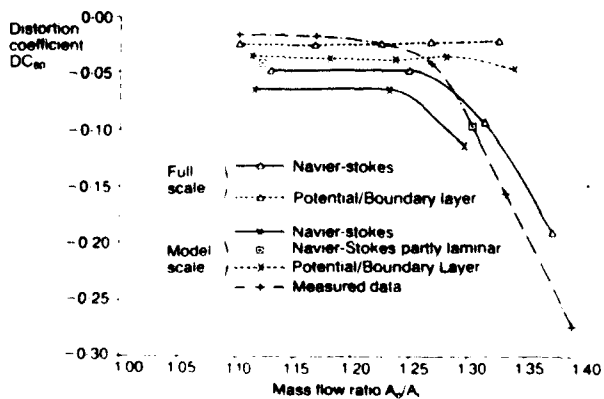


Figure 7. Distortion coefficient (DC_{60}) of 3D intake at $M = 0.35$, $\alpha = 21^\circ$

Figures 6 and 7 show model scale measured data for pressure recovery and , along with the potential/boundary layer and Navier-Stokes predictions at both full and model scale. For the highest mass flow the model scale Navier-Stokes solution has a large flow separation with inflow at the downstream boundary, violating the assumptions of the code. Hence this case has been omitted from Figs. 6 and 7. At lower mass flows the potential method agrees fairly well with the measurements. Model scale predictions have somewhat greater losses than full scale, since the boundary layer is thicker relative to the geometry. As mass flow increases the potential method fails to predict the rapid increase in loss, since it does not take into account the shock losses and associated shock/boundary layer interaction. Eventually the inviscid-viscous coupling procedure breaks down and results cannot be obtained.

The Navier-Stokes solutions predict the reduction in pressure recovery and distortion coefficient with mass flow the curves (Figs. 6 and 7) quite well. Full and model scale predictions of pressure recovery lie respectively above and below the model measured data, showing the correct trend with scale (i.e. Reynolds number) but indicating that there are additional predicted losses. These could be due to numerical truncation error but may also be attributable to the assumption of fully turbulent flow, since in reality there will be a region of laminar flow followed by transition to turbulence. To investigate this latter possibility, two additional model scale calculations have been performed by specifying a region of laminar flow axially upstream of the point of transition predicted by the potential flow/integral boundary layer method on the bottom lip intake profile. This transition point is approximately at the shock position in the throat as seen in Fig. 5a. This is only a crude estimate of transition location as it ignores the circumferential variation around the intake. The resulting points, labelled "partly laminar" in Figs. 6 and 7, lie significantly closer to the measured data than the full turbulent predictions. Hence, it appears that an accurate transition model is necessary to provide an accurate prediction of model scale behaviour.

A more detailed study of the dependence of the solutions on grid density would be required to investigate further the possibility of any spurious losses arising from numerical truncation error, connected with grid skewness and density. In the current grid, excessively skewed cells have been avoided, drawing on the experience of Section 3.1 above.

Figure 8 shows predicted and measured isentropic Mach number distributions on the intake bottom line for the same case as in Fig. 5. The peak is underpredicted by the potential flow solutions. The Navier-Stokes solutions predict the peak Mach number better, and the shock position and strength are seen to be sensitive to both scale and the assumed laminar/turbulent transition location. Predicting the surface Mach number here is quite difficult

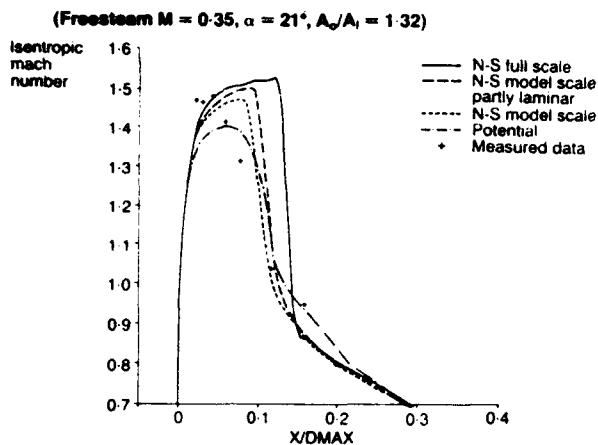


Figure 8. 3D intake bottom lip surface Mach number

as the distribution will be strongly affected by viscous effects associated with the shock/ boundary layer interaction. In these situations, adequate grid resolution and realistic turbulence modelling are necessary to capture the details of this complex feature. Perhaps surprisingly, although the details of the surface Mach number distribution are not accurately predicted, the trends in total pressure recovery and distortion shown in Figs. 6 and 7 are well captured.

4. FUTURE WORK

This paper has only shown predictions for intake flow at a single type of off-design condition, namely at low speed with high incidence. The work represents part of an ongoing programme to develop the Navier-Stokes method for civil intakes and nacelles. Future work will be aimed at exploring the capabilities of the Navier-Stokes method at other off-design conditions, e.g., crosswind, drag rise and climb/ engine out (see Fig. 1). In addition, in view of the sensitivity of the predicted results to Reynolds number, more evaluation of the method against test data at a range of Reynolds number is envisaged.

5. CONCLUSIONS

A Navier-Stokes method has been applied to calculate axisymmetric and three-dimensional civil engine intake flows. The method is particularly aimed at off-design conditions where potential flow calculations with coupled boundary layer are inaccurate or break down. A C-type computational grid has been used, in common with the established potential flow method. Results for the axisymmetric intake for a subsonic case show good agreement between the potential flow method, the Navier-Stokes method and the experimental data. For a transonic case, the potential flow method fails to predict the external shock on the intake. This feature is well captured by the Navier-Stokes method. For the 3D intake at off-design conditions, the potential flow

method fails to predict the sudden reduction in pressure recovery with increasing mass flow, and at the very highest flows, the inviscid-viscous iteration procedure breaks down. The Navier-Stokes method correctly predicts both the reduction of pressure recovery, and increased distortion. The predicted effects of intake scale (Reynolds number) and of imposing a laminar boundary layer over the intake leading edge indicate that an accurate model of laminar-turbulent transition is required to predict model scale behaviour. A grid dependency study would be necessary to quantify the levels of any numerically generated loss. Even without this, on the modest grid sizes used, the present method clearly shows advantages over traditional inviscid/viscous interaction methods in determining intake separation and shock loss boundaries. The indications are also that the Navier-Stokes method can be used to account for Reynolds number effects, overcoming some of the difficulties associated with sub-scale model testing. Overall the results are sufficiently accurate to suggest that the Navier-Stokes method will have a useful rôle in the increasing refinement of the intake design process.

6. ACKNOWLEDGEMENTS

The authors wish to thank Rolls-Royce plc for permission to publish this paper. Thanks are also due to Y. K. Ho of Rolls-Royce plc, for carrying out much of the program development work and to G. Austin who carried out the potential flow computations. This work has been carried out with the support of Procurement Executive, Ministry of Defence.

The results and opinions expressed in this paper are those of the authors; they do not necessarily reflect the views of Rolls-Royce plc.

REFERENCES

1. Chen, L. T., and Caughey, D. A. Calculation of Transonic Inlet Flowfields Using Generalised Co-ordinates. *J. Aircraft*, Vol. 17, No. 3, March 1980, pp167-174.
2. Vadyak, J. and Atta, E. H. Three-Dimensional Transonic Nacelle/Inlet Flowfield Computations Using an Efficient Approximate Factorization Algorithm. *AIAA-83-1417*, 1983.
3. Nakamura, T. Computation of Three-Dimensional Transonic Inlet Flowfields Using an Approximate Factorization Algorithm. *J. Propulsion and Power*, Vol. 4, No. 3, May-June 1988, pp285-287.
4. Peace, A. J. Transonic Flow Calculations Around Isolated Inlet Configurations. *Aero. J.*, Vol. 90, No. 893, March 1986, pp103-110.

5. Reyhner, T. A. Transonic Potential Flow computation about Three-Dimensional Inlets, Ducts and Bodies. AIAA Journal, Vol. 19, No. 9, September 1981, pp1112-1121.
6. Schmilovich, A. Calculation of Transonic Flows with Separation Past Arbitrary Inlets at Incidence. AIAA-88-0707, 1988.
7. Cebeci, T. and Smith, A. M. O. Analysis of Turbulent Boundary Layers. Academic Press, New York, 1974.
8. Chen, H. C., Yu, N. J. and Rubbert, P. E. Flow Simulations for General Nacelle Configurations Using Euler Equations. AIAA-83-0539, 1983.
9. Hirose, N. and Akai, K. 3-D Euler Flow Analysis of Fanjet Engine and Turbine Powered Simulator with Experimental Comparison in Transonic Speed. AIAA-89-1835, 1989.
10. Vadyak, J. Simulation of Transonic Three-Dimensional Nacelle/Inlet Flowfields Using an Euler/Navier-Stokes Algorithm. AIAA-85-0084, 1985.
11. Shrewsbury, G.D., Vadyak, J., Schuster, D. M. and Smith, M. J. Computation of Aircraft Component Flow Fields at Transonic Mach Numbers Using a Three-Dimensional Navier-Stokes Algorithm. NASA-CP-3020, 1988.
12. Jameson, A., Schmidt, W. and Turkel, E. Numerical Solutions of the Euler Equations by Finite Volume Methods Using Runge-Kutta Time-Stepping Schemes. AIAA-81-1259, 1981.
13. Swanson, R.C. and Turkel, E. A Multi-Stage Time-Stepping Scheme for the Navier-Stokes Equations. AIAA-85-0035, 1985.
14. Moore, J. and Moore, J. G. Calculations of Three-Dimensional, Viscous Flow and Wake Development in a Centrifugal Impeller. ASME J.Eng. for Power, Vol. 103, April 1981, pp367-372.
15. Jameson, A. Iterative Solution of Transonic Flows Over Airfoils and Wings, Including Flows at Mach 1. Comm. Pure Appl. Math., Vol. 27, 1974, pp283-309.
16. Baker, T.J., and Forsey, C.R. A Fast Algorithm for the Calculation of Transonic Flow Over Wing/Body Combinations. AIAA J., Vol. 21 No. 1, January 1983, pp60-67.
17. Langley, M. J. The Design of Axisymmetric Cowls for Poddled Nacelles for High Bypass Ratio Turbofan Engines. ARC R&M 3846, May 1979.

Discussion


K. BROICHHAUSEN, MTU, MÜNCHEN, GERMANY

In the computation of the internal intake flow you have imposed a "free-stream" boundary condition with fixed static pressure. However, in the critical case of internal separation (e.g., the high incidence case) the fan might have an influence on the separation itself. Do you think this influence is negligible or how do you intend to cover it?

AUTHOR'S REPLY

The authors are grateful to the questioner for raising this point. Several workers (e.g., Refs. 1 and 2) have shown that the intake flow near separation can be strongly influenced by the presence of the fan, in particular by suppressing the tendency of the flow to separate and reducing circumferential distortion. The boundary condition at the fan face described in the paper certainly is not appropriate in the case where a fan is present, but is appropriate when comparing with isolated intake model test data, such as that presented. In the near future, the authors are intending to incorporate alternative boundary conditions into the Navier-Stokes code that model the effect of the fan via an actuator or semi-actuator disk approach, similar to that adopted in Ref. 3. The successful implementation of such a model will then enable the calculation of both an isolated model intake (without a fan) and the true engine situation.

REFERENCES

1. Hodder, B.K.: "An Investigation of Engine Influence on Inlet Performance." NASA CR-166136, 1981.
 2. Motycka, D.L.: "Reynolds Number and Fan/Inlet Coupling Effects on Subsonic Transport Inlet Distortion." AIAA J. Propulsion, Vol. 1, No. 3, pp. 229-234, 1985.
 3. Billet, G., Huard, J., Chevalier, P., and Laval, P.: "Experimental and Numerical Study of the Response of an Axial Compressor to Distorted Inlet Flow." ASME J. Fluid Eng., Vol. 110, pp. 355-360, Dec. 1988.
- 



CFD CONTRIBUTIONS DURING HYPERSONIC AIRPLANE INTAKE DESIGN

N. C. Bissinger
A. Eberle

Military Aircraft Division
Messerschmitt-Bölkow-Blohm GmbH
P.O. Box 80 11 60
D-8000 München 80
Germany

92-16085

SUMMARY

With increasing Mach numbers of high speed vehicles there is a growing need for the design people to get information on the steadily growing complexity of the flows outside and inside these airplanes. Today, this need can only be satisfied by computational fluid dynamics (CFD) because above certain Mach numbers flows in windtunnels can no longer fully simulate the actual flow physics. Especially for the design of optimal propulsion systems which are capable of economically propelling aircraft to hypersonic Mach numbers understanding of the "real" flow is mandatory.

This paper will address recently developed numerical elements of an advanced CFD code regarding computational speed and accuracy. Results will be presented of several calculations performed to gain insight into the flow in hypersonic intakes.

1. INTRODUCTION

The task for the intake designer consists in designing an intake that delivers a specified mass flow with specified flow conditions at the engine face. On its way the intake air is compressed from free-stream to engine face conditions. The compression can be achieved by supersonic compression through shocks and/or subsonic diffusers depending on flight Mach number. This flow process has to be accomplished with as little losses as possible. In addition the flow distortion of the intake air can be limited by the distortion tolerance level of the engine attached to the intake. For hypersonic air vehicles the selection of a specific intake design can be governed by the overall performance of the vehicle, i.e. it may no longer be possible to select an intake that is optimized by itself.

The design of hypersonic intakes usually is accomplished by the use of a method of characteristics (MOC) coupled with a boundary layer code. To determine the performance of such an intake (or its alternatives) models have to be built and tested. This approach, however, becomes increasingly difficult with increasing hypersonic flight Mach numbers. For very high flight Mach numbers testing facilities with realistic flow conditions do not exist. Also, testing techniques are not proven and pose considerable problems.

But even at moderate hypersonic Mach numbers wind tunnel testing today produces

overall performance data with little flow details only. However, flow details are needed for flow diagnostics during the optimization of an intake design.

Today Computational Fluid Dynamics (CFD) shows great promise in contributing to flow diagnostics. There are various codes to calculate forebody compression, shock/boundary layer interactions on ramps of 2D intakes or on sidewalls (glancing shocks). Calculations of the flow in front of blunt intake lips can help in the structural design and dimensioning of cooling systems. Duct flows with wall bleed can be calculated by modeling the actual bleed geometry or by simplified bleed models. Thus optimal bleed locations can be determined.

Sensor systems for the determination and stabilization of the location of the final shock in internal compression intakes can be developed only when flow details (e.g. the existence of a shock train and its extent) are known. CFD can provide those. With CFD it is even possible to investigate surge interaction between close coupled intakes. On an engineering level there seems to be no CFD model to determine the stability of shock boundary layer interactions in realistic intakes and its assurance by bleed, although on the academic level much has been done in this area also.

CFD has the capability even to support wind tunnel testing during the scaling of the measured data to "realistic" Mach and Reynolds numbers. CFD should be able to discern radiation effects on boundary layers and give guidelines to windtunnel engineers when and how to perform hot model/cold tunnel tests.

For all these calculations listed above CFD codes for the full Navier-Stokes equation NS (steady or unsteady) seem to be inevitable. However, not for all flow problems relevant turbulence models do exist. Also, computer costs can become prohibitive especially for complex three-dimensional unsteady flow calculations. Therefore, Euler calculations can still be attractive for flow problems where viscous effects can be expected to be small. The difference between their results and NS solutions indicates the effect viscosity has on the flow. A further reason is still "play" (work) with Euler solvers is the fact that most NS codes are based on Euler codes to which the viscosity terms have been added. It is therefore absolutely necessary to find out whether the Euler

solution gives a solution for a particular flow problem with a minimum of numerical dissipation. These are the main reasons why this paper deals with the solution of the Euler equations for hypersonic intake flows.

2. OUTLINE OF THEORY

2.1 Flux Formulation

The present code used for the theoretical prediction of intake flows is a cell centered Finite Volume Method (FVM). This concept has become classic two decades before with the work of MacCormack (Ref.1), Inouye and Rizzi (Ref.2). The implementation of the flux evaluation at the cell faces, however, is innovative and incorporates the newest developments in characteristic theory. The fluxes occurring in the Euler equations call for the flow variables at the cell face. In a cell centered finite volume scheme, however, it is assumed that each cell carries its own set of flow quantities such that exactly at the cell face the flow variables are represented by step functions, which do not allow the straight forward definition of the latter values there. In the present work this observation leads to a sound theory based on the method of characteristics. The system of equations to be solved reads:

$$\begin{aligned} \dot{\rho} + (\rho u)_x + (\rho v)_y + (\rho w)_z &= 0 \\ (\rho u) + (p + \rho u^2)_x + (\rho uv)_y + (\rho uw)_z &= 0 \\ (\rho v) + (\rho uv)_x + (p + \rho v^2)_y + (\rho vw)_z &= 0 \\ (\rho w) + (\rho uw)_x + (\rho vw)_y + (p + \rho w^2)_z &= 0 \\ \dot{e} + [u(p+e)]_x + [v(p+e)]_y + [w(p+e)]_z &= 0 \\ p &= (\gamma - 1) \left(e - \rho \frac{u^2 + v^2 + w^2}{2} \right) \end{aligned}$$

The symbolic form is

$$\dot{U} + \tilde{E}_x + \tilde{F}_y + \tilde{G}_z = 0$$

It can be transformed to curvilinear computational grids to read

$$D\dot{U} + \tilde{E}_\xi + \tilde{F}_\eta + \tilde{G}_\zeta = 0$$

D is the geometric mapping determinant (or the discrete cell volume) and the new fluxes E, F, G are functions of the cartesian fluxes indicated by the tilde:

$$\begin{aligned} E &= \tilde{E}\xi_x + \tilde{F}\xi_y + \tilde{G}\xi_z \\ F &= \tilde{E}\eta_x + \tilde{F}\eta_y + \tilde{G}\eta_z \\ G &= \tilde{E}\zeta_x + \tilde{F}\zeta_y + \tilde{G}\zeta_z \end{aligned}$$

The geometric quantities ξ_x, ξ_y, ξ_z are the cartesian components of a $\xi = \text{const}$ surface area vector of a finite volume. Similarly η_x, η_y, η_z are the components of a $\eta = \text{const}$ surface area vector and $\zeta_x, \zeta_y, \zeta_z$ are those of a $\zeta = \text{const}$ surface. The numerical representation of the flux differences is

$$\begin{aligned} E_\xi &= E_{i+1/2, j, k} - E_{i-1/2, j, k} \\ F_\eta &= F_{i, j+1/2, k} - F_{i, j-1/2, k} \\ G_\zeta &= G_{i, j, k+1/2} - G_{i, j, k-1/2} \end{aligned}$$

2.2 Left/Right State Definition

As an example a $\xi = \text{const}$ cell face labeled $i+1/2$ is considered, which separates the cells labeled i (left cell) and $i+1$ (right cell). The states are determined such that the finite spatial difference occurring in the model equation

$$\dot{U} + \lambda U_\xi = 0$$

is of second order accuracy. A useful ansatz is

$$\begin{aligned} U_{i, i+1/2} &= U_i + \left(\frac{1}{4} - \phi\right)(U_i - U_{i-1}) + \\ &\quad + \left(\frac{1}{4} + \phi\right)(U_{i+1} - U_i) \\ U_{i+1, i+1/2} &= U_{i+1} - \left(\frac{1}{4} - \phi\right)(U_{i+2} - U_{i+1}) + \\ &\quad + \left(\frac{1}{4} + \phi\right)(U_{i+1} - U_i) \end{aligned}$$

The parameter ϕ is restricted to values in the range $|\phi| < 0.25$ for stability and controls the accuracy and dispersion of different schemes:

ϕ	scheme
-1/4	upwind
0	symmetric (Fromm's scheme)
1/12	third order biased
1/4	central

In the present work also another base point interpolation has been investigated with minimum dispersion resulting from crossing out the first uneven truncation error:

$$\begin{aligned} U_{i, i+1/2} &= aU_i + bU_{i-1} + cU_{i+1} + dU_{i+2} \\ U_{i+1, i+1/2} &= aU_{i+1} + bU_{i+2} + cU_i + dU_{i-1} \end{aligned}$$

were a, b, c, d are expressed by two parametric quantities A, B:

$$\begin{aligned} a &= \frac{1}{24}(14 + 15A + 3B) & b &= -\frac{1}{24}(2 + A + B) \\ c &= \frac{1}{24}(14 - 15A - 3B) & d &= \frac{1}{24}(A + B - 2) \end{aligned}$$

The difference representations provided so far need flux limiting to first order being incorporated for shock capturing. This is achieved by a coefficient L which is unity in smooth flow regions and zero at shocks:

$$\begin{aligned} U_{i, i+1/2} &= U_i + L_i \left[\left(\frac{1}{4} - \phi\right)(U_i - U_{i-1}) + \right. \\ &\quad \left. + \left(\frac{1}{4} + \phi\right)(U_{i+1} - U_i) \right] \\ U_{i+1, i+1/2} &= U_{i+1} - L_{i+1} \left[\left(\frac{1}{4} - \phi\right)(U_{i+2} - U_{i+1}) - \right. \\ &\quad \left. - \left(\frac{1}{4} + \phi\right)(U_{i+1} - U_i) \right] \end{aligned}$$

For the minimum dispersion base point interpolation the parameters A and B become:

$$A = \frac{2}{3}(1 - L), \quad B = B_0(1 - \frac{3}{2}A) + 2A$$

where B_0 is a user specified constant controlling smoothing by the fourth order truncation error.

There is much latitude with the limiter L . Four possibilities have been tried out:

$$L = \max(0, 1 - \alpha |M^2_{\xi\xi\xi}|) \quad (\text{Mach sensor})$$

$$\alpha_i = \frac{2D_1 D_r + \epsilon U^{*2}}{D_1^2 + D_r^2 + \epsilon U^{*2}} \quad (\text{van Albada, Ref.3})$$

$$D_1 = U_i - U_{i-1} \quad D_r = U_{i+1} - U_i \quad U^* = U_{i+1} + U_{i-1}$$

The parameters α and ϵ are user specified constants. A further refinement is achieved by increasing the order of the original van Albada limiter:

$$L_i = \frac{2D_1 D_r \max(|D_1|, |D_r|)^{\sigma} + \epsilon U^{*2}}{(D_1^2 + D_r^2) \max(|D_1|, |D_r|)^{\sigma} + \epsilon U^{*2}} \quad (\text{van Albada/Eberle, Ref.4})$$

with σ being a user specified constant. Unfortunately the van Albada-type limiters may assume negative values at extrema of the variables distributions. So we cut away the negative part by the modification

$$\beta_i = \max(0, \alpha_i)$$

In order to restore differentiability a new limiter using β as the argument is

$$L_i = 1 - (1 + n\beta_i)(1 - \beta_i)^n \quad (\text{Eberle, Ref.5})$$

where n is an input parameter to adjust the limiter to any sharpness desired. Differentiability is guaranteed for $n > 2$.

2.3 Enhancing the Accuracy

Numerous choices are at our disposal which set of flow variables should be entry to the left and right state: the primitive variables ρ, u, v, w, p for example, the conservative variables $\rho, l = \rho u, m = \rho v, n = \rho w, e$, etc. In this section we try to find out why the latter are best suited for maximum accuracy. For this purpose we investigate the impact of a small change of the flow variables on the change of the fluxes. Let us take a representative flux of the momentum equations:

$$f = \rho u w \quad (\text{non-conservative variables})$$

$$f = \frac{\ln}{\rho} \quad (\text{conservative variables})$$

Now we assume a relative change of the non-conservative flow variables vector $r = dU^*/U^*$ and calculate the relative change of the flux such as to estimate the consequence of a numerical error in the flow variables on the accuracy of the fluxes.

$$\frac{df}{f} = \frac{u w d\rho + \rho w d u + \rho u d w}{\rho u w} = \frac{d\rho}{\rho} + \frac{d u}{u} + \frac{d w}{w} = 3r$$

If we did the same exercise for a flux occurring in the continuity equation, we obtained a value for the relative flux change being $2r$ and the energy equation would give $4r$. With the conservative variables we obtain for any of the fluxes the same value r , for example:

$$\frac{df}{f} = \left(\frac{d \ln + n d l}{\rho} - \frac{\ln}{\rho^2} \right) \frac{\rho}{\ln} = \frac{d l}{l} + \frac{d n}{n} - \frac{d \rho}{\rho} = r$$

Only in the case of the conservative flow variables the accuracy of a difference representation of the flow variables is

identically transferred to the difference representation of the fluxes. Therefore they are chosen as entries for the left/right state formulas.

2.4 The Riemann Solution

Now we try to evaluate the flow variables vector at a $\xi = \text{const}$ cell face from the left/right state. For this purpose it is convenient to use the governing equations in their possibly simplest form:

$$\frac{D}{A} s + \lambda_0 s_{\xi} + \frac{\gamma-1}{2} s (x u_{\xi} + y v_{\xi} + z w_{\xi}) + T^s = 0$$

$$\frac{D}{A} u + \lambda_0 u_{\xi} + \frac{\gamma s^2}{\gamma-1} (2 \frac{s_{\xi}}{s} - \frac{s_{\xi}}{\gamma}) + T^u = 0$$

$$\frac{D}{A} v + \lambda_0 v_{\xi} + \frac{\gamma s^2}{\gamma-1} (2 \frac{s_{\xi}}{s} - \frac{s_{\xi}}{\gamma}) + T^v = 0$$

$$\frac{D}{A} w + \lambda_0 w_{\xi} + \frac{\gamma s^2}{\gamma-1} (2 \frac{s_{\xi}}{s} - \frac{s_{\xi}}{\gamma}) + T^w = 0$$

$$\frac{D}{A} s + \lambda_0 s_{\xi} + T^s = 0$$

This form requires some explanations. s is the speed of sound, $s = (\gamma p / \rho)^{1/2}$. S is an entropy defined by $p = e^S \rho^{\gamma}$. ξ is the curvilinear abscissa usually aligned with the i -direction. Suppose, that we are considering a $\xi = \text{const}$ cell face, then $\lambda_0 = x u + y v + z w$ is the normal velocity of that cell face, the unit normal of which is $(x, y, z)^T$, and its area surface is A . D is the local mapping determinant, which needs not be calculated explicitly as we will see later. The T -vector is a symbol for all remaining (tangential) derivatives with respect to the η and ζ -direction. The above system of equations is nothing but the chainruled original non-conservative Euler equations written in the S, g, s variables. Since all the derivatives are undefined due to the cell face step functions of the flow variables, the partial time derivative is replaced by the total derivative along a line passing through the cell face placed at ξ at time $t + dt$ and a point on the initial data level at $\xi - d\xi$ and at time t :

$$U_{i,n} = U(\xi - d\xi, t) = U(\xi, t + dt) - \dot{U} dt - U_{\xi} d\xi$$

'in' denotes the initial state. If the value of $d\xi$ is positive, the initial state is taken from left side of the cell face (U_i) otherwise from the right side (U_r). With the time step being replaced by the ratio of a length (D/A) and a wave speed λ

$$dt = \frac{D}{A \lambda} d\xi$$

the Euler equations assume the form

$$\lambda (s - s_{i,n}) + [(\lambda_0 - \lambda) s_{\xi} + \frac{\gamma-1}{2} s (x u_{\xi} + y v_{\xi} + z w_{\xi}) + T^s] d\xi = 0$$

$$\lambda (u - u_{i,n}) + [(\lambda_0 - \lambda) u_{\xi} + \frac{\gamma s^2}{\gamma-1} (2 \frac{s_{\xi}}{s} - \frac{s_{\xi}}{\gamma}) + T^u] d\xi = 0$$

$$\lambda (v - v_{i,n}) + [(\lambda_0 - \lambda) v_{\xi} + \frac{\gamma s^2}{\gamma-1} (2 \frac{s_{\xi}}{s} - \frac{s_{\xi}}{\gamma}) + T^v] d\xi = 0$$

$$\lambda (w - w_{i,n}) + [(\lambda_0 - \lambda) w_{\xi} + \frac{\gamma s^2}{\gamma-1} (2 \frac{s_{\xi}}{s} - \frac{s_{\xi}}{\gamma}) + T^w] d\xi = 0$$

$$\lambda (S - S_{i,n}) + [(\lambda_0 - \lambda) S_{\xi} + T^s] d\xi = 0$$

Performing the limiting process $d\xi \rightarrow 0$ removes all tangential derivatives to first

order:

$$\lambda(s-s_{1n}) + (\lambda_0 - \lambda)ds + \frac{\gamma-1}{2}s(xdu + ydv + zdw) = 0$$

$$\lambda(u-u_{1n}) + (\lambda_0 - \lambda)du + \frac{\gamma s^2}{\gamma-1}(2\frac{ds}{s} - \frac{dS}{\gamma}) = 0$$

$$\lambda(v-v_{1n}) + (\lambda_0 - \lambda)dv + \frac{\gamma s^2}{\gamma-1}(2\frac{ds}{s} - \frac{dS}{\gamma}) = 0$$

$$\lambda(w-w_{1n}) + (\lambda_0 - \lambda)dw + \frac{\gamma s^2}{\gamma-1}(2\frac{ds}{s} - \frac{dS}{\gamma}) = 0$$

$$\lambda(S-S_{1n}) + (\lambda_0 - \lambda)dS = 0$$

$\lambda = \lambda_0$ is an eigenvalue and generates the streamline relations:

$$\lambda = \lambda_0: S-S_0=0 \quad u=u_0+ax \quad v=v_0+ay \quad w=w_0+az$$

where 'a' is a velocity parameter to be specified later. The interpretation involving the left U_1 and the right state U_r is evident: If the eigenvalue is positive (negative) then the flow variables labeled '0' are taken from the left (right) state defined above. The pressure wave eigenvalues produce the solution for the speed of sound and the velocity parameter a:

$$\lambda_1 = \lambda_0 + s, \lambda_2 = \lambda_0 - s:$$

$$s = \frac{s_1 + s_2 + \frac{\gamma-1}{2}[x(u_1 - u_2) + y(v_1 - v_2) + z(w_1 - w_2)]}{2 + \frac{S_1 + S_2 - 2S_0}{2\gamma}}$$

$$a = \frac{r_1 - r_2}{\gamma - 1}$$

$$r_1 = s_1 + \frac{1}{2}[(\gamma-1)[x(u_1 - u_0) + y(v_1 - v_0) + z(w_1 - w_0)] + \frac{s}{\gamma}(S_0 - S_1)]$$

$$r_2 = s_2 - \frac{1}{2}[(\gamma-1)[x(u_2 - u_0) + y(v_2 - v_0) + z(w_2 - w_0)] - \frac{s}{\gamma}(S_0 - S_2)]$$

The Riemann solver developed so far needs no iterations but violates the homogeneous property since it works with non-conservative variables. Therefore it is recast in conservative variables using the differentials of the density and the pressure by which the difference representations are rewritten:

$$d\rho = -\frac{\rho}{\gamma-1}(2\frac{ds}{s} - dS) \quad dp = \frac{\rho s^2}{\gamma-1}(2\frac{ds}{s} - \frac{dS}{\gamma})$$

Further expansions of these differentials with respect to the conservative variables $\rho, l = \rho u, m = \rho v, n = \rho w, e$ centered around the streamline state labeled '0' leads to the final homogeneous Riemann solver:

$$\begin{aligned} \rho &= \rho_0 + r_1 + r_2 \\ l &= l_0 + (u+sx)r_1 + (u-sx)r_2 \\ m &= m_0 + (v+sy)r_1 + (v-sy)r_2 \\ n &= n_0 + (w+sz)r_1 + (w-sz)r_2 \\ e &= e_0 + (H+s\lambda_0)r_1 + (H-s\lambda_0)r_2 \end{aligned}$$

$$\begin{aligned} r_1 &= -\frac{1}{2s^2}[(\frac{\gamma-1}{2}q^2 - s\lambda_0)(\rho_1 - \rho_0) + \\ &\quad + [sx - (\gamma-1)u](l_1 - l_0) + \\ &\quad + [sy - (\gamma-1)v](m_1 - m_0) + \\ &\quad + [sz - (\gamma-1)w](n_1 - n_0) + \\ &\quad + (\gamma-1)(e_1 - e_0)] \end{aligned}$$

$$\begin{aligned} r_2 &= -\frac{1}{2s^2}[(\frac{\gamma-1}{2}q^2 + s\lambda_0)(\rho_2 - \rho_0) - \\ &\quad - [sx + (\gamma-1)u](l_2 - l_0) - \\ &\quad - [sy + (\gamma-1)v](m_2 - m_0) - \\ &\quad - [sz + (\gamma-1)w](n_2 - n_0) + \\ &\quad + (\gamma-1)(e_2 - e_0)] \end{aligned}$$

$$q^2 = u^2 + v^2 + w^2$$

$$H = \frac{e+p}{\rho} \text{ (total enthalpy)}$$

This Riemann solver contains only the velocity vector and the speed of sound as coefficients which are taken from the s, g, S solver described previously. Therefore also the homogeneous solver needs no iterations for improving the coefficients. It combines both, homogeneity and high accuracy.

2.5 Shock Capturing

All classic Riemann solvers cause problems at shocks, if their strength exceeds a certain bound, since they produce diffusionless centered differences at all places where one of the eigenvalues changes sign. Flux vector splitting, however, retains a considerable positive matrix diagonal contribution also at places where the eigenvalues change sign. So blending of the Riemann solution with fluxvector splitting at shocks is an excellent tool to keep the iterations stable. The split flux vector chosen for this purpose is in our case a second order polynomial of the acoustic eigenvalues with the streamline eigenvalue being neglected. This way the total temperature can be preserved to high accuracy. After specifying the polynomials:

$$r_{11} = \{\rho A(\lambda_1 + |\lambda_1|)[M - \frac{1}{4} + (\lambda_1 + |\lambda_1|)\frac{1-2M}{8s}]\}_1$$

$$r_{1r} = \{\rho A(\lambda_1 - |\lambda_1|)[M - \frac{1}{4} + (\lambda_1 - |\lambda_1|)\frac{1-2M}{8s}]\}_r$$

$$r_{21} = \{\rho A(\lambda_2 + |\lambda_2|)[M - \frac{1}{4} - (\lambda_2 + |\lambda_2|)\frac{1-2M}{8s}]\}_1$$

$$r_{2r} = \{\rho A(\lambda_2 - |\lambda_2|)[M - \frac{1}{4} - (\lambda_2 - |\lambda_2|)\frac{1-2M}{8s}]\}_r$$

where M is a user specified input parameter .25 < M < .75 controlling the desired diffusion. A is the cell face area. If M is put zero, the splitting is that proposed by Einfeldt (Ref.6). M=.25 recovers the van Leer fluxes (Ref.7). M=.5 is a flux splitting developed by the present authors (Ref.5) for overcoming extremely strong shocks occurring in high speed flow. It is the possibly simplest form of flux vector splitting and requires least arithmetic. M=.75 improves slightly the total temperature preservation feature (Ref.5). The split fluxes are:

$$F^0 = r_{11} + r_{1r} + r_{21} + r_{2r}$$

$$\begin{aligned} F^0 u &= [(\tilde{u} + \frac{sx}{2\gamma M})r_1 + (\tilde{u} - \frac{sx}{2\gamma M})r_2]_1 + \\ &\quad + [(\tilde{u} + \frac{sx}{2\gamma M})r_1 + (\tilde{u} - \frac{sx}{2\gamma M})r_2]_r \end{aligned}$$

$$F^v = [(\tilde{v} + \frac{SV}{2\gamma M})r_1 + (\tilde{v} - \frac{SV}{2\gamma M})r_2]_1 + \\ + [(\tilde{v} + \frac{SV}{2\gamma M})r_1 + (\tilde{v} - \frac{SV}{2\gamma M})r_2]_r$$

$$F^w = [(\tilde{w} + \frac{SZ}{2\gamma M})r_1 + (\tilde{w} - \frac{SZ}{2\gamma M})r_2]_1 + \\ + [(\tilde{w} + \frac{SZ}{2\gamma M})r_1 + (\tilde{w} - \frac{SZ}{2\gamma M})r_2]_r$$

$$F^* = [H(r_1 + r_2)]_1 + [H(r_1 + r_2)]_r$$

$$\tilde{u} = u + x \frac{2M-1}{2M\gamma} \lambda_0$$

$$\tilde{v} = v + y \frac{2M-1}{2M\gamma} \lambda_0$$

$$\tilde{w} = w + z \frac{2M-1}{2M\gamma} \lambda_0$$

$$\lambda_0 = ux + vy + wz$$

$$(x, y, z)^T = \frac{(A_x, A_y, A_z)^T}{A}$$

$$\lambda_1 = \lambda_0 + s \quad \lambda_2 = \lambda_0 - s$$

With the Riemann solver and the flux vector splitting two independent ways are available to evaluate characteristic based inviscid flux vectors. The Riemann fluxes are very accurate and do exhibit only very little diffusion. At strong shocks the Riemann fluxes fail to avoid spikes in the flow variable distribution. An intelligent interpolation between the two different flux formulations uses a sensor η discovering flow discontinuities:

$$F = F_{\text{Riemann}}(1-\eta) + \eta F_{\text{split}}$$

In order to keep the whole scheme differentiable the interpolation abscissa $1/\eta > 0$ is made a symmetric polynomial with vanishing slopes at $\eta=1$ and $\eta=0$:

$$\eta = (3-2\xi)\xi^2$$

The coordinate ξ at a cell face $i+1/2$ is composed from the minimum of all the limiter values on both sides of the common cell face:

$$\xi = \min\{1, \alpha[1 - \min(L_i, L_{i+1})]\}$$

The number α is an input constant by means of which the sensing characteristic can be adjusted to the flow problem under consideration. The parameter α allows to switch off flux vector splitting completely when the flow is subsonic everywhere.

2.6 Real Gas Incorporation

Real gas effects of equilibrium flow can be easily incorporated if only the steady state solution is of interest. What is necessary for the physical modelling is a table or splines telling the computer program the relation

$\gamma_{\text{variable}} = \gamma_v(p, \rho)$. In this particular case the whole theory about the Riemann solution and the flux vector splitting can be retained with the consideration that γ (without subscript) is now a constant reference value. The only line in the Euler equations where γ occurs is the energy equation, which for convenience is written for 1D:

$$\dot{\tilde{e}} + (u(\tilde{e}+p))_x = 0$$

The tilde (\sim) indicates that this value is formed with the real gas variable γ_v :

$$\tilde{e} = \frac{p}{\gamma_v - 1} + \rho \frac{q^2}{2}$$

Upon specifying an inner energy e using the constant reference value γ

$$e = \frac{p}{\gamma - 1} + \rho \frac{q^2}{2}$$

the energy equation may be written as

$$\dot{\tilde{e}} + \tilde{e} - \dot{\tilde{e}} + [u(\tilde{e} + e - p)]_x = \dot{e} + \Delta \dot{e} + [u(\tilde{e} + e - p)]_x = 0$$

Because time accuracy is not of interest at present, the time derivative of Δe may be neglected. After rearrangement, the energy equation is obtained with a source term on the right side:

$$\dot{e} + [u(e+p)]_x = [u(e-\tilde{e})]_x = [up(\frac{1}{\gamma-1} - \frac{1}{\gamma_v-1})]_x$$

Written in general terms we have then

$$\dot{e} + \text{div}[q(e+p)] = \text{div}[qp(\frac{1}{\gamma-1} - \frac{1}{\gamma_v-1})]$$

$$p = (\gamma-1)(e - \rho \frac{q^2}{2})$$

This way the left hand side remains unaltered.

2.7 Implicit Formulation

The system of equations is solved using a Newton timelike extrapolation. The Jacobian matrix is taken from the flux vector splitting and not from the homogeneous Riemann solver, since it turned out that the Jacobian taken from the split fluxes tolerates much larger local time steps. In the smooth regions of the flow the time step is switched to infinity. The time step is based on a comparison of the size of the maximum local eigenvalue and the smallest matrix diagonal element. Although the arithmetic work of establishing the left hand side matrix is considerable (a multiple of that required for the fluxes) improved convergence rates usually justify the implicit approach. The system of the linearized algebraic equations is solved by a repeated block Jacobi update, thus allowing a high degree of vectorization and portability to any vector or parallel computer.

2.8 Iterative Grid Generation

Although there are numerous grid generation schemes, we found in our work that there is obviously no general method which overcomes all the problems occurring with complicated configurations. The simplest grid topology particularly well suited for industrial flow calculations past complex configurations still seems to be the monoblock H-type grid. It requires least man power, which only needs to be invested in the surface point distribution, where most of the 'handwork' has to be done. Once the surfaces of the configuration are discretized, the space grid generation is fully automatic and requires no user interaction. The theory of the method is based on the fact that the grid point distribution should be stationary:

$$dx = dy = dz = 0$$

The first order Taylor expansion of this statement in time and space with respect to the computational grid coordinates is

$$\begin{aligned} dx &= \dot{x}dt + x_\xi d\xi + x_\eta d\eta + x_\zeta d\zeta = 0 \\ dy &= \dot{y}dt + y_\xi d\xi + y_\eta d\eta + y_\zeta d\zeta = 0 \\ dz &= \dot{z}dt + z_\xi d\xi + z_\eta d\eta + z_\zeta d\zeta = 0 \end{aligned}$$

The displacement vector in the computational space $(d\xi, d\eta, d\zeta)^T$ can be expressed by velocities multiplied by the time increment:

$$d\xi = Udt \quad d\eta = Vdt \quad d\zeta = Wdt$$

By inserting the constituting equations can be written:

$$\begin{aligned} \dot{x} + Ux_\xi + Vx_\eta + Wx_\zeta &= 0 \\ \dot{y} + Uy_\xi + Vy_\eta + Wy_\zeta &= 0 \\ \dot{z} + Uz_\xi + Vz_\eta + Wz_\zeta &= 0 \end{aligned}$$

Upon modifying the nomenclature of the velocities in the computational space by the following definitions

$$U = -\frac{2s_\xi u}{dt} \quad V = -\frac{2s_\eta v}{dt} \quad W = -\frac{2s_\zeta w}{dt}$$

the update formulas for the grid coordinates are

$$\begin{aligned} x^{n+1} &= x + 2(s_\xi ux_\xi + s_\eta vx_\eta + s_\zeta wx_\zeta) \\ y^{n+1} &= y + 2(s_\xi uy_\xi + s_\eta vy_\eta + s_\zeta wy_\zeta) \\ z^{n+1} &= z + 2(s_\xi uz_\xi + s_\eta vz_\eta + s_\zeta wz_\zeta) \end{aligned}$$

The derivatives on the RHS are upwinded:

$$\begin{aligned} x^{n+1} &= x + s_\xi [(u+|u|)x_{\xi d} + (u-|u|)x_{\xi u}] + \\ &\quad + s_\eta [(v+|v|)x_{\eta d} + (v-|v|)x_{\eta u}] + \\ &\quad + s_\zeta [(w+|w|)x_{\zeta d} + (w-|w|)x_{\zeta u}] \\ &= x + s_\xi (ux_\xi + |u|x_{\xi\xi}) + \\ &\quad + s_\eta (vx_\eta + |v|x_{\eta\eta}) + \\ &\quad + s_\zeta (wx_\zeta + |w|x_{\zeta\zeta}) \\ y^{n+1} &= \dots \quad z^{n+1} = \dots \end{aligned}$$

Smoothing properties are enhanced by introducing a parameter p

$$\begin{aligned} x^{n+1} &= x + s_\xi [ux_\xi + (|u|+p)x_{\xi\xi}] + \\ &\quad + s_\eta [vx_\eta + (|v|+p)x_{\eta\eta}] + \\ &\quad + s_\zeta [wx_\zeta + (|w|+p)x_{\zeta\zeta}] \\ y^{n+1} &= \dots \quad z^{n+1} = \dots \end{aligned}$$

Finally the numbers s_ξ, s_η, s_ζ can be used for weighting the coordinate directions in order to avoid overflows in the vicinity of highly curved surfaces. For this purpose an accompanying potential ϕ is calculated, the gradient of which is used for identifying the weights:

$$\begin{aligned} s_\xi &= \frac{|\phi_\xi|}{\phi} \quad s_\eta = \frac{|\phi_\eta|}{\phi} \quad s_\zeta = \frac{|\phi_\zeta|}{\phi} \\ S &= \frac{\omega}{s_\xi + s_\eta + s_\zeta} \\ s_\xi &= SS_\xi \quad s_\eta = SS_\eta \quad s_\zeta = SS_\zeta \end{aligned}$$

All distributed functions (ϕ, u, v, w) are found from the solution of Laplace equations in the computational space. Suitable boundary conditions allow for the attraction of grid lines to the body surfaces such that the grids exhibit even

NS quality. The coefficient ω is an under relaxation parameter which is less than unity if the equations are solved by the block Jacobi procedure rather than point Gauss-Seidel method, which may become necessary on vector and parallel computers.

3. RESULTS

3.1 Scramjet Results

The geometry for this two-dimensional SCRAMJET can be found in the literature (Ref.8). The grid used in these calculations is shown in fig.1 in which every 5th point in x - and every 2nd point in z -direction is shown. It is a simple algebraic grid with constant but different grid distributions in different areas. That is, no smoothing has been applied in the distribution of the grid points. The number of grid points was 407 in x -direction and 155 in z -direction. The Euler code used was the original EUFLEX code (Ref.9). This upwind biased code used the Mach sensor (see chapter 2) and second and fourth order smoothing. The result for $M_\infty = 3.0$ is shown in figs.2 to 5. The lines of constant density in fig.2 clearly show that the code reproduces clearly all flow phenomena to be expected: ramp shocks, reflected shocks, expansion waves, crossing shocks, interactions between shocks and expansion waves. The slip stream originating from the trailing edge of the strut can best be recognized in the plot of constant Mach number lines in fig.3. The maximum mass flow deficit with respect to the entrance mass flow is below 0.2 %, the total temperature varies between -0.67 and +0.92 % of the entrance total temperature (fig.4). In fig.5 the Mach numbers behind the shocks (along a line $K = \text{const}$) are compared with those derived from oblique shock tables. To remove the pre- and post-shock wiggles in this solution some more smoothing would have been necessary (and successful).

At a Mach number of $M = 5.0$ the shocks are steeper and stronger. The result of this calculation is plotted in figs.6 to 8. At this Mach number the reflected shocks in the outer duct hit the trailing edge of the strut. Nonetheless the code produces all flow phenomena without any difficulty. The lines of constant density and Machnumber in figs.6 and 7, respectively, indicate this clearly. The Machnumber distribution along the centerline in fig.8 no longer depicts pre- or post-shock wiggles, i.e. the smoothing for this calculation has been sufficient. However, at the same time it made the shocks somewhat thicker.

Increasing the Mach number to $M = 10.0$ increases the shock strengths and angles even further. The interaction between the expansion waves and the shocks between the struts become so strong that the shocks are highly curved (figs.9 and 10). The mass flow deficit has not been changed dramatically (fig.11). The maximum deviation is about 0.25 %. The total temperature varies between -1.96 and +0.6 % of the entrance total temperature. That the shocks are rather thick at this Machnumber can be seen in fig.12. The Machnumbers derived from

oblique shock tables again compare quite well with those from the calculations.

In order to improve the shock resolution of the $M = 10.0$ results several modifications to the code have been tried. First the flux of the vector splitting according to Steger/Warming (Ref.10) was (at shocks) blended into the solution. This blending in was accomplished with the help of the M' switch. Later the flux vector splitting was modified. Also, the switch was replaced by the van Albada limiter (Ref.3). Roe averaging (Ref.4) was incorporated, too. However, all these modifications have not worked satisfactorily. A result of one of these flow calculations (basic code plus modified Steger/Warming flux plus van Albada switch) is depicted in fig.13. Between the struts and behind the first shock crossing the lines of constant density reveal (unphysical?) "peaks" which could not be damped out even by increased smoothing. Compared with the solution of the basic code in fig.9 the result in fig.13 clearly depicts shocks and expansion fans that are more smeared out.

3.2 2D Hypersonic Intake Calculations

Although the calculations of the SCRAMJET flows "proved" that the EUFLEX code is capable to cope with the flow phenomena in hypersonic intakes they also showed that its results could still be improved at high Mach numbers. This experience led to the development of the fluxes and switches described in the theoretical part of this paper. In addition the more refined grid generation method described in the theoretical part has been implemented. With this method it is possible to smoothly distribute grid points in the flow field and to attract grid lines towards solid walls. The distribution of points along solid walls has been done in a CATIA system. At the users choice points can be distributed evenly or with attraction to specified wall points. The findings from these investigations will be demonstrated by results of flow calculations for realistic 2D airbreathing engine (turbo or RAM) intakes.

The geometries of the intakes considered differ from one another mainly in the geometry behind the throat. The ramp angles and lengths are practically identical.

Grid Effects

For this intake two different grids have been produced. The medium grid plotted in fig.14 consists of 161 grid points in x-direction and 65 grid points in z-direction. There are 26 grid cells spanning the height of the intake duct. The fine grid (fig.15) consists of 300 grid points in x-direction and 106 grid points in z-direction. 52 grid cells are spanning the height of the intake duct. The length of the intake duct behind the throat is somewhat shorter for the fine grid than for the medium grid. Some crude shock fitting has been attempted by arranging the surface grid points such that the point on the leading edge of the third ramp corresponds to the point on the tip of the intake lip (fig.14).

The Mach number distribution for the Euler calculations on the two grids is plotted in fig.16 with the results for the medium grid in fig.16a and the results for the fine grid in fig.16b. It can be clearly seen that the finer grid produces the sharper shocks and the area where the three ramp shocks coalesce is much clearer. Especially the third ramp shock for which the grid is adapted best is extremely thin in the fine grid solution. However, as a result of this "shock fitting" the shock originating at the intake lip appears to be thicker than expected. The distribution of the mass flow deficit has been improved by the increase in grid points (compare fig.17a with 17b).

The details of the results are good in both calculations. In fig.18 a close-up of the flow around the intake lip (calculated with the fine grid) is plotted. The external ramp shocks merge outside the intake just below and behind the tip of the intake lip. On the outside of the intake lip an expansion wave is created which interacts with the slip stream behind the intersection point of the external ramp shocks and the shock formed by coalescence of these shocks. The coalescence shock is curved which results in a Mach number gradient normal to the flow direction.

Mach Number Effects

By increasing the Mach number from $M = 5.25$ to $M = 5.65$ the external first and second ramp shocks coalesce in front of the tip of the intake lip. This coalescence shock merges with the third ramp shock just in front and slightly below the intake lip (fig.19). As can be seen the slip stream downstream of this coalescence point nearly touches the wall of the intake lip. The curved part of the shock below the intake lip is much shorter than in the flow of fig.16b ($M = 5.25$) and therefore the resulting Mach number gradient is distributed in a much thinner "layer". This layer is also much closer to the intake wall than in the $M = 5.25$ flow. The detailed effects of this flow along the external wall of the intake lip onto the state of the boundary layer and its consequences concerning friction and heat loads are still unknown to both the experimentalists and the computational people.

Start of Internal Compression with Bleed

For a given entrance Mach number of an internal compression intake the ratio throat area to entrance area must lie between two limiting values (Ref.11). These two boundaries are determined from isentropic, inviscid flow calculations. For Euler calculations this means that if the area ratio is too close to these boundaries the calculations will produce the unstart flow of the intake. For such a case where the area ratio was too close to the lower boundary (fig.20) wall bleed has been applied on the third ramp inside the intake. As in the experiment it is thus possible to establish a started flow condition for the intake. In fig.21 the bleed area can be identified by the expansion wave originating from the mass removal of the bleed on the third ramp.

Real Gas Calculations

In order to be able to consider real gas effects the gas tables by Tannehill/Mugge in the form of Reference 12 have been incorporated into the code. The flow calculation with the medium grid in fig.14 has been repeated. As expected for these "low" Mach numbers the plot with lines of constant Mach numbers (fig.22) is not much different from that of the ideal gas calculation (fig.16a). The ratio of specific heats Γ varies between 1.375 and 1.401 in the whole flow field. Fig.23 shows the Γ variation of the grid line along the intake duct bottom.

First Order Coefficients for the Riemann Solver

This investigation has been performed with the fine grid in fig.15. Here, instead of the higher order coefficients, i.e. the extrapolated flow variables at the cell faces, first order coefficients, i.e. the neighbouring cell flow variables were used for the Riemann solver. The plot with lines of constant Mach number (fig.24) indicates very smooth shocks although they are thicker than those for the higher order coefficients solution in fig.16b. For this solution to become smooth the limiter had to be tuned to be extremely sharp, i.e. limiting took place at the smallest waviness of a flow variable. This is quite in contrast to the solution with higher order coefficients for which only little limiting has been necessary. From this result it could be concluded that the higher order coefficient Riemann solver is superior to the first order one.

Subsonic Region

The calculation performed on the medium grid (130 x 60 grid points) in fig.25 revealed an interesting flow behind the intake throat. For a Mach number of $M = 5.25$, i.e. slightly below the shock-on-lip Mach number, a subsonic flow region occurred on the ramp side. Between the third ramp and the curved intake duct there is a "corner" point. At this point the reflected internal compression shock was meant to extinguish itself at design conditions. For this off-design condition this jump in wall slope leads to an expansion which is immediately followed by a shock after which subsonic recirculating flow exists (fig.26). If this flow is "real", i.e. not due to numerical effects, it can be suspected that this is a flow that is most likely to lead to separation and possibly to unstart of the intake. In addition the slip stream behind the shock interaction that goes down the duct can be the source of instabilities of the intake flow. Euler calculations like this one can give valuable hints on the existence of such problems (well before an intake model has been built and tested).

Complete Duct Flow

The Euler equations are able to describe both the supersonic and subsonic part of the flow in a mixed compression intake. In

an Euler code this means that at the duct exit a special "subsonic" boundary condition has to be implemented. Here, prescribing in the exit grid cells a given static pressure and extrapolating mass flows and density from the duct was applied. The result from one of the calculations is plotted in fig.27 in which for Mach numbers larger than one lines of constant Mach number are shown. Clearly, the final shock can be identified. Downstream of it the flow is completely subsonic. This final shock is not a normal shock (fig.28) because remnants of the reflected shocks of the internal compression reach him. Therefore the flow towards this shock is not uniform. This also leads to a non-uniform flow downstream of this shock. The velocity vectors in fig.29 indicate that in the upper part of the duct the flow is nearly stagnant, whereas in the lower part most of the intake mass flow is transported towards the engine face.

The flow calculation was started by assuming free stream flow on the outside and inside the intake up to a selected station downstream of the throat. There a normal shock was assumed to exist followed by subsonic flow. One-dimensional flow theory was used to prescribe the flow from there down to the engine face.

The calculation of this flow is very difficult because the final shock not only reacts to very small changes of the duct exit pressure but also to small changes of the numerical smoothing during the iteration process. Especially when the shock is very close to the throat it is extremely difficult to select the appropriate exit pressure and code parameters. However, Euler investigations like this are absolutely necessary if one wants to gain some sort of "feeling" for the reliability of Navier-Stokes solutions based on this Euler code.

Three Dimensional Intake Flow

For highly integrated configurations the flow from the forebody can be three-dimensional. It is also varying with flight Mach number. That means an optimization problem for the intake designer who has to account for these three-dimensional flows when designing sidewall and lip shapes. In addition sidewalls have a finite thickness. This again means an optimization problem with the two possibilities of choosing either very long sidewalls with subsonic leading edges or shorter sidewalls with additional shocks entering the intake. Euler calculations are very helpful for the solution of the latter optimization problem because the effects of the additional compression due to sidewall shocks can be investigated and accounted for.

The geometry of the three-dimensional intake used in this calculation is shown in fig.30. It possesses three external ramps. The sidewalls start at the second ramp. Their leading edge is a sharp wedge. In order to have the maximum thickness of the sidewall at the tip of the sharp intake lip the wedges of the sidewalls extend in front and below the intake lip.

For this geometry the surface grid was constructed on a CATIA system (Ref.13). As can be seen in fig.31 this grid is somewhat coarse. The space grid was determined with the three-dimensional version of the method described in chapter 2.8. It is a one block H-type grid.

The calculation has been performed for a Mach number of $M = 5.63$ in front of the first ramp. The intake is an belly-type intake. In the calculations the bottom of the vehicle has been simulated by a flat plate surface. In the following the result is depicted in lines of constant Mach numbers on surface planes or on grid planes in the flow.

In fig.32 a view of the intake in flow direction and from below is shown. In addition to those on the body surfaces lines of constant Mach number are also shown on the vertical centerline plane of the intake. On this plane the three external shocks are recognizable. These three shocks coalesce in front of the intake lip. The resultant shock below the intake lip is very thick due to the coarse grid in this region. There is an expansion taking place around the lower corner on the outside of the intake (bottom/sidewall corner).

In fig.33 the centerline plane is replaced by the sidewall plane. The external shocks appear to be somewhat clearer. Also, it can be seen on the ramp surfaces that whereas the footprint of the first ramp shock indicates its two-dimensionality the second and third ramp shocks are more or less curved due to the sidewall effects on the flow. To demonstrate this even better in fig.34 a horizontal plane has been added. On this plane the lines of constant Mach number show that the second ramp shock and the sidewall shocks merge and form a highly three-dimensional surface. It can also be seen, how the first ramp shock wraps around the intake.

4. CONCLUDING REMARKS

This paper describes in detail newly developed numerical elements of an Euler code. Flow calculations have been accomplished and results are presented for a variety of both two- and three-dimensional intake flows.

Results indicate that the code is able to produce all possible flow phenomena occurring in high-speed intakes with very high accuracy. Shock resolution is high if the grid is fine enough. Changes in flow variables across shocks agree with values from oblique shock tables in NACA1135. Intake mass flow conservation is excellent.

A newly developed grid generation procedure is described also. This procedure is able to produce grids both for Euler and Navier-Stokes calculations. Calculations have been performed with a simple algebraic grid and with the new procedure. A sort of "shock fitting" improved results only locally. In other regions of the intake flow results at least degraded slightly. Grid embedding should be able to overcome this.

The Euler code versions EU2DIN and EU3DIN (developed from the MBB EUFLEX code) for two- and three-dimensional intake flows, respectively, are being used during intake design to validate the design procedures and to calculate intake lip drags. Determination of the effects of real gas and mass removal by bleed is possible and will be carried out.

Validation of the codes will be performed in the near future by comparing calculated and measured data of a hypersonic intake model.

REFERENCES

1. MacCormack, R.W., "A Numerical Method for Solving the Equations of Compressible Viscous Flows", AIAA-Paper 81-110, 1981
2. Rizzi, A., Inouye, M., "Time-Split Finite-Volume Method for Three-Dimensional Blunt-Body Flow", AIAA Journal, Vol. 11, No. 11, Nov. 1973, pp. 1478-1485
3. Van Albada, G.D., Van Leer, B., Roberts, W.W., "A Comparative Study of Computational Methods in Cosmic Gas Dynamics", Astro. Astrophys. 108, 1982
4. Eberle, A., Rizzi, A., Hirschel, E.H., "Numerical Solution of the Euler Equations for Steady Flow Problems", Volume 33 of Notes on Numerical Fluid Mechanics, Vieweg, Braunschweig, Wiesbaden, 1991, to appear
5. Eberle, A., Schmatz, M., Bissinger, N., "Generalized Fluxvectors for Hypersonic Shock-Capturing", AIAA Paper 90-0390, 1990
6. Einfeldt, B., "Ein schneller Algorithmus zur Lösung des Riemann Problems", Report 38, Institut für Geometrie und Praktische Mathematik, RWTH Aachen, Germany, 1986
7. Van Leer, B., "Flux Vector Splitting for the Euler Equations", Lecture Notes in Physics 170, 1982
8. Shapiro, R.A., "An Adaptive Finite Element Solution Algorithm for the Euler Equations", Ph.D. Thesis, MIT, Cambridge, Massachusetts, 1988
9. Eberle, A., "Characteristic Flux Averaging Approach to the Solution of Euler's Equations", VKI-Lecture Series 1987-04
10. Steger, J.L., Warming, R.F., "Flux vector splitting of the inviscid gasdynamic equations with application to finite difference methods", J. Comp. Phys., Vol. 40, 1981, pp. 263-293
11. Schwab, R.R., Göing, M., Aulehla, F., Weinreich, H.-L., "Einige Gesichtspunkte zur Auslegung eines Hyperschall-Antriebssystems im Hinblick auf die Abstimmung von Einlauf und Heck mit dem Triebwerk", DGLR Jahrestagung, Darmstadt, Sept. 1988

12. Mundt, Ch., Keraus, R., Fischer, J.: "New, accurate, vectorized approximations of state surfaces for the thermodynamic and transport properties of equilibrium air", paper accepted for publication in zfw, 1989

13. S. HeiB, "Generierung von Oberflächennetzen aus CATIA-Kurven", MBB-FE122-AERO-MT-853, 20.11.1989

ACKNOWLEDGEMENTS

This work has been supported by the German Ministry of Research and Technology (BMFT). The authors would also like to acknowledge the support and discussions with their colleagues during this work.

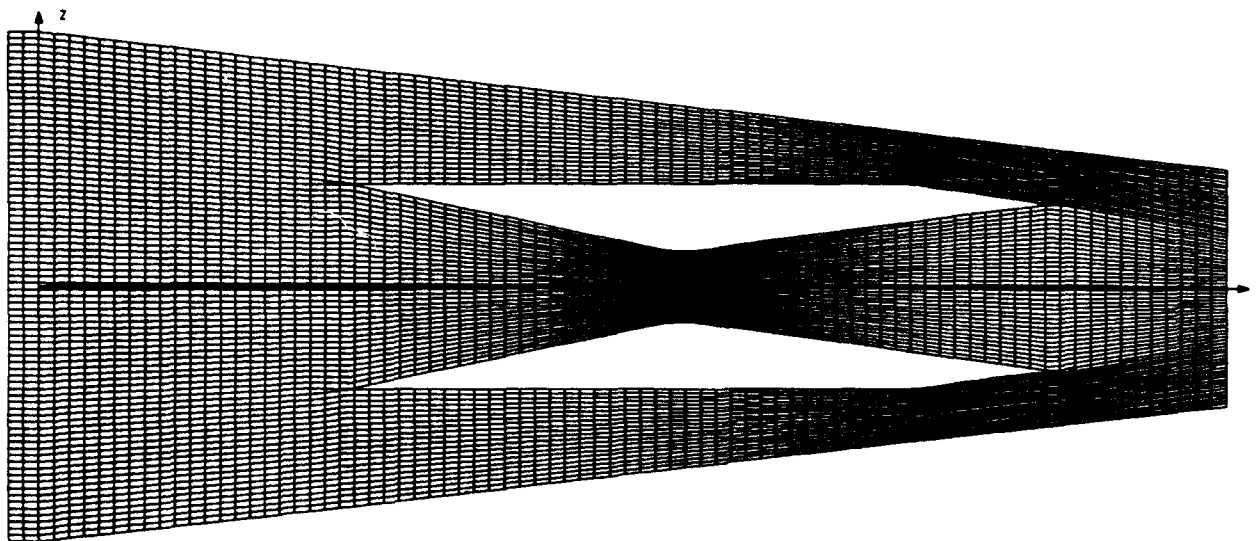


Fig.1: Grid for Scramjet (407x155 grid points)

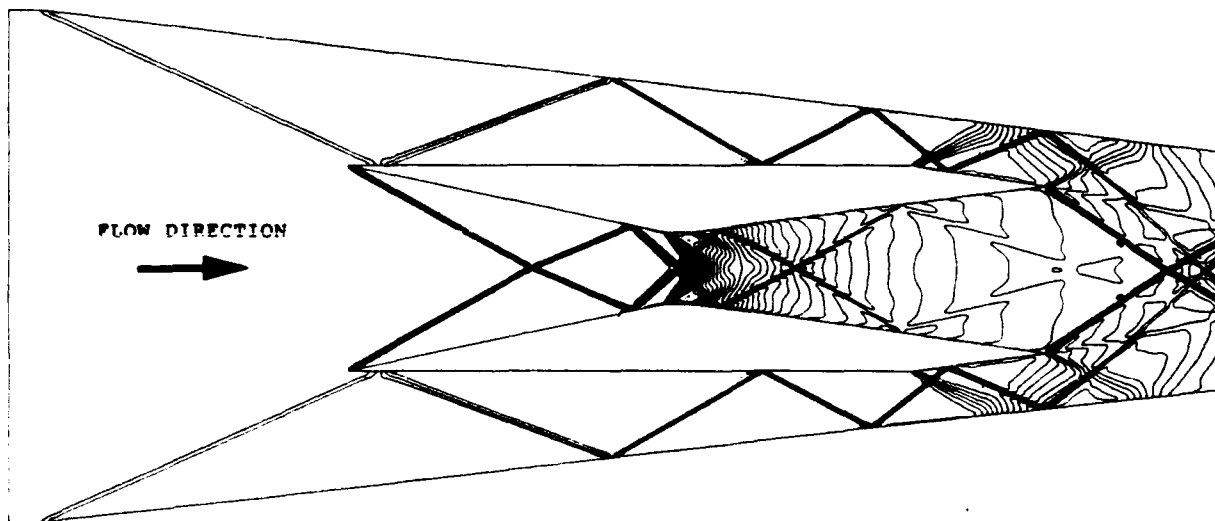
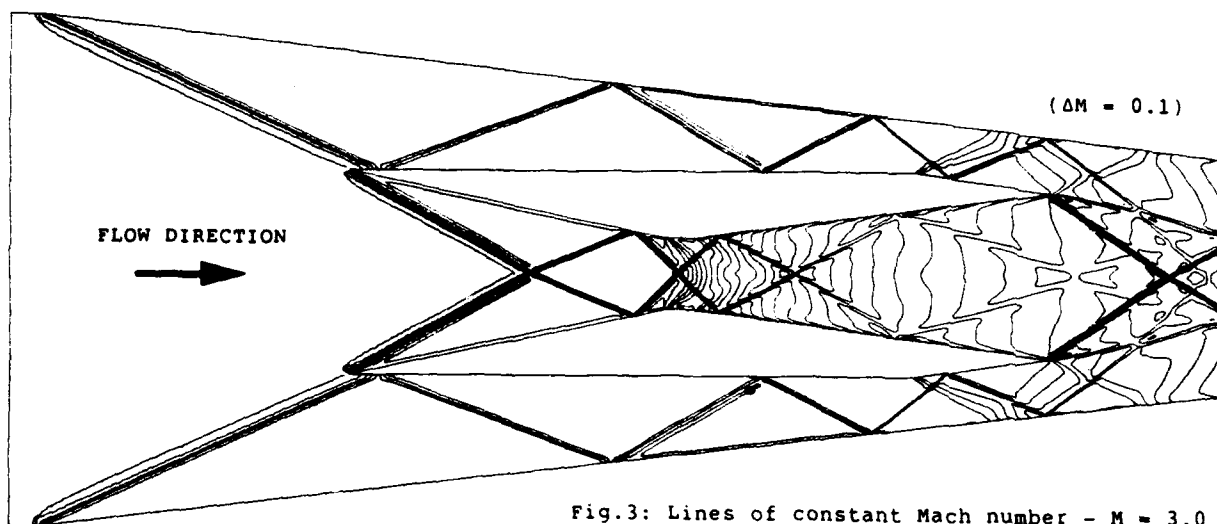
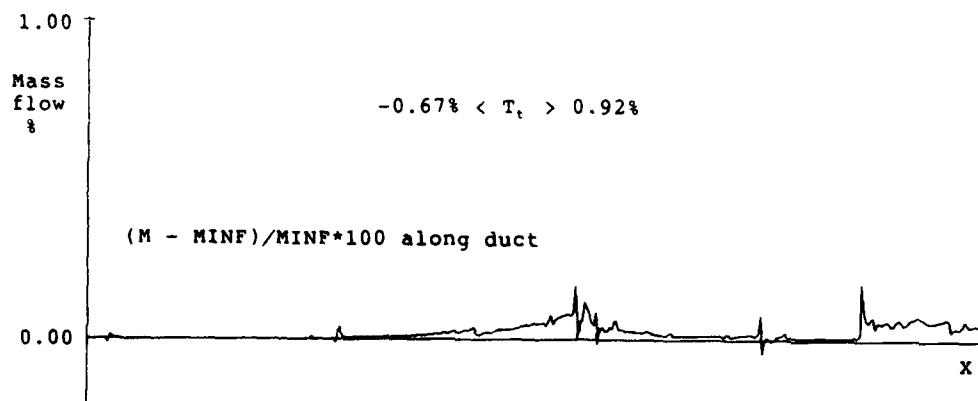
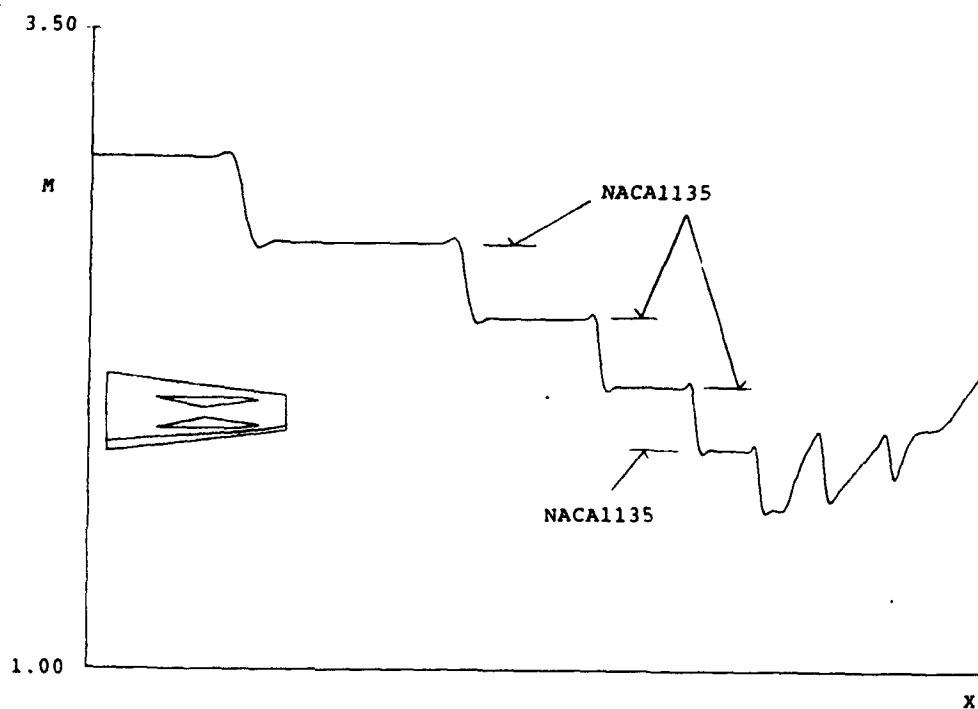


Fig.2: Lines of constant density - $M = 3.0$

Fig.3: Lines of constant Mach number - $M = 3.0$ Fig.4: Mass flow and total temperature deviation - $M = 3.0$ Fig.5: Mach number along grid line $k = 20$ - $M = 3.0$

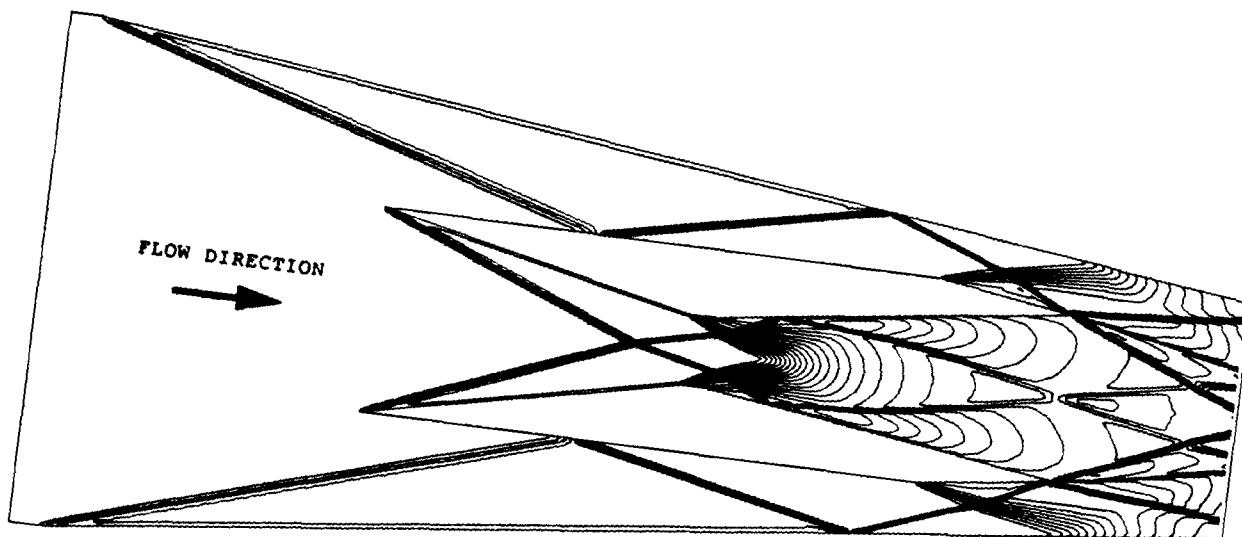


Fig.6: Lines of constant density - $M = 5.0$

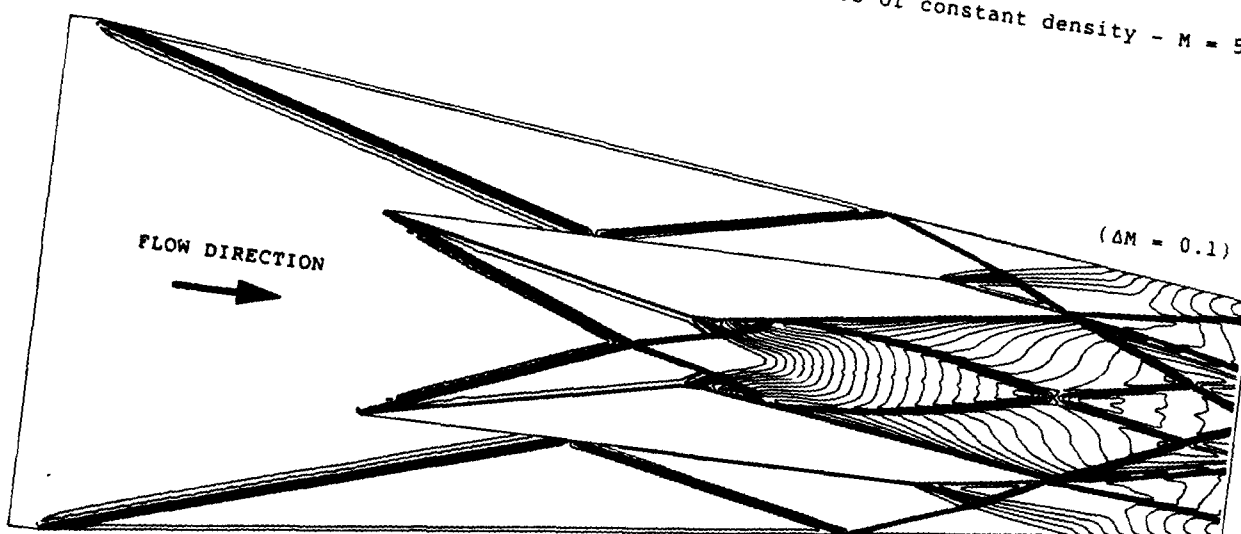


Fig.7: Lines of constant Mach number - $M = 5.0$

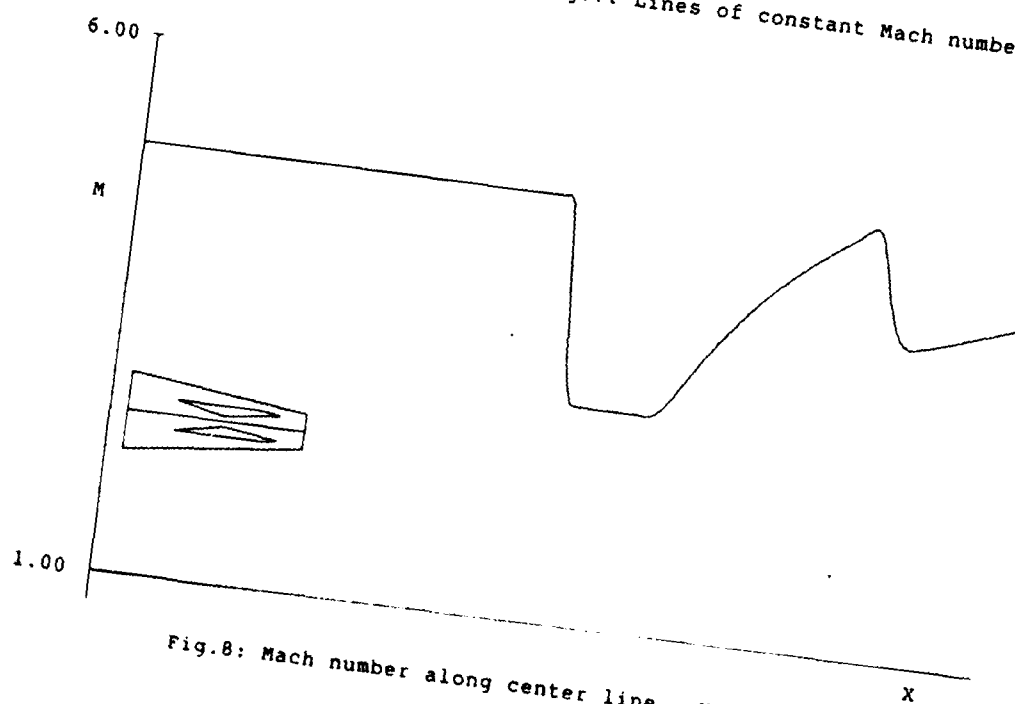


Fig.8: Mach number along center line - $M = 5.0$

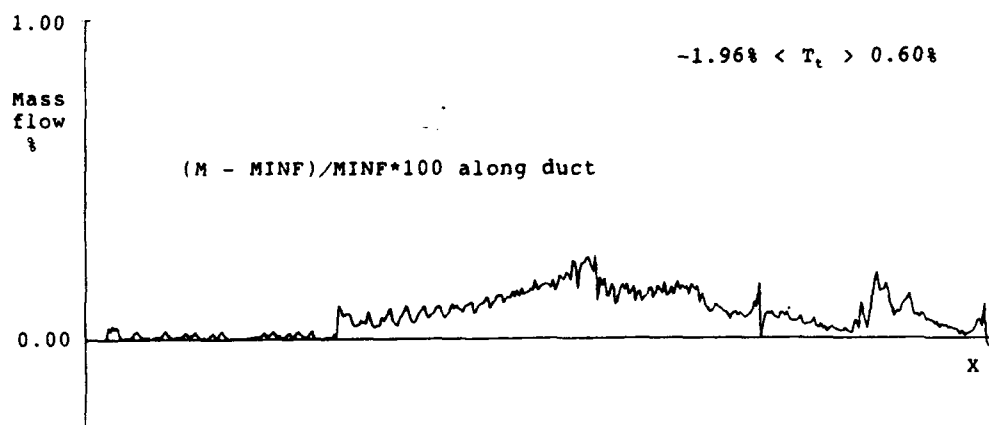
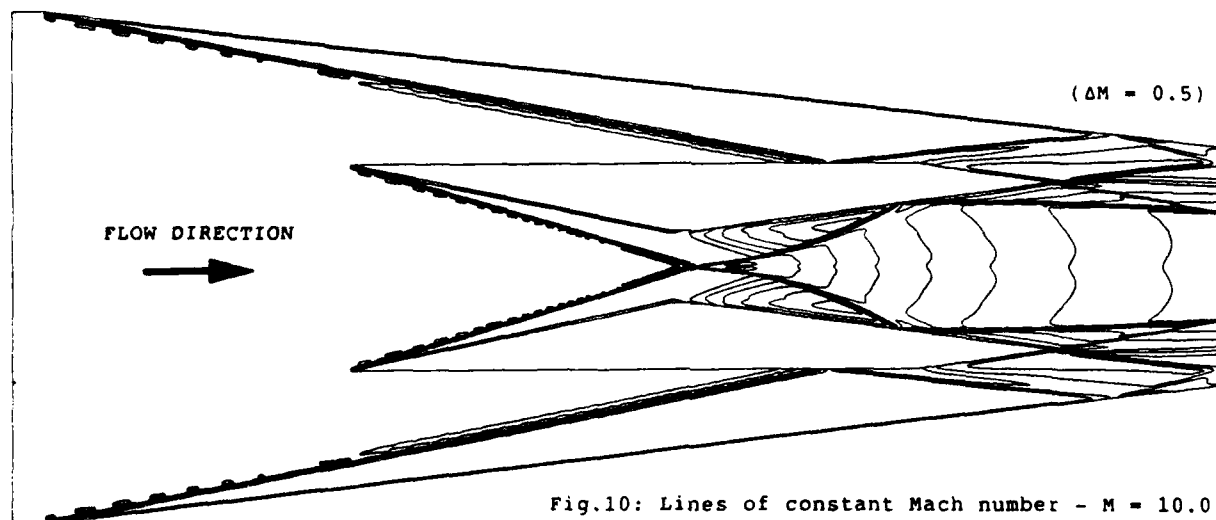
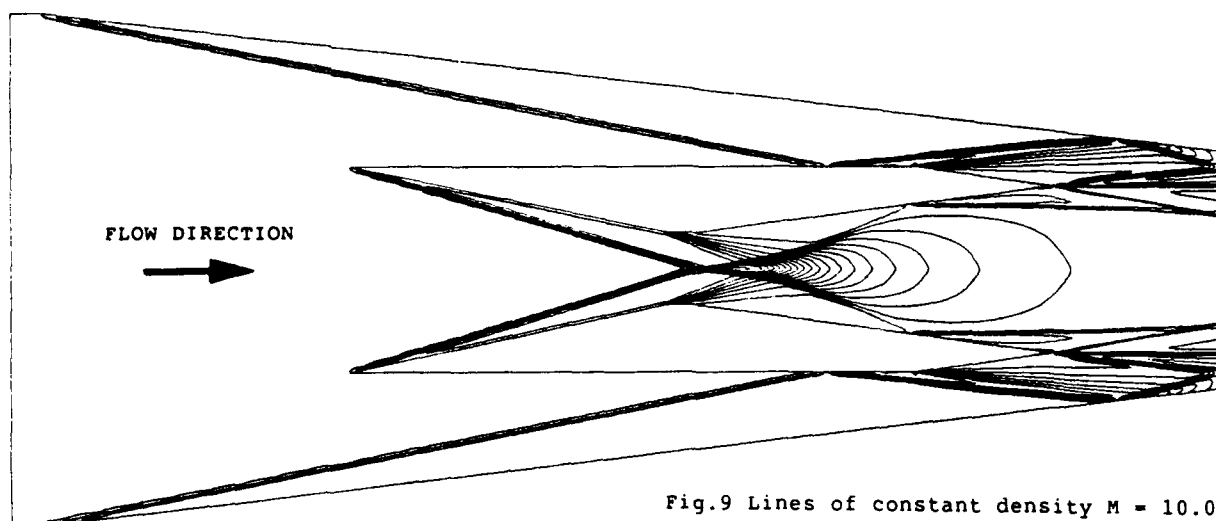


Fig.11: Mass flow and total temperature deviation - $M = 10.0$

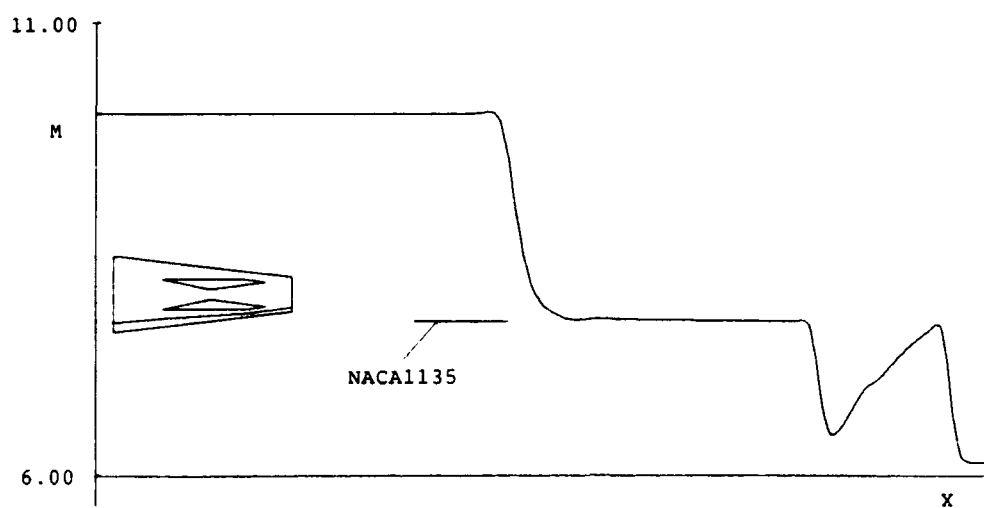


Fig.12: Mach number along grid line $k = 20$ - $M = 10.0$

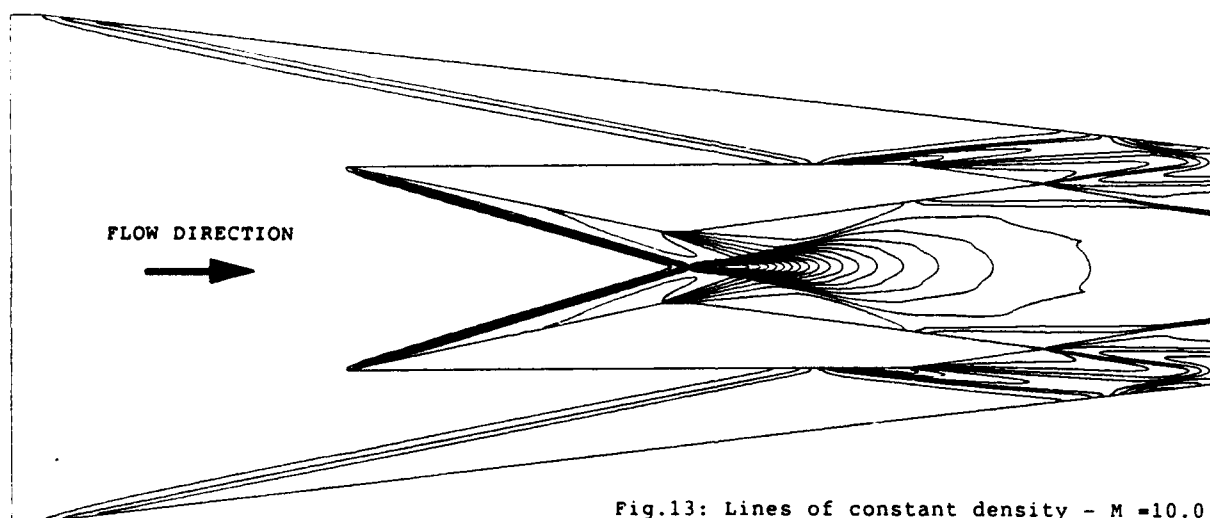


Fig.13: Lines of constant density - $M = 10.0$

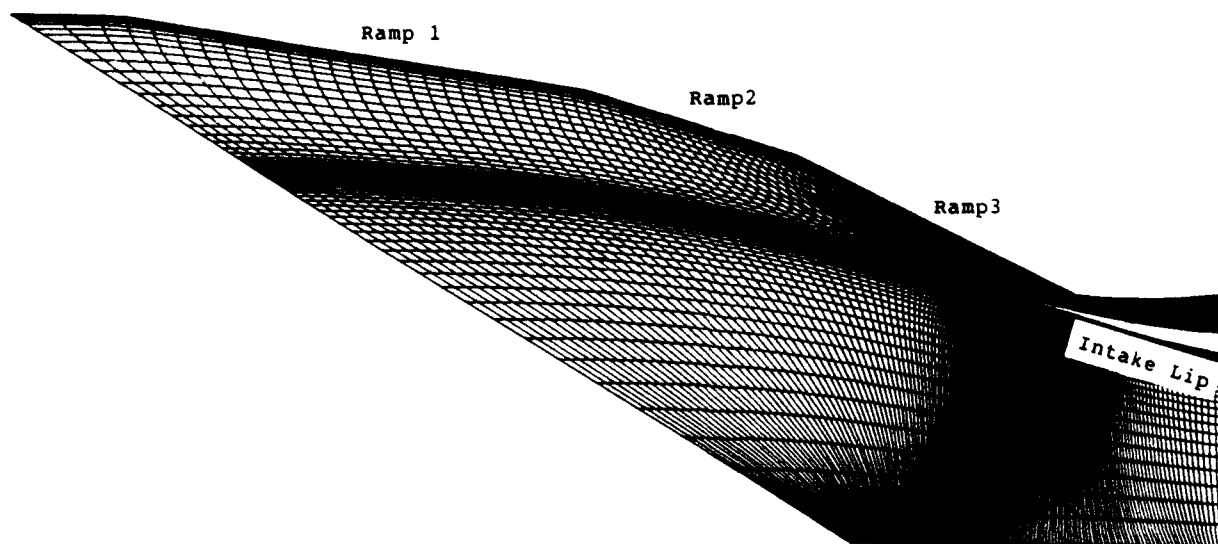


Fig.14: Medium grid for 2D mixed compression intake (161x65 grid points)

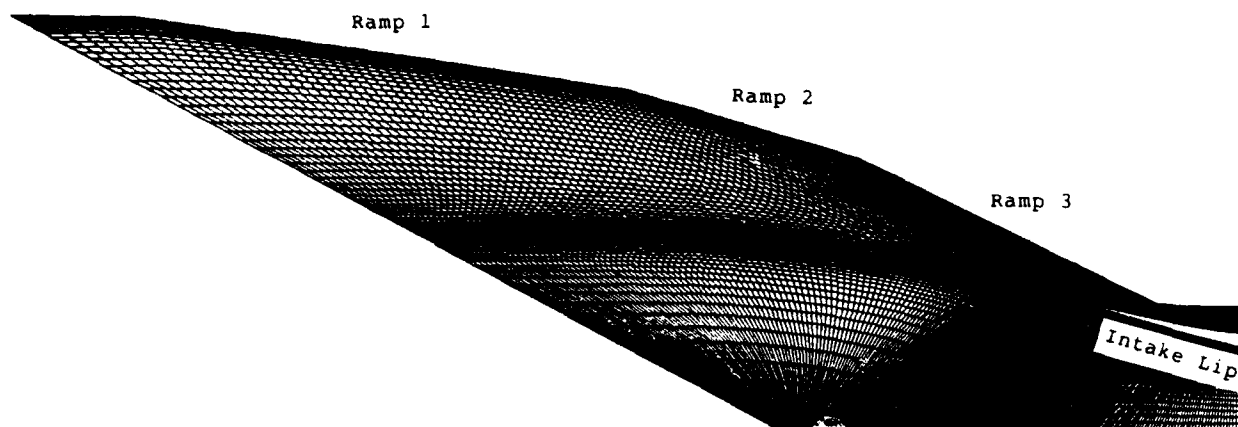


Fig.15: Fine grid for 2D mixed compression intake (301x107 grid points)

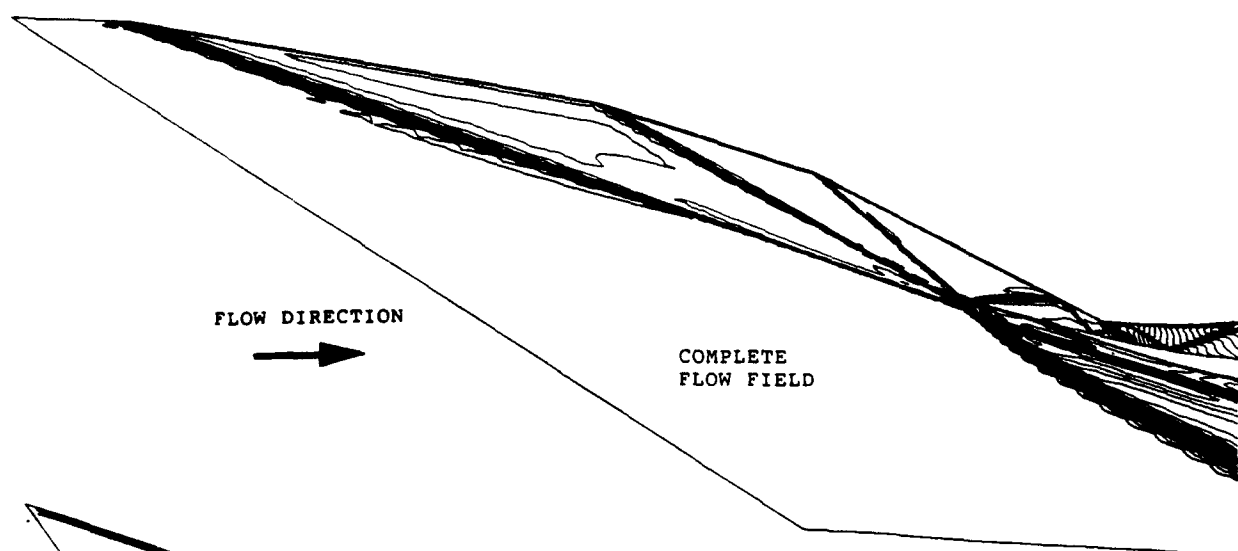
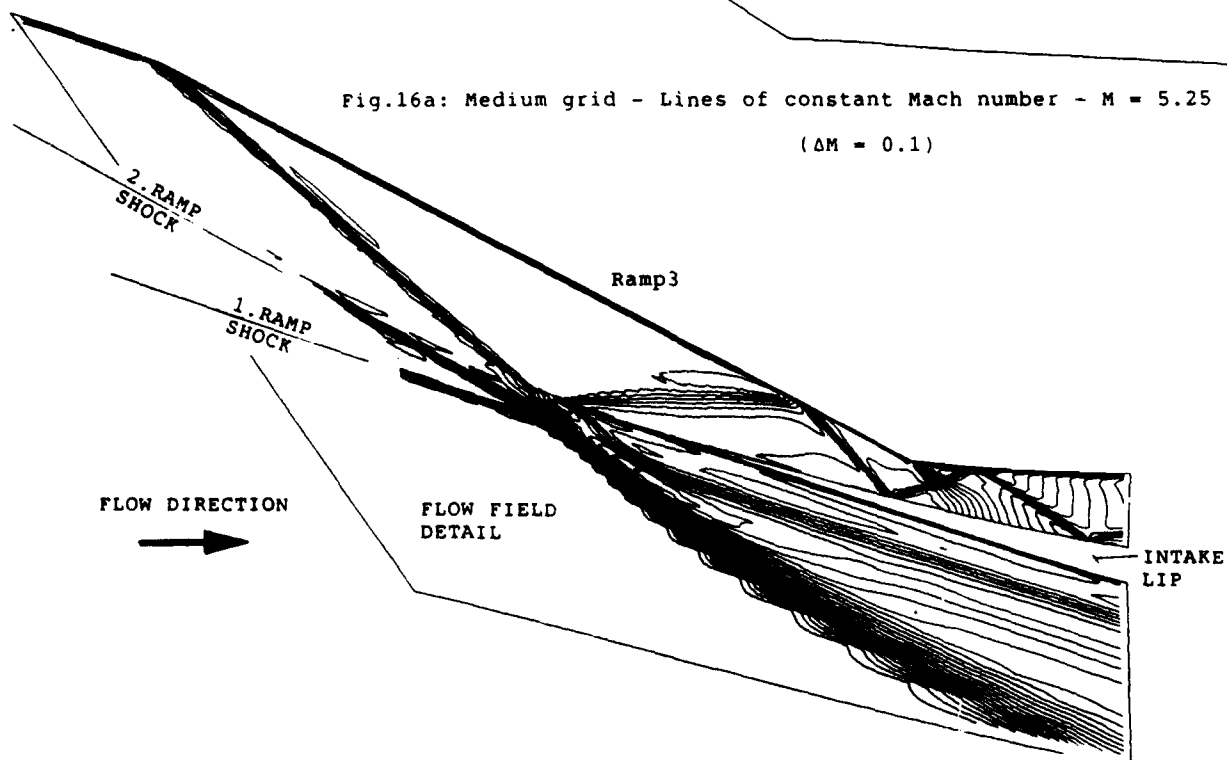


Fig.16a: Medium grid - Lines of constant Mach number - $M = 5.25$
($\Delta M = 0.1$)



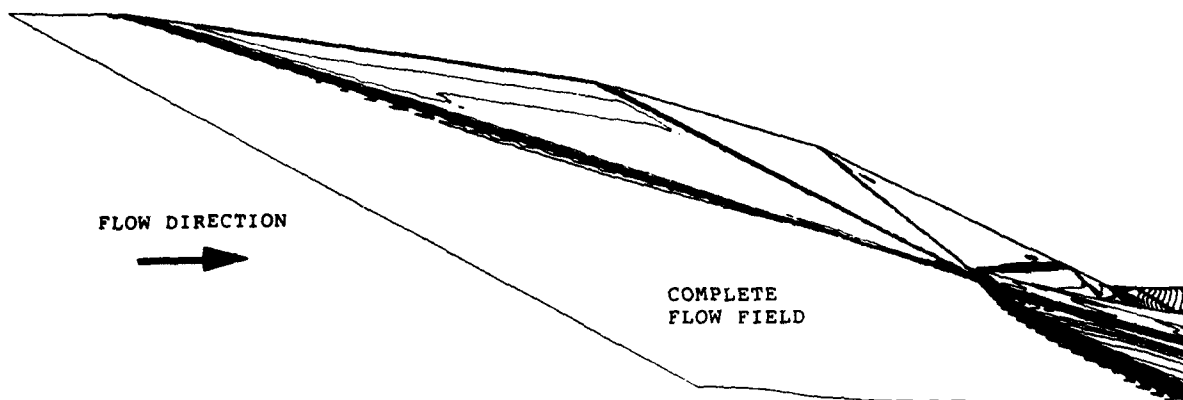
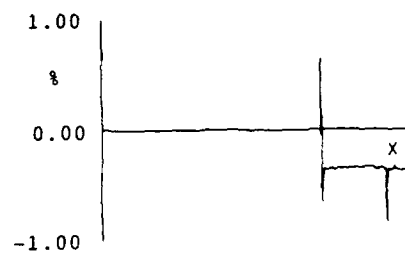
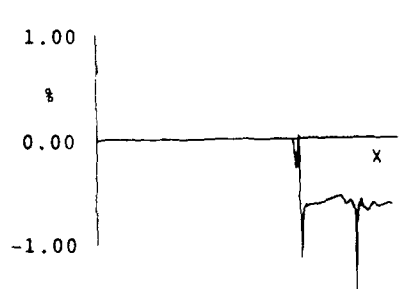
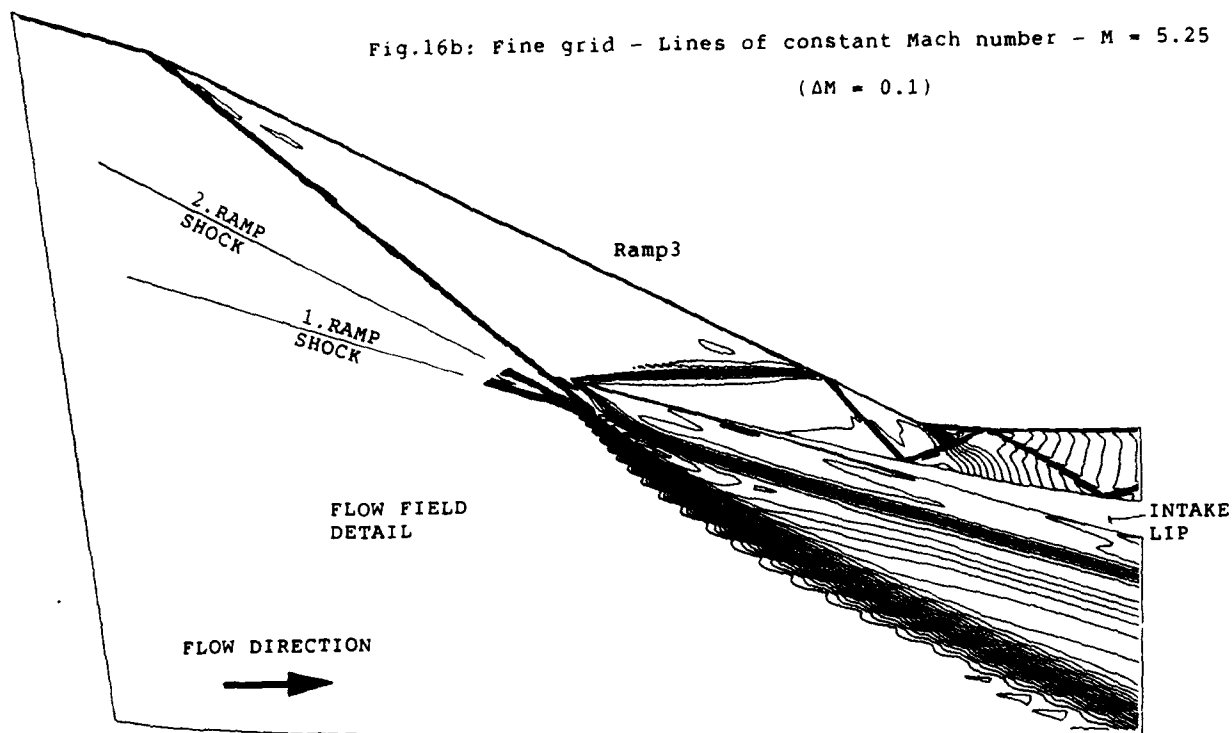


Fig.16b: Fine grid - Lines of constant Mach number - $M = 5.25$
($\Delta M = 0.1$)



$(M - M_{INF})/M_{INF} \times 100$ along duct

Fig.17a: Medium grid
Mass flow deviation
 $M = 5.25$

Fig.17b: Fine grid
Mass flow deviation
 $M = 5.25$

Fig.18: Fine grid - $M = 5.25$
 Close-up of the shock system at the intake lip:
 Lines of constant Mach number ($\Delta M = 0.1$)

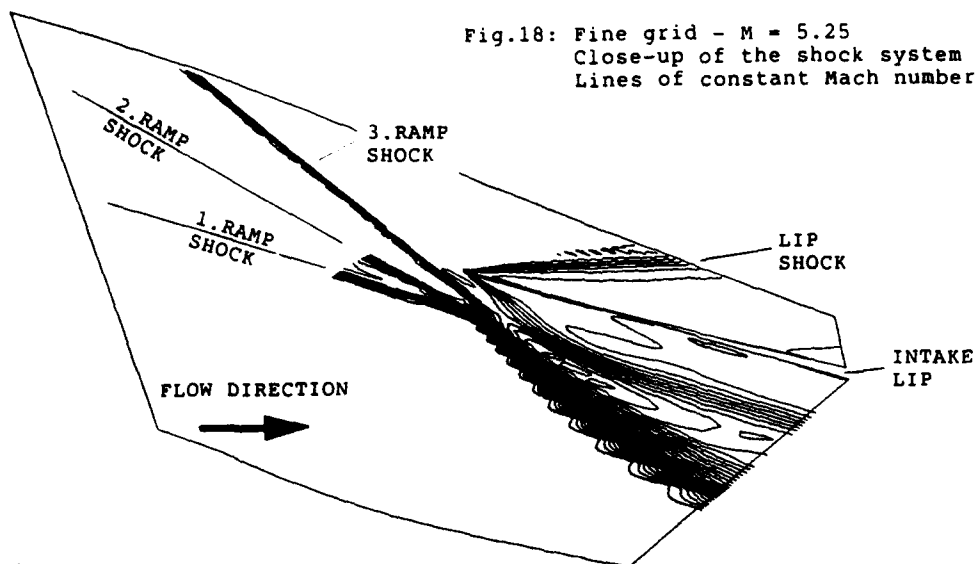


Fig.19: Fine grid - $M = 5.65$
 Close-up of the shock system at the intake lip:
 Lines of constant Mach number ($\Delta M = 0.1$)

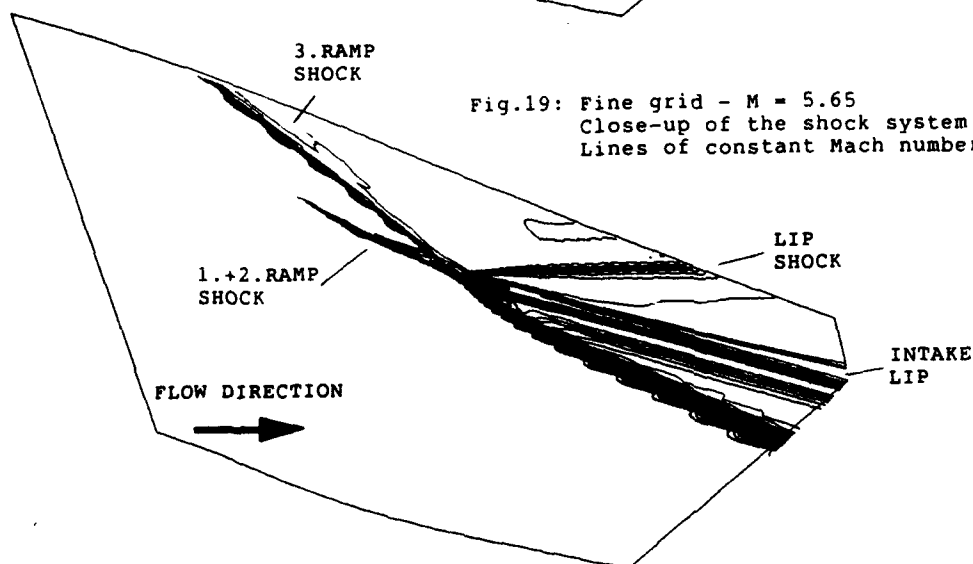
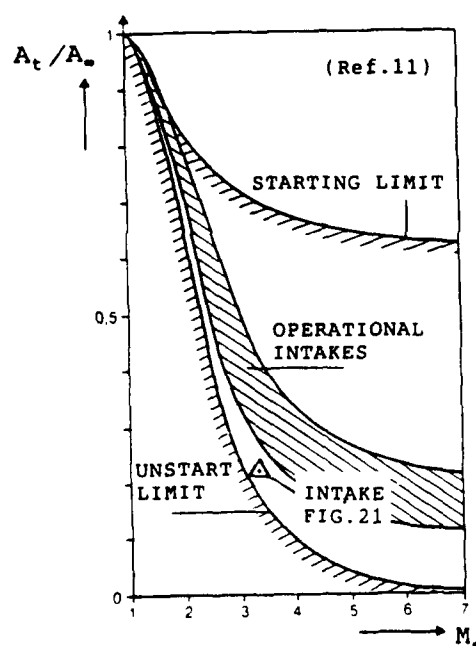


Fig.20: Throat area limits
 for internal compression
 (derived for isentropic flow)



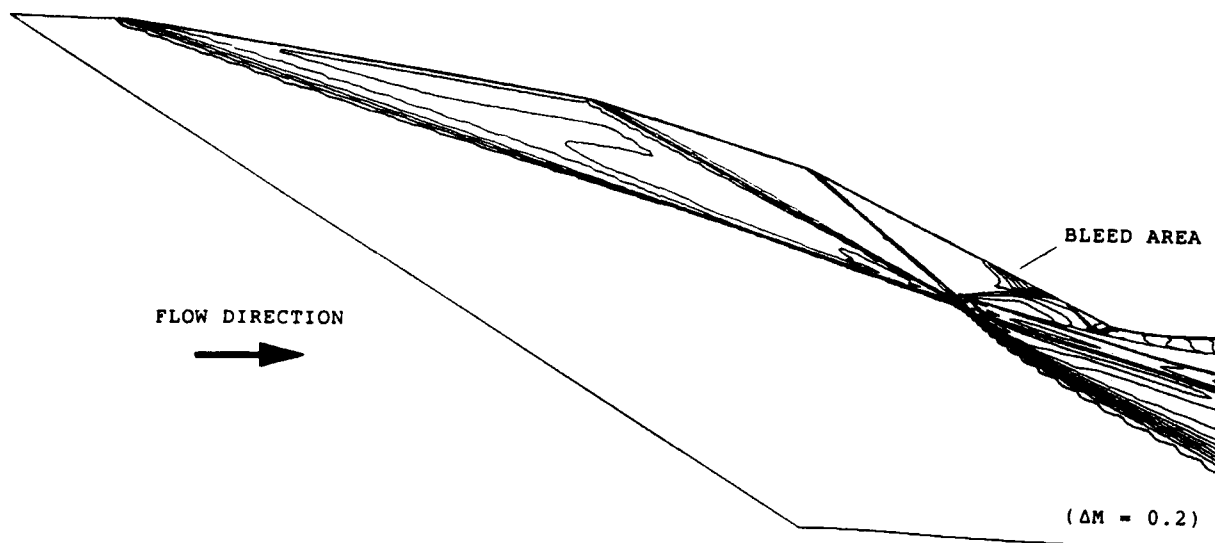


Fig.21: Starting of internal compression by ramp bleed
Lines of constant Mach number - $M = 5.25$ - Medium grid

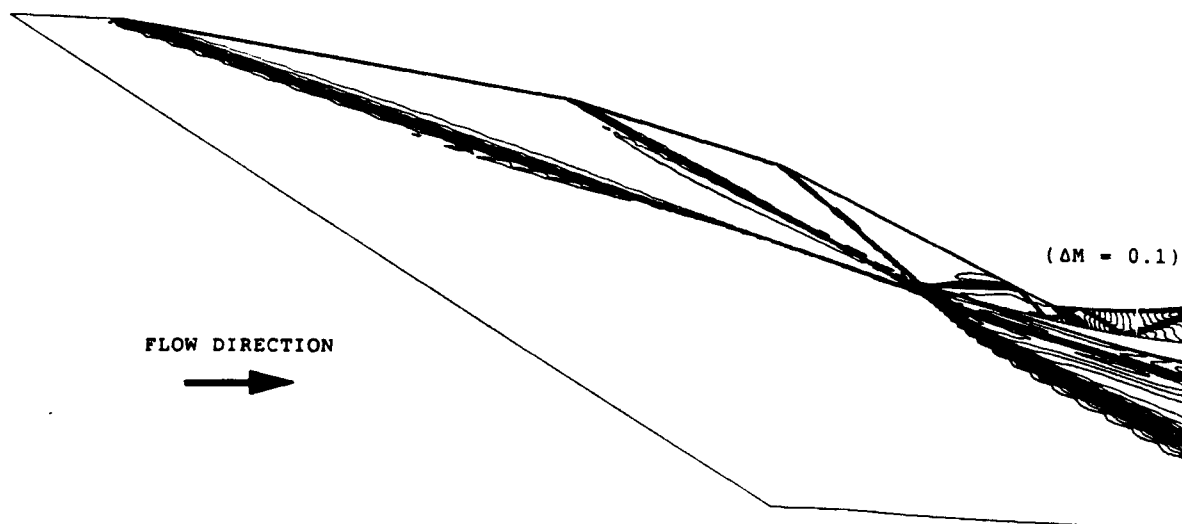


Fig.22: Real gas calculation
Lines of constant Mach number - $M = 5.25$ - Medium grid

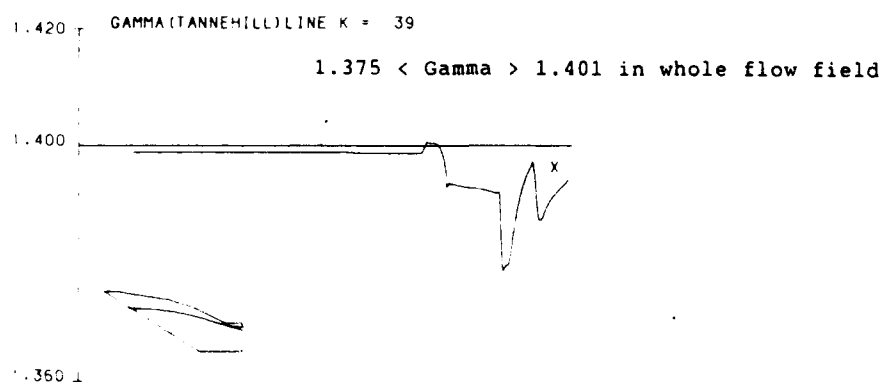


Fig.23: Real gas calculation
Ratio of specific heats along grid line $k = 39$ (intake bottom)

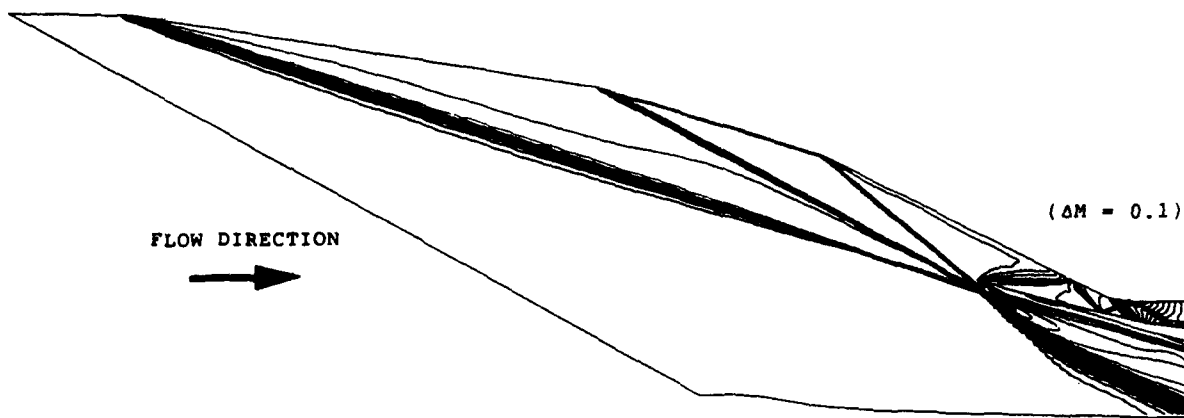


Fig.24: First order coefficients result
Lines of constant Mach number - $M = 5.25$ - Fine grid

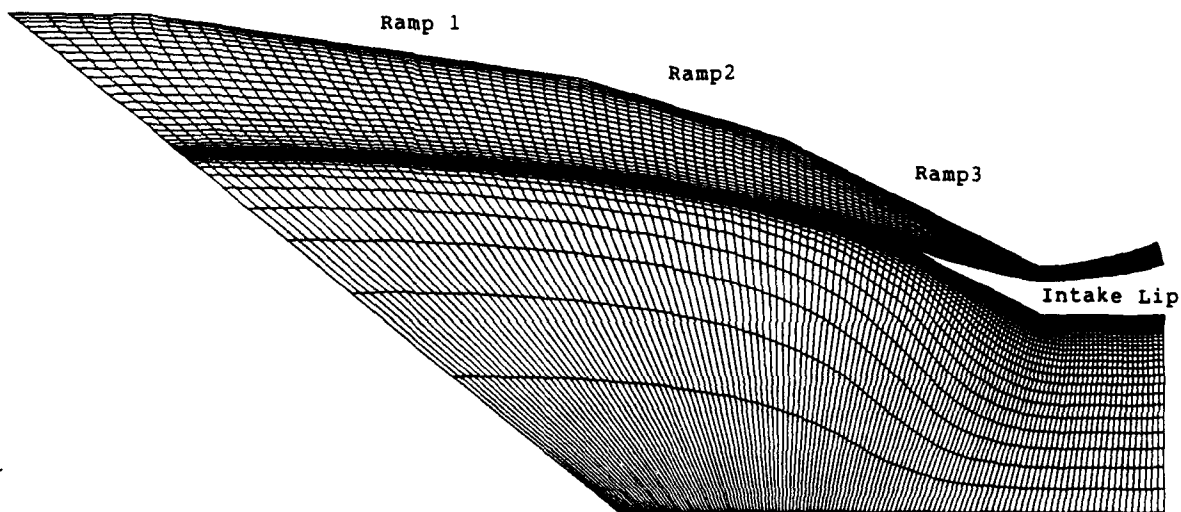


Fig.25: Medium grid for second intake duct shape (130x60 grid points)

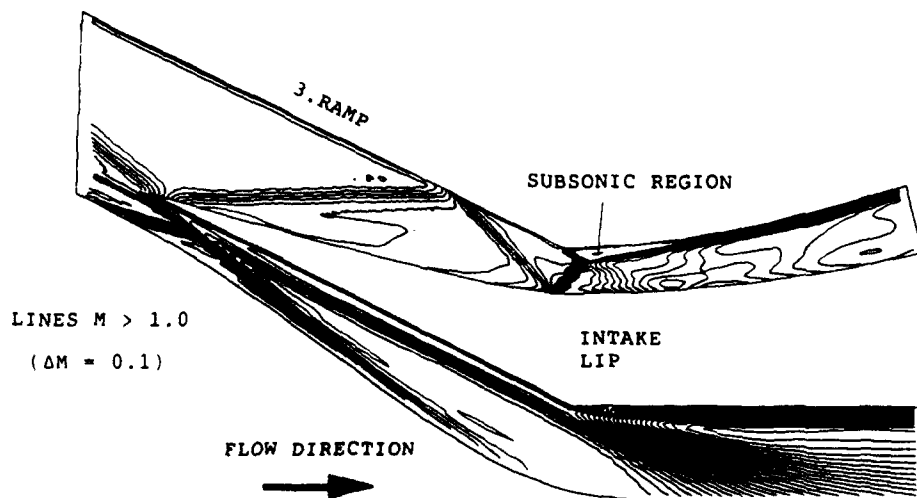


Fig.26a: Subsonic region downstream of throat
Lines of constant Mach number - $M = 5.25$ - Medium grid

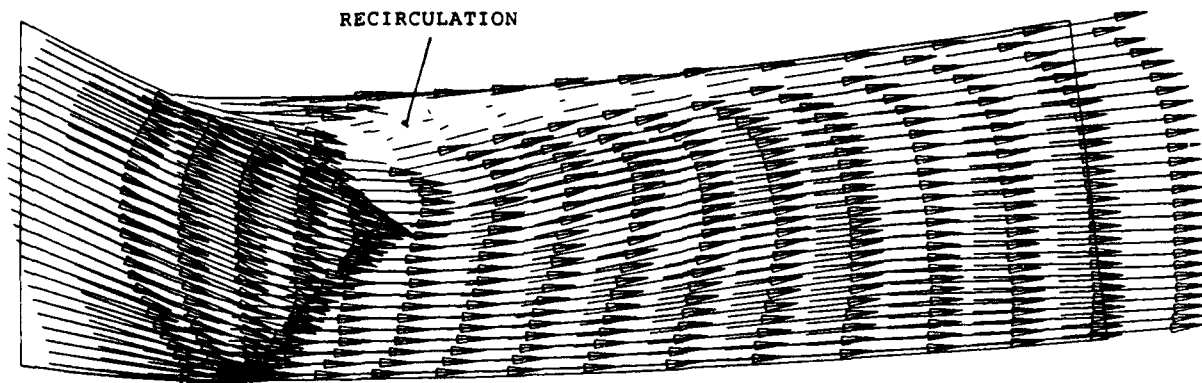


Fig.26b: Subsonic region downstream of throat
Velocity vectors showing recirculation region
 $M = 5.25$ - Medium grid

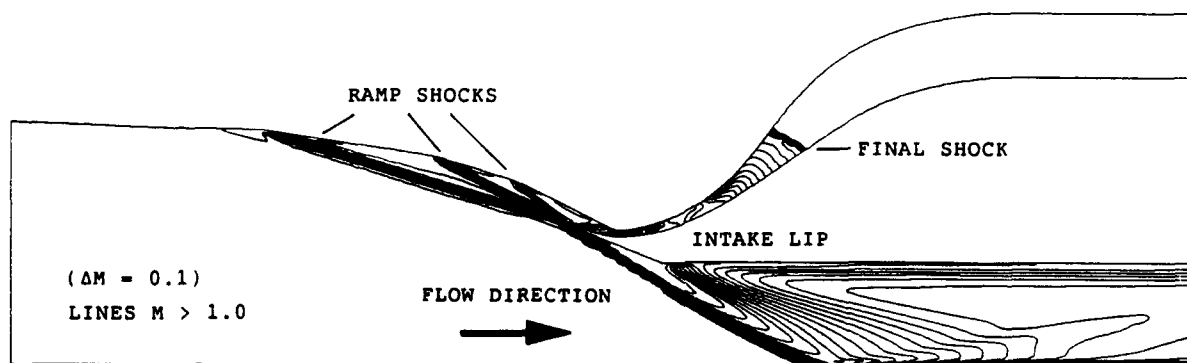


Fig.27: Complete duct flow
Lines of constant Mach number - $M = 5.65$ - Medium grid

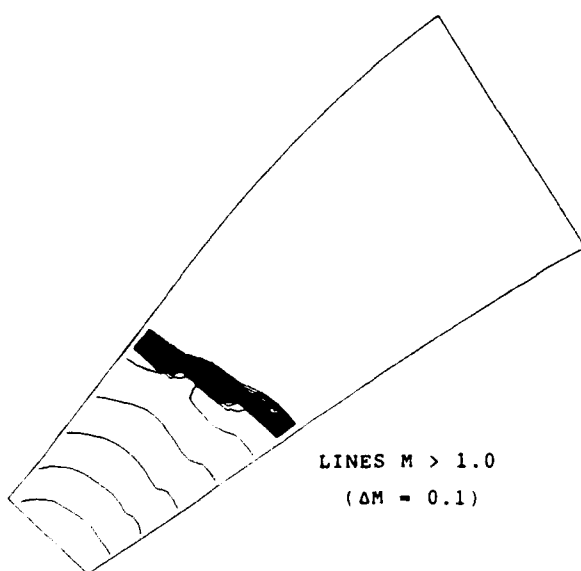


Fig.28: Final shock of supersonic
internal compression
Lines of constant Mach number
 $M = 5.65$ - Medium grid

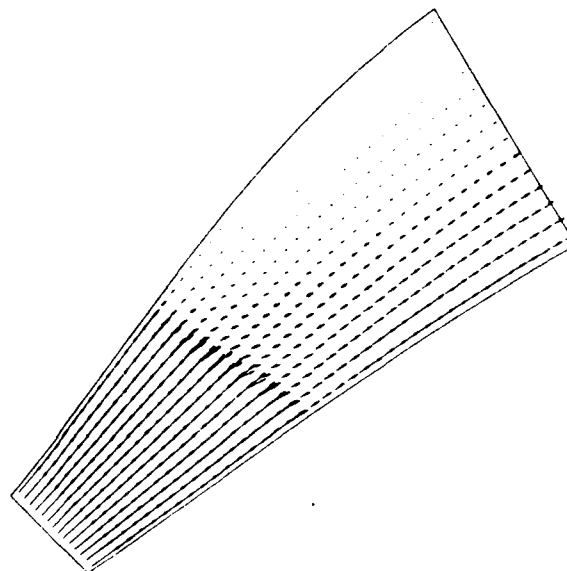


Fig.29: Velocity vectors at final shock
of supersonic internal compression
 $M = 5.65$ - Medium grid

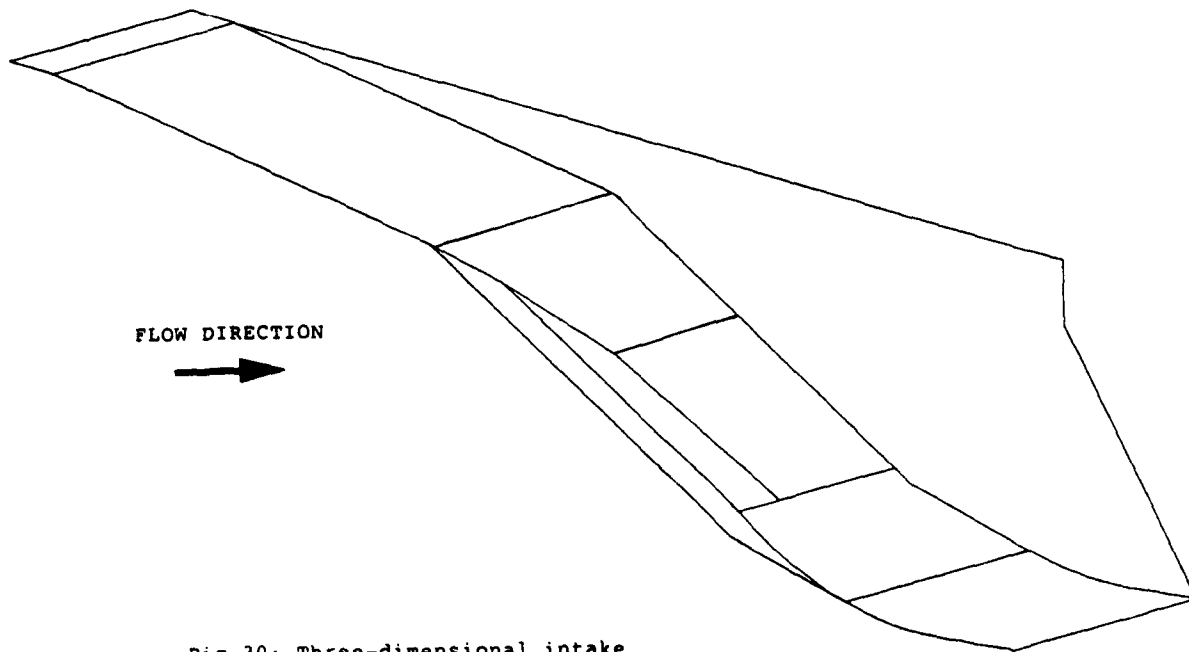


Fig.30: Three-dimensional intake

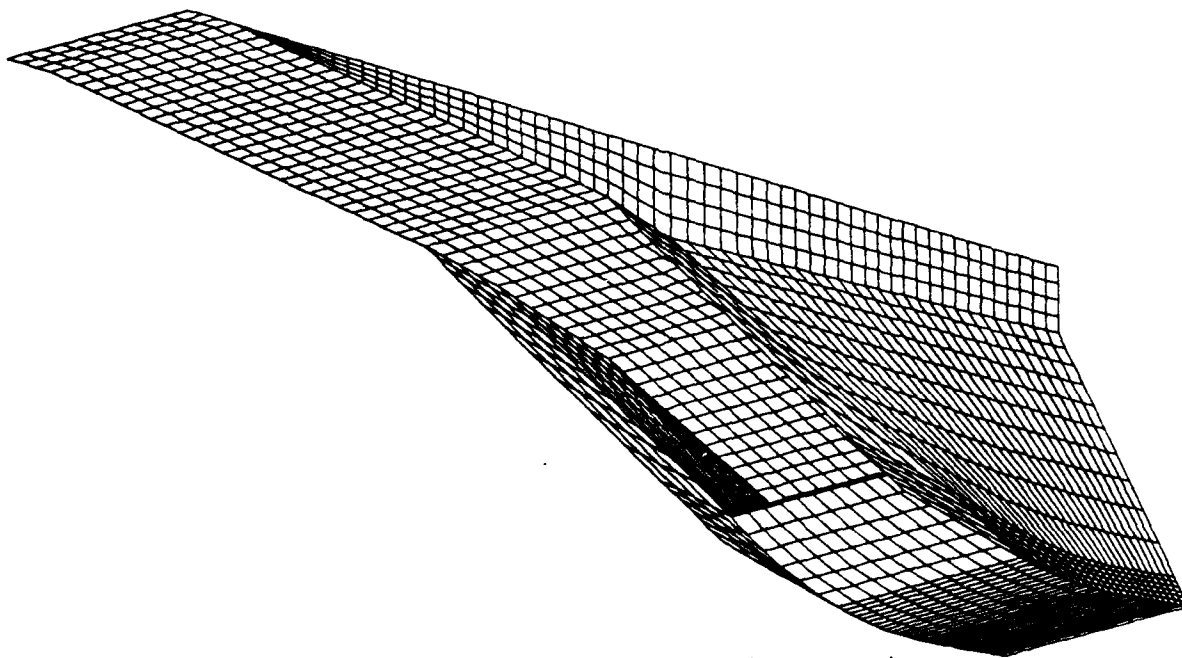


Fig.31: Surface grid for three-dimensional intake

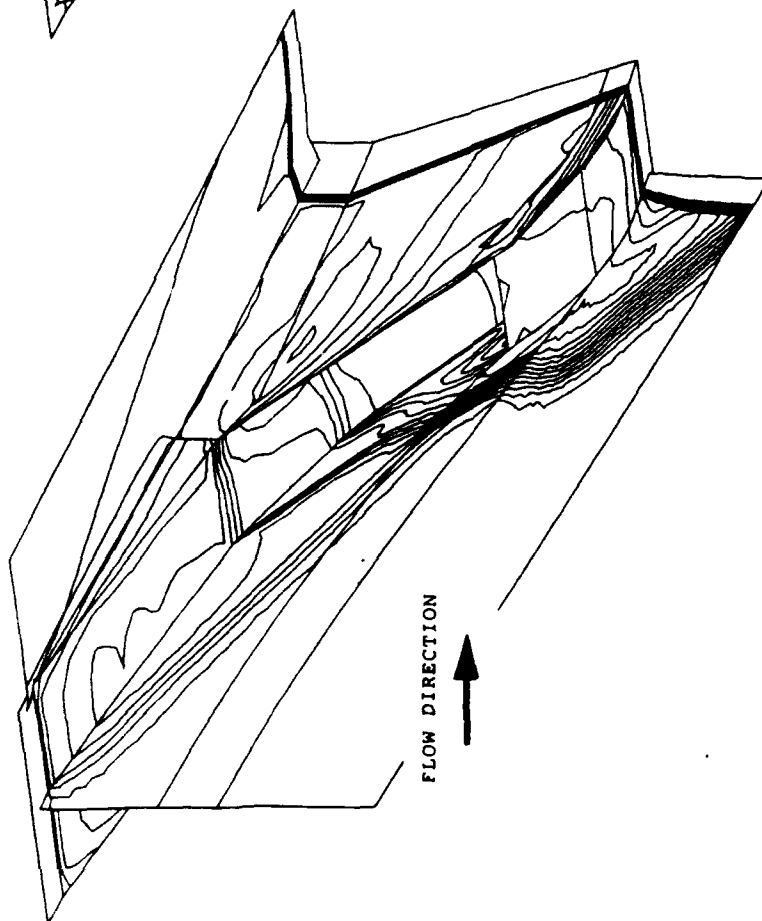


Fig.32: Three-dimensional intake
Lines of constant Mach number on surface
and vertical centerline plane
 $M = 5.63 - \Delta M = 0.2$

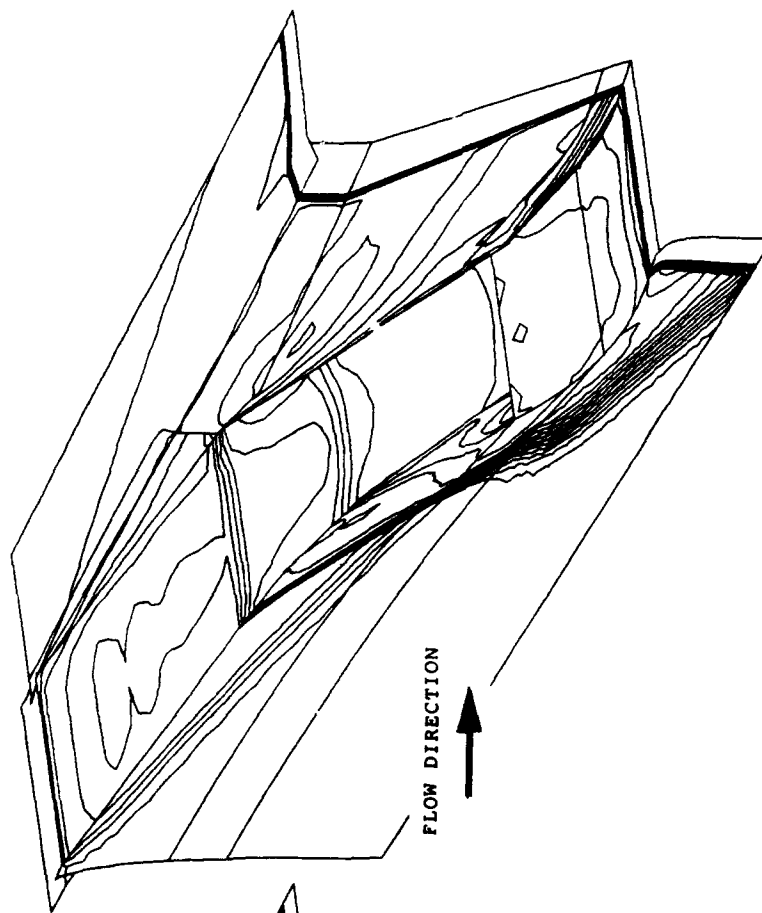


Fig.33: Three-dimensional intake
Lines of constant Mach number on surface
and sidewall grid plane
 $M = 5.63 - \Delta M = 0.2$

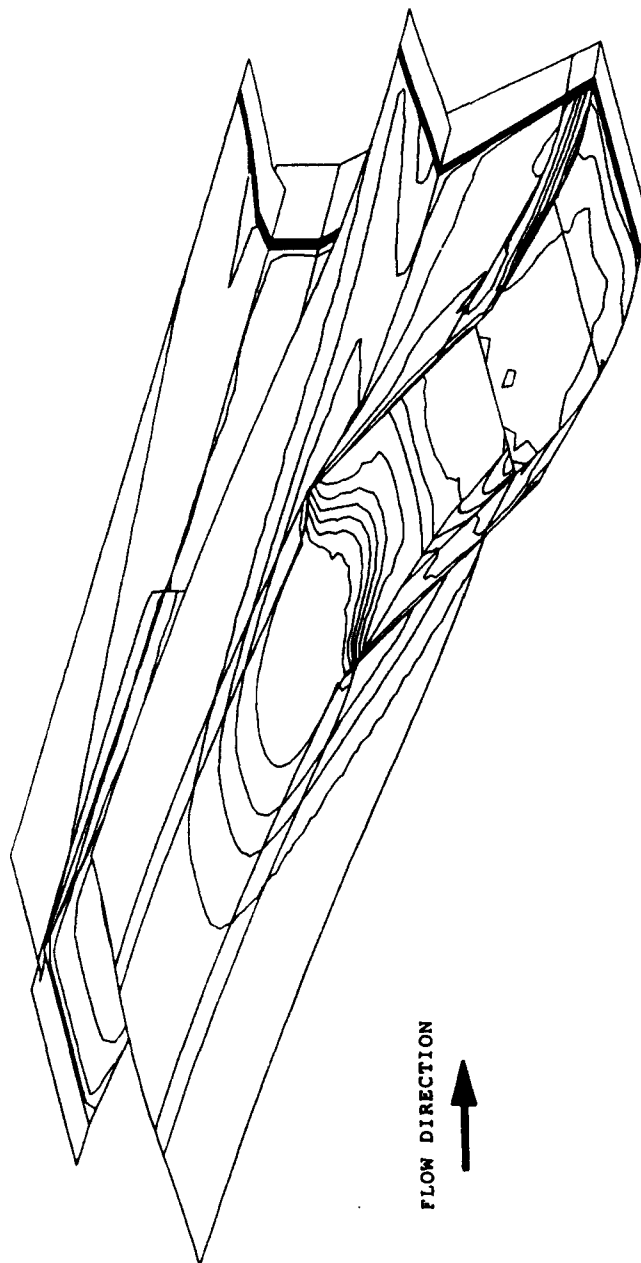


Fig.34: Three-dimensional intake
Lines of constant Mach number on surface and horizontal middle plane
 $M = 5.63 - \Delta M = 0.2$

Discussion

M. FORDE, UNIV. OF TRONDHEIM, NORWAY

In Fig. 16(a) the shocks shows a wavy pattern, what is the reason for this?

AUTHOR'S REPLY

The solution in Fig. 16(a) has been calculated with the medium grid of Fig. 14. In Fig. 14 it can be seen that at the location of the shock below the intake (Fig. 16(a)) the distance between the "horizontal" grid lines is large compared to the distance between the "vertical" ones. Therefore, it can be concluded that the waviness of this shock is due to the grid density, i.e., cell aspect ratio, and possibly to the angle at which the shock is crossing these elongated grid cells.

T. VOGEL, DLR, GERMANY

Which boundary condition did you apply for the lower boundary in Fig. 27?

AUTHOR'S REPLY

The lower boundary in Fig. 27 is far from the area of interest of this calculation. (The calculation was aimed at determining the flow inside the intake.) Therefore at this boundary, free stream conditions have been set and held fixed there. As a result of this some disturbance is entering the flow where the shock hits this boundary.





THREE DIMENSIONAL SOLUTION OF INTERNAL FLOWS USING A CELL VERTEX FINITE VOLUME METHOD

Erdal Oktay, İ.Sinan Akmandor, Ahmet Ş. Üçer
Middle East Technical University
06531, Ankara - Türkiye

ABSTRACT:

The numerical solutions of internal three dimensional Euler flows have been obtained, using a cell vertex finite volume method. The solver which has been developed, has been applied to a wide range of subsonic, transonic and supersonic test cases among which are the Ni-bump channel, the supersonic wedge cascade and the Squire and Winter 90° bend channel. A second order accurate, one step Lax-Wendroff scheme has been used to solve the unsteady equations, discretized in strong conservation form. Characteristic boundary conditions have been used along with appropriate artificial viscosity and smoothing models. The results illustrate the established flow symmetry in a subsonic Ni-bump channel, the shock - boundary interaction in transonic and supersonic Ni-channels and wedge cascade and finally, the secondary flow within a 90° bend channel. Despite the wide range in the Mach number and the diversity of flow geometries which have been tested, close agreement have been obtained with available analytical and numerical results associated with these test cases.

INTRODUCTION:

In recent years, Computational Fluid Dynamics (CFD) codes have been increasingly used for studying advanced aerodynamic phenomena in internal and external flow situations. Within this fertile environment, very efficient time marching finite volume methods have been developed for solving the 3-D Euler equations. Among others, two main strategies are popularly followed in the approximations of (mass, momentum, energy) integrals over the surface of control volumes in the computational mesh: These are the cell centered and cell vertex schemes. These two approach have fundamental differences in the formulation of discretized equations for internal and boundary points.

a) Cell centered scheme: As it names implies, the flow properties are calculated at the center of the computational cell. This scheme was applied by Jameson, Schmidt and Turkel [1] and by Allmaras and Giles [2] to 2-D flow fields. Jameson and Baker [3] and Rizzi [4] have also successfully applied this scheme to compute complex 3-D configurations.

b) Cell vertex scheme: In this scheme, the flow properties are assigned at the vertices of the cell, once the changes in conserved quantities have been evaluated at the center of each face surrounding each nodal point. Ni [5] and Hall [6] applied this scheme to inviscid 2-D flows, while Koeck [7] and Denton [8] employed cell vertex schemes to calculate 3-D flow solutions.

A comparison of accuracy of cell centered and cell vertex finite volume schemes have been reported by Rossow, Kroll, Radespiel and Scherr [9]. Furthermore, a third order accurate, conservative cell vertex formulation have recently been developed by Powell and Leer [10] by coupling this scheme with a downwind-weighted distribution step. The 2-D and 3-D problems are solved using a direction split method with the upwinding directions normal to the faces of the computational cells.

The aim of the present paper is to apply a Lax-Wendroff based cell vertex scheme to several internal flow problems including the subsonic, transonic and supersonic Ni-bumps [5], the Agard PEP WG-18 supersonic wedge cascade [11] and the secondary subsonic flow within Squire and Winter 90° bend channel [12]. The algorithm is second order accurate in space. In the central differenced first order accurate version of the finite volume formulation, the residual for the central cell is distributed equally to the eight nodes surrounding this cell. Since the Lax-Wendroff scheme is used, the distribution of the property changes are modified by the 2nd order terms and the nodes receives a flux weighted fraction of the residual when the governing equations are integrated over the finite volume.

The test cases which have been mentioned above are different from each other because of the wide range of the inlet Mach number and the differences in complex flow geometries. The validation of the code for all test cases shows the robustness of the present algorithm. First the Ni-bump will be investigated in subsonic, transonic and supersonic flow fields. This is a well known case which exhibits flow symmetry in subsonic flows around the channel center. In transonic regime, the shock is located at 72% of the arc bump and the supersonic regime exhibit shock-shock and shock-boundary interactions. The second test case examines the flow around a supersonic wedge cascade. This problem demonstrate the capability of the algorithm to capture and reflect the shock waves. Shock-boundary, shock-shock and shock-expansion wave interactions are illustrated in this example. The last test case which has been considered is a subsonic incompressible three dimensional flow within a 90° bend Squire and Winter channel. The inlet velocity profile have a boundary layer-like profile at the bottom wall. This radially non-uniform profile develops into a secondary flow as the fluid moves through the bend channel. Because of the 90° turning, the axial velocity component is not always the predominant component and a strong coupling between the governing equations is expected. The test cases will be thoroughly reviewed before the presentation of the computed results. By using such physically different flow cases, it is hoped that the present computer program is pretested and will be able to resolve flow details within highly loaded, high speed, low aspect ratio fans, blades and ducts of todays modern ultra high by-pass ratio engines.

GOVERNING EQUATIONS :

Three dimensional Euler equation for unsteady compressible inviscid flows written in conservation form using a cartesian coordinate system is

$$\frac{\partial Q}{\partial t} + \nabla \cdot F = 0$$

where

92-16086



$$\vec{E} = F \vec{i} + G \vec{j} + H \vec{k}$$

$$Q = \begin{bmatrix} \rho \\ \rho u \\ \rho v \\ \rho w \\ e \end{bmatrix} \quad F = \begin{bmatrix} \rho u \\ \rho u^2 + p \\ \rho uv \\ \rho uw \\ (e + p)u \end{bmatrix} \quad G = \begin{bmatrix} \rho v \\ \rho uv \\ \rho v^2 + p \\ \rho vw \\ (e + p)v \end{bmatrix} \quad H = \begin{bmatrix} \rho w \\ \rho uw \\ \rho vw \\ \rho w^2 + p \\ (e + p)w \end{bmatrix}$$

Here ρ is the density ; p is the pressure ; u , v and w the velocity components in the x , y , z cartesian directions respectively ; and e is the total energy per unit volume. The pressure is related to the total energy and density by the equation of state for a polytropic gas as

$$p = (\gamma - 1) \left[e - \frac{1}{2} \rho (u^2 + v^2 + w^2) \right]$$

where γ is the ratio of specific heats.

FINITE VOLUME DISCRETIZATION :

The Taylor - series expansion for the component Q in Eqs. (1) is written by the second order approximation

$$\delta Q = \left(\frac{\partial Q}{\partial t} \right)^n \Delta t + \frac{1}{2} \left(\frac{\partial}{\partial t} \left(\frac{\partial Q}{\partial t} \right)^n \right) \frac{\Delta t^2}{2} \quad (2)$$

where the superscript n denotes the value of a variable at the time level n , $\delta Q = Q^{n+1} - Q^n$ and time increment $\Delta t = t^{n+1} - t^n$. Substituting from Eqs. (1) and changing the order of differentiation yields ,

$$\delta Q = - \nabla \cdot \vec{E} \Delta t - \frac{1}{2} \nabla \cdot \left(\frac{\partial \vec{E}}{\partial t} \right)^n \frac{\Delta t^2}{2} \quad (3)$$

by defining $\frac{\partial \vec{E}}{\partial t} \cdot \Delta t = \Delta \vec{E}$

$$\delta Q = - \nabla \cdot \vec{E} \Delta t - \nabla \cdot \Delta \vec{E} \frac{\Delta t}{2} \quad (4)$$

where $\Delta \vec{E} = \Delta F \vec{i} + \Delta G \vec{j} + \Delta H \vec{k}$

A finite volume cell in its most general form in the physical domain is shown in Fig.1 . For a finite volume discretization , Eq. (4) is integrated over the control volume specified around nodal points as shown in Fig. 2a. In this figure, grid points are denoted by numbers and capital letters. The vertices of the control volume of grid point 1 are located at the center of the faces defined by neighbouring nodal points.

Integrating Eq.(4) over the control volume k-h-e-z-s-o-w-v

$$\delta Q_1^n = - \frac{\Delta t}{\Delta V} \iiint_{C.V.} \nabla \cdot \vec{E} dV - \frac{\Delta t}{2\Delta V} \iiint_{C.V.} \nabla \cdot \Delta \vec{E} dV \quad (5)$$

where ΔV is the volume of the finite volume cell

The first term can be split into eight separate volume integrals around (1-a-b-c-d-e-f-g) etc. , and each of these can be approximated as a 1/8 of volume integral around the larger cell (1-2-3-4-5-6-7-8), which are labeled I, II, III, IV, V, VI, VII, VIII. In this manner δQ_1 is split into eight parts:

$$\delta Q_1 = \delta Q_{1I} + \delta Q_{1II} + \delta Q_{1III} + \delta Q_{1IV} + \delta Q_{1V} + \delta Q_{1VI} + \delta Q_{1VII} + \delta Q_{1VIII} \quad (6)$$

where

$$\delta Q_{1I} = - \frac{\Delta t}{8\Delta V} \iiint_{I} \nabla \cdot \vec{E} dV - \frac{\Delta t}{2\Delta V} \iiint_{I} \nabla \cdot \Delta \vec{E} dV \quad (7)$$

Using Gauss' divergence theorem

$$\delta Q_{1I} = - \frac{\Delta t}{8\Delta V} \iint_{I} \vec{E} \cdot d\vec{s} - \frac{\Delta t}{2\Delta V} \iint_{I} \Delta \vec{E} \cdot d\vec{s} \quad (8)$$

If the first order change is denoted in Q

$$\Delta Q = - \Delta t \nabla \cdot \vec{E} \quad (9)$$

Eq. (8) takes following form

$$\delta Q_{1I} = \frac{\Delta Q}{8} - \frac{\Delta t}{2\Delta V} \iint_{I} \Delta \vec{E} \cdot d\vec{s} \quad (10)$$

where

$$\Delta Q_1 = - \frac{\Delta t}{\Delta V_1} \iint_{\text{CELL } 1} \vec{E} \cdot d\vec{S} \quad (11)$$

Eq. (11) is evaluated using surface area vectors (Fig 2b). This vectors are calculated as [1] , [2]

$$\begin{aligned} d\vec{S}_1 &= \left\{ \left(\frac{\xi_z}{J} \right)_1 \vec{i} + \left(\frac{\xi_y}{J} \right)_1 \vec{j} + \left(\frac{\xi_x}{J} \right)_1 \vec{k} \right\} = \frac{1}{2} (\vec{r}_2 - \vec{r}_1) \times (\vec{r}_3 - \vec{r}_1) \\ d\vec{S}_2 &= \left\{ \left(\frac{\xi_z}{J} \right)_2 \vec{i} + \left(\frac{\xi_y}{J} \right)_2 \vec{j} + \left(\frac{\xi_x}{J} \right)_2 \vec{k} \right\} = \frac{1}{2} (\vec{r}_3 - \vec{r}_2) \times (\vec{r}_6 - \vec{r}_2) \\ d\vec{S}_3 &= \left\{ \left(\frac{\eta_z}{J} \right)_3 \vec{i} + \left(\frac{\eta_y}{J} \right)_3 \vec{j} + \left(\frac{\eta_x}{J} \right)_3 \vec{k} \right\} = \frac{1}{2} (\vec{r}_6 - \vec{r}_3) \times (\vec{r}_8 - \vec{r}_3) \\ d\vec{S}_4 &= \left\{ \left(\frac{\eta_z}{J} \right)_4 \vec{i} + \left(\frac{\eta_y}{J} \right)_4 \vec{j} + \left(\frac{\eta_x}{J} \right)_4 \vec{k} \right\} = \frac{1}{2} (\vec{r}_6 - \vec{r}_4) \times (\vec{r}_7 - \vec{r}_4) \\ d\vec{S}_5 &= \left\{ \left(\frac{\xi_z}{J} \right)_5 \vec{i} + \left(\frac{\xi_y}{J} \right)_5 \vec{j} + \left(\frac{\xi_x}{J} \right)_5 \vec{k} \right\} = \frac{1}{2} (\vec{r}_2 - \vec{r}_5) \times (\vec{r}_6 - \vec{r}_5) \\ d\vec{S}_6 &= \left\{ \left(\frac{\xi_z}{J} \right)_6 \vec{i} + \left(\frac{\xi_y}{J} \right)_6 \vec{j} + \left(\frac{\xi_x}{J} \right)_6 \vec{k} \right\} = \frac{1}{2} (\vec{r}_3 - \vec{r}_6) \times (\vec{r}_7 - \vec{r}_6) \end{aligned} \quad (12)$$

where ξ , η , ζ are cell based coordinate axes shown in Fig.1 and J is the Jacobian. The vector \vec{r} represents the position vector of the cell vertices.

$$\Delta Q_1 = - \frac{\Delta t}{\Delta V_1} \iint_{\text{CELL } 1} \vec{E} \cdot d\vec{S} \quad (13)$$

$$= - \frac{\Delta t}{\Delta V} \left\{ -\vec{E}_{1265} d\vec{S}_5 + \vec{E}_{3467} d\vec{S}_6 - \vec{E}_{1564} d\vec{S}_4 + \vec{E}_{2673} d\vec{S}_3 - \vec{E}_{1234} d\vec{S}_1 + \vec{E}_{5678} d\vec{S}_2 \right\}$$

$$\begin{aligned} \Delta Q_1 &= \frac{\Delta t}{\Delta V_1} \left\{ \frac{F_1 + F_2 + F_6 + F_9}{4} \left(\frac{\xi_z}{J} \right)_{s_5} + \frac{G_1 + G_2 + G_6 + G_9}{4} \left(\frac{\xi_y}{J} \right)_{s_5} + \frac{H_1 + H_2 + H_6 + H_9}{4} \left(\frac{\xi_x}{J} \right)_{s_5} \right. \\ &\quad - \frac{F_3 + F_4 + F_8 + F_7}{4} \left(\frac{\xi_z}{J} \right)_{s_6} - \frac{G_3 + G_4 + G_8 + G_7}{4} \left(\frac{\xi_y}{J} \right)_{s_6} - \frac{H_3 + H_4 + H_8 + H_7}{4} \left(\frac{\xi_x}{J} \right)_{s_6} \\ &\quad + \frac{F_1 + F_5 + F_9 + F_4}{4} \left(\frac{\eta_z}{J} \right)_{s_3} + \frac{G_1 + G_5 + G_9 + G_4}{4} \left(\frac{\eta_y}{J} \right)_{s_3} + \frac{H_1 + H_5 + H_9 + H_4}{4} \left(\frac{\eta_x}{J} \right)_{s_3} \\ &\quad - \frac{F_2 + F_6 + F_7 + F_3}{4} \left(\frac{\eta_z}{J} \right)_{s_4} - \frac{G_2 + G_6 + G_7 + G_3}{4} \left(\frac{\eta_y}{J} \right)_{s_4} - \frac{H_2 + H_6 + H_7 + H_3}{4} \left(\frac{\eta_x}{J} \right)_{s_4} \\ &\quad + \frac{F_1 + F_2 + F_3 + F_4}{4} \left(\frac{\zeta_z}{J} \right)_{s_1} + \frac{G_1 + G_2 + G_3 + G_4}{4} \left(\frac{\zeta_y}{J} \right)_{s_1} + \frac{H_1 + H_2 + H_3 + H_4}{4} \left(\frac{\zeta_x}{J} \right)_{s_1} \\ &\quad \left. - \frac{F_5 + F_6 + F_7 + F_9}{4} \left(\frac{\zeta_z}{J} \right)_{s_2} - \frac{G_5 + G_6 + G_7 + G_9}{4} \left(\frac{\zeta_y}{J} \right)_{s_2} - \frac{H_5 + H_6 + H_7 + H_9}{4} \left(\frac{\zeta_x}{J} \right)_{s_2} \right\} \end{aligned} \quad (14)$$

where ΔQ_1 is first - order change in Q for the cell 1 in time - step Δt ; ΔV_1 is the volume of cell 1. F, G, H are specified at time-level n. In Ref.2 Kordulla gives an efficient formula for calculating cell volume as

$$\begin{aligned} \Delta V_1 &= \frac{1}{3} \vec{r}_1 \cdot \{ d\vec{S}_1 + d\vec{S}_3 + d\vec{S}_5 \} \\ &= \frac{1}{3} \left\{ \left(\left(\frac{\xi_z}{J} \right)_1 + \left(\frac{\eta_z}{J} \right)_3 + \left(\frac{\xi_z}{J} \right)_5 \right) (x_7 - x_1) \right. \\ &\quad + \left(\left(\frac{\xi_y}{J} \right)_1 + \left(\frac{\eta_y}{J} \right)_3 + \left(\frac{\xi_y}{J} \right)_5 \right) (y_7 - y_1) \\ &\quad \left. + \left(\left(\frac{\xi_x}{J} \right)_1 + \left(\frac{\eta_x}{J} \right)_3 + \left(\frac{\xi_x}{J} \right)_5 \right) (z_7 - z_1) \right\} \end{aligned} \quad (15)$$

The part (1-a-b-c-d-e-f-g) of the control volume in cell-1 has three outer face. The surface area vectors of this inner small cell is approximated as a quarter of the surface area vector taken in the center of cell-1 (Fig 2). Thus Eq.(10) is evaluated as

$$\delta Q_{11} = \frac{1}{8} \left\{ \Delta Q + \frac{\Delta t}{\Delta V} \left(\Delta \vec{E} \cdot d\vec{S}_{e1} + \Delta \vec{E} \cdot d\vec{S}_{e1} + \Delta \vec{E} \cdot d\vec{S}_{e1} \right) \right\} \quad (16)$$

where $d\vec{S}_6$, $d\vec{S}_4$, and $d\vec{S}_2$ are always facing outwards.

$$\begin{aligned} d\vec{S}_{e1} &= \left\{ \left(\frac{\xi_z}{J} \right)_1 \vec{i} + \left(\frac{\xi_y}{J} \right)_1 \vec{j} + \left(\frac{\xi_x}{J} \right)_1 \vec{k} \right\} \\ d\vec{S}_{e1} &= \left\{ \left(\frac{\eta_z}{J} \right)_1 \vec{i} + \left(\frac{\eta_y}{J} \right)_1 \vec{j} + \left(\frac{\eta_x}{J} \right)_1 \vec{k} \right\} \end{aligned} \quad (17)$$

$$d\vec{S}_i = \left\{ \frac{\xi_z}{J} \right\}_i \vec{i} + \left\{ \frac{\xi_z}{J} \right\}_i \vec{j} + \left\{ \frac{\xi_z}{J} \right\}_i \vec{k}$$

Substitution Eq. (17) into the Eq. (16) yields

$$\delta Q_{1i} = -\frac{1}{8} \left\{ \Delta Q + \frac{\Delta t}{\Delta V} (-\Delta f - \Delta g - \Delta h) \right\} \quad (18)$$

where

$$\begin{aligned} \Delta f_i &= \left\{ \frac{\xi_z}{J} \right\}_i \Delta F_i + \left\{ \frac{\xi_z}{J} \right\}_i \Delta G_i + \left\{ \frac{\xi_z}{J} \right\}_i \Delta H_i \\ \Delta g_i &= \left\{ \frac{\eta_z}{J} \right\}_i \Delta F_i + \left\{ \frac{\eta_z}{J} \right\}_i \Delta G_i + \left\{ \frac{\eta_z}{J} \right\}_i \Delta H_i \\ \Delta h_i &= \left\{ \frac{\zeta_z}{J} \right\}_i \Delta F_i + \left\{ \frac{\zeta_z}{J} \right\}_i \Delta G_i + \left\{ \frac{\zeta_z}{J} \right\}_i \Delta H_i \end{aligned} \quad (19)$$

here, $\Delta F_i \equiv (\partial F / \partial Q)_i \Delta U_i$, $\Delta G_i \equiv (\partial G / \partial Q)_i \Delta U_i$, and $\Delta H_i \equiv (\partial H / \partial Q)_i \Delta U_i$ being the Jacobians of F, G , and H are given in Appendix; and components of surface area vectors (metrics) are found in a similar way as in Eq. 12.

Eq. (18) gives the contribution to node member 1, coming from the cell 1. The contribution to the other nodes of this cell can be found similarly

$$\begin{aligned} \delta Q_{1i} &= -\frac{1}{8} \left\{ \Delta Q + \frac{\Delta t}{\Delta V} (-\Delta f - \Delta g - \Delta h) \right\}_i \\ \delta Q_{2i} &= -\frac{1}{8} \left\{ \Delta Q + \frac{\Delta t}{\Delta V} (-\Delta f + \Delta g - \Delta h) \right\}_i \\ \delta Q_{3i} &= -\frac{1}{8} \left\{ \Delta Q + \frac{\Delta t}{\Delta V} (\Delta f + \Delta g - \Delta h) \right\}_i \\ \delta Q_{4i} &= -\frac{1}{8} \left\{ \Delta Q + \frac{\Delta t}{\Delta V} (\Delta f - \Delta g - \Delta h) \right\}_i \\ \delta Q_{5i} &= -\frac{1}{8} \left\{ \Delta Q + \frac{\Delta t}{\Delta V} (-\Delta f - \Delta g + \Delta h) \right\}_i \\ \delta Q_{6i} &= -\frac{1}{8} \left\{ \Delta Q + \frac{\Delta t}{\Delta V} (-\Delta f + \Delta g + \Delta h) \right\}_i \\ \delta Q_{7i} &= -\frac{1}{8} \left\{ \Delta Q + \frac{\Delta t}{\Delta V} (\Delta f + \Delta g + \Delta h) \right\}_i \\ \delta Q_{8i} &= -\frac{1}{8} \left\{ \Delta Q + \frac{\Delta t}{\Delta V} (\Delta f - \Delta g + \Delta h) \right\}_i \end{aligned} \quad (20)$$

By means of above Eq. (20), first order changes in a cell are distributed to its vertices.

The time increment Δt is limited by the CFL numerical stability criterion as

$$\Delta t = CFL * \min \left\{ \frac{\Delta V}{\left| \left\{ \frac{\xi_z}{J} \right\}_i u + \left\{ \frac{\xi_z}{J} \right\}_i v + \left\{ \frac{\xi_z}{J} \right\}_i w + a \sqrt{\left\{ \frac{\xi_z}{J} \right\}_i^2 + \left\{ \frac{\xi_z}{J} \right\}_i^2 + \left\{ \frac{\xi_z}{J} \right\}_i^2} \right|}, \frac{\Delta V}{\left| \left\{ \frac{\eta_z}{J} \right\}_i u + \left\{ \frac{\eta_z}{J} \right\}_i v + \left\{ \frac{\eta_z}{J} \right\}_i w + a \sqrt{\left\{ \frac{\eta_z}{J} \right\}_i^2 + \left\{ \frac{\eta_z}{J} \right\}_i^2 + \left\{ \frac{\eta_z}{J} \right\}_i^2} \right|}, \frac{\Delta V}{\left| \left\{ \frac{\zeta_z}{J} \right\}_i u + \left\{ \frac{\zeta_z}{J} \right\}_i v + \left\{ \frac{\zeta_z}{J} \right\}_i w + a \sqrt{\left\{ \frac{\zeta_z}{J} \right\}_i^2 + \left\{ \frac{\zeta_z}{J} \right\}_i^2 + \left\{ \frac{\zeta_z}{J} \right\}_i^2} \right|} \right\} \quad (21)$$

where a is the speed of sound. $0 < CFL < 1$.

NUMERICAL SMOOTHING :

For transonic and supersonic flows artificial viscous damping is added to the algorithm to stabilize captured shocks. Thus certain highly oscillatory steady-state modes which are allowed by the basic Lax-Wendroff scheme may be suppressed.

In this algorithm, an artificial smoothing model similar to Ni's [5] original formulation is used by adding smoothing terms in the distribution formulas (20). Hence, after adding the numerical smoothing term, the new distribution formula for δQ_{1i} takes following form

$$\delta Q_{1i} = -\frac{1}{8} \left\{ \Delta Q + \frac{\Delta t}{\Delta V} (-\Delta f - \Delta g - \Delta h) + \alpha (Q_i - Q_{1i}) \right\}_i \quad (22)$$

where

$$Q_i = \frac{1}{8} [Q_1 + Q_2 + Q_3 + Q_4 + Q_5 + Q_6 + Q_7 + Q_8]$$

$$\mu = \sigma \frac{\Delta t}{\Delta V} [DL + DM + DN]$$

$$0 < \sigma < 0.1$$

$$DL = \sqrt{\left(\frac{\xi_1}{j}\right)_h^2 + \left(\frac{\xi_2}{j}\right)_h^2 + \left(\frac{\xi_3}{j}\right)_h^2}$$

$$DM = \sqrt{\left(\frac{\eta_1}{j}\right)_h^2 + \left(\frac{\eta_2}{j}\right)_h^2 + \left(\frac{\eta_3}{j}\right)_h^2}$$

$$DN = \sqrt{\left(\frac{\zeta_1}{j}\right)_h^2 + \left(\frac{\zeta_2}{j}\right)_h^2 + \left(\frac{\zeta_3}{j}\right)_h^2}$$

This formula must be modified at the boundaries because of the control volume disparities.

BOUNDARY CONDITIONS :

Each of the boundary conditions used has been implemented in a predictor/corrector form as in Ref.[15]. The predictor/corrector form is based on a second order numerical integration scheme for internal points incorporates a mathematical signal propagation phenomena analogous to the theory of characteristics. In the same sense Ni [5] suggests that the "distribution" formula represent similar wave solutions.

On boundaries the predictor step consists of summing contributions from cells interior to the boundary. The corrector step consists of enforcement of the appropriate boundary conditions.

To make a characteristic analysis, linearized nonconservative form of Euler equations are written in a coordinate system tangential and normal to the boundary as presented by Coakley [6].

$$Q_t + AQ_n = 0 \quad (23)$$

where A is the Jacobian matrix. The above equation is transformed to characteristic form by the similarity matrix as in Ref. [16] and Ref.[17]

$$W_t + \Lambda W_n = 0 \quad (24)$$

where $\Lambda = \text{diag} \{\lambda_1, \lambda_2, \lambda_3, \lambda_4, \lambda_5\}$ and $\lambda_1 = \lambda_2 = \lambda_3 = u_n$, $\lambda_4 = u_n + a$, $\lambda_5 = u_n - a$

$$W = \begin{bmatrix} \rho - \frac{p}{a} \\ u_s \\ u_b \\ u_n + \frac{p}{\rho a} \\ -u_n + \frac{p}{\rho a} \end{bmatrix} \quad (25)$$

where n,s, and b represent normal,tangential, and binormal directions respectively. Barred quantities are calculated from interior.

The number of boundary conditions which are specified at the boundary is equal to the number of positive eigenvalues.

For subsonic inflow ($0 < u_n < a$) the four positive eigenvalues require four boundary conditions to be specified while W_5 must come from the flow interior to the boundary. The boundary conditions are set by defining W_1 , W_2 , W_3 , and W_4 in terms of known flow parameters. Thus it is constructed a system of equation and solving this system simultaneously corrected values are obtained.

For supersonic inflow ($u_n > 0$) all eigenvalues are positive and five boundary conditions are specified. For subsonic outflow ($-a < u_n < 0$) there is only one positive eigenvalue ($\lambda_4 > 0$) and therefore one boundary condition is set and W_1 , W_2 , W_3 , and W_5 are taken from flow interior. In the case of supersonic outflow, since all eigenvalues become negative, all characteristic values are taken from predicted values ($W_{corrected} = W_{predicted}$). Characteristic analysis is also used for solid wall. In that case there is only one positive eigenvalue and require one boundary condition. This condition is $u_n = 0$. W_5 is determined from predictor state.

RESULTS AND DISCUSSION OF THE TEST CASES :

The cell vertex scheme which has been presented above has been used to compute results applied to a wide range of test cases. All 2-D and 3-D results were obtained with the same three dimensional Euler code. For the two dimensional test cases, the geometrical cross section along the x-axis was assumed to be constant at all spanwise y-locations. First channel flow cases will be presented for subsonic ($M_{inlet} = 0.5$), transonic ($M_{inlet} = 0.675$) and supersonic ($M_{inlet} = 1.6$) flows over a 20% thick bi-circular arc cascade at zero incidence. For these test cases, the grid was algebraically generated with constant x along the bump and an algebraic stretching away from the bump. In Fig.3, this $65 \times 9 \times 17$ grid is shown. Secondly, the algorithm will be adapted to a supersonic wedge cascade sensitive to

shock reflection and correct shock strength calculations. For this test case, an algebraic $110 \times 5 \times 33$ grid was used and is shown in Fig.11. Finally, the capability of the algorithm will be illustrated by calculating the flow through a 90° bend channel (Fig.14) where secondary flow development is of prime importance. The $(33 \times 33 \times 17)$ algebraic grid shown in Fig.15 has been used for this test case. All test cases were run on IBM 3090-180S.

A - Subsonic Ni bump :

The test case from the subsonic bi-circular arc cascade, which is also described as the 10% thick circular arc bump in a channel, is widely known in the literature as the Ni's bump. The corresponding results are shown from Fig.4 to Fig.6. The initial flow conditions are taken to be uniform. The variables are calculated from the isentropic Mach number obtained from the ratio of exit static pressure to inlet total pressure. The boundary conditions are specified as follows:

- At the inlet: Total temperature, total pressure and flow angles are specified.
- At the exit: The static pressure is imposed.

As it can be seen from these figures, the stagnation points at the leading and trailing edges of the bump and the maximum Mach number occurs -as expected- at the maximum thickness location of the bump. The figures illustrate the symmetry of the flow with respect to the bump center. The smoothness of the flow demonstrate the adequate amount of artificial dissipation used in the flow, in order to prevent any oscillations near high gradient regions (leading and trailing edges). The total pressure loss which indicate the degree of accuracy of the Euler solver is given in Fig.5. Since the flow is subsonic, no shock induced total pressure loss exists. However, the numerical smoothing and the truncation errors produce total pressure variations. This figures shows clearly that the total pressure errors are small and does not cause any asymmetries in the flows.

B - Transonic Ni bump:

The corresponding runs for the transonic Ni's bump are presented for Mach number $M_{inlet} = 0.675$. In this test case, the same initial and boundary conditions were used as in the subsonic case described earlier. Fig.7 and Fig.8 show the strength and the location of the shock. The isomach contours show no significant oscillations at upstream and downstream of the shock, probably because of increased effect of the artificial viscosity. The shock is at the 72% of the chord, on the bump. The shock is smeared over two finite volume cells. The convergence rate for this transonic flow decreases due to the presence of high frequency errors in the vicinity of the shock.

C - Supersonic Ni bump :

For this test case, the inlet Mach number is taken as 1.6. This flow field is dominated by oblique shock generation, reflection and (shock-shock, shock-boundary, shock-expansion wave) interactions. All inlet conditions are specified for $M_{inlet} = 1.6$. At the exit plane, all the flow variables are taken from the interior. These results are shown from Fig.9 to Fig.10. Isomach lines show that an oblique shock is formed at the leading edge. This shock is weakened and curved by the expansion waves emanating from the surface of the bump; and intersects the upper symmetry line as a normal shock. Further downstream, it reflects downward to intersect another oblique shock leaving the trailing edge. The same flow configuration was also tested by Chima [18]. Close agreement is observed between the two calculations are good.

D - Supersonic staggered wedge cascade :

Test case A/CAC-2 from AGARD EP WG-18 [Ref.11] has been chosen. This is a fully supersonic flow in a compressor cascade. The analytical solution given in [11] is derived from characteristic theory and oblique shock relations. This test case is different from previous test cases because the present flow structure with an inlet Mach number of 1.6 involves shock reflection and shock suppression through the upper and lower sides of the cascade blades. Furthermore, the flow direction and the magnitude of the Mach number are very sensitive to the location of these shocks and also to the exit pressure. The leading edge wedge leads to the oblique shock wave attached to the nose of the upper blade with a 45° inclination to the incoming flow. The shock reflects from the lower blade with 48.2° reflection angle; and -most important of all- the second reflection from the upper blade is suppressed with proper wall inclination. The numerical result is plotted in Fig.12 and Fig.13 along with the corresponding analytical results. As it can be seen from the comparison of these figures, there are disagreements between the observed numerical and analytical results at the downstream portion of this cascade. This region extends from the trailing edge of the lower blade to the exit boundary of the cascade. This highly nonuniform region calculated by the present algorithm is thought to be caused by constant pressure condition imposed at the exit boundary. Here, in this region, the shock emanating from the trailing edge of the upper blade is affected by the expansion waves originating from the trailing edge of the lower blade; and then, this shock impinges on the exit boundary. This causes non-uniform pressure at the downstream boundary. Therefore, it is incorrect to force a uniform pressure at this boundary. It is thought that the uniformity of the flow structure at the downstream portion of the cascade is related to how well the exit static pressure can be relaxed.

E - Squire and Winter 90° bend channel flow:

Description of the problem : The developed code was also used in calculating the subsonic incompressible flow field within a severley bend (90° turning) duct. The geometry of this duct has been designed by Squire and Winter and is given in Fig.14. It consists of a quarter of quasi-circular portion flanked at both ends by straight channel sections. The rectangular cross-section is constant throughout the channel axial length and has an aspect ratio of $b/c = 2/15$. The geometry is taken from Ref.[19]. The incoming stream is taken to be non-uniform over a large part of the span of the channel vanes. The boundary layer like velocity profile imposed at the inlet boundary may have been created by frictional effects. As a result, a large rotating vortex is formed on the downstream portion of the channel near the exit plane. The development of this secondary flow is mainly due to the acceleration of the axially non-uniform velocity profile through the curved duct. Therefore, in this case, the secondary flow mechanism is considered to be mainly an inviscid, rotational phenomena which can be accurately simulated using Euler solver.

Initial and boundary conditions : The initial condition imposed is such that the unsteady solver will mimic the discharge of the flow through this curved duct. No flow is specified within the channel and the solution is driven by the pressure boundary condition imposed at both ends. The upstream boundary condition consists of specifying the total temperature and imposing the inlet velocity profile as given in Ref.[20]

The downstream boundary conditions are also of characteristic type. Static exit pressure is prescribed.

Results: The calculated secondary flow velocity component in spanwise and radial directions are shown in Fig.16 to Fig.19. The corresponding analytical results obtained from Squire and Winter [12] is also given. It can be seen that the agreement is good. The vortex at the cross location at $\theta = 45^\circ$ is plotted in Fig.20. This agrees well with the plot

given in Ref.[20]. Especially, the location of the core of the vortex is predicted numerically very well. It can be seen that the vortex pair is located symmetrically with respect to the top and bottom walls at a distance of 13% of the span above the side wall. The strength of the secondary flow illustrated by the flow velocity components mentioned above and the location of the vortex core agrees with available data in the literature.

CONCLUSION :

An efficient Euler solver for three dimensional transonic internal flow has been presented. A cell vertex finite volume method have been applied to a wide variety of subsonic,transonic and supersonic channel, curved duct and cascade flows. With such algorithm, it has been possible to capture the symmetry over a bump channel and the shock strength and location of a transonic and supersonic flows. The algorithm has also been tested against a fully supersonic wedge cascade where oblique shock strength and location have been successfully calculated. Furthermore, for an incompressible subsonic flow, it has been possible to capture the development of a secondary flow generated by the presence of a boundary-like streamwise velocity profile.

REFERENCES :

- [1] Jameson, A , Schmidt, W , Turkel, E. "Numerical solution of the Euler Equations by finite Volume Method using Runge - Kutta Time Stepping Schemes" AIAA Paper 81-1259 , 1981.
- [2] Allmaras, S.R. , Gles, M.B. "A Second Order Flux Split Scheme for the Unsteady 2-D Euler Equations on Arbitrary Meshes" AIAA Paper 87-11, 19 , 1987.
- [3] Jameson, A. , Baker, T. "Solution of the Euler Equations for Complex Configurations" AIAA Paper 83-1929 , 1983.
- [4] Rizzi, A. , "Damped Euler Equation Method to Compute Transonic Flow Around Wing-Body Combinations" AIAA Journal, Vol. 20 pp.1321-1328 , 1982.
- [5] Ni, R.H. "Multiple Grid Scheme for Solving the Euler Equations" AIAA Paper 81-1025 , 1981.
- [6] Hall, M.G. "Cell-Vertex Multiple Grid Scheme for the Solution of the Euler Equations" Proceedings of the Conference on Numerical Methods for Fluid Dynamics, Reading U.K. , 1985.
- [7] Koeck, C. "Computation of Three Dimensional Flow Using the Euler Equations and Multiple Grid Scheme." Int.Journal for Numerical Methods in Fluids, Vol.5 ,pp.483-500 , 1985.
- [8] Denton, J.D. "The Computation of Fully Three Dimensional Flow Through Any Type of Turbomachinery Blade Row" AGARD-LS-140 , 1985.
- [9] Rossow, C. , Kroll, N. , Radespiel, R. , Scherr, S. "Investigation of the Accuracy of Finite Volume Methods For 2- and 3-Dimensional Flows" AGARD-CP-437 p14.1-14.11 , 1988.
- [10] Powell, K.G. , Van Leer, B. "A Genuinely Multi-Dimensional Upwind Cell-Vertex Scheme for the Euler Equations" Paper AIAA 89-0095 , 1989.
- [11] Denton, J.D. , Hirsch, Ch. , Meauze, G. "Test Case A/CA-2: Supersonic Staggered Wedge Cascade" AGARD-AR-275, Propulsion and Energetics Panel Working Group 18 on Test Cases for Computation of Internal Flows in Aero-Engine Components. pp. 22-23 , 1990.
- [12] Squire, H.B. , Winter, K.B. "The Secondary Flow in a Cascade of Airfoils in a Non-uniform Stream" Journal of the Aeronautical Sciences pp.271-277 , 1951.
- [13] Lawrence, S.L. , Chaussee, D.S. , Tannehill, J.C. "Application of An Upwind Algorithm to the Three-Dimensional Parabolized Navier-Stokes Equations" Paper AIAA 87-1112 , 1987.
- [14] Hung, C.M. , Kordulla, W. "A Time-Split Finite Volume Algorithm for the Three Dimensional Flow Field Simulation" Paper AIAA 83-1957 , 1983.
- [15] Usab, W.J. "Embedded Mesh Solutions of the Euler Equation Using a Multiple Grid Method" Ph.D. Thesis MIT , 1983.
- [16] Coakley, T.J. "Numerical Method for Gas Dynamics Combining Characteristic and Conservation Concepts" AIAA 81-1257 , 1981.
- [17] Rizzi, A. , Eriksson, L.E. "Computation of Flow Around Wings Based on the Euler Equations" J.Fluid Mech. Vol.148 pp.45-71 , 1984.
- [18] Chima, R.A. , Johnson, G.M. "Efficient Solution of the Euler and Navier-Stokes Equation With a Vectorized Multiple Grid Algorithm" AIAA Journal, Vol.23, No.1 , 1985.
- [19] Ecer, A. , Akay, H.U. "Finite Element Solution of Steady Inviscid Flows in Turbomachinery". In Thermodynamics and Fluid Mechanics of Turbomachinery, Vol.II NATO ASI Series, Series E: Applied Sciences, No. 97 A. , edited by A.S. Leer, P. Stow, Ch. Hirsch , 1985.
- [20] Pandolfi, M. , Colasurdo, G. "Three Dimensional Inviscid, Compressible, Rotational Flows". In Flow in Primary, Non-rotating Passages in Turbo-machines, edited by H.J. Herrings et al. The Winter Annual Meeting of the ASME, December 2-7, 1979, New York, New York-USA.

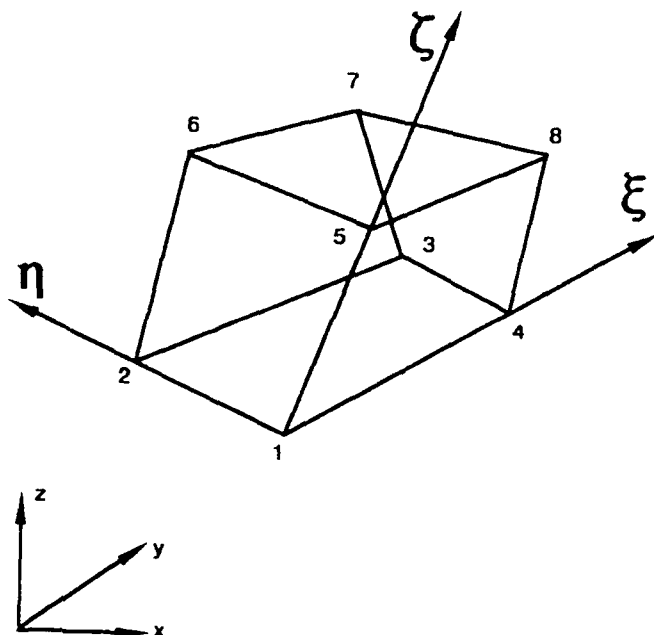
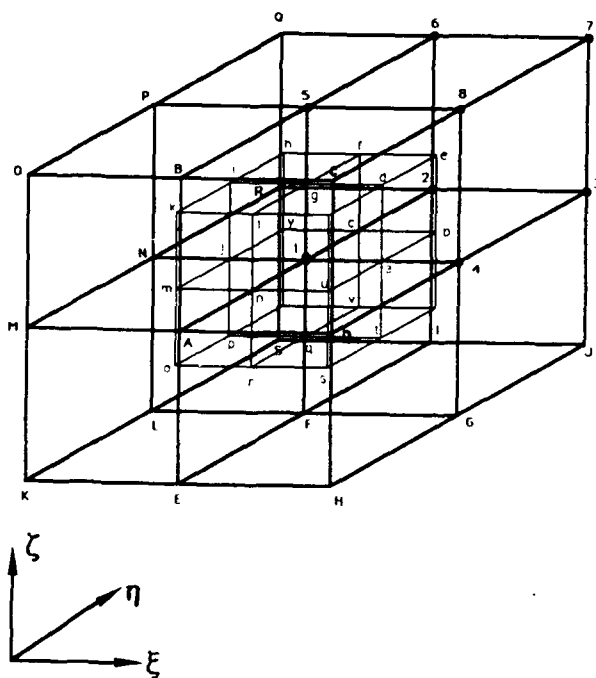
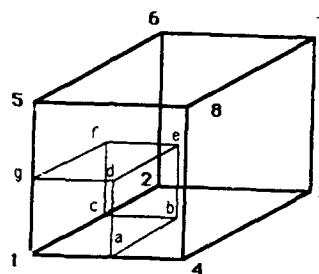


Fig. 1 A hexahedron finite volume cell in the physical domain

Fig. 2.a A sample control volume for the nodal point 1
(in the computational domain)Fig. 2.b Portion of the control volume for
node 1 within the finite volume cell
(in the computational domain)
 $S_1: 1\ 2\ 3\ 4$
 $S_2: 5\ 6\ 7\ 8$
 $S_3: 1\ 5\ 8\ 4$
 $S_4: 2\ 3\ 7\ 6$
 $S_5: 1\ 2\ 6\ 5$
 $S_6: 3\ 4\ 8\ 7$

CELL I	12345678
CELL II	1234I J6H
CELL III	14DAF6HE
CELL IV	1485ADCB
CELL V	1265NRQP
CELL VI	12I FNLSR
CELL VII	1FLNAEKM
CELL VIII	15PNABOM

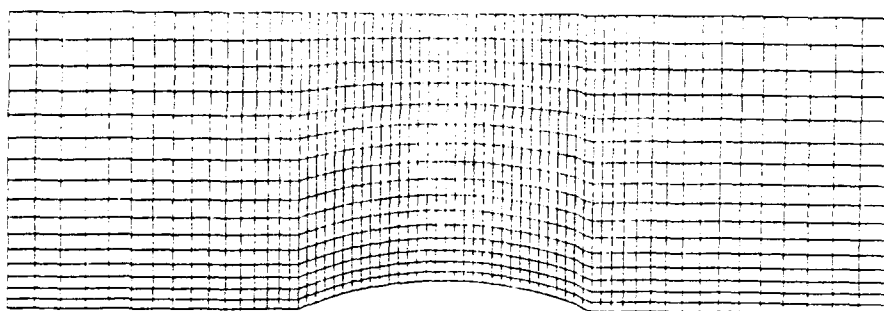


Fig.3 Computational grid for test case 1 (Ni bump)

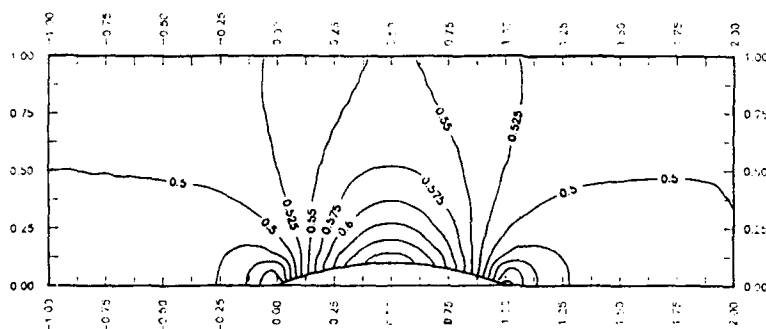


Fig.4 Isomach lines for the subsonic Ni bump flow ($M_{\infty}=0.5$)

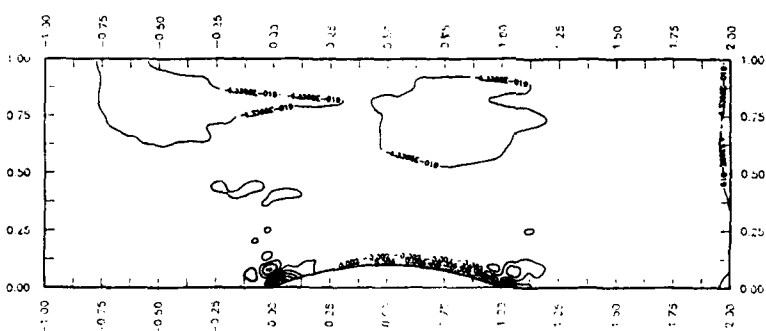


Fig.5 Total pressure loss contours for the subsonic Ni bump flow ($M_{\infty}=0.5$)

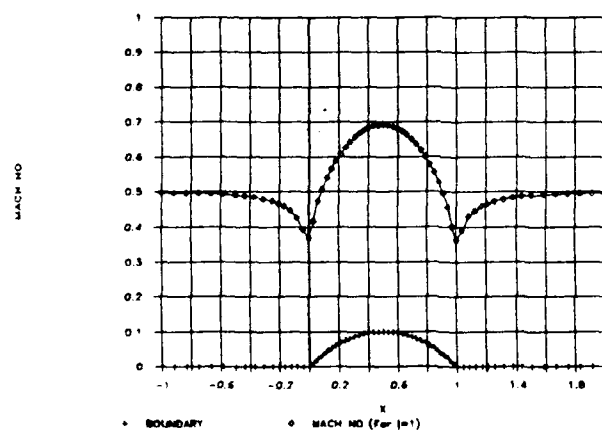


Fig.6 Surface Mach number distribution of the subsonic Ni bump flow ($M_{\infty}=0.5$)

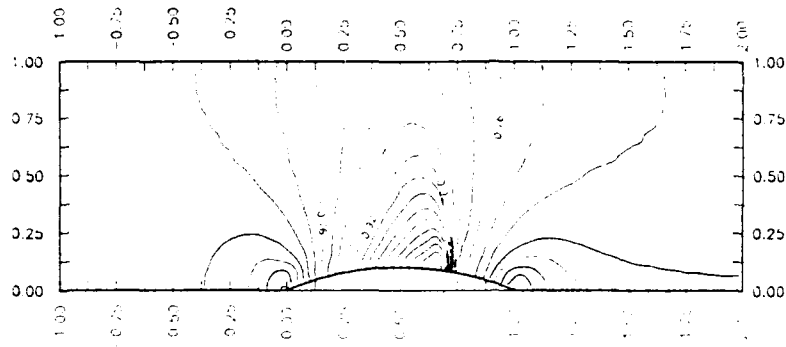


Fig.7 Isomach lines for the transonic Ni bump flow ($M_{\infty}=0.675$)

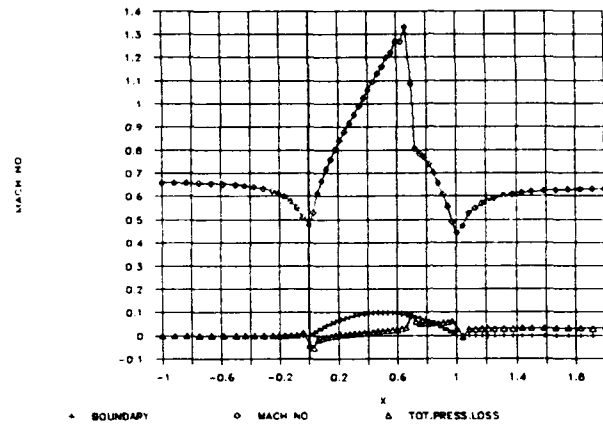


Fig.8 Surface Mach number distribution for the transonic Ni bump flow ($M_{\infty}=0.675$)



Fig.9 Isomach lines for the supersonic Ni bump flow ($M_{\infty}=1.6$)

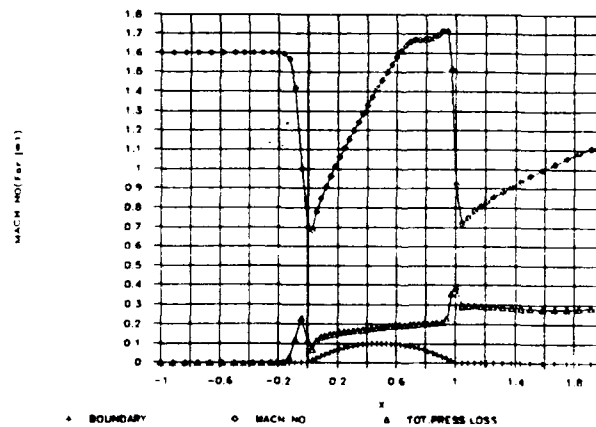


Fig.10 Surface Mach number and total pressure loss distributions for the supersonic Ni bump flow ($M_{\infty}=1.6$)

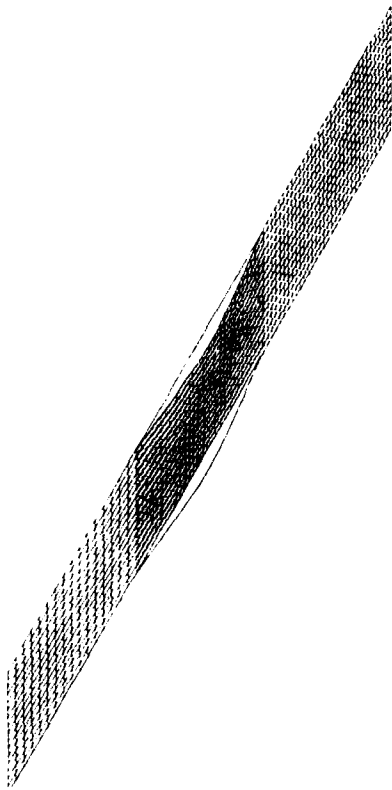


Fig.11 Computational grid for test case 2
(Supersonic staggered wedge cascade)

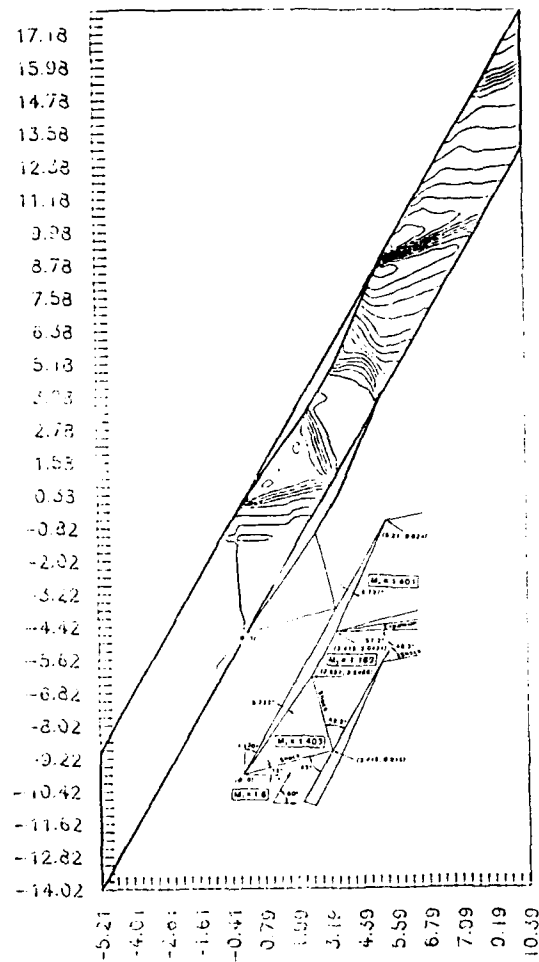


Fig.12 Isomach lines for the supersonic
wedge cascade, as compared to
the analytical results.

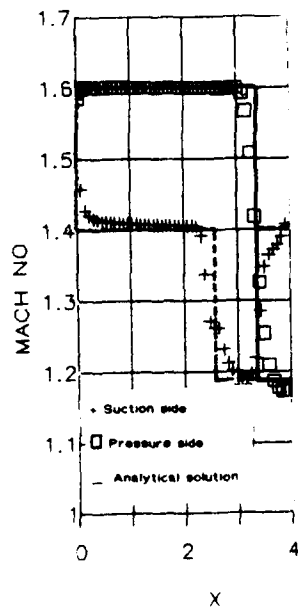


Fig.13 Analytical vs calculated pressure
distribution over the cascade walls

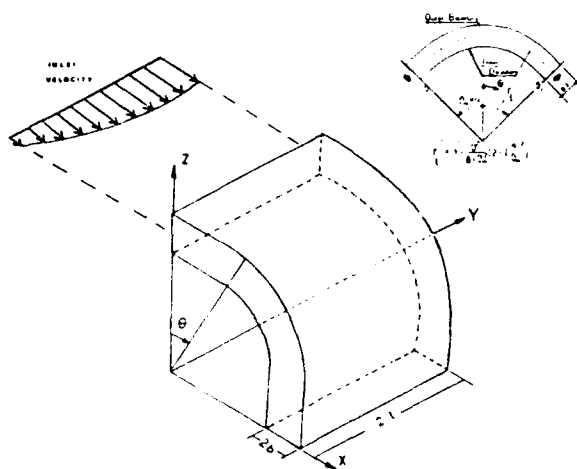
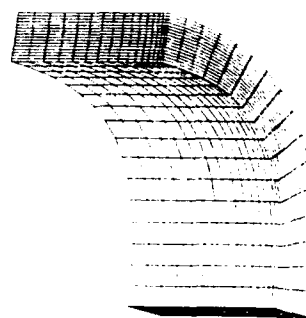
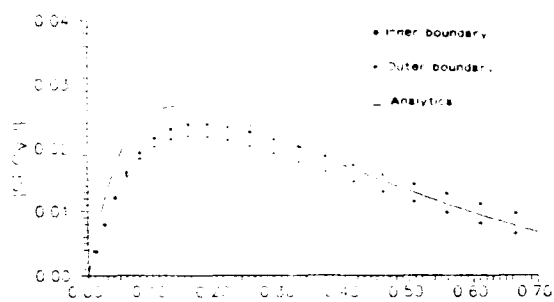
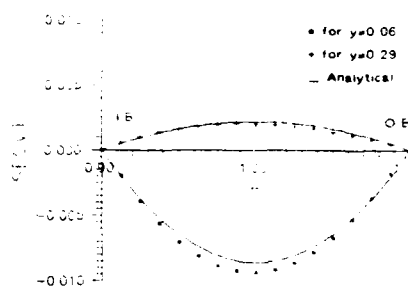
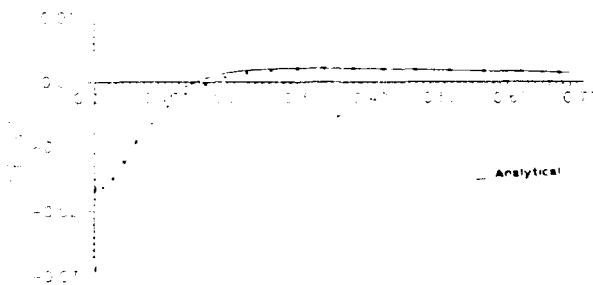
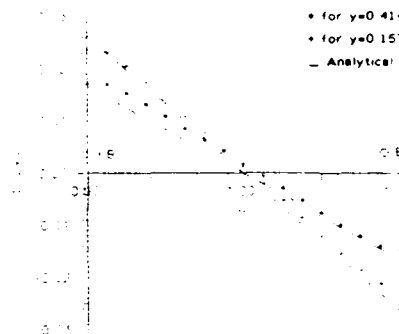
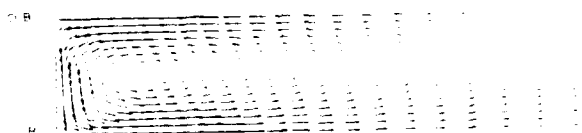


Fig.14 Duct geometry and coordinate system

Fig.15 Computational grid for test case 3
(Squire and Winter 90° bend)Fig.16 Radial component of the secondary flow velocity at $\theta=\pi/4$ Fig.17 Spanwise component of the secondary flow velocity at $\theta=\pi/4$ Fig.18 Spanwise component of the secondary flow velocity on the channel centerline at $\theta=\pi/4$ Fig.19 Radial component of the secondary flow velocity at $\theta=\pi/4$ Fig.20 Secondary flow velocity vectors at $\theta=\pi/4$

APPENDIX

Expression for ΔF , ΔG and ΔH

$$\Delta Q = \begin{bmatrix} \Delta \rho \\ \Delta \rho u \\ \Delta \rho v \\ \Delta \rho w \\ \Delta e \end{bmatrix} \quad \Delta F = \begin{bmatrix} \Delta \rho u \\ u(\Delta \rho u) + \rho u \Delta u + \Delta p \\ v(\Delta \rho u) + \rho u \Delta v \\ w(\Delta \rho u) + \rho u \Delta w \\ h_n(\Delta \rho u) + \rho u \Delta h_n \end{bmatrix}$$

$$\Delta G = \begin{bmatrix} \Delta \rho v \\ u(\Delta \rho v) + \rho v \Delta u \\ v(\Delta \rho v) + \rho v \Delta v + \Delta p \\ w(\Delta \rho v) + \rho v \Delta w \\ h_n(\Delta \rho v) + \rho v \Delta h_n \end{bmatrix} \quad \Delta H = \begin{bmatrix} \Delta \rho w \\ u(\Delta \rho w) + \rho w \Delta u \\ v(\Delta \rho w) + \rho w \Delta v \\ w(\Delta \rho w) + \rho w \Delta w + \Delta p \\ h_n(\Delta \rho w) + \rho w \Delta h_n \end{bmatrix}$$

$$\rho \Delta u = \Delta(\rho u) - u(\Delta \rho)$$

$$\rho \Delta v = \Delta(\rho v) - v(\Delta \rho)$$

$$\rho \Delta w = \Delta(\rho w) - w(\Delta \rho)$$

$$\Delta p = (\gamma - 1) \left\{ \Delta e - \frac{1}{2} [u(\Delta \rho u) + v(\Delta \rho v) + w(\Delta \rho w) + \rho u \Delta u + \rho v \Delta v + \rho w \Delta w] \right\}$$

$$\rho \Delta h_n = \Delta e + \Delta p - h_n \Delta \rho$$

Discussion

F. BASSI, UNIV. OF CATANIA, ITALY

Which kind of boundary condition do you use at the downstream of the staggered cascade?

AUTHOR'S REPLY

For all the test cases, we use characteristic type boundary conditions. For test case D (supersonic staggered wedge cascade); although the flow is supersonic at the downstream, axial velocity component (normal to the boundary) is subsonic; accordingly a subsonic boundary condition is used by imposing a constant static pressure which corresponds to the desired inlet Mach number.

C. HAH, NASA LEWIS, U.S.A.

Your last example; is it incompressible flow or subsonic flow? If it is incompressible flow did you use an artificial compressibility method or something else?

AUTHOR'S REPLY

The last test case (E-Squire and Winter 90° bend channel flow) is a low subsonic flow ($M \approx 0.3$).

B. NOLL, UNIV. OF KARLSRUHE, GERMANY

What is the advantage of the cell vertex finite volume method?

AUTHOR'S REPLY

Cell vertex finite volume method maintains higher order accuracy independent of the smoothness of the grid for nonuniform meshes, whereas cell centered schemes do not. Cell vertex schemes are more flexible for the control volume definitions.





NUMERICAL REPRESENTATION OF HEAT TRANSFER INTO TURBINE BLADE COOLING DUCTS

by

C.Taylor*, J.Y.Xia*, J.O.Medwell† and W.D.Morris†

* Department of Civil Engineering

† Department of Mechanical Engineering

University College of Swansea

Singleton Park

Swansea SA2 8PP

United Kingdom

92-16087



ABSTRACT

A numerical representation of three dimensional turbulent flow within cooling ducts located in turbine blades and heat transfer into such ducts is effected using the finite element method. The importance of a coupled solid/fluid numerical model, when investigating heat transfer, is demonstrated by comparing numerical results with experimentally determined values relating to smooth, cylindrical rotating passages. Having verified the numerical model, the technique is then used to evaluate heat transfer into a multi-ribbed rotating cylindrical duct. The enhancement of heat transfer, due to Coriolis induced secondary motion and the incorporation of ribs, is predicted and compared with experimental measurements.

1. INTRODUCTION

For over a decade the quest for improved aero gas turbine power and fuel economy has stimulated research directed at the design of high performance cooling systems for rotor blade airfoil sections. Current state-of-the-art cooling systems require complex air flow passages within the rotating airfoil section. These passages channel compressor-bled air in a spanwise direction along the blade and may have a variety of smooth or artificially roughened cross sectional shapes, with interconnecting bends if the coolant flows in a multi-pass manner.

As a consequence of the introduction of cooling passages, there is a requirement for an accurate predictive technique for evaluating the heat transfer characteristics within the coolant passages. The heat transfer in these can be significantly affected by the incorporation of repeated ribs on the duct surface and the secondary Coriolis induced transverse flows which arise due to blade rotation.

When studying confined convection problems it is customary to associate the fluid flow with a solid bounding surface via prescribed boundary conditions. For confined strongly turbulent flow, the computational domain can be defined in one of three ways. In the first, the domain is treated as a whole and an appropriate numerical technique used to solve the governing equations. This is, in practice, inadmissible since a computationally unacceptable fine discretisation adjacent to boundary surfaces would be necessary to accommodate rapid variations in the independent variables. The second technique consists of a flow domain separated from boundaries by a spatially narrow strip, the 'near wall' zone. In this zone the variation in the variables can be depicted via empirical universal profiles [1], in a direction normal to the boundary surface, using special spatial discretisations [2] or unidimensional representations [3].

In the present investigation, universal profiles are adopted and the governing equations are then solved, using an advocated numerical approach, outside the near wall zone. The boundary conditions specified at the edge of the resulting thin zone are subject to simultaneous correspondence between the main flow domain and the near wall zone.

However, convective heat transfer associated with such confined turbulent flows is not straightforward, since,

- (i) no empirical functions exist at the edge of the near wall zone to provide boundary conditions for heat transfer,
- and,
- (ii) the source of heat is usually known either on the outer extremity of or within the confining solid.

During the course of this investigation, it was recognised that conduction inside the wall material, from which a rotor blade is manufactured, plays an important role in the establishment of the prevailing thermal boundary conditions at the interface between the coolant and the internal bounding surface. For this reason, and also to permit a better numerical model of the experimental apparatus used to obtain results for comparison, the conjugated system, in which the fluid and the containing metal duct are treated as a total system, was used.

In this paper, the coupled solid/fluid model, based on finite element method, is used to evaluate heat transfer into smooth rotating cylindrical cooling ducts. The importance of using a conjugate system over conventional models, which seek to effect a separate heat balance at the solid/fluid interface, is observed by comparing computed results with the experimental measurements. Furthermore, the effectiveness of this proposed model is demonstrated for more complex flows and turbulent heat transfer by considering flow and heat transfer into a multi-transverse ribbed rotating cylindrical cooling duct. The numerical predictions relating to heat transfer are compared with experimental values.

2. COUPLED SOLID/FLUID MODEL FOR TURBULENT HEAT TRANSFER

The relevant equations used to predict the turbulent flow within coolant passages are presented elsewhere [4] and the main body of the current text is devoted to details relating to the equations depicting heat transfer within rotating, ribbed ducts.

The heat transfer within a gas under steady state turbulent flow conditions may be written,

$$\rho C u_i \frac{\partial T}{\partial x_i} = \frac{\partial}{\partial x_i} \left[C \left(\frac{\mu}{\sigma} + \frac{\mu_t}{\sigma_t} \right) \frac{\partial T}{\partial x_i} \right] \quad (1)$$

Within the encompassing solid, since no convection terms exist, the governing equation becomes,

$$\frac{\partial}{\partial x_i} \left[k \frac{\partial T}{\partial x_i} \right] = 0 \quad (2)$$

where U and T are the time averaged velocity and temperature, respectively. ρ , C , μ and k are the fluid density, specific heat of fluid at constant pressure, fluid viscosity and thermal conductivity of the solid respectively. μ_t is a turbulent viscosity which is determined from a suitable turbulence model, such as the one- or two-equation model [5]. σ and σ_t are the Prandtl number and turbulent Prandtl number respectively, the values of which for air flowing in the fully developed region of a pipe are 0.7 and 0.95, respectively. Close to the solid wall, outside the central fully turbulent core region ($0 < Y^+ < 30$), the turbulent Prandtl number is subject to change. During attempts to quantify a relationship in agreement with experimental predictions of surface heat flux have led to the following, [5]

$$\sigma_t = \begin{cases} 0.7 & Y^+ < 5 \\ 1.4 - 0.7 (13 - Y^+)/8 & 5 < Y^+ < 13 \\ 1.4 & 13 < Y^+ < 17 \\ 0.95 + 0.45 (25 - Y^+)/8 & 17 < Y^+ < 25 \\ 0.95 & Y^+ > 25 \end{cases} \quad (3)$$

where Y^+ is defined as,

$$Y^+ = \frac{y}{\mu} \sqrt{\rho \tau_0}$$

in which τ_0 is wall shear stress and y is measured along the inward normal to the solid surface.

In general, the temperature distribution is evaluated from a simultaneous solution of the continuity, momentum and energy equations. The momentum equations are coupled to the energy equation, by a temperature-dependent buoyancy term, and includes the effect of variations in fluid density due to temperatures. In the present work, the buoyancy term is ignored since its effect proved to be negligible relative to convection for the range of parameters studied [6], so that the momentum equations are assumed to be independent of temperature; the converse is not true. The dependence of temperature on velocity is represented by the convection term in equation (1) and the dependence on viscosity is incorporated via the 'heat conduction' term.

Since velocity and turbulent viscosity are assumed independent of temperature, the velocity distribution within the duct can be calculated using standard techniques [5] employing either a one or two equation turbulence model.

In order to obtain an accurate simulation of heat transfer from the outer face of the solid into the flow, corresponding to experiment, the solid is included as part of the discretised domain, in a finite element context, as shown for a smooth cylindrical duct, Figure 1. The mesh is constructed so that each twenty noded isoparametric element comprises either a solid or a fluid. Along the interface between the solid and fluid, the continuity of heat transfer is automatically satisfied since the finite element method used for present purposes assumes continuity of flux along the internal element boundaries, i.e.,

$$\int_{\text{fluid}} C \left[\frac{\mu}{\sigma} + \frac{\mu_t}{\sigma_t} \right] \frac{\partial T}{\partial n} dS = \int_{\text{solid}} k \frac{\partial T}{\partial n} dS \quad (4)$$

where n is the outward normal to the interface.

The computational mesh used to evaluate the velocity in the main flow domain remains unchanged and an additional mesh is added to represent the near wall zone and the solid wall. When dealing with strongly convective heat transfer, a fine mesh in the near wall region of flow field is essential in order to accommodate the relatively large variations in temperature. From a computational viewpoint, the extra mesh required to simulate heat transfer is acceptable since only one variable (temperature) per node is involved and the front

width is much smaller than that required when computing the flow field when each node is associated with three/four variables.

Due to the dependence of temperature on velocity and viscosity, the nodal values of velocity within the near wall zone must be evaluated. These have, in the current investigation, been determined using 'wall functions' [1]. The values of Y^+ at each near wall node, located along the interface between the near wall region and the main flow, are already known. The Y^+ values for nodes within the near wall zone can be linearly extrapolated according to the nodal distance from the solid surface. Having obtained Y^+ , the velocity profiles can be determined utilising the wall functions. If the near wall zone modelling is based on unidimensional elements [3], the velocity profiles in the near wall zone is already known and no interpolation is required.

For heat transfer, based on the present coupled solid/fluid approach, the specified boundary conditions are as shown on Figure 2. At inlet, experimental values of temperature are imposed at the solid wall, T_{w0} , and fluid, T_{f0} ; along outer wall surface, an experimentally determined heat flux is applied. At exit, since, flux conditions inside the flow domain are unknown, arbitrary heat flux values,

$$f_i = \left[\frac{\mu}{\sigma} + \frac{\mu_t}{\sigma_t} \right] \frac{\partial T}{\partial x_i} \ell_i \quad (5)$$

in which ℓ_i is the component of an unit outward to the boundary, are imposed as an initial condition and subsequently updated to be compatible with the heat flux from within the flow domain. This results in a necessarily iterative solution procedure terminating when convergence is achieved. Around the solid surface, either temperature or heat flux profiles can be specified.

3. HEAT TRANSFER INTO A SMOOTH DUCT

The first example corresponds to conditions where the Reynolds number is 15,000, Rossby number 0.0406 and a Rayleigh number of 1.586×10^6 . A ribless smooth duct is analysed where the boundary flux is either applied at the wall/fluid interface or at the outer extremity of the solid, as in Figure 2a.

The introduction of the conduction in the solid boundary, $k = 35$ (W/mK), into the analyses has the immediate effect of averaging the circumferential wall temperature. The importance of the wall condition is clearly portrayed in Figure 3 where the variation of the temperature is plotted against axial position along the cylindrical duct. Under the same input boundary conditions, excellent agreement is obtained between the predicted values and the experimental data when wall conduction is included. However, the numerical values from the method when conduction is excluded, under-predict measured values by a maximum of 20%. Figure 4 depicts the axial variations of local Nusselt number using the same format as the previous diagrams. For present purposes the local Nusselt number is defined as

$$Nu = \frac{q}{k_a} \frac{d}{\Delta T}$$

in which q is the local flux, k_a the thermal conductivity of the fluid, d the duct diameter and ΔT the difference between the wall temperature and the bulk fluid temperature. Here the predicted results straddle the curve corresponding to measured values, the better agreement being again achieved by including wall conduction. In this case, no attempt has been made to average the numerical results in order to illustrate the difference in wall temperature gradients, and therefore heat flux, that occur at the leading and trailing edges.

4. HEAT TRANSFER INTO MULTI-RIBBED DUCT

The computational model detailed in the previous section is used for estimating heat transfer into a multi-ribbed cylindrical duct which rotates about an axis orthogonal to its

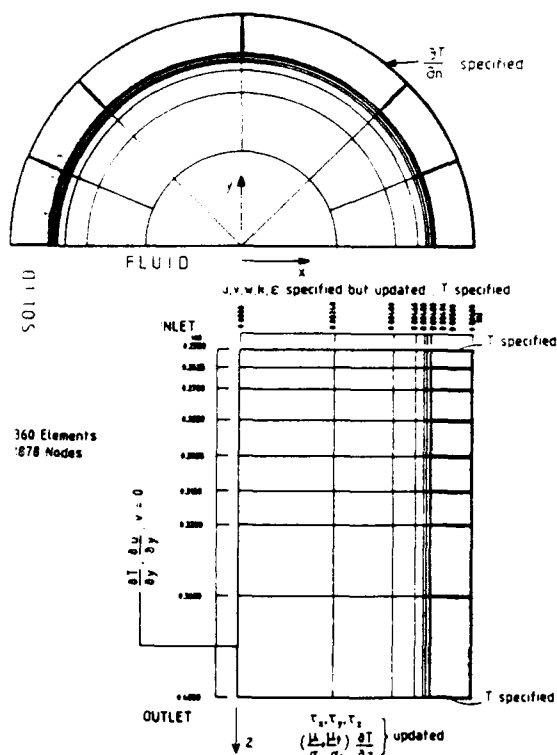


Figure 1 Fluid-solid mesh in x-y and y-z planes and boundary conditions

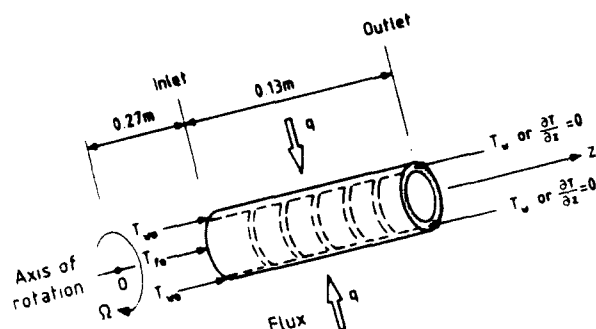


Figure 2 Geometry and boundary conditions for heat transfer

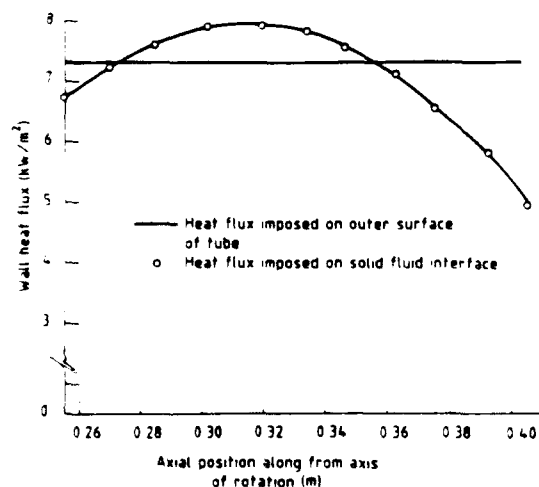


Figure 2a Imposed heat flux along duct wall

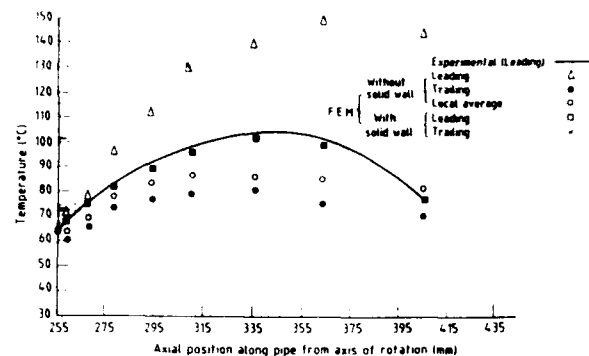


Figure 3 Comparison of predicted wall temperature distributions with experimental values ($Re=15,000$, $Ro=0.0406$, $Ra=1.586 \times 10^6$)

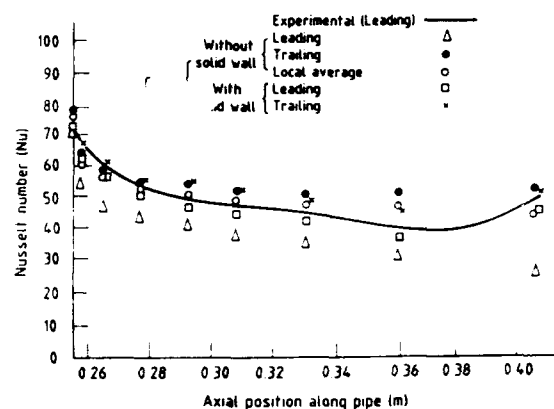


Figure 4 Comparison of predicted variation of heat transfer with experimental values ($Re=15,000$, $Ro=0.0406$, $Ra=1.586 \times 10^6$)

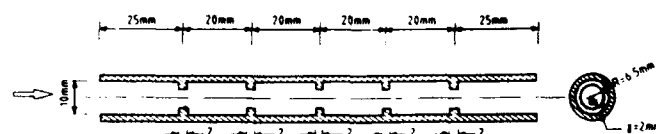


Figure 5 Geometry of multi-ribbed duct

longitudinal centre line. The geometry of the computational domain is shown as on Figure 5. The ratio of the rib height to inner duct diameter (h/d) is 0.2 and the ratio of rib height to pitch (h/p) is 0.1. The entry section of the duct is 270mm from the centre of rotation, as shown on Figure 2, and physical parameters are as defined previously. Figure 6 shows the finite element mesh used, comprising twenty noded isoparametric elements, for the prediction of the primitive variables (a) and heat transfer (b). The upstream boundary conditions relating to velocity correspond to a zero transverse flow and an axial velocity profile based on the $1/7$ th power law corresponding to a Reynolds number of 15,000. The upstream kinetic energy profile is taken as 1% of the axial velocity component squared. Updated traction boundary conditions [4] are applied at the downstream boundary. In the near wall zone [3], a logarithmic universal law [1] is used to depict variations in the velocity.

The coupled solid/fluid model for heat transfer in a complex geometry comprising the multi-ribbed duct is extremely effective since the distribution of heat flux around each ribbed surface from rib front to rib back, Figure 7, varies rapidly and is automatically evaluated in the numerical model and would be extremely difficult to measure.

Figure 8 is a plot of the developing turbulent flow pattern over the first and second rib which clearly shows the

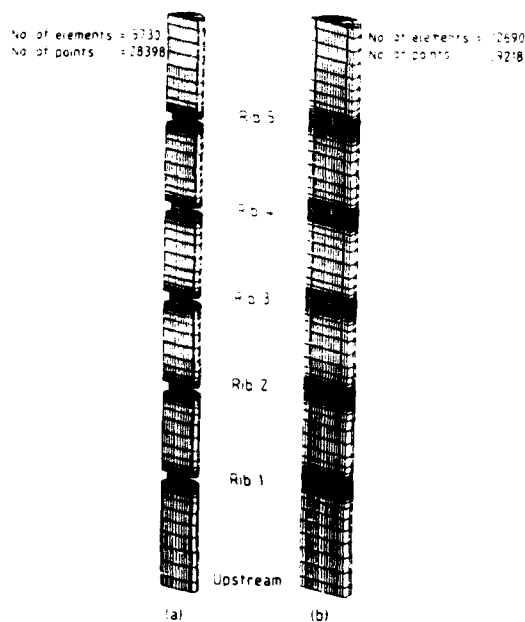


Figure 6 Finite element mesh distribution (a) for evaluation of flow and (b) for evaluation of heat transfer

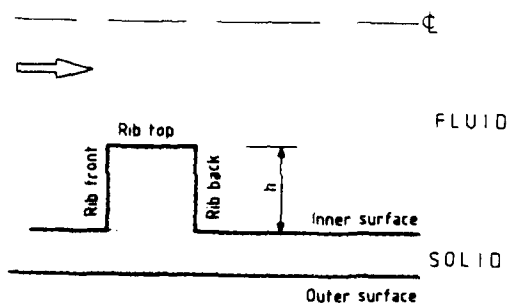


Figure 7 Definition of some terms relating to a rib

variation in velocity from rib to rib in this developing region. However, a similar plot, Figure 9, from ribs 2 to 4 shows that the pattern is essentially repetitive. The Coriolis force due to the orthogonal rotation produces a larger separation zone at both the leading and trailing edges and are also larger than those at the 90° plane. A typical development of the secondary flow between each pair of ribs, say from rib 3 to rib 4, is illustrated in Figure 10. The rapid change in the secondary flow pattern corresponds to the momentum transfer between the axial and transverse direction, especially adjacent to the ribs, which serves to increase heat transfer from the solid surface into the flow domain.

The temperature contours, degrees centigrade, within the solid wall as well as the flow domain, corresponding to $T_{wo} = 86.3^\circ\text{C}$ and $T_{fo} = 25.3^\circ\text{C}$ and a flux distribution with $k = 1.29$ (w/mk) as shown on Figure 11 are plotted on Figure 12. Within the fluid, the temperature steadily increases in a downstream direction as heat is transferred from the solid wall into the fluid. The contours are distorted towards the trailing edge, which is to be expected, such that the heat flux into the fluid is larger than that at the leading edge. The hotter zones are within the solid approximately midway between the ribs where both the axial flow component and the transverse flow component are relatively weak. Figure 13 shows the temperature variation across the solid wall and is compared with experimental measurements which were taken at 1mm from the outer surface of the duct. A marked drop in temperature on the inside face occurred along the top edge of each rib, corresponding to the larger velocities, and is mirrored by a decrease on the outer wall surface. The

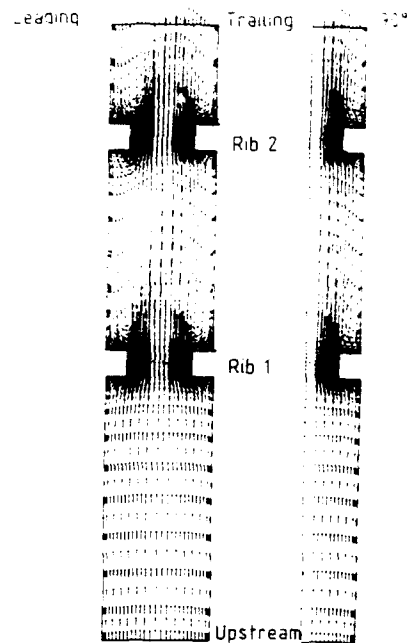


Figure 8

Velocity vectors from inlet and over the first and second rib ($Re=15,000$, $Ro=0.04$, $1\text{mm} = 6\text{m/s}$)
(a) in the symmetric plane
(b) at 90° plane to the symmetric plane

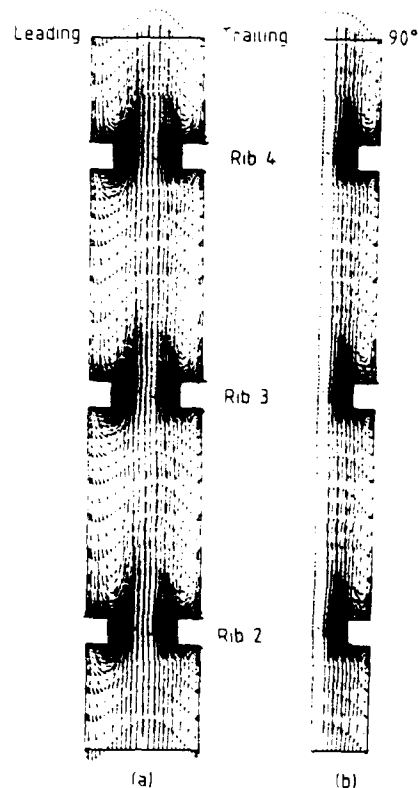


Figure 9

Velocity vectors over second, third and fourth rib ($Re=15,000$, $Ro=0.04$, $1\text{mm} = 6\text{m/s}$)
(a) in the symmetric plane
(b) at 90° plane to the symmetric plane

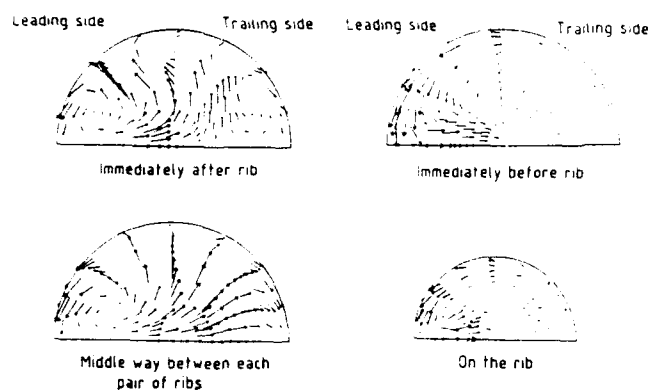


Figure 10 Typical pattern of the development of secondary flow at and between ribs ($Re=15,000$, $Ro=0.04$)

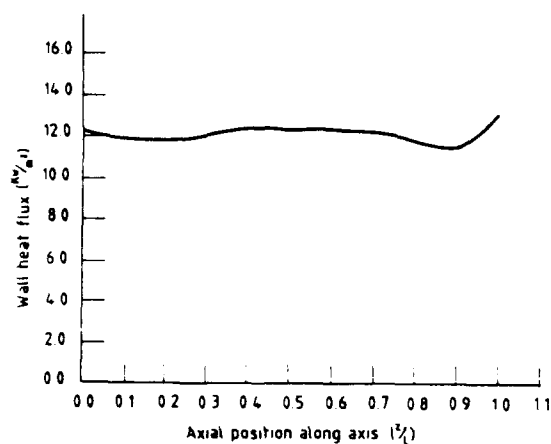


Figure 11 Imposed axial variation of heat flux on external surface of the ribbed duct

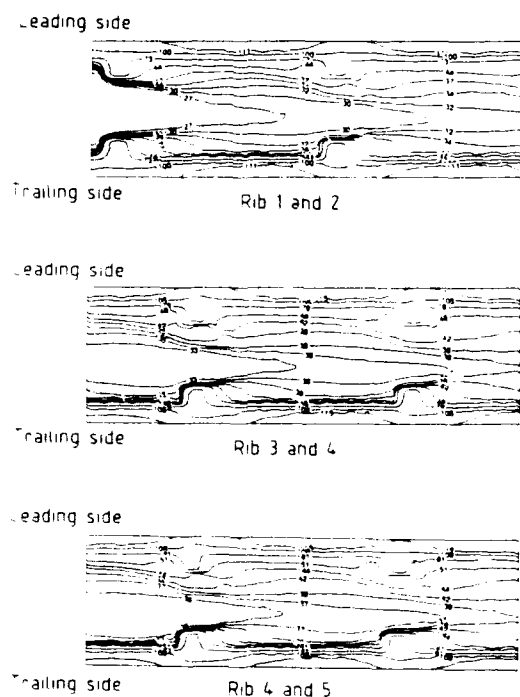


Figure 12 Temperature contours ($^{\circ}C$) in a rotating ribbed cylindrical duct ($Re=15,000$, $Ro=0.04$, $Ra=1.5 \times 10^6$)

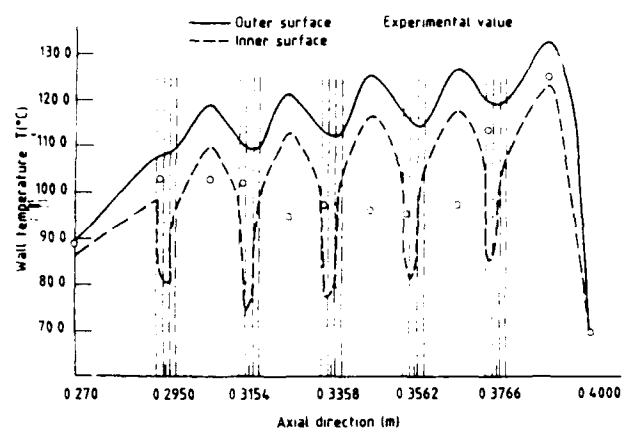


Figure 13 Comparison of wall temperature along the leading edge across the solid of a rotating ribbed cylindrical duct ($Re=15,000$, $Ro=0.04$, $Ra=1.56 \times 10^6$)

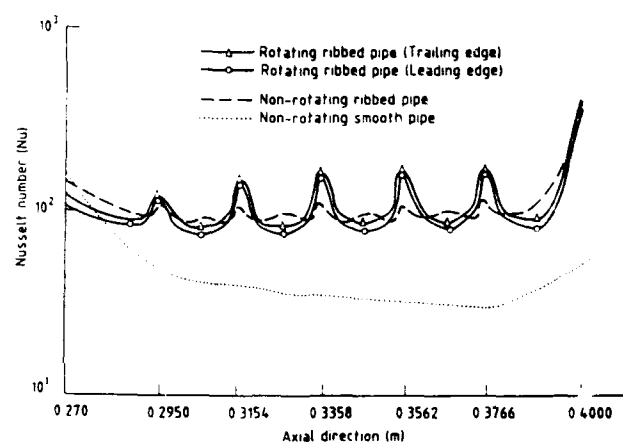


Figure 14 Comparison of heat transfer (Nu) along the inner surface of a ribbed cylindrical duct ($Re=15,000$, $Ro=0.04$, $Ra=1.5 \times 10^6$)

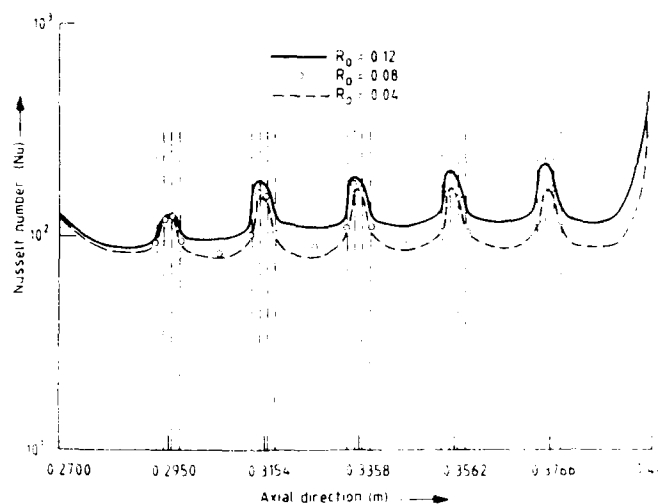


Figure 15 Predicted effects of Rossby number on the heat transfer (Nu) along the trailing edge of a ribbed cylindrical duct ($Re=15,000$)

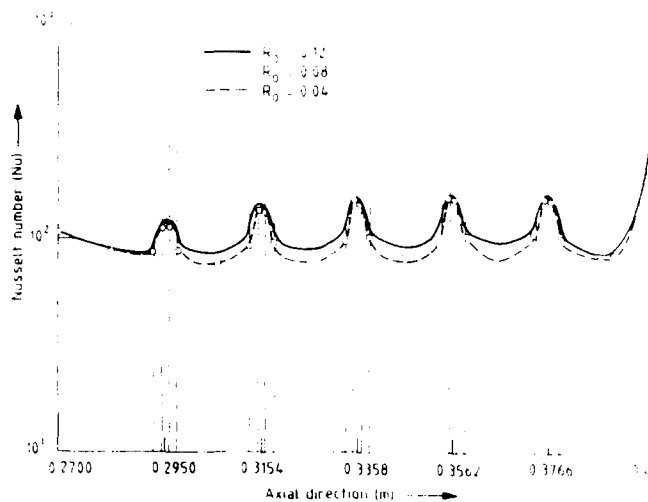


Figure 16 Predicted effects of Rossby number on the heat transfer (Nu) along the leading edge of a ribbed cylindrical duct ($Re=15,000$)

predicted rapid local variations in temperature, up to 50% of the local mean value, were not, probably due to limits on the number of thermocouples incorporated into the wall, apparent in the experimental measurements. However, general agreement is within acceptable limits.

The enhancement of heat transfer due to the incorporation of ribs is apparent, as shown in Figure 14, and is enhanced by up to 50% compared with that in a smooth duct. The influence of rotation is generally quantified in terms of the non-dimensional parameter representing Coriolis, the Rossby number Ro . For present purposes, the Rossby number is defined as,

$$Ro = \frac{\Omega d}{w}$$

in which Ω is the rotational speed (radians per second), w the mean axial velocity of the fluid where the diameter, d , is 10mm.

For a Rossby number 0.04, the effect of rotation on heat transfer in a ribbed duct is only local, Figure 14, and there is no discernible overall increase in heat transfer. However, with the increase in Rossby number, a certain amount of overall increase of heat transfer is predicted, as shown in Figures 15 and 16 for rotating trailing and leading edges respectively. Rossby numbers from 0.04 to 0.08 do not result in a significant variation in heat transfer particularly at the ribs. This indicates that for the range of parameters studied, the rib effect is still dominant in terms of heat transfer. At values of Rossby numbers greater than 0.08, the Coriolis effect increases and the profile reflecting the heat transfer demonstrates a general increase, Figure 15, for the trailing edge. In contrast to Figure 15, Figure 16 for the leading edge shows a relatively small variation and is limited to the regions away from the ribs.

5. CONCLUSIONS

It is evident that the finite element based coupled solid/fluid simulation of heat transfer into rotating ducts is extremely effective particularly for geometrically complex ribbed ducts. The availability of such a model enhances the experimental investigation and also acts as an indicator as to where experimentation needs to be refined.

It is evident that the present investigation is not exhaustive and parametric studies, relating to both geometry, physical conditions and modelling of the near wall zone need to be studied. However, the effectiveness of including ribs in such a situation has been demonstrated and areas of further work highlighted.

6. ACKNOWLEDGEMENTS

The authors wish to acknowledge the financial support of the M.O.D. (U.K.) and Rolls Royce Plc (Bristol) during this research.

7. REFERENCES

1. Davies, J.T., 1972, *Turbulence Phenomena*, Academic Press.
2. Taylor, C., Hughes, T.G. and Morgan, K. 1977, 'A numerical analysis of turbulent flow in pipes', *Int. J. Comp. Fluids*, 5, 181-203.
3. Xia, J.Y., Taylor, C. and Medwell, J.O., 1989, 'Finite element modelling of the near wall zone of confined turbulent flows', *Eng. Comput.* Vol.66, 127-132.
4. Taylor, C., Rance, J. and Medwell, J.O., 1986, 'A method for the prediction of Coriolis induced secondary flows and their influence on heat transfer in rotating ducts', *Eng. Comput.* vol.2, No.1, 1-12.
5. Xia, J.Y. 1990, *Finite element method and complex turbulent flow and heat transfer*, Ph.D. Thesis, University College of Swansea, Wales.
6. Morris, W.D. and Salemi, R. 1991, 'An attempt to experimentally uncouple the effect of Coriolis and buoyancy forces on heat transfer in smooth circular tubes which rotate in the orthogonal mode', *ASME Gas Turbine and Aeroengine Congress and Exposition*, Orlando, Florida.

Discussion

HANAKER, DARMSTADT, GERMANY

- 1) The boundary condition at pipe entry is already affected by Coriolis forces. How was it determined?
- 2) It is our experience that turbulence is affected by swirl and Coriolis forces, leading even to local relaminarization. Therefore, refined turbulence modeling should be included in list of future work required.
- 3) The increase in heat transfer due to ribs is "paid for" by an increase in pressure drop which has to be known to the designer. Have you calculated and measured the pressure drop?
- 4) Were your results affected by buoyancy forces? What were the Rayleigh Numbers?

AUTHOR'S REPLY

- 1) The boundary conditions are the values obtained from a preliminary analysis of flow within a rotating ribless duct. Entry boundary values correspond to numerically compatible velocities, turbulence kinetic energy and, if required, dissipation rates. This method was undertaken and applied since the only value available from experiment was the bulk flow rate.
- 2) This is a very valid point. However, to date, the correspondence between measured and predicted values have been acceptable and such refinement may not be necessary. A program of work should be undertaken to corroborate or disprove this statement.
- 3) The pressure drop was calculated as part of the primitive variable solution procedure. These show that the mean pressure variation, nondimensionalized with respect to the mean longitudinal energy, is approximately 2.5 times that when no ribs are present. As expected the local loss and recovery of pressure in the vicinity of the ribs is quite appreciable, as illustrated in the figure.
- 4) The calculations were undertaken including and excluding buoyancy terms. The difference in numerical values proved negligible. The Rayleigh number was 1.586×10^6 . We would expect buoyancy to have a measurable effect at Rayleigh numbers above 1×10^7 .

M. IACOVIDES, UMIST, U.K.

- 1) Our recent computations of rotating flows at UMIST indicate that rotational buoyancy effects start to become important for Rayleigh values greater than 10^7 . This is consistent with the findings of this paper.
- 2) Is the failure of the $k-\epsilon$ model to predict flows over ribs due to the treatment of the near-wall regions or do the authors feel that it represents a basic weakness of the $k-\epsilon$ model?

AUTHOR'S REPLY

- 1) The first question is in accord with our observations. The problem was analyzed both excluding and including buoyancy. It was observed that no discernable effects were apparent. Rayleigh numbers for the current problem is of the order 10^6 .
- 2) The authors have analyzed flow over a single rib using universal laws in the "near wall" region and also discretizing this zone using finite elements. In both cases the $k-\epsilon$ model underpredicts the recirculation zone length by 35 to 40 percent. In view of this it seems that the $k-\epsilon$ model is basically not applicable to such flows with strong recirculation.





VALIDATION OF NON-ORTHOGONAL THREE DIMENSIONAL LAMINAR FLOW PREDICTIONS

P.J. Coelho

J.C.F. Pereira

92-16088



*Instituto Superior Técnico
Mechanical Engineering Department
Av. Rovisco Pais
1096 Lisboa Codex
Portugal*

SUMMARY

Most of the flow geometries for aeronautical engineering are complex and cannot be discretized using orthogonal coordinates. In addition, some of those flows can only be described by the fully form of the Navier-Stokes equations. In this paper the Navier-Stokes equations are solved for three-dimensional complex geometries using a non-orthogonal, non-staggered coordinate system. The strong conservation form of the governing equations for laminar flows is discretized using a finite volume method. A numerical grid generation method is employed in order to easily generate the meshes. The flow through a square diffuser, the flow through a transforming duct of elliptical cross-section and the flow through a square cross-section S-shaped duct were analysed. The predictions reveal good agreement with the available data demonstrating the accuracy and generality of the present method. The present solution algorithm can easily be extended to calculate subsonic compressible flows.

- β Metric coefficient of the coordinate transformation.
 ϕ Dependent variable.
 λ Independent solution parameter in equations (5) to (7).
 μ Dynamic viscosity.
 θ Angle between the axis of the duct and the sidewall of the square-cross section diffuser; angle between the axis of the duct and the semi-minor axis of the elliptical cross section duct.
 ρ Density.
 ξ_i Non-orthogonal coordinate in i direction.

Subscripts

- ϕ Dependent variable.
 P Grid node P .
 p Pressure.
 V Velocity.

LIST OF SYMBOLS

- a_i Combined convection/diffusion coefficient of the discretized equation at node i .
 b Source term of the discretized equation.
 \overline{E}_ϕ Average absolute error of variable ϕ .
 J Jacobian.
 N Number of grid nodes.
 p Pressure.
 R^* Non-dimensionalized radial coordinate.
 S_ϕ Source term of the discretized ϕ -equation.
 U, V, W Velocity components in x, y, z directions, respectively.
 u_i Velocity component in i direction.
 V_b Bulk velocity.
 V_n Streamwise velocity.
 V_r Radial velocity.
 x, y, z Coordinates.
 ξ_i Cartesian coordinate in i direction.
 Z^* Non-dimensionalized spanwise coordinate.
 α Under relaxation parameter.

1. INTRODUCTION

Most of the flows found in engineering applications are characterized by complex geometries which cannot be properly simulated using Cartesian coordinates. Curved boundaries have often been treated in a stepwise fashion permitting the use of Cartesian coordinates but this technique is unable to provide accurate predictions near such boundaries. A special treatment using non-rectangular control volumes close to curved boundaries and Cartesian coordinates elsewhere has also been attempted [1] but it is complicated, specially for three-dimensional flows. Therefore, boundary-fitted coordinates have become increasingly more popular to deal with complex geometries. In addition, many flows of practical interest can only be described by the fully form of the Navier-Stokes equations.

In this paper a finite-volume solution method for the Navier-Stokes equations using a non-orthogonal curvilinear coordinate system is presented. Orthogonal coordinates lead to discretized equations similar to those obtained using Cartesian coordinates and there are

powerful and well established solution techniques available [2]. However, since it is difficult and in some cases impossible to generate an orthogonal grid for arbitrary three-dimensional geometries [3], non-orthogonal coordinates are used in the present work.

There are many different choices available to write the Navier-Stokes equations when non-orthogonal coordinates are employed, as discussed in Ref. [4]. They are physically equivalent but they imply the use of different solution methods and computational effort. The main options available are the conservation form of the governing equations (weak, semi-strong or strong), the velocity components taken as dependent variables (Cartesian, covariant or contravariant) and grid variable arrangement (staggered or non-staggered grids). The strong conservation form of the equations is generally preferred because it becomes easier to ensure conservation of the fluxes. Staggered grids were almost universally used in the past but, since the appearance of pressure-velocity coupling techniques able to prevent nonphysical oscillations in the pressure field, non-staggered grids constitute an attractive alternative. The Cartesian velocity components are preferred when non-staggered grids are chosen because they lead to a simpler form of the equations. In the present work the strong conservation form of the governing equations is used with non-staggered grids and cartesian velocity components as dependent variables in the momentum equations.

The final aim of this work is to develop a numerical algorithm for three-dimensional compressible flows [5]. As a first step only 3D incompressible flows are considered and validation of the code under this phase is a major objective of this paper. Only laminar flows will be considered in order to avoid errors due to turbulence models. Simple flows for which the analytical solution is known are examined and the flow in a geometry with engineering applications (S-shaped ducted) is calculated and the predictions are compared with experimental data. These results are shown and discussed in Section 3, after the presentation of the method in Section 2. The paper closes with a list of conclusions.

2. THE NUMERICAL METHOD

The strong conservation form of the Navier-Stokes equations for a steady flow can be written as follows:

$$\frac{\partial}{\partial \xi^j} (\rho u_k \beta_k^j) = 0 \quad (1)$$

$$\begin{aligned} \frac{\partial}{\partial \xi^j} (\rho u_k \beta_k^j u) = & \frac{\partial}{\partial \xi^j} \left[\mu \left(\frac{\partial u_i}{\partial \xi^m} \beta_k^m \beta_k^j + \right. \right. \\ & \left. \left. + \frac{\partial u_k}{\partial \xi^m} \beta_i^m \beta_k^j \right) \right] - \frac{\partial}{\partial \xi^j} (\rho \beta_k^j) \end{aligned} \quad (2)$$

where

$$\beta_k^j = J \frac{\partial \xi^j}{\partial x^k} \quad (3)$$

The non-orthogonal coordinate system (ξ^1, ξ^2, ξ^3) and the Cartesian coordinate system (x^1, x^2, x^3) are related by the coordinate transformation $x^i = x^i(\xi^j)$ whose Jacobian was denoted by J (see Figure 1). The Einstein summation convention is utilized.

The governing equations are discretized over a non-staggered mesh using the finite volume/finite difference method. The equations are integrated over each control volume in the computational domain and the Gauss divergence theorem is applied. In the discretization process the fluxes through the boundaries of each control volume must be related to the nodal values. The diffusive terms are discretized using central differences and the convective terms are discretized using the hybrid upwind/central differences scheme.

The discretization of the diffusive flux through each boundary yields three distinct terms representing a normal derivative and two cross-derivatives arising from non-orthogonality of the grid lines. The two cross-derivatives terms are treated explicitly as, e.g., in references [6] and [7]. This treatment does not influence the accuracy of the results and Peric [8] has shown that provided the skewness of the grid is not too high and the grid aspect ratios are not too large the convergence rate is not significantly affected.

Evaluation of the convective fluxes through the cell faces requires the calculation of the velocity components at those cell faces. Pressure-velocity coupling is ensured by a special interpolation method [7]. According to this method, expressions for the velocities at the two adjacent control volumes are obtained from the discretized momentum equation. Then, the cell face velocity is calculated by linear interpolation of the terms in the two expressions, with the exception of the pressure difference between the two grid nodes which is evaluated as in the staggered approach. Under-relaxation factors, which have to be used to ensure convergence due to the non-linearity and coupling of the equations, are taken into account in the interpolation formula, following the recommendations of references [9], [10] and [11].

The discretized equations can be expressed as follows:

$$a_p \phi_p = \sum_i a_i \phi_i + b \quad (4)$$

where the summation extends over the neighbours of grid node P . Coefficients a_i include the convective fluxes and the normal derivative fluxes and coefficient b accounts for the source terms.

The velocities and the pressure are linked via the SIMPLE algorithm [12]. Velocity and pressure corrections are introduced as in the original algorithm, neglecting the pressure gradients along the cell faces arising from non-orthogonality of the grid lines (see e.g. [6], [7], [8]). This simplification has no influence on the solution accuracy. According to reference [13], the convergence rate is not improved when these terms are taken explicitly into account. In a recent study, Peric [14] concluded that neglecting those

pressure gradients is computationally more efficient if the grid skewness is not too severe. However, when the grid skewness is high the algorithm becomes inefficient and it may not converge.

The explicit treatment of the cross-derivatives diffusive fluxes and the forementioned simplification in the velocity correction leads to a discretized equation (4) with only seven non-zero coefficients associated with the grid node P and the six closer neighbours. The Gauss-Seidel line-by-line iteration procedure was used to solve the sets of discretized equations.

The iteration procedure was terminated when the residual sums, normalised by the inlet mass or momentum fluxes, decreased below 10^{-3} for all the dependent variables.

3. RESULTS AND DISCUSSION

The first step towards the development of a code for the solution of the Navier-Stokes equations is the solution of a scalar transport equation. Moreover, it is desirable, for validation purposes, to choose an equation with a known analytical solution. The test case selected here is an extension for 3D of the proposal of Ref. [15] for 2D. The computational domain, shown in Figure 2a), was mapped using an elliptic grid generation procedure [16]. The velocity field is prescribed as follows:

$$U = -\frac{\lambda}{\pi} \frac{x}{x^2 + y^2} \sin\left(\pi \sqrt{x^2 + y^2}\right) \sin(\pi z) \quad (5)$$

$$V = -\frac{\lambda}{\pi} \frac{y}{x^2 + y^2} \sin\left(\pi \sqrt{x^2 + y^2}\right) \sin(\pi z) \quad (6)$$

$$W = -\frac{\lambda}{\pi} \frac{1}{\sqrt{x^2 + y^2}} \cos\left(\pi \sqrt{x^2 + y^2}\right) \cos(\pi z) \quad (7)$$

and the source term, driving the flow, is given by:

$$S_\phi = 2\pi \phi \cdot \frac{\pi}{\sqrt{x^2 + y^2}} \cos\left(\pi \sqrt{x^2 + y^2}\right) \cos(\pi z) \quad (8)$$

The analytical solution is given by:

$$\phi = \sin\left(\pi \sqrt{x^2 + y^2}\right) \cos(\pi z) \quad (9)$$

The average absolute error over all the computational domain, defined as:

$$\bar{E}_\phi = \frac{\sum_{i=1}^N (\phi_i - \phi_{i,anal})}{N} \quad (10)$$

is used for comparison between the analytical and numerical solutions. The λ parameter was set equal to 1 as well as the density and the diffusion coefficient.

Table 1 summarizes the results obtained using a cylindrical grid and the non-orthogonal grid shown in Figure 2a). It can be seen that the number of iterations required to achieve convergence is not influenced by non-orthogonality of the grid lines but the solution accuracy decreases with grid skewness. This behaviour may be attributed to the numerical errors associated with the computation of the extra terms due to non-orthogonality of the grid lines. Grid refinement leads to a decrease of the average absolute error for both grids, as expected.

Since the scalar transport equation was successfully solved, we may now pass to the solution of the Navier-Stokes equations. Two test cases suggested by Prakash *et al.* [17] are examined next. They correspond to artificial flows but they are quite close to some real physical problems. Motivation for the prediction of these flows arises from recognition that, for ducts of varying cross section, nothing is available in literature that can be used as a benchmark. These two flows have known exact solutions and they can be used to validate the numerical method.

The first test case is the flow through a duct of square cross section varying along axial direction (see Figure 2b), and the second one is the flow through an elliptical duct whose cross section changes also along axial direction, but with the area of the cross section remaining constant (see Figure 2c).

The influence of the under relaxation parameters on the convergence rate was investigated and the results are displayed in Figure 3. They reveal that the increase of the under relaxation parameters for velocity, α_v , leads to a smaller number of iterations required to achieve convergence, provided that the under relaxation parameters for

Grid Nodes (x, y, z)		Cylindrical Mesh	Non-Orthogonal Mesh
10 x 10 x 5	\bar{E}_ϕ	0.0065	0.0117
	Number of Iterations	44	43
20 x 20 x 10	\bar{E}_ϕ	0.0016	0.0036
	Number of Iterations	153	151
30 x 30 x 15	\bar{E}_ϕ	0.0007	0.0019
	Number of Iterations	337	333

Table 1 — Average Absolute Error and Number of Iterations for the Transport of a Scalar in a Prescribed Flow Field

pressure, α_p , are properly selected. However, as α_v becomes higher, the influence of α_p becomes crucial. Optimum under relaxation parameters are $\alpha_v = 0.8$ and $\alpha_p = 0.4$, for the square cross-section duct whereas for the elliptical cross-section duct optimum values are $\alpha_v = 0.9$ and $\alpha_p = 0.3$ or $\alpha_v = 0.8$ and $\alpha_p = 0.4$. These results are in agreement with the findings of reference [8], where a relation $\alpha_p = 1.0 - \alpha_v$ is suggested for $\alpha_v < 0.8$, and reference [14] where $\alpha_p = 1.1 - \alpha_v$ is recommended for all values of α_v .

Table 2 summarizes the average absolute errors and the number of iterations required to achieve convergence for different grids and geometries. In this table θ is the angle between the axis of the duct and the diffuser side walls for the square

cross-section duct. For the elliptical cross-section duct, θ stands for the angle between the axis of the duct and the semi-minor axis of the elliptical cross section which increases linearly along axial direction. In both cases, as θ increases the cross section changes more rapidly and the grid skewness increases as well.

The results obtained follow the trends found for the transport of a scalar in a prescribed flow field analysed earlier. The convergence rate is only slightly affected by the grid skewness but for the square cross-section duct a significant increase in the number of iterations was found when θ increased from 22.5° to 45° . The solution accuracy decreases with the departure from orthogonality in both cases. In addition, the average absolute error decreases with grid refinement, as expected.

Duct	Grid Nodes (x, y, z)		$\theta = 0^\circ$	$\theta = 10^\circ$	$\theta = 22.5^\circ$	$\theta = 45^\circ$
Square Cross Section	5x5x5	$\bar{E}_u = \bar{E}_v$	1.3×10^{-3}	4.8×10^{-3}	8.2×10^{-3}	1.2×10^{-2}
		\bar{E}_w	6.9×10^{-3}	6.3×10^{-3}	8.2×10^{-3}	1.6×10^{-2}
		No. Iterations	32	32	33	40
	10x10x10	$\bar{E}_u = \bar{E}_v$	3.5×10^{-4}	1.5×10^{-3}	2.6×10^{-3}	3.8×10^{-3}
		\bar{E}_w	2.3×10^{-3}	2.3×10^{-3}	2.8×10^{-3}	4.6×10^{-3}
		No. Iterations	48	51	55	84
	20x20x20	$\bar{E}_u = \bar{E}_v$	8.5×10^{-5}	5.2×10^{-4}	9.2×10^{-4}	1.4×10^{-3}
		\bar{E}_w	6.1×10^{-4}	7.4×10^{-4}	9.5×10^{-4}	1.4×10^{-3}
		No. Iterations	173	185	191	271
Elliptical Cross Section	5x5x5	\bar{E}_u	2.0×10^{-4}	5.1×10^{-4}	1.3×10^{-3}	6.9×10^{-3}
		\bar{E}_v	2.0×10^{-4}	5.8×10^{-4}	1.8×10^{-3}	7.3×10^{-3}
		\bar{E}_w	9.0×10^{-4}	1.2×10^{-3}	3.0×10^{-3}	1.3×10^{-2}
		No. Iterations	17	18	20	29
	10x10x10	\bar{E}_u	7.6×10^{-5}	1.8×10^{-4}	5.0×10^{-4}	2.2×10^{-3}
		\bar{E}_v	7.6×10^{-5}	2.2×10^{-4}	6.9×10^{-4}	3.2×10^{-3}
		\bar{E}_w	3.6×10^{-4}	5.2×10^{-4}	1.2×10^{-3}	5.0×10^{-3}
		No. Iterations	37	37	37	41
	20x20x20	\bar{E}_u	2.7×10^{-5}	6.1×10^{-5}	2.1×10^{-4}	8.7×10^{-4}
		\bar{E}_v	2.7×10^{-5}	8.3×10^{-5}	2.5×10^{-4}	1.2×10^{-3}
		\bar{E}_w	1.9×10^{-4}	2.6×10^{-4}	5.9×10^{-4}	2.2×10^{-3}
		No. Iterations	123	123	122	128

Table 2 — Average Absolute Errors and Number of Iterations for the Flow Through Ducts of Varying Cross Section

Streamwise velocity profiles at different cross sections for the flow in the square cross-section duct are presented in Figure 4. They prove the excellent agreement between the predictions and the analytical solution. Corresponding profiles for the flow in the elliptical cross-section duct are shown in Figure 5. Once again, the accuracy of the predictions is good.

Finally, the method developed will be used to predict the flow in a S-shaped duct of square cross-section. S-shaped ducts occur in many industrial applications including intakes in aircrafts, internal combustion engine passages and river bends. An experimental study for the geometry shown in Figure 2d) is reported in [18] and the available data will serve for validation purposes. Due to symmetry only one half of the duct, mapped using $12 \times 24 \times 46$ grid nodes in Z^* , R^* and streamwise direction, respectively, was considered in the computations. Measurements available at Section 1 (see Figure 2d) were used as inlet boundary conditions.

Some selected results are displayed in Figures 6 and 7. Figure 6 shows radial and streamwise velocity profiles at $R^* = 0.3$ for the sections indicated in Figure 2d), where measurements are available. Here, R^* and Z^* are non-dimensionalized coordinates ranging from 0 to 1. Figure 7 shows experimental and predicted contours of radial and streamwise velocities.

At the inlet section there is a high velocity core flow which is displaced along the first bend towards the outer wall, due to the duct curvature (see Figure 7a). A region of low streamwise velocity close to the inner wall, at Section 3, near the exit of the first bend, is characteristic of the secondary flow. The vortex developed along the first bend can be observed in Figure 7b) where positive radial velocities occur near the upper and bottom walls of the duct and negative radial velocities prevail close to the symmetry plane. This vortex tends to be reversed along the second bend and the high core velocity flow towards the outer wall, observed along the first bend, does not continue along the second one. These characteristics are correctly predicted although the vortex reversal occurs faster than suggested by the predictions (see Figures 6g) and 6h).

In general, qualitative agreement between the measurements and the predictions was found but there is qualitative disagreement in some profiles at the exit section. One possible reason for the differences observed is the coarseness of the grid. However, calculations performed using a finer grid ($20 \times 40 \times 46$) did not yield significant improvement in the numerical solution. Other possible sources of error are the experimental errors and the limited knowledge of the boundary conditions. According to [18], experimental errors are estimated to be of the order of 1% rising to 2-3% in the regions of steep gradients. Errors in boundary conditions arise from the inlet boundary conditions, calculated from only 12×5 experimental velocities which do not include measurements in the spanwise direction, and from the outlet boundary condition based on the assumption of zero streamwise gradients.

4. CONCLUSION

A general finite-volume method for the prediction of three-dimensional laminar incompressible flows, governed by the full Navier-Stokes equations, in complex geometries was presented. The geometry is mapped using non-staggered grids and non-orthogonal curvilinear coordinates. The strong conservation form of the governing equations with the Cartesian velocity components as dependent variables is employed. The pressure-weighted interpolation method is used to calculate the velocities at the cell faces, ensuring a strong pressure-velocity coupling.

Validation of the method developed was made by comparing numerical and analytical solutions for the transport of a scalar in a prescribed flow field and for two benchmark flows. Prediction of the flow in a S-shaped duct of square-cross section has demonstrated the capability of the method to simulate flows in geometries of practical interest. Comparison of the predictions with available data reveals satisfactory agreement. Possible sources of inaccuracy are the coarseness of the grid, the insufficient knowledge of the boundary conditions and the experimental errors. The algorithm is validated and their extension to compressible all Mach number flows is in progress.

REFERENCES

1. P.D. Frymier Jr., H.A. Hassan and M.D. Salas, "Navier-Stokes Calculations Using Cartesian Grids: I. Laminar Flows". *AIAA J.*, 26, 1181 - 1188 (1988).
2. S.B. Pope, "The Calculation of Turbulent Recirculating Flows in General Orthogonal Coordinates". *J. Comp. Physics* 22, 197-217 (1978).
3. J.F. Thompson, Z.U.A. Warsi and C.W. Mastin, *Numerical Grid Generation - Foundations and Applications*, North - Holland, Amsterdam (1985).
4. I.A. Demirdzic, "A Finite Volume Method for Computation of Fluid Flow in Complex Geometries". Ph.D. Thesis, University of London (1982).
5. M.H. Kobayashi and J.C.F. Pereira, "Pressure Based Calculation Procedure for Compressible Viscous Flows Using Non-Staggered Non-Orthogonal Grid Systems". Submitted to *AIAA Journal*.
6. K.C. Karki and S.V. Patankar, "Calculation Procedure for Viscous Incompressible Flows in Complex Geometries". *Numerical Heat Transfer*, 14, 295 - 307 (1988).
7. C.M. Rhie and W.L. Chow, "Numerical Study of the Turbulent Flow Past an Airfoil with Trailing Edge Separation". *AIAA J.*, 21, 1525 - 1532 (1983).

8. M. Peric, "A Finite Volume Method for the Prediction of Three-Dimensional Fluid Flow in Complex Ducts". Ph.D. Thesis, University of London (1985).
9. M. Majumdar, "Role of Underrelaxation in Momentum Interpolation for Calculation of Flow with Non-Staggered Grids". Numerical Heat Transfer, 13, 125 - 132 (1988).
10. T.F. Miller and F.W. Schmidt, "Use of a Pressure-Weighted Interpolation Method for the Solution of the Incompressible Navier-Stokes Equations on a Non-Staggered Grid System". Numerical Heat Transfer, 14, 213 - 233 (1988).
11. M.H. Kobayashi and J.C.F. Pereira, "Calculation of Incompressible Laminar Flows on Non-Staggered Non-Orthogonal Grids". To be published in Numerical Heat Transfer.
12. S.V. Patankar, D.B. Spalding, "A Calculation Procedure for Heat, Mass and Momentum Transfer in Three-Dimensional Parabolic Flows". Int. J. Heat and Mass Transfer, 15, 1787 - 1806 (1972).
13. W. Shyy, S.S. Tong and S.M. Correa, "Numerical Recirculating Flow Calculation Using a Body-Fitted Coordinate System". Numerical Heat Transfer, 8, 99-113 (1985).
14. M. Peric, "Analysis of Pressure-Velocity Coupling on Non-Orthogonal Grids". Numerical Heat Transfer, Part B, 17, 63-82 (1990).
15. J.J.D. Domingos, J.B. Lopes, "Numerical Stability and False Diffusion in Recirculating Flows". Technical Institute of Lisbon, Internal Report 16/81 (1981).
16. P.D. Thomas, J.F. Middlecoff, "Direct Control of Grid Point Distribution in Meshes Generated by Elliptic Equations". AIAA J., 18, No. 6, 652-656 (1979).
17. C. Prakash, S.V. Patankar, "A Control-Volume Finite-Element Method for Predicting Flow and Heat Transfer in Ducts of Arbitrary Cross-Sections - Part II: Application to Some Test Problems". Numerical Heat Transfer, 12, 413 - 437 (1987).
18. A.M.K.P. Taylor, J.H. Whitelaw and M. Yianneskis, "Developing Flow in S-Shaped Ducts, I-Square Cross-Section Duct". NASA CR - 3550 (1982).

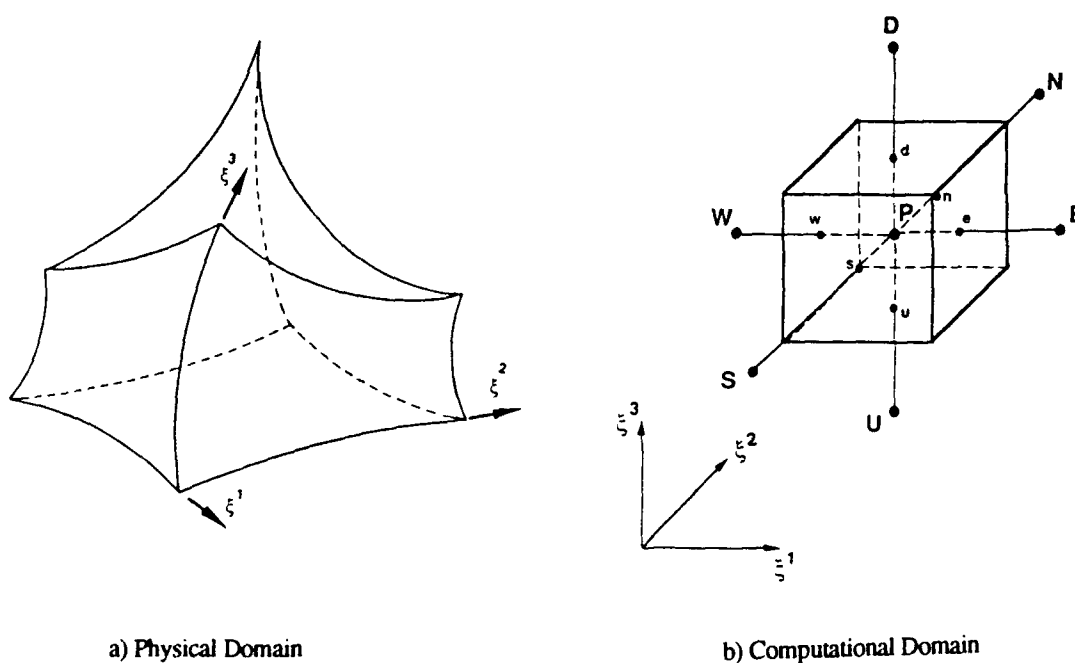


Figure 1 — Typical Control Volume.

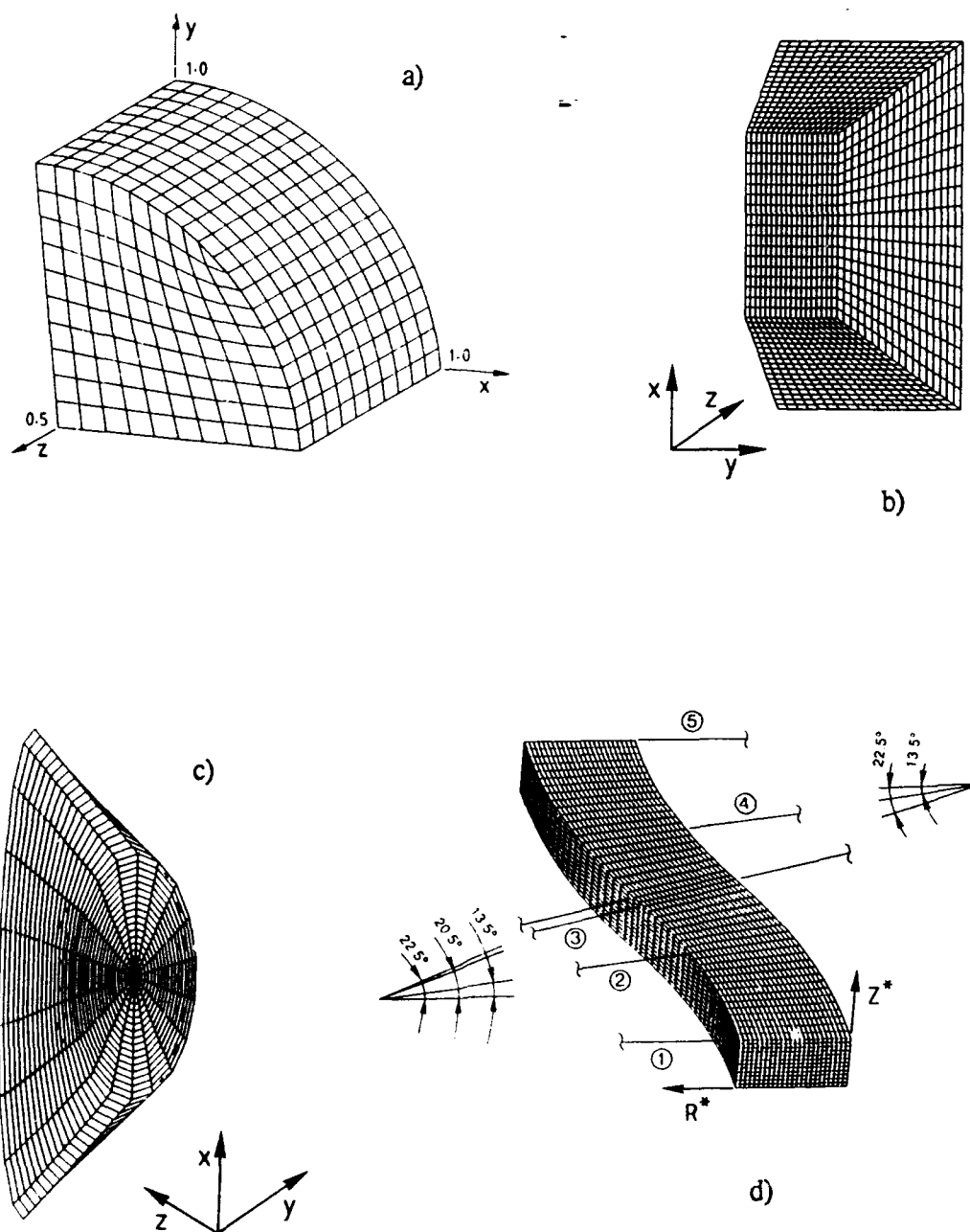


Figure 2 — Range of Geometries Under Investigation.

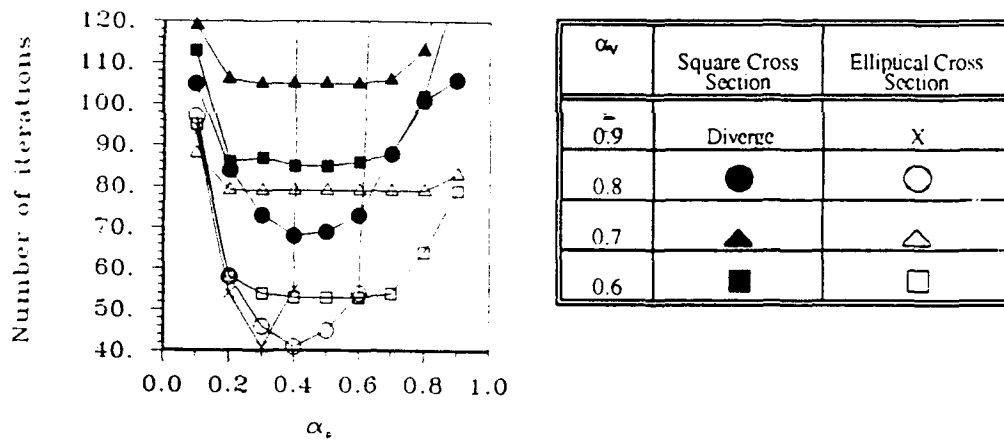


Figure 3 — Influence of the Under Relaxation Parameters on the Convergence Rate.

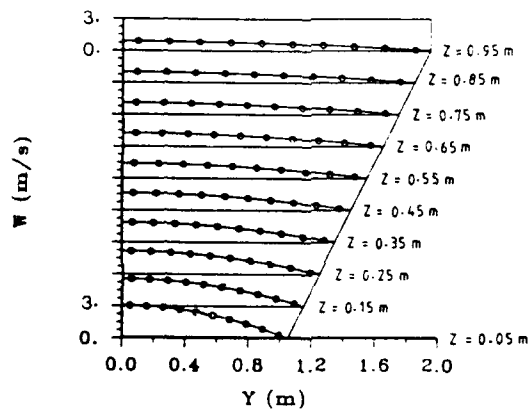


Figure 4 — Streamwise Velocity Profiles for the Flow through a Square Cross-Section Diffuser ($x = 0$ m).

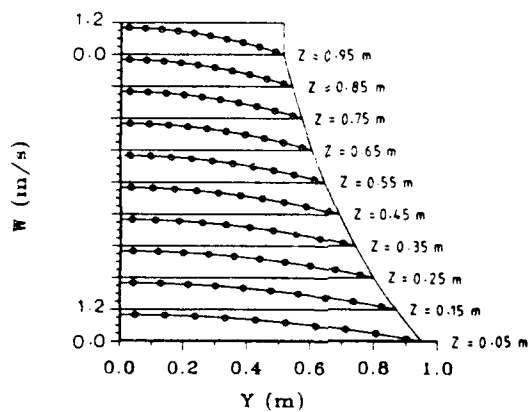


Figure 5 — Streamwise Velocity Profiles for the Flow through an Elliptical Cross-Section Duct ($x = 0$ m).

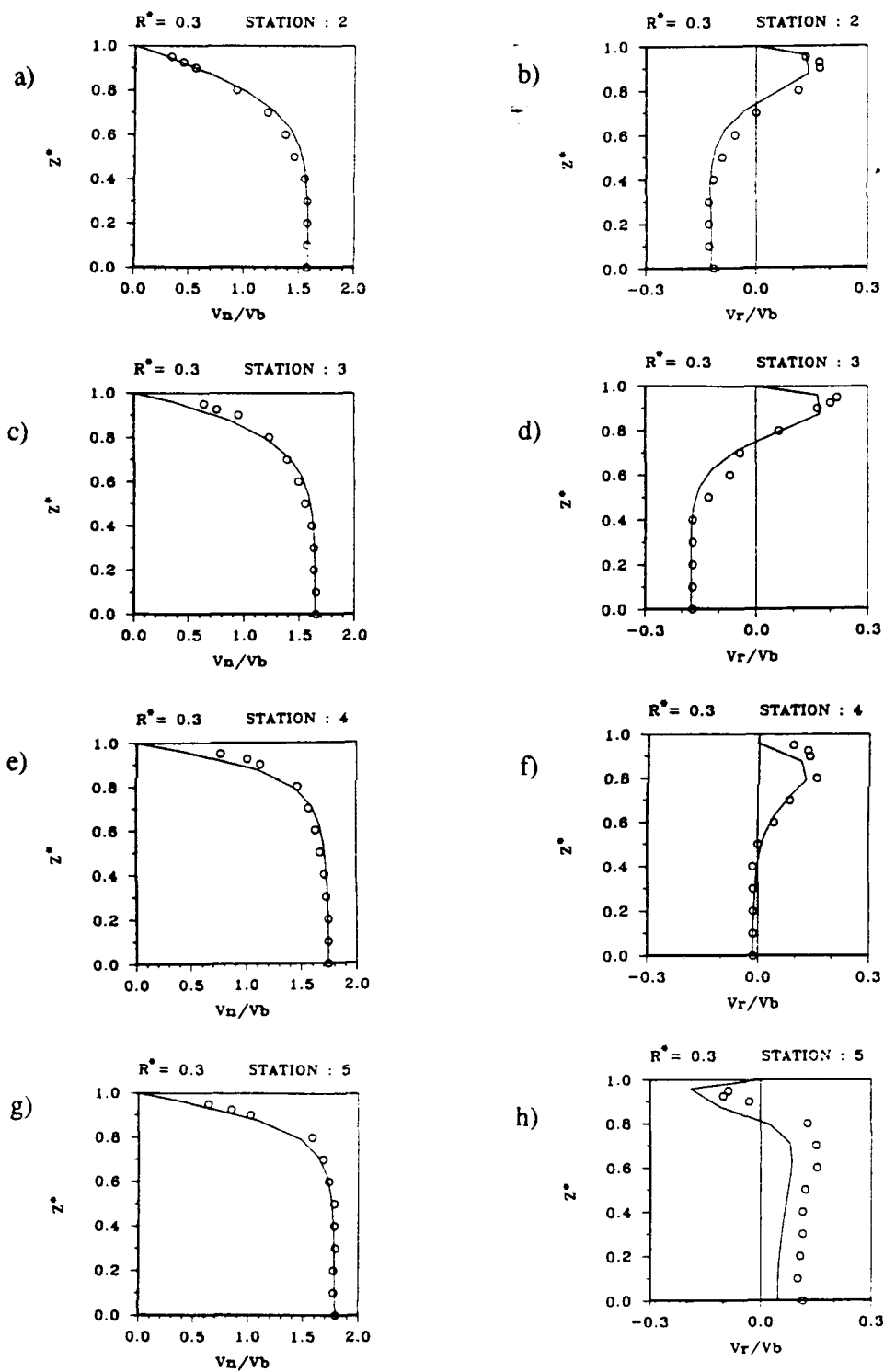


Figure 6 — Velocity Profiles for the Flow through a S-Shaped Duct.

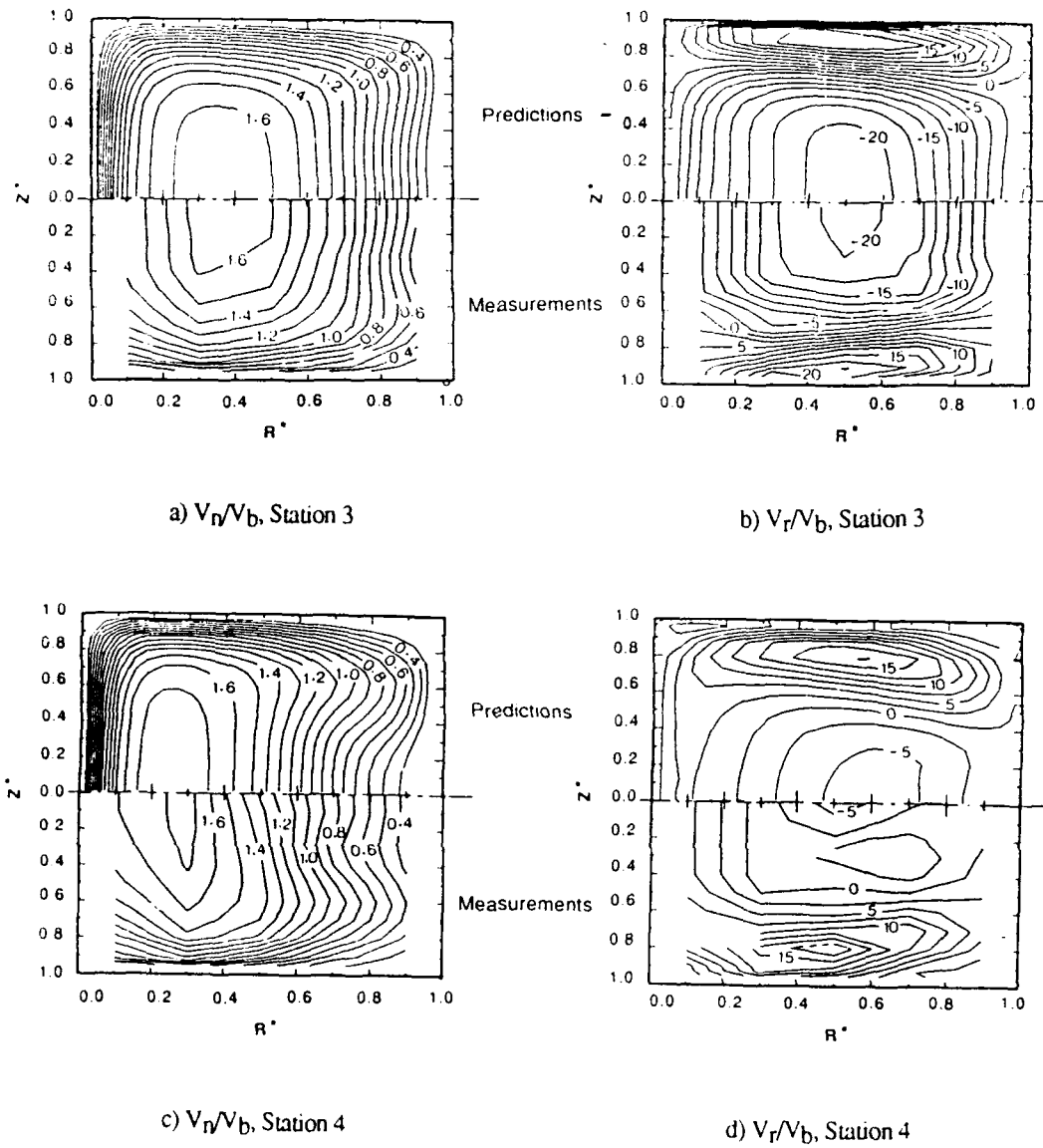


Figure 7 — Velocity Contours for the Flow through a S-Shaped Duct.

Discussion

C. TAYLOR, UNIV. OF SWANSEA, U.K.

The downstream boundary condition imposed is inadmissible since flow is not fully developed. Imposition of flow field here and at entry is also inadmissible. Suggest authors use either an updated traction boundary condition (a "natural" B.C. from the conservative form of the equations) or extend the computational domain downstream.

AUTHOR'S REPLY

In order to place the exit section in a fully developed flow region it would be necessary to extend the computational domain at least 20 hydraulic diameters downstream of the exit of the second bend. This would increase dramatically the computational requirements. The curvature of this particular duct is not very strong and the rate of change of the streamwise velocity is not large. Therefore, although we agree that the assumption of zero streamwise gradients at the exit section may be a source of inaccuracy (see section 3 of the paper) we believe that the main reason that justifies the observed discrepancies arises from the inaccuracy in the specification of the inlet velocity profiles which propagates downstream. The outlet velocity profile was not prescribed. However, this could be done according to the experimental data provided that care is taken such that the mass flow rate is the same at the inlet and outlet sections.

M. IACOVIDES, UMIST, U.K.

In our experience for accurate curved duct flow computations the computational domain should begin at least three diameters upstream of the bend exit and the exit boundary should be located several diameters downstream of the bend exit. This may account for the disagreement between the predictions and the experimental data.

AUTHOR'S REPLY

We fully agree that the main source of disagreement between the predictions and the experimental data arises from the prescribed boundary conditions of the inlet and exit sections, as stated in the last paragraph of section 3 of the paper. If there are detailed velocity measurements at the inlet section in order to permit the accurate specification of the inlet profile, the inlet boundary condition that we have used is the best one. Otherwise, the inlet section can be placed several hydraulic diameters upstream as you suggest. In such a case, however, a previous computation must be carried out in order to calculate the fully developed flow in the straight duct which would be prescribed as a boundary condition for the computations in the curved duct. The placement of the exit section several hydraulic diameters downstream the second bend could also improve the results at the expense of an increase in CPU time. Although we agree with your comments, no additional efforts were directed towards the improvement of the present predictions because:

- (1) The first three test cases revealed an excellent agreement between the measurements and the predictions.
- (2) The disagreement found for the flow through a S-shaped square cross-section duct is restricted to some profiles at stations 4 and 5 and is not very significant.
- (3) The primary objective of this paper is not the computation of the flow in this S-shaped duct but rather the development and validation of the solution method.

M. RACHNER, DLR, COLOGNE, GERMANY

What pressure-difference quotient did you use in the momentum equation of the boundary cells normal to the boundary?

AUTHOR'S REPLY

The pressure term is computed from the difference between the pressure on the cell face opposite to the boundary and the pressure on the boundary. The pressure on the opposite cell face is linearly interpolated from the two grid nodes on each side of the cell face. The pressure on the boundary is linearly extrapolated from the two closer grid nodes in the direction normal to the wall.





FINITE ELEMENT SOLUTION OF VISCOUS COMPRESSIBLE FLOWS IN GAS TURBINE DUCTS AND DIFFUSERS

by

W.G.Habashi***, M.F.Peeters**, M.P.Robichaud**, V-N.Nguyen** and M.V.Bhat**

* Concordia University, Montreal, Quebec

** Pratt & Whitney Canada

1000 Marie Victorin

Longueuil, Quebec J4G 1A1

Canada

92-16089



ABSTRACT

Aerodynamic losses incurred in gas turbine ducting are often substantial, contributing in a significant way to the overall compression or power loss. A finite element Navier-Stokes compressible turbulent code, NS3D, has been under development between Pratt & Whitney Canada and Concordia University to help in the understanding of the flow field in such ducts and diffusers, in order to control the loss mechanisms. The code is based on a Newton-Galerkin finite element method, with equal order interpolation for velocities and pressure. The system of linear equations, at each Newton iteration, is solved for the primary variables (u, v, w, p) simultaneously, with either iterative methods designed to run on engineering workstations or with direct methods on supercomputers. Turbulence is modeled through the well-known (k, ϵ) model, with wall functions.

The code has been applied to the compressible turbulent analysis of intercompressor ducts and diffusers, and compares reasonably well to experiments. In addition, the code is being currently used to obtain improvement of duct performance through numerical re-design.

Greek symbols

Δ	change in a variable
ϵ	pressure dissipation parameter
μ	viscosity
ρ	density

Subscripts

art	artificial viscosity
i, j	nodal indices
p	related to continuity equation
t	related to turbulence
u	related to x-momentum equation
v	related to y-momentum equation
\vec{V}	pertaining to momentum equations
w	related to z-momentum equation
x, y, z	differentiation with respect to x, y, z

Superscripts

LHS	left hand side
n	iteration number
p	contribution to the pressure term
RHS	right hand side
u	contribution to the u -velocity term
v	contribution to the v -velocity term
w	contribution to the w -velocity term

LIST OF SYMBOLS

e	element index
E	total number of elements
$[k]$	element influence matrix
$[K]$	global influence matrix
$[L], [U]$	lower/upper composition of $[K]$
\dot{m}	mass flow
$[M]$	global mass matrix
p	pressure
$\{R\}, \ R\ $	residual vector at nodes, residual norm
Re	Reynolds number
t	time
u, v, w	velocity components
\vec{V}	velocity vector

1. INTRODUCTION

The simulation of complex turbomachinery fields by means of inviscid and viscous flow equations is becoming the preferred analysis and design tool in the gas turbine industry. There is no shortage of methods for discretizing the governing fluid flow equations, with these methods differing in their discretization of the time terms, space terms, linearization and algebraic equations solution method.

The predominant space discretization methods in industrial practice are the Finite Difference (FDM) and Finite Volume (FVM) Methods, with the Finite Element Method (FEM) a distant third, since it is wrongly perceived as taxing on computer memory. Space discretization methods differ in applying the dissipation necessary to

stabilize the numerical solution and two approaches are common: centered schemes, with dissipation introduced through an explicit artificial viscosity and upwind schemes, applied directly to the convective terms. For time discretization, explicit and implicit approximations can be used. Explicit schemes trade the speed of convergence for simplicity by not requiring matrix inversion and are easily vectorizable and parallelizable. Large-scale problems are therefore more amenable to solution on today's computers, with a sacrifice of large solution times but manageable memory resources. Implicit schemes, on the other hand, allow much larger time steps at the cost of inverting some matrices at each step. These range from fully-coupled schemes, to ADI schemes, all the way to schemes that only require the solution of scalar tridiagonal matrices.

This hierarchy of simplifications via explicitness and/or segregation in the solution of the coupled system of equations is, however, at the cost of additional iterations to obtain the same overall convergence of the nonlinear system. It can be argued that coupled methods of solutions are impractical because of their memory requirements: nevertheless their convergence is faster and simpler, as the usual bells and whistles of uncoupled methods are not needed. The slow convergence of explicit methods, in addition, leads to the temptation of accepting partially converged results under the guise of sufficient engineering accuracy. This is not without danger as was demonstrated by Pulliam [1].

These reasons led us into a Pratt & Whitney-Concordia joint research program to develop simple, but effective, methods for the solution of the fully-coupled system of inviscid (Euler) [2] and viscous (Navier-Stokes) [3] equations. The scheme developed is a Newton-Galerkin formulation, with a Laplacian pressure dissipation term added to the continuity equation for Navier-Stokes formulations. The space discretization is by finite elements, the linearization of the system is carried out by a Newton method, and the solution of the coupled system of linear equations, at each iteration, is either by a direct method (for supercomputers) or by iterative methods (for workstations) [4].

2. GOVERNING EQUATIONS

The steady, three-dimensional compressible, variable viscosity, Navier-Stokes equations can be written as:

Continuity:

$$\nabla \cdot (\rho \vec{V}) = \epsilon \nabla^2 p \quad (1)$$

Momentum:

$$\rho (\vec{V} \cdot \nabla) \vec{V} + \vec{V} (\nabla \cdot \rho \vec{V}) = -\nabla p + \frac{1}{Re} \left[-\frac{2}{3} \nabla (\mu_t \nabla \cdot \vec{V}) + \nabla \times \mu_t (\nabla \times \vec{V}) + 2 (\nabla \cdot \mu_t \nabla) \vec{V} \right] \quad (2)$$

Simplified energy equation:

$$H_o = \frac{\gamma}{\gamma-1} \frac{p}{\rho} + \frac{1}{2} \vec{V} \cdot \vec{V} \quad (3)$$

Equation of state:

$$\frac{p}{\rho} = RT \quad (4)$$

It is well known that odd-even decoupling or checkerboarding would occur unless unequal order interpolation or staggered grids are used. To overcome decoupling in a simpler manner, a pressure dissipation term $\epsilon \nabla^2 p$, has been added to the continuity equation for the regularization needed for equal order interpolation of velocities and pressure.

After FEM discretization and Newton linearization, the following delta form of the equations must be assembled in terms of the cell-vertex unknowns of pressure and velocity components:

$$([k_{ij}^p] \Delta \hat{p}_j + [k_{ij}^u] \Delta \hat{u}_j + [k_{ij}^v] \Delta \hat{v}_j + [k_{ij}^w] \Delta \hat{w}_j) = -(R_i)_p$$

$$([k_{ij}^p] \Delta \hat{p}_j + [k_{ij}^u] \Delta \hat{u}_j + [k_{ij}^v] \Delta \hat{v}_j + [k_{ij}^w] \Delta \hat{w}_j) = -(R_i)_u$$

$$([k_{ij}^p] \Delta \hat{p}_j + [k_{ij}^u] \Delta \hat{u}_j + [k_{ij}^v] \Delta \hat{v}_j + [k_{ij}^w] \Delta \hat{w}_j) = -(R_i)_v$$

$$([k_{ij}^p] \Delta \hat{p}_j + [k_{ij}^u] \Delta \hat{u}_j + [k_{ij}^v] \Delta \hat{v}_j + [k_{ij}^w] \Delta \hat{w}_j) = -(R_i)_w$$

After assembly, this can be written in the matrix form:

$$\begin{bmatrix} [K^{\vec{V}}]_{\vec{V}} & [K^p]_{\vec{V}} \\ [K^{\vec{V}}]_{\vec{p}} & [K^p]_{\vec{p}} \end{bmatrix} \begin{Bmatrix} \Delta \vec{V} \\ \Delta p \end{Bmatrix} = - \begin{Bmatrix} R_{\vec{V}} \\ R_p \end{Bmatrix} \quad (5)$$

The remainder of the variables are solved in a segregated manner. Turbulence is modelled with the classical (k - ϵ) model using standard wall-functions [5]. After FEM discretization the turbulence matrix is solved with a direct (frontal) solver.

The next two sections describe the direct and iterative schemes developed for the solution of the matrices resulting from the present coupled approach. These include preconditioned conjugate gradient-like methods suitable to run on advanced Engineering Work Stations (EWS) and direct solvers suitable to run on supercomputers.

3. DIRECT SOLVERS: GAUSS ELIMINATION ON SUPERCOMPUTERS

Some pioneering work has been initiated by Storaasli, Agarwal and Nguyen [6] who, using the computing power of a Cray Y-MP with 8 processors were able to achieve impressive execution rates for the direct solution of a symmetric set of 54,870 equations for the structural analysis of the Space Shuttle Solid Rocket Booster. In our solver, their ideas have been further extended by the following important features:

- the CFD system matrix is non-symmetric,
- a larger set of equations, with a larger bandwidth, is solved,
- a group of equations is eliminated in each processor, rather than a single equation,
- no special language, other than Fortran, is used,
- the parallel-vector strategy is highly optimized.

3.1 The Vector-Parallel Gauss Elimination

The matrix is stored in a continuous vector containing the entries row-by-row, with a variable bandwidth, i.e. in a skyline mode. Two indices are defined: the first to indicate the start of each row and the second to point out the farthest row above it affecting its elimination.

Unlike the classical Gauss elimination procedure which starts elimination from the top of the matrix, Storaasli et al [6] invert the procedure by selecting a row to be operated on and all previous rows affecting it then are used to eliminate the corresponding columns of that row. This is more amenable to parallel computing since at the row being eliminated synchronization is needed only with a number of preceding rows equal to the number of processors, i.e. much less than the continuous synchronization that would be required by the classical Gauss elimination. In addition, the fact that many rows are available for elimination of the selected row allows loop unrolling.

The decomposition therefore proceeds by assigning a group of equations, here 5, to each processor. The elimination is performed in parallel on the processors, using all previously

completed factorized rows. As soon as a processor has completed the factorization of its group of rows, it operates on the next unfactorized group. The vectorization is carried out on the row operations using loop unrolling of various levels with the vector length controlled by the bandwidth and the stride being 1 since all vector components are contiguous.

3.2 Speeding Up the Process

It should be remarked that the best effort of Storaasli et al. yielded a speed of 1.57 Gigafllops, which is impressive, but substantially below the peak of the Cray Y-MP. We have introduced the following features which add substantial speed to the process:

3.2.1 Dynamic Assignment of Equations to Processors

Since each processor must be initiated, taking some finite time to come on stream, speed is gained by dynamically assigning groups of equations to be operated on to the available processors.

3.2.2 Dynamic Loop Unrolling

Loop unrolling is a technique to minimize the fetching and storing of data to and from memory in a compute intensive application. It consists of explicitly writing out portions of a DO-loop to minimize the number of times data is stored back to memory. Storaasli et al [6] use level-9 loop unrolling and pre-divide the matrix into blocks of 9 rows each. In such cases two special short blocks can occur: one at the elimination row and one at the farthest row used to eliminate it. By dynamically sizing blocks to start at the first row affecting the elimination, only one special short block can occur and, over the large number of operations involved in the matrix decomposition, this can translate into a sizeable saving.

3.2.3 Dynamic Elimination

In a static elimination procedure, a block is only processed if all information within that block is ready, i.e. the whole block has already been operated on. This implies a wait state with a processor idle if the entire block operations are not yet complete. In a dynamic elimination, instead of spending CPU cycles in an idle state, the processor is allowed to start operating on the completed portion of the equation block. While this partial-block operation affects the level of loop unrolling, the penalty is less than allowing a processor to remain idle.

3.2.4 Load Balancing

Another aspect of dynamic allocation is that it provides a mechanism to balance the load across

the processors. As soon as a processor has completed the elimination of its group of rows, a new group is assigned to it. A scheme has been introduced where, instead of waiting for the completion of the previous rows of equations, the processor suspends the elimination of its group of rows and goes back to get the next group to be eliminated. This minimizes the idle time of a processor and provides a continuous fine-grain load balancing throughout the elimination.

3.3 Gauss Elimination for the Navier-Stokes Equations

The Gauss elimination benchmarks have been obtained on a Cray YMP-8 computer as well as on an IBM-3090/600J-VF. The equation sets solved are from the discretization of the Navier-Stokes equations for the three-dimensional flow in a gas turbine diffuser and test cases size information is shown in Table 1.

	# ELEMS	# EQNS	MAX BAND	Storage Mwords
TEST1	1,785	6,804	476	5.5
TEST2	2,208	8,496	492	7.5
TEST3	3,168	12,192	688	14.7
TEST4	3,762	14,630	964	25.1
TEST5	21,936	50,470	1,269	116
TEST6	26,078	100,334	620	110
TEST7	7,500	24,021	2,258	91.7

Table 1: 3-D Navier-Stokes Gauss solver Test Case Information

Tables 2 and 3 present the performance of the Cray YMP, obtained in dedicated mode. Table 2 presents the results obtained on 8 processors with 32 Megawords of memory and using multitasking. Results indicate that the speedup from 1 to 8 processors has an efficiency of the order of 96% and that the larger the problem, the better the parallel efficiency.

	1-CPU Mflops	8-CPU Gflops	SPEED 1 TO 8
TEST1	224	1.577	88%
TEST2	227	1.635	90%
TEST3	238	1.796	94%
TEST4	247	1.899	96%

Table 2: 3-D Navier-Stokes Gauss solver on CRAY YMP-8/32

The largest test cases attempted were on a 128 Megawords YMP and are shown in Table 3. Autotasking has been used for these cases. Test

case 6 has a large number of unknowns and a moderate bandwidth, while test case 5 has half the unknowns but double the bandwidth. The ratio between the two speeds works out exactly to be proportional to NB^2 , where N is the number of equations and B the bandwidth. The fastest execution rate, 2.307 Gigafllops, is obtained in test case 7 selected for its large bandwidth, which enhances vectorization by increasing the vector length. In November 1990, this solver proved to be the fastest scientific code on a Cray, worldwide.

	8-CPU Gflops	ELAPSED SECS
TEST5	2.276	59
TEST6	1.980	31
TEST7	2.307	77

Table 3: 3-D Navier-Stokes Gauss solver on CRAY YMP-8/128

Table 4 presents the speed on 6 processors of the IBM-3090, in production mode. Results marked with an asterisk indicate estimates based on timing for other test cases. The Table shows that speeds of the order of 80 Mflops are attained on a single processor, i.e. 58% of the peak rate of the IBM-3090.

Parallelization indicates an efficiency of up to 99%, with rates of 435 Mflops attained on 6 processors. The results point out that the speed that can be achieved corresponds to the memory transfer rate of the IBM-3090.

	6-CPU Mflops	SPEED 1 TO 6	ELAPSED SECS
TEST 1	402	5.5	5.4
TEST 2	410	5.5	7.6
TEST 3	423	5.6	21
TEST 4	433	5.5	51
TEST 5	435*	5.5	311*
TEST 6	402*	5.5	156*
TEST 7	424*	5.5	421*

Table 4: 3-D Navier-Stokes Gauss solver on IBM-3090/600J-VF: speedup factors and execution times

The execution rates demonstrated here, coupled with the rapid convergence rates of the Newton-Galerkin algorithm, illustrate convincingly that it is possible to solve large-scale Navier-Stokes problems, of about 100,000 unknowns, to machine accuracy, in a few minutes on supercomputers.

4. ITERATIVE SOLVERS: PRECONDITIONED CONJUGATE GRADIENT-LIKE ALGORITHMS

Direct methods such as Gauss elimination require $O(NEQ^{2.33})$ operations for the factorization step, and $O(NEQ^{1.67})$ operations for the substitution step, while storage requirements are proportional to $O(NEQ^{1.67})$ on an $(NxNxN=NEQ)$ mesh. Iterative methods for the Newton correction, on the other hand, can offer the advantage of $O(NEQ)$ storage and, under certain conditions, preconditioned conjugate-gradient methods can produce a machine accurate solution in $O(NEQ^{1.17})$ operations [7]. These estimates must, however, be tempered by the sensitivity of iterative methods to matrix conditioning.

Because of their low storage requirements and operation count, iterative methods are well adapted to engineering workstations which are characterized by large memory (512 Megabytes) and fast scalar performance (25 Mflops).

The choice of iterative methods for the systems arising from the linearization of the Navier-Stokes equations is, however, complicated by the non-symmetry and non-positive definiteness of the matrix. Classical conjugate gradient methods, highly efficient for symmetric problems, become inapplicable. One must use variants, based either on minimization of the residuals, such as the Generalized Minimum Residual (GMRES) method [8] or on extensions of the bi-conjugate gradient, such as the Conjugate Gradient Squared (CGS) method [9]. We have adopted a CGS method, preconditioned by incomplete factorization (PCGS). Given a matrix $[K]$, we transform the system,

$$[K] \{\Delta x\} = -\{R\} \quad (6)$$

into the preconditioned one,

$$[L]^{-1}[K][U]^{-1}\{\Delta z\} = -[L]^{-1}\{R\} \quad (7)$$

$$\text{where } \{\Delta z\} = [U] \{\Delta x\} \quad (8)$$

The introduction of a time dependent term in the equations is found necessary to improve the conditioning of the matrix by the addition of a mass matrix, $[M]/\Delta t$, on the diagonal:

$$\begin{bmatrix} [M] + \Delta t [K \vec{V}]_{\vec{V}} & \Delta t [K^p]_{\vec{V}} \\ -\Delta t [K \vec{V}]_p & [M] + \Delta t [K^p]_p \end{bmatrix} \begin{Bmatrix} \Delta \vec{V} \\ \Delta p \end{Bmatrix} = - \begin{Bmatrix} R_{\vec{V}} \\ R_p \end{Bmatrix} \quad (10)$$

In addition, for coarse grids, a streamline diffusion is added to the problem on both sides of the equation. This can be represented in the condensed form:

$$[K(\epsilon, \mu_{art})] \begin{Bmatrix} \Delta \vec{V} \\ \Delta p \end{Bmatrix} = - \begin{Bmatrix} R_{\vec{V}}(\mu_{art}) \\ R_p(\epsilon) \end{Bmatrix} \quad (11)$$

This leads to an algorithm where the iteration matrix, $[K]$, is computed with progressively lower values of the parameters ϵ and μ_{art} , referred to as ϵ^{LHS} , μ_{art}^{LHS} , but higher than those in the residual, denoted by ϵ^{RHS} , μ_{art}^{RHS} . The residual is therefore computed with the smallest possible values of these parameters for which the outer Newton iteration converges.

This hybrid artificial viscosity algorithm can be described as follows:

1. Set: $\mu_{art}^{RHS} = \mu_{art}^{LHS}$
 $\epsilon^{RHS} = \epsilon^{LHS}$
2. \vec{V} , p being given, compute $\|R_V, R_p\|_0$

Newton Iteration:

3. Solve $\Delta \vec{V}_i$ and Δp_i with PCGS at each Newton iteration,
$$[K(\epsilon^{LHS}, \mu_{art}^{LHS})] \begin{Bmatrix} \Delta \vec{V} \\ \Delta p \end{Bmatrix} = - \begin{Bmatrix} R_{\vec{V}}(\mu_{art}^{RHS}) \\ R_p(\epsilon^{RHS}) \end{Bmatrix} \quad (12)$$

4. Update \vec{V} and p :

$$\begin{Bmatrix} \vec{V}_{i+1} \\ p_{i+1} \end{Bmatrix} = \begin{Bmatrix} \vec{V}_i \\ p_i \end{Bmatrix} + \begin{Bmatrix} \Delta \vec{V}_i \\ \Delta p_i \end{Bmatrix}$$

till $\|R_V, R_p\|_{i+1} / \|R_V, R_p\|_0 < 10^{-m}$, repeat from 3.

5. Lower ϵ^{RHS} , μ_{art}^{RHS} and repeat from 2, if necessary.
($m=3$ for the first cycle and $m=6$ for a second and subsequent cycles)

Normally two such cycles are sufficient.

Convergence results are investigated for various time steps. The solutions are obtained for the analysis of a gas turbine diffuser, at a Reynolds number of 1,000 on a structured grid consisting of 25 planes in the flow direction, each with 135 nodes, leading to a total of 11,521 unknowns. Table 5 shows the effect of the time step on the convergence properties of the Newton method and that of PCGS. It can be seen that increasing the time step from 0.5 to 5.0 reduces the number of Newton iterations by a factor of nearly 6, while the number of PCGS iterations per Newton step only increases by a factor of 3. The PCGS method could not, even with very high damping values of ϵ and μ_{art} , converge for the steady-state equations. The penalty of solving the unsteady-state equations is, however, minimal: 26 Newton steps for the iterative method versus 22 for the steady-state equations with a direct solver.

Time Step	Newton Iterations	Avg. PCGS Iterations per Newton step	Total CPU hours (SGI 4D/310)
0.5	152	10	3.14
1.0	75	17	2.13
5.0	26	31	1.39
∞^*	22	-	9.27

* Steady state with Frontal solver

Table 5: Convergence properties of PCGS as function of time step; $\epsilon_{RHS} = \epsilon_{LHS} = 0.05$; $\mu_{art}^{RHS} = 0.025$; $\mu_{art}^{LHS} = 0.05$

It is important to note that the hybrid artificial viscosity scheme is the key feature that allows the significantly large time steps that make the use of iterative methods viable for steady-state problems.

The theoretical optimal rate of $O(NEQ^{1.17})$ for the computational time of the PCG method on symmetric problems is also attained by the PCGS method for non-symmetric test problems here. It can also be shown that the fraction of the total computational time required for matrix integration and assembly is $O(NEQ)$ and relatively important when compared to the incomplete factorization [4].

5. APPLICATION TO DIFFUSER ANALYSIS AND DESIGN

A preliminary validation study for the current code, NS3D, has been initiated at Pratt & Whitney Canada.

4.1 Diffuser 1

4.1.1 Experimental Setup

A schematic of the experimental setup is shown in Figure 1. A screen is placed before the diffuser throat to duplicate the measured velocity profile at the inlet to the diffuser in the actual engine. A calibration of loss versus mass flow for the screen was obtained and used to determine the mass-averaged total pressure just downstream of it, at the inlet to the diffuser. The exit pressure was measured with a five-probe rake which is rotated to measure both the vertical and horizontal pressure variations.

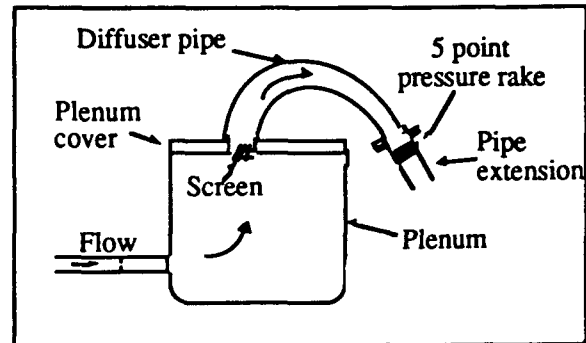


Figure 1: Schematic experimental setup for diffuser 1 rig test.

The loss definition for the diffuser is based on total pressure, P_t , using the following equation:

$$\text{Loss \%} = \frac{P_{t \text{ in}} - P_{t \text{ out}}}{P_{t \text{ in}}} \times 100$$

where:

$$P_{t \text{ in}} = P_{\text{plenum}} - \text{Screen Loss}$$

$$= P_{\text{plenum}} * (1.0 - 1.67 \dot{m}^2)$$

$$P_{t \text{ out}} = \text{Average of rake values}$$

4.1.2 Numerical Boundary Conditions

The inlet numerical boundary conditions used were based on the Mach number profile given by the screen, at a mass flow corresponding to $M=1$ at the throat. This profile is then scaled down to give the operating mass flow corresponding to the actual inlet Mach number. This somewhat exaggerates the total pressure variation at the inlet, as the actual total pressure loss through the screen varies with the square of the mass flow while linear scaling assumes that the loss varies linearly with mass flow.

At exit, the static pressure obtained in the test is specified.

The flow is computed with these boundary conditions and a specified inlet total temperature.

4.1.3 Computational Results

Two geometries were considered: an original version of this diffuser and a redesigned one for loss reduction. Figures 2 and 3 present the vertical Mach number profiles for the original version and a redesigned version of diffuser 1, including the computed inlet and exit profiles, as well as the experimental exit profile¹.

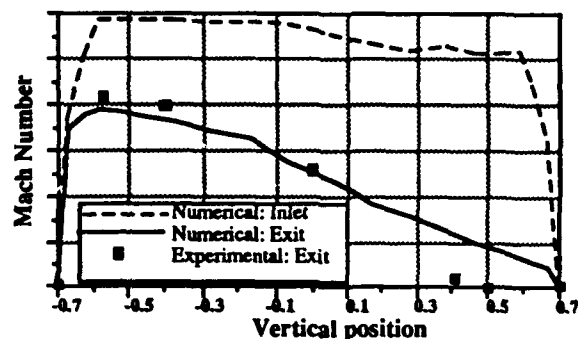


Figure 2: Vertical Mach number profile: original diffuser 1

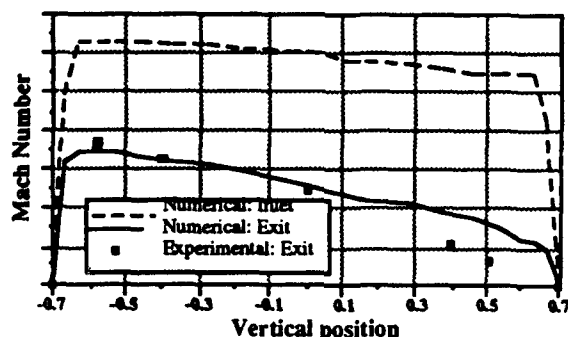


Figure 3: Vertical Mach number profile: redesigned diffuser 1

There is a noticeable skew in the exit Mach number profile, although the computed profile has less skew than the experimental one. Table 7 shows the computed and experimental loss prediction. The computed values were obtained on fine meshes (25,830 nodes) and are somewhat higher than the experimental ones. A comparison of the two diffusers based on computed loss shows a 7% (experimental inlet profile imposed) to 10% (uniform inlet profile imposed) loss reduction with the redesigned diffuser while a 30% loss reduction is observed in the experiment.

¹ All the results presented in this section have been non dimensionalized and represent relative rather than absolute values.

The correct trend is thus predicted, although the level of loss reduction is underpredicted. More detailed experimental data, particularly at the inlet, as well as further numerical tests, are needed to fully assess NS3D's capabilities for this geometry.

Diffuser 1	Loss % Measured	Loss % Computed	
		Uniform profile	Expt'l profile
Original	1.00	1.19	1.40
Redesign	0.66	1.06	1.30

Table 7: Experimental and computed loss % for diffuser 1

In addition to the computations with the experimentally derived inlet profile, the table also shows numerical tests using a uniform inlet profile. The results show that such inlet profile reduces the loss by 15% for both the original and redesigned diffusers.

Sensitivity of the computed loss to grid size in the flow direction was also evaluated since the grids generally used in diffuser analysis are coarser in that direction. Tests were performed using grids with 287 nodes per plane and between 20 to 90 planes in the flow direction. The results presented in Figure 4 shows that the loss level asymptotically flattens out at around 90 planes, suggesting that grids of 20,000 to 30,000 nodes should give grid independent solutions. More importantly, it also shows that, while the loss level changes with grid refinement, coarse grids still yield reasonable flow characteristics and give the ability to make relative loss comparisons.

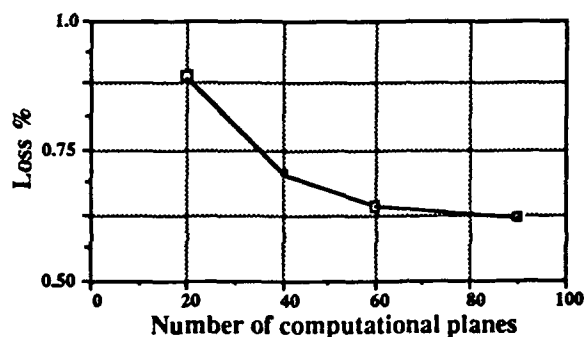


Figure 4: Effect of number of planes on the computed loss; original diffuser 1

4.2 Diffuser 2

4.2.1 Experimental Setup

The basic experimental setup is similar to that of the previous case but with no screen, leading

The diffuser was also preceded by a straight section of pipe, in order to develop the flow. There is a static pressure tap one half throat diameter upstream of the inlet. Using this measurement together with the mass flow and the assumption that the peak total pressure is equal to that of the plenum, a fairly accurate inlet profile can be constructed. There is no rake at the exit, and instead, the exit flow is measured by traversing just downstream of the exit.

4.2.2 Numerical Boundary Conditions

The flow is analyzed with a straight section added upstream of the diffuser inlet to allow the flow to develop to the point where the peak total pressure and the static pressure match the experiment. Unfortunately, the static pressure tap was matched at the throat instead of its actual position slightly upstream of it, leading to a peak Mach number at the static pressure tap location of 0.77 compared to 0.80 in the experiment, a 4% difference.

At exit, the static pressure was set equal to the barometric pressure.

4.2.3 Computational Results

Two geometries were considered: the original diffuser 2 and the same diffuser with an added horizontal splitter blade. This arrangement is thought to decrease the pressure loss by reducing secondary flows.

The experimental and computed exit Mach number contours are compared in Figures 5a and 5b for the original diffuser. The contours are similar, with two high speed zones where the Mach number peaks at 0.24 and 0.25 for the experimental and computed solutions, respectively, and a fairly quiescent zone at the lower section of the exit. The mass-averaged Mach number is 0.187 for the computed solution compared to 0.175 in the experiment.

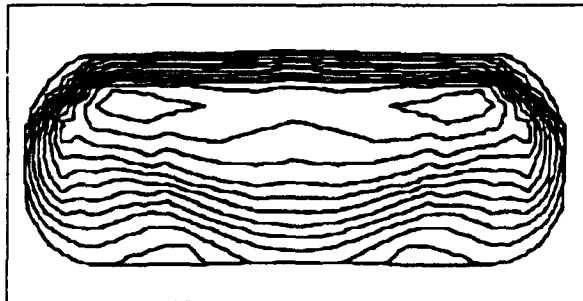


Figure 5a: Experimental Mach number contours for the original diffuser 2

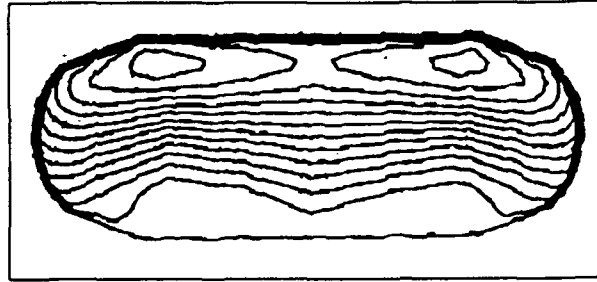


Figure 5b: Computed Mach number contours for the original diffuser 2

In Figure 6 the mass-averaged static and total pressure distributions for the original version of diffuser 2 are presented. The figure also points out some geometric features: where the cross section changes from circular to oblong and where the meanline starts to bend.

It can be seen from the results that static pressure rises quickly at the beginning and then tails off, while the total pressure drop is quite mild. As the meanline curvature begins, secondary flows induce strong mixing. This process raises the static pressure but also generates loss, eventually causing the static pressure to fall, leading to a peak of static pressure well before diffuser exit.

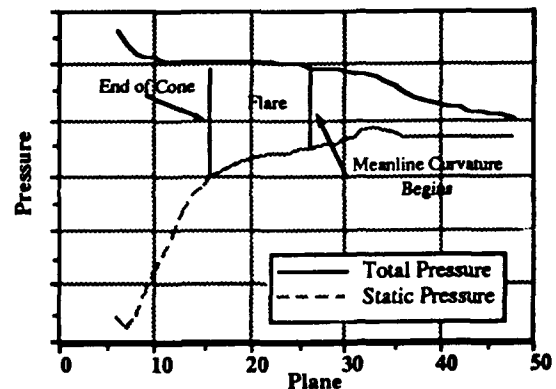


Figure 6: Static and total pressure distributions for the original diffuser 2

To obtain a more steady rise in the pressure, a horizontal splitter plate is added just upstream of the bend, effectively doubling the aspect ratio of the channel. This should reduce secondary flow losses and allow the static pressure to rise more uniformly. The mass-averaged total and static pressure distributions for diffuser 2, with a splitter, are shown in Figure 7. The effects of the splitter plate are as expected: a more gradual total pressure drop, as well as a more uniform rise in static pressure.

Table 8 compares the total pressure loss and static pressure rise coefficients for the two diffusers. The splitter version generates more loss but has a higher static pressure rise. This higher static pressure rise leads to a better performance since the diffuser outflow is dumped into the combustor with little or no recovery. It should be noted that these conclusions are based on a best case scenario since the analysis assumes a splitter with zero thickness and a diffuser with a clean axisymmetric inlet profile, minimizing incidence losses at the splitter.

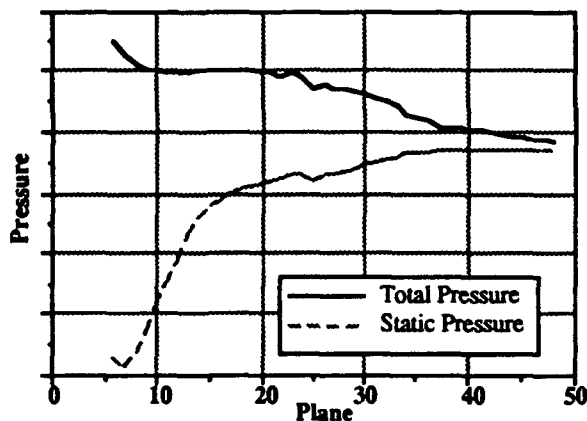


Figure 7: Static and total pressure distributions for diffuser 2 with a splitter

Diffuser 2	Loss %	C _p
Original	1.00	1.000
Splitter	1.05	1.043

Table 8: Loss and static pressure rise coefficients for diffuser 2

When the diffuser with a splitter was finally tested in an engine, it showed a slight performance increase compared to the original diffuser. The improvement was somewhat smaller than predicted by the Navier-Stokes analysis, the inlet conditions in the engine being likely different from this best case scenario analysis.

4.3 Diffuser 3

In this section we examine how a Navier-Stokes-based design system can be used to optimize diffuser performance. In a first attempt to improve performance, we restrict geometry modifications only to area distribution optimization along the meanline. Figure 8 shows the total and static pressure distributions for diffuser 3 which are quantitatively similar to that of diffuser 2. An effective design process requires optimization via the evaluation of a large number of geometries, which can only be achieved by a code that

converges reliably and rapidly. The current sequential optimization process involved ten geometries, analyzed over a two weeks period using a Silicon Graphics 4D/340 EWS.

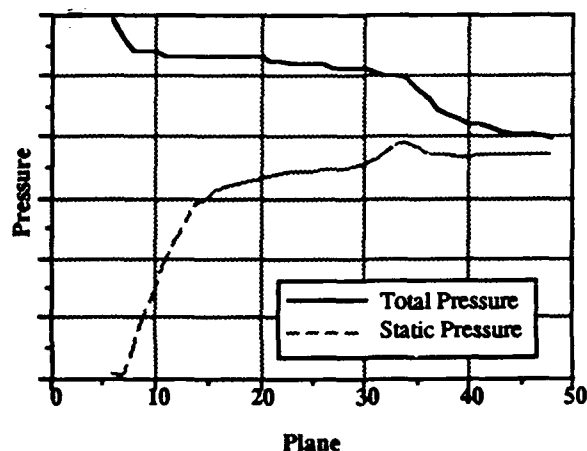


Figure 8: Static and total pressure distributions for the original diffuser 3

The analyses revealed two main shortcomings of the original area distribution: the area ratio was too large and too much diffusion was occurring in the narrowest part of the bend. The redesign thus aimed at reducing the area ratio and the diffusion in that part. The effects of these changes are shown in Figure 9. As can be seen, the amplitude of the irregularity in static pressure rise, as well as the steepness of the total pressure loss are reduced. The loss and static pressure rise coefficients are given in Table 9. The redesigned diffuser has noticeably reduced loss and increased static pressure rise coefficient. Testing of this improved geometry is currently under way and will further help in validating NS3D.

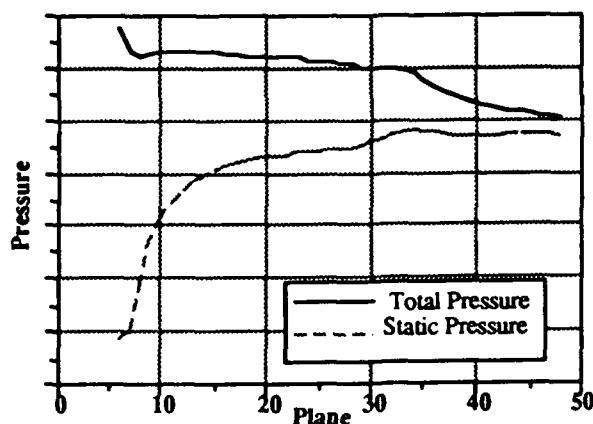


Figure 9: Static and total pressure distributions for redesign of diffuser 3

Diffuser 3	Loss %	C_p
Original	1.00	1.000
Redesign	0.81	1.053

Table 8: Loss and static pressure rise coefficients for diffuser 3

6. CONCLUSIONS

Based on this preliminary validation study, it can be concluded that FEM-based Navier-Stokes analysis is a cost effective tool to improve gas turbine diffusers' performance. The following remarks must also be made:

- Relative loss comparisons between diffusers can be predicted on coarse grids (6K-10K elements) enabling same day turnaround on a SGI 4D/340 EWS.
- Absolute loss levels in diffusers can be predicted with reasonable accuracy on finer grids (20,000 - 30,000 elements).
- The inlet velocity profile to a diffuser has a noticeable impact on its loss level.
- Detailed flowfield measurements are required for further code validation.

As far as solvers are concerned, the present application of preconditioned iterative methods such as Preconditioned Conjugate Gradient Squared, to the solution of linearized problems associated with the incompressible and compressible Navier-Stokes equations, is quite successful. The introduction of time dependent terms in the equations improves matrix conditioning. When this is coupled with a hybrid artificial viscosity method, i.e. higher in the iteration matrix than in the physical matrix, a robust and very efficient scheme is obtained. Iterative approaches are shown to be particularly efficient when used on advanced engineering workstations.

It was also shown that the availability of advanced computers like the Cray YMP and IBM 3090 series enable the use of large-scale direct solvers for the solution of Navier-Stokes problems. In that respect, it has been demonstrated that a direct solution of the coupled sets of equations resulting from the Navier-Stokes analysis of fluid problems is practical and that Gaussian elimination procedures vectorize and parallelize well on such computers. Execution rates of over 2.3 Gigafllops can be attained and work is continuing on an out-

of-core version of the method, to handle even larger CFD problems.

Undoubtedly, the continuing evolution of hardware will permit to take increasing advantage of the properties of fully-coupled strategies for fluid dynamics problems.

ACKNOWLEDGEMENTS

The continuous support of Pratt & Whitney Canada is gratefully acknowledged. This work is also partially supported under Strategic Grant STREQ040 and Operating Grant OGPIN013 of the Natural Sciences and Engineering Research Council of Canada (NSERC), and Grant 91-ER0517 of the Fonds pour la Formation de Chercheurs et l'Aide à la Recherche (FCAR) of the Quebec Government, held by the first author.

The authors would like to thank Cray Research (Canada) Inc. and Cray Research Inc. for their generosity in providing all necessary YMP access times, in dedicated mode, on their computers. Computing time on the Cornell National Supercomputing Facility is also gratefully acknowledged.

The authors would also like to thank SiliconGraphics Computer Systems (Canada) Inc. for graciously providing the Concordia-Pratt & Whitney team with the 4D/340 platform on which all iterative methods were developed and are currently run.

REFERENCES

1. Pulliam, T.H., "A Computational Challenge: Euler Solution for Ellipses", AIAA Paper 89-0469, Reno, Nevada, 1989, also *AIAA Journal*, Vol. 28, No. 10, October 1990, pp. 1703-1704.
2. Baruzzi, G., Habashi, W.G. and Hafez, M.M., "Finite Element Solutions of the Euler Equations for Transonic External Flows", AIAA Paper 90-0405, Reno, Nevada, 1990. (in press, *AIAA Journal*, June 1991).
3. Peeters, M.F., Habashi, W.G., Nguyen, B.Q. and Kotiuga, P.L., "Finite Element Solutions of the Navier-Stokes Equations for Compressible Internal Flows", AIAA Paper 90-0441, 1990. (in press, *AIAA Journal of Power and Propulsion*).

4. Habashi, W.G., Fortin M., Liu J.W.H., Robichaud M.P., Nguyen V-N. and Ghaly W.S., "Large-Scale Computational Fluid Dynamics by the Finite Element Method", AIAA Paper 91-0120, Reno, Nevada, January 1991.
5. Launder, B.E. and Spalding D.B., "The Numerical Computation of Turbulent Flows", Computer Methods in Applied Mechanics and Engineering, Vol. 3, 1974, pp. 269-289.
6. Storaasli, O.O., Nguyen, D.T. and Agarwal, T.K., "Parallel-Vector Solution of Large-Scale Structural Analysis Problems on Supercomputers", AIAA Journal, Vol. 28, No. 7, 1990, pp. 1211-1216.
7. Axelsson, O.A. and Barker, V.A., *Finite Element Solution of Boundary Value Problems*, Academic Press, 1984.
8. Saad, Y. and Schultz, M.H., "GMRES: A Generalized Minimum Residual Algorithm for Solving Nonsymmetric Linear Systems", *SIAM Journal of Scientific and Statistical Computing*, Vol. 17, 1986, pp. 856-869.
9. Sonneveld, P., "CGS: A Fast Lanczos-type Solver for Nonsymmetric Linear Systems", *SIAM Journal of Scientific and Statistical Computing*, Vol. 20, 1989, pp. 36-52.

Discussion

T. VOGEL, DLR, GERMANY

I would like to see the geometry of the diffusers one to three. Do you have any viewgraphs which show the designs?

AUTHOR'S REPLY

Geometry of the diffusers used in this code validation study are not available for external distribution.

D. HAARMEYER, MTU MÜNCHEN, GERMANY

Have you ever tried to apply a multigrid algorithm to solve the equations iteratively instead of the CGS or PCGS method?

AUTHOR'S REPLY

We have not yet considered using multigrid methods but have not ruled it out. Before trying the multigrid (MG) method, we will first try to use mesh interpolation from coarse to fine grid to improve the computational efficiency. We would also try using mesh refinement and mesh adaptivity before multigrid. Multigrid could then be used as an extension of the previous approach. We should mention that PCG-like methods are currently being used as smoother in MG to improve its robustness. In that sense, MG could be viewed as complementary to PCG-like methods with interpolation, mesh refinement and mesh adaptivity.

F. BASSI, UNIV. OF CATANIA, ITALY

Do you think that your method could be extended, with the same efficiency to transonic and supersonic flows?

AUTHOR'S REPLY

We have successfully extended our method to transonic flows (choking flows) and there were no noticeable degradation in the iterative solver efficiency. We have not tried supersonic flows.





AEROTHERMODYNAMICS OF NOZZLE FLOWS FOR ADVANCED HYPERSONIC PROPULSION SYSTEMS

by

C. Weiland, G. Hartmann, S. Menne
Messerschmitt-Bölkow-Blohm GmbH
Space Group
PO Box 80 11 69
W-8000 Munich 80
Germany

92-16090



Summary

One of the major tasks for the development of novel airbreathing space transportation systems, operating from usual airports by horizontal take off and landing, is the integration of an advanced propulsion system in the cell of that spacecraft. The air intake and in particular the free expansion nozzle affect not only the efficiency of the engine but also severely the forces and moments, and with that the control, of the complete spacecraft. Therefore, of course, it is necessary to know in detail the flow fields through such nozzles and its interaction with the external airflow. Another project deals with conventional rocket motor nozzles where by injection of turbine exhaust gases in the expansion part of the nozzle the wall of the nozzle is cooled (filmcooling concept) and the thrust is slightly increased. Theoretical investigation of these and other nozzles is the objective of this paper. Euler and boundary layer methods will be applied to predict the flow fields of the nozzles whereat special emphasis is laid on the consideration of real gas effects. The theory of the Euler method used will be described in detail while for the second order boundary layer method the governing equations are presented and the range of its applicability is shortly discussed. Finally results for a variety of nozzles will be given.

1 Introduction

In recent years the interest in hypersonic flows has grown very rapidly. This is due to the fact that around the world the development of new space transportation systems has been discussed. Besides the National Aerospace Plane in USA, particularly in Europe the projects Ariane V, Hermes, Sänger and Hotol play an important role in this field. In order to deal with the aerothermodynamics in a proper way national and international hypersonic research programs are initiated which encourage experimental and above all numerical investigations. This new challenge brings together aerodynamicists, thermodynamicists, chemists and people working in the area of gas-kinetics. There is a growing significance for Computational Fluid Dynamics (CFD) predictions of the flow field behaviour and flow phenomena, since for hypersonic flows not all of the similarity parameters can be reproduced simultaneously in the related windtunnels.

Windtunnel investigations are important for studying basic physical phenomena and for validation purposes of the numerical prediction methods.

All the above-mentioned space transportation systems need either propulsion systems and/or Reaction Control Systems (RCS), which may be given for example by rocket motors, thrusters, scramjets, ramjets and turbojets. The efficiency of those systems depends strongly on the expansion nozzles used. Besides the conventional rocket motor or thruster nozzles, the airbreathing propulsion systems of hypersonic spacecraft require new concepts for expanding the gas exhausting from the combustion chamber (e.g.: free expansion nozzles). One of the major tasks for the development of such hypersonic space transportation systems is the integration of the propulsion system in the cell of that spacecraft. The air intake and the free expansion nozzle affect not only the efficiency of the engine but also severely the forces and moments of the complete spacecraft. This makes it necessary to know in detail the flow behaviour through these devices and their interaction with the external flow field.

An advanced concept of a rocket motor nozzle considers the injection (in the expansion part of the nozzle) of turbine exhaust gases tangential to the nozzle contour in order to utilize the cooling effect of the gas (film-cooling of the nozzle wall) and to increase the thrust. In the afore-mentioned cases real gas effects cannot be neglected and have to be accounted for. If various gases interact

with each other having completely different equations of thermodynamic state, the numerical description of such flow fields is complicated because the location of the shear layer (inviscid approach) or the mixing zone (viscous approach) are a priori not known. In inviscid flow one possibility to overcome this problem consists in to fit the shear layer, which means that one has to employ time-dependent grids. This strategy will be followed here and examples (considering real gas effects in chemical and thermal equilibrium) will be discussed in this paper. Hypersonic windtunnel (shock tubes, vacuum tunnels) are mainly working with conical nozzles. The flow quality in such nozzles which is affected by the evolution of the boundary layer and the real gas effects will be investigated, too.

The goal of this paper is to

- present different nozzle concepts
- describe the theoretical tools developed to compute the flow fields through the various nozzles
- discuss the results.

2 Thermodynamic Formulation

Euler and 2.order boundary layer methods are applied in order to calculate the various flow fields. These methods are formulated considering equilibrium real gas effects. In thermodynamic equilibrium there exist two independent variables. Two equations are necessary combining the four variables p (pressure), ρ (density), T (temperature) and ϵ (internal energy per unit mass). These equations are the caloric and the thermal equations of state. The thermal equation of state for real gas can be written as

$$p = \rho RT \cdot Z(\rho, T) \quad (1)$$

Z : compressibility factor

R : specific gas constant per unit mass

For non-dissociating and non-ionizing gases one has $Z \approx 1$ if the pressure is low enough that van-der-Waals effects are not important. In this case the thermal equation of state for thermally ideal gas can be applied:

$$p = \rho RT \quad (2)$$

The caloric equation of state connects the internal energy ϵ per unit mass to the density and temperature and can be written in general as

$$\epsilon = \epsilon(\rho, T) \quad (3)$$

in a dilute non-dissociating and non-ionizing gas the energy does not depend on the density and one has

$$\begin{aligned} \epsilon &= \epsilon(T) \\ \epsilon(T) &= \int c_v(T) dT + \text{const} \\ c_v(T) &: \text{specific heat at constant volume} \end{aligned} \quad (4)$$

Below 500°C the specific heat in air is independent of the temperature

$$\begin{aligned} c_v &= 5/2R \\ \epsilon &= c_v T \end{aligned} \quad (5)$$

and air behaves as thermally and calorically ideal gas (perfect gas). Above 500°C molecular vibration can be excited, leading to a temperature dependence of c_v .

The thermal and caloric equations of state can be combined to give the desired expression connecting the pressure with density and energy

$$p = \rho RT(\rho, \epsilon) Z(\rho, \epsilon) \quad (6)$$

The speed of sound is defined by

$$c^2(\rho, \epsilon) = \left(\frac{\partial p}{\partial \rho} \right)_\epsilon = \frac{\left(\frac{\partial h}{\partial \rho} \right)_\epsilon}{\frac{1}{\rho} - \left(\frac{\partial h}{\partial \epsilon} \right)_\epsilon} \quad (7)$$

$$\begin{aligned} h &= \epsilon + p/\rho, & h &: \text{specific enthalpy} \\ s &: \text{specific entropy} \end{aligned}$$

With the definition eq. 7 the speed of sound can be expressed by any two independent thermodynamic variables for example the density ρ and the internal energy ϵ which are governing variables in the fluiddynamic equations

$$c^2(\rho, \epsilon) = \frac{p}{\rho^2} \left(\frac{\partial p}{\partial \epsilon} \right)_\rho + \left(\frac{\partial p}{\partial \rho} \right)_\epsilon \quad (8)$$

For perfect gas the speed of sound is given by

$$c^2 = \gamma p / \rho \quad (9)$$

with $\gamma = c_p/c_v$ the relation of specific heats. Various isentropic exponents can be defined which have their importance for different assumptions of the state of the gas.

- definition by the ratio of specific heats

$$\gamma = \frac{c_p}{c_v} = \frac{\left(\frac{\partial h}{\partial T} \right)_p}{\left(\frac{\partial h}{\partial T} \right)_v} = \frac{dh}{d\epsilon} = \frac{h}{\epsilon}$$

thermally ideal perfect gas

- definition by the speed of sound

$$\gamma_{eff1} = \frac{\partial(\ln p)}{\partial(\ln \rho)} \Big|_\epsilon = \frac{\partial h}{\partial \epsilon} \Big|_\epsilon = \frac{dh}{d\epsilon} = \frac{h}{\epsilon}$$

thermally ideal perfect gas

- definition by the internal energy

$$\gamma_{eff2} = 1 + \frac{p}{\rho \epsilon} = \frac{h}{\epsilon}$$

perfect gas

In the case of perfect gas all three definitions are identical. For thermally ideal gas γ and γ_{eff1} are still identical. For a completely real gas the definitions are quite different. In the latter case the most useful definition is the third one γ_{eff2} . The implementation of the state equation of real gases in equilibrium in an Euler method requires the knowledge of $p(\rho, \epsilon)$ and the derivatives $\left(\frac{\partial p}{\partial \rho} \right)_\epsilon$ and $\left(\frac{\partial p}{\partial \epsilon} \right)_\rho$ if the speed of sound is needed by the algorithm. The boundary layer equations require the determination of the viscosity and the heat conduction coefficient as a function of the internal energy ϵ and the density ρ as well as the derivatives of the temperature T with respect to ϵ and ρ , $\left(\frac{\partial T}{\partial \epsilon} \right)_\rho$ and $\left(\frac{\partial T}{\partial \rho} \right)_\epsilon$. For air the real gas description can be taken from Mollier - fit routines defined in [1] or from routines approximating the related dependent variables as a function of density and internal energy by the aid of bicubic splines [2]. For other mixtures of gases the equations of thermodynamic state were calculated by the computer code of Gordon & McBride [3], which contains also the equilibrium chemical kinetics of combustion.

3 Fluiddynamic Formulation

3.1 Euler Equations

The basic equations governing the inviscid flowfield describe the conservation of mass, momentum and energy. If one chooses the conservative variables

$$Q^T = (\rho, \rho u, \rho v, \rho w, e),$$

these equations can be written in the divergence form

$$\frac{\partial Q}{\partial t} + \frac{\partial F}{\partial x} + \frac{\partial G}{\partial y} + \frac{\partial H}{\partial z} = 0 \quad (10)$$

$$F^T = (\rho u, \rho u^2 + p, \rho uv, \rho uw, u(e + p))$$

$$G^T = (\rho v, \rho uv, \rho v^2 + p, \rho vw, v(e + p))$$

$$H^T = (\rho w, \rho uw, \rho vw, \rho w^2 + p, w(e + p))$$

ρ : density

u, v, w : cartesian velocity components

e : total energy per unit of volume

p : static pressure

This system of equations is closed by a relation between the pressure and the dependent variables Q , which has to be derived from the thermodynamic equation of state. The total energy is defined by

$$e = \rho \epsilon - \frac{1}{2}(\rho(u^2 + v^2 + w^2)) \quad (11)$$

and for a perfect gas one obtains the familiar result for the pressure

$$p = (\gamma - 1)(e - \frac{1}{2}\rho(u^2 + v^2 + w^2))$$

For an equilibrium real gas eq. 6 is applied. In practice the full equilibrium Euler code with the equation of state approximated by the methods, mentioned in section 1, needs approximately 25 % more computer time than the corresponding perfect gas code. The general strategy is to integrate the Euler equations by applying a split-matrix method [4,5,6]. Therefore eq. 10 is rewritten in

a quasi-conservative form (quasi-linear, conservative variables) and then transformed to a generalized curvilinear time-dependent coordinate system (ξ, η, ζ, τ) . In three dimensions one obtains

$$\frac{\partial Q}{\partial \tau} + \mathcal{J} \frac{\partial Q}{\partial \xi} + \mathcal{K} \frac{\partial Q}{\partial \eta} + \mathcal{L} \frac{\partial Q}{\partial \zeta} = 0 \quad (12)$$

with

$$\begin{aligned} \xi &= \xi(x, y, z, t); & \eta &= \eta(x, y, z, t); \\ \zeta &= \zeta(x, y, z, t); & \tau &= t \end{aligned}$$

and

$$\begin{aligned} \mathcal{N} &= j n_x + k n_y + l n_z + n_t \\ \mathcal{N} &=: (\mathcal{J}, \mathcal{K}, \mathcal{L}) \text{ for } n = (\xi, \eta, \zeta) \\ j &= \frac{\partial F}{\partial Q}; \quad k = \frac{\partial G}{\partial Q}; \quad l = \frac{\partial H}{\partial Q} \end{aligned}$$

The quasilinear form eq. 12 can be derived for any set of dependent variables Q . If conservative variables with $Q^T = (\rho, \rho u, \rho v, \rho w, e)$ are selected eq. 12 is called quasi-conservative. The shock capturing capability of this formulation is excellent what has been demonstrated in [6] with the exception of strong hypersonic shocks. The matrices \mathcal{N} in eq. 12 for perfect gas can be found in [7] for time independent grids. For time dependent grids, which are necessary using fitting procedures, either for shocks or shear layers, the term $n_t \cdot I$ (I = identity matrix) has to be added to \mathcal{N} . To deal with a general equation of state to take into account equilibrium real gas effects, one has to rederive the Jacobians \mathcal{N} of the flux vectors. Applying eq. 11 one gets for the generalized Jacobian \mathcal{N} [6]

$$\mathcal{N} = \begin{pmatrix} 0 & n_x & n_y \\ n_x \Phi_R - u \Theta_n & n_x u(1 - \bar{p}_e) + \Theta_n & n_y u - n_x v \bar{p}_e \\ n_y \Phi_R - v \Theta_n & n_x v - n_y u \bar{p}_e & n_y v(1 - \bar{p}_e) + \Theta_n \\ n_z \Phi_R - w \Theta_n & n_x w - n_z u \bar{p}_e & n_y w - n_z v \bar{p}_e \\ (\Phi_R - \frac{e+p}{\rho}) \Theta_n & n_x \frac{e+p}{\rho} - \Theta_n u \bar{p}_e & n_y \frac{e+p}{\rho} - \Theta_n v \bar{p}_e \end{pmatrix} + \begin{pmatrix} n_x & 0 \\ n_x u - n_x w \bar{p}_e & n_x \bar{p}_e \\ n_x v - n_y w \bar{p}_e & n_y \bar{p}_e \\ n_x w(1 - \bar{p}_e) + \Theta_n & n_z \bar{p}_e \\ n_x \frac{e+p}{\rho} - \Theta_n w \bar{p}_e & \Theta_n(1 + \bar{p}_e) \end{pmatrix} + n_t \cdot I$$

with

$$\begin{aligned} \bar{p}_e &= \frac{1}{\rho} \left(\frac{\partial p}{\partial e} \right)_\rho \\ c_R^2 &= \frac{p}{\rho \bar{p}_e} + \left(\frac{\partial p}{\partial \rho} \right)_e \\ \Phi_R &= \bar{p}_e (u^2 + v^2 + w^2 - \frac{e+p}{\rho}) + c_R^2 \\ \Theta_n &= n_x u + n_y v + n_z w \end{aligned}$$

where c_R is the speed of sound for equilibrium real gases. In the perfect gas limit one has

$$\begin{aligned} \bar{p}_e &= (\gamma - 1) \\ c_R^2 &= \gamma \frac{p}{\rho} \\ \Phi_R &= \frac{\gamma - 1}{2} (u^2 + v^2 + w^2) \end{aligned}$$

The scheme used for the integration of the Euler equations is based on the split matrix algorithm [4,5]. For that the Jacobian \mathcal{N} has to be diagonalized and then split according to the sign of the eigenvalues. The eigenvalues of the Jacobians are given by

$$\begin{aligned} \lambda_{1,2,3} &= U_n \\ \lambda_4 &= U_n + c_R |\nabla n| \\ \lambda_5 &= U_n - c_R |\nabla n| \end{aligned} \quad (14)$$

where

$$U_n = \bar{\Theta}_n + n_t, \quad |\nabla n| = (n_x^2 + n_y^2 + n_z^2)^{1/2}; \quad n = (\xi, \eta, \zeta)$$

$$\bar{\Theta}_n = \Theta_n / |\nabla n|$$

For the three dimensional case the left and right hand eigenvectors arranged in the matrices T_n, T_n^{-1} can be found in [6,8]. The similarity transformation is then given by

$$\begin{aligned} \mathcal{N} &= T_n \Lambda_n T_n^{-1} \\ \Lambda_n &= \text{diag}(\lambda_1, \lambda_2, \lambda_3, \lambda_4, \lambda_5). \end{aligned} \quad (13)$$

The Jacobian \mathcal{N} has the threefold eigenvalue $\lambda_{1,2,3} = U_n$. Supposed the rank of \mathcal{N} is fully decreased the corresponding eigenvectors have three free components which have to be chosen such that they are linear independent with each other. In three dimensions the choice of the related eigenvectors with respect to the references [6,7,8] is appropriate, but a reduction of these eigenvector matrices to two dimensions (plane or axisymmetric flows) leads to linear dependent eigenvectors for the corresponding twofold eigenvalues $\lambda_{1,2}$.

Nozzle flows are often 2-D or axisymmetric. Therefore another, more suitable choice of the eigenvector matrices \tilde{T}_n and \tilde{T}_n^{-1} in two dimensions has to be made

$$\tilde{T}_n = \begin{pmatrix} 1 & 0 & 1 \\ u & \tilde{n}_y & u + c_R \tilde{n}_x \\ v & -\tilde{n}_x & v + c_R \tilde{n}_y \\ \frac{e+p}{\rho} - \frac{c_R^2}{\bar{p}_e} & u \tilde{n}_y - v \tilde{n}_x & \frac{e+p}{\rho} + c_R(u \tilde{n}_x + v \tilde{n}_y) \end{pmatrix}$$

$$\tilde{T}_n^{-1} = \begin{pmatrix} 1 - \Phi_R & \frac{u \bar{p}_e}{c_R} & \frac{v \bar{p}_e}{c_R} & -\frac{\bar{p}_e}{c_R} \\ -(u \tilde{n}_y - v \tilde{n}_x) & \tilde{n}_y & -\tilde{n}_x & 0 \\ \frac{\Phi_R - (u \tilde{n}_x + v \tilde{n}_y)}{2c_R} & \frac{c_R \tilde{n}_x - u \bar{p}_e}{2c_R} & \frac{c_R \tilde{n}_y - v \bar{p}_e}{2c_R} & \frac{\bar{p}_e}{2c_R} \\ \frac{\Phi_R (u \tilde{n}_x + v \tilde{n}_y)}{2c_R} & \frac{-c_R \tilde{n}_x - u \bar{p}_e}{2c_R} & \frac{-c_R \tilde{n}_y - v \bar{p}_e}{2c_R} & \frac{\bar{p}_e}{2c_R} \end{pmatrix} \quad (15)$$

$$\Phi_R = \bar{p}_e (u^2 + v^2 - \frac{e+p}{\rho}) + c_R^2; \quad \tilde{n}_i = n_i / |\nabla n|$$

For axisymmetric flows (x, y) have to be replaced by the cylindrical coordinates (z, r) and the curvature terms

$$H^T = \frac{1}{r} (\rho v, \rho v v, \rho v^2, (e+p)v)$$

have to be added to eq. 12, while $\frac{\partial}{\partial \zeta} \equiv 0$.

3.2 Numerical Algorithm

The general idea of every flux vector splitting or split-matrix method is to discretize the spatial derivatives with regard to the direction of the characteristic wave propagation. For a one-dimensional consideration the region of influence changes with the sign of the eigenvalues of the related jacobian matrix. Therefore the Jacobian \mathcal{N} is split according to the sign of the eigenvalues of Λ_n yielding

$$\mathcal{N} = T_n(\Lambda_n^+ + \Lambda_n^-)T_n^{-1} \equiv \mathcal{N}^+ + \mathcal{N}^- \quad (16)$$

with

$$\Lambda_n^\pm = \frac{1}{2}(\Lambda_n \pm |\Lambda_n|).$$

Eq. 12 becomes for the three-dimensional problem

$$\begin{aligned} \frac{\partial Q}{\partial \tau} + \mathcal{J}^+ \frac{\partial Q}{\partial \xi} + \mathcal{J}^- \frac{\partial Q}{\partial \xi} + \mathcal{K}^+ \frac{\partial Q}{\partial \eta} + \mathcal{K}^- \frac{\partial Q}{\partial \eta} \\ + \mathcal{L}^+ \frac{\partial Q}{\partial \zeta} + \mathcal{L}^- \frac{\partial Q}{\partial \zeta} = 0 \end{aligned} \quad (17)$$

The space derivatives of Q are discretized using third order accurate upwind-biased formulas [9]

$$\begin{aligned} Q_n^+ &= \frac{1}{6\Delta n}(Q_{m-2} - 6Q_{m-1} + 3Q_m + 2Q_{m+1}) \\ Q_n^- &= -\frac{1}{6\Delta n}(Q_{m+2} - 6Q_{m+1} + 3Q_m + 2Q_{m-1}) \end{aligned} \quad (18)$$

The formula is unconditionally stable as long as no shocks are present in the flowfield. To prevent oscillations near shock waves a non-linear artificial diffusion term d of MacCormack type is added

$$\begin{aligned} d &= d_\xi + d_\eta + d_\zeta \\ d_n &= \alpha_n \Delta n^3 (|U_n| + c_R) \frac{\partial}{\partial n} \left[\frac{1}{4p} \frac{\partial^2 p}{\partial n^2} \frac{\partial Q}{\partial n} \right] \\ \alpha_n &\approx 0.5 \\ n &:: (\xi, \eta, \zeta) \end{aligned} \quad (19)$$

In [10] a systematic study of three step time stepping schemes in conjunction with different kinds of upwind space discretisation has been conducted. The iterative Runge-Kutta scheme for the stepping from time level (n) to time level $(n+1)$ has the general form [11]

$$\begin{aligned} Q^{(0)} &= Q^n \\ Q^{(1)} &= Q^n - a_1 \Delta t \mathcal{P}(Q^n) \\ Q^{(2)} &= Q^n - a_2 \Delta t \mathcal{P}(Q^{(1)}) \\ Q^{(3)} &= Q^n - a_3 \Delta t \mathcal{P}(Q^{(2)}) \\ Q^{(n+1)} &= Q^{(3)} \end{aligned} \quad (20)$$

where the operator \mathcal{P} contains the space derivatives and the diffusion terms. An advantage of the iterative Runge-Kutta schemes is that only one intermediate set of flow variables has to be stored in addition to the time levels Q^n and Q^{n+1} . A linear investigation of eq. 20 shows that the scheme is third order accurate in time if the coefficients are chosen $a_1 = 1/3$; $a_2 = 1/2$; $a_3 = 1$. Considering non-linear effects the time accuracy of the scheme cannot increase beyond second order and a von Neumann stability analysis, performed at a one-dimensional test equation, has yielded that the optimal stability region is achieved for $a_1 = 0.275$; $a_2 = 1/2$; $a_3 = 1$ allowing a maxi-

mum value of the CFL number ($CFL = u\Delta t/\Delta x$) of $CFL = 1.75$ [10].

3.3 Boundary Conditions

For subsonic and supersonic inflow and outflow boundaries characteristic compatibility relations based on one-dimensional characteristic equations are employed. At the wall boundary, the flow is normally directed towards the wall and consequently all characteristics except one are included in the prediction step. The resulting flow values Q^* do not satisfy the boundary condition

$$\begin{aligned} (\vec{\mu} \cdot Q^*) &= 0 \\ \vec{\mu} &= (0, n_x, n_y, n_z, 0)^T / |\nabla n| \end{aligned}$$

and have to be corrected using the eigenvector \vec{t}_i corresponding to the characteristic directed away from the body

$$\begin{aligned} Q &= Q^* - \beta \vec{t}_i \\ \beta &= (\vec{\mu} \cdot Q^*) / (\vec{\mu} \cdot \vec{t}_i) \end{aligned} \quad (21)$$

As mentioned in the introduction in some nozzle concepts various gases with quite different thermodynamic equations of state interact with each other. In inviscid flows a shear layer or contact streamsurface (in 2-D a streamline) separates the regions of different gases (inviscid approach \rightarrow no diffusion). But the location of this contact surface is a priori not known and will be part of the solution. For the calculations discussed in this paper the shear layers are fitted by aligning a coordinate surface (here the $n = \text{const}$ surface) to that layer using the appropriate one-dimensional characteristic variables on both sides of the layer and utilizing the condition that the pressure has to be continuous. For the two-dimensional case the derivation of the conditions will be given below

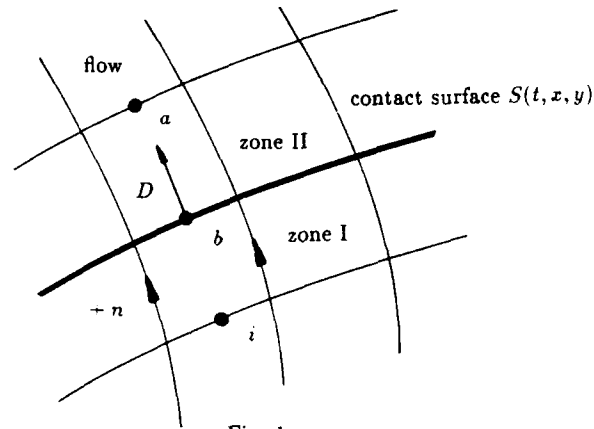


Fig. 1

Using the one-dimensional, non-conservative characteristic variables employed for subsonic inflow conditions from zone I into zone II (Fig. 1) one gets the relations $[7]$ (for a conservative formulation see [12])

$$\begin{aligned} p_b &= \frac{1}{2}(p_a + p_i - 2\rho_0 c_0(\tilde{n}_x(u_a - u_i) + \tilde{n}_y(v_a - v_i))) \\ u_b &= u_a - \tilde{n}_x \frac{p_a - p_b}{\rho_0 c_0} \\ v_b &= v_a - \tilde{n}_y \frac{p_a - p_b}{\rho_0 c_0} \end{aligned} \quad (22)$$

\circ denotes a reference state

Combining these three equations under the assumption that the contravariant velocity component $U_b = n_a u_b + n_b v_b = D$ ($U_a \equiv -U_i$) has to be vanished in the limit $t \rightarrow \infty$ (D denotes the normal velocity of the contact surface $S(t, x, y)$) one obtains

$$D = \frac{p_i - p_a}{2\rho_0 c_0} |\nabla n| \quad (23)$$

Further it is

$$\frac{\partial S}{\partial t} = D |\nabla S| \quad (24)$$

The contact surface coincides with the coordinate surface $n = \text{const} = n_{\text{sup}}$. In the computational space (τ, ξ, η) the point distributions along the arc length of the n -coordinates ($n = \xi, \eta$) is defined by

$$R(\tau, \xi, \eta) = \Psi(\xi) F(\tau, \eta) \quad (25)$$

with

$$0 \leq \Psi(\xi) \leq 1$$

$$0 \leq \xi \leq 1$$

$$R(\tau, 1, \eta) = F(\tau, \eta)$$

$F(\tau, \eta) =$: contour function of the contact surface in the computational space.

The time derivative of the contour function $F(\tau, \eta)$ is then given by

$$F_\tau = D |\nabla \xi| F \Psi_\xi \quad (26)$$

The final position of the time-dependent grid will be reached for $D \rightarrow 0$ when the contact surface S agrees with the contour function F .

3.4 Boundary Layer Equations

In flow regions where weak viscous-inviscid interactions occur (flows without separation) the concept of matching Euler and boundary layer methods can be applied for the calculation of viscous drag and thermal loads at the wall. For the flow fields discussed in this paper a second order boundary layer method formulated for equilibrium real gases is used. The three-dimensional second order boundary layer equations are derived by an order of magnitude analysis of the terms of the Navier-Stokes equations whereas -besides the terms of order one- the terms of order $\text{Re}^{-1/2}$ are retained, too. The second order terms are mainly related to curvature effects. Curvature plays an important role in the boundary layer development when locally the boundary layer thickness is not small compared to the smallest radius of curvature of the body surface. Centrifugal forces produce a pressure gradient normal to the body surface, which means that the related terms in the momentum equation normal to the wall do not vanish in the second order theory. The references [13,14,15] describe the details of the second order boundary layer theory.

The second order, three-dimensional boundary layer equations formulated in locally monoclinic surface oriented coordinates (perfect gas) employing tensorial notation including the summation convention have the form [13]

continuity:

$$(\sqrt{a} M \rho v^a)_{,a} + \sqrt{a} (M \rho v^3)_{,3} = 0 \quad (27)$$

x^1 - and x^2 - momentum equations ($\alpha = 1, 2$):

$$\rho(v^a_{,3} v^3 + v^a_3 v^3 + \Gamma^a_{\gamma\beta} v^\gamma v^\beta - 2\Lambda^a_{\delta} b^{\delta}_3 v^3 v^3) = -g^{\alpha\beta} p_{,\beta} + ((\mu v^a_{,3})_{,3} - 2\Lambda^a_{\gamma} b^{\gamma}_3 \mu v^{\delta}_{,3} - \Lambda^{\delta}_3 b^{\gamma}_3 \mu v^{\delta}_{,3}) / \text{Re} \quad (28)$$

x^3 - momentum equation (wall normal direction):

$$M^{\delta}_a b^{\delta}_3 \rho v^{\gamma} v^{\gamma} = -p_{,3} \quad (29)$$

energy:

$$\rho c_p (v^a T_{,a} + v^3 T_{,3}) - \text{Ec} (v^a p_{,a} + v^3 p_{,3}) = \frac{\text{Ec}}{\text{Re}} g_{\alpha\beta} \mu v^{\alpha}_{,3} v^{\beta}_{,3} + ((k T_{,3})_{,3} - \Lambda^a_{\gamma} b^{\gamma}_3 k T_{,3}) / \text{PrRe} \quad (30)$$

$\rho, v^a, v^3, p, T, c_p, \mu$ denote density, contravariant components of the velocity vectors in x^a and x^3 direction, pressure, temperature, specific heat at constant pressure and the viscosity coefficient; $k = \mu c_p / \text{Pr}$ thermal conductivity.

Greek letters have the values 1 or 2.

$\sqrt{a}, g^{\alpha\beta}, g_{\alpha\beta}, b^{\alpha}_3, b_{\alpha 3}, M^{\alpha}_3, M, \Gamma^{\alpha}_{\beta\gamma}$ are metric and curvature quantities (see [15]).

The quantities $\text{Re}, \text{Pr}, \text{Ec}$, are the Reynolds, Prandl and Eckert numbers defined in the usual way [13].

The underlined terms in eqs. (27)-(30) are the second order terms which are low or even vanish if the curvature of the surface is very small compared with the boundary layer thickness. The set of equations for the three-dimensional equilibrium real gas case can be found in [16]. Because most of the nozzle flow fields are two-dimensional or axisymmetric a reduced form of the second order boundary layer equations is used. For the axisymmetric case one obtains from eqs. (27)-(30) with

$$v^2 = 0; \quad \frac{\partial v^2}{\partial x^2} = 0; \quad \frac{\partial a}{\partial x^2} = 0 \quad (\text{equilibrium real gas})$$

continuity:

$$(\sqrt{a} M \rho v^1)_{,1} + \sqrt{a} (M \rho v^3)_{,3} = 0 \quad (27a)$$

x^1 - momentum equation:

$$\rho(v^1_{,1} v^1 + v^1_3 v^3 + \Gamma^1_{11} v^1 v^1 + 2\text{Re}^{-1/2} \Gamma^1_{31} v^1 v^3) = -g^{11} p_{,1} + (\mu v^1_{,3})_{,3} + \text{Re}^{-1/2} (3\Gamma^1_{31} + \Gamma^2_{32}) \mu v^1_{,3} \quad (28a)$$

x^3 - momentum equation (wall normal direction):

$$\rho \text{Re}^{-1/2} \Gamma^3_{11} v^1 v^1 = -p_{,3} \quad (29a)$$

energy:

$$\rho(v^1 \epsilon_{,1} + v^3 \epsilon_{,3}) - \text{Ec} \gamma p \rho^{-1} (v^1 \rho_{,1} + v^3 \rho_{,3}) =$$

$$\text{Ec} \gamma \mu g_{11} v^1_{,3} v^1_{,3} + \gamma \text{Pr}^{-1} [k(T_{,e} \epsilon_{,33} + T_{,e} \rho_{,33} + T_{,e3} \epsilon_{,3} +$$

$$T_{,e3} \rho_{,3} + \text{Re}^{-1/2} (\Gamma^1_{31} + \Gamma^2_{32}) k T_{,3} + k_{,3} T_{,3}] \quad (30a)$$

γ and ϵ denote the ratio of specific heats of the freestream and the internal energy. In the case of plane 2-D flow the Cristoffel symbols Γ_{32}^2 vanish (see [17]).

The boundary layer equations are of parabolic type and will be integrated by using a space-marching procedure. The discretisation is done employing a Crank - Nicolson scheme. The coupling of the Euler and the boundary layer solutions is carried out by calculating an equivalent source distribution from the boundary layer results, with which the displacement effects of the boundary layer itself is simulated in the Euler calculations. At the outer edges of the boundary layers the profiles of the velocities and the thermodynamic variables are used as boundary conditions of that boundary layers. Further details of the integration and coupling procedure may be found in [13, 16, 17].

4 Results

First an overview will be given about the different nozzle flows to be considered here. For axisymmetric nozzles (e.g. HM60 and HM60 with injection of turbine exhaust gases) the main interest from the project side consists in the determination of the thrust and the efficiency coefficient. In the case of windtunnel nozzles (shock tube, vacuum windtunnel) the quality of the flow at the nozzle exit will be mainly considered. Strong interactions between nozzle flows and external air flows take place at free expansion nozzles. Two examples of such nozzles (a plane and a plug nozzle) will be considered here, where the objective of the investigations is to learn something about the flow field phenomena and the thrust, the thrust angle and the efficiency coefficient of such nozzles. The quality of the predictions depends on the aerodynamical and thermodynamical model equations used. Therefore for some cases the influence of the boundary layer and the equilibrium real gas effects on the flow topology and above-mentioned global values are studied.

The first example is an axisymmetric nozzle where the influences of the equilibrium real gas effects and the boundary layer on the flow pattern and the thrust are investigated. As one can see in Fig. 2 the flow field contains a recompression zone (or weak shock wave) which is due to the change of wall curvature from convex to concave. The position of this recompression zone depends strongly on the thermodynamic state of the gas. The variations are shown in the Figs. 2a, 2c, 2e where in the first two plots perfect gas with $\gamma = 1.4$ and $\gamma = 1.17$ has been assumed. The solution using the equilibrium real gas assumption (Fig. 2e) lies in between. The thrust for the $\gamma = 1.4$ case has the value 1045.9 [KN] while for $\gamma = 1.17$ the thrust is 1172.7 [KN]. Assuming equilibrium real gas the thrust amounts to 1103.8 [KN]. This means that there exists a severe dependency of the thrust on the thermodynamic state of the gas [18].

Solutions of the Euler and boundary layer method (turbulent flow), in a closed coupled version [17], are shown for $\gamma = 1.4$ (Fig. 2b) and $\gamma = 1.17$ (Fig. 2d). The differences in the flow pattern between the pure inviscid (Figs. 2a, 2c) and the viscous solutions (Figs. 2b, 2d) are small, except in the region of the boundary layer itself. The viscous effects diminish the thrust only slightly. The deviations are of order 1/2 %.

An extended configuration of the HM60 contour is considered in Fig. 3. The goal of this investigation is cooling the wall (film-cooling principle) with an gas tangentially injected in the expansion part of the nozzle. As already mentioned in section 3.3 the flow consists of two gases with quite different thermodynamic equations of state. In the inviscid case the contact surfaces (shear layers) are fitted with the procedure described in section 3.3. Fig. 3a shows the Euler reference solution without gas injection.

The gas is a mixture of hydrogen/oxygen with a prescribed ratio of components. Fig. 3b shows the two block grid for the flow situation with gas injection. The gas to be injected has a fixed static pressure. The Fig. 3c shows the inviscid flow field when the static pressure of the expanding gas, coming from the combustion chamber, coincide, while doubling the static pressure of the injected gas leads to a perturbation of the flowfield (the main flow has to change its direction) which is clearly shown in Fig. 3d. The injection of the gas leads to an increase of the thrust which is proportional to the increase of the mass flux.

Modern concepts of hypersonic spacecrafts have an air-breathing propulsion system which is highly integrated in the cell of that spacecraft. This means that the flow through the expansion nozzle (the same is valid for the air intake) interacts with the external airflow around the spacecrafts and influences very strongly the forces and moments of the complete spacecraft. In the Figures 4 and 5 a plane nozzle and a plug nozzle concept will be investigated. A three block grid is used in the case of the nozzle in order to deal with the external leeward - windward and nozzle flow (Fig. 4a). The calculations have been carried out employing perfect gas with a ratio of specific heats $\gamma = 1.27$ and equilibrium real gas as well. In the latter case it is assumed that γ is only a function of the

temperature alone for both gases (the external air and the combusted gas) and that the chemical degrees of freedom are frozen. This means that only vibrational excitations are considered. Fig. 4b shows that under these assumptions the curves describing the thermodynamic equation of state of the two gases can be matched together [19]. The Figs. 4c and 4d, where the isolines of Machnumbers are plotted for the perfect gas $\gamma = 1.27$ and the equilibrium real gas case, show clearly the shock waves which are due to the displacement of the external airflow through the expanded nozzle gas and the contact surfaces (shear layers) which separate the various gases from one another. The flow pattern in both cases looks not so different and the calculated quantities of the thrust are very similar. This implies that the γ value selected in the perfect gas case, is a good approximation of the thermodynamics of this flow. For completeness Fig. 4e shows the pressure distribution where further shock waves can be detected, created inside the nozzle owing to rapid changes of the curvature.

The plug nozzle is a complicated nozzle concept, where the position of the plug controls the state of the engine. The nozzle part is usually axisymmetric and the free-expansion surface evolves in the aft part to a plane surface. In general a complete three-dimensional calculation is necessary for solving this problem. In order to study the generating flow phenomena both an axisymmetrical and a plane calculation of the flow through such a nozzle configuration are carried out using the Euler equations with a perfect gas assumption (Figs. 5a, 5b) [20]. In the plane case where the displacement effects by the plug is much stronger than in the axisymmetric case the shock waves and shear layers are more pronounced. Adding the interaction of the external windward airflow to the nozzle flow leads to so complicated flow fields as they can be seen in Figs. 5c and 5d. As it is well known from other calculations (e.g.: the backward facing step) the Euler methods are able to predict flow separations which is true also here at the plug contour where the curvature has its largest value. There is no doubt that Navier-Stokes solutions would predict flow separation at the afore-mentioned position, too. The remaining question is how compare the topology of the separation and the influence of the viscous effects of the flow the governing flow quantities in the Euler and the Navier-Stokes calculations.

The reliability of windtunnel experiments depends considerably on the flow quality at the exit of the wind tunnel nozzles. The design goal for such nozzles is to obtain a flowfield which is as homogeneous as possible. Here flow field calculations through a nozzle of a high enthalpy shock tube are presented. Fig. 6a shows the Euler grid used. For a perfect gas with $\gamma = 1.17$ the Fig. 6b shows the inviscid result $M_{exit} = 5.0$ and in Fig. 6c the inviscid/viscous result obtained by an Euler / second order boundary layer solution [17] is plotted. As one is aware the turbulent boundary layer is relatively thick and leads to an reduced Machnumber $M_{exit} = 4.9$ in the inviscid core flow in the nozzle exit plane. Considering equilibrium real gas effects the nozzle flow fields for vessel conditions stipulated to $T_0 = 5180[K]$ and $p_0 = 670[bar]$ are displayed in Figs. 6d and 6e. While in Fig. 6d the isolines of Machnumbers of the inviscid flow are shown, in Fig. 6e the inviscid/viscous (laminar) flow is presented. The laminar boundary layer thickness is much thinner than the turbulent one and the influence of the boundary layer on the flow pattern seems to be small.

5 Concluding Remarks

From the present computations it can be concluded that the influence of the viscous effects is much less than the one of the real gas effects. The high temperature of the gas coming from the combustion chamber and the strong expansion of it in the divergent part of the related nozzle leads in reality to some non-equilibrium effects which have to be accounted for in future investigations. On the other hand there are surely some flow situations which are completely three-dimensional and should be regarded as such. In the case of nozzle flow interactions with external airflow the viscous effects in the free mixing zone have to be investigated and the problem of considering different gases with different thermodynamic state has to be solved for the Navier-Stokes solutions.

6 References

- [1] Srinivasan S., Tannehill J.C., Weilmuenster K.J.: Simplified Curve Fits for the Thermodynamic Properties of Equilibrium Air, ISU-ERI-AMES-86401, Iowa State University, (1986).
- [2] Fischer J.: Entwicklung verbesserter Approximationen der Zustandsfunktion für atmosphärische Luft im thermochemischen Gleichgewicht, MBB/FE122/5-PUB/380, (1989).
- [3] Gordon, McBride.: NASA SP-273, (1976).
- [4] Chakravarthy S.R., Anderson D.A., Salas M.D.: The Split-Coefficient Method for Hyperbolic Systems of Gas Dynamic Equations, AIAA Paper 80-0268, (1980).
- [5] Weiland C.: A Split-Matrix Method for the Integration of the Quasi-Conservative Euler Equations, Notes on Numerical Fluid Dynamics, Vol.13, Vieweg, (1986).
- [6] Pfitzner M., Weiland C.: 3-D Euler Solutions for Hypersonic Mach Numbers, AGARD-CP 428, Paper No.22, (1987).
- [7] Whitfield D.L., Janus J.M.: Three-Dimensional Unsteady Euler Equations Solution Using Flux Vector Splitting, AIAA Paper 84-1552, (1984).
- [8] Weiland C., Hartmann G., Menne S., Pfitzner M., Schröder W.: Numerical Methods for Aerodynamic Design I Proceedings: Space Course on Low Earth Orbit Transportation and Orbit Systems, Volume III, Paper No.61. Aachen, March 1991.
- [9] Weiland C., Pfitzner M.: 3-D and 2-D Solutions of the Quasi-Conservative Euler Equations, Lecture Notes in Physics, Vol.264, Springer (1986) pp.654-659
- [10] Pfitzner M.: Runge-Kutta Split-Matrix Method for the Simulation of Real Gas Hypersonic Flows, Notes on Numerical Fluid Dynamics, Vol.24, Vieweg, (1988) pp.489-498
- [11] Turkel E., Van Leer B.: Flux Vector Splitting and Runge-Kutta Methods, Lecture Notes in Physics, Vol 218, Springer (1985) pp.566-570
- [12] Riedelbauch S., Weiland C.: Inviscid Laval Nozzle Flowfield Calculation, J.of Spacecraft and Rockets, Vol.25, No.1, (1988), pp. 88
- [13] Monnoyer F.: Calculation of Three-Dimensional Attached Viscous Flow on General Configurations Using Second-Order Boundary Layer Theory ZfW, Vol.14, 1990, pp.95-108.
- [14] Monnoyer F., Wanie K.M., Schmatz M.A.: Calculation of the Three-Dimensional Viscous Flow Past Ellipsoids at Incidence by Zonal Solutions Notes on Numerical Fluid Mechanics, Vol. 20, Vieweg, 1988, pp.229-238.
- [15] Monnoyer F.: The Effects of Surface Curvature on Three-Dimensional, Laminar Boundary Layers, Doctoral Thesis, Université libre de Bruxelles, (1985).
- [16] Mundt Ch., Pfitzner M., Schmatz M.A.: Calculation of Viscous Hypersonic Flows Using a Coupled Euler / Boundary Layer Method Notes on Numerical Fluid Mechanics, Vol. 29, Vieweg, 1990, pp.419-429.
- [17] Vilsmeier R.: Düsenströmung mit Grenzschichteffekten Diploma Thesis, University of Stuttgart, Report MBB-UK-0030-89, PUB=OTN-010426, (1989).
- [18] Hartmann G.: Berechnung von reibungsfreien Düsenströmungen DGLR - Paper No. 89-148, Jahrestagung der DGLR, Hamburg (1989).
- [19] Hermann O., Rick H.: Propulsion Aspects of Hypersonic Turbo-Ramjet Engines with Special Emphasis on Nozzle / Aft Body Interactions Proceedings: ASME - Turboexpo Conference, Orlando, USA, June (1991).
- [20] Hampel K.: Strömungen in einer freien Expansionsdüse Diploma Thesis, University of Munich, Report MBB-UK-0088-90, PUB=OTN-030718, (1990).

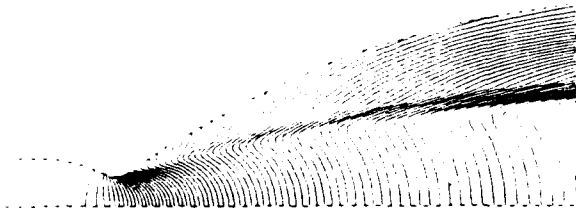
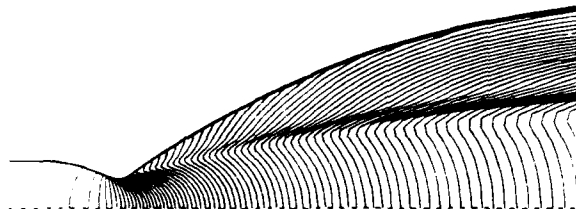
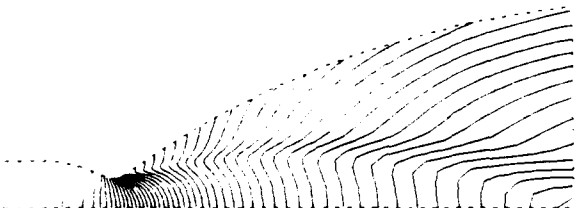
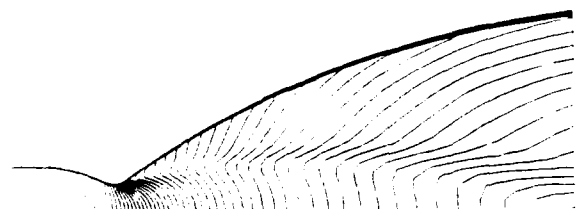
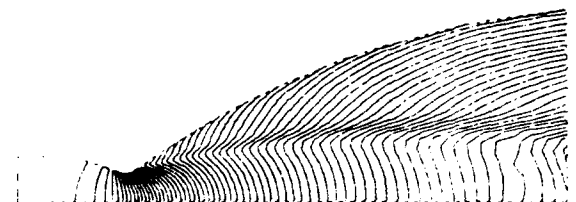
ACKNOWLEDGEMENT:

THE AUTHORS THANK DR.MONNOYER OF MBB MILITARY AIRCRAFT DIVISION FOR VERY HELPFUL DISCUSSIONS AND THE SUPPORT DURING THE ADJUSTMENT OF HIS BOUNDARY LAYER METHOD.

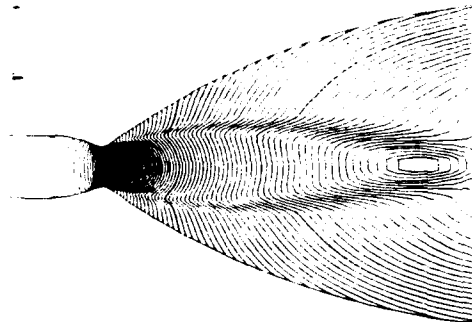
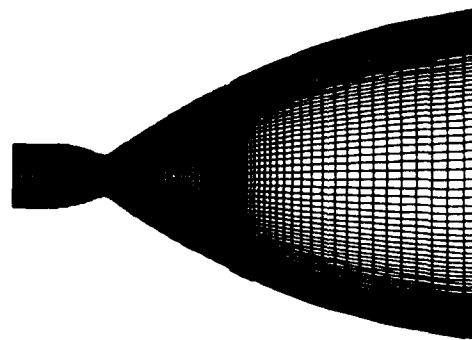
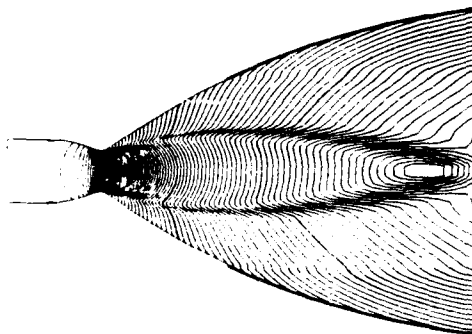
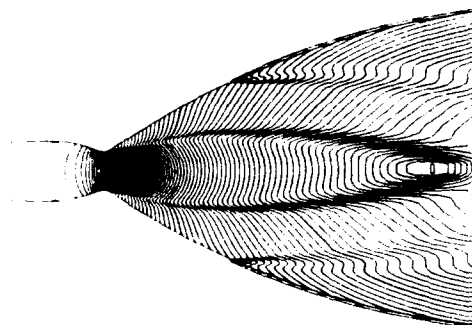
Rocket Motor Nozzle Flow

Lines of constant Machnumbers

HM60

 $p_{\text{envir.}} = 0 \text{ [Pa]}$, grid : (101x41) pointsFig. 2a Euler solution $\gamma = 1.4$ thrust = 1045.9 [kN]Fig. 2b Euler/ boundary layer (turbulent) solution
 $\gamma = 1.4$ thrust = 1040.8 [kN]Fig. 2c Euler solution $\gamma = 1.17$ thrust = 1179.2 [kN]Fig. 2d Euler/ boundary layer (turbulent) solution
 $\gamma = 1.17$ thrust = 1172.7 [kN]Fig. 2e Euler solution equilibrium real gas (air)
thrust = 1103.8 [kN]

HM60 Extension

Fig. 3a Euler solution equilibrium real gas
($H_2/LOX - MIX(O/F) = 7.09$) thrust = 1293.0 [kN]Fig. 3b Grid for Euler solution with turbine
exhaust gas (TEG) injection tangential to the wallFig. 3c Euler solution equilibrium real gas
($H_2/LOX - MIX(O/F) = 7.09$)
with TEG injection ($H_2/LOX - MIX(O/F) = 0.93$)
injection pressure 10^5 [Pa] thrust = 1316.0 [kN]Fig. 3d Euler equilibrium: real gas
($H_2/LOX - MIX(O/F) = 7.09$)
with TEG injection ($H_2/LOX - MIX(O/F) = 0.93$)
injection pressure $2 \cdot 10^5 \text{ [Pa]}$

Free - Expansion Nozzle (plane)
simulated freeflight $M_\infty = 6.8$

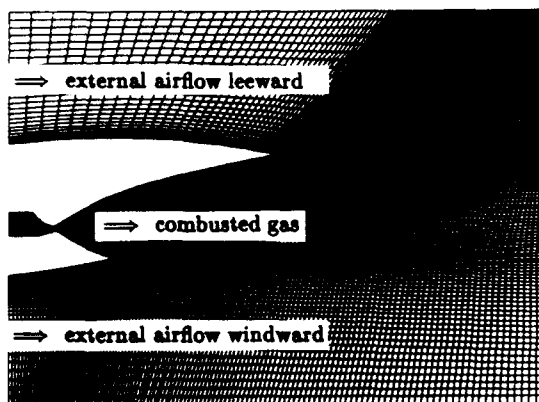


Fig. 4a Three block grid

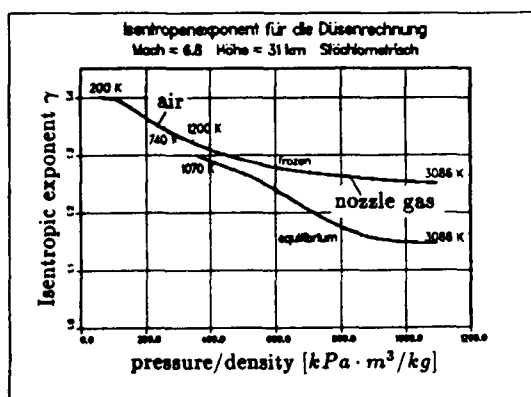


Fig. 4b Isentropic exponent γ

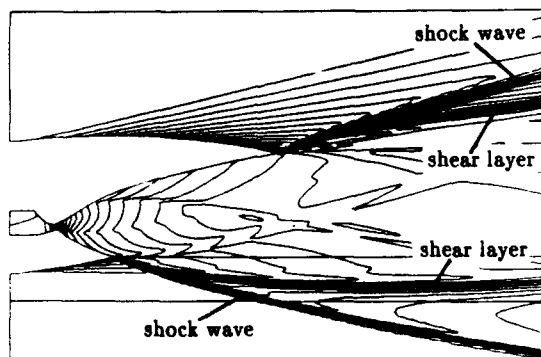


Fig. 4c Euler solution, perfect gas $\gamma = 1.27$
Machnumber distribution, thrust = 290.5 [KN/m]

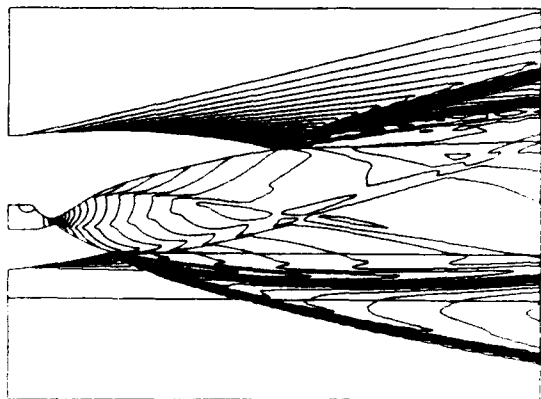


Fig. 4d Euler solution equilibrium real gas
Machnumber distribution, thrust = 288.8 [KN/m]

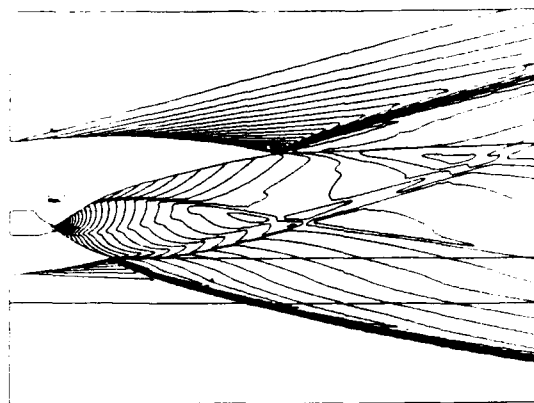


Fig. 4e Euler solution equilibrium real gas (air)
pressure distribution

Free - Expansion Nozzle (plug)
perfect gas; simulated freeflight $M_\infty = 3.5$

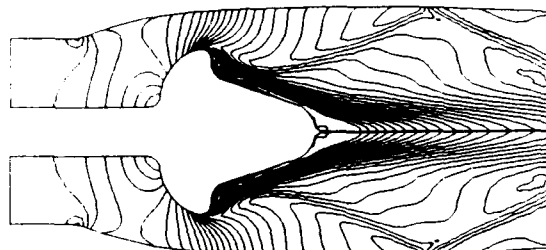


Fig. 5a Euler solution (axisym.)
Machnumber distribution, no external air flow

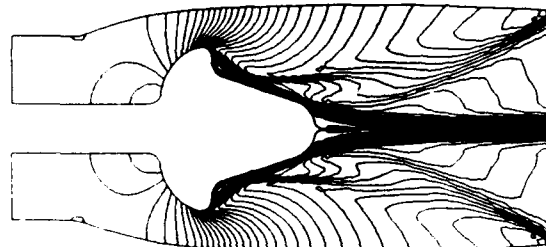


Fig. 5b Euler solution (plane)
Machnumber distribution, no external air flow

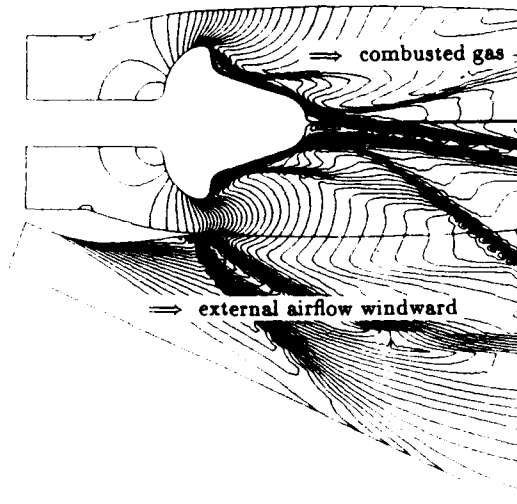


Fig. 5c Euler solution (plane)
Machnumber distribution, with external air flow

Shock Tube Nozzle

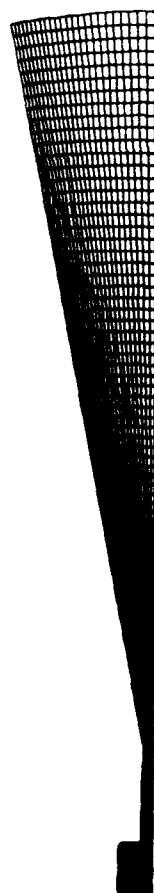


Fig. 6a Grid for Euler calculations

Shock Tube Nozzle

Lines of constant Machnumbers



Fig. 6d Euler solution, equilibrium real gas
 $T_v = 5180[K]$, $p_v = 670[\text{bar}]$, $\Delta M = 0.05$



Fig. 6e Euler / boundary layer solution(laminar),
equilibrium real gas
 $T_v = 5180[K]$, $p_v = 670[\text{bar}]$, $\Delta M = 0.05$

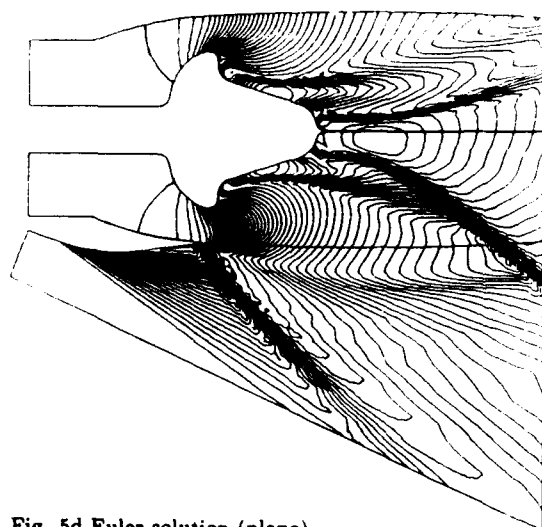


Fig. 5d Euler solution (plane)
pressure distribution, with external air flow

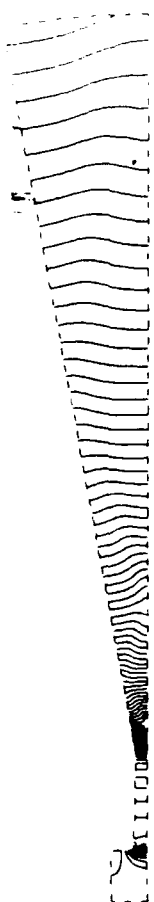


Fig. 6b Euler solution, perfect gas $\gamma = 1.17$, $\Delta M = 0.05$



Fig. 6c Euler / boundary layer solution(turbulent)
perfect gas $\gamma = 1.17$, $\Delta M = 0.1$

Discussion

R. WALTHER, MTU MÜNCHEN, GERMANY

With your plug nozzle example, I wonder about the strong gradient in Mach number distribution normal to the rearward plug contour (Figs. 5(a) to (c)). Can you comment on this feature?

AUTHOR'S REPLY

It has been well-known for a couple of years that the Euler equations may calculate flow separations in cases where strong curvatures in the surface contour occurs. This is due to the fact that in the limit when we have an edge in the contour, the geometrical singularity leads to the production of vorticity and the flow separates. In this case here the flow separates at the rearward edge of the plug creating a shear layer and reverse flow directions.

H. WEYER, DLR, COLOGNE, GERMANY

You mentioned three fields (Real Gas Effects, Turbulence, Mixing) being decisive for nozzle flow. I am missing chemical nonequilibrium which is of even greater influence. Can you comment on the status of modeling?

AUTHOR'S REPLY

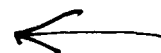
The methods applied are formulated for real gas effects in equilibrium and nonequilibrium. This means that viscous flows in the manner considered in the paper can be computed with a coupling procedure of Euler and boundary layer methods. Up to now only chemical nonequilibrium is accounted for and work is on the way to implement also thermal nonequilibrium (vibrational excitations).

T. VOGEL, DLR, GERMANY

- 1) Figure 6(c): Did you apply an inverse boundary layer method?
- 2) Figure 3(d): I think you cannot neglect the viscous effects for film cooled flows. What is the blowing rate or the momentum ratio of the injected flow?

AUTHOR'S REPLY

- 1) This is not an inverse boundary layer method.
- 2) I never said that viscous effects should be neglected in the case of the film cooling problem. The conclusions in the paper present the appropriate explanation for that.





APPLICATION OF FINITE ELEMENT METHOD TO HYPERSONIC NOZZLE FLOW COMPUTATIONS

by
W. Koschel, W. Rick and S. Bikker
Institute for Jet Propulsion and Turbomachinery
Technical University of Aachen
Templergraben 55, D-5100 Aachen

92-16091

SUMMARY

An explicit Taylor-Galerkin FEM algorithm used for the solution of Euler/Navier-Stokes equations is applied for the computation of steady-state frozen equilibrium flow in single expansion ramp nozzles (SERN) and in plug nozzles for hypersonic propulsion systems. External flow conditions are taken into account. For the determination of nozzle performance a detailed 2D/3D-flow analysis in regions with complex geometries has been performed using unstructured computational grids with adaptive mesh refinement. Some results for the investigated nozzle configurations at different flight conditions are presented and discussed. Thrust vectoring by modification of the lower nozzle flap shape has been studied additionally.

NOMENCLATURE

C_e element limiter
 C_v specific heat
 C_{gt} gross thrust coefficient
 E specific total energy
 F flux vector
 M mass matrix
 M_l lumped mass matrix
 N_i, P_i shape functions
 P pressure
 R specific gas constant
 t time
 T temperature
 U solution vector
 u_j component of velocity

ρ density
 ψ mole fraction
 Ω computational domain

Subscripts

e number of elements
 h high order solution
 i number of nodal points
 j direction of Cartesian coordinates
 l low order solution
 m molar

Superscripts

n time level

INTRODUCTION

In the design process of propulsion systems for hypersonic aerospaceplanes there is a primary emphasis on the accurate prediction of exhaust nozzle performance because of its strong effect on net thrust [1].

The single expansion ramp (SERN) nozzle exhibits the capability to be highly integrated with hypersonic airplanes offering reduced propulsion system weight [2]. Another exhaust nozzle concept, which is of interest, is the combination of a plug nozzle with a single expansion ramp characterized by a smaller overall design length compared to the SERN nozzle concept. This inherent design advantage is obtained at the expense of more complex asymmetric nozzle flowfields involving three-dimensional internal/external flow interfaces.

An analysis of these nozzle concepts is performed by use of a 2D/3D Euler finite element code for flow computation providing first informations on integral parameters such as inviscid thrust coefficient, thrust vector angle and mass flow.

The computations so far carried out for 2D nozzle flows show a large variation of the thrust vector especially in the transonic flight regime so that thrust vectoring will be indispensable due to operational requirements [3]. Therefore the present investigation was aimed to analyze if the thrust vector in the transonic flight regime could be influenced by modification of the cowl flap.

The computations for the two-dimensional SERN nozzle flow and for the three-dimensional plug nozzle flow as well are performed by applying a two-step Taylor-Galerkin finite element method with the extension of flux corrected transport for use on unstructured grids [4].

The computational results are compared with predictions obtained by using a method-of-characteristics [5].

NUMERICAL SCHEMEGOVERNING EQUATIONS

The Euler equations governing time dependent three-dimensional compressible inviscid flow can be expressed in the conservation form using the summation convention for repeated indices:

$$\frac{\partial U}{\partial t} + \frac{\partial F_j}{\partial x_j} = 0 \quad j = 1, \dots, 3 \quad (1)$$

where

$$U = \begin{pmatrix} \rho \\ \rho u_i \\ \rho E \end{pmatrix} \quad F_j = \begin{pmatrix} \rho u_i u_j + \delta_{ij} p \\ u_j (\rho E + p) \end{pmatrix} \quad (2)$$

Herein U is the solution vector and F_j represents the convective flux vector in the direction x_j of a Cartesian coordinate system.

- Thermally perfect gas is assumed to complete the set of equations. This means that the perfect gas equation of state holds:

$$p = \rho R T \quad (3)$$

The temperature dependence of the specific heat accounts for the excitation of vibrational energy within the molecules of the gas, so that the caloric equation of state gives

$$e = \int c_{vm}(T) dT / \sum \Psi_i M_i \quad (4)$$

e : internal energy
 c_v : specific heat at constant volume

The molar specific heat $c_{vm}(T)$ of a mixture of perfect gases reads:

$$c_{vm}(T) = \sum_i \Psi_i c_{vmi}(T), \quad \sum_i \Psi_i = 1 \quad (5)$$

where Ψ_i denotes the mole fraction of the gas component i due to the gas mixture composition.

The molar specific heat $c_{vmi}(T)$ of each gas component is provided by a polynomial fitting:

$$c_{vmi}(T) = a_0 + a_1 T + a_2 / T^2 + a_3 T^2 \quad (6)$$

The coefficients a_j of the above approach are taken from tables of gas properties [6].

The specific gas constant R of the gas mixture is specified by:

$$R = R / \sum \Psi_i M_i \quad (7)$$

where R represents the universal gas constant and M_i denotes the mole mass of the gas component i .

The presented results of this study are based either on chemically frozen or chemically as well as vibrationally frozen flows. The latter case is represented by calorically perfect gas.

DISCRETIZATION

The Euler equations (1) are integrated inside the domain after its subdivision into triangles in case of two-dimensional and into tetrahedra for three-dimensional domains.

The algorithm refers to the two-step type of the Lax-Wendroff scheme with a spatial discretization due to the Galerkin weighted residual method using C^0 linear shape functions [7].

The first step of the scheme is based on a Taylor expansion in time truncated to first order.

Predictor step:

$$U^{n+1} = U^n - \frac{\Delta t}{2} \frac{\partial F_j}{\partial x_j}^n \quad (8)$$

The above equation can be rewritten in a weighted residual form employing piecewise constant weighting functions:

$$\int_{\Omega} P_\bullet U^{n+1/2} d\Omega = \int_{\Omega} P_\bullet U^n d\Omega - \frac{\Delta t}{2} \int_{\Omega} P_\bullet \frac{\partial F_j}{\partial x_j}^n d\Omega \quad (9)$$

and inserting the following function approximations:

$$\begin{aligned} U^{n+1/2} &= P_\bullet U_\bullet^{n+1/2} \\ F_j^n &= N_i F_j^{in} \\ U^n &= N_i U_i^n \end{aligned} \quad (10)$$

where $F_j^{in} = F_j(U_i^n)$ and N_i, P_\bullet denote piecewise linear respectively constant shape functions.

The equation (9) can be solved directly for each element in turn leading to the solution vector at time level $t = t^{n+1/2}$.

Advancing the solution towards time level $t = t^{n+1}$ the second step makes use of the Gauss divergence theorem applied to the integral of equation (11).

Corrector step:

$$U^{n+1} = U^n - \Delta t \frac{\partial F_j^{n+1/2}}{\partial x_j} \quad (11)$$

which represents the corresponding weak integral formulation:

$$M \Delta U = \Delta t \int_{\Omega} F_j^{n+1/2} \frac{\partial N_k}{\partial x_j} d\Omega - \Delta t \int_{\Gamma} F_j^{n+1/2} N_k n_j d\Gamma \quad (12)$$

where

$$\begin{aligned} \Delta U &= U^{n+1} - U^n \\ F_j^{n+1/2} &= P_e F_e^{n+1/2} \\ U^n &= N_i U_i^n \\ U^{n+1} &= N_i U_i^{n+1} \end{aligned} \quad \text{with} \quad F_e^{n+1/2} = F_j(U_e^{n+1/2}) \quad (13)$$

n_j denotes the outward normal unit vector on the boundary of the domain Ω and M describes the consistent mass matrix given by:

$$M_{ijk} = \int_{\Omega} N_i N_k d\Omega \quad (14)$$

All integrations in equation (12) may be performed exactly and result in an assembled equation system of the form:

$$M_{ijk} \Delta U_k = \Delta t_i R S_i \quad (15)$$

where $\Delta U_k = U_k^{n+1} - U_k^n$ and $R S_i$ is the vector of all assembled element contributions to node i .

This equation system (15) can be solved iteratively utilizing the property of diagonal dominance of the matrix M .

The following scheme suggested by Donea and Giuliani [8] is applied to transient solutions with three iterations and does not require storing the global matrix:

$$\begin{aligned} M_i \Delta U^v &= (M_i - M) \Delta U^{v-1} + \Delta t R S \\ \Delta U^0 &= 0 \end{aligned} \quad (16)$$

where v represents the number of iterations and M_i describes the diagonalized mass matrix also called lumped mass matrix.

ARTIFICIAL VISCOSITY MODEL

The application of symmetric shape functions within the algorithm leads to a centred space discretization, so that artificial dissipative terms need to be added in order to stabilize the scheme for shock capturing.

According to Morgan, Peraire [7], [9] the used artificial damping consists of a second order difference term controlled by a pressure switch:

$$U_e^{n+1} = U^{n+1} + c M_i^{-1} \sum_j S_e (M - M_i) U_j^{n+1} \quad (17)$$

U_e^{n+1} is the modified solution and S_e represents the element switch coefficient, which nodal value is given by:

$$S_i = \sum_j \frac{(M - M_i) p}{|(M - M_i) p|} \quad (18)$$

S_i always varies between 0 to 1 depending on the local smoothness of the solution U^{n+1} .

BOUNDARY CONDITIONS

The fluxes $F_j^{n+1/2}$ in the boundary integral of equation (12) are specified according to the corrected variables $U^{n+1/2}$ obtained by applying linearized characteristics analysis [10] requiring that the number of boundary conditions imposed at the boundaries of the domain are equal to the number of incoming characteristics.

STABILITY

The explicit character of the time stepping scheme implies that the local Courant number criterion is satisfied:

$$\Delta t \leq \frac{\alpha \Delta h_e}{|u_j u_i|^{1/2} + a} \quad (19)$$

where a is the local speed of sound and Δh_e is a characteristic element length represented by the

minimum height of each element. The value of the factor α depends on the number of passes through the iterative scheme (16). In case of one pass, which means only employing the lumped mass matrix, the factor is taken to be equal to 1, otherwise α is determined to be $\alpha = 1/\sqrt{3}$ resulting from stability analysis [7].

HIGH RESOLUTION SCHEME

The above described artificial viscosity model introduced in the algorithm for shock capturing only appears to work well in transonic flow regions. It fails for the computation of hypersonic flows involving embedded strong discontinuities by tending to oscillating or smeared shocks due to an a priori unknown appropriate amount of artificial viscosity. This fact motivates to turn to other shock capturing techniques providing improved shock resolution capabilities on unstructured meshes.

The principle of flux corrected transport (FCT) originated by Boris, Book [11] consists of the combination of a low order monotonic solution with the solution obtained by a high order scheme, which turns out oscillations, in a way that the corrected solution exhibits no overshoots.

Following a suggestion of Löhner et al. [4] to implement a multidimensional generalization of the concept of flux corrected transport first introduced by Zalesak [13] in context of the finite element method allows an application of a high resolution scheme to unstructured meshes.

The FCT solution is given by limiting the difference between a high and a low order element contribution, denoted by AEC, at every time step:

$$U_i^{n+1} = U_i^{n+1} + \sum_j C_{ij} (HEC - LEC) \quad 0 \leq C_{ij} \leq 1 \quad (20)$$

HEC : high order element contribution
LEC : low order element contribution

where U_i^{n+1} represents the advanced low order solution at $t = t^{n+1}$. The limiter C_{ij} of every element is constructed by relating the maximum allowable change Q_i^{\pm} of node i to its sum of antidiffusive element contributions AEC_i^{\pm} :

$$C_{ij} = \min \begin{cases} R_j^+ & AEC_j > 0 \\ R_j^- & AEC_j < 0 \end{cases} \quad j=1,4 \quad (21)$$

j : nodes of a tetrahedron

$$\text{where} \quad R_i^{\pm} = \begin{cases} \min(1, Q_i^{\pm} / AEC_i^{\pm}) & |AEC_i| > 0 \\ 0 & AEC_i = 0 \end{cases} \quad (22)$$

The value Q_i^{\pm} describes the previously mentioned maximum allowable change of all nodes around i including itself with respect to the low order solution U_i^{n+1} and the previously obtained solution U^n so that no oscillations are introduced into the corrected solution U^{n+1} .

$$Q_i^{\pm} = \max_{\min} (U_i^{n+1}, U^n)_k - U_i^{n+1} \quad (23)$$

K : surrounding nodes of $i \sim 1 \leq k$

The above described two-step Taylor-Galerkin algorithm is taken to be the high order scheme whereas the same scheme employing the lumped mass matrix (16) and the artificial viscosity model (18) with $S_i = 1$ is used as the low order scheme.

The limiter of equation (21) is provided by the minimum of the limiters obtained for the density and the pressure. Particularly for the nozzle flow computations at high pressure ratios it has been found to be necessary to limit the pressure for preventing negative values in regions e.g. where strong expansions of the flow occur.

VECTORIZATION

The algorithm can be vectorized to a large extent on machines supporting gather and scatter loops efficiently by use of special hardware routines [13].

The computation of the equation system (15) represents a typical finite element assembling process, which involves indirectly addressed element loops. For running the code in a most efficient way vectorization of these loops is necessary. Opposed to the gathering of nodal quantities to each element in the predictor step, the corrector step leads to a recursive scatter assembling process relating element quantities back to the nodes. Recurrences associated with this assembling process prevent an immediate vectorization. An alteration by renumbering of the elements enables a subdivision of the entire scatter loop into smaller loops without recurrences each running in a vector mode. Such a modification provides a vectorization rate of the code of about 95 % equal to a vector/scalar speed-up factor of 12 on a Siemens SNI 400/10.

2D MESH GENERATION WITH ADAPTIVE REFINEMENT

The triangulation of arbitrary shaped computational domains with embedded interior boundaries is accomplished by an automatic mesh generation scheme following the generalized advancing front method [7],[14]. The shape of the triangles is controlled by the mesh parameters: element size, element stretching and stretching direction. A spatial distribution of these parameters is provided by a coarse

background grid, which consists of linear triangular elements completely covering the computational domain.

The adaptive remeshing method applied here offers the ability to improve the solution quality in a computationally efficient manner. The adaption process is achieved by regenerating completely the computational mesh based upon information provided by the computed solution on the current grid. The new mesh is constructed using the generation scheme described in the previous section allowing a significant variation in element size and stretching of the elements in the vicinity of one-dimensional flow features. The initial computational mesh is now acting as a background grid providing the spatial distribution of the mesh parameters. In order to determine the nodal values for these mesh parameters in an optimal manner it is necessary to perform some method of error estimation. In this process the second derivatives of a certain scalar variable, e.g. density, are used to give some indication of the error magnitude and direction. Detailed information on this method may be taken from references [14],[15]. An example of the application of this method to the case of a SERN nozzle flow computation is given in Fig. 1.

Further on adaptive mesh enrichment is used widely for 2D computations. This mesh refinement method starts with relatively coarse initial grids, which are locally refined by subdivision of triangles into smaller elements. This process depends on an error estimation, which is also based on the second derivative of a key variable, e.g. density, computed from a solution obtained on the coarser grid and not accounting for the error direction. In contrary to the above described remeshing the grid is not completely regenerated but only locally refined by adding equilateral triangles. Thus to avoid highly distorted elements particularly after a sequence of refinements newly introduced nodes are only added to the sides of the elements, which should be substituted [7],[16]. One example of a two-dimensional mesh adapted by this procedure is shown in Fig. 2.

3D MESH GENERATION

In this case a more straightforward strategy is applied temporarily before starting a three-dimensional extension of the described two-dimensional automatic mesh generator [9], [17]. The mesh generation proceeds by mapping of a two-dimensional unstructured grid generated by the methods described above into different planes. These planes are linked by fictitious prisms, which relate corresponding triangles of adjacent planes as illustrated in Fig. 3. In the following these prisms are thought being subdivided into tetrahedra providing a semi-unstructured three-dimensional mesh. When badly deformed tetrahedra are encountered by sweeping over all elements the edges of the tetrahedra exceeding a certain ratio C , defined in the following equation, are marked and elements concerned are replaced by subdivision into smaller less distorted tetrahedra.

$$\frac{S_i}{S_{\min}} > C \quad (24)$$

$$S_{\min} = \min(S_i)$$

where S_i denotes the edge length of a tetrahedron.

ADAPTIVE 3D MESH ENRICHMENT

The three-dimensional mesh refinement procedure is an extension of the 2D mesh enrichment concept described before. Depending on an error indicator, which can be derived from the requirement of constant interpolation error in every element [7], one tetrahedron can be refined by adding up to six new nodes placed in the middle of the element edges. The corresponding subdivision may lead to three different geometrical bodies namely smaller tetrahedra, pyramids and prisms. In a further step these pyramids and prisms in return can be splitted into tetrahedral elements. The flow scheme of the mesh refinement is illustrated in Fig. 4 by a decomposition of one tetrahedron being refined for the case of adding five new nodes.

COMPUTATIONAL RESULTS

Inviscid flow computations for thrust nozzles of a turbo-ramjet propulsion system designed for hypersonic spaceplanes covering transonic up to hypersonic flight conditions have been carried out based on the finite element code and making extensive use of the above described meshing techniques.

Computational results for the flow through a single expansion ramp nozzle (SERN) at different flight conditions as well as for the three-dimensional flow field of a plug nozzle combined with a single expansion ramp at design speed, taking external flow interaction in all cases into account, will be presented and discussed.

SERN NOZZLE FLOWFIELD ANALYSIS

The computational domain and the boundary conditions, which have been applied to flow computations of the SERN-type nozzle at hypersonic flight conditions, are schematically shown in Fig. 5. The modifications for the transonic regime are discussed later on. All nozzle flow computations reported herein are based on different stagnation conditions for the exhaust gas flow and the external air flow. Both flows represented by different specific gas constants can be characterized by specifying temperature ranges, which is justified by the strong temperature drop across the jet boundary. The inner flow conditions are taken from a performance analysis of a combined turbofan ramjet propulsion system burning hydrogen.

The design condition for the SERN nozzle is given by a flight Mach number of $M = 3.45$ where the

propulsion system is switched over from the turbojet into the ramjet mode. A typical Mach number isolines plot obtained for this case is shown in Fig. 6. For supersonic respectively hypersonic flight conditions the described FCT algorithm is employed in combination with the mentioned remeshing procedure providing highly resolved discontinuities which is illustrated by this result. As well the plume shock originating from the cowl flap as the jet boundary can be clearly detected. For the hypersonic flight condition at $M = 6.8$ a similar flow field is obtained as can be seen from Fig. 7. Herein the nozzle flow regime is widened up and has displaced the jet boundary to the lower side.

For the case of flight Mach number 1.2 the boundary is splitted into an inflow freestream boundary and an outflow boundary with extrapolated conditions. For the flight Mach number 0.9 the outflow part of the lower boundary is iteratively fitted to a streamline imposed by the ambient static pressure, as is depicted in Fig. 8. The computation of the nozzle flow at transonic flight operation conditions have been performed on unstructured meshes similar to that of Fig. 1 using the mesh enrichment method and applying the artificial viscosity model.

Overexpanded nozzle flow condition occurs at transonic flight speeds which can be seen from the plot of isolines of the Mach number shown in Fig. 9 and in Fig. 10 which is in line with the interpretation given by Trefny [18] who described the different behaviour of SERN nozzle flow at transonic and hypersonic flight conditions. These flow phenomena are sketched schematically in Fig. 11. At transonic flight with turbofan operation and low nozzle pressure ratios the cowl flap is deflected upward to prevent a strongly overexpanded exhaust flow involving shocks upstream of the cowl trailing edge, which would result in considerable increased nozzle drag. At hypersonic speeds with the engine operating in the ramjet mode high nozzle pressure ratios are provided due to inlet recovery, thus the limiting characteristic of the inner flow emanating from the trailing edge of the cowl flap does not incident on the expansion ramp. In this case the external flow has only little effect on the exhaust flow, which is slightly underexpanded according to the length optimization of the nozzle.

Particularly in the transonic flight range the interaction between inner and outer flow has a strong effect on the thrust vector. Although a large part of this effect can be compensated by similar aerodynamic moments [3] it is expected that thrust vectoring capabilities will be necessary to satisfy flight operation requirements. For this reason the outer shape of the cowl flap was modified in order to produce a more severe expansion in the external flow leading to smaller pressure impressed on the exhaust flow at the cowl trailing edge. In Fig. 12 the results for the flap cowl modification are presented as a plot of Mach number isolines. As the jet boundary adjusts to an angle that equalizes pressure in the internal and external flow the thrust vector angle could be reduced only by about three degrees increasing simultaneously the drag on the external flap surface. Imposed stronger expansion of the external flow around the cowl flap tends to separation effects, which does not give evidence in combination with Euler solutions and requires the inclusion of viscous effects. The thrust vector angles obtained from the computations for the SERN nozzles including the cowl flap modification are shown in Fig. 13. The comparison of the thrust vector angles with those found by MTU [5] applying the method-of-characteristics turns out to be in good agreement.

3D PLUG NOZZLE FLOWFIELD COMPUTATION

The three-dimensional flow through a plug nozzle including internal/external flow interactions with different stagnation conditions for both flows has been simulated for nozzle design conditions at $M = 6.8$ using the FCT-algorithm.

In Fig. 14 the rear half of the nozzle with its planes of symmetry is shown schematically. The boundary conditions are similar to those specified for the 2D SERN nozzle flow computation given by Fig. 5. The grid for the nozzle flow field computation considering afterbody interactions consists of two coupled blocks each generated by rotational respectively translational mapping of 2D unstructured grids. The discretised axially adjustable plug as well as the expansion ramp integrated into the fuselage with a transition from annular to rectangular contour is illustrated in Fig. 15.

The computational grid and the plot of the Mach number isolines for the x,y-plane through the nozzle axis are presented in Fig. 16. The Mach number isolines indicate that there is a slightly underexpanded nozzle flow involving shocks except of the recompression zone at the rear side of the plug. In this case the overall error of massflow related to the exhaust massflow is found to be 1.8 % for a mesh with about 190,000 elements.

A 3D mesh refinement by increasing the number of elements up to 380,000 has been applied. The enriched grid and the corresponding results for the Mach number distribution are presented in Fig. 17. It can be seen from this plot that the shock originating from the lower cowl and the jet boundary become more pronounced by mesh refinement.

Finally an evaluation of the thrust vector coefficient $c_{t\theta}$ for all the investigated nozzles was carried out. The results are plotted in Fig. 18. All nozzles show a good performance in the hypersonic flight regime whereas at transonic speeds lower values of the thrust coefficient are obtained due to the before discussed nozzle flow phenomena.

CONCLUSION

Computations of SERN thrust nozzle performance of a hypersonic spaceplane at design and off-design conditions are performed using a Taylor-Galerkin finite element algorithm on unstructured grids. Comparison of the results with predictions of a method-of-characteristics shows good agreement.

A strongly reduced axial thrust coefficient corresponding to a large thrust vector angle is revealed for

transonic flight conditions, which requires further studies on possibilities for thrust vectoring including viscous effects.

Finally the three-dimensional flow through a plug nozzle including external flow effects has been computed with flux corrected transport extension of the code applying an adaptive grid refinement to get improved quality of steady state Euler solutions.

This study demonstrates the capability of the 2D/3D finite element method for analysing complex inviscid high-speed flows through propulsion components of hypersonic aircrafts.

ACKNOWLEDGEMENT

This study was carried out within the frame of the Collaborative Research Center (SFB 253) at the RWTH Aachen 'Fundamentals of Aerospace Plane Design' funded by the Deutsche Forschungsgemeinschaft (DFG). Additional support by MTU München is gratefully acknowledged.

REFERENCES

- [1] A.P. Kuchar: Variable Convergent-Divergent Exhaust Nozzle Aerodynamics, Aircraft Propulsion Systems Technology and Design, ed. G.C. Oates, AIAA Education Series, 1989
- [2] A.P. Kuchar, J.P. Wolf: Preliminary Assessment of Exhaust Systems For High Mach (4 to 6) Fighter Aircraft, AIAA-89-2356
- [3] D.E. Koelle, H. Kuczera: SÄNGER Space Transportation System - Progress Report 1990, IAF-90-175, 41st IAF Congress, Dresden, Oct. 1990
- [4] R. Löhner, K. Morgan, J. Peraire, M. Vahdati: Finite Element Flux-Corrected Transport (FEM-FCT) for the Euler and Navier-Stokes Equations, Int. J. for Num. Methods in Fluids, Vol. 7, 1093-1109, 1987
- [5] M. Göing: Nozzle Design Optimization by Method-of-Characteristics, AIAA-90-2024, Orlando USA, 1990
- [6] C. Barin, O. Knacke: Thermochemical Properties of Inorganic Substances, Springer Verlag, Berlin 1973
- [7] K. Morgan, J. Peraire: Finite Element Methods for Compressible Fluids, von Karman Institute, Belgium 1987
- [8] J. Donea, S. Giuliani: A Simple Method to Generate High Order Accurate Convection Operators for Explicit Schemes Based on Linear Finite Elements, Int. J. Num. Methods in Eng. 1, 1981
- [9] J. Peraire, J. Peiro, L. Formaggia, K. Morgan, O.C. Zienkiewicz: Finite Element Euler Computations in Three Dimensions, AIAA-87-0032, Reno, 1988
- [10] W.J. Usab, E.M. Murman: Embedded Mesh Solution of the Euler Equations Using a Multiple-Grid Method, Advances in Computational Transonics, Pineridge Press, 447-472, 1985
- [11] J.P. Boris, D.L. Book: Flux-Corrected Transport. I SHASTA, A Transport Algorithm that Works, J. Comp. Phys. 11, 1973
- [12] S.T. Zalesak: Fully Multidimensional Flux-Corrected Transport Algorithm for Fluids, J. Comp. Phys. 31, 1979
- [13] R. Löhner, K. Morgan: Finite Element Methods on Supercomputers: The Scatter-Problem, Proc. NUMETA '85 Conf., Rotterdam, 1985
- [14] R. Löhner, P. Parikh, M.D. Salas: Generation of Unstructured Grids and Euler Solutions for Complex Geometries, Springfield USA, 1988
- [15] J. Peraire, M. Vahdati, K. Morgan, O.C. Zienkiewicz: Adaptive Remeshing for Compressible Flow Computations, J. Comp. Phys. 72, 1987
- [16] J.T. Oden, T. Strouboulis, P. Devloo: Adaptive Finite Element Method for the Analysis of Inviscid Compressible Flow: Part I Fast Refinement/Unrefinement and Moving Mesh Methods for Unstructured Meshes, Comp. Meth. Appl. Mech. Eng. 59, 1986
- [17] R. Löhner, P. Parikh: Generation of Three-Dimensional Unstructured Grids by the Advancing-Front Method, AIAA-88-0515, 1988
- [18] Trefny, C.: On the Use of External Burning to Reduce Aerospace Vehicle Transonic Drag, AIAA-90-1935, Orlando USA, 1990

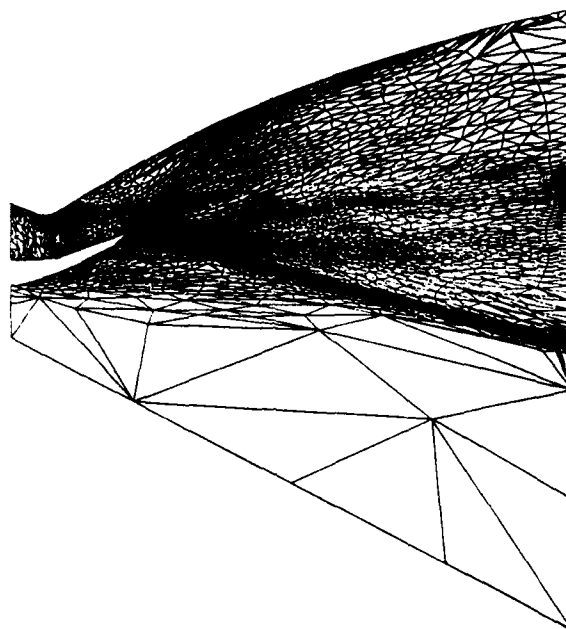


Fig. 1: Adaptive mesh refinement; computational grid for the case of flight Mach number 3.45

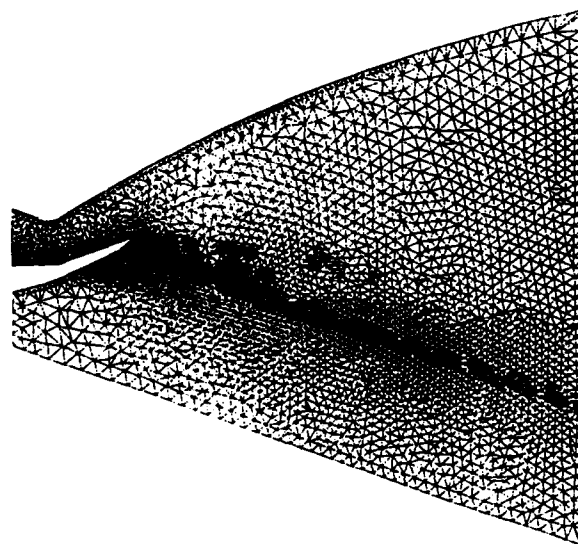


Fig. 2: Adaptive enrichment; computational grid

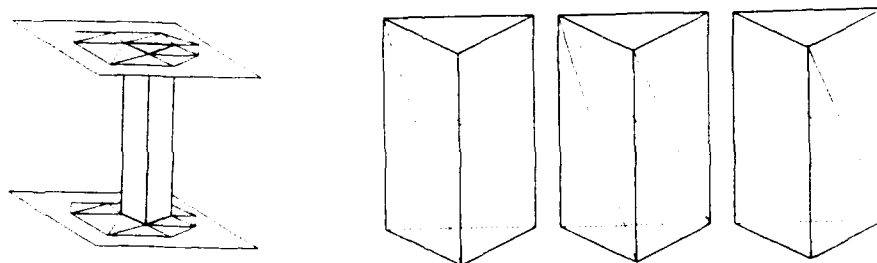


Fig. 3: 3D mesh generation method

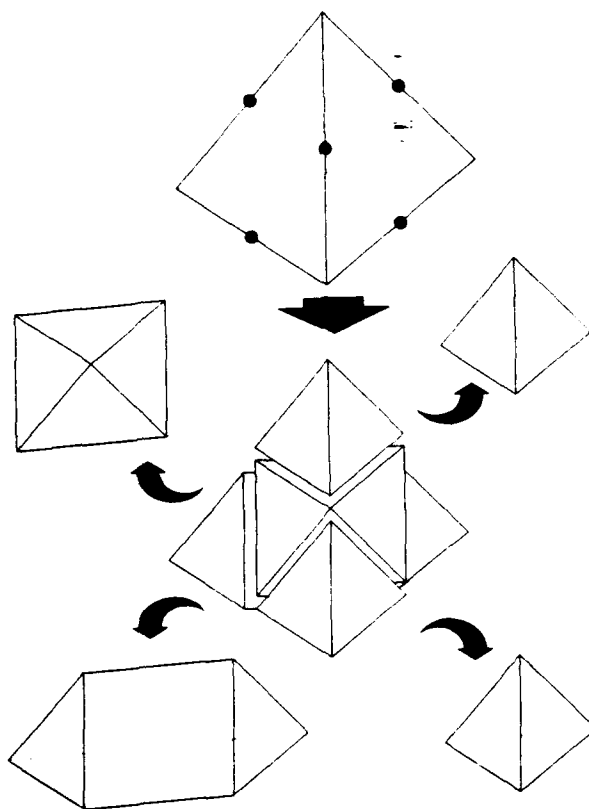


Fig. 4: Adaptive 3D mesh enrichment

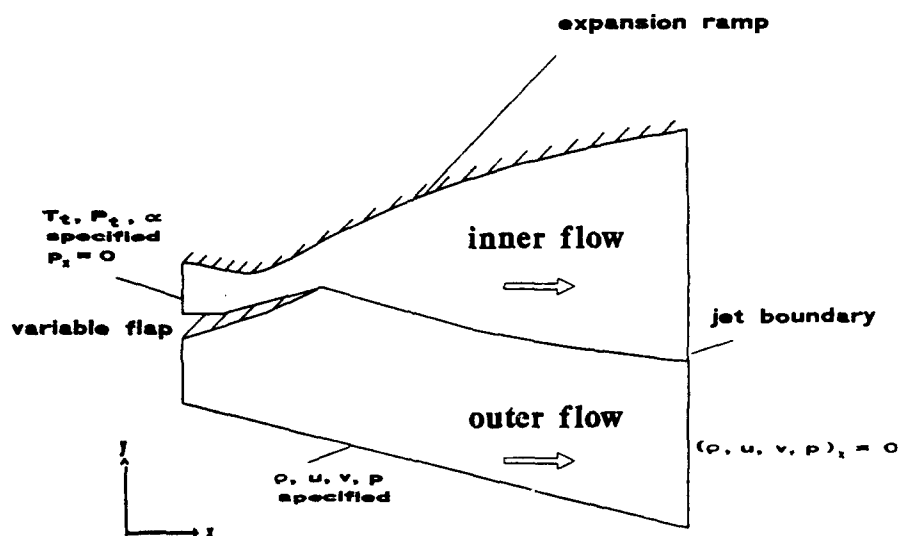


Fig. 5: Computational domain and boundary conditions for SERN nozzle at hypersonic speed

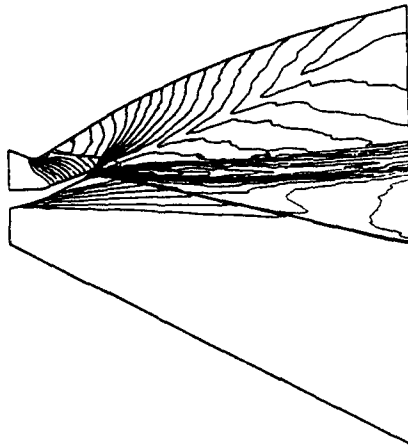


Fig. 6: Mach number isolines for flight Mach number 3.45

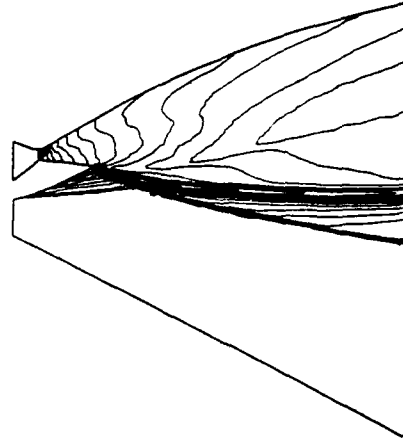


Fig. 7: Mach number isolines for flight Mach number 6.8

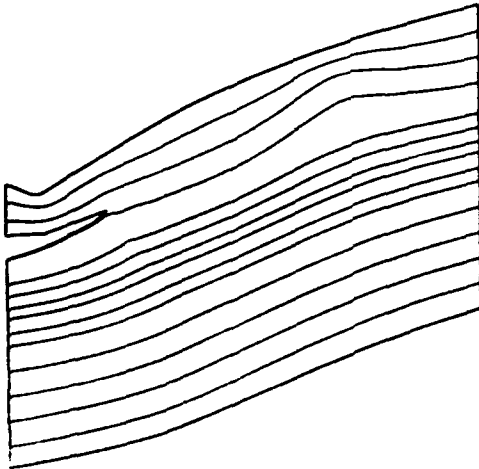


Fig. 8: Streamlines for flight Mach number 0.9

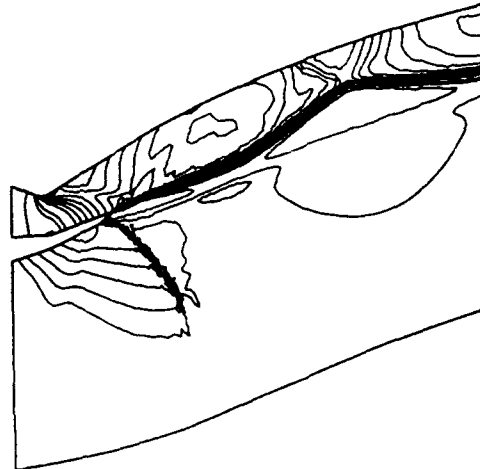


Fig. 9: Mach number isolines for flight Mach number 0.9

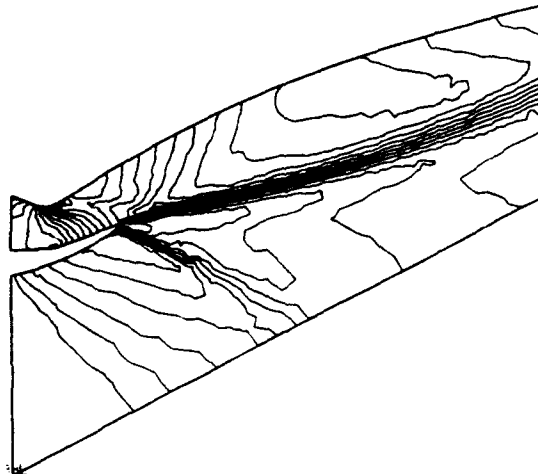


Fig. 10: Mach number isolines for flight Mach number 1.2

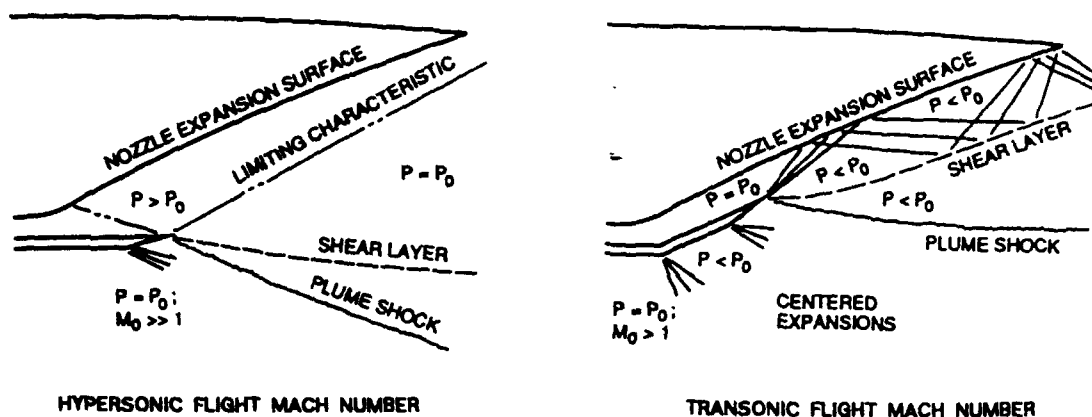


Fig. 11: SERN nozzle flow phenomena [18]

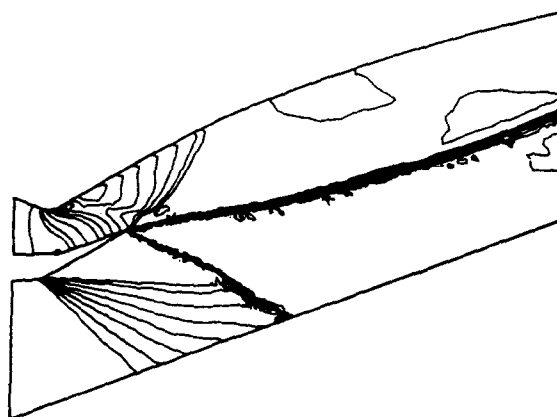


Fig. 12: Mach number isolines for flight Mach number 1.2; Thrust vectoring by cowl flap modification

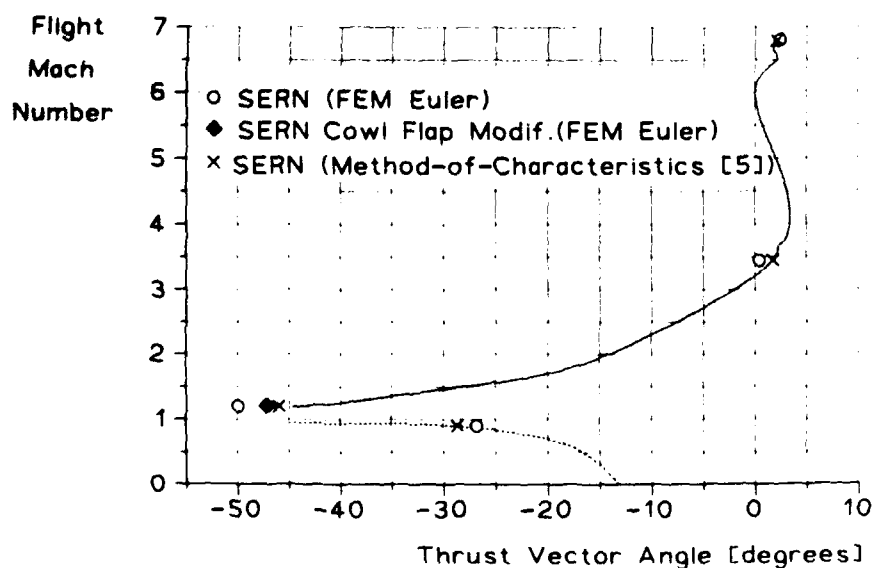


Fig. 13: Thrust vector angle variation with flight Mach number for SERN nozzle

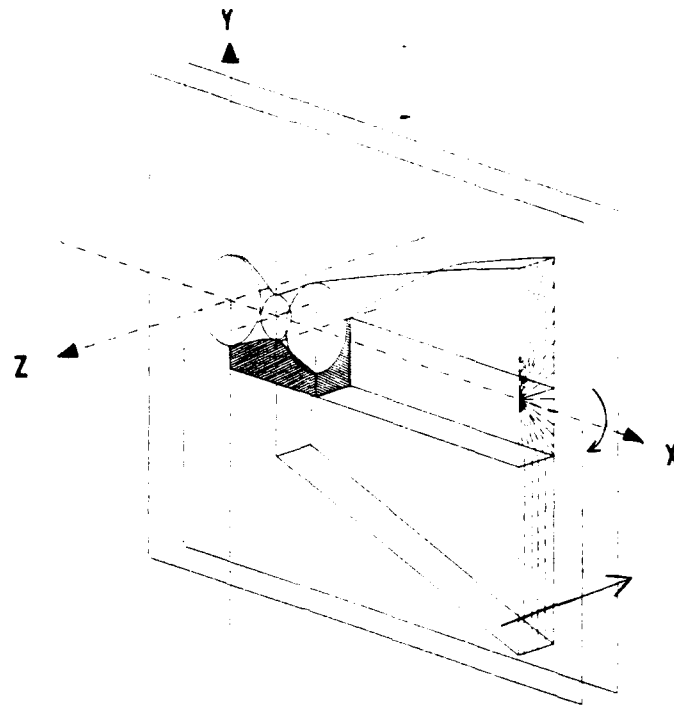


Fig. 14: 3D computational domain for the plug nozzle

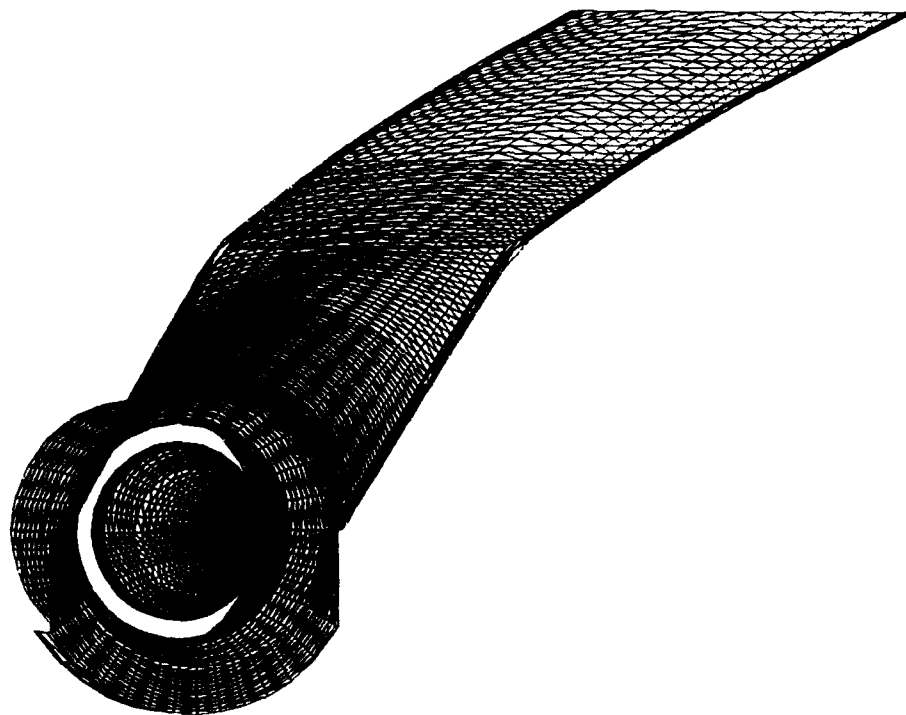


Fig. 15: Discretized plug nozzle contour seen from the rear side

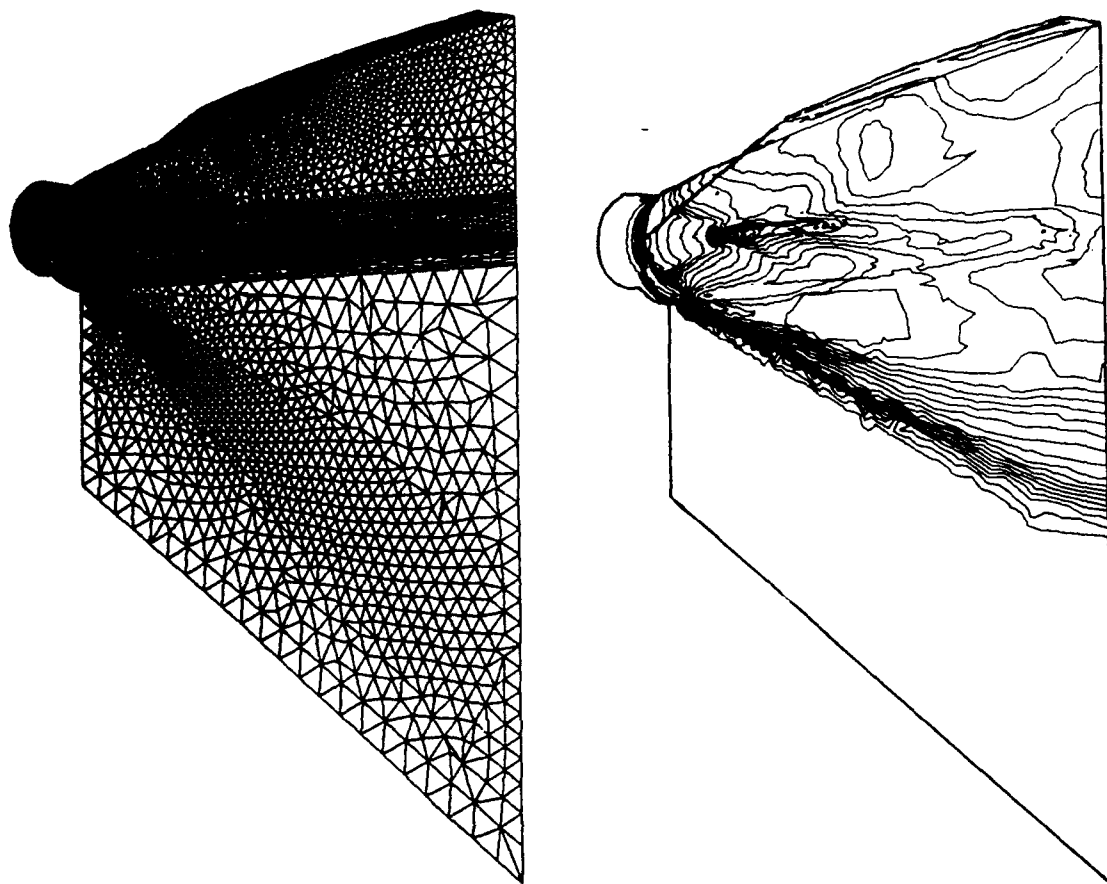


Fig. 16: Grid and Machnumber isolines for plug nozzle at flight Mach number 6.8
(x,y-plane at nozzle axis seen from the rear side, 150 000 elements)

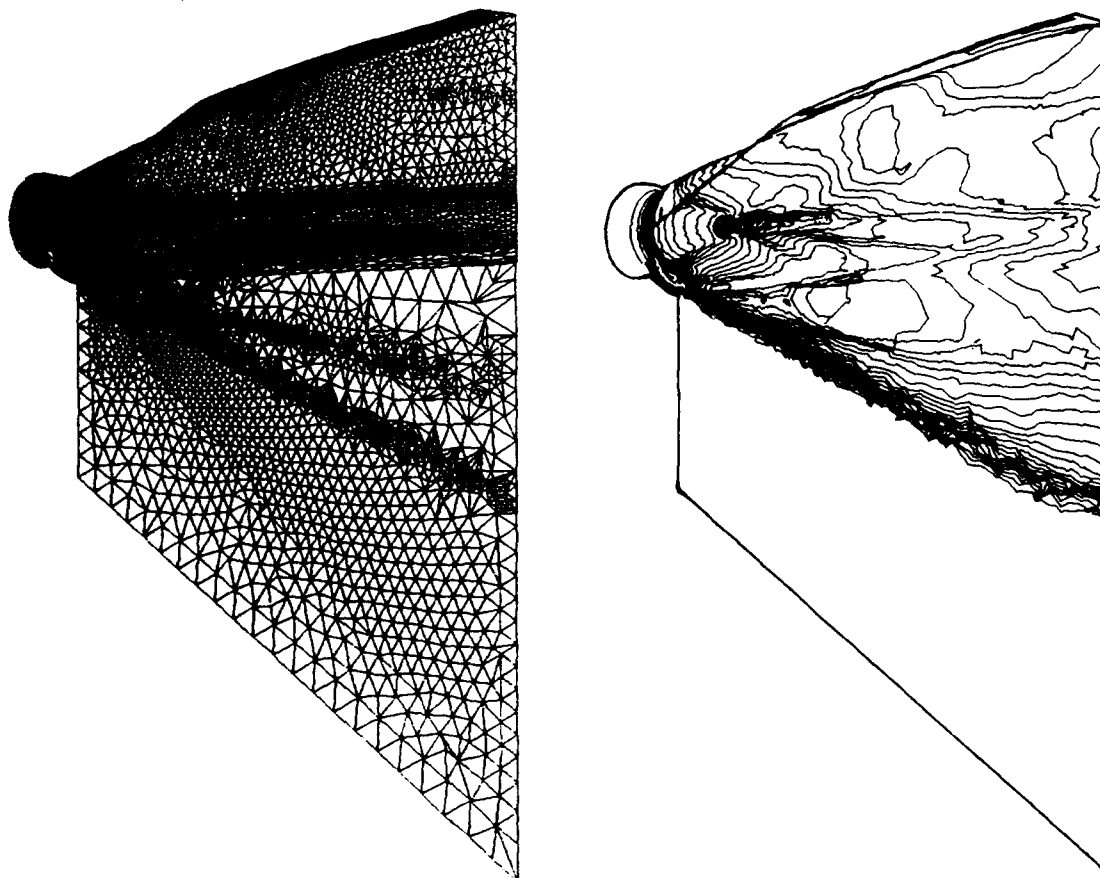


Fig. 17: Grid and Machnumber isolines for plug nozzle at flight Mach number 6.8
(x,y-plane at nozzle axis seen from the rear side, 380 000 elements)

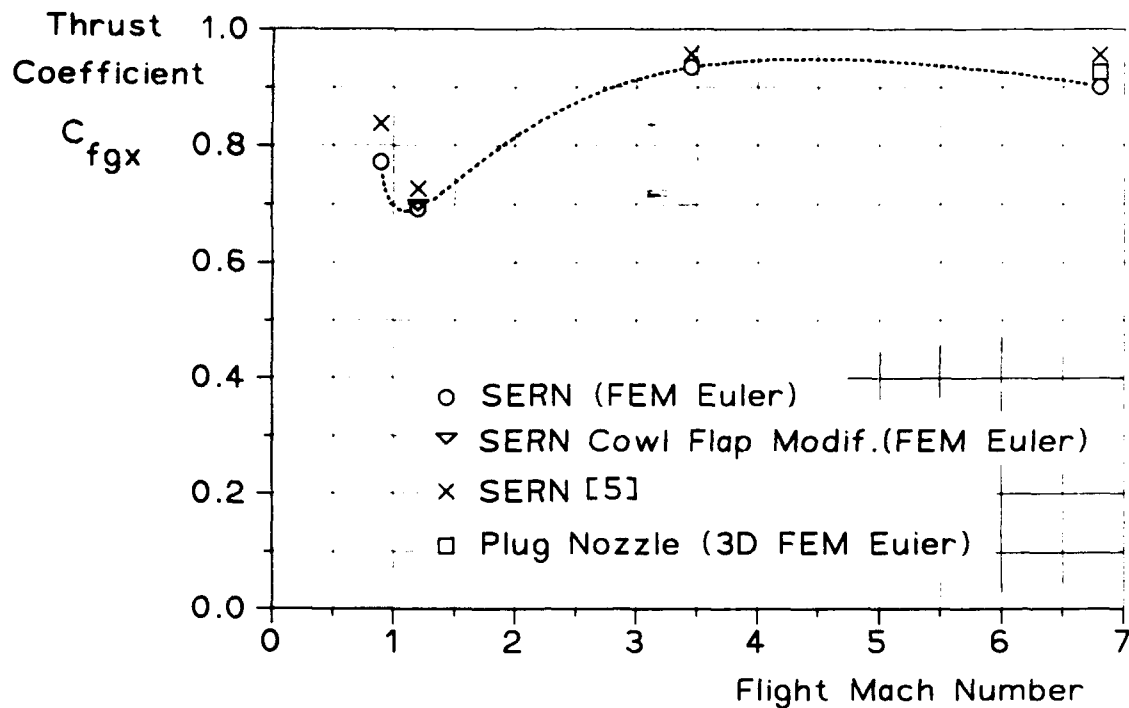


Fig. 18: Thrust coefficient for SERN nozzles and for plug nozzle at design and off-design flight conditions

Discussion

C. HAH, NASA LEWIS, U.S.A.

For the case of Fig. 15, what is the total CPU to calculate the flow?

AUTHOR'S REPLY

The code requires about 5 hr CPU time on a Siemens SNI400/40 vector computer to decrease the density residual by around four orders of magnitude.

R. WALTHER, MTU, GERMANY

For your three-dimensional plug nozzle computation you mentioned a computation time of 5 hr on a vector computer. Can you give a rough estimation on the computing time which has to be expected when finite rate chemistry will be included?

AUTHOR'S REPLY

I have no idea. We will first implement chemistry in a two-dimensional version of the code.





COMPUTATIONAL MODELLING OF TURBULENT FLOW IN S-BENDS

N.I. ABOU HAIDAR, H. IACOVIDES & B.E. LAUNDER

Dept of Mechanical Engineering

UMIST

PO Box 88

Manchester

M60 1QD. U.K.

ABSTRACT

The paper considers the computation of turbulent flow through circular sectioned S-bends, a flow generically similar to those arising in various types of jet-engine intake ducting. A fully elliptic, finite-volume discretization of the Reynolds equations is adopted. For the main part of the flow the standard algebraic second-moment (ASM) closure is adopted while over the thin viscosity-affected sublayer adjacent to the wall three levels of model have been explored: namely, one- and two-equation eddy viscosity models or a two-equation ASM closure. Although the main features of the flow development are well captured even with the simplest near-wall treatment the pressure drop through the second half of the S-bend is seriously underestimated. The successive refinement of the model across the sublayer is found to bring the computed behaviour into very close accord with the detailed experimental data. The findings indicate the desirability of using a high-level turbulence model not just in the main part of the flow but across the low-Reynolds-number sublayer also.

1. INTRODUCTION

In both civil and military aircraft the intake passage leading to the jet engine is commonly of S-duct form. Since the engine performance is significantly affected by the quality of the flow at the fan or compressor inlet plane, the ability to predict accurately the three-dimensional turbulent flow development through S-bends would be of considerable help in guiding the design of the intake passage.

While notable computational studies of flow in curved ducts and S-bends have been contributed by McDonald and co-workers and the collaborating group at NASA Lewis, e.g. [1,2] turbulent transport in these cases has been represented by very simple turbulence models, usually at the level of the mixing-length hypothesis. Reasonably satisfactory behaviour has nevertheless been obtained arguably reflecting the relatively small importance of the viscous layers, provided separation is not encountered. At UMIST, since the early 1980's, there has been an effort at predicting complex three-dimensional flows in ducts. Attention was initially given to flow around U-bends with fully-developed flow conditions at inlet and to the prediction of convective heat transfer coefficients [3]. At the time it was

supposed that these features placed heavier demands on the model of turbulent transport than did the S-bend test cases - at any rate those studied experimentally at Imperial College by Professor Whitelaw and co-workers which had formed the basis of the reported computational studies. In those cases the boundary layers at inlet were thin and the total straining imposed by the bend was considerably less than in the U-bends.

A more leisurely consideration might have arrived at different conclusions. Turbulence is known to be greatly affected by small amounts of streamline curvature; but it is relatively less affected by strong curvature (see, for example, Gibson [4]). Moreover, an S-bend involves the successive application of strains of opposite sign, the consequences of which - so far as the turbulence is concerned - cannot easily be foreseen. Accordingly, the invitation by British Aerospace to examine turbulent flow in S-ducts has been seized as an opportunity to explore the sensitivity of the predicted flow to refinements in the near-wall turbulence model. The study has so far been limited to bends of uniform cross-sectional area and shape but has included both circular and square cross sections. In view of space constraints, however, only the former case is considered in the present paper; the latter will be reported elsewhere [5] though it is pertinent to add that experience with the square S-bend is entirely consistent with that for the circular-sectioned bend reported below.

2. THE COMPUTATIONAL PROCEDURE2.1 The Numerical Solver

The basic numerical scheme has been described in several earlier publications [3,6,7] and thus does not require a detailed presentation here. It provides a finite-volume solution of the three-dimensional momentum and continuity equations in toroidal coordinates adopting, for the most part, the solution methodology of the TEACH family of programmes e.g. a staggered velocity/pressure grid and the use of the SIMPLE algorithm for correcting the pressure field. When the ASM turbulence model is employed the stress field is evaluated on a staggered mesh so that the stress components are located on the boundaries of the velocity control volumes on which (via the relevant momentum equations) they act. Quadratic upwind interpolation has been employed on the secondary flow momentum equations though mesh densities are fine enough that

results show no important differences from those obtained using the stabler but more diffusive 'Hybrid' differencing. While earlier versions of the code have adopted a semi-elliptic methodology, in which only the pressure is stored 3-dimensionally over the whole solution domain, in the present study the software has been adapted to a fully elliptic scheme in which all dependent variables are stored 3-dimensionally. This change of strategy reflected the increased storage now available to us and the fact that an elliptic treatment was expected to produce a much faster rate of convergence for the complex static pressure field created by the S-bend.

2.2 The Turbulence Models

2.2.1 The High Reynolds Number Core

In all the computations reported in Section 3 turbulent stresses over most of the cross section have been obtained from the following widely used algebraic second-moment closure based on the proposals of Gibson and Launder [8].

$$\frac{\overline{u_i u_j}}{k} = \frac{2}{3} \delta_{ij} + \frac{(1-c_2)}{\epsilon (c_1 - 1 + P_k/\epsilon)} \quad (1)$$

$$\left\{ P_{ij} - \frac{2}{3} P_k \delta_{ij} \right\} + \frac{\Phi_{ij}^w}{\epsilon (c_1 - 1 + P_k/\epsilon)}$$

where

$$P_k = - \overline{u_i u_j} \partial u_i / \partial x_j \quad (2)$$

$$P_{ij} = - \overline{u_i u_k} \partial u_j / \partial x_k - \overline{u_j u_k} \partial u_i / \partial x_k \quad (3)$$

Φ_{ij}^w is the wall-echo part of the pressure-strain correlation. It is approximated via the proposal given in [8]. n_q is the unit vector normal to the wall, Y the nominal distance from the wall to the point in question and ℓ the local turbulent length scale defined as

$$\ell = k^{3/2} / (C_\ell \epsilon) \quad (4)$$

The function $f(\ell/Y)$ is assumed to take the following form

$$f(\ell/Y) = \frac{\ell}{R-\ell} + \frac{\ell}{R+\ell} \quad (5)$$

where r is the distance from the pipe centre. The turbulent kinetic energy k and its rate of viscous dissipation ϵ are obtained from

$$\frac{\partial (\rho U_j k)}{\partial x_j} = \frac{\partial}{\partial x_j} \left\{ (\mu \delta_{ij} + C_\mu \rho \frac{k}{\epsilon} \overline{u_i u_j}) \frac{\partial k}{\partial x_j} \right\} + \rho P_k - \rho \epsilon \quad (6)$$

$$\frac{\partial}{\partial x_j} (\rho U_j \epsilon) = \frac{\partial}{\partial x_j} \left\{ (\mu \delta_{ij} + C_\mu \rho \frac{k}{\epsilon} \overline{u_i u_j}) \frac{\partial \epsilon}{\partial x_j} \right\} + C_{\epsilon 1} \frac{\epsilon}{k} P_k - C_{\epsilon 2} \frac{\epsilon^2}{k} \quad (7)$$

2.2.2 The Low-Reynolds-Number Sublayer

From the wall, extending to a distance of approximately 3% of the pipe radius R - an area that includes the whole region where direct viscous transport is important - a different turbulence model has been adopted. While our early computations of U-bends employed a mixing-length treatment in this sublayer, the most recent published work has used a 1-equation turbulence model [9] allowing transport effects on the turbulence energy to be accounted for. The model, adapted from the work of Wolfshtein [10] and Yap [11] takes the form:

$$\overline{u_i u_j} = \frac{2}{3} k \delta_{ij} - \nu_T \left(\frac{\partial u_i}{\partial x_j} + \frac{\partial u_j}{\partial x_i} \right) \quad (8)$$

$$\text{where } \nu_T = c_\mu \ell_\mu k^{1/2} \quad (9)$$

$$\ell_\mu = 2.4 Y \{1 - \exp(-0.016 Y^*)\} \quad (10)$$

$$Y^* = Y k^{1/2} / \nu \quad (11)$$

k is obtained from

$$\frac{\partial}{\partial x_j} (\rho U_j k) = \frac{\partial}{\partial x_j} \left\{ \left(\mu + \frac{\mu_T}{\sigma_k} \right) \frac{\partial k}{\partial x_j} \right\} + \rho P_k - \rho k^{3/2} / \ell_\mu \quad (12)$$

$$\text{where } \ell_\mu = 2.4 Y \{1 - \exp(-0.236 Y^*)\} \quad (13)$$

This representation was adopted for the first phase of the U-bend computations in the present study. However, in view of systematic differences between computations and measurements - most notably in the static pressure variation through the bend - a two-stage refinement of the near-wall has been introduced. The first was the replacement of the one-equation scheme by the Launder-Sharma [12] form of 2-equation eddy viscosity model.

The k and ϵ transport equations now take the following forms:

$$\frac{\partial}{\partial x_j} (\rho U_j k) = \frac{\partial}{\partial x_j} \left\{ \left(\mu + \frac{\mu_T}{\sigma_k} \right) \frac{\partial k}{\partial x_j} \right\} + \rho P_k - \rho \epsilon - 2\mu \left(\frac{\partial \sqrt{k}}{\partial x_j} \right)^2 \quad (14)$$

$$\frac{\partial}{\partial x_j} (\rho U_j \epsilon) = \frac{\partial}{\partial x_j} \left(\left(\mu + \frac{\mu_T}{\sigma_\epsilon} \right) \frac{\partial \epsilon}{\partial x_j} \right) + C_{\epsilon 1} \frac{\epsilon}{K} P_k - C_{\epsilon 2} \rho \frac{\epsilon^2}{K} + 2\mu_T \nu \left(\frac{\partial^2 U_i}{\partial x_j \partial x_k} \right)^2 \quad (15)$$

$$\text{where } \mu_T = f_\mu c_\mu \frac{k^2}{\epsilon} \quad f_\mu = \exp \left(\frac{-3.4}{(1+0.02R_T)^4} \right)$$

$$R_T = k^2 / \nu \epsilon$$

$$C_{\epsilon 2} = C_{\epsilon 2} \left\{ 1 - \frac{0.4}{1.8} \exp(-R_T^2/36) \right\} \quad (16)$$

$$\epsilon = \epsilon - 2\nu \left(\frac{\partial \sqrt{k}}{\partial x_j} \right)^2$$

The empirical constants appearing in equations (1) to (16) are given the following standard values

C_1	C_2	C_1	C_2	$C_{\epsilon 1}$
1.8	0.6	0.5	0.3	1.44
$C_{\epsilon 2}$	C_k	C_ϵ	C_μ	C_η
1.92	0.22	0.15	0.09	2.55
σ_k	σ_ϵ			
1	1.22			

The second stage was the replacement of the eddy viscosity stress-strain formula by an ASM formulation. No suitable ASM proposals for the near-wall sublayer were known to us so the following version has been devised in the present work

$$\frac{U_i U_j}{K} = \frac{2}{3} \delta_{ij} + \frac{(1-C_2) (P_{ij} - \frac{2}{3} P_k \delta_{ij})}{\epsilon (C_1 - 1 + f_s + P_k/\epsilon)} + \frac{f_\mu \phi_{ij}^w}{\epsilon (C_1 - 1 + f_s + P_k/\epsilon)} + \frac{(H_{ij} - \frac{1}{3} H_k \delta_{ij})}{\epsilon (C_1 - 1 + f_s + P_k/\epsilon)} \quad (17)$$

$$+ \frac{0.06k \left(\frac{\partial U_i}{\partial x_j} + \frac{\partial U_j}{\partial x_i} \right) \exp(-R_t/8)}{\epsilon (C_1 - 1 + f_s + P_k/\epsilon)}$$

$$f_s = \exp(-R_T/12)$$

$$f_w = [1 - \exp(-R_T/25)] [1 + \exp(-R_T/100)] \quad (18)$$

$$H_{ij} = f_H \left\{ \frac{U_i U_j}{\nu} \frac{\partial \sqrt{k}}{\partial x_i} \frac{\partial \sqrt{k}}{\partial x_j} + \frac{U_j U_i}{\nu} \frac{\partial \sqrt{k}}{\partial x_i} \frac{\partial \sqrt{k}}{\partial x_j} \right\} \frac{\nu}{K} \quad (19)$$

$$f_H = (15.6 + 2.4R_T) \exp(-R_T/20) \quad (20)$$

The k and ϵ equations now become:

$$\frac{\partial}{\partial x_j} (\rho U_j k) = \frac{\partial}{\partial x_j} \left\{ \left(\mu \delta_{ij} + c_k \frac{\rho k}{\epsilon} \frac{U_i U_j}{\nu} \right) \frac{\partial k}{\partial x_j} \right\} + \rho P_k - \rho \epsilon - 2\mu \left(\frac{\partial \sqrt{k}}{\partial x_j} \right)^2 \quad (21)$$

$$\frac{\partial}{\partial x_j} (\rho U_j \epsilon) = \frac{\partial}{\partial x_j} \left\{ \left(\mu \delta_{ij} + c_\epsilon \frac{\rho k}{\epsilon} \frac{U_i U_j}{\nu} \right) \frac{\partial \epsilon}{\partial x_j} \right\} + C_{\epsilon 1} \rho \frac{\epsilon}{K} P_k - C_{\epsilon 2} \rho \frac{\epsilon^2}{K} + 2\mu_T \nu \left(\frac{\partial^2 U_i}{\partial x_j \partial x_k} \right)^2 \quad (22)$$

All the constants are the same as previously defined apart from f_μ which is now:

$$f_\mu = \exp \left\{ \frac{-2.9}{(1+0.003R_T)(1+0.004R_T)} \right\} \quad (23)$$

The above version reflects our desire to produce, rather quickly, a low-Reynolds-number extension of the basic ASM that generated broadly the correct shear stress variation across the sublayer. No attempt has been made to satisfy the two-component turbulence limit or other kinematic constraints that are becoming popular with more elaborate (full) second-moment closures. The low-Reynolds-number terms in the present ASM formulation have been calibrated by reference to fully-developed flow in a straight pipe.

3. APPLICATION TO FLOW IN AN S-BEND

The test-case considered here is the flow through a circular sectioned S-bend measured by Taylor et al [13]. The duct consists of two identical curved sections of 22.5 degrees arc, the radius of curvature being 14 times the pipe radius. The four measuring stations are shown in Fig 1. Most attention will be given to the final station just prior to the end of the S-bend as the flow there is more strongly affected by the straining history than at earlier stations.

The numerical computations began 3 diameters upstream of the bend. The entry conditions for the computation were generated by making a separate computation of flow in a straight tube. The position at which the straight-tube profile of streamwise mean velocity agreed most closely with the measured upstream data was used to fix the initial conditions for the S-bend computations for all dependent variables. The 3D computations covered one half of the duct lying on one side of the flow's (presumed) plane of symmetry. The following grids were adopted: for the 1-equation sublayer model: 36 (radial) x 31 (circumferential) x 76 (streamline); for the two-equation models: 50 x 31 x 76. Extensive grid refinement studies with variants of the present code applied to similar flows (see, for example, Iacovides and Launder [3], Launder and Loizou [14]) provide evidence that these grid densities

lead to a sensibly grid-independent numerical solution.

Figure 2 provides comparisons between the experimental streamwise velocity profiles (measured along the non-parallel radial lines indicated in the inset sketch) and the corresponding computations obtained with the 1-equation sublayer model. The left side of the figures (- R) corresponds with the inside of the bend over the first 22.5 degrees of arc. At stations 1 and 2 the computed behaviour closely mimics the measurements. Over the second half of the S-bend, however, it is seen that the fluid near the mid-plane to the left of the figure has considerably smaller velocity than in the computations.

The corresponding predicted behaviour over the final two stations using the more elaborate near-wall turbulence models is shown in Fig 3. The two-equation eddy viscosity scheme brings a moderate improvement in the level of accord achieved while the ASM scheme does considerably better. Another way of comparing the streamwise velocity field is by way of contour plots, Fig 4. These bring out the much stronger low-velocity bulge (near what from station 3 onwards has become the outside of the bend) produced when the low-Reynolds-number ASM scheme is employed. The different contour shapes could reflect the different response of the axial flow to the very steep streamwise pressure gradients encountered near the entry to the second half of the S-bend (see Fig 8); or it could indicate differences in the secondary flow pattern. Probably both factors are influential. Unfortunately the secondary velocities were measured only along the diametral line perpendicular to the plane of symmetry. It is seen from Fig 5 that at the final station the low-Reynolds-number ASM scheme does exhibit closer agreement with the near-wall secondary flow measurements. It might be noted, however, that the main differences in the secondary flow pattern among the three sets of predictions are to be found near the inside of the bend. Fig 6, which presents the secondary velocity at station 4, shows that near the symmetry plane towards the inside of the bend there is virtually no secondary motion with the 1-equation model while a distinct return flow is present with the other models, and is particularly noticeable with the ASM treatment.

The changes in the near-wall model bring about a moderate improvement in the fidelity with which the normal stress field is predicted. Figure 7, for example, compares the measured streamwise turbulence intensities at station 4 with predictions generated by the 1-equation and ASM sublayer models. The experimental profiles indicate that the higher turbulence intensities occur to the left of the figure; the 1-equation computations show the reverse. The ASM sublayer scheme produces higher near-wall velocity fluctuations on the left side (at this position the concave surface) bringing closer accord with the experimental

distribution, albeit incomplete.

The final comparison in Fig 8 concerns the variation of wall static pressure through the S-bend at 90 degree intervals around the perimeter. For all three models the computed variation through the first S-bend is rather satisfactory, partly reflecting the relatively small contribution that the boundary layers exert on the static pressure during the initial rapid straining. The one-equation scheme seriously underestimates the loss of static pressure during the "changeover" between the two halves of the bend. The two-equation near-wall treatment achieves a somewhat improved variation while the ASM scheme a considerably better accord. These results while perhaps not surprising, in view of the progressive improvement in the streamwise velocity field arising from successively upgrading the sublayer turbulence model, are nevertheless satisfying in that they are entirely consistent with the behaviour considered in Figure 2 and thus lend weight to the conclusions that that comparison suggested.

A companion set of computations for an identically proportioned square-sectioned U-bend has been carried out using the 1-equation sublayer model which will be reported elsewhere [5]. These results, too, appear to be fully consistent with the behaviour found here for the circular sectioned duct and thus help to reinforce some of the conclusions drawn.

4. CONCLUDING REMARKS

The present study has examined the sensitivity of the predicted flow in a circular sectioned S-bend to the near-wall model of turbulence. The initial computations, employing a 1-equation model across the sublayer and the usual algebraic second-moment closure for the fully turbulent core flow exhibited what were felt to be surprisingly large disagreements with the measurements of the streamwise velocity distribution near the bend exit and the static pressure drop through the bend.

This discovery led us to focus attention on refining the near-wall turbulence model, first to a two-equation eddy viscosity form and thereafter to an algebraic second-moment closure. The former refinement allows non-equilibrium distributions of near-wall turbulent length scale to arise should rapid streamwise rates of change occur while the latter also allows the sublayer region (as well as the fully turbulent core fluid) to be sensitive to the effects of streamline curvature on the strain field. This elaboration in the near-wall treatments led to clear-cut improvements in the quality of the predictions, particularly the switch to an ASM treatment.

The study thus seems to indicate that the increasingly popular practice of interfacing a 1-equation eddy viscosity treatment in the sublayer with a two-equation eddy viscosity or ASM model

for the core fluid is not an adequate representation for bend flows when high accuracy is required. For the future it is the authors' view that further research on the computational modelling of three-dimensional flows in curved ducts should most usefully be directed at employing a full second-moment closure (rather than the algebraic truncation used here) over the complete cross section. It is difficult for us to envisage that any simpler formulation will be widely seen as a useful level at which to standardize given the very rapid increases in numerical processing rates that are becoming possible thanks to hardware and software developments.

5. ACKNOWLEDGEMENTS

The research has been sponsored by British Aerospace (Military Aircraft) Ltd. under contract GR/F70495 with further support provided by Rolls Royce plc. The camera-ready manuscript has been prepared by Mrs J. Buckley.

Authors' names are listed alphabetically.

6. REFERENCES

1. Levy, R., Briley, W.R. and McDonald, H., (1983), "Viscous Primary/Secondary Flow Analysis for Use with Nonorthogonal Coordinate Systems", AIAA-83-0556, 21st Aero Sciences Meeting, Reno, Nevada, 1983.
2. Anderson, B.H., (1991), "The Aerodynamic Characteristics of Vortex Ingestion for the FIA-18 Inlet Duct", AIAA-91-0139, 29th Aero Sciences Meeting, Reno, Nevada, 1991.
3. Iacovides, H. and Launder, B.E., (1985), "ASM Predictions of Turbulent Momentum and Heat Transfer in Coils and U-Bends", Proc. 4th Int. Conf. on Num. Meth. in Lam. and Turb. Flows, Swansea, 1985.
4. Gibson, M.M., "Effects of Surface Curvature on the Law of the Wall", Proc. Zoric Memorial International Seminar on Wall Turbulence, Dubrovnik, Yugoslavia, Hemisphere Publishing Corp., 1988.
5. Abou-Haidar, N.I. and Iacovides, H., (1991), "The Computation of Turbulent Flow Through an S-Bend of Square Cross-Section", In preparation.
6. Iacovides, H. and Launder, B.E., (1984), "The Computation of Momentum and Heat Transport in Turbulent Flow around Pipe Bends", 1st UK National Heat Transfer Conf., Leeds, 1984.
7. Choi, Y-D, Iacovides, H. and Launder, B.E., (1989), "Numerical Computation of Turbulent Flow in a Square-Sectioned 180-deg Bend", ASME J. Fluids Engrg., March 1989.
8. Gibson, M.M. and Launder, B.E., (1978), "Ground Effects on Pressure Fluctuations in the Atmospheric Boundary Layers", J.F.M., 85, p.491.
9. Iacovides, H. and Launder, B.E., (1990), "Parametric and Numerical Study of Fully-Developed Flow and Heat Transfer in Rotating Rectangular Ducts", ASME 90-GT-24, ASME Int. Gas Turb. Congress, Brussels, 1990.
10. Wolfshtein, M., (1969), "The Velocity and Temperature Distribution in One-Dimensional Flow with Turbulence Augmentation and Pressure Gradient", Int. J. Heat and Mass Transfer, 12, p.301.
11. Yap, C.R., (1987), "Turbulent Heat and Momentum Transfer in Recirculating and Impinging Flows", PhD. Thesis, Faculty of Technology, University of Manchester.
12. Launder, B.E. and Sharma, B.J., (1974), "Application of the Energy-Dissipation Model of Turbulence to the Calculation of Flow near a Spinning Disc", Lett. Heat and Mass Transfer, 2, p.1.
13. Taylor, A.M.K.P., Whitelaw, J.H. and Yianneskis, M., (1982), "Developing Flow in S-Shaped Ducts - Part II: Circular Cross-Section Duct", Report FS/82/7, Imperial College, Fluids Section (NASA CR3759).
14. Launder, B.E. and Loizou, P.A., (1989), "Laminarization in 3-Dimensional Accelerating Flow Through Curved Rectangular Ducts", 7th Turb. Shear Flows Symp., Stanford, California, 1989.

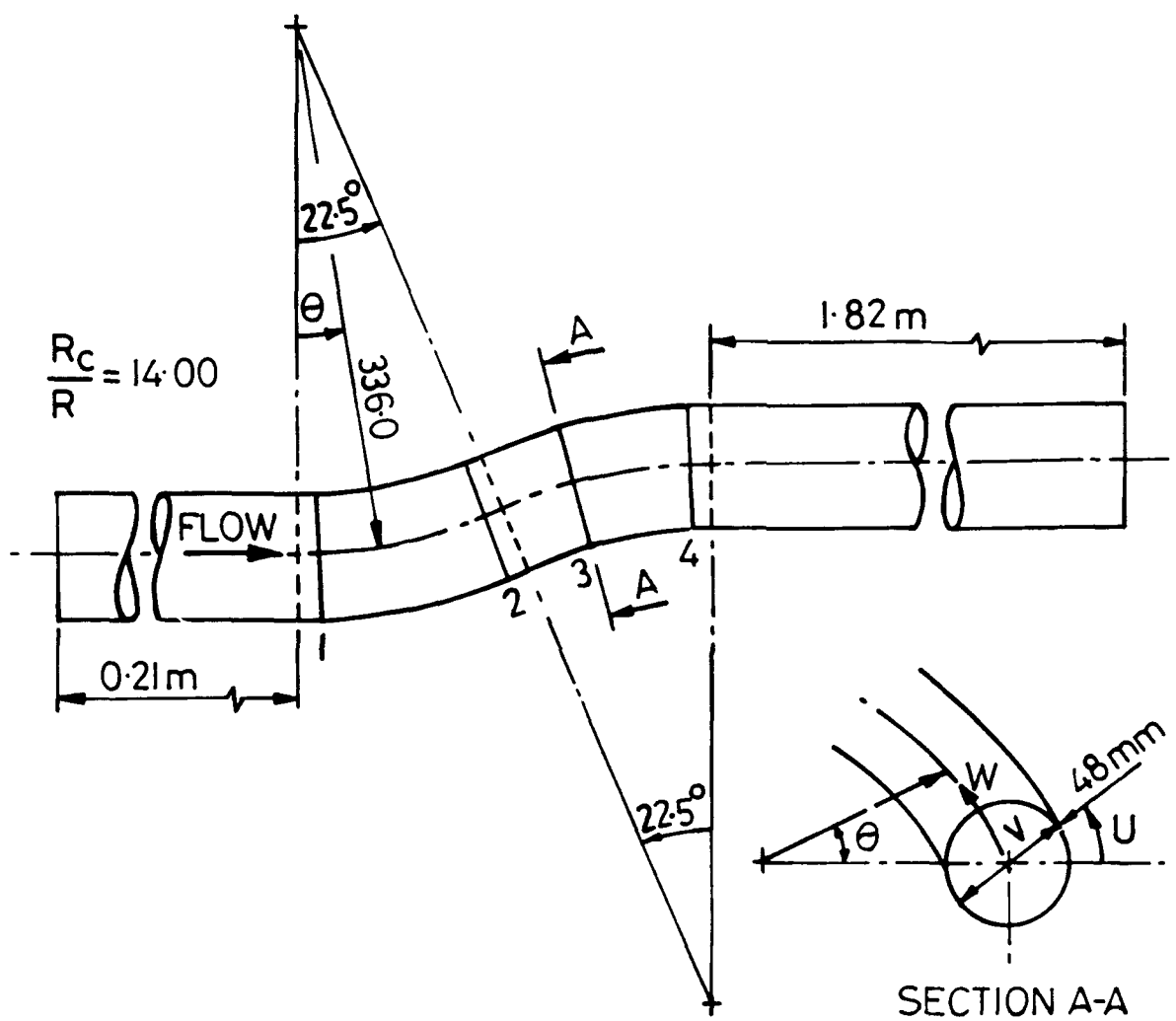
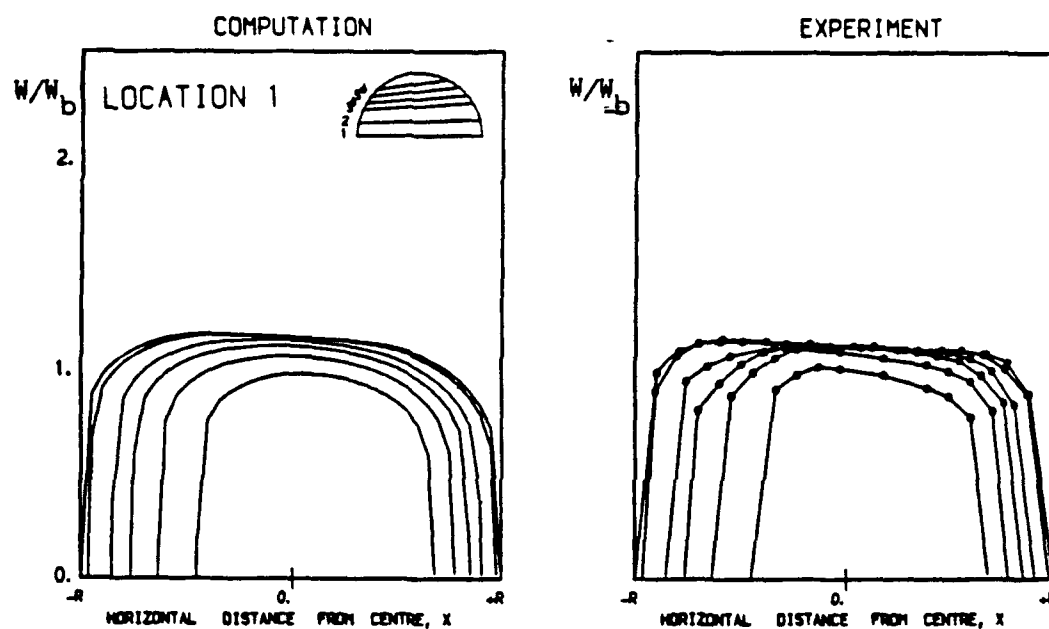
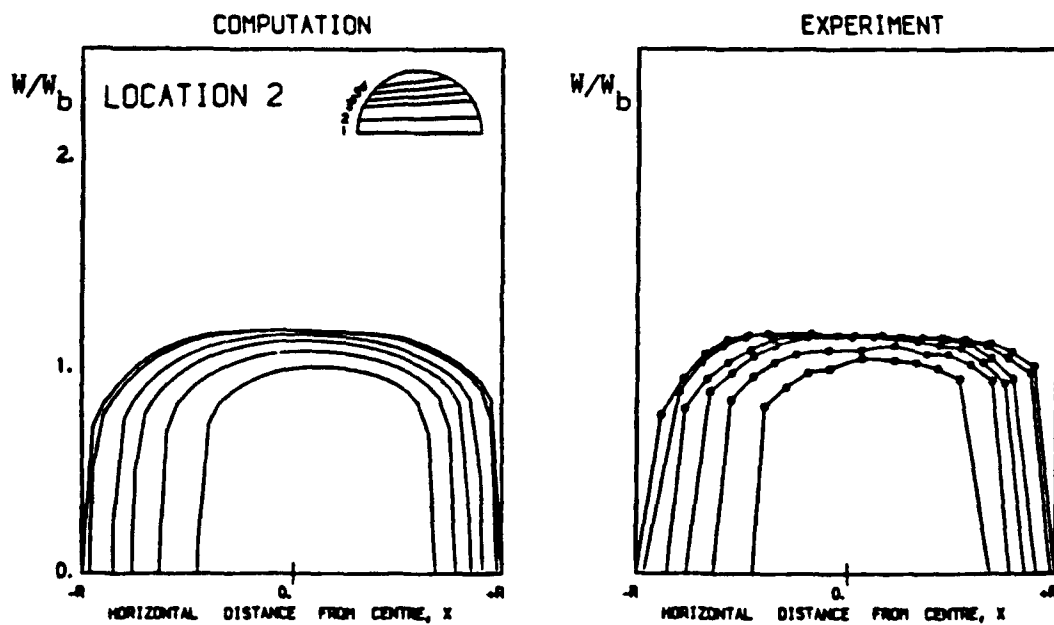


Figure 1 Flow Geometry

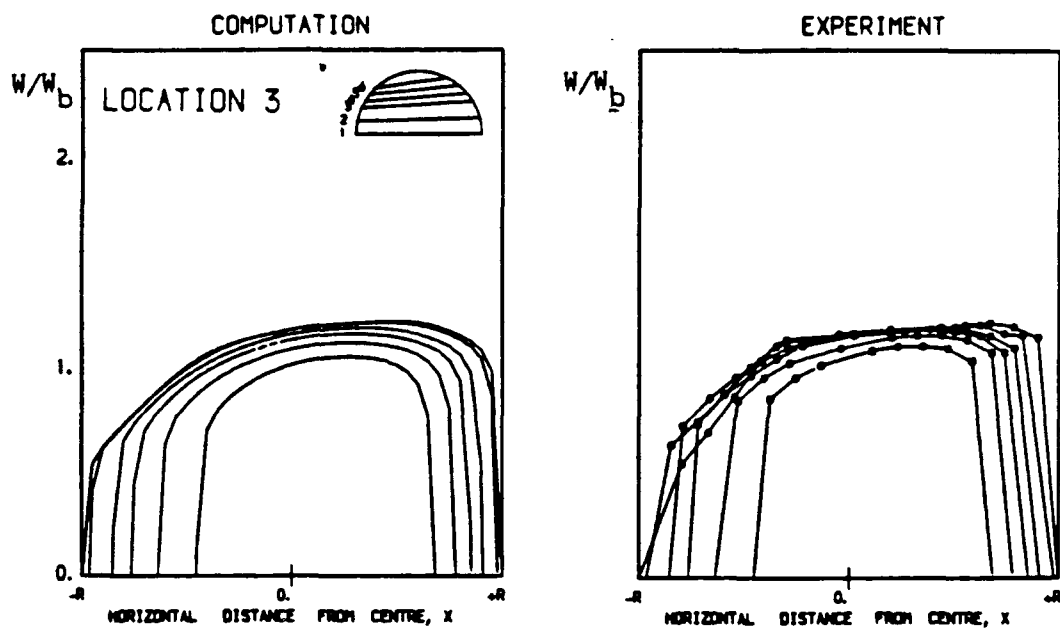


(a) Location 1

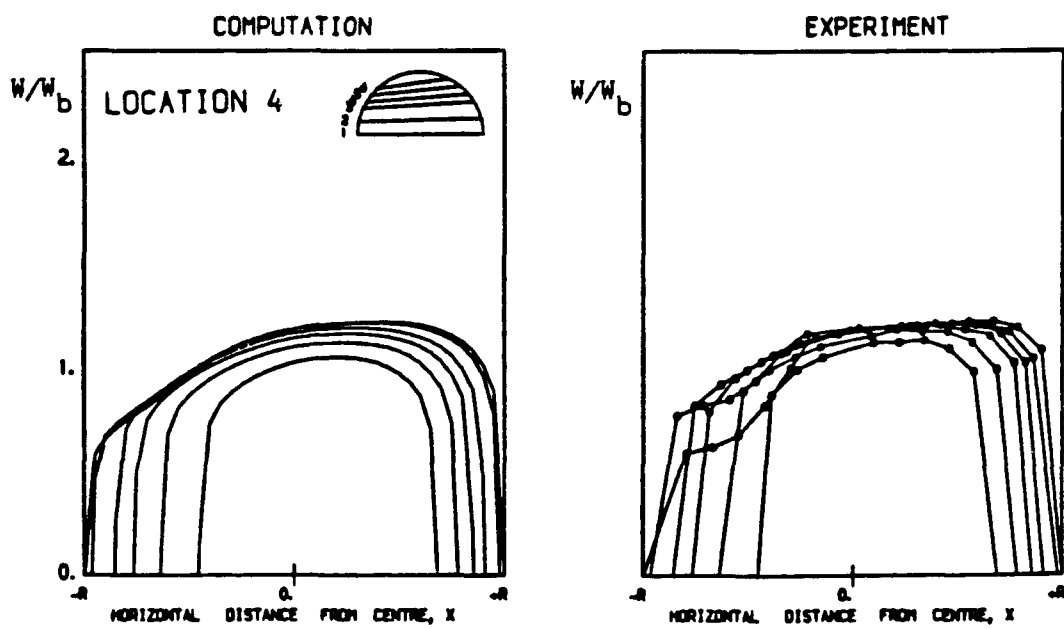


(b) Location 2

Figure 2 Comparisons between predicted and experimental streamwise velocity profiles using the ASM/1-EQN model

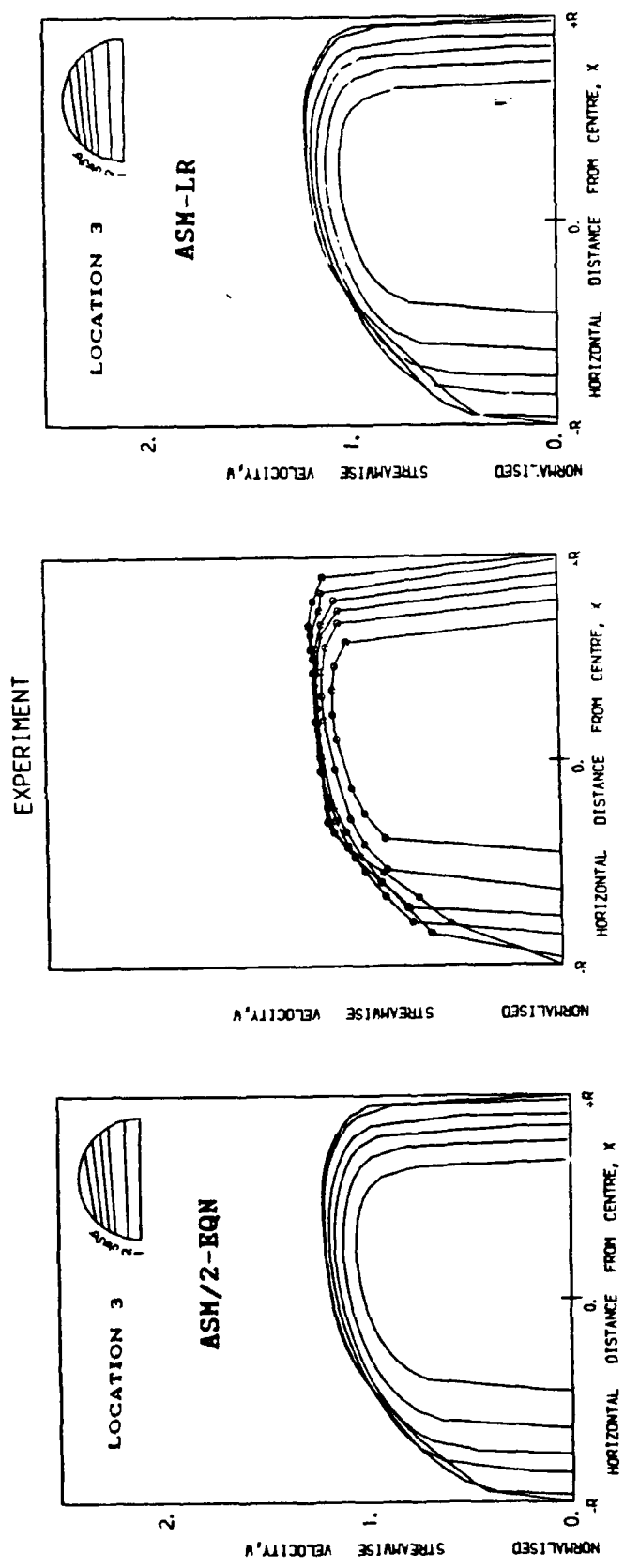


(c) Location 3



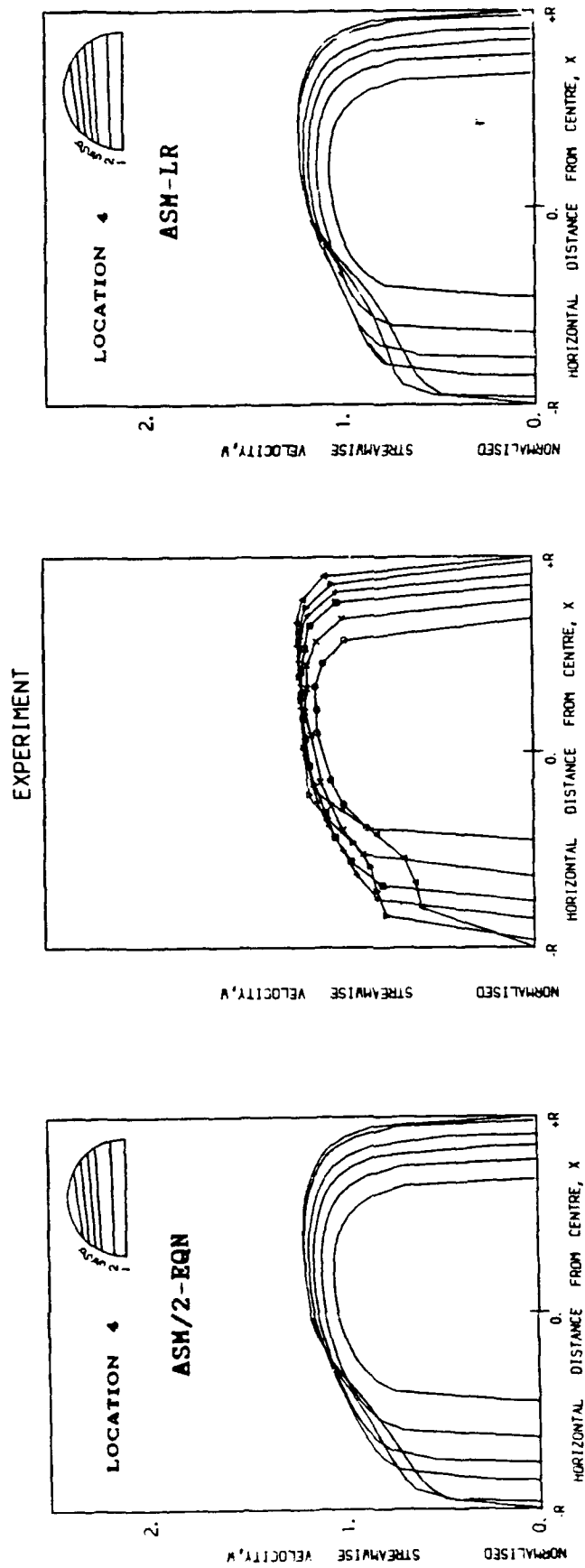
(d) Location 4

Figure 2 continued



(a) Location 3

Figure 3 Effects of near-wall model refinements on the streamwise velocity profiles



(b) Location 4

Figure 3 continued

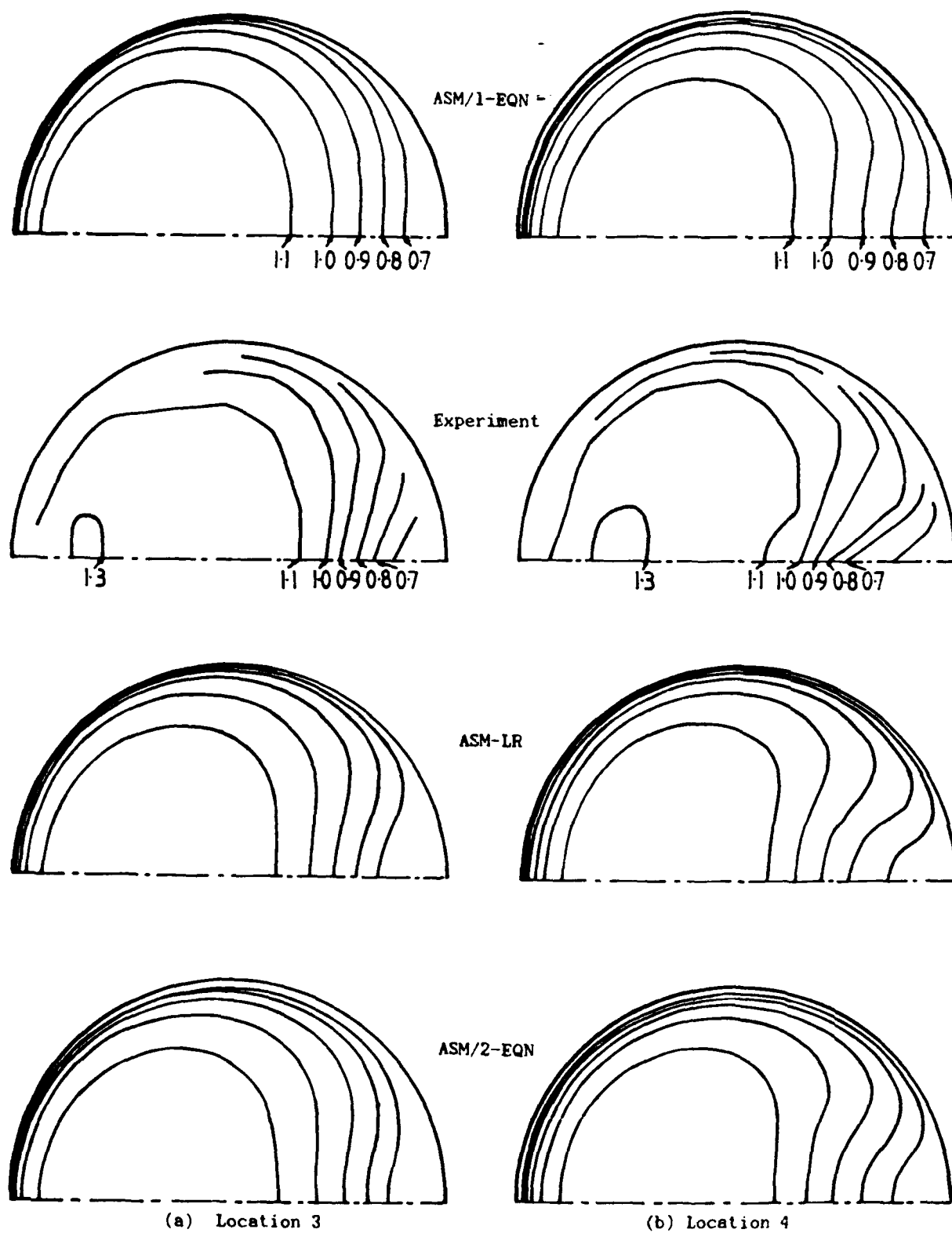


Figure 4 Comparisons between experimental and predicted streamwise velocity contours

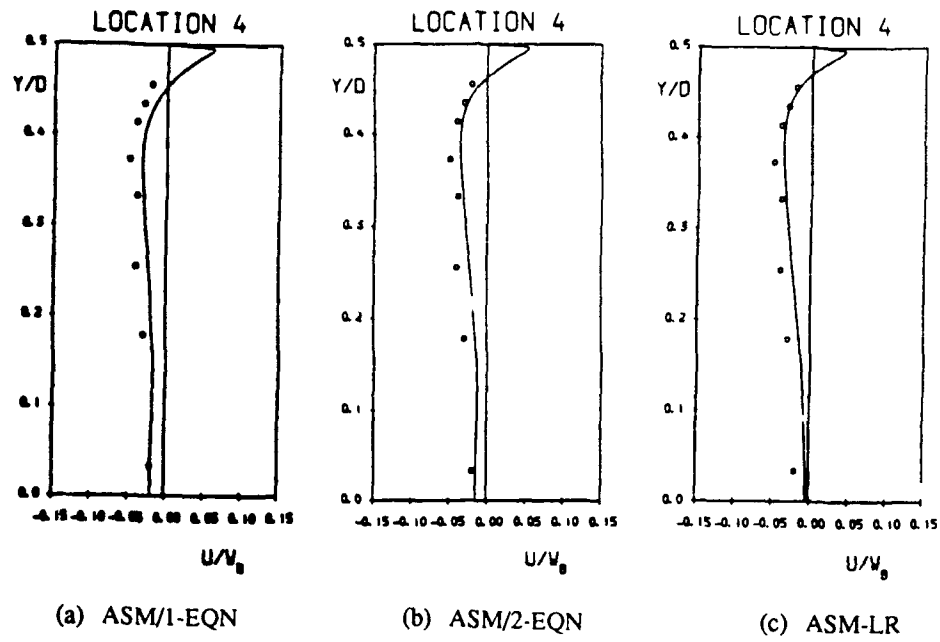
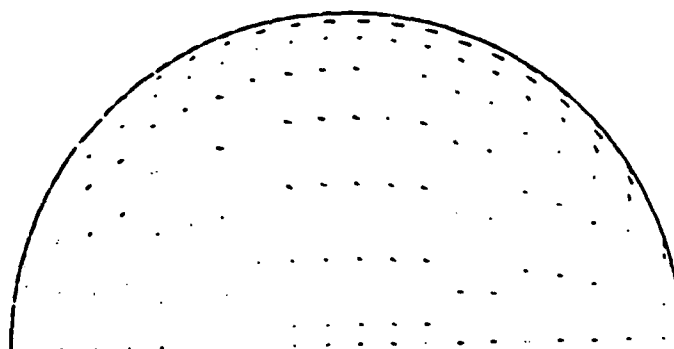
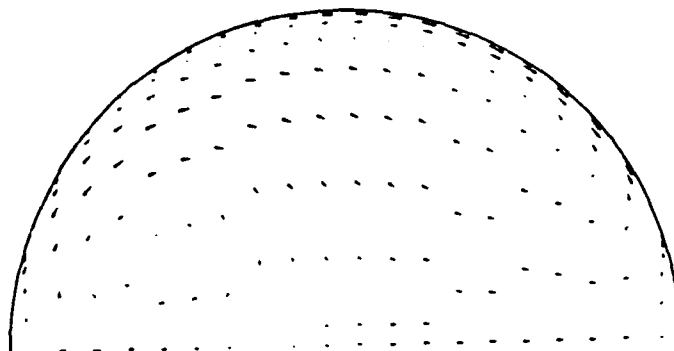


Figure 5 Comparisons of circumferential velocity profiles along the radius normal to the symmetry plane at location 4

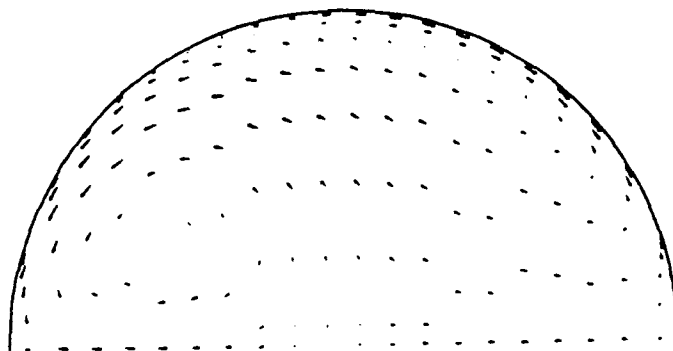
Figure 6 Predicted secondary velocity
field at location 4



(a) ASM/1-EQN



(b) ASM/2-EQN



(c) ASM-LR

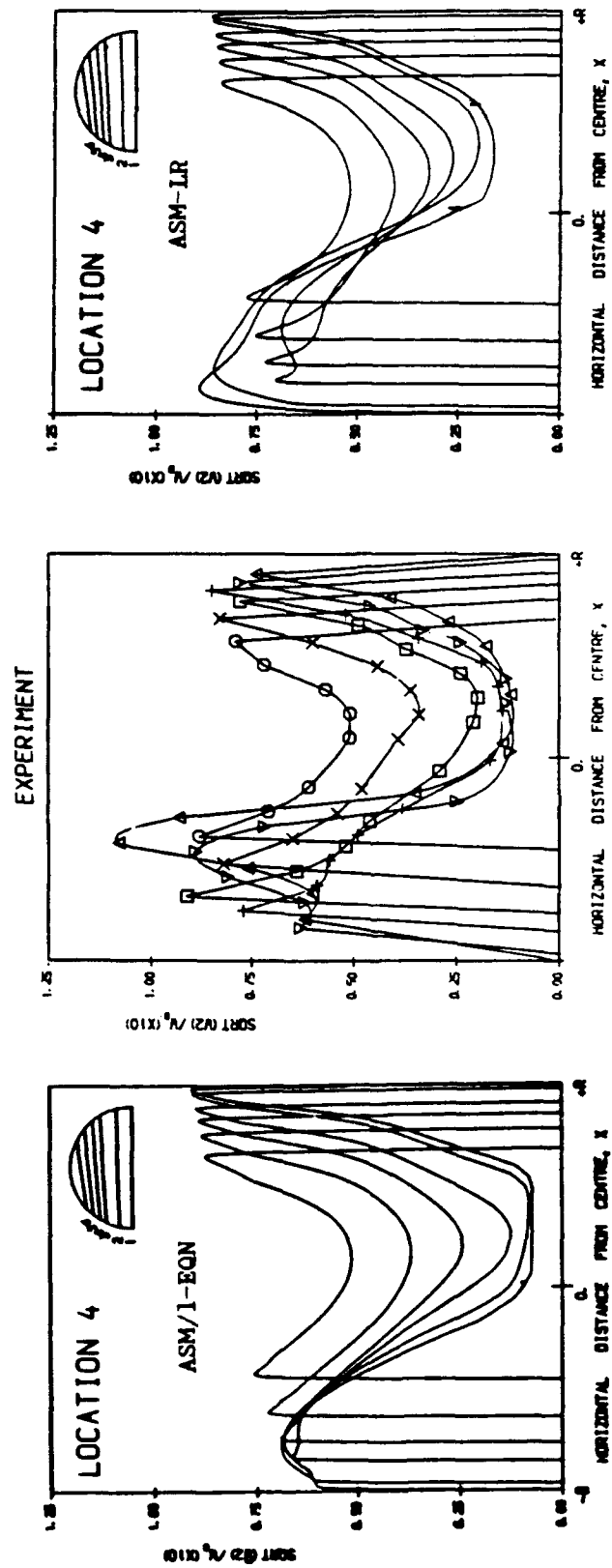
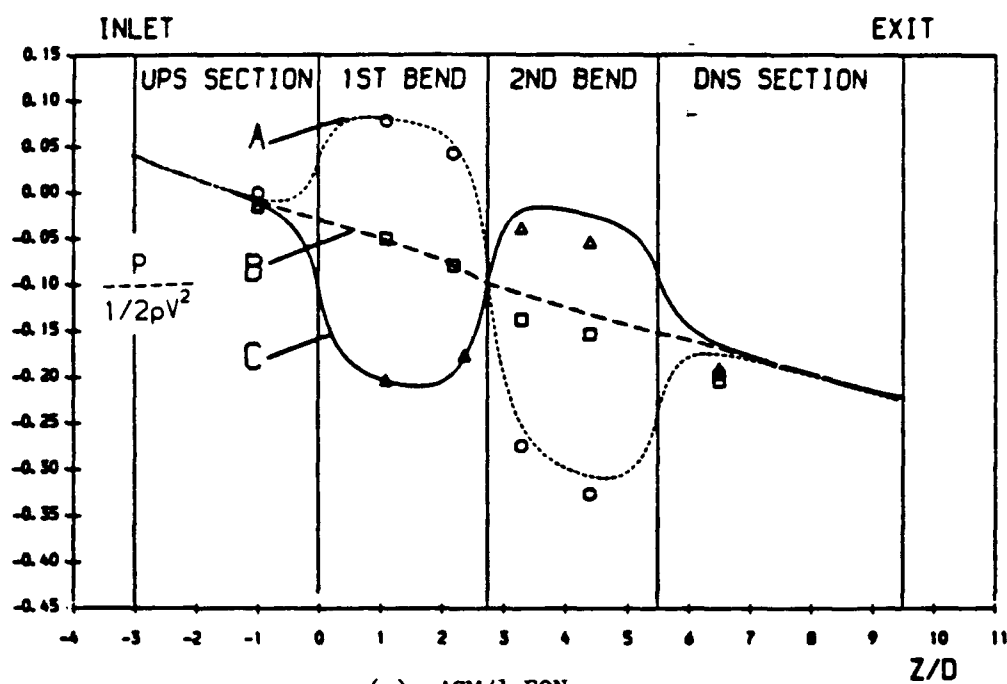


Figure 7 Comparisons of streamwise normal stress profiles at location 4



(a) ASM/1-EQN

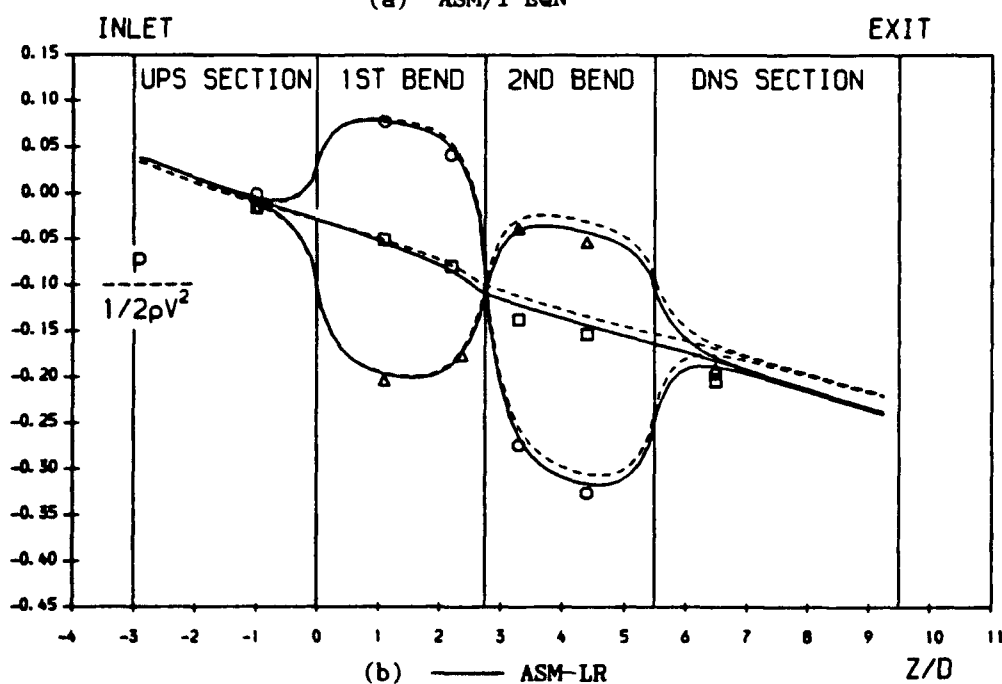
(b) — ASM-LR
----- ASM/2-EQN

Figure 8 Comparisons between measured and predicted wall static pressure

Discussion

P. COELHO, INST. SUPERIOR TECNICO, PORTUGAL

- 1) When the low Reynolds number $k-\epsilon$ model was used, 50 grid nodes were employed in the radial direction. How many of them were placed in the near wall region?
- 2) Can you compare the convergence rate for two different near wall treatments: standard wall functions and low Reynolds number model?
- 3) Did you use the QUICK scheme only for the corrective terms in the momentum conservation equations? Or was it applied also for k and ϵ transport equations?

AUTHOR'S REPLY

- 1) When the low-Reynolds versions of the $k-\epsilon$ and of the ASM model were employed 20 to 24 radial grid nodes were placed in the near-wall region. Earlier investigations included in Ref. 14 of this paper indicate that this number is sufficient.
- 2) No such convergence comparisons were carried out in the course of this study. Use of a low-Reynolds near-wall model however (instead of the wall function approach) involves the employment of a finer mesh and inevitably leads to an increase in the number of iterations required for convergence. It must also be pointed out that as the complexity of the near-wall model increases a further increase in the number of required iteration occurs.
- 3) In this investigation the QUICK scheme was only used for the discretization of the cross-stream convective terms of the mean momentum transport equations. Because the mesh employed in this study however was sufficiently fine, results obtained using the QUICK scheme were identical to those computed using the HYBRID scheme.

H. WEYER, DLR, GERMANY

- 1) Please comment on the type of measurements you based your calculations on and what is the level of accuracy?
- 2) Are these three-dimensional LDV measurements and what is the size of the particles the flow is seeded with?

AUTHOR'S REPLY

The experimental measurements, with which the present computations have been compared, have been obtained by Prof. Whitelaw's group at Imperial College London, using Laser-Doppler velocimetry. For the mean flow measurements the experimentalists quote a systematic error of up to 3 percent and a random error of up to 1-1/2 percent. For the measurement of the turbulence quantities the corresponding errors quoted by the experimentalists are up to 3 percent and 5 percent respectively. Water was used as the working fluid and it was seeded with only minute quantities of milk.

C. TAYLOR, UNIV. OF SWANSEA, U.K.

Did the authors analyze the flow in a straight rectangular/square duct? Our experience shows that both $k-l$ and $k-\epsilon$ models cannot predict perturbation induced secondary flows.

AUTHOR'S REPLY

This version of the near-wall ASM model has not yet been applied to square-ducts. Our earlier experiences with the standard high-Reynolds ASM version are in agreement with the questioner's findings.





THREE DIMENSIONAL FLOW IN SHARP BENDS

K. Fotea
P. Prinos
A. Goulas

Lab. of Fluid Mechanics and Turbomachinery
Dept. of Mechanical Engineering
Aristotle University of Thessaloniki
54006 Thessaloniki, GREECE

Aristotle

SUMMARY

The three - dimensional flow in sharp bends is computed by solving the fully elliptic three - dimensional Navier - Stokes equations in conjunction with a $k - \epsilon$ model of turbulence. Computed isovelocity patterns before and after the sharp bend and recirculation lengths are compared with experimental measurements taken using Laser Doppler Anemometry. In general good agreement is obtained although refinements in the turbulence modelling can improve the predictions. The computational results show that the recirculating region to depends strongly on the inlet velocity profile. Finally an increase of the aspect ratio of the duct indicates an increase of the region of the recirculation.

1. INTRODUCTION

Flow in sharp bends is encountered in many engineering applications , such as fluid machinery , heat exchangers , heating and ventilating systems, chemical processing plants , etc. While the geometry is apparently simple , the flow characteristics are quite complex. With a change of flow direction in the sharp bend a transverse secondary motion is initiated and this is superimposed on the primary flow field.

In the past , the flow through bends and especially bend curvature has been studied extensively .(1,4,6, among others). Also, studies of two-dimensional flow in a channel with a variable angle branch (5,8) and three-dimensional turbulent flow in a splitting T-junction (11,12) have been carried out. Recently , the flow in two-dimensional sharp bends has been studied numerically (3) with emphasis on the effect of the turbulence model on the recirculation region. However, to the authors ' knowledge , the three dimensional character of flow in sharp bends, has not examined yet so extensively.

In this study, three-dimensional flow in sharp bends is studied numerically by solving the fully elliptic three-dimensional Navier-Stokes equations, for steady, incompressible, turbulent flow. Computational results are compared with initial experimental results (2) taken by Laser-Doppler anemometry. The system of Navier-Stokes equations is "closed" with the $k - \epsilon$ model of turbulence and is solved with a finite volume method in primitive variables , based on Patankar's (9) procedure.

Also , the effect of inlet profile on the flow characteristics is considered using three initial profiles (uniform , experimental and fully developed). In general , good agreement between predictions and experiments is achieved but some discrepancies are observed mainly due to the turbulence model as grid independance has been checked by changing the size of the grid. Of special interest is the effect of the aspect ratio (duct width / height) of the duct on the characteristics of the flow (secondary flow, reattachment lengths etc.), hence , calculations were performed for three aspect ratios ($W/H=3, 2$ and 1). For $W/H=2$, experimental measurements are also available and a comparison between experimental and computational results are made.

2. EXPERIMENTAL APPARATUS

The L- shaped duct with an aspect ratio of 2 was set up at the suction side of a centrifugal fan . The inlet duct had an L/D_h ratio of 20 , where D_h is the hydraulic diameter of the duct. The corner region itself was made of plexiglas to allow optical access for the L.D.A. system. A considerable distance $L/D_h = 20$, was set between the inlet plenum of the fan and the corner in order to avoid any interference from the flow in the fan . A honeycombe was set at the inlet to the duct in order to achieve a symmetrical profile upstream of the corner. The symmetry was checked using a Pitot tube assembly.

Measurements were taken using a forward scatter laser Doppler system with frequency shift and a counter. Naturally occurring dust was used as seeding. Preliminary results are given here. The main problem encountered is in the region of the recirculation , where the particles because of their size and the relatively large relaxation time did not respond quickly to the reverse flow conditions . As a result the magnitude of the velocity within the recirculation region and very close to the corner was smaller than expected. Further measurements with the aim of refining the data acquisition system within the recirculation region are already under way.

3. THE GOVERNING EQUATIONS

The three-dimensional, Reynolds -averaged, Navier-Stokes equations for steady , incompressible turbulent flow are used for calculating the flow characteristics in sharp bends, assuming that the turbulent stresses are estimated via the eddy viscosity concept:

Continuity equation:

$$\frac{\partial u}{\partial x} + \frac{\partial v}{\partial y} + \frac{\partial w}{\partial z} = 0. \quad (1)$$



x- momentum

$$\begin{aligned} \frac{\partial}{\partial x}(UU) + \frac{\partial}{\partial y}(UV) + \frac{\partial}{\partial z}(UW) - \frac{1}{\rho} \frac{\partial p}{\partial x} \\ + \frac{\partial}{\partial x} \left[2v_{eff} \frac{\partial U}{\partial x} \right] + \frac{\partial}{\partial y} \left[v_{eff} \left(\frac{\partial U}{\partial y} + \frac{\partial V}{\partial x} \right) \right] \\ + \frac{\partial}{\partial z} \left[v_{eff} \left(\frac{\partial U}{\partial z} + \frac{\partial W}{\partial x} \right) \right] \end{aligned} \quad (2)$$

y- momentum

$$\begin{aligned} \frac{\partial}{\partial x}(VU) + \frac{\partial}{\partial y}(VV) + \frac{\partial}{\partial z}(VW) - \frac{1}{\rho} \frac{\partial p}{\partial y} \\ + \frac{\partial}{\partial y} \left[2v_{eff} \frac{\partial V}{\partial y} \right] + \frac{\partial}{\partial x} \left[v_{eff} \left(\frac{\partial U}{\partial y} + \frac{\partial V}{\partial x} \right) \right] \\ + \frac{\partial}{\partial z} \left[v_{eff} \left(\frac{\partial V}{\partial z} + \frac{\partial W}{\partial y} \right) \right] \end{aligned} \quad (3)$$

z- momentum

$$\begin{aligned} \frac{\partial}{\partial x}(WU) + \frac{\partial}{\partial y}(WV) + \frac{\partial}{\partial z}(WW) - \frac{1}{\rho} \frac{\partial p}{\partial z} \\ + \frac{\partial}{\partial z} \left[2v_{eff} \frac{\partial W}{\partial z} \right] + \frac{\partial}{\partial x} \left[v_{eff} \left(\frac{\partial U}{\partial z} + \frac{\partial W}{\partial x} \right) \right] \\ + \frac{\partial}{\partial y} \left[v_{eff} \left(\frac{\partial V}{\partial z} + \frac{\partial W}{\partial y} \right) \right] \end{aligned} \quad (4)$$

where: U, V, W : velocity components in the traverse ($-x$), vertical ($-y$) and longitudinal ($-z$) directions respectively, p = effective pressure, v_{eff} = effective viscosity ($v_{eff} = \nu + \nu_t$)
 ν = kinematic viscosity, ν_t = turbulent viscosity, ρ = fluid

density.

In the above equations the eddy viscosity concept was assumed to be valid. The Reynolds stresses are calculated through the eddy viscosity which in turn is determined by the $k - \epsilon$ model of turbulence.

The eddy viscosity is determined from the following relationship :

$$\nu_t = c_\mu \frac{k^2}{\epsilon} \quad (5)$$

where k = the turbulent kinetic energy

ϵ = the rate of dissipation of k
 and c_μ = constant = (0.09).

The $k - \epsilon$ model uses two transport equations for k and ϵ ,

which close the system of equations
 (1) - (4), and are written as follows :

k - equation

$$\begin{aligned} \frac{\partial}{\partial x}(Uk) + \frac{\partial}{\partial y}(Vk) + \frac{\partial}{\partial z}(Wk) - \\ \frac{\partial}{\partial x} \left[\left(\nu + \frac{\nu_t}{\sigma_k} \right) \frac{\partial k}{\partial x} \right] + \frac{\partial}{\partial y} \left[\left(\nu + \frac{\nu_t}{\sigma_k} \right) \frac{\partial k}{\partial y} \right] \\ + \frac{\partial}{\partial z} \left[\left(\nu + \frac{\nu_t}{\sigma_k} \right) \frac{\partial k}{\partial z} \right] + P_k - \epsilon \end{aligned} \quad (6)$$

 ϵ - equation

$$\begin{aligned} \frac{\partial}{\partial x}(U\epsilon) + \frac{\partial}{\partial y}(V\epsilon) + \frac{\partial}{\partial z}(W\epsilon) - \\ \frac{\partial}{\partial x} \left[\left(\nu + \frac{\nu_t}{\sigma_\epsilon} \right) \frac{\partial \epsilon}{\partial x} \right] + \frac{\partial}{\partial y} \left[\left(\nu + \frac{\nu_t}{\sigma_\epsilon} \right) \frac{\partial \epsilon}{\partial y} \right] \\ + \frac{\partial}{\partial z} \left[\left(\nu + \frac{\nu_t}{\sigma_\epsilon} \right) \frac{\partial \epsilon}{\partial z} \right] + c_1 P_k \frac{\epsilon}{k} - c_2 \frac{\epsilon^2}{k} \end{aligned} \quad (7)$$

where P_k = the rate of production of k and $c_1, c_2, \sigma_k, \sigma_\epsilon$ constants (= 1.44, 1.92, 1.0, 1.3 respectively).

The term P_k is given by the following relationship:

$$\begin{aligned} P_k = -\overline{u^2} \frac{\partial U}{\partial x} - \overline{v^2} \frac{\partial V}{\partial y} - \overline{w^2} \frac{\partial W}{\partial z} \\ - \overline{uv} \left(\frac{\partial U}{\partial y} + \frac{\partial V}{\partial x} \right) - \overline{uw} \left(\frac{\partial U}{\partial z} + \frac{\partial W}{\partial x} \right) \\ - \overline{vw} \left(\frac{\partial V}{\partial z} + \frac{\partial W}{\partial y} \right) \end{aligned} \quad (8)$$

where $\overline{u^2}, \overline{v^2}, \overline{w^2}, \overline{uv}, \overline{uw}, \overline{vw}$ the three normal and shear stresses respectively. The above stresses used in the production term, are also calculated using the eddy viscosity concept.

4. SOLUTION PROCEDURE

The solution of equation (1) - (7) is based on the primitive pressure - velocity approach using a finite volume method described extensively by Pantankar (9).

The pressure is deduced using the SIMPLE algorithm of Pantakar and Spalding (10).

The procedure incorporates displaced grids for the velocity components which are placed between nodes where the pressure is stored. Solution of the resulting algebraic equations is achieved using a plane-by-plane algorithm for all variables. Typical values of underrelaxation factors for convergence are .5 for velocity and pressure and .7 for k and ϵ .

5. BOUNDARY CONDITIONS

In the computational domain, shown in fig. 1, the following boundary conditions have been applied.

INLET: Three different profiles have been used to study the effect of inlet conditions with a Re-number ($Re = (W D_h) / \nu$) of 200,000. These are:

- (a) a uniform profile of the main (z-component) velocity W and values of k and ϵ such that $v_t = 10 \nu$,
- (b) a fully developed profile of W, k, ϵ obtained by a three-dimensional parabolic code applied to a straight rectangular duct and
- (c) experimental values of W, k at $z/H = .5$ and values of ϵ chosen such that $v_t = 100 \nu$. Furthermore the x- and y-components of the inlet velocity are assumed zero.

OUTLET: The gradients of all variables with respect to the duct cross-section are set equal to zero.

WALLS: The wall-function approach described by Launder and Spalding (7) is adopted. At the first computational point outside the viscous sublayer the logarithmic law of the wall prevails and the turbulence is nearly in local equilibrium. In such a point at a distance y from the wall, the velocity U_i is related to the friction velocity U_τ by the following expression:

$$U_i = U_\tau \frac{1}{\kappa} \ln(Ey^+) \quad , \quad y^+ = \frac{U_\tau y}{\nu} \quad (9)$$

where κ = von Karman constant ($\approx .41$) and E = friction parameter (≈ 9 , for smooth walls).

U_τ = friction velocity based on the resultant wall shear stress, τ_{ws} . In the numerical procedure, this wall shear stress is related to the resultant parallel velocity at the first grid point away from the wall, U_{res} , by the following relationship:

$$\tau_{ws} = \rho U_\tau^2 = \Gamma \frac{U_{res}}{y} \quad , \quad \text{where} \quad (10)$$

$$\Gamma = \frac{\rho \nu k y^+}{\ln(Ey^+)}$$

The boundary conditions for k and ϵ are also specified at the first grid point in the region of the logarithmic velocity distribution. With the assumption of the local equilibrium at this point there follows:

$$k = \frac{U_\tau^2}{\sqrt{c_\mu}} \quad (11)$$

$$\epsilon = \frac{k^3}{\kappa y} \quad (12)$$

In the corner region, U_τ is taken as a weighed average of the friction velocities at the two or three walls, which form the corner.

SYMMETRY PLANE: the gradients of all variables, except U , with respect to the plane are set to zero, while the value of the normal to the symmetry plane velocity component was set to zero.

6. COMPUTATIONAL RESULTS

For the three dimensional sharp bend, shown in fig. 1, computations have been performed using a typical grid $17 \times 68 \times 40$. Grid independence checks were carried out but they did not show any significant changes, from those obtained with the above grid. The grid positioning though affected the results particularly those close to the corners. Therefore the grid was more dense close to the solid surfaces.

Fig.2 shows the isovelocity contours normal to the cross section upstream of the 90° angle. The experimental results were also used as input to one of the predictions. The results are compared with a fully developed duct flow computed using a parabolic code and a Reynolds stress model. It is obvious that the flow is not fully developed. This is of course expected because of the small L/D_h ratio (≈ 20).

Fig.3 shows the isovelocity contours experimental and computational at station $y/h=0$. A separation region is shown in both cases at the opposite to the sharp bend, corner of the duct and remarkable agreement exists between computational and experimental results. It is also interesting to note the high velocity ridge present at a region approximately $1/3$ from the plane of symmetry which is indicative of a strong secondary flow field.

Fig.4 shows the isovelocity of the normal to the cross section velocity component at a plane immediately downstream of the sharp bend. The computational results predict the main features of the flow in the recirculation region and the extension of the high velocity area towards the inner wall but it failed to predict correctly the shear gradients at the interface between the core flow and the recirculation region although the positioning is given correctly. Extensive search showed that this "rapid" diffusion was not grid dependent. It is felt that this is the result of the $k-\epsilon$ turbulence model used for the calculations which is an isotropic model applied to a highly non-isotropic region. This is corroborated by the fact that further downstream the computational and experimental results in this flow region agree very well.

Fig.5 and 6 show the isovelocity contours at the plane further downstream of the sharp corner which support the above agreement. Furthermore the extend of the recirculation region is predicted very well.

This though is not the case towards the end of the recirculation region where the computed results show a smaller recirculation area while the experimental results indicate a velocity peak at the side wall of the duct. The explanation for such a discrepancy lies in the inability of the $k-\epsilon$ turbulence model to predict correctly the development of shear-induced secondary flow due again to the isotropic nature of the model.

It is worth remarking here that Reynolds stress modelling was attempted with the present elliptic code but was not successful due to problems of convergence while the same model worked remarkably well with the 3-D Navier-Stokes parabolic code.

Fig. 8 shows the effect the inlet profile has on the development of the flow downstream of the bend. In the case of the fully developed profile the recirculation region almost disappears at station $y/h=2.5$.

Fig. 9 shows the velocity profiles at selected stations along the plane of symmetry. The core flow and the extent of the recirculating region is predicted very well. The velocity profiles within the recirculation region and close to the corner are not predicted well. It is felt that this is the result of the poor quality of the seeding in the area. This is still under study.

Fig. 10 and 11 show the effect of the inlet profile on the extent of the three-dimensional recirculation region. For the same aspect ratio ($W/H=2.0$) the computed size of the recirculation region is compared for three different initial profiles (uniform, fully developed, experimental).

Fig. 10 shows that fully developed profile produces the smallest recirculation regions while the experimental profile (the more disturbed) produces the largest.

Finally the effect of the aspect ratio on the magnitude of the recirculation region and on the flow characteristics has been studied numerically using three different aspect ratios ($W/H=3.0, 2.0, 1.0$) and for an uniform inlet profile. Fig. 11 shows that an increase of the length of the recirculation region results from an increase of the aspect ratio. Similar results were obtained from a two-dimensional study (3). For large aspect ratios the flow at the symmetry plane tends to 2-D.

6. CONCLUSIONS

Three-dimensional flow in sharp bends has been studied numerically and a comparison with experimental measurements indicates the following:

(a) Satisfactory agreements between computed and

experimental results is obtained before the sharp bend. The model tends to overpredict the velocities in the strong recirculating region.

(b) The dimensions of the recirculating region appearing in the inner wall are affected by the inlet profile. Beyond the sharp bend qualitative agreement has been obtained close to the sharp bend itself. Further downstream the agreement is again quite good. It is thought that the turbulence model, $k-\epsilon$, used been isotropic cannot predict correctly such regions. Further refinements therefore are needed in the turbulence model to improve the prediction in the region close to the corner.

(c) An increase of the duct aspect ratio produces an increase of the recirculating region length and an decrease at its height. This indicates the significant effect the side walls have on the recirculation region.

REFERENCES

1. Choi Y. D., Iacovides H., Launder B. E., "Numerical Computation of turbulent Flow in a Square - Sectioned 180 Deg Bend", 1989, J. Fluids Eng., Vol 111., pp 59-68.
2. Dimos K., Papoutsidis K., "Measurements with L.D.A in a 3-d L shaped bend" Dipl. Thesis Thessaloniki 1991.
3. Fotea K., Prinos P., Goulas A., "Modelling of flow in sharp bends", to be presented in 7th International Conference on Numerical Methods in Laminar and Turbulent Flow, July 15-19 1991.
4. Humphrey J.A.C., Whitelaw J. H., Yee G., "Turbulent Flow in a square duct with strong curvature", J. Fluid Mech., 1981, vol 103, pp 443-463.
5. Kawashima Y., Nakagawa M., "The two dimensional pattern of flow at right-angled, T-shaped confluence", Int. Chem. Eng., 1983, Vol 23, pp 717-724.
6. Kotb N. A. E., Mokhtarzadeh-Dehghan M. R., Ward-Smith A. J., "A Numerical study of Laminar and Turbulent flows in a two dimensional bend with or without a guide vane.", 1988, Int. Journal for Numerical Methods in Engineering, Vol 26, pp 245-262.
7. Launder B.E., Spalding D.B., "The numerical computation of turbulent flows", Comp. Methods Applied Mech. Eng., 1974, vol 3, pp 269 - 289.
8. Liepsch D., Moravec S., Rastogi A. K., Vlachos N. S., "Measurement and calculations of Laminar flow in a ninety degree bifurcation", J. Biomech., 1982, vol 15, pp 473-485.
9. Pantankar S.V., "Numerical Heat Transfer and Fluid Flows", 1980, Hemisphere Publishing Corp., McGraw-Hill.
10. Pantankar S.V., Spalding D.B., "A Calculating Procedure For Heat, Mass and Momentum Transfer in Three-Dimensional Flows", 1972, Int. J. Heat Mass Transfer, Vol. 15 pp 1787 - 1806.
11. Pollard A., Spalding D. B., "The prediction of three-dimensional turbulent flow field in a flow -splitting Tee-junction", Computer Methods in Applied Mechanics and Engineering, 1978, vol 13, pp 293-306.
12. Samagaio A., Vlachos N. S., "Calculation of three-dimensional Laminar flows in T-shaped Junctions", Computer Methods in Applied Mechanics and Engineering, 1989, vol 75, pp 393-407.

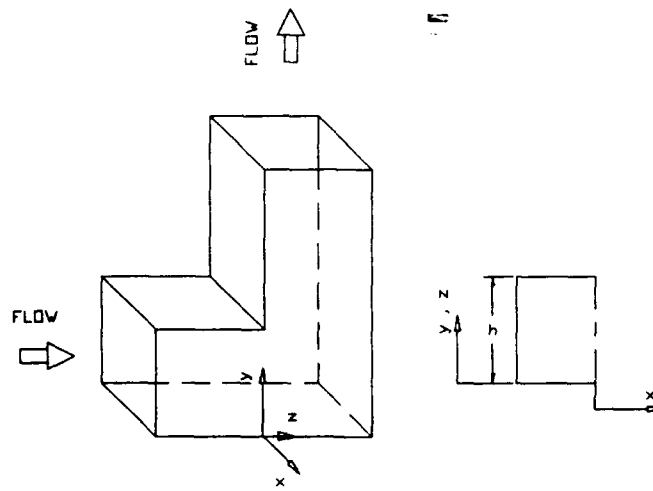


Fig. 1 : Three - dimensional domain
for a L- shaped sharp bend

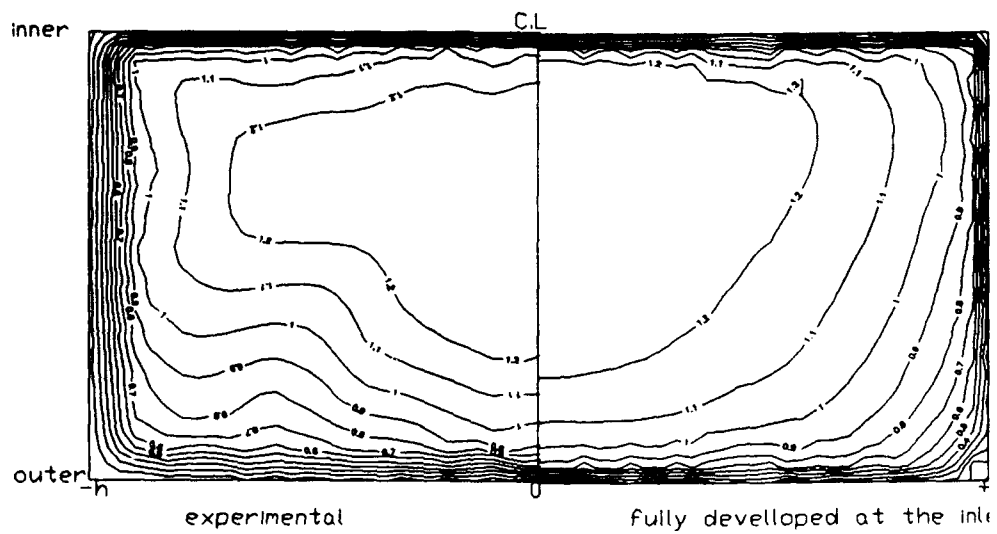


Fig.2 Isovelocity contours at the $z/h = -0.5$

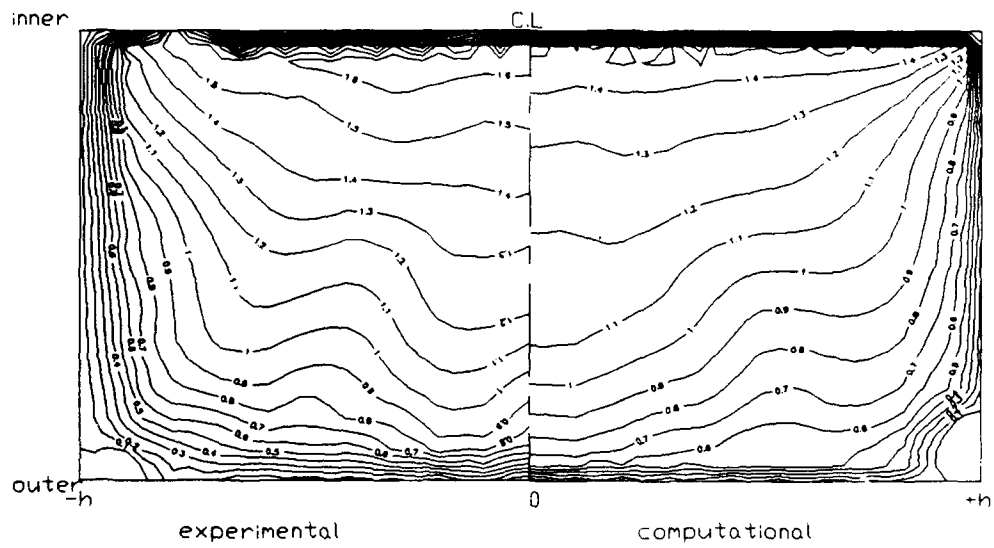


Fig. 3 Isovelocity contours at $z/h=0$.

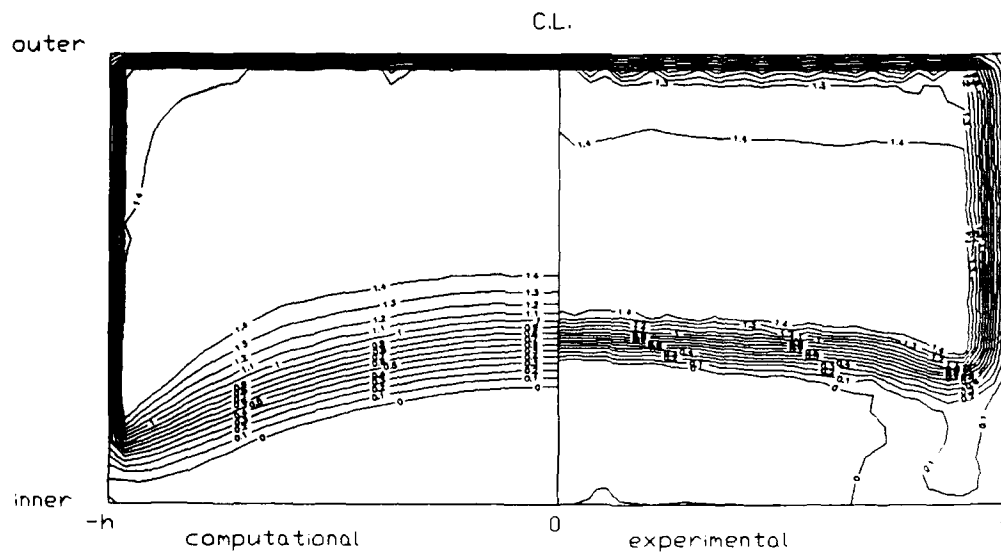


Fig. 4 Isovelocity contours at $y/h = 13$

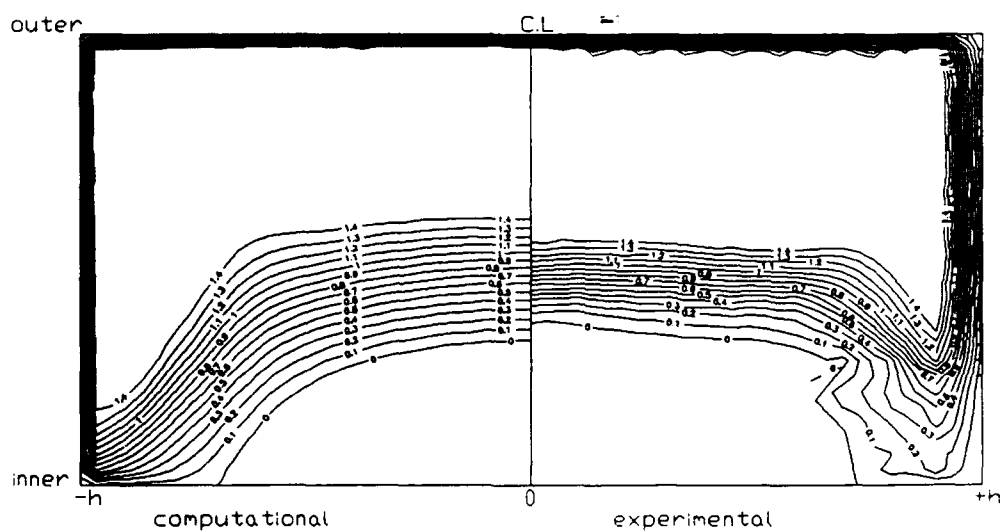


Fig. 5 Isovelocity contours at $y/h=1.9$

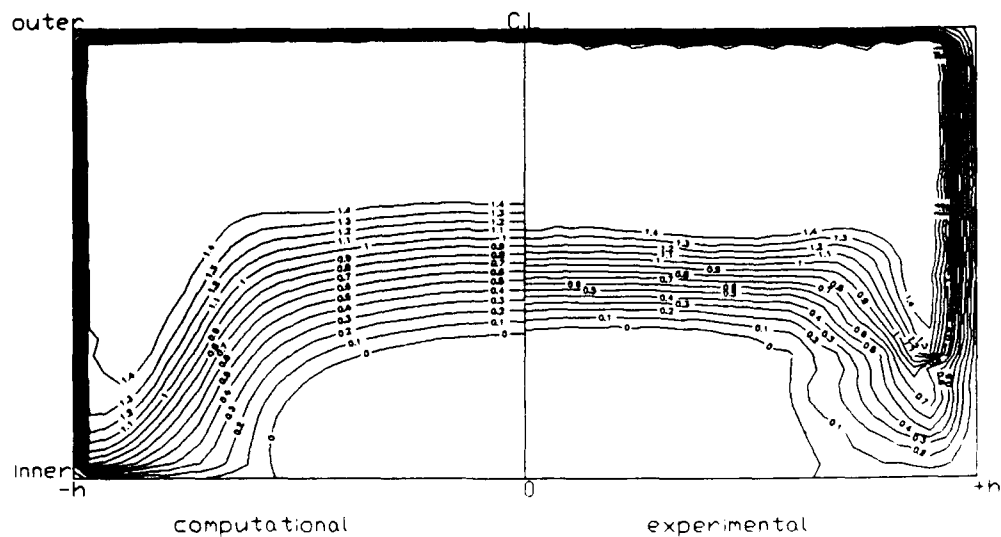
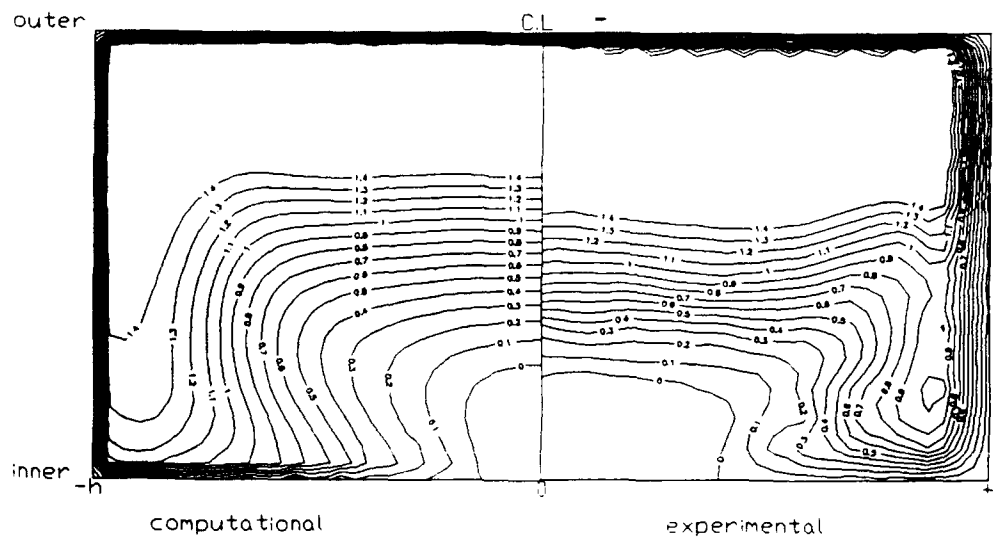
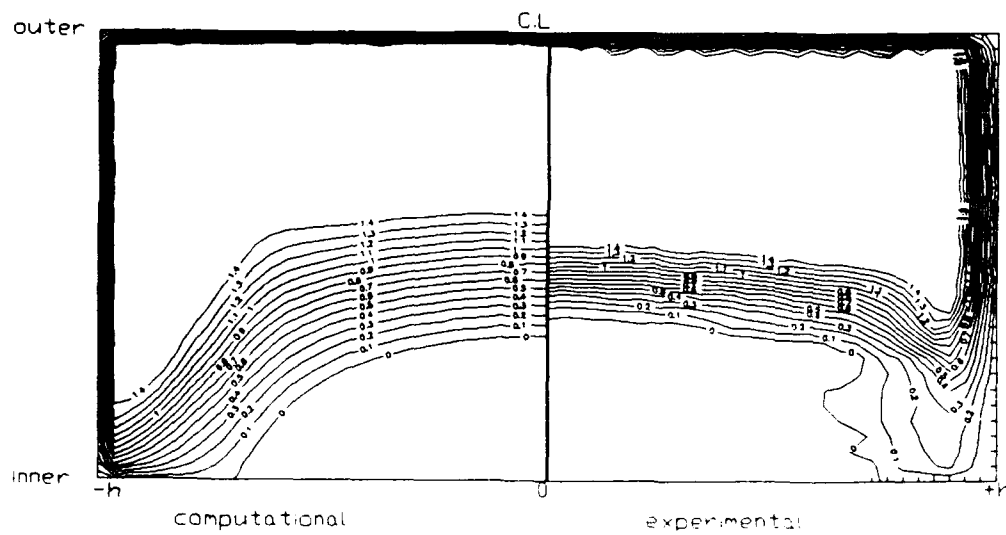


Fig. 6 Isovelocity contours at $y/h=2$

Fig.7 Isevelocity contours at $y/h = 2.5$ Fig. 8 Isevelocity contours at $y/h = 1.9$

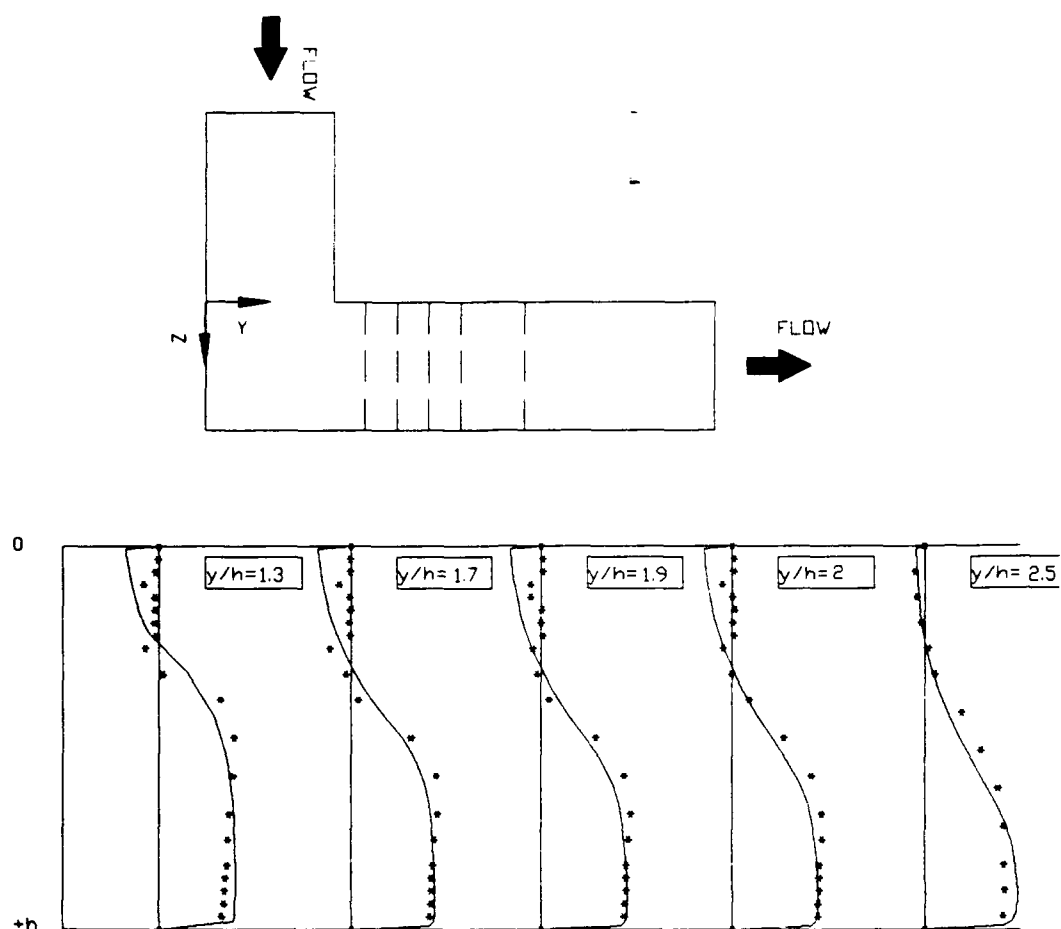


Fig.9 Computational and experimental velocity disturbance at selected verticals of the symmetry plane

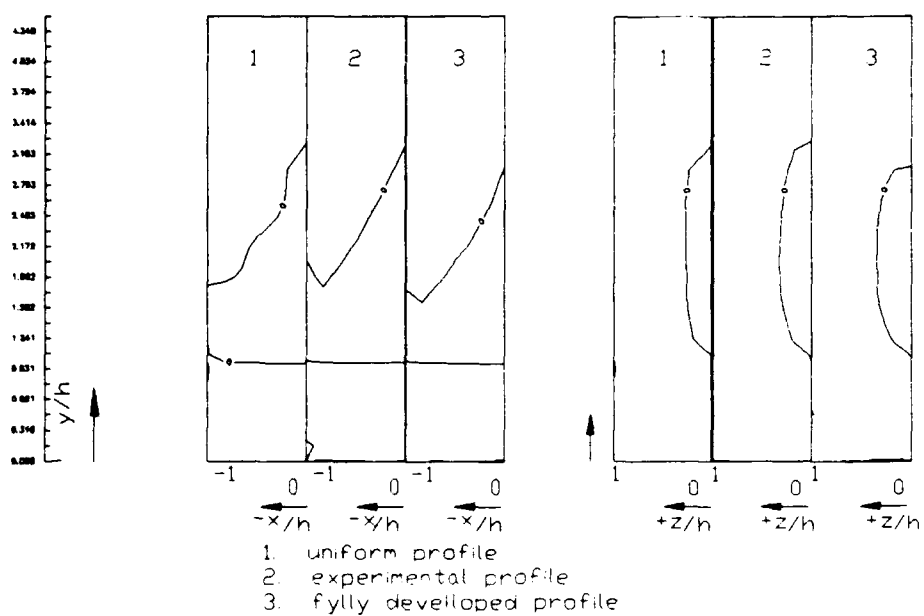


Fig. 10 Effect of the inlet profile on the recirculation region

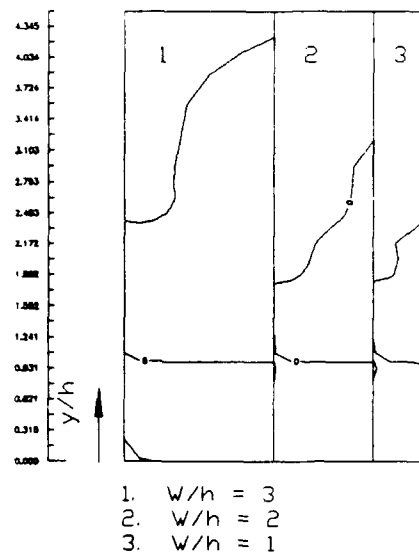


Fig. 11 Effect of the duct aspect ratio on the recirculation region

Discussion

D. GREGORY-SMITH, DURHAM UNIVERSITY, UNITED KINGDOM

Did you carry out any continuity checks to satisfy yourself as to the accuracy of the non-recirculating velocities?

The boundary layer on the side walls seems much thicker measured than computed (Figs 4, 5, 6, 7, 8). Do you have any comment?

AUTHOR'S REPLIES

Continuity tests were carried out in the upstream duct and downstream of the recirculation zone. Both were correct within the experimental error $\pm 4\%$.

The appearance of thicker boundary layer in the experimental results relative to computational is artificial and due to the graphics package used, in conjunction with the limited number of experimental data close to the specific wall. (Nearest experimental point was 1.3 mm from the wall in the recirculation region and 13 mm in the side wall).

H. WEYER, DLR INSTITUT FUR ANTRIEBSTECHNIK, GERMANY

Following the question of Dr. Gregory-Smith: LDV measurements near the side walls in the normal mode are difficult. The large ($10\text{ }\mu\text{m}$) particles you use tend to reveal thinner (turbulent) BL's than they are because of particles' bias. The large particles are also the reason for successful near-wall measurements.

AUTHOR'S REPLY

We agree with Dr Weyer's comment. We are at present redesigning the seeding apparatus to include small diameter particles $1\text{ }\mu\text{m}$ in the recirculation zone.

P. COELHO, INSTITUTO SUPERIOR TECNICO, PORTUGAL

Did you perform any calculations in order to ensure that the predictions are grid independent?

No predictions of turbulent quantities are shown. Could you comment on that?

AUTHOR'S REPLIES

Grid independence tests were carried out and the results presented are grid independent. It was found out though that the whole solution was very sensitive to grid shape close to solid walls.

Predictions of turbulence quantities will be published soon. In the recirculating region k (is?) the shapes of k distribution in the centerline are correct although the position of maximum k is predicted closer to the wall (recirculation region) than in the shear flow region. In the other areas the predictions seem to be good.

H. IACOVIDES, UMIST, UNITED KINGDOM

In our experience grid refinement has a greater effect on the k and ϵ predictions. Did the authors also observe this phenomenon?

AUTHOR'S REPLY

Grid refinement affects the k - ϵ predictions when it was carried out close to the boundary walls. No significant changes were observed when grid refinement took place in the high shear flow region. This allowed us to conclude that it was the k - ϵ formulation in this region which created the "problematic" predictions rather than the grid.





3-D NAVIER-STOKES FLOW AND TEMPERATURE FIELD COMPUTATION FOR A FORCED MIXER NOZZLE

K. Katheder
MTU Motoren- und Turbinen-Union München GmbH
Dachauer Str. 665
D-8000 München-50
GERMANY

92-16095



SUMMARY

To increase the temperature mixing efficiency in the common nozzle of an existing turbofan engine, a forced mixer is to be developed. Its design is generally based on empirically derived knowledge and requires some verification testing. To minimize the scope of testing, a numerical investigation has been performed, computing the complete flow path through the mixer up to the thrust nozzle. The computational domain is formed by a body fitted H-type grid. The simulated air flow is compressible adiabatic including variable specific heat and viscosity and the standard k-epsilon model is used. Resulting velocity and temperature fields are presented together with the temperature mixing efficiency. Use of the velocity field to shape the scallops at the mixer trailing edge is demonstrated. Comparison with test results indicates that CFD is a useful engineering tool to check and improve a new design before testing.

1. INTRODUCTION

The decision to adapt a forced mixer to the splitter upstream of the common nozzle of an existing turbofan engine was the starting point for the construction of a model test set-up as well as for the numerical investigation of a preliminary mixer geometry. Since the design point for the mixer is cruise at a Mach number of 0.8 in an altitude of 12192 meters, it was obvious, that model testing meant to accept severe compromises due to the restricted operational capabilities of the available test cell. Thus the numerical computation of the flow field was the only method to obtain an early full scale verification of the mixer effectiveness. Furthermore it was obvious, that a thorough interpretation of the computed, strongly three dimensional flow field could support and reduce testing of this geometrically complex gas turbine part.

2. GENERAL FEATURES OF A FORCED MIXER

2.1 Operating characteristics

To reduce noise and specific fuel consumption, forced mixers are often integrated into high by-pass turbofan engines. Generally a lobed mixer is installed well upstream of the thrust nozzle, fig. 1a. Its purpose is to mix the hot gas from the low pressure turbine exit into the cold air leaving the by-pass duct. Thereby the initially coflowing annular streams are mixed to an approximately uniform flow in the thrust nozzle. The mixing process is initiated by the lobes of the mixer, fig. 1b. They part

the hot and cold annular streams into individual jets with opposite radial velocity components, fig. 1c. Due to the radial components of the momentum, axial vortices are generated downstream of each more or less radial lobe wall. Besides the shear flow, essentially these swirls effect the mixing process. The quality of the mixing process is expressed by the thermal mixing efficiency obtained up to the thrust nozzle and the level of additional total pressure losses occurring between splitter and nozzle.

2.2 Mixer geometry

Generally the design of a lobed mixer is based on a large amount of empirically derived knowledge. This has been accumulated by numerous series of model and full scale tests like those of Frost [1], Hartmann [2], Kozlowski [3], Shumpert [4], Blackmore [5], Cullom [6], Anderson [7], Kuchar [8] and Skebe [9].

Some of the essential design recommendations concerning the geometry of the lobes are:

- limit hot and cold total flow turning angles to approximately 25 degree relative to the axis
- provide a large radial lobe penetration, defined as the ratio between lobe and duct height at lobe exit
- keep the aspect ratio at lobe exit below four
- ratio of hot and cold cross-sections at lobe exit is the same as without lobe
- lobe side walls approximately parallel
- scalloping of lobe side walls is favourable
- large number of lobes is favourable.

Also some physical parameters have been defined:

- static pressures of hot and cold stream balanced at lobe exit
- no diffusion within lobes
- no flow separation at lobe walls
- no boundary layer merger within lobes
- avoid wall impingement of lobe jets.

Besides the large range of tests to define these global criteria only some investigations have been initiated in the last years to explore the physics of mixing in more detail. Especially the research of Werle [10], Skebe [9], Russell [11], Koutmos [12] and Eckerle [13] was concentrated on the formation process of vortices and of the velocity and turbulence structure in relation to the geometrical parameters of the mixer.

Taking care of most of the relevant information, an individual forced mixer has been designed for integration into an existing turbofan engine, fig. 2. Essentially an axially long mixer with 12 lobes and a penetration of 80 % seemed to be appropriate to replace the splitter. Scalloping of the initial layout had been dropped, since the scallop-form should be developed from the computed flow field.

3. REVIEW OF NUMERICAL MIXER FLOW SIMULATION

Although most of the attempts to simulate numerically the flow field of forced mixers had in view the reduction of tests and the improved understanding of the flow development, the strongly three-dimensional flow structure is also a test field for CFD-models and the power of the computers. With respect to this evolution, a review has been carried out to check to which detail forced mixer flow fields have been computed. Thereby some computation field trends could be revealed:

- computation of only the primary flow in the lobe by Blackmore [5]
- computation of the flow in the mixing chamber alone by Birch [14], Povinelli [15] and Kreskovsky [16, 17]
- separate computation of the hot and cold lobe streams as well as the mixing chamber flow with iterative adaption of the flow field results at domain boundaries; Goyal [18], Barber [19], Koutmos [20], Yamamoto [21].

Further trends can be recognized concerning the computational grids and the simulation of the flow structure. In every case the available fluid dynamics code not only dictates the achievable depth of realism, but also the type of grid to be used. Often relatively coarse cylindrical polar grids have been used, which required special handling of wall to mesh intersections; Birch [14], Koutmos [20]. Only a few simulations have been carried out using body fitted coordinates, Goyal [18], Yamamoto [21]. Simulation of the flow structure grew more and more sophisticated with increasing computer power. Now there are computations which use potential flow analysis combined with boundary layer calculations to demonstrate the basic inviscid nature of the vortical mixing process (Barber [19, 22]) and even low Reynolds-number type Reynolds stress models, to reproduce more correctly the anisotropy near the lobe walls; Yamamoto [21].

Compared to the reviewed reports, it was tried to simulate the complete mixer flow field using a CFD-code like an usual engineering tool. This implicated the requirement for a high degree of maturity of the code, which should allow to do the computation within a body fitted grid beginning at lobe entry and ending at thrust nozzle exit.

4. COMPUTATIONAL MODEL

4.1 Numerical code

To compute the 3D velocity, temperature and pressure fields, a commercially available CFD-code, Ref. [23, 24], has been used. Its general features are:

- Reynolds averaged Navier-Stokes code
- first order accurate
- fully implicit, upwind solver
- primitive variables like pressure, velocity components and enthalpy
- built-in turbulence models
- built-in wall functions for friction and heat transfer
- user friendly modular set-up.

4.2 Grid

The main tasks of the grid are:

- describe the geometry of the mixer, plug and nozzle walls accurately
- set the boundaries of the computational domain
- resolve the flow domain by octagonal volume elements which are positioned dense enough to allow a grid independent solution.

Since the flow field possesses symmetry planes, these are used to build a 15 degree sector model representing only half a lobe. Thus the computational domain is confined circumferentially by angular cuts intersecting lobe trough and lobe peak. The radial boundaries are formed by the axis and the mixing chamber wall. Splitter, lobe and plug walls are represented to a fair degree by the body fitted option of the code.

4.2.1 Demands on the computational grid

Although the work to build a grid for a complex three dimensional flow domain is very pretentious by nature, the creation of the grid can be severely complicated by additional constraints dictated by the numerics of the code.

For this simulation one essential restriction resulted from the requirement to use a H-type grid, where the number of cells per direction must be constant. The consequence thereof is, that a locally necessary increase in the number of cells cannot be canceled in those parts of the grid where a much smaller number of cells would be sufficient. This would be possible with an unstructured or block structured grid, which is not accepted by the code used.

It is generally recommended to build a smooth grid. This means, grid lines should follow streamlines or stream surfaces and volume elements should be approximately orthogonal. The latter requirement can be achieved by an - due to computer capacity restraints not always advisable-local increase in the number of cells. A more economical method to approach orthogonality is to cut the flow field into large blocks of hexahedral or

better cuboidal character. This can be achieved by introduction of auxiliary lines which describe the edges of those blocks. They have to be placed carefully between and on boundary surfaces. That means, auxiliary lines which are crossing the flow field and connecting body or domain surfaces should be orthogonal at these surfaces. This is also true for intersections between auxiliary lines. Subsequently the desired kind of volume elements can be produced by a regular or irregular subdivision of opposing block edges.

Since it is not always possible to create volume elements with a brick like shape, there are some further limitations to be regarded to avoid divergence problems. Highly critical in this context are cell vertex angles smaller than approximately 30 degree. Less critical but detrimental to the quality of the result and the speed of convergence are cell edge aspect ratios larger than 10. Also a discontinuous increase or decrease of cell size and grid curvature should be avoided.

Additionally the simulated physical processes affect the grid structure to an appreciable extent. Thus, large local gradients of any variable have to be resolved through an increase in mesh density. Examples for those regions are boundary and mixing layers, wakes and recirculation zones. One more strategy influencing grid design, is to provide plane domain entry and exit slabs. This facilitates the introduction of physical boundary conditions as well as the handling, especially averaging of the data fields resulting from these regions.

In every case it is very useful to develop a precise idea of the flow field to be calculated in advance of grid generation.

4.2.2 Building the grid

To get most of the partially contradicting grid design requirements into line, it is essential to use an efficient grid generator. Therefore a commercially available interactive graphics pre-processor, Ref. 25, has been selected instead of the grid generator provided together with the numerical code. The chosen pre-processor is predominantly used for finite element analysis, but its flexibility and naturally its ability to generate fields of six sided volume elements made it suitable to the requirements posed by the flow solver.

With this pre-processor the mesh is built reversing the so called "top down" method as follows:

- define the cartesian coordinates of basic points of the computational domain and of blocks. Declare sets of points to define arbitrary contours
- define lines between points; that is straight lines, arcs and track lines (splines)
- subdivide lines to the locally appropriate number of volume elements
- define surfaces from 4 rim lines each
- define hexagonal blocks from the surfaces
- activate the mesh interpolator for the space within each block.

The resulting mesh is to be checked slabwise in three dimensions by the aid of a graphical display terminal. This whole procedure is a very time consuming process since it must be repeated sometimes to get favourable block profiles from adjusted auxiliary lines.

After final corrections in the grid, like careful relocation of singular nodes, the nomenclature of the nodes is converted by an interface program to fit the conventions of the CFD-code.

The result of the grid generation process for the mixer is a grid of $13 \times 63 \times 64 = 52\,416$ volume elements. Figure 3 presents the mesh at all physical walls of the computational sector. Thereby the by-pass duct casing and mixing chamber inner wall surfaces have been meshed fairly regular with exception of the region above the lobe entry. This local irregularity results from the increase in mesh density required to model the lobe.

The wall surface meshes at the splitter are nearly ideal. Not shown is the grid contained between the splitter walls. There the part of the grid starts, which is necessary downstream of the splitter to mesh the lobe walls as well as the flow field between the lobe walls. At the end of the splitter this part of the grid is compressed to a very small ring and only a small step in the middle of the splitter trailing edge allows to form the lobe wall as shown. The unavoidable concentration of volume elements can be seen best in figure 4. This region deserves special attention during the course of iteration to avoid numerical instability.

To resolve the boundary layers, the grid density near walls has been increased and wherever possible a smooth grid has been created. Figure 5 demonstrates once more the lot of complex grid adjustments necessary to distort the regular entry grid into the s-like shape of the lobe exit without changing the number of volume elements per slab and direction.

4.3 Modeling the physics of the flow

Throughout the flow path from by-pass duct and low pressure turbine exit through the mixer up to the nozzle the gas streams were defined to be turbulent, subsonic, compressible and adiabatic. Kinematic viscosity and specific heat capacity were calculated from local temperatures. To account for wall friction, the logarithmic law of the wall was activated. Production and dissipation of turbulent kinetic energy was modelled with the k-epsilon model using standard coefficients.

To approximate correct engine working conditions, measured velocity and temperature profiles were chosen to describe the boundary conditions at computation domain entry. The profiles showed no swirl and were assumed to be axis symmetric. The entry conditions for turbulent kinetic energy and dissipation were derived assuming an isotropic turbulence structure and a turbulence level of 1.5 % respectively 4 % for by-pass duct and core entry, together with a mixing length of 10 % of the initial shear layer width.

At nozzle exit, a constant ambient pressure was set, insinuating that the flow angles will be small at this cross-section. To capture eventually developing recirculation zones, the elliptical mode of the numerical solver was activated.

5. RESULTS

Some actions had to be taken in the course of the numerical computation. Firstly, only the continuity and momentum equations were solved before starting the energy equation. Then, after stabilization of this set of equations, the turbulence model was included. Additionally the high density grid at the lobe entrance was dampened more conservatively than the whole field to overcome numerical instabilities resulting from this unfavourable part of the domain. Convergence was obtained after about 4000 iterations over the complete domain. Subsequently the flow field had been analysed using the graphic post-processor supplied with the code, Ref. [26]. This facilitated the task to select readable and interpretable 2D-plots from the 3D-data fields to a large degree.

5.1 Temperature field

Temperature mixing is driven by an axial vortex which starts from the radial trailing edge of the lobe. Due to this flow rotation, hot gas leaves the top of the hot sector downstream of the lobe with a circumferential velocity component and cold gas enters the initially hot sector at smaller radii. Figure 6 demonstrates this development through isolines of the total temperature in an angular cut intersecting the lobe peak. The corresponding cut through the lobe trough is shown in fig. 7. The separated cold and hot and the partially mixed regions are clearly recognizable as well as the nearly unmixed region at the axis. Due to the short mixing chamber mixing is not completed. The thermal mixing efficiency achieved at nozzle exit was calculated to be 74 %. The comparable value for coflowing streams - without forced mixer - is 32 %.

Some radial cuts through prominent cross-sections are plotted in fig. 8. There, the axial development of the temperature distribution can be traced from entry into the lobe over the exit of the lobe up to the thrust nozzle exit. In accordance with engine test results the hot and cold streams were simulated with nearly no temperature profile at computation domain entry. Just downstream of the lobe exit both streams are separated by small temperature boundary layers and the resultant total temperature distribution at mixing chamber exit is comparable to the one known from measurements. A closer inspection of this profile indicates, that the upper part of the hot jet impinges at the mixing chamber wall.

This is supported by fig. 9, which presents the temperature field close to the inner mixing chamber wall downstream of a complete lobe.

5.2 Velocity field

In fig. 10 the velocity fields of three prominent sectors are plotted in form of constant Mach-lines. At entry of the computation domain the axis-symmetric by-pass flow is simulated by a profile with a peak Mach-number of 0.65 near the duct inner wall. The also axis-symmetric hot gas flow downstream of the low pressure turbine has only small boundary layers and a flat profile maximum. Wakes resulting from upstream struts have not been simulated. Due to the flow redistribution enforced by the lobes, the boundary layers at lobe exit assume a characteristic profile. That is, the cold flow is heavily decelerated in the lobe trough, while the maximum velocity of the by-pass flow remains nearly unchanged. Additionally the thickness of the cold boundary layer at the lobe peak is reduced. The hot gas boundary layer thickness has also been diminished markedly. This results from the redistribution of the turbine exit outer boundary layer onto a much larger perimeter.

From lobe exit to thrust nozzle exit the mixing chamber cross-section is steadily reduced. Thereof results an increase in flow velocity and the wanted leveled-off exit profile. Despite the flow acceleration there remain small vortex velocity components, fig. 11. They reduce the achievable thrust level by a small but nevertheless remarkable extent. The computed flow angles have also been used during the design of the total pressure rake at rig exit to assure its insensitivity to flow direction.

5.3 Scallop the lobes

Scalloping the lobes means to cut out a shell like contour at the radially oriented side walls of the lobes. This serves to save weight and is said to be possible without a reduction of mixing efficiency. As there are some examples of forced mixers with scallops, there exists also a large variety of differing forms, but no recommendations are published concerning the layout of the cutting line. Thus it was tried to derive the scallop line from the computed flow field. Since it is accepted, that the kinetic energy of a vortex is dependent on circulation, parameters to describe the circulation produced by the lobe, are the radial velocity components at the hot respectively cold side of the lobe wall, fig. 12. To simplify the delineation procedure for the scallop outline, lines of constant angle difference between hot and cold streamlines have been derived from the vector fields close to the lobe walls and the result are shell like isolines, fig. 13. Hence it is possible to cut back the trailing edge of a lobe along such an isoline without loss of vortex energy compared to the unmachined trailing edge. Furthermore the axial length of the mixing vortex is increased and regions of small angle differences are recognized. To include the revealed advantages into lobe design, the mixer was scalloped according to fig. 14.

6. COMPARISON TO TEST RESULTS

To check the initial lobe design and the influence of scalloping, full scale water tunnel tests and hot gas rig tests have been carried out with a 60 degree sector model in addition to the numerical investigation. The observations during the water tunnel tests confirmed the computed flow field to a large degree:

- efficient mixing identified by dye streaks
- vortex motion observed
- no separation at lobe walls
- enhanced mixing due to scalloping.

These results allowed to concentrate on the scalloped version of the lobe during hot gas rig tests. A comprehensive instrumentation was provided to traverse radially and circumferentially the total pressure and temperature fields downstream of the lobes and downstream of the thrust nozzle. Although cruise conditions could not be reproduced with this rig, some of the measured effects compared favourably to the computations:

- total pressure loss from lobe entry up to nozzle exit approximately 4 % of the mass weighted entry total pressure
- hot jets from the lobes impinge on mixing duct wall.

No coincidence could be achieved concerning mixing efficiency. From the rig tests a value of 90 % was derived compared to 74 % from the numerical analysis. A similar trend has been observed also by other authors, ref. [8, 14]. It is partially caused due to deviations of the turbulence levels, different entry profiles, deficiencies of the k-epsilon model to represent wall jets and swirls and to unsufficient approximation of the real geometry.

7. CONCLUSIONS

Realizing the intention to use a commercially available numerical code like a standard engineering tool can be successful only if there are also available a powerful computer, grid generator, post-processor and graphical display. Otherwise the numerical computation of 3D flow fields can be too time consuming to be able to support and reduce rig tests effectively.

In the case presented here, a fruitful interaction between computational and testing efforts could be achieved. Above all, it was possible through analysis of the numerical results to:

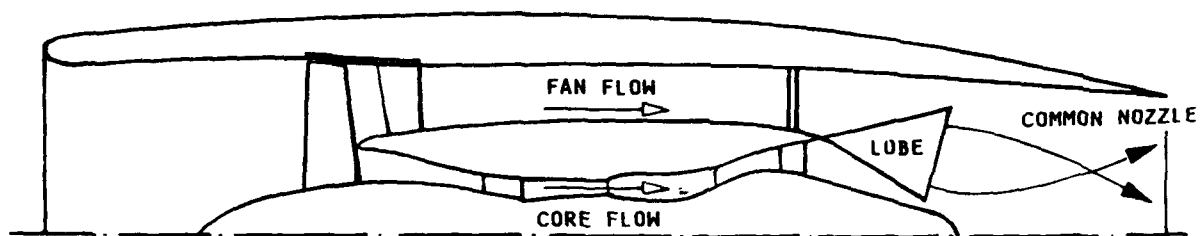
- increase insight into a complex flow field development prior to tests
- check and improve an initially empirical forced mixer design
- verify details of the flow field like jet impingement and total pressure losses
- derive a method for the scalloping of lobes.

With regard to the thermal mixing efficiency, the discrepancy between numerical and rig result is remarkable but not alarming. On one hand this could be expected due to differences between numerical and rig simulation and on the other hand both results have to be checked in an altitude test bed. Only there the net effect of the forced mixer can be demonstrated through rematching of engine components to the added part.

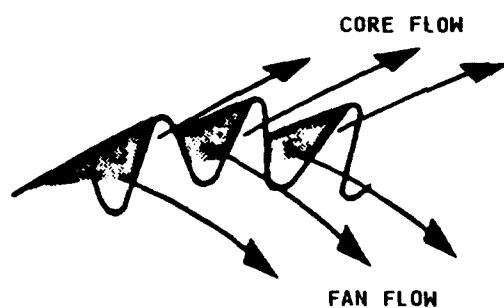
8. REFERENCES

1. T.H. Frost
Practical Bypass Mixing Systems for Fan Jet Aero Engines
The Aeronautical Quarterly, May 1966, p. 141 - 160
2. A. Hartmann
Untersuchungen über die Mischung bei Zweikreisturbinenluftstrahltriebwerken
Diss. RWTH-Aachen, Fak. Maschinenwesen 1966
3. H. Kozlowski, G. Kraft
Experimental Evaluation of Exhaust Mixers for an Energy Efficient Engine
AIAA-80-1088
4. P.K. Shumpert
An Experimental Model Investigation of Turbofan Engine Internal Exhaust Gas Mixer Configurations
AIAA-80-0228
5. W.L. Blackmore, C.E. Thompson
Design and Development of a Mixer Compound Exhaust System
AIAA/SAE/ASME Paper 81-1494
6. R.R. Cullom, G.A. Bobula, L.A. Burkardt
Mixing Effectiveness Test of an Exhaust Gas Mixer in a High Bypass Turbofan at Altitude
AIAA-81-1495
7. B.H. Anderson, L.A. Povinelli
Factors Which Influence the Behavior of Turbofan Forced Mixer Nozzles
NASA-TM-81668, (AIAA-81-0274)
8. A.P. Kuchar, R. Chamberlin
Subscale-Model and Full-Scale Engine Mixed-Flow Exhaust System Performance Comparison
J. Aircraft, Vol. 22, Nov. 1985, No. 11, p. 950-955
9. S.A. Skebe, R.W. Paterson, T.J. Barber
Experimental Investigation of Three-Dimensional Forced Mixer Lobe Flow Fields
AIAA-88-3785-CP
10. M.J. Werle, R.W. Paterson, W.M. Presz, Jr.
Flow Structure in a Periodic Axial Vortex Array
AIAA-87-0610
11. W.D. Russell
Lobed Nozzle Afterbody Research
AIAA-87-1867

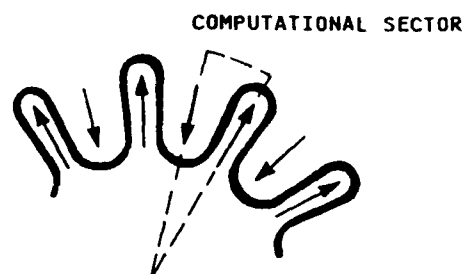
12. P. Koutmos, J.J. McGuirk
Isothermal velocity and turbulence
measurements downstream of a model
multilobed turbofan mixer.
Experiments in Fluids, Vol. 8, 1989,
p. 183 - 191
13. W.A. Eckerle, H.S.J. Awad
Experimental Measurement of the
Vortex Development Downstream of a
Lobed Mixer Flow
ASME-90-GT-27
14. S.F. Birch, G.C. Paynter,
D.B. Spalding, D.G. Tatchell
Numerical Modeling of
Three-Dimensional Flows in Turbofan
Engine Exhaust Nozzles
AIAA-77-204
15. L.A. Povinelli, B.H. Anderson
W. Gerstenmaier
Computation of Three-Dimensional Flow
in Turbofan Mixers and Comparison
with Experimental Data
AIAA-80-0227
16. J.P. Kreskovsky, W.R. Briley
H. McDonald
Turbofan Forced Mixer-Nozzle
Internal Flowfield III - A Computer
Code for 3-D Mixing in Axisymmetric
Nozzles
NASA-CR-3494, 1982
17. J.P. Kreskovsky, L.A. Povinelli,
B.H. Anderson
Investigation of Mixing in a Turbofan
Exhaust Duct
Part I: Analysis and Computational
Procedure
Part II: Computer Code Application
and Verification
AIAA J., Vol. 22, 1984, No. 3/4,
p. 374 - 382, p. 518 - 525
18. R.K. Goyal, W.L. Blackmore,
V. Head, L. Povinelli
Three Dimensional Compressible
Viscous Analysis of Mixer Nozzles
AIAA-83-1401
19. T.J. Barber, G.L. Muller,
S.M. Ramsay, E.M. Murman
Three-Dimensional Inviscid Flow in
Mixers, Part I:
Mixer Analysis Using a Cartesian Grid
J. Propulsion, Vol. 2, No. 3,
May-June 1986, p. 275 - 281
20. P. Koutmos, J.J. McGuirk
Turbofan forced mixer nozzle
temperature and flow field modeling
Int. J. Heat Mass Transfer, Vol. 32,
1989, No. 6, p. 1141 - 1153
21. M. Yamamoto, C. Arakawa, T. Tagori
Development of a New
Low-Reynolds-Number Type Reynolds
Stress Model and it's Application to
a Lobe Mixer Flow
7th Symposium on Turbulent Shear
Flows,
Stanford University, Aug. 21 - 23,
1989, Paper 13 - 3
22. T. Barber
Turbofan Forced Mixer Lobe Flow
Modeling, Part II
Three-Dimensional Inviscid Mixer
NASA-CR-4147-Pt-2, 1988
23. H.I. Rosten, D.B. Spalding
The Phoenix Beginners Guide
-CHAM TR/100, Version 1.4, Oct. 1987
24. H.I. Rosten, D.B. Spalding
The Phoenix Reference Manual
CHAM TR/200, Version 1.4, Oct. 1987
25. FEMGEN User Manual
Version 8.5
FECS Ltd., Oakington Cambridge CB45BA
26. H.I. Rosten, D.B. Spalding,
J.A. Templeman
The Photon User Guide
CHAM TR/140, Version 1.4, Nov. 1987



a: FORCED MIXER IN A TURBOFAN ENGINE



b: BASIC FLOW TURNING



c: RADIAL COMPONENTS

FIG.1 FLOW TURNING CHARACTERISTICS OF A FORCED MIXER NOZZLE
(largely from ref.9)

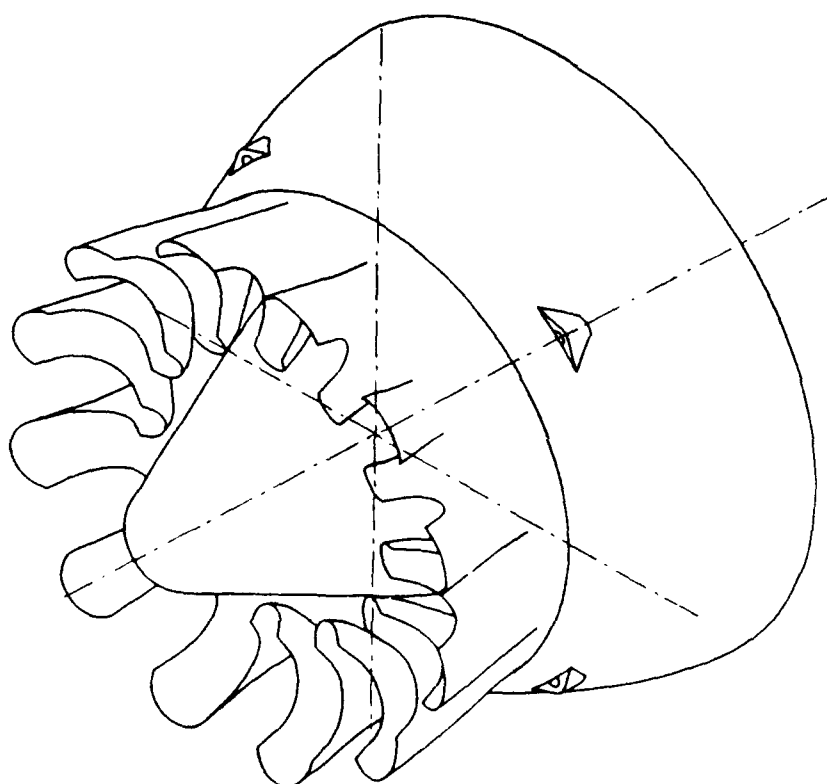


FIG.2 3D-VIEW OF PROPOSED FORCED MIXER NOZZLE

FIG.3 GRID AT WALLS

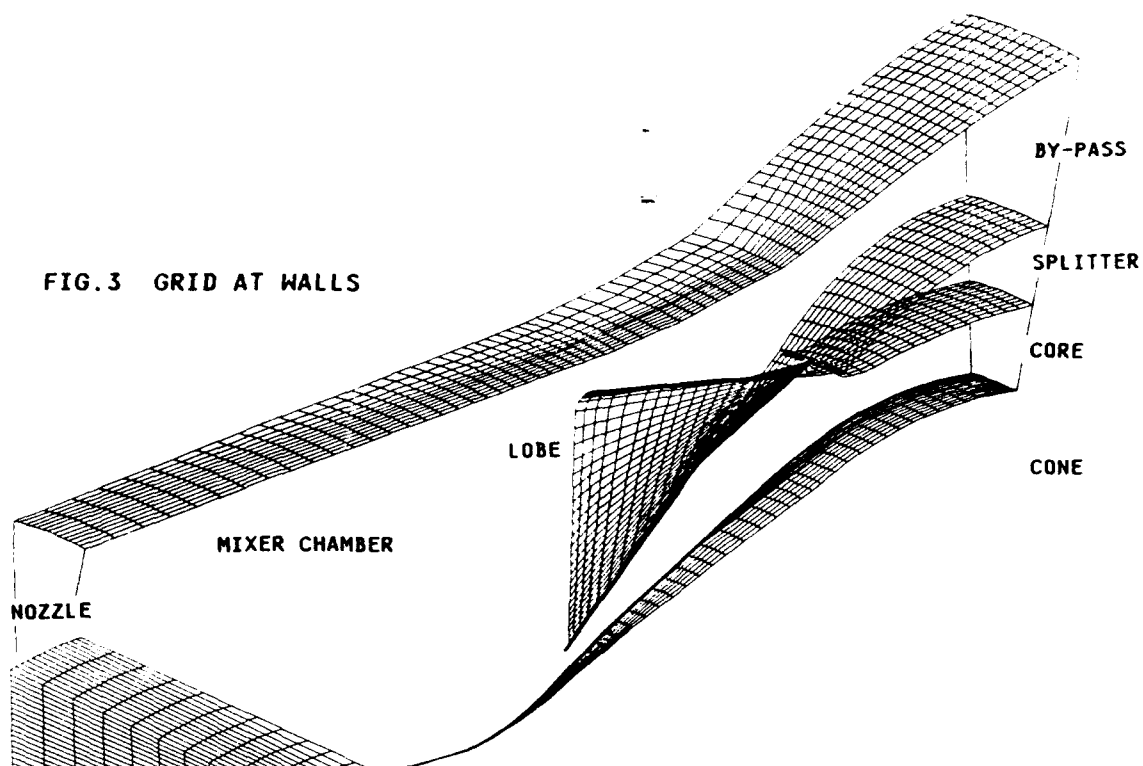
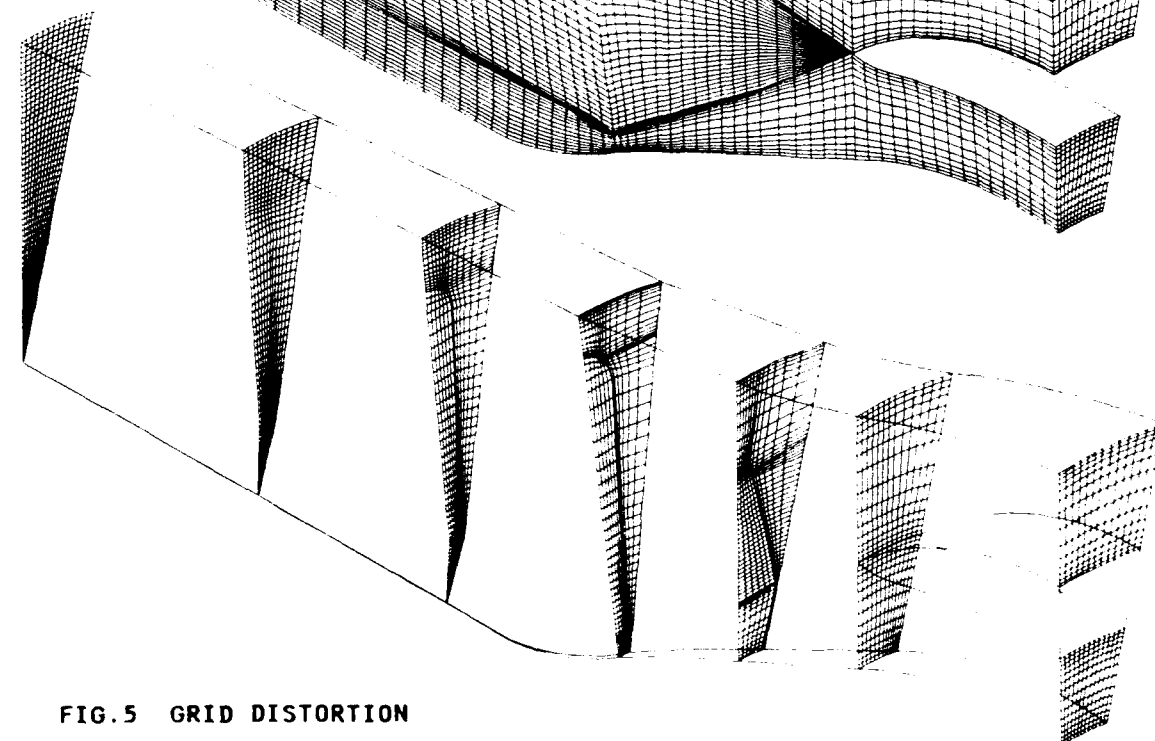
FIG.4 3D-VIEW OF
COMPUTATIONAL DOMAIN
13 × 63 × 64

FIG.5 GRID DISTORTION

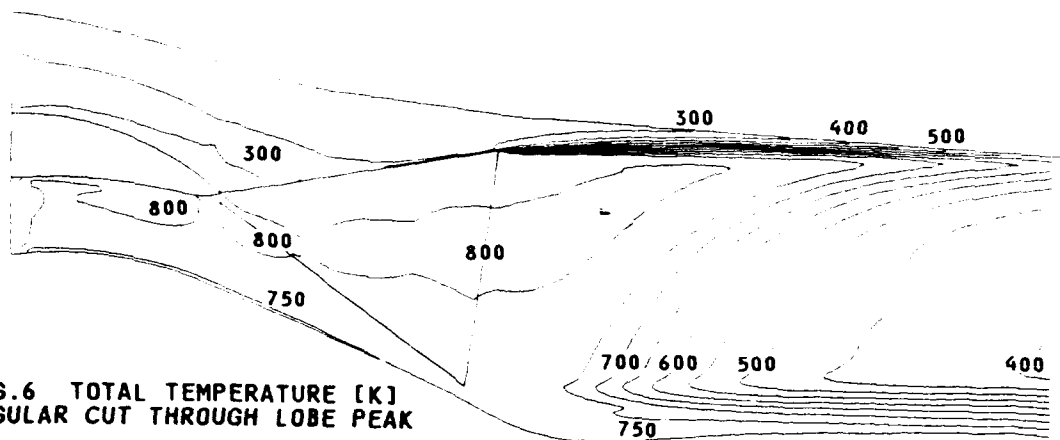


FIG.6 TOTAL TEMPERATURE [K]
ANGULAR CUT THROUGH LOBE PEAK

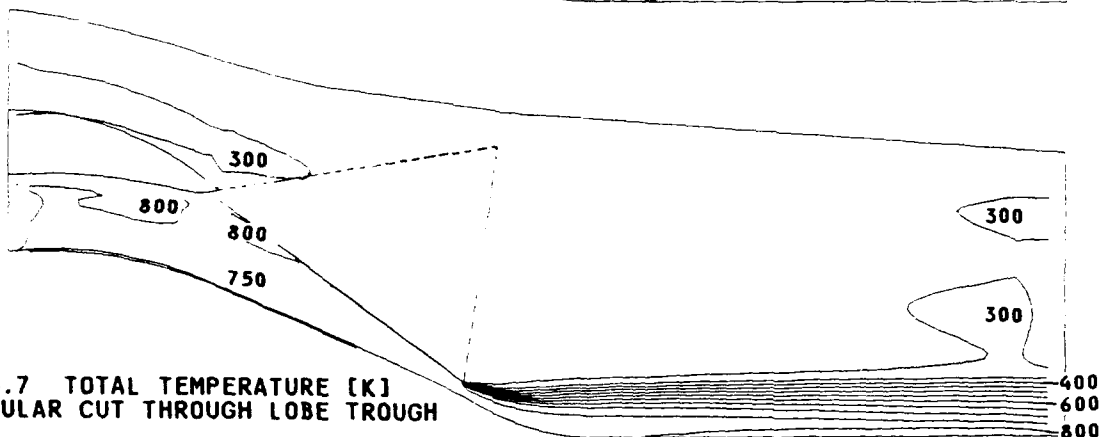


FIG.7 TOTAL TEMPERATURE [K]
ANGULAR CUT THROUGH LOBE TROUGH

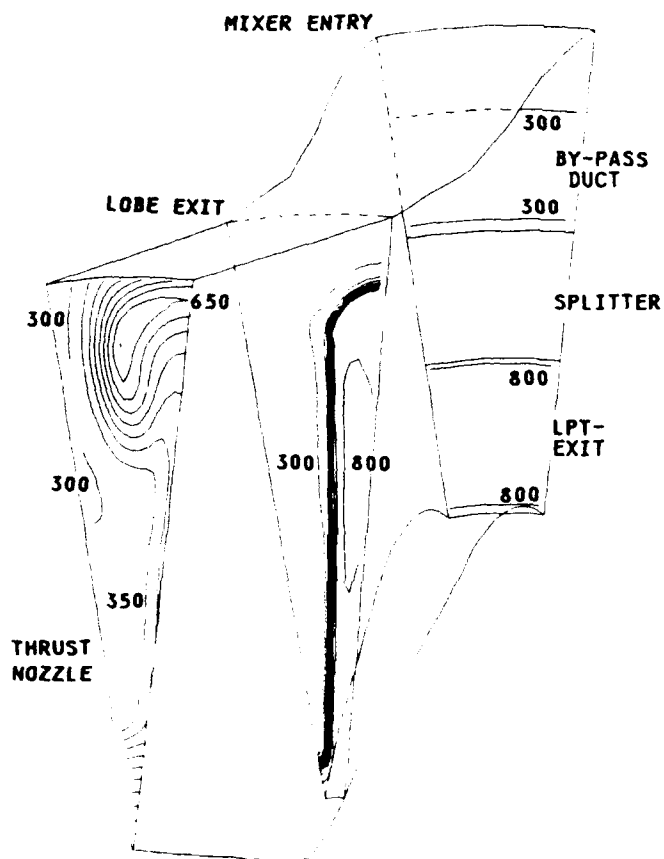


FIG.8 TOTAL TEMPERATURE [K]
PROMINENT CROSS-SECTIONS

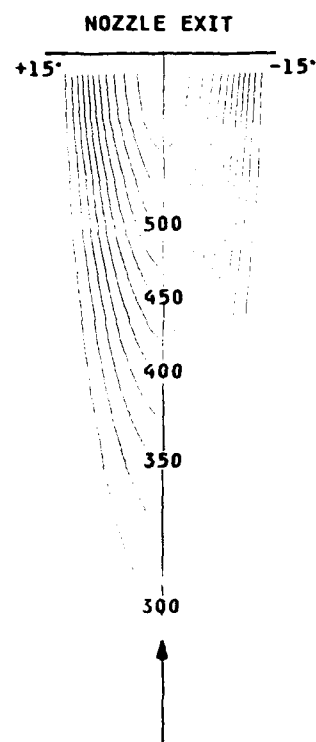


FIG.9 TOTAL TEMPERATURE [K]
DOWNSTREAM LOBE EXIT
NEAR MIXING CHAMBER WALL

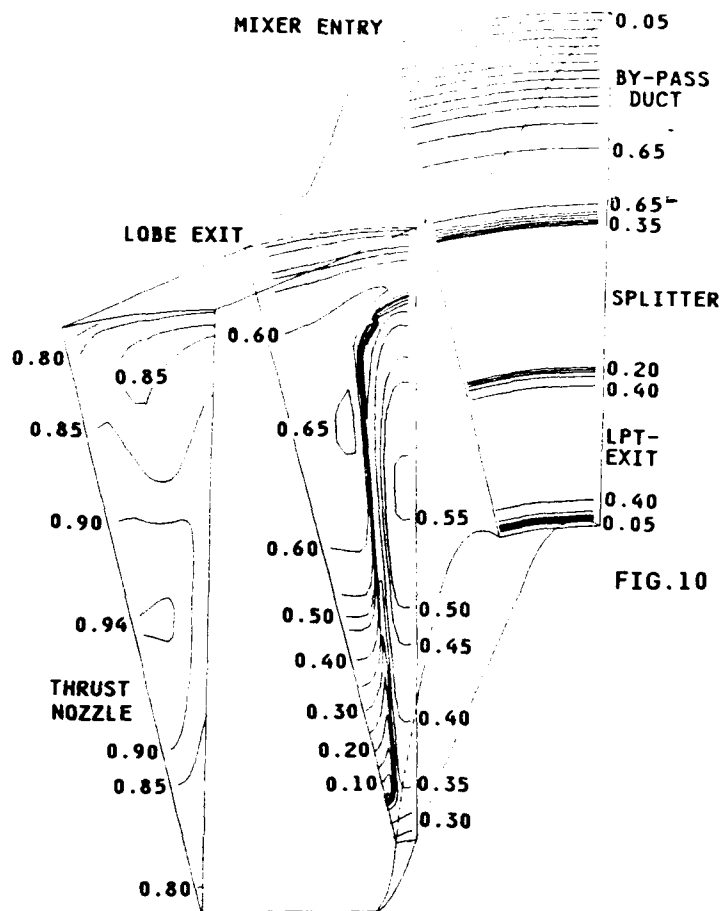
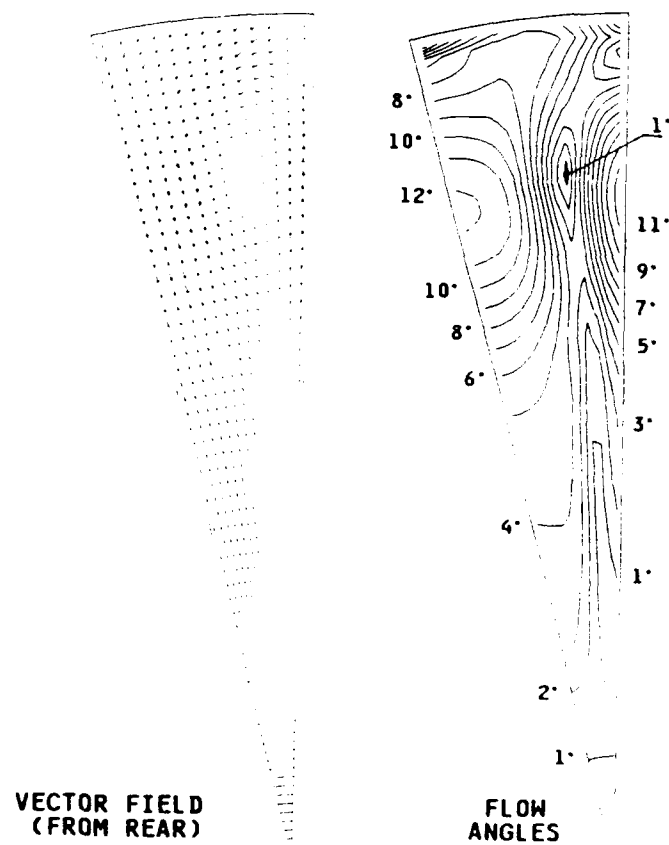


FIG. 10 MACH-NUMBER DISTRIBUTION
IN PROMINENT CROSS-SECTIONS

FIG. 11 NOZZLE EXIT
FLOW DIRECTION



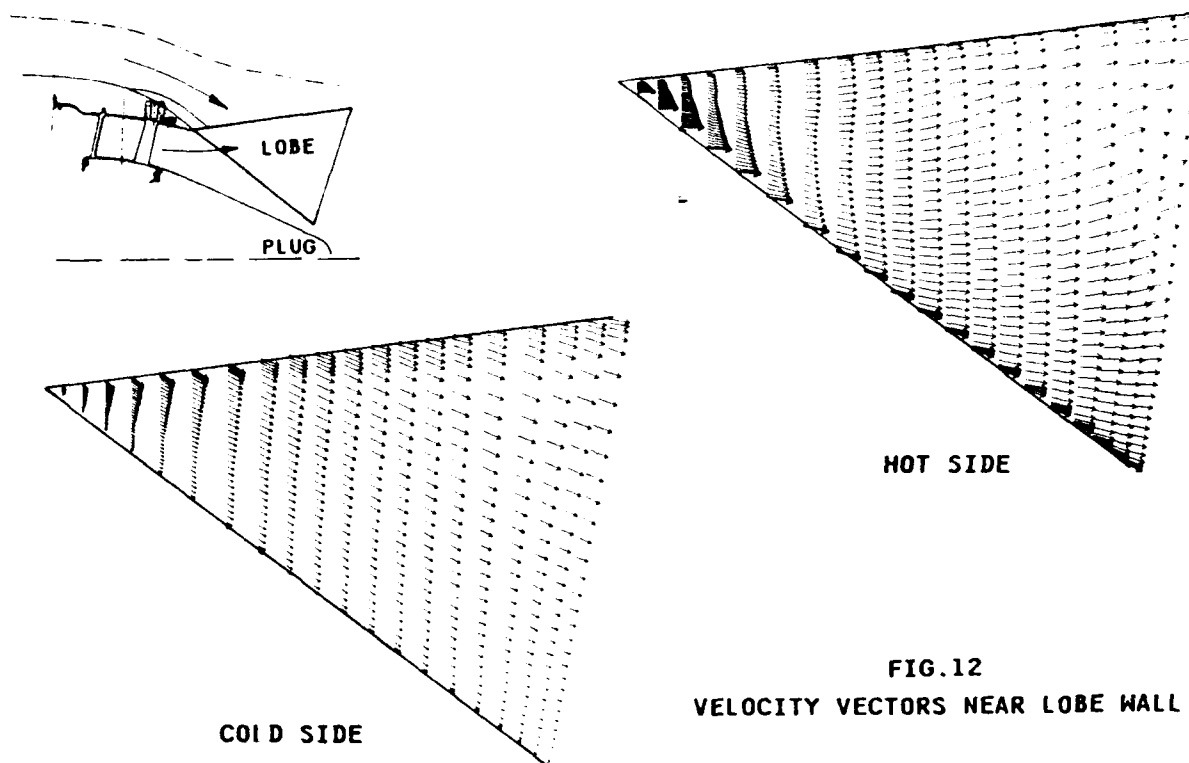


FIG. 12
VELOCITY VECTORS NEAR LOBE WALL

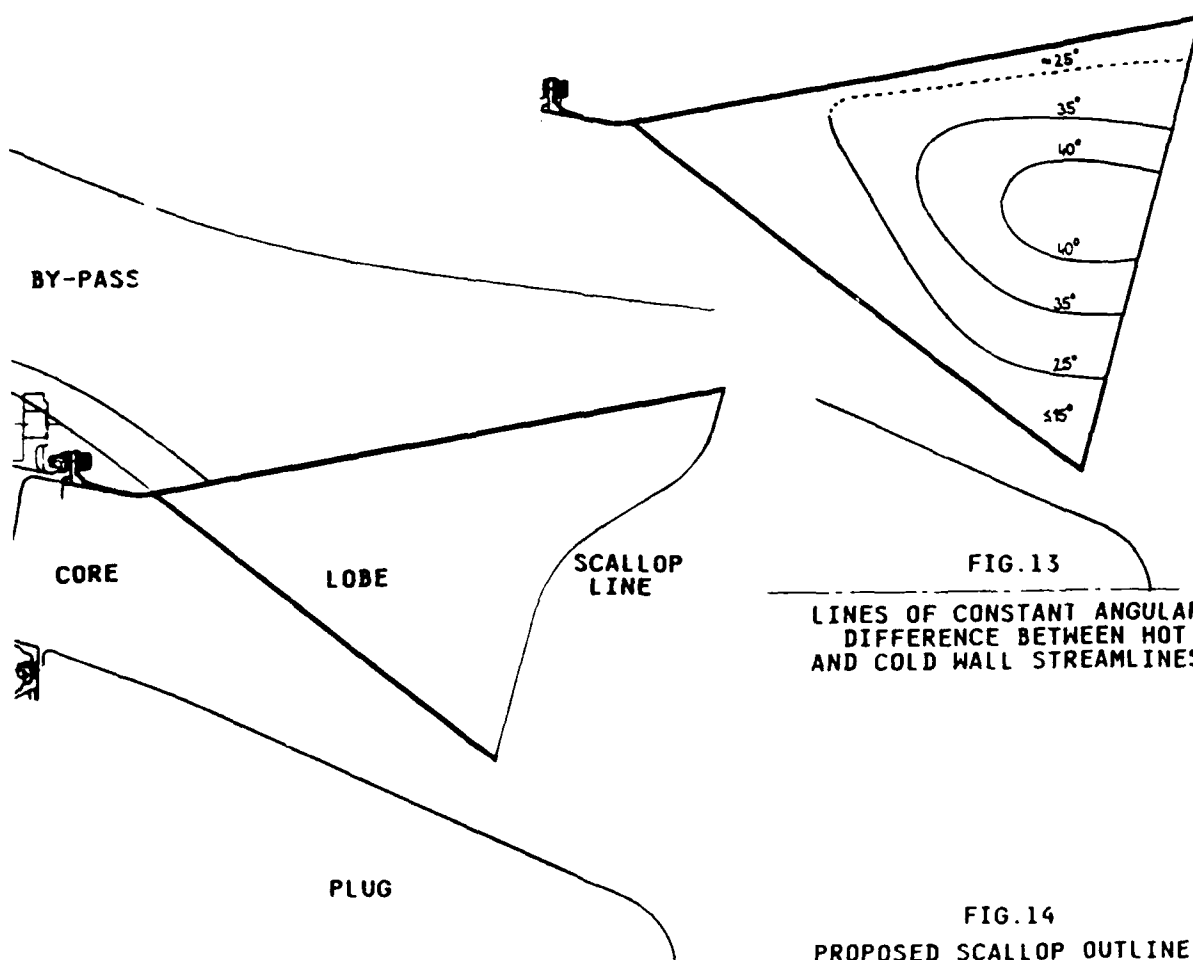


FIG. 13
LINES OF CONSTANT ANGULAR
DIFFERENCE BETWEEN HOT
AND COLD WALL STREAMLINES

Discussion

W. CALVERT, RAE PYESTOCK, U.K.

- 1) What was the computation time for your calculation?
- 2) Did you carry out any further calculations with different lengths of mixer?

AUTHOR'S REPLY

- 1) Computation time on a VAX 6800 was approximately 6 CPU-days including several restarts.
- 2) No. Only one single computation has been carried out.

L. POVINELLI, NASA LEWIS, U.S.A.

I would like to comment on the effect of turbulence modeling. In Ref. 17 (Povinelli and Anderson), a Navier-Stokes analysis was carried with a $k-\epsilon$ turbulence model and also with a simple eddy viscosity model. No discernable difference in temperature profiles or the mixing were found. This is to be expected since the inviscid flow turning of the fan and core streams generate the primary vortex structure which predominates the mixing phenomena and the temperature distributions.

R. GRAY, WRIGHT LABS, U.S.A.

What was the definition of mixing efficiency?

AUTHOR'S REPLY

Mixing efficiency was the standard definition which is described by the ratio of the difference between partially mixed and unmixed thrust over the difference between completely mixed and unmixed thrust.





FLOW COMPUTATION IN COMBUSTION CHAMBERS USING ZONAL NONSTAGGERED GRIDS

by

M. Rachner

German Aerospace Research Establishment (DLR)

Institute of Propulsion Technology

Linder Höhe, 5000 Köln 90

Germany

SUMMARY

A Rhie-type nonstaggered grid 3D-Navier-Stokes Code working on overlaid subdomains by a zonal technique is applied on two model combustion chambers.

In case of the swirling turbulent combustor flow investigated, a locally unrealistic flow behavior at domain boundaries was found on the coarse grid. This is caused by strong overshoots of the momentum interpolated cell face mass fluxes, not reported up to now in the literature. The influence of the pressure gradient discretization at boundaries on these overshoots is shown.

At inter grid boundaries the discretization of the pressure gradient can give rise to wiggles in the numerical solution as observed in the case of the reacting turbulent crossflow- H_2 -jet in a rectangular channel.

Moreover the influence of fully, partially and lacking local flux conservativity in coupling the numerical fluxes across inter grid boundaries of the subdomains is studied. The fully conservative coupling scheme turned out to be not a robust method.

List of symbols and abbreviations

a	coefficient in discretization eqn
$a_p^{p,u}$	main diagonal coefficient a_p in u-discretization eqn at grid point W
$A_w^{p,u}$	cell crosssectional area
B	overshoot [m/s]
C	mass flux
DIVG	cell mass source
DQ	difference quotient
DV	pressure-velocity coefficient
H	defined by eqn (4)
k	kinetic turbulence energy
MI	momentum interpolation
p	pressure
PVD	pressure-velocity decoupling
r	radial direction
S_c, S_p	portions of integrated linearized source term $S = S_c + S_p \cdot \phi$
\vec{v}	velocity vector
Vol	cell volume
u,v,w	velocity components in x,y,z-direction
x,y,z	cartesian coordinates
Z	pressure term, defined by eqn (5)
α	linear blending factor
δp	pressure difference quotient
$\delta p'$	pressure correction difference quotient
ϵ	turbulence dissipation
Δh	grid spacing
ρ	density
ϕ	stands for a quantity governed by an own transport eqn

Superscripts

*	old value (before correction)
'	correction
c	quantity based on central p-DQ
+	quantity based on first order forward p-DQ
-	quantity based on first order backward p-DQ
--	quantity based on second order backward p-DQ
o	quantity based on central p-DQ but assuming zero p-gradient between grid point and boundary

Subscripts

lin	linear interpolated
mom	momentum interpolated
P	grid point P
N,S,E,W,T,B	neighbour grid points to P
n,s,e,w,t,b	cell faces midway between P and the respective neighbour grid point
nb	stands for neighbour grid points N,S,E,W,T,B

92-16096



1. Introduction and motivation

In recent years the gasturbine combustion chamber has achieved increasingly more attention due to the impending requirement of drastic reduction of emissions, higher turbine inlet temperatures and compact chambers. The search for new combustion chamber concepts (see e.g. /1/, p. 466ff), where experience is limited or lacking, forms the background for an enhanced future employment of CFD for combustor flow investigation.

In gasturbine combustion chambers we are facing a subsonic (order ~ 50 m/s), recirculating, highly turbulent flow in 3d, complex domains. As the flow is subsonic, special care must be taken to avoid the occurrence of oscillations in the pressure and/or velocity field computed, which may arise owing to a pressure-velocity decoupling. The conventional remedy, the circumstantial staggered arrangement of pressure and velocity nodes, is seemingly being replaced slowly but steadily by the nonstaggered arrangement, as an observation of the nonstaggered grid publications indicates, see /2/. Most of nonstaggered grid methods (also called colocated grid methods) for low speed flow base on a concept called the "momentum interpolation" (MI) of cell face normal velocities, which was first introduced by Rhie /3/ and Hsu /4/ in their Finite volume methods and at the same time in the Finite element context by Prakash /5/ in 1981. The MI-concept has been applied successfully to numerous low speed laminar and turbulent 2d and 3d flows, see e.g. /6,7,8/. However it may produce locally unrealistic flowfields on coarse grids due to overshooting MI. This is the first issue addressed in this paper.

Another problem arises due to the complex geometry of combustors. Here a development during the recent years can be pursued: In order to handle complex domains adequately the first generation codes typically basing on staggered grids with cartesian or polar grid lines are being more and more replaced by second generation codes, which employ curvilinear, nonorthogonal (or at least orthogonal) staggered or nonstaggered meshes /9/. Although the gain in geometrical flexibility is considerable, it may be not yet sufficient. For instance typical annular gasturbine combustor arrangements comprise of a number of nozzles firing into the chamber, whereby nozzle axis and chamber axis are mutually deferred, see /1, p. 375/. Such a flow configuration cannot be computed on a single, even curvilinear, structured grid. It asks for a zonal scheme, splitting up the entire computational domain in coupled subdomains each having their own grid. The elliptic nature of the flow with large recirculation zones may result in a strong feedback of flow information between coupled subdomains. In addition considerable gradients occur in case of combustor flow. Therefore the treatment of zonal boundary conditions may have a strong influence on the solution obtained. Although there are numerous applications of zonal schemes to transsonic and supersonic flows, zonal procedures applied to the low speed, recirculating, highly turbulent internal flow type (as in combustion chambers) are only few. None of these compares different ways of zonal grid coupling. This is done here in a limited extent, whereas a more comprehensive investigation of the grid coupling and the nonstaggered grid momentum interpolation will be given in /2/.

2. Some theory of the computational method

The investigations shown in this paper base on results obtained with our MUG3D-Code. It is an extension of the Garret code /10/ for the computation of steady 3d, turbulent flow in combustion chamber geometries by a local relaxation procedure, see e.g. /11/. The governing transport eqns are integrated over cartesian or cylindrical grids and solved repeatedly in a successive manner until convergence is obtained. The iteration sequence is well known as the SIMPLE algorithm, employing a pressure correction equation derived from the integrated continuity- and momentum eqns (see e.g. /12/). Turbulence model is the standard k, ϵ -model, which requires the additional solution of transport eqns for the kinetic turbulence energy k and its dissipation ϵ . The turbulent hydrogen-air combustion for the crossflow jet investigated was modelled by a one-step finite rate chemistry of Eddy-Break-Up type /13/.

In the context of this paper two other code features (not yet contained in /11/) are of main interest here: the nonstaggered grid formulation and the zonal scheme, which enables the grid coupling in three different manners. Some theory concerning them is given now in 2.1 and 2.2, respectively, followed by the application of the nonstaggered grid zonal scheme on two cases in chapter 3.

2.1 Nonstaggered grid

2.1.1 The problem of pressure-velocity decoupling

What is the reason that made the circumstantial staggered grid standard for Navier-Stokes computations in the low speed range up to the 80 years? It is the fact that at speeds substantial lower than speed of sound, pressure changes in the flowfield are so small, that they have only little or (in the incompressible limit) vanishing influence on density, which influences velocity field. Therefore the coupling between p and \vec{v} is less tight than in a compressible flow. This makes the problems. Due to the weak p - \vec{v} -coupling an improper treatment of pressure gradient terms and discretization of continuity eqn (first derivatives!) may lead (but need not always) to a p - \vec{v} -decoupling (PVD) of the numerical solution, which then exhibits spatial 1-4h oscillations in the pressure and velocity field. For a staggered grid, where the respective u, v, w -nodes are placed between the "driving" p -nodes, this decoupling does not occur, see /12/. The straightforward extension to a nonstaggered arrangement would be: retaining the central diffe-

rence quotient (DQ) for the pressure gradient terms in the momentum eqns and for the mass fluxes in the continuity eqn and obtain the needed pressure- and normal mass flux values on the cell faces by linear interpolation from the two adjacent grid nodes. However it is this linear interpolation that makes the momentum eqns actually use a $2\Delta h$ -central p-DQ and the continuity eqn a $2\Delta h$ central mass flux-DQ. Therefore short waved $1\Delta h$ pressure and/or velocity disturbances, which may arise during the iteration process towards convergence, are ignored by the numerical scheme and not damped out. They remain in the converged solution and appear as checkerboard-like $1\Delta h$ wiggles in the p and/or \vec{v} -field obtained. Fig. 1 gives an impression of that.

As already mentioned, such a PVD can be avoided - at least for rectilinear grids - by a staggered arrangement of pressure- and velocity nodes, which due to the staggering does not require the interpolation of the pressure on momentum cell faces or normal velocity values on continuity cell faces. This results in $1\Delta h$ -DQs for pressure and mass fluxes, so that no $1\Delta h$ wiggles can occur in the converged solution. However the staggered grid has its own shortcomings. A discussion of the relative merits of staggered and nonstaggered grid can be found in /14, 15/.

In order to obtain a nonstaggered grid scheme not susceptible to PVD one could employ forward or backward DQs (i.e. $1\Delta h$ -DQs) for the pressure gradient terms and in the continuity eqn, as was done by /16, 17/. However the second order accuracy of the central DQ is lost.

Another way is to retain central differencing, but modify the linear interpolation of cell face values, as is done in the idea of the so called momentum interpolation also called pressure-weighted interpolation, originated by /3, 4, 5/. The MI concept retains linear interpolation for the pressure values on the cell face boundaries, but employs a special interpolation of cell face normal velocities, introducing the $1\Delta h$ p-DQ across the cell face in order to avoid PVD.

2.1.2 Momentum interpolation

Our own MI-version, which is similar to that used by Perić /15/ is sketched now. Let's consider a finite volume cell surrounding a grid node P. Neighbour gridpoints are labelled by capital letters according to the points of the compass. Cell faces are located midway between adjacent nodes and denoted by lower case letters. As an example, the integration of the u-momentum eqn over the P-cell yields the discretized algebraic eqn (1). For reasons of clearness we consider a cartesian grid and unrelaxed equations. The influence of relaxation on MI is analysed elsewhere /18/.

$$a_P \cdot u_P = \sum_{nb} a_{nb} \cdot u_{nb} + S_C \quad nb = \{N, S, E, W, T, B\} \quad (1)$$

$$\text{where } a_P = \sum_{nb} a_{nb} - S_P \quad (2)$$

The a_{nb} are the discretization coefficients arising from convection and diffusion, whereas S_C , S_P represent the portions of the integrated linearized source term $S = S_C + S_P \cdot u_P$. For convenience we split up S_C in the integrated pressure gradient term plus a rest \tilde{S}_C and introduce some abbreviations. Then eqn (1) appears:

$$u_P = H_P + Z_P \quad (3)$$

$$\text{where } H_P := \frac{\sum_{nb} a_{nb} \cdot u_{nb}}{a_P} + \frac{\tilde{S}_C}{a_P} \quad (4)$$

$$Z_P := -DV_P \cdot \delta p_P \quad \text{"pressure term"} \quad (5)$$

$$DV_P := \frac{Vol_P}{a_P} \quad (6)$$

The pressure term Z [m/s] consists of the p-DQ δp_P times a factor, the pressure-velocity coefficient DV, times -1. Both H and Z can be positive or negative.

Let's denote quantities based on the central, first order forward, first order backward p-DQ by the superscripts c, +, -, respectively.

We consider point P and its axial neighbour gridpoint W:

$$u_W = H_W + Z_W \quad ; \quad u_P = H_P + Z_P \quad (7)$$

If we replaced δp_P by δp_P^- and δp_W by δp_W^+ , we would i.g. get some changed velocity values from the u-momentum eqn:

$$u_W^+ = H_W + Z_W^+ \quad ; \quad u_P^- = H_P + Z_P^- \quad (8)$$

Note that $\delta p_p \equiv \delta p_w^+$ is the $1 \cdot \Delta h$ p-DQ across the w-cell face. Instead of linear interpolation of cell face normal velocity from adjacent nodal values:

$$u_{w,lin} := \frac{1}{2} \cdot (u_w + u_p) = \frac{1}{2} \cdot (H_w + Z_w + H_p + Z_p) \quad (9)$$

we use the fictive nodal values:

$$u_{w,mom} := \frac{1}{2} \cdot (u_w^+ + u_p^-) = \frac{1}{2} \cdot (H_w + Z_w^+ + H_p + Z_p^-) \quad (10)$$

In my opinion this is the most clear, straightforward realization of the MI-idea.

As the normal cell face velocities appear not isolated but always incorporated in cell face mass fluxes C [kg/s], it is advantageous to store the latter rather than the former in the code. I use:

$$C_{w,mom} := \frac{1}{2} \cdot \left(\underbrace{S_w u_w^+ A_w}_{C_w^+} + \underbrace{S_p u_p^- A_p}_{C_p^-} \right) \quad (11)$$

In contrast the alternative definition

$$C_{w,mom} := \frac{S_w + S_p}{2} \cdot \frac{u_w^+ + u_p^-}{2} \cdot \frac{A_w + A_p}{2} \quad (12)$$

does not ensure boundedness condition

$$\min(C_w^+, C_p^-) \leq C_{w,mom} \leq \max(C_w^+, C_p^-) \quad (13)$$

In case of combustor crossflow- H_2 -jet (see 3.2) locally steep gradients of density and velocity appear at the boundary of the jet flame. There eqn (12) produced unrealistic overshooting values due to the local density variation and should not be used.

Employing the momentum interpolated cell face mass fluxes in the continuity eqn integrated over the cell surrounding P , we arrive with the common SIMPLE assumption (see /12/) at a pressure correction eqn:

$$a_p \cdot p_p' = \sum_{nb} a_{nb} \cdot p_{nb}' - \text{DIVG}^* \quad (14)$$

$$\text{where } \text{DIVG}^* := C_{n,mom}^* - C_{s,mom}^* + C_{e,mom}^* - C_{w,mom}^* + C_{t,mom}^* - C_{b,mom}^* \quad (15)$$

$$a_p = \sum_{nb} a_{nb} \quad (16)$$

$$a_w = \frac{1}{2} \cdot \left(S_w A_w \frac{\text{Vol}_w}{a_{p,u_w}} + S_p A_p \frac{\text{Vol}_p}{a_{p,u_p}} \right) \cdot \frac{1}{x_p - x_w} \quad (17)$$

$$a_e = \frac{1}{2} \cdot \left(S_e A_e \frac{\text{Vol}_e}{a_{p,u_e}} + S_p A_p \frac{\text{Vol}_p}{a_{p,u_p}} \right) \cdot \frac{1}{x_e - x_p} \quad (18)$$

(The other coefficients are formed analogously)
 a_{p,u_w} is coefficient a_p of u -eqn at point w

It is crucial for the avoidance of PVD that the cell mass source DIVG now consists of cell face mass fluxes containing $1 \cdot \Delta h$ p-DQs. The p' -eqn is solved with zero normal gradient boundary conditions. This is consistent to given mass flow rates through domain boundaries. If a p' -field has been obtained, the present old (index *) values of cell face mass fluxes, cell center velocities and pressure are updated, e.g.

$$C_{w,mom} = C_{w,mom}^* + C_w' \quad (19)$$

$$u_p = u_p^* + u_p' \quad (20)$$

$$p_p = p_p^* + p_p' \quad (21)$$

$$\text{where } C_w' = -\frac{1}{2} \cdot \left(S_w A_w \frac{\text{Vol}_w}{a_{p,u_w}} + S_p A_p \frac{\text{Vol}_p}{a_{p,u_p}} \right) \cdot \delta p_p' \quad (22)$$

$$\text{and } u_p' = - \frac{Vol_p}{a_{p,u_p}} \cdot \delta_{p_p}' \quad (23)$$

Inside domain $\delta_{p_p}' = \delta_{p_p}^c$ is used, whereas for cells at domain boundaries the zero p' -gradient between the grid point and the boundary is taken into account. It should be mentioned here that eqn (22) follows directly from the derivation of the p' -eqn (14). In contrast, the nodal velocity correction formula eqn (23) is somewhat arbitrary /5, p. 124/ and was chosen in analogy to eqn (22). Note that all corrections vanish in the converged state. In the pressure terms (eqn(5)) of the discretized momentum eqns apart from boundaries, the central DQ $\delta_{p_p} = \delta_{p_p}^c$ is used. If P-cell is boundary cell, the respective forward or backward p-DQ is used, as pressure values on the boundary are i.g. not given. The choice of p-DQ there can have strong effect on the appearance of overshooting momentum interpolated cell face mass fluxes. This will be treated now.

2.1.3 Overshooting

The subject of overshooting MI-cell face mass fluxes has not yet been analyzed in nonstaggered grid literature. /19/ mention "extensive testing by ASC has demonstrated that this potential problem is relatively minor", whereas /20/ state, that overshooting "in some cases is quite large". Only /21/ give some quantitative values of (more or less small) overshooting axial cell face velocities occurring in the "region of the peak and most rapidly changing axial p-gradients" in a laminar constriction near the contraction plane. My own experience indicates that on coarse grids considerable overshoots can occur, which may be accompanied by convergence problems.

For reason of clearness consider a constant density flow on a cartesian grid. Then ρ and A are constant and we can consider velocities rather than mass fluxes. It is clear from eqn (10) that momentum interpolated cell face normal velocities are not bounded, i.e.

$$\min(u_W, u_p) \leq u_{w \text{ mom}} \leq \max(u_W, u_p) \quad (24)$$

is not a priori fulfilled.

Therefore we want to investigate the circumstances of overshooting of a cell face velocity u_w located midway between adjacent grid points W and P. We define the overshoot B_w :

$$B_w := u_{w \text{ mom}} - u_{w \text{ lin}} \quad (25)$$

and its corresponding "overshoot portions" at points W and P:

$$B_w^+ := u_w^+ - u_W \quad ; \quad B_p^- := u_p^- - u_P \quad (26)$$

With eqns (5,7 - 10) it follows:

$$B_w = \frac{1}{2} \cdot (B_w^+ + B_p^-) \quad (27)$$

and also

$$B_w = \frac{1}{2} \cdot \left[\underbrace{DV_W \cdot (\delta_{p_W} - \delta_{p_W}^+)}_{B_w^+} + \underbrace{DV_P \cdot (\delta_{p_P} - \delta_{p_P}^-)}_{B_p^-} \right] \quad (28)$$

Fig. 2 illustrates that. We want to discuss the magnitude of the cell face velocity overshoot B_w . It can be seen from eqn (28) that B_w will be small, if both overshoot portions are small, or if both are large but compensate to a small value. Moreover, as the DV are always positive and $\delta_{p_W}^+ = \delta_{p_P}^+$, it follows from eqn (28) that a (i.g. incomplete) compensation of the overshoot portions requires the absence of a turning point of the pressure profile $p(x)$ in the vicinity of grid points W and P. More exactly speaking:

$$\text{compensation} \iff \begin{pmatrix} \delta_{p_W} < \delta_{p_W}^+ < \delta_{p_P} \\ \vee \delta_{p_W} > \delta_{p_W}^+ > \delta_{p_P} \end{pmatrix} \quad (29)$$

However this alone does not protect against large overshoots. We have to consider the magnitude of the overshoot portions B_w^+, B_p^- now. In the special case of a locally linear pressure profile $p(x)$, which is always achieved in the limit of a very fine grid, the differences in the p-DQs disappear in eqn (28) and therefore B_w vanishes. However in general these differences are not zero. Then the magnitude of the pressure velocity coefficients DV (defined in eqn (6)) is important, because they act as an amplification factor for the p-DQ-differences in B_w^+ and B_p^- . Large DV values make MI prone to overshoots.

The value of DV depends on flow field and grid spacing. A tight convective or diffu-

sive coupling between the gridpoint and its neighbours reduces DV. Moreover it approaches zero, if the grid spacing in any of the three coordinate directions goes to zero. At least in the limit of small grid spacing, i.e. small grid-Peclet numbers, this dependency is a quadratic one, because the effect of diffusion in the respective coordinate direction on DV becomes dominating.

Eqn (28) was evaluated for the four p-DQ combinations for δ_{p_W} and δ_{p_P} shown in Fig.3. For a sufficiently small, constant x-grid spacing $\Delta h \rightarrow 0$ the following relations were derived from eqn (28):

$$I: (\delta_{p_W} = \delta_{p_W}^c \wedge \delta_{p_P} = \delta_{p_P}^c) \quad B_W = \frac{\Delta h^2}{4} \cdot \frac{DV_W + DV_P}{2} \cdot \frac{\partial^3 p}{\partial x^3} \Big|_W \quad (30)$$

$$IIa: (\delta_{p_W} = \delta_{p_W}^c \wedge \delta_{p_P} = \delta_{p_P}^0) \quad B_W = -\frac{1}{6} \cdot DV_P \cdot \frac{\partial p}{\partial x} \Big|_W \quad (31)$$

$$b: (\quad \quad \quad \wedge \delta_{p_P} = \delta_{p_P}^-) \quad B_W = -\frac{\Delta h}{4} \cdot DV_W \cdot \frac{\partial^2 p}{\partial x^2} \Big|_W \quad (32)$$

$$c: (\quad \quad \quad \wedge \delta_{p_P} = \delta_{p_P}^{--}) \quad B_W = -\frac{\Delta h}{4} \cdot (3 DV_W - 2 DV_P) \cdot \frac{\partial^2 p}{\partial x^2} \Big|_W \quad (33)$$

In case I, where neither W nor P are boundary cells, B_W^+ and B_P^- are governed by $\partial^2 p / \partial x^2$ -values, whereas B_W depends on the gradient of $\partial^2 p / \partial x^2$. So curvature changes of pressure profil play an important role. In case II, where P is a boundary cell, the expressions for the three investigated different p-DQs at the boundary reveal: The zero normal p-gradient assumption (using $\delta_{p_P}^0$) makes B_W proportional to pressure gradient, whereas a first order ($\delta_{p_P}^-$) or second order ($\delta_{p_P}^{--}$) backward p-DQ results in a dependence from the second derivative of pressure. Among the three boundary treatments, the overshoot expression B_W for the zero normal p-gradient assumption (eqn (31)) is of lower Δh -order than in the first order backward p-DQ case (eqn (32)). It is interesting, that a switching over to the second order backward p-DQ does not raise the Δh -order of B_W (eqn (33)), which remains lower than apart from boundaries (eqn (30)).

So regions at domain boundaries are prone to MI-overshoots in the velocity component normal to the boundary. The use of the zero normal p-gradient assumption in the normal momentum eqn of boundary cells is less favourable. This is confirmed by the experience gained from the swirl nozzle flow, see 3.1. When using the first or second order backward p-DQ at boundaries, no remarkable overshooting can occur there, if the normal distance between the three grid lines adjacent next to the boundary is chosen sufficiently small.

2.1.4 Linear blending

The nonlinear behaviour of the MI is a remedy to avoid PVD on nonstaggered grid arrangements. Therefore nonvanishing overshoots B are welcome. However the cell face normal velocity u_w should remain a reasonable representation of the nodal values u_w and u_p . Otherwise (sometimes wavy) distortions in the computed flow field are observed, see e.g. Fig. 11a.

In order to reduce too strong overshoots, the originally pure MI-cell face mass fluxes were replaced by a combination with the linear interpolated cell face mass fluxes:

$$C_w = (1 - \alpha) \cdot C_{w_{\text{mom}}} + \alpha \cdot C_{w_{\text{lin}}} \quad (34)$$

By a choice of the linear blending factor α ($0 \leq \alpha \leq 1$) one can balance between the eventual occurrence of strong overshoots and the eventual occurrence of PVD-oscillations. Experience gained from the two flow cases below reveals that both phenomena, if they appear strong enough, are accompanied by convergence problems, as certain underlying assumptions of the pressure correction scheme are poorly fulfilled then.

2.2 Grid coupling

Composite grid or zonal methods can be categorized in three groups. Following the terminology of Thompson /25/ these are:

- block grid or patched grid methods, where the structured subgrids share a common interface with or without continuity of grid lines and line slope across the boundary, e.g. /26/
- overlaid or Chimera methods, which abandon the constraint of a common interface, employing instead an overlap area (or -volume in 3d), where solution on both structured grids is computed, e.g. /27/

- hybrid methods, which use an unstructured grid as connecting grid bridging the gap between the structured grids, e.g. /28/.

Such composite grid methods have become popular for about a decade in the simulation of aircraft aerodynamics and turbomachinery flow. Most of these applications employ the inviscid Euler eqns and the thin layer Navier-Stokes eqns in the transsonic or upper subsonic flow regime. In contrast, zonal grid applications of the full Navier-Stokes eqns for low speed flow are not yet widespread in use. These are more reported for laminar flow, e.g. /29-31/ than for the turbulent case, e.g. /32-34/. Sheemingly only /33, 34/ computed combustng turbulent flow with a zonal scheme.

The question whether grid coupling should be flux conservative is a debated issue. For compressible flow it is a common view, that lacking local conservation of the numerical fluxes across grid interfaces may give rise to distortions and instabilities in the computed flowfield near shocks. For turbulent recirculating low speed flow, however, the influence of interface flux conservation has not yet been studied. Therefore the chosen Chimera zonal grid feature in the MUG3D-Code was designed to treat subgrid interfaces optional in three different manners:

- a) nonconservative
However global mass conservation is enforced on each subgrid by a cell face area weighted additive correction of receiving cell face mass fluxes, as the finite volume approach requires at least global mass conservation for convergence.
- b) locally mass conservative
Only mass fluxes are transferred locally conserved across the interfaces.
- c) locally fully conservative
The numerical fluxes of all transported quantities ϕ are transferred locally conserved across the interfaces.

The nonconservative coupling interpolates receiver grid interface values from the sender grid (Diriclet-b.c.). This is done by trilinear Lagrange interpolation. The geometrical data contained in the interpolation factors are distances between grid points. In contrast the mass conservative or fully conservative coupling mode require additionally intersection areas and -volumes, whose determination for an arbitrary orientation of sender and receiver grid cells can become a cumbersome task.

The conservative flux transmission in mode b and c is performed as follows: The flux from a sender grid cell into the i.g. intersecting receiver grid surface (called the interface), is obtained from a flux balance for its remaining cell portion that is not occupied by the receiver grid. Doing this for all respective sender grid cells and assuming a constant distribution of these interface fluxes inside their respective sender grid cell, we get a stepwise constant flux density distribution on the interface. From that, the local receiver cell face fluxes are then obtained straightforward according to location and area of the respective cell face on the interface. The transmitted mass flux values are used regularly to form convective terms in the ϕ -transport eqns and enter the mass source DIVG of the pressure correction eqn (14). This differs from the implementation of conservative ϕ -flux values: Here a deferred correction is used, i.e. in the ϕ -eqn of a receiver cell P the flux difference between the conservative, say, west cell face flux and its i.g. nonconservative counterpart, which is obtained by the regular use of the interpolated ϕ -value ϕ_w , is introduced as an additional contribution to the explicit source term S_C (e.g. in eqn (1)).

3. Applications

Some results of the application of the MI zonal procedure on two flow cases are given now.

3.1 Swirling axisymmetric model combustor flow

This flow case consists of a model swirl nozzle expanding axisymmetric in a chamber. In order to reduce the outer recirculation zone, a weak axial blowing from the frontside of the chamber is added. Swirler and combustor geometry were developed for numerical and experimental investigations of turbulent particle dispersion at the DLR. For more details see /22, 23/. Results shown here confine to axisymmetric, isothermal, single phase flow. Fig. 4 gives an impression of geometry and the turbulent flowfield computed on three overlapping grids. Owing to the strong swirl imposed (swirl number was 1.66), an inner recirculation zone results, reaching almost to the axial front wall of the nozzle. Inside the nozzle strong MI overshoots of radial velocity v were observed adjacent to the left axial wall ($x = 1$ mm, Fig. 5a) and also at the outer nozzle wall (e.g. $x=32.5$ mm Fig. 5b). The computed radial profiles $v(r)$ shown in Fig. 5-7 were obtained on two grids: the coarse grid had 13 radial grid points inside the nozzle, whereas the fine grid had twice as many radial grid points and additionally an axial refinement near $x=0$. At $x=1$ mm an unrealistic $v(r)$ -profil below $r \approx 12$ mm was found. This has two reasons:

First, the remarkable influence of the boundary normal p-DQ treatment on the coarse grid solution indicates a too coarse axial grid spacing near $x=0$, causing MI-overshooting u-velocities, which in turn distort the wall-tangential $v(r)$ -profile, where u and v are of the same order (and that happens at $x=1$ mm for r below ≈ 12 mm).

Second, a considerable MI-overshooting of v -velocities can be observed on the coarse grid. This is exhibited in Fig. 6a and for comparison purposes also for the fine grid (Fig. 6b). The curvature changes in the radial pressure profile cause strong differences between v^+ , v , v^- (defined analogously to eqns (7,8)), resulting in locally severe overshoot portions B^+ , B^- . Apart from the pressure turning point at $r \approx 11\text{mm}$ there is fortunately compensation of these overshoot portions but it is locally very incomplete, so that the resulting cell face overshoots B are still high. These can be obtained quantitatively from Fig. 6 as the vertical distance between v_{nom} (denoted by the symbol \odot) and the line interpolating v_p values (denoted by \times). Note that it is the nodal point velocities v_p that behaved locally unrealistic, whereas the v_{nom} -profile did not exhibit any wiggles. This might be due to the continuity eqn, which in the limiting case of a 1d-flow prohibits any wiggles of the MI cell face mass fluxes, regardless of eventual MI-overshoots. The fine grid results of Fig. 6b exhibit clearly an amendment of the situation, but also reveal that the refinement is not yet sufficient, so that the two fine grid profiles $v(r)$ in Fig. 5a do not yet behave as should be expected from physics for $r < 11\text{mm}$.

The $v(r)$ -profiles at $x=32.5\text{mm}$ are instructive for boundary normal p-DQ influence on MI. As can be seen from Fig. 5b, apart from the outer nozzle wall ($r=25\text{mm}$) overshooting is not a problem there. However the normal velocity component v_p nearest to the wall exhibits unrealistic values up to 13 m/s (note that the axial component u_p is of order 20 m/s there)! As overshooting at boundaries is of lower Δh -order when using δ_{pp} rather than δ_p (see eqn (31) and (32)) a more realistic behaviour can be expected in the latter case. This is confirmed by Fig. 5b, which also contains a warning: In the δ_{pp} -case the grid refinement resulted in a still more unrealistic value v_p than on the coarse grid! The reason for that is an improper grid refinement at the boundary: in the δ_{pp} -case rather than using δ_{pp} or δ_p , MI-overshooting depends on grid expansion factor normal to the boundary (not featured in eqn (31), which was derived for constant grid spacing Δh). As no additional grid line between the original boundary-neighbouring coarse grid grid line was introduced by the grid refinement, grid expansion factor rose and worsened the situation.

In Fig. 7 it is shown that the diminishing of overshoots by linear blending resulted in more realistic $v(r)$ -profiles. Moreover convergence problems encountered on the coarse grid due to the strong overshoots at $x=1\text{mm}$ did not occur with linear blending (already with $\alpha=0.5$). However it was found, that increasing linear blending factor α tended to roughen pressure and velocity profiles in high gradient regions. In the swirl nozzle flow case this effect was only weak, but could be more clearly observed in the crossflow jet case with its steeper gradients. This is a consequence of the less tight pressure - velocity coupling introduced by linear blending. Based on present experience only a mild linear blending of, say, $\alpha=0.5$ can be recommended, although in the swirl nozzle case unique improvements of the computed flow field in the nozzle could be achieved by raising α up to 0.9.

All fine grid results shown were obtained by a division of the computational domain in three overlapping subgrids, see Fig. 4. (For the coarse grid computations the fine subgrid 1 was dropped and instead subgrid 2 extended into the whole nozzle.) In both overlap regions the respective two subgrids had identical axial grid spacing but different radial spacing being increasingly coarser from subgrid 1 to 3. The axial overlap in the nozzle took two cells, whereas a three-cell overlap was employed in the chamber. For comparison purposes a single grid computation was performed on a grid that maintained the radial grid spacing of subgrid 1 and 2 up to the right boundary ($x = 560\text{mm}$) of the chamber.

It was found that the nonconservative and mass conservative coupling method gave very similar results being in good agreement with the single grid computation. Hereby the nonconservative coupling scheme was marginally better than the mass conservative one. The fully conservative scheme gave also good agreement with the single grid results in the grid overlap region in the chamber, where a recirculating flow across the interfaces still exists, but flow gradients are low. However at the grid interfaces in the nozzle partially strong distorted profiles were obtained with the fully conservative mode, arising from receiver cells, in which the respective sender grid fluxes had been coupled in. This is due to a basic problem of conservative ϕ -flux coupling, as it inherently bears the danger of coupling improper downstream information to upstream by force, what may be unphysically, if locally no (or weak) transfer mechanism of ϕ from downstream to upstream exists. Such an unphysical flux prescription can result in distorted profiles or even ill conditioned or singular discretization eqns for such receiver cells. Improper flux values coupled in may be caused by the fact that:

- a) flux transfer from sender to receiver grid may require higher order assumptions on flux distribution. However for arbitrary orientated grids the realization of a conservative flux transfer being of higher order than the stepwise constant flux profile assumption is not an easy task.
- b) the flux information may stem from a sender grid, whose solution is locally too different from the one of the receiver grid. This may happen, if grid spacing of the two grids are too different in a region, where flow gradients are not small. This may also happen in an intermediate state of the iteration process towards the converged solution, due to the occurrence of a too different (quasi-) time advancement of the solutions on the coupled grids at the interfaces. Indeed this was the reason, why the converged solution of the fully conservative coupling scheme could only be obtained in the swirl nozzle flow case from a restart of the converged

(e.g.) mass conservative solution. However also then convergence was much slower. In the crossflow jet case no converged solution could be obtained with the fully conservative coupling scheme.

In Fig. 8 velocity profiles from the three-grid zonal computation of the MUG3D-code are compared with LDA-measurements and results from another code (staggered grid code CPTR, using single grid) at an axial position 2 mm downstream of the sudden expansion. These measurements and CPTR results are taken from Blümcke /35/ at my institute. The profiles are predicted fairly well by the zonal scheme and are in close agreement to those produced by the MUG3D single grid calculation already mentioned. The zonal scheme reduced drastically the CPU-time on an IBM 3091 from ~13 hours to 2 hours, whereby number of active grid points decreased from ~4500 to 2700, but the single grid accuracy was retained (except locally for the fully conservative mode). It was found that the CPU-time overhead arising from coupling operations to be performed by the code, were about the same for the three coupling modes.

3.2 Single crossflow jet in rectangular channel

In the context of a national technology program for hypersonic airbreathing propulsion concepts basic investigations on hydrogen crossflow jets in subsonic air stream are being made at our DLR-Institute of Propulsion Technology. In order to gain insight into jet penetration, mixing and stabilization the basic arrangement shown in Fig. 9 was investigated experimentally and numerically, see /24/. The reacting H_2 -jet issues from a small rectangular aperture ($l \times b = 0.5 \times 1.7\text{mm}$) perpendicularly into an air crossflow in a rectangular channel ($B \times H = 25 \times 40\text{mm}$). Computations started 40mm upstream of jet center assuming a constant distribution of air velocity $u_{\text{air}} = 31\text{m/s}$. Channel pressure was 6 bars. Hydrogen velocity in the nozzle orifice was taken to be 1150m/s, what is still subsonic. H_2 -air momentum density ratio was 95, whereas mass flux ratio was 0.0022. Fig. 10 gives an impression of the spreading and deflection of the burning jet by means of equivalence ratio isolines $\varphi = \text{const}$. Hereby the value $\varphi = 0.1$ represents the lean burning limit of a well stirred H_2 -air mixture.

Computations were performed on a $43 \times 40 \times 17$ single grid as well as with a 2-grid zonal arrangement, where a rectangular fine grid $33 \times 40 \times 16$ covering the high gradient region around the H_2 -orifice was overlaid to the global $43 \times 40 \times 17$ grid. The latter extended overlapping into the fine grid domain. Coarse grid points beyond the overlap region, i.e. coarse grid points far inside the fine grid domain were formally computed, but fixed to a constant value (passive region).

The single grid computations predicted the main features of the flow in the high gradient jet region roughly according to the fine grid solution of the zonal scheme, although flow details were captured rather poor and sometimes unrealistic. Linear blending changed the single grid results locally sometimes remarkably, but an overall better agreement with the fine grid solution of the zonal scheme could not be stated. As expected, in the limiting case $\alpha = 1$ severe PVD-oscillations were observed. In my opinion the single grid resolution was too coarse in the high gradient jet region to allow a meaningful evaluation of linear blending influence by a comparison with the fine zonal grid solution.

No severe MI-overshooting effects at domain boundaries were observed, where the respective (first order) backward p-DQ was employed. However at zonal boundaries originally the central p-DQ in the receiver grid momentum eqn normal to the interface was employed. This had a strongly destabilizing effect on convergence behaviour as well as on the solution obtained, see Fig. 11a: The fine grid mass flux density normal to the axial fine grid boundaries (at $x = -3\text{mm}$ and $x = +5\text{mm}$) exhibits a strong MI-overshooting at the boundary cells inducing wiggles and distorted profiles. The reason for that is, that the normal central p-DQ of receiver cell uses an interpolated pressure value from the sender grid. However here the local pressure profiles of sender and receiver grid are too different, so that the use of this pressure value imposes a sudden pressure jump on the receiver boundary cell. This in turn results in a large difference between central and backward p-DQ of the cell, leading to a considerable overshoot B. Linear blending reduced these overshoots, but yet worsened the situation, because the pressure jump stimulated PVD-oscillations arising from the boundary. It could be clearly seen, that raising blending factor α attenuated the ability of the solution to damp out the oscillations excited from the pressure jump. This problem cannot be remedied here by a higher order interpolation of the pressure value from the sender grid, because sender grid profiles were smooth near the receiver zonal boundary. In order to avoid the use of such pressure values, the original p-DQ in the normal momentum eqn of receiver grid cells at zonal boundaries was replaced by the respective first order backward p-DQ. That removed the difficulties, as can be seen from Fig. 11b. It should be mentioned here, that in the swirl nozzle flow case the central p-DQ was still used without problems, because there sender and receiver grid pressure fields at the zonal boundaries did fit, owing to weaker gradients.

All three zonal coupling modes were applied on the crossflow jet flow case. The non-conservative and the mass conservative scheme showed a similar convergence behaviour, what was also found for the swirl nozzle flow case. In contrast no converged solution could be obtained with the fully conservative coupling scheme for the crossflow jet. For the two former schemes a control of the obtained zonal grid solutions by means of a sufficiently fine single grid solution is hardly feasible in this 3d flow, as the CPU-time for that would be tremendous (days). However LDA-measurements have been made. According

to the experimental facility the flow conditions were changed from those given before: The isothermal mixing of an air-in-air crossflow jet at ambient pressure was studied. Channel width B was somewhat enlarged to 30 mm and velocity at jet orifice was decreased to 296 m/s, retaining roughly the original momentum density ratio. At present the LDA measurements are not yet completed. They are continued to control and refine the existing experimental results gained up to now. The preliminary comparison of the zonal grid solutions with the present LDA data indicates a somewhat better agreement of the nonconservative results with the measurement than the mass conservative solution did. However a unique superiority of the nonconservative mode cannot be concluded from that. The choice of coupling mode had locally a strong influence on the coarse and fine grid solution obtained. In addition locally strong differences between the coupled coarse and fine solution in the overlap region were found for each coupling mode. An example of this situation represent the profiles of axial velocity $u(y)$ 2mm downstream of jet center at symmetry plane $z = 0$ shown in Fig. 12. It can be seen from this figure, how different the coupled coarse and fine grid solution can locally be. Linear blending with $\alpha = 0.5$ as well as a local blending scheme, which determined α -values locally between 0.5 and 0.9, gave slightly better agreement with the LDA measurements than pure MI ($\alpha = 0$).

4. Conclusions

The nonstaggered grid zonal procedure was outlined and applied on two flow cases. Locally unrealistic flowfields computed by the momentum interpolation scheme employed were shown to be caused by strong overshoots of the momentum interpolated cell face mass fluxes. In extrem cases the overshoots were accompanied by convergence problems. Fortunately strong overshooting is a coarse grid effect. The connection between grid spacing, curvature of pressure profiles and overshooting was analyzed. At boundaries overshooting is more sensitive to grid spacing than apart from boundaries. The analysis reveals that the zero pressure gradient assumption at boundaries is -as far as overshooting is concerned- inferior to an extrapolation of boundary pressure in the p-DQ of the normal momentum eqn. This was confirmed by experience. At zonal boundaries pressure values from the sender grid should not be used to form the p-DQ in the normal momentum eqn of receiver grid cells at the interface. Otherwise this may have a destabilizing effect if grids are too different. The respective backward p-DQ remedied the difficulties encountered. Experience with the two flow cases indicates, that linear blending of the momentum interpolated cell face mass fluxes can be a measure to attenuate the drawbacks of strong MI-overshooting, if pressure-velocity decoupling effects do not occur.

In variable density flow (combustion!) locally an unrealistic overshooting of cell face mass fluxes due to a distinct interpolation of density and velocity values could be observed. That was avoided by interpolation of mass flux densities itself.

The Chimera zonal scheme was applied in three coupling modes: nonconservative, locally mass flux conservative, locally fully flux conservative mode. The latter turned out to be not a robust method and cannot be recommended for general grid combinations. Experience gained so far with the two other modes, which worked well, does not indicate a clear superiority of one of them, neither in accuracy, convergence behaviour or CPU-overhead. However the mass conservative mode requires more geometrical coupling data, whose determination may be a cumbersome task for an arbitrary orientation of the grids.

In my opinion the question of the conservativity of inter grid flux transfer becomes less important if the grids coupled together produce too different approximations of the flowfield near the interface. Then the solutions don't fit and distort one another, what cannot be cured by an even sophisticated coupling scheme employing higher order interpolations. As only patched grid coupling methods with grid line continuity across the interface are a priori free of that sort of problem, one has to take care that interfaces are not placed in high gradient regions if the grid spacings are too different near the interfaces.

5. References

- /1/ W.J. Dodds "Combustion system design", in: "Design of modern turbine combustors", edited by A.M. Mellor, Academic Press, 1990
- /2/ M. Rachner Dissertation, Fakultät für Maschinenbau der Ruhr-Universität Bochum, to appear in 1992 (also as DLR Forschungsbericht DLR-FB 92-xxx)
- /3/ C.M. Rhie "A numerical study of the flow past an isolated airfoil with separation", PhD Thesis, University of Illinois at Urbana-Champaign, 1981
- /4/ C.F. Hsu "A curvilinear-coordinate method for momentum, heat and mass transfer in domains of irregular geometry", PhD Thesis, University of Minnesota, Minneapolis, 1981
- /5/ C. Prakash "A finite element method for predicting flow through ducts with arbitrary cross sections", PhD Thesis, University of Minnesota, Minneapolis, 1981

- /6/ A.D. Gosman
M. Perić "ein Finites-Volumen-Berechnungsverfahren für dreidimensionale, komplexe Strömungen", Proc. 6. DGLR-Fach-Symposium "Strömungen mit Ablösung", held Nov. 1988 in Braunschweig, DGLR-Bericht 88-05, pp. 313-326, 1988
- /7/ A.O. Demuren "Calculation of 3d turbulent jets in crossflow with a multigrid method and a second-moment closure model", in: "Engineering turbulence modelling and experiments", edited by W. Rodi and Ganić, Elsevier Science Publ., 1990
- /8/ G.V. Hobson
B.Lakshminarayana "Prediction of cascade performance using an incompressible Navier-Stokes technique", ASME 90-GT-261, 1990
- /9/ M.A.Leschziner "Modeling turbulent recirculating flows by finite-volume methods - current status and future directions", Int. J. Heat and Fluid Flow, Vol. 10, No. 3, Sept. 1989
- /10/ H.C. Mongia
R.S. Reynolds "Combustor design criteria validation", Volume III - User's Manual, USARTL-TR-78-55C, Febr. 1979
- /11/ H. Eickhoff
J. Koopman
W. Neuberger
M. Rachner "Entwicklung eines Berechnungsverfahrens zur Bestimmung der dreidimensionalen Strömungs- und Verbrennungsvorgänge in Gasturbinenbrennkammern", FVV-Abschlußbericht Gasturbinen-Brennkammern, Vorhaben Nr. 300, Forschungsberichte Verbrennungskraftmaschinen, Heft 363, 1985
- /12/ S.V. Patankar "Numerical heat transfer and fluid flow", Hemisphere Publishing Corp., 1980
- /13/ M. Rachner
J. Koopman "Fundamentals and application of CFD to combustors", lecture script No. 64, at "Space Course on Low Earth Orbit Transportation and Orbital Systems", RWTH Aachen, 18.2. - 8.3.1991
- /14/ M. Perić
R. Kessler
G. Scheuerer "Comparison of finite-volume numerical methods with staggered and colocated grids", Computers and Fluids, Vol. 16, No. 4, pp. 389-403, 1988
- /15/ M. Perić "A finite volume method for the prediction of three-dimensional fluid flow in complex ducts", PhD Thesis, University of London, 1985
- /16/ D.F. Roscoe "The numerical solution of the Navier-Stokes equations for three-dimensional laminar flow in curved pipes using finite difference methods", J. of Engineering Mathematics, Vol. 12, No. 4, pp. 303-323, 1978
- /17/ L. Fuchs
H.-S. Zhao "Solution of three-dimensional viscous incompressible flows by a multi-grid method", Int. J. Numerical Methods in Fluids, Vol. 4, pp. 539-555, 1984
- /18/ S. Majumdar "Role of underrelaxation in momentum interpolation for calculation of flow with nonstaggered grids", Numerical Heat Transfer, Vol. 13, pp. 125-132, 1988
- /19/ (Company
brochure) "Technical summary of ASC's CFD technology", Advanced Scientific Computing Ltd., Waterloo, Canada, June 1989
- /20/ S.Acharya
F.H.Moukalled "Improvements to incompressible flow calculation on a nonstaggered curvilinear grid", Numerical Heat Transfer, Part B, Vol. 15, pp. 131-152, 1989
- /21/ T.F.Miller
F.W.Schmidt "Use of a pressure-weighted interpolation method for the solution of the incompressible Navier-Stokes equations on a nonstaggered grid system", Numerical Heat Transfer, Vol. 14, pp. 213-233, 1988
- /22/ Ch.Hassa
E.Blümcke
M.Rachner
H.Eickhoff "The influence of a radial swirl generator on the flow field from a fuel nozzle model", Proc. 4th Int. Symp. on Application of Laser Techniques to Fluid Mechanics, Lisbon, 1988
- /23/ E.Blümcke
H.Eickhoff
Ch.Hassa "Dispersion of monosized droplets in a turbulent swirling flow", Proc. 4th Int. Conf. on Liquid Atomization and Spray Systems, Sendai, Japan, 22.-24.8.1988
- /24/ J.Koopman
M.Rachner
H.Wiegand
H.Eickhoff "Aerodynamics and stabilization of combustion of hydrogen jets injected into subsonic airflow", 75th Symp. AGARD PEP on "Hypersonic Combined Cycle Propulsion", AGARD-CP-479, Madrid, 1990
- /25/ J.F.Thompson "General structured grid generation systems", AGARD FDP Specialists' Meeting on "Application of Mesh Generation to Complex 3-D Configurations", AGARD-CP-464, Loen, Norway, May 1989

- /26/ M.M.Rai "A conservative treatment of zonal boundaries for Euler equation calculations", AIAA-paper No. 84-0164, January 1984
- /27/ J.A.Benek
J.L.Steger
F.C.Dougherty "A flexible grid embedding technique with application to the Euler equations", AIAA 83-1944-CP, July 1983
- /28/ K.Nakahashi
S.Obayashi "FDM-FEM zonal method for viscous flow computations over multiple-bodies", Technical Report of National Aerospace Laboratory NAL TR-925T, Tokyo, Japan, March 1987
- /29/ B.E.Launder
T.H.Massey "The numerical prediction of viscous flow and heat transfer in tube banks", J. Heat Transfer, Vol. 100, pp. 565-571, Nov. 1978
- /30/ R.E.Phillips
F.W.Schmidt "A multilevel-multigrid technique for recirculating flows", Numerical Heat Transfer, Vol. 8, pp. 573-594, 1985
- /31/ R.L.Meakin
R.L.Street "Simulation of environmental flow problems in geometrically complex domains. Part 2: A domain-splitting method", Computer Methods in Applied Mechanics and Engineering, Vol. 68, pp. 311-331, 1988
- /32/ C.-N.Yung
T.G.Keith
K.J.De Witt "Numerical simulation of axisymmetric turbulent flow in combustors and diffusers", Int. J. Num. Methods in Fluids, Vol. 9, pp. 167-183, 1989
- /33/ T.Mukerjee
L.T.Tam
S.K.Jain
N.C.Costes "A multidomain and multidimensional numerical analysis of flow in fuelside preburner, high pressure turbine, hot gas manifold and main injector assembly of the space shuttle main engine", AIAA-87-1802, 1987
- /34/ P.N.Wild
F.Boysan
J.Swithenbank
X.Lu "3-dimensional gas turbine combustor modelling", 70th Symp. AGARD PEP on "Combustion and fuels in gas turbine engines", AGARD-CPP-422, Chania, Greece, 1987
- /35/ E.Blümcke "Turbulente Partikeldispersion in eingeschlossenen Drallströmungen", Dissertation, Ruhr-Universität Bochum, to appear 1991 (also as DLR Forschungsbericht)

Figures

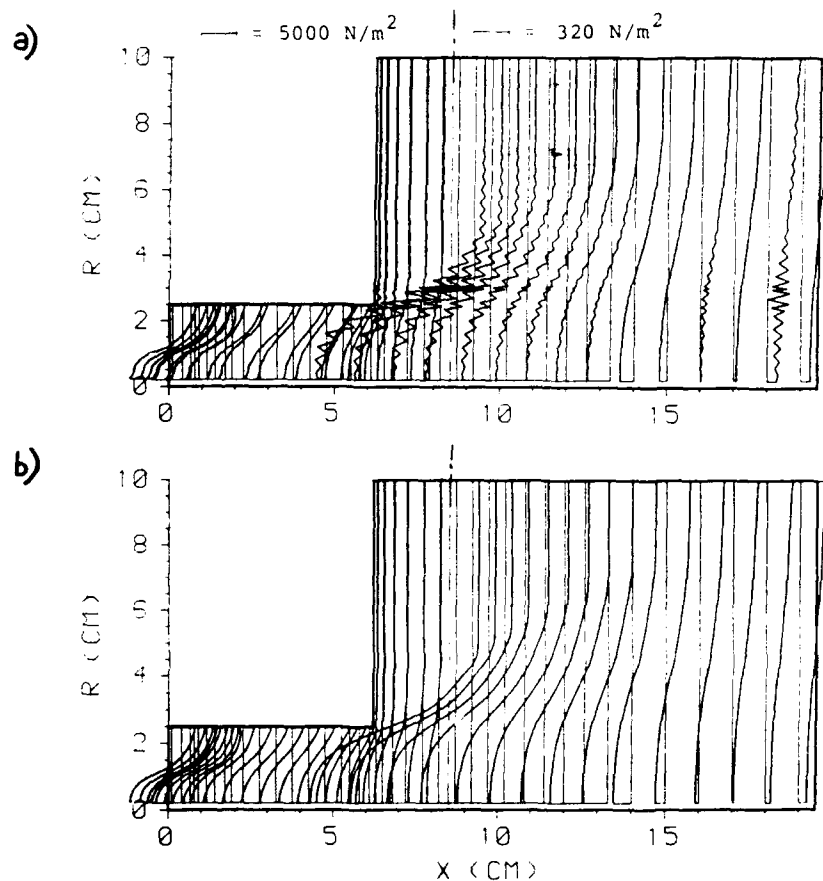


Fig. 1 Swirl nozzle flow: Effect of pressure-velocity decoupling on computed pressure profiles $p(r)$

- a) PVD promoted by linear interpolation of cell face mass fluxes ($\alpha=1$)
 b) PVD prevented by momentum interpolation of cell face mass fluxes ($\alpha=0$)

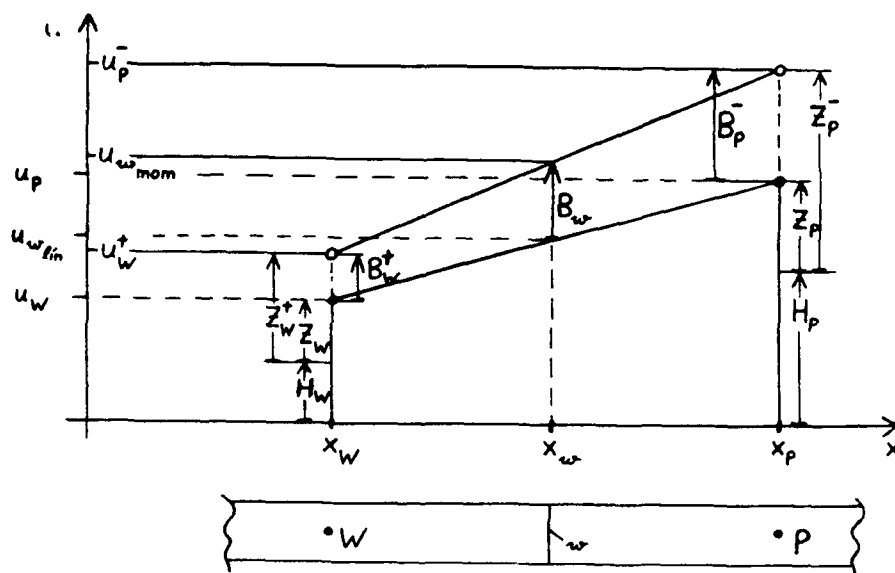
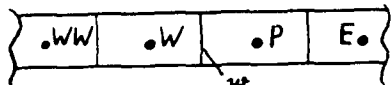
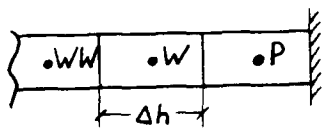


Fig. 2 Momentum interpolation of cell face normal velocity u_w : Sketch of quantities involved

I: 

$$\delta_{p_P} = \delta_{p_P}^e = \frac{p_E - p_W}{2 \cdot \Delta h}$$

II: 

a)
$$\delta_{p_P} = \delta_{p_P}^o = \frac{p_P - 0.5(p_P + p_W)}{\Delta h} = 0.5 \cdot \delta_{p_P}^-$$

b)
$$\delta_{p_P} = \delta_{p_P}^- = \frac{p_P - p_W}{\Delta h}$$

c)
$$\delta_{p_P} = \delta_{p_P}^{--} = \frac{p_{WW} + 4p_W - 3p_P}{2 \cdot \Delta h}$$

Fig. 3 Different choice of p-DQ of cell P for $\Delta h = \text{const}$

- I) cell P is apart from east domain boundary
 II) cell P is east boundary cell

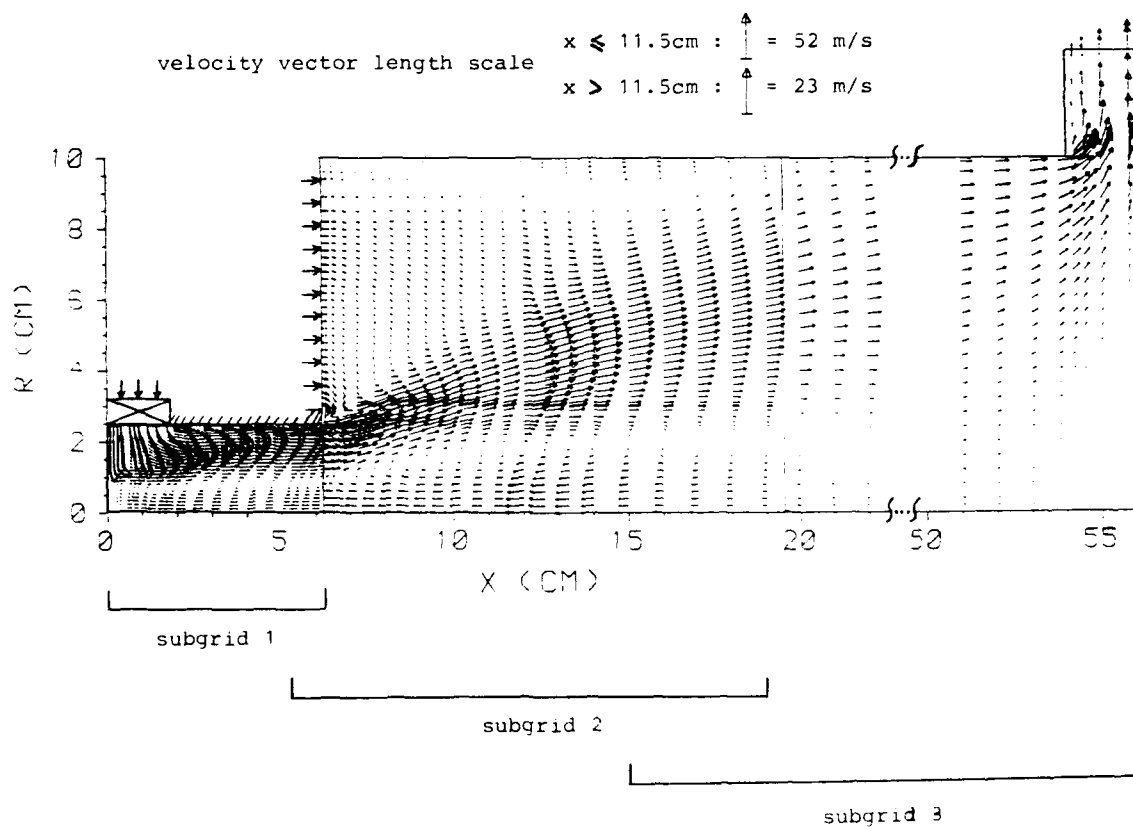


Fig. 4 Swirl nozzle flow: velocity field computed by the zonal scheme

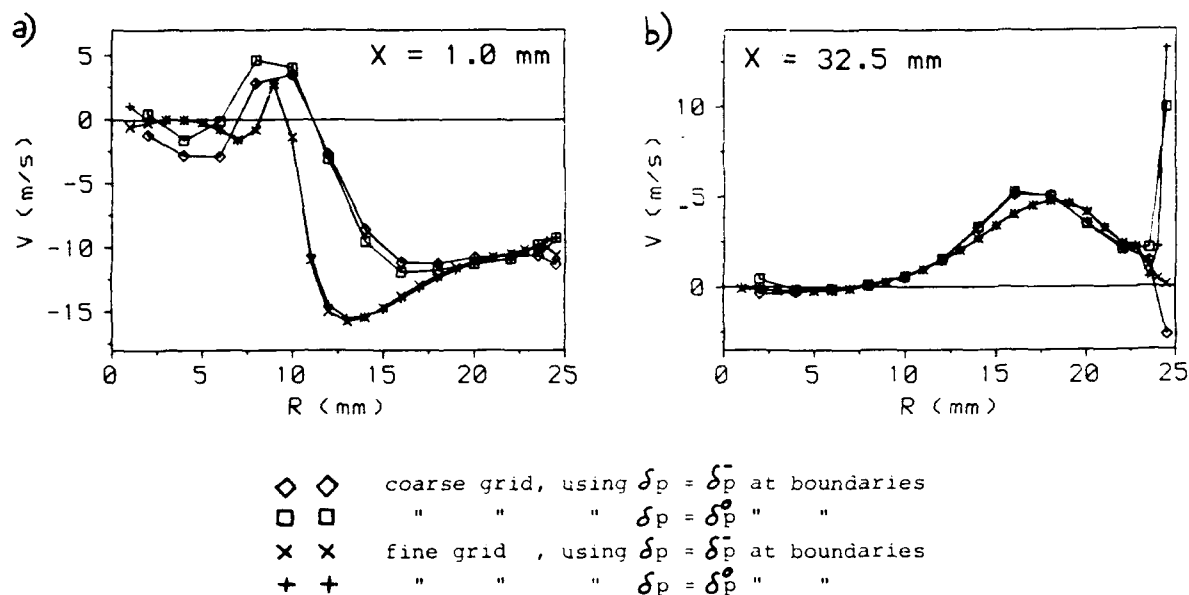


Fig. 5 Swirl nozzle flow: Influence of grid refinement and the discretization of normal pressure gradient at boundaries on radial velocity profiles $v(r)$ (pure MI used: $\alpha=0$)

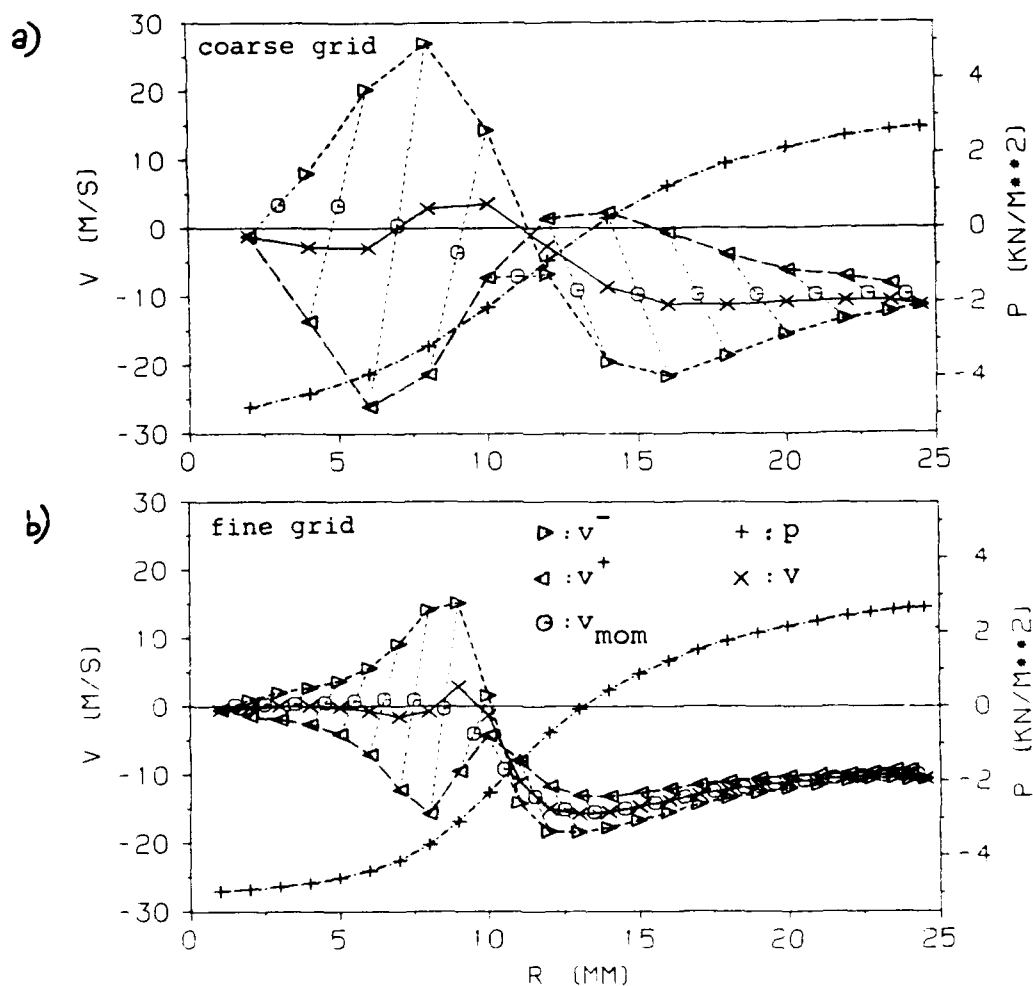


Fig. 6 Swirl nozzle flow: Analysis of overshooting radial velocities at $x=1$ mm ($\delta_p = \delta_p^-$ at boundaries used; pure MI)

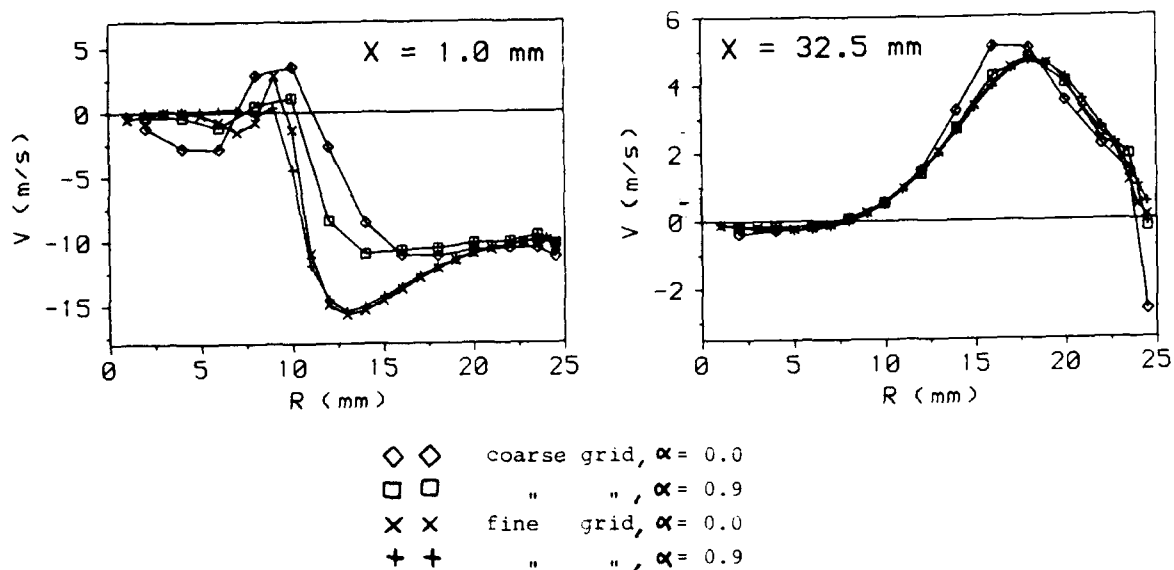


Fig. 7 Swirl nozzle flow: Influence of linear blending on radial velocity profiles $v(r)$ ($\delta p = \delta \bar{p}$ at boundaries used)

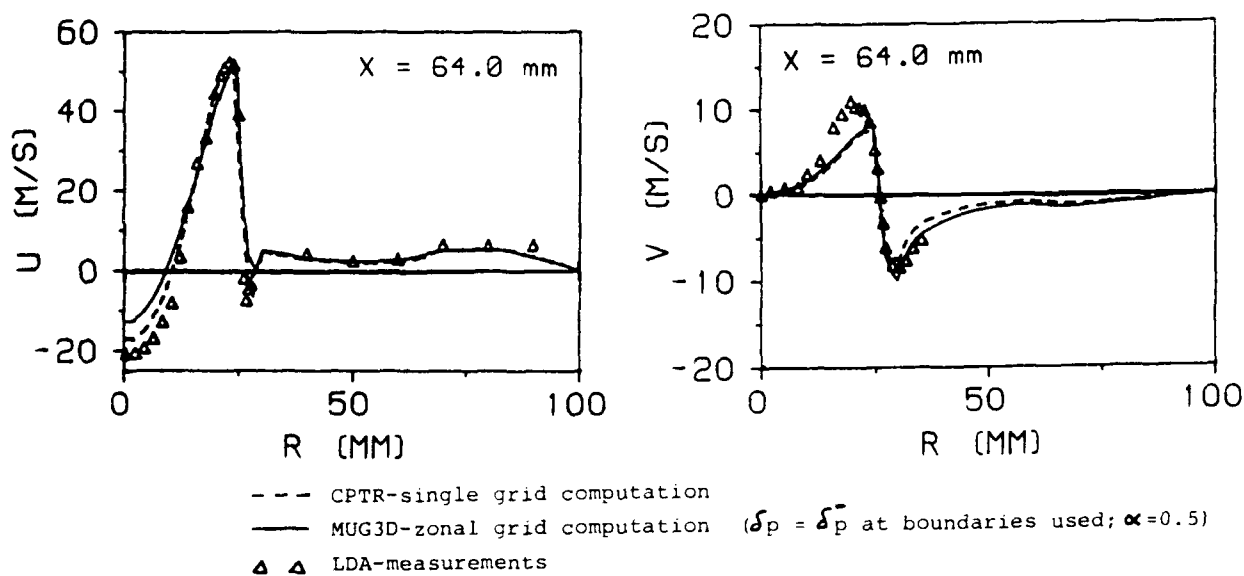
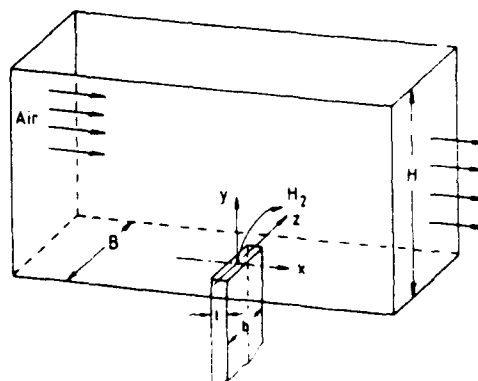


Fig. 8 Swirl nozzle flow: Comparison of computed velocity profiles with LDA-measurements at $x=64$ mm

Fig. 9 Crossflow jet:
Basic channel geometry



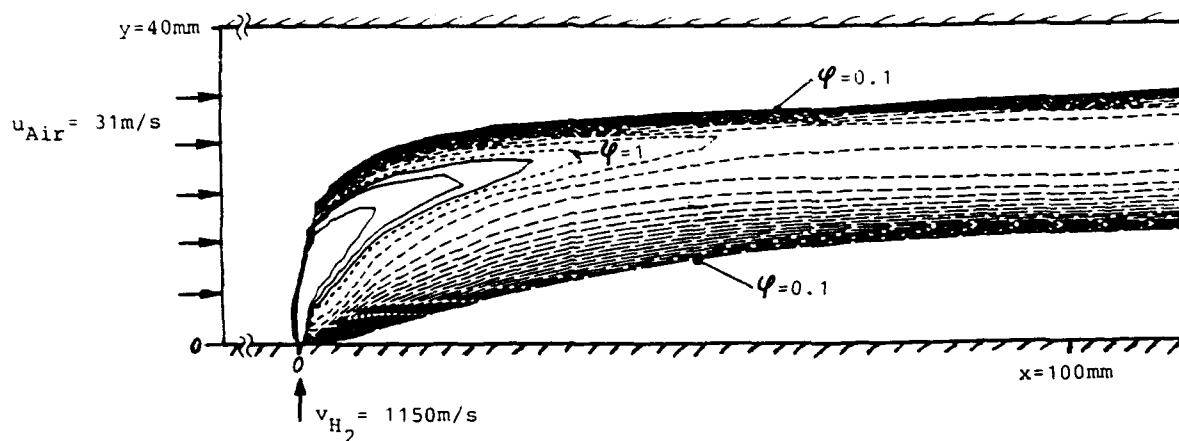


Fig. 10 Crossflow jet: Computed isolines of equivalence ratio ϕ at symmetry plane $z=0$ (combusting flow)

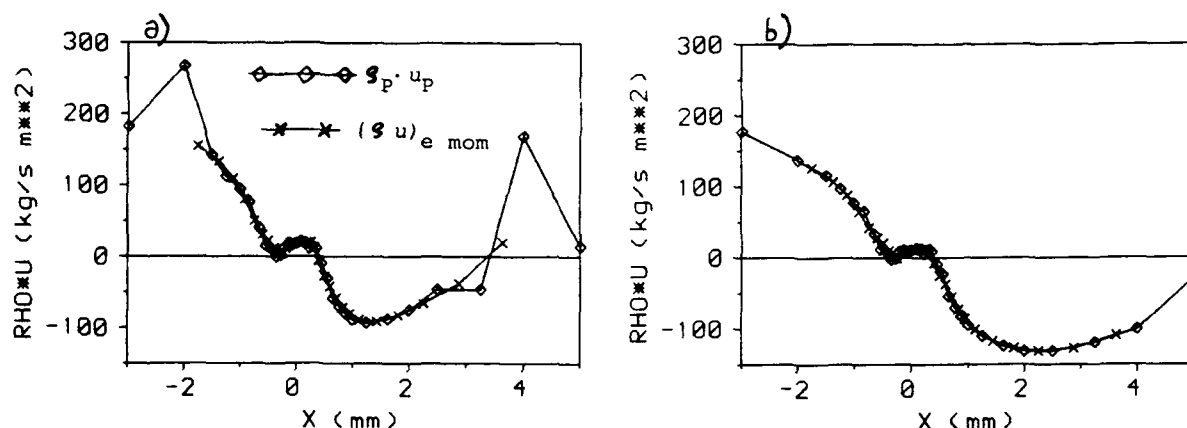


Fig. 11 Crossflow jet: Influence of the discretization of normal pressure gradient at zonal boundaries on the computed axial mass flux density of the fine grid at $y=1\text{mm}$, $z=0$ (combusting flow, pure MI: $\alpha=0$)
a) using δ_p at zonal boundaries
b) using δ_p at zonal boundaries

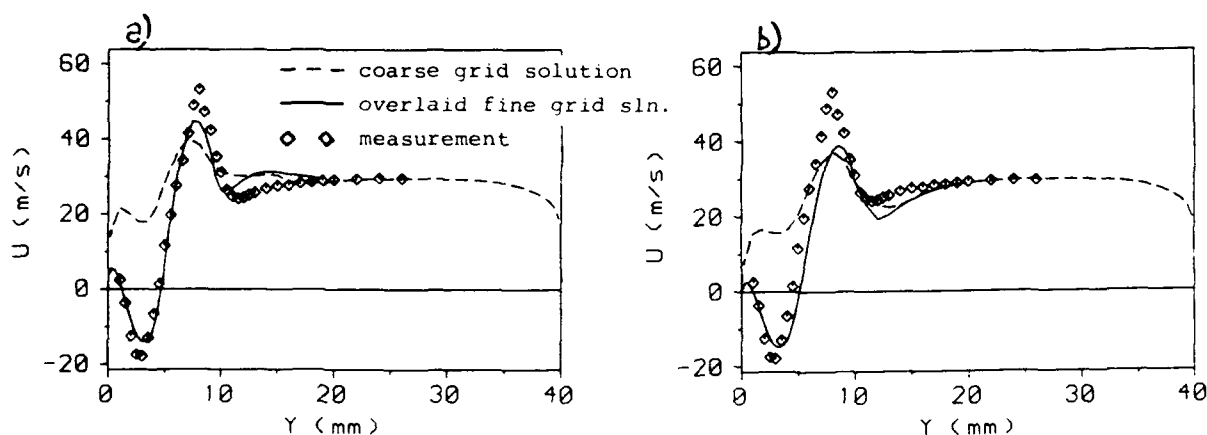


Fig. 12 Crossflow jet: Comparison of computed axial velocity profiles with LDA measurement at $x=2\text{mm}$, $z=0$ (isothermal air-in-air flow, $0.5 \leq \phi \leq 0.9$ from a local scheme)
a) nonconservative zonal coupling mode
b) locally mass conservative zonal coupling mode

Discussion

P. COELHO, INST. SUPERIOR TECNICO, PORTUGAL

1) You have defined overshooting in an unusual way. Considering, for example, cell face e , overshooting is generally considered to occur if $u_e > \max(u_E, u_F)$ whereas you defined overshooting as $u_e - 0.5(u_E + u_F)$ for a uniform grid. According to your definition overshooting or undershooting will always occur if momentum interpolation is used, unless the pressure gradient is zero. This overshooting in the sense you have defined, is necessary in order to ensure pressure-velocity coupling. Why did you choose this definition for overshooting?

2) In Fig. 4 of your paper the overlapping region has about five rows of overlapping, whereas only one or two are usually considered. Which criteria did you use to choose the number of overlapping rows?

AUTHOR'S REPLY

1) I agree that an i.g. nonvanishing overshoot B of cell face normal fluxes is the measure of the momentum interpolation to avoid PVD. In the limiting case of a fine grid, momentum interpolation and linear interpolation become identical. Then no overshooting problems occur. So it is reasonable to define B in a way, that it vanishes in this limit. This is fulfilled by the definition Eq. (25). Moreover this definition is convenient for analysis. I want to mention in that context of your question, that I observed distorted velocity profiles due to strong overshoots already in situations, where the cell face mass flux was still bounded in the sense, that its value lay between the flux values at the neighbored nodal points. Such a case can be seen in Fig. 11(a).

2) Overlap looks greater in Fig. 4 than it actually is, but those velocity vector profiles on a receiver grid, which were obtained from interpolation from the respective receiver grid must be disregarded in order to count the number of overlap cells from Fig. 4. Experience with a 2d, laminar driven cavity showed, that an overlap of only one cell gave slower convergence than with 3 or 5 cells in that case. From that it was decided, to choose an overlap of 3 cells for coupling subgrid 2 and 3, and an overlap of two cells for coupling subgrid 1 and 2 (see p. 37-8 in the swirl nozzle flow case).

C. HAH, NASA LEWIS, U.S.A.

Have you tried any convergence acceleration technique?

AUTHOR'S REPLY

No multigrid technique was employed to accelerate convergence.

F. LACAS, CNRS, FRANCE

In the case of reactive flows, what kind of approach are you using in regard of turbulent combustion modeling?

AUTHOR'S REPLY

The combustng hydrogen-air-crossflow jet of Fig. 10 was computed employing a global one-step-reaction, where reaction rate was assumed to be only turbulence controlled (Eddy-Break-Up model used).





MODELLING THE VAPORISER AND PRIMARY ZONE FLOWS FOR A MODERN
GAS TURBINE COMBUSTION CHAMBER

N R Bond
J M Le Vallois
K R Menzies

Combustion Technology Department
Rolls-Royce plc
Filton
Bristol BS12 7QE
United Kingdom

92-16097



ABSTRACT

A three-dimensional curvilinear finite-volume CFD code has been applied to aid understanding of the mechanisms leading to observed baseplate temperature patterns on a modern vaporiser combustion chamber. This code calculates recirculating, turbulent, combusting flows with a $k-\epsilon$ turbulence model and a conserved scalar / local chemical equilibrium combustion model. Predictions were obtained for both the vaporiser internal flows and for the complete flametube; the latter used the predicted vaporiser exit flow patterns as boundary conditions. The vaporiser flow models displayed a sensitivity to the fuel injector location which was subsequently confirmed by water analogy experiments. In conjunction with the flametube calculations, the effect of injector geometry and location on the primary zone flow patterns and temperatures were assessed, explaining the experimental results. The computational studies suggested a modified fuel injector geometry to reduce sensitivity and improve fuel distribution, which was validated by subsequent experiments in the full combustor.

INTRODUCTION

The role of computational methods in the design and development of gas turbine combustors has become more pronounced in recent years due to influences from a number of sources. From a computational viewpoint, the availability of more powerful computer hardware has enabled the routine calculation of complex flowfields with a predictive capability improved through the use of more accurate numerical schemes and physical models. In addition, the pressures to design combustion chambers exhibiting, for example, improved durability and reduced pollutant emissions, has made the task of the combustion engineer more challenging, necessitating

a move away from the traditional 'cut and try' approach or the use of empirical correlations based on a database of previous results, as described in [1]. In consequence, advanced computational fluid dynamics (CFD) techniques are now an essential tool for use in the design and development processes.

This paper describes one recent application of CFD within Rolls-Royce plc to the diagnosis and elimination of a particular integrity problem on a research combustor. The modelling approach is described with particular emphasis on the representation of the fuel injector system. Results are presented both for the initial problem diagnosis and a potential cure found through modelling. These results are compared with available data from experiments.

THE GAS TURBINE COMBUSTION
CHAMBER

The function of the gas turbine combustion chamber is to provide the power input for the engine by means of the high pressure and high temperature oxidation of fuel. Due to the arduous operating conditions and the stringent requirements of, for example, durability, low pollutant emissions and good stability, combustion chamber design has become ever more complex.

The particular combustor geometry studied here is shown in Figure 1 and can be classified as an annular vaporiser combustor ([2]). The vaporiser concept is employed with a single skin combustor head, 'dump' diffuser and rear mounting arrangement as shown, to produce a short, lightweight unit. The combustor head is cooled by the main diffuser flow, thanks to the single skin arrangement, while the vaporiser is cooled by its internal flows.

Given the hostile operating environment, it proves difficult to obtain measurements of conditions inside the combustor. The best that can usually be achieved is the measurement of the exit temperature distribution ('pattern factor'), combustor exit emissions and wall temperatures, often from temperature sensitive paints. This information is supplemented with cold flow studies, for example on water analogy rigs. However, these cannot mimic the large fluid volumetric expansion associated with combustion. Experimental studies have also been carried out to investigate the internal flows and efflux for the vaporiser fuel injector ([3], [4]).

As a consequence of this difficulty in obtaining measurements at the conditions of interest, the potential for the use of CFD is very large which is a great incentive to the production of robust, validated codes which can produce accurate and meaningful simulations in a wide variety of geometries and operating conditions.

MODELLING APPROACH FOR GAS TURBINE COMBUSTORS

The flow in a modern gas turbine combustion chamber is characterised as being three dimensional, turbulent, recirculating, variable density and enclosed in a geometrically complex domain. All of these features must be reflected in the equations solved and the coordinate system chosen.

The task of calculating a three dimensional, turbulent, chemically reacting flow poses a number of problems. For practical flows, the instantaneous Navier-Stokes equations cannot be solved directly and so some form of averaging must be used. For constant density flows, conventional Reynolds averaging is sufficient, where a quantity ϕ is decomposed as $\phi = \bar{\phi} + \phi'$, where $\bar{\phi}$ is the (time averaged) mean value and ϕ' is the fluctuating component. In the case of a variable density flow, it is more convenient to use Favre (density-weighted) averaging, where the quantity ϕ is decomposed as $\phi = \bar{\phi} + \phi''$. The resulting mean flow equations may be calculated with the aid of closure models which, for a reacting flow, take three forms: turbulence closure, a chemical closure model and a model

describing the interaction of turbulence with combustion. The flow in a gas turbine combustion chamber is predominantly pressure driven and so the standard high Reynolds number k- ϵ model [5] is generally sufficient to provide turbulence closure. The job of describing the turbulent combustion process is somewhat more problematic; a review of some possible approaches is given in [6].

In the case of a practical gas turbine combustor, the combustion problem involves the high temperature and high pressure oxidation of a complex hydrocarbon mixture fuel, typically kerosene. A detailed description of this process involves a large number of steps, many of which are not well known, with unknown reaction rates. If, however, we make the simplifying assumption that the chemical kinetic times are very much shorter than turbulent mixing and residence times then we may suppose that the reactions will proceed to equilibrium. If we further assume that all components of the fuel have equal diffusivities then fuel transport may be described by specifying the values of a conserved scalar, the fuel fraction f . The density may be related to the fuel fraction through an equilibrium relationship. In the case of a turbulent flame, the equilibrium state will be subjected to fluctuations and so, due to the nonlinearity of the density - fuel fraction relationship, the mean density is not obtained from the mean fuel fraction. To incorporate the effects of these fluctuations, a probability density function (pdf) approach is used to describe the variation of fuel fraction; see [6]. Here, the pdf is assumed to be a Beta function of f and its Favre-averaged variation \bar{f}''^2 . This leads to a further equation to be solved for the variance of f .

As a consequence of this modelling, the equations to be solved may be written (using general tensor notation) as specified in Table 1. The constants for the k- ϵ model are taken as standard ([5]): $C_\mu = 0.09$, $C_{\epsilon 1} = 1.44$, $C_{\epsilon 2} = 1.92$

This equation set is closed by the prescription of the mean density ρ as:

$$\bar{\rho} = \left(\int_0^1 \frac{p(f, x_i)}{\rho(f)} df \right)^{-1}$$

where p is the Beta function pdf of f and \bar{f}''^2 . A more complete discussion of these equations is to be found in [7] and [8].

As noted above, the geometry of a modern gas turbine combustion chamber is quite complex, see Figure 1 for example. This naturally affects the choice of coordinate system for the solution of the above governing equations. Here, an orthogonal curvilinear coordinate system was used for the two-dimensional (x,y) plane, with the angular dimension being accounted for as a body of revolution, as described in [7] and [8]. This approach is a reasonable compromise between the simple cartesian grid which lacks flexibility and makes the imposition of boundary conditions difficult, and the general nonorthogonal grid, transformation to which introduces a large number of extra terms in the equations to be solved. By using a curvilinear orthogonal system, no cross derivative terms appear in the transformation tensor, thus limiting the extra work incurred. The orthogonal transformation is obtained by the application of Schwarz - Christoffel mappings as described in [8].

Given the orthogonal coordinate system, the governing equations are discretised on a staggered grid arrangement with either Hybrid or QUICK differencing [7] for convection approximation. The equations are usually solved in steady state form using the SIMPLE algorithm [9] for pressure-velocity coupling. This derives an equation for the pressure correction based on the momentum and continuity equations to overcome the lack of any obvious pressure equation in the set to be solved. This algorithm is of the predictor - corrector type and solves the momentum, pressure correction and scalar equations in a sequential iteration process. The linear equations arising at each stage can be solved by, for example, the Tri-Diagonal Matrix Algorithm. The iteration process is judged to be converged when both residual errors for each equation and the continuity imbalances are less than some particular value.

CALCULATIONS AND EXPERIMENTAL VERIFICATION

The calculations reported here were initiated following experimental testing of the research combustor in Figure 1 displayed excessive head ~~over~~heating as shown from the thermal paint result in Figure 2. An initial model of a sector of the flametube was set up as shown in Figure 3. The vaporiser was defined as blockages in the flow domain as shown with a flat exit profile for both fuel and air. The resulting flowfield is shown in Figure 4 with the near wall gas temperatures shown in Figure 5. It is clear that this prediction shows a reasonable temperature distribution with the areas of concern being upstream of the shoulder cooling rings.

This solution represents the case where the vaporiser efflux is perfectly mixed. This boundary condition is likely to have a strong influence on the primary zone flowfield, so to check the correctness of this assumption and also to further investigate the behaviour of the vaporiser, it was decided to model the flows internal to the vaporiser unit.

The vaporiser geometry with its fuel injector is shown in Figure 6. Note that the injector is free to move within the vaporiser as the combustor expands. The corresponding computational domain is shown in Figure 7. It contains over 190000 nodes in order to give adequate resolution of the geometry.

In modelling the vaporiser flows, both fuel and air flows must be considered. To model the liquid fuel completely would require consideration of the complex ligament breakup and droplet coalescence processes in addition to evaporation and droplet trajectories. In this case, however, it was felt appropriate to simply model the fuel as a dense gas. Subsequent comparison with experimental results indicated that this simplified approach was still able to capture the essential details of the vaporiser flows. Since combustion does not occur within the vaporiser, density changes occur through mixing only.

The datum flowfield and fuel distributions are shown in Figure 8, which yield an airflow split between the two arms of 49.9% / 50.1% and a fuel flow split of 49.4% / 50.6%. Of particular note is the wake downstream of the injector head. Thus the vaporiser flows in this configuration are shown to be essentially symmetrical, although the exit profiles are not flat.

These profiles were then transferred as boundary conditions to the flametube solution.

The near wall gas temperatures from the revised flametube solution are shown in Figure 9, displaying a generally hotter combustor head. Note that the external aerodynamics for both solutions would be the same, so the increased gas temperatures near the walls would result in increased metal temperatures. However, the combustor distress observed experimentally implies that there is a further mechanism influencing the flowfield and gas temperatures which is not being modelled here. It was therefore decided to investigate possible mechanisms for fuel maldistribution in the vaporiser flows.

A possible cause of maldistribution in the vaporiser flows which was investigated was a sensitivity to the fuel injector location on the fuel and air flow splits. The vaporiser calculation was repeated with the fuel injector head offset so that it was in contact with the vaporiser stem. The resulting flowfield and fuel concentrations are shown in Figure 10. It can clearly be seen that the fuel flow is now heavily biased in the direction of the injector offset, with significant fuel entrainment in the recirculation formed in the wake of the injector head. The predicted airflow splits have not changed significantly, being 47.9% / 52.1%, but the fuel flow split is now 25.9% / 74.1%.

To model the effect of this fuel distribution on the primary zone flows, a model of a complete vaporiser sector of the flametube was set up (compared with the symmetric half segments modelled before), utilising the biased vaporiser flows as boundary conditions. The results are shown in Figures 11 and 12. Although the primary zone flow patterns have not changed significantly between the rich and weaker halves of the solution, the near wall gas temperatures correctly predict the single sided head overheat observed in experiments (as in Figure 2).

The prediction of the head overheat pattern could be seen in itself as sufficient validation of the modelling effort, but in order to effect a remedy to the problem, it was necessary to check that the vaporiser flows really were as dependent on injector location as the model suggested. Consequently, cold flow measurements were performed on an airflow rig using water in

place of fuel to check the fuel flow split for various injector positions. A sample of results from this study are shown in Figure 13. For the maximum injector displacement case (corresponding to that modelled), the measured fuel splits were 23.2% / 76.8%. Thus, despite the assumptions adopted in the vaporiser modelling, the sensitivity of this particular geometry to injector location had been correctly predicted. This obviously gave confidence that similar techniques could be used to remedy the problem.

The initial calculations for the whole combustor, shown in Figures 4 and 5, illustrate an acceptable temperature distribution over much of the combustor head with a well mixed vaporiser efflux. In addition, the vaporiser internal flow calculations had shown fuel entrainment in the wake of the bluff injector head. Consequently, it was decided to attempt to reduce this wake effect and assess the sensitivity of the resulting geometry. From a variety of options modelled, the most promising avenue for reducing the wake was to switch to a bifurcated head injector (Figure 14). This was modelled in the same manner as the previous vaporiser geometries, giving results such as Figures 15 and 16. The predicted airflow split for the offset bifurcated injector was 49.3% / 50.7%, with a fuel split of 44.0% / 56.0%. Measurements confirmed the greatly reduced sensitivity of this geometry, with a measured fuel split of 38% / 62%. On the strength of these predictions and their experimental validation, this injector geometry was specified for full rig testing where it did indeed yield a more acceptable combustor head temperature distribution.

CONCLUSIONS

A modelling approach for three dimensional, turbulent, recirculating, combustor flows has been outlined and its application to the calculation of flows in a gas turbine combustion chamber and vaporiser fuel injector unit have been shown. The ability of the method to illustrate the sensitivity of the vaporiser flow splits to injector location has been demonstrated and compared with available experimental data for the same geometry. Incorporating the predicted vaporiser efflux profiles as boundary conditions, full combustor models were able to predict head temperature

patterns which agreed with, and explained mechanisms for, experimentally observed temperature distributions. The vaporiser modelling was able to indicate a modified fuel injector geometry to reduce the sensitivity of the system which was subsequently validated by experiment. The calculations have also demonstrated the ability of CFD methods to produce meaningful and useful data in areas where experimental access may be very limited.

These results illustrate that, while much work remains to be done in improving the methodologies and physical models used for prediction of turbulent reacting flows, the techniques outlined here have reached a sufficient state of maturity to be used with confidence in the design and development stages for gas turbine combustors to supplement and direct experimental testing.

ACKNOWLEDGEMENTS

The authors would like to thank their colleagues in the Combustion Department, Rolls Royce plc, who have contributed to the work presented here. They would also like to thank Rolls Royce plc and the Ministry of Defence for permission to publish this paper.

REFERENCES

1. Lefebvre A H : 'Gas Turbine Combustion', Hemisphere (1983)
2. Sotheran A : 'The Rolls-Royce Annular Vaporizer Combustor', ASME-83-GT-49, 28th International Gas Turbine Conference and Exhibit, Phoenix, Az (1983)
3. Jasuja A K : 'Vaporiser Research Studies', Internal Report, Cranfield Institute of Technology (1982)
4. Low H C : 'Recent Research on the Efflux of the Rolls-Royce Vaporiser Fuel Injector', AGARD-CP-353 (Combustion Problems in Turbine Engines) (1983)
5. Launder B E and D B Spalding : 'The Numerical Computation of Turbulent Flows', Comp Meth Appl Mech Eng vol 3, pp269-289 (1974)
6. Priddin C H 'Turbulent Combustion Modelling, A Review', presented at 3rd European Turbulence Conference, Stockholm (1990)
7. Coupland J and C H Priddin : 'Modelling the Flow and Combustion in a Production Gas Turbine Combustor', Proceedings, Turbulent Shear Flows 5, Springer-Verlag (1987)
8. Manners A P : 'The Calculation of Flows in Gas Turbine Combustion Systems', Ph.D Thesis, University of London (1988)
9. Patankar S V and D B Spalding : 'A Calculation Procedure for Heat, Mass and Momentum Transfer in Three-Dimensional Parabolic Flows', Int J Heat Mass Transfer, vol 15, pp1718-1806 (1972)

TABLE 1 : GOVERNING EQUATIONS SOLVED

For a three-dimensional, turbulent, combusting flow the equations to be solved may be written as :

$$\frac{\partial \bar{\rho}}{\partial t} + \frac{\partial \bar{\rho} \tilde{U}_i}{\partial x_i} = 0 \quad (\text{continuity})$$

$$\begin{aligned} \frac{\partial \bar{\rho} \tilde{U}_i}{\partial t} + \frac{\partial}{\partial x_j} (\bar{\rho} \tilde{U}_i \tilde{U}_j) = & - \frac{\partial \bar{p}}{\partial x_i} + \frac{\partial}{\partial x_j} \left((\mu + \mu_t) \left(\frac{\partial \tilde{U}_i}{\partial x_j} + \frac{\partial \tilde{U}_j}{\partial x_i} \right) \right. \\ & \left. - \frac{2}{3} \mu_t \delta_{ij} \frac{\partial \tilde{U}_l}{\partial x_l} - \frac{2}{3} \delta_{ij} \bar{\rho} \tilde{k} \right) \end{aligned}$$

(momentum)

(i, j = 1, 2, 3)

This equation set is closed by the inclusion of :

$$\frac{\partial (\bar{\rho} \tilde{k})}{\partial t} + \frac{\partial (\bar{\rho} \tilde{U}_i \tilde{k})}{\partial x_i} = \frac{\partial}{\partial x_i} \left(\Gamma \frac{\partial \tilde{k}}{\partial x_i} \right) + P - \bar{\rho} \tilde{\epsilon}$$

(turbulent kinetic energy)

$$\frac{\partial (\bar{\rho} \tilde{\epsilon})}{\partial t} + \frac{\partial (\bar{\rho} \tilde{U}_i \tilde{\epsilon})}{\partial x_i} = \frac{\partial}{\partial x_i} \left(\Gamma \frac{\partial \tilde{\epsilon}}{\partial x_i} \right) + \frac{\tilde{\epsilon}}{K} (C_{\epsilon 1} P - C_{\epsilon 2} \bar{\rho} \tilde{\epsilon})$$

(dissipation of k)

$$\frac{\partial (\bar{\rho} \tilde{f})}{\partial t} + \frac{\partial (\bar{\rho} \tilde{U}_i \tilde{f})}{\partial x_i} = \frac{\partial}{\partial x_i} \left(\frac{\mu}{\sigma_t} \frac{\partial \tilde{f}}{\partial x_i} \right)$$

(fuel fraction)

$$\frac{\partial (\bar{\rho} \tilde{f}''^2)}{\partial t} + \frac{\partial (\bar{\rho} \tilde{U}_i \tilde{f}''^2)}{\partial x_i} = \frac{\partial}{\partial x_i} \left(\frac{\mu}{\sigma_t} \frac{\partial \tilde{f}''^2}{\partial x_i} \right) + 2 \bar{\rho} \frac{\mu_t}{\sigma_t} \frac{\partial \tilde{f}}{\partial x_i} \frac{\partial \tilde{f}}{\partial x_i} - 2 \bar{\rho} \tilde{\epsilon} \frac{\tilde{f}''^2}{K}$$

(fuel fraction variance)

where

$$P = \mu_t \left(\frac{\partial \tilde{U}_i}{\partial x_j} + \frac{\partial \tilde{U}_j}{\partial x_i} \right) \frac{\partial \tilde{U}_i}{\partial x_j} \quad : \quad \text{production of turbulent kinetic energy}$$

$$\Gamma = \frac{\mu_t}{\sigma_t} + \frac{\mu}{\sigma} \quad : \quad \text{diffusion coefficient}$$

$$\mu_t = C_\mu \bar{\rho} \tilde{k}^2 / \tilde{\epsilon} \quad : \quad \text{'turbulent' viscosity}$$

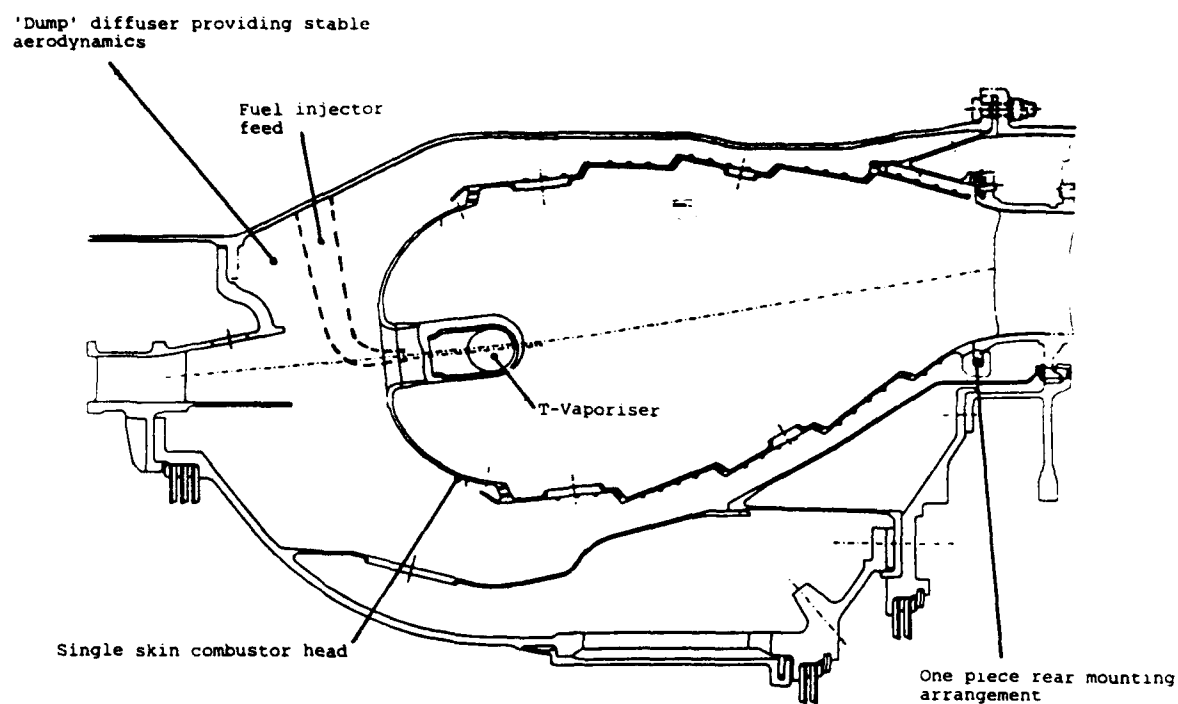


FIGURE 1 : VAPORISER COMBUSTOR GEOMETRY

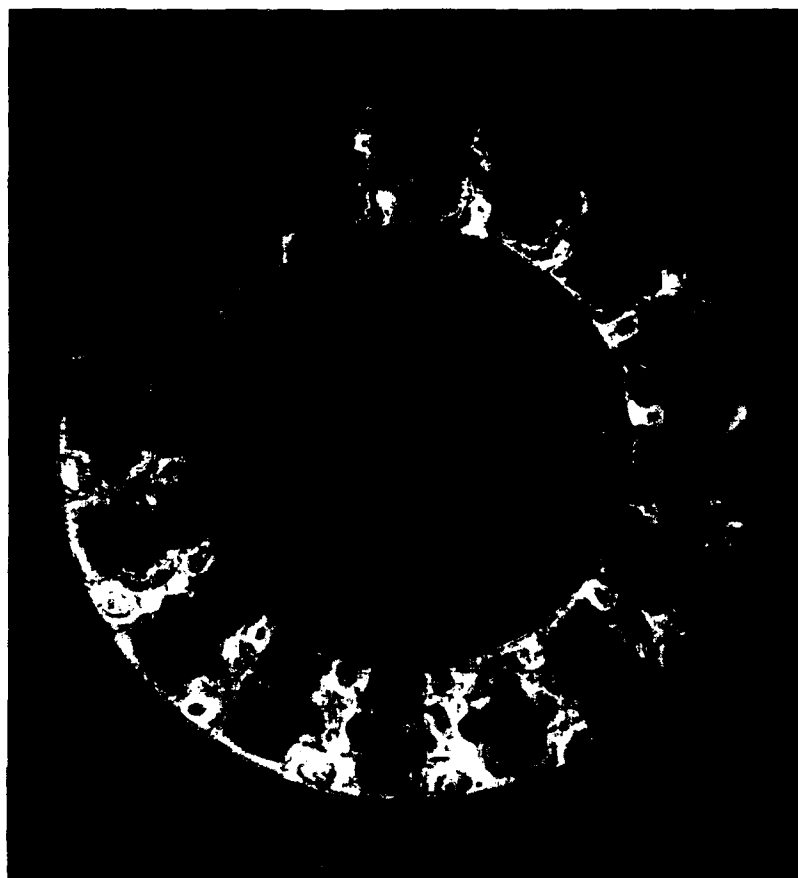


FIGURE 2 : COMBUSTOR HEAD TEMPERATURES FROM THERMAL PAINTS

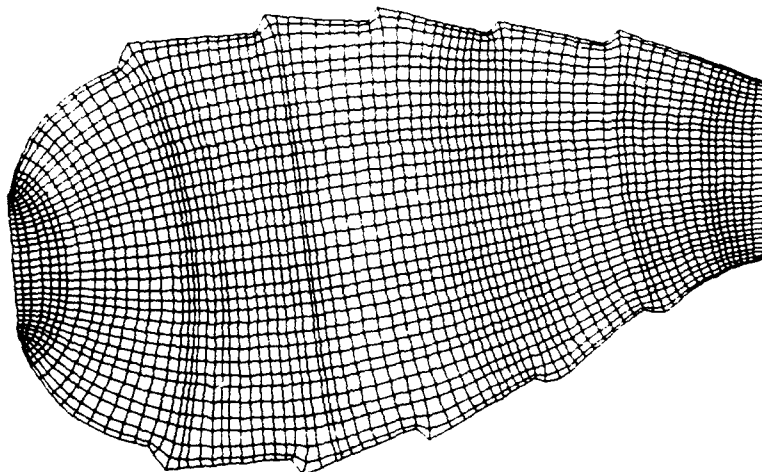


FIGURE 3 : MODELLED GEOMETRY AND GRID

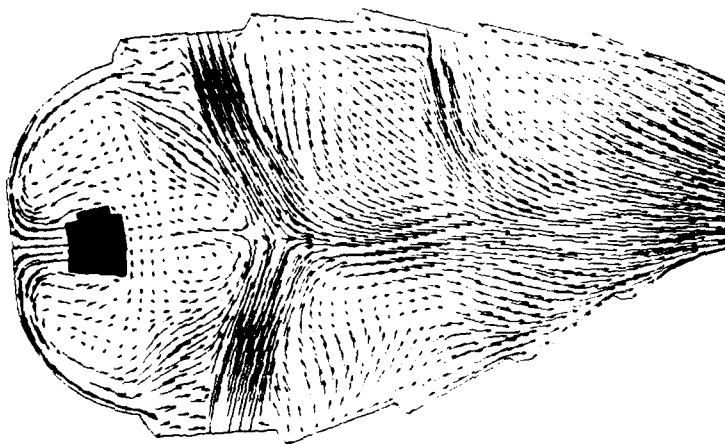


FIGURE 4 : DATUM SOLUTION, FLOW STREAKLINES

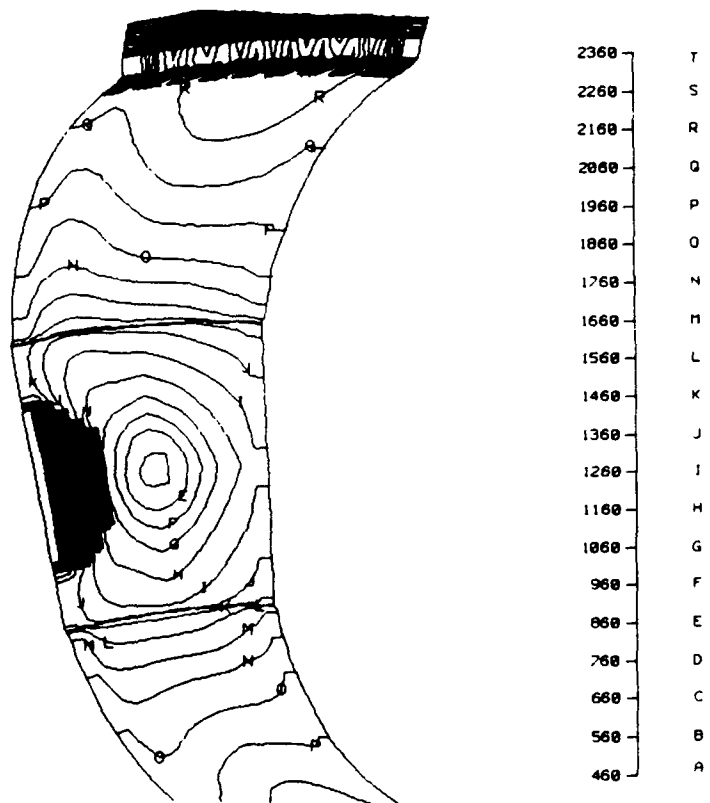


FIGURE 5 : DATUM SOLUTION, GAS TEMPERATURES AT HEAD OF COMBUSTOR

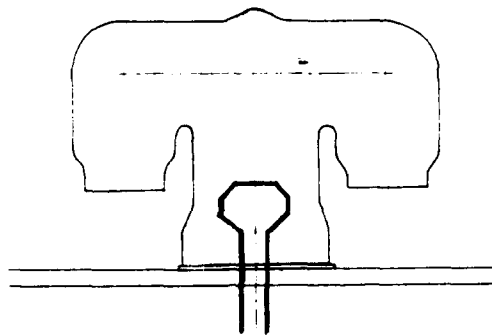


FIGURE 6 : GEOMETRY OF T-VAPORISER WITH STANDARD FUEL INJECTOR

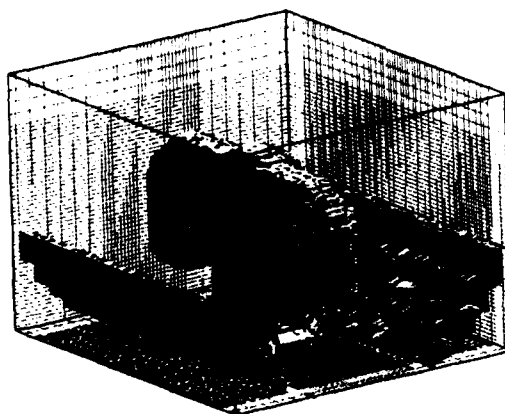
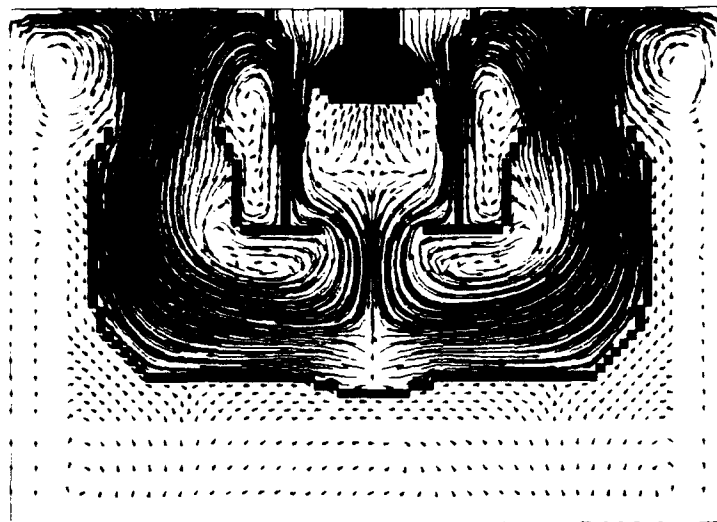
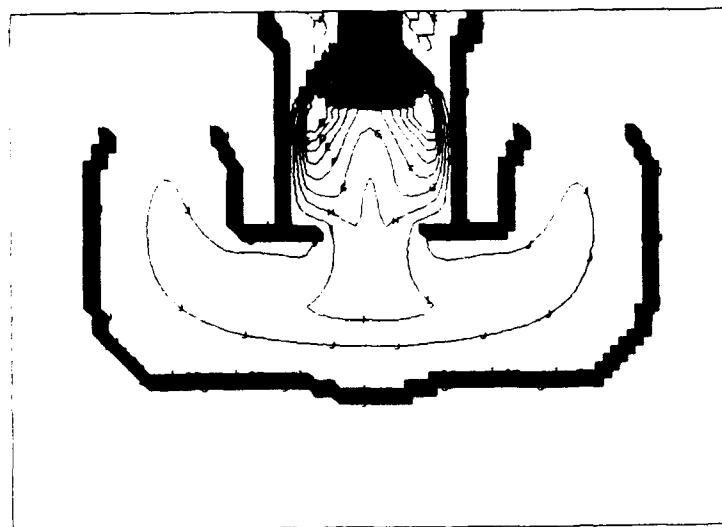


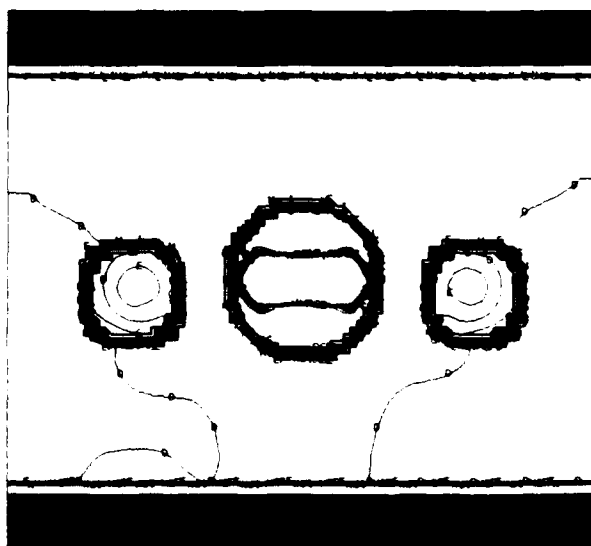
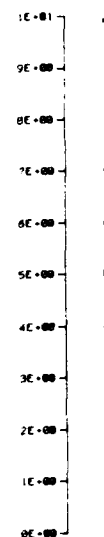
FIGURE 7 : MODELLING OF VAPORISER, GRID AND GEOMETRY REPRESENTATION



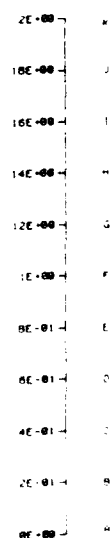
(a) Flow streamlines



(b) Fuel concentrations on plane through injector centreline



(c) Fuel concentrations on plane through vaporiser exits

**FIGURE 8 : DATUM SOLUTION, FLOWFIELD AND FUEL CONCENTRATION**

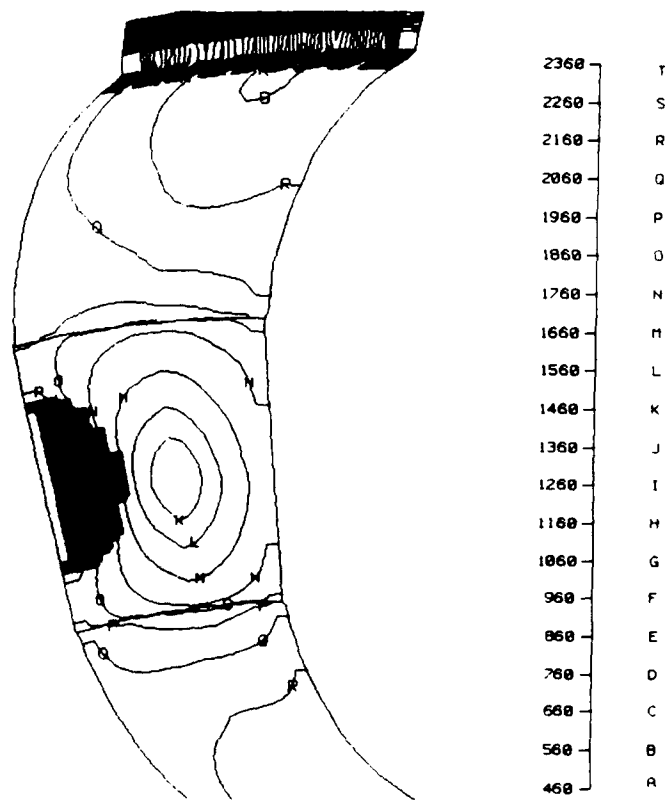
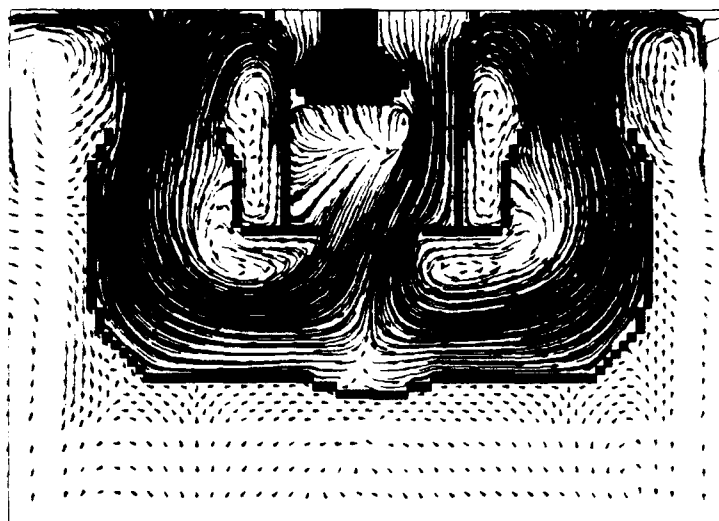
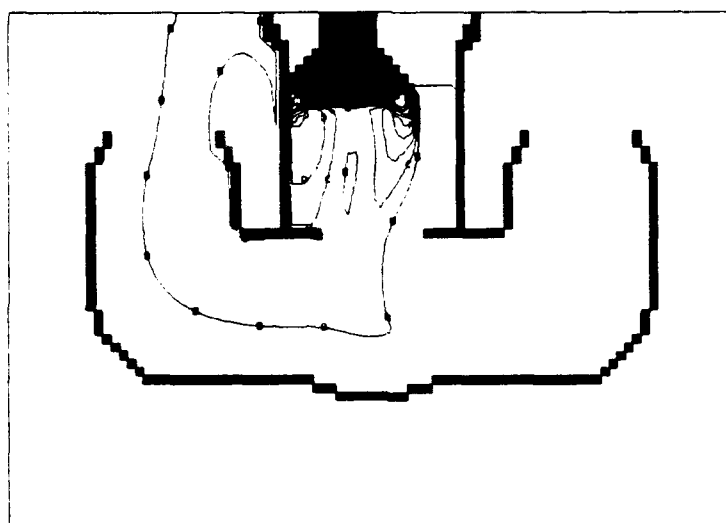


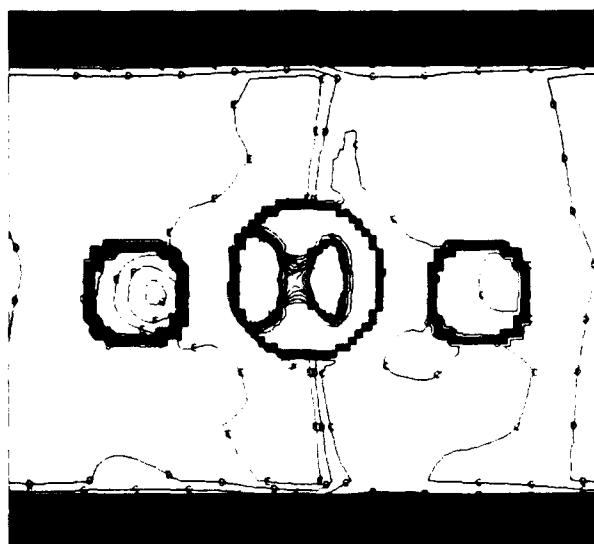
FIGURE 9 : NEAR WALL TEMPERATURES FOR FLAMETUBE SOLUTION WITH
PROFILED VAPORISER BOUNDARY CONDITION



(a) Flow streaklines

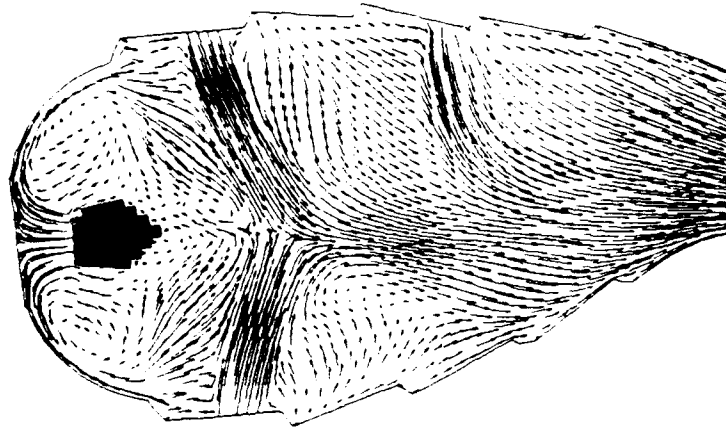


(b) Fuel concentrations on plane through injector centreline

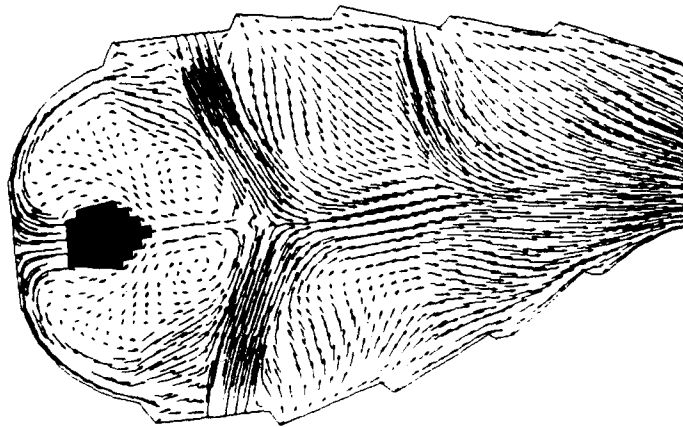


(c) Fuel concentrations on plane through vaporiser exits

FIGURE 10 : OFFSET INJECTOR SOLUTION, FLOWFIELD AND FUEL CONCENTRATION



(a) Plane through weak vaporiser outlet



(b) Plane through richer vaporiser outlet

FIGURE 11 : FLOWFIELD FOR FLAMETUBE SOLUTION WITH OFFSET INJECTOR
VAPORISER BOUNDARY CONDITION

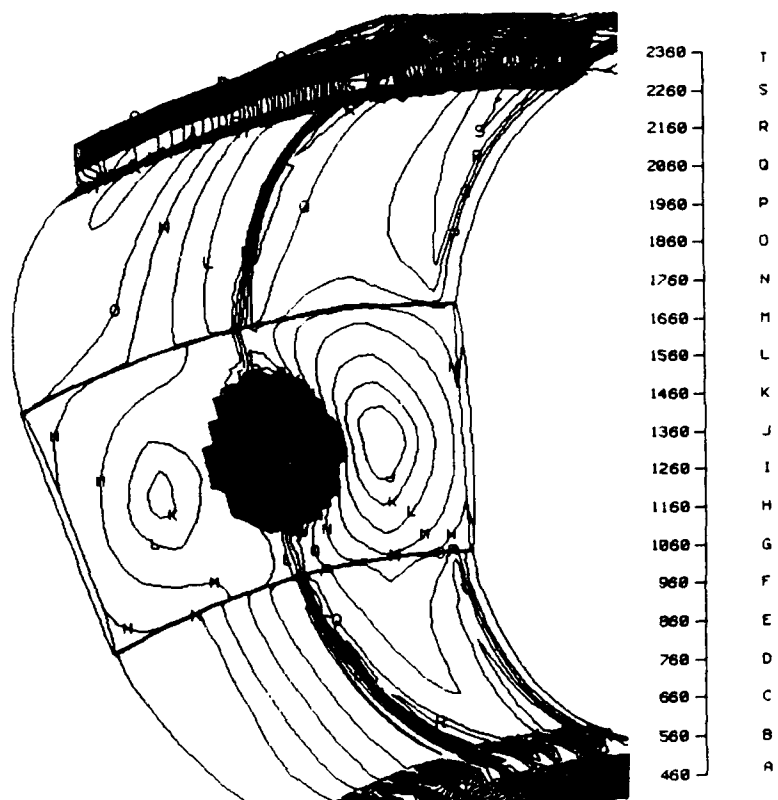


**FIGURE 12 : NEAR WALL GAS TEMPERATURES FOR FLAMETUBE SOLUTION
WITH OFFSET INJECTOR VAPORISER BOUNDARY CONDITION**

Flow Proportion

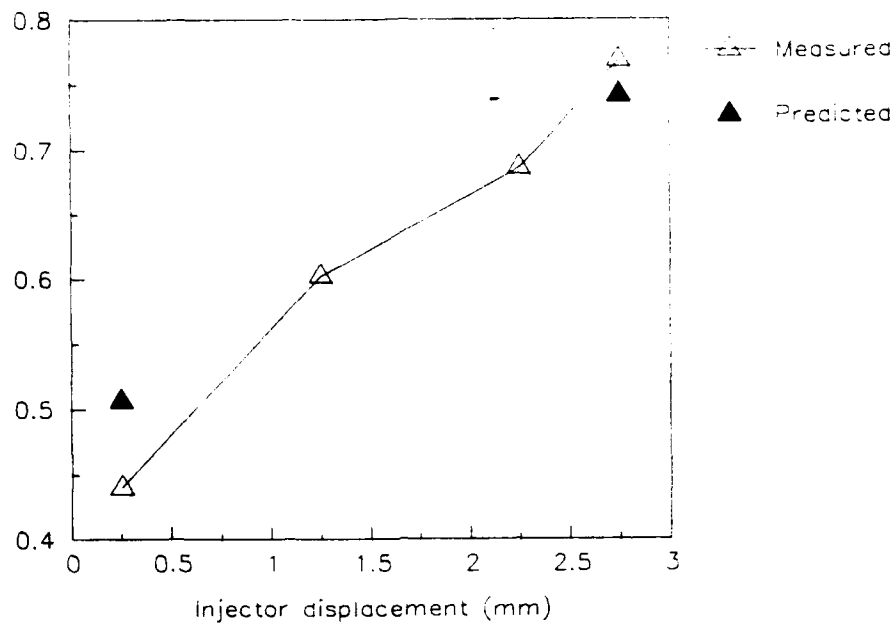


FIGURE 13 : EXPERIMENTAL MEASUREMENTS OF DEPENDENCE OF FUEL FLOW SPLIT ON INJECTOR OFFSET

The injector was displaced from the central position and the proportion of the total fuel flow (represented by water) passing through the arm in the direction of the offset was measured.

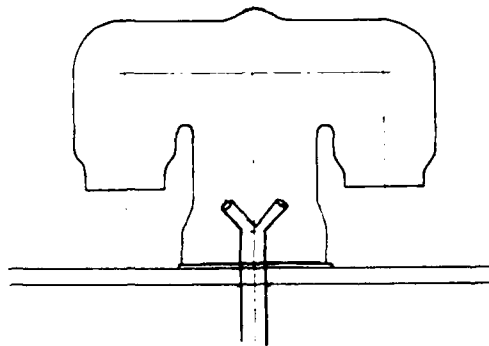
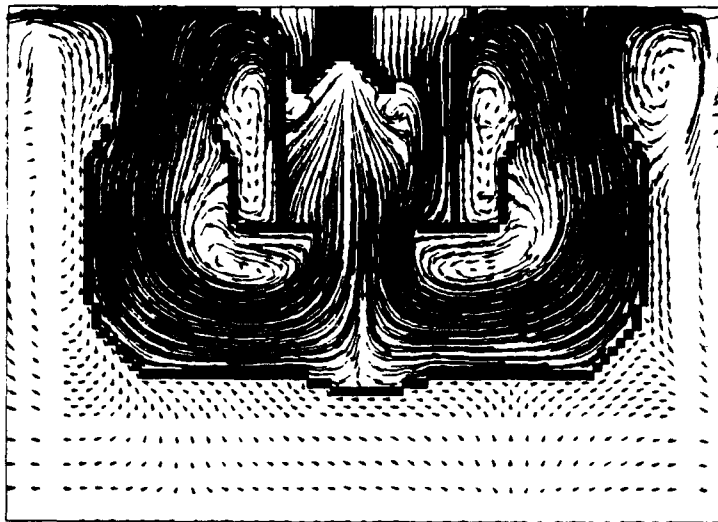
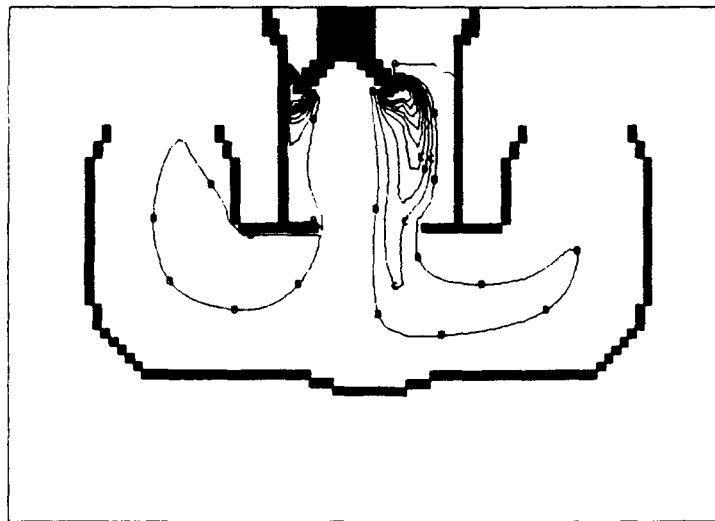


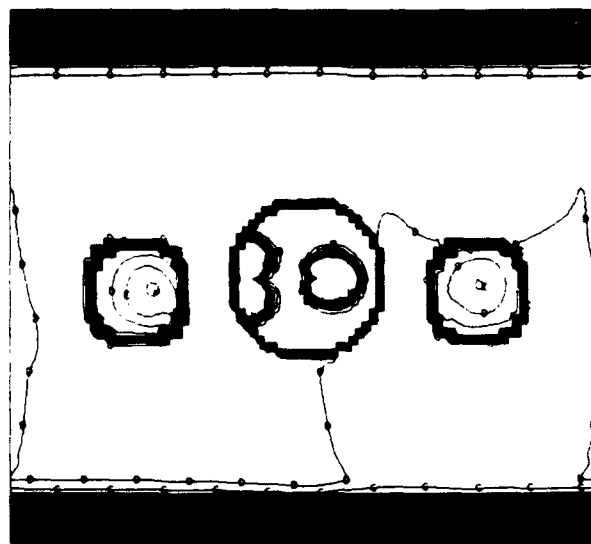
FIGURE 14 : VAPORISER WITH BIFURCATED HEAD FUEL INJECTOR



(a) Flow streaklines



(b) Fuel concentrations on plane through injector centreline



(c) Fuel concentrations on plane through vaporiser exits

FIGURE 15 : OFFSET BIFURCATED HEAD INJECTOR SOLUTION, FLOWFIELD AND FUEL CONCENTRATION

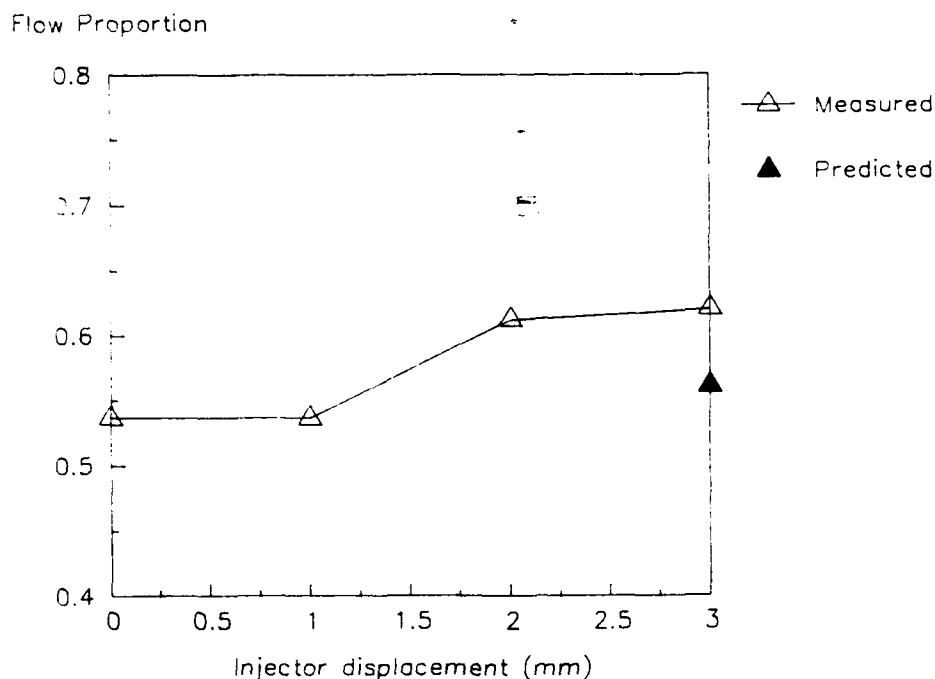


FIGURE 16 : EXPERIMENTAL MEASUREMENTS OF DEPENDENCE OF FUEL FLOW SPLIT ON INJECTOR OFFSET : BIFURCATED HEAD INJECTOR

Experimental technique as for Figure 13.

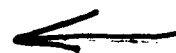
Discussion

R. WALTHER, MTU, GERMANY

- 1) Can you comment on the physical background which leads to the better full concentration distribution at the vaporizer exits gained by the bifurcated head injector?
- 2) Is there any potential for self-ignition of the fuel-air mixture within the vaporizer tubes and if yes have you ever tried to simulate it?

AUTHOR'S REPLY

- 1) The original injector had a bluff head which tended to promote recirculation and entrainment with a consequent redistribution of the fuel at the operating conditions being considered. The modified head reduced this tendency for fuel entrainment at its base.
- 2) It is not the intention that combustion should take place within the vaporizer and I am not sure what investigations have been carried out in this field. To some extent the vaporized tubes rely on full flow over their internal surfaces to act as a coolant.





APPLICATION OF MONTE CARLO SIMULATION FOR THREE-DIMENSIONAL FLOWS

M. Scheurlen, B. Noll, S. Wittig

Lehrstuhl und Institut für Thermische Strömungsmaschinen
Universität Karlsruhe
Kaiserstr. 12, D-7500 Karlsruhe
Federal Republic of Germany

92-17460



SUMMARY

A Monte Carlo technique is outlined for the simulation of the transport of a joint scalar probability density function (pdf). The discretisation of the partial differential equations is based on a finite-volume approximation. The problem of frozen solutions is addressed if the number of stochastic elements is limited. Non-adiabatic boundary conditions are discussed if the energy equation is solved by a Monte Carlo simulation.

The Monte Carlo simulation is compared with deterministic calculations and with an experiment in a three-dimensional non-isothermal non-reacting jet-mixing flow. The results of the simulation agree very well with the experiment and the deterministic calculations. However, the computer time and storage requirements for a three-dimensional simulation of the transport of a single scalar pdf increases dramatically in comparison to deterministic calculations. The results also indicate the need for a simulation procedure that is free of numerical diffusion.

LIST OF SYMBOLS

A_l	side area of the finite-volume ($l=e,w,n,s,h,l$)
$E(\psi)$	mixing term
k	turbulence kinetic energy
N	number of stochastic elements at each grid point
N_P	number of grid points
$p(\psi)$	joint pdf of ψ
h	enthalpy
Pr	Prandtl number
Sc	Schmidt number
T	temperature
t	time
u_i	velocity in x_i direction
u, v, w	velocity components
x_i	spatial coordinates ($i = 1, 2, 3$)
\underline{x}	spatial vector

greek symbols

Γ_t	turbulent diffusion coefficient
Δt	time increment
ΔV	finite-volume
δ	Dirac-delta function
ϵ	rate of dissipation of k
κ	constant of the wall function
μ	viscosity
ρ	density
σ	dimensionality of ψ -space
τ_P	characteristic time
τ_w	wall shear stress
$\underline{\psi}$	independent composition space
ω	turbulence frequency

superscripts

-	Favre averaging
-	time averaging
'	fluctuation

subscripts

0	inlet
j	jet
P	grid point
t	turbulent

1. INTRODUCTION

Determination of mean values of coupled nonlinear scalar variables in turbulent reacting flow requires the knowledge of a joint probability density function (pdf) of the variables involved in the problem. A deterministic solution of the transport equation of the joint pdf with large dimensionality seems impractical. Therefore, often a Monte Carlo technique is proposed for the simulation of the transport and the evolution of the joint pdf.

The advantage of this technique is that the computational work rises only linearly with the dimensionality of the pdf (Pope (1981)). In addition, no modelling is required to treat the chemical source term for reacting flows.

Contrary to simple test cases there is limited experience with the performance and the application of Monte Carlo methods for calculations of three-dimensional complex recirculating flows. A drawback, for instant, is the large storage requirement if three-dimensional elliptic flows are considered and one has to ask for the influences of practical storage limitations. An other problem is associated with the use of the upwind scheme to derive the finite difference equations for the Monte Carlo simulation. It is well known that this scheme suffers from numerical diffusion (cfe. Noll (1991)). To apply higher order differencing schemes to a Monte Carlo simulation of the transport of a joint pdf seems to be a formidable task.

In this paper, a Monte-Carlo technique is outlined for the simulation of the transport of a joint scalar pdf. Finite-volume equations are derived for use of the Monte Carlo simulation and the simulation process itself is described. An implementation of non-adiabatic boundary conditions is given and some numerical problems are discussed for practical applications. Finally, numerical calculations are compared with an experimental test case.

2. FINITE - VOLUME SCHEME

In this section a finite-volume difference scheme is outlined for the transport equation of the Favre averaged joint scalar pdf. The differential equation to start with is

taken from Pope (1979) where a complete derivation and description of this equation is given. Here, the transport equation is written in the following form:

$$\begin{aligned} & \frac{\partial}{\partial t} (\bar{\rho}(\underline{x}, t) \bar{p}(\underline{\psi}; \underline{x}, t)) + \frac{\partial}{\partial x_i} (\bar{\rho}(\underline{x}, t) \bar{p}(\underline{\psi}; \underline{x}, t) \bar{u}_i(\underline{x}, t)) \\ &= \frac{\partial}{\partial x_i} \left(\Gamma_i \frac{\partial \bar{p}(\underline{\psi}; \underline{x}, t)}{\partial x_i} \right) - \frac{\partial}{\partial \psi_\alpha} (\bar{\rho}(\underline{x}, t) \bar{p}(\underline{\psi}; \underline{x}, t) S_\alpha(\underline{\psi})) \\ & \quad + \bar{\rho}(\underline{x}, t) E(\underline{\psi}; \underline{x}, t). \end{aligned} \quad (1)$$

$\bar{p}(\underline{\psi}; \underline{x}, t)$ is the Favre averaged joint pdf of the σ scalars with the independent scalar space given by $\underline{\psi} = \psi_1 \dots \psi_\sigma$. The first three terms of Eq. (1) represent the change of \bar{p} in time and physical space whereas the last two terms on the right hand side describe the influence of reaction and molecular mixing in scalar space. It is of predominant importance that the chemical source term appears in closed form, thus, it does not require any model assumptions. In this equation molecular diffusion is neglected in comparison to turbulence exchange processes. In addition, for the simulation procedure equal diffusion coefficients have to be assumed for all σ scalar variables of the joint pdf.

A mathematical description of the mixing process is not straight forward, however, a model proposed by Curl (1963) proved to give qualitatively correct results and is applicable to multi dimensional pdf's (cfe. Pope (1979, 1981, 1982)). In addition, this mixing model can be very efficiently applied to Monte Carlo techniques. Curl's model yields:

$$E(\underline{\psi}; \underline{x}, t) = 2^\sigma \omega \int \bar{p}(\underline{\psi} + \underline{\psi}') \bar{p}(\underline{\psi} - \underline{\psi}') d\underline{\psi}' - \omega \bar{p}(\underline{\psi}). \quad (2)$$

The rate of mixing is directly proportional to a turbulence frequency ω . This frequency or time scale may be derived from the turbulent kinetic energy and its rate of dissipation if the turbulent flow field calculation is based on a k, ϵ -model.

For the derivation of the finite-volume transport equation the time derivative in Eq. (1) is replaced by a first order accurate forward difference scheme in time

$$\begin{aligned} & \frac{\partial}{\partial t} (\bar{\rho}(\underline{x}, t) \bar{p}(\underline{\psi}; \underline{x}, t)) = \\ & \frac{(\bar{\rho}(\underline{x}, t + \Delta t) \bar{p}(\underline{\psi}; \underline{x}, t + \Delta t)) - (\bar{\rho}(\underline{x}, t) \bar{p}(\underline{\psi}; \underline{x}, t))}{\Delta t} \end{aligned} \quad (3)$$

and subsequently the entire equation is integrated over a finite-volume ΔV . To perform the integration the volume integrals related to convection and diffusion are changed to surface integrals by means of Gauss' theorem. Integration and rearrangement yield:

$$\begin{aligned} \bar{p}_P(\underline{\psi}; t + \Delta t) &= \left(1 - \frac{\Delta t}{\tau_P}\right) \bar{p}_P(\underline{\psi}; t) + \sum_l \frac{\Delta t}{\tau_P} \frac{a_l}{a_P} \bar{p}_l(\underline{\psi}; t) \\ & \quad - \Delta t \frac{\partial}{\partial \psi_\alpha} (S_\alpha(\underline{\psi}) \bar{p}_P(\underline{\psi}; t)) + \Delta t E_P(\underline{\psi}; t) \end{aligned} \quad (4)$$

with $l = E, W, N, S, H, L$. The coefficients a_l describe

the transport by diffusion and convection into the finite-volume

$$\Delta V = \Delta x_P \Delta y_P \Delta z_P \quad (5)$$

which is located at the grid point P . The grid denotations and correspondences used are illustrated in Fig. 1. The coefficients of Eq. (4) are defined by:

$$a_E = \left(\frac{\Gamma_{t,e}}{\Delta x_e} + [[0, -(\bar{\rho}\bar{u})_e]] \right) A_e \quad (6a)$$

$$a_W = \left(\frac{\Gamma_{t,w}}{\Delta x_w} + [[0, (\bar{\rho}\bar{u})_w]] \right) A_w \quad (6b)$$

$$a_N = \left(\frac{\Gamma_{t,n}}{\Delta y_n} + [[0, -(\bar{\rho}\bar{v})_n]] \right) A_n \quad (6c)$$

$$a_S = \left(\frac{\Gamma_{t,s}}{\Delta y_s} + [[0, (\bar{\rho}\bar{v})_s]] \right) A_s \quad (6d)$$

$$a_H = \left(\frac{\Gamma_{t,h}}{\Delta z_h} + [[0, -(\bar{\rho}\bar{w})_h]] \right) A_h \quad (6e)$$

$$a_L = \left(\frac{\Gamma_{t,l}}{\Delta z_l} + [[0, (\bar{\rho}\bar{w})_l]] \right) A_l \quad (6f)$$

and

$$a_P = a_E + a_W + a_N + a_S + a_H + a_L \quad (6g)$$

where a central differenc and upwind scheme has been used to describe the diffusion and convection flux, respectively. The mathematical operator $[[a, b]]$ gives the maximum of a and b . Beside the turbulence frequency ω and

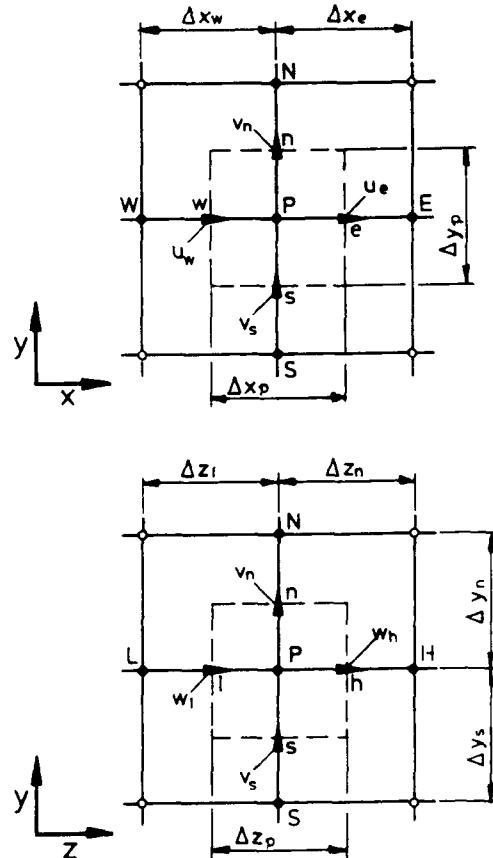


Fig. 1: Grid denotations.

the fixed time increment Δt Eq. (4) exhibits a third time scale τ_P which is defined as:

$$\tau_P = \frac{\bar{p}_P(t) \Delta V}{a_P} \quad (7)$$

This time scale may be interpreted as a characteristic residence time associated with the finite-volume under consideration.

It should be pointed out that Eq. (4) only tends to a correct solution if the change of \bar{p} in time is small, i.e. $\bar{p}(t + \Delta t) \rightarrow \bar{p}(t)$. This can be assured if Δt is very small or a steady state solution is sought.

To apply a Monte Carlo simulation to Eq. (4) it is advantageous to rearrange this equation in terms of an operator product. The result of the manipulation is shown in Eq. (8):

$$\bar{p}_P(\underline{\psi}; t + \Delta t) = (\mathbf{I} + \Delta t \mathbf{T})(\mathbf{I} + \Delta t \mathbf{S})(\mathbf{I} + \Delta t \mathbf{E}) \bar{p}_P(\underline{\psi}; t) + 0(\Delta t^2) \quad (8)$$

where \mathbf{I} is the identity operator and \mathbf{T}, \mathbf{S} , and \mathbf{E} represent finite-volume operators for spatial transport, reaction, and mixing, respectively. The definitions of these operators are as follows:

$$\mathbf{T} \bar{p}_P(\underline{\psi}; t) = \frac{\sum_l a_l \bar{p}_l(\underline{\psi}; t) - a_P \bar{p}_P(\underline{\psi}; t)}{\tau_P a_P}, \quad (9)$$

$l = E, W, N, S, H, L$

$$\mathbf{S} \bar{p}_P(\underline{\psi}; t) = -\frac{\partial}{\partial \phi_\alpha} (S_\alpha(\underline{\psi}) \bar{p}_P(\underline{\psi}; t)) \quad (10)$$

$$\mathbf{E} \bar{p}_P(\underline{\psi}; t) = E_P(\underline{\psi}; t). \quad (11)$$

The notation $0(\Delta t^2)$ in Eq. (8) means that the first term neglected in the derivation is of order Δt^2 .

The operator product may now be split in a sequence of operations acting on \bar{p} according to the following scheme:

$$\bar{p}_P(\underline{\psi}; t + \frac{1}{3} \Delta t) = (\mathbf{I} + \Delta t \mathbf{T}) \bar{p}_P(\underline{\psi}; t) \quad (12a)$$

$$\bar{p}_P(\underline{\psi}; t + \frac{2}{3} \Delta t) = (\mathbf{I} + \Delta t \mathbf{S}) \bar{p}_P(\underline{\psi}; t + \frac{1}{3} \Delta t) \quad (12b)$$

$$\bar{p}_P(\underline{\psi}; t + \Delta t) = (\mathbf{I} + \Delta t \mathbf{E}) \bar{p}_P(\underline{\psi}; t + \frac{2}{3} \Delta t) \quad (12c)$$

The intermediate time steps do not represent a physical state but rather aid as a tool to calculate the effects of transport, reaction and mixing sequentially. The sequential operator splitting is utilized for simulating the transport of \bar{p} by a Monte Carlo technique.

3. MONTE CARLO SIMULATION

The fundamentals of the Monte Carlo simulation technique used are described by Pope (1981) and the reader is referred to this publication for detailed information. However, some changes arise due to the finite-volume approach chosen here and by the definition of the spatial operator \mathbf{T} which includes convection as well as diffusion fluxes whereas Pope (1981) treats both transport processes separately. Therefore, the concept of the simulation is briefly described in this section.

For the simulation process the density weighted joint pdf at each grid point is represented by an ensemble of N stochastic elements, and the stochastic elements itself

comprise the σ scalars of the problem under consideration. The discrete representation of $\bar{p}(\underline{\psi}; \underline{x}, t)$ may be written in the following form:

$$\Phi_P(\lambda \Delta t) \equiv \begin{pmatrix} \phi_P^{(1)}(\lambda \Delta t) & = & \phi_1^{(1)}, \phi_2^{(1)} \dots \phi_\alpha^{(1)} \dots \phi_\sigma^{(1)} \\ \phi_P^{(2)}(\lambda \Delta t) & = & \phi_1^{(2)}, \phi_2^{(2)} \dots \phi_\alpha^{(2)} \dots \phi_\sigma^{(2)} \\ \vdots & & \vdots \\ \phi_P^{(n)}(\lambda \Delta t) & = & \phi_1^{(n)}, \phi_2^{(n)} \dots \phi_\alpha^{(n)} \dots \phi_\sigma^{(n)} \\ \vdots & & \vdots \\ \phi_P^{(N)}(\lambda \Delta t) & = & \phi_1^{(N)}, \phi_2^{(N)} \dots \phi_\alpha^{(N)} \dots \phi_\sigma^{(N)} \end{pmatrix} \quad (13)$$

where the independent scalar space $\underline{\psi}$ corresponds to $\underline{\phi}$. For a correct simulation it has to be assured that the number N of stochastic elements is large enough such that the ensemble average of any function $Q(\underline{\phi})$ is sufficiently close to the average based on the continuous pdf, i.e.

$$\frac{1}{N} \sum_{n=1}^N Q(\phi_P^{(n)}(\lambda \Delta t)) \rightarrow \int Q(\underline{\psi}) \bar{p}_P(\underline{\psi}; \lambda \Delta t) d\underline{\psi}. \quad (14)$$

The transport and the evolution of the discrete representation of \bar{p} now proceeds according to the sequential operations given by Eq. (12). The spatial transport

$$\begin{aligned} \bar{p}_P(\underline{\psi}; t + \frac{1}{3} \Delta t) &= (\mathbf{I} + \Delta t \mathbf{T}) \bar{p}_P(\underline{\psi}; t) \\ &= \left(1 - \frac{\Delta t}{\tau_P}\right) \bar{p}_P(\underline{\psi}; t) + \sum_l \frac{\Delta t a_l}{\tau_P a_P} \bar{p}_l(\underline{\psi}; t), \end{aligned} \quad (15)$$

$$l = E, W, N, S, H, L$$

is simulated by replacing n_{tl} elements at $\Phi_P(t)$ by randomly selected elements at $\Phi_l(t)$. The selected element number n_{tl} is the nearest integer to

$$n'_{tl} = \frac{\Delta t a_l}{\tau_P a_P} N. \quad (16)$$

It is evident from Eq. (15) that a necessary criterion for stability is

$$\frac{\Delta t}{\tau_P} < 1. \quad (17)$$

This criterion has to be fulfilled for all grid points at the same time. Thus, the maximum time increment chosen has to be less than the smallest τ_P in the calculation domain.

The operations for reaction and mixing specified by Eqs. (12b) and (12c) are identical to the formalism given by Pope (1981). Their simulation is as follows. Reaction is simulated by moving all stochastic elements according to the differential equation

$$\frac{d\phi_\alpha^{(n)}}{dt} = S_\alpha^{(n)}(\underline{\phi}), \quad \alpha = 1, 2, \dots, \sigma \quad (18)$$

in scalar space. The time increment of integration is Δt . S_α is the source term of the scalar variable α , which, in general, is a function of all σ scalars. However, in this paper only non-reacting flows are considered. Thus, S_α is zero for all scalars.

The continuous mixing model specified by Eq. (2) is realized for the discrete representation of the pdf by selecting pairs of elements from Φ_P , say $\phi_P^{(m)}$ and $\phi_P^{(n)}$, and assigning these two elements their mean value:

$$\begin{aligned}\phi_P^{(m)}(t + \Delta t) &= \phi_P^{(n)}(t + \Delta t) \\ &= \frac{1}{2} \left(\phi_P^{(m)} \left(t + \frac{2}{3} \Delta t \right) + \phi_P^{(n)} \left(t + \frac{2}{3} \Delta t \right) \right).\end{aligned}\quad (19)$$

The number of pairs n_m selected is the nearest integer to

$$n'_m = \frac{1}{2} \Delta t \omega N \quad (20)$$

and the turbulence frequency ω is defined by

$$\omega = 2C_\phi \frac{\epsilon}{k}. \quad (21)$$

C_ϕ is an empirical constant and has been set to 1.79. k and ϵ are given by the turbulence model.

4. NUMERICAL ASPECTS

In this section some numerical aspects of the Monte Carlo simulation are discussed. These are concerned with the influence of computer storage limitations and non-equally spaced grids.

Pope (1981) showed that the computational work for the Monte Carlo simulation is proportional to the number of stochastic elements, the dimensionality of the pdf, and the time, i.e.

$$W \propto N \sigma t. \quad (22)$$

An interesting feature of this equation is that the work is independent of the time increment Δt . Consequently, one may choose a very small Δt to decrease numerical errors. However, there exists a dependency between the smallest allowable N and Δt which is deduced from Eq. (16). This equation describes the spatial transport from neighbouring grid cells into the finite-volume around P . There will be only a transport if the number of shifted elements is greater than one. This implies:

$$N > \frac{1}{2} \left[\frac{\Delta t a_l}{\tau_P a_P} \right]^{-1}, \quad l = E, W, N, S, H, L. \quad (23)$$

In addition one is interested to reduce the sampling error, which indicates the difference between the left and right hand side of Eq. (14). The sampling error causes disturbances of the deterministic flow field calculations if the density is a function ϕ . Pope (1981) showed that the sampling error is proportional to $N^{-\frac{1}{2}}$. Therefore, to reduce the sampling error and to account for the criterion of Eq. (23) the element number N should be as large as possible but storage restrictions set a limit on N . Nguyen (1984) did extensive numerical tests with a boundary layer type program for two dimensional parabolic flows to study the influence of limited N on the accuracy of the simulation. For this type of program it is only necessary to store Φ at two grid lines: the line where iteration is performed and the preceding one. Thus, the suggested value for N of the order of 10^3 does not require too much storage. In case of three dimensional elliptic flow predictions Φ has to be stored at all grid points to allow for iterations over the entire domain. The storage requirement SR , given in MBytes, for this case is estimated by

$$SR = N_P \cdot N \cdot \sigma \cdot 4 \cdot 10^{-6} \quad (24)$$

where N_P , N , and σ are the number of grid points, number of stochastic elements of Φ , and its dimensionality, respectively. For a combustor type flow the minimum of grid points is of the order of 10^4 and the number of scalars may vary in the range of 1 to 5, depending what kind of reaction model is used. With these benchmarks the storage requirement is of the order of 100 MBytes and more which is only processed by large computers in a justifiable time. In addition practically no advantage can be taken of present vector computers because of the recursive nature of the simulation process.

For typical combustor type flow configurations as shown in Fig. 2a the criterion of Eq. (23) may introduce severe problems even if N is set to a relatively large value. The configuration shown is that of an initially high velocity jet issuing into a main stream with moderate speed.

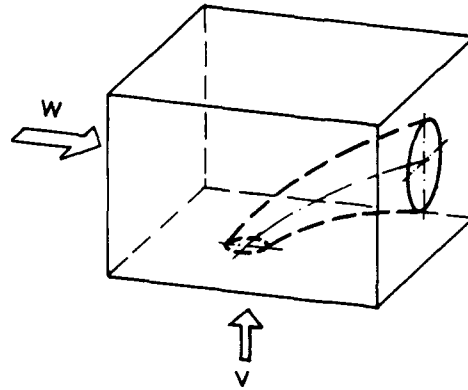


Fig. 2a: Jet in a cross flow.

The allowable maximum time increment Δt in this configuration is governed by the smallest resident time τ_P which occurs close to the injection hole. This is because of the increased convective flux at the jet inlet (see Eq. (7)). Thus, a limited region of the flow field calls for a very small Δt . In the main stream region, where low velocities prevail, the value of τ_P is much higher and Eq. (23), therefore, may no more be satisfied. In this regions the solution is considered to be 'frozen' because no elements are shifted.

So far, only the influence of the time scales Δt and τ_P has been discussed and it is in question if the quotient of the coefficients a_l and a_P in Eq. (23) behaves well. To clear this question one considers a finite-volume grid as shown in Fig. 2b. The characteristic of this grid is that the spacing in y and z -direction is very coarse in comparison to the spacing in x -direction, i.e. $\Delta y > \Delta z$ and $\Delta z > \Delta x$. This situation leads to a large diffusion coefficient $\Gamma_t/\Delta x$ in Eq. (6) which may cause a dominance of the coefficients in E, W -direction. The worst effect of this dominance for a limited N is that there is only a diffusive exchange of stochastic elements in x -direction. The transport in the remaining directions is frozen because Eq. (23) is not fulfilled for this directions.

It is concluded from this discussion that the large storage requirement for three-dimensional flow problems sets a limit on the number N of stochastic elements. By this limitation one has to account for the criterion given by Eq. (23) if there are large variations of τ_P in the flow field and/or if the finite-volume cells are distort.

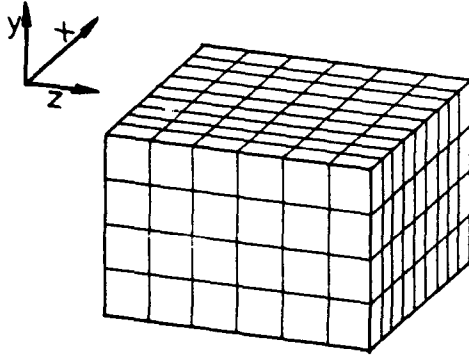


Fig. 2b: Three dimensional grid.

5. HIGHER ORDER DIFFERENCING SCHEMES

The derivation of the transport equation for \bar{p} has been based on the upwind scheme to assure stability if the flow is dominated by convection. It is well known that this scheme suffers from numerical diffusion if the flow direction is oblique relative to the grid. This problem, in general, is of minor importance for parabolic or boundary layer flows. In case of recirculating flows there are always discretisation errors due to numerical diffusion to some extent and one has to check very carefully if this is acceptable. A differencing procedure free of numerical diffusion is the QUICK scheme where the convective flux of any variable through a finite-volume surface is based on three values; two of the values are located upstream and one downstream of the surface under consideration. The QUICK scheme is implemented in the transport equation by adding a correction factor $Q_P(\psi; t)$ to the spatial transport operator T in the following form:

$$T\bar{p}_P(\psi; t) = \frac{\sum_l a_l \bar{p}_l(\psi; t) - a_P \bar{p}_P(\psi; t) + Q_P(\psi; t)}{\tau_P a_P}, \quad (25)$$

$$l = E, W, N, S, H, L$$

with

$$Q_P(\psi; t) = \sum_l \bar{p}_l \bar{u}_l A_l f_l, \quad l = e, w, n, s, h, l. \quad (26)$$

and f_l is the quadratic interpolation function, see Noll (1986). For example f_e is given by

$$f_e = \frac{(x_e - x_P)(x_e - x_E)}{(x_W - x_P)(x_W - x_E)} (\bar{p}_W(\psi; t) - \bar{p}_P(\psi; t)) + \frac{(x_e - x_W)(x_e - x_P)}{(x_E - x_W)(x_E - x_P)} (\bar{p}_E(\psi; t) - \bar{p}_P(\psi; t)) \quad (27)$$

if the flow direction is from W to E . The basic problem is the occurrence of differences of two pdf's as shown in Eq. (27) whenever the modified operator T is applied to a Monte Carlo simulation. There is no efficient algorithm known by the authors to solve this problem in the framework of statistical methods.

If one just likes to investigate the influence of numerical diffusion for a specific problem it may be sufficient to correct the means of the σ scalars independently. This is done by shifting all stochastic elements $\phi_\sigma^{(n)}$ by the quan-

tity q_σ in scalar space where q_σ is defined as

$$q_\sigma = \frac{\Delta t}{a_P \tau_P} \sum_l \bar{p}_l \bar{u}_l A_l \bar{f}_{\sigma l}, \quad \begin{cases} l = e, w, n, s, h, l \\ \sigma = 1, 2, \dots, \sigma \end{cases} \quad (28)$$

and for example $\bar{f}_{\sigma e}$ is given by

$$\bar{f}_{\sigma e} = \frac{(x_e - x_P)(x_e - x_E)}{(x_W - x_P)(x_W - x_E)} (\bar{\phi}_{\sigma W} - \bar{\phi}_{\sigma P}) + \frac{(x_e - x_W)(x_e - x_P)}{(x_E - x_W)(x_E - x_P)} (\bar{\phi}_{\sigma E} - \bar{\phi}_{\sigma P}). \quad (29)$$

Whenever this method is used one has to keep in mind that statistical independency of the σ scalars is assumed and that due to this numerical procedure the variance is artificially increased by the order of q_σ^2 .

6. NON-ADIABATIC BOUNDARY CONDITIONS

The implementation of boundary conditions for \bar{p} is straightforward if these are cyclic or if the gradients of the dependent variables normal to the boundaries vanish. Problems arise if the value of a variable itself is prescribed at the boundary. This situation is of practical interest whenever the energy equation is solved, i.e. one of the σ scalars of \bar{p} represents the specific enthalpy h , and the wall temperature is given. In this case there will be a temperature gradient which induces a specific wall heat flux \dot{q}_w and an efficient algorithm is needed to simulate this heat flux by a Monte Carlo technique.

The simulation of the heat flux takes advantage of wall functions to avoid very small grid node distances near the boundary. An extensive study of wall functions is given for example by Scherer (1989) and the reader is referred to this publication for more information. Here, the heat flux is described by (Pun and Spalding (1976)):

$$\frac{\dot{q}_w}{(h_N - h_P) |\bar{u}_P| \bar{\rho}_P} = \frac{\tau_w / (\bar{\rho}_P \bar{u}_P^2)}{Pr_t (1 + P_j \sqrt{\tau_w / (\bar{\rho}_P \bar{u}_P^2)})} \quad (30)$$

with the empirical function

$$P_j = 9.0 \left(\frac{Pr}{Pr_t} - 1 \right) \left(\frac{Pr}{Pr_t} \right)^{-\frac{1}{4}} \quad (31)$$

where τ_w is the wall shear stress which corresponds to the grid point P , see Fig. 3, and Pr_t is the turbulent Prandtl number.

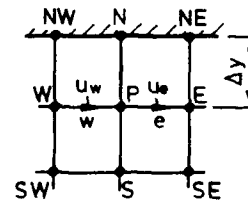


Fig. 3: Grid denotations for wall functions.

An efficient implementation of Eq. (30) into the Monte Carlo simulation is given by changing the coefficients of Eq. (6) which describe a boundary. Referring to the example of Fig. 3 the wall coefficient a_N of Eq. (6c) is substituted by

$$a_N = \frac{(\tau_w / |\bar{u}_p|) A_N}{Pr_t (1 + P_j \sqrt{\tau_w / (\bar{\rho}_p \bar{u}_p^2)})} \quad (32)$$

where A_N is the wall area of the finite-volume. Combination of the coefficient a_N with Eq. (16) yields the number of stochastic elements of Φ_p that are substituted by elements of Φ_N . The latter discrete pdf is predetermined by the boundary conditions. It is interesting to note that the number of transferred elements is independent of the difference $h_N - h_p$. This difference is buried in the changed values of the substituted elements. Hence, the heat flux simulated by this process is given by a combination of the number of transferred elements and the change in the values of the substituted elements. The advantage of this implementation is that there is only a modification of the wall coefficients needed to account for non-adiabatic boundary conditions.

7. COMPUTER CODE EPOS

The Monte Carlo process outlined to simulate the transport of a joint scalar pdf is incorporated in the finite-volume computer code EPOS (Elliptic Package On Shear flow), which has been previously described by Elbahar (1982), Elbahar et al. (1986), Noll (1986), and Noll et al. (1987). The code has been developed at the Institut für Thermische Strömungsmaschinen (ITS), University of Karlsruhe, and is capable of solving stationary three-dimensional turbulent elliptic flow problems including chemical reactions. In the present work, EPOS incorporates the standard version of the k, ϵ -model.

The seven dependent variables, relevant to the problem under consideration, are calculated in the following consecutive order: velocity components, pressure, \bar{k} , $\bar{\epsilon}$, and \bar{p} . For solution the program permanently changes between iterating over the first five variables and the Monte Carlo simulation to solve for \bar{p} . Iteration is stopped whenever the maximum residuum of the finite-volume equations falls below a certain value r_{ref} . In case of Eq. (4) the residuum has been defined for the mean of the σ scalars in stationary non-reacting flows by

$$|\sum_i a_i \bar{\phi}_{ai} - a_p \bar{\phi}_{ap}| = r_a \leq r_{ref}, \quad l = E, W, N, S, H, L. \quad (33)$$

8. TEST CASE

The test case considered is a non-isothermal jet-mixing flow. The experimental setup for this flow configuration, illustrated in Fig. 4a, and the experimental results presented here have been previously described by Wittig et al. (1984) and Noll (1986).

The main feature of the configuration are the two opposite rows of cold jets penetrating the hot main flow under atmospheric pressure. The jet diameter D_j is 8 mm, the spacing s between two jets is 20 mm, and the height of the channel H is 100 mm. The temperature T_j of 308 K is constant for all jets. The jet inlet velocities at the top and bottom are slightly different. At the top the jet velocity v_{jT} is 75.6 m/s and at the bottom v_{jB} is 75.0 m/s. The inlet velocity w_0 of the main flow is 13.7 m/s and the mean inlet air temperature T_0 is 460.0 K.

Because of symmetry the finite-volume grid expands only between the central and mid plane as shown in Fig. 4b.

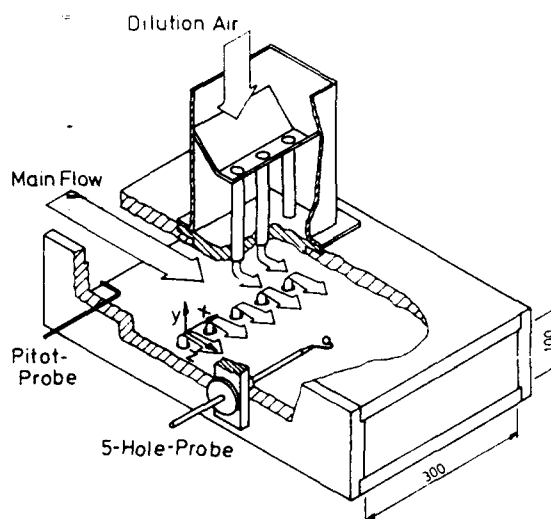


Fig. 4a: Test section.

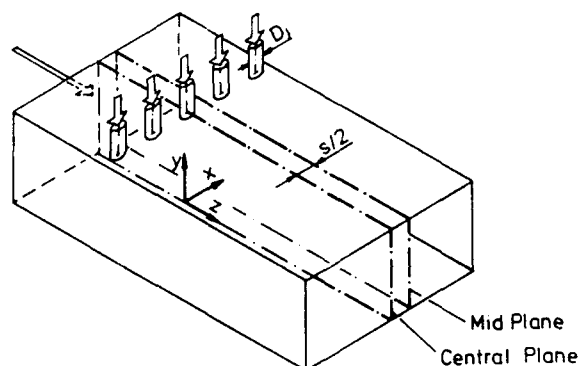


Fig. 4b: Calculation field.

The number of grid points used are $10 \times 30 \times 33$ in x -, y -, and z -direction, respectively. For the Monte Carlo simulation of the energy equation a constant specific heat capacity c_p is assumed and the discrete pdf of the enthalpy h is represented by $N = 150$ stochastic elements, which is at the lower limit. The pdf's at the main inlet and the jet holes are characterized by a delta impuls.

For solution alternately 50 sweeps over the entire domain are performed to solve for the first five variables and to solve for \bar{p} by the Monte Carlo simulation, respectively, until a converged solution is achieved. The storage requirement for this simple test case is 10 MByte and the CPU time for one sweep over the entire flow field for the first five variables is approximately 1 second whereas a sweep for the Monte Carlo simulation needs 15 seconds. Thus, 93% of the time is spent for the pdf simulation process. This times are measured on a vector computer VP400-EX. As previously mentioned, the increased computer time for the simulation is basically due to the recursive nature of the Monte Carlo process which restricts vectorisation. A converged solution needs approximately four hours.

The quality of the Monte Carlo simulation is not only judged by the agreement of the numerical results with the

experimental data but also by comparison of the simulation with deterministic solutions of the energy equation as commonly applied. In detail, the following six calculation models are considered.

1st model: The Favre averaged energy equation is solved deterministically with the upwind scheme.

2nd model: The transport equation of the pdf of h is solved by the Monte Carlo method with the upwind scheme. The mean temperature and density are calculated by means of the density weighted pdf:

$$\bar{\rho} = \left[\int \frac{\bar{p}(\psi)}{\rho(\psi)} d\psi \right]^{-1} \quad (34)$$

$$\bar{T} = \bar{\rho} \int \frac{T(\psi) \bar{p}(\psi)}{\rho(\psi)} d\psi. \quad (35)$$

where the independent scalar space ψ is one-dimensional and represents the enthalpy.

3rd model: The transport equation of the pdf of h is solved by the Monte Carlo method with the upwind scheme but the mean temperature and enthalpy are calculated by means of \bar{h} :

$$\bar{\rho}^* = \rho(\bar{h}) \quad (36)$$

$$\bar{T}^* = T(\bar{h}) \quad (37)$$

with

$$\bar{h} = \bar{\rho} \int \frac{\psi \bar{p}(\psi)}{\rho(\psi)} d\psi. \quad (38)$$

The models 4, 5, and 6 correspond to the first three models but the QUICK scheme is used instead of the upwind scheme. As already mentioned, the first model has been chosen as a reference to conventional prediction methods. The third model has been selected because the results are independent of the shape of the pdf. Therefore, the predictions obtained with this model should be identical with the first one if the transport of \bar{p} is simulated correctly by the Monte Carlo method. For all model calculations the QUICK scheme was employed for the discretisation of the momentum equations.

Typical results presented here are taken from two downstream locations relative to the jet inlets in the central plane; see the coordinate system indicated in Fig. 4b. The velocity profiles shown in Fig. 5 at this locations are practically identical for all models. This indicates that the density, which couples the energy and the momentum equation, is equally well predicted. In general, the calculated velocities agree very well with the experiment. However, some differences occur near the walls for v and w at $z/H = 0.4$. These may be due to the QUICK scheme used to solve the momentum equation.

The temperature profiles at $z/H = 0.4$ are shown in Fig. 6. There is a distinct difference between the group of the first three models based on the upwind scheme and the second group based on the QUICK scheme. As expected the upwind scheme yields a more leveled profile due to numerical diffusion in this region. Further downstream the flow is nearly parallel and by this the QUICK scheme does not improve the solution any more as shown in Fig. 7 and 8. Comparison with the experimental data indicate that the predicted heat exchange in y -direction is slightly too low.

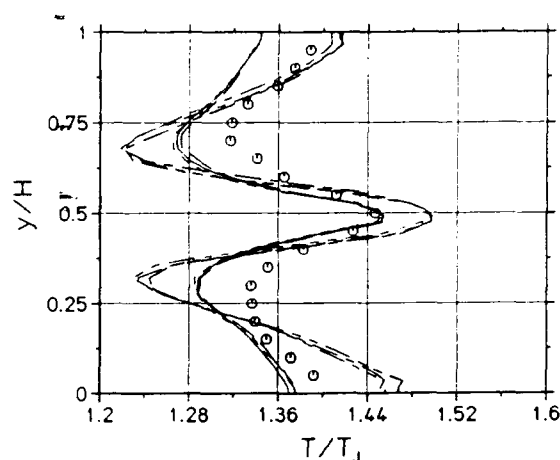


Fig. 6: Temperature profiles at $z/s = 0$ and $z/H = 0.4$. Symbols same as Fig. 5.

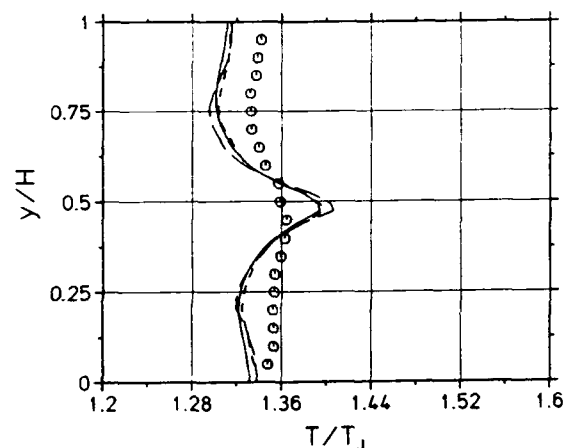


Fig. 7: Temperature profiles of models 1 to 3 at $z/s = 0$ and $z/H = 1.4$. Symbols same as Fig. 5.

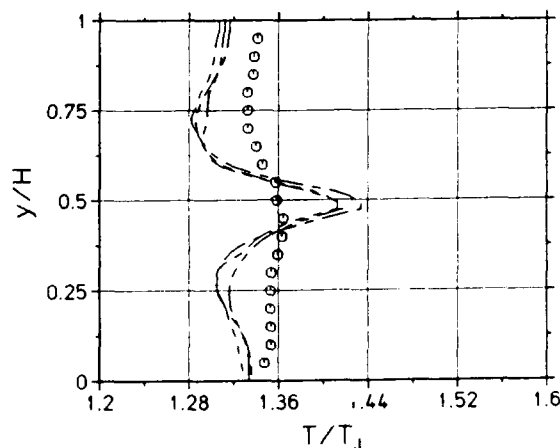


Fig. 8: Temperature profiles of models 4 to 6 at $z/s = 0$ and $z/H = 1.4$. Symbols same as Fig. 5.

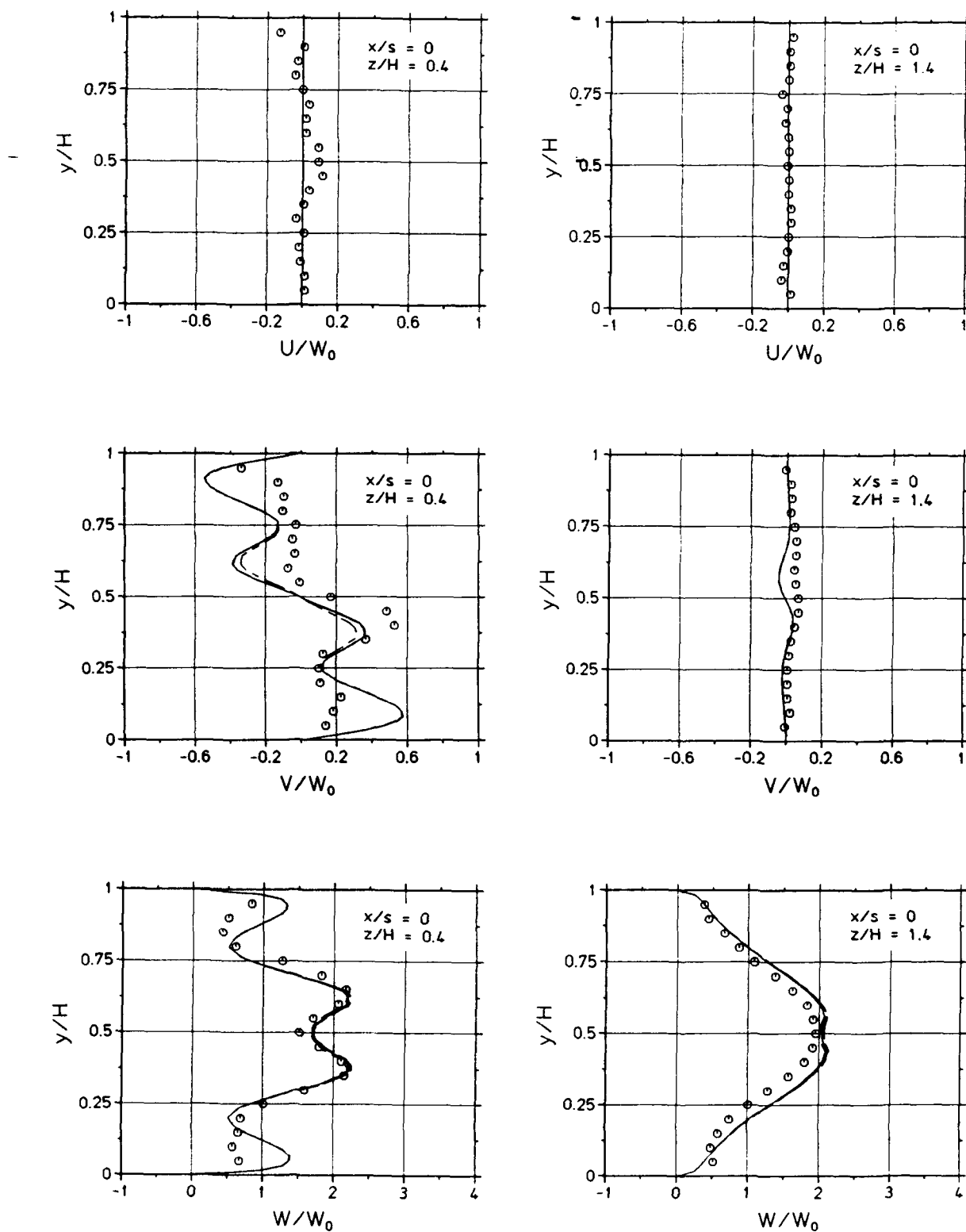


Fig. 5: Velocity profiles at $x/s = 0$. \circ experiment,
 — model 1, - - - model 2, model 3,
 - · - model 4, - - - model 5, - · - model 6

The calculated temperature distributions for each group are practically identical. This indicates that the transport simulated by the Monte Carlo technique is the same as for deterministic approaches as required. The fact that the results of the models 2 and 3 are very close together is caused by the flow considered. Due to the high turbulence level, induced by the interaction of the jets with the main flow, there is an intense mix which decreases the variance of h rapidly. By this effect the results of model 2 has to approach the results of model 3. The same holds true if the QUICK scheme is applied to correct the mean although this method increases the variance. Finally, Fig. 9 shows a comparison of a pdf determined by the Monte Carlo method and a pdf calculated by the well known beta-function which is based on transport equations for the mean and the variance of h . For this test case both approaches result in very similar shapes of the pdf's throughout the entire flow field. This similarities may explain the successful use of the beta-function in simple problems where no joint pdf is required, otherwise the Monte Carlo method is more appropriate.

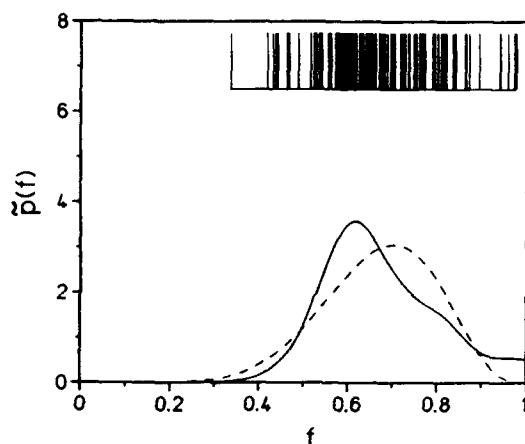


Fig. 9: Pdf of normalized enthalpy at $x/s = 0$, $z/H = 0.4$ and $y/H = 0.4$. f is defined by:
 $f = (h - h_j)/(h_0 - h_j)$.
 — Monte Carlo method model 2
 - - - - Beta-function based on transport equations of the first two moments

9. CONCLUSIONS

A finite-volume equation for the transport of a joint scalar pdf has been outlined. It has been shown that the computer storage requirements are very large whenever three-dimensional elliptic flow problems are considered. This is caused by the necessity to store the discrete pdf at all grid points. It has been shown that the number of stochastic elements can not be decreased arbitrarily to save storage if there are large variations of the characteristic residence time τ_P in the flow field. An analysis of the influence of distort grids showed that large variations in the spatial directions of the finite-volume cells hinder convergence. The simulation of three-dimension non-isothermal jet-mixing flow showed that the algorithm gives quantitatively correct results. However, the differences between the temperature predictions caused by numerical diffusion indicate the need for an efficient simulation scheme that is free of numerical diffusion but also applicable to joint pdf's.

10. REFERENCES

- Curl, R.L. (1963): Dispersed phase mixing. American Institute of Chemical Engineers, Vol. 9, No. 2, pp. 175-181
- Elbahar, O. (1982): Zum Einfluß von Kühlluftstrahlen und Mischzonengeometrie auf die Temperaturprofilentwicklung in Gasturbinen-Brennkammern. Dissertation Universität Karlsruhe
- Elbahar, O., Noll, B., Wittig, S. (1986): Investigation of the flow-field and temperature profiles in gas turbine combustors: the results of three finite difference schemes. 6th International Conference on Mechanical Power Engineering
- Nguyen, T.V., Pope, S.B. (1984): Monte Carlo calculations of turbulent diffusion flames. Combustion Science and Technology, Vol. 42, pp. 13-45
- Noll, B. (1986): Numerische Berechnung brennkammertypischer Ein- und Zweiphasenströmungen. Dissertation Universität Karlsruhe
- Noll, B. (1991): Evaluation of a bounded high resolution scheme for combustor flow computations. Accepted for publication in AIAA-Journal
- Noll, B., Wittig, S., Steinebrunner, K. (1987): Numerical analysis of the flame-stabilizing flow in the primary zone of a combustor. Proceeding of the ASME/JSME Thermal Engineering Joint Conference, Vol. 1, pp. 151-159
- Pope, S.B. (1979): The statistical theory of turbulent flames. Philosophical Transactions of the Royal Society of London, Vol. 291A
- Pope, S.B. (1981): A monte carlo method for the pdf equation of turbulent reactive flow. Combustion Science and Technology, Vol. 25, pp. 159-174
- Pope, S.B. (1982): An improved turbulent mixing model. Combustion Science and Technology, Vol. 28, pp. 131-135
- Wittig, S., Elbahar, O., Noll, B. (1984): Temperature profile development in turbulent mixing of coolant jets with a confined hot crossflow. Journal of Engineering for Gas-Turbines and Power, Vol. 106, pp. 193-197

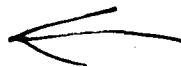
Discussion

L. DELUCA, POLITECNICO DI MILANO, ITALY

Can you compute the distribution of heat release rates? For which specific kinetic scheme?

AUTHOR'S REPLY

In general it is possible to compute the mean heat release rate because no restrictions are imposed by theory on the dimension of the pdf. By this, more detailed kinetic schemes can be applied. For the combustion of hydrocarbons, reaction schemes including one passive and three reactive scalars have been used in connection with this Monte Carlo method.





THE COHERENT FLAMELET MODEL FOR PROPULSION APPLICATIONS

D. Veynante, F. Lacas, P. Boudier*, B. Dillies,
J. M. Samaniego, T. Poinso and S. Candel

E.M2.C. Laboratory, CNRS, Ecole Centrale Paris
92295 Chatenay-Malabry Cedex, FRANCE
*and IFP, Rueil Malmaison, FRANCE

92-16098



This article reports our recent progress in the modeling of turbulent combustion for propulsion applications. The description of the reactive flow relies on the flamelet concept and uses a transport equation for the flame surface density. The coherent flamelet description which has evolved from a series of numerical and experimental studies is first reviewed and its recent improvements are explained. We then focus on the premixed version of the model. Two applications of relevance to aeronautical propulsion are then described. The first concerns a flame stabilized by a hot stream of combustion products. The second deals with a ramjet configuration comprising two lateral injection jets. In both cases the model predictions are compared with experiments. It is shown that the model provides viable representations of these two cases.

Cet article décrit les progrès que nous avons accomplis récemment dans la modélisation de la combustion turbulente pour les applications à la propulsion. La représentation de l'écoulement réactif est basée sur le concept de flammelette et utilise une équation de bilan pour la densité de surface de flamme. Le modèle de flamme cohérente développé à partir d'une série d'études numériques et expérimentales est d'abord brièvement revu et les améliorations récentes sont expliquées. On considère ensuite la version prémélangée du modèle. Deux applications intéressantes la propulsion aéronautique sont ensuite présentées. La première concerne une flamme stabilisée par un écoulement de gaz chauds résultant de la combustion d'un prémélange d'air et de méthane. La seconde configuration est de type stato-réacteur et elle comprend deux entrées d'air latérales alimentées par un prémélange d'air et de propane. Dans les deux cas, le modèle donne une description convenable de l'écoulement.

1. INTRODUCTION

Turbulent combustion is a central problem in the design and development of propulsion systems. Some progress has been accomplished in this field and applications have been rapidly conducted in various configurations (jet-engine main combustors, afterburners, ramjets, liquid rocket motors). A variety of models has been used to perform calculations in simple and more complex situations. The theoretical basis of turbulent combustion modeling is reviewed in many books and papers (see for example Libby and Williams 1980 and Williams 1985 for basic presentations and Correa and Shyy 1987 for a recent survey of computational models of continuous turbulent combustion, Candel et al. 1990a and b for reviews of flamelet models). Classical models have usually been founded on stochastic descriptions. In general the determination of the local average reaction rates has involved a probability density function. While this pdf is often presumed, it may be also be determined as a solution of an evolution equation (see Borghi 1988 and Pope 1990 for reviews). This last approach is attractive because it relies on a framework of stochastic techniques but it is not very practical especially if complex chemistry is to be considered. In addition the exact evolution equation is always replaced by a modeled equation which requires a set of closure assumptions. This approach has been most notably developed by Borghi (1988) and Pope (1990). An important drawback of pdf models is that they do not distinguish the fluctuations existing in a turbulent flow in terms of their scale. As a consequence large, intermediate or small scale eddies are treated indifferently while their effects on the flame are not comparable.

Alternative descriptions of turbulent combustion have relied on flamelet concepts. A variety of physical models use this idea and treat the reactive field as a collection of flame elements propagating in the turbulent flow (Carrier et al. 1975, Williams 1975, Marble and Broadwell 1977, 1979, Clavin and Williams 1982, Peters 1984, 1986, Spalding 1978, Bray et al. 1984, Bray 1987). The flamelet idea is represented schematically in Fig.1 in the case of premixed turbulent combustion. The instantaneous flame is constituted by localized reactive sheets. According to certain authors the flame sheet should remain uninterrupted and the local instantaneous structure of the flow should be exactly that of a laminar flame. An extended view of the concept allows for discontinuities in the flame sheet and it is then assumed that the reactive sheets are distributed in the flowfield and that their structure may be identified and analysed separately. Using the flamelet concept it is possible to uncouple complex chemistry and molecular transport problems from the analysis of the turbulent flow field. In certain cases a simplified model for the reactive laminar sheets is utilized while in others a more elaborate flamelet library is first constructed yielding specific properties such as the consumption rates per unit flame area, ignition and extinction conditions that are required in the computation of the turbulent flow field.

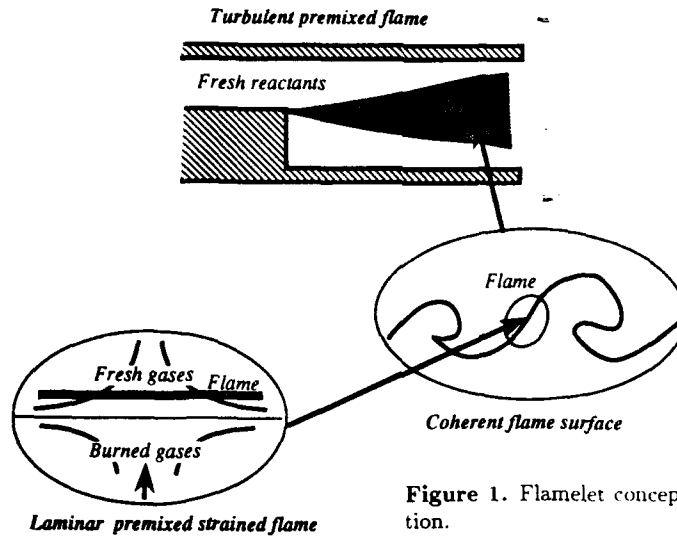


Figure 1. Flamelet concept for premixed combustion.

The domain of application of flamelet models is still not well defined at this time (but this is also the case for other models). This aspect is a subject of discussion but it is generally agreed that the concept is applicable in the range of large Damkohler numbers and for characteristic turbulent scales much larger than a typical flame thickness. These conditions are satisfied in many practical situations and the flamelet regime probably exists in many cases and at least in certain ranges of operation of IC engines and continuous flow aircraft combustors, ramjets and rocket motors. The limits of the flamelet regime have been defined up to now on purely intuitive grounds (Barrère 1974, Borghi 1985, Williams 1985, Peters 1986) but new results have become available from direct numerical simulations and a revision of current criteria and beliefs is required (see Poinso et al. 1990 a and b for an analysis of quenching and combustion regimes in turbulent premixed reactive flows). While the question of applicability is still not settled recent evidence indicates that the flamelet concept may be used over a domain which is wider than previously thought. It is then reasonable to leave this issue and evaluate the flamelet models in specific situations by comparing their predictions with experimental results.

At this point it is important to note that flamelet descriptions are far from being unique. They have in common the following ingredients: (1) A laminar flamelet submodel (or submodels) providing the local structure and properties of the reactive elements. (2) A description of the turbulent flow comprising mass average equations describing the mean flow variables and the main species mass fractions and relevant closure equations. (3) A rule or a set of rules which couple the flamelet submodels to the turbulent flow description. (4) Additional submodels accounting for chemical reactions taking place outside the flamelets.

The specification of these elements is however flexible and many alternative ways have been explored. Reviews due to Peters (1984, 1986) and Bray (1987) describe some of the possibilities but they are incomplete and do not make reference to **models based on the flame surface density concept**. An initial application of this idea is developed in Candel et al. 1982 and further progress along this line is reported in Darabiha (1984) Darabiha et al. (1987a and b), Maistret et al. (1989) and Candel et al. (1990a and b) and it is further illustrated in the present article.

In certain flamelet models a probability density function is used to couple the local analysis to the flow description. This method devised by Liew et al (1984) and Peters (1984) to treat turbulent diffusion flames requires that at a given point in space the instantaneous structure of the turbulent flame will be that of a laminar reactive sheet. The individual reactive elements belong to a family and are described in terms of a reactant composition (the mixture fraction) and the strain rate (or the scalar dissipation) that is imposed to the flame sheet by the flow field. It is then assumed that there is a unique definition between a scalar quantity ϕ and the normalised conserved scalar ξ : $\phi = \phi(\xi, \chi_{st})$. In this expression χ_{st} designates the scalar dissipation at the stoichiometric point. This quantity has dimensions of s^{-1} and it may be related to the strain rate. The couple (ξ, χ_{st}) may be treated as a random variable having a joint pdf and this function must be presumed or calculated. One usually assumes that the conserved scalar and the scalar dissipation are independent stochastic variables so that the joint pdf may be written as a product: $P(\xi, \chi_{st}) = P_1(\xi)P_2(\chi_{st})$. The shape of the conserved scalar pdf P_1 is presumed and its coefficients are determined from the moments of the conserved scalar. The scalar dissipation pdf P_2 is taken as a log-normal distribution and its coefficients are determined from the moments of ξ which are themselves related to the other moments of the turbulent variables.

Other models use the flamelet passage frequency to evaluate the mean reaction terms (see Bray 1987 for a survey of this method). The reaction rate is first written as the product of the flamelet crossing frequency by the mean reaction rate per flame crossing. A statistical analysis of the flamelet crossing frequency then leads to the following expression for the mean reaction term

$$\bar{w} = \frac{g\bar{c}(1-\bar{c})}{\bar{L}_y |\sigma_y|} \rho_R S_L^0 I_0 \quad (1)$$

where g is a constant of order 1, \bar{c} is the Reynolds mean of a reaction progress variable, \bar{L}_y is an integral scale of the wrinkled flame, σ_y is a geometrical factor, S_L^0 is the burning velocity of a freely propagating laminar flame and I_0 is an integral over the strain rate

$$I_0 = \int_0^\infty \frac{W(a)}{W(0)} P(a) da \quad (2)$$

where $P(a)$ is the probability density of the strain rate a . $W(a)$ is the consumption rate per unit area of strained flame and $W(0)$ is the consumption rate per unit area of an unstrained flame. The mean consumption rate has the final form

$$\bar{w} = \frac{g\bar{c}(1-\bar{c})}{\bar{L}_y |\sigma_y|} \int_0^\infty W(a) P(a) da \quad (3)$$

Still other flamelet models rely on a balance equation for the flame area. This equation describes the transport of the mean reactive surface by the turbulent flow field and the physical mechanisms which produce and destroy this quantity. While descriptions of turbulent combustion in terms of flame area may be found in the early literature its use in the form of a transported quantity was originally developed by Marble and his co-workers in an analysis of non-premixed combustion (Carrier, Fendell and Marble 1975, Marble and Broadwell 1977, 1979). It is suggested in these studies that turbulent combustion of unmixed reactants is controlled in the early stages by a competition between straining of the flame elements and mutual annihilation of the flame area due to mutual destruction of neighbouring flame sheets. The Coherent Flame Model identifies important physical mechanisms of turbulent combustion such as the production of flame area by stretching, its destruction by flame shortening and the central influence of the strain rate acting on the local flamelets (Fig. 2). Because these aspects are important in the large scale coherent motions found in shear flows (as those made evident in the classical study of Brown and Roshko 1974), the model accounts in some sense for the presence of these organized fluctuations.

Our own effort has been to extend the coherent flame description to premixed flow configurations (Candel et al. 1982, Darabiha 1984, Darabiha et al. 1987a and b, Maistret et al. 1989, Candel et al. 1990a and b) and to explore its potential

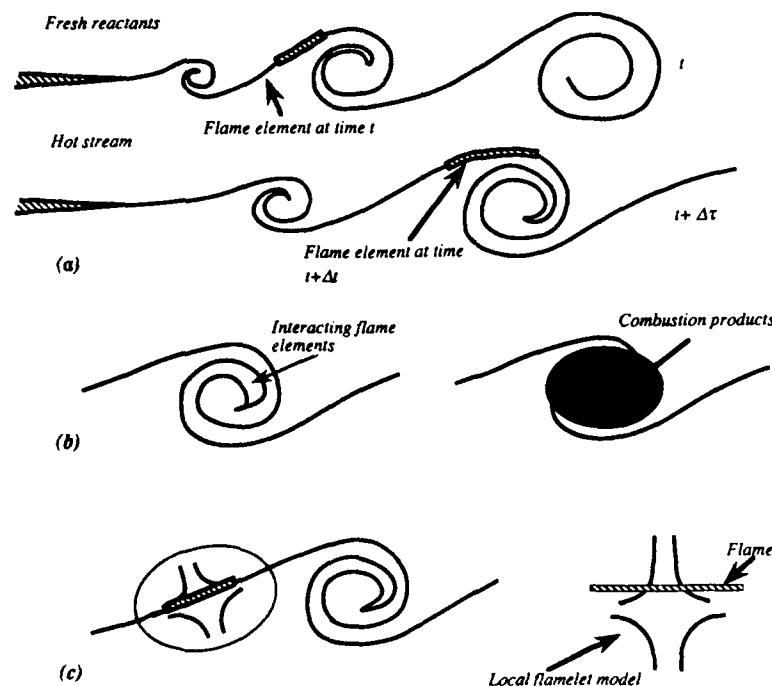


Figure 2. Basic mechanisms of turbulent premixed combustion. (a) Flame surface generation by the rates of strain. (b) Flame surface destruction by mutual interactions of adjacent reactive sheets. (c) Local flamelet structure.

in non-premixed situations (Veynante et al. 1987, Lacas et al. 1987). A new description which accounts for premixed and non-premixed flamelets was recently presented (Veynante et al. 1989a). The case of propagating turbulent fronts is treated in separate papers (Lacas et al. 1989, Veynante et al. 1989b). Non-uniformly premixed flames are considered by Veynante et al. (1989c). Application to the analysis of combustion in cryogenic rocket motors is developed in Lacas (1989). Comparisons between calculations and experiments have also been conducted systematically in the case of a flame stabilized on a V gutter and the results obtained are discussed in our previous papers (for example Darabiha et al. 1987a or Maistret et al. 1989).

In this article we will examine two other configurations which have fundamental and practical interest. The first is a classical experiment on a premixed flame stabilized by a stream of hot products (Moreau 1977, 1981, Moreau and Boutier 1977, Magre et al. 1985). In this situation we will directly compare calculated and measured profiles of temperature and main species.

In the second case we consider a side dump combustor simulating a typical ramjet motor. The experimental device is two-dimensional and allows direct optical access. The comparison will be carried in this geometry between the predicted distribution of mean heat release rate and the observed distribution of this quantity as obtained from images from free radical light emission. While the comparison is not exactly quantitative it still provides clues on the validity of the model in a geometry which is not studied extensively in the technical literature but which is of practical interest. At this point it is worth indicating why such a comparison is worthwhile. Examining the available experimental data (see Libby et al. 1986 for a review of premixed turbulent flame experiments) one finds that measurements of temperature, velocity or concentration profiles are usually emphasized. Little information is reported on the source terms. Now there are good reasons which justify an experimental determination of these terms. First, it is found that the spatial distributions of the mean heat release are influenced by the equivalence ratio and the flow velocity. Observation of the heat release rates will thus provide a unique view of the interaction between the chemical kinetics and the flow turbulence. Second the data also allow a direct evaluation of the theoretical expressions used to model the mean consumption rates appearing in the averaged balance equations. Of course we are also perfectly aware that standard measurements of the flow variables and of their fluctuations are also valuable but it is clear that much can be learnt from a less standard type of analysis. The detailed examination of the mean source term differs from the more common tests performed in the literature on velocity, temperature and mass fraction profiles all of which are only indirectly related to the modeled reaction rates. Because the flow variables are obtained by integrating the dynamic equations they are less sensitive to the modeling assumptions and do not allow a direct assessment of the combustion models. It is a fact that reasonable mean flow profiles may be obtained with the simplest assumptions and hence it is then difficult to see if the model is adequate.

If one wishes to describe the effects of finite rate chemistry and turbulence on the structure of the flame it is clear that the mean source terms should be examined and precisely represented. With this goal in mind a large set of experiments has been carried to measure the distribution of light emission from C2 and CH radicals in the side-dump ramjet configuration. The spatial distributions of the radiated light may be interpreted as giving a qualitative mapping of the local mean heat release in the turbulent flame. Because finite-rate chemistry effects are quite pronounced the modeling of the flow is a challenging problem. Indeed standard "fast" chemistry models are unable to reproduce the trends observed. Improved descriptions are needed which account explicitly for the interaction between the chemical kinetics and the flow.

We begin with a rapid survey of the basic elements of the coherent flamelet model and with a review of recent progress in the modeling (Section 2). Experiments and calculations are then compared in Section 3 in the case of a flame stabilized by a hot stream. The lateral injection combustor is treated in Section 4.

2. REVIEW OF COHERENT FLAMELET MODEL

In this section we will briefly present the basic elements of the coherent flame model. Further details may be found in previous articles (for example Candel et al. 1990a and b). Consider again the configuration shown in Figure 1. A representation which describes this situation and leads to a detailed balance of the flame elements is provided by the Coherent Flame Model. One assumes in this model that the flame elements are convected and distorted by the turbulent motion but keep an identifiable structure. In this sense, the flamelets remain "coherent" (i.e. "organized"). This is so if the thickness of the reactive sheet δ_r is sufficiently small when compared to the typical scales l_t of the energy containing turbulent motion. Some authors believe that δ_r should be less than all the scales existing in the turbulent flow i.e. that it should be smaller than the Kolmogorov scale. However recent numerical simulations (Poinsot et al. 1990) indicate that there exists a cut-off scale in each turbulent flow so that fluctuations which have a size smaller than this scale are unable to interact with the flame. As a consequence the flame thickness could certainly exceed the Kolmogorov scale and the flow would still be in the flamelet regime.

While a definitive answer to this question is not yet available we now consider that the combustion regime is of the flamelet type and examine the processes which govern the combustion mechanism. To fix the ideas it is worth using the idealized sketch of a reactive shear layer separating a fresh mixture and hot combustion products as shown in Figure 2. A flame element placed in the flowfield is mainly affected by the local strain rate which acts in the plane of the flame, modifies its structure and changes the local reaction rate. As a consequence, the local consumption rate per unit of flame area may be obtained from an analysis of strained laminar premixed. The simplest geometry allowing this analysis is shown in Figure 2-c. This geometry adopted in many studies allows detailed calculations of the consumption rates per unit flame surface (for example Darabiha et al. 1988, Djavdan et al. 1990).

The strain rate imposed by the turbulent motion has also the effect of increasing the available reactive area. This production process is balanced by various destruction mechanisms such as flame shortening (mutual annihilation of adjacent flamelets by consumption of one of the reactant, Figure 2-b) or flame quenching (due, for example, to an excessively large strain rate). This mechanism is well illustrated by a generic problem devised by Marble (1985) and Karagozian and Marble (1986). One considers an initially plane flame interacting with a vortex. The flame is wound up by the flow field and flame area is created by the local strain rates acting on the flame sheet. The local production of surface is actually proportional to the strain component acting in the plane tangent to the flame. The reactive elements formed near the vortex core interact and the intervening fuel or oxidizer is rapidly consumed giving place to a burnt core of products and in this region the flame surface disappears. This process is well illustrated by calculations performed by Laverdant and Candel in non-premixed and premixed situations (1988 and 1989).

The previous considerations indicate that the mean consumption rate of a species i per unit volume at a point of the flow, W_i , may be determined as the product of the mean flame surface density at that point (i.e. the flame surface per unit of volume), Σ_f , by the consumption rate per unit of flame area, V_{D_i} , obtained from the analysis of local strained laminar flamelets: $W_i = \rho V_{D_i} \Sigma_f$. In its simplest form, the coherent flame description of turbulent reactive flows combines the three following elements: (1) A model for the turbulent flow comprising a standard set of Reynolds or mass average dynamic equations and a turbulence closure model (2) A local model for the laminar strained flame elements providing

the consumption rates per unit flame area. Complex molecular transport and detailed chemistry may be incorporated into this model which is essentially decoupled from the turbulent flow calculation (3) A balance equation for the flame surface density accounting for transport, diffusion, production and destruction of flame area. A schematic representation of the model is given in Figure 3.

One originality of this description lies in the use of the flame surface density to relate the local flamelet analysis to the global turbulent flow field calculation. This equation takes into account transport, diffusion, production and destruction of flame area and has the general form : $\{\text{transport}\} = \{\text{turbulent diffusion}\} + \{\text{production}\} - \{\text{destruction}\}$. A balance equation of this type is proposed by Marble and Broadwell (1977) to describe the evolution of the flame surface density in the case of a turbulent diffusion flame. While the balance equation for the flame surface was initially devised on the basis of some intuitive arguments it may be derived from basic principles (see for example Candel and Poinso 1990). Considering a non-premixed flame involving a global reaction between the two main species F and O the balance of flame surface may be written :

$$\frac{\partial \Sigma_f}{\partial t} + v_k \frac{\partial \Sigma_f}{\partial x_k} = \frac{\partial}{\partial x_k} \left[D \frac{\partial \Sigma_f}{\partial x_k} \right] + \epsilon_s \Sigma_f - \left(\frac{V_{DF}}{X_F} + \frac{V_{DO}}{X_O} \right) \Sigma_f^2 \quad (4)$$

where Σ designates the flame surface density, D is a turbulent diffusion coefficient, V_{DO} and V_{DF} are the volume rates of consumption of oxidizer and fuel per unit flame area and X_O and X_F are the oxidizer and fuel mole fractions. The

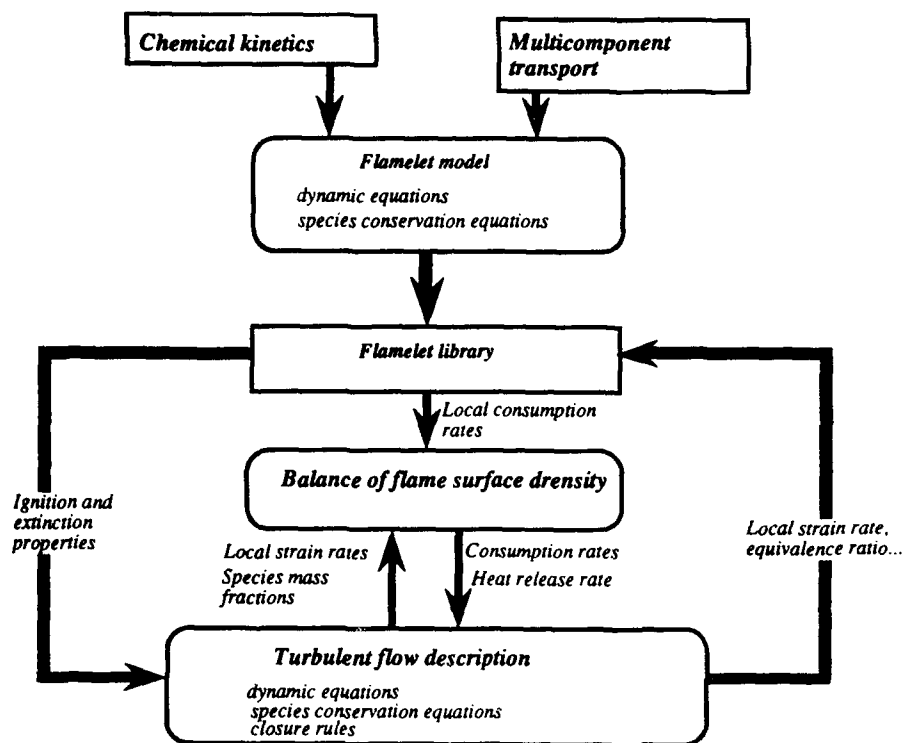


Figure 3. General organization of the coherent flamelet model.

production term describes the increase of flame area due to the local strain rate ϵ_s whereas the destruction term only takes into account the flame shortening mechanism due to mutual interaction of adjacent flame elements. The local strain rate plays an important role in this flamelet model and must be derived from known variables characterizing the turbulent flow (turbulent kinetic energy, dissipation, typical turbulent length scale, ...). In the case of a two dimensional mixing layer such as that shown in Figure 2 an estimate of the local strain rate ϵ_s may be deduced from the transverse gradient of the mean axial velocity :

$$\epsilon_s = \alpha |\partial u / \partial y|$$

This expression is applicable in simple flows like shear layers but it is not adequate in more complex situations where the strain rate may be evaluated in terms of the turbulent kinetic energy and dissipation.

Balance equation for the flame surface density in premixed configurations

The balance equation for the flame area plays a key role in this model. This equation describes the competition between the various processes which create or destroy flame area. It may be derived from first principles but some additional closure assumptions are also required. In the basic Coherent Flame Model the balance equation relating the local and

global description levels was written for the flame area per unit volume designated as Σ_f . Now, our recent applications to reactive flows with nonsteady changes of the mean pressure as found for example in studies of internal combustion engines indicate that a slightly different quantity is more adequate. In fact the flame area per unit mass S_f arises quite naturally in the derivation of an instantaneous balance of flame surface. The two quantities are of course related by $\Sigma_f = \rho S_f$. The balance equation for the mean flame area per unit mass may be derived by adopting the same procedure as that used for S_f (see Darabiha et al. 1987b). It is also possible to follow a different path and start from a general expression for the flame stretch as shown by Candel and Poinso (1990). In terms of the flame surface per unit mass, the following equation may be derived:

$$\frac{\partial(\rho S_f)}{\partial t} + \nabla \cdot \rho \mathbf{v} S_f = \rho [(\nu \nu + \eta \eta) : \nabla \mathbf{v}] S_f - n \cdot \nabla (\rho S_L S_f) \quad (5)$$

where ν and η are two unit vectors in the tangent plane to the flame.
Introducing the strain rate tensor

$$s_{ij} = \frac{1}{2} \left(\frac{\partial v_i}{\partial x_j} + \frac{\partial v_j}{\partial x_i} \right) \quad (6)$$

and using indices the previous expression becomes

$$\frac{\partial}{\partial t} (\rho S_f) + \frac{\partial}{\partial x_k} [\rho (v_k + S_L n_k) S_f] = \rho [(\nu_i \nu_j + \eta_i \eta_j) s_{ij}] S_f + \rho (S_L \nabla \cdot \mathbf{n}) S_f \quad (7)$$

The effect of the strain rate acting in the plane of the flame and of flame curvature appear explicitly in this balance. The combination of these two terms is known as the flame stretch (the fractional variation of flame surface element per unit time). In the following development we will neglect the terms containing the flame speed S_L and we use ϵ_S to designate the strain acting in the plane of the flame

$$\epsilon_S = (\nu_i \nu_j + \eta_i \eta_j) s_{ij} \quad (8)$$

These assumptions are adopted for simplicity but it is possible to write a more exact average equation including the flame relative motion and the curvature terms. Introducing the mass average decomposition of the different variables appearing in the balance equation for the flame surface one gets

$$\frac{\partial}{\partial t} (\bar{\rho} \tilde{S}) + \frac{\partial}{\partial x_k} (\bar{\rho} \tilde{v}_k \tilde{S}) = \bar{\rho} \tilde{\epsilon}_S \tilde{S} + \bar{\rho} \tilde{\epsilon}_S'' \tilde{S}'' + \frac{\partial}{\partial x_k} (-\bar{\rho} \tilde{v}_k \tilde{S}'') \quad (9)$$

At this point it is necessary to make use of closure assumptions. Adopting a gradient diffusion representation for the turbulent flux term one may write:

$$-\bar{\rho} \tilde{v}_k \tilde{S}'' = \frac{\mu_t}{\sigma_s} \frac{\partial \tilde{S}}{\partial x_k} \quad (10)$$

The first two terms on the right hand side of equation (9) may be estimated as

$$\bar{\rho} \tilde{\epsilon}_S \tilde{S} + \bar{\rho} \tilde{\epsilon}_S'' \tilde{S}'' = \alpha \bar{\rho} \tilde{\epsilon}_S \tilde{S} \quad (11)$$

where ϵ_S is a mean strain rate. This term describes the augmentation of material surface by the rate of strain. This expression of the production term differs slightly from that used in our previous work because we now consider the flame surface per unit mass. These assumptions are sufficient to close the balance of mean flame surface per unit mass S_f . However certain processes are not described by the previous equation. More specifically it is necessary to include a chemical shortening term similar to that appearing in the balance equation for the flame surface density S_f . This destruction term describing the process of flame shortening (the reduction of flame area by consumption of the reactants separating adjacent flame sheets) may take different forms. For premixed flames, one may consider that the fractional rate of annihilation of flame surface is proportional to the mass of fuel burnt per second and inversely proportional to the mass of fuel in the control volume V :

$$\left(\frac{1}{\bar{\rho} \tilde{S}_f} \frac{d \bar{\rho} \tilde{S}_f}{dt} \right)_A = -\beta \frac{\bar{\rho} \tilde{Q} \tilde{S}_f V / (-\Delta h_f^0)}{\bar{\rho} \tilde{Y}_F V} \quad (12)$$

where the heat release rate per unit flame area Q is obtained from the local flamelet calculations and $(-\Delta h_f^0)$ designates the heat release per unit mass of fuel. The annihilation term is then written as :

$$-\beta \bar{\rho} \frac{Q}{(-\Delta h_f^0) \tilde{Y}_F} \tilde{S}_f^2 \quad (14)$$

and the balance equation of flame surface per unit mass becomes

$$\frac{\partial}{\partial t} (\bar{\rho} \tilde{S}_f) + \frac{\partial}{\partial x_k} (\bar{\rho} \tilde{v}_k \tilde{S}_f) = \frac{\partial}{\partial x_k} \left[\frac{\mu_t}{\sigma_s} \frac{\partial \tilde{S}_f}{\partial x_k} \right] + \alpha \bar{\rho} \tilde{\epsilon}_S \tilde{S}_f - \beta \bar{\rho} \frac{Q}{(-\Delta h_f^0) \tilde{Y}_F} \tilde{S}_f^2$$

Numerical simulations based on this equation as well as physical arguments also indicate that the production term describing the effect of the strain rate should be modified to take into account limiting mechanisms like extinction. Furthermore the determination of the effective strain rate should take into account the scale of the turbulent eddies which are acting on the flame surface. It is shown by Poinso et al. (1990 a and b) that certain turbulent eddies are too small to interact efficiently with the flame and hence do not participate to the production of flame area by strain. There is a cut-off scale below which the turbulent fluctuations do not have a noticeable effect on the flame. It is also shown that quenching of the flame may take place in a range intermediate turbulent scales. When this process takes place some of the turbulent eddies (essentially the large scale eddies) participate to the production of flame area by the strain they impose to the reactive sheet while other turbulent scales have a contrary effect and tend to diminish the flame surface by quenching some portions of the reaction sheets. The production of flame surface associated with the strain rate is less efficient as this quantity takes large values. In a field of very high strain the process may even become completely ineffective and the strain may then only contribute to the destruction of flame surface. The analytical consequences of the study carried by Poinso et al. (1990 a) have not yet been fully exploited but it is nevertheless possible to write some simple models to account for these features. One idea is to modify the production term if the strain rate becomes too large. This may be done in various ways. For instance, one may consider a certain critical strain rate ϵ_{Se} (which depends on the local conditions and is determined from

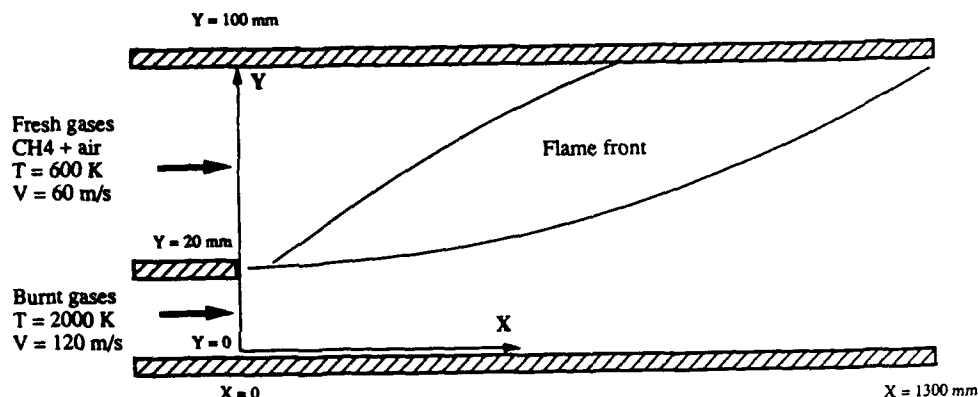


Figure 4. Experimental geometry of a turbulent methane-air flame stabilized by a parallel flow of burnt gases. (Experiment developed at ONERA by Moreau).

the local analysis or from direct simulations of the kind performed by Poinso et al. 1990 a) and write the destruction term as

$$-2\alpha\rho(\epsilon_S - \epsilon_{Se})h(\epsilon_S - \epsilon_{Se})S_f$$

where $h(x)$ is the Heavyside function $h(x) = 1$ if $x > 0$ and $h(x) = 0$ if $x < 0$. Another possibility is to multiply the production term by a function representing the efficiency of the strain rate (close to 1 for low strain rates and close to 0 for high strain rates). The function Q/Q_0 (where Q is the heat release rate per unit flame area -obtained from the local flamelet analysis- and Q_0 is the value of Q for $\epsilon_S = 0$) adequately represents the influence of the strain rate. The production term becomes

$$\alpha\tilde{\rho}\tilde{\epsilon}_S\tilde{S}_f\frac{Q}{Q_0} \quad (15)$$

This expression is used in the calculations presented in this paper. The balance equation for S_f is finally written as

$$\frac{\partial}{\partial t}(\tilde{\rho}\tilde{S}_f) + \frac{\partial}{\partial x_k}(\tilde{\rho}\tilde{v}_k\tilde{S}_f) = \frac{\partial}{\partial x_k}\left[\frac{\mu_t}{\sigma_S}\frac{\partial\tilde{S}_f}{\partial x_k}\right] + \alpha\tilde{\rho}\tilde{\epsilon}_S\tilde{S}_f\frac{Q}{Q_0} - \beta\tilde{\rho}\frac{Q}{(-\Delta h_f^0)}\tilde{S}_f^2 \quad (16)$$

The strain rate appearing in this equation may be evaluated from $\epsilon_S = C_s c/k$ and the constants used in the model take the following values : $\sigma_S = 1$, $\alpha = 10$, $\beta = 0.4$ and $C_s = 0.17$. It is probable that the final form of the balance equation for the flame area will also differ from that presented in this paper and the values of the constants will have to be adjusted. The consequences of some recent studies like those of Poinso et al. (1990 a and b) are not being incorporated in the model and many other ideas are being tested.

3. A TURBULENT PREMIXED FLAME STABILIZED IN A DUCT

The model is now tested in the case of a two dimensional high velocity turbulent premixed flame, stabilized by a parallel flow of burnt gases. The experimental setup shown in Fig. 4 was designed by Moreau at ONERA (Moreau 1977, Moreau and Boutier 1977). The reaction of a premixed air-methane stream in a square duct (100 mm x 100 mm) is initiated and stabilized in a mixing layer with a high velocity flow of hot gases produced by the stoichiometric burning of a secondary stream of air and methane. The velocity and temperature are respectively 60 m/s and 600 K for the fresh gases, 120 m/s

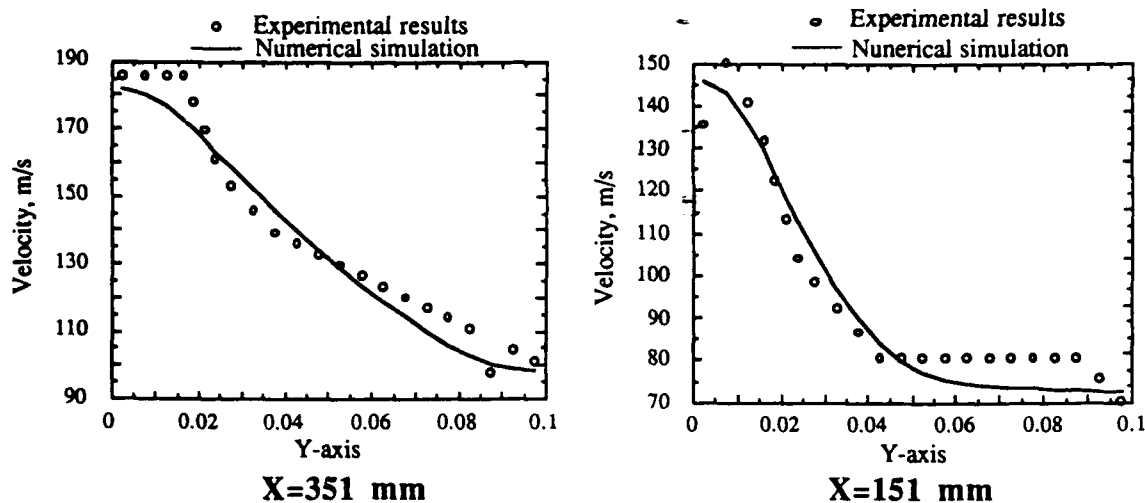


Figure 5. Comparison between calculated velocity profiles and measurements by laser Doppler anemometry (data from Moreau and Boutier 1977)

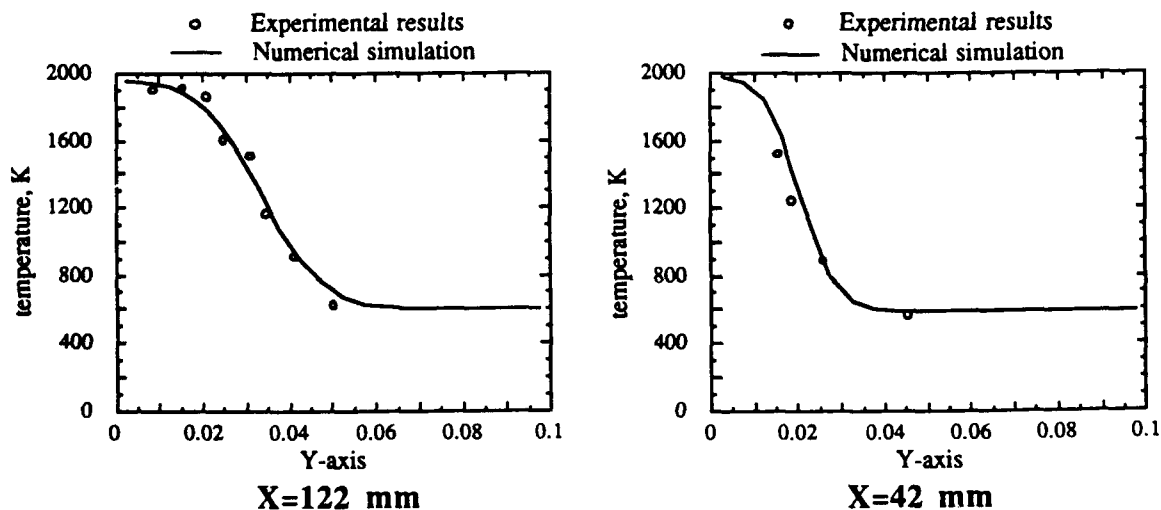


Figure 6. Comparison between calculated temperature profiles and measurements obtained by coherent anti-Stokes Raman scattering (CARS). Experimental data presented by Magre et al. 1985.

and 2000 K for the burnt gases. The turbulence level of the premixed fresh stream was about 10 percent and could be modified by introducing different sizes of grids in the upstream flow.

Numerical results are provided for an equivalence ratio of 0.8 where most experimental data are available. The calculations are compared with velocity profiles (from Laser Doppler Velocimetry measurements), temperature profiles from Coherent Anti-Stokes Raman Spectroscopy (CARS) and species mass fractions obtained with sampling probes and chromatography analysis. The experimental data are taken from Moreau (1977), Moreau and Boutier (1977), Moreau (1981) and Magre et al. (1985). Velocity profiles were measured for many sections all along the combustion chamber. Unfortunately, the experimental tests could not last more than 30 s because the combustor walls were not cooled during the run. The measured quantities are then only available for few sections of the flow, depending on the kind of measurement (locations $x = 42$ mm and $x = 122$ mm downstream from the splitter plate in the case of CARS measurements, locations $x = 130$ mm, $x = 330$ mm and $x = 430$ mm for chromatography analysis). Results of calculations are displayed in Fig. 5 to 7 together with the available data. The agreement is fairly good, both for the flame location and for the angle of the flame with respect to the mean flow, as may be seen in the velocity profiles (Fig. 5), temperature profiles (Fig. 6) and methane mass fractions profiles (Fig. 7). The model used in the calculations incorporates the results of the ITNFS analysis of Meneveau and Poinso (1990) in the balance equation for the mean flame surface density. The general flame structure is made apparent in Fig. 8 by plotting the calculated mean heat release source term, temperature and fuel mass fraction distribution.

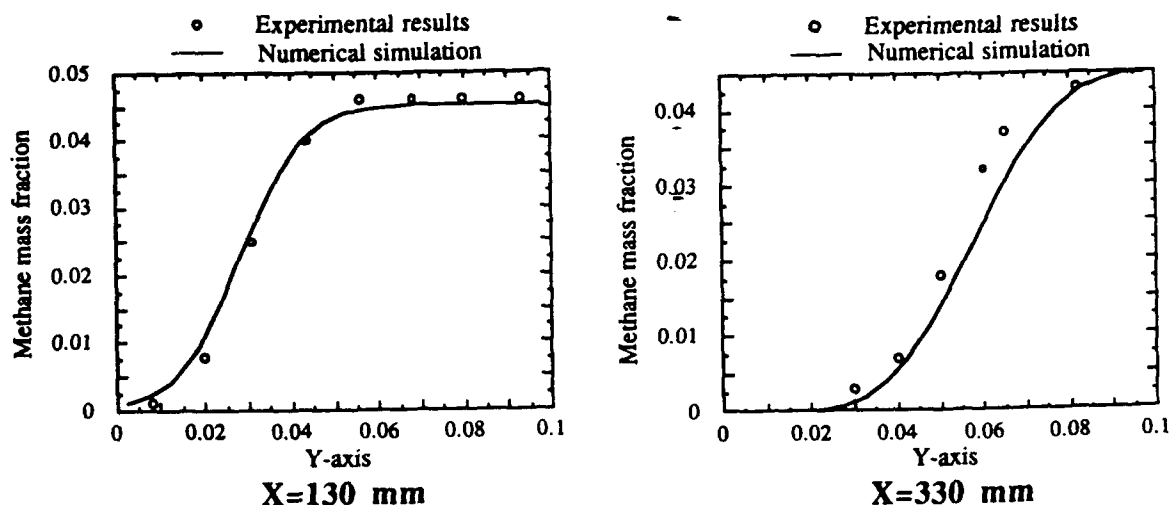


Figure 7. Comparison between calculated mass fraction profiles and experimental values determined by gas phase chromatography. Data from Moreau (1977, 1981)

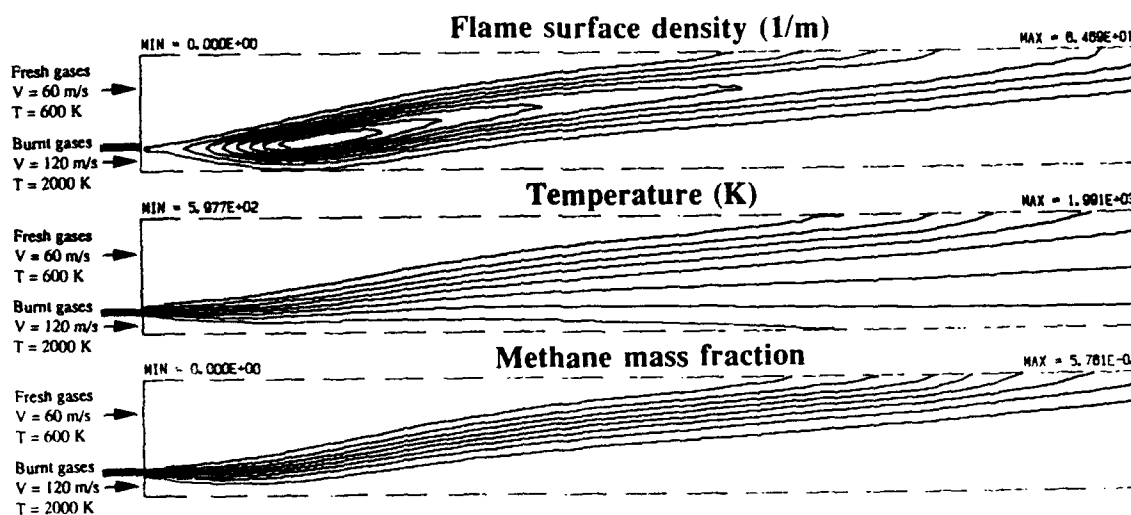


Figure 8. Flame structure. The distributions of mean heat release source terms, temperature and fuel mass fraction are plotted as iso-contours.

4. A MODEL RAMJET CONFIGURATION

Let us now consider experiments and calculations carried in a side dump two dimensional model of a ramjet combustor. In this case we will compare spatial maps of light emission from free radicals and computed distributions of heat release source terms.

Experimental configuration

Experiments are performed in a two-dimensional combustion chamber of constant cross-sectional area. A stream of air and propane is injected through two opposed inlets located on the top and bottom walls of the combustion chamber (fig. 9), the dimensions are reported in this figure). The top, bottom and rear walls of this chamber are made of an insulating material. The device is also equipped with quartz side-wall windows allowing a maximum optical access into the combustion zone. The outlet is of the same cross-sectional area as the combustion chamber and acts as an acoustically open

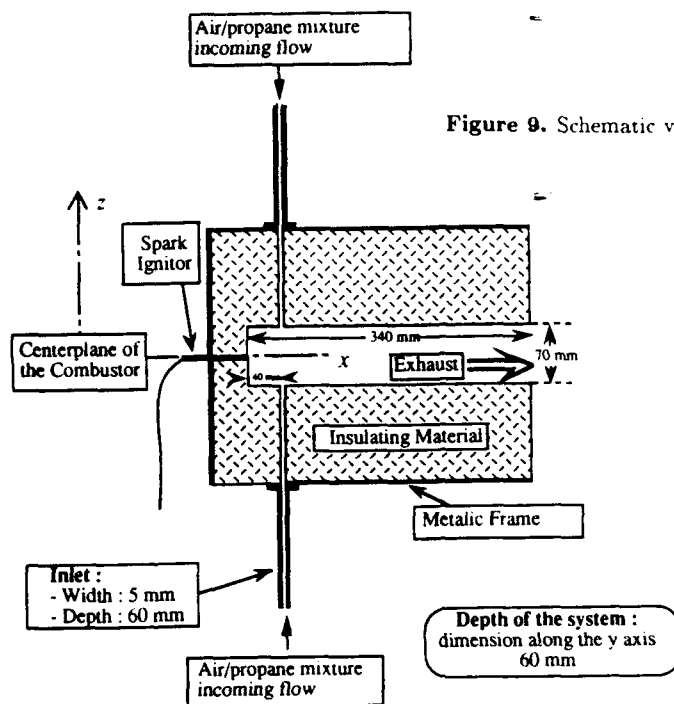


Figure 9. Schematic view of the model ramjet combustor.

end. The burnt gases are evacuated from the room by a separated exhaust system, not connected with the combustor. Ignition is triggered by a spark ignitor located in the rear wall of the combustion chamber. Four parameters determine the operating conditions of this experimental set-up (two parameters for each inlet): the two inlet velocities of the air/propane mixture, which range from 15 to 100 m/s and the two equivalence ratios (defined as $\Phi = (\dot{m}_f/\dot{m}_o)/(\dot{m}_f/\dot{m}_o)_{st}$), which range from 0.00 to 2.00. The present results correspond to symmetric operating conditions: inlet velocities equal to 20 m/s and equivalence ratios equal to 0.85, for both inlets. The average Reynolds number of the flow in the inlets, based on the inlet width (5 mm), is about 5000. Imaging of the C_2 free-radical emission distribution has been performed and provides experimental information which is interpreted as mean rates of heat release and can be compared with numerical calculations. C_2 free-radicals are created in the reaction zones and have short lifetimes (Dibble, Long, and Masri 1986). Consequently their natural chemiluminescence is a good indicator of the reaction zones. Images of the C_2 emission field can qualitatively be interpreted as heat release rate fields, thus allowing comparison with the computed fields.

Imaging system

Images are acquired with a video PULNIX TM 440 CCD camera (422 x 579 pixels at CCIR video standard) equipped with a C-mount BERTHLOT lens (20 mm focal length, $f/1.5$) and an interference filter at 516 nm (peak transmission 0.55 at 516 nm, bandwidth 8 nm). The camera was located at about 1 meter from the combustion chamber and oriented perpendicularly to the quartz windows, thus integrating the C_2 emission over the transverse dimension of the combustion chamber. The output video signal was digitized with a PHOTON frame-grabber and the resulting digital images were stored on a Macintosh II. The time exposure of each image is of 1/50 s. due to the video standard. Averaging of 10 images is performed to minimize the effects of turbulent fluctuations.

Numerical method

The reacting flow inside the two-dimensional combustion chamber is computed using a finite volume method (Dupoirieux and Scherrer 1985, Lacas 1989). Only the upper half part of the different fields is computed (due to the symmetry of the experimental operating conditions). A cartesian non-uniform grid of 19 x 41 cells is used. The boundary conditions are shown in Fig. 10. An acoustic impedance was imposed in the exhaust section to evacuate every longitudinal acoustic oscillation, thus achieving a faster convergence towards the steady-state solution.

At $t = 0$, the domain is filled with premixed air and propane with an equivalence ratio and temperature equal to those imposed in the injection section. A linear increase of the variables imposed in the injection plane, such as the mass flow-rate, is performed until the nominal value is attained. These values are then kept constant. Ignition is obtained by imposing a flame surface density in a small number of computational cells during one time step.

The calculations were performed for an injection velocity of 20 m/s and an equivalence ratio of 0.85. About 20000 steps were necessary to reach the convergence towards the steady-state solution.

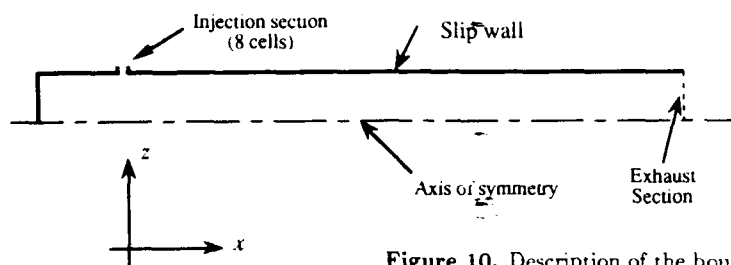


Figure 10. Description of the boundary conditions.

Results

A typical C_2 emission image (Fig. 11 a) shows the presence of two distinct zones of high intensity separated by the two impinging jets. These two main zones are distributed along the central axis of the combustion chamber and can be interpreted as turbulent combustion zones. Also, on both sides of the two jets, one observes elongated regions of significant intensity associated with the main combustion zones. They can be viewed as mixing layers where some laminar processes are still predominant and where laminar combustion occurs. Significant C_2 emission is observed in the jet interaction region. Finally, there is a dissymmetry of the C_2 emission pattern which may be due to slightly different values of the inlet velocity or the equivalence ratio in the two inlets. Comparison with the computed heat release rate field (fig. 11 b) shows that the CFM model is able to reproduce the general pattern of combustion inside the test section. The presence of two main combustion zones is fairly well predicted, especially regarding the locations of the heat release rate maxima. Some differences may be observed : extinction near the impingement region is not predicted and the interaction between the mixing layers and the combustion processes is not well reproduced. A research effort is currently being pursued in order to determine the origins of these discrepancies. Measurements of turbulence using LDV and comparison with computations is being planned and the results will be presented in a future publication.

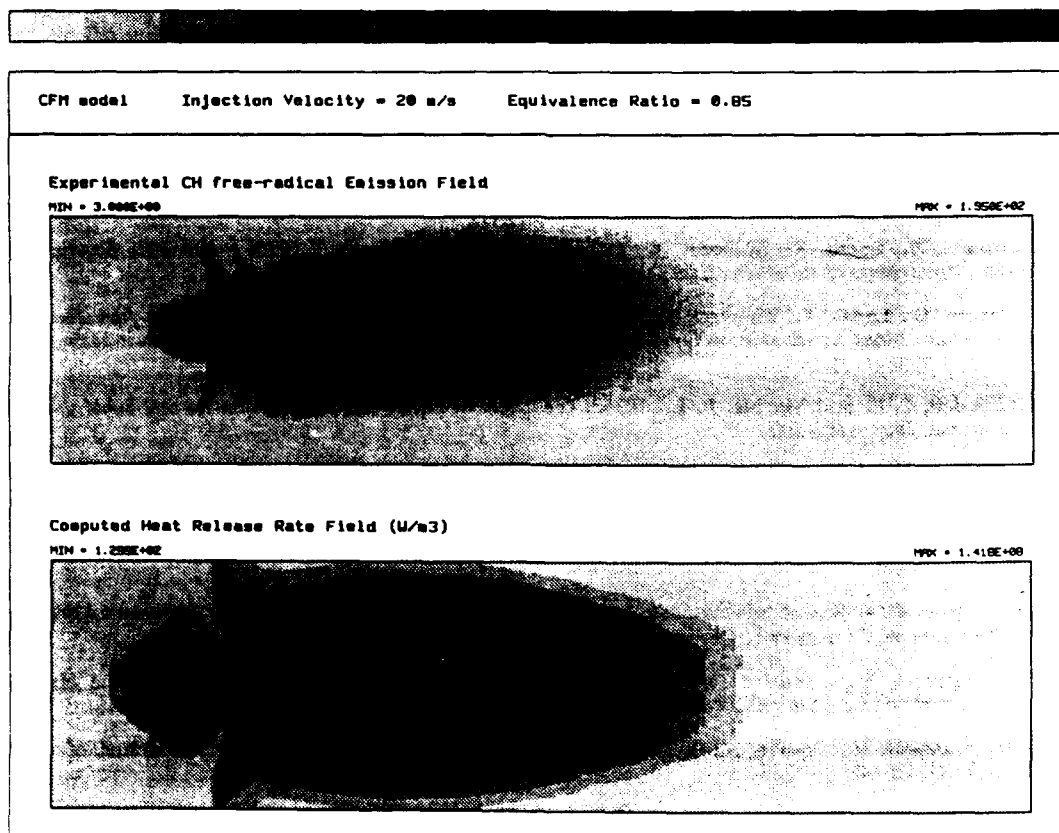


Figure 11. Comparison between calculations and experiments for an injection velocity of 20 m/s and an equivalence ratio $\Phi = 0.85$. Top view : experimental CH free-radical emission field. Bottom view : computed mean heat release field using the CFM model.

6. CONCLUSION

It is shown in this article that flamelet models based on the concept of flame surface and making use of a transport equation for the flame surface density provide a suitable description of turbulent reactive flows. Two cases of interest to propulsion applications are considered as examples. In the first a flame is stabilized by a hot stream of products. In the second the reaction takes place in a lateral injection model ramjet. In both cases the model predictions agree with experiments. While these results are quite encouraging as those obtained in other configurations treated previously, modifications of the model are being devised to describe extinction effects and to account for pollutant formation.

ACKNOWLEDGMENTS

The support provided to this research by SNECMA, DRET and Aérospatiale is gratefully acknowledged.

REFERENCES

- Barrère, M.** 1974, Modèles de combustion. *Revue Générale de Thermique*, vol. 148, 295-308.
- Borghi, R.** 1985, On the structure and morphology of turbulent premixed flames. *Recent Advances in Aeronautical Science*. C. Casci and C. Bruno, ed. Pergamon, pp. 117-138.
- Borghi, R.** 1988, Turbulent combustion modelling. *Progress in Energy and Combustion Science*, 14, p. 245
- Bray, K. N. C.** 1987, Methods on including realistic chemical reaction mechanisms in turbulent combustion model. *Complex Chemical Reactions*. J. Warnatz and W. Jager, ed. Springer Verlag, Heidelberg. pp. 356-375.
- Bray, K. N. C., Libby, P. A. and Moss, J. B.** 1984, Flamelet crossing frequencies and mean reaction rates in premixed turbulent combustion, *Combustion Science and Technology*, vol. 41, pp. 143-172.
- Brown, G.L. and Roshko, A.** 1974, On density effects and large structure in turbulent mixing layers, *Journal of Fluid Mechanics* vol. 64, pp. 775-816.
- Candel, S., Darabiha, N. and Esposito, E.** 1982, Models for a turbulent premixed turbulent combustor, *AIAA 18th Joint Propulsion Conference*, Cleveland, AIAA Paper 82-1261.
- Candel, S. M. and Poinso, T.** 1990, Flame stretch and the balance equation for the flame area, *Combustion Science and Technology*, vol. 70, pp. 1-15
- Candel, S., Veynante, D., Lacas, F., Maistret, E., Darabiha, E. and Poinso, T.** 1990a, Flamelet descriptions of turbulent combustion. *Proceedings of the 9th Int. Heat Transfer Conf.*, Jérusalem, August 1990.
- Candel, S., Veynante, D., Lacas, F., Maistret, E., Darabiha, E. and Poinso, T.** 1990b, Coherent flamelet model : applications and recent extensions. In *Advances in Combustion Modelling*, B. Laroutou, ed., Series on Advances in Math. for Appl. Sci., World Scientific, Singapore. pp. 19-64.
- Carrier, G. F., Fendell, F. E. and Marble, F. E.** 1975, The effect of strain rate on diffusion flames, *SIAM Journal of Applied Mathematics*, vol. 28, pp. 463-500.
- Clavin, P. and Williams, F. A.** 1982, Effects of molecular diffusion and of thermal expansion on the structure and dynamics of premixed flames in turbulent flows of large scales and low intensity, *Journal of Fluid Mechanics*, vol. 116, pp. 215-282.
- Correa, S. M. and Shyy, W.** 1987, Computational models and methods for continuous gaseous turbulent combustion, *Progress in Energy and Combustion Science*, vol. 13, pp. 249-292.
- Darabiha, N.** 1984, *Un modèle de flamme cohérente pour la combustion prémélangée. Analyse d'un foyer turbulent à élargissement brusque*, Doctoral Thesis, Ecole Centrale Paris, Chatenay-Malabry.
- Darabiha, N., Giovangigli, V., Candel, S. and Smooke, M. D.** 1988, Extinction of strained premixed propane-air flames with complex chemistry, *Combustion Science and Technology*, vol. 60, pp. 267-285.
- Darabiha, N., Giovangigli, V., Trouvé, A., Candel, S.M. and E. Esposito** (1987) Flamelet modeling of turbulent premixed flames, AGARD CP 442, 33-1, 33-16.
- Darabiha, N., Giovangigli, V., Trouvé, A., Candel, S. and Esposito, E.** 1987, Coherent flame description of turbulent premixed ducted flames. *Proceedings of the France-USA Joint Workshop on Turbulent Combustion. Turbulent Reactive Flows*. R. Borghi and S. N. B. Murthy, ed. Springer Verlag, New York. pp. 591-637.
- Dibble, R.W., M.B. Long, and A. Masri.** 1986, *In Progress in Astronautics and Aeronautics*. pp. 99-109. AIAA, New-York.

- Djavdan, E., Darabiha, N., Giovangigli, V. and Candel, S. M. 1990, Strained propane-air flames with detailed and reduced kinetic schemes, *Combustion Science and Technology*, Accepted for publication.
- Dupoirieux, F. and Scherrer, D. 1985, Methodes numériques à convergence rapide utilisées pour le calcul d'écoulements réactifs. *Numerical simulation of combustion phenomena*. R. Glowinski, B. Larrouturou and R. Temam, ed. Springer, Berlin. pp. 32-45.
- Karagozian, A. R. and Marble, F. E. 1986, Study of a diffusion flame in a stretched vortex, *Combustion Science and Technology*, vol. 46, pp. 65-84.
- Lacas, F. 1989, *Modélisation et simulation numérique de la combustion turbulente dans les moteurs fusée cryotechniques*. PhD Thesis, Ecole Centrale de Paris, France.
- Lacas, F., Veynante, D. and Candel, S. M. 1989, A numerical study of propagating premixed turbulent flames, *Numerical Combustion*, Antibes. A. Dervieux and B. Larrouturou, ed., Springer Verlag, Berlin. pp. 395-406.
- Lacas, F., Zikikout, S. and Candel, S. 1987, A comparison between calculated experimental mean source terms in non premixed turbulent combustion, *AIAA/SAE/ASME 23rd Joint Propulsion Conference*, AIAA Paper 87-1782.
- Laverdant, A. M. and Candel, S. M. 1988, A numerical analysis of a diffusion flame vortex interaction, *Combustion Science and Technology*, vol. 60, pp. 79.
- Laverdant, A. M. and Candel, S. 1989a, Computation of diffusion and premixed flames rolled up in vortex structures, *Journal of Propulsion and Power*, vol. 5, pp. 134-143.
- Libby, P. A., Sivasegram, S. and Whitelaw, J. A. 1986, Premixed combustion, *Progress in Energy and Combustion Science*, vol. 12, pp. 393-405.
- Libby, P. A. and Williams, F. A., ed. 1980, *Turbulent reacting flows*. Springer Verlag, New York.
- Liew, S. K., Bray, K. N. C. and Moss, J. B. 1981, A flamelet model of turbulent non premixed combustion, *Combustion Science and Technology*, vol. 27, pp. 69-73.
- Liu, J. T. C. 1988, Coherent mode interaction in developing free shear layers with application to coherent flames., Caltech, Pasadena. Marble Symposium.
- Magre, P., Moreau, P., Pealat, M. and Collin G., 1985 *Mesures par DRASC des températures instantanées dans une flamme turbulente air-méthane*, Technical Report ONERA 46/7104 EY, ONERA Chatillon.
- Maistret, E., Darabiha, E., Poinot, T., Veynante, D., Lacas, F., Candel, S. and Esposito, E. 1989, Recent developments in the coherent flamelet description of turbulent combustion, *Numerical Combustion*, Antibes. A. Dervieux and B. Larrouturou, ed., Springer Verlag, Berlin. pp. 98-117.
- Marble, F. E. 1985, Growth of a diffusion flame in the field of a vortex, *Advances in Aerospace Science*, C. Bruno and C. Casci eds., Plenum Press, New York, pp. 395-413.
- Marble, F. E. and Broadwell, J. E. 1977, *The coherent flame model of non-premixed turbulent combustion*. Report: TRW-9-PU.
- Marble, F. E. and Broadwell, J. E. 1979, *A theoretical analysis of nitric oxide production in a methane-air turbulent diffusion flame*. EPA Technical Report.
- Moreau, P. 1977, Turbulent flame development in a high velocity premixed flow. AIAA Paper 77-49, *15th Aerospace Science Meeting*, Los Angeles.
- Moreau, P. and Boutier A. 1977 Laser velocimeter measurements in a turbulent flame, *16th Symposium (Int) on Combustion*. The Combustion Institute, Pittsburgh.
- Moreau, P. 1981 Détermination expérimentale des fonctions de densités de probabilité de vitesse et de température dans une flamme turbulente, *La Recherche Aérospatiale* n°4 (1981) pp. 233-244.
- Peters, N. 1984, Laminar diffusion flamelets in non-premixed turbulent combustion, *Progress in Energy and Combustion Science*, vol. 10, pp. 319-339.
- Peters, N. 1986, Laminar flamelet concepts in turbulent combustion, *21st Symposium (International) on Combustion*, The Combustion Institute, Pittsburgh. pp. 1231-1250.
- Peters, N. 1988, *Turbulent modeling, scales and flame structure of premixed turbulent flames*. Report: Technical report.
- Poinot, T., Veynante, D. and Candel, S. M. 1990a, Diagrams of Premixed Turbulent Combustion Based on Direct Simulation, *23rd Symposium (Int) on Combustion*, The Combustion Institute, Pittsburgh.
- Poinot, T., Veynante, D. and Candel, S. M. 1990b, Direct simulation of quenching in premixed turbulent combustion, *accepted Journal of Fluid Mechanics*.
- Poinot, T. and Meneveau 1990 Submitted for publication to *Combustion and Flame*.
- Pope, S. B. and Cheng, W. K. 1988, The stochastic flamelet model of turbulent combustion, *22nd Symposium (International) on Combustion*, The Combustion Institute, Pittsburgh. pp. 781-789.
- Pope, S. B. 1990, *23rd Symposium (International) on Combustion*, The Combustion Institute, Pittsburgh.

Spalding, D. B. 1978. The influence of laminar transport and chemical kinetics on the time mean reaction rate in a turbulent flame. *17th Symposium (International) on Combustion*, Pittsburgh. The Combustion Institute, Pittsburgh. pp. 431.

Veynante, D., Candel, S. and Martin, J. P. 1987. Coherent flame modelling of chemical reaction in a turbulent mixing layer. *Complex Chemical Reactions*, J. Warnatz and W. Jager, eds. Springer Verlag, Berlin, Heidelberg. pp. 386-398.

Veynante, D., Lacas, F. and Candel, S. 1989a. A new flamelet combustion model combining premixed and nonpremixed turbulent flames, *Aerospace Science Meeting*, AIAA Paper 89-487.

Veynante, D., Lacas, F. and Candel, S. 1989b. Numerical simulation of the transient ignition regime of a turbulent diffusion flame, *accepted for publication in AIAA Journal*.

Veynante, D., Lacas, F., Maistret, E. and Candel, S. 1989c. Coherent flame model in non uniformly premixed turbulent flames, *7th Symposium on Turbulent Shear Flows*, Stanford. pp. 26.2.1-26.2.6.

Williams, F. A. 1975. A review of some theoretical combustions of turbulent flame structure. *AGARD Conference Proceedings*, pp. II.1.1-25.

Williams, F. A. 1985, *Combustion Theory*. Benjamin Cummings, Menlo Park, CA.

Discussion

F. PITT, ONERA, FRANCE

Dans ce modèle, comment tenez vous compte des effets de richesse?

AUTHOR'S REPLY

Dans ce type de modèle où les calculs de cinétique chimique sont découplés des calculs d'aérothermochimie, les effets de richesse interviennent au niveau du taux de dégagement chaleur par unité de surface de flamme (Q dans les équations). Il faut cependant pouvoir disposer de concentration en combustible dans les gaz frais. Il est donc nécessaire d'écrire une équation de bilan pour cette quantité. Cette équation intervient surtout par ces valeurs aux frontières, qui peuvent subir d'importantes variations (cas de la zone primaire et du met d'air secondaire dans une chambre de combustion de turboréacteur par exemple).

M. FORDE, UNIV. OF TRONDHEIM, NORWAY

1) How much does the model depend on the chemical reaction rates?

2) Have you done any variation of the parameters in order to see the sensitivity of your model?

AUTHOR'S REPLY

1) In the case of common fuels and steady flows, we could observe only little dependence on the chemistry of the reaction. But for unsteady flows, this effect is much more important. In that case, we could observe some flames which were blown out in the case of propane as fuel, while they were steady turbulent flames for hydrogen. So we were able to conclude that our model is able to represent some chemistry effects on the flame. We have made a parametric study of our model (regarding the parameters of the model itself and the effect of heat release rate per unit flame area). These computations were made in the case of propagating turbulent flames. See for instance LACAS et al. or FICHOT et al.

REFERENCES

Lacas, F., Veynante, D., and Candel, S.: "A numerical study of propagating premixed turbulent flames," 3rd International Conference on Numerical Combustion, Antibes, France, May 23-26, 1989.

Fichot F., Lacas, F., Veynante, D., Candel, S.: "One dimensional propagation of a premixed turbulent flame with the coherent flame model," submitted to Combustion Science and Technology, 1991.





NONEQUILIBRIUM 3D FLOWS OF AIR THROUGH INLETS

Roberto Marsilio and Maurizio Pandolfi

Dipartimento di Ingegneria Aeronautica e Spaziale
Politecnico di Torino
C.so Duca degli Abruzzi, 24 - 10129 Torino, ITALY

92-16099



Abstract

The hypersonic nonequilibrium flow of air through inlets of propulsion devices is investigated. The fluid dynamics is described by the Euler equations and a chemical model accounts for finite rate equations. The numerical procedure is based upon a space-marching technique, under the hypothesis of fully developed supersonic flow. The conservative form of the Euler and finite-rate chemical equations are integrated, following a finite volume discretization and a flux-difference splitting procedure. The numerical scheme is of the second order accuracy, with a proper TVD technique to avoid spurious oscillations at flow discontinuities. Numerical results are presented and discussed.

1. Introduction

The physics of hypersonic flows is rather complicated. Some of the fluid dynamics aspects, such as shock waves and contact surfaces, are described by the Euler equations. Effects related to viscosity and thermal conductivity and due to transport phenomena are accounted by the additional terms of the Navier-Stokes equations. Moreover, the large amount of kinetic energy available in the hypersonic regime promotes variations of thermodynamical characteristics and the generation of new chemical species, even in pure air flows. Depending on the scale of the physical problem, thermodynamics and chemistry can be approximated by equilibrium conditions or have to be described as nonequilibrium phenomena, according to additional differential equations.

In this paper, we confine our attention to the interaction of the basic fluid dynamics, described by the Euler equations, with the chemical nonequilibrium, predicted on the basis of the finite

rate equations.

In the following we present the governing equations for supersonic steady flow in chemical non-equilibrium and report on the numerical method based upon a space marching technique. The approximation is founded on a finite volume approach and the fluxes at the side walls of the volumes are evaluated according to a flux-difference splitting procedure, specifically conceived for steady supersonic flows. A second order of accuracy scheme is shown and the treatment at the boundary (solid walls) is presented. Finally numerical results are reported and discussed.

2. Equations

We consider the Euler equations for steady flows and adopt the model proposed in [1] for the chemical relaxation in the air. We take into account five species (O , N , NO , O_2 , N_2) and seventeen reactions. The thermodynamics is assumed to be frozen, with the vibrational energy corresponding to the half-excited mode. Such a hypothesis is rather crude, but our attention in the present investigation is focused on the chemical relaxation. A more realistic description of nonequilibrium thermodynamics will be introduced in the next future.

We define ρ_i , the partial density of the i -species:

$$\rho_i = \rho Y_i = \rho \mu_i q_i$$

where Y_i and q_i denote respectively the mass and molar concentrations and μ_i the molecular mass.

Owing to the conservation of the atomic species, we will consider the finite rate equations only for three species. In particular, we look at the generation of O , N , NO , ($i = 1, 2, 3$) and obtain the concentration of O_2 , N_2 , ($i = 4, 5$) by:

$$Y_4 = Y_{4\infty} - \frac{\mu_4}{2} \left(\frac{Y_1}{\mu_1} + \frac{Y_3}{\mu_3} \right)$$

$$Y_5 = Y_{5\infty} - \frac{\mu_5}{2} \left(\frac{Y_2}{\mu_2} + \frac{Y_3}{\mu_3} \right)$$

where the ∞ -values refer to the upstream undisturbed air concentrations ($Y_{1\infty} = Y_{2\infty} = Y_{3\infty} = 0$, $Y_{4\infty} = 0.233$, $Y_{5\infty} = 0.767$).

The rates of the production of the species per unit volume are denoted hereafter by Ω_i and are evaluated on the basis of formulas and constants suggested in [1].

Being $R_i = R/\mu_i$ the elasticity constant of the i -species, the specific heat at constant pressure is given by:

$$c_{p,i} = \frac{5}{2} R_i \quad (\text{for } N, O)$$

$$c_{p,i} = \left(\frac{7}{2} + \frac{1}{2} \right) R_i \quad (\text{for } NO, O_2, N_2)$$

The additional 1/2 for the molecules refers to the approximation of the half-excited vibration.

The air in the non-equilibrium evolution is considered as a mixture of perfect gases. Therefore, the equation of state is given by:

$$\frac{p}{\rho} = \sum_{i=1}^5 R_i Y_i T$$

where the density of the mixture is $\rho = \sum_{i=1}^5 \rho_i$.

The enthalpy is defined as

$$h = h_{for} + \sum_{i=1}^5 c_{p,i} Y_i T$$

where h_{for} represents the total heat of formation:

$$h_{for} = \sum_{i=1}^3 Y_i h_i^0$$

and h_i^0 is the heat of formation of the i species.

Finally it is convenient to introduce γ as the frozen ratio of the specific heats:

$$\gamma = \frac{\sum_{i=1}^5 c_{p,i} Y_i}{\sum_{i=1}^5 (c_{p,i} - R_i) Y_i}$$

The frozen speed of sound is given by:

$$a_f^2 = \gamma \frac{p}{\rho}$$

The governing equations are represented by the laws of conservation written as:

$$\begin{aligned} \int_{\partial Vol} \rho_i \mathbf{V} \cdot d\mathbf{S} &= \int_{Vol} \Omega_i dVol \\ \int_{\partial Vol} \rho \mathbf{V} \cdot d\mathbf{S} &= 0 \\ \int_{\partial Vol} \rho \mathbf{V} (\mathbf{V} \cdot d\mathbf{S}) + \int_{\partial Vol} p d\mathbf{S} &= 0 \\ \int_{\partial Vol} (p + e) \mathbf{V} \cdot d\mathbf{S} &= 0 \end{aligned} \quad (1)$$

for $i = 1, 3$. Here e is the total internal energy by unit volume, \mathbf{V} is the velocity vector, Vol , ∂Vol , and $d\mathbf{S}$ are the control volume, the whole surface of the control volume and the surface elementary element, respectively.

The first three equations ($i = 1, 3$) refer to the continuity the species O , N , NO . The convective flux of the mass for each i -species over the surface ∂Vol is balanced by the rate of production Ω_i in the volume Vol , being the diffusion of the i -species neglected. The fourth, fifth and sixth equations represent the continuity of the mixture, the equilibrium of the forces and the energy balance.

3. Finite Volume Approach

The finite volume approach is applied straightforward to the integral form of the governing equations (1). For simplicity, the two-dimensional case is considered in the present analysis. Only formal and not fundamental difficulties are added in the three-dimensional problem.

Let x and y be two space coordinates, \mathbf{n} the unit vector of the control surface S , n_x and n_y the corresponding components of \mathbf{n} , respectively. With reference to the Fig. 1 the governing equations (1) may be written as

$$\int_{\partial Vol} w n_x dS + \int_{\partial Vol} f n_y dS = \int_{Vol} g dVol \quad (2)$$

where

$$w = \begin{Bmatrix} \rho_1 u \\ \rho_3 u \\ \rho u \\ p + \rho u^2 \\ \rho u v \\ (p + e)u \end{Bmatrix}; \quad f = \begin{Bmatrix} \rho_1 v \\ \rho_3 v \\ \rho v \\ \rho u v \\ p + \rho v^2 \\ (p + e)v \end{Bmatrix};$$

$$g = \begin{Bmatrix} \Omega_1 \\ \Omega_2 \\ \Omega_3 \\ 0 \\ 0 \\ 0 \\ 0 \end{Bmatrix}$$

Here, u and v are the components of the velocity vector \mathbf{V} along x and y , w , f and g are the flux vectors in the directions x and y and the rate of production of the species vector, respectively.

Now, let x be the hyperbolic direction (the flow is supersonic along it), so that it plays the role of the marching direction. Hence, being the flux values known at the abscissa x , we may determine, using Eq. (2), the new values of the flux at the abscissa $x + Dx$, according with the space-marching technique. We divide the computational domain into quadrilateral cells (volumes) where the geometry is completely known, as sketched in Fig. 2. The computational points of the cell are A and C . The point A is an initial data point whilst C is the point where the solution has to be computed. Therefore, the Eq. (2) takes the following approximated form:

$$\begin{aligned} & w_A^k(y_2 - y_1) + w_D^k(y_3 - y_2) + w_C^k(y_4 - y_3) + \\ & w_D^k(y_1 - y_4) + f_B^k(x_3 - x_2) + f_D^k(x_1 - x_4) = \\ & g^k \frac{(y_2 - y_1) + (y_3 - y_4)}{2} \end{aligned} \quad (3)$$

where w_j^k and f_j^k are the k flux components ($k = 1, 7$) computed at the points j ($j = A, B, C, D$) and g^k is the vector component computed at the center of the cell. The flux vectors w and f , at the cell interfaces (points B, D), are evaluated according to the flux difference splitting procedure, as shown hereafter.

4. Flux Difference Splitting

The basic steps of the flux difference splitting formulation are the definition and the solution of an appropriate Riemann problem. We would like to address the reader not familiar with this formulation conceived for steady supersonic flows to [2] for more details on this matter.

Let us point our attention to the point B (see Fig. 2). In order to predict w_D and f_D , we consider the flow properties at the points (N) and $(N + 1)$, and define the Riemann problem with piecewise constant values distributions, by

generating a discontinuity at the interface location $(N + 1/2)$, as shown in Fig. 3. The collapse of this discontinuity generates three waves, two acoustic waves (I, III) and one contact surface (II). On the basis of the two initial uniform regions (a and b , corresponding to N and $N + 1$), the two new uniform regions c and d are generated (see Figs. 4a,b,d).

We proceed to the approximate solution of this Riemann problem, according to the suggestions proposed in [2]. In addition, we make the approximation of considering frozen the concentrations of the species after the collapse of the discontinuity. Therefore, the initial concentrations in regions a and b , given by the initial data and generally different each other, remain unchanged through the acoustic waves (I, III), respectively in regions c and d . This approximation is added, in agreement to the original assumption of considering isentropic the evolution through the acoustic waves.

Let us consider the Euler equations for the steady supersonic flow and the finite rate equations written in the quasi-linear form. It is convenient to introduce, as dependent variables, the logarithm of the pressure ($P = \ln(p)$), the slope of the streamline ($\sigma = v/u$) and the enthalpy (h). Owing to their hyperbolic nature, the quasi-linear equations may be replaced by the compatibility equations which describe the convection of signals. The collapse of the initial discontinuity shown in Fig. 3 is governed by these compatibility equations. The discontinuity generates a pattern of waves I, II and III (Figs. 4a,b,c) and the two new uniform flow regions c and d can be predicted from the initial ones a and b , as it follows. We define the slopes of the characteristic lines:

$$\begin{aligned} \lambda_1 &= \frac{u^2\sigma - a_f^2\beta}{u^2 - a_f^2} \\ \lambda_2 &= \sigma \\ \lambda_3 &= \frac{u^2\sigma + a_f^2\beta}{u^2 - a_f^2} \end{aligned}$$

and the signals dR_1 , dR_2 and dR_3 that propagate along them, according to compatibility equations:

$$dR_1 = dP - \frac{\gamma u^2}{a_f^2\beta} d\sigma \quad (4)$$

$$dR_2 = dh - \frac{P}{\rho} dP \quad (5)$$

$$dR_3 = dP + \frac{\gamma u^2}{a_f^2\beta} d\sigma \quad (6)$$

where $\beta = \sqrt{M^2 - 1}$, where M is denoting the Mach number.

With reference to any of Figs. 4a,b,c, we consider the definitions in equations (5 and 6) and we note that through the wave I we have:

$$P_c + \left(\frac{\gamma u^2}{a_f^2 \beta} \right)_a \sigma_c = R_{3a}$$

$$h_c - \left(\frac{p}{\rho} \right)_a P_c = R_{2a}$$

where:

$$R_{3a} = P_a + \left(\frac{\gamma u^2}{a_f^2 \beta} \right)_a \sigma_a$$

$$R_{2a} = h_a - \left(\frac{p}{\rho} \right)_a P_a$$

On the contact surface (wave II) we impose the usual continuity of pressure and the stream-line direction:

$$P_c = P_d \quad ; \quad \sigma_c = \sigma_d$$

Finally, on the basis of definitions in equations (4 and 5), the compatibility equations through the wave III , give:

$$P_d - \left(\frac{\gamma u^2}{a_f^2 \beta} \right)_b \sigma_d = R_{1b}$$

$$h_d - \left(\frac{p}{\rho} \right)_b P_d = R_{2b}$$

where:

$$R_{1b} = P_b - \left(\frac{\gamma u^2}{a_f^2 \beta} \right)_b \sigma_b$$

$$R_{2b} = h_b - \left(\frac{p}{\rho} \right)_b P_b$$

The evaluation of unknowns p , h and σ in regions c and d proceeds straightly from the above conditions. We have:

$$\sigma_c = \sigma_d = \frac{R_{3a} - R_{1b}}{\left(\frac{\gamma u^2}{a_f^2 \beta} \right)_a + \left(\frac{\gamma u^2}{a_f^2 \beta} \right)_b}$$

$$P_c = P_d = R_{3a} - \left(\frac{\gamma u^2}{a_f^2 \beta} \right)_a \sigma_c$$

$$h_c = R_{2a} + \left(\frac{p}{\rho} \right)_a P_c$$

$$h_d = R_{2b} + \left(\frac{p}{\rho} \right)_b P_d$$

Being the concentrations frozen through the acoustic waves, we have:

$$Y_{ic} = Y_{ia} \quad Y_{id} = Y_{ib}$$

and therefore:

$$(h_{for})_c = (h_{for})_a \quad (h_{for})_d = (h_{for})_b$$

All the flow properties in regions c and d , in particular w and f , follow immediately. We look now at the direction of propagation of each wave and identify the region (one among a , c , d or b) that includes the volume interface between two adjacent cells. For instance, in the case of Fig. 4a the interface falls in region c . In the cases of Fig. 4b and Fig. 4c, we have the regions d and a , respectively. Then, we define the flux vectors w , f at the interface on the basis of the flow properties that pertain to this region. Namely, the variable $w_{N+\frac{1}{2}}^k$ is evaluated as:

$$w_{N+\frac{1}{2}}^k = w_{N+1}^k - \Delta^l w^k \quad (7)$$

or

$$w_{N+\frac{1}{2}}^k = w_N^k + \Delta^r w^k$$

where $\Delta^l w^k$ (or $\Delta^r w^k$) is the flux difference through the waves propagating with slopes greater (or smaller) than of the slope of volume interface. For the first order scheme, in the case of Fig. 4a, we have:

$$\Delta^l w^k = (w_b^k - w_d^k) + (w_d^k - w_c^k) \quad (8)$$

or

$$\Delta^r w^k = (w_c^k - w_a^k)$$

for the case of Fig. 4b

$$\Delta^l w^k = (w_b^k - w_d^k) \quad (9)$$

or

$$\Delta^r w^k = (w_d^k - w_c^k) + (w_c^k - w_a^k)$$

and for the case of Fig. 4c

$$\Delta^l w^k = (w_b^k - w_d^k) + (w_d^k - w_c^k) + (w_c^k - w_a^k) \quad (10)$$

or

$$\Delta^r w^k = 0$$

A similar evaluation is done for the interface flux $f_{N+\frac{1}{2}}$.

The same procedure is developed at the point D (see Fig. 2), at the location $(N - 1/2)$, solving the Riemann problem defined with the points (N) and $(N - 1)$, for computing the values of $w_{N-\frac{1}{2}}$ and $f_{N-\frac{1}{2}}$.

The most interesting cases occur when a sonic transition shows up within one of the fans that describe the acoustic waves *I*, *III*. These are the cases where the volume interface is embedded in a compression or an expansion fan. We refer the reader to [2] for more details.

5. Second Order

We have developed a second order of accuracy numerical scheme. This is shown hereafter. The flux difference $\Delta^l w^k$ in Eq. (7) may be defined as:

$$\Delta^l w^k = (\Delta^l w^k)' + (\Delta^l w^k)'' \quad (11)$$

where $(\Delta^l w^k)'$ is the first order flux difference, computed by Eqs. (8), (9), (10). The term $(\Delta^l w^k)''$ is the second order flux difference correction, defined as:

$$(\Delta^l w^k)'' = \frac{\delta(r^k)}{2} \sum_{i=1}^3 \left[\frac{|\lambda_i|}{\lambda_i} - \frac{\Delta x}{\Delta y} \lambda_i \right] (w_{N+1}^k - w_N^k) \quad (12)$$

where λ_i is the slope *i*-characteristic line, $\delta(r^k)$ is the flux limiter to ensure the scheme be TVD (Total Variation Diminishing). In our case we have chosen the Van Albada flux limiter [3], defined as:

$$\delta(r) = \frac{r + r^2}{1 + r^2}$$

The argument r^k depends of the gradient of the flux w

$$r^k = \frac{w_N^k - w_{N-1}^k}{w_{N+1}^k - w_N^k} \quad \text{if } \lambda_i > 0$$

or

$$r^k = \frac{w_{N+2}^k - w_{N+1}^k}{w_{N+1}^k - w_N^k} \quad \text{if } \lambda_i < 0$$

More details on the TVD schemes may be found in [4] and [5].

6. Boundary Conditions

The boundary we consider here is represented by solid walls. We assume the volume at the boundary lying on the wall, as shown in Fig. 5. Let *C* be the point of the surface of the cell where we predict the flow, *A* the initial data point and *D* the interface point on the boundary where we need the appropriate values of w_D and f_D . Since there are no volumes below the point *D* at the boundary, we can not define a Riemann problem as at the interior volumes. Instead, we define a half Riemann problem, by assuming the flow in the region *b* determined by the point *A* and imposing the slope of the streamline in the region *d* equal to the slope of the wall (σ_w). The wave *I* does not appear, the wave *II* runs along the wall and only the wave *III* propagates in the flow field. The values of w_D and f_D are computed from the flow properties in the region *d*. The latter are obtained by the approximate solution of the half Riemann problem, through the wave *III*:

$$P_d = P_b - \left(\frac{\gamma u^2}{a_f^2 \beta} \right)_b (\sigma_b - \sigma_w)$$

$$\sigma_d = \sigma_w$$

$$h_d = h_b - \left(\frac{p}{\rho} \right)_b (P_b - P_d)$$

7. Numerical Experiments

We have carried out some preliminary computations in order to validate the numerical methodology. Here we refer on two sets of numerical experiments: 2D hypersonic non-equilibrium flows and 3D supersonic non-reacting flows.

In the first set of numerical experiments, we have considered the hypersonic flow over a 30° ramp and the upstream conditions already prescribed in [6]: $V_\infty = 6.7[km/sec]$, $p_\infty = 10.85[N/m^2]$, $T_\infty = 237.1[K]$. The initial data needed in the space marching technique are given by the exact analytical solution of the non-reacting flow over a ramp, which represents a correct physical solution at very small distances from the corner of the ramp. We have assumed the finite volumes defined by a grid obtained with rays originated at the ramp corner and planes normal to the abscissa *x*. Therefore, the grid is described in a self-similar fashion. The computational region is confined by the outer boundary, a ray inclined by 37.2° over the

x -axis and by the inner one, the ramp at 30° . The shock layer for the frozen flow at the initial x -station extends, along the y -coordinate, through about 80% of the computational domain. The results shown in the following have been obtained with a 40 intervals grid along y .

Since in the initial exact data the shock is a sharp discontinuity, we have performed some integration steps to build up a stable structure of the numerically captured shock. The distribution of the pressure of the initial frozen flow, along the normalized coordinate y/x , with initial frozen flow, is shown in Fig. 6. We have assumed these initial data given at the abscissa $x = 10^{-3}$ [m]. Here the concentrations of the species are practically the same as in the upstream flow. Indeed, no time is allowed to the particles in the shock layer to develop any appreciable reaction over such short distances, even if the rate of production of the new species are the highest.

We have carried out the integration from the initial station, ($x = 10^{-3}$ [m]), very far downstream, up to $x = 10^3$ [m]. There, the flow is in full equilibrium all over the shock layer, except through the chemical layer, just behind the shock, the width of which becomes infinitesimally small with respect to whole width of the shock layer.

We have found the same description of the non equilibrium phenomenology as already reported by [6] and [7]. It is convenient to compare our present results with those shown in these two references. Note that the results from [6] and [7] are based upon a slightly different chemical model and on the assumption of a constant average molecular mass for the gas mixture all over the flow field. Moreover, the method of characteristics has been used in [6] and the lambda formulation (a finite difference version of the method of characteristics) matched to the shock fitting technique, in [7].

The distribution of the pressure at the wall, along the ramp, is shown in Fig. 7. Close to the ramp corner, the pressure is at the level of the frozen flow. Then, it goes smoothly down to the level of the equilibrium flow. The solid line refers to the present computations, and the circles to [7]. Note the peaks in pressure that show up periodically in our results. We have studied the problem and found that these disturbing oscillations are due to the passage of the shock across the grid points, as the shock itself moves towards the wall, going from the frozen to the equilibrium configuration. In fact, the problem was predictable already from the pressure distribution for the frozen flow plotted in Fig. 6. We note the overshooting of the pressure just behind

the shock and the too sharp and unusual transition of the captured shock. The problem does not appear at lower Mach number. More precisely, it shows up when the component of the upstream Mach number normal to the oblique shock grows over certain values. In these cases, the approximate solver of the Riemann problem, in particular the assumption of isentropic transition across the acoustic waves (I, III), becomes too rough. Therefore, the prediction of the domains of dependence in the approximate solution results too far from the correct one, which is consistent with the proper dissipation and jump of entropy. The violation of the domains of dependence makes the flux difference splitting incorrect and the overshooting shows up. Let us remark that the problem is originated when the difference of the flux is split. Nevertheless, since the numerical integration is conservative, the correct jump in entropy is predicted in the updated solution. We have understood the problem, we know how to fix it and we will do it in the next future. For the present time, let us accept this overshooting that is responsible for the disturbing peaks of the pressure in Fig. 7.

The development of the slope of the oblique shock is shown in Fig. 8, where the angle θ_h is plotted. Because the shock is numerically captured, we have denoted the shock location by the interval of the grid where the highest dissipation (increasing of entropy) occurs. This explains the discontinuous behaviour of the present results. Here we have the comparison with results from [6] (triangles) and [7] (circles).

The evolution of the chemical relaxation is shown in Figs. 9 and 10, with reference to the concentration of O and NO, respectively. Note that the agreement in the concentrations with the results from [6] and [7] is due to the close similarity of the chemical model used here and there, while the difference in the pressure and slope of the shock are probably related to the different equation of state, because of the different definition of the molecular weight.

Finally the distribution of the pressure over the shock layer, very far downstream and corresponding to the equilibrium configuration, is shown in Fig. 6. Note that the disturbing overshooting at the shock is disappeared, because the Mach number component normal to the shock is lower in the equilibrium configuration.

More comments on the physical aspects of this non-equilibrium flow are reported in [6] and [7]. We would like to address the reader to this references for more detailed information on this matter.

The second set of numerical results refers to three-dimensional flows, in the supersonic

regime, so that no appreciable chemical relaxation occurs. We have computed the conical pattern of corner flows, generated by two adjacent ramps. The flow pattern is quite complex and characterized by shocks and contact surfaces. A typical case is shown in Figs. 11 and 12, where contour lines for the pressure and the entropy are plotted over a plane normal to the x -axis, with the normalized coordinates y/x and z/x . We observe the irregular reflection of the shocks generated by the two ramps and the formation of a Mach stem. Moreover, in Fig. 12 we see the contact surfaces originated at the shock intersections and pointing towards the entropy singularity at the corner line. The results refer to two orthogonal ramps, both presenting the angle of 12.2° and $M_\infty = 2.47$. The grid size in the y/x and z/x plane is 145×145 . The upstream flow condition and the geometry of the ramps are the same presented in [8], where the flow has been predicted on the basis of the lambda formulation and a sophisticated shock fitting technique. The comparison of the present results, given in Figs. 11 and 12, with similar plots reported in [8] is very good and no differences can be detected by superimposing the two sets of results. The distribution of the pressure over the wall of one ramp is shown in Fig. 13. The ordinate refers to the normalized difference between the local pressure and the value of the 2D ramp (p_R), namely $(p - p_R)/p_R$. The solid line represents the results from [8] and the symbols denote our present results.

8. Conclusions

A space marching technique has been developed for the prediction of 3D non equilibrium steady flows through inlets in the hypersonic regime. The physics is governed by the Euler equations and a five species model for describing the chemical relaxation. The discretization follows the finite volume approach and shocks and contact surfaces are captured numerically. The values of the fluxes on the side walls of each finite volume are predicted according to a flux-difference splitting technique, conceived for steady supersonic flows.

Numerical results have been carried out for the 2D non-equilibrium hypersonic flows over a ramp and for 3D supersonic non-reacting flows over the corner generated by two ramps.

Overshootings of the pressure have been found behind the shock in extreme conditions of very high Mach number component normal to oblique shocks, even with the plain first order scheme and for non-reacting flows. A proper

investigation has shown that the overshootings are due to the violation of the domains of dependence, due to the too drastic assumptions introduced in the approximate solver of the Riemann problem. The fact does not hamper the robustness of the method and the inconvenience will be fixed in a short time. The comparison of the present results with others reported in the literature is satisfactory.

Numerical experiments have been also carried out for 3D computations, with non-reacting flows. Complex patterns of shocks and contact surfaces have been predicted. The comparison with results available in literature is very good.

The above validations about 2D non-equilibrium and 3D non-reacting flows allow us to proceed towards the merging of these experiences, in order to investigate 3D non-equilibrium flow problems.

REFERENCES

- [1] Park, C., "On Convergence of Computation of Chemically Reacting Flows", AIAA Paper-85-0247, Jan. 1985.
- [2] Pandolfi, M., "Computation of Steady Supersonic Flows by a Flux-Difference Splitting Method", *Comp. & Fluids*, Vol. 10, No. 1, pp. 37-46, 1985.
- [3] Van Albada, G. D., Van Leer, B., and Roberts, W. W., "A Comparative Study of Computations Methods in Cosmic Gas Dynamics", *Astron. Astrophys.* 108, pp 76-84, 1982.
- [4] Sweby, P. K., "High Resolution Schemes Using Flux Limiters for Hyperbolic Conservation Laws", *SIAM J. Num. Anal.*, Vol. 21, pp. 995-1011, 1984.
- [5] Roe, P. L., "Some Contributions to the Modelling of Discontinuous Flows", *Lect. in Appl. Mathem.*, Vol. 22, Amer. Math. Soc., Providence, R.I., 1985.
- [6] Rakich, J. V., Bailey, K. E., and Park, C., "Computation of Non-Equilibrium Three-Dimensional Inviscid Flow over Blunt-Nosed Bodies", *AIAA J.*, Vol. 21, No. 6, 1983, pp. 834-841.
- [7] Pandolfi, M., Arina, R., and Botta, N., "Non-Equilibrium Hypersonic Flows Over Corners", to appear in a next issue of *AIAA J.*
- [8] Marconi, F., "Supersonic, Inviscid, Conical Corner Flowfields", *AIAA J.*, Vol. 18, No. 1, pp. 78-84, 1980.

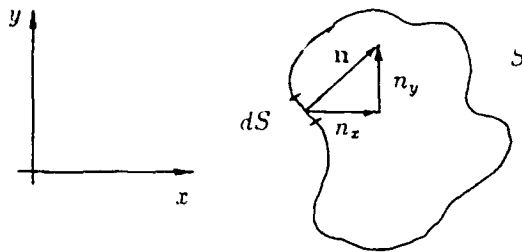


Fig. 1

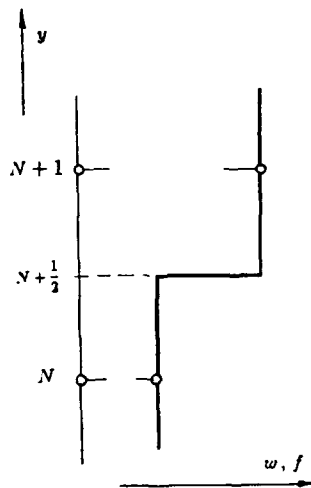


Fig. 3. Definition of the Riemann Problem

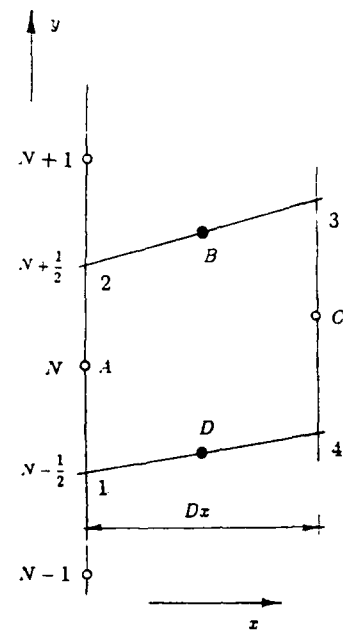


Fig. 2. Finite Volume

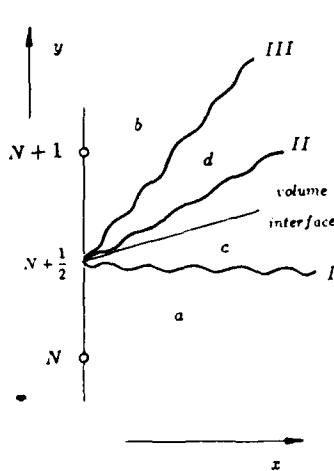


Fig. 4a.

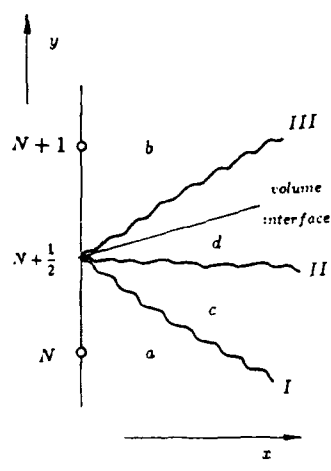


Fig. 4b.

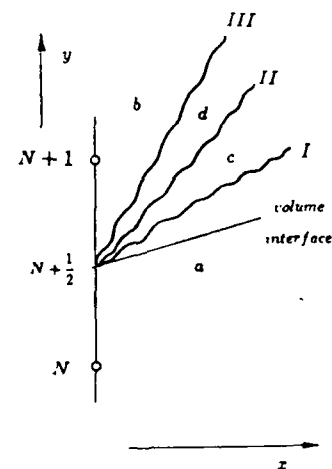


Fig. 4c.

Evolution of the discontinuity
of the R. P.

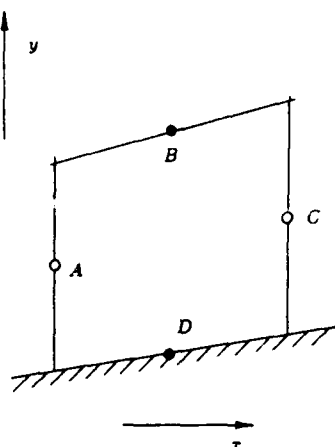


Fig. 5. Finite Volume at the wall

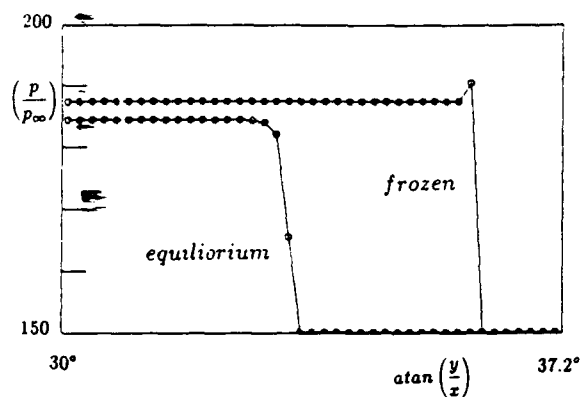


Fig. 6. Distribution of the pressure in the shock layer for the frozen and equilibrium configurations

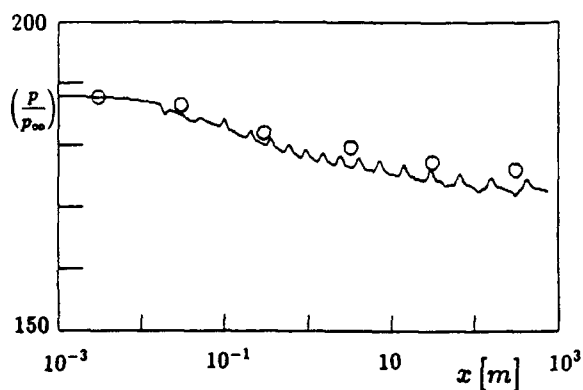


Fig. 7. Evolution of the pressure at the wall, along the ramp

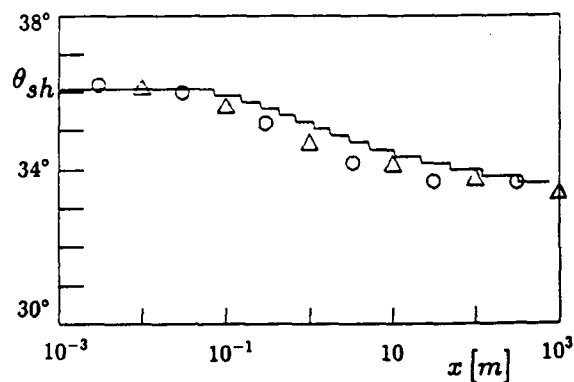


Fig. 8. Evolution of the oblique shock angle, along the ramp

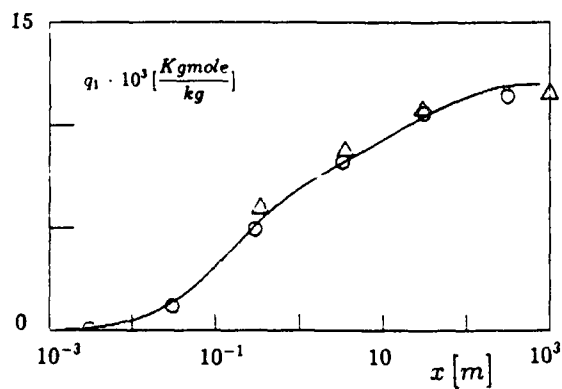


Fig. 9. Molar concentration of atomic oxygen at the wall, along the ramp

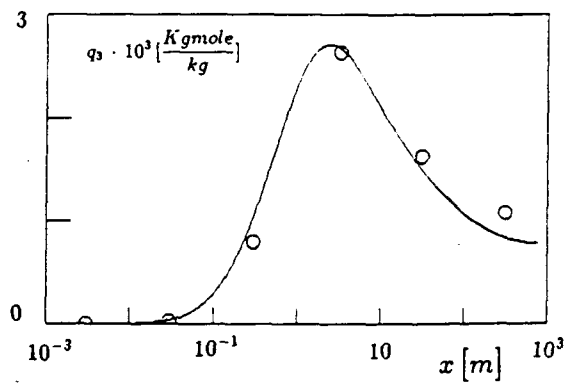


Fig. 10. Molar concentration of nitric oxide at the wall, along the ramp

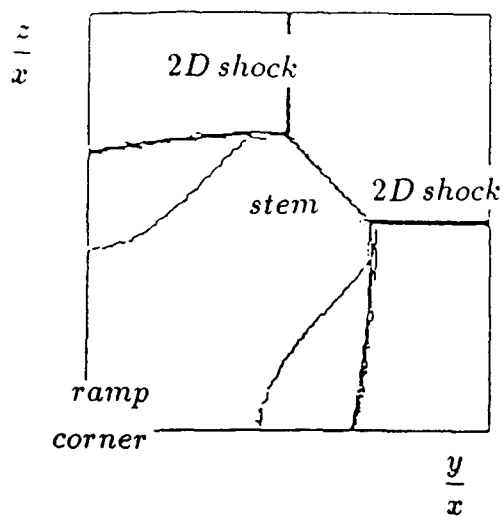


Fig. 11. Corner Flow: Contour lines of pressure

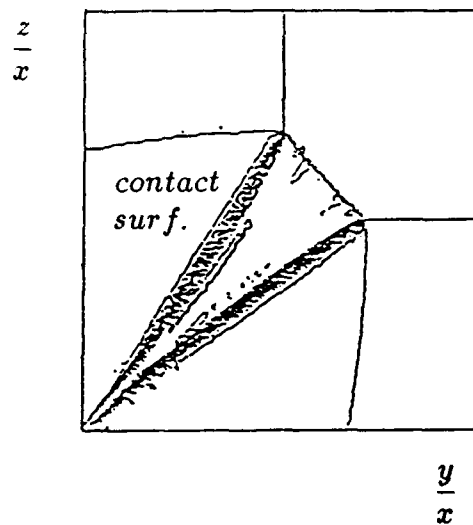


Fig. 12. Corner Flow: Contour lines of entropy

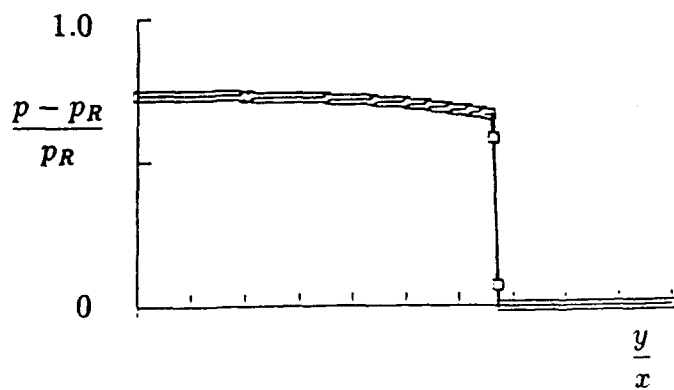


Fig. 13. Corner Flow: pressure over one ramp





EVALUATION OF THE EFFECTS OF FINITE RATE CHEMISTRY ON NOZZLE PERFORMANCE

M. Onofri*

Dipartimento di Meccanica e Aeronautica

Università di Roma "La Sapienza"

Via Eudossiana, 18 - Roma (IT) 00184

92-16100



SUMMARY

Predictions of nozzle performance may be strongly affected by the choice of the flow model: large discrepancies with actual behaviours could occur if the two-dimensional gasdynamic effects and the variations of chemical composition are not suitably accounted for, especially when the nonequilibrium region is wide enough and 2D gasdynamic phenomena interact significantly with chemical kinetics.

In order to assess the accuracy of different simulations, a comparison among inviscid numerical solutions is performed for different classes of axisymmetric nozzles. The role of the two-dimensional effects on the global propulsive parameters is analysed by comparing 1-D with 2-D solutions, while their influence on chemical kinetics is evaluated by considering frozen and nonequilibrium flow models.

The numerical solution of the nonequilibrium nozzle flow model is performed by an implicit integration technique based on an operator splitting between gasdynamics and chemistry. While gasdynamic equations are integrated by a fast solver, the energy and mass fraction conservation equations are integrated in steady form along streamlines with a variable step procedure. This approach yields very efficient and accurate solutions even when the chemical variables display steep gradients.

- α_k exponent of θ in Arrhenius expression of k -th reaction rate
- α_0 angle between coordinate grid line and x -axis
- γ ratio of frozen specific heats
- δ $(\gamma - 1)/2$
- A_i characteristic lines
- μ_i chemical potential of i -th species
- ρ density
- θ temperature
- τ local unit vector along transversal grid lines

1. INTRODUCTION

An accurate evaluation of the effects of finite rate chemical kinetics on the performance of propulsive nozzles is mandatory in order to design rocket nozzles, since a correct evaluation of specific impulse may result in a significant gain in terms of payload. Moreover these effects may also have considerable importance in designing efficient airbreathing propulsive devices such as those considered in the hypersonic aerospace-plane vehicles.

The variations of chemical composition that mainly affect the propulsive performance of supersonic nozzles are connected with dissociation/recombination reactions. At the nozzle inlet the gas mixture shows a certain amount of dissociated species, produced by endothermic reactions occurring in the combustion chamber. In these processes thermal energy is absorbed from the fluid to break molecular bonds, and it is thus subtracted to propulsive purposes. On the contrary, during the expansion phase, the flow experiences a large temperature drop, which yields exothermic recombination reactions. In this case chemical energy is released to the flow, resulting in an increase of the total energy available for thrust. This recover of energy is usually analysed as occurring in three phases. In the first part of the convergent nozzle the flow is close to equilibrium conditions. A nonequilibrium regime takes place up to the throat region, and then the further temperature drop in the divergent duct results in a strong slowing down of the reaction rates, that yields a freezing of the flow chemical composition.

Mathematical modeling assuming frozen conditions cannot obviously account for variations of chemical composition, while numerical solutions of equilibrium flow models may show discrepancies with the actual behaviour when the nonequilibrium region is wide enough. The more general nonequilibrium model seems thus preferable in predicting the behaviour of nozzle flows.

To this end computer codes have been developed that include the modeling of chemical kinetics. Since they are generally characterized by large computational times, quasi one-dimensional solutions are often used for flow predictions. Nevertheless, the one-dimensional hypothesis dis-

LIST OF SYMBOLS

A	a/δ
a	frozen sound speed
B_k	constant in Arrhenius expression of k -th reaction rate
c_p	specific heat at constant pressure
c_v	specific heat at constant volume
e_i	internal energy of i -th species
E_k	activation energy of k -th reaction
G	transformation metric
N	number of species
n	local unit vector along longitudinal grid lines
p	pressure
q	velocity
R	R/\bar{W}
\bar{R}	universal gas constant
R_1, R_2, R_3, R_4	Riemann variables
s	entropy
t	time
u	velocity component along n -direction
v	velocity component along τ -direction
x, y	cartesian coordinates
Y_i	mass fraction of i -th species

*Associate Professor

regards the actual gasdynamic phenomena occurring in radial direction, and consequently their interaction with the chemical kinetics, that may affect the nozzle performance in not negligible fashion. For instance, short nozzles with large expansion ratios may show significant radial effects, while possible oblique shock waves may locally increase the temperature: in both cases the recombination reactions or the freezing conditions occurring in the divergent duct could be strongly affected by these phenomena.

Aim of the present study is to evaluate the role of the two-dimensional effects on the chemical kinetics in nozzles and to assess their influence on the global propulsive parameters. A comparison is carried out among numerical solutions based on frozen and nonequilibrium models of inviscid axisymmetric nozzle flows. To this end, classical quasi one-dimensional calculations are compared with two-dimensional ones for different classes of nozzles and different operational conditions.

The numerical solution of the nonequilibrium nozzle flow model is performed by an integration technique for inviscid steady flows presented in [1,2], recently improved and tested for external hypersonic flows [3,4]. The technique is based on an operator splitting between gasdynamics and chemistry. While gasdynamic equations are integrated by a fast solver [5], the energy and mass fraction conservation equations are integrated in steady form along streamlines with a variable step procedure. This approach yields very efficient and accurate solutions even when the chemical variables display steep gradients, as behind shock waves [6].

2. MATHEMATICAL MODEL

The working fluid is assumed to be a mixture of N gases, each one considered as thermally and calorically perfect, and the flow is considered adiabatic, inviscid, and non-conducting. With these assumptions the system of conservation equations may be written in quasi linear form as

$$A_i + q \cdot \nabla A + a \nabla \cdot q = \dot{A} \quad (1a)$$

$$q_i + q \cdot \nabla q + a \nabla A - \theta \nabla s = \dot{q} \quad (1b)$$

$$s_i + q \cdot \nabla s = \dot{s} \quad (1c)$$

$$Y_{i1} + q \cdot \nabla Y_i = \dot{Y}_i \quad i = 1, N \quad (1d)$$

denoting with \dot{Y}_i the rate of production of each i -species, which takes into account the effects of all reactions. The other source terms \dot{A} , \dot{q} , \dot{s} are given by

$$\begin{aligned} \dot{A} &= a \sum_i P_i \frac{DY_i}{Dt} \\ \dot{q} &= \theta \sum_i Q_i \nabla Y_i \\ \dot{s} &= - \frac{1}{\theta} \sum_i \mu_i \dot{Y}_i \end{aligned} \quad (2)$$

where μ_i are the chemical potentials, and with

$$P_i \equiv \frac{1}{2\delta} \frac{\partial}{\partial Y_i} \left[\ln \left(\frac{\gamma R}{\delta^2} \right) \right] - \frac{c_i}{R\theta}$$

$$Q_i \equiv c_i \frac{\partial}{\partial Y_i} \left[\ln \left(\frac{\gamma R}{\delta^2} \right) \right] - s_i$$

Following the procedure described in [1,3] to extend the quasi-linear lambda formulation [7] to chemical nonequilibrium flows, four compatibility equations are obtained in terms of Riemann variables $R_j = A + w_j \cdot q$, with $j = 1, 4$ and respectively $w_j = n, -n, \tau, -\tau$, as:

$$(R_j)_t + A_j \cdot \nabla R_j + a w'_j \cdot \nabla (w'_j \cdot q) = \theta w \cdot \nabla s + \dot{R}_j + \beta + F \quad (3)$$

with $w'_j = \tau, -\tau, -n, n$, and

$$\begin{aligned} \beta &= q \cdot \nabla \alpha_0 & F &= a k \times q \cdot \nabla \alpha_0 \\ A_1 &= q + a n & R_1 &= A + n \cdot q \\ A_2 &= q - a n & R_2 &= A - n \cdot q \\ A_3 &= q + a \tau & R_3 &= A + \tau \cdot q \\ A_4 &= q - a \tau & R_4 &= A - \tau \cdot q \end{aligned}$$

where the corresponding source terms are:

$$\begin{aligned} \dot{R}_1 &= \dot{A} + n \cdot \dot{q}, & \dot{R}_2 &= \dot{A} - n \cdot \dot{q}, \\ \dot{R}_3 &= \dot{A} + \tau \cdot \dot{q}, & \dot{R}_4 &= \dot{A} - \tau \cdot \dot{q} \end{aligned}$$

On the contrary, the energy and species conservation equations are used in the compatibility form above reported (1c,1d).

3. INTEGRATION TECHNIQUE

Studies concerning the numerical integration of the equation system (1) or (3,1c,1d) date back to the '60 [8,9,10,11], and have recently received a new interest from the need to predict hypersonic external flows about reentry vehicles. As a result of these studies is known that the numerical integration of these equation systems displays basically three numerical problems:

- i) the stiffness of the equation system when approaching the equilibrium conditions,
- ii) large computational times when considering complex reaction mechanisms,
- iii) the need for high spatial resolution when steep gradients of the thermofluiddynamic variables occur.

A method was presented a few years ago in order to face the first two problems [1,2]. The technique has been recently improved to solve also the third problem, and it has been successfully applied to predict hypersonic external flows about blunt bodies [3,4].

Instead of solving the system (3,1c,1d) by integrating the fully coupled equations, as indicated in [12,13,14,15], the method follows the approach firstly proposed by Li [11] and then widely adopted [16,17,18,19,20,21], based on an operator splitting between the the gasdynamic operator, describing the mass and momentum conservation of the mixture, and the chemical operator, describing the conservation of the energy of the mixture and of the mass of each individual chemical species.

As a matter of fact, the fully coupled integration requires a very large computational work when implemented on multidimensional flows. This computational work is actually not needed. In fact, the high resolution required for

integrating the finite rate chemistry is often not necessary for the gasdynamic integration, since in reacting nozzle flows generally the variations of species concentration and temperature display a mild influence on pressure and velocity fields.

The advantage of using integration schemes based on an operator splitting is that the numerical problems relevant to the stiff nature of the equation system and to the nonlinearity of the solution can be restricted to the chemical operator only, while the gasdynamic operator can be solved by standard approaches. In particular the two operators are integrated independently of each other by an iterative procedure: the mixture is considered frozen when integrating the gasdynamic equations, while the flowfield is considered frozen when integrating the chemical operator.

The proposed technique takes full advantage of this approach performing the integration over two different grids: a standard grid for the gasdynamic equations, and steps along streamlines for the chemical operator. Due to its one-dimensional nature, the integration along streamlines can be easily performed by using a variable step procedure. In this way high resolution can be provided where it is actually required, without becoming cumbersome elsewhere.

3.1 The gasdynamic operator

The system of equations (3) is integrated by a semi implicit fast solver [5]. In particular the integration is performed by solving the four compatibility equations independently of each other along the appropriate propagation directions of the relevant Riemann variable. A body-fitted non-orthogonal grid is adopted.

The compatibility equations are discretised as follows.

The terms containing derivatives of the Riemann variables are discretised in space by means of upwind derivatives computed according to the sign of the characteristics. The terms containing the entropy, as well as the chemical source terms, are treated by an upwind discretisation according to the discretisation of the relevant Riemann variable term. The metric source term is evaluated locally.

3.2 The chemical operator

The energy conservation equation written in terms of entropy is particularly suited to be coupled to the species conservation equations in the chemical operator (1c,1d). As a matter of fact, both of them have the velocity vector q as characteristic direction. Thus, in order to preserve their physical meaning, the integration of these equations should be performed along streamlines.

The implementation of this type of integration yields relevant advantages from a numerical point of view. First, the multidimensional problem is reduced, for the chemical operator, to a certain number of one-dimensional integrations. Second, an integration algorithm with variable step can be easily carried out, which allows to increase the spatial resolution locally, where the variable gradients are larger. In practice the procedure results equivalent to the implementation of a subgridding, but with a minimum computational burden.

At each grid point the incoming streamline is reconstructed within the cell boundaries moving backward from it up to an initial point of the streamline, that is assumed to be its intersection with a cell side. The in-

tegration is performed marching along this path, starting from the values of Y_i , velocity, pressure and entropy at the initial point, which are obtained by interpolating between the nodes.

For steady state solutions, the equations can be written in the form:

$$u Y_s = \dot{Y}$$

denoting here $Y = (Y_i, s)^T$

The integration is performed marching along the streamline in the direction of the velocity by an implicit scheme based on the following discretized form of the equations:

$$u \frac{(Y^{n+1} - Y^n)}{\Delta z} = \frac{(\dot{Y}^n + \dot{Y}^{n+1})}{2}$$

where the source term \dot{Y}^{n+1} is expressed by a first order Taylor expansion with respect to the dependent variables.

A variable integration step is implemented by checking the solution obtained with a tentative step. Once the increment ΔY has been computed, the integration step is considered inappropriate if the new concentration values are negative or if $\Delta Y/Y$ is too large or too small. In this case, the integration step is reduced according to the criterion suggested in [9], and the integration performed again.

4. RESULTS AND DISCUSSION

4.1 Descriptions of the numerical tests

In order to perform a sensitivity analysis of the chemical kinetics effects on the nozzle flow expansion, three different classes of geometrical configurations of axisymmetric nozzles are considered.

The first is a conical nozzle with an area ratio of 32.7, whose regular expansion allows to have a description of the fundamental behaviour of the chemical kinetics in the nozzle.

The second is a contoured nozzle of the same class experimented in NASA Lewis Research Center [22,23]. The considered area ratios are 32.7 and 23. The divergent has an initial angle of 35° and an exit angle of 13° . This geometry produces a sudden expansion in the throat region and a light recompression downstream, such that two-dimensional phenomena may have a significant role on the chemical behaviour.

The third group of numerical tests concerns the same class of nozzles, but with a divergent exit angle of 2° . In this case the compression on the divergent wall region is stronger and the larger consequent rise of temperature could affect the chemical trend. Moreover different lengths are considered for the same area ratio, in order to analyze the effect of different divergent expansion angles right behind the nozzle throat.

Oxygen and hydrogen are used as propellants with an excess of hydrogen to limit the temperature rise. The conditions in the combustion chamber are determined by adiabatic combustion of H_2 and O_2 with an equivalence ratio of 1.42 at a pressure of 23 Atm.

The evaluation of the species mass fractions at the inlet section has been done by assuming equilibrium conditions in the combustion chamber. The values are obtained by using the chemical equilibrium code reported in [24], in a suitably modified version to consider constant specific

heats for each species, according to the nonequilibrium model above described.

The reaction mechanism including 6 species and 8 reactions reported in [25] is used (see Table 1).

TABLE 1			
	B_k	α_k	E_k
$H+O_2 \rightleftharpoons OH+O$	$3 \cdot 10^{11}$	0	73.25
$O+H_2 \rightleftharpoons OH+H$	$3 \cdot 10^{11}$	0	33.50
$OH+H_2 \rightleftharpoons H_2O+H$	$3 \cdot 10^{11}$	0	25.10
$2OH \rightleftharpoons H_2O+O$	$3 \cdot 10^{11}$	0	25.10
$2H+M \rightleftharpoons H_2+M$	10^9	0	0
$H+OH+M \rightleftharpoons H_2O+M$	10^9	0	0
$H+O+M \rightleftharpoons OH+M$	10^9	0	0
$2O+M \rightleftharpoons O_2+M$	10^9	0	0
$B_k = m^3/(\text{kmole s})$ (two-body forward reaction) $B_k = m^6/(\text{kmole}^2 \text{ s})$ (three-body forward reaction) $E_k = \text{MJ/kmole}$			

4.2 Numerical results

The flow in the conical nozzle allows to analyse the fundamental chemical behaviour of the mixture during its expansion. In Figs. 1,2 iso-contours are reported for Mach and temperature. As expected they respectively increase and decrease regularly with axial distance, with a semi-circular shape.

The chemical process can be described as evolving in two phases. The first phase, approximately up to the throat, is characterised by higher temperatures and chemical processes close to equilibrium. During this phase the main role in the reaction mechanism (Table 1) is played by the reactions with higher activation energy and essentially H_2O and radicals are produced. The second phase of the expansion is characterised by lower temperatures and radicals consumption up to the possible freezing: reactions with zero activation energy, which form final products, become prevalent.

In Figs. 5(a-f) the mass fractions of the chemical species are reported. As an overall result H_2O is produced, while all other concentrations decay with axial distance. From Fig. 5f it appears that atomic hydrogen displays a particular trend, characterised by a minimum right behind the throat and a growth downstream. A possible explanation can be obtained by looking at the reaction mechanism of Table 1. In the convergent, where T is still high, the first reaction destroys H rapidly and forms OH . Thus H reaches a minimum right behind the throat. Moving downstream, the dropping T slows down this reaction, while the third, favored by the concentration of OH and by a lower activation energy, is still active and produces enough H to more than compensate for its consumption. In fact, all H -consuming reactions -excepted the first- are three-body recombinations, that are slower compared to

those forming radicals and thus relatively slow in this nozzle region. Further downstream, as T keeps dropping, all reactions H -forming and H -destroying slow down, and so does the rate of H formation. An inversion of this trend, with a diminishing of H , is to be expected when the third reaction freezes up, and a vanishingly small H is to be expected at equilibrium; however, in the conditions considered the freezing point value is such that does not allow to check quantitatively this prediction.

The results concerning the contoured nozzle are reported in Figs. 3,4 in terms of iso-contour lines of Mach number and temperature. Unlike the gradual expansion in the conical nozzle, here a sudden expansion takes place at the throat, followed by a light compression in the wall region of the divergent, which yields a local temperature rise. The temperature at the exit has an average value of 850K, about 150K lower than the conical nozzle with same area ratio. Since the difference is 70K for the inert cases, the different chemical phenomena should be responsible for about 8% of difference on the temperature recovery. In particular, consequences of the two-dimensional gasdynamic phenomena on chemical kinetics can be evaluated from Figs. 6(a-f), where iso-contours are reported for the species mass fractions. The comparison of the mass fractions with those of Figs. 5 shows that the consumption of most species is slowed down by the strong expansion behind the throat. In fact the reaction velocity becomes lower and the temperature rise is too small and comes too downstream, when most of reactions are close to frozen conditions. As a general effect, the flow seems to pass rapidly from conditions of quasi-equilibrium to a frozen regime. The different temperature recovery achieved in the two cases is the consequence of the two different chemical processes.

A representative trend is shown by O_2 (Fig. 6b): the strong expansion behind the throat propagates downstream along the direction of the characteristic line, freezing the reaction so suddenly that different concentration values are then carried along each streamline in the divergent.

The same general considerations made above for the hydroxyl trend here held. Nevertheless, contrary to the case of the conical nozzle, where the expansion is more regular, here due to the different intensity of the expansion going from wall to centerline, the freezing of the first reaction of Table 1 is faster in the wall region than along the axis. At throat, when the reaction freezes up at wall, it is still weakly active in the corresponding abscissas along the centerline: the zone of minimum concentration is thus wider there than at wall, and it takes a triangular form (Fig. 6f).

Another group of numerical tests considers the same class of nozzles, but with a stronger compression in the wall region, generated by a divergent exit angle of 2° . Results concerning the species mass fractions of atomic hydrogen, oxygen and hydroxyl, are reported in Figs. 7(a-c) for a nozzle shape with same length and same expansion angle at throat above considered. Due to the stronger compression in the wall exit region the temperature rises locally. Its overall effect is to emphasize consumption of all species except H_2O . Locally the temperature recovery is about 200K larger than in the previous test, and it is partially due to the chemistry, since an inert gas solution predicts a difference of only 100K. However, since it is limited to the wall zone of the exit section, the recovery in terms of specific impulse seems not to be significant.

If the expansion angle at the throat of the nozzle is reduced from 35 to 20 with a longer divergent, the process becomes more regular and the nonequilibrium region wider, yielding a gain of specific impulse (about 2.5%). The results for some species mass fractions are reported in Figs. 8(a-c) and should be compared with the results of Figs. 7. While the quantity of water formation does not change, the consumption of O_2 is higher and the atomic hydrogen rise is reduced by the higher temperature in the wall region, which enhances the role of the consumption reactions.

Finally a difference of 2.3% is noted between predictions computed by the above described method, integrating the chemical operator with small integration steps along streamlines, and by the old integration scheme [2,1], using coarser chemical steps (the same used for the gasdynamic operator).

Of course the higher accuracy obtained by using a finer resolution requires larger computational times. With a computational grid of 50×10 mesh points, the approximate CPU time to obtain a residual of $1.E-06$ is 300 seconds for the older version of the code [1,2], and 1200 seconds for this version, for calculations performed on an IBM 3090/600J (scalar) computer.

4.3 Effect of modeling on numerical predictions

The results obtained by a systematic series of tests are here reported, to evaluate the consequences on the specific impulse of the different behaviour of chemical kinetics, induced by different two-dimensional gasdynamic effects.

Conical nozzle $A_R = 32.7$ The nonequilibrium model predicts a specific impulse 10.4% larger than the inert gas model (see Table 2). The same comparison for one-dimensional calculations gives a difference of 13.1%. The loss in specific impulse due to two dimensional effects is 1% for inert flows, while it is 4.2 % for the nonequilibrium models. Thus, it can be evaluated that 3.2% of specific impulse is due to the chemical effects produced by two-dimensional gasdynamic phenomena.

Contoured nozzle (exit angle = 13.5° , $A_R = 32.7$).

The nonequilibrium model predicts (see Table 3) a specific impulse 9.7% larger than the inert gas model. The same comparison for one-dimensional calculations gives a difference of 12.4%. The loss in specific impulse due to two dimensional effects is 4.2% for inert flows, while it is 7.0% for the nonequilibrium models. Here the two-dimensional effects interacting with chemical kinetics are therefore responsible for 2.7% of specific impulse. This value is .5% lower than the conical nozzle since the sudden expansion produced by the nozzle shape behind the throat results in a faster freezing of reactions, thus reducing the recover of energy connected to them.

Contoured nozzle (exit angle = 2.0° , $A_R = 23$). In this case two different nozzle divergent profiles are considered. The first with the same expansion angle at throat above examined, the second with an angle of 20° and thus a longer divergent duct. The nonequilibrium model predicts a specific impulse that is 4.8% larger than the inert gas model for the first case, while for the longer nozzle the results of the nonequilibrium model are 7.3% larger than the inert model. Since the comparison of results for inert models does not give in the two cases substantial variations of specific impulse, the evaluation of the chemical effects yields to a gain of 2.5% in the specific impulse

for the longer nozzle, mainly due to an expansion more regular from the fluid dynamic point of view.

In conclusion, from the tests performed the influence on the specific impulse of the chemical kinetics induced by two-dimensional gasdynamic effects can be evaluated. These effects depend on the different degree of expansion behind the nozzle throat, which can anticipate the freezing of some reactions, reducing the level of energy recover connected with them.

For instance, they are responsible for a 3.2 % of the value of the specific impulse in the case of conical nozzle, while this influence is lowered of .5% if nozzle shapes with sudden expansions in the throat region are considered.

On the contrary, the compression occurring in the wall exit region of contoured nozzles seems to play a weak effect on the specific impulse.

While these results should be definitely checked with different sets of Arrhenius data for the O_2/H_2 reaction, they are backed by recent work of Straub [26] and also by the interest NASA seems to have at the moment in precise measurements of exhaust velocity for the SSME. As a matter of fact these measurements are intended to assess the validity of the simple one-dimensional rocket nozzle codes such as [24].

5. CONCLUSIONS

A semi-implicit technique to compute nozzle flows with chemical kinetics has been implemented on different axisymmetric nozzles. The comparison of the results with frozen and one-dimensional solutions shows that for some conditions the two-dimensional phenomena affect significantly chemical kinetics, and their effects should be accurately taken into account by suitable simulations to have precise predictions of nozzle performance.

A more comprehensive analysis of the above phenomena will require more a quantitative evaluation of the discrepancies coming from the use of frozen, equilibrium and nonequilibrium models on the global propulsive parameters. Moreover a modeling including variable specific heats should be more realistic.

Further studies will be carried on on this aspects.

ACKNOWLEDGEMENTS

A special acknowledgement is due to Paolo Peronti for his precious and valuable assistance in running the test cases and visualizing the results.

This study comes from the common activity of the research group of Gasdynamics and Propulsion of the Department of Meccanica and Aeronautica of University of Rome. The role of B. Favini, D. Lentini, F. Sabetta and M. Valorani that cooperated with the author in the development of the numerical techniques here used must be stressed. The author's thanks go to them and also to C. Bruno and M. Di Giacinto for the helpful suggestions and the endless critical discussions.

References

- [1] Lentini D., and Onofri M., "Nonequilibrium Chemically Reacting Flows in Nozzles" in "Analysis and Design of Advanced Energy Systems: Fundamen-

- als", AES ASME, Vol 3-1, (Eds.: Morgan M.J. and Gaggioli R.A.), New York, 1987.
- [2] Lentini D., and Onofri M., "Fast Numerical Technique for Nozzle Flows with Finite Rate Kinetics", in *Computational Fluid Dynamics* (Eds.: De Vahl Davis G. and Fletcher C.), North Holland, 1987.
 - [3] Valorani M., Onofri M., Favini B., Sabetta, F., "Nonequilibrium Hypersonic Inviscid Steady Flows", *AIAA Journal*, July 1991.
 - [4] Sabetta F., Favini B., Moretti G., Onofri M., Valorani M., "Euler Flows About Ellipse and Double Ellipse", Workshop on Hypersonic Flows for Reentry Problems, INRIA-GAMNI, Antibes, 1990.
 - [5] Onofri, M., Lentini, D., "Fast Numerical Solver for Transonic Flows", *Computers & Fluids*, 17, n.1, 1989.
 - [6] Onofri M., "Reacting Shock Waves In Hypersonic Propulsion", AGARD CP-479, Madrid, 1990.
 - [7] Moretti, G., "A Technique for Integrating Two-dimensional Euler Equations", *Computers & Fluids* 15, 59-75, 1987.
 - [8] Treanor C.E., "A Method for the Numerical Integration of Coupled First-Order Differential Equations with Greatly Different Time Constants", *Math. Comp.*, Vol. 20, Jan. 1966.
 - [9] Lomax, H., and Bailey, H.E., "A Critical Analysis of Various Integration Methods for Computing the Flow of a Gas in Chemical Nonequilibrium", *NASA TN D-4109*, 1967.
 - [10] Moretti G., "A New Technique for the Numerical Analysis of Nonequilibrium Flows", *AIAA Journal*, Vol. 3, Feb. 1965.
 - [11] Li, C.P., "Time-Dependent Solutions of Nonequilibrium Dissociating Gases Past a Blunt Body", *Journal of Spacecraft and Rockets*, 9, 571-572, 1972.
 - [12] Drummond J.P., Hussaini M.Y. and Zang T.A. "Spectral Methods for Modelling Supersonic Chemically Reacting Flowfields", *AIAA Journal*, Vol. 9, Sept. 1986.
 - [13] Grossman B., Cinnella P. "The Development of Flux Splitting Algorithms for Flows with Nonequilibrium Thermodynamics and Chemical Reactions", *AIAA Paper* 88-3596.
 - [14] Bussing, R.A., and Murmann, E.M., "Numerical Investigation of Two-Dimensional H_2 -Air Flamehold-ing over Ramps and Rearward-Facing Steps", *J. Propulsion and Power*, 3, No. 5, 448-54, 1987.
 - [15] Shuen J.S., and Yoon S., "Numerical Study of Chemically Reacting Flows Using LU-SSOR Scheme", *AIAA Journal*, Vol. 27, no. 12, Dec. 1989.
 - [16] Rakich, J.V., Bailey, H.E., and Park, C., "Computation of Nonequilibrium, Supersonic Three-Dimensional Inviscid Flow over Blunt-Nosed Body", *AIAA Journal*, 21, no. 6, 834-841, 1983.
 - [17] Li, C.P., "Implicit Methods for Computing Chemically Reacting Flow", *NASA TM* 58274, September 1986.
 - [18] Gnoffo, P.A., Mc Candless, R.S., and Yee, H.C., "Enhancements to Program LAURA for Computation of Three-Dimensional Hypersonic Flows", *AIAA Paper*, 87-0280, 1986.
 - [19] Stiles R.J., Hoffman J.D., "Analysis of Steady, Two-Dimensional, Chemically Reacting, Nonequilibrium, Inviscid Flow in Nozzles", *AIAA Journal*, Vol. 23, Mar. 1985.
 - [20] Schetz J.A., Billig F.S., Favin S., "Numerical Solution of Ramjet Nozzle Flows", *AIAA Paper* 85-1270, Jul. 1985.
 - [21] Dash S.M., Sinha N., Wolf D.E. and York B.J., "Computational Models for the Analysis/Design of Hypersonic Scramjet Components", *AIAA Paper*, A86-42737, June 1986.
 - [22] McAmis R., and Lankford D., "Application of a Chemically Reacting Navier-Stokes Code for Predicting Nozzle Performance of a High Area Ratio Liquid Propellant Rocket Engine", *AIAA Paper* 91-0307, Jan. 1991.
 - [23] VanOverbeke T.J., and Shuen J.S., "A Numerical Study of Chemically Reacting Flow in Nozzle", *AIAA Paper* 89-2793, Jan. 1991.
 - [24] Gordon S., and McBride B.J., "Computer Program for Calculation of Complex Chemical Equilibrium Compositions, Rocket Performance, Incident and Reflected Shocks, and C-J Detonations", *NASA SP*-273, 1976.
 - [25] Ferri A., Libby P.A., Zakkay V., "Theoretical and Experimental Investigation of Supersonic Combustion", Third ICAS Congress, Stockholm, 1962.
 - [26] Straub D., *Thermofluid-dynamics of Optimized Rocket Propulsion*, Birkhauser Verlag, Berlin 1989.

TABLE 2

	1 D		2 D
Inert		1%	
	13.1%		10.4%
Nonequilibrium		4.2%	
CONICAL NOZZLE (Differences in I_{sp} prediction between different models)			

TABLE 3

	1 D		2 D
Inert		4.2%	
	12.4%		9.7%
Nonequilibrium		7%	
CONTOURED NOZZLE (Differences in I_{sp} prediction between different models)			

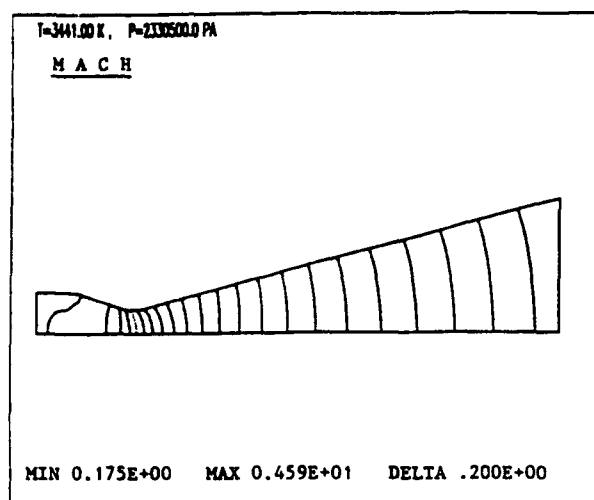


Fig. 1. Iso-contours of Mach number for a conical nozzle with $A_R = 32.7$.

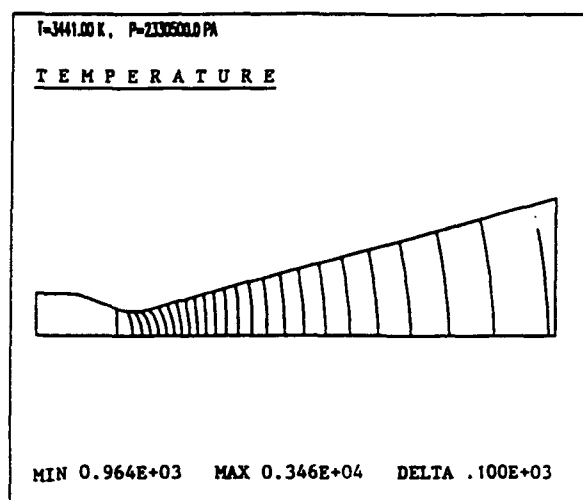


Fig. 2. Iso-contours of temperature for a conical nozzle with $A_R = 32.7$.

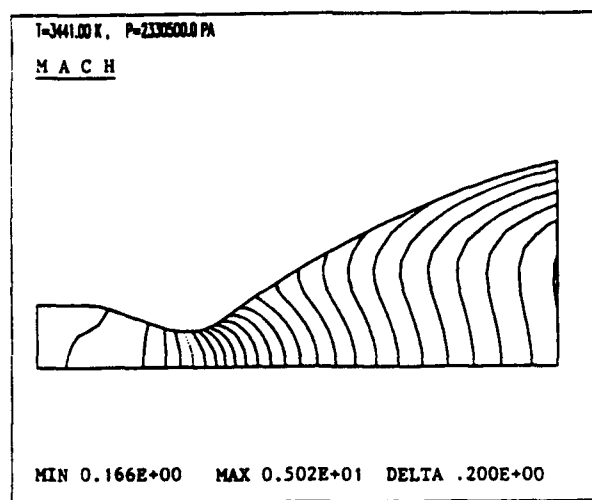


Fig. 3. Iso-contours of Mach number for a contour nozzle with $A_R = 32.7$.

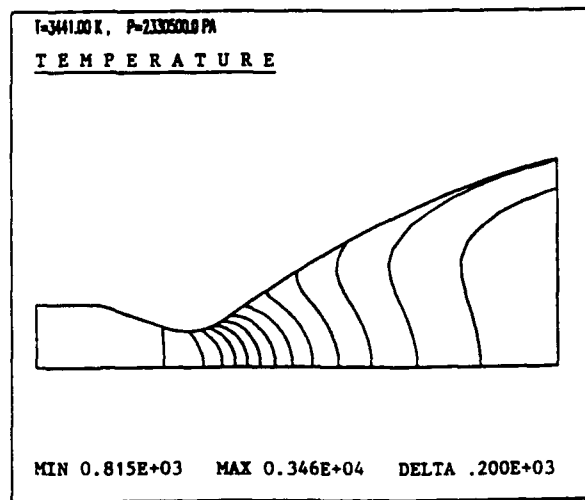
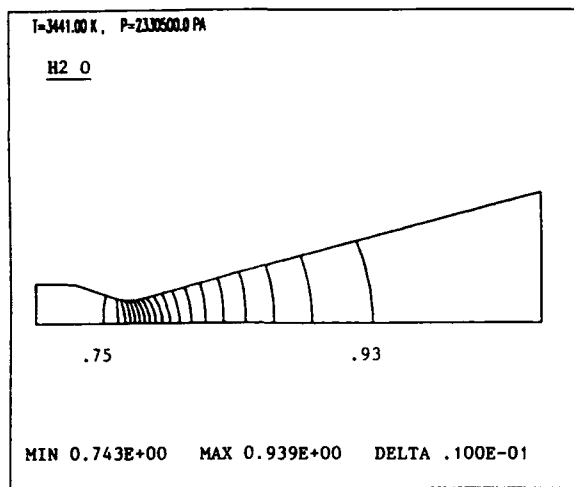
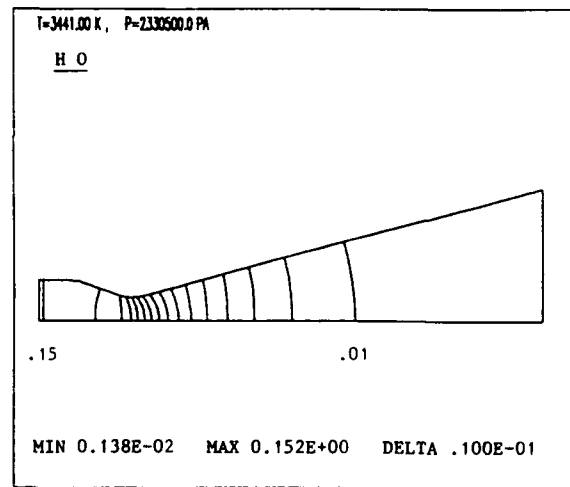


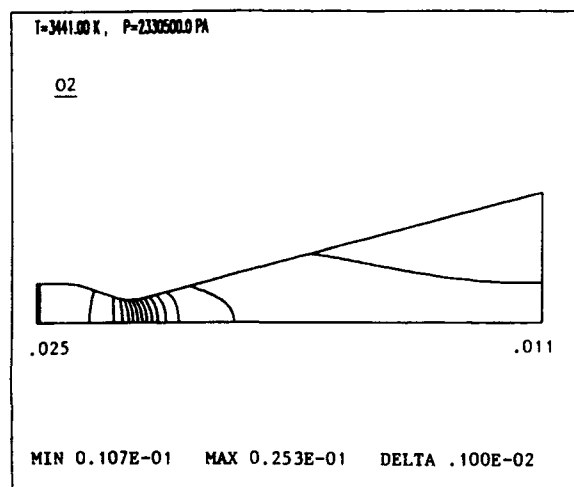
Fig. 4. Iso-contours of temperature for a contour nozzle with $A_R = 32.7$.



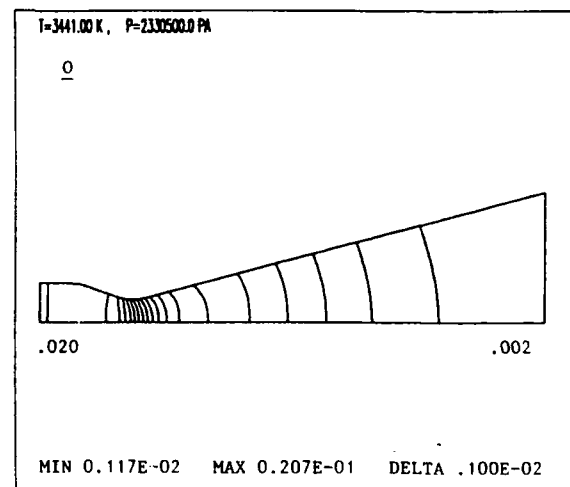
a)



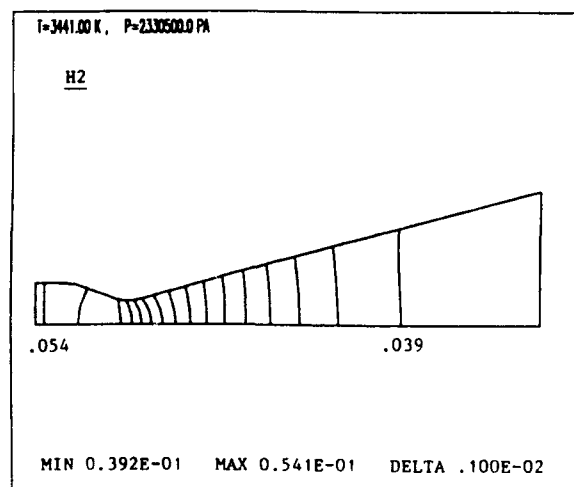
d)



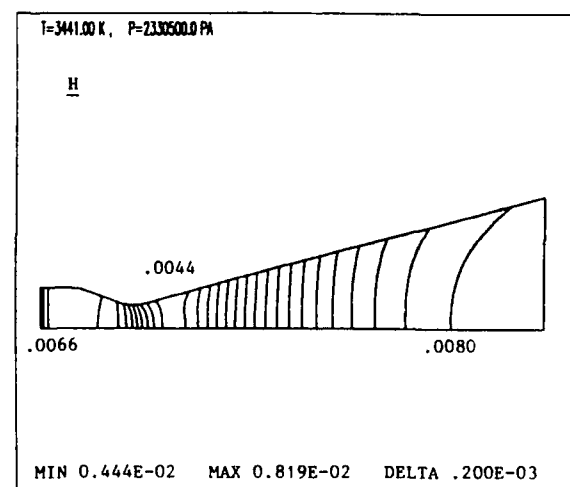
b)



e)

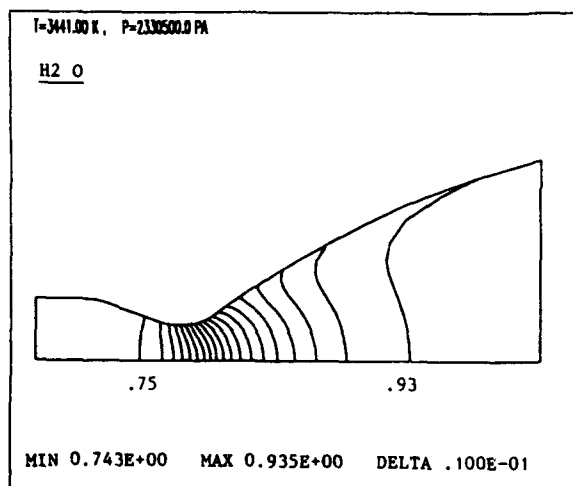


c)

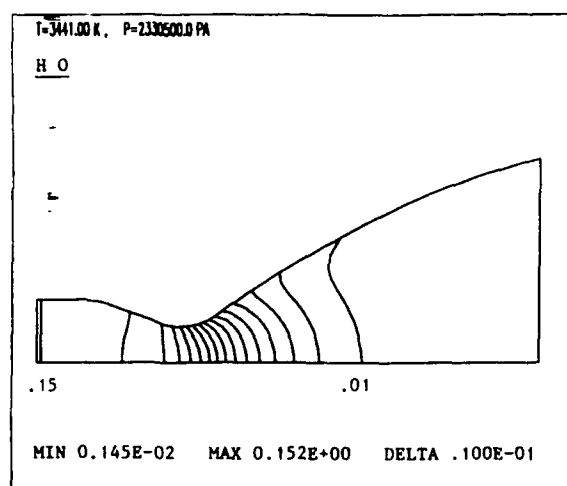


f)

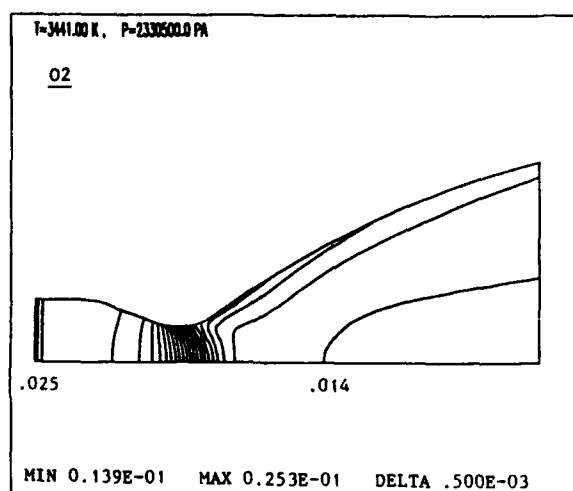
Fig. 5. Iso-contours of species mass fractions for a conical nozzle with $A_R = 32.7$.



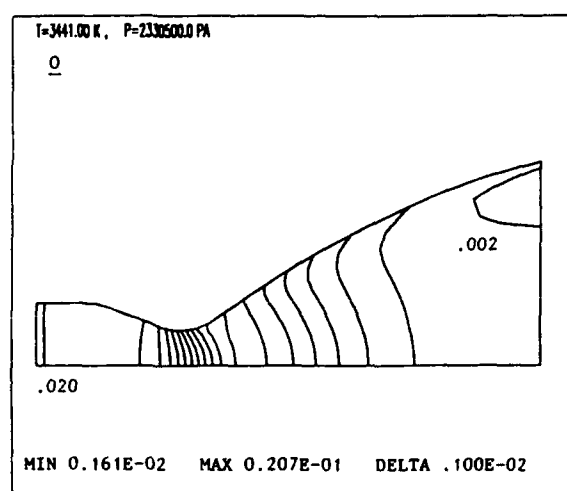
a)



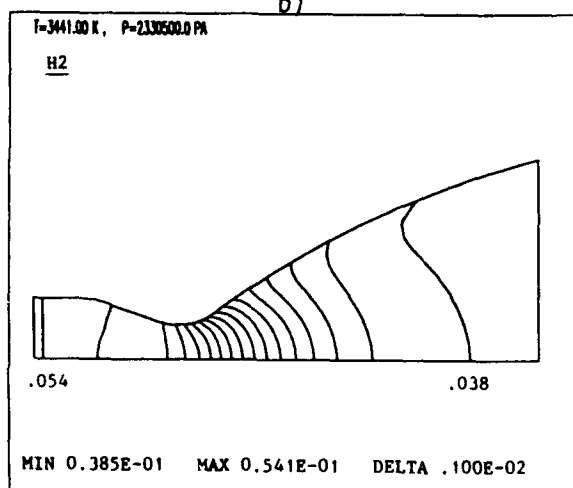
d)



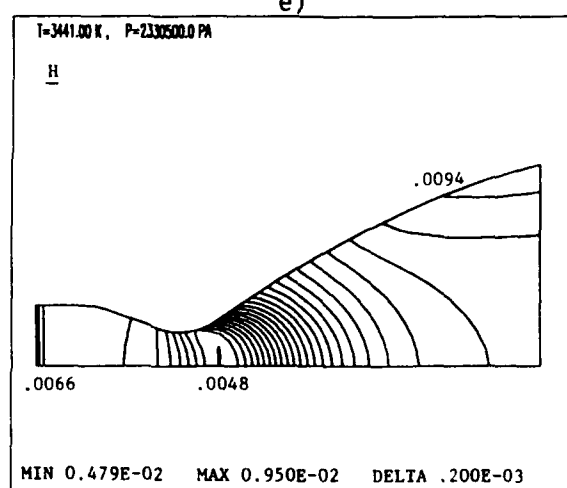
b)



e)

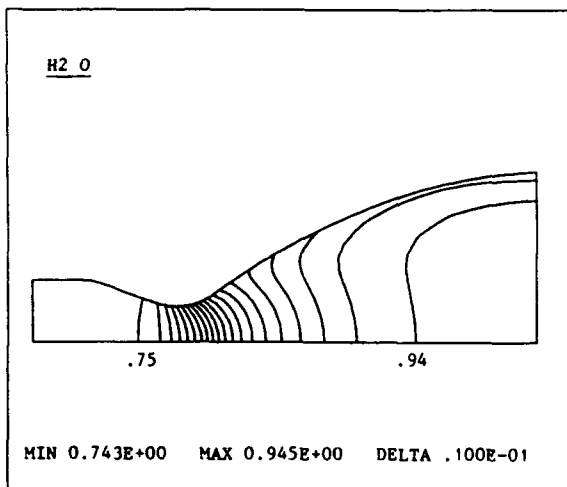


c)

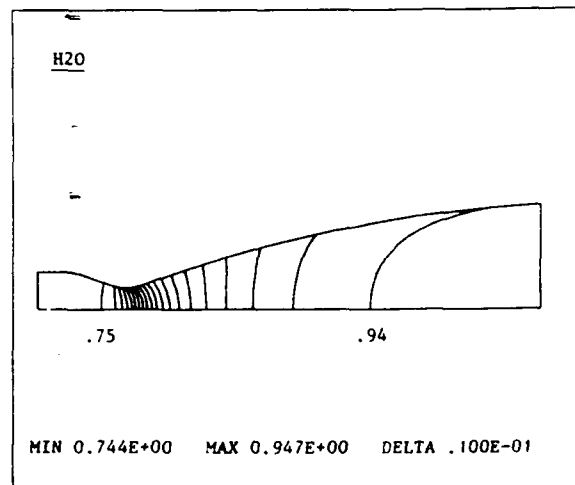


f)

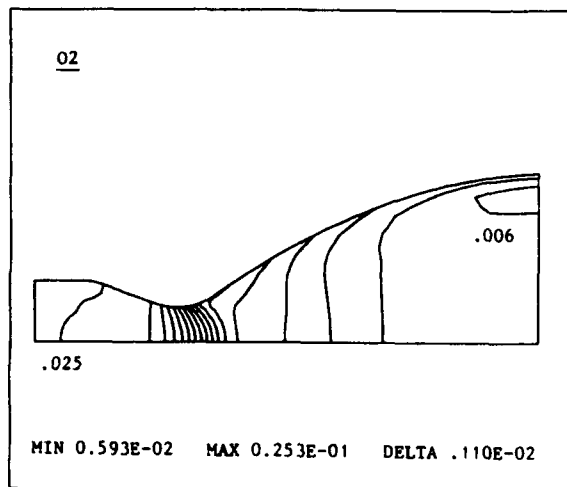
Fig. 6. Iso-contours of species mass fractions for a contoured nozzle with $A_R = 32.7$.



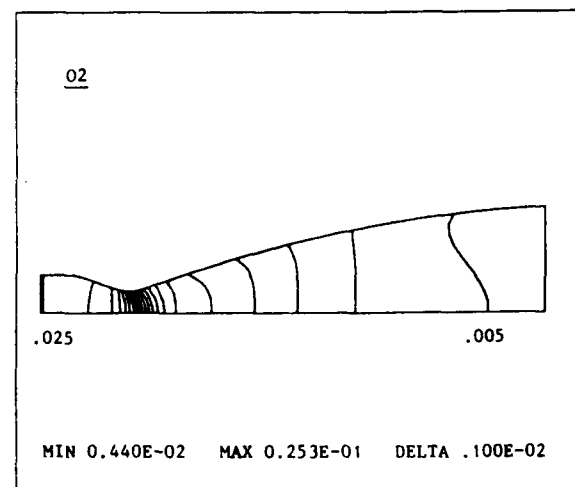
a)



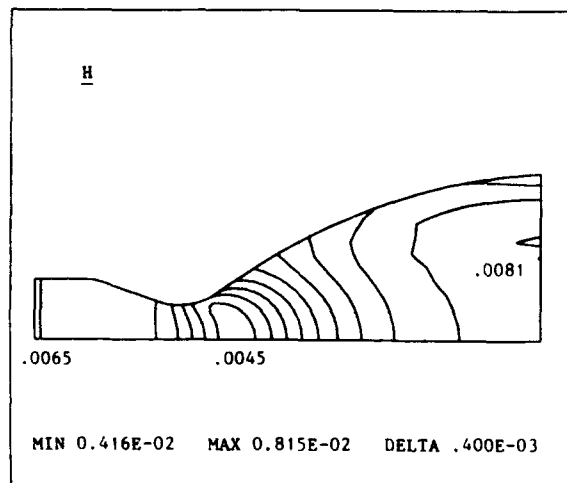
a)



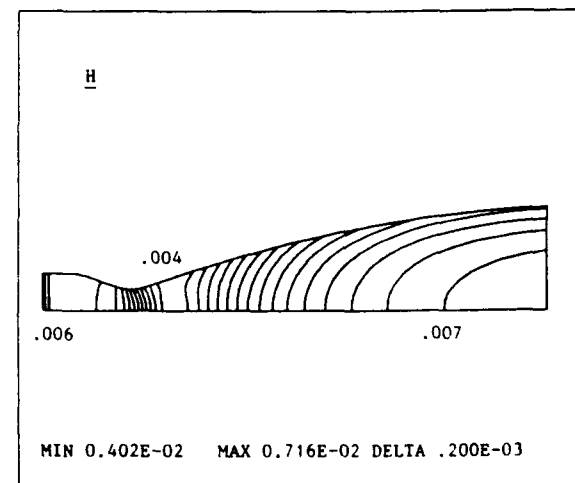
b)



b)



c)



c)

Fig. 7. Iso-contours of species mass fractions for a contoured nozzle with $A_R = 23$ and divergent angles $\alpha_1 = 35$, $\alpha_2 = 2$.

Fig. 8. Iso-contours of species mass fractions for a contoured nozzle with $A_R = 23$ and divergent angles $\alpha_1 = 20$, $\alpha_2 = 2$.

Discussion

K. BROICHHAUSEN, MTU, MÜNCHEN, GERMANY

Taking into account the chemical reaction in the numeric scheme is equivalent to additional source terms. Thus, the formulation of these source terms (modeling of the chemistry) can contribute to a artificial viscosity of the solution. Have you done any investigations on this problem?

AUTHOR'S REPLY

I have not done systematic tests on this aspect, but I think it could be an interesting point to be investigated.





NUMERICAL ANALYSIS OF CONVERGING-DIVERGING NOZZLE FLOWS IN CHEMICAL NON-EQUILIBRIUM

by

R. Walther

MTU Motoren- und Turbinen-Union München GmbH

Postfach 50 06 40

D-8000 München 50

Germany

92-16101



SUMMARY

The converging-diverging nozzle geometries, which are presently proposed for hypersonic propulsion systems, are characterized by large expansion area ratios, and by a geometrically variable nozzle throat to control the engine mass flow. Within the expanding nozzle flow, chemical recombination reactions of the combustor exhaust gas products will occur; the limited chemical reaction rates generally leading to a relaxation of the chemical species composition. In addition, changes in mixture composition and heat release due to chemical reactions influence the flow field.

Based on Moretti's λ -scheme (a method for the solution of the time-dependent 2D Euler equations) a numerical model was developed which couples the gas dynamic phenomena with the chemistry effects that occur within the flow field. The chemical reaction rates are described by a kinetic model involving a satisfactory reaction mechanism. The developed scheme was applied to the expanding nozzle flow of a stoichiometric H_2 -air exhaust gas. For comparison purposes, four different physical models have been considered to describe the chemical phenomena:

- Chemically frozen flow including a temperature-dependent specific heat ratio.
- Flow which is in chemical equilibrium.
- Upstream of the nozzle throat the flow is assumed to be in local chemical equilibrium, whereas downstream it is considered as frozen.
- Flow which is in chemical non-equilibrium.

The results are discussed in terms of flow properties, gas mixture composition and nozzle exit momentum. It is concluded, that a physically inadequate model of the chemical phenomena will lead to unacceptable discrepancies in net engine thrust predictions.

LIST OF SYMBOLS

c_v, c_p	specific heats of the reacting mixture
h	enthalpy
κ	specific heat ratio of the reacting mixture $c_p/(c_p - R)$
l	length
p	pressure
P	natural logarithm of pressure
R	averaged gas constant of the reacting mixture $\approx \text{const.}$
ρ	density

s	entropy
S	dimensionless entropy s/c_v
θ	temperature
$V(u, v)$	velocity vector
ξ_i	mass fraction of species i
X, Y, T	computational coordinates
x, y, t	physical coordinates

Subscripts

ch	source term due to chemical reactions
i	denotes quantities of the species i , with $i=1, n$
o	reference quantities

Superscripts

$-$	denotes averaged integral values
-----	----------------------------------

1 INTRODUCTION

Typical features of the converging-diverging nozzle geometries, projected for hypersonic propulsion systems, are large expansion area ratios at high flight Mach numbers and a geometrically variable nozzle throat to control the engine mass flow. Preferably, the nozzle should be highly integrated with the airframe so that the upper wall of the nozzle is actually the aft end of the airframe, Fig. 1.

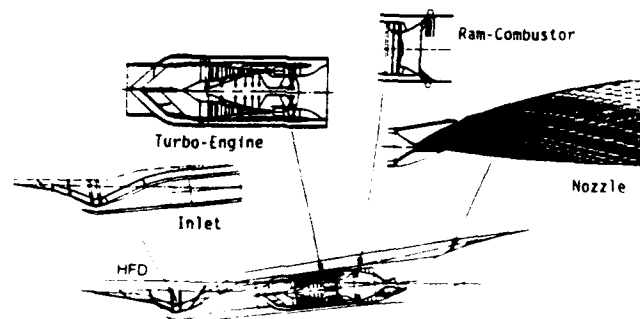


Fig. 1. Propulsion System Integration

Within the flight Mach number range 6 to 7, where the upper stage of the German 2-stage hypersonic transport system SANGER (TSTO) is projected to separate from the air-

breathing lower stage, the engine inlet momentum may be as high as 80% of the nozzle exit momentum. Consequently, the predicted net engine thrust will be highly sensitive to small inaccuracies in the computation of the nozzle exit momentum. Therefore, for an accurate prediction of nozzle performance, the inclusion of chemical non-equilibrium effects becomes important.

Recent analytical studies on nozzle performance were reported from Harloff et al /1/. Solving the full 2D Reynolds-averaged Navier-Stokes equations by the implicit Beam and Warming scheme, the flow fields, wall pressures, wall skin friction values, heat transfer values and overall nozzle performance were determined for a scramjet-type nozzle over a wide range of flight conditions. However, the nozzle flow was considered as chemically frozen and the ratio of specific heats as well as the gas constant were held constant throughout the entire flow field. In addition, the investigated nozzle geometry was typical for scramjet applications, i.e. it was completely divergent.

Rizkalla et al /2/ expanded a frozen chemistry method-of-characteristics computer program, for designing and analyzing divergent scramjet engine nozzles, to incorporate finite-rate chemistry and vibrational relaxation. One interesting result of this work was, that finite-rate chemical recombination and viscous effects are of major consequence in determining nozzle performance, whereas vibrational relaxation times appear to be quite short at Mach 20 flight conditions (nozzle inlet stagnation conditions: 1.5 bar, 3000 K). Thus, the flow is mainly in vibrational equilibrium throughout its passage through the nozzle.

In the work presented here, a convergent-divergent nozzle contour typical for hypersonic ramjet propulsion systems was chosen as a basis. Thus, the 2D investigations of chemical non-equilibrium effects also include the kinetic highly sensitive, transonic throat region. In addition, the analyses investigate the influence of different chemistry modelling techniques, such as frozen, local equilibrium and finite-rate chemistry on nozzle exit momentum and net engine thrust.

For solving the 2D inviscid flow equations, a numerical model based on the λ -scheme of Moretti /3/ is applied. This scheme takes into consideration the physical background of unsteady inviscid flows which are governed by the propagation of sound waves and by the convection of entropy along particle paths.

Since the basic phenomena of hyperbolic flows are still present with chemically reacting flows, the λ -scheme should also be an appropriate basic method for reacting flows.

In order to account for the different time scales characteristic of the fluid and chemical processes, during the explicit integration of the time-dependent basic equations the chemical source terms for species and energy are replaced by averaged integral values.

2 GOVERNING EQUATIONS

For a dimensionless form of the equations relating to the problem, we introduce the reference values ρ_0, p_0 and l_0 . The corresponding units of temperature, velocity and

enthalpy are defined as:

$$\theta_0 = p_0 / R \rho_0, \quad u_0 = (p_0 / \rho_0)^{1/2}$$

$$t_0 = l_0 / u_0, \quad h_0 = p_0 / \rho_0$$

Following the form of Moretti /4/, we use as flow variables, in addition to the velocity vector, the logarithm of the dimensionless pressure and the dimensionless entropy:

$$P = \ln p, \quad dS = ds / c_v$$

Then, the equations defining the conservation of mass, momentum and energy of a reacting, inviscid flow in vector form are:

$$\begin{aligned} \frac{DP}{Dt} + \kappa \nabla \cdot \mathbf{V} &= \frac{DS}{Dt} \\ \frac{D\mathbf{V}}{Dt} + \theta \nabla P &= 0 \\ \frac{DS}{Dt} + Q_{ch} &= 0 \end{aligned} \quad (1)$$

with

$$Q_{ch} = \frac{(\kappa - 1)}{\theta} \sum_i h_i (\dot{\xi}_i)_{ch} \quad i = 1, n.$$

Thermal conduction as well as molecular and turbulent transport processes have been neglected. The term Q_{ch} expresses the released or absorbed chemical energy. For a chemically frozen flow, this term vanishes and the equations represent the Euler equations of gas dynamics. The distribution of the individual chemical species in the flow is defined by the following set of transport equations:

$$\frac{D\dot{\xi}_i}{Dt} = (\dot{\xi}_i)_{ch} \quad i = 1, n. \quad (2)$$

The term $(\dot{\xi}_i)_{ch}$ expresses the chemical production or loss processes of the species i . These source terms are governed by the laws of chemical kinetics; they form another set of first-order, coupled, ordinary differential equations. For a chemically frozen flow, the source terms vanish and the equations simply state the invariance of the mass fractions along particle paths.

3 NUMERICAL MODEL

The finite-rate chemistry model applied in this work solves the basic equations (1) and (2) for a 2D nozzle flow. In order to account for the different time-steps characteristic of the fluid and chemical processes, we split off the chemical source terms and replace them during the integration of the remaining terms by averaged integral values. The integration of the modified problem equations is carried out by applying the λ -scheme. With the solution of the energy equation, special regard is given to the physical fact, that the entropy is transported along particle paths. Moretti and Pandolfi /5/. That means, the space derivatives are approximated in such a way that information is never carried upstream. Since the same physical fact holds for the species mass fractions, the integration technique is also applied to the

species transport equations (2). Chemical production processes of heat and species occur during the transport of the particles. Special regard is given to this fact with the definition of averaged integral values for the chemical source terms. To describe the technique in more detail, we consider a cut-out of grid points in a rectangular computational grid, Fig. 2.

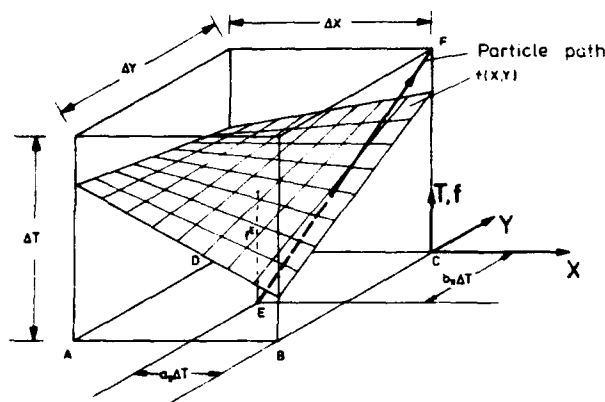


Fig. 2. Sub-Model for the Computation of Chemical Source Terms

The coefficients a_{11} and b_{11} correspond to the components of velocity at point C and define the slope of the particle path segment E-F. The change in mixture composition along E-F results from the integration of the chemical rate equations. The initial values of mass fractions, pressure and temperature at point E are interpolated, as shown, for a typical value f . Therefore, a curved plane is fitted to the values of f at the grid points A, B, C and D. The integration is carried out by an implicit scheme based on the method of Lomax and Bailey /6/. This method keeps the pressure along the particle path segment constant. After the composition of the flow is known at the points E and F, an averaged integral value of each species can be defined as:

$$(\bar{\xi})_{\text{ch}} = \frac{1}{\Delta T} \int_E^F (\xi)_{\text{ch}} dT = \frac{1}{\Delta T} (\xi_i^F - \xi_i^E).$$

A corresponding value for the chemical heat is:

$$\bar{Q}_{\text{ch}} = \frac{(\kappa - 1)}{\theta} \sum h_i (\bar{\xi})_{\text{ch}} = \frac{(\kappa - 1)}{\theta \Delta T} \sum h_i (\xi_i^F - \xi_i^E)$$

To reduce computer time, the averaged source terms are calculated only once per grid point. These source terms are then inserted for both the predictor and corrector step.

4 PROBLEM DESCRIPTION

The problem is specified by three different boundary conditions: a subsonic inlet; a supersonic outlet; and an upper and lower inviscid rigid wall, Fig. 3. At the wall, the velocity component perpendicular to the wall vanishes. A post-correction method reported by de Neef /7/ is used to satisfy this boundary condition.

At the subsonic inlet boundary, a characteristic-based formulation published by Moretti and Pandolfi /8/ is applied.

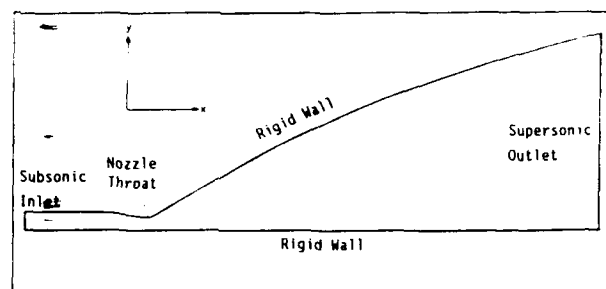


Fig. 3. Problem Specification

At each time-step, the mixture composition at the nozzle inlet equals the chemical equilibrium composition of a stoichiometric H_2 -air exhaust gas determined for the local values of static temperature and pressure. At the supersonic outlet boundary, information will never be carried backwards. Therefore, the λ -scheme does not require any specified boundary condition.

In order to reduce the complexity of the problem, the lower wall of the nozzle is extended to the nozzle exit. This implies a certain simplification with regard to actually projected nozzle specifications, where the lower wall is cut shorter than the upper wall to reduce weight. In the latter case, the ambient flow will interact with the nozzle exit flow. The interaction itself will depend on flight Mach number and on whether the nozzle flow is over- or underexpanded. Similar interactions have been previously studied by Semmler /9/, but without considering the impact of chemical effects.

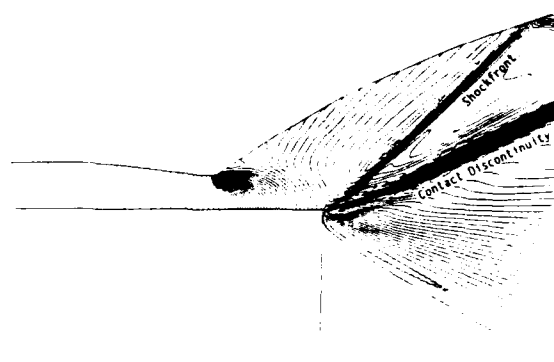


Fig. 4. Lines of Constant Mach Number for an Overexpanded Nozzle Flow

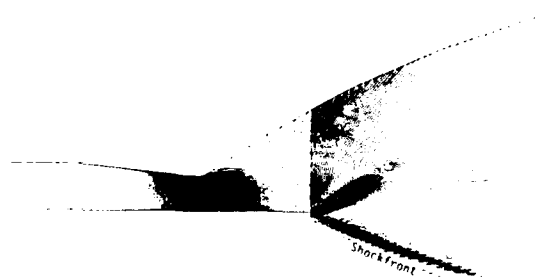


Fig. 5. Isobars for an Underexpanded Nozzle Flow

Fig. 4 shows the results for a typically overexpanded nozzle flow. The computations were carried out by use of the λ -scheme without any fitting procedure for embedded discontinuities. Nevertheless, the lines of constant Mach number clearly indicate an embedded oblique shock front and a contact discontinuity. In Fig. 5, the isobars for a typically underexpanded nozzle flow are plotted.

For the simulation of the finite-rate chemistry, a simplified reaction mechanism of the H_2 -air system is used. The chemical kinetics model includes six reacting species and the six reactions listed in Table 1 (Nitrogen is regarded as inert). The simplified mechanism is derived by means of a successive sensitivity analysis from a more comprehensive mechanism including 38 reaction paths, Rebhan /10/.

Table 1. Simplified Reaction Mechanism of the H_2 -Air-System

		A (m ³ , mol, s)	α	E/R (K)
Nr. 1:	$H_2 + O_2 = 2 OH$	$2.5 \cdot 10^8$	0	$1.964 \cdot 10^4$
Nr. 2:	$H + O_2 = OH + O$	$7.9 \cdot 10^8$	0	$8.863 \cdot 10^3$
Nr. 3:	$O + H_2 = OH + H$	$1.2 \cdot 10^7$	0	$4.663 \cdot 10^3$
Nr. 4:	$OH + H_2 = H_2O + H$	$4.0 \cdot 10^7$	0	$2.870 \cdot 10^3$
Nr. 5:	$H + O + M = OH + M$	$3.6 \cdot 10^8$	-1	0
Nr. 6:	$H + OH + M = H_2O + M$	$9.0 \cdot 10^8$	-1	0

5 DISCUSSION OF RESULTS

In the example presented below, the total length and the area ratio of the nozzle geometry shown in Fig. 3 are 12.3 m and 13.9, respectively. The nozzle inlet stagnation pressure and temperature (8 bar and 2780 K) are representative of a projected flight Mach number of 6.8. For these conditions, the mean residence time of the flow within the nozzle is about 9 msec.

Due to the physical compatibility of the numerical scheme applied, a rather coarse computational grid can be used without causing any substantial numerical inaccuracies. Fig. 6 shows a typical grid consisting of 60 x 15 grid points. Since most of the chemical behaviour and the fastest reactions occur in the throat region, the grid is refined here to maintain accuracy.

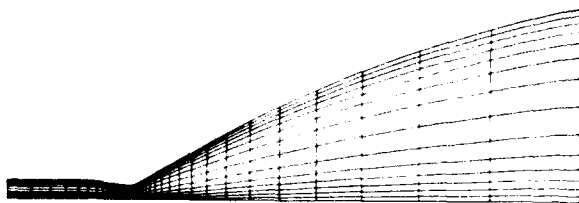


Fig. 6. Typical Grid

As initial start conditions for chemically frozen flow field computations, a 1D analytical calculation of the flow field variables proved to be sufficient. Preferably, the solution for the inert flow may then serve as the initial condition for the com-

putation of the chemically reacting flow field. In doing so, at the initial condition, the mass fractions of the chemical species are set constant within the flow field according to the chemical equilibrium composition of a stoichiometric H_2 -air exhaust gas determined for the nozzle inlet values of static pressure and temperature. In order to compare the results gained by the λ -scheme with the results of the classical method-of-characteristics, first calculations considered a chemically frozen flow in a divergent nozzle section, under the assumption of a constant specific heat ratio. In Fig. 7, the Mach number distribution along the upper nozzle wall is plotted for both methods, indicating a rather good agreement.

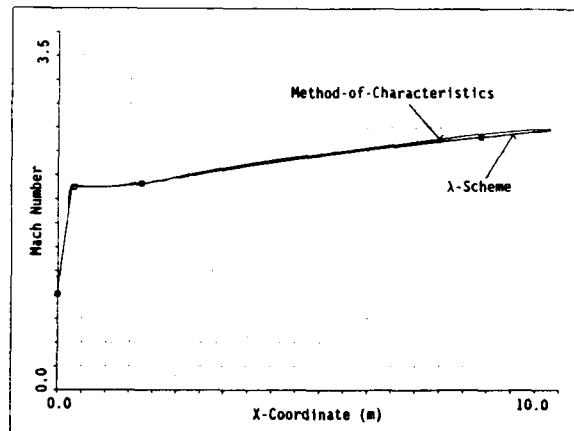


Fig. 7. Comparison of Mach Number Distributions

The major part of the numerical analyses, however, has been focussed on the simulation of chemistry effects comprising four special cases:

In the first case, as an extension of the computations mentioned above, the flow is regarded as chemically frozen but this time including a temperature-dependent specific heat ratio.

In the second case, the flow is considered to be in chemical equilibrium, implying that the local chemical reactions proceed infinitely fast. Thereby, the local equilibrium calculations are carried out analytically.

In the third case, the flow upstream of the nozzle throat is considered to be in chemical equilibrium, whereas downstream it is assumed to be frozen. Thus, this simulation technique corresponds to the well-known "Bray-approach", usually applied in 1D nozzle analyses, with the freezing cross section located at the nozzle throat. Finally, the fourth case performs the simulation of the finite-rate chemistry flow by use of the reaction mechanism listed in Table 1.

In Fig. 8, one interesting detail of the 2D results is extracted by plotting the temperature distributions against the lower nozzle wall length. Besides a general strong decrease of the static mixture temperature in the throat region, an obvious rise in temperature with increasing degree of chemical recombination can be observed. The difference between the inert and equi-

librium mixture temperature at the nozzle exit corresponds to approximately 6%. The chemical recombination effects, suppressed within the inert flow and completely unlocked within the equilibrium flow, are mainly associated with exothermic reactions giving rise to an increase in temperature.

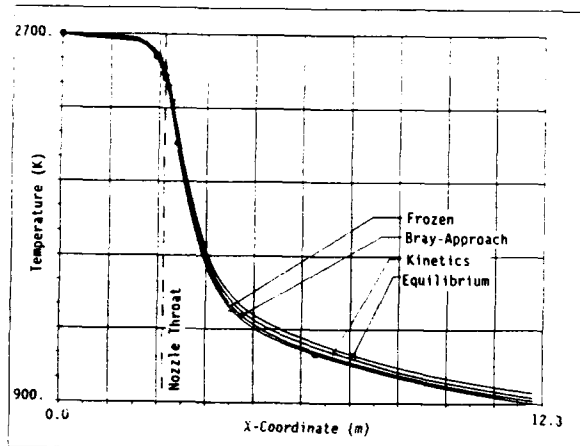


Fig. 8. Comparison of Temperature Distributions

Fig. 9 shows the isobars of the finite-rate chemistry calculation. The pressure distribution is rather insensitive to the modeling method. At the nozzle exit, the maximum pressure difference between the frozen and equilibrium flow is 3%, the pressure of the equilibrium flow being higher; the sensitivity of the Mach number is even smaller. At the nozzle exit, the Mach number of the frozen flow exceeds that of the equilibrium flow by a maximum of 1.5%, indicating that the increase in exit velocity is more than compensated by the temperature rise.

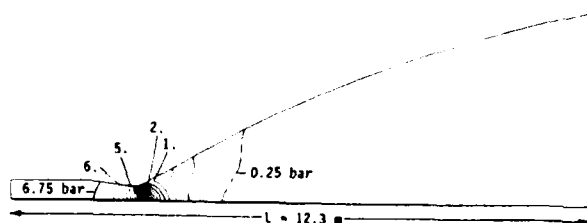


Fig. 9. Isobars for the Finite-Rate Chemistry Flow

Fig. 10 illustrates the time-marching solution technique by means of the transient variation of atomic hydrogen (H) distributions along the lower nozzle wall. Starting from a constant initial distribution, which corresponds to the equilibrium value at the nozzle inlet, the final steady state is achieved after about 10,000 time-steps. As expansion proceeds, and static temperature as well as pressure decrease accordingly, the amount of H mass fraction also tends to decrease. However, immediately downstream of the throat, a minimum is reached beyond which the mass fraction increases. This behaviour is due to the local production and depletion rates for the H-atom, which de-

pend on local mixture composition, flow temperature and pressure, constituting the complexity of the chemical kinetics mechanism.

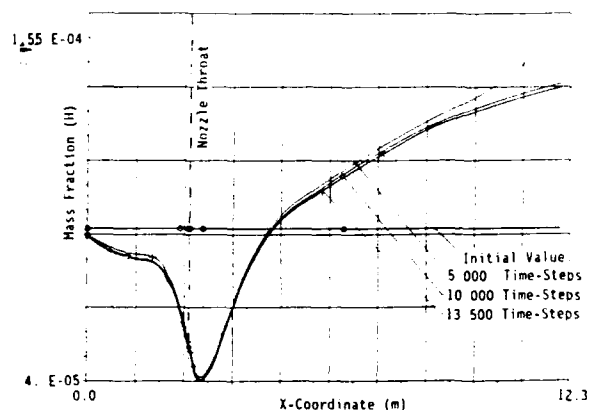


Fig. 10. Transient Variation of H - Mass Fraction Distributions

Figs. 11 and 12 reveal the field contours of the atomic hydrogen (H) and the highly reactive hydroxyl radical (OH) distributions respectively.

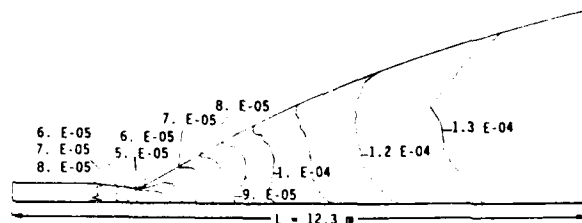


Fig. 11. Field Distribution of Atomic Hydrogen (H)

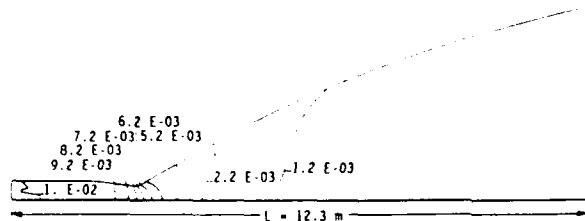


Fig. 12. Field Distribution of Hydroxyl Radical (OH)

In order to compare the local gas mixture compositions of the equilibrium and finite-rate chemistry flow, the mass fractions of the individual species along the upper wall are plotted in Figs. 13 and 14. Especially downstream of the throat region, the recombination of the species O, H, OH, as well as the depletion of fuel mass H_2 , proceed evidently faster with the equilibrium

flow.

Fig. 15 shows the corresponding distributions for the so-called "Bray-approach", assuming equilibrium upstream of the nozzle throat, and frozen chemistry downstream.

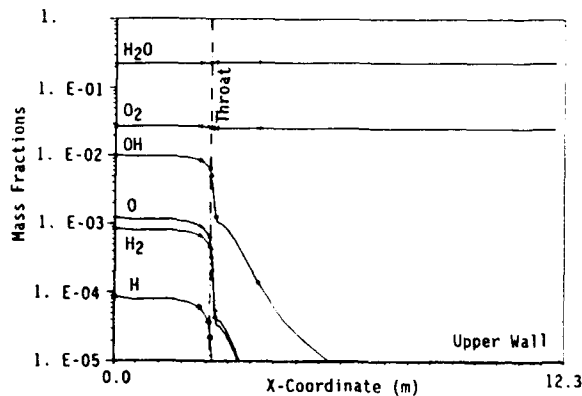


Fig. 13. Species Mass Fractions with the Equilibrium Flow

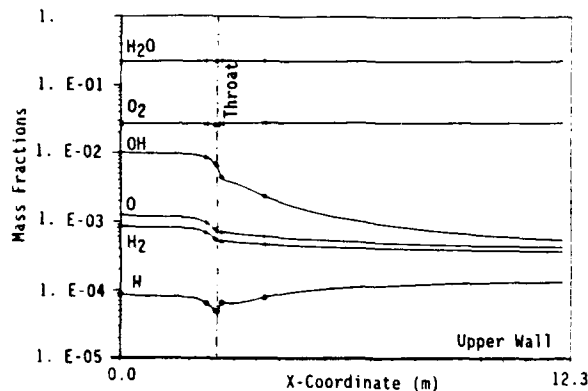


Fig. 14. Species Mass Fractions with the Finite-Rate Chemistry Flow

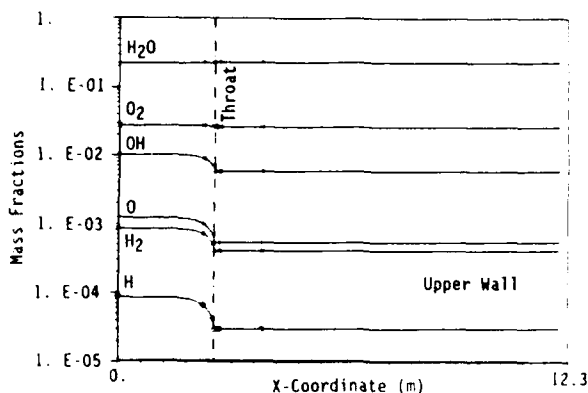


Fig. 15. Species Mass Fractions with the "Bray-Approach"

Finally, one of the most important results remains to be addressed: the influence of different chemistry modelling techniques on net engine thrust prediction.

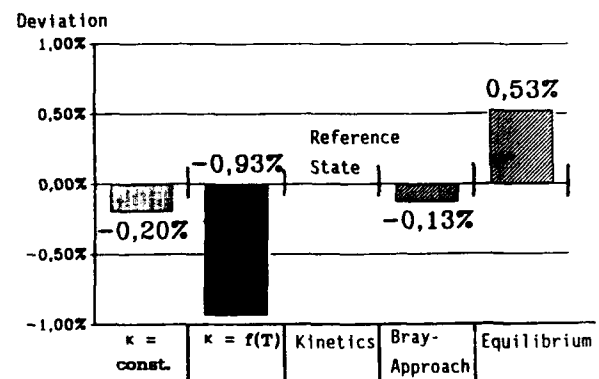
To describe the effects, Table 2 illustrates the specific impulses at the nozzle exit provided by the different chemistry models. The results are related to the physically most realistic finite-rate chemistry model.

The equilibrium model predicts the exit impulse to be approximately 0.5% too high. Bearing in mind that within the high flight Mach number range 6 to 7 the ratio of engine inlet to nozzle exit momentum may be as high as 0.8, this deviation results in an overprediction of net engine thrust by about 3%.

When considering the frozen model, the predicted impulse is recognized to be approximately 0.9% smaller compared to the finite-rate chemistry model, leading to an underprediction of net engine thrust by nearly 5%.

The so-called "Bray-approach" favourably approximates the finite-rate chemistry model in terms of nozzle exit impulse. As well as a reduction in the variation of the net thrust (in this case 0.7%) additional benefits can be obtained from a considerable reduction in the computing time.

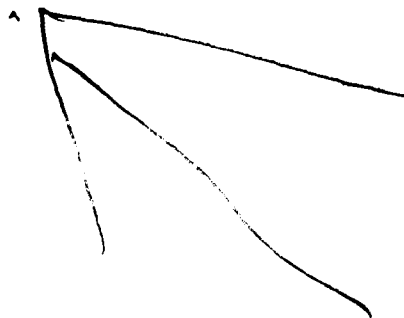
Table 2. Comparison of Specific Nozzle Exit Impulses



It is concluded, that the sensitivity of net engine thrust to different chemistry modelling techniques is rather high and that a physically inadequate model may lead to unacceptable defects in net thrust prediction. This is particularly true for the high-flight Mach number range, where the engine inlet momentum is high compared to that of the nozzle exit, and where the projected thrust reserves are generally low.

REFERENCES

- /1/ Harloff G.J., Lai H.T., Nelson E.S.: Two-Dimensional Viscous Flow Computations of Hypersonic Scramjet Nozzle Flowfields at Design and Off-Design Conditions, AIAA-88-3280, AIAA 24th Joint Propulsion Conference, 1988, Boston, Mass.
- /2/ Rizkalla O., Chinitz W., Erdos J.I.: Calculated Chemical and Vibrational Non-equilibrium Effects in NASP-Type Nozzles, AIAA 88-3263, AIAA 24th Joint Propulsion Conference, 1988, Boston, Mass.
- /3/ Moretti G.: The Lambda Scheme, Computers & Fluids 7, 191, 1979.
- /4/ Moretti G.: A Numerical Analysis of Muzzle Blast Precursor Flow, Computers & Fluids 10, 51, 1982.
- /5/ Moretti G. and Pandolfi M.: Entropy Layers, Computers & Fluids 1, 19, 1971.
- /6/ Lomax H. and Bailey H.E.: A Critical Analysis of Various Numerical Integration Methods for Computing the Flow of a Gas in Chemical Non-equilibrium, NASA TN D-4109 1967.
- /7/ De Neef T.: Treatment of Boundaries in Unsteady, Inviscid Flow Computations, Delft Univ. of Technology, Dept. of Aerospace Engineering, Report LR-262, 1978.
- /8/ Moretti G. and Pandolfi M.: Critical Study of Calculations of Subsonic Flows in Ducts, AIAA Journal 19, Nr. 4 1981.
- /9/ Semmler K.: Numerische Berechnung der reibungsfreien Strömung in 2-dimensionalen konvergent-divergenten Überschall-düsen, Studienarbeit TU Stuttgart 1989.
- /10/ Rebhan D.: Numerische Berechnung der NO_x -Emissionen eines Staustrahltriebwerkes für Hyperschall-Transportsysteme, Studienarbeit TU Stuttgart, 1989.



Discussion

M. ONOFRI, UNIV. OF ROME, ITALY

I noticed in your results a small variation of H_2O and O_2 concentrations during the expansion phase - Is that due to your operational temperature or to a low initial ion concentration of H_2 ? Can you please comment on this point?

AUTHOR'S REPLY

The nozzle inlet temperature and the inlet pressure are 2700 K and 7 atm, respectively. The gas composition at the inlet is equal to the equilibrium composition of a stoichiometric exhaust gas. The H_2O concentration increases by chemical recombination processes along the nozzle flow by about 10 percent, and the increase in O_2 is accordingly. However, due to the logarithmic scale chosen for Fig. 14, this change is hardly visible.

**CALCULS TRIDIMENSIONNELS D'ÉCOULEMENTS REACTIFS DANS LES CHAMBRES
DE COMBUSTION AERONAUTIQUES EFFECTUES A L'AIDE DE DEUX MODELES
DE COMBUSTION**

par

Fabienne PIT, Hélène TICHITSKY, Pascale GILBANK, Francis DUPOIRIEUX

**Office National d'Etudes et de Recherches Aérospatiales
29, Avenue de la Division Leclerc
92320 CHATILLON (FRANCE)**

Des calculs tridimensionnels ont été effectués afin de prévoir l'écoulement réactif dans les chambres de combustion aéronautiques. Deux types de modèle de combustion ont été testés : d'une part un modèle qui a recours à l'hypothèse de chimie rapide mais qui peut cependant prendre en compte certains aspects de la cinétique chimique par l'intermédiaire de délais d'inflammation, d'autre part, le modèle eulérien-lagrangien PEUL qui traite directement des lois d'Arrhenius au moyen du sous-modèle IEM (Interaction par Echange avec la Moyenne) et donc ne fait pas appel à l'hypothèse de chimie rapide.

**THREE DIMENSIONAL CALCULATIONS OF REACTIVE FLOWS WITHIN AIRCRAFT
COMBUSTION CHAMBERS INCLUDING SOME COMBUSTION MODELS**

by

Fabienne PIT, Hélène TICHITSKY, Pascale GILBANK, Francis DUPOIRIEUX

Some 3D calculations have been performed in order to predict the reactive flow within aircraft combustion chambers. Two kinds of combustion models have been tested: on one hand a model which makes the assumption of fast chemistry but can however take roughly into account some aspects of the chemical kinetics through an ignition delay and, on the other hand, the lagrangian-eulerian PEUL model which can deal directly with some Arrhenius laws by means of the IEM (Interaction by Exchange with the Mean) submodel and hence does not include some assumption of fast reaction.

INTRODUCTION:

L'amélioration des méthodes numériques et des modèles, la puissance croissante des ordinateurs permettent maintenant de calculer des flammes dans des configurations industrielles.

Ces calculs sont basés sur la résolution des équations de bilan moyennées de la mécanique des fluides contenant en particulier, les bilans d'espèces chimiques et d'énergie. Ces équations nécessitent des hypothèses de fermeture qui donnent lieu à des modèles. Ceux-ci sont déduits de l'analyse physique des phénomènes.

Ainsi, les flux turbulents sont obtenus au moyen du modèle $k-\epsilon$ (1-2) adapté aux écoulements à densité variable. Pour les écoulements réactifs, un autre problème crucial apparaît : il s'agit de la modélisation du (ou des) taux de réaction moyen(s). Différents modèles de combustion turbulente concernant des écoulements turbulents réactifs non parfaitement prémélangés sont présentés et deux de ces modèles sont appliqués à une configuration industrielle.

1- EQUATIONS EULERIENNES DE LA MECANIQUE DES FLUIDES.

Les équations de bilan régissant les écoulements réactifs turbulents peuvent se mettre sous la forme intégrale suivante :

$$\frac{\partial}{\partial t} \left(\iiint_V \bar{\rho} \tilde{f} dv \right) + \iint_{\Sigma} \vec{\Phi}_f \cdot \vec{n} d\sigma = \iiint_V \bar{\rho} \bar{S}_f dv$$

où $\bar{\rho}$ représente la valeur moyenne statistique de la masse volumique; \tilde{f} la moyenne de Favre (pondérée par la masse) des quantités suivantes: la masse volumique ($\tilde{f}=1$); la vitesse ($\tilde{f}=\tilde{u}_\alpha, \alpha=1,2,3$); l'énergie ($\tilde{f}=\tilde{e}$); la fraction massique du combustible ($\tilde{f}=\tilde{Y}_F$); la fraction massique d'un traceur inerte ($\tilde{f}=\tilde{Tr}$); $\vec{\Phi}_f$ représente le flux surfacique de la grandeur \tilde{f} par unité de surface et Σ la surface entourant le volume V ; \bar{S}_f représente le taux de production (ou de disparition) volumique de la quantité \tilde{f} (par exemple, production ou consommation par les réactions chimiques dans le cas d'un bilan d'espèce, forces volumiques dans le cas d'un bilan de quantité de mouvement).

Les flux turbulents sont modélisés par l'intermédiaire de l'énergie cinétique k et de sa dissipation ϵ dont on résout les équations de bilan. L'hypothèse classique de couche limite logarithmique permet de déduire les conditions à la paroi des équations de k et ϵ (3). Ces équations de bilan sont résolues numériquement par le code tridimensionnel DIAMANT (23) qui utilise une technique de volumes finis implicite.

Le taux de production moyen des espèces chimiques s'écrit sous la forme:

$$\tilde{W}_f = \int y_1 \int y_2 \dots \int y_n \int T w(y_1, y_2, \dots, y_n, T) * P(y_1, y_2, \dots, y_n, T) * dy_1 dy_2 \dots dy_n dT$$

où w est le taux de production instantané, P est la fonction densité de probabilité multi-espèces associée et n est le nombre d'espèces chimiques mises en jeu.

Pour déterminer ce terme, plusieurs approches sont possibles (4-5):

- les modèles où on résout l'équation de transport pour la fonction densité de probabilité $P(y_1, y_2, \dots, y_n, T)$ (6-11);
- les modèles hybrides ou à p.d.f. présumée dans lesquels on fait des hypothèses sur la forme de la fonction P (12-17);
- les modèles lagrangiens dans lesquels on introduit la notion de trajectoires de particules fluides (18-20);
- les modèles de type flamme cohérente liés au concept de flamme mince (21-22).

Nous avons testé deux modèles de combustion turbulente : le modèle hybride CRAMER et le modèle lagrangien PEUL dans le cas d'un écoulement réactif turbulent non parfaitement prémélangé à richesse globale faible.

2. LE MODELE HYBRIDE CRAMER.

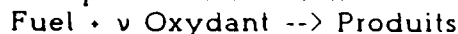
Le modèle CRAMER fait l'hypothèse que les réactions chimiques sont rapides. Il prend en compte le fait qu'un niveau minimal de richesse et de température est requis pour l'inflammation. Dans ce modèle, le taux de production instantané w et la fonction densité de probabilité associée sont évalués.

Dans le cas d'un foyer de turboréacteur, les gaz pénètrent soit sous forme d'air pur par les trous primaires, les trous de dilution et les films de refroidissement, soit sous forme d'un mélange air-combustible par les injecteurs de combustible. Pour simplifier l'exposé, on suppose que la richesse est inférieure à 1 (excès de comburant), y compris à la sortie des injecteurs de combustible. Dans le plan de coordonnées (Y_F, φ) (φ variable de Schwab-Zeldovich), toutes ces entrées sont représentées par seulement deux points notés A et B ; au point A, on a $Y_F - Y_{FA} > 0$ alors qu'au point B, $Y_F - Y_{FB}$ est nul. Dans l'espace des phases (Y_F, φ) représenté figure 1, la droite AB correspond à une ligne de mélange sans combustion de particules fluides issues des deux entrées. La droite CO correspond à une ligne où les particules brûlent. Les particules fluides contenues dans le triangle BCD ($\varphi < \varphi_C$) ne brûlent pas car leur richesse est supposée trop faible.

Considérons une particule fluide, non brûlée, initialement au point M de la droite AB. Avec l'hypothèse de chimie rapide, la particule consomme tout son combustible instantanément et se retrouve au point M' de la droite CO tel que :

$$\varphi_M = (v.M_O / M_F).Y_{FM} - Y_{OM} = \varphi_{M'} = -Y_{OM}$$

v coefficient stoechiométrique de la réaction :



M_O et M_F représentent la masse molaire de l'oxydant et du fuel, Y_O et Y_F les fractions massiques de l'oxydant et du fuel.

Ainsi, pour toute particule fluide telle que $\varphi > \varphi_C$, on a :

$$\text{si } Y_F \neq 0, w=0 \quad \text{et si } Y_F=0, w \neq 0.$$

Tant que $Y_F \neq 0$, la température de la particule fluide est faible et l'inflammation n'a pas lieu ($w=0$). Dès que Y_F se rapproche de 0 la température se rapproche de la température de fin de combustion (cela peut se vérifier facilement à partir d'un bilan d'énergie) et l'inflammation a lieu, ce qui conduit à un taux de réaction non nul, le combustible échangé avec l'extérieur maintient un taux de production non nul à l'intérieur de la particule fluide.

Les équations lagrangiennes déduites du modèle I.E.M. décrit plus loin s'écrivent :

$$\frac{dY_F}{dt} = \frac{\tilde{Y}_F - Y_F}{\tau} - w$$

avec τ temps caractéristique du mélange.

En particulier, pour $Y_F=0$ extréma, on a

$$\left. \frac{dY_F}{dt} \right|_{Y_F=0} = 0 = \frac{\tilde{Y}_F}{\tau} - W$$

En moyennant l'équation ci-dessus et en tenant compte des considérations précédentes, on obtient pour le taux de réaction moyen :

$$\tilde{W} = \frac{\tilde{Y}_F}{\tau} \int P(Y_F) dY_F$$

Dans le cas particulier d'un écoulement prémélangé avec un excès de comburant, la formule ci-dessus se simplifie :

$$\tilde{W} = \frac{\tilde{Y}_F}{\tau} \left(1 - \frac{\tilde{Y}_F}{\tilde{Y}_F} \right)$$

τ est un temps caractéristique d'échange ; en principe il est proportionnel à $\tilde{Y}^2/\varepsilon_y$ (ε_y taux moyen de destruction de \tilde{Y}^2). Etant donné l'analogie entre les équations de \tilde{Y}^2 et de k d'une part, de ε_y et de ε d'autre part, on considère pour simplifier que τ est proportionnel à k/ε .

3- MODELE LAGRANGIEN PEUL.

Une autre façon de calculer le taux moyen de production des espèces W est de faire une moyenne arithmétique de w sur un grand nombre d'événements : $W = 1/N \sum w_n$. Cette méthode permet de s'affranchir de la connaissance de la fonction densité de probabilité. En revanche, il faut déterminer le taux de production instantané dans les particules fluides. Pour cela, il faut déterminer la trajectoire physique de ces particules ainsi que l'évolution en fonction du temps de leur concentration et leur température.

3.1 - MODELISATION DE LA DISPERSION TURBULENTE.

Pour déterminer la trajectoire d'une particule fluide, il faut résoudre l'équation :

$$\frac{d\vec{x}(t)}{dt} = \vec{u}(\vec{x}(t)) = \vec{u} + \vec{u}'$$

avec \vec{u} vitesse moyenne de la particule à l'instant t . Cette vitesse est déduite d'un calcul eulérien précédent effectué par exemple avec le modèle CRAMER. La fluctuation de la vitesse U' est évaluée à l'aide d'un modèle de dispersion turbulente (24). Pour cela, on fait les hypothèses suivantes :

- la densité de probabilité du couple de vitesses $(U(t_1), U(t_2))$ à deux instants différents et le coefficient de corrélation lagrangienne $R_L(t)$ ne dépendent que de la différence de temps $\tau = |t_1 - t_2|$;

- la corrélation lagrangienne $R_L(\tau)$ s'exprime à l'aide de fonctions de Frenkiel (25) :

$$R_L(\tau) = \exp(-\tau/(m^2+1)\vartheta_L) \cos(m\tau/(m^2+1)\vartheta_L)$$

avec $\tau = |t_1 - t_2|$ et ϑ_L échelle temporelle lagrangienne, m est un paramètre réel fonction du nombre et de l'importance des boucles négatives dans la corrélation ;

- les fonctions densité de probabilité de vitesse sont gaussiennes ;
- les corrélations spatio-temporelles peuvent s'exprimer simplement à l'aide des corrélations spatiales et de la corrélation lagrangienne $R_L(\tau)$.

Avec ces hypothèses, on peut modéliser la matrice de corrélations associée à la loi de probabilité de U' (matrice notée A). A partir de cette matrice A et d'un vecteur Y dont les composantes résultent du tirage de variables aléatoires normales centrées indépendantes, il est possible d'obtenir une évaluation de U' : si la modélisation est correcte, A est symétrique définie positive de sorte qu'il existe une matrice B telle que $A = BB^T$ (B^T transposée de B) ; le vecteur U' est alors égal à BY . La matrice B est obtenue au moyen de l'algorithme de CHOLESKI.

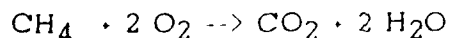
3.2 - MODELE I.E.M. .

A tout instant, on connaît la position des particules fluides suivies ; pour connaître leur évolution chimique, il est possible d'utiliser le modèle d'Interaction par Echange avec la Moyenne (I.E.M.) (27). Ce modèle tient compte de l'interaction entre la particule et son environnement extérieur. Il est écrit ici sous une forme adaptée au problème de la combustion turbulente :

$$\frac{dY_i}{dt} = \frac{(\tilde{Y}_i - Y_i)}{\tau} + w_i$$

Y_i est la fraction massique de l'espèce i dans la particule ; w_i est le taux de production ou de consommation instantané de l'espèce i dans cette même particule. Le terme $(\tilde{Y}_i - Y_i)/\tau$ représente le taux d'échange massique de l'espèce i entre la particule et son environnement ; \tilde{Y}_i représente la fraction massique moyenne de l'espèce i à l'endroit où se trouve la particule. Ce modèle permet de prévoir l'avancement de réactions chimiques simples ou complexes.

Nous l'avons appliqué à une cinétique chimique (28) à une étape qui se traduit, dans le cas où le combustible est le méthane, par :



La vitesse de production chimique est donnée par la loi d'Arrhenius :

$$w = K \cdot Y_{\text{CH}_4}^a \cdot Y_{\text{O}_2}^b \cdot T^c \cdot \exp(E_A/RT)$$

avec $a=0.7$; $b=0.8$; $c=0$; $K=3 \cdot 10^{13}$; $E_A=48000 \text{ J}$.

τ est le temps caractéristique du mélange comme précédemment, on considère qu'il est proportionnel à k/ϵ .

3.3 TAUX DE PRODUCTION MOYEN.

En un endroit déterminé de l'écoulement, on voit passer un nombre N' de particules fluides. Dans l'espace des phases associé (Y_p, φ) (figure 2), on observe un nuage de points, chaque point correspond à la composition chimique d'une particule fluide. En fait, si N' est assez grand, cet ensemble de points correspond à la projection de la fonction densité de probabilité dans ce plan.

On peut évaluer le taux de production moyen en effectuant une moyenne arithmétique dans chaque maille de l'écoulement. Ces grandeurs étant définies, nous pouvons les introduire comme terme source dans le code eulérien DIAMANT. On obtient un écoulement moyen modifié par rapport au premier calcul. On peut à nouveau calculer des trajectoires et le taux moyen de production associé. On poursuit ce processus itératif jusqu'à convergence des résultats.

4. RESULTATS NUMERIQUES.

L'écoulement turbulent réactif dans une chambre de combustion aéronautique a été calculé. Le maillage extérieur correspondant à la demi chambre est représenté figure 3. Sur le fond avant, on peut voir la trace d'un demi-injecteur ; sur la paroi supérieure, on voit la trace d'un orifice primaire et de deux orifices secondaires ; de même sur la paroi inférieure, on peut voir la trace d'un orifice primaire et de deux demi orifices secondaires.

Au niveau de l'injecteur aérodynamique (entrée A), le débit surfacique de gaz est de $14 \text{ kg/m}^2\text{s}$, la fraction massique de combustible est 0,05. Au niveau des orifices primaires et secondaires (entrée B), le débit surfacique est de $48 \text{ kg/m}^2\text{s}$. La température d'entrée de tous les gaz est de 746K . Le niveau de pression, qui est fixé par la pression de sortie, est de l'ordre de une atmosphère.

Un premier écoulement stationnaire, sans combustion, a été effectué. La combustion a été initiée en simulant une étincelle dans une cellule où la vitesse des gaz est faible. Un nouvel état stationnaire a été obtenu avec le code DIAMANT et le modèle CRAMER. Sur les figures 4 et 5, nous avons représenté les champs de vitesse et de température obtenus dans les plans longitudinaux J-1 (dans lequel on voit la trace du demi-injecteur et de deux trous secondaires), J-9 (où on observe la trace de l'injecteur, de trous primaires et secondaires), J-15 (où on voit la trace de trous secondaires) et en plus pour la température, les plans transversaux I-1 et I-30. La figure 6 représente le taux moyen de production \bar{W} en fonction de la concentration \bar{Y}_F et de la température \bar{T} . La courbe est en forme de cloche. On distingue bien les deux entrées A et B. On observe qu'une température minimale environ 1000°K est requise pour l'inflammation des particules fluides.

Au total 12600 particules fluides ont été injectées (7000 dans le demi-injecteur et 5600 dans les trous primaires et secondaires). La figure 7 représente le champ de température \bar{T} obtenu par moyenne arithmétique des résultats lagrangiens dans les plans J-1, J-9, J-15. La température des jets à leur sortie reste proche de la température d'injection sur une distance non négligeable et la température dans les zones chaudes près du fond avant sont proches de la température de fin de combustion. Aussi, il existe de forts gradients de température. La température en sortie de chambre est de l'ordre de 1500K . La figure 8 représente le taux moyen de production en fonction de \bar{Y}_F et de \bar{T} (valeurs obtenues par moyenne arithmétique). On peut faire les mêmes constatations que sur les températures.

Les figures 9 et 10 montrent l'évolution, en fonction du temps, de la fraction massique du combustible et de la température de deux particules fluides. La première particule fluide est issue du demi-injecteur, sa fraction massique de combustible est proche de 0,05. Initialement elle se mélange avec l'écoulement moyen, ce qui provoque son échauffement, puis elle brûle. Enfin, elle se refroidit au contact des jets primaires et secondaires. La seconde particule est issue d'un trou primaire, sa fraction massique, initialement faible 0,005, augmente par échange avec l'écoulement moyen, en même temps la particule s'échauffe, puis brûle et se refroidit au contact des jets secondaires. Ce travail étant en cours de développement, la partie itérative n'a pas été faite.

5 - CONCLUSIONS

Dans les écoulements industriels, différents régimes de combustion sont possibles. L'influence de la chimie sur les caractéristiques de l'écoulement est aussi importante que la turbulence elle-même. Le processus de modélisation de la combustion doit-être le plus réaliste possible : il doit comporter plusieurs schémas réactionnels et de nombreuses espèces chimiques.

Afin de prédire les caractéristiques aérothermochimiques d'un écoulement de type industriel, nous avons utilisé un modèle hybride CRAMER et un modèle lagrangien PEUL. Le modèle CRAMER fait appel à l'hypothèse de chimie rapide et à une cinétique chimique globale. Le taux de production est fonction de la fraction massique du combustible et d'un traceur inerte. Le modèle PEUL peut prendre en compte des hétérogénéités de richesse et des cinétiques chimiques complexes. Même si nous n'avons utilisé qu'une cinétique chimique à une étape, le taux de production est fonction des espèces chimiques mises en jeu.

Ce nouveau modèle est prometteur pour le traitement des écoulements réactifs turbulents tridimensionnels dans les foyers aérobies.

- (1) LAUNDER B. E., SPALDING D. B., Computer methods in applied Mechanics and Engineering, vol. 3, n°2, p 269 (1974).
- (2) LAUNDER B. E., Turbulence, P. BRADSHAW ed., Topics in Applied Physics, SPRINGER VERLAG (1976).
- (3) PIT F., TICHITSKY H., DUPOIRIEUX F., 3D calculations of reacting flows within aircraft engine combustion chambers, 3rd International Seminar on Flame Structure, Alma-Ata U.R.S.S. September 18-22th. (1989).
- (4) BORCHI R.
- (5) WILLIAMS F. A., Combustion Theory (1965).
- (6) POPE S. B., The probability approach to the modeling of turbulent reacting flows, Comb. and Flame vol. 27, p 299-312 (1976).
- (7) ANAND M. S., POPE S. B., Calculations of premixed turbulent flames by p.d.f. methods, Comb. and Flame, vol. 67 p.127-142 (1987).
- (8) DOPAZO C., Relaxation of initial probability density function in the turbulent convection of scalar field, Phys. Fluids 22.20 (1979).
- (9) O'BRIEN E. E., The probability density function approach to reacting turbulent flows, in LIBBY P. A. and WILLIAMS F. A. ed. Turbulent reacting flow SPRINGER VERLAG Berlin Chap. 5.
- (10) JANIKA J., KOLBE W., KOLLMAN W., Closure of the transport equation for the probability density function scalar field, J. Non equilibri. Thermodyn. 4, 47.
- (11) CHEN J. Y., KOLLMAN W., p.d.f. modeling non equilibrium effects in turbulent non-premixed hydrocarbon flames, 22nd Symposium (Int.) Combust. The Combustion Institut Pa. (1988).
- (12) SPALDING D. B., MA A. S. C., NOSEIR M. A., An application of the E.S.C.I.M.O. Theory of turbulent combustion, AIAA 80-0014.
- (13) BILGER R. W., The structure of diffusion flame, Project Squid T.R. USCD T PU (1975).
- (14) LOCKWOOD F. C., NAGUIB A. S., Second Combustion Institute European Symposium p.502 (1975).
- (15) WILLIAMS F. A., LIBBY P. A., Some implications of recent theoretical studies in turbulent combustion, AIAA 80-0012 (1980).
- (16) BORCHI R., MOREAU P., Turbulent combustion in a premixed flow, Acta Astronautica, vol. 4, p.321-341 (1977).
- (17) BRAY K. N. C., MOSS, LIBBY,
- (18) BORCHI R., POURBAIX E., On the coupling of complex chemistry with a turbulent combustion model, Physico-chemical Hydrodynamics vol. 2, p.65-77 n°1981-1.
- (19) BORCHI R., GONZALES M., Applications of the lagrangian models to turbulent combustion, Comb. and Flame vol.63, p.239-250 (1986).
- (20) GILBANK P., Contribution à la modélisation de la combustion turbulente dans le cas d'une stabilisation par accroche-flamme, Thèse de Doctorat de l'Université PARIS VI.
- (21) MARBLE F. E., BROADWELL J. E., Project Squid technical report TRW9PU, Purdue University (1977).
- (22) MAISTRET E., DARABIHIA N., POINSOT T., VEYNANTE D., CANDEL S., ESPOSITO S., Recent developments in the coherent flamelet description of the turbulent combustion, 3eme Conférence internationale sur la combustion numérique Antibes (1989).
- (23) PIT F., DUPOIRIEUX F., TICHITSKY H., LACAS F., 3D numerical simulation for an aircraft engine type combustion chamber, 9th ISABE, Athènes, September 4-9 (1989).
- (24) BERLEMONT A., DEJONQUERES P., GOUESBET G., Particule lagrangian simulation in turbulent flows, Int. J. Multiphase flow vol. 16, n°1, p.19-34 (1990).
- (25) FRENKIEL F. N., Etude statistique de la turbulence: fonctions spectrales et coefficients de corrélations, Rapport Technique O.N.E.R.A. n°34 (1948).
- (26) CIARLET P. G., Introduction à l'analyse numérique matricielle, Masson Paris (1982).
- (27) AUBRY C., VILLERMAUX J., Représentation d'un mélange imparfait de deux courants réactifs dans un réacteur agité continu, Chemical Engineering Sci., vol.30, p.457-464 (1975).
- (28) CATHONNET M., BOETTNER J. C., GAILLARD F., Etude cinétique des réactions en combustion, C.R.C.C.H.T. CNRS Orleans.

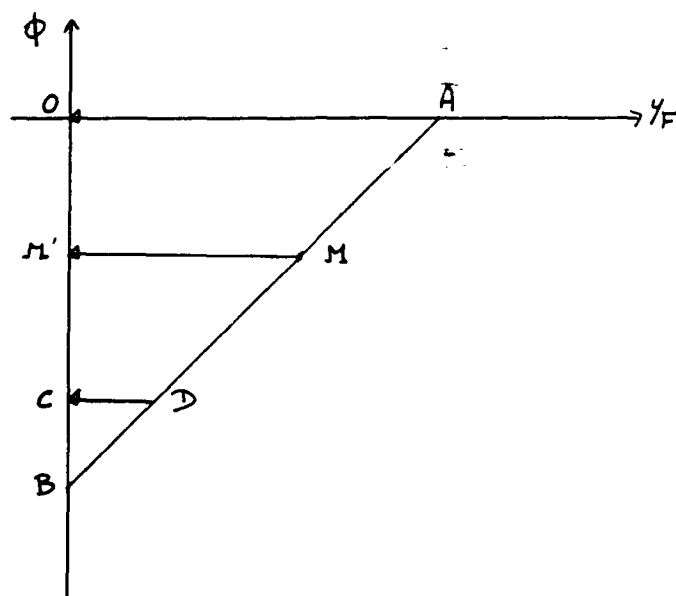


figure 1: Espace des phases (modèle I. E. M.).

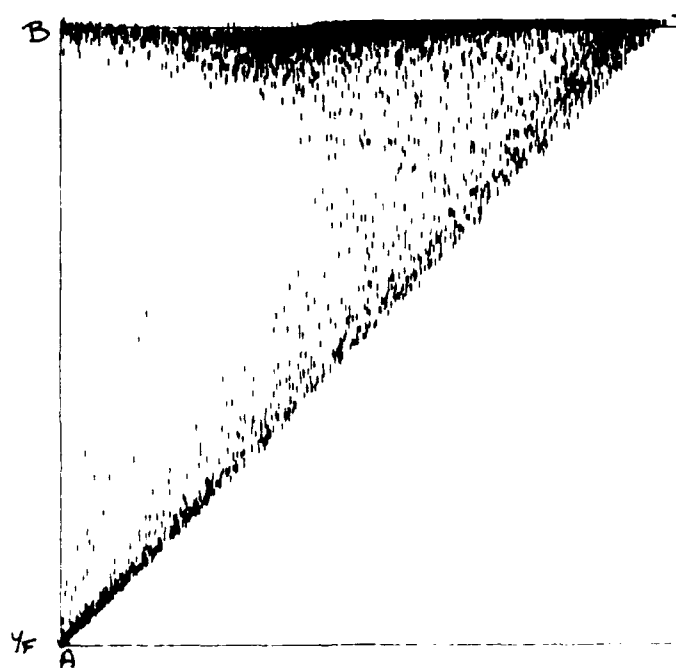


figure 2: Espace des phases (modèle P.E.U.L.).

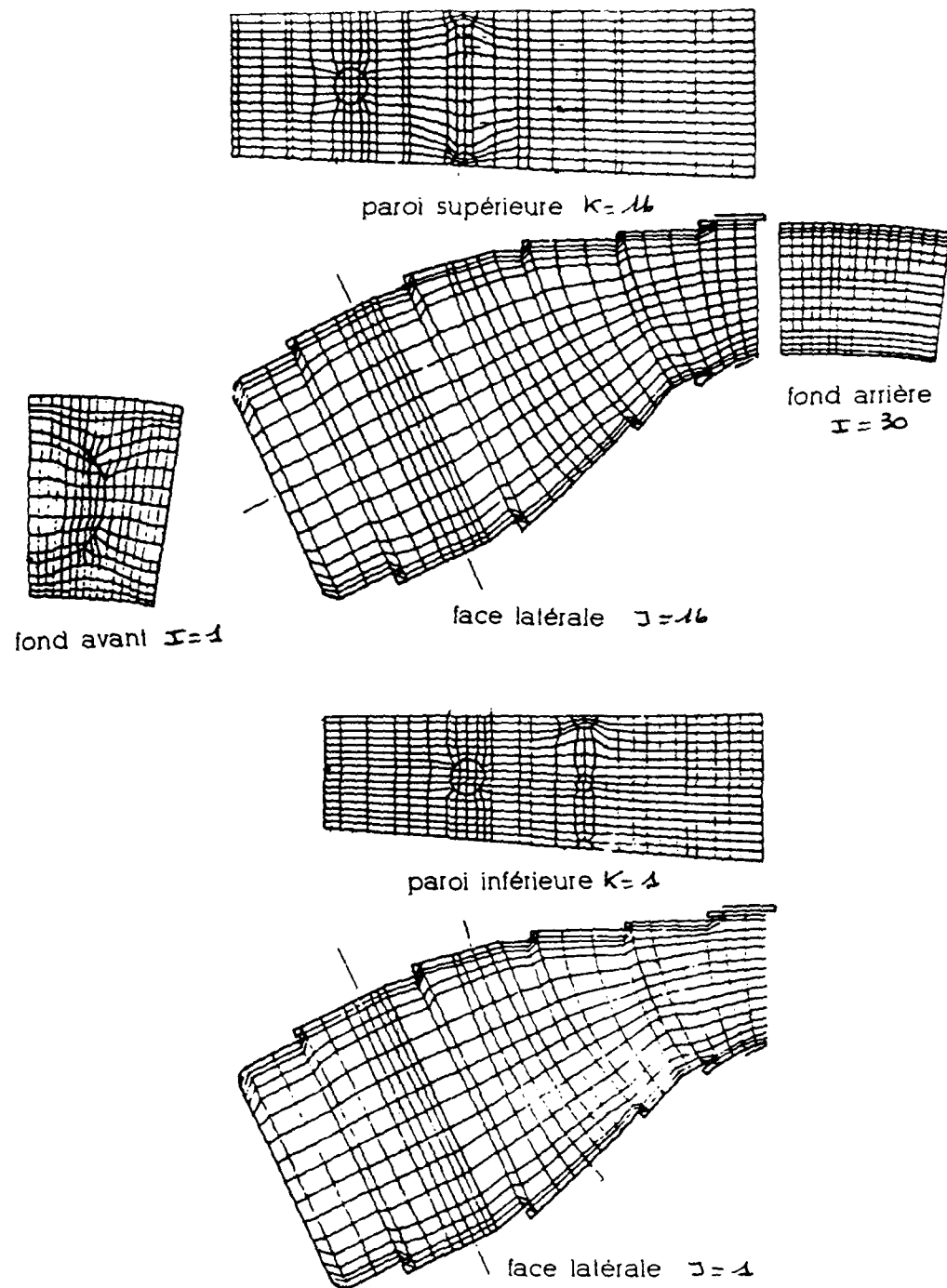


figure 3: Maillage extérieur de la chambre de combustion.
 $30 \times 16 \times 16$

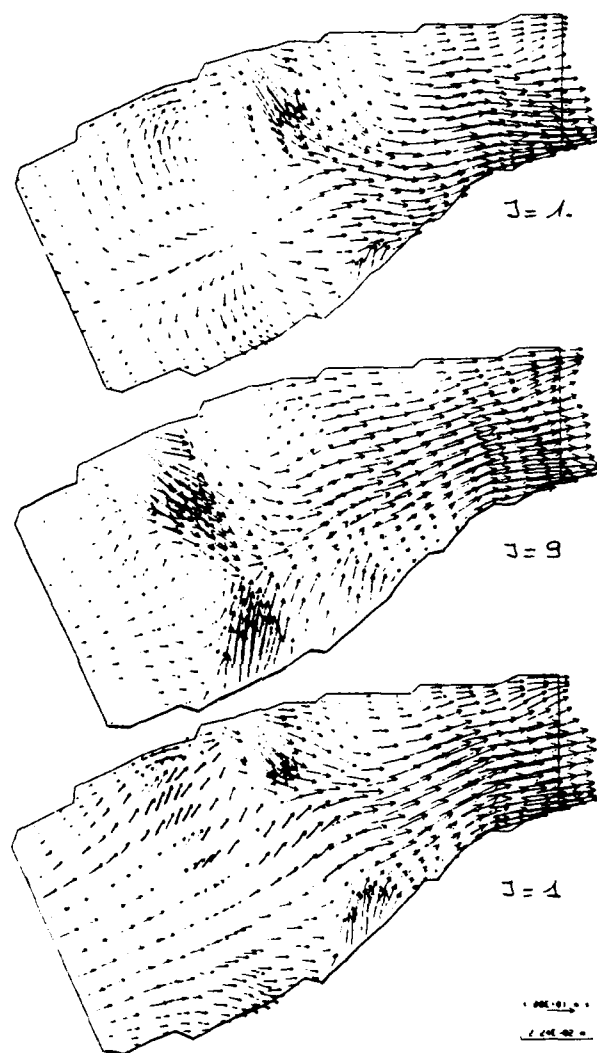


figure 4: Champ de vitesse (modèle CRAMER).

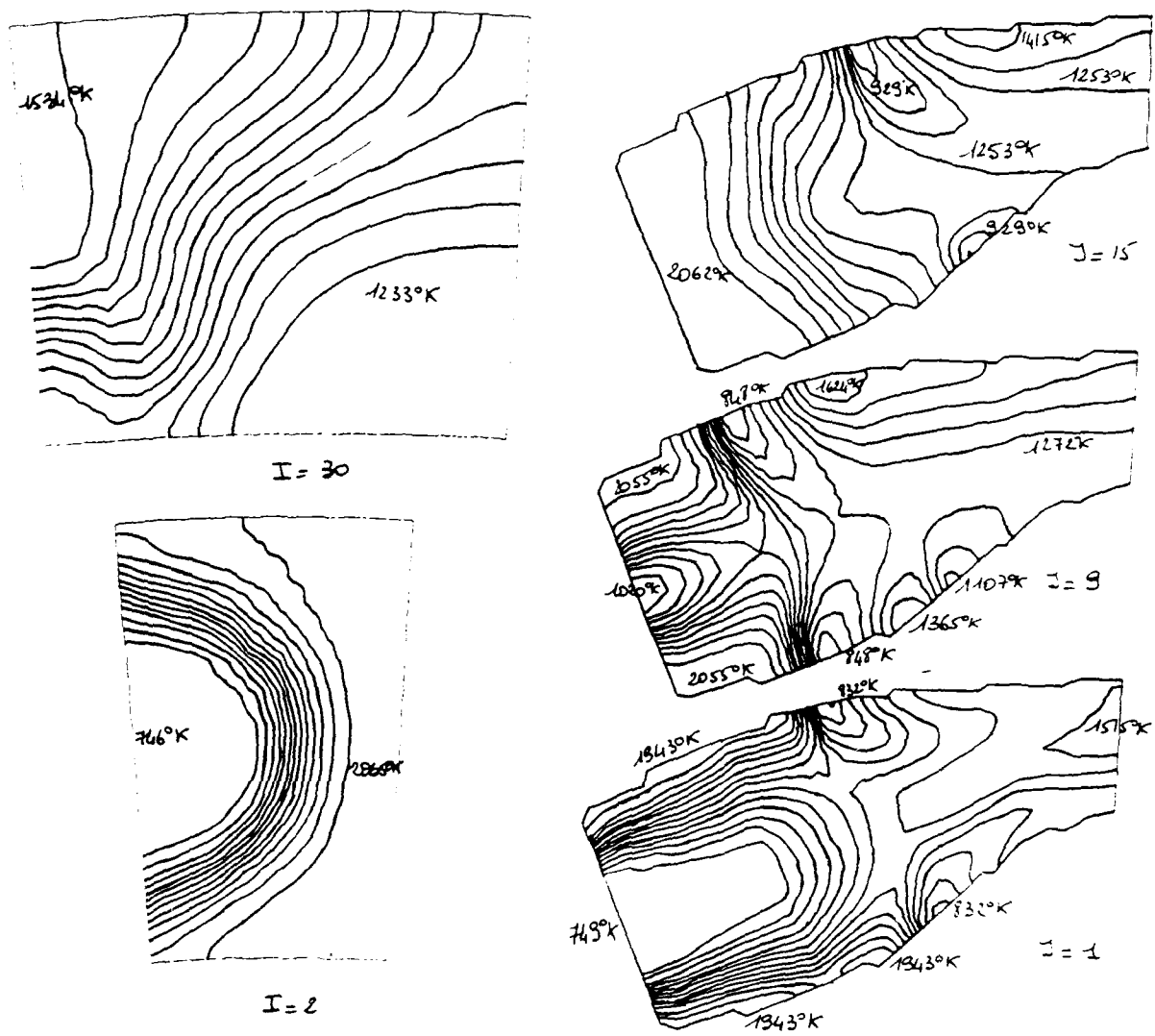


figure 5: Champ de température (modèle CRAMER).

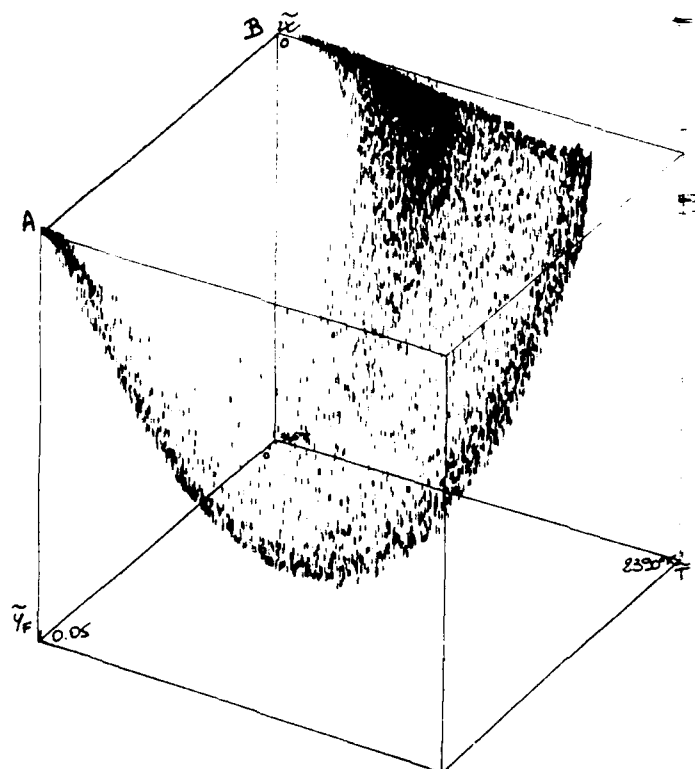


figure 6: Taux de production moyen
(modèle CRAMER).

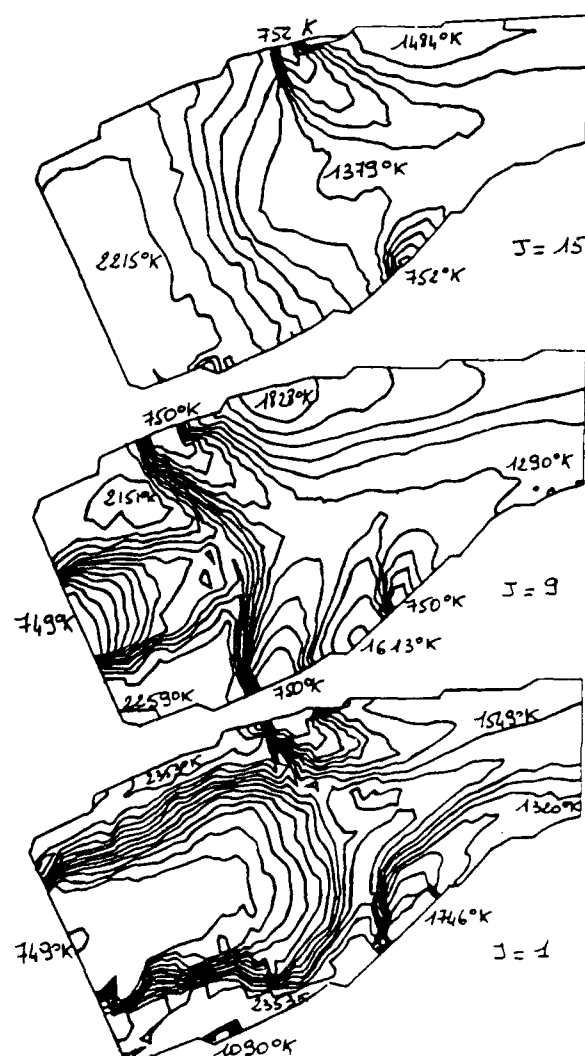


figure 7: Champ de température
(modèle PEUL).

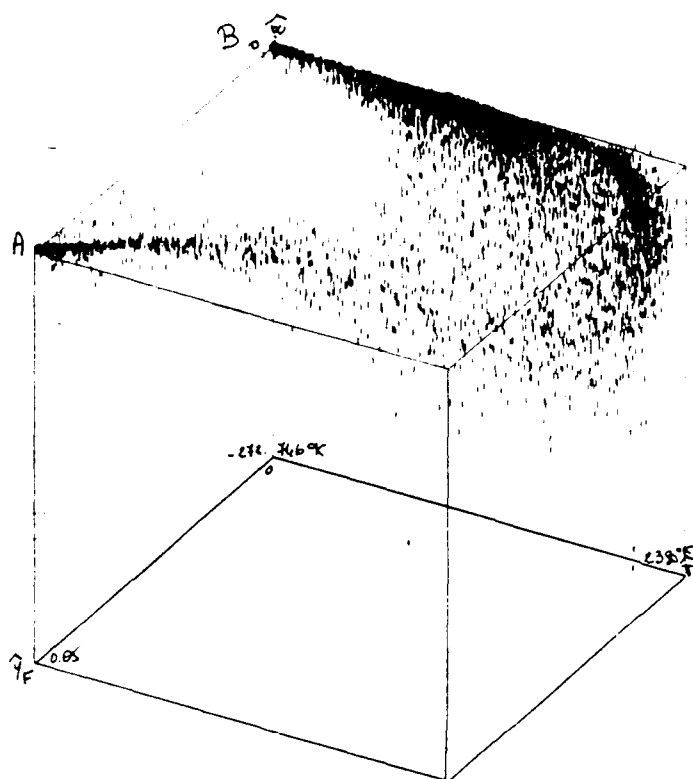


figure 8: Taux de production moyen
(modèle PEUL).

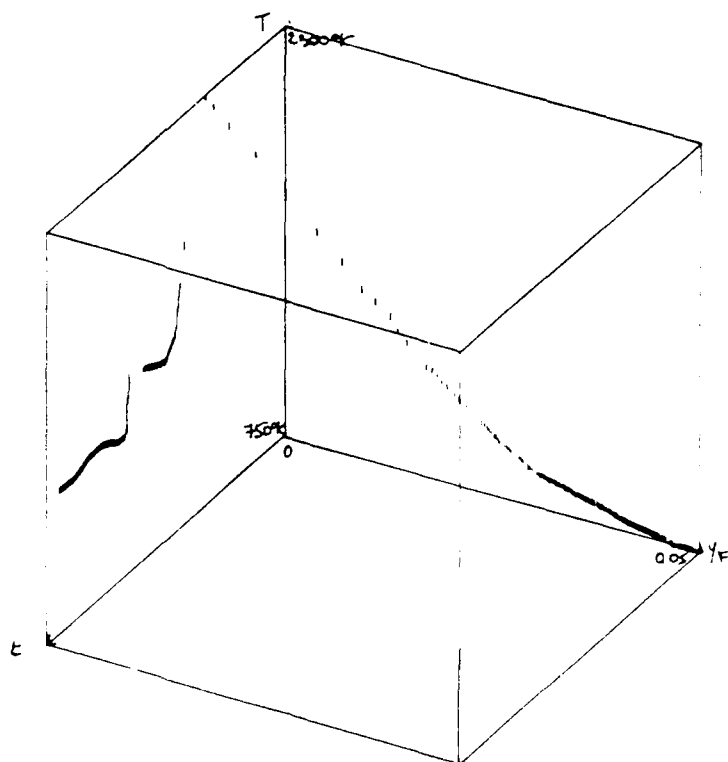


figure 9: Evolution en fonction
du temps de y_f et T d'une
particule fluide issue
de l'injecteur.

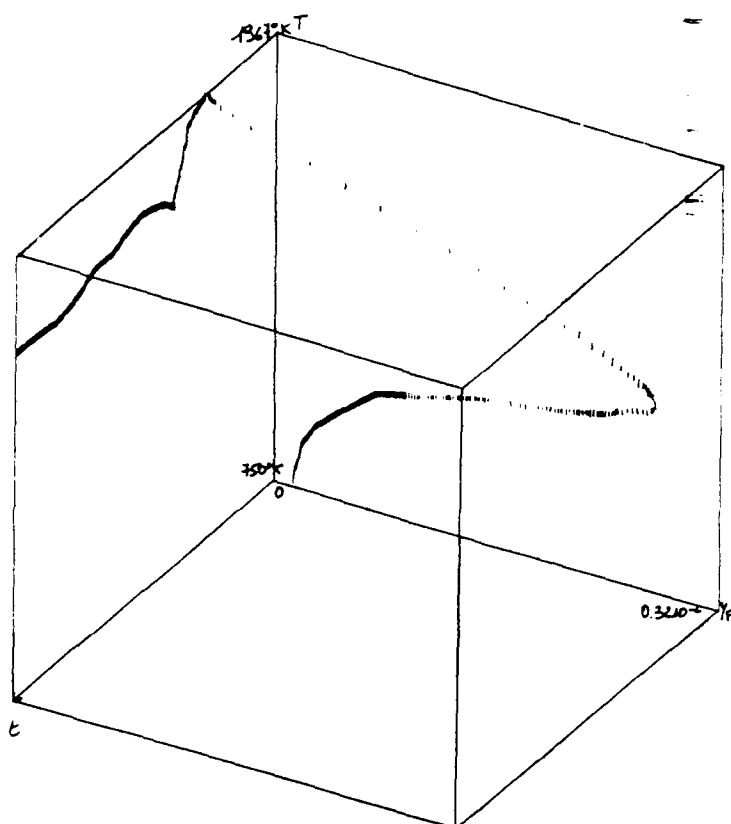


figure 10: Evolution en fonction du temps de y_f et T d'une particule fluide issue d'un trou primaire.

Discussion

R. WALTHER, MTU, GERMANY

Do you see any possibility to extend your model for the simulation of pollutant formation processes, for example NO_x ?

AUTHOR'S REPLY

Oui, nous espérons pouvoir introduire la simulation des processus de création des polluants. Ces derniers seront introduits au niveau du choix de la cinétique chimique.

REPORT DOCUMENTATION PAGE

1. Recipient's Reference	2. Originator's Reference	3. Further Reference	4. Security Classification of Document
	AGARD-CP-510	ISBN 92-835-0659-6	UNCLASSIFIED
5. Originator	Advisory Group for Aerospace Research and Development North Atlantic Treaty Organization 7 rue Ancelle, 92200 Neuilly sur Seine, France		
6. Title	CFD TECHNIQUES FOR PROPULSION APPLICATIONS		
7. Presented at	the Propulsion and Energetics Panel 77th Symposium held in San Antonio, Texas, United States, 27th to 31st May 1991.		
8. Author(s)/Editor(s)	Various		9. Date February 1992
10. Author's/Editor's Address	Various		11. Pages 596
12. Distribution Statement	This document is distributed in accordance with AGARD policies and regulations, which are outlined on the back covers of all AGARD publications.		
13. Keywords/Descriptors			
Computational fluid dynamics Jet propulsion Three dimensional flow Viscous flow Unsteady flow Computer programs Proving		Hypersonic flow Navier-Stokes equations Turbomachinery Numerical analysis Intakes Jet engine nozzles	
14. Abstract			
<p>The Conference Proceedings contains the 40 papers and the Technical Evaluation presented at the Propulsion and Energetics Panel 77th Symposium on "CFD Techniques for Propulsion Applications", which was held 27th—31st May 1991 in San Antonio, Texas, United States.</p> <p>The Symposium was composed of the following sessions: Turbomachinery Computations and Validations (21); Flow in Ducts, Intakes and Nozzles (11); Reacting Flows (8). Questions and answers of the discussions follow most papers in the Proceedings.</p> <p>The papers presented covered full three-dimensional code validation and numerical techniques, multi-dimensional reacting flow and unsteady viscous flow for the entire spectrum of propulsion system components. The capabilities of the various numerical techniques were assessed, and significant new developments were identified. The Technical Evaluation spells out in detail where progress has been made and that the present state of the art has almost reached the level necessary to tackle the comprehensive topic of CFD Validation for Propulsion.</p>			

<p>AGARD Conference Proceedings 510 Advisory Group for Aerospace Research and Development, NATO CFD TECHNIQUES FOR PROPULSION APPLICATIONS Published February 1992 596 pages</p> <p>The Conference Proceedings contains the 40 papers and the Technical Evaluation presented at the Propulsion and Energetics Panel 77th Symposium on "CFD Techniques for Propulsion Applications", which was held 27th-31st May 1991 in San Antonio, Texas, United States.</p> <p>The Symposium was composed of the following sessions: Turbomachinery Computations and Validations (21); Flow in Ducts, Intakes and Nozzles (11); Reacting Flows (8). Questions and answers of the discussions follow most papers in the Proceedings.</p> <p>P.T.O.</p>	<p>AGARD-CP-510</p> <p>Computational fluid dynamics Jet propulsion Three dimensional flow Viscous flow Unsteady flow Computer programs Proving Hypersonic flow Navier-Stokes equations Turbomachinery Numerical analysis Intakes Jet engine nozzles</p>	<p>AGARD Conference Proceedings 510 Advisory Group for Aerospace Research and Development, NATO CFD TECHNIQUES FOR PROPULSION APPLICATIONS Published February 1992 596 pages</p> <p>The Conference Proceedings contains the 40 papers and the Technical Evaluation presented at the Propulsion and Energetics Panel 77th Symposium on "CFD Techniques for Propulsion Applications", which was held 27th-31st May 1991 in San Antonio, Texas, United States.</p> <p>The Symposium was composed of the following sessions: Turbomachinery Computations and Validations (21); Flow in Ducts, Intakes and Nozzles (11); Reacting Flows (8). Questions and answers of the discussions follow most papers in the Proceedings.</p> <p>P.T.O.</p>	<p>AGARD-CP-510</p> <p>Computational fluid dynamics Jet propulsion Three dimensional flow Viscous flow Unsteady flow Computer programs Proving Hypersonic flow Navier-Stokes equations Turbomachinery Numerical analysis Intakes Jet engine nozzles</p>
<p>AGARD Conference Proceedings 510 Advisory Group for Aerospace Research and Development, NATO CFD TECHNIQUES FOR PROPULSION APPLICATIONS Published February 1992 596 pages</p> <p>The Conference Proceedings contains the 40 papers and the Technical Evaluation presented at the Propulsion and Energetics Panel 77th Symposium on "CFD Techniques for Propulsion Applications", which was held 27th-31st May 1991 in San Antonio, Texas, United States.</p> <p>The Symposium was composed of the following sessions: Turbomachinery Computations and Validations (21); Flow in Ducts, Intakes and Nozzles (11); Reacting Flows (8). Questions and answers of the discussions follow most papers in the Proceedings.</p> <p>P.T.O.</p>	<p>AGARD-CP-510</p> <p>Computational fluid dynamics Jet propulsion Three dimensional flow Viscous flow Unsteady flow Computer programs Proving Hypersonic flow Navier-Stokes equations Turbomachinery Numerical analysis Intakes Jet engine nozzles</p>	<p>AGARD Conference Proceedings 510 Advisory Group for Aerospace Research and Development, NATO CFD TECHNIQUES FOR PROPULSION APPLICATIONS Published February 1992 596 pages</p> <p>The Conference Proceedings contains the 40 papers and the Technical Evaluation presented at the Propulsion and Energetics Panel 77th Symposium on "CFD Techniques for Propulsion Applications", which was held 27th-31st May 1991 in San Antonio, Texas, United States.</p> <p>The Symposium was composed of the following sessions: Turbomachinery Computations and Validations (21); Flow in Ducts, Intakes and Nozzles (11); Reacting Flows (8). Questions and answers of the discussions follow most papers in the Proceedings.</p> <p>P.T.O.</p>	<p>AGARD-CP-510</p> <p>Computational fluid dynamics Jet propulsion Three dimensional flow Viscous flow Unsteady flow Computer programs Proving Hypersonic flow Navier-Stokes equations Turbomachinery Numerical analysis Intakes Jet engine nozzles</p>

<p>The papers presented covered full three-dimensional code validation and numerical techniques, multi-dimensional reacting flow and unsteady viscous flow for the entire spectrum of propulsion system components. The capabilities of the various numerical techniques were assessed, and significant new developments were identified. The Technical Evaluation spells out in detail where progress has been made and that the present state of the art has almost reached the level necessary to tackle the comprehensive topic of CFD Validation for Propulsion.</p> <p>ISBN 92-835-0659-6</p>	<p>The papers presented covered full three-dimensional code validation and numerical techniques, multi-dimensional reacting flow and unsteady viscous flow for the entire spectrum of propulsion system components. The capabilities of the various numerical techniques were assessed, and significant new developments were identified. The Technical Evaluation spells out in detail where progress has been made and that the present state of the art has almost reached the level necessary to tackle the comprehensive topic of CFD Validation for Propulsion.</p> <p>ISBN 92-835-0659-6</p>
<p>The papers presented covered full three-dimensional code validation and numerical techniques, multi-dimensional reacting flow and unsteady viscous flow for the entire spectrum of propulsion system components. The capabilities of the various numerical techniques were assessed, and significant new developments were identified. The Technical Evaluation spells out in detail where progress has been made and that the present state of the art has almost reached the level necessary to tackle the comprehensive topic of CFD Validation for Propulsion.</p> <p>ISBN 92-835-0659-6</p>	<p>The papers presented covered full three-dimensional code validation and numerical techniques, multi-dimensional reacting flow and unsteady viscous flow for the entire spectrum of propulsion system components. The capabilities of the various numerical techniques were assessed, and significant new developments were identified. The Technical Evaluation spells out in detail where progress has been made and that the present state of the art has almost reached the level necessary to tackle the comprehensive topic of CFD Validation for Propulsion.</p> <p>ISBN 92-835-0659-6</p>

AGARD

NATO  OTAN

7 RUE ANCELLE · 92200 NEUILLY-SUR-SEINE

FRANCE

Téléphone (1)47.38.57.00 · Telex 610 176
Telecopie (1)47.38.57.99

DIFFUSION DES PUBLICATIONS

AGARD NON CLASSIFIEES

L'AGARD ne détient pas de stocks de ses publications, dans un but de distribution générale à l'adresse ci-dessus. La diffusion initiale des publications de l'AGARD est effectuée auprès des pays membres de cette organisation par l'intermédiaire des Centres Nationaux de Distribution suivants. A l'exception des Etats-Unis, ces centres disposent parfois d'exemplaires additionnels; dans les cas contraire, on peut se procurer ces exemplaires sous forme de microfiches ou de microcopies auprès des Agences de Vente dont la liste suit.

CENTRES DE DIFFUSION NATIONAUX

ALLEMAGNE

Fachinformationszentrum,
Karlsruhe
D-7514 Eggenstein-Leopoldshafen 2

BELGIQUE

Coordonnateur AGARD-VSL
Etat-Major de la Force Aérienne
Quartier Reine Elisabeth
Rue d'Evere, 1140 Bruxelles

CANADA

Directeur du Service des Renseignements Scientifiques
Ministère de la Défense Nationale
Ottawa, Ontario K1A 0K2

DANEMARK

Danish Defence Research Board
Ved Idraetsparken 4
2100 Copenhagen Ø

ESPAGNE

INTA (AGARD Publications)
Pintor Rosales 34
28008 Madrid

ETATS-UNIS

National Aeronautics and Space Administration
Langley Research Center
M/S 180
Hampton, Virginia 23665

FRANCE

O.N.E.R.A. (Direction)
29, Avenue de la Division Leclerc
92320, Châtillon sous Bagneux

GRECE

Hellenic Air Force
Air War College
Scientific and Technical Library
Dekelia Air Force Base
Dekelia, Athens TGA 1010

ISLANDE

Director of Aviation
c/o Flugrad
Reykjavik

ITALIE

Aeronautica Militare
Ufficio del Delegato Nazionale all'AGARD
Aeroporto Pratica di Mare
00040 Pomezia (Roma)

LUXEMBOURG

Voir Belgique

NORVEGE

Norwegian Defence Research Establishment
Attn: Biblioteket
P.O. Box 25
N-2007 Kjeller

PAYS-BAS

Netherlands Delegation to AGARD
National Aerospace Laboratory NLR
Kluyverweg 1
2629 HS Delft

PORTUGAL

Portuguese National Coordinator to AGARD
Gabinete de Estudos e Programas
CLAFAs
Base de Alfragide
Alfragide
2700 Amadora

ROYAUME UNI

Defence Research Information Centre
Kentigern House
65 Brown Street
Glasgow G2 8EX

TURQUIE

Milli Savunma Başkanlığı (MSB)
ARGE Daire Başkanlığı (ARGE)
Ankara

LE CENTRE NATIONAL DE DISTRIBUTION DES ETATS-UNIS (NASA) NE DETIENT PAS DE STOCKS
DES PUBLICATIONS AGARD ET LES DEMANDES D'EXEMPLAIRES DOIVENT ETRE ADRESSEES DIRECTEMENT
AU SERVICE NATIONAL TECHNIQUE DE L'INFORMATION (NTIS) DONT L'ADRESSE SUIT.

AGENCES DE VENTE

National Technical Information Service
(NTIS)
5285 Port Royal Road
Springfield, Virginia 22161
Etats-Unis

ESA Information Retrieval Service
European Space Agency
10, rue Mario Nikis
75015 Paris
France

The British Library
Document Supply Division
Boston Spa, Wetherby
West Yorkshire LS23 7BQ
Royaume Uni

Les demandes de microfiches ou de photocopies de documents AGARD (y compris les demandes faites auprès du NTIS) doivent comporter la dénomination AGARD, ainsi que le numéro de série de l'AGARD (par exemple AGARD-AG-315). Des informations analogues, telles que le titre et la date de publication sont souhaitables. Veuillez noter qu'il y a lieu de spécifier AGARD-R-nnn et AGARD-AR-nnn lors de la commande de rapports AGARD et des rapports consultatifs AGARD respectivement. Des références bibliographiques complètes ainsi que des résumés des publications AGARD figurent dans les journaux suivants:

Scientific and Technical Aerospace Reports (STAR)
publié par la NASA Scientific and Technical
Information Division
NASA Headquarters (NTT)
Washington D.C. 20546
Etats-Unis

Government Reports Announcements and Index (GRA&I)
publié par le National Technical Information Service
Springfield
Virginia 22161
Etats-Unis

(accessible également en mode interactif dans la base de
données bibliographiques en ligne du NTIS, et sur CD-ROM)



Imprimé par Specialised Printing Services Limited
40 Chigwell Lane, Loughton, Essex IG10 3TZ